

平成 27 (2015) 年度 研究成果
著書・総説・発表論文等

著書・総説・発表論文等リスト

著書・総説・解説

1. 増川一、北島正治、櫻井英博、井上和仁
「ヘテロシスト形成型シアノバクテリアのニトロゲナーゼを利用した光生物学的水素生産」
バイオインダストリー, **2015**, Vol.33, 1, 36-42
2. R. S. Poudyal, I. Tiwari, A. R. Koirala, H. Masukawa, K. Inoue, T. Tomo, M. M. Najafpour, S. I. Allakhverdiev, T. N. Veziroglu
Hydrogen production using photobiological methods
In Compendium of Hydrogen Energy, Woodhead Publishing Series in Energy, **2015**, pp. 523-531, Elsevier
3. Three-Dimensionally Ordered Macroporous (3DOM) Perovskite Mixed Metal Oxide, M. Sadakane, W. Ueda, *Perovskites and Related Mixed Oxides: Concepts and Applications* (ed. P. Granger, V. I. Parvulescu, S. Kallaguine, W. Prellier) Wiley, **2015**, 113-142
4. Assembly of e-Keggin-Type Polyoxometalates to Form Crystalline Microporous Metal Oxides, Z-X. Zhang, M. Sadakane, W. Ueda, *Trends in Polyoxometalates Research* (ed. L. Ryhlmann, D. Schamig) NOVA, New york, **2015**, Ch. 15, 409-427
5. 大坂 武男, 岡島 武義, 松本 太, 北村 房男 (共訳)
「電気化学 基礎と応用」
東京化学同人, ISBN 9784807908479 (2015).
6. Tsuyoshi Ohira
Crustacean hyperglycemic hormone. In: Y. Takei et al (eds) Handbook of hormones. Elsevier, 2015, 403-404

発表論文

1. Shigeo Yamaguchi, Tadzunu Suzuki, Kazuhito Inoue and Yoshitaka Azumi
DC-driven thermoelectric Peltier device for precise DNA amplification
Japanese Journal of Applied Physics, **2015**, 54, 057001:1-4
2. Yusuke Tsukatani, Yuu Hirose, Jiro Harada, Naomi Misawa, Keita Mori, Kazuhito Inoue, Hitoshi Tamiaki
Complete Genome Sequence of the Bacteriochlorophyll *b*-Producing Photosynthetic Bacterium *Blastochloris viridis*
Genome Announcements, **2015**, 3, e01006-15:1-2
3. Jiro Nomata, Maki Maeda, Atsuko Isu, Kazuhito Inoue and Toru Hisabori
Involvement of thioredoxin on the scaffold activity of NifU in heterocyst cells of the diazotrophic cyanobacterium *Anabaena* sp. strain PCC 7120
J. Biochem., **2015**, 158, 253–261
4. Ultrathin inorganic molecular nanowire based on polyoxometalates, Z. Zhang, T. Murayama, M. Sadakane, H. Ariga, N. Yasuda, N. Sakaguchi, K. Asakura, W. Ueda, *Nature commun.*, **2015**, 6, 7731
5. Direct Imaging of Octahedral Distortion in a Complex Molybdenum Vanadium Mixed Oxide, T. Lunkenbein, F. Girgsdies, A. Wernbacher, J. Noack, G. Auffermann, A. Yashuhara, A. K-Hoffmann, W. Ueda, M. Eichelbaum, A. Trunschke, R. Schlogel, M. G. Willinger, *Angew. Chem. Int. Ed.*, **2015**, 54, 6828-6831
6. Redox treatment of orthorhombic $M_{0.29}V_{11}O_{112}$ and relationships between crystal structure, microporosity and catalytic performance for selective oxidation of ethane, S. Ishikawa, D. Kobayashi, T. Konya, S. Ohmura, T. Murayama, N. Yasuda, M. Sadakane, W. Ueda, *J. Phys. Chem., C*, **2015**, 119, 7195-7206
7. Supercritical Preparation of TiO_2 with Tailored Anatase/Rutile Composition for Application in Redox Catalysis and Photocatalysis, R. Marin, S. Ishikawa, H. Bahruji, G. Shaw, S. Kondrat, P. Miedziak, D. Morgan, S. Taylor, J. Bartley, J.

Edwards, M. Bowker, W. Ueda, G. Hutchings, *Appl. Catal., General A*, **2015**, *504*, 62-73.

8. Selective Synthesis of Primary Amines by Reductive Amination of Ketones with Ammonia over supported Pt catalysts, Y. Nakamura, Abeda, K. Kon, T. Murayama, W. Ueda, K. Shimizu, *ChemCatChem.*, **2015**, *7*, 921-924
9. Synthesis of Crystalline Mo-V-W-O Complex Oxides with Orthorhombic and Trigonal Structures and Their Application as Catalysts Catalysis, Structure and Reactivity, C.T. Qiu, C. Chen, S. Ishikawa, T. Murayama, W. Ueda, *Catal. Structure and Reactivity*, **2015**, *2*, 71-77
10. Selective Carbon Dioxide Adsorption of ϵ -Keggin-type Zincomolybdate-based Purely-Inorganic 3D Frameworks, Z.-X Zhang, M. Sadakane, S. Noro, T. Murayama, T. Kamachi, K. Yoshizawa, W. Ueda, *J. Mat. Chem. A*, **2015**, *3*, 746-755
11. Anti-obesity activities of the yoshinone A and the related marine γ -pyrone compounds.
Koyama T, Kawazoe Y, Iwasaki A, Ohno O, Suenaga K, Uemura D.
J Antibiot (Tokyo) (in press) 2016 Mar 2. doi: 10.1038/ja.2016.19.
12. Isolation of Monovalerianester A, an Inhibitor of Fat Accumulation, from *Valeriana fauriei*.
Yuki K, Ikeda M, Yoshida S, Ohno O, Suenaga K, Yamada K, Uemura D, Miyamoto K.
Nat Prod Commun. 2015 Aug;10(8):1333-4.
13. Stereodivergent Synthesis and Stereochemical Reassignment of the C79-C104 Fragment of Symbiodinolide.
Takamura H, Fujiwara T, Kawakubo Y, Kadota I, Uemura D.
Chemistry. 2016 Feb;22(6):1984-1996. doi: 10.1002/chem.201503881.
14. Stereoselective Synthesis of the Proposed C79-C104 Fragment of Symbiodinolide.
Takamura H, Fujiwara T, Kawakubo Y, Kadota I, Uemura D.

Chemistry. 2016 Feb;22(6):1979-1983. doi: 10.1002/chem.201503880.

15. Hisao Saneyoshi*, Kazuhiko Kondo, Naoki Sagawa, Akira Ono*
“Glutathione-triggered activation of the model of pro-oligonucleotide with benzyl protecting groups at the internucleotide linkage”
Bioorg. Med. Chem. Lett., **2016**, 26, 622-625.
16. Tatsuo Kurokawa,* Manabu Igawa, Akira Ono, and Itaru Okamoto*
“Selective Transport of Mercury(II) Ions across Supported Liquid Membrane with Thymine Derivative as Carrier”
Chem. Lett., **2015**, 44, 1732–1734. | doi:10.1246/cl.150769
17. Takenori Dairaku, Kyoko Furuita, Hajime Sato, Yoshinori Kondo, Chojiro Kojima, Akira Ono & Yoshiyuki Tanaka*
“Exploring a DNA Sequence for the Three-Dimensional Structure Determination of a Silver(I)-Mediated C-C Base Pair in a DNA Duplex By ¹H NMR Spectroscopy”
Nucleosides Nucleotides Nucleic Acids. **2015**, 34 (12), 877-900.
18. Hisao Saneyoshi,* Yuki Hiyoshi, Koichi Iketani, Kazuhiko Kondo, Akira Ono*
“Bioreductive deprotection of protected thymine bases in oligonucleotides for the activation of duplex formation”
Bioorg. Med. Chem. Lett., **2015**, 25, 5632-5635.
19. Yoshiyuki Tanaka,* Jiro Kondo, Vladimír Sychrovský, Jakub Šebera, Takenori Dairaku, Hisao Saneyoshi, Hidehito Urata, Hidetaka Torigoe and Akira Ono*
“Structures, physicochemical properties, and applications of T–Hg^{II}–T, C–Ag^I–C, and other metallo-base-pairs”
Chem. Comm., **2015**, 51(98), 17343-17360. (Feature Article)
20. Jiro Kondo*, Yoshinari Tada, Takenori Dairaku, Hisao Saneyoshi, Itaru Okamoto, Yoshiyuki Tanaka, Akira Ono
“High-resolution crystal structure of Ag^I-RNA hybrid duplex containing Watson-Crick-like C–Ag^I–C metallo-base pairs”
Angew. Chem. Int. Ed., **2015**, 54, Issue 45, 13323–13326.

21. Takenori Dairaku, Kyoko Furuita, Hajime Sato, Jakub Šebera, Daichi Yamanaka, Hiroyuki Otaki, Shoko Kikkawa, Yoshinori Kondo, Ritsuko Katahira, F. Matthias Bickelhaupt, Célia Fonseca Guerra, Akira Ono, Vladimír Sychrovský, Chojiro Kojima, and Yoshiyuki Tanaka
 “Direct detection of the mercury–nitrogen bond in the thymine–Hg^{II}–thymine base-pair with ¹⁹⁹Hg NMR spectroscopy”
Chem. Comm., **2015**, *51*, 8488-8491.
22. Hisao Saneyoshi,* Kanami Shimamura, Naoki Sagawa, Yuki Ando, Takahito Tomori, Itaru Okamoto, Akira Ono*
 “Development of a photolabile protecting group for phosphodiester in oligonucleotides”
Bioorg. Med. Chem. Lett., **2015**, *25*, 2129-2132.
23. Yusuke Kataoka, Natsumi Yano, Tatsuya Kawamoto, and Makoto Handa
 Isolation of a Tetranuclear Intermediate Complex in the Synthesis of Paddlewheel-Type Dirhodium Tetraacetate
Eur. J. Inorg. Chem. **2015**, 5650-5655.
24. Yuki Ide, Takahisa Ikeue, Yusuke Kataoka, Ryoko Inoue, Mikio Nakamura, Daisuke Yoshioka, Masahiro Mikuriya, Tatsuya Kawamoto, and Makoto Handa
 Preparation, structure, and dynamic and electrochemical behaviors of dinuclear rhodium(I) complexes with bridging formamidinato ligands
J. Organomet. Chem. **2016**, *803*, 92-103.
25. T. Yoshida, E. Nagashima, H. Arai, S. Matsunaga, and K. Nomiya
 Aggregation of Dinuclear Cations [$\{Au(PR_3)_2(\mu-OH)\}^+$] into Dimers Induced by Polyoxometalate (POM) Template Effects
Z. Anorg. Allgem. Chem., **641**, (10), 1688-1695 (2015).
26. Y. Inoue, S. Matsunaga, and K. Nomiya
 Al₁₆-hydroxide cluster-containing tetrameric polyoxometalate, [$\{\alpha-Al_3SiW_9O_{34}(m-OH)_6\}_4\{Al_4(\mu-OH)_6\}^{22-}$]
Chem. Lett., **44**, (12), 1649-1651 (2015).
27. Y. Matsuki, T. Hoshino, S. Takaku, S. Matsunaga, and K. Nomiya
 Synthesis and Molecular Structure of a Water-Soluble, Dimeric

Tri-Titanium(IV)-Substituted Wells-Dawson Polyoxometalate Containing Two Bridging (C₅Me₅)Rh²⁺ Groups
Inorg. Chem., **54**, (23), 11105-11113 (2015).

28. F. Odden, Y. Chiba, J. Nakazawa, T. Ohta, T. Ogura, and S. Hikichi
Characterization of Mononuclear Non-heme Iron(III)-Superoxo Complex with a Five-Azole Ligand Set
Angew. Chem. Int. Ed., **2015**, *54*, 7336-7339.
29. H. Hori, H. Saito, H. Sakai, T. Kitahara, T. Sakamoto
Efficient decomposition of a new fluorochemical surfactant: perfluoroalkane disulfonate to fluoride ions in subcritical and supercritical water
Chemosphere, **2015**, *129*, 27-32.
30. H. Hori, H. Tanaka, K. Watanabe, T. Tsuge, T. Sakamoto, A. Manseri, B. Ameduri
Hydrogen peroxide induced efficient mineralization of poly(vinylidene fluoride) and related copolymers in subcritical water
Industrial & Engineering Chemistry Research, **2015**, *54*, 8650-8658.
31. H. Hori, H. Yokota
Efficient oxygen-induced decomposition of triphenylsulfonium trifluoromethanesulfonate to fluoride ions in subcritical water
Journal of Fluorine Chemistry, **2015**, *178*, 1-5.
32. H. Hori, Y. Yoshimura, T. Otsu, K. Kume, Y. Mitsumori, S. Kutsuna, K. Koike
Efficient photochemical recovery of rhenium from aqueous solutions
Separation and Purification Technology, **2015**, *156*, 242-248.
33. 堀 久男
有機フッ素化合物の国際規制動向と分解無害化・再資源化反応の開発
オレオサイエンス, **2016**, *16*, 111-118.
34. Hideki Abe, Hideki Yoshikawa, Naoto Umezawa, Ya Xu, Govindachetty Saravanan, Gubbala V. Ramesh, Toyokazu Tanabe, Rajesh Kodiyath, Shigenori Ueda, Nobuaki Sekido, Yoko Yamabe-Mitarai, Masahiko Shimoda, Takahisa Ohno, Futoshi Matsumoto and Takayuki Komatsu

Correlation between the surface electronic structure and CO-oxidation activity of Pt alloys

Phys. Chem. Chem. Phys., **17**, 4879-4887 (2015).

35. Takao Gunji, Arockiam John Jeevagan, Masanari Hashimoto, Toshiaki Nozawa, Toyokazu Tanabe, Shingo Kaneko, Masahiro Miyauchi and Futoshi Matsumoto
Photocatalytic Decomposition of Various Organic Compounds Over WO₃-Supported Ordered Intermetallic PtPb co-Catalysts
Applied Catalysis B: Environmental, **181**, 475-480 (2016).
36. 金子信悟, 横溝美衣子, 望月康正, 嵐田敏彦, 笹元貴弘, 田邊豊和, 松本 太
マグネトロンスパッタ法により作製したリン酸リチウムオキシナイトライド 固体電解質薄膜のイオン伝導性に及ぼす導入ガス中窒素濃度の影響
表面技術, **66(11)**, 540-543 (2015).
37. Fuma Ando, Takao Gunji, Hikaru Fujima, Tsuyoshi Takeda, Toyokazu Tanabe, Shingo Kaneko, Futoshi Matsumoto
Preparation of PtPb/TiO₂/Cup-Stacked Carbon Nanotube Composite for Enhancement of Electrocatalytic Reaction of Oxygen Reduction Reaction
Chem Lett., **44(12)**, 1741-1743(2015).
38. Genki Kobayashi, Yuta Irii, Futoshi Matsumoto, Atsushi Ito, Yasuhiko Ohsawa, Shinji Yamamoto, Yitao Cui, Jin-Young Son, Yuichi Sato
Improving Cycling Performance of Li[Li_{0.2}Ni_{0.18}Co_{0.03}Mn_{0.58}]O₂ through Combination of Al₂O₃-based Surface Modification and Stepwise Pre-cycling
J. Power Sources, **303**, 250-256(2016).
39. K. Notake, T. Gunji, S. Kosemura, Y. Mochizuki, T. Tanabe, S. Kaneko, S. Ugawa, H. Lee, F. Matsumoto
The Application of a Water-Based Hybrid Polymer Binder to a High-Voltage and High-Capacity Li-rich Solid-Solution Cathode and Its Performance in Li-Ion Batteries
J. Appl. Electrochem., **46(3)**, 267-278 (2016).
40. Toshiaki Matsubara* and Tomoyoshi Ito
Quantum Mechanical and Molecular Dynamics Studies of the Reaction Mechanism of the Nucleophilic Substitution at the Si Atom
J. Phys. Chem. A, in press (2016), DOI: 10.1021/acs.jpca.6b02308.

プロシーディング

1. Arockiam John Jeevagan, Takao Gunji, Toyokazu Tanabe, Shingo Kaneko, Futoshi Matsumoto
Photocatalytic Activity of Pd-Au Alloy Nanoparticle Co-Catalyst/TiO₂ for Acetic Acid Decomposition
ECS Transactions, Electrochemical Society, Inc., **64(25)**,9-16 (2015).
2. Gunji, K. Sasaki, A. J. Jeevagan, T. Tanabe, S. Kaneko, F. Matsumoto
Enhanced Oxygen Reduction Reactions and Stable Long-term Activity on TiO₂-supported Dealloyed PtCu Nanoparticles in Acidic Aqueous Solutions
ECS Transactions, Electrochemical Society, Inc., **66(39)**,1-8 (2015).
3. Takuya Kuzuoka, Tomohiro Kouno, Tomohiro Koyama, Yuji Morita, Keitaro Yamazaki, Takao Gunji, Toyokazu Tanabe, Shingo Kaneko, Ben Nanzai, Futoshi Matsumoto,
Development of Moving Micro-Machines That Use Hydrogen Peroxide and Glucose as Fuels
ECS Transactions, Electrochemical Society, Inc., **69(39)**,17-26 (2015).
4. Takao Gunji, Masanari Hashimoto, Toyokazu Tanabe, Shingo Kaneko, Futoshi Matsumoto
Preparation of Ordered Intermetallic PtBi co-Catalyst Nanoparticles/WO₃ and its Photocatalytic Activity towards Decomposition of Acetic Acid
ECS Transactions, Electrochemical Society, Inc., **69(39)**,11-16 (2015).
5. Kazuma Uehara, Takao Gunji, Toyokazu Tanabe, Shingo Kaneko, Futoshi Matsumoto
The effect of Brightener on the Fabrication of Electroplated Bright Aluminum Films Using an AlCl₃-EMIC-Toluene Bath
ECS Transactions, Electrochemical Society, Inc., **69(29)**,7-13 (2015)..

報告書・紀要

1. 力石紀子、野宮健司、松永 諭、両角宗一郎、高山晃彦、高木由貴、井上ちさと、柳田貢助、吉川理絵
2014年度神奈川大学総合理学研究所共同研究助成論文「ヒスチジンを中心

とした塩基性アミノ酸を配位子とするポリマー性銀(I)錯体の合成、構造解析及び抗菌活性」

Science J. of Kanagawa University, **26**, 47-52 (2015).

ヘテロシスト形成型シアノバクテリアの ニトロゲナーゼを利用した光生物学的水素生産

Photobiological Hydrogen Production using the Nitrogenase of Heterocyst-Forming Cyanobacteria

増川 一^{*1} 北島正治^{*2} 櫻井英博^{*3} 井上和仁^{*4}

一部のシアノバクテリアは、窒素栄養欠乏条件下で、窒素固定に特化したヘテロシストと呼ばれる異型細胞を分化させる。窒素固定酵素であるニトロゲナーゼの反応では必然的副産物として水素が生産される。筆者らはヘテロシスト形成型シアノバクテリアを遺伝子工学的に改良して水素生産を高めることに成功した。

1. はじめに

地表に到達する太陽光エネルギーは、人類が消費する化石燃料エネルギーの6,000倍以上と膨大であり、量的に再生可能エネルギー源として有望であるが、その平均エネルギー密度は約 $1,500\text{kWh}\cdot\text{m}^{-2}\cdot\text{yr}^{-1}$ と低く、いかにして経済性を確保しつつこれを利用するかが課題となる。植物や藻類などの光合成生物を利用したバイオ燃料の研究は様々に行われているが、エネルギー変換効率、経済性、大規模化、食料生産との競合など克服すべき課題は多い。本稿では、ヘテロシスト形成型シアノバクテリアを利用した光生物学的水素生産に関する研究の現状について、筆者らが行っている研究を中心に紹介する。

2. ヘテロシスト形成型シアノバクテリア

シアノバクテリアは植物や藻類と同様に水を光

合成の電子供与体として用いる酸素発生型の光合成を行う原核生物（細菌）である。紅色光合成細菌や緑色細菌等のいわゆる光合成細菌は水を光合成の電子供与体を用いることができず、硫化水素や有機酸などを用いて光合成を行う。資源量を考えると、水を使って光合成を行うシアノバクテリアを利用したバイオ燃料の生産は非常に有利であると考えられる。シアノバクテリアは形態学的にも、生態学的にも非常に大きな多様性を持つ細菌群である。この中で一部の糸状性シアノバクテリア（*Anabaena* や *Nostoc* 属等）は、硝酸塩類などの窒素栄養源が欠乏した条件下では、通常酸素発生型光合成を行う栄養細胞の一部が、約10~20細胞の間隔で異型細胞（ヘテロシスト）へと分化し、窒素固定酵素ニトロゲナーゼの反応により大気中の N_2 を還元しアンモニアを生産する。

ヘテロシスト内部は、酸素発生源となる光化学系IIが不活性化され、加えて細胞壁を肥厚させて

^{*1}Hajime Masukawa 大阪市立大学 複合先端研究機構 特任准教授

^{*2}Masaharu Kitashima 神奈川大学 総合理化学研究所 客員研究員

^{*3}Hidehiro Sakurai 神奈川大学 光合成水素生産研究所 プロジェクト研究員；早稲田大学名誉教授

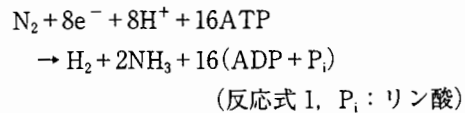
^{*4}Kazuhito Inoue 神奈川大学 理学部 生物科学科 教授；光合成水素生産研究所 所長

外部から細胞内への酸素透過を防ぎ、呼吸活性を増加させて酸素を除去しており、細胞内部の酸素濃度は低い状態に保たれている。ニトロゲナーゼは酸素により失活しやすいが、上述のように、ヘテロシスト内部は酸素濃度が低いため活性を維持することができる。糸状体全体としては通常の光合成を行う栄養細胞と窒素固定を行うヘテロシストで役割を分業させており、糸状体はあたかも多細胞生物のような細胞共同体として存在している。糸状体の細胞間には細胞間連絡が存在し、栄養細胞で酸素発生型光合成による糖質合成が行われ、その糖質がヘテロシストへ運ばれ、ニトロゲナーゼ反応を駆動する還元力の源となる。ニトロゲナーゼ反応にはATPも必要であるが、これはヘテロシストに存在する光化学系I周辺の循環的な電子伝達系による光リン酸化反応、および呼吸による酸化的リン酸化反応により供給される。窒素固定により合成されたアンモニアはグルタミンに変換されて栄養細胞へと輸送される。このように光合成と窒素固定が空間的に分離されることにより、糸状体全体として酸素発生型光合成とニトロゲナーゼ反応の両立が可能となる(図1)。

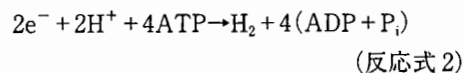
3. ニトロゲナーゼ

ニトロゲナーゼは、空気中の窒素ガス N_2 を固定する酵素として知られているが、必然的な副産物として H_2 も生産される(反応式1)。シアノバクテリアの他、マメ科植物の根に共生する根粒菌など一部の原核生物がその活性を持つ。酸素発生

型光合成生物のうちニトロゲナーゼを持つのは、一部のシアノバクテリアに限られ、クロレラなどの真核光合成生物は持たない。ニトロゲナーゼの触媒サブユニットは、一般にモリブデン(Mo)、鉄(Fe)、硫黄(S)からなる金属クラスター(FeMo-cofactor)を結合している(Mo型ニトロゲナーゼ)が、Moの代わりにバナジウム(V)(V型ニトロゲナーゼ)やFeのみ(Fe-only型ニトロゲナーゼ)を持つものもある。窒素固定の効率が最も高いとき(N_2 濃度が十分高いとき)、Mo型酵素の反応は、次式のように表され、電子の1/4が水素生産に向けられる。



窒素ガスが存在しない条件下(例:Ar気相)では、全ての電子が水素生産に向かう。



ニトロゲナーゼは、上記反応式に示されるように大量のATP(生体の高エネルギー物質)を消費するので理論的最高エネルギー変換効率は低いが、水素生産が不可逆的に起こることが、その利点である。

水素生産に利用できる酵素として、シアノバクテリアは、ヒドロゲナーゼも持つ。ヒドロゲナーゼは水素生産の理論的最高エネルギー変換効率が、高いが、反応は可逆的なため、光合成により生成する酸素の存在下では生産された水素の再吸収が

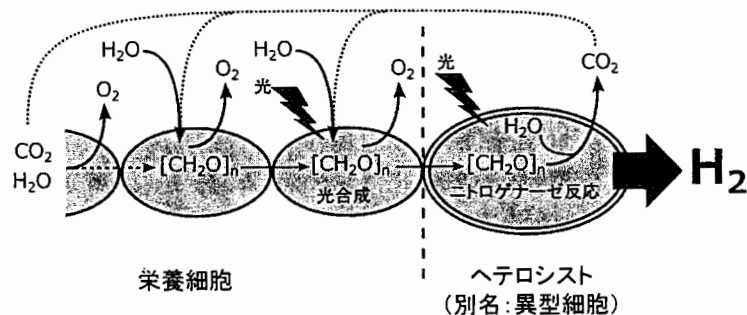


図1 糸状性シアノバクテリアにおけるヘテロシストと栄養細胞の分業
ニトロゲナーゼは、反応式1または2で示される窒素固定・水素発生反応を行う。

起こりやすい。また、ほとんどの窒素固定生物は、ニトロゲナーゼによって発生した H_2 を再吸収する取り込み型ヒドロゲナーゼ (Hup) を持ち、Hup 活性の存在は、水素生産を妨げる。

筆者らは、このような総合的判断から、ニトロゲナーゼを基礎とする水素生産方式を採用し、その研究開発に取り組んでいる¹⁻⁵⁾。

4. 遺伝子工学による改良

4.1 形質転換法

光合成の研究に良く用いられる *Synechocystis* sp. PCC 6803 は自然形質転換が可能で、単に DNA と細胞を混合するだけで DNA は細胞内に取り込まれて、相同組換えでゲノムに取り込ませることが可能である。一方、多くのシアノバクテリア (*Nostoc*, *Anabaena* など) は、独自の制限酵素系を持っているため、切断を防ぐために、その認識部位を大腸菌内でメチル化する必要がある。筆者らは、Wolk らの開発した triparental mating⁶⁾ を用いて、*Nostoc* や *Anabaena* の形質転換を行っている。この方法は、形質転換させたいシアノバクテリア株と、その株が持つ制限酵素の認識部位をメチル化するメチラーゼ遺伝子と導入したい遺伝子の両方を持つ大腸菌株、さらに接合性プラスミドを持つ大腸菌の合計 3 種の細菌細胞を混合する。遺伝子は、大腸菌からシアノバクテリアへ接合により導入され、得られた形質転換シアノバクテリア株を薬剤スクリーニングする。*Nostoc* や *Anabaena* では、ほとんどの場合、相同組換えは 1 点 (1 ヲ所) でしか起こらない (1 点交差変異株)。これは復帰突然変異が起こる可能性があり、安定な変異体を得るには 2 点交差株を選抜する必要がある。それには、薬剤耐性および *sacB* 遺伝子 (スクロース致死遺伝子) を持つプラスミドを利用して、1 点交差株を単離後、もう一度接合による形質転換、スクロース耐性によるスクリーニングを行うので、自然形質転換法に比べて時間と労力が必要となる。

4.2 取り込み型ヒドロゲナーゼ HupL の遺伝子破壊

Anabaena sp. PCC 7120 株は、窒素固定シアノバクテリアとして初めて全ゲノム塩基配列が明らかにされた株である⁷⁾。この株は、取り込み型 (Hup) および双方向型 (Hox) の 2 種類のヒドロゲナーゼの遺伝子を持つ^{2,8)}。また、*Nostoc* sp. PCC 7422 株は、筆者らが 13 種のシアノバクテリア株の中から光合成に基づくニトロゲナーゼ活性が最も高い野生株として選抜した株である⁹⁾。この株は Hox 活性がほとんどなく、Hup 活性のみが高い。筆者らは、この 2 株を主に用いて遺伝子工学的な改良を進めている。

Nostoc sp. PCC 7422 の Hup 活性を遺伝子工学的に不活性化した変異株 Δ Hup 株では、水素生産活性が野生株に比べて 3 倍程度増加し、光合成による酸素発生を行いながら水素を約 30% (v/v) まで蓄積できた⁹⁾。

4.3 ホモクエン酸合成酵素 NifV の破壊

Mo 型ニトロゲナーゼは N_2 還元触媒活性部位である FeMo-cofactor と呼ばれる金属クラスターを結合するモリブデン・鉄タンパク質 (ジニトロゲナーゼ) とこれに電子を供給する鉄タンパク質 (ジニトロゲナーゼレダクターゼ) から構成される¹⁰⁾。モリブデン・鉄タンパク質は *nifD* 遺伝子

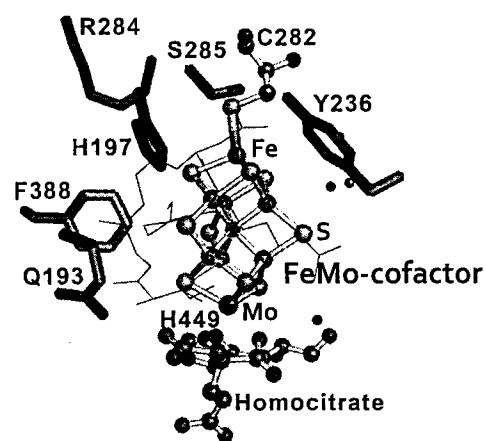


図 2 Mo 型ニトロゲナーゼの FeMo-cofactor 周辺の立体構造 (文献 14) より改変)

がコードする α サブユニット 2 個と *nifK* 遺伝子がコードする β サブユニット 2 個からなるヘテロ四量体から構成されるが、結晶構造解析によると FeMo-cofactor はシステイン残基とヒスチジン残基を介して α サブユニットに結合している (図 2)。FeMo-cofactor の Mo 原子に結合するホモクエン酸は、効率的な窒素固定反応を行うためには必須であり、従属栄養細菌 *Klebsiella pneumoniae* では、ホモクエン酸の合成酵素遺伝子 *nifV* を破壊すると、ホモクエン酸の代わりに炭素鎖が 1 つ短いクエン酸が FeMo-cofactor に結合するようになり¹¹⁾、 N_2 還元はほとんどできなくなるが、水素生産は野生株と同程度の活性を持つ¹²⁾。Masukawa ら¹³⁾ は *Anabaena* PCC 7120 の Δ Hup 株を親株としてヘテロシスト内で発現するホモクエン酸合成酵素の遺伝子 *nifVI* の破壊株を作製した。この株は親株である Δ Hup 株に比べて培養液当たり水素生産性が 2 倍程度増加した。

4.4 FeMoCo 周辺を取り巻くアミノ酸残基の部位特異的置換株

続いて、Masukawa ら¹⁴⁾ は、 N_2 ガス存在下のニトロゲナーゼ反応 (反応式 1) における電子の大部分 (約 3/4) が窒素固定に使われ、水素生産に使われる電子が僅か (約 1/4) であるため、この電子配分比率を遺伝子工学的手法により変更し、 N_2 存在下の窒素固定活性が低く、水素生産活性が上昇する変異株を作製した。ニトロゲナーゼは、その活性部位にモリブデン (Mo) と鉄 (Fe) からなる金属クラスターを持ち、その近傍には高度に保存されたアミノ酸残基が位置している。他の細菌のニトロゲナーゼ立体構造情報を基に、活性中心近傍アミノ酸残基の中から 6 つの残基を選び (図 2)、別の残基へ置換した変異株を合計 49 株作成した。ほとんどの変異株で窒素固定活性が大幅に低下したが、そのうちのいくつかの株は、 N_2 ガス存在下でも水素生産の低下が見られず、親株 Δ Hup 株と比較して、約 3~4 倍高い水素生産活性を示した。これらの中から最も優れた置換株を選び、長期間にわたる水素生産性について評価し

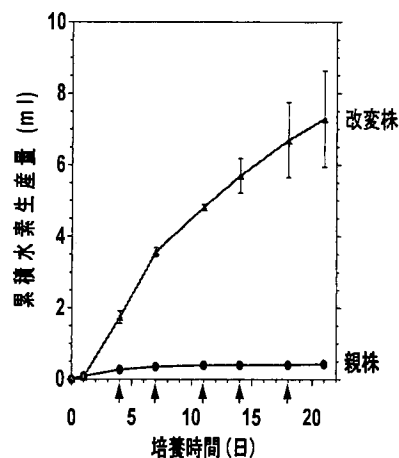


図 3 窒素気相中で培養したシアノバクテリア株の水素生産
初期気相は 95% N_2 /5% CO_2

た¹⁵⁾。親株は窒素固定活性が高いので窒素栄養充足になりニトロゲナーゼ活性が低下する結果、水素生産の活性も持続せず、低いレベルとなる (図 3)。一方、置換株では、窒素固定活性が大幅に低下しているため、 N_2 存在下でも窒素栄養飢餓状態が持続し、比較的高い水素生産活性が約 3 週間にわたり持続するようになった (図 3)。これまでは、気相中の N_2 ガスを Ar ガスで置換することで、窒素栄養飢餓状態にして高活性を持続させることができたが、このような改変株の利用により、コストのかかる Ar ガスは必要なくなり、水素生産のための培養ガスのコストを削減できる。

5. 水素バリアー性プラスチック素材を利用したバイオリクター

Amos¹⁶⁾ は藻類の光合成を利用した大規模エネルギー生産において、経済性を確保するためにはバイオリクターのコスト低減が重要な課題だと指摘し、受光面 $1 m^2$ 当たり数十 US ドル以下のバイオリクターが必要だと結論している。筆者らは水素バリアー性プラスチック膜を含む 3 層のプラスチックバックを用いることで、安価なバイオリクターの作成が可能であると提案している¹⁷⁾。水素バリアー性プラスチック膜を用いた実験用に

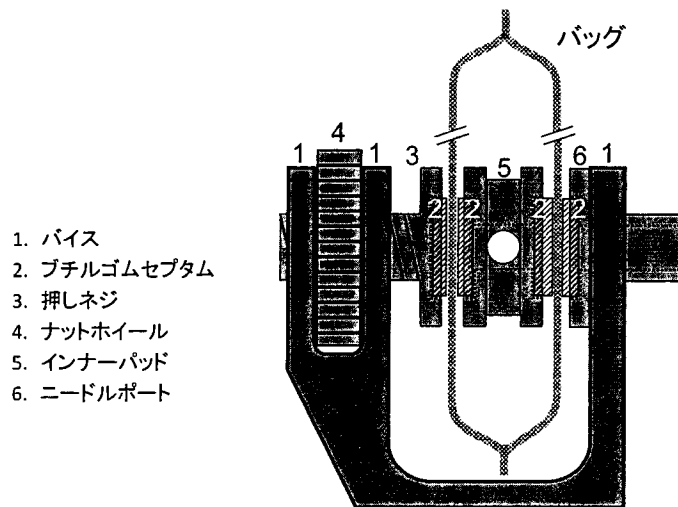


図4 ガスサンプリングデバイス (文献17) より改変)

ガスサンプリングポートの開発を行った (図4)。ガスサンプリングポートは、バッグ内にブチルゴムセプタムを付けたインナーパッドを入れ、プラスチックフィルムの外からブチルゴムセプタムを付けた押しネジもしくはニードルポートで挟み込み、ナットホイールで押しネジを繰り出すことで、プラスチックフィルムの内側と外側からブチルゴムセプタムで挟み込む構造のものを設計した。高温水蒸気滅菌可能な水素バリアー性透明プラスチックバッグとして、(株) Wakhy 研究所により製作されたもの (Wakhy バッグ) 2種類がGLサイエンスから発売されている。無延伸ポリプロピレン層がラミネートされたものは耐熱温度120℃でややヘイズがかかっており、直鎖状低密度ポリエチレン層がラミネートされたものは耐熱温度100℃で透明度が前者よりも高い。前者をオートクレーブ滅菌処理 (120℃, 20min), 前者および後者を間歇滅菌処理 (100℃, 20min, 3回) したもの、および未加熱処理のものについて、水素透過性を試験した (表1)。これらプラスチックバッグの水素透過性は $20\sim 90\text{cm}^3 \cdot \text{m}^{-2} \cdot \text{day}^{-1} \cdot \text{atm}^{-1}$ 程度であり、バイオリクターとして将来の実用化の素材の候補となりうると考えられる。

また、加熱処理のGI-Eを用いて、密閉容器内での水素生産量とプラスチックバッグ内での水素

表1 Besela フィルムおよびGLフィルムの水素透過性 (文献17) より改変)

処理方法	プラスチック 素材	Km : H ₂ 透過性 ($\text{cm}^3 \cdot \text{m}^{-2} \cdot \text{day}^{-1} \cdot \text{atm}^{-1}$)
未処理	Be-E	87
	Be-P	44
	GI-E	49
	GI-P	44
100℃×20min 3回間歇滅菌	Be-E	22
	Be-P	53
	GI-E	29
	GI-P	48
120℃×20min オートクレーブ 滅菌	Be-E	89
	Be-P	67
	GI-P	41

Be : Besela フィルム, GI : GL フィルム ; E : 直鎖状低密度ポリエチレン, P : 無延伸ポリプロピレン

生産量を比較した。窒素栄養充足培地 (BG11) から窒素欠乏培地 (BG11₀) へと移した *Nostoc* sp. PCC 7422 ΔHupL 株の細胞培養液を、同じ直径のガラス容器に等量ずつ分注し、一方の容器はブ



図5 水素バリアー性プラスチックバッグを用いたシアノバクテリアの培養

チルゴム栓で密封，もう一方の容器はガスサンプリングデバイスをつけたプラスチックバッグに入れた。プラスチックバッグ内の初期気相は等量の1%N₂/5%CO₂/94%Arにして，12時間ごとの明暗周期光照射を行いながら生産された水素の蓄積量を測定した。その結果，3日目まではどちらの水素蓄積量もほぼ同等であったが，光照射後9日目ではプラスチックバッグの水素蓄積量が密閉容器に比べて約30%程度多かった。水素バリアー性プラスチックバッグでのシアノバクテリアの培養および水素生産測定の典型例を図5に示す。

6. 今後の課題

シアノバクテリアを利用した水素生産の実用化のためには，経済的に大規模に行うための様々な課題を克服する必要がある。水素生産の低コスト化につながる改変として，上述で筆者らは，ニトロゲナーゼのアミノ酸残基置換により，コストのかかるArガスを使用せず，N₂気相下でも高い水素生産活性を数週間にわたり持続させることに

成功したが，今後，エネルギー変換効率や長期の生産安定性をさらに向上させる必要がある。そのための改変として，現在，筆者らが取り組んでいる研究例を最後に紹介する。

1) 水素生産に最適なシアノバクテリア株を作出するために，水素生産を行う細胞であるヘテロシストの形成頻度を通常5~10%から増加させることが考えられ，これまでにその頻度を10%以上に増加させた変異株を多数作製することに成功している。これらの変異株では，特定の条件下で水素生産性がさらに向上する可能性がある。2) N₂気相下での水素生産の変換効率は，優先的に発現するMo型ニトロゲナーゼよりも，V型やFe-only型ニトロゲナーゼの方が高いので，後者のタイプのニトロゲナーゼを発現させたシアノバクテリア株の作成が有効である可能性がある。3) 屋外での水素生産では強光阻害を受けやすい。強光により光合成活性が低下しないように，光化学系や色素系などの改変や，水素生産の大規模化のために，プラスチックバッグの大型化，多層化も今後必要である。これらの改良を積み重ねることで，水素生産が強光下で数週間持続するようにし，光から水素へのエネルギー変換効率を1%以上に高めることが今後の目標である。

また，光生物学的水素生産の大規模実用化においては，生物学的側面以外の課題も多々ある。例を挙げると，水素と酸素の両方を含む混合気体からの水素の分離（光半導体触媒を利用した水素生産にも同じ課題がある），遺伝子組換え生物の屋外における培養の社会的受容等である。これらの困難があるものの，酸素発生型光合成微生物を利用した水素生産は，地球温暖化を軽減するための有力な候補だと考える。

文 献

- 1) H. Masukawa *et al.*, *Ambio*, 41, 169 (2012)
- 2) H. Sakurai *et al.*, *J. Photochem. Photobiol. C*.

- Photochem. Rev.*, 17, 1 (2013)
- 3) H. Sakurai *et al.*, *Mar. Biotechnol.*, 9, 128 (2007)
- 4) 増川一ほか, 微細藻類によるエネルギー生産と事業展望, p.80, シーエムシー出版 (2012)
- 5) H. Sakurai *et al.*, *Life*, 5, 997 (2015)
- 6) T. Thiel *et al.*, *Methods Enzymol.*, 153, 232 (1987)
- 7) T. Kaneko *et al.*, *DNA Res.*, 8, 205 (2001)
- 8) P. Tamagnini *et al.*, *Microbiol. Mol. Biol. Rev.*, 66, 1 (2002)
- 9) F. Yoshino *et al.*, *Mar. Biotechnol.*, 9, 101 (2007)
- 10) L. C. Seefeldt *et al.*, *Annu. Rev. Biochem.*, 78, 701 (2009)
- 11) S. M. Mayer *et al.*, *J. Biol. Chem.*, 277, 35263 (2002)
- 12) P. A. McLean *et al.*, *Nature*, 292, 655 (1981)
- 13) H. Masukawa *et al.*, *Appl. Environ. Microbiol.*, 73, 7562 (2007)
- 14) H. Masukawa *et al.*, *Appl. Environ. Microbiol.*, 76, 6741 (2010)
- 15) H. Masukawa *et al.*, *Int. J. Hydrogen Energ.*, 39, 19444 (2014)
- 16) W. A. Amos, <http://www.nrel.gov/docs/fy04osti/35593.pdf> (2014年5月3日アクセス), Milestone Completion Report NREL, Golden, CO, 2004, Jan.
- 17) M. Kitashima *et al.*, *Biosci. Biotech. Bioch.*, 76, 831 (2012)



難培養微生物研究の最新技術Ⅲ—微生物の生き様に迫り課題解決へ—

監修：大熊盛也(理化学研究所)、野田悟子(山梨大学)

★2004年、2010年に続く大好評「難培養微生物研究」シリーズの第3弾!

★ゲノム解析技術が広まり、細胞ひとつひとつの役割解明や相互作用への理解が進む!

★環境・エネルギー問題や食糧問題を解決する鍵を微生物が握る!

【第1編 基盤技術・情報の進展】

- 第1章 微生物ゲノム研究の動向
- 第2章 微生物統合データベースによる微生物と環境の研究への貢献
- 第3章 メタゲノム情報からの難培養微生物ポピュレーションゲノムの抽出・再構築技術
- 第4章 シングルセルゲノム解析技術の現状と展望
- 第5章 難培養微生物の機能解析研究の進展
- 第6章 メタオミクス解析による微生物群集代謝ネットワーク解析
- 第7章 二次イオン質量分析法による同位体の高分解能イメージング解析—微生物学研究での利用—

【第2編 共生微生物の機能と応用】

- 第8章 腸内細菌が産生する短鎖脂肪酸と宿主免疫・生体防御
- 第9章 口腔内環境と微生物
- 第10章 農業害虫の生存を支えるオルガネラ様共生細菌
- 第11章 昆虫に新機能を賦与する微生物
- 第12章 昆虫と酵母の共生

- 第13章 糸状菌の細胞に内生する細菌
- 第14章 植物と病原微生物の相互作用と作物保護
- 第15章 C1微生物と植物の共生
- 第16章 深海生物の微生物共生
- 第17章 微生物間の電子移動に基づく共生

【第3編 微生物と環境の研究】

- 第18章 鉄酸化細菌研究の現状と展望
- 第19章 微生物腐食：微生物による金属腐食
- 第20章 微生物の細胞外電子伝達と汚染浄化
- 第21章 有機塩素化合物の還元脱ハロゲン呼吸細菌の研究と浄化利用の動向
- 第22章 環境中における可動性遺伝因子の動態解析
- 第23章 植物に生息する環境応答微生物の特定と分離
- 第24章 海洋細菌の新しい光エネルギー利用機構:ロドブシン
- 第25章 二酸化炭素地中貯留と地下微生物生態系への影響
- 第26章 地下圏微生物によるメタン生成と分散型エネルギー生産技術への応用
- 第27章 蛇紋岩水系地下生命圏に生息する微生物群の生態系

■体裁/B5判・261頁 ■発行/2015年8月 ■本体/66,000円+税

申込 FAX: 03(3293)2069 <http://www.cmcbooks.co.jp/>

シーエムシー出版

Hydrogen production using photobiological methods

10

R.S. Poudyal^{1,2,#}, I. Tiwari^{1,#}, A.R. Koirala³, H. Masukawa⁴, K. Inoue⁴, T. Tomo⁵, M.M. Najafpour⁶, S.I. Allakhverdiev^{7,8,9}, T.N. Veziroğlu¹⁰

¹Pusan National University, Busan, Republic of Korea; ²Tribhuvan University, Kirtipur, Kathmandu, Nepal; ³Sogang University, Shinsu-dong, Seoul, Republic of Korea;

⁴Research Institute for Photobiological Hydrogen Production, Kanagawa University,

Tsuchiya, Hiratsuka, Kanagawa, Japan; ⁵Tokyo University of Science, Kagurazaka,

Shinjuku-ku, Tokyo, Japan; ⁶Institute for Advanced Studies in Basic Sciences (IASBS),

Zanjan, Iran; ⁷Institute of Plant Physiology, Russian Academy of Sciences, Moscow, Russia;

⁸Institute of Basic Biological Problems, Russian Academy of Sciences, Moscow Region,

Russia; ⁹M.V. Lomonosov Moscow State University, Moscow, Russia;

¹⁰International Association for Hydrogen Energy, Miami, FL, USA

10.1 Introduction

Hydrogen is a versatile energy carrier that can release energy through a number of different processes such as direct combustion, catalytic combustion, steam production, and fuel cell operations. In terms of environmental impact, hydrogen may be the best alternative to fossil fuels because it drastically reduces the release of climate-changing gases and compounds harmful to human health (Zattel et al., 2008). Photobiological hydrogen production is an attractive option to generating hydrogen by photoautotrophic organisms from sunlight and water. This process is most effective and important for avoiding using fossil fuel (Ghirardi, Dubini, Yu, & Maness, 2009; Kruse, Rupprecht, Mussgnug, Dismukes, & Hankamer, 2005; Prince & Kheshgi, 2005). Photobiological hydrogen production consumes naturally occurring carbon dioxide gas to produce oxygen and biomass; hence, it is renewable and sustainable. Microorganisms such as green algae, cyanobacteria, purple non-sulfur bacteria, and dark fermentative bacteria are used to generate biohydrogen. In the light, solar energy is converted into adenosine triphosphate (ATP) and nicotinamide adenine dinucleotide phosphate (NADPH) as a source of energy and reductants, respectively. In the dark, organic compound is synthesized from CO₂ and H₂O. There are two different methods for photobiological hydrogen production: (1) direct photobiological hydrogen production, in which hydrogen gas is produced directly by the activity of hydrogenase without intermediate molecules such as carbohydrates; and (2) indirect photobiological hydrogen production, in which hydrogen

These authors contributed equally to this work.

gas is produced after the storage of carbohydrates or glycogen (Dasgupta et al., 2010; Eroglu & Melis, 2011). For photobiological H₂ production, microalgae require sunlight to donate e⁻ from electron-donating substances. This process can be categorized as oxygenic and non-oxygenic photobiological H₂ production, depending on oxygen generation during the process.

Oxygenic photobiological H₂ production is carried out during photoautotrophic growth of eukaryotic microalgae and cyanobacteria in water. The former organisms possess [FeFe] hydrogenases whereas the latter ones possess [NiFe] hydrogenases, with ferredoxin and NAD(P)H, respectively, as a direct electron donor (Ghirardi et al., 2009).

Although non-oxygenic photobiological H₂ production is carried out by purple non-sulfur bacteria (PNSB), these bacteria convert organic acids to produce H₂ by using sunlight as a source of energy, in a reaction catalyzed by nitrogenase. In a non-oxygenic or photofermentation process by PNSB, O₂ is not produced, so there is no debate about the repression of nitrogenase by oxygen.

Currently, several researchers are trying to achieve renewable hydrogen production with environmentally safe resources by using molecular biology, biotechnology, genetic engineering, and organometallic chemistry. Apart from this, artificial photosynthesis by biomimetic systems is a good candidate for generating hydrogen, and knowledge of the biochemical or biophysical study of hydrogenase and nitrogenase enzymes is exploited by organometallic chemists to synthesize biomimetic compounds for artificial photosynthesis.

Biohydrogen is a potentially useful gas to fulfill energy consumption with a high demand for hydrogen energy. Currently, around 80% of global energy is generated by fossil fuels (Kim, Jo, Jo, & Cha, 2012; Quintana, der Kooy, de Rhee, Voshol, & Verpoorte, 2011). However, the use of fossil fuels is comparatively costly and requires more energy consumption to generate hydrogen gas. Owing to the high demand for energy in the world, biohydrogen using microorganisms can be considered an alternative renewable source of energy, because it is estimated that energy consumption will increase at the rate of 44% by 2030 (Nel & Cooper, 2009; Rout et al., 2008).

10.2 Methods to generate photobiological hydrogen production

Previously, biological hydrogen production was categorized into five different groups; (1) direct biophotolysis of water, (2) indirect biophotolysis of water, (3) biophotofermentation, (4) hydrogen production by water gas reaction, and (5) dark fermentation (Das & Veziroğlu, 2001; Hallenbeck & Benemann, 2002; Nandi & Sengupta, 1998). The main available pathways to improved photosynthetic H₂ production have been summarized elsewhere (Allakhverdiev et al., 2009, 2010). Similarly, available methods to generate biohydrogen by using microorganisms have been summarized (Poudyal et al., in press). Although biohydrogen production is mediated by the

activity of two different enzymes, i.e., hydrogenase and nitrogenase, the activities of these enzymes depend on the availability of molecular oxygen (Bothe, Schmitz, Yates, & Newton, 2010; Ghirardi et al., 2007; Tsygankov, 2007). Hence, enhanced activation of these two enzymes will be more interesting in the future. As we know, the production of biohydrogen by microorganisms is inhibited by the presence of molecular oxygen generated by photosynthesis. Therefore, researchers are trying to overcome the inhibitory effect of molecular oxygen and enhance hydrogen production, which has been considered a major focus of photobiological hydrogen production. The enzymes are inactivated by molecular oxygen that diffuses into the catalytic center of the enzymes (Sundaram, Tripathi, & Gupta, 2010) to overcome this problem, some hypotheses have been applied in cyanobacteria.

Cyanobacteria (or blue-green algae) have characteristic features of both algae and bacteria. The algal character shows photosynthesis producing hydrogen; these cyanobacteria have [NiFe] hydrogenase but not an [FeFe] hydrogenase enzyme. NiFe enzyme is less sensitive to molecular oxygen, and hence it is favorable for hydrogen production. Based on this finding, an organism i.e., *Rubrivivax gelatinosus* CBS, has been identified that has the capacity for oxygen-tolerant hydrogenase during non-oxygenic photosynthesis (Ghirardi et al., 2005; Maness, Smolinski, Dillon, Heben, & Weaver, 2002). Some cyanobacteria may yield more hydrogen by a genetically engineered, optimized metabolic network (Quintana et al., 2011). Photobiological hydrogen production uses sunlight, which algae and cyanobacteria use to produce hydrogen as their metabolic processes. As these organisms grow in water, they can easily split water into hydrogen and oxygen. Some technology has been developed to increase the conversion efficiency of sunlight. According to the current status, the following photobiological methods are significantly applied to generate biohydrogen.

10.2.1 Direct and indirect biophotolysis

Direct biophotolysis means the production of H₂ gas under the illumination of light in biological organisms. In the chloroplast of algae and cyanobacteria, the thylakoid membranes consist of chlorophyll pigments in both photosystems, i.e., photosystem I (PSI) and photosystem II (PSII). The light energy absorbed by these pigments raises the energy level of electrons from water oxidation to PSII to PSI to ferredoxin, where a portion of the light energy is directly stored in hydrogen gas. Direct photobiological H₂ production from water using solar energy is a good example of massive (large-scale) production of hydrogen gas by photosynthesis, in which solar energy is used to split water into H₂ gas. Microorganisms include single-cell cyanobacteria (*Synechocystis*), multicellular cyanobacteria (*Nostoc* sp.), and green algae (*Chlamydomonas* sp.). Overall, the reaction of direct biophotolysis can be described as (Shaishav, Singh, & Tripathi, 2013):



However, indirect biophotolysis refers to the production of H₂ from intracellular energy reserves including carbohydrates such as starch and glycogen in microalgae and cyanobacteria (Antal & Lindblad, 2005; Dauvillée et al., 2006; Miura et al., 1995). Hence, this process is composed of two stages: carbohydrates synthesis in the light and dark fermentation of carbohydrates for H₂ production (Lee, Klaus, Maness, & Spear, 2007; Melis & Melnicki, 2006; Miura et al., 1995; Skjånes, Rebours, & Lindblad, 2013). Hence, indirect biophotolysis can be described as the following reactions:



In overall, (Shaishav et al., 2013):



10.2.2 Photobiological H₂ production by hydrogenase and nitrogenase

Photobiological H₂ production in algae and cyanobacteria is mediated by the activity of two enzymes: hydrogenase and nitrogenase (Bothe et al., 2010; Ghirardi et al., 2007; Tsygankov, 2007), both of which are sensitive to oxygen (Poudyal et al., in press). Generation of hydrogen by algae and cyanobacteria employs the activity of two distinct hydrogenases, i.e., [FeFe], also known as algal hydrogenase, and [NiFe], also known as cyanobacterial bidirectional hydrogenase enzyme, which that can consume and produce hydrogen (i.e., $2\text{H}^+ + 2\text{e}^- \leftrightarrow \text{H}_2$).

The exact mechanism of algal [FeFe] hydrogenase for H₂ production is not clear. It is theorized that electrons from ferredoxin are delivered to the metallocluster, making reduced iron atoms (Fe₂). This reduced iron atom is stabilized by the presence of CO and CN ligands and the proton pathway from the protein surface to the catalytic site is deconvoluted, which acts as the final binding site for one proton. Simultaneously, the second proton binds to Fe₂, where is doubly reduced to a hydride anion. Finally, the reaction involved in the process producing hydride anion recombines with the bound proton to release H₂ gas (Ghirardi et al., 2009).

In cyanobacteria, [NiFe] bidirectional hydrogenase has four different metal centers in which an NiFe active site for the catalytic domain and three Fe-S clusters for electron transfer have been identified. The NiFe active site is composed of bimetallic nickel and iron atoms; the nickel atom has four conserved cysteine residues, two of which bridge to the iron ion (Shima et al., 2008). However, it has been reported that [NiFe] hydrogenase is reversibly inactivated by molecular oxygen (Ogata et al., 2009). The [NiFe] enzyme catalyzes both the uptake and evolution of H₂. When the bridge ligand of [NiFe] is removed, the enzyme is activated and molecular hydrogen is produced. [NiFe] hydrogenases are bidirectional because they couple the reversible

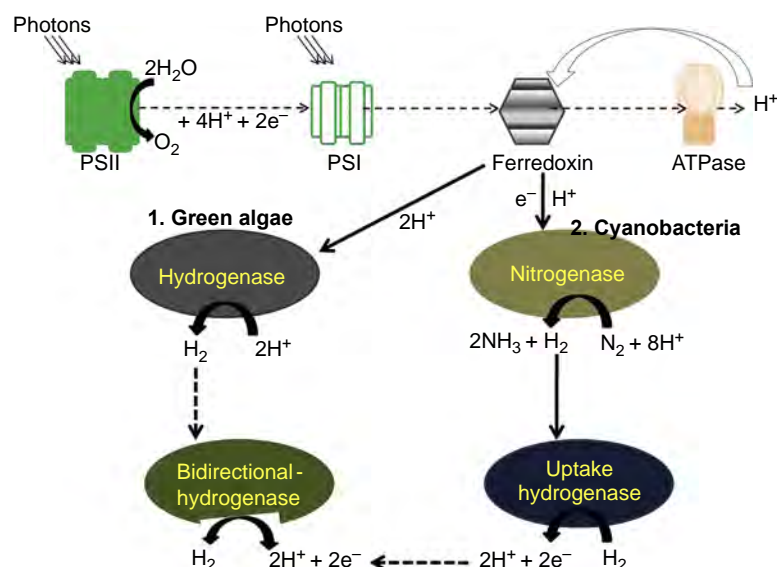


Figure 10.1 Summary of mechanism of photobiological H_2 production by algae. Light-dependent electron transport pathway for hydrogen production is shown in green algae and cyanobacteria with the involvement of their respective catalytic enzymes.

The figure is modified from Mathews and Wang (2009).

cleavage of hydrogen to the redox conversion of NAD(P)H (Horch, Lauterbach, Lenz, Hildebrandt, & Zebger, 2012). In green algae, only hydrogenase is present whereas in cyanobacteria two enzymes (hydrogenase and nitrogenase) work separately to catalyze H_2 production. A detailed scheme for two types of hydrogenases, uptake enzyme and bidirectional one, and nitrogenase in the respective microalgae, is given in Figure 10.1.

Similarly, nitrogenase enzyme is present in both unicellular and heterocystous nitrogen-fixing cyanobacteria and has a potential application for producing hydrogen. However, because of the higher energetic reaction, hydrogen production by nitrogenase is not efficient during nitrogen fixation, because most of the energy consumed by nitrogenase is used to produce ammonia (Tamagnini et al., 2002). The overall reaction under conditions optimal for nitrogen fixation can be written as:



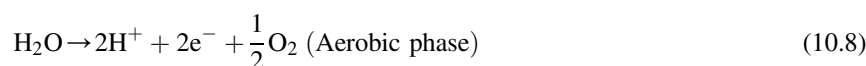
However, in the absence of N_2 , all electrons and ATP are used for H_2 production:



10.2.3 Mechanism of photobiological H_2 production

Two phases of photobiological hydrogen production in microalgae have been reported previously: aerobic and anaerobic (Melis, Zhang, Forestier, Ghirardi, & Seibert, 2000).

These two phases have different reactions to the contribution of hydrogen. The overall reactions are described as (Nguyen et al., 2008):



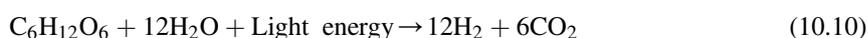
During the aerobic phase in microalgae, the H_2O is split into protons (H^+), electrons (e^-), and oxygen (O_2). Hence, the H^+ and e^- generated by water in PSII are stored as different metabolic products, such as proteins and carbohydrates, and these H^+ and e^- are essential precursors for H_2 production (Melis et al., 2000). During the anaerobic phase, H_2 is produced by hydrogenase. Mostly [FeFe] hydrogenase is rapidly activated under anaerobic conditions that catalyze the reduction of H^+ to H_2 using ferredoxin as an e^- donor. There, PSII contributes direct and indirect pathways for the source of e^- . In a direct pathway, e^- driven from the water-splitting activity of PSII (Najafpour & Allakhverdiev, 2012) is delivered into the electron transport chain (ETC) during state transition (Lemeille, Turkina, Vener, & Rochaix, 2010) and finally reaches [FeFe] hydrogenase, which reduces H^+ to H_2 . However, in an indirect pathway, proteins, carbohydrates, or starches that are stored during the aerobic phase are subsequently fermented and enter into an ETC (Posewitz, Dubini, Meuser, Seibert, & Ghirardi, 2009).

The basic mechanism and biochemical pathway for photobiological H_2 production are shown in (Figure 10.1). The thylakoid membrane of algae and cyanobacteria contains a photosystem with a light-harvesting protein complex, reaction center, and chlorophyll. It has the ability to capture light energy, which facilitates water oxidation to release protons (H^+) and electrons (e^-). These electrons are transported via the ETC, and iron-sulfur protein ferredoxin (PetF) or NAD(P)H via FNR (ferredoxin/NAD(P)H oxidoreductase) acts as an e^- donor to [FeFe] or [NiFe] hydrogenase, respectively. In algae, ferredoxin directly linked to synthesize H_2 via the ETC and in cyanobacteria NAD(P)H donates e^- to [NiFe] bidirectional hydrogenase to synthesize H_2 (Kufryk et al., 2013). Adenosine triphosphate and NADPH generated by light reaction are used to fix CO_2 during a dark reaction. Based on current progress, three pathways have been employed for biohydrogen production in cyanobacteria: (1) The first is light-driven ETC from water via PSII to PSI, ferredoxin (Fd) to ferredoxin: NADP⁺ oxidoreduction (FNR). Finally, H_2 is produced by [NiFe] bidirectional hydrogenase from the electrons supplied by reduced NADP. (2) Hydrogen is produced by the degradation of lipids, starches, and carbohydrates. In this pathway, NAD(P)H is oxidized and electrons are transported through plastoquinone (PQ) for H_2 production. (3) The last is cyanobacterial nitrogen fixation by nitrogenase, in which H_2 is produced as a byproduct under anaerobic conditions or in heterocysts that provide a microaerobic environment.

10.2.4 Hydrogen production by photofermentation

Hydrogen gas can also be produced by photofermentation. Some organic compounds such as acetic acids, lactic acids, and butyric acids are converted into H_2 and CO_2 by

photosynthetic bacteria in the presence of sunlight. However, this process also requires anaerobic conditions. During photofermentation, both hydrogenase and nitrogenase enzymes are involved in H_2 production depending on the physiological conditions of microorganisms. Five factors limit nitrogenase-mediated photofermentation in PNSB: (1) the occurrence of an H_2 uptake enzyme; (2) low photofermentation efficiency for H_2 production; (3) the low turnover rate of nitrogenase; (4) a low rate of carbon conversion; and (5) the availability of organic acids (Akkerman, Janssen, Rocha, & Wijffels, 2002). The overall reaction in photofermentation by PNSB for the reduction of organic compounds can be summarized as:



The overall pathway is (Das, Khanna, & Veziroğlu, 2008):



These PNSB has some advantages owing to the lack of PSII, which creates difficulties for H_2 generation because of the presence of O_2 (Das et al., 2008). Purple non-sulfur bacteria have the action of nitrogenase and hydrogenase enzymes. Nitrogenase produces H_2 under nitrogen-deficient conditions in PNS bacteria (Figure 10.2). Thus, the question arises regarding the role of hydrogenase in PNS bacteria. Hence, hydrogenase produces H_2 under anaerobic conditions and hydrogenase oxidizes H_2 to recycle e^- , H^+ , and ATP for energy metabolism (Koku, Eroğlu, Günfüz, Yücel, & Türker, 2002; Mathews & Wang, 2009; Oh, Raj, Jung, & Park, 2011). Some hydrogenases consume H_2 if a suitable e^- acceptor is present, or produce H_2 if anaerobic conditions are favorable (Vignais, Magnin, & Willison, 2006).

Several factors such as light intensity, duration of light, temperature, and age of inoculum are important for photofermentative H_2 production by photosynthetic bacteria. For example, 31 °C and 36 °C are the optimum temperatures for *Rhodobacter* sp. (Hey et al., 2013). These bacteria are able to convert organic acids into H_2 and CO_2

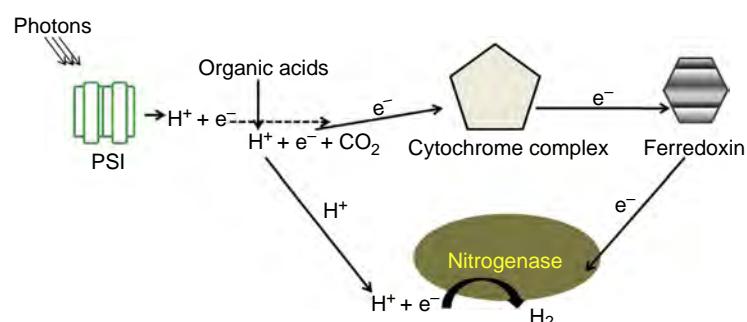


Figure 10.2 Mechanism of photofermentative H_2 production by PNSB by nitrogenase. Hydrogen gas is generated by the activity of nitrogenase after the breakdown of organic acids. The figure is modified from Androga, Özgür, Eroglu, Gündüz, and Yücel (2012).

under anaerobic conditions by using nitrogenase enzyme (Koku et al., 2002). It has been reported that supplementing micronutrients such as iron (Fe) and molybdenum (Mo) in a growth medium of some *Rhodobacter* increased photofermentative H₂ production (Kars, Gündüz, Yücel, Türker, & Eroğlu, 2006; Özgür et al., 2010; Uyar, Schumacher, Gebicki, & Modigell, 2009). Apart from this, the role of other nutrients such as iron (Fe), nickel (Ni), and magnesium (Mg) has been observed in *Rhodospseudomonas* sp (Liu, Ren, Ding, Xie, & Guo, 2009). Some strategies for the combination of dark and photofermentation have been applied to enhance H₂ production, because dark fermentation can produce lower amounts (2–4 mol H₂) from 1 mol of hexose. In addition, this process produced acetate and butyrate, which are environmental pollutants (Su, Cheng, Zhou, Song, & Cen, 2009a). To solve this problem, a combination of dark and photofermentation processes has been applied to *Rhodospseudomonas palustris* and greatly improved the production of H₂ from 240 to 402 ml H₂ per gram of starch (Su, Cheng, Zhou, Song, & Cen, 2009b). It was also revealed that H₂ production by mixed bacteria through dark and photofermentation increased the productivity of H₂. Dark fermentation by mixed anaerobic bacteria (*Clostridium* species) produced 351 ml H₂ per gram of starch, and during photofermentation by mixed photosynthetic bacteria (*Rhodospseudomonas palustris* species) produced 489 ml H₂ per gram of starch. These data clearly demonstrate that mixed bacteria can be used to improve dark and photofermentation (Cheng, Su, Zhou, Song, & Cen, 2011).

10.2.5 Hydrogen production by metabolic and genetic engineering of green algae

Both metalloprotein hydrogenase and nitrogenase enzymes are capable of reducing H⁺ to H₂. However, O₂ molecules generated during photosynthesis inhibit the activity of these enzymes. To overcome this problem, some researchers studied the different biochemical mechanisms of algae and cyanobacteria. Genetic engineering of green algae is considered as pioneering research to enhance H₂ gas; genetic and other biochemical modifications as well as the generation of new strains of cyanobacteria to enhance H₂ production have been applied (Bonenthe et al., 2011; Ghysels & Franck, 2010; Nguyen et al., 2011; Papazi, Andronis, Loannidis, Chaniotakis, & Kotzabasis, 2012; Philipps, Happe, & Hemschemeier, 2012; Tiwari & Pandey, 2012; Winkler, Kuhlger, Hippler, & Happe, 2009).

Some genetically modified cyanobacterial strains such as *Synechococcus* PCC 6301 and PCC 7942 and *Synechocystis* PCC 6803 have been considered good model organisms to enhance H₂ production (Thiel, 1994). Similarly, genetic transformation has been conducted in filamentous algae such as *Nostoc* and *Anabaena* to enhance photo-biological H₂ production (Hansel & Lindblad, 1998). In addition, structural gene-encoding FeFe hydrogenase from *Clostridium pasteurianum* has been transformed into cyanobacterium strain, *Synechococcus elongatus* PCC 7942 for better H₂ production (Asada et al., 2000; Miyake, Schnackenberg, Nakamura, Asada, & Miyake, 2001). Genetic engineering was employed to obtain transformed strains to generate renewable biofuel in some cyanobacterial strains such as *Synechocystis* sp PCC6803 (Lindberg, Park, & Melis, 2010).

Genetic engineering has been conducted not only in cyanobacteria but also in some photosynthetic bacteria such as *Rhodobacter sphaeroides*. For example, the mutation of *pucBA* depleting B800–850 light-harvesting complex in *R. sphaeroides* RV increased H₂ production (Kondo et al., 2002, Kim, Kim, Kim, & Lee, 2006a), and mutation of *cyt cbb3* oxidase in *Rhodobacter* species enhanced hydrogen production because the deletion of *cyt cbb3* oxidase induced nitrogenase activity and inhibited uptake hydrogenase (Öztürk et al., 2006). Deletion of light-harvesting antenna complexes in *R. sphaeroides* and of uptake hydrogenase showed higher H₂ production (Eltsova, Vasilieva, & Tsygankov, 2010; Liang et al., 2009). Similarly, the composition of gene-encoding pathways involved in pyruvate catabolism and end-product synthesis pathways and genetic biomarkers were studied to identify potential methods for optimizing hydrogen production and metabolic engineering for biofuel production in bacteria (Carere et al., 2012; Cha, Chung, Elkins, Guss, & Westpheling, 2013).

10.2.6 Enhancement of photobiological H₂ production by repression of hydrogen uptake system in microorganisms

As mentioned elsewhere, hydrogenases are key enzymes for biohydrogen production and can be classified as H₂ uptake hydrogenase and H₂ production hydrogenase. Thus, an uptake hydrogenase mostly consumes molecular H₂ and gives protons (H⁺), resulting in the inhibition of H₂ production. It is known that both aerobic and anaerobic microorganisms possess uptake hydrogenase to use H₂ as a source of energy (Richau, Kudahettige, Pujic, Kudahettige, & Sellstedt, 2013). Uptake hydrogenase oxidizes H₂ produced during nitrogen fixation by the activity of nitrogenase (Tamagnini et al., 2007). When uptake hydrogenase is repressed, the activity of H₂ production is enhanced in several species of *Nostoc* and *Anabaena* (Happe, Schütz, & Böhme, 2000; Lindberg, Schütz, Happe, & Lindblad, 2002; Masukawa, Mochimaru, & Sakurai, 2002; Yoshino, Ikeda, Masukawa, & Sakurai, 2007).

Many photosynthetic microorganisms including cyanobacteria have nitrogenase [FeFe], and/or [NiFe] bidirectional hydrogenases (Ghirardi et al., 2007; Prince & Kheshgi, 2005; Rupprecht et al., 2006; Tamagnini et al., 2002, 2007; Vignais & Billoud, 2007). Nitrogenase reduces H⁺ to H₂ as a side reaction of nitrogen fixation and H₂ produced by nitrogenase is consumed by uptake hydrogenase to yield protons (H⁺). Although bidirectional hydrogenase catalyzes both uptake and evolution of H₂, it cannot replace the function of uptake hydrogenase (Masukawa et al., 2002). Therefore, mutation of uptake hydrogenase is a good example for protecting generated H₂ molecules by nitrogen-fixing microorganisms (Cournac, Guedeney, Peltier, & Vignais, 2004; Tamagnini et al., 2007, Vignais & Billoud, 2007).

This uptake hydrogenase is a heterodimeric enzyme containing two functional subunits, i.e., HupS (small subunit) and HupL (large subunit). HupS, encoded by *hupS*, contains three FeS clusters that have the role of transferring electrons from the active site of HupL to ETC, whereas HupL, encoded by *hupL*, contains a bimetallic active site composed of four conserved cysteine residues (Khetkorn, Lindbald, & Incharoen-sakdi, 2012). In this way, uptake hydrogenase inhibits biohydrogen production by

consuming molecular H₂ (Figure 10.1). To overcome this problem, research has been carried out to knock out uptake hydrogenase for better bihydrogen production. Liang et al. (2009) knocked out membrane-bound [NiFe] hydrogenase (MBH) in photosynthetic bacterium *Allochromatium vinosum* to improve the H₂ production rate. Similarly, H₂ evolution activities were increased by the mutation of *hupW*, which encodes putative hydrogenase-specific protease in *Nostoc* strain PCC 7120 of cyanobacterium (Lindberg, Devine, Stensjö, & Lindblad, 2011), inactivation of functional uptake hydrogenase (*hupS*) in nitrogen-fixing cyanobacterium *Anabaena siamensis* TISTR 8012 (Khetkorn et al., 2012), and substitution of amino acid, which alters the ligation of Fe-S clusters of [NiFe] uptake hydrogenase even in marine bacterium *Alteromonas macleodii* (Yonemoto, Matteri, Nguyen, Smith, & Weyman, 2013).

10.2.7 Strategies for cultivation and growth of cyanobacteria and green algae to enhance H₂ production

In algae and cyanobacteria, physiological, biochemical, and environmental conditions have an important role for biological H₂ production. In addition, growth conditions, light intensity, carbon source, nitrogen source, sulfur, salinity, oxygen, and temperature are also essential for improving bihydrogen production by microorganisms (Poudyal et al., in press). Cyanobacteria are good sources for photobiological H₂ production and may be considered the most important microorganisms for a renewable source of H₂ gas (Dutta, De, Chaudhuri, & Bhattacharya, 2005). Among many microorganisms, cyanobacteria can grow with less nutrition and can use sunlight as a source of energy. The autotrophic nature of cyanobacteria produces H₂ as the final product of photosynthesis. Therefore, it is urgent to conduct research on photobiological H₂ production using cyanobacteria, because some species of *Chlamydomonas* such as *Chlamydomonas reinhardtii* and *Chlamydomonas noctigama* produce more H₂ under sulfur-deprived photoheterotrophic conditions (Skjånes, Knutsen, Källqvist, & Lindblad, 2008). According to Kosourov, Tsygankov, Seibert, and Ghirardi (2002), sulfur-deprived algal cultures have five phases: aerobic, anaerobic, O₂ anaerobic consumption, H₂ production, and 5) end of H₂ production. Research has been conducted in these five phases in *C. reinhardtii*, including light intensity and the effect of pH on the culture medium (Kosourov, Seibert, & Ghirardi, 2003), optimization of culture medium (Jo, Lee, & Park, 2006), and the addition of a small amount of sulfate in sulfur-deprived culture medium (Kosourov et al., 2005). Sulfur-deprived *C. reinhardtii* was able to produce photobiological H₂ production under photoautotrophic, photoheterotrophic, and photomixotrophic growth conditions (Kosourov et al., 2005). The remodeling of photosystem II light-harvesting complex, *LHCBM9* in *C. reinhardtii* for photobiological H₂ production under sulfur starvation conditions was also identified (Nguyen et al., 2008). Different strategies have been applied for photobiological H₂ production by adding iron to the growth medium of *Anabaena* (Prabina & Kumar, 2010), depriving culture medium of nitrogen to enhance H₂ production (Philipps et al., 2012), and mechanistically modeling sulfur-deprived photobiological H₂ production by including dense *C. reinhardtii* in culture medium, as well as changing light intensity and delaying the growth of cyanobacteria (Williams & Bees, 2013).

In addition, the intensity of light is important for photobiological H₂ production in cyanobacteria; Kim, Kang, Park, Kim, and Sim (2006b) observed maximum H₂ production by *C. reinhardtii* at 200 $\mu\text{mol}/\text{m}^2$ s. Oxygen molecules are thought to inhibit H₂ evolution by hydrogenase. To examine this phenomenon, Markov, Eivazova, and Greenwood (2006) used high-intensity light to suppress oxygen evolution in *C. reinhardtii* to evaluate H₂ generation. When 2000 $\mu\text{mol}/\text{m}^2$ s light intensity was applied for 30 s, and then 15 $\mu\text{mol}/\text{m}^2$ s, H₂ production increased, demonstrating that the photoinhibition of photosynthetic O₂ evolution leads to anaerobiosis favorable for H₂ production (Markov et al., 2006).

Hence, light intensity is required for better H₂ evolution in cyanobacteria; however, the effect of light intensity depends on the species of different cyanobacteria (Dutta et al., 2005). For example, *Arthrospira platensis* produces H₂ by day and night under anaerobic conditions. However, *Spirulina platensis* and *Synechococcus elongatus* PCC 7942 produce H₂ only in the dark under anaerobic conditions (Asada & Miyake, 1999) some species (*Azospirillum brasilense* and *A. lipoferum*) produce H₂ only in the presence of light (Stal & Krumbein, 1985). Therefore, we need to focus on the role of photoperiod and light intensity for H₂ production in cyanobacteria. Generally, 30–40 °C is the optimal temperature for cyanobacterial H₂ production. However, it has been also demonstrated that species of cyanobacteria produce more H₂ at 22 °C and others at 30 °C or 40 °C (Datta, Nikki, & Shah, 2000; Ernst, Kerfin, Spiller, & Böger, 1979; Serebryakova, Shremetieva, & Lindbald, 2000). The nutrient present in culture medium is also important for generating H₂ from cyanobacteria. For example, 8 mM NH₄⁺, 1.11 mM PO₄³⁻, and 0.69 mM SO₄²⁻ in Tris-acetate phosphate medium was the optimal condition for H₂ evolution in *C. reinhardtii* (Jo et al., 2006).

10.2.8 Designing bioreactors to harvesting green algae

After the identification of suitable strains of algae and cyanobacteria, various bioreactors can be used for photobiological H₂ production by microorganisms in which light energy is converted into biochemical energy. Some factors such as area–volume ratio, temperature, agitation, and gas exchange also influence the performance of bioreactors (Dasgupta et al., 2010). Bioreactors can be used to harvest light energy more easily and minimize energy loss. A few decades ago, Sathiyamoorthy and Shanmugasundaran (1994) developed a polypropylene bag that was a simple and inexpensive culture vessel on which to grow cyanobacteria. Later, tubular, flat panel, and bubble column types of major bioreactors had been designed for photobiological H₂ production (Akkerman et al., 2002). Several types of photobioreactors have been designed; a typical dual photobioreactor that uses sunlight to generate electricity and produce H₂ is depicted in Figure 10.3.

Based on the growth conditions of microorganisms, bioreactors are classified as two types: one-phase and two-phase. In a one-phase bioreactor, H₂ is produced by PSII turnover and the activity of HydA enzyme (chloroplast hydrogenase enzyme) under microoxic condition. The microoxic condition does not inhibit hydrogenase for H₂ production. Similarly, the two-phase bioreactor consists of both aerobic and anaerobic conditions for H₂ production. In the two-phase type, cells are grown under aerobic

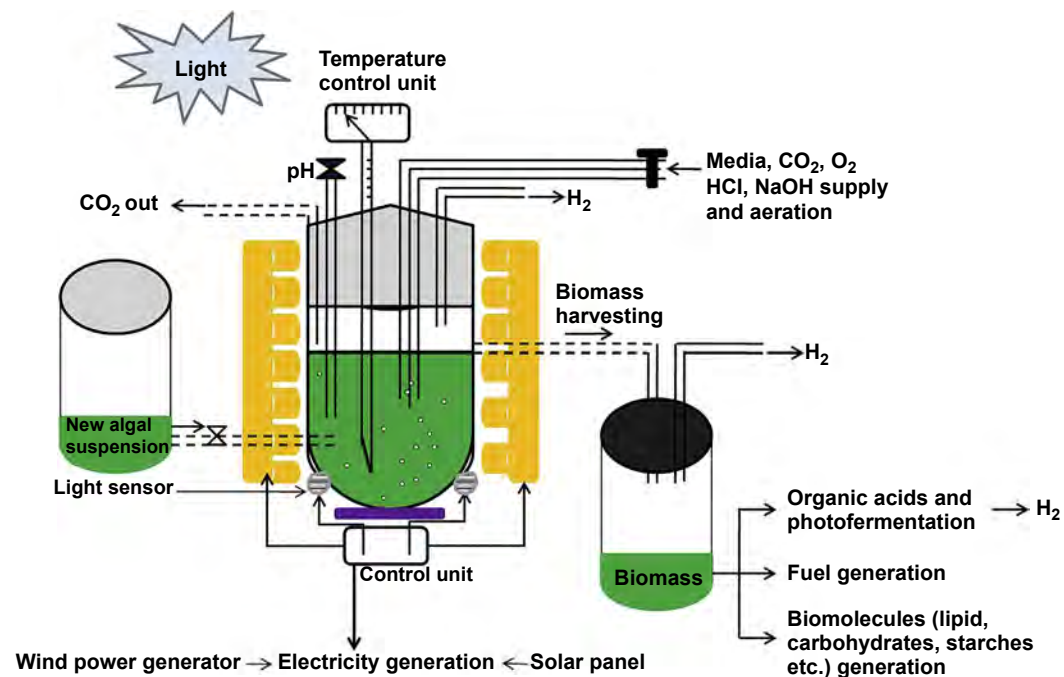


Figure 10.3 Schematic description of dual photobioreactor system for solar energy conversion by microorganisms. A photobioreactor with sunlight and light-emitting diode light sources with a solar panel and wind power generator is shown in the middle panel. Similarly, cultivation of microalgae for biomass and H₂ gas generation is shown.

The figure is modified from [Chen, Yeh, Aisyah, Lee, and Chang \(2011\)](#); [Show, Lee, and Chang \(2011\)](#); [Kwon, Rögner, and Rexroth \(2012\)](#); [Rosner and Wagner \(2012\)](#).

conditions to accumulate more biomass, and then cells are transferred into sulfur-deprived medium to induce H₂ production (Hankamer et al., 2007). The quality and quantity of light are also important for growing phototrophic microorganisms within the bioreactor. To achieve this goal, a tank bioreactor and high surface area–volume ratio bioreactor were developed. Owing to the shading effects of light, tank bioreactors have been considered less effective (Hankamer et al., 2007).

In addition, based on the effective production of biomass and H₂ by microorganisms, bioreactors are classified into two types: open system and closed system (Dasgupta et al., 2010). The open system bioreactor is a simple and traditional system in which algae and cyanobacteria can grow under natural conditions such as small ponds, lakes, or artificial containers for biomass production. However, the efficiency and collection of H₂ are inconvenient. Hence, closed-system bioreactors are considered safe reactors for improving the biomass and H₂ production efficiency of microorganisms in a modern way, because photobioreactors have been designed to multiply rapidly with a high density of microalgae biomass production (Evens, Chapman, Robbins, & D'Asaro, 2000). Some important points for designing bioreactors for photobiological H₂ production are summarized by (Dasgupta et al., 2010):

1. Temperature control and an agitation system in photobioreactors
2. Use of mixed microorganisms for better employment of solar energy
3. More research on genetic and metabolic engineering of microorganisms to improve better yield for overall performance of photobioreactors
4. Bioreactor performance with the same volume but different area–volume ratio for a given microorganism for H₂ production

In addition, the genetic study of microorganisms and the design of an effective photobioreactor for the long-term cultivation of microorganisms are essential because to date, photobioreactors have been developed only for laboratory purposes (Rosner & Wagner, 2012). Apart from this, two-stage culture strategies have been developed to induce the productivity of microalgae such as *Chlorophyta* and *Scenedesmaceae*. These processes consist of fast growth induction in stage 1 followed by lipid induction in stage 2. With this strategy, overall productivity was improved and a better quality of biodiesel was obtained (Xia, Ge, Zhou, Zhang, & Hu, 2013). Comparatively, two-stage culture strategies were more effective than biomass production by microalgae in open ponds (Lin & Lin, 2011) or vertical tank bioreactors (Chinnasamy, Bhatnagar, Claxton, & Das, 2010).

10.2.9 Feedstocks for photobiological H₂ production

Hydrogen is the most abundant element in the universe but it does not exist alone in nature. Therefore, H₂ can be produced from hydrogen-containing substances or feedstocks such as water (H₂O), natural gas by CH₄, biomass (cellulose, hemicellulose, or lignin), and hydrocarbons such as coal. Because of inadequate research on the mass production of H₂ by photobiological methods, H₂ has been produced from different varieties of feedstocks, from fossils to coal and natural gases. It has been predicted that H₂ will have a major role in the energy supply by 2100. Therefore, feedstock

for biohydrogen production has significant value for future generations (Saratale, Chen, Lo, Saratale, & Chang, 2008).

In the fermentative process, carbohydrates such as cellulose, hemicellulose, and starch are popular feedstocks that are freely available in plant biomass and agricultural waste (Nowak et al., 2005). Normally, organic acids are transferred from dark fermentation to photofermentation, and thus the feedstock must contain low nitrogen compound for nitrogenase-mediated H₂ production (Chen, Yang, Yeh, Liu, & Chang, 2008; Özgür et al., 2010).

Hydrogen production by lignocellulosic fermentation uses the feedstock of corn stover and microbial electrolysis cells (MEC) use fermentation waste as a feedstock; thus, integration of lignocellulosic fermentation and MEC consume the fermentative waste of fermentation as the MEC feedstock. Three main systems have been examined for a fermentative system (James, Baum, Perez, & Baum, 2009):

- H₂ production using dark fermentation of algal waste
- H₂ production using dark fermentation of lignocellulosic feedstock (corn stover)
- H₂ production from MEC using fermentation waste as a feedstock

Biogas is generated by anaerobic digestion of algal waste combined with several feedstocks (Weiss, Patyk, & Schebek, 2011). Research has been conducted into optimizing feedstock for photobiological H₂ production; to produce H₂, photosynthetic bacteria *Rhodospseudomonas* used sewage and wastewater (Sunita & Mitra, 1993), *Rhodospseudomonas* and *Cyanobacterium anacystis* used dairy and sugarcane wastewater (Thangaraj & Kulandaivelu, 1994), *Rhodobacter sphaeroides* used feedstock tofu wastewater (Zhu, Suzuki, Tsygankov, Asada, & Miyake, 1999), *R. sphaeroides* O.U. 001 used sugar refinery wastewater (Yetis et al., 2000), and *R. sphaeroides* O.U. 001 used brewery wastewater (Seifert, Waligorska, & Laniecki, 2010). Because several different feedstocks such as organic waste and algal biomass are used, both photofermentation and dark fermentation are considered to have potential advantages (Ferreira, Ribau, & Silva, 2011; Yang, Guo, Xu, Fan, & Luo, 2011). Similarly, the highest production of H₂ was produced using pretreated biomass of microalgae *Nannochloropsis* sp. as substrates for fermentation by immobilized *Clostridium acetobutylicum* cells among pretreated biomass of various microalgae such as *Arthrospira platensis*, *Nannochloropsis* sp., *Dunaliella tertiolecta*, *Galdieria partita*, *Chlorella vulgaris*, *Cosmarium* sp., and *Nostoc* sp. (Efremenko et al., 2012). Nobre et al. (2013) found the *Nannochloropsis* sp. to be a potential feedstock for dark and photofermentative H₂ production.

10.2.10 Hydrogen production by artificial photosynthetic systems

Artificial photosynthesis as a chemical process replicates natural photosynthesis to reduce anthropogenic carbon dioxide (CO₂), increase fuel security, and provide a sustainable global economy (Faunce et al., 2013). Because of the development of some suitable technologies, we can develop artificial photosynthesis using artificial leaves for the efficient conversion of solar energy into H₂ and other fuels (Centi & Perathoner,

2010, 2011). This method may be a potential technology for H₂ production by mimicking natural photosynthesis by green leaves. Therefore, research has been carried out to harvest solar energy to produce H₂ by artificial photosynthesis (Lewis & Nocera, 2006; Nocera, 2009). In artificial photosynthesis, the artificial leaf must be able to use sunlight and water to reduce CO₂ and water into H₂ (Centi & Perathoner, 2010, 2011; Roy, Varghese, Paulose, & Grimes, 2010). Hence, artificial photosynthesis has created great interest owing to the employment of photoelectrochemical cells (PEC) to use sunlight to produce solar fuel (Bensaid, Centi, Garrone, Perathoner, & Saracco, 2012; Listorti, Durrant, & Barber, 2009; Walter et al., 2010). In practice, solar-driven electrochemical fuel generation needs the integration of light-absorbing and electrochemical components able to separate product fuels (Modestino et al., 2013). Natural photosynthesis synthesizes glucose and oxygen in the presence of sunlight. In the presence of sunlight, the excitation of chlorophyll molecules in PSII and PSI generates ATP and NADPH along the ETC with the involvement of different protein complexes. Similarly, in artificial photosynthesis, the use of solar energy to produce NADPH as an electron donor by PSI must be achieved (Amao, Hamano, & Shimizu, 2012). Thus, we have to know all biochemical pathways before constructing an artificial photosynthetic system, because natural photosynthesis consists of the involvement of several pigments, proteins, and enzymes. The main barrier is producing artificial leaves for artificial photosynthesis to mimic the overall reactions of natural photosynthesis (Cogdel et al., 2010).

In artificial photosynthesis, model molecular systems, electron donor and acceptor assemblies, solar energy conversion by photo-induced charge separation, examination of photoelectrochemical cells to convert solar energy into fuels, light-harvesting component, charge separation, and catalysis in photosynthesis have been compared with natural photosynthesis. The three key components for solar energy conversion in artificial photosynthesis are light harvesting, charge separation, and catalysis (McConnell, Li, & Brudvig, 2010). According to Nocera (2012), a light-dependent reaction is required to mimic photosynthesis. Hence, artificial leaves were constructed by adding catalysts (Co-OEC and NiMoZn) to a light-harvesting silicon-based semiconductor to split water. Those silicon semiconductors in artificial leaves may be considered photosynthetic membranes in natural photosynthesis. The silicon junction harvests sunlight and converts it into a wireless current through Si. Then, Co-OEC is integrated with Si that functionalizes single-junction PEC. Several photochemical reactions that occur in this solar cell generate the photovoltage used for the water-splitting reaction to generate H₂ (Figure 10.4). In addition, electrocatalysts have been designed for a light-driven charge separation system for solar fuel production (Tran, Wong, Barber, & Loo, 2012). Based on the current situation, the concept of an artificial leaf has been developed as a source of clean fuel. An artificial leaf can be developed using a silicon-coated sheet that splits water into hydrogen and oxygen. Silicon has become an attractive material with which to design an artificial leaf because silicon is cheap and abundant and such cells can capture and store energy. Although the development of an artificial leaf is still a scientific challenge, some concepts have been developed to overcome technical difficulties. To overcome those difficulties, some researchers have focused on artificial leaves for artificial photosynthesis to

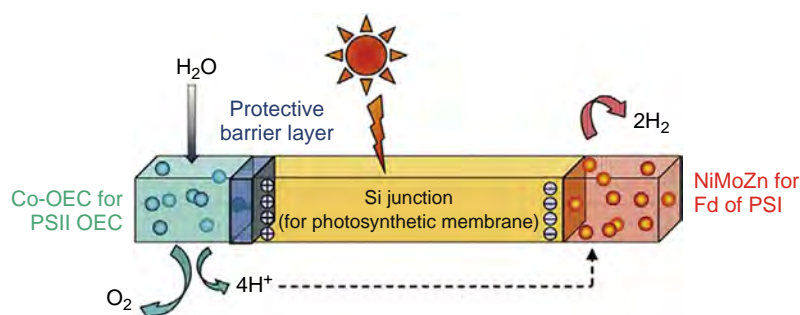


Figure 10.4 Construction of an artificial leaf. The photosynthetic membrane is replaced by an Si junction that performs light capture and conversion to a wireless current. The oxygen-evolving complex and ferredoxin reductase of the photosynthetic membrane are replaced by Co-OEC and NiMoZn OER and HER catalysts, respectively, to perform water splitting. Figure and legend adopted from Nocera (2012).

generate clean hydrogen. Hybrid strategies for solar water splitting based on dye-sensitized photoelectrosynthetic cells (Alibabaei et al., 2013), by proposing natural to artificial photosynthesis with artificial photocatalysts, hybrid photocatalysts for water oxidation/proton reduction and hydrogen evolution, as well as construction of complete photocatalytic system for hydrogen and oxygen evolution from water (Barber and Tang, 2013), used a photovoltaic reactor for artificial photosynthesis, based on water electrolysis to produce high-energy hydrogen atoms (Nong et al., 2014). An artificial photosynthetic system using TiO_2 was developed that has the features of photosynthesis to overcome the challenge of solar-driven water splitting and CO_2 reduction. In addition, the photoreduction of CO_2 into hydrocarbon fuels (CO and CH_4) has been demonstrated, which solves the architectural model of artificial photosynthesis to produce solar cells, fuel cells, or battery electrodes (Zhou et al., 2013).

The Joint Center for Artificial Photosynthesis developed an idea for artificial photosynthesis using a water-splitting photoconversion system that produces H_2 directly from water. As in plants, water oxidation takes place in PSII with the help of visible light and electrons are transferred to the PSI with the help of electron transport mediators in which carbon dioxide is reduced to carbohydrates during a dark reaction. Plants prepare food (carbohydrates) with the help of water and carbon dioxide in the presence of visible light (Figure 10.5(a)). Scientists are trying to mimic the wonderful work carried out by green leaves. In this regard, different concepts have been proposed to prepare artificial leaves. The Joint Center for Artificial Photosynthesis proposed a model to design artificial leaves, is illustrated in Figure 10.5(b).

According to this model, water oxidation and reduction half-reaction take place separately in two different systems, as in natural photosynthesis. Semiconductor nanowires are used for water oxidation as well as the reduction half-reaction after modification with water oxidation and reduction catalyst, respectively. Upon irradiation of visible light, the nanowires absorb visible light and water is oxidized to produce oxygen, electrons, and protons. Electrons travel through semiconductor wires to the reduction side whereas protons are transferred to the reduction side with the help of

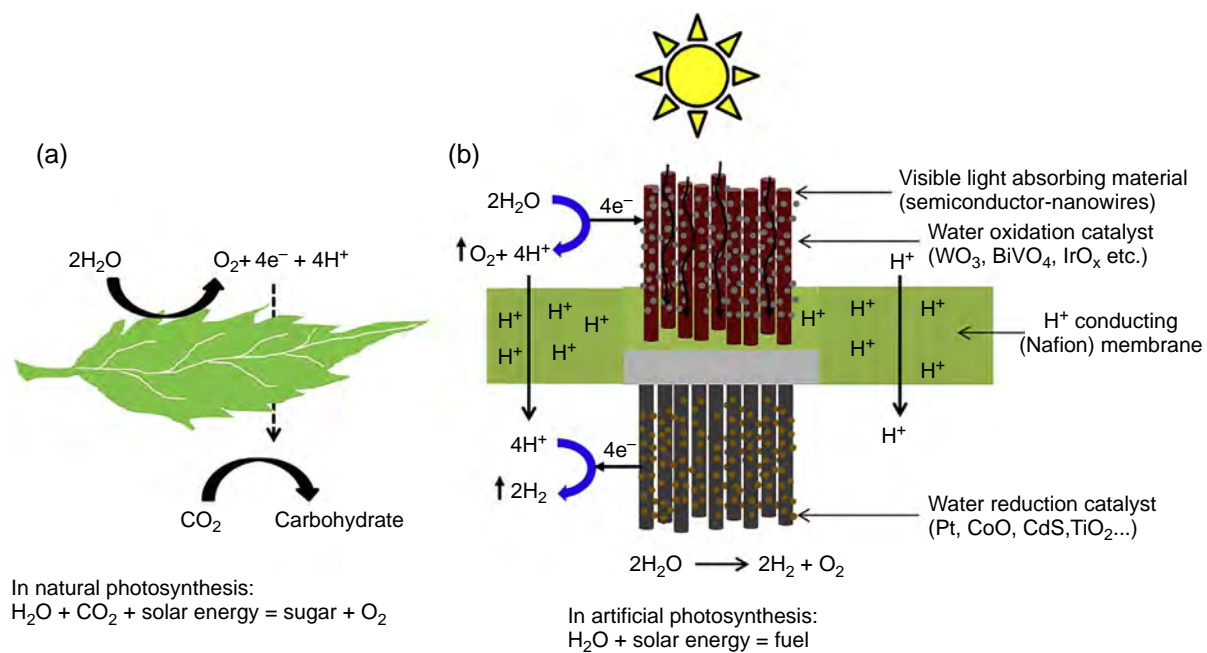


Figure 10.5 Schematic illustration of natural photosynthetic system (NPS) and artificial photosynthetic system (APS). (a) Basic process of photosynthesis in NPS. (b) Structural design of artificial photosynthesis in APS. In APS, electrons and protons are liberated by the water-splitting reaction and are passed through a proton-conducting membrane (Nafion), where protons are reduced to H_2 . Figure (b) is adopted and modified from the concept of [Warren, Atwater, and Lewis \(2014\)](#).

proton-conducting membrane (Nafion), in which protons are reduced to hydrogen gas. In this way, water splitting (generation of H₂ and O₂) can be achieved with high efficiency separately in two different systems. The development of an efficient catalyst for water oxidation to evolve O₂ is a key task for yielding breakthrough water splitting. Ruthenium- and iridium-based catalysts show better performance but they are scarce and expensive (Liu & Wang, 2012; Singh & Spiccia, 2013). Thus, earth-abundant elements are more promising (Hocking et al., 2011).

10.3 Advantages and disadvantages of hydrogen production using photobiological methods

Photobiological H₂ production has several advantages as compared with other methods such as petroleum refining, coal gasification, fossil fuel, and thermochemical techniques because those processes are hazardous. Hence, photobiological H₂ production can be considered as an effective method for producing pure and clean H₂ gas, although it has some disadvantages; therefore, the advantages and disadvantages of photobiological production are given below.

10.3.1 Advantages of hydrogen production using photobiological methods

- Photobiological H₂ production uses microorganisms to convert solar energy into hydrogen gas.
- Photobiological H₂ production, especially by photosynthetic microorganisms, has several advantages because it requires simple techniques and low-cost energy (natural sunlight) compared with electrochemical H₂ production based on water splitting. Hence, these methods only use sunlight and water as renewable sources of energy.
- Photobiological H₂ production does not emit environmentally polluting gases and toxic compounds.
- Pure and clean H₂ can be produced by photobiological methods.
- Green algae, cyanobacteria, and photosynthetic bacteria are abundant everywhere and we can easily grow them under suitable artificial conditions. Most of these microorganisms are not environmentally harmful. Hence, we can easily grow such microorganisms to fulfill our goal.
- During photobiological H₂ production, many photosynthetic bacteria can use wide-spectrum light energy and organic waste (Hussy, Hawkes, Dinsdale, & Hawkes, 2003).
- Photobiological H₂ production by microorganisms under anaerobic conditions produces valuable metabolites such as lactic acid, butyric acid, and acetic acid as byproducts (Lay, 2000; Lin & Chang, 1999).
- The photon conversion efficiency to produce H₂ from sunlight is high: ~10–16% (Kruse et al., 2005, Prince & Kheshgi, 2005).
- This method is useful for carbon sequestration. Solar-powered H₂ production by microorganisms has a unique process for CO₂ sequester. In the aerobic phase, CO₂ is converted into biomass; in the anaerobic phase H₂ is subsequently produced (Hankamer et al., 2007).
- Biohydrogen production by photosynthetic microorganisms requires the use of a simple solar reactor such as a transparent closed box with a low energy requirement (Parmar, Singh, Pandey, Gnansounou, & Madamwar, 2011).

- Hydrogen production by sunlight is cheap compared with the current fossil fuel system and the synthetic fossil fuel system for H₂ production.

10.3.2 Disadvantages of hydrogen production using photobiological methods

- Hydrogenase is inactivated in the presence of molecular oxygen in microorganisms.
- In green algae the simultaneous production of O₂ and H₂ inhibits hydrogenase activity by O₂. The presence of uptake hydrogenase in cyanobacteria and photosynthetic bacteria also decreases H₂ production (Dasgupta et al., 2010).
- Production of H₂ by photofermentation is low (Hussy et al., 2003).
- The exact metabolic pathway for H₂ production by microorganisms is not clear. In addition, there is no clear contender for a robust, industrially capable microorganism that can be metabolically engineered to produce more H₂. Several engineering issues need to be addressed, including an appropriate bioreactor design for H₂ production (Bhutto et al., 2011).
- Photosynthetic bacteria do not produce more H₂ that will fulfill public demands (Bhutto et al., 2011).
- The development of a new strain of microorganisms is required to enhance high solar conversion efficiency for H₂ production.
- Mass cultivation of green algae and cyanobacteria is difficult because it may require a large surface area. Also, the yield of H₂ production by these microorganisms is not high, which may not fulfill demand.
- Scaling-up and materials for construction of several photobioreactors are costly, and there are many disadvantages (Dasgupta et al., 2010).
- Storing hydrogen is expensive because it needs to be compressed.
- Construction of artificial leaves for artificial photosynthesis is an expensive method for generating H₂.

10.4 Future trends to improve photobiological H₂ production

Photobiological H₂ production using photosynthetic microorganisms such as bacteria, algae, and cyanobacteria is an exciting topic for research. Currently, H₂ is considered a fuel for the future as a renewable source of energy that does not create greenhouse gases. In addition, the method of photobiological H₂ production using photosynthetic microorganisms shows promise and great interest for generating carbon-free, clean, and pure H₂ from abundant natural resources such as water and sunlight. However, feasible and commercial exploration for better yield of H₂ is required. Further exploration is needed to improve photosynthetic microorganisms by either metabolic or genetic engineering. There are some ideas for improving photobiological H₂ production: (1) identifying the most suitable microorganisms and incorporating hydrogenase and nitrogenase into selected microorganisms, (2) optimizing culture conditions, (3) stabilizing photobioreactors, (4) improving feedstocks, (5) performing comparative analyses of photobiological H₂ production, (6) improving H₂ yield using cheap or cost-effective raw materials, (7) exploring novel species of photosynthetic microorganisms that use better solar energy to improve H₂ production, and (8) improving photobioreactors for better propagation of microalgae for effective H₂ production.

List of acronyms

ATP	Adenosine triphosphate
NADPH	Nicotinamide adenine dinucleotide phosphate
NADH	Nicotinamide adenine dinucleotide
CO₂	Carbon dioxide
H₂O	Water
H₂	Hydrogen
O₂	Oxygen
PNSB	Purple non-sulfur bacteria
e⁻	Electron
H⁺	Proton
PSII	Photosystem II
PSI	Photosystem I
Fd	Ferredoxin
FNR	Ferredoxin-NADP ⁺ -reductase
PQ	Plastoquinone
LED	Light-emitting diode
MEC	Microbial electrolysis cell
PEC	Photoelectrochemical cell
Si	Silicon
JCAP	Joint Center for Artificial Photosynthesis

Acknowledgments

This work was supported by grants from the Russian Science Foundation (No: 14-14-00039) to SIA. MMN is grateful to the Institute for Advanced Studies in Basic Sciences and the National Elite Foundation for financial support. KI was supported in part by grant-in-aid for Scientific Research on Innovative Areas (No. 24107004) and Strategic Research Base Development Program for Private Universities from MEXT, Japan. TT and HM were supported by a grant from JST PRESTO.

References

- Akkerman, I., Janssen, M., Rocha, J., & Wijffels, R. H. (2002). Photobiological hydrogen production: photochemical efficiency and bioreactor design. *International Journal of Hydrogen Energy*, 27(11–12), 1195–1208.
- Alibabaei, L., Brennaman, M. K., Norris, M. R., Kalanyan, B., Song, W., Losego, M. D., et al. (2013). Solar water splitting in a molecular photoelectrochemical cell. *Proceedings of the National Academy of Sciences of the United States of America*, 110(50), 20008–20013.
- Allakhverdiev, S. I., Kreslavski, V. D., Thavasi, V., Zharmukhamedov, S. K., Klimov, V. V., Nagata, T., et al. (2009). Hydrogen photoproduction by use of photosynthetic organisms and biomimetic systems. *Photochemical and Photobiological Sciences*, 08(2), 148–156.
- Allakhverdiev, S. I., Thavasi, V., Kreslavski, V. D., Zharmukhamedov, S. K., Klimov, V. V., Ramakrishna, S., et al. (2010). Photosynthetic hydrogen production. *Journal of Photochemistry and Photobiology C: Photochemistry Reviews*, 11(2–3), 101–113.

- Amao, Y., Hamano, A., & Shimizu, K. (2012). Development of artificial leaf for solar hydrogen production. *Energy Procedia*, 29, 21–25.
- Androga, D. D., Özgür, E., Eroglu, I., Gündüz, U., & Yücel, M. (2012). Photofermentative hydrogen production in outdoor conditions. In D. Minic (Ed.), *Hydrogen Energy—Challenges and Perspectives*, ISBN 978-953-51-0812-2. <http://dx.doi.org/10.5772/50390>.
- Antal, T. K., & Lindblad, P. (2005). Production of H₂ by sulphur-deprived cells of the unicellular cyanobacteria *Gloeocapsa alpicola* and *Synechocystis* sp. PCC 6803 during dark incubation with methane or at various extracellular pH. *Journal of Applied Microbiology*, 98(01), 114–120.
- Asada, Y., Koike, Y., Schnackenberg, J., Miyake, M., Uemura, I., & Miyake, J. (2000). Heterologous expression of clostridial hydrogenase in the cyanobacterium expression of clostridial hydrogenase in the cyanobacterium *Synechococcus* PCC7942. *Biochimica et Biophysica Acta (BBA)—Gene Structure and Expression*, 1490(3), 269–278.
- Asada, Y., & Miyake, J. (1999). Photobiological hydrogen production. *Journal of Bioscience and Bioengineering*, 88(1), 1–6.
- Barber, J., & Tran, P. D. (2013). From natural to artificial photosynthesis. *Journal of The Royal Society Interface*, 10(81), 20120984. <http://dx.doi.org/10.1098/rsif.2012.0984>
- Bensaid, S., Centi, G., Garrone, E., Perathoner, S., & Saracco, G. (2012). Towards artificial leaves for solar hydrogen and fuels from carbon dioxide. *ChemSusChem*, 05(3), 500–521.
- Bhutto, A. W., Bazmi, A. A., Kardar, M. N., Yaseen, M., Zahedi, G., & Karim, K. (2011). Developments in hydrogen production through microbial processes; Pakistan's prospective. *International Journal of Chemical and Environmental Engineering*, 02(3), 189–205.
- Bonente, G., Formighieri, C., Mantelli, M., Catalanotti, C., Giuliano, G., Morosinotto, T., et al. (2011). Mutagenesis and phenotypic selection as a strategy toward domestication of *Chlamydomonas reinhardtii* strains for improved performance in photobioreactors. *Photosynthesis Research*, 108(2–3), 107–120.
- Bothe, H., Schmitz, O., Yates, M. G., & Newton, W. E. (2010). Nitrogen fixation and hydrogen metabolism in cyanobacteria. *Microbiology and Molecular Biology Reviews*, 74(4), 529–551.
- Carere, C. R., Rydzak, T., Verbeke, T. J., Cicek, N., Levin, D. B., & Sparling, R. (2012). Linking genome content to biofuel production yields: a meta-analysis a major catabolic pathways among select H₂ and ethanol-producing bacteria. *BMC Microbiology*, 12, 295.
- Centi, G., & Perathoner, S. (2010). Towards solar fuels from water and CO₂. *ChemSusChem*, 03(2), 195–208.
- Centi, G., & Perathoner, S. (2011). CO₂-based energy vectors for the storage of solar energy. *Greenhouse Gases: Science and Technology*, 01(1), 21–35.
- Cha, M., Chung, D., Elkins, J. G., Guss, A. M., & Westpheling, J. (2013). Metabolic engineering of *Caldicellulosiruptor bescii* yields increased hydrogen production from lignocellulosic biomass. *Biotechnology for Biofuels*, 6, 85.
- Cheng, J., Su, H., Zhou, J., Song, W., & Cen, K. (2011). Hydrogen production by mixed bacteria through dark and photo fermentation. *International Journal of Hydrogen Energy*, 36(1), 450–457.
- Chen, C.-Y., Yang, M.-H., Yeh, K.-L., Liu, C.-H., & Chang, J.-S. (2008). Biohydrogen production using sequential two-stage dark and photo fermentation processes. *International Journal of Hydrogen Energy*, 33(18), 4755–4762.
- Chen, C.-Y., Yeh, K.-L., Aisyah, R., Lee, D.-J., & Chang, J.-S. (2011). Cultivation, photobioreactor design and harvesting of microalgae for biodiesel production: a critical review. *Bioresource Technology*, 102(1), 71–81.

- Chinnasamy, S., Bhatnagar, A., Claxton, R., & Das, K. C. (2010). Biomass and bioenergy production potential of microalgae consortium in open and closed bioreactors using untreated carpet industry effluent as growth medium. *Bioresource Technology*, *101*(17), 6751–6760.
- Cogdell, R. J., Brotsudarmo, T. H. P., Gardiner, A. T., Sanchez, P. M., & Cronin, L. (2010). Artificial photosynthesis—solar fuels: current status and future prospects. *Biofuels*, *01*(6), 861–876.
- Cournac, L., Guedeney, G., Peltier, G., & Vignais, P. M. (2004). Sustained photoevolution of molecular hydrogen in a mutant of *Synechocystis* sp. strain PCC 6803 deficient in the type I NADPH-dehydrogenase complex. *Journal of Bacteriology*, *186*(6), 1737–1746.
- Dasgupta, C. N., Gilbert, J. J., Lindbald, P., Heidorn, T., Borgvang, S. A., Skjånes, K., et al. (2010). Recent trends on the development of photobiological processes and photobioreactors for the improvements of hydrogen production. *International Journal of Hydrogen Energy*, *35*(19), 10218–10238.
- Das, D., Khanna, N., & Veziroğlu, T. N. (2008). Recent developments in biological hydrogen production processes. *Chemical Industry and Chemical Engineering Quarterly*, *14*(2), 57–67.
- Das, D., & Veziroğlu, T. N. (2001). Hydrogen production by biological processes: a survey of literature. *International Journal of Hydrogen Energy*, *26*(1), 13–28.
- Datta, M., Nikki, G., & Shah, V. (2000). Cyanobacterial hydrogen production. *World Journal of Microbiology and Biotechnology*, *16*(8–9), 757–767.
- Dauvillée, D., Chochois, V., Steup, M., Haebel, S., Eckermann, N., Ritte, G., et al. (2006). Plastidial phosphorylase is required for normal starch synthesis in *Chlamydomonas reinhardtii*. *The Plant Journal*, *48*(2), 274–285.
- Dutta, D., De, D., Chaudhuri, S., & Bhattacharya, S. K. (2005). Hydrogen production by Cyanobacteria. *Microbial Cell Factories*, *4*, 36. <http://dx.doi.org/10.1186/1475-2859-4-36>.
- Efremenko, E. N., Nikolskaya, A. B., Lyagin, I. V., Senko, O. V., Makhlis, T. A., Stepanov, N. A., et al. (2012). Production of biofuels from pretreated microalgae biomass by anaerobic fermentation with immobilized *Clostridium acetobutylicum* cells. *Bioresource Technology*, *114*, 342–348.
- Eltsova, Z. A., Vasilieva, L. G., & Tsygankov, A. A. (2010). Hydrogen production by recombinant strains of *Rhodobacter sphaeroides* using a modified photosynthetic apparatus. *Applied Biochemistry and Microbiology*, *46*(5), 487–491.
- Ernst, A., Kerfin, W., Spiller, H., & Böger, P. (1979). External factors influencing light-induced H₂ evolution by the blue-green algae, *Nostoc muscorum*. *Zeitschrift für Naturforschung*, *34*, 820–825.
- Eroglu, E., & Melis, A. (2011). Photobiological hydrogen production: recent advances and state of art. *Bioresource Technology*, *102*(18), 8403–8413.
- Evens, T. J., Chapman, D. J., Robbins, R. A., & D'Asaro, E. A. (2000). An analytical flat-plate photobioreactor with a spectrally attenuated light source for the incubation of phytoplankton under dynamic light regimes. *Hydrobiologia*, *434*(1–3), 55–62.
- Faunce, T., Styring, S., Wasielewski, M. R., Brudvig, G. W., Rutherford, W., Messinger, J., et al. (2013). Artificial photosynthesis as a frontier technology for energy sustainability. *Energy and Environmental Science*, *6*(6), 1074–1076.
- Ferreira, A. F., Ribau, J. P., & Silva, C. M. (2011). Energy consumption and CO₂ emissions of potato peel and sugarcane biohydrogen production pathways, applied to Portuguese road transportation. *International Journal of Hydrogen Energy*, *36*(21), 13547–13558.

- Ghirardi, M. L., Dubini, A., Yu, J., & Maness, P.-C. (2009). Photobiological hydrogen-producing systems. *Chemical Society Reviews*, 38(12), 3505.
- Ghirardi, M. L., King, P. W., Posewitz, M. C., Maness, P. C., Fedorov, A., Kim, K., et al. (2005). Approaches to developing biological H₂-producing organisms and processes. *Biochemical Society Transactions*, 33, 70–72.
- Ghirardi, M. L., Posewitz, M. C., Maness, P. C., Dubini, A., Yu, J., & Seibert, M. (2007). Hydrogenases and hydrogen photoproduction in oxygenic photosynthetic organisms. *Annual Review of Plant Biology*, 58, 71–91.
- Ghysels, B., & Franck, F. (2010). Hydrogen photo-evolution upon S deprivation stepwise: an illustration of microalgal photosynthetic and metabolic flexibility and a step stone for future biotechnological methods of renewable H₂ production. *Photosynthesis Research*, 106(1–2), 145–154.
- Hallenbeck, P. C., & Benemann, J. R. (2002). Biological hydrogen production; fundamentals and limiting processes. *International Journal of Hydrogen Energy*, 27(11–12), 1186–1194.
- Hankamer, B., Lehr, F., Rupprecht, J., Mussgnug, J. H., Posten, C., & Kruse, O. (2007). Photosynthetic biomass and H₂ production by green algae: from bioengineering to bioreactor scale-up. *Physiologia Plantarum*, 131(1), 10–21.
- Hansel, A., & Lindblad, P. (1998). Towards optimization of cyanobacteria as biotechnologically relevant producers of molecular hydrogen, a clean and renewable energy source. *Applied Microbiology and Biotechnology*, 50(2), 153–160.
- Happe, T., Schütz, K., & Böhme, H. (2000). Transcriptional and mutational analysis of the uptake hydrogenase of the filamentous cyanobacterium *Anabaena variabilis* ATCC 29413. *Journal of Bacteriology*, 182(6), 1624–1631.
- Hay, J. X. W., Wu, T. Y., Juan, J. C., & Jahim, J. M. (2013). Biohydrogen production through photo fermentation or dark fermentation using waste as a substrate: overview, economics, and future prospects of hydrogen usage. *Biofuels Bioproducts and Biorefining*, 07(3), 334–352.
- Hocking, R. K., Brimblecombe, R., Chang, L., Singh, A., Cheah, M. H., Glover, C., et al. (2011). Water-oxidation catalysis by manganese in a geochemical-like cycle. *Nature Chemistry*, 3, 461–466.
- Horch, M., Lauterbach, L., Lenz, O., Hildebrandt, P., & Zebger, I. (2012). NAD(H)-coupled hydrogen cycling-structure-function relationships of bidirectional [NiFe] hydrogenase. *FEBS Letters*, 586(5), 545–556.
- Hussy, I., Hawkes, F. R., Dinsdale, R., & Hawkes, D. L. (2003). Continuous fermentative hydrogen production from a wheat starch co-product by mixed microflora. *Biotechnology and Bioengineering*, 84(6), 619–626.
- James, B. D., Baum, G. N., Perez, J., & Baum, K. N. (2009). Technoeconomic Boundary analysis of biological pathways to hydrogen production. In *National Renewable Energy Laboratory, Subcontract Report NREL/SR-560-46674* (pp. 1–193). Arlington, Virginia: Directed Technologies, Inc.
- Jo, J. H., Lee, D. S., & Park, J. M. (2006). Modeling and optimization of photosynthetic hydrogen gas production by green alga *Chlamydomonas reinhardtii* in sulfur-deprived circumstance. *Biotechnology Progress*, 22(2), 431–437.
- Kars, G., Gündüz, U., Yücel, M., Türker, L., & Eroğlu, I. (2006). Hydrogen production and transcriptional analysis of *nifD*, *nifK* and *hupS* genes in *Rhodobacter sphaeroides* O.U.001 grown in media with different concentrations of molybdenum and iron. *International Journal of Hydrogen Energy*, 31(11), 1536–1544.

- Khetkorn, W., Lindbald, P., & Incharoensakdi, A. (2012). Inactivation of uptake hydrogenase leads to enhanced and sustained hydrogen production with high nitrogenase activity under high light exposure in the cyanobacterium *Anabaena siamensis* TISTR 8012. *Journal of Biological Engineering*, *06*, 19.
- Kim, J. Y. H., Jo, B. H., Jo, Y., & Cha, H. J. (2012). Improved production of biohydrogen in light-powered *Escherichia coli* by co-expression of proteorhodopsin and heterologous hydrogenase. *Microbial Cell Factories*, *11*, 2.
- Kim, J. P., Kang, C. D., Park, T. H., Kim, M. S., & Sim, S. J. (2006). Enhanced hydrogen production by controlling light intensity in sulfur-deprived *Chlamydomonas reinhardtii* culture. *International Journal of Hydrogen Energy*, *31*(11), 1585–1590.
- Kim, E.-J., Kim, J.-S., Kim, M.-S., & Lee, J. K. (2006). Effect of changes in the level of light harvesting complexes of *Rhodobacter sphaeroides* on the photoheterotrophic production of hydrogen. *International Journal of Hydrogen Energy*, *31*(4), 531–538.
- Koku, H., Eroğlu, I., Günfüz, U., Yücel, M., & Türker, L. (2002). Aspects of the metabolism of hydrogen production by *Rhodobacter sphaeroides*. *International Journal of Hydrogen Energy*, *27*(11–12), 1315–1329.
- Kondo, T., Arakawa, M., Hirai, T., Wakayama, T., Hara, M., & Miyake, J. (2002). Enhancement of hydrogen production by a photosynthetic bacterium mutant with reduced pigment. *Journal of Bioscience and Bioengineering*, *93*(2), 145–150.
- Kosourov, S., Makarova, V., Fedorov, A. S., Tsygankov, A., Seibert, M., & Ghirardi, M. L. (2005). The effect of sulfur re-addition on H₂ photoproduction by sulfur-deprived green algae. *Photosynthesis Research*, *85*(3), 295–305.
- Kosourov, S., Seibert, M., & Ghirardi, M. L. (2003). Effects of extracellular pH on the metabolic pathways in sulfur-deprived, H₂-producing *Chlamydomonas reinhardtii* cultures. *Plant and Cell Physiology*, *44*(2), 146–155.
- Kosourov, S., Tsygankov, A., Seibert, M., & Ghirardi, M. L. (2002). Sustained hydrogen photoproduction by *Chlamydomonas reinhardtii*: effects of culture parameters. *Biotechnology and Bioengineering*, *78*(7), 731–740.
- Kruse, O., Rupprecht, J., Mussgnug, J. H., Dismukes, G. C., & Hankamer, B. (2005). Photosynthesis: a blueprint for solar energy capture and biohydrogen production technologies. *Photochemical and Photobiological Sciences*, *04*(12), 957–970.
- Kufryk, G. (2013). Advances in utilizing cyanobacteria for hydrogen production. *Advances in Microbiology*, *03*(6A), 60–68.
- Kwon, J.-H., Rögner, M., & Rexroth, S. (2012). Direct approach for bioprocess optimization in a continuous flat-bed photobioreactor system. *Journal of Biotechnology*, *162*(1), 156–162.
- Lay, J. J. (2000). Modeling and optimization of anaerobic digested sludge converting starch to hydrogen. *Biotechnology and Bioengineering*, *68*(3), 269–278.
- Lee, J. Z., Klaus, D. M., Maness, P.-C., & Spear, J. R. (2007). The effect of butyrate concentration on hydrogen production via photofermentation for use in a Martian habitat resource recovery process. *International Journal of Hydrogen Energy*, *32*(15), 3301–3307.
- Lemeille, S., Turkina, M. V., Vener, A. V., & Rochaix, J.-D. (2010). Stt7-dependent phosphorylation during state transitions in the green alga *Chlamydomonas reinhardtii*. *Molecular and Cellular Proteomics*, *09*(6), 1281–1295.
- Lewis, N. S., & Nocera, D. G. (2006). Powering the planet: chemical challenges in solar energy utilization. *Proceedings of the National Academy of Sciences of the United States of America*, *103*(43), 15729–15735.
- Liang, Y., Wu, X., Gan, L., Xu, H., Hu, Z., & Long, M. (2009). Increased biological hydrogen production by deletion of hydrogen-uptake system in photosynthetic bacteria. *Microbiological Research*, *164*(6), 674–679.

- Lin, C.-Y., & Chang, R.-C. (1999). Hydrogen production during the anaerobic acidogenic conversion of glucose. *Journal of Chemical Technology and Biotechnology*, 74(6), 498–500.
- Lindberg, P., Devine, E., Stensjö, K., & Lindblad, P. (2011). HupW Protease specifically required for processing of the catalytic subunit of the uptake hydrogenase in the cyanobacterium *Nostoc* sp. strain PCC 7120. *Applied and Environmental Microbiology*, 78(1), 273–276.
- Lindberg, P., Park, S., & Melis, A. (2010). Engineering a platform for photosynthetic isoprene production in cyanobacteria, using *Synechocystis* as the model organism. *Metabolic Engineering*, 12(1), 70–79.
- Lindberg, P., Schütz, K., Happe, T., & Lindblad, P. (2002). A hydrogen producing, hydrogenase-free mutant strain of *Nostoc punctiforme* ATCC 29133. *International Journal of Hydrogen Energy*, 27(11–12), 1291–1296.
- Lin, Q., & Lin, J. (2011). Effects of nitrogen source and concentration on biomass and oil production of a *Scenedesmus rubescens* like microalga. *Bioresource Technology*, 102(2), 1615–1621.
- Listorti, A., Durrant, J., & Barber, J. (2009). Artificial photosynthesis: solar to fuel. *Nature Materials*, 08(12), 929–930.
- Liu, B.-F., Ren, N.-Q., Ding, J., Xie, G.-J., & Guo, W.-Q. (2009). The effect of Ni²⁺, Fe²⁺ and Mg²⁺ concentration on photo-hydrogen production by *Rhodospseudomonas faecalis* RLD-53. *International Journal of Hydrogen Energy*, 34(2), 721–726.
- Liu, X., & Wang, F. (2012). Transition metal complexes that catalyze oxygen formation from water: 1979–2010. *Coordination Chemistry Reviews*, 256, 1115–1136.
- Maness, P.-C., Smolinski, S., Dillon, A. C., Heben, M. J., & Weaver, P. F. (2002). Characterization of the oxygen tolerance of a hydrogenase linked to a carbon monoxide oxidation pathway in *Rubrivivax gelatinosus*. *Applied and Environmental Microbiology*, 68(6), 2633–2636.
- Markov, S. A., Eivazova, E. R., & Greenwood, J. (2006). Photostimulation of H₂ production in the green alga *Chlamydomonas reinhardtii* upon photoinhibition of its O₂-evolving system. *International Journal of Hydrogen Energy*, 31(10), 1314–1317.
- Masukawa, H., Mochimaru, M., & Sakurai, H. (2002). Disruption of the uptake hydrogenase gene, but not of the bidirectional hydrogenase gene, leads to enhanced photobiological hydrogen production by the nitrogen-fixing cyanobacterium *Anabaena* sp PCC 7120. *Applied Microbiology and Biotechnology*, 58(5), 618–624.
- Mathews, J., & Wang, G. (2009). Metabolic pathway engineering for enhanced biohydrogen production. *International Journal of Hydrogen Energy*, 34(17), 7404–7416.
- McConnell, I., Li, G., & Brudvig, G. W. (2010). Energy conversion in natural and artificial photosynthesis. *Chemistry and Biology*, 17(5), 434–447.
- Melis, A., & Melnicki, M. R. (2006). Integrated biological hydrogen production. *International Journal of Hydrogen Energy*, 31(11), 1563–1573.
- Melis, A., Zhang, L., Forestier, M., Ghirardi, M. L., & Seibert, M. (2000). Sustained photobiological hydrogen gas production upon reversible inactivation of oxygen evolution in the green alga *Chlamydomonas reinhardtii*. *Plant Physiology*, 122(1), 127–136.
- Miura, Y., Akano, T., Fukatsu, K., Miyasaka, H., Mizoguchi, T., Yagi, K., et al. (1995). Hydrogen production by photosynthetic microorganisms. *Energy Conversion and Management*, 36(6–9), 903–906.
- Miyake, M., Schnackenberg, J., Nakamura, C., Asada, Y., & Miyake, J. (2001). Molecular handling of hydrogenase. In J. Miyake, T. Matsunaga, & A. San Pietro (Eds.), *Biohydrogen II* (pp. 205–219). Oxford, United Kingdom: Elsevier Science Ltd.

- Modestino, M. A., Walczak, K. A., Berger, A., Evans, C. M., Haussener, S., Koval, C., et al. (2013). Robust production of purified H₂ in a stable, self-regulating, and continuously operating solar fuel generator. *Energy and Environmental Science*, *07*(1), 297–301.
- Najafpour, M. M., & Allakhverdiev, S. I. (2012). Manganese compounds as water oxidizing catalysts for hydrogen production via water splitting: from manganese complexes to nano-sized manganese oxides. *International Journal of Hydrogen energy*, *37*(10), 8753–8764.
- Nandi, R., & Sengupta, S. (1998). Microbial production of hydrogen: an overview. *Critical Reviews in Microbiology*, *24*(1), 61–84.
- Nel, W. P., & Cooper, C. J. (2009). Implications of fossil fuel constraints on economic growth and global warming. *Energy Policy*, *37*(1), 166–180.
- Nguyen, A. V., Thomas-Hall, S. R., Malnoë, A., Timmins, M., Mussgnug, J. H., Rupprecht, J., et al. (2008). Transcriptome for photobiological hydrogen production induced by sulfur deprivation in the green alga *Chlamydomonas reinhardtii*. *Eukaryotic Cell*, *07*(11), 1965–1979.
- Nguyen, A. V., Toepel, J., Burgess, S., Uhmeyer, A., Blifernez, O., Doebbe, A., et al. (2011). Time-course global expression profiles of *Chlamydomonas reinhardtii* during photobiological H₂ production. *PLoS ONE*, *06*(12), e29364.
- Nobre, B. P., Villalobos, F., Barragán, B. E., Oliveira, A. C., Batista, A. P., Marques, P. A. S. S., et al. (2013). A biorefinery from *Nannochloropsis* sp. microalga—extraction of oils and pigments. Production of biohydrogen from the leftover biomass. *Bioresource Technology*, *135*, 128–136.
- Nocera, D. G. (2009). Personalized energy: the home as a solar power station. *ChemSusChem*, *02*(5), 387–390.
- Nocera, D. G. (2012). The artificial leaf. *Accounts of Chemical Research*, *45*(5), 767–776.
- Nong, G., Chen, S., Xu, Y., Huang, L., Zou, Q., Li, S., et al. (2014). Artificial photosynthesis of oxalate and oxalate-based polymer by a photovoltaic reactor. *Scientific Reports*, *04*, 3572. <http://dx.doi.org/10.1038/srep03572>.
- Nowak, J., Florek, M., Kwiatek, W., Lekki, J., Chevallier, P., Zieba, E., et al. (2005). Composite structure of wood cells in petrified wood. *Materials Science and Engineering: C*, *25*(2), 119–130.
- Ogata, H., Lubitza, W., & Higuchi, Y. (2009). [NiFe] hydrogenases: structural and spectroscopic studies of the reaction mechanism. *Dalton Transactions Issue*, *37*, 7577–7587.
- Oh, Y.-K., Raj, S. M., Jung, G. Y., & Park, S. (2011). Current status of the metabolic engineering of microorganisms for biohydrogen production. *Bioresource Technology*, *102*(18), 8357–8367.
- Özgür, E., Mars, A. E., Peksel, B., Louwse, A., Yücel, M., Gündüz, U., et al. (2010). Biohydrogen production from beet molasses by sequential dark and photofermentation. *International Journal of Hydrogen Energy*, *35*(2), 511–517.
- Öztürk, Y., Yücel, M., Daldal, F., Mandac, S., Gündüz, U., Türker, L., et al. (2006). Hydrogen production by using *Rhodobacter capsulatus* mutants with genetically modified electron transfer chains. *International Journal of Hydrogen Energy*, *31*(11), 1545–1552.
- Papazi, A., Andronis, E., Loannidis, N. E., Chaniotakis, N., & Kotzabasis, K. (2012). High yields of hydrogen production induced by meta-substituted dichlorophenols biodegradation from the green alga *Scenedesmus obliquus*. *PLoS ONE*, *7*(11), e49037. <http://dx.doi.org/10.1371/journal.pone.0049037>.
- Parmar, A., Singh, N. K., Pandey, A., Gnansounou, E., & Madamwar, D. (2011). Cyanobacteria and microalgae: a positive prospect for biofuels. *Bioresource Technology*, *102*(22), 10163–10172.

- Philipps, G., Happe, T., & Hemschemeier, A. (2012). Nitrogen deprivation results in photosynthetic hydrogen production in *Chlamydomonas reinhardtii*. *Planta*, 235(04), 729–745.
- Posewitz, M. C., Dubini, A., Meuser, J. E., Seibert, M., & Ghirardi, M. L. (2009). Hydrogenases, hydrogen production, and anoxia. In D. B. Stern (Ed.), *The Chlamydomonas sourcebook: Organellar and metabolic processes* (2nd ed.), (Vol. 02, pp. 217–246). Academic Press.
- Poudyal, R.S., Tiwari, I., Najafpour, M.M., Los, D.A., Carpentier, R., Shen, J-R., Allakhverdev, S.I. Current insights to enhance hydrogen production by photosynthetic organisms. In D. Stolten & B. Emonts (Eds.), *Hydrogen science and engineering*, Wiley-VCH Books, in press.
- Prabina, B. J., & Kumar, K. (2010). Studies on the optimization of cultural conditions for maximum hydrogen production by selected cyanobacteria. *ARPN Journal of Agricultural Science and Biological Science*, 05(5), 22–31.
- Prince, R. C., & Kheshgi, H. S. (2005). The photobiological production of hydrogen: potential efficiency and effectiveness as a renewable fuel. *Critical Reviews in Microbiology*, 31(1), 19–31.
- Quintana, N., der Kooy, F. V., de Rhee, M. D. V., Voshol, G. P., & Verpoorte, R. (2011). Renewable energy from cyanobacteria: energy production optimization by metabolic pathway engineering. *Applied Microbiology and Biotechnology*, 91(3), 471–490.
- Richau, K. H., Kudahettige, R. L., Pujic, P., Kudahettige, N. P., & Sellstedt, A. (2013). Structural and gene expression analyses of uptake hydrogenases and other proteins involved in nitrogenase protection in Frankia. *Journal of Bioscience*, 38(4), 703–712.
- Rosner, V., & Wagner, H.-J. (2012). Life cycle assessment and process development of photobiological hydrogen production—from laboratory to large scale applications. *Energy Procedia*, 29, 532–540.
- Rout, U. K., Akimoto, K., Sano, F., Oda, J., Homma, T., & Tomoda, T. (2008). Impact assessment of the increase in fossil fuel prices on the global energy system, with and without CO₂ concentration stabilization. *Energy Policy*, 36(9), 3477–3484.
- Roy, S. C., Varghese, O. K., Paulose, M., & Grimes, C. A. (2010). Toward solar fuels: photocatalytic conversion of carbon dioxide to hydrocarbons. *ACS Nano*, 04(3), 1259–1278.
- Rupprecht, J., Hankamer, B., Mussgnug, J. H., Ananyev, G., Dismukes, C., & Kruse, O. (2006). Perspectives and advances of biological H₂ production in microorganisms. *Applied Microbiology and Biotechnology*, 72(3), 442–449.
- Saratale, G. D., Chen, S.-D., Lo, Y.-C., Saratale, R. G., & Chang, J.-S. (2008). Outlook of biohydrogen production from lignocellulosic feedstock using dark fermentation—a review. *Journal of Scientific and Industrial Research*, 67(11), 962–979.
- Sathiyamoorthy, P., & Shanmugasundaran, S. (1994). A low-cost bioreactor for cyanobacterial biomass production. *Bioresource Technology*, 49(3), 279–280.
- Seifert, K., Waligorska, M., & Laniecki, M. (2010). Brewery wastewaters in photobiological hydrogen generation in presence of *Rhodobacter sphaeroides* O.U. 001. *International Journal of Hydrogen Energy*, 35(9), 4085–4091.
- Serebryakova, L. T., Shremetieva, M. E., & Lindbald, P. (2000). H₂-uptake and evolution in the unicellular cyanobacterium *Chroococciopsis thermalis* CALU 758. *Plant Physiology and Biochemistry*, 38(6), 525–530.
- Shaishav, S., Singh, R. N., & Tripathi, S. (2013). Biohydrogen from algae: fuel of the future. *International Research Journal of Environment Sciences*, 02(4), 44–47.
- Shima, S., Pilak, O., Vogt, S., Schick, M., Stagni, M. S., Meyer-Klaucke, W., et al. (2008). The crystal structure of [Fe]-hydrogenase reveals the geometry of the active site. *Science*, 321(5888), 572–575.

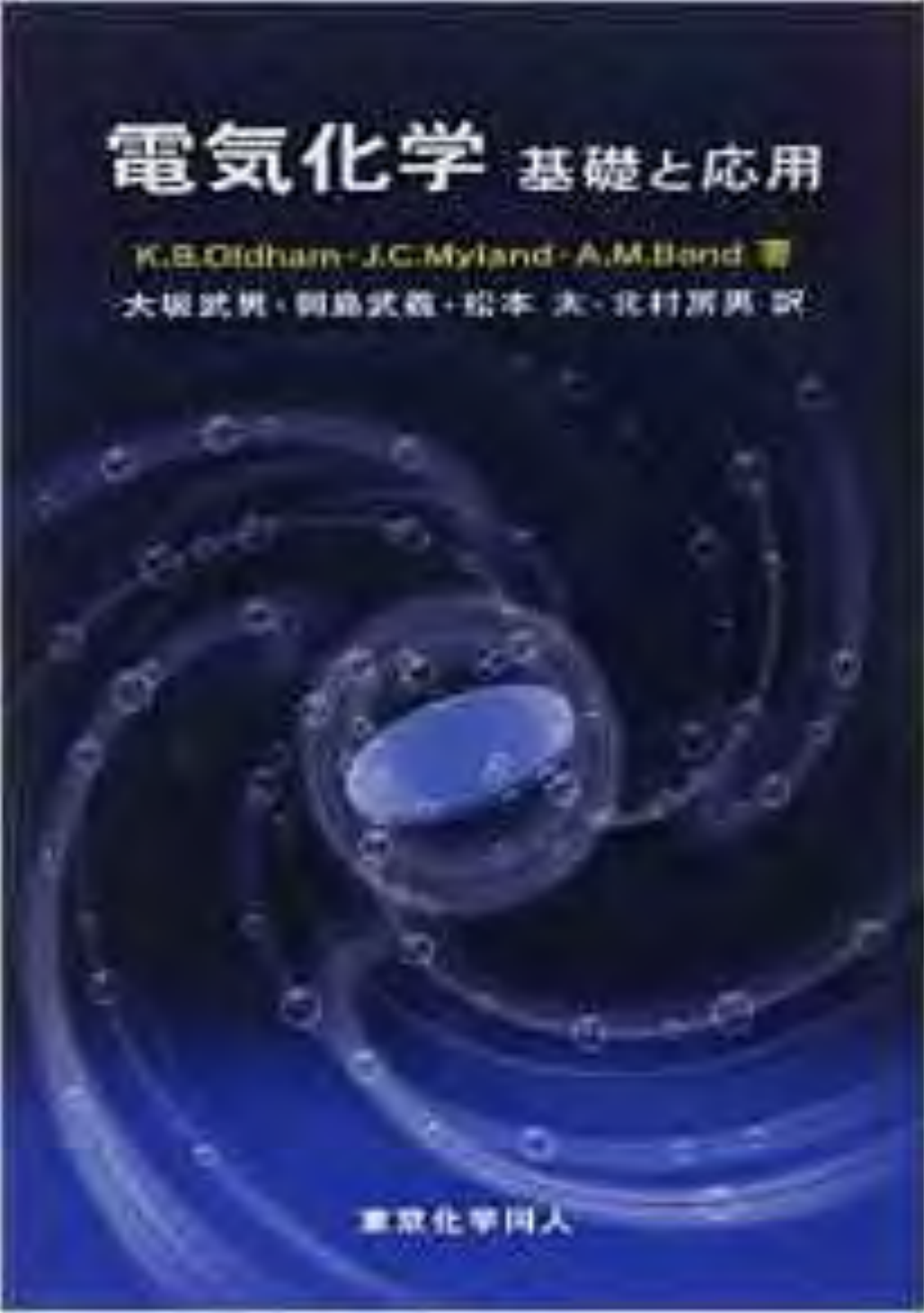
- Show, K.-Y., Lee, D.-J., & Chang, J.-S. (2011). Bioreactor and process design for biohydrogen production. *Bioresource Technology*, *102*(18), 8524–8533.
- Singh, A., & Spiccia, L. (2013). Water oxidation catalysts based on abundant 1st row transition metals. *Coordination Chemistry Reviews*, *257*, 2607–2622.
- Skjånes, K., Knutsen, G., Källqvist, T., & Lindblad, P. (2008). H₂ production from marine and fresh water species of green algae during sulfur deprivation and considerations for bioreactor design. *International Journal of Hydrogen Energy*, *33*(2), 511–521.
- Skjånes, K., Rebours, C., & Lindblad, P. (2013). Potential for green microalgae to produce hydrogen, pharmaceuticals and other high value products in a combined process. *Critical Reviews in Biotechnology*, *33*(2), 172–215.
- Stal, L. J., & Krumbein, W. E. (1985). Oxygen protection of nitrogenase the aerobically nitrogen fixing, non-heterocystous cyanobacterium *Oscillatoria* sp. *Archives of Microbiology*, *143*(1), 72–76.
- Su, H., Cheng, J., Zhou, J., Song, W., & Cen, K. (2009a). Combination of dark- and photo-fermentation to enhance hydrogen production and energy conversion efficiency. *International Journal of Hydrogen Energy*, *34*(21), 8846–8853.
- Su, H., Cheng, J., Zhou, J., Song, W., & Cen, K. (2009b). Improving hydrogen production from cassava starch by combination of dark and photo fermentation. *International Journal of Hydrogen Energy*, *34*(4), 1780–1786.
- Sundaram, S., Tripathi, A., & Gupta, V. (2010). Structure prediction and molecular simulation of gases diffusion pathways in hydrogenase. *Bioinformation*, *05*(4), 177–183.
- Sunita, M., & Mitra, C. K. (1993). Photoproduction of hydrogen by photosynthetic bacteria from sewage and waste water. *Journal of Biosciences*, *18*(1), 155–160.
- Tamagnini, P., Axelsson, R., Lindberg, P., Oxelfelt, F., Wünschiers, R., & Lindblad, P. (2002). Hydrogenases and hydrogen metabolism of cyanobacteria. *Microbiology and Molecular Biology Reviews*, *66*(01), 1–20.
- Tamagnini, P., Leitão, E., Oliveira, P., Ferreira, D., Pinto, F., Harris, D. J., et al. (2007). Cyanobacterial hydrogenases: diversity, regulation and applications. *FEMS Microbiology Review*, *31*(6), 692–720.
- Thangaraj, A., & Kulandaivelu, G. (1994). Biological hydrogen photoproduction using dairy and sugarcane waste waters. *Bioresource Technology*, *48*(1), 9–12.
- Thiel, T. (1994). Genetic analysis of cyanobacteria. In D. A. Bryant (Ed.), *The molecular biology of cyanobacteria. Advances in photosynthesis and respiration* (pp. 581–611). Dordrecht, The Netherlands: Kluwer Academic Publishers.
- Tiwari, A., & Pandey, A. (2012). Cyanobacterial hydrogen production—a step towards clean environment. *International Journal of Hydrogen Energy*, *37*(1), 139–150.
- Tran, P. D., Wong, L. H., Barber, J., & Loo, J. S. C. (2012). Recent advances in hybrid photocatalysts for solar fuel production. *Energy and Environmental Science*, *05*(3), 5902–5918.
- Tsygankov, A. A. (2007). Nitrogen-fixing cyanobacteria. A review. *Applied Biochemistry and Microbiology*, *43*(3), 250–259.
- Uyar, B., Schumacher, M., Gebicki, J., & Modigell, M. (2009). Photoproduction of hydrogen by *Rhodobacter capsulatus* from thermophilic fermentation effluent. *Bioprocess and Biosystems Engineering*, *32*(5), 603–606.
- Vignais, P. M., & Billoud, B. (2007). Occurrence, classification, and biological function of hydrogenases: an overview. *Chemical Reviews*, *107*(10), 4206–4272.
- Vignais, P. M., Magnin, J.-P., & Willison, J. C. (2006). Increasing biohydrogen production by metabolic engineering. *International Journal of Hydrogen Energy*, *31*(11), 1478–1483.

- Walter, M. G., Warren, E. L., McKone, J. R., Boettcher, S. W., Mi, Q., Santori, E. A., et al. (2010). Solar water splitting cells. *Chemical Reviews*, *110*(11), 6446–6473.
- Warren, E. L., Atwater, H. A., & Lewis, N. S. (2014). Silicon microwire arrays for solar energy-conversion applications. *The Journal of Physical Chemistry*, *118*(2), 747–759.
- Weiss, A., Patyk, A., & Schebek, L. (2011). Nutrient recycling and energy production with microalgae from a life cycle perspective. In Gesellschaft zur Förderung des Instituts für Siedlungswasserwirtschaft der Technischen Universität Braunschweig e.V. (Ed.), *Tagungsband 3. Internationales Symposium "Re-Water Braunschweig" 21. und 22. November 2011. Braunschweig: Institut für Siedlungswasserwirtschaft* (Vol. 81).
- Williams, C. R., & Bees, M. A. (2013). Mechanistic modeling of sulfur-deprived photosynthesis and hydrogen production in suspensions of *Chlamydomonas reinhardtii*. *Biotechnology and Bioengineering*, *111*(2), 320–335.
- Winkler, M., Kuhlger, S., Hippler, M., & Happe, T. (2009). Characterization of key step for light-driven hydrogen evolution in green algae. *The Journal of Biological Chemistry*, *284*(52), 36620–36627.
- Xia, L., Ge, H., Zhou, X., Zhang, D., & Hu, C. (2013). Photoautotrophic outdoor two-stage cultivation for oleaginous microalgae *Scenedesmus obtusus* XJ-15. *Bioresource Technology*, *144*, 261–267.
- Yang, Z., Guo, R., Xu, X., Fan, X., & Luo, S. (2011). Fermentative hydrogen production from lipid-extracted micro algal biomass residues. *Applied Energy*, *88*(10), 3468–3472.
- Yetiş, M., Gündüz, U., Eroğlu, I., Yücel, M., & Türker, L. (2000). Photoproduction of hydrogen from sugar refinery wastewater by *Rhodobacter sphaeroides* O.U. 001. *International Journal of Hydrogen Energy*, *25*(11), 1035–1041.
- Yonemoto, I. Y., Matteri, C. W., Nguyen, T. A., Smith, H. O., & Weyman, P. D. (2013). Dual organism design cycle reveals small subunit substitutions that improve [NiFe] hydrogenase hydrogen evolution. *Journal of Biological Engineering*, *07*, 17.
- Yoshino, F., Ikeda, H., Masukawa, H., & Sakurai, H. (2007). High photobiological hydrogen production activity of a *Nostoc* sp. PCC 7422 uptake hydrogenase-deficient mutant with high nitrogenase activity. *Marine Biotechnology*, *09*(1), 101–112.
- Zhou, H., Guo, J., Li, P., Fan, T., Zhang, D., & Ye, J. (2013). Leaf-architected 3D hierarchical artificial photosynthetic system of perovskite titanates towards CO₂ photoreduction into hydrocarbon fuels. *Scientific Report*, *3*, 1667. <http://dx.doi.org/10.1038/srep01667>.
- Zhu, H., Suzuki, T., Tsygankov, A. A., Asada, Y., & Miyake, J. (1999). Hydrogen production from tofu wastewater by *Rhodobacter sphaeroides* immobilized in agar gels. *International Journal of Hydrogen Energy*, *24*(4), 305–310.
- Zuttel, A., Borgschulte, A., & Schlapbach, L. (Eds.). (2008). *Hydrogen as a future energy carrier* (Vol. 427). Weinheim: John Wiley & VCH, ISBN 978-3-527-30817-0.

電気化学 基礎と応用

K.B.Oldham・J.C.Myland・A.M.Bond 著

大塚武貴・朝島武哉・松本 大・北村眞真 訳



東京化学同人

Crustacean Hyperglycemic Hormone

Tsuyoshi Ohira

Abbreviation: CHH

Additional names: family members include molt-inhibiting hormone (MIH), vitellogenesis-inhibiting hormone (VIH), and mandibular organ-inhibiting hormone (MOIH)

Pleiotropic hormones referred to as eyestalk hormones are produced by the most important crustacean endocrine organ, the X-organ sinus gland complex, and are members of the CHH family peptides.

Discovery

A CHH regulating hemolymph glucose levels as a hyperglycemic factor was first isolated and sequenced from the shore crab *Carcinus maenas* in 1989 [1]. Subsequently, a MIH and a VIH were isolated and characterized from *C. maenas* [2] and from the American lobster *Homarus americanus* [3], respectively. MIH controls molting by suppressing synthesis and/or secretion of ecdysteroids by the Y-organ. VIH regulates the onset of vitellogenesis by suppression of vitellogenin synthesis. Later, MOIH, inhibiting methyl farnesoate synthesis and/or secretion by the mandibular organ, was purified and structurally determined from the crab *Cancer pagurus* [4]. In *C. maenus*, it has been shown that CHH is produced in non-eyestalk tissues such as the pericardial organ and the gut [5,6].

Structure

Structural Features

CHH, MIH, VIH, and MOIH are members of the CHH family peptides. These peptides are mostly 72–78 aa residues in length, having 6 conserved cysteine residues that form three intramolecular disulfide bonds. CHH family peptides are divided into two subtypes based on the absence (type I) or presence (type II) of a glycine residue at position 12 in the mature peptide (Figure 53.1).

Primary Structure

Most eyestalk CHH belongs to type I and consists of 72 aa residues with a C-terminal amide. The C-terminal amide is important for its hyperglycemic activity [5]. In *H. americanus* and several crayfish species, stereoisomer isoforms (D-phenylalanine) have been found [5]. Long-type CHH isoforms (non-eyestalk type) produced by alternative splicing have been found in *C. maenas* and the giant freshwater prawn *Macrobrachium rosenbergii* [5]. N-terminal aa sequences of

eyestalk CHH and non-eyestalk CHH are common (positions 1–40), but the remaining C-terminal sequences differ considerably. MIH, VIH, and MOIH are grouped as type II, because they have a characteristic glycine residue at position 12 [6]. MIH, VIH, and MOIH are longer than CHH. All of the peptides have a free N-terminus, and most of them are not amidated at the C-terminus. The molecular weights of CHHs range from 8,200 to 8,700, and those of MIHs, VIHs, and MOIHs range from 9,000 to 9,500.

Synthesis and Release

Gene, mRNA, and Precursor

CHH genes occur in multiple isoforms of two-exon (*Penaeus monodon* CHH1) [7], three-exon (*Metapenaeus ensis* CHHA and CHHB) [6], or four-exon genes (*C. maenas* and *M. rosenbergii* CHHs) [5]. Four-exon CHH genes express multiple mRNAs, eyestalk CHH mRNA (Exons 1, 2, and 4), and non-eyestalk CHH mRNA (Exons 1–4) by alternative splicing. The CHH precursor consists of a signal peptide, CHH-precursor related peptide, dibasic cleavage site, mature CHH, and an amidation signal (eyestalk CHH only). MIH and MOIH genes consist of three-exon genes only. There have been no data for VIH genes. Type II peptide (MIH, VIH, and MOIH) precursors consist of a signal peptide and mature peptide. The organization of a type II peptide precursor is apparently different from that of type I (CHH).

Distribution of mRNA

Eyestalk CHH mRNA is detected most abundantly in the X-organ, but also in non-eyestalk tissues such as the ventral nerve cord and gut. Long-type CHH isoforms (non-eyestalk type) are expressed in the pericardial organ in *C. maenus*, and in the heart, gills, antennal glands, and thoracic ganglion in *M. rosenbergii* [5]. Most type II peptide genes are expressed only in eyestalk neurons.

Regulation of Synthesis and Release

CHH is secreted to hemolymph in response to stressful conditions such as emersion, hypoxia, drastic thermal change, bacterial endotoxins, parasitism by dinoflagellates, and heavy metal pollutants [5]. Exercise also stimulates CHH release from the sinus gland. Serotonin (5-hydroxy-tryptamine; 5HT) is a CHH-releasing agent, while Leu-enkephalin and glucose are inhibitory chemicals.

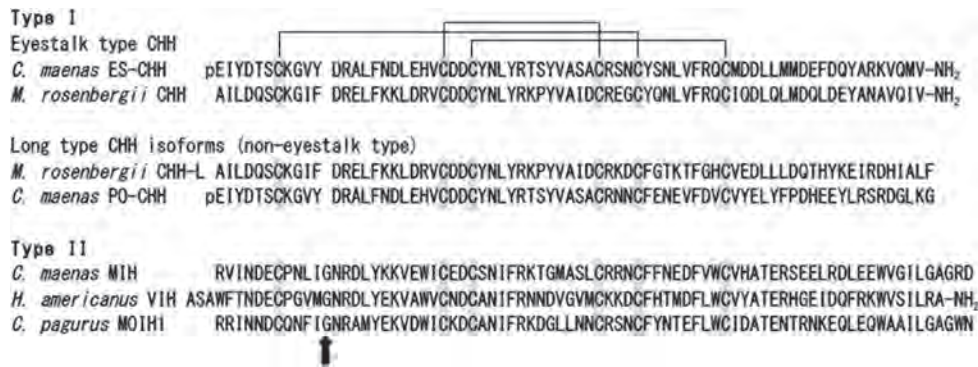


Figure 53.1 Alignment of CHH, MIH, VIH, and MOIH. N-terminal “pE” indicates pyroglutamic acid residue. Conserved cysteine residues are gray-boxed. Disulfide bridges are indicated by lines. Characteristic glycine residues in type II are indicated by an arrow. ES, eyestalk; PO, pericardial organ.

Receptors

CHH-, MIH-, VIH-, and MOIH-receptors have not yet been identified. Membrane-bound guanylate cyclase (GC) is presumed to be a candidate as a CHH receptor, because cGMP is used as a second messenger of CHH signaling [5]. Regarding second messengers involved in MIH signaling, both cAMP and cGMP are implicated in the regulation of ecdysteroidogenesis in various crustacean species [5]. Therefore, several reports suggest that the MIH receptor is a GPCR but not a membrane-bound GC.

Biological Functions

Crustacean Hyperglycemic Hormone

Eyestalk CHH controls crustacean hemolymph glucose levels as a hyperglycemic factor. Hyperglycemia is a result of mobilization of glycogen in target tissues such as the hepatopancreas and abdominal muscles. Steady CHH hemolymph levels of *Carcinus maenas* are 25 fmol/ml in the winter and 50–55 fmol/ml in the summer [8]. Recent studies have revealed that eyestalk CHHs in many species have pleiotropic functions, such as MIH, MOIH, and VIH activities [5,8,9]. Eyestalk CHH also possesses a role in osmo/ionoregulation at the gill in euryhaline crustacean species. CHH expressed in the gut, the aa sequence of which is identical with that of eyestalk CHH, contributes as another osmoregulator in, for example, ion transport at the gills and water uptake for the purpose of enlarging body size after molting. A few studies have shown that eyestalk CHH is probably involved with inhibitory regulation of the androgenic gland (AG). The biological functions of long-type CHH isoforms (non-eyestalk type) have not yet been elucidated.

Molt-Inhibiting Hormone

MIH inhibits molting by suppressing synthesis and/or secretion of the molting hormone (ecdysteroid) by the Y-organ, except at the premolt stage when ecdysteroids are released to trigger ecdysis. The MIH hemolymph level of the American crayfish *Procambarus clarkii* is around 5–6 fmol/ml at the intermolt stage and decreases to 1.28 fmol/ml at the early premolt stage [10]. American lobster, *H. americanus*, CHH also showed MIH activity [5].

Vitellogenesis-Inhibiting Hormone

VIH inhibits vitellogenin synthesis by the ovary and/or hepatopancreas as well as vitellin accumulation in the oocytes, thus negatively controlling crustacean vitellogenesis. In some penaeid shrimp species, CHHs decrease vitellogenin gene expression in the cultured ovary *in vitro* [8].

Mandibular Organ-Inhibiting Hormone

The mandibular organ is the site of synthesis of methyl farnesoate (MF), the unepoxidated precursor of insect juvenile hormone III. The biological functions of MF in crustaceans have not yet been well defined. MOIH inhibits MF synthesis and/or secretion by the mandibular organ. In the spider crab *Libinia emarginata*, CHH showed both hyperglycemic activity and MF synthesis inhibition activity [5].

References

1. Kegel G, Reichwein B, Weese S, et al. Amino acid sequence of the crustacean hyperglycemic hormone (CHH) from the shore crab, *Carcinus maenas*. *FEBS Lett.* 1989;255:10–14.
2. Webster SG. Amino acid sequence of putative moult-inhibiting hormone from the crab *Carcinus maenas*. *Proc R Soc Lond B.* 1991;244:247–252.
3. Soyez D, Le Caer JP, Noel PY, Rossier J. Primary structure of two isoforms of the vitellogenesis inhibiting hormone from the lobster *Homarus americanus*. *Neuropeptides.* 1991;20:25–32.
4. Wainwright G, Webster SG, Wilkinson MC, Chung JS, Rees HH. Structure and significance of mandibular organ-inhibiting hormone in the crab, *Cancer pagurus*. *J Biol Chem.* 1996;271:12749–12754.
5. Webster SG, Keller R, Dirksen H. The CHH-superfamily of multifunctional peptide hormones controlling crustacean metabolism, osmoregulation, moulting, and reproduction. *Gen Comp Endocrinol.* 2012;175:217–233.
6. Wiwiegweaw A, Udomkit A, Panyim S. Molecular structure and organization of crustacean hyperglycemic hormone genes of *Penaeus monodon*. *J Biochem Mol Biol.* 2004;37:177–184.
7. Chan SM, Gu PL, Chu KH, Tobe SS. Crustacean neuropeptide genes of the CHH/MIH/GIH family: implications from molecular studies. *Gen Comp Endocrinol.* 2003;134:214–219.
8. Chung JS, Zmora N, Katayama H, Tsutsui N. Crustacean hyperglycemic hormone (CHH) neuropeptides family: functions, titer, and binding to target tissues. *Gen Comp Endocrinol.* 2010;166:447–454.
9. Katayama H, Ohira T, Nagasawa H. Crustacean peptide hormones: structure, gene expression and function. *Aqua-BioSci Monogr.* 2013;6:49–90.
10. Nakatsuji T, Sonobe H. Regulation of ecdysteroid secretion from the Y-organ by molt-inhibiting hormone in the American crayfish, *Procambarus clarkii*. *Gen Comp Endocrinol.* 2004;135:358–364.

Supplemental Information Available on Companion Website

- Phylogenetic tree of the CHH family members/E-Figure 53.1
- Accession numbers of genes and cDNAs for precursors of CHH, MIH, VIH, and MOIH/E-Table 53.1

DC-driven thermoelectric Peltier device for precise DNA amplification

Shigeo Yamaguchi^{1*}, Tadzunu Suzuki², Kazuhito Inoue³, and Yoshitaka Azumi³

¹Department of Electrical, Electronic, and Information Engineering, Kanagawa University, Yokohama 221-8686, Japan

²Research Institute for Engineering, Kanagawa University, Yokohama 221-8686, Japan

³Department of Biological Sciences, Kanagawa University, Hiratsuka, Kanagawa 259-1293, Japan

E-mail: yamags18@kanagawa-u.ac.jp

Received August 30, 2014; accepted February 24, 2015; published online April 8, 2015

Using a DC-driven Peltier device, we fabricated a DNA amplification system [polymerase chain reaction (PCR) system] with the aim of increasing its speed and precision. The Peltier device had a well block sandwiched by $\text{Bi}_2\text{Se}_{0.37}\text{Te}_{2.36}$ as an N-type thermoelectric material and $\text{Bi}_{0.59}\text{Sb}_{1.30}\text{Te}_3$ as a P-type material. The well block was directly controlled by the electric current, leading to a high thermal response. Using the Peltier device with the well block, we performed thermal cycles of a PCR, and we demonstrated that our PCR system produces a smaller amount of nonspecific products for the genome DNA (gDNA) of *Arabidopsis thaliana*, leading to a more precise DNA amplification system.

© 2015 The Japan Society of Applied Physics

1. Introduction

The polymerase chain reaction (PCR) system is an extremely important and well-established technique for DNA amplification, which is widely used in genome sequencing, forensics, and the diagnosis of various diseases. For a successful PCR, precise temperature control is required, and during a PCR process, specimens are subjected to multiple thermal cycles (~ 25 cycles) typically at three temperatures: 94, 55, and 72 °C. Transitions between these temperatures must be conducted rapidly and within a certain temperature resolution (± 0.2 °C). To perform these thermal cycles, commercially available PCR systems include a Peltier module as a thermal cyler. The Peltier modules have a structure called the π -structure¹⁾ and they are widely used to precisely control the temperature of devices such as infrared detectors, thermal stabilizers for laser diodes, charge-coupled devices, and cooling stage.²⁾

In commercially available PCR systems, the Peltier module controls the temperature of the metallic blocks embedded in the PCR system. This fact significantly means that the thermal response of a PCR system cannot in principle exceed that of the Peltier module itself. Consequently, to overcome this problem, we have proposed and fabricated a PCR system with a novel thermal cyler using a Peltier device with a higher thermal response.

To realize rapid PCR systems, their miniaturization has so far been performed using a microreactor, a capillary, or silicon technology.^{3–20)} However, the improvement of our novel system compared with conventional systems in terms of the reduction in the amount of nonspecific products cannot be attributed to the miniaturization itself because reagents act differently in a miniaturized space compared with in the space of conventional tubes. To clarify the effect of our Peltier device on the PCR, the use of conventional PCR tubes, in which sufficient heat convection occurs, is necessary. In this study, we used polypropylene tubes, which are commonly used in PCR systems.

We previously fabricated devices with a PN sandwich structure.^{21–24)} Recently, we have incorporated such devices into a customized PCR system. As shown in Fig. 1, the device is characterized by a metallic tip directly sandwiched between a P-type thermoelectric material and an N-type material. The tip is cooled or heated directly by the Peltier

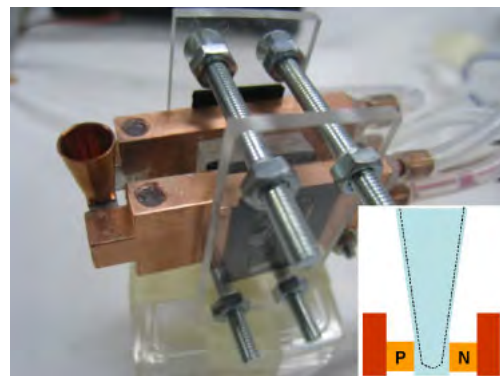


Fig. 1. (Color online) Photograph of our Peltier device and (inset) schematic structure of our PN-sandwiched well block.

effect, resulting in a high thermal response. Using this DC-driven Peltier device, we have recently fabricated a PCR system with the ultimate aim of realizing a rapid and precise PCR system for early diagnoses that can be used at home or outside laboratories.

2. Experiment

2.1 Device structure

Figure 1 shows the schematic structure (inlet) and a photograph of our Peltier device embedded in a thermal cyler. The P- and N-type thermoelectric bulks are located between Cu heat sinks, which also serve as electrodes. Our device has a well block of copper placed between the P- and N-type bulks. This well block is formed by transforming an electrode so that it partially protrudes from the matrix bulks, and the well block is used to directly cool or heat objects. A conventional π -type Peltier device is difficult to modify or adapt, whereas for our device, the block shape can be easily changed. Our structure has the following advantages: (i) the absolute absorption of heat at the well block is sufficiently large because the matrix bulks are large; (ii) to apply the device to different-size areas, the well block is simply exchanged for one of an appropriate size; (iii) nanotechnology can be used for the fabrication of the well block; (iv) efficient Peltier heating can be applied, which has not been achieved so far; and (v) its fabrication has a low cost. Advantage (i) has the greatest importance when a very small object is cooled. If the

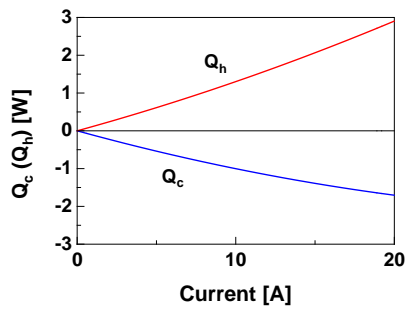


Fig. 2. (Color online) Current dependence of heat absorption or radiation for our device.

size of the Peltier device is decreased, the absolute cooling power will decrease markedly because it is strongly related to the volume of the device, even when the absolute power per unit area is unchanged.

The well block of copper between the P- and N-type bulks has a square base of $3.5 \times 3.5 \text{ mm}^2$ and a circular top with a diameter of 5.5 mm. The inner shape of the well block was manufactured to fit the shape of the PCR tube used. The thermoelectric materials were $\text{Bi}_2\text{Se}_{0.37}\text{Te}_{2.36}$ for the N-type material and $\text{Bi}_{0.59}\text{Sb}_{1.30}\text{Te}_3$ for the P-type material. The size of the materials was $3.2 \times 3.2 \times 1.7 \text{ mm}^3$. The use of a metallic well block allows the Peltier effect to occur thermally with high electrical efficiency at the interface between the well block and the N- or P-type material. Because our PCR system has a single well block of copper directly sandwiched between the P- and N-type materials mentioned above, the well block can be directly cooled or heated by the Peltier effect.

2.2 Fundamental properties of the device

Here we describe the fundamental properties of our Peltier device with a PN sandwich structure. The rate of heat absorption Q_c and that of heat radiation Q_h of our Peltier device are expressed in terms of Q_{pc} (heat absorption on cold side), Q_{ph} (heat radiation on hot side), Q_j (Joule heat), and Q_k (heat by thermal conduction). Thus, as follows:

$$Q_c = Q_{pc} - Q_j - Q_k = \alpha T_c I - \frac{1}{2} R I^2 - K(T_0 - T_c), \quad (1)$$

$$Q_h = Q_{ph} + Q_j - Q_k = \alpha T_h I + \frac{1}{2} R I^2 - K(T_h - T_0). \quad (2)$$

Here α , R , K , and T_0 are the Seebeck coefficient, electric resistance, and thermal conductance of the device, and the temperature of the radiation plates (equal to that of the cooling water), respectively. The values for the Peltier device are $\alpha = 400 \times 10^{-6} \text{ V/K}$, $R = 3.4 \times 10^{-5} \Omega$, $K = 0.0374 \text{ W m}^{-1} \text{ K}^{-1}$, and $T_0 = 15^\circ \text{C}$.²¹⁾ On the basis of the above values, the estimated values of Q_c and Q_h as a function of current are plotted in Fig. 2. The maximum values of Q_c and Q_h were 1.6 and 2.9 W, respectively, at a current of 20 A.

For an actual PCR system, a high thermal response is required as well as high heat absorption and radiation. Using the experimental data obtained from the transient characteristics of the temperature of our Peltier device, the time constants τ_c (for cooling) and τ_h (for heating) were estimated using the expressions below, and their minima were 1.2 and 2.0 s, respectively, at a current of 20 A.

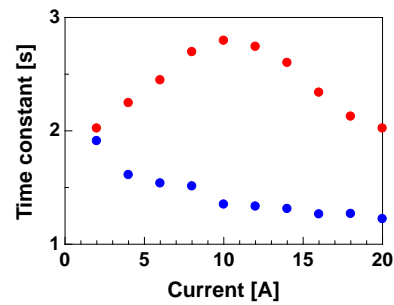


Fig. 3. (Color online) Current dependence of time constants of our device.

The thermal time constants were evaluated through a time-transient experiment, in which the temperature of the well block was measured as a function of time. Then, the thermal time constants were estimated using the following equations:

$$T = T_c + \Delta T_c \exp\left(-\frac{t}{\tau_c}\right), \quad (3)$$

$$T = T_h + \Delta T_h \exp\left(-\frac{t}{\tau_h}\right) \quad (4)$$

for the cooling operation and for the heating operation. Here, T_c and T_h are the saturated temperatures during cooling and heating, and ΔT_c and ΔT_h are $(T_0 - T_c)$ and $(T_h - T_0)$, respectively.

The time constants for cooling (blue points) and heating (red points) are plotted in Fig. 3. Note that these time constants indicate the net thermal response of the Peltier device, reflecting its controllability for an ideal thermal cycle.

For conventional Peltier devices, the thermal response is limited by that of the PN elements themselves.

From this viewpoint, Fig. 3 shows the thermal response of the PN elements of our Peltier device. For a conventional Peltier device, the time constant is typically approximately 30 s.²⁵⁾

Note that these time constants indicate the net thermal response of the Peltier device, reflecting its controllability for an ideal thermal cycle.

2.3 PCR system

The Peltier device with the above characteristics was set in a thermal cycler that was electrically connected to a temperature controller and a power supply as shown in Fig. 4. To induce the radiation of the Peltier device, water flows in the copper electrodes. The power supply (a driver in the case of our Peltier device) was laboratory-built to make it suitable for the low voltage and high current of the device. The structure of the power supply is shown in Fig. 5. The resultant electrical resistance of the device was as small as 10 mΩ, and, consequently, the typical applied voltage and current were 0.3 V and 20 A, respectively; no power supply that can drive such a device is commercially available.

Conventional regulators are classified into two types: switching regulators and linear regulators. Although a switching regulator has higher efficiency, it is impossible to apply a voltage of 0.3 V to a device as a current source. On the other hand, although a linear regulator has the advantage that a continuous voltage can be applied to a device as a

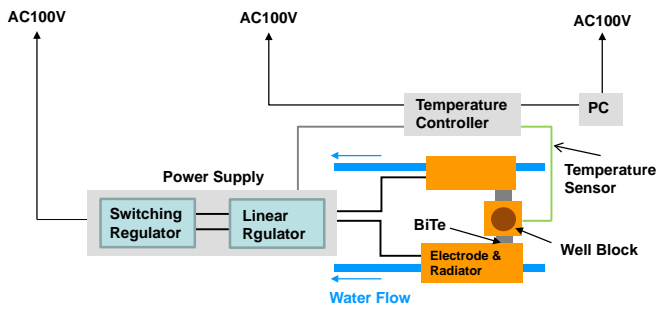


Fig. 4. (Color online) Schematic structure of our PCR system.

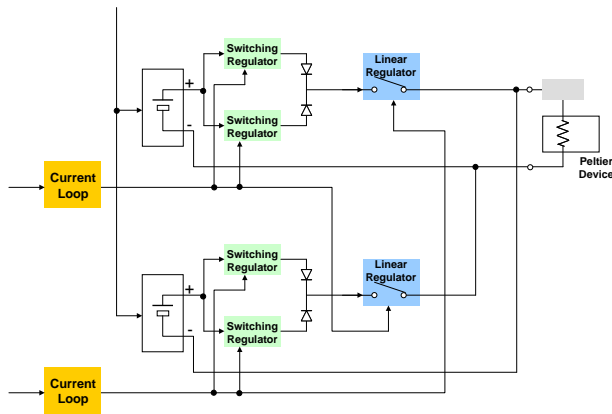


Fig. 5. (Color online) Electrical structure of the driver (power supply) for our Peltier device.

current source, the loss between the input power and output power is large, leading to heat generation. Consequently, a radiator is necessary, and particularly in this case, a rather large amount of radiation is inevitable; if a typical power supply ($\pm 15\text{ V}$, $\pm 5\text{ A}$) for a conventional commercially available Peltier module is introduced into our Peltier device, the heat produced is estimated to be as large as 294 W. To radiate such a large amount of heat, an extremely large radiation system will be necessary, which is not practical. To overcome this problem, as shown in Fig. 5, we have developed and introduced our own power supply involving the combination of a switching regulator and a linear regulator to drive the device, where, depending on the output voltage of the switching regulator, the roles of the two types of regulator are changed: for lower voltages, the linear regulator is used, and for higher voltages, the switching regulator is used. The control signals were added through analog current loops of 4–20 mA. The switching regulator is a DC–DC converter (Fujitsu FPLR12TR7530PA) and the linear regulator is mainly composed of a MOSFET (Renesas 2SK3163).

Using the PCR system embedded together with the PN-sandwiched Peltier device and the custom driver, 25 thermal cycles under the same conditions given below were performed, and the first two cycles are shown in Fig. 6. It is shown that almost rectangular thermal cycles were performed using our Peltier device and system with a PCR tube containing 30 μL water. The temperature was measured at the well block. As shown in the next section, our system showed clearer PCR amplification of the target DNA than a commercially available system.

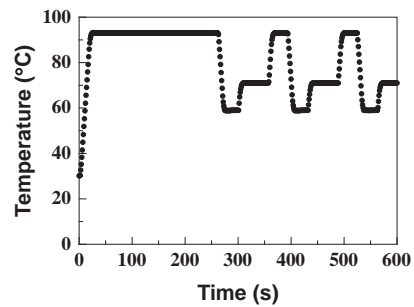


Fig. 6. First two cycles of a PCR sequence (4 min for the initial denaturation and a subsequent set of 30 s for denaturation, 20 s for annealing, and 60 s for extension).

3. Results and discussion

To compare the performance between our thermal cycler and an iCycler (BioRad), a PCR was performed using genomic DNA (gDNA) of *Arabidopsis thaliana* (L.) Heynh. (ecotype Columbia) as the template. The primer sequences were 5'-GTCTGCGACTAGAGGCGGAG-3' and 5'-TCCTTGCTCACCACCACCG-3'. The target was a 1,000 bp region in the AT1G15830 gene on chromosome 1 (GenBank accession: CP002684). The gDNA was extracted from *Arabidopsis thaliana* plants grown at 25 °C under a short-day condition with a light period of 14 h. The gDNA was prepared in accordance with the technique in Ref. 26. Whole plants were crushed into a fine powder in liquid nitrogen using a mortar and pestle. The powder was suspended in an extraction buffer [100 mM Tris–HCl, pH 8, 20 mM EDTA, 3% (w/v) hexadecyltrimethylammonium bromide, 1% (w/v) poly(vinyl pyrrolidone) (M_w 40,000)]. The suspension was incubated at 65 °C for 30 min. Then, an equal volume of chloroform was added, which was followed by mixing by gentle shaking at room temperature for 30 min. Following centrifugation at 17,000 g for 10 min, the upper aqueous layer was collected. The gDNA was separated by 2-propanol precipitation and resolved in 10 mM Tris–HCl (pH 8) and 0.1 mM EDTA. The PCR solution was composed of 0.5 ng/ μL gDNA, 0.2 μM of each primer, 0.2 mM of each dNTP, 2.0 mM MgCl_2 , 1 \times Ex Taq buffer, and 0.025 unit/ μL Ex Taq DNA polymerase (Takara Bio). The reaction conditions for our PCR were as follows: 94 °C for 4 min for the initial denaturation, 25 cycles (94 °C for 30 s for denaturation, 48–62 °C for 20 s for annealing, and 72 °C for 60 s for extension steps), and then 72 °C for 3 min for additional extension.^{27,28)} The maximum rate of ramping up and down was 3 °C/s in all steps. The PCR using the iCycler was carried out with the following program: 94 °C for 4 min, 25 cycles (94 °C, 30 s for denaturation, 48–62 °C for 20 s for annealing, and 72 °C for 60 s for extension), and 72 °C for 3 min. Figure 7 shows that the primers caused several non-specific amplifications and less amplification of the targets for the iCycler, while the nonspecific products were less amplified and the target was amplified by our system. The blur in Fig. 7 indicates the generation of nonspecific products. Moreover, in Fig. 7, T_a is the annealing temperature, at which primer bases combined with DNAs, and kb denotes kilobases of DNA pairs. The intensity of blur for DNA nonspecific products as a function of annealing temperature T_a is shown in Fig. 8. PI and PNS correspond the conven-

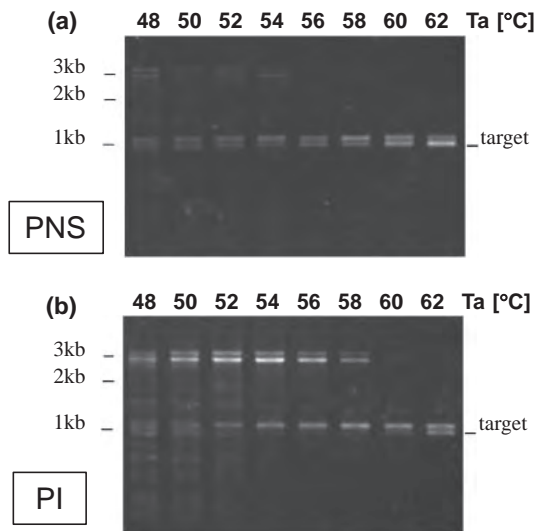


Fig. 7. Images of PCR product observed through agarose gel electrophoresis: (a) our system and (b) commercially available system.

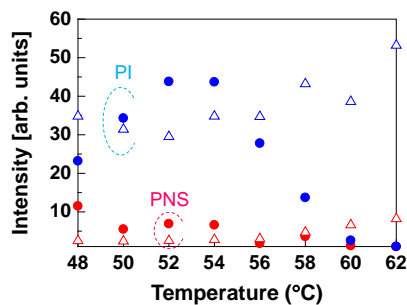


Fig. 8. (Color online) Intensities of DNA bands in Fig. 7 for our device (PNS) and a conventional system (PI).

tional system used in this study and our system, respectively. At any annealing temperature, the intensities for PNS are much weaker than those for PI. In other words, the degree of blur in DNA nonspecific products is outstandingly reduced using our PCR system. The above results demonstrate that the rapid thermal response of our PCR system leads to a smaller amount of nonspecific products than that for the commercially available PCR system; the temperature ramping rate significantly affects the annealing process of DNA. This is because the apparently longer time for annealing process causes primers to be annealed nonspecifically, namely, the primers are mismatched: in other words, for our system, before primers are nonspecifically annealed, the temperature rapidly changes to the desired temperature. We intentionally employed commonly used standard PCR tubes because the experimental results for PCR products can be easily compared between our PCR system and other systems.

Note that greatly superior results are expected when smaller tubes are used. This can be easily achieved since the well block is fabricated in accordance with the size of the tube then is simply sandwiched between the P- and N-type thermoelectric materials. Furthermore, if our PCR system is

linked to a microdevice, such as a microreactor, a portable PCR system with high speed and precision will be realized in the future.

4. Conclusions

Using our novel PCR system with a current-driven PN sandwich structure, it was demonstrated that the thermal response of the system produces a smaller amount of non-specific products for the gDNA of *Arabidopsis thaliana* than that for commercially available PCR systems.

Acknowledgment

This study was partly supported by a JST A-STEP Grant for Exploratory Research.

- 1) D. M. Rowe, *CRC Handbook of Thermoelectrics* (CRC Press, Boca Raton, FL, 1995).
- 2) S. B. Riffat and X. Ma, *Appl. Therm. Eng.* **23**, 913 (2003).
- 3) P. Wilding, M. A. Shoffner, and L. J. Kricka, *Clin. Chem.* **40**, 1815 (1994).
- 4) E. K. Wheeler, W. Benett, P. Stratton, J. Richards, A. Chen, A. Christian, K. D. Ness, J. Ortega, L. G. Li, T. H. Weisgraber, K. Goodson, and F. Milanovich, *Anal. Chem.* **76**, 4011 (2004).
- 5) J. Yang, Y. Liu, C. B. Rauch, R. L. Stevens, R. H. Liu, R. Lenigk, and P. Grodzinski, *Lab Chip* **2**, 179 (2002).
- 6) J. Khandurina, T. E. McKnight, S. C. Jacobson, L. C. Waters, R. S. Foote, and J. M. Ramsey, *Anal. Chem.* **72**, 2995 (2000).
- 7) T. M. Lee and I. M. Hsing, *Anal. Chim. Acta* **556**, 26 (2006).
- 8) M. Hashimoto, P. C. Chen, M. W. Mitchell, D. E. Nikitopoulos, S. Soper, and M. Murphy, *Lab Chip* **4**, 638 (2004).
- 9) P. Belgrader, J. K. Smith, V. W. Weedn, and M. A. Northrup, *J. Forensic Sci.* **43**, 315 (1998).
- 10) E. K. Wheeler, C. A. Hara, J. Frank, J. Deotte, S. B. Hall, W. Benett, C. Spadaccini, and N. R. Beer, *Analyst* **136**, 3707 (2011).
- 11) Y. Fuchiwaki, H. Nagai, M. Saito, and E. Tamiya, *Biosens. Bioelectron.* **27**, 88 (2011).
- 12) H. Tsuchiya, M. Okochi, N. Nagao, M. Shikida, and H. Honda, *Sens. Actuators B* **130**, 583 (2008).
- 13) L. C. Waters, S. C. Jacobson, N. Kroutchinina, J. Khandurina, R. S. Foote, and J. M. Ramsey, *Anal. Chem.* **70**, 5172 (1998).
- 14) Z. Zhao, Z. Cui, D. Cui, and S. Xia, *Sens. Actuators A* **108**, 162 (2003).
- 15) T. M.-H. Lee, M. C. Carlesb, and I.-M. Hsing, *Lab Chip* **3**, 100 (2003).
- 16) P. Liu, T. S. Seo, N. Beyor, K.-J. Shin, J. R. Scherer, and R. A. Mathies, *Anal. Chem.* **79**, 1881 (2007).
- 17) E. T. Lagally, J. R. Scherer, R. G. Blazej, N. M. Toriello, B. A. Diep, M. Ramchandani, G. F. Sensabaugh, L. W. Riley, and R. A. Mathies, *Anal. Chem.* **76**, 3162 (2004).
- 18) D. M. Jenkins, R. Kubota, J. Dong, Y. Li, and D. Higashiguchi, *Biosens. Bioelectron.* **30**, 255 (2011).
- 19) T. M.-H. Lee and I.-M. Hsing, *Anal. Chim. Acta* **556**, 26 (2006).
- 20) N. Park, S. Kim, and J. H. Hahn, *Anal. Chem.* **75**, 6029 (2003).
- 21) S. Yamaguchi, T. Anzai, and A. Yamamoto, *Electrochem. Solid-State Lett.* **11**, H103 (2008).
- 22) T. Anzai and S. Yamaguchi, *J. Micro/Nanolithogr. MEMS MOEMS* **8**, 021115 (2009).
- 23) K. Arakawa and S. Yamaguchi, *ECS Trans.* **25** [33], 75 (2010).
- 24) Y. Okuwaki and S. Yamaguchi, *Adv. Mater. Res.* **254**, 128 (2011).
- 25) *Netsuden Henkan Shisutemu Gijutsu Soran* (The New Edition of Thermoelectric Energy Conversion Systems), ed. T. Kajikawa, S. Sano, and J. Morimoto (Realize Science & Engineering, Tokyo, 2004) [in Japanese].
- 26) T. Suzuki, S. Yamaguchi, Y. Azumi, and K. Inoue, *Sci. J. Kanagawa Univ.* **22**, 83 (2011).
- 27) M. J. McPherson and S. G. Moller, *PCR* (Taylor & Francis, New York, 2006) 2nd ed.
- 28) *PCR applications*, ed. M. A. Innis, D. H. Gelfand, and J. J. Sninsky (Academic Press, London, 1999).

Complete Genome Sequence of the Bacteriochlorophyll *b*-Producing Photosynthetic Bacterium *Blastochloris viridis*

Yusuke Tsukatani,^{a,b} Yuu Hirose,^{c,d} Jiro Harada,^e Naomi Misawa,^d Keita Mori,^a Kazuhito Inoue,^f Hitoshi Tamiaki^g

Earth-Life Science Institute, Tokyo Institute of Technology, Tokyo, Japan^a; PRESTO, Japan Science and Technology Agency, Saitama, Japan^b; Department of Environmental and Life Sciences, Toyohashi University of Technology, Aichi, Japan^c; Electronics Inspired-Interdisciplinary Research Institute (EIRIS), Toyohashi University of Technology, Aichi, Japan^d; Department of Medical Biochemistry, Kurume University School of Medicine, Fukuoka, Japan^e; Department of Biological Sciences, Kanagawa University, Kanagawa, Japan^f; Graduate School of Life Sciences, Ritsumeikan University, Shiga, Japan^g

We report the complete genome sequence of the purple photosynthetic bacterium *Blastochloris viridis* belonging to α -Proteobacteria. This is the first completed genome sequence of a phototroph producing bacteriochlorophyll *b*. The genome information will be useful for further analysis of the photosynthetic energy conversion system and bacteriochlorophyll pigment biosynthesis.

Received 24 July 2015 Accepted 25 July 2015 Published 3 September 2015

Citation Tsukatani Y, Hirose Y, Harada J, Misawa N, Mori K, Inoue K, Tamiaki H. 2015. Complete genome sequence of the bacteriochlorophyll *b*-producing photosynthetic bacterium *Blastochloris viridis*. *Genome Announc* 3(5):e01006-15. doi:10.1128/genomeA.01006-15.

Copyright © 2015 Tsukatani et al. This is an open-access article distributed under the terms of the [Creative Commons Attribution 3.0 Unported license](https://creativecommons.org/licenses/by/3.0/).

Address correspondence to Yusuke Tsukatani, tsukatani@elsi.jp.

Blastochloris viridis is a member of anoxygenic phototrophic bacteria in the phylum *Proteobacteria* (α -2 subclass) (1, 2), which are often called “purple bacteria.” This bacterium is unique because it produces bacteriochlorophyll (BChl) *b* which has an absorption maximum in the near-infrared light region (3, 4), whereas most isolated purple bacteria produce BChl *a* (5, 6). Photochemical reaction center complexes of *B. viridis* were the target proteins for the study revealing the first crystal structure of membrane protein complexes (7), and three of the authors won the Nobel Prize in Chemistry in 1988. In 2004, we sequenced the photosynthetic gene cluster of *B. viridis* using an inverse PCR and Sanger method, and some genes in the cluster have already been deposited at GenBank (accession no. AB738834). For the better understanding of photosynthetic processes based on BChl *b* and the biosynthetic pathways of the pigment, we determined the complete genome sequence of *B. viridis* DSM 133 (1).

Genome sequencing was performed using the MiSeq system (Illumina). An 800-bp paired-end library and an 8-kbp mate-pair library were prepared using the TruSeq DNA PCR-free sample preparation kit (Illumina) and Nextera mate-pair sample preparation kit (Illumina), respectively. The libraries were sequenced with the MiSeq Reagent kit v3 (600-cycles; Illumina). The reads were filtered using ShortReadManager based on 17-mer frequency (8). A total of 198-Mbp paired-end reads and 218-Mbp mate-pair reads were assembled using Newbler version 2.9 (Roche), yielding 1 scaffold and 58 large contigs (>1 kbp). Gap sequences between the contigs were determined *in silico* using GenoFinisher and AceFileViewer (8), followed by PCR and Sanger sequencing. We succeeded in determining the complete genome sequence of *B. viridis* strain DSM 133, which comprises one circular chromosome of 3,861,362 bp. The G+C content of the genome was calculated to be 67%. Gene prediction and functional annotation were carried out with Rapid Annotations using Subsystems Technology (RAST)

(9), revealing 3,576 protein-coding genes, 9 rRNAs, and 47 tRNAs.

Most of the genes related to photosynthetic activities were clustered in a region on the genome forming the so-called photosynthetic gene cluster (PGC) (10). The PGC of *B. viridis* includes genes for photochemical reaction center complexes (*pufLMC* and *pufH*), light-harvesting proteins (*pufBA*), bacteriochlorophyll biosynthesis (*bchPGFNBHLMIDCXYZ*), and carotenoid biosynthesis (*crtIBE*). A characteristic of the PGC of this organism is the presence of genes for carbon fixation in the middle of PGC. The *bchE* and *bchJ* genes are known to be involved in bacteriochlorophyll biosynthesis (11, 12), but are not located in PGC. As we already reported using the draft genome sequence (4), the *bciA* gene encoding divinyl-chlorophyllide reductase found in BChl *a*-producing purple bacteria are missing in the genome of *B. viridis*. This genome information will contribute to our understanding of bacteriochlorophyll biosynthetic pathways and photosynthetic apparatuses in *B. viridis*.

Nucleotide sequence accession number. The complete genome sequence of *B. viridis* DSM 133 has been deposited at the DNA Data Bank of Japan (DDBJ) under accession number [AP014854](https://www.ncbi.nlm.nih.gov/nuccore/AP014854).

ACKNOWLEDGMENTS

This work was partially supported by Grants-in-Aid for Young Scientists (B) (26840099 to Y.T.) and Scientific Research (C) (15K05577 to J.H.) as well as on Innovative Areas “Artificial Photosynthesis (AnApple)” (24107002 to H.T. and 24107004 to K.I.) from the Japan Society for the Promotion of Science (JSPS). Y.T. is supported by a PRESTO (Precursory Research for Embryonic Science and Technology) fellowship from the Japan Science and Technology Agency (JST).

REFERENCES

1. Drews G, Giesbrecht P. 1966. *Rhodospseudomonas viridis*, nov. spec., ein neu isoliertes, obligat phototrophes Bakterium. *Arch Microbiol* 53: 255–262.
2. Hiraishi A. 1997. Transfer of the bacteriochlorophyll *b*-containing pho-

- trophic bacteria *Rhodospseudomonas viridis* and *Rhodospseudomonas sulfoviridis* to the genus *Blastochloris* gen. nov. *Int J Syst Bacteriol* 47:217–219. <http://dx.doi.org/10.1099/00207713-47-1-217>.
3. Jay F, Lambillotte M, Stark W, Mühlethaler K. 1984. The preparation and characterisation of native photoreceptor units from the thylakoids of *Rhodospseudomonas viridis*. *EMBO J* 3:773–776.
 4. Tsukatani Y, Yamamoto H, Harada J, Yoshitomi T, Nomata J, Kasahara M, Mizoguchi T, Fujita Y, Tamiaki H. 2013. An unexpectedly branched biosynthetic pathway for bacteriochlorophyll *b* capable of absorbing near-infrared light. *Sci Rep* 3:1217. <http://dx.doi.org/10.1038/srep01217>.
 5. Stomp M, Huisman J, Stal LJ, Matthijs HCP. 2007. Colorful niches of phototrophic microorganisms shaped by vibrations of the water molecule. *ISME J* 1:271–282. <http://dx.doi.org/10.1038/ismej.2007.59>.
 6. Mizoguchi T, Harada J, Tamiaki H. 2006. Structural determination of dihydro- and tetrahydrogeranylgeranyl groups at the 17-propionate of bacteriochlorophylls-*a*. *FEBS Lett* 580:6644–6648. <http://dx.doi.org/10.1016/j.febslet.2006.11.020>.
 7. Deisenhofer J, Epp O, Miki K, Huber R, Michel H. 1985. Structure of the protein subunits in the photosynthetic reaction centre of *Rhodospseudomonas viridis* at 3Å resolution. *Nature* 318:618–624. <http://dx.doi.org/10.1038/318618a0>.
 8. Ohtsubo Y, Maruyama F, Mitsui H, Nagata Y, Tsuda M. 2012. Complete genome sequence of *Acidovorax* sp. strain kks102, a polychlorinated-biphenyl degrader. *J Bacteriol* 194:6970–6971. <http://dx.doi.org/10.1128/JB.01848-12>.
 9. Overbeek R, Olson R, Pusch GD, Olsen GJ, Davis JJ, Disz T, Edwards RA, Gerdes S, Parrello B, Shukla M, Vonstein V, Wattam AR, Xia F, Stevens R. 2014. The SEED and the Rapid Annotation of microbial genomes using Subsystems Technology (RAST). *Nucleic Acids Res* 42:D206–D214. <http://dx.doi.org/10.1093/nar/gkt1226>.
 10. Alberti M, Burke DH, Hearst JE. 1995. Structure and sequence of the photosynthesis gene cluster, p 1083–1106. *In* Blankenship RE, Madigan MT, Bauer CE (ed), Anoxygenic photosynthetic bacteria. Kluwer Publishers, Dordrecht, The Netherlands.
 11. Chew AGM, Bryant DA. 2007. Chlorophyll biosynthesis in bacteria: the origins of structural and functional diversity. *Annu Rev Microbiol* 61:113–129. <http://dx.doi.org/10.1146/annurev.micro.61.080706.093242>.
 12. Tsukatani Y, Harada J, Nomata J, Yamamoto H, Fujita Y, Mizoguchi T, Tamiaki H. 2015. *Rhodobacter sphaeroides* mutants overexpressing chlorophyllide *a* oxidoreductase of *Blastochloris viridis* elucidate functions of enzymes in late bacteriochlorophyll biosynthetic pathways. *Sci Rep* 5:9741. <http://dx.doi.org/10.1038/srep09741>.

Involvement of thioredoxin on the scaffold activity of NifU in heterocyst cells of the diazotrophic cyanobacterium *Anabaena* sp. strain PCC 7120

Received March 2, 2015; accepted April 17, 2015; published online May 6, 2015

Jiro Nomata^{1,2,*}, Maki Maeda^{1,*}, Atsuko Iisu^{1,2}, Kazuhito Inoue³ and Toru Hisabori^{1,2,†}

¹Chemical Resources Laboratory, Tokyo Institute of Technology, Nagatsuta 4259, Midori-ku, Yokohama 226-8503, Japan; ²Core Research for Evolutional Science and Technology (CREST), Japan Science and Technology Agency (JST), Chiyoda-Ku, Tokyo 102-0076, Japan; and ³Department of Biological Sciences, Kanagawa University, Tsuchiya 2946, Hiratsuka, Kanagawa 259-1293, Japan

*These authors contributed equally to this work.

†Toru Hisabori, Chemical Resources Laboratory, Tokyo Institute of Technology, Nagatsuta 4259-R1-8, Midori-ku, Yokohama 226-8503, Japan. Tel: 81-45-924-5234, Fax: 81-45-924-5268, email: thisabor@res.titech.ac.jp

The diazotrophic cyanobacterium *Anabaena* sp. strain PCC 7120 (A.7120) differentiates into specialized heterocyst cells that fix nitrogen under nitrogen starvation conditions. Although reducing equivalents are essential for nitrogen fixation, little is known about redox systems in heterocyst cells. In this study, we investigated thioredoxin (Trx) networks in *Anabaena* using TrxM, and identified 16 and 38 candidate target proteins in heterocysts and vegetative cells, respectively, by Trx affinity chromatography (Motohashi *et al.* (Comprehensive survey of proteins targeted by chloroplast thioredoxin. *Proc Natl Acad Sci USA*, 2001;98, 11224–11229)). Among these, the Fe–S cluster scaffold protein NifU that facilitates functional expression of nitrogenase in heterocysts was found to be a potential TrxM target. Subsequently, we observed that the scaffold activity of N-terminal catalytic domain of NifU is enhanced in the presence of Trx-system, suggesting that TrxM is involved in the Fe–S cluster biogenesis.

Keywords: cyanobacteria/heterocyst/nitrogen fixation/redox regulation/thioredoxin.

Abbreviations: DTT, dithiothreitol; GSH, glutathione; GSSG, oxidized glutathione; MALDI-TOF MS, matrix-assisted laser desorption ionization time-of-flight mass; NTR, NADPH-thioredoxin reductase; PEO, maleimide-PEG11-Biotin; PMF, peptide mass fingerprint; RbcL, ribulose-1,5-bisphosphatase large precursor; SDS–PAGE, sodium dodecyl sulphate–polyacrylamide gel electrophoresis; TCA, tricarboxylic acid; Trx, thioredoxin.

Thioredoxin (Trx) is a ubiquitous redox protein that contributes to a number of physiological processes by controlling target enzyme activities and supplying

reducing equivalents to anti-oxidative stress proteins. The dithiol/disulphide exchange active site of Trx bears the sequence motif ‘WCGPC’ and was originally characterized by Holmgren *et al.* (1). Subsequently, the molecular mechanism for reduction of target proteins by Trx was elucidated (2). In 2001, Motohashi *et al.* developed a Trx affinity chromatography (3, 4) to capture potential Trx-targeted proteins by immobilizing mutant Trx containing the substituted motif WCGPS on chromatographic resin. The absence of the second cysteine results in suspension of the dithiol/disulphide exchange reaction at the mixed disulphide intermediate, allowing capture of Trx-targeted proteins on the resin. Following biochemical studies revealed that enzymatic activities of various metabolic enzymes are actually regulated by Trx through the reduction of disulphide bond in the enzyme in plant cells, chloroplasts, mitochondria and bacteria (5–9).

The filamentous cyanobacterium *Anabaena* sp. strain PCC 7120 (A.7120) has an ability for nitrogen fixation by forming specialized heterocysts under nitrogen starvation conditions, and is often used in studies on cell differentiation as a model (10). Heterocysts are terminally differentiated cells that contribute to microoxic environments, which are necessary for the function of nitrogen-fixing enzyme, nitrogenase. Differentiation of heterocysts from vegetative cells is established by a number of morphological and biochemical changes, including the disassembly of photosystem II, biosynthesis of glycolipid or polysaccharide for formation of specialized envelopes and enhancement of oxidase activity to protect nitrogenase from oxygen (11, 12).

The A.7120 genome encodes eight Trxs (*alr0052*, *all1866*, *all2367*, *alr2341*, *alr3955*, *all1893*, *asl7641* and *alr2205*), two NADPH-dependent Trx reductases (*all0737* and *alr2204*) and two ferredoxin-dependent Trx reductases (*alr4065* and *asl2469*). Based on sequence homology and the presence of conserved sequences, Trx genes have been classified into four distinct types: TrxM (*alr0052* and *all1866*), TrxX (*alr2341*), TrxY (*all1893*) and TrxZ (*alr3955*), which exclude *asl7641* and *alr2205* (13). However, few reports demonstrate interactions between Trx and its binding partners in A.7120 cells. Gleason *et al.* (14) demonstrated that glucose-6-phosphate dehydrogenase, which catalyses the first reaction in the oxidative pentose phosphate pathway, was reductively inactivated by TrxM (*Alr0052*) or TrxX (*Alr2341*). More recently, Ehira and Ohmori (15) reported that TrxM (*All1866*) reduces intramolecular disulphide bonds and restores DNA-binding activity of the transcriptional regulator RexT (*Alr1867*). However, the Trx system in A.7120 cells remains uncharacterized, and direct capture of

Trx target proteins in A.7120 cells has been rarely attempted. In this study, we used Trx affinity chromatography to comprehensively investigate TrxM target proteins in vegetative cells and heterocysts from A.7120, and revealed 54 potential target proteins including proteins involved in nitrogen fixation. Within them, we focused on the heterocyst-specific Fe–S cluster scaffold protein NifU, which plays an important role in the maturation of nitrogenase, the key enzyme for nitrogen fixation. NifU is composed of three distinct domains, N-terminal catalytic domain which is highly homologous to IscU and contains three conserved cysteines critical to provide a scaffold activity, the central domain containing four conserved cysteines which coordinate one redox-active [2Fe-2S] cluster (16). In addition, C-terminal domain contains two conserved cysteines and possibly provides a second transient cluster assembly site. Then we studied the interaction between the N-terminal catalytic domain of NifU (NifU1) and TrxM, and showed that Trx-system is required to maintain the scaffold activity of NifU1. Our results indicate heterocyst-specific role of TrxM.

Materials and Methods

Cloning, expression and purification of TrxM and its variants

The coding region of *trxM* (*alr0052*) was amplified from A.7120 genomic DNA using polymerase chain reaction (PCR) with the primers *alr0052*-Nd-fl (*5'*-ATCATATGTCAGCAGCCGCACAAGT TACAG-3') and *alr0052*-Xh-r1 (*5'*-ATCTCGAGTTACAGATGC TTTTCTAGGG-3') or *pAsk3*-*Alr0052*-fl (*5'*-AAAGGTGGTCTC TAATGTCAGCAGCCGCACAAGTTAC-3') and *pAsk3*-*Alr0052*-fl (*5'*-TTACTAGGTCTCCGCGCTTACAGATGCTTTT CTAGGG-3'). Restriction sites are underlined. Amplified DNA fragments were cloned into the *Nde*I and *Xho*I sites of pET23c (Novagen) or into the *Bsa*I site of *pAsk*-IBA3⁺ to produce recombinant proteins with C-terminal 6 × histidine tag or Strep-tag II, respectively. The DNA sequences of the resulting plasmids were confirmed by DNA sequencing (Prism 3100, Applied Biosystems). The plasmids pET23c-*TrxM* and *pAsk3*-*TrxM* were then transformed into the *Escherichia coli* BL21 (DE3) expression host and the proteins were overexpressed.

Harvested cells overexpressing 6 × His-tagged *TrxM* were suspended in 25 mM HEPES–KOH (pH 7.5) and were disrupted by sonication. After centrifugation at 118,000 × *g* for 1 h, supernatants were loaded onto a Ni-NTA Sepharose column (10 ml of Ni-NTA Sepharose, QIAGEN) that had been equilibrated with wash buffer containing 25 mM HEPES–KOH (pH 7.5) and 20 mM imidazole. After washing, 6 × His-tagged *TrxM* was eluted from the column using a wash buffer containing 25 mM HEPES–KOH (pH 7.5) and 100–200 mM imidazole. The protein solution was applied to a Butyl-Toyopeal column (40 ml; TOSOH, Japan), which had been equilibrated with a solution containing 1.5 M ammonium sulphate, 25 mM HEPES–KOH (pH 7.5) and 2.5 mM ethylenediaminetetraacetic acid (EDTA). The protein was eluted from the column using a 1.5–0 M inverse gradient of ammonium sulphate. Fractions containing proteins of interest were collected, and proteins were confirmed using sodium dodecyl sulphate–polyacrylamide gel electrophoresis (SDS–PAGE).

Harvested cells overexpressing *TrxM* with Strep-tagII were suspended in a solution containing 100 mM HEPES–KOH (pH 8.0), 150 mM NaCl, 5 mM EDTA and 5 mM dithiothreitol (DTT) and were disrupted by sonication. After centrifugation at 118,000 × *g* for 1 h, supernatants were loaded onto a Strep-Tactin Sepharose column (4 ml of Strep-Tactin Sepharose; IBA, Germany) that had been equilibrated with wash buffer containing 100 mM HEPES–KOH (pH 8.0) and 150 mM NaCl. The column was washed with 40 ml of wash buffer and Strep-tagged proteins were then eluted using wash buffer containing 1.0 mM desthiobiotin.

Protein concentrations were determined using the BCA method (Protein Assay; Bio-Rad) using bovine serum albumin as a standard.

Preparation of the Trx mutant

The *TrxM* mutant plasmids *TrxM*-C35S and *TrxM*-C32S/C35S were generated with WCGPS and WSGPS mutations in active site sequences, respectively, using pET23c-*TrxM* as a template. Mutations were performed using PCR with the primers *TrxM*-C35S-f (*5'*-CTTGGTGTGGTCTCCAGA-3') and *TrxM*-C35S-r (*5'*-TCTGGAAGGACCACACCAAG-3') for the *TrxM*-C35S mutant, or *TrxM*-C32S/C35S-f (*5'*-CTTGGTCCGGTCTCTCCAGA-3') and *TrxM*-C32S/C35S-r (*5'*-TCTGGAAGGACC GGACCAAG-3') for the *TrxM*-C32S/C35S mutant. Introduced nucleotide substitutions are underlined. The mutant protein was expressed in *E. coli* and was purified by the method used for the wild-type *TrxM*.

Cloning, expression and purification of NADPH-thioredoxin reductase, IscS and NifU1

The coding region of NADPH-*Trx* reductase (NTR) from *E. coli*, the coding region of cysteine desulfurase (IscS) from *Azotobacter vinelandii*, and the N-terminus region of the NifU (NifU1) from A.7120 were amplified using PCR with the following combinations of primers: *Ask3*-*EcNTR*-fl (*5'*-ACTATGGGTCTCTAATGGGC ACGACCAACACAGTAAAC-3') and *Ask3*-*EcNTR*-r1 (*5'*-TAC TGAGGTCTCAGCGCTTTTTCGTCAGCTAAACATCG-3') for NTR; *AvIscS*-Nd-fl (*5'*-AGAGACATATGAAGTTGCCGATT TATCTGG-3') and *AvIscS*-Xh-r1 (*5'*-GAAGGCTCGAGGTGGG CCTGCCACTCGATC-3') for IscS; and *Ask3*-*AnNifU*-fl (*5'*-ACT CGGGTCTCTAATGTGGGACTACACAGATAAAG-3') and *Ask3*-*NifU*-Nter-r1 (*5'*-GAAGCAGGTCTCTGCGCTACCTTCG TCATCTTC-3') for NifU1. Restriction sites are underlined. The amplified DNA fragment encoding IscS was then cloned into *Nde*I and *Xho*I sites of pET-23a (Novagen), and the fragments encoding NTR and NifU were cloned into the *Bsa*I site of *pAsk*-IBA3⁺ (IBA, Germany). After confirmation of DNA sequences, the plasmids *pAsk3*-*EcNTR*, pET23a-*AvIscS* and *pAsk3*-*NifU1* were transformed into the expression host *E. coli* BL21 (DE3) and the proteins were overexpressed.

Harvested cells overexpressing 6 × His-tagged IscS were suspended in buffer containing 100 mM Tris-HCl (pH 8.0) and 150 mM NaCl and were disrupted by sonication. After centrifugation at 118,000 × *g* for 1 h, supernatants were loaded onto a Ni-NTA Sepharose column (5 ml of Ni-NTA Sepharose, QIAGEN) that had been equilibrated with wash buffer containing 100 mM Tris-HCl (pH 8.0), 150 mM NaCl and 20 mM imidazole. After washing with 100 ml of the wash buffer, 6 × His-tagged IscS was eluted from the column with elution buffer containing 100 mM Tris-HCl (pH 8.0), 150 mM NaCl and 100 mM imidazole.

Strep-tagged NTR and NifU1 were purified using the same method used for strep-tagged *TrxM*. After isolation, NifU1 was incubated with a 10-fold excess of dithionite and a 40-fold excess of EDTA for 30 min to remove transient Fe–S clusters and adventitiously-bound iron. Excess dithionite and EDTA were removed using an Amicon ultra centrifugal filter unit 10K (Merck-Millipore, Germany). Prior to use in IscS-mediated cluster assembly experiments, samples were oxidized with 5 mM oxidized glutathione (GSSG), and were again desalted to remove GSSG using the Amicon ultra centrifugal filter unit (Merck-Millipore).

Preparation of the Trx-immobilized resin

The *TrxM*-C35S mutant was incubated with cyanogen bromide-activated Sepharose 4B in 100 mM sodium carbonate buffer (pH 8.3) containing 500 mM NaCl according to the manufacturer's instructions. After termination of the coupling reaction, unreacted side chains on the resin were blocked by incubation with 100 mM Tris-HCl (pH 8.0) for 12 h at 4°C. *Trx*-immobilized resin was incubated with 100 mM Tris-HCl (pH 8.0) containing 10 mM DTT for 30 min, and was then washed with 100 mM sodium carbonate buffer (pH 8.3) containing 500 mM NaCl. The amounts of immobilized *Trx* on the gel were calculated as the difference between that added and that remaining in solution after the coupling reaction.

Preparation of cytosolic fraction from A. 7120 vegetative cells

A.7120 cultures were photo-autotrophically grown at 31°C under continuous illumination with white light at an intensity of 30 μmol

photons $m^{-2} s^{-1}$. BG11 growth medium was supplemented with 1 g/l $NaHCO_3$ and was bubbled with 1% (v/v) CO_2 in air. Cells at an optical density of 0.6–0.8 at 730 nm were harvested and suspended in a buffer containing 50 mM Tris-HCl (pH 8.0), 100 mM EDTA (pH 8.0) and lysozyme (1 mg/ml) and were incubated for 1 h at room temperature. Cells were then disrupted by sonication and unbroken cells were pelleted by centrifugation at $5,000 \times g$ for 10 min. Collected unbroken cells were again disrupted by sonication and cell debris was removed by centrifugation at $118,000 \times g$ for 1 h, yielding a supernatant containing vegetative cytosolic proteins.

Isolation and preparation of cytosolic fraction from *A. 7120* heterocyst cells

A. 7120 cultures were grown as described above. Cells at an optical density of 0.3–0.5 at 730 nm were harvested and resuspended into the BG11 medium without combined nitrogen sources. After 48 h, cells were harvested and suspended in a buffer containing 50 mM Tris-HCl (pH 8.0), 50 mM EDTA (pH 8.0) and 8% sucrose (SET buffer) with lysozyme (1 mg/ml) and were incubated for 1 h at 35°C. Vegetative cells were disrupted by sonication and remained heterocyst cells were pelleted by centrifugation at $3,000 \times g$ for 5 min. After washing with SET buffer, heterocyst cells were washed two times with 25 mM HEPES-NaOH (pH 7.5) and were lysed using a French pressure cell (Ohtake, Tokyo) in the same buffer. Cell debris was removed by centrifugation at $118,000 \times g$ for 1 h, yielding a supernatant containing heterocyst cytosolic proteins.

Immunoblotting

Heterocyst purity was initially estimated using optical microscopy. Because heterocysts contain very little Rubisco (17, 18), purity was confirmed using immunoblotting with an anti-ribulose-1,5-bisphosphatase large precursor (RbcL) antibody.

Isolation of Trx target proteins

Cytosolic fractions from vegetative cells or heterocysts contained 55 mg of proteins, and were incubated with 2 ml of Trx-immobilized resin (a total of 5 mg of TrxM was immobilized) for 1 h. The resin was completely washed as previously described (Motohashi *et al.* (3)), and the resin incubated with vegetative cell lysates was washed with SDS-free buffer. The resin was then suspended in a solution containing 50 mM Tris-HCl (pH 7.5), 200 mM NaCl and 10 mM DTT, and was incubated for 30 min at 25°C with gentle stirring. The eluted proteins were then fractionated from the resin by centrifugation.

Protein identification

Eluted proteins were separated using two-dimensional (2D) SDS-PAGE with IPG strips (Bio-Rad, pH 3–10) and 15% (w/v) polyacrylamide gels for the second dimension. Separated protein bands were visualized by Coomassie brilliant blue (CBB) staining. Protein spots were then excised from the gel, were in-gel digested with trypsin, and were extracted as previously described (9). The resulting peptides were desalted using a ZipTipC18 pipette (Merck-MilliPore, Germany) and were analysed using matrix-assisted laser desorption ionization time-of-flight mass (MALDI-TOF MS) spectrometry (AXIMA-CFR, SHIMADZU, Japan). Proteins were identified using the MASCOT peptide mass fingerprint (PMF) search engine (Matrix Science, London, UK) with a monoisotopic peptide mass tolerance of 0.2 Da, a peptide charge state of 1+, and a maximum of 1 missed cleavage.

Trx-dependent reduction of NifU1

Oxidized NifU1 was incubated with ascorbate, glutathione (GSH), or the combination of NTR, NADPH and TrxM as indicated in the figure legends. The redox states of NifU1 protein were then determined as follows. The protein was precipitated with 10% (w/v) trichloroacetic acid and was collected by centrifugation. Protein precipitates were then washed with prechilled ethanol and were dissolved in a freshly prepared solution containing 1% (w/v) SDS, 50 mM Tris-HCl (pH 7.5) and 5 mM maleimide-PEG11-Biotin (PEO). Labelled proteins were then separated using SDS-PAGE with 12% (w/v) polyacrylamide gel. Protein bands were visualized by CBB staining.

Trx-associated Fe-S cluster assembly on NifU

All procedures for the cluster assembly study were performed under anaerobic conditions (<1 ppm O_2) in an anaerobic chamber (model A; Coy Laboratory Products). The cluster assembly reaction mixture is composed of 90–125 μ M oxidized-NifU1, 0.63 μ M IscS, 1 mM L-cysteine, 1 mM Fe^{2+} , 1.4 μ M TrxM, 1.4 μ M NTR and 1.4 mM NADPH. Assays were initiated by addition of IscS and were performed at 25°C for 2.5 h. To monitor changes in absorption of the NifU1 reaction mixture, the assay mixture was prepared in a cuvette with an air-tight screw cap in the anaerobic chamber, and absorption spectra were recorded using a JASCO V-550 spectrophotometer (JASCO, Japan). After incubation, NifU1 was repurified using Strep-Tactin Sepharose as described above. The iron content of repurified NifU1 was determined using a metallo assay kit Fe (Metallogenics, Japan).

Results

Preparation of heterocyst extracts.

To identify potential Trx targets in heterocysts, intact heterocysts were isolated from *A. 7120*. Phycobiliprotein degradation is increased during heterocyst differentiation (19). A decrease of absorption at 620 nm is therefore a good indicator of the purity of the heterocysts (Fig. 1A). Because heterocysts contain very low levels of Rubisco proteins, heterocyst cell purity was also assessed using western blotting analyses of the Rubisco large subunit (RbcL) (17, 18). Although RbcL was detected in cell lysate of vegetative cells, no band was observed in the isolated heterocyst fraction (Fig. 1B).

Trx affinity chromatography and identification of possible Trx target proteins

To identify potential cytosolic target proteins of TrxM in vegetative cells and heterocysts, Trx affinity chromatography using TrxM-C35S was examined (3). After the chromatography, captured proteins were analysed using conventional SDS-PAGE (Fig. 2) and 2D gel electrophoresis (Fig. 3). A TrxM-C32S/C35S double mutant, in which both cysteine residues were substituted with serine, was used as a negative control. SDS-PAGE profiles of DTT-eluted fractions (Fig. 2A) showed multiple-specific bands of possible TrxM target proteins when heterocyst lysates were used. In contrast, the profile of eluted fractions from vegetative cell lysates showed more various target candidate proteins (Fig. 2B). Protein spots were excised from 2D SDS-PAGE gels, and trypsin-mediated in-gel digestion was performed. The obtained peptides were then analysed using PMF analyses with MALDI-TOF MS spectroscopy. Among proteins captured by the immobilized TrxM mutant, 16 and 38 cytosolic proteins were identified from heterocyst and vegetative cell lysates, respectively (Tables I and II). These were then classified as (i) nitrogen fixation (3 proteins), (ii) glycolytic pathway (3 proteins), (iii) tricarboxylic acid (TCA) cycle (5 proteins), (iv) nitrogen assimilation (2 proteins), (v) protein synthesis and folding (10 proteins), (vi) antioxidant (3 proteins), (vii) sulphur metabolism (1 protein), (viii) amino acid metabolism (3 proteins), (ix) CO_2 fixation (1 protein), (x) light-harvesting (5 proteins) and (xi) hypothetical (15 proteins) proteins. Although five phycobiliproteins were captured from vegetative cell lysates, their

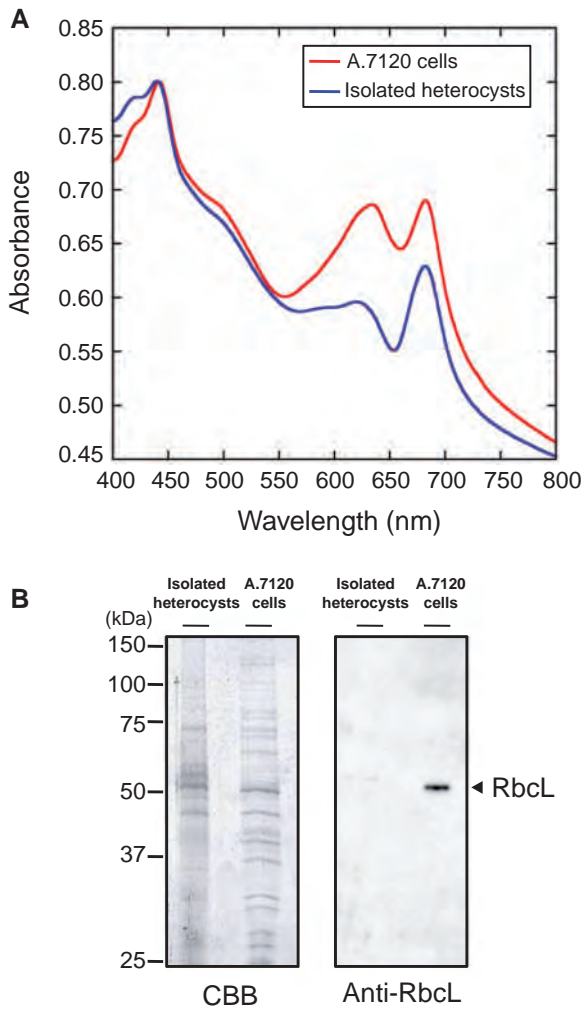


Fig. 1 Isolation of heterocysts from A.7120. (A) Absorption spectra of A.7120 cells and isolated heterocyst as indicated; vegetative cells were disrupted by sonication and heterocysts were isolated by centrifugation. (B) Immuno-blotting validation of heterocysts; Rubisco subunit RbcL was used as the indicative marker protein.

interaction with Trx should be further investigated as they were captured by TrxM-C32S/C35S double mutant immobilized resin as well (Fig. 2B).

Trx-dependent reduction of the N-terminal catalytic domain of NifU

As shown in Table I, the nitrogenase-maturing protein NifU, was identified as a possible target of TrxM (Table I). As a scaffold protein, NifU is involved in the assembly of Fe–S clusters, and activates Fe and MoFe proteins by providing [4Fe–4S] clusters or Fe–S cluster precursors (20, 21). Although no published reports describe interaction between Trx and NifU so far, their interaction is worth to be elucidated judging from the significance of reducing equivalents for NifU function. Thus, to confirm the interaction between NifU and TrxM in A.7120, recombinant NifU was expressed in *E. coli* and protein–protein interaction was examined *in vitro*. However, these analyses were complicated by the labile [2Fe–2S] cluster in the central domain of NifU, which is bound to cysteine residues that are exposed as free thiols during degradation of the

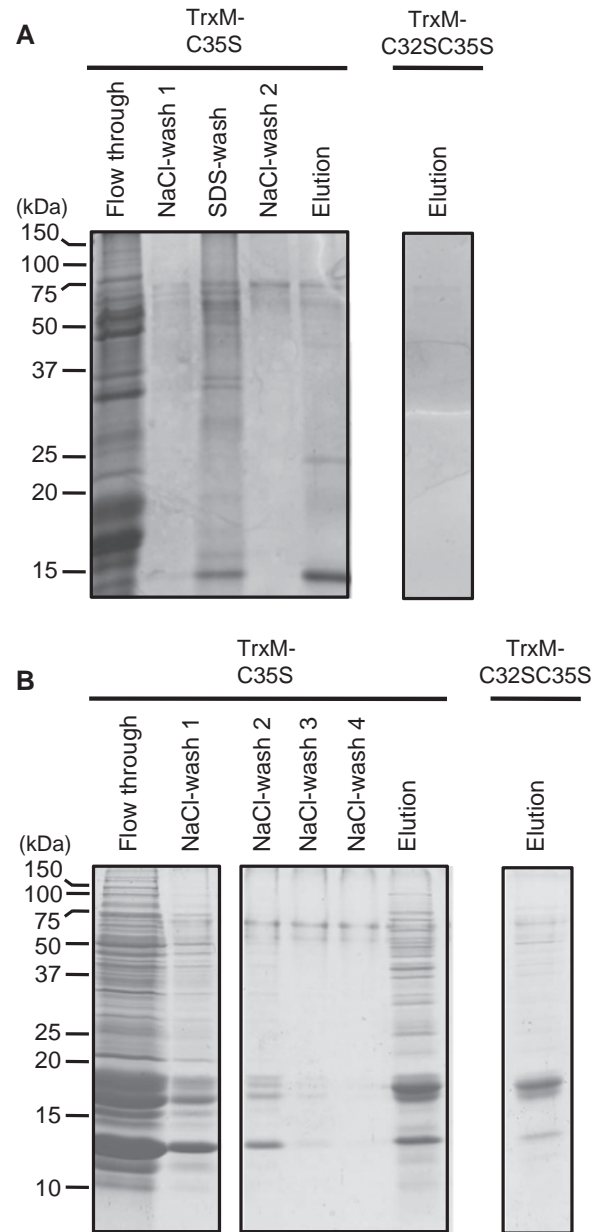


Fig. 2 SDS-PAGE profiles of proteins eluted from Trx affinity chromatography. A.7120 TrxM target proteins were isolated from heterocysts (A) and vegetative cells (B) with TrxM-C35S immobilized on resin. Unbound proteins (Flow throw), proteins eluted with buffer containing 200 mM NaCl (NaCl wash) or 0.1% SDS (SDS wash), and TrxM-C35S-bound proteins that were eluted in buffer containing 10 mM DTT (Elution) were electrophoresed on 12% polyacrylamide gel and were stained with CBB. To check for non-specifically bound proteins, the cysteine-free mutant TrxM-C32S/C35S was used as a control.

cluster. Thus, the N-terminal catalytic domain of NifU was expressed and isolated from *E. coli* with a C-terminal Strept-tag II (first 141 residues; NifU1). Interactions of NifU1 with TrxM were confirmed by biochemical analyses. Because NifU1 contains three catalytic cysteine residues (Cys⁴¹, Cys⁶⁸ and Cys¹¹²) as mentioned, the redox state of NifU1 was initially determined by SDS-PAGE mobility shifts after modification with the thiol-binding maleimide compound, PEO (Fig. 4A). Under these conditions, disulphide bonds within the NifU1 molecule were reduced in the

presence of TrxM, NADPH-Trx-reductase from *E. coli* (NTR), and NADPH but were not reduced in the absence of one of these components (Fig. 4A). Additions of reduced GSH or ascorbate did not

significantly affect the reduction of NifU1. In addition, the PEO-labelling study indicated that oxidized NifU1 forms intermolecular disulphide bond(s). To confirm the intermolecular disulphide bond formation and resulted NifU1-dimer, CuCl₂- or GSSG-oxidized NifU1 was analyzed by non-reducing SDS-PAGE (Fig. 4B, ox). Subsequently, the oxidized NifU1 was treated with 2-mercaptoethanol and separated by non-reducing SDS-PAGE (Fig. 4B, red). Oxidized and re-reduced NifU1 showed the apparent molecular mass of 36 and 17 kDa, respectively.

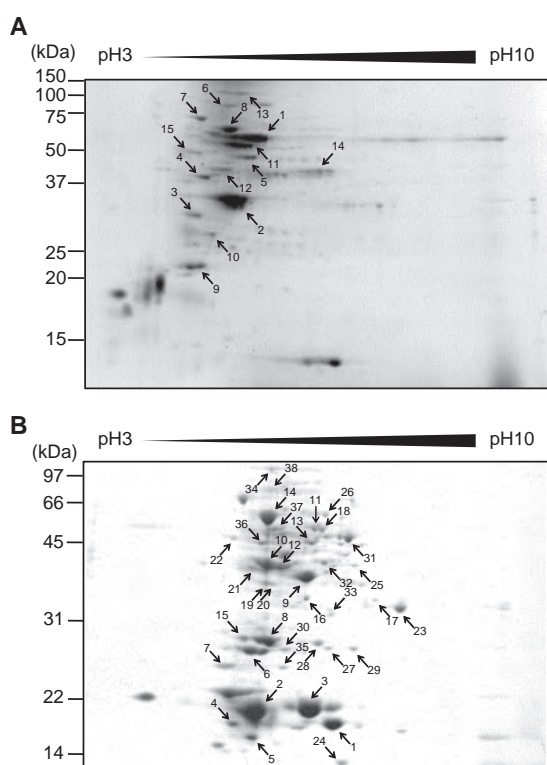


Fig. 3 2D-SDS-PAGE of proteins captured using TrxM-C35S immobilized resin. Proteins captured from heterocysts (A) and vegetative cells (B) were separated by 2D-SDS-PAGE and were identified using PMF analysis and MALDI-TOF MS spectroscopy. Identified proteins are numbered and presented in Tables I and II.

Table I. TrxM target candidates identified by PMF analysis followed by MALDI-TOF MS spectroscopy in A.7120 heterocysts

Category	Spot No. ^a	ORF	Annotation	MW	No. of cyst	No. of peptide matched	Sequence coverage (%)
Nitrogen fixation	1	all1440	Nitrogenase molybdenum-iron protein beta chain NifK	57,851	6	27	47
	2	all1455	Nitrogenase iron protein NifH	32,574	5	12	40
	3	all1456	Nitrogen fixation protein NifU	32,625	9	15	54
Glycolytic pathway	12	all3538	Enolase	45,994	1	11	42
TCA cycle	13	all1267	Aconitate dehydratase	95,217	11	24	29
	14	alr0222	Citrate synthase	43,078	3	17	39
Nitrogen assimilation	11	alr2328	Glutamate ammonia ligase	53,314	6	16	28
Protein synthesis and folding	4	all4191	RNA polymerase alpha subunit	35,165	2	6	26
	5	all4337	Translation elongation factor EF-Tu	44,840	1	16	41
	6	all4338	Translation elongation factor EF-G	76,268	3	17	26
	7	alr1742	DnaK-type molecular chaperone	68,037	3	7	13
	8	alr3662	Chaperonin GroEL	57,973	1	28	51
Anti-oxidative stress system	10	all3822	Two-component response regulator ycf27	27,134	1	13	49
	9	alr4641	Peroxiredoxin	22,731	2	7	55
Other/hypothetical	6 ^b	all4396	Polyribonucleotide nucleotidyltransferase	77,856	2	20	34
	15	alr4550	Hypothetical protein	60,658	2	15	35

^aSpot numbers correspond to those presented in Fig. 3A.

^bTwo proteins were identified from spot 6 presented in Fig. 3A.

Table II. TrxM target candidates identified by PMF analysis followed by MALDI–TOF MS spectroscopy in A.7120 vegetative cells

Category	Spot No. ^a	ORF	Annotation	MW	No. of cyst	No. of peptide matched	Sequence coverage (%)
Glycolytic pathway	9	all4563	Fructose-1,6-bisphosphate aldolase	38,764	3	6	20
	10	alr1041	Fructose-1,6-bisphosphatase	37,056	6	8	33
	26	all4008	Pyruvate kinase	63,037	4	14	38
TCA cycle	16	all0122	Pyruvate dehydrogenase E1 beta chain	36,387	1	10	38
	20	alr2708	Pyruvate dehydrogenase E1 alpha chain	38,193	3	6	22
Anti-oxidative stress system	6	alr4404	AhpC/TSA family protein	23,740	1	6	34
	7	alr4641	Peroxiredoxin	22,731	2	8	55
Sulphur metabolism	8	all4464	Phosphoadenosine phosphosulphate reductase	27,596	1	9	44
Amino acid metabolism	18	alr1890	Phosphoglycerate dehydrogenase	55,921	2	9	32
	11	all3555	Acetolactate synthase	59,830	8	12	34
Protein synthesis and folding	14	alr3662	Chaperonin GroEL	57,973	1	23	54
	15	all3822	Two-component response regulator ycf27	27,134	1	9	55
	38	all4338	Translation elongation factor EF-G	76,268	3	8	18
	21	all0723	Probable GTP-binding protein	39,345	2	15	61
CO ₂ fixation	31	alr1524	Ribulose 1,5-bisphosphate carboxylase/oxygenase large chain	53,411	7	17	36
Nitrogen assimilation	37	alr2328	Glutamate ammonia ligase	53,136	6	10	30
	12	all2906	Molybdopterin biosynthesis protein	42,969	6	10	43
Phycobilisome	1	alr0529	Phycocyanin alpha chain	17,504	1	8	59
	2	alr0523	Phycocyanin beta chain	18,500	4	8	57
	3	alr0524	Phycocyanin alpha chain	17,615	3	5	40
	4	alr0021	Allophycocyanin alpha chain	17,392	1	7	49
	5	alr0022	Allophycocyanin beta chain	17,351	1	5	43
Other/hypothetical	13	all0982	Thiamin biosynthesis protein	51,180	7	14	46
	17	alr0657	dTDP-glucose 4-6-dehydratase	35,593	4	14	63
	19	alr4380	Delta-aminolevulinic acid dehydratase	35,792	4	7	35
	27	alr1207	Uridylate kinase	26,140	2	7	50
	29	alr1675	Protein-methionine-S-oxide reductase	24,571	4	7	42
	30	all4358	ATP-dependent Clp protease proteolytic subunit	24,203	2	5	26
	32	alr3343	3-oxoacyl-ACP synthase beta chain	44,335	8	12	53
	33	alr2880	Bicarbonate transport ATP-binding protein cmpD	1E+05	3	8	43
	34	alr3809	Carbamoyl phosphate synthetase large chain	22,670	11	14	15
	35	alr1238	ATP-dependent Clp protease proteolytic chain	48,300	2	5	27
	22	alr4550	Hypothetical protein alr4550	60,658	2	11	32
	23	alr0882	Hypothetical protein alr0882	30,875	5	11	59
24	asl0060	Hypothetical protein asl0060	10,645	1	4	53	
25	alr0893	Hypothetical protein alr0893	39,766	3	8	33	
28	alr2001	Hypothetical protein alr2001	30,004	1	7	33	
36	all5218	Hypothetical protein pmbA	53,445	1	7	25	

^aSpot numbers correspond to those presented in Fig. 3B.

Discussion

A proteomic study of Trx-interacting proteins from A.7120

The cyanobacterium *Anabaena* sp. PCC 7120 forms heterocysts that fix nitrogen under nitrogen-deficient conditions. Although this process requires a large amount of ATP and reducing power, little is known about the redox systems that provide energy and redox metabolites in heterocysts. In this study, we performed Trx affinity chromatography to identify proteins that are involved in the Trx network, and captured 16 and 38 candidate Trx-interacting proteins from heterocysts and vegetative cells, respectively. Among these, the nitrogenase component of NifH and NifK, the scaffold protein NifU, aconitate dehydratase, citrate synthase and enolase were captured only from heterocysts,

suggesting the involvement of Trx system in nitrogen fixation, glycolysis, and the TCA cycle in heterocysts.

Assistance of the scaffold activity of NifU by TrxM

It is striking that we captured two subunits of nitrogenase and NifU as potential Trx targets from heterocysts lysate (Table I). The nitrogen-fixing protein nitrogenase contains Fe protein and MoFe protein components (23), which are specifically expressed in heterocysts (17). Maturation of Fe protein and MoFe protein requires the participation of at least 15 proteins, including NifU (24, 25). Moreover, this process requires biosynthesis of [4Fe–4S] clusters, FeMo cofactors and P clusters. To date, there have been no reports describing the interaction between Trx and nitrogenase or its maturing protein components. In this study, we focused on the possible involvement of

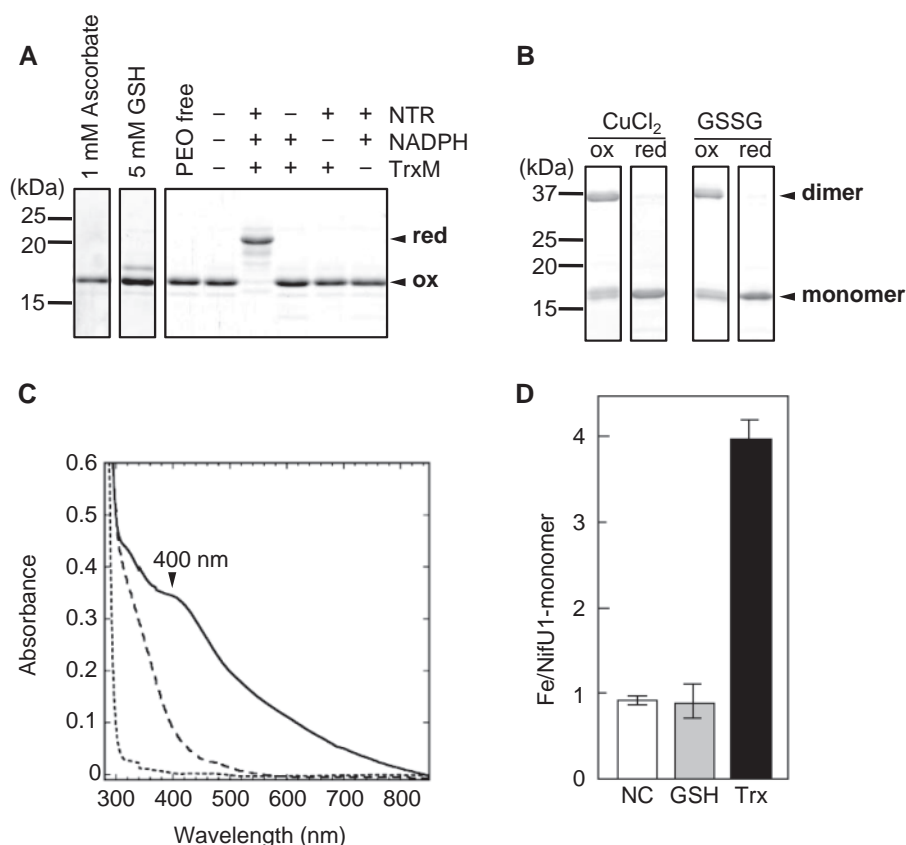


Fig. 4 Reduction of NifU1 by Trx-system and Fe-S cluster assembly on NifU1. **(A)** Trx-dependent reduction of NifU1; Oxidized NifU1 (50 μ M) was incubated with or without 1.6 μ M NTR, 1.5 mM NADPH and 1.6 μ M TrxM for 45 min at 31°C (lanes 4–8) or was incubated with 1 mM ascorbate or 5 mM GSH for 45 min at 31°C (lane 1 or 2). After TCA precipitation, reduction of NifU1 was determined by the incorporation of PEO and mobility shifts during SDS-PAGE. Protein bands were visualized by CBB staining. **(B)** Mobility shifts of NifU1 upon oxidation on non-reducing SDS-PAGE; Purified NifU1 (30 μ M) was incubated with 30 μ M CuCl_2 or 1 mM GSSG for 10 min or 30 min, respectively, at 31°C (ox). The oxidized NifU1 proteins were then incubated with 50 mM 2-mercaptoethanol for 30 min at 31°C (red). NifU1-dimer formation was confirmed by SDS-PAGE. Protein bands were visualized by CBB staining. **(C)** UV-VIS absorption spectrum of re-purified NifU1 after Fe-S cluster assembly in the presence or absence of complete Trx-system. After cluster assembly for 2.5 h, NifU1 was re-purified using Strep-Tactin Sepharose under anaerobic conditions (solid line). The shoulder at 400 nm, which is indicative of [4Fe-4S] cluster formation, is indicated with an arrowhead. As a negative control, NifU1 was incubated with Fe-S cluster assembly mixture in the presence of incomplete Trx-system (NADPH was omitted) and re-purified (dashed line). The dotted line is a spectrum of re-purified NifU1 before Fe-S cluster assembly. Conditions for Fe-S cluster assembly are described in 'Materials and Methods'. **(D)** Determination of iron content of re-purified NifU1; Fe-S assembly assays for NifU1 were performed in the absence (NC) or presence of GSH or the Trx-system (Trx). After the reaction, NifU1 was re-purified and iron contents were determined using a metallo-assay kit for Fe. Data are presented as the mean of three independent experiments.

TrxM in the heterocyst-specific Fe-S cluster assembly by NifU. The present data show that NifU interacts with TrxM in a functional manner, and analyses of the catalytic domain of NifU (NifU1) using PEO-labelling assays showed reduction of NifU1 disulphide bonds in the presence of TrxM, NTR and NADPH, indicating involvement of the Trx system for the function of NifU (Fig. 4A). Also, disulphide-linked dimer formation of NifU1 was examined by non-reducing SDS-PAGE (Fig. 4B). CuCl_2 - or GSSG-oxidized NifU1 forms dimer (Fig. 4B, ox) and both dimers are dissociated upon reduction (Fig. 4B, red), indicating that NifU1 forms dimer via intermolecular disulphide bond(s). Moreover, analyses of NifU1 scaffold activity using absorption spectra of re-purified NifU1 indicates the enhanced formation of Fe-S clusters on NifU1 when Trx-system was supplemented (Fig. 4C). Determination of iron contents in the re-purified NifU1 showed the presence of a 3.8 Fe/NifU1 monomer (Fig. 4D), indicating that a single [4Fe-4S]

cluster is assembled on the reduced NifU1 monomer (26). Although this spectrum is somehow different from the typical spectrum of 4Fe-4S cluster containing protein, it was very similar with that of diazotrophic bacterium *A. vinelandii* (24, 25). Because the iron contents of NifU1 monomer was slightly lower, the re-purified NifU1 may partially contain 2Fe-2S clusters, which is emerged during the 4Fe-4S assembly process, and it makes the spectrum slightly different. These data suggest that the NifU protein is a novel TrxM-targeted protein, and its scaffold activity is enhanced by Trx-system. It was demonstrated previously that Trx-system promotes the [2Fe-2S] cluster assembly in apo-IscU from *E. coli* (22). Also, Achebach *et al.* (27) showed that glutaredoxin (Grx) system stimulates the [4Fe-4S] cluster formation of oxygen sensor fumarate nitrate reductase regulator. Taken together, our results imply that TrxM is involved in the Fe-S cluster assembly in NifU1. In addition to the

disulphide bond reduction of NifU1, TrxM possibly provides a reductant for Fe–S cluster assembly in NifU. This finding warrants further biochemical studies on the Trx-dependent Fe–S cluster assembly and the physiological role of TrxM in Fe–S cluster biosynthesis as well.

Conclusions

For more than 10 years, proteomic studies using Trx affinity chromatography and biochemical analyses have revealed numerous roles of Trx in various organisms. In this study, we identified 16 and 38 proteins from heterocyst and vegetative cells, respectively, as potential targets of TrxM in A.7120. Among these, six were involved in nitrogen fixation, glycolysis or the TCA cycle, and were only captured from heterocyst lysates. In addition, several proteins were captured only from the vegetative cells, and were not related to nitrogen fixation or redox pathways. Given that heterocysts metabolism is highly adapted to nitrogen fixation, the captured proteins might be up-regulated to sustain the energy requirements of nitrogen fixation in heterocysts. Indeed, proteomic analysis by Ow *et al.* (28) showed that the abundance of aconitate dehydratase was more prominent in the heterocyst than that in the vegetative cells. Moreover, the present biochemical analyses suggest that Fe–S cluster assembly in NifU1 is enhanced by TrxM-mediated reduction in heterocysts. These data suggest the significance of the Trx-system in nitrogen fixation. Thus, further biochemical studies on the Trx-dependent reduction or the redox regulation of the proteins that were captured in this study must demonstrate significant roles of TrxM in heterocysts.

Acknowledgements

We thank S. Hara and K. Yoshida for their helpful discussions.

Funding

This work was supported by the Core Research of Evolutional Science & Technology programme (CREST) from the Japan Science and Technology Agency (JST), and was supported in part by the Network Joint Research Center for Materials and Devices, MEXT, Japan, in part by JSPS KAKENHI (24770040) (to J.N.), and in part by grant-in aid for Scientific Research on Innovative Areas (24107004) and Strategic Research Base Development Program for Private Universities from MEXT, Japan (to K.I.).

Conflict of Interest

None declared.

References

- Holmgren, A., Soderberg, B.O., Eklund, H., and Branden, C.I. (1975) Three-dimensional structure of *Escherichia coli* thioredoxin-S2 to 2.8 Å resolution. *Proc. Natl Acad. Sci. U. S. A.* **72**, 2305–2309
- Holmgren, A. (1989) Thioredoxin and glutaredoxin systems. *J. Biol. Chem.* **264**, 13963–13966
- Motohashi, K., Kondoh, A., Stumpp, M.T., and Hisabori, T. (2001) Comprehensive survey of proteins targeted by chloroplast thioredoxin. *Proc. Natl Acad. Sci. U. S. A.* **98**, 11224–11229
- Hisabori, T., Hara, S., Fujii, T., Yamazaki, D., Hosoya-Matsuda, N., and Motohashi, K. (2005) Thioredoxin affinity chromatography: a useful method for further understanding the thioredoxin network. *J. Exp. Bot.* **56**, 1463–1468
- Lindahl, M. and Florencio, F.J. (2003) Thioredoxin-linked processes in cyanobacteria are as numerous as in chloroplasts, but targets are different. *Proc. Natl Acad. Sci. U. S. A.* **100**, 16107–16112
- Hosoya-Matsuda, N., Inoue, K., and Hisabori, T. (2009) Roles of thioredoxin in the obligate anaerobic green sulfur photosynthetic bacterium *Chlorobaculum tepidum*. *Mol. Plant.* **2**, 336–343
- Montrichard, F., Alkhalfoui, F., Yano, H., Vensel, W.H., Hurkman, W.J., and Buchanan, B.B. (2009) Thioredoxin targets in plants: the first 30 years. *J. Proteomics* **72**, 452–474
- Buchanan, B.B., Holmgren, A., Jacquot, J.P., and Scheibe, R. (2012) Fifty years in the thioredoxin field and a bountiful harvest. *Biochim. Biophys. Acta* **1820**, 1822–1829
- Yoshida, K., Noguchi, K., Motohashi, K., and Hisabori, T. (2013) Systematic exploration of thioredoxin target proteins in plant mitochondria. *Plant Cell Physiol.* **54**, 875–892
- Meeks, J.C. and Elhai, J. (2002) Regulation of cellular differentiation in filamentous cyanobacteria in free-living and plant-associated symbiotic growth states. *Microbiol. Mol. Biol. Rev.* **66**, 94–121; table of contents.
- Murry, M.A. and Lopez, M.F. (1989) Interaction between hydrogenase, nitrogenase, and respiratory activities in a Frankia isolate from *Alnus rubra*. *Canad. J. Microbiol.* **35**, 636–641
- Kumar, K., Mella-Herrera, R.A., and Golden, J.W. (2010) Cyanobacterial heterocysts. *Cold Spring Harb. Perspect. Biol.* **2**, a000315
- Florencio, F.J., Perez-Perez, M.E., Lopez-Maurry, L., Mata-Cabana, A., and Lindahl, M. (2006) The diversity and complexity of the cyanobacterial thioredoxin systems. *Photosynth. Res.* **89**, 157–171
- Gleason, F.K. (1996) Glucose-6-phosphate dehydrogenase from the cyanobacterium, *Anabaena* sp. PCC 7120: purification and kinetics of redox modulation. *Arch. Biochem. Biophys.* **334**, 277–283
- Ehira, S. and Ohmori, M. (2012) The redox-sensing transcriptional regulator RexT controls expression of thioredoxin A2 in the cyanobacterium *Anabaena* sp. strain PCC 7120. *J. Biol. Chem.* **287**, 40433–40440
- Agar, J.N., Yuvaniyama, P., Jack, R.F., Cash, V.L., Smith, A.D., Dean, D.R., and Johnson, M.K. (2000) Modular organization and identification of a mononuclear iron-binding site within the NifU protein. *J. Biol. Inorg. Chem.* **5**, 167–177
- Elhai, J. and Wolk, C.P. (1990) Developmental regulation and spatial pattern of expression of the structural genes for nitrogenase in the cyanobacterium *Anabaena*. *EMBO J.* **9**, 3379–3388
- Cardona, T., Battchikova, N., Zhang, P., Stensjo, K., Aro, E.M., Lindblad, P., and Magnuson, A. (2009) Electron transfer protein complexes in the thylakoid membranes of heterocysts from the cyanobacterium *Nostoc punctiforme*. *Biochim. Biophys. Acta.* **1787**, 252–263
- Wood, N.B. and Haselkorn, R. (1980) Control of phycobiliprotein proteolysis and heterocyst differentiation in *Anabaena*. *J. Bacteriol.* **141**, 1375–1385

20. Fu, W., Jack, R.F., Morgan, T.V., Dean, D.R., and Johnson, M.K. (1994) nifU gene product from *Azotobacter vinelandii* is a homodimer that contains two identical [2Fe-2S] clusters. *Biochemistry* **33**, 13455–13463
21. Yuvaniyama, P., Agar, J.N., Cash, V.L., Johnson, M.K., and Dean, D.R. (2000) NifS-directed assembly of a transient [2Fe-2S] cluster within the NifU protein. *Proc. Natl Acad. Sci. U. S. A.* **97**, 599–604
22. Ding, H., Harrison, K., and Lu, J. (2005) Thioredoxin reductase system mediates iron binding in IscA and iron delivery for the iron-sulfur cluster assembly in IscU. *J. Biol. Chem.* **280**, 30432–30437
23. Igarashi, R.Y. and Seefeldt, L.C. (2003) Nitrogen fixation: the mechanism of the Mo-dependent nitrogenase. *Crit. Rev. Biochem. Mol. Biol.* **38**, 351–384
24. Dos Santos, P.C., Dean, D.R., Hu, Y., and Ribbe, M.W. (2004) Formation and insertion of the nitrogenase iron-molybdenum cofactor. *Chem. Rev.* **104**, 1159–1173
25. Hu, Y. and Ribbe, M.W. (2011) Biosynthesis of nitrogenase FeMoco. *Coord. Chem. Rev.* **255**, 1218–1224
26. Smith, A.D., Jameson, G.N., Dos Santos, P.C., Agar, J.N., Naik, S., Krebs, C., Frazzton, J., Dean, D.R., Huynh, B.H., and Johnson, M.K. (2005) NifS-mediated assembly of [4Fe-4S] clusters in the N- and C-terminal domains of the NifU scaffold protein. *Biochemistry* **44**, 12955–12969
27. Achebach, S., Tran, Q.H., Vlamis-Gardikas, A., Mullner, M., Holmgren, A., and Uden, G. (2004) Stimulation of Fe-S cluster insertion into apoFNR by *Escherichia coli* glutaredoxins 1, 2 and 3 in vitro. *FEBS Lett.* **565**, 203–206
28. Ow, S.Y., Cardona, T., Taton, A., Magnuson, A., Lindblad, P., Stensjo, K., and Wright, P.C. (2008) Quantitative shotgun proteomics of enriched heterocysts from *Nostoc* sp. PCC 7120 using 8-plex isobaric peptide tags. *J. Proteome Res.* **7**, 1615–1628

ARTICLE

Received 2 Feb 2015 | Accepted 4 Jun 2015 | Published 3 Jul 2015

DOI: 10.1038/ncomms8731

OPEN

Ultrathin inorganic molecular nanowire based on polyoxometalates

Zhenxin Zhang¹, Toru Murayama¹, Masahiro Sadakane^{2,3}, Hiroko Ariga¹, Nobuhiro Yasuda⁴, Norihito Sakaguchi⁵, Kiyotaka Asakura¹ & Wataru Ueda^{1,6}

The development of metal oxide-based molecular wires is important for fundamental research and potential practical applications. However, examples of these materials are rare. Here we report an all-inorganic transition metal oxide molecular wire prepared by disassembly of larger crystals. The wires are comprised of molybdenum(VI) with either tellurium(IV) or selenium(IV): $\{(NH_4)_2[XMo_6O_{21}]\}_n$ ($X = \text{tellurium(IV) or selenium(IV)}$). The ultrathin molecular nanowires with widths of 1.2 nm grow to micrometre-scale crystals and are characterized by single-crystal X-ray analysis, Rietveld analysis, scanning electron microscopy, X-ray photoelectron spectroscopy, ultraviolet-visible spectroscopy, thermal analysis and elemental analysis. The crystals can be disassembled into individual molecular wires through cation exchange and subsequent ultrasound treatment, as visualized by atomic force microscopy and transmission electron microscopy. The ultrathin molecular wire-based material exhibits high activity as an acid catalyst, and the band gap of the molecular wire-based crystal is tunable by heat treatment.

¹Catalysis Research Center, Hokkaido University, N-21, W-10, Kita-ku, Sapporo 001-0021, Japan. ²Department of Applied Chemistry, Graduate School of Engineering, Hiroshima University, 1-4-1 Kagamiyama, Higashi Hiroshima 739-8527, Japan. ³JST, PRESTO, 4-1-8 Honcho, Kawaguchi, Saitama, 332-0012, Japan. ⁴Japan Synchrotron Radiation Research Institute/SPring-8, 1-1-1 Kouto, Sayocho, Sayogun, Hyogo 679-5198, Japan. ⁵High Voltage Electron Microscope Laboratory, Center for Advanced Research of Energy and Materials, Faculty of Engineering, Hokkaido University, Sapporo 060-8626, Japan. ⁶Department of Material and Life Chemistry, Faculty of Engineering, Kanagawa University, Rokkakubashi, Kanagawa-ku, Yokohama-shi, Kanagawa 221-8686, Japan. Correspondence and requests for materials should be addressed to W.U. (email: uedaw@kanagawa-u.ac.jp).

Nanowires, in which two dimensions of the materials are on a scale of tens of nanometres or less and the length of the remaining dimension can be increased without confinement, have been attracting attention because of their large surface area and quantum mechanical effects that result in unique material properties. Different compounds, such as metallic compounds¹, semiconducting compounds^{2–10}, metal oxides^{11–13} and organic polymers^{14–17}, can be grown to form nanowires for use in functional materials and devices that have been successfully applied as sensors¹³, transistors^{2,5}, semiconductors³, photonics devices^{7,11} and solar cells^{4,6}.

Among the various types of nanowires, molecular wires, which grow by repeating a single molecular unit along a certain axis, have garnered much interest. The most common type of molecular wire is an organic or organometallic polymer^{14–17}, which has been widely applied in nanotechnology, semiconductors, electrochemistry and cell biology. A more interesting material is a molecular wire with an all-inorganic composition; inorganic compounds have various advantages over organic molecular wires, including stable structures, tunable chemical compositions and tunable properties. However, all-inorganic molecular wires are rare, leaving a field that is full of challenges. One example of an inorganic molecular wire is the $\text{Mo}_6\text{S}_{9-x}\text{I}_x$ molecular wire^{18,19}, which was assembled with molecular units of $\text{Mo}_6\text{S}_{9-x}\text{I}_x$ along its c axis to form a nanowire. The material exhibits excellent electron transport, magnetic, mechanical, tribological and optical properties and has been applied in chemisensors, biosensors, field emission devices, composites, lubricants, nonlinear optical limiting materials, Li batteries and molecular-scale connectors for molecular electronics.

Assembly of transition metal–oxygen octahedral building blocks is an attractive approach to form nanostructured materials²⁰. Both zero-dimensional molecular nanodots, which are known as polyoxometalates (POMs)^{21,22}, and two-dimensional molecular nanosheets^{23,24} can be obtained by this approach. However, no isolated molecular nanowire assembled with transition metal oxide octahedra has been reported to date.

POMs are ideal subunits for constructing one-dimensional (1D) metal oxides that are based on transition metal–oxygen octahedra, and a few examples of all-inorganic POM-based chain structures in crystals have been reported^{25–27}. However, isolation of individual ultrathin molecular wires that are based on transition metal oxides has not yet been realized to the best of our knowledge.

Herein, we report an isolable transition metal oxide-based molecular wire that is formed by repeating a hexagonal molecular unit of $[\text{X}^{\text{IV}}\text{Mo}^{\text{VI}}\text{O}_{21}]^{2-}$ along its c axis, where $\text{X} = \text{Te}$ or Se and denoted as Mo–Te oxide and Mo–Se oxide, respectively. These molecular wires assemble in a hexagonal manner on interaction with water and ammonium cations to form crystals, and the molecular wires are isolable from the crystal. The ultrathin molecular wire-based material acts as an active acid catalyst, and the band gap of the molecular wire-based crystal is easily altered, indicating its potential application in catalysis and electronic devices²⁸.

Results

Material synthesis and characterization. Crystalline transition metal oxide molecular wires were synthesized using a hydrothermal method. The starting materials contained $(\text{NH}_4)_6\text{Mo}_7\text{O}_{24} \cdot 4\text{H}_2\text{O}$ as a source of Mo, and Se^{IV} or Te^{IV} ions were assembled into the materials, forming Mo–Se oxide or Mo–Te oxide, respectively. The Se or Te ions with IV oxidation state were essential in obtaining these samples. Mo–Se oxide was easily

obtained via hydrothermal synthesis of $(\text{NH}_4)_6\text{Mo}_7\text{O}_{24} \cdot 4\text{H}_2\text{O}$ and a $\text{Se}^{\text{IV}}\text{O}_2$ solution. For Mo–Te oxide, soluble $\text{Te}^{\text{VI}}(\text{OH})_6$ was used with a reducing agent ($\text{VOSO}_4 \cdot 5\text{H}_2\text{O}$) to form Te^{IV} ions. X-ray photoelectron spectroscopy (XPS) with curve fitting (Supplementary Fig. 1a–d) was used to confirm that the Mo, Te and Se ions in both materials were present as Mo^{VI} , Te^{IV} and Se^{IV} , respectively. Ultraviolet–visible (ultraviolet–vis) spectra of Mo–Te oxide and Mo–Se oxide are presented in Supplementary Fig. 2. No absorption was detected over a range of 500–600 nm, which was attributed to Mo^{V} and confirmed that the Mo ions in the materials were present as Mo^{VI} . Elemental analysis, XPS and energy dispersive X-ray spectroscopy analysis confirmed that there was no vanadium present in the Mo–Te oxide (Supplementary Fig. 3); vanadium was therefore not a building block of the material and only acted as a reducing agent to reduce $\text{Te}^{\text{VI}}(\text{OH})_6$ to Te^{IV} ion. Elemental analysis of Mo–Te oxide and Mo–Se oxide revealed that the ratio of $\text{Mo}:\text{Te}:\text{NH}_4^+:\text{H}_2\text{O}$ and $\text{Mo}:\text{Se}:\text{NH}_4^+:\text{H}_2\text{O}$ was 6:1:2:3 and 6:1:2:2, respectively.

Powder X-ray diffraction (XRD) patterns of Mo–Te oxide and Mo–Se oxide are shown in Fig. 1 and Supplementary Fig. 4. The powder XRD peaks of Mo–Te oxide and Mo–Se oxide could be indexed by a trigonal cell with lattice parameters of $a = 12.48 \text{ \AA}$ and $c = 3.94 \text{ \AA}$ for Mo–Te oxide and $a = 12.51 \text{ \AA}$, $c = 3.93 \text{ \AA}$ for Mo–Se oxide (Supplementary Table 1). Similar unit cells

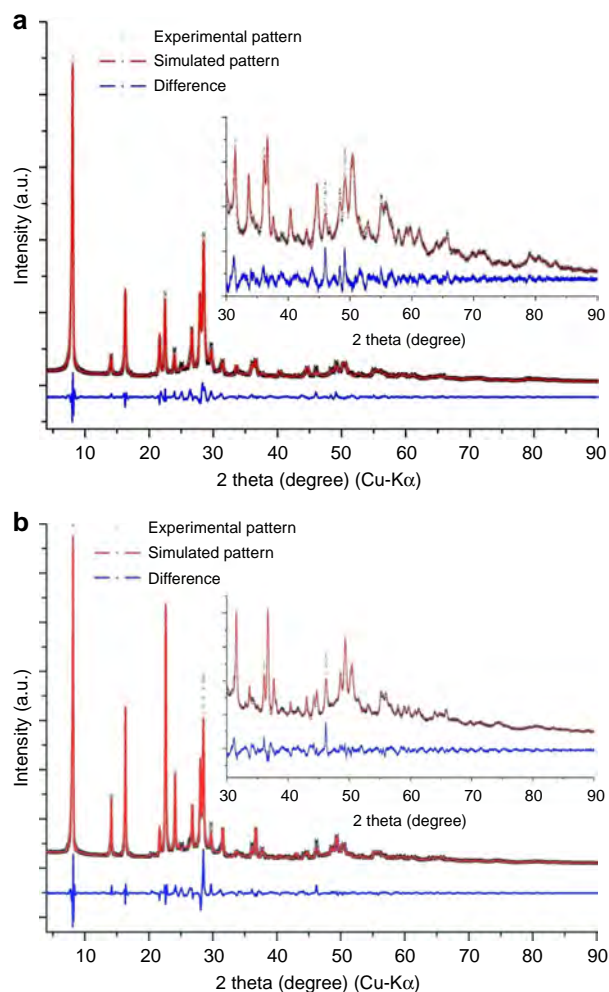


Figure 1 | Comparison of the experimental XRD patterns with the simulated XRD patterns using the Rietveld method. (a) Mo–Te oxide, $R_{\text{wp}} = 7.06\%$ and **(b)** Mo–Se oxide, $R_{\text{wp}} = 7.49\%$. Insert: magnification of high-angle area.

indicated that the structures of the two materials were similar. The Fourier transform infrared (FTIR) spectra (Supplementary Fig. 4) of Mo–Te oxide and Mo–Se oxide were similar, indicating that water ($1,620\text{ cm}^{-1}$) and NH_4^+ ($1,400\text{ cm}^{-1}$) were present in the materials and that the molecular structures were the same. The presence of water and NH_4^+ were also confirmed by thermogravimetric-differential thermal analysis (TG-DTA) (Supplementary Fig. 5) and temperature-programmed desorption mass spectrometry (TPD-MS) (Supplementary Fig. 6).

Morphologies of the as-synthesized materials were characterized by scanning electron microscopy (SEM). Interestingly, the morphologies of the Mo–Te and Mo–Se oxides were completely different. Mo–Te oxide was a rod-like material (Fig. 2), whereas Mo–Se oxide was a plate-shaped material.

The hydrothermally synthesized Mo–Te and Mo–Se oxides were too small to perform single-crystal analysis (Fig. 2a,b). A large single crystal of Mo–Te oxide was obtained by low-temperature crystallization (see Methods section). The SEM images in Fig. 2a,c show that the Mo–Te oxide synthesized by the low-temperature method was much larger than that synthesized by the hydrothermal method. XRD and FTIR confirmed that the basic structure of the material obtained from the low-temperature synthesis was identical to that of the material obtained from hydrothermal synthesis (Supplementary Fig. 4b).

Single-crystal X-ray structural analysis combined with elemental analysis showed that six Mo–O octahedra surrounded one Te ion in the a – b plane, forming a molecular unit of $[\text{Te}^{\text{IV}}\text{Mo}^{\text{VI}}_6\text{O}_{21}]^{2-}$. The Mo–O octahedra units were connected

to each other through two edge-sharing oxygen atoms on one side with equatorial Mo–O bond lengths of $1.97(4)$ – $1.99(6)$ Å and a corner-sharing oxygen atom on another side with equatorial Mo–O bond lengths of $1.79(6)$ – $1.84(5)$ Å (Fig. 3a,b). The Te ion inside of the Mo–O cluster was coordinated to three oxygen atoms (Te–O bond lengths of $2.05(3)$ – $2.05(4)$ Å), and a lone pair of Te ions was directed parallel along the c direction. The distance between the Te ions was 3.94 Å, and thus there was no interaction between the Te ions. The hexagonal $[\text{TeMo}_6\text{O}_{21}]^{2-}$ units were stacked along the c axis through sharing of the axial oxygen atoms with Mo (axial Mo–O bond lengths of $1.90(5)$ – $2.15(5)$ Å) to form prismatic clusters (Fig. 3c) as molecular wires. The molecular wires were further packed parallel in a hexagonal manner to form the material (Fig. 3d), and ammonium cations and water were present in between the molecular wires. The nanowires were ca. 1.2 nm in width and micrometre scale in length. The size distribution of the Mo–Te oxide crystals based on SEM images (Fig. 4) showed that most of the particles had widths of 50 – 200 nm and lengths of 500 – $3,000$ nm with distribution maxima at 150 nm in width and $1,500$ nm in length, indicating that over $3,800$ hexagonal $[\text{TeMo}_6\text{O}_{21}]^{2-}$ units accumulated along the c direction to form the material. The Mo–Te oxide crystal typically terminated at a sharp tip with a size of 150×150 nm in the a – b plane, with each bundle containing over $14,000$ ordered single molecular wires.

The Mo–Se oxide structure was proposed on the basis of powder diffraction Rietveld analysis and elemental analysis (Mo:Se = 6:1), showing that the basic structure of the material

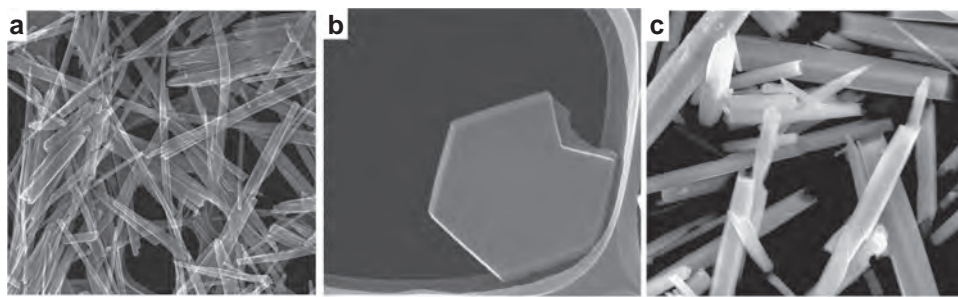


Figure 2 | SEM images. (a) Mo–Te oxide, scale bar, $3\text{ }\mu\text{m}$; (b) Mo–Se oxide, scale bar, 800 nm ; and (c) Mo–Te oxide synthesized under refrigeration, scale bar, $5\text{ }\mu\text{m}$.

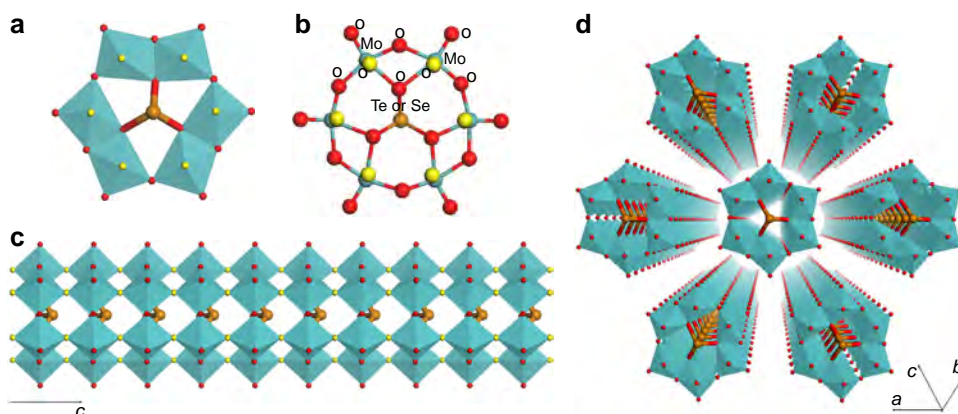


Figure 3 | Structural representations. (a) Polyhedral representation of a hexagonal unit of $[\text{Te}^{\text{IV}}\text{Mo}^{\text{VI}}_6\text{O}_{21}]^{2-}$ or $[\text{Se}^{\text{IV}}\text{Mo}^{\text{VI}}_6\text{O}_{21}]^{2-}$. (b) Ball-and-stick representation of a hexagonal unit of $[\text{Te}^{\text{IV}}\text{Mo}^{\text{VI}}_6\text{O}_{21}]^{2-}$ or $[\text{Se}^{\text{IV}}\text{Mo}^{\text{VI}}_6\text{O}_{21}]^{2-}$ with labels. (c) A single molecular wire of Mo–Te oxide. The bridge oxygen atoms that connect the hexagonal units are highlighted in yellow. (d) Assembly of single molecular wires into crystalline Mo–Te oxide (or Mo–Se oxide). Mo: blue, Te (Se): brown and O: red.

was the same as that of Mo–Te oxide. The structures of Mo–Te oxide and Mo–Se oxide were refined with Rietveld refinement. The resulting simulated patterns of the materials were similar to those of the experimental data, and the R_{wp} values of the Mo–Te and Mo–Se oxides were 7.06% and 7.49%, respectively, indicating that the proposed structures were correct (Fig. 1). The powder samples were pure because no obvious additional peaks were observed.

According to the structural analysis, ultraviolet–vis spectra, and elemental analysis, the chemical formulae were estimated to be $(\text{NH}_4)_2[\text{Te}^{\text{IV}}\text{Mo}^{\text{VI}}_6\text{O}_{21}] \cdot 3\text{H}_2\text{O}$ for Mo–Te oxide and $(\text{NH}_4)_2[\text{Se}^{\text{IV}}\text{Mo}^{\text{VI}}_6\text{O}_{21}] \cdot 2\text{H}_2\text{O}$ for Mo–Se oxide.

The molecular wires of Mo–Te oxide and Mo–Se oxide were inorganic polymers formed by accumulation of the $[\text{X}^{\text{IV}}\text{Mo}^{\text{VI}}_6\text{O}_{21}]^{2-}$ ($\text{X}=\text{Te}$ or Se) monomers along the c direction; their monomers, with the same or iso-structural molecular structure, have been previously synthesized using bidentate organic ligands, such as carboxylates, to stabilize the monomer structure^{29,30}.

Isolation of molecular wire from crystals. The order of the molecular wires in the Mo–Te oxide and Mo–Se oxide crystals were observed by high-resolution transmission electron microscopy (HR-TEM) as shown in Fig. 5. Because of the different crystal orientations of Mo–Te oxide and Mo–Se oxide, different lattice planes were observed. In the case of Mo–Te oxide, the molecular wires were packed parallel to the c direction with distances of ca. 1.1 nm, and the hexagonal $[\text{TeMo}_6\text{O}_{21}]^{2-}$ building blocks were accumulated with distances of ca. 0.4 nm, which corresponded to d values of (100) and (001) planes, respectively (Fig. 5a). The HR-TEM image of Mo–Se oxide showed a

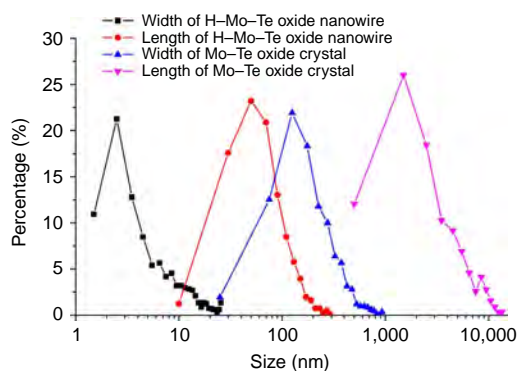


Figure 4 | Comparison of morphology and size. Size distributions of the Mo–Te oxide crystals from SEM and the H–Mo–Te oxide molecular wires from TEM. More than 800 particles were counted.

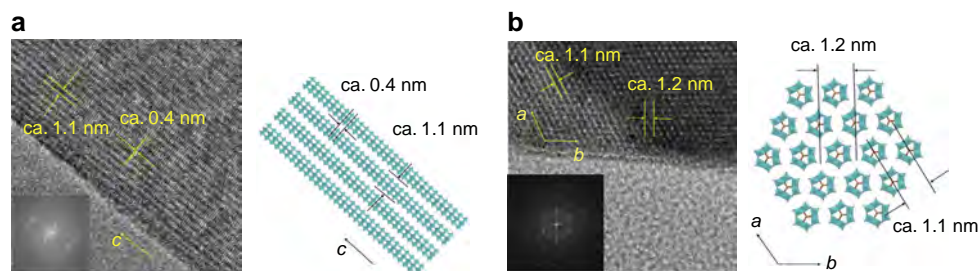


Figure 5 | Comparison of polyhedral structural images with HR-TEM images. (a) Mo–Te oxide, scale bar, 5 nm and (b) Mo–Se oxide, scale bar, 5 nm. Insert images: power spectra.

hexagonal arrangement of the molecular wires in the a – b plane (Fig. 5b). The HR-TEM images were in good agreement with the crystal structures from the structural analysis.

The molecular wire arrays in the crystals were readily disassembled to form single molecular wires by a simple process (Fig. 6a). Ion exchange with protons made the molecular wire isolated from the crystal easily. Ammonium cations in Mo–Te oxide and Mo–Se oxide were replaced by protons to form proton-exchanged materials, denoted as H–Mo–Te oxide and H–Mo–Se oxide, after reaction at room temperature for 15 h. The resulting solids were characterized by powder XRD and FTIR. The diffraction peaks of both materials broadened after proton exchange, indicating that the size of the materials decreased (Supplementary Fig. 4). Furthermore, all characteristic infrared bands of the materials were retained in the materials after proton exchange, demonstrating that the molecular structures of the materials did not change after ion exchange with protons (Supplementary Fig. 4). Elemental analysis confirmed that approximately half of the ammonium cations were replaced by protons, and formulae of the proton-exchanged materials were estimated to be $(\text{NH}_4)_{1.1}[\text{H}_{0.9}\text{TeMo}_6\text{O}_{21}] \cdot 5\text{H}_2\text{O}$ and $(\text{NH}_4)_{1.1}[\text{H}_{0.9}\text{SeMo}_6\text{O}_{21}] \cdot 6\text{H}_2\text{O}$.

Proton exchange helped to crack the materials. H–Mo–Te oxide remained a rod-shaped material after proton exchange, and several open gaps could be observed in the crystal surface (Fig. 6b). Crystal breakage after proton exchange was more evident in H–Mo–Se oxide. The material was no longer a plate-like shape compared with the as-synthesized material. The crystals were broken into several small rods (Fig. 6h).

H–Mo–Te oxide could be disassembled into thin rod-like particles and even single molecular wires by dispersion in ethanol with ultrasound. The material was characterized by HR-TEM, which confirmed that nanowires with smaller sizes were generated after ultrasound, and some isolated molecular wires with widths of 1.5 nm (Fig. 6c; Supplementary Fig. 7) were observed. The isolated nanowires were further characterized by atomic force microscopy (AFM). An AFM image of H–Mo–Te oxide after isolation experiments revealed wire-shaped particles. Some ultrathin nanowires were observed in the AFM image, and the thicknesses of typical particles in Fig. 6d were ca. 1.2 nm (particle i) and ca. 4.8 nm (particle ii). The thickness of particle (i) was consistent with that of a single H–Mo–Te oxide molecular wire deduced from the crystallographic data on Mo–Te oxide (Fig. 6e), and particle (ii) was ascribed to a structure with four layers of molecular wires (Fig. 6e). One possible structure is shown in Fig. 6f. The width of the particles appeared to be much larger than that of a single molecular wire (1.2 nm) in the AFM image, which resulted from the large size of the AFM cantilever compared with that of the particles (Supplementary Fig. 8).

The size distribution of the H–Mo–Te oxide nanowires (Fig. 4; Supplementary Fig. 9) indicated that most of the nanowires had

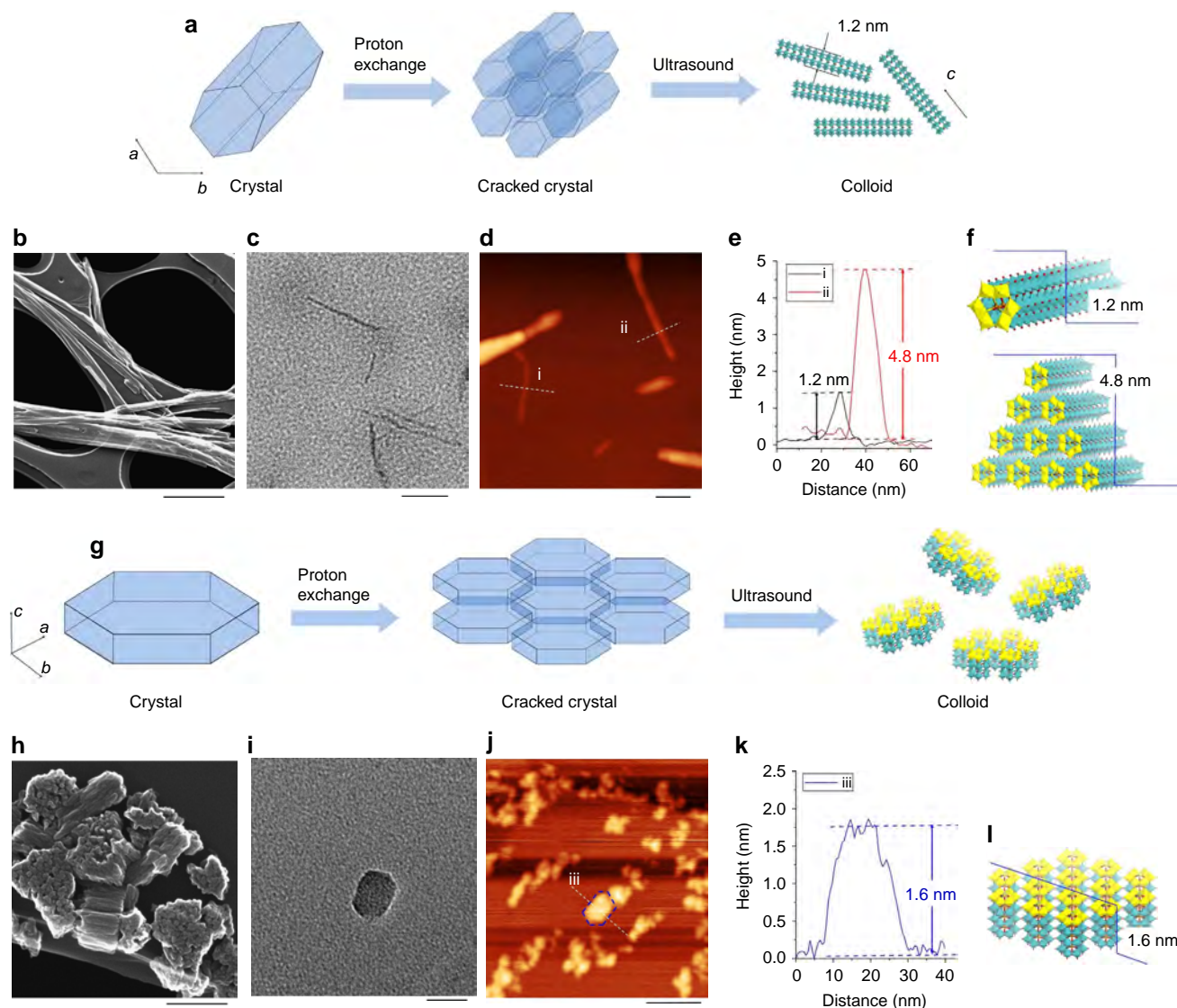


Figure 6 | Isolation of crystals into molecular wires. (a) Isolation of H-Mo-Te oxide to obtain small particles. (b) SEM images of H-Mo-Te oxide, scale bar, 1 μm . (c) HR-TEM images of a colloid sample of H-Mo-Te oxide, scale bar, 50 nm. (d) AFM images of a colloid sample of H-Mo-Te oxide, scale bar, 50 nm. (e) Line profiles from the AFM images. (f) Proposed structures from the line profile analysis, with yellow highlighting the *a-b* plane of the materials. (g) Isolation of H-Mo-Se oxide to obtain small particles. (h) SEM images of H-Mo-Se oxide, scale bar, 200 nm. (i) HR-TEM images of a colloid sample of H-Mo-Se oxide, scale bar, 20 nm. (j) AFM images of a colloid sample of H-Mo-Se oxide, scale bar, 50 nm. (k) Line profiles from the AFM images. (l) Proposed structures from the line profile analysis, with yellow highlighting the *a-b* plane of the materials.

widths <10 nm and length between 20 and 80 nm, which were much smaller than those of the Mo-Te oxide crystals.

The H-Mo-Te oxide nanowires were recovered from ethanol by evaporating the ethanol. The recovered material was characterized by XRD (Supplementary Fig. 10). The diffraction peak positions of the recovered H-Mo-Te oxide were similar to those of the as-synthesized Mo-Te oxide, but the peaks of the recovered H-Mo-Te oxide had broadened; this indicated that the basic structure of the wires did not change, but the ordering of the nanowires decreased during the isolation process. These results indicate that the material dispersed in ethanol was a mixture of single molecular wires and nanowires with hexagonally packed molecular wires. The crystallite size estimated by the Scherrer equation using the (100) peak was 16 nm, the order of which was the same as that obtained from the TEM observations.

TEM (Fig. 6i) and AFM (Fig. 6j) images showed that the H-Mo-Se oxide colloid was composed of small nanoplates, which was different from H-Mo-Te oxide. The thickness of the

hexagonal-shaped nanoplates was ~ 1.6 nm (Fig. 6k), which corresponded to four layers of $(\text{NH}_4)_{1.1}[\text{H}_{0.9}\text{SeMo}_6\text{O}_{21}]$ along the *c* axis (Fig. 6l).

Acid catalysis of the H-Mo-Te oxide nanowires. Nanomaterials are anticipated to have applications in catalysis, because nanomaterials have a large surface area due to their small particle size. Approximately half of the ammonium cations in Mo-Te oxide were able to be replaced by protons, and the material was thus acidic. H-Mo-Te oxide was used to esterify ethanol with acetic acid at 365 K, and the results are summarized in Fig. 7. The acetic acid conversion of large H-Mo-Te oxide particles before ultrasound treatment (17%) was close to that in the reaction without a catalyst (11%), indicating that large H-Mo-Te oxide particles before ultrasound treatment had low catalytic activity under the present conditions. The catalytic activity of the H-Mo-Te oxide nanowires after ultrasound treatment (58%) was much higher

than that of the large H–Mo–Te oxide particles due to the smaller particle size of the former, as well as the catalytic activities of other homogeneous acid catalysts such as $\text{H}_3\text{PW}_{12}\text{O}_{40}$ (30%) and $\text{H}_3\text{PMo}_{12}\text{O}_{40}$ (38%). The catalyst was recyclable and reused three times with only a slight decrease in activity (Supplementary Fig. 11).

Altering the band gap of Mo–Te oxide. 1D nanostructured materials have potential applications in the emerging field of nanoelectronics, including applications as functional components and as conductive connections^{31–33}. Nanostructured molybdenum oxides have been reported as good candidates for applications in electronic devices.²⁸ As a molybdenum oxide-based molecular wire, Mo–Te oxide is also expected to have applications in electronic devices. Electroconductivity of a material is important for electronic applications. However, bulk molybdenum (VI)-based oxides, such as $\alpha\text{-MoO}_3$, were shown to have poor electroconductivity because of the large band gap of the material ($>2.7\text{ eV}$)³⁴, and the material was therefore not suitable as a semiconductor²⁸. Reducing the Mo^{VI} ions by reaction under reducing conditions decreased the band gap of the material^{28,33}.

For Mo–Te oxide, the use of heat treatment without an additional reducing agent enables easy manipulation of the

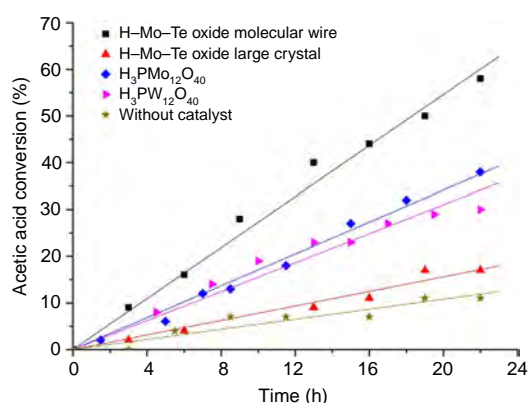


Figure 7 | Ethanol esterification with acetic acid. Reaction conditions, catalyst, 0.1 mg; ethanol, 5 ml; acetic acid, 0.1 ml; decane as internal standard, 0.1 ml; reaction temperature, 365 K. The selectivity of ethyl acetate was 99% and the carbon balance was over 95% in all cases.

oxidation states of the Mo ions in the material, and the band gap of the material can thus be tuned continuously. Mo–Te oxide was calcined under N_2 (180 ml min^{-1} , 1 h, 473–573 K). Powder XRD patterns and FTIR spectra of the calcined samples were similar to those of the as-synthesized material, indicating that the basic structure did not change (Supplementary Fig. 12). Further heating of the material damaged its structure (Supplementary Fig. 12g,h). The diffraction peaks shifted to a higher angle after the material had been treated at a high temperature, and this shift in diffraction peaks was caused by a decrease in the distances between the molecular wires after removal of some water or ammonia from the material. The calcined Mo–Te oxide at 573 K was further characterized, and it remained a rod-shaped material (Supplementary Fig. 13a). The particle size and morphology did not change with calcination, which was indicated by the size distribution (Supplementary Fig. 14). The arrangement of the molecular wire was observed by TEM (Supplementary Fig. 13b) and was in good agreement with the powder XRD patterns. Thus, calcination did not affect the morphology of the material.

Photo images of the Mo–Te oxide showed that the colour of the material gradually changed to blue with an increase in the treatment temperature (Supplementary Fig. 15), indicating that reduced Mo species were generated in the material. The resulting materials were further characterized by ultraviolet–vis spectroscopy, which revealed that Mo ions in the material were reduced by heating (Fig. 8a). The band gap calculated from the ultraviolet–vis spectra indicated that the band gap had decreased with the reduction of Mo ions in the material (Fig. 8b). The band gap of the original Mo–Te oxide was 2.93 eV. After calcination, the band gap of the material decreased to 2.28 eV. The oxidation states of the Mo and Te ions in the material were further studied by XPS. Most of the Mo^{VI} ions were reduced to Mo^{V} ions after heat treatment at 573 K under N_2 , whereas the Te ions in the material were not oxidized (Supplementary Fig. 1f–h). TPD-MS profiles (Supplementary Fig. 6a) of Mo–Te oxide revealed that N_2 had desorbed from the material during heat treatment, indicating that the NH_3 in the material had been oxidized to N_2 , whereas the Mo^{VI} ions had been reduced to Mo^{V} ions. Therefore, the Mo ions were reduced in their reaction with NH_3 in the material. It has been reported that any charge transfer or n -type electron doping in a conduction band causes lattice distortion of Mo-based oxides and consequently a reduction in the band gap³⁵. Regarding Mo–Te oxide under heat treatment, electrons were transferred from

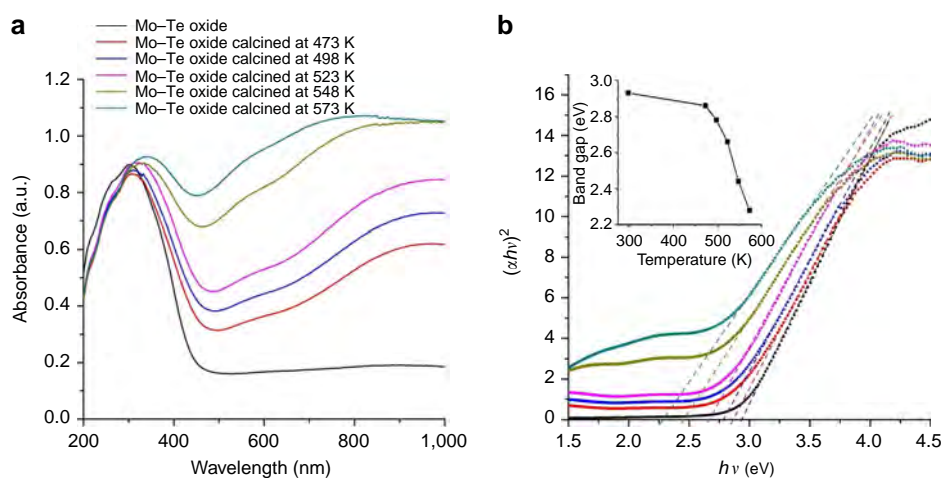


Figure 8 | Band gap change in Mo–Te oxide. (a) Diffuse reflectance ultraviolet–vis spectra of the materials and (b) plots of $h\nu$ versus $(\alpha h\nu)^2$, where α stands for the absorption coefficient: as-synthesized Mo–Te oxide (black) and Mo–Te oxide calcined for 1 h at 473 K (red), 498 K (blue), 523 K (pink), 548 K (yellow) and 573 K (cyan). Insert: band gap changed with the treatment temperature; dotted lines indicate the band gaps.

NH_4^+ to the conduction band of the material (formed in the molecular wires from the d -orbitals of Mo), and therefore the band gap could be reduced. The XRD peak at ca. 22 degree shifted after calcination (Supplementary Fig. 12C), which was ascribed to lattice distortion of the molecular wire.

Discussion

It is interesting that Mo–Te oxide and Mo–Se oxide had similar basic structure, but different morphologies. The lattice parameters of Mo–Te oxide and Mo–Se oxide were similar, and the negative charge and counter cation were the same. Mo–Te oxide was a rod-like material that exhibited preferential crystal growth along the c direction. By contrast, Mo–Se oxide was a hexagonal plate-shaped material that preferred crystal growth along the a – b plane. Several factors affecting this difference in morphology were considered.

First, the difference in the central elements, Te^{IV} and Se^{IV} , was considered. In α -Keggin-type POMs, $[\text{X}^{n+}\text{W}_{12}\text{O}_{40}]^{(8-n)-}$ ($\text{X}:\text{Si}(n=4)$, $\text{Ge}(n=4)$, $\text{P}(n=5)$, $\text{As}(n=5)$, $\text{Co}(n=2)$ and $\text{Zn}(n=2)$), properties such as the redox potential and affinity for protons depend on the identity of the central element. These differences result from the ionic size and electronegativity of the central element³⁶. Differences in the ionic radii and electronegativity of Te^{IV} and Se^{IV} might have affected the morphology of the Mo–Te oxide and Mo–Se oxide crystals.

Second, the synthetic preparations of the materials were different. Soluble SeO_2 was used as a Se^{IV} source in Mo–Se oxide, whereas $\text{Te}(\text{OH})_6$ with a reducing reagent (VOSO_4) was used as a Te^{IV} source in Mo–Te oxide. An obvious difference is that a large amount of Mo–Se oxide (ca. 10% of the yield) was formed within 10 min at room temperature (material characterization in Supplementary Fig. 16 and Supplementary Methods), whereas nearly no solid was observed in the Mo–Te oxide system even after 1 day. Only a small amount of Mo–Te oxide (ca. <0.06% of the yield) was produced after 2 days at room temperature (Supplementary Fig. 17; Supplementary Methods). This indicates that formation rate of Mo–Se oxide was faster than that of Mo–Te oxide. Mo–Se oxide was produced immediately after mixing the Mo and Se sources, which might result from the high concentration of Se^{IV} species in the initial solution due to the soluble SeO_2 . In Mo–Te oxide, Te^{IV} was produced slowly *in situ* by reduction of $\text{Te}(\text{OH})_6$ by VOSO_4 (Supplementary Fig. 18). Furthermore, Te^{IV} is typically insoluble in water compared with Se^{IV} , which might affect the concentration of Te^{IV} (Supplementary Fig. 19). These factors could result in the slow generation of Mo–Te oxide. Therefore, the different synthetic conditions and formation processes might also affect the morphology of the materials.

Mo–Se oxide can also be synthesized through reduction of $\text{Se}(\text{OH})_6$ with VOSO_4 (synthesis and characterization in Supplementary Methods, Supplementary Fig. 20 and Supplementary Fig. 21), which slowly generated Se^{IV} (Supplementary Fig. 18). FTIR (Supplementary Fig. 20b) indicated that the structures of the molecular wires in the resulting material were identical to that obtained using SeO_2 . Powder XRD Rietveld analysis indicated an identical molecular structure in the molecular wires with slightly different packing (Supplementary Fig. 20; Supplementary Fig. 21). SEM images and size distributions (Supplementary Fig. 22) showed that the a – b plane of the material using $\text{Se}(\text{OH})_6$ was much smaller than that using SeO_2 . This result also supports the fact that synthetic conditions affected the morphology of the products.

Proton exchange facilitates the isolation of the molecular wires from the Mo–Te oxide crystal. The density functional theory (DFT) calculation was used to further understand the process.

In the Mo–Te oxide crystals, there were three main interactions organizing the molecular wires into the crystal: electrostatic interactions between anionic molecular wires and ammonium cations, hydrogen bond interactions and van der Waals forces. Generally, the electrostatic interaction is stronger than the other two interactions. Weakening the electrostatic interaction through proton exchange drove isolation from the crystal to form the molecular wires, as demonstrated by the DFT calculation.

Single-crystal structure analysis revealed that the distance of the N in NH_4^+ and the O in the Mo=O terminal bond ($\text{O}(\text{Mo}=\text{O}_t)$) was ca. 2.669–2.814 Å, indicating the presence of electrostatic interactions in the materials. After optimizing the geometry with the DFT calculation, the distance of the N in NH_4^+ and $\text{O}(\text{Mo}=\text{O}_t)$ was 2.753–2.762 Å, similar to the single-crystal data. Moreover, the DFT calculation demonstrated that the distance between the H in NH_4^+ ($\text{H}(\text{NH}_4^+)$) and $\text{O}(\text{Mo}=\text{O}_t)$ was 1.825–1.831 Å (Fig. 9a,b), indicating no covalent bond between $\text{H}(\text{NH}_4^+)$ and $\text{O}(\text{Mo}=\text{O}_t)$. Therefore, electrostatic interactions existed in the material. The chemical formula of molecular wire was $(\text{NH}_4)_{2n}[\text{TeMo}_6\text{O}_{21}]_n$, indicating that $[\text{TeMo}_6\text{O}_{21}]^{2-}$ interacted with two NH_4^+ .

In the second model, all ammonium cations were ideally replaced by protons. The DFT calculation showed that two Mo=O_t bonds were protonated because the O–H bond length was 0.987–0.989 Å (Fig. 9c,d). Protonation of the terminal M=O is common in POMs. Therefore, after proton exchange, the anionic molecular wire was neutralized by protons, destroying the electrostatic interactions.

The third model is the closest to the proton-exchanged material (Fig. 9e,f), in which half of the ammonium cations were replaced by protons. After geometry optimization only one Mo=O_t was protonated in a cell. The anionic molecular wire was partly neutralized by proton exchange. The chemical formula of the molecular wire was $(\text{NH}_4)_n[\text{HTeMo}_6\text{O}_{21}]_n$, indicating that one $[\text{HTeMo}_6\text{O}_{21}]^-$ interacted with only one NH_4^+ . Therefore, the electrostatic interaction was weakened by proton exchange.

The energy to isolate of the crystal and form the molecular wire (ΔE_{iso}), denoted as $\Delta E_{\text{iso}} = E_{\text{molecular wire}} - E_{\text{crystal}}$, was calculated; ΔE_{iso} decreased with increasing protons in the material (Fig. 9g). Thus, proton exchange decreased the electrostatic interaction (ΔE_{iso}), which caused the crystal to crack into small molecular wires.

Furthermore, Raman spectra and FTIR spectra (Supplementary Fig. 23) contained shifts in the Raman band at 964 cm^{-1} and the IR band at 939 cm^{-1} after proton exchange, indicating that the Mo=O bond lengths were altered after proton exchange and protonation of Mo=O³⁷.

In summary, self-assembly of Mo–O octahedra with Se^{IV} or Te^{IV} formed the transition metal oxide-based molecular wires. The structures of Mo–Te oxide and Mo–Se oxide were determined by single-crystal X-ray analysis and powder XRD Rietveld analysis combined with XPS, FTIR and elemental analysis. The materials were composed of $[\text{X}^{\text{IV}}\text{Mo}_6\text{O}_{21}]_n$ ($\text{X} = \text{Se}$ and Te) hexagonal-shaped 1D molecular wires with water and NH_4^+ . Because of their unique structural properties, these materials will give rise to new transition metal oxide nanowire technologies based on their 1D properties.

The metal oxide molecular wires exhibited acid-catalyst activities, which will open up a new field of heterogeneous catalysts based on molecular wires. Moreover, the band gap of the material can be easily manipulated, which may alter the electroconductivity of the material. These molecular wire-based materials are expected to have applications in the fields of thermochromic materials and semiconductors, as well as other related fields.

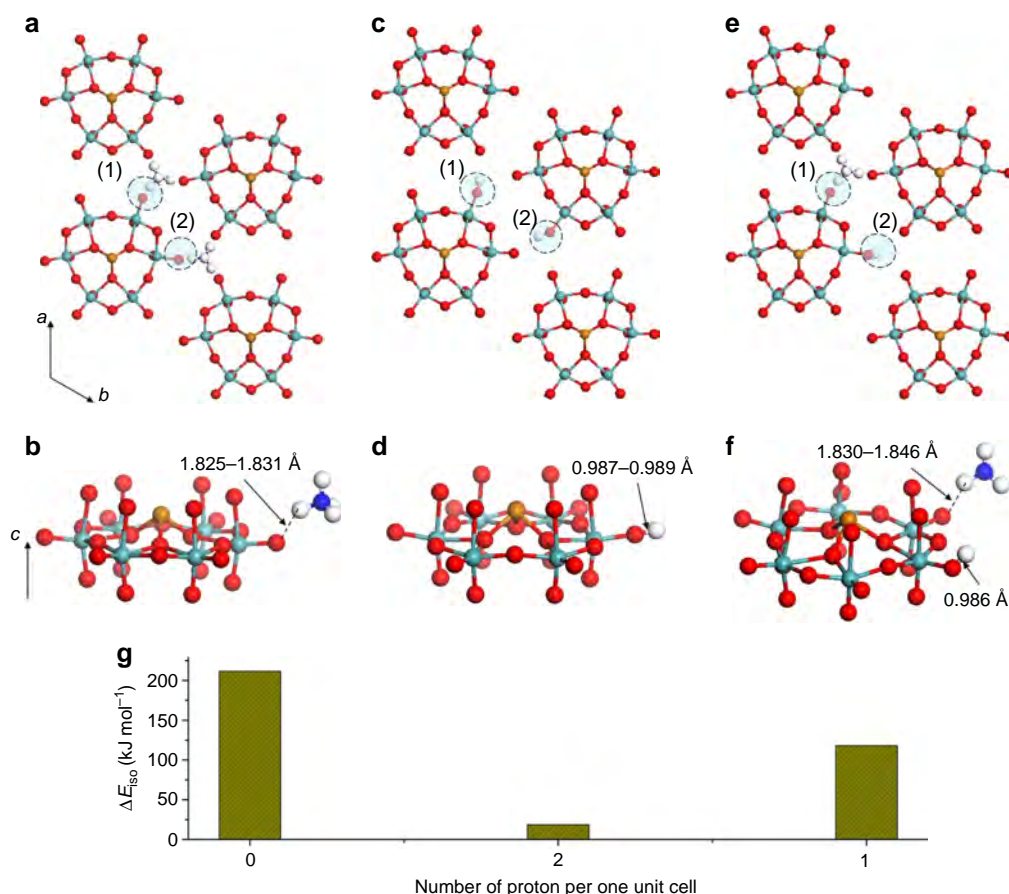


Figure 9 | Structure in unit cells after geometry optimization. (a) Mo-Te oxide with two ammonium cations in a unit cell. (b) Magnified image of a hexagonal unit of [TeMo₆O₂₁] with an ammonium cation. (c) Mo-Te oxide with two protons in a unit cell. (d) Magnified image of a hexagonal unit of [TeMo₆O₂₁] with a proton. (e) Mo-Te oxide with an ammonium cation and a proton in a unit cell. (f) Magnified image of a hexagonal unit of [TeMo₆O₂₁] with an ammonium cation and a proton. (g) Calculated ΔE_{iso} .

Methods

Synthesis of Mo-Te oxide. (NH₄)₆Mo₇O₂₄·4H₂O (1.766 g, 10 mmol based on Mo) was dissolved in 20 ml of water, followed by addition of Te(OH)₆ (0.391 g, 1.7 mmol) to the (NH₄)₆Mo₇O₂₄·4H₂O solution to form solution A. Then, VOSO₄·5H₂O (0.6438 g, 2.5 mmol) was dissolved in 20 ml of water to form solution B. Solution B was poured rapidly into solution A. The mixture was stirred at room temperature for 10 min and degassed by N₂ bubbling for 10 min (pH 2.8). The mixture was introduced into the 50-ml Teflon-liner of a stainless-steel autoclave, which was heated at 448 K for 24 h. After the autoclave had cooled to room temperature, the resulting solid was recovered from the solution by filtration. The obtained solid was washed with 10 ml of water three times and dried at 353 K overnight. Then, 1.07 g of Mo-Te oxide was obtained (yield of 58% based on Mo). Elemental analysis: calculated for N₂Mo₆Te₁O₂₄H₁₄: N, 2.48; Mo, 50.98; Te, 11.30; H, 1.24; V, 0, found: N, 2.49; Mo, 51.59; Te, 11.13; H, 1.22; V, 0.

Synthesis of large Mo-Te oxide crystals. (NH₄)₆Mo₇O₂₄·4H₂O (1.766 g, 10 mmol based on Mo) was dissolved in 20 ml of water, followed by addition of Te(OH)₆ (0.391 g, 1.7 mmol) to the (NH₄)₆Mo₇O₂₄·4H₂O solution to form solution A. Then, VOSO₄·5H₂O (0.6438 g, 2.54 mmol) was dissolved in 20 ml of water to form solution B. Solution B was poured rapidly into solution A. The mixture was stirred at room temperature for 10 min and degassed by N₂ bubbling for 10 min (pH of 2.8). The solution was sealed and stored in a refrigerator for ~3 months. The large well-crystallized Mo-Te oxide was collected by centrifugation (3,500 r.p.m., 5 min). Then, 5 mg of Mo-Te oxide was obtained (yield of 0.3% based on Mo).

Synthesis of Mo-Se oxide. (NH₄)₆Mo₇O₂₄·4H₂O (1.766 g, 10 mmol based on Mo) was dissolved in 20 ml of water, followed by addition of SeO₂ (0.189 g, 1.7 mmol) to the (NH₄)₆Mo₇O₂₄·4H₂O solution. The pH of the solution was adjusted to 2.8 by H₂SO₄ (1 M), and the solution was stirred at room temperature for 10 min (yellow solid was generated during this process) and degassed by N₂ bubbling for 10 min. The mixture was introduced into the 50-ml Teflon-liner of a

stainless-steel autoclave, which was heated at 448 K for 24 h. After the autoclave had cooled to room temperature, the resulting solid was recovered from the solution by filtration. The obtained solid was washed with 10 ml of water three times and dried at room temperature overnight. Then, 0.17 g of Mo-Se oxide was obtained (yield of 9.6%). Elemental analysis: calculated for N₂Mo₆Se₁O₂₃H₁₂: N, 2.64; Mo, 54.17; Se, 7.43; and H, 1.13, found: N, 2.72; Mo, 54.19; Se, 7.58; and H, 1.25.

Ion exchange with protons. Mo-Te oxide or Mo-Se oxide (0.6 g) was dispersed in 24 ml of water. HCl (36%, 2 ml) was added to the solution. The mixture was stirred for 15 h. The resulting solid was recovered by filtration and dried at room temperature. Elemental analysis: calculated for N_{1.1}Mo₆Te₁O₂₆H_{15.3} (denoted as H-Mo-Te oxide): N, 1.34; Mo, 50.06; Te, 11.10; and H, 1.33, found: N, 1.44; Mo, 50.34; Te, 11.18; and H, 1.51. Elemental analysis: calculated for N_{1.1}Mo₆Se₁O₂₇H_{17.3} (denoted as H-Mo-Se oxide): N, 1.38; Mo, 51.43; Se, 7.05; and H, 1.55, found: N, 1.52; Mo, 51.68; Se, 7.05; and H, 1.58.

Separation of molecular wires. H-Mo-Te oxide or H-Mo-Se oxide (5 mg) was dispersed in 5 ml of ethanol, followed by ultrasonication (200 W, 37 kHz) for 1 h. The solution was centrifuged for 2 h (3,500 r.p.m.). The upper 50% of the colloid was used in further characterization. Approximately 2 wt% of H-Mo-Te oxide formed nanoparticles, as determined by measuring the weight of remaining solid in the solution.

Catalytic activity. A catalyst (0.1 g) was dispersed in 5 ml of ethanol. Acetic acid (0.1 ml) and decane (0.1 ml) were added to the ethanol solution. The mixture was heated at 365 K. The reaction was monitored by gas chromatography with flame ionization detector. Conversion was calculated based on acetic acid. The selectivity was calculated by $n(\text{ethyl acetate})/n(\text{all products})$, and the carbon balance was calculated by $n(\text{all products})/n(\text{acetic acid})$, where n is the molar amount. The carbon balance was over 95% and the selectivity of ethyl acetate was 99% in all cases.

Calcination. Mo–Te oxide (0.1 g) was calcined in a glass tube that was set into a furnace under N₂ flow (180 ml min⁻¹) at 473, 498, 523, 548 and 573 K for 1 h with a rate of increase in temperature of 10 K min⁻¹.

Characterization. XRD patterns were obtained on RINT2200 (Rigaku, Japan) with Cu K α radiation (tube voltage: 40 kV, tube current: 20 and 40 mA for structural analysis). FTIR spectroscopy was carried out on a Perkin Elmer PARAGON 1000 (Perkin Elmer, USA). Diffuse reflectance ultraviolet–vis spectra were obtained using a JASCO V-570 spectrophotometer equipped with an ISN-470 reflectance spectroscopy accessory (JASCO, Japan). The band gap of the material was obtained from the figure of $h\nu$ versus $(\alpha h\nu)^2$ via the equation of $(\alpha h\nu)^2 = k(h\nu - E_g)$, where E_g is the band gap; α is the absorption coefficient; $h\nu$ is the incident light energy; and k is a constant³⁸. XPS was performed on a JPS-9010MC (JEOL, Japan). The spectrometer energies were calibrated using the Au 4f_{7/2} peak at 84 eV. Raman spectra were recorded on a Renishaw inVia Raman Microscope (Renishaw, UK).

TPD-MS measurements were carried out from 313 to 893 K at a heating rate of 10 K min⁻¹ under He flow (flow rate: 50 ml min⁻¹). Samples were set up between two layers of quartz wool. A TPD apparatus (BEL Japan, Inc., Japan) equipped with a quadrupole mass spectrometer (M-100QA, Anelva) was used to detect NH₃ ($m/z = 16$), H₂O ($m/z = 18$), N₂ ($m/z = 28$) and O₂ ($m/z = 32$). TG-DTA was carried out up to 773 K at a heating rate of 10 K min⁻¹ under nitrogen flow (flow rate: 50 ml min⁻¹) on a Thermo plus TG-8120 (Rigaku, Japan).

SEM images were obtained with a HD-2000 (HITACHI) and a JSM-6360LA (JEOL, Japan). TEM images were taken with a 200-kV TEM (JEOL, JEM-2010F, Japan). AFM images were obtained on an Agilent 5500 scanning probe microscope (Agilent Technologies, USA) in air by a silicon cantilever with a 7-nm radius.

Elemental compositions were determined using an inductively coupled plasma atomic emission spectroscopy method (ICPE-9000, Shimadzu, Japan). The CHN elemental compositions were determined in the Instrumental Analysis Division, Equipment Management Center, Creative Research Institution, Hokkaido University.

Single-crystal X-ray analysis of Mo–Te oxide. The crystals obtained at room temperature were still too small for the diffractometer in the laboratory single-crystal analysis system, and data collection was performed on a high-precision diffractometer installed in the SPring-8 BL40XU beamline^{39,40}. The synchrotron radiation emitted from a helical undulator was monochromated by an Si(111) channel cut monochromator and focused with a Fresnel zone plate. A Rigaku Saturn724 charge-coupled device detector was used. The measurement was performed at 100 (2) K. An empirical absorption correction based on Fourier series approximation was applied. The data were corrected for Lorentz and polarization effects. The structure was solved by direct methods and refined by full-matrix least-squares (SHELX-97)⁴¹, where the unweighted and weighted agreement factors of $R = \sum |F_o| - |F_c| / \sum |F_o|$ ($I > 2.00\sigma(I)$) and $wR = [\sum w(F_o^2 - F_c^2)^2 / \sum w(F_o^2)]^{1/2}$ were used. Crystallographic data, atom position and bond lengths for Mo–Te oxide are shown in Supplementary Tables 2–4. The Cif file is available in Supplementary Data 1.

Structure determination by powder X-ray diffraction. The structure of Mo–Se oxide was determined from powder XRD. A powder XRD pattern for structural analysis was obtained on a RINT2200 (Rigaku, Japan) with Cu K α radiation (tube voltage: 40 kV, tube current: 40 mA, scan speed: 1° min⁻¹, step: 0.01°). First, the powder XRD pattern was indexed by the DICVOL06 (ref. 42) and X-cell programs⁴³. After performing Pawley refinement, the most reasonable space group was obtained. Then, the Le Bail method⁴⁴ was applied for intensity extraction with the EdPCR program. The initial structure was solved by a charge-flipping algorithm⁴⁵. The positions and types of atoms were obtained by analysing the generated electron density maps (Supplementary Table 5). The initial structure was refined by Rietveld analysis.

Rietveld refinement. The structures of Mo–Te oxide (from single-crystal analysis) and Mo–Se oxide (from powder XRD) were refined by powder XRD Rietveld refinement⁴⁶. Pattern parameters and lattice parameters of the materials were refined by the Pawley method. The atomic temperature factor of Mo–Te oxide was from the single-crystal analysis. Then, isotropical temperature factors were given for every atom in the initial structure of Mo–Se oxide. Rietveld analysis was initiated with the initial models of the materials, and lattice parameters and pattern parameters were from the Pawley refinement. Every atom position was refined. Occupancy of atoms in the framework was fixed without further refinement, and occupancies of atoms in water and the cations were refined with consideration of elemental analysis results. Finally, the pattern parameters were refined again to obtain the lowest R_{wp} value. The crystallographic parameters, atom positions and bond lengths of Mo–Se oxide are shown in Supplementary Table 2, Supplementary Table 6 and Supplementary Table 7, and the Rietveld analysis parameters of Mo–Te oxide and Mo–Se oxide are shown in Supplementary Table 1.

DFT calculations. The structures of the Mo–Te oxide crystals and the Mo–Te oxide molecular wires were optimized using the DMol³ program^{47,48}. The Perdew–Burke–Ernzerhof generalized gradient functional and DND basis sets

were employed. The lattice parameters and atom coordination of the initial structure of the Mo–Te oxide crystal were from the single-crystal analysis. For the Mo–Te oxide molecular wires, the structure was optimized in a cell with lattice parameters of $a = b = 30 \text{ \AA}$, $c = 3.944 \text{ \AA}$ and $\alpha = \beta = \gamma = 90^\circ$, which insured that the interaction between each molecular wire was negligible. The relative positions of the atoms in the molecular wires were the same as that from the single-crystal analysis.

References

- Hong, B. H., Bae, S. C., Lee, C. W., Jeong, S. & Kim, K. S. Ultrathin single-crystalline silver nanowire arrays formed in an ambient solution phase. *Science* **294**, 348–351 (2001).
- Ernst, T. Controlling the polarity of silicon nanowire transistors. *Science* **340**, 1414–1415 (2013).
- Storm, K. *et al.* Spatially resolved Hall effect measurement in a single semiconductor nanowire. *Nat. Nanotechnol.* **7**, 718–722 (2012).
- Holm, J. V. *et al.* Surface-passivated GaAsP single-nanowire solar cells exceeding 10% efficiency grown on silicon. *Nat. Commun.* **4**, 1498 (2013).
- Tomioka, K., Yoshimura, M. & Fukui, T. A III–V nanowire channel on silicon for high-performance vertical transistors. *Nature* **488**, 189–192 (2012).
- Wallentin, J. *et al.* InP nanowire array solar cells achieving 13.8% efficiency by exceeding the ray optics limit. *Science* **339**, 1057–1060 (2013).
- Heiss, M. *et al.* Self-assembled quantum dots in a nanowire system for quantum photonics. *Nat. Mater.* **12**, 439–444 (2013).
- Ouyang, L., Maher, K. N., Yu, C. L., Mccarty, J. & Park, H. Catalyst-assisted solution-liquid-solid synthesis of CdS/CdSe nanorod heterostructures. *J. Am. Chem. Soc.* **129**, 133–138 (2007).
- Schumacher, T., Giessen, H. & Lippitz, M. Ultrafast spectroscopy of quantum confined states in a single CdSe nanowire. *Nano Lett.* **13**, 1706–1710 (2013).
- Laochareonsuk, R. *et al.* Flow-based solution-liquid-solid nanowire synthesis. *Nat. Nanotechnol.* **8**, 660–666 (2013).
- Liu, X. *et al.* All-printable band-edge modulated ZnO nanowire photodetectors with ultra-high detectivity. *Nat. Commun.* **5**, 4007 (2014).
- Joo, J., Choh, B. Y., Prakash, M., Boyden, E. S. & Jacobson, J. M. Face-selective electrostatic control of hydrothermal zinc oxide nanowire synthesis. *Nat. Mater.* **10**, 596–601 (2011).
- Koka, A. & Sodano, H. A. High-sensitivity accelerometer composed of ultra-long vertically aligned barium titanate nanowire arrays. *Nat. Commun.* **4**, 2682 (2013).
- Gothard, C. M., Rao, N. A. & Nowick, J. S. Nanometer-sized amino acids for the synthesis of nanometer-scale water-soluble molecular rods of precise length. *J. Am. Chem. Soc.* **129**, 7272–7273 (2007).
- Sakaguchi, H., Matsumura, H. & Gong, H. Electrochemical epitaxial polymerization of single-molecular wires. *Nat. Mater.* **3**, 551–557 (2004).
- Davis, W. B., Svec, W. A., Ratner, M. A. & Wasielewski, M. R. Molecular-wire behaviour in p-phenylenevinylene oligomers. *Nature* **396**, 60–63 (1998).
- Mahato, R. N. *et al.* Ultrahigh magnetoresistance at room temperature in molecular wires. *Science* **341**, 257–260 (2013).
- Remskar, M. *et al.* Self-assembly of subnanometer-diameter single-wall MoS₂ nanotubes. *Science* **292**, 479–481 (2001).
- Mihailovic, D. Inorganic molecular wires: Physical and functional properties of transition metal chalcogenide polymers. *Prog. Mater. Sci.* **54**, 309–350 (2009).
- Long, D.-L., Tsunashima, R. & Cronin, L. Polyoxometalates: building blocks for functional nanoscale systems. *Angew. Chem. Int. Ed. Engl.* **49**, 1736–1758 (2010).
- Hill, C. L. Special thematic issue on polyoxometalates. *Chem. Rev.* **98**, 1–390 (1998).
- Cronin, L. & Müller, A. Special thematic issue on polyoxometalates. *Chem. Soc. Rev.* **41**, 7325–7648 (2012).
- Ma, R. & Sasaki, T. Nanosheets of oxides and hydroxides: ultimate 2D charge-bearing functional crystallites. *Adv. Mater.* **22**, 5082–5104 (2010).
- Nicolosi, V., Chhowalla, M., Kanatzidis, M. G., Strano, M. S. & Coleman, J. N. Liquid exfoliation of layered materials. *Science* **340**, 1226419 (2013).
- Galán-Mascarós, J. R. *et al.* A novel chainlike heteropolyanion formed by Keggin units: synthesis and structure of (ET)_{8n}[PMnW₁₁O₃₉]_n · 2nH₂O. *Angew. Chem. Int. Ed. Engl.* **34**, 1460–1462 (1995).
- Chen, L. *et al.* Three transition-metal substituted polyoxotungstates containing Keggin fragments: from trimer to one-dimensional chain to two-dimensional sheet. *Cryst. Growth Des.* **11**, 1913–1923 (2011).
- Wang, Y. *et al.* Cs₄Mo₅P₂O₂₂: a first Strandberg-type POM with 1D straight chains of polymerized [Mo₅P₂O₂₃]⁶⁻ units and moderate second harmonic generation response. *Chem. Commun.* **49**, 306–308 (2013).
- Balendhran, S. *et al.* Enhanced charge carrier mobility in two-dimensional high dielectric molybdenum oxide. *Adv. Mater.* **25**, 109–114 (2013).
- Kortz, U. *et al.* Heteropolymolybdates of As^{III}, Sb^{III}, Bi^{III}, Se^{IV}, and Te^{IV} functionalized by amino acids. *Angew. Chem. Int. Ed. Engl.* **41**, 4070–4073 (2002).

30. Yang, D., Li, S., Ma, P., Wang, J. & Niu, J. Controlled assembly of inorganic-organic frameworks based on $[\text{SeMo}_6\text{O}_{21}]^{4-}$ polyanion. *Inorg. Chem.* **52**, 14034–14039 (2013).
31. Javey, A., Nam, S. W., Friedman, R. S., Yan, H. & Lieber, C. M. Layer-by-layer assembly of nanowires for three-dimensional, multifunctional electronics. *Nano Lett.* **7**, 773–777 (2007).
32. Pauzauskie, P. J., Sirbully, D. J. & Yang, P. Semiconductor nanowire ring resonator laser. *Phys. Rev. Lett.* **96**, 143903 (2006).
33. Hu, X. K. *et al.* Comparative study on MoO_3 and H_xMoO_3 nanobelts: structure and electric transport. *Chem. Mater.* **20**, 1527–1533 (2008).
34. Bouzidi, A. *et al.* Effect of substrate temperature on the structural and optical properties of MoO_3 thin films prepared by spray pyrolysis technique. *Mater. Sci. Eng. B* **97**, 5–8 (2003).
35. Huang, P., He, Y., Cao, C. & Lu, Z. Impact of lattice distortion and electron doping on α - MoO_3 electronic structure. *Sci. Rep.* **4**, 7131 (2014).
36. Eda, K. & Osakai, T. How can multielectron transfer be realized? A case study with Keggin-type polyoxometalates in acetonitrile. *Inorg. Chem.* **54**, 2793–2801 (2015).
37. Wachs, I. E. & Roberts, C. A. Monitoring surface metal oxide catalytic active sites with Raman spectroscopy. *Chem. Soc. Rev.* **39**, 5002–5017 (2010).
38. Debanath, M. K. & Karmakar, S. Study of blueshift of optical band gap in zinc oxide (ZnO) nanoparticles prepared by low-temperature wet chemical method. *Mater. Lett.* **111**, 116–119 (2013).
39. Yasuda, N., Fukuyama, Y., Toriumi, K., Kimura, S. & Takata, M. Submicrometer single crystal diffractometry for highly accurate structure determination. *AIP Conf. Proc.* **1234**, 147–150 (2010).
40. Yasuda, N. *et al.* X-ray diffractometry for the structure determination of a submicrometre single powder grain. *J. Synchrotron Radiat.* **16**, 352–357 (2009).
41. Sheldrick, G. M. *SHELX-97, Program for Crystal Structure Analysis* (Universität Göttingen, 1997).
42. Boulton, A. & Louer, D. Powder pattern indexing with the dichotomy method. *J. Appl. Crystallogr.* **37**, 724–731 (2004).
43. Neumann, M. A. X-Cell: a novel indexing algorithm for routine tasks and difficult cases. *J. Appl. Crystallogr.* **36**, 356–365 (2003).
44. Le Bail, A. Frontiers between crystal structure prediction and determination by powder diffractometry. *Powder Diffr.* **23**, S5–S12 (2008).
45. Palatinus, L. & Chapuis, G. SUPERFLIP—a computer program for the solution of crystal structures by charge flipping in arbitrary dimensions. *J. Appl. Crystallogr.* **40**, 786–790 (2007).
46. Young, R. A. *The Rietveld method* (Oxford Univ. Press, 1995).
47. Delley, B. From molecules to solids with the DMol³ approach. *J. Chem. Phys.* **113**, 7759–7764 (2000).
48. Delley, B. An all-electron numerical method for solving the local density functional for polyatomic molecules. *J. Chem. Phys.* **92**, 508–517 (1990).

Acknowledgements

This work was financially supported by a Grant-in-Aid for Scientific Research (A) (grant No. 2324-6135) from the Ministry of Education, Culture, Sports, Science and Technology, Japan. The synchrotron radiation experiments were performed at the BL40XU of SPring-8 with the approval of the Japan Synchrotron Radiation Research Institute (JASRI) (Proposal No. 2013A1052 and 2014A1177). M.S. thanks PRESTO, JST for financial support. A part of this work was conducted at Hokkaido University, supported by the 'Nanotechnology Platform' Program of the Ministry of Education, Culture, Sports, Science and Technology (MEXT), Japan.

Author contributions

Z.Z. and T.M. performed the material synthesis, characterization, and other corresponding experiments. N.Y., M.S., and Z.Z. performed the single-crystal analysis. N.S. and Z.Z. performed the TEM observations. H.A., Z.Z., and K.A. performed the AFM analysis. Z.Z. and M.S. wrote the paper. W.U. designed the research.

Additional information

Accession codes: The X-ray crystallographic coordinates for structures reported in this Article have been deposited at the Cambridge Crystallographic Data Centre (CCDC), under deposition number CCDC 1401200. These data can be obtained free of charge from The Cambridge Crystallographic Data Centre via www.ccdc.cam.ac.uk/data_request/cif.

Supplementary Information accompanies this paper at <http://www.nature.com/naturecommunications>

Competing financial interests: The authors declare no competing financial interests.

Reprints and permission information is available online at <http://npg.nature.com/reprintsandpermissions/>

How to cite this article: Zhang, Z. *et al.* Ultrathin inorganic molecular nanowire based on polyoxometalates. *Nat. Commun.* **6**:7731 doi: 10.1038/ncomms8731 (2015).



This work is licensed under a Creative Commons Attribution 4.0 International License. The images or other third party material in this article are included in the article's Creative Commons license, unless indicated otherwise in the credit line; if the material is not included under the Creative Commons license, users will need to obtain permission from the license holder to reproduce the material. To view a copy of this license, visit <http://creativecommons.org/licenses/by/4.0/>

Direct Imaging of Octahedral Distortion in a Complex Molybdenum Vanadium Mixed Oxide**

Thomas Lunkenbein, Frank Girgsdies, Anna Wernbacher, Johannes Noack, Gudrun Auffermann, Akira Yasuhara, Achim Klein-Hoffmann, Wataru Ueda, Maik Eichelbaum, Annette Trunschke, Robert Schlögl, and Marc G. Willinger*

Abstract: Complex Mo,V-based mixed oxides that crystallize in the orthorhombic M1-type structure are promising candidates for the selective oxidation of small alkanes. The oxygen sublattice of such a complex oxide has been studied by annular bright field scanning transmission electron microscopy. The recorded micrographs directly display the local distortion in the metal oxygen octahedra. From the degree of distortion we are able to draw conclusions on the distribution of oxidation states in the cation columns at different sites. The results are supported by X-ray diffraction and electron paramagnetic resonance measurements that provide integral details about the crystal structure and spin coupling, respectively.

In the past 25 years, high-resolution transmission electron microscopy (HRTEM) has been developed to a powerful tool for direct imaging of atomic structures.^[1] However, direct imaging of elements with low atomic number, such as oxygen, nitrogen, and hydrogen is difficult due to their low scattering power. For instance, in high-angle annular dark field scanning transmission electron microscopy (HAADF-STEM) the intensity is due to Rutherford scattering by the nuclei and, therefore, approximately proportional to Z^2 .^[2] As a result, the intensity of heavy elements generally overwhelms the signal of light ones. Nonetheless, individual oxygen columns have been observed by advanced techniques, such as exit wave reconstruction,^[3] spherical aberration corrected TEM,^[4] and

high voltage HRTEM.^[5] Although these methods show concepts to pinpoint the oxygen columns, their utilization is limited.

Pioneering work on the direct imaging of oxygen columns was mainly accomplished on structures derived from thermodynamically stable, high-temperature perovskites characterized by negligible beam sensitivity.^[4b,5] In catalysis and energy conversion, however, metastable and specifically beam-sensitive phases exhibiting defects and distortions in the metal-oxygen polyhedra are generally used. Direct imaging of light elements in beam-sensitive materials is, however, possible by using an annular bright field (ABF) detector^[6] in combination with STEM. Small-angle scattering occurs at the edge of the atoms where all elements have comparable charge densities. Thus the scattering intensities of light and heavy elements are more balanced.^[7] Here we present the direct imaging of the oxygen sublattice in beam-sensitive, binary orthorhombic (Mo,V)O_x. Images were recorded with a double corrected JEOL ARM 200F equipped with a cold field emission gun (CFEG) using HAADF and ABF detectors.

(Mo,V)O_x crystallizes in an orthorhombic structure (Pba2) closely related to the so-called M1 phase of MoVTeNbO_x (ICSD no. 55097, Figure 1).^[8] It has been considered as catalyst in the oxidative activation of short-chain alkanes in the light of prospected raw material changes from crude oil to natural gas.^[9] The obtained ABF-STEM images enable a direct measurement of the metal-oxygen bond angles for the different metal sites. Although the measured distortions correspond to a projection onto the basal plane, they give a hint on the oxidation state of each metal site.^[10] Our findings are compared with Rietveld refined X-ray diffraction (XRD) data and electron paramagnetic resonance (EPR) spectroscopy.

Aberration-corrected HAADF-STEM imaging has been used before^[2,11] to directly observe the characteristic metal framework of the orthorhombic (Mo,V)O_x structure in the [001] projection. It provided valuable insights on different metal site occupancies and defect structures.^[2,12] In the case of highly crystalline (Mo,V)O_x (Figure SI1), the analysis of HAADF images (Figure 2A) showed a similar trend in the Mo site occupancy (Figure SI2). Using the labeling scheme suggested by DeSanto^[8] et al., the Mo content in the respective sites decreases in the order S9 ≈ S5 ≈ S6 > S8 ≈ S10 ≈ S11 > S2 > S4 ≈ S3 ≈ S7 > S1. This result is in good agreement with the preferential positions of Mo and V obtained by Rietveld refinement of the XRD data (Figure 1, Table 1, and Table SI1). However, occupancies diverge slightly from observations reported previously, thus indicating

[*] Dr. T. Lunkenbein, Dr. F. Girgsdies, A. Wernbacher, Dr. J. Noack, A. Klein-Hoffmann, Dr. M. Eichelbaum, Dr. A. Trunschke, Prof. R. Schlögl, Dr. M. G. Willinger
Department of Inorganic Chemistry
Fritz-Haber-Institut der Max-Planck-Gesellschaft
Faradayweg 4–6, 14195 Berlin (Germany)
E-mail: willinger@fhi-berlin.mpg.de

Dr. G. Auffermann
Max Planck Institut für Chemische Physik Fester Stoffe
Nöthnitzer Straße 40, 01187 Dresden (Germany)

A. Yasuhara
Jeol Ltd.
Tokyo (Japan)
Prof. W. Ueda
Catalysis Research Center, Hokkaido University
Sapporo (Japan)

Prof. R. Schlögl, Dr. M. G. Willinger
Max-Planck-Institut für Chemische Energiekonversion
Stiftstrasse 34–36, 45470 Mülheim an der Ruhr, Germany

[**] J.N. thanks BasCat for a fellowship.

Supporting information for this article is available on the WWW under <http://dx.doi.org/10.1002/anie.201502236>.

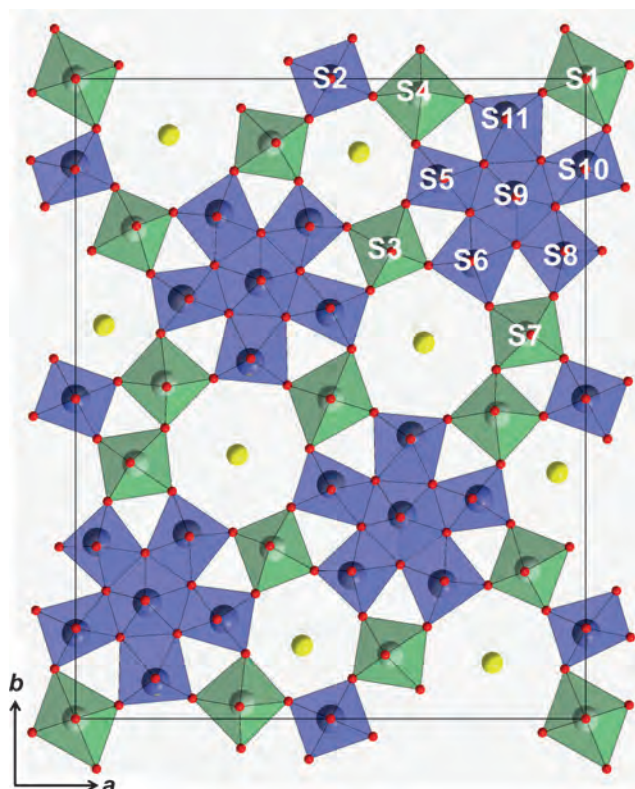


Figure 1. Polyhedron model of the orthorhombic $(\text{Mo},\text{V})\text{O}_x$ structure viewed along $[001]$ obtained from Rietveld refined XRD pattern (Figures S14 and S15). Mo- or V-dominated, channel and oxygen sites are denoted by blue or green polyhedra/atoms, yellow and red atoms, respectively.

Table 1: Measured oxygen-metal-oxygen bond angles within the basal plane of a low, medium, and high distorted metal site, preferred metal site occupation, and proposed oxidation states of Mo and V in the orthorhombic $(\text{Mo},\text{V})\text{O}_x$ structure. Additional bond angles for various metal sites are listed in the Supporting Information (Table S11).

Oxygen site ^[a]	Metal site	Oxygen site ^[a]	Bond angle $[\circ]^{[b]}$	Metal ^[c]	Population [at.%] ^[d]	d^1 (OS) ^[e]
O26	S1	O13	$90^{[f]}$	V	87	high
O13	S1	O26'	90 ± 1			(4+)
O26'	S1	O13'	$90^{[f]}$			
O13'	S1	O26	90 ± 1			
O30	S3	O17	88 ± 4	V	69	low
O17	S3	O14	97 ± 3			(5+)
O14	S3	O15	89 ± 4			
O15	S3	O30	85 ± 3			
O19	S5	O30	109 ± 2	Mo	90	low
O30	S5	O18	83 ± 4			(6+)
O18	S5	O22	73 ± 4			
O22	S5	O19	95 ± 4			

[a] An oxygen site map is given in the Supporting Information (Figure S11). [b] Measured metal–oxygen bond angles in the basal plane. Given numbers are averages of different spots. [c] Preferred metal at the corresponding metal site as determined from the XRD data (Figures 1 and S15) and HAADF-STEM image (Figures 2A and S12). [d] Occupancy of the dominating metal as obtained from XRD. The difference to 100% corresponds to the minor element. [e] Probability of realizing a d^1 state and proposed oxidation state. [f] Symmetry centers: The angle of neighboring metal–oxygen bonds has to be 180° .

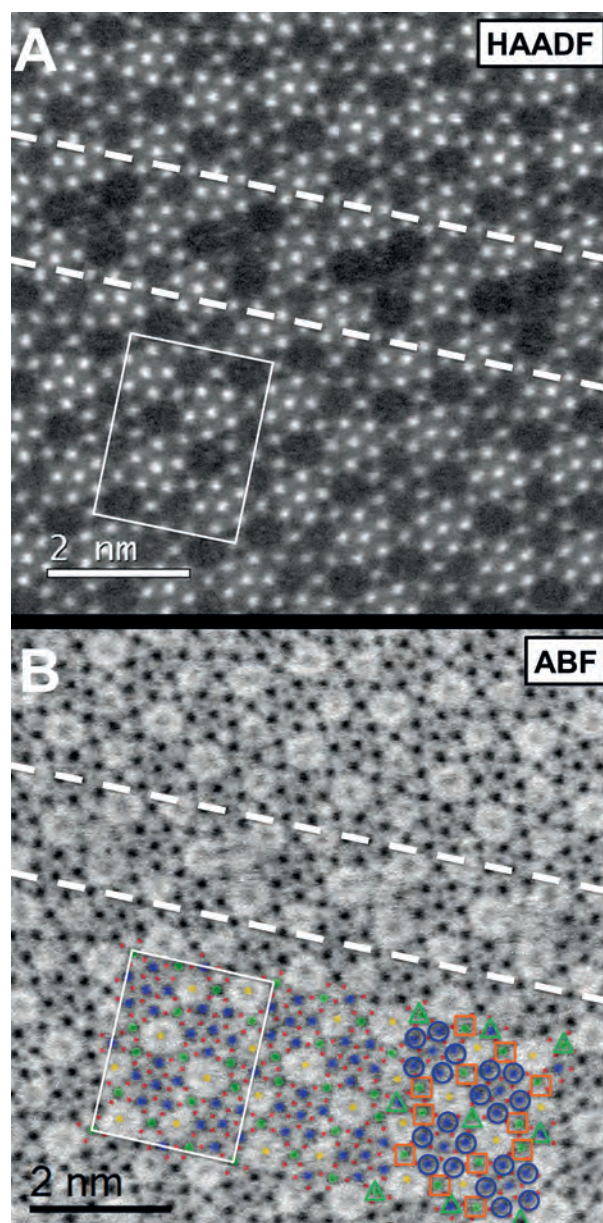


Figure 2. A) Atomic resolution HAADF-STEM image and simultaneously recorded ABF-image (B) of $(\text{Mo},\text{V})\text{O}_x$. The white rectangles in (A) and (B) display the orthorhombic unit cell. The white dashed lines in (A) and (B) denote a trigonal intergrowth. In (B) Mo-, V-dominating metal, channel, and oxygen sites are highlighted in blue, green, yellow, and red, respectively. In addition, metal sites with high, intermediate, and no distortions are indicated by blue circles, orange squares, and green triangles, respectively. Original ABF images are given in the Supporting Information (Figures S17 and S18).

a certain chemical flexibility of orthorhombic $(\text{Mo},\text{V})\text{O}_x$. Variations in the Mo and V distribution could be related to the fact that thermal treatment after hydrothermal synthesis was omitted. It is important to note here that STEM is a very local method and therefore allows resolving statistic occupation of inequivalent sites for individual unit cells (Figure S13), whereas XRD averages over the whole sample.

The simultaneously recorded annular bright field (ABF)-STEM image is depicted in Figure 2B. In ABF, channels

appear bright, whereas individual metal and oxygen sites appear dark. As opposed to HAADF, the oxygen columns in the vicinity of the metal sites can clearly be observed in the ABF images. In agreement with the XRD measurements (Figures 1, SI4, and SI5), ABF shows that heptagonal^[14] and hexagonal channels exhibit additional electron density indicating at least a partial occupancy of both channels. Interestingly, the highly localized contrast due to the oxygen columns indicates a relative confined distribution of O atoms, suggesting an equal distortion of the MO₆ octahedra stacks along [001] columns, regardless of the mixed Mo/V ratio. If the distortion at one site would vary, a diffuse contrast of the oxygen atoms would be expected. The direct imaging of the metal oxygen polyhedra provides information about bond angles that can otherwise only be obtained by a combination of different physical methods. However, direct measurement of structural parameters requires distortion-free imaging. To validate the absence of scan distortions a Pt reference sample was investigated using the same settings (see Figure SI6). Improved room design and the high stability of modern TEM platforms allow distortion-free imaging and abstraction of structural parameters as demonstrated in several recent publications.^[15] The STEM images in Figure 2 and the measured angles correspond to a 2D projection of (Mo,V)O_x. Thus, the apical M–O bonds are not accessible. The measured bond angles of the different metal sites in (Mo,V)O_x are listed in Tables 1 and SI1 and are schematically illustrated in Figure 2B. Almost no distortion was obtained in the basal plane of the S1 and S2 sites, medium distortions were measured at the S3, S4, and S7 sites, and the highest distortions were observed for the metal sites S5, S6, S8, S9, S10, and S11, which are located in the pentagonal units.

The distortion in transition metal oxides is a result of symmetry breaking due to energy minimization and depends on the spin configuration of the central cation^[10] and the local surrounding.^[16] Fully oxidized polyhedra consisting of Mo or V are known to always show a high out-of-center distortion tendency toward various directions^[8,10] due to their ability to form stable “molybdenyl” or “vanadyl” (M=O; M=Mo,V) species. Structurally, the M1 phase represents a group of nonstoichiometric oxides such as Mo₅O₁₄, Mo₈O₂₃, and Mo₁₇O₄₇.^[17] Mo₈O₂₃ for instance also exhibits a complex framework, composed of distorted edge-shared octahedra hosting Mo=O species and less distorted bands of corner-shared polyhedra.^[18] In the case of vanadium, V⁵⁺ polyhedra are generally distorted through one shortened bond length forming the characteristic V=O bond.^[10b,19] While the strong distortion in highly oxidized Mo generally arises from a shortening of two metal oxygen bonds, in vanadium only one bond is compressed.^[18,19] It has further been highlighted that the majority of Mo⁶⁺ cations tend to shift toward edges of the corresponding octahedra,^[10b] leading to the occurrence of significant changes in the projected metal–oxygen bond angles. In the case of fully oxidized V, the metal centers are known to be mostly shifted toward the vertices,^[10b] thus resulting in lower projected bond distortions. This is reflected in our measured metal–oxygen bond angles which are highest for the molybdenum oxide octahedra (Tables 1 and SI1) in the pentagonal building block.

Based on the measured projected distortions we therefore propose that medium and highly distorted sites (S3, S4, S7, S5, S6, S8, S10, and S11) contain empty d-orbitals and accommodate highly charged V and Mo cations, respectively. In contrast, almost no distortions are observed for symmetric S1 and S2 sites. Thus, these sites might exhibit an increased probability for hosting one d-electron at the respective metal centers. Finally, in the case of the pentagonal bipyramidal S9 site, no strong distortions were observed, although XRD data and HAADF-STEM analysis indicate that it is mainly occupied by Mo (Figure 2B, Table 1) and, according to charge neutrality, should be in a d⁰ oxidation state. Hence, we cannot draw conclusions on the relation between distortion and d-occupancy in the case of the pentagonal bipyramid.

To verify the presence of unpaired electrons an EPR measurement was conducted. The corresponding spectrum (Figure SI9) can be fitted by two broad featureless signals and two signals containing hyperfine splitting (Figure SI10). The g-factors for the broad signals are typical for strongly interacting V (or Mo) species with 3d (or 4d) electrons. These features are indicating the presence of two distinguishable metal sites in the bulk phase and were therefore used for correlation. The signals with resolved hyperfine structure correspond to isolated ⁵¹V⁴⁺ in an axial crystal field. Quantification of the spin numbers in the sample under the assumption that only d⁰ and d¹ cations are present, reveals that at least 1–2% of the metals carry unpaired d-electrons (Tables SI2–SI5). In line with our assignment, the results could be translated to the presence of d¹ electrons at the S1 and S2 site. It should be mentioned that the EPR-detected amount of unpaired electrons represents a minimum value for d¹ electrons present in the unit cell of (Mo,V)O_x.

Our assignments of the metal site occupancy, distortion in the oxygen sublattice and oxidation state based on STEM micrographs are in very good agreement with XRD and EPR measurements. The combination of edge- and corner-shared M–O polyhedra (M=Mo, V) with different degrees of distortion relieve lattice strain and lead to the realization of this energetically favored, complex network structure. Such structures can be obtained by Mo or V because they are able to form discrete molybdenyl (Mo=O) and vanadyl (V=O) species, respectively. As the distortions are also affected by the electronic configuration, imaging of distortions in the oxygen sublattice enables a way to conclude on the oxidation state. The knowledge of the oxidation state of each single metal site will contribute to a better understanding of the redox chemistry of these materials and their function as prospective catalysts. Contrary to the HAADF-STEM image which gives the impression of empty channels which cannot be found by gas adsorption, the ABF image shows occupied channels. This result further underlines the power of modern chemical TEMs equipped with an ABF detector to verify the filling of nominal channels in inorganic structures. This report demonstrates that we are getting closer to Feynman’s wish of understanding the atomic arrangement by just looking at it.

In conclusion, we have demonstrated that modern electron microscopy provides detailed chemical information that could otherwise only be obtained by a combination of

different analytical methods and could therefore be labeled as chemical electron microscopy (ChemEM). Abstracting local oxidation states from the atomic position in images provides an alternative to electron energy loss spectrometry for cases of beam-sensitive materials.

Experimental Section

The (Mo,V) oxide (FHI-SN: 11345) was prepared by hydrothermal synthesis and analyzed without further thermal treatment.^[14] Details regarding synthesis and the applied analytical techniques are summarized in the Supporting Information.

Keywords: annular bright field microscopy · bond angles · electron microscopy · light elements · transmission electron microscopy

How to cite: *Angew. Chem. Int. Ed.* **2015**, *54*, 6828–6831
Angew. Chem. **2015**, *127*, 6932–6935

- [1] a) K. W. Urban, *Nat. Mater.* **2009**, *8*, 260–262; b) M. Haider, S. Uhlemann, E. Schwan, H. Rose, B. Kabius, K. Urban, *Nature* **1998**, *392*, 768–769; c) P. E. Batson, N. Dellby, O. L. Krivanek, *Nature* **2002**, *418*, 617–620.
- [2] W. D. Pyrz, D. A. Blom, M. Sadakane, K. Kodato, W. Ueda, T. Vogt, D. J. Buttrey, *Chem. Mater.* **2010**, *22*, 2033–2040.
- [3] a) C. Kisielowski, C. J. D. Hetherington, Y. C. Wang, R. Kilaas, M. A. O’Keefe, A. Thust, *Ultramicroscopy* **2001**, *89*, 243–263; b) K. Yoshida, T. Kawai, T. Nambara, S. Tanemura, K. Saitoh, N. Tanaka, *Nanotechnology* **2006**, *17*, 3944.
- [4] a) C.-L. Jia, S.-B. Mi, K. Urban, I. Vrejoiu, M. Alexe, D. Hesse, *Nat. Mater.* **2008**, *7*, 57–61; b) C. L. Jia, M. Lentzen, K. Urban, *Science* **2003**, *299*, 870–873.
- [5] Z. Zhang, W. Sigle, F. Phillipp, M. Rühle, *Science* **2003**, *302*, 846–849.
- [6] W. O. Saxton, W. K. Jenkins, L. A. Freeman, D. J. Smith, *Optik* **1978**, *49*, 505–510.
- [7] P. E. Batson, *Nat. Mater.* **2011**, *10*, 270–271.
- [8] P. DeSanto, J. Buttrey Douglas, K. Grasselli Robert, G. Lugmair Claus, F. Volpe Anthony, H. Toby Brian, T. Vogt, *Z. Kristallogr.* **2004**, *219*, 152.
- [9] T. Konya, T. Katou, T. Murayama, S. Ishikawa, M. Sadakane, D. Buttrey, W. Ueda, *Catal. Sci. Technol.* **2013**, *3*, 380–387.
- [10] a) M. Kunz, I. D. Brown, *J. Solid State Chem.* **1995**, *115*, 395–406; b) K. M. Ok, P. S. Halasyamani, D. Casanova, M. Llundell, P. Alemany, S. Alvarez, *Chem. Mater.* **2006**, *18*, 3176–3183.
- [11] W. D. Pyrz, D. A. Blom, T. Vogt, D. J. Buttrey, *Angew. Chem. Int. Ed.* **2008**, *47*, 2788–2791; *Angew. Chem.* **2008**, *120*, 2830–2833.
- [12] W. D. Pyrz, D. A. Blom, M. Sadakane, K. Kodato, W. Ueda, T. Vogt, D. J. Buttrey, *Proc. Natl. Acad. Sci. USA* **2010**, *107*, 6152–6157.
- [13] E. J. Kirkland, *Advanced Computing in Electron Microscopy*, Springer, New York, **2010**.
- [14] S. Ishikawa, T. Murayama, S. Ohmura, M. Sadakane, W. Ueda, *Chem. Mater.* **2013**, *25*, 2211–2219.
- [15] a) I. MacLaren, Q. M. Ramasse, *Int. Mater. Rev.* **2014**, *59*, 115–131; b) X. Li, X. Ma, D. Su, L. Liu, R. Chisnell, S. P. Ong, H. Chen, A. Toumar, J.-C. Idrobo, Y. Lei, J. Bai, F. Wang, J. W. Lynn, Y. S. Lee, G. Ceder, *Nat. Mater.* **2014**, *13*, 586–592.
- [16] K. Amakawa, L. Sun, C. Guo, M. Hävecker, P. Kube, I. E. Wachs, S. Lwin, A. I. Frenkel, A. Patlolla, K. Hermann, R. Schlögl, A. Trunschke, *Angew. Chem. Int. Ed.* **2013**, *52*, 13553–13557; *Angew. Chem.* **2013**, *125*, 13796–13800.
- [17] L. Kihlberg in *Nonstoichiometric Compounds, Vol. 39*, American Chemical Society, Washington, DC, **1963**, pp. 37–45.
- [18] E. Canadell, M. H. Whangbo, *Inorg. Chem.* **1990**, *29*, 2256–2260.
- [19] H. Björk, S. Lidin, T. Gustafsson, J. O. Thomas, *Acta Crystallogr. Sect. B* **2001**, *57*, 759–765.

Received: March 10, 2015

Published online: April 27, 2015

Redox Treatment of Orthorhombic $\text{Mo}_{29}\text{V}_{11}\text{O}_{112}$ and Relationships between Crystal Structure, Microporosity and Catalytic Performance for Selective Oxidation of Ethane

Satoshi Ishikawa,^{*,†,‡} Daichi Kobayashi,[†] Takeshi Konya,[†] Shunpei Ohmura,[†] Toru Murayama,[†] Nobuhiro Yasuda,[§] Masahiro Sadakane,^{||} and Wataru Ueda^{*,†}

[†]Catalysis Research Center, Hokkaido University, N-21, W-10, Sapporo 001-0021, Japan

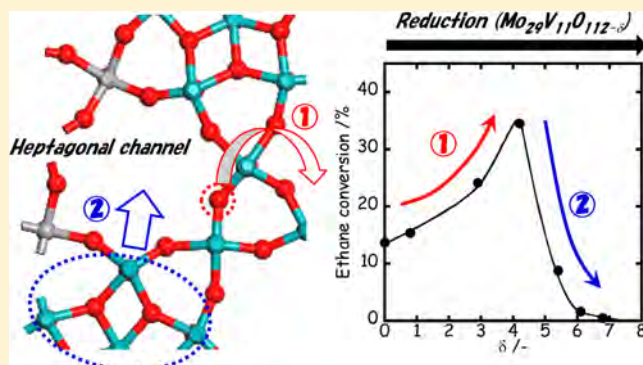
[‡]Japan Society for the Promotion of Science, Kojimachi Business Center Building, 5-3-1 Kojimachi, Chiyoda-ku, Tokyo 102-0083, Japan

[§]JASRI/SPring-8, 1-1-1 Kouto, Sayo-cho, Sayo-gun, Hyogo 679-5198, Japan

^{||}Department of Applied Chemistry, Graduate School of Engineering, Hiroshima University, 1-4-1 Kagamiyama, Higashi-Hiroshima 739-8527, Japan

Supporting Information

ABSTRACT: Redox treatments of an orthorhombic $\text{Mo}_{29}\text{V}_{11}\text{O}_{112}$ catalyst (MoVO) were conducted and its crystal structure, microporosity, and catalytic activity were investigated. TPR and TG revealed that MoVO evolved two kinds of lattice oxygen (α -oxygen and β -oxygen) from the structure by reduction treatment. In the early stage of reduction, α -oxygen was evolved from the structure, causing expansion of the micropore channel. With further reduction, the atoms in the pentagonal $[\text{Mo}_6\text{O}_{21}]^{6-}$ unit moved toward the micropore channel, resulting in a decrease in micropore size. Expansion of the micropore drastically increased catalytic activity for selective oxidation of ethane, but the activity was decreased by a reduction in the micropore channel size. Strong relationships were found between crystal structure, microporosity, and catalytic activity for selective oxidation of ethane.



1. INTRODUCTION

Orthorhombic Mo_3VO_x oxide (MoVO) has attracted much attention because of its outstanding catalytic performance for selective oxidation of ethane^{1–8} and acrolein.^{3,9–12} A structural model of MoVO constructed on the basis of HAADF-STEM images is shown in Figure 1.^{13,14} The a – b plane is composed of pentagonal $[\text{Mo}_6\text{O}_{21}]^{6-}$ units (shown by purple) and $\{\text{MO}_6\}$ ($M = \text{Mo}, \text{V}$) octahedra which stacks on each other to form layered material of MoVO. In the a – b plane, the network arrangement of the pentagonal $[\text{Mo}_6\text{O}_{21}]^{6-}$ units and Mo/V octahedra forms the framework unit (shown by the blue enclosure). Voids in the framework are filled with pentamer units comprised of five octahedra (shown by a red circle), resulting in the formation of hexagonal and heptagonal channels. In these channels, the heptagonal channel provides molecular sieving properties on the basis of the channel size (0.40 nm) and can adsorb small molecules such as N_2 or light alkanes.^{15–18}

We have reported that the sorption behavior of MoVO derived from the heptagonal channel is continuously and reversibly tunable by redox treatment.¹⁷ This is a unique feature

of this material since it is impossible for other crystalline porous materials such as zeolites and MOFs, because zeolites are comprised of elements that are redox-inactive, and the organic moiety of MOFs is unstable under redox conditions. Apart from the sorption behavior, we have reported that the heptagonal channel converts ethane to ethene in the channel without diffusion effects, resulting in outstanding catalytic performance.^{2,3} This fact suggests that the catalytic performance for selective oxidation of ethane should depend on the properties of the heptagonal channel. More specifically, the microporosity derived from the heptagonal channel may be a key factor for the catalysis of ethane. It is important to reveal the relationship of microporosity and catalytic activity for selective oxidation of ethane in order to understand the catalysis of this reaction at the molecular level. We also believe that such findings will lead to a deep understanding of general selective oxidations.

Received: December 24, 2014

Revised: March 17, 2015

Published: March 17, 2015

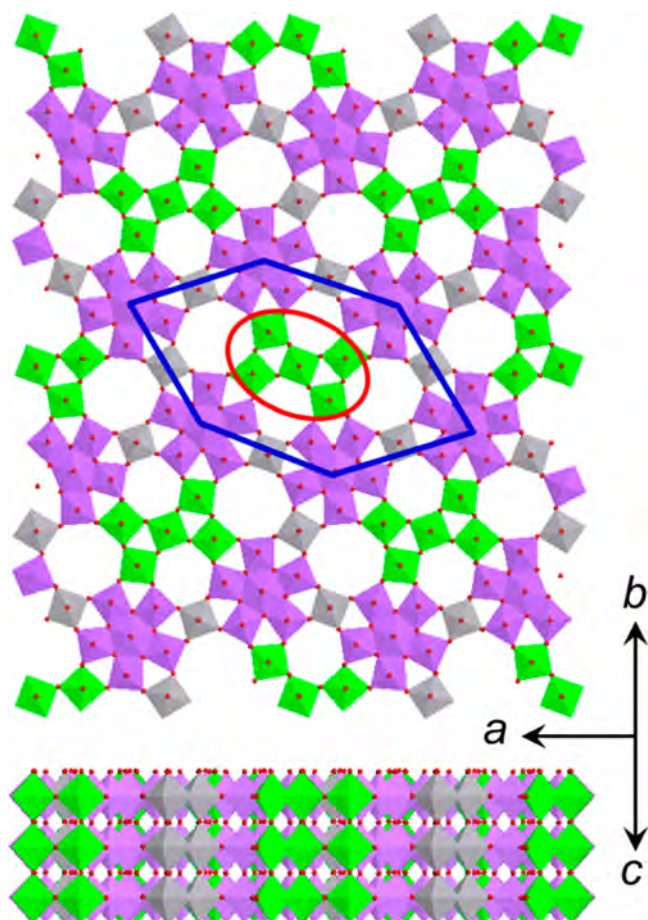


Figure 1. Structural model of MoVO. The blue enclosure represents a framework structure comprised of pentagonal $[\text{Mo}_6\text{O}_{21}]^{6-}$ units. The red circle represents pentamer units embedded in the framework structure. Key: purple, pentagonal unit (Mo); gray, linker of two pentagonal units (mixture of Mo and V); green, pentamer unit (mixture of Mo and V).

In this study, we carried out redox treatments of MoVO and we evaluated the relationships between crystal structure, microporosity, and catalytic activity for selective oxidation of ethane.

2. EXPERIMENTS

2.1. Catalyst Preparation. The orthorhombic $\text{Mo}_{29}\text{V}_{11}\text{O}_{112}$ oxide (MoVO) was synthesized by the hydrothermal method. First, 8.83 g of $(\text{NH}_4)_6\text{Mo}_7\text{O}_{24}\cdot 4\text{H}_2\text{O}$ (Mo: 50 mmol, Wako) was dissolved in 120 mL of distilled water. Separately, an aqueous solution of VOSO_4 was prepared by dissolving 3.29 g of hydrated VOSO_4 (V: 12.5 mmol, Mitsuwa Chemicals) in 120 mL of distilled water. The two solutions were mixed at ambient temperature and stirred for 10 min. At this stage, the pH value of the solution was 3.2. Then the obtained mixed solution was introduced into an autoclave with a 300 mL-Teflon inner vessel and 4000 cm^2 of a Teflon thin sheet to occupy about half of the Teflon inner vessel space. This sheet is indispensable for obtaining well-crystallized samples. After the introduction, N_2 was fed into the solution in the vessel to remove residual oxygen. The hydrothermal reaction was started at 175 $^\circ\text{C}$ for 48 h under static conditions in an electric oven. The gray solid formed on the Teflon sheet was separated by filtration, washed with 1000 mL of distilled

water, and dried at 80 $^\circ\text{C}$ overnight. Since the obtained solid contained amorphous types of materials as an impurity phase, so the dried sample was treated with oxalic acid for purification. To 25 mL of an aqueous solution (0.4 mol l^{-1} , 60 $^\circ\text{C}$) of oxalic acid (Wako), 1 g of the dried material was added, and the mixture was stirred for 30 min and then washed with 500 mL of distilled water. The obtained solid was dried at 80 $^\circ\text{C}$ overnight. MoVO was ground for 5 min with an agate mortar before heat treatment under air as an oxidative gas at 400 $^\circ\text{C}$ for 2 h with a 10 $^\circ\text{C min}^{-1}$ ramp in a muffle furnace. The oxidized MoVO is abbreviated as MoVO(0). The formula from elemental analysis was $\text{Mo}_{28.8}\text{V}_{11.2}\text{O}_{112}(\text{N}_2)_2(\text{O}_2)_{0.5}(\text{H}_2\text{O})_{4.5}$ (Anal. Calcd: Mo, 52.7; V, 11.0; O, 35.8; N, 1.0; H, 0.2. Found: Mo, 52.3; V, 10.8; O, 35.6; N, 1.1; H, 0.2; total, 100.7).

2.2. Redox Treatment. Redox treatment for MoVO was carried out by heat treatment under an oxidative or reductive gas atmosphere. As a reduction treatment, the oxidized sample (MoVO(0)) was heat-treated under 70 mL min^{-1} of 5% H_2/Ar flow with a fixed bed Pyrex tubular furnace equipped with a TPR apparatus. The temperature was increased from room temperature to 400 $^\circ\text{C}$ with a 10 $^\circ\text{C min}^{-1}$ ramp rate and was kept for x h (0, 0.2, 0.5, 1.0, 1.5, and 2.0), 0 h meaning that the temperature was decreased soon after the temperature had reached 400 $^\circ\text{C}$. The obtained samples are abbreviated as MoVO(δ) ($\delta = 0.8, 2.9, 4.2, 5.4, 6.1, 6.8$), where δ represents the amount of lattice oxygen evolved from the unit cell of MoVO ($\text{Mo}_{29}\text{V}_{11}\text{O}_{112-\delta}$) and was estimated by a TCD equipped with a TPR apparatus. As an oxidative treatment, MoVO(2.9) and MoVO(6.8) were heat-treated under air atmosphere at 400 $^\circ\text{C}$ for 2 h with a 10 $^\circ\text{C min}^{-1}$ ramp in a muffle furnace, and the obtained samples are abbreviated as MoVO(2.9)-AC and MoVO(6.8)-AC, respectively.

2.2. Characterization of Synthesized Materials. The obtained catalysts were characterized by the following techniques. TPR was conducted by using CHEMBET 3000 (Quantachrome). First, 1.7 g of MoVO(0) was put into a U-type quartz tube and was set in a furnace equipped with a TPR apparatus. The temperature was increased to 400 $^\circ\text{C}$ with a 10 $^\circ\text{C min}^{-1}$ ramp and kept for x h (0, 0.2, 0.5, 1.0, 1.5, 2.0) under 70 mL min^{-1} of 5% H_2/Ar flow. The amount of lattice oxygen evolved was estimated from the signal area of TPR from 200 $^\circ\text{C}$ to the signal end. Prior to the calculation, the TPR signal area was calibrated with CuO (99.9%, Wako). The amount of lattice oxygen evolved was calculated by assuming that consumed H_2 is used to reduce MoVO and consumed H_2 was removed as H_2O , which is confirmed by TG-DTA measurements. TG analysis was conducted with a TG/DTA 7200 (SEIKO Instrument). After placing 0.01 g of Al_2O_3 as a reference and 0.01 g of MoVO(0) in a furnace equipped with a TG, the temperature was increased to 400 $^\circ\text{C}$ with a 10 $^\circ\text{C min}^{-1}$ ramp and kept for 2 h under 70 mL min^{-1} of 5% H_2/Ar flow or 70 mL min^{-1} Ar flow. After holding for 2 h at 400 $^\circ\text{C}$, the gas was switched to air and kept for another 2 h at the same temperature. The amount of lattice oxygen evolved was estimated from the weight loss from 200 $^\circ\text{C}$. Powder XRD patterns were recorded with a diffractometer (RINT Ultima+, Rigaku) using $\text{Cu-K}\alpha$ radiation (tube voltage, 40 kV; tube current, 40 mA). For XRD measurements, 0.16 g of the catalyst was mixed with 0.04 g of Si, as an external standard to correct the peak positions, and was set in a rotation attachment (Rigaku). Diffractions were recorded in the range of 4–80 $^\circ$ with 1 $^\circ \text{min}^{-1}$ at a rotation rate of 10 rpm. Unit cell parameters were refined by the Rietveld program with Materials Studio 6.1

(Accelrys) using the XRD patterns after the peak positions had been corrected. In situ XRD experiments were carried out to evaluate the structural behavior upon redox treatment. After 0.20 g of MoVO(0) had been set in a furnace attachment, the temperature was increased from room temperature to 400 °C with a 10 °C min⁻¹ ramp under 50 mL min⁻¹ air flow (oxidative gas). When the temperature had reached 400 °C, the gas was switched to 100 mL min⁻¹ of 5% H₂/N₂ mixture (reductive gas) and kept for 1 h. Then the gas was switched to 50 mL min⁻¹ of air (oxidative gas) and kept for 0.5 h, and the gas was again switched to 100 mL min⁻¹ of 5% H₂/N₂ mixture (reductive gas) and kept for 1 h. This cycle was repeated 4 times. In-situ XRD measurement by using 100 mL min⁻¹ of 10% C₂H₆/N₂ mixture as a reductive gas instead of 100 mL min⁻¹ of 5% H₂/N₂ mixture was also performed at 300 °C. In addition, in situ XRD measurement at 300 °C using C₂H₆/O₂/N₂ = 10/10/80 mL min⁻¹ mixture was conducted for 12 h to evaluate the structural behavior of MoVO during the reaction. Molecular adsorption (N₂, CO₂, CH₄, C₂H₆, C₃H₈) experiments were performed to estimate the external surface area and the micropore volume. When CO₂, CH₄, C₂H₆, and C₃H₈ were used, isotherms were obtained at 25 °C using an autoadsorption system (BELSORP MAX, Nippon BELL). N₂ adsorption isotherms at liquid N₂ temperature were obtained by using the same apparatus. Prior to the adsorption, the catalysts were evacuated under vacuum at 300 °C for 2 h. FT-IR spectra were obtained using a spectrometer (Paragon 1000, PerkinElmer) at room temperature in the range of 500–2000 cm⁻¹. Raman spectra (inVia Reflex Raman spectrometer, RENISHAW) were obtained in air on a static sample with an Ar laser (532 nm). Elemental compositions of the bulk were determined by ICP-AES (ICPE-9000, Shimadzu). Complete elemental analysis for MoVO(0) was carried out by Mikroanalytisches Labor Pascher (Remagen, Germany). Single crystal analysis was carried out for MoVO(0). Crystals of MoVO(0) are too small (cross-sectional size, <1 μm; length, more than 10 μm; Figure S1) to perform single-crystal structural analysis using a laboratory system. Therefore, X-ray single-crystal structure analysis was performed using synchrotron radiation. Data collection was performed on a high-precision diffractometer installed in the SPring-8 BL40XU beamline.^{19,20} Synchrotron radiation emitted from a helical undulator was monochromated by using a Si(111) channel cut monochromator and focused with a Fresnel zone plate. A Rigaku Saturn724 CCD detector was used. The measurement was performed at 100 (2) K. Empirical absorption correction based on Fourier series approximation was applied. The data were corrected for Lorentz and polarization effects. The structure was solved by direct methods and refined by full-matrix least-squares (SHELX-97 and SHELX-2014),^{21,22} where the unweighted and weighted agreement factors of $R = \sum |F_0| - |F_c| / \sum |F_0|$ ($I > 2.00\sigma(I)$) and $wR = [\sum w(F_o^2 - F_c^2)^2 / \sum w(F_o^2)]^{1/2}$, respectively, were used. Nitrogen atoms of a nitrogen molecule, oxygen atoms of an oxygen molecule, and oxygen atoms of water were modeled as oxygen atoms because nitrogen atoms could not be distinguished from oxygen atoms. All oxygen atoms were refined isotropically, and Mo and V atoms were refined anisotropically. Obtained crystallographic data of MoVO(0) are shown in Table 1. The Mo/V atom ratio (The numbers of Mo and V atoms were 7.2 and 2.8, respectively.) estimated by complete elemental analysis was different from that obtained by single crystal structure analysis (the numbers of Mo and V atoms were 7.6 and 2.4,

Table 1. Crystallographic Data for Orthorhombic MoVO(0)

MoVO(0)	
formula	Mo _{7.62} V _{2.38} O _{29.23}
formula weight	1320.25
crystal system	orthorhombic
space group	<i>Pba</i> 2
<i>a</i> (Å)	20.9864(5)
<i>b</i> (Å)	26.4023(6)
<i>c</i> (Å)	3.98755(9)
volume (Å ³)	2209.46(9)
temperature (K)	100(2)
<i>Z</i>	4
ρ_{calcd} (g cm ⁻³)	3.969
<i>F</i> ₀₀₀	2435
λ (Å)	0.83077
absorption coefficient (mm ⁻¹)	7.986
measured reflections	38157
unique reflections	4016
<i>R</i> 1 ($I > 2\sigma(I)$)	0.0351
<i>wR</i> 2 (all data)	0.0832
goodness of fit	1.049

respectively), due to the difference in the crystal sample and bulk sample. The total number of oxygen atoms of water, oxygen atoms, and nitrogen atoms was smaller than the total number of oxygen atoms of water, oxygen atoms and nitrogen atoms estimated by elemental analysis. This is also due to the difference in the crystal sample and bulk sample. The sample for elemental analysis may contain surface waters. CIF files are available in Supporting Information. CSD-428978 contains crystallographic data for MoVO(0) (data available from ref 50). In order to obtain structural models of the catalysts with various reduction states, Rietveld refinement was carried out by using the structural model of MoVO(0) obtained by single crystal analysis as a base structure. The Rietveld program with Materials Studio 6.1 (Accelrys) was used for refinement. The XRD patterns after peak position corrections were subjected to the refinement. The occupancy of metals in the framework and temperature factors of all atoms were fixed without further refinement from those of MoVO(0). As shown the Results and Discussion, there are two kinds of lattice oxygen in the structure (α -oxygen and β -oxygen). α -oxygen was assumed to be O₂₉ (Figure 8, Tables S1–S10) and β -oxygen was assumed to be axial oxygen (Tables S1–S10: O₁–O₃, O₁₅, and O₁₇–O₂₃). Occupancies of these oxygen atoms were calculated based on the results of TPR, assuming that the evolution oxygens from MoVO(6.8)-AC was all attributed all to β -oxygen. All metal atom positions were refined. After the refinement of metal positions, oxygen atom positions were refined to set a proper metal–oxygen length. The pattern parameters were refined for obtaining the lowest *R*_{wp} value. Atom positions are shown in Tables S3–S10, and Rietveld analysis parameters are shown in Tables S11–S19.

2.3. Catalytic Test. Selective oxidation of ethane in gas phase was carried out at atmospheric pressure in a conventional vertical flow system with a fixed bed Pyrex tubular reactor. After 0.50 g of the catalyst had been diluted with 2.30 g of SiO₂, the mixture was put into the tubular reactor for ethane oxidation. The reactor was heated gradually from room temperature at a rate of 10 °C min⁻¹ to 300 °C under a nitrogen flow (40 mL min⁻¹ from the top of the reactor). The temperature was measured with a thermocouple inserted in the middle of the

catalyst zone. When the temperature had reached 300 °C, a reactant gas with the composition of $C_2H_6/O_2/N_2 = 10/10/80$ (mol %) was fed in at a total flow rate of 50 mL min^{-1} and the catalytic test was started at that temperature. Reactants and products were analyzed with three online gas chromatographs (molecular sieve 13X for O_2 , N_2 and CO with a TCD detector, Gaskuropack for CO_2 , C_2H_4 and C_2H_6 with a TCD detector, and Porapak Q for acetic acid with an FID detector). Blank runs showed that homogeneous gas-phase reactions were negligible under the experimental conditions used in this study. Carbon balance was always ca. 98–100%. After catalytic oxidation, the catalysts were cooled down to room temperature under an N_2 flow and were subjected to various characterizations.

3. RESULTS AND DISCUSSION

3.1. Single Crystal Analysis of MoVO. First, we introduce the detailed crystal structure of MoVO(0) as a base structure for redox treatments. Single crystal structural analysis revealed the detailed structure of MoVO(0), and metal coordinates, occupancies, and metal–oxygen bond lengths are summarized in Tables S1 and S2. It was shown that the pentagonal units consist exclusively of Mo atoms and that V prefers linking polyhedra connecting the pentagonal units. Both Mo and V atoms occupy nonpentagonal unit metal sites (M7, M8, M9, M10, and M11) with Mo occupancy ranging from 0.11 to 0.75, which is consistent with HAADF-STEM results for orthorhombic $Mo_{29}V_{11}O_{112}$ and single crystal structure analysis results for orthorhombic Mo–V–Sb oxide.^{13,23} Mo and V in octahedral sites have out-of-center distortions with significant elongation of one apical M–O bond and with subsequent shortening of the other apical M–O bond. These findings are similar to the results of a previous study obtained by using combined Rietveld analysis of synchrotron X-ray and neutron powder data for orthorhombic Mo–V–Nb–Te oxide and results of single crystal structure analysis of orthorhombic Mo–V–Sb oxide.^{23,24} The apical short distance ranged from 1.63 to 1.73 Å, the long distance ranged from 2.28 to 2.36 Å, and equatorial M–O bonds ranged from 1.76 to 2.08 Å; these distances are reasonable for molybdenum oxides containing pentagonal units.^{24–29} Disordering of some metal sites (M7, M8, and M9) along the z direction was detected (black balls and gray balls in Figure 2). Such disordering is often observed in single-crystal structural analyses of polyoxomolybdates and

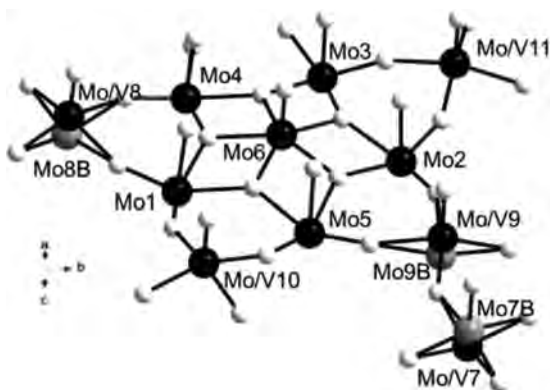


Figure 2. Site map of an asymmetric unit in MoVO(0) obtained from single crystal structural analysis: metals with high occupancy (black ball), low occupancy (gray ball), and oxygen (small white ball).

molybdenum oxides.^{25,30–34} Neither Mo atoms nor V atoms were found in the hexagonal and heptagonal channels, being consistent with HAADF-STEM results for orthorhombic $Mo_{29}V_{11}O_{112}$.¹³

3.2. Physicochemical Properties of MoVO after Redox Treatment. Table 2 shows the physicochemical properties of MoVO catalysts after redox treatment. The redox treatment caused no change in the V/Mo ratio, which was in the range of 0.37–0.39. TPR spectra and TG spectra of MoVO(0) are shown in Figures S2 and S3, respectively, and the estimated amounts of lattice oxygen evolved (δ) from the unit cell (shown as $Mo_{29}V_{11}O_{112-\delta}$) are shown in Table 2. For TG, weight loss was measured under 70 mL min^{-1} of Ar or 70 mL min^{-1} of 5% H_2/Ar . Under Ar flow, weight loss was only observed below 150 °C and the weight loss was due to desorption of N_2 , O_2 , and H_2O trapped in the heptagonal channel.¹⁷ On the other hand, under 5% H_2/Ar flow, as well as the weight loss at 150 °C, weight loss was observed from 250 °C and proceeded when the temperature was held at 400 °C. This weight loss corresponds to the evolution of lattice oxygen from the structure since weight increase was observed when 5% H_2/Ar was switched to air at the same temperature because of the incorporation of gaseous O_2 into the structure.

For TPR, the peak around 150 °C was derived from the desorption of N_2 , O_2 , and H_2O from the heptagonal channel as was also observed by TG. With increase in the temperature, the TPR signal rapidly increased and the signal rapidly decreased and became flat when the temperature was held at 400 °C. As indicated earlier, this TPR signal corresponds to the evolution of lattice oxygen by the reduction.¹⁷ The values of δ estimated from TPR and TG were almost the same. Therefore, for further experiments, δ estimated from TPR was used. Figure 3 shows TPR spectra of MoVO(0), MoVO(2.9)-AC, and MoVO(6.8)-AC. The temperature was increased to 400 °C with a 10 °C min^{-1} ramp and kept at 400 °C for 2 h under 70 mL min^{-1} of 5% H_2/Ar flow. As already shown in Figure S3, the TPR signal of MoVO(0) rose rapidly with increase in temperature and was maximum when the temperature reached 400 °C. The signal decreased and became flat when the temperature was held at 400 °C. The TPR spectrum of MoVO(2.9)-AC was similar to that of MoVO(0), but a small decrease in the initial rise at 400 °C was observed. MoVO(6.8)-AC showed no initial rise in the TPR signal. These experimental results suggest that there are two kinds of lattice oxygen in the structure. One is evolved in the early stage of the reduction and hardly returns to the structure even with reoxidation. The other is evolved continuously by the reduction and reversibly comes back to the structure with reoxidation. We abbreviated the former oxygen as α -oxygen and the latter oxygen as β -oxygen. We calculated the total amount of α -oxygen to be 2.7 on the basis of the TPR signal area by assuming that the TPR signal area of MoVO(6.8)-AC is all attributed to the evolution of β -oxygen. Based on this assumption, it was implied that the evolution of α -oxygen was almost completed by the reduction at MoVO(4.2).

Figure 4 shows XRD patterns, lattice parameters, and peak intensity ratios of the catalysts. All of the catalysts showed peaks at 6.6° , 7.9° , 9.0° , and 22.1° , corresponding to diffractions of (020), (120), (210), and (001) in MoVO, respectively.¹ No XRD peaks related to impurities appeared during the reduction. With increase in δ , XRD peaks attributed to (020), (120), and (210) were shifted to lower degrees, but the XRD peak attributed to (001) was shifted to a higher degree.

Table 2. Physicochemical Properties of MoVO

catalyst	bulk V/Mo ^a	$\delta^b/-$		lattice parameter ^c /nm			external surface area ^f /m ² g ⁻¹	micropore volume/10 ⁻³ cm ³ g ⁻¹				
		TPR ^e	TG ^d	a	b	c		V _{N₂} ^f	V _{CO₂} ^g	V _{CH₄} ^g	V _{C₂H₆} ^g	V _{C₃H₈} ^g
MoVO(0)	0.38	—	—	2.100	2.645	0.4015	5.8	13.0	27.7	27.8	15.8	3.7
MoVO(0.8)	0.39	0.8	1.0	2.109	2.646	0.4010	5.8	15.4	26.1	25.0	20.5	2.8
MoVO(2.9)	0.37	2.9	1.8	2.112	2.653	0.4004	5.7	13.3	26.2	23.6	22.1	6.2
MoVO(4.2)	0.37	4.2	2.8	2.114	2.662	0.3998	6.5	17.6	25.5	23.0	22.0	13.8
MoVO(5.4)	0.38	5.4	5.1	2.118	2.668	0.3988	5.8	4.4	15.1	1.8	1.5	1.6
MoVO(6.1)	0.37	6.1	6.6	2.121	2.671	0.3979	6.2	1.3	2.6	0.3	0.7	0.1
MoVO(6.8)	0.38	6.8	7.3	2.122	2.674	0.3977	6.3	1.2	0.0	0.0	0.0	0.0
MoVO(2.9)-AC	0.39	0.5	—	2.099	2.645	0.4013	5.7	11.2	24.3	25.4	16.3	5.5
MoVO(6.8)-AC	0.37	2.7	—	2.100	2.647	0.4010	5.8	10.7	23.9	23.0	20.8	10.0

^aDetermined by ICP. ^bNumber of lattice oxygen atoms evolved from the unit cell. ^cEstimated from the TPR signal area from 200 °C. ^dEstimated from the weight loss based on the weight loss at 200 °C. ^eMeasured by XRD and calculated by Rietveld refinement. ^fMeasured by N₂ adsorption at liquid N₂ temperature and calculated by a *t*-plot. V_{N₂} represents the micropore volume measured by using N₂. ^gMicropore volume measured by CO₂, CH₄, C₂H₆, and C₃H₈ adsorption and estimated by the DA method.

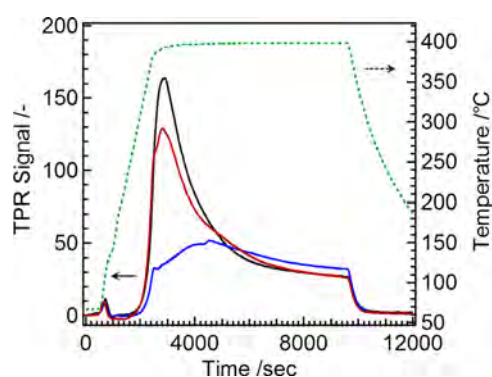


Figure 3. TPR spectra of MoVO(0) (black solid line), MoVO(2.9)-AC (brown solid line), and MoVO(6.8)-AC (blue solid line). Temperature (green dotted line) was increased at a 10 °C min⁻¹ ramp rate and was held at 400 °C for 2 h.

Lattice parameters of the catalysts were calculated by Rietveld refinement and are shown in Figure 4 (B) and Table 2. With increase in δ , the lattice parameters in the *a*–*b* plane continuously increased and the lattice parameter in the *c*

axis continuously decreased. The lattice parameter changes are due to cation size changes of Mo and V, which were suggested by UV analysis to be changes in the oxidation states of Mo and V (Figure S4).^{17,35–40} A drastic increase in the lattice parameter to *a* axis between MoVO(0) to MoVO(0.8) was observed. The reduction of MoVO(0) may cause desorption of oxygen incorporated in the heptagonal channel (see Figure S10). This drastic change in the lattice parameter to the *a* axis between MoVO(0) to MoVO(0.8) is thought to be caused by the desorption of oxygen in the heptagonal channel as well as cation size changes. It is notable that the lattice parameters of MoVO(2.9)-AC and MoVO(6.8)-AC were almost the same as that of MoVO(0) (Table 2). The difference between MoVO(2.9)-AC and MoVO(6.8)-AC is only the amount of α -oxygen in the structure. This experimental fact clearly indicates that the evolution of α -oxygen does not cause any change in lattice parameters. Therefore, the change in lattice parameters with reduction would be caused solely by the evolution of β -oxygen. As shown in Figure 1, MoVO is composed of the framework and pentamer units. It has been reported that the pentamer unit is structurally less stable than the framework unit.⁴¹ Therefore, we propose that evolution of

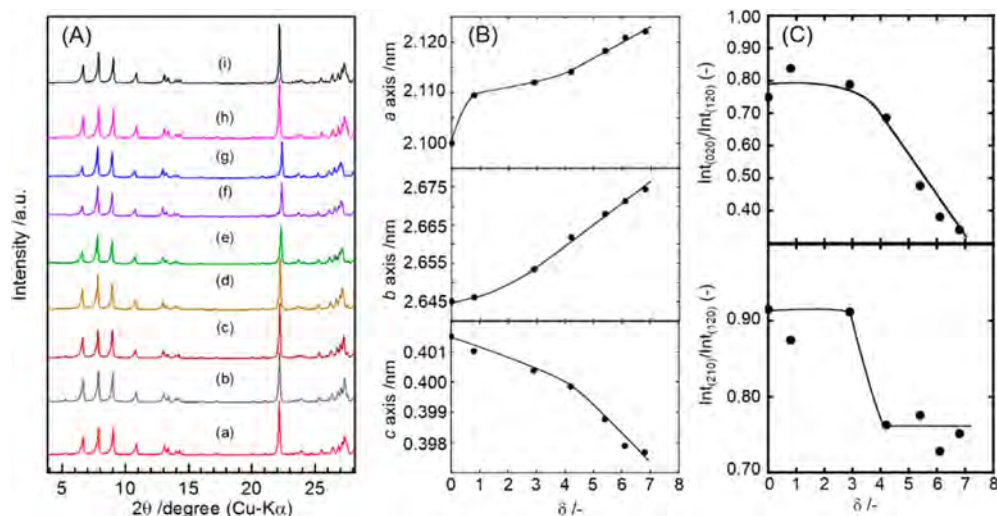


Figure 4. (A) XRD patterns of MoVO: (a) MoVO(0), (b) MoVO(0.8), (c) MoVO(2.9), (d) MoVO(4.2), (e) MoVO(5.4), (f) MoVO(6.1), (g) MoVO(6.8), (h) MoVO(2.9)-AC, and (i) MoVO(6.8)-AC. Lattice parameters (B) and peak intensity ratios based on (120) (C) of MoVO as a function of δ .

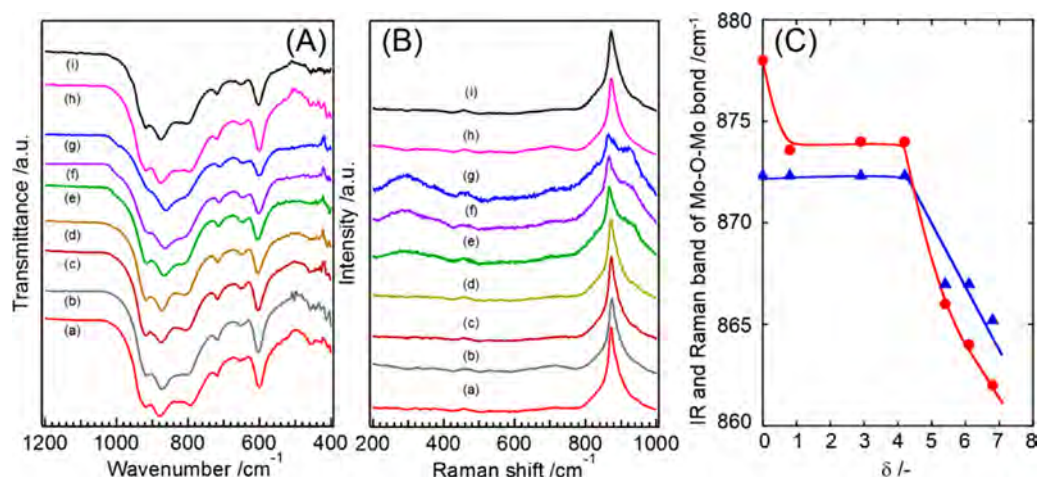


Figure 5. IR (A) and Raman (B) spectra of MoVO: (a) MoVO(0), (b) MoVO(0.8), (c) MoVO(2.9), (d) MoVO(4.2), (e) MoVO(5.4), (f) MoVO(6.1), (g) MoVO(6.8), (h) MoVO(2.9)-AC, and (i) MoVO(6.8)-AC. (C) IR (circle) and Raman (triangle) bands attributed to the Mo–O–Mo bond in the pentagonal $[\text{Mo}_6\text{O}_{21}]^{6-}$ unit as a function of δ .

oxygen from the framework strongly affects the lattice parameters rather than the pentamer units. Based on this idea, β -oxygen should be located in the framework unit and α -oxygen should be located in the pentamer unit.

The peak intensity ratios of (020) to (120), $\text{Int}_{(020)}/\text{Int}_{(120)}$, and (210) to (120), $\text{Int}_{(210)}/\text{Int}_{(120)}$, are shown in Figure 4 (C). Small differences in $\text{Int}_{(020)}/\text{Int}_{(120)}$ were observed in the range of MoVO(0)–MoVO(4.2) and the ratio was continuously decreased by reduction above MoVO(5.4). The change in $\text{Int}_{(020)}/\text{Int}_{(120)}$ implies a continuous structural change in the a – b plane above MoVO(5.4). In the case of $\text{Int}_{(210)}/\text{Int}_{(120)}$, the ratio was almost the same in the range of MoVO(0)–MoVO(2.9). The ratio was decreased and became constant by reduction above MoVO(4.2). In the TPR part, it was implied that the evolution of α -oxygen was almost completed by reduction up to MoVO(4.2). The change in $\text{Int}_{(210)}/\text{Int}_{(120)}$ may be related to the structural change caused by evolution of α -oxygen from the structure.

Figure 5 shows IR and Raman spectra of the catalysts. Characteristic IR absorption at 915 cm^{-1} attributed to $\text{V}=\text{O}$, 874 , 800 , 720 , and 652 cm^{-1} to Mo–O–Mo, 604 cm^{-1} to V–O–Mo, and 458 cm^{-1} to Mo–O were observed. All of those were characteristic absorption of MoVO.^{1,42–44} For the band at 874 cm^{-1} , the wavenumber rapidly decreased in the range of MoVO(0) to MoVO(0.8), possibly due to the desorption of oxygen incorporated in the heptagonal channel. In the range of MoVO(0.8) to MoVO(4.2), there was almost no peak shift, but the continuous downward shift of the wavenumber was observed with reduction above MoVO(5.4) (Figure 5C). This wavenumber was reversibly shifted from 862 to 874 cm^{-1} by reoxidation. For the Raman spectrum, the Raman band at 873 cm^{-1} was shifted in a lower direction by reduction above MoVO(5.4) and was restored by reoxidation in the same manner as IR. The band around 873 – 874 cm^{-1} found by IR and Raman is attributed to the Mo–O–Mo bond in the pentagonal $[\text{Mo}_6\text{O}_{21}]^{6-}$ unit.^{44–46} This band shift indicates that the strength of the Mo–O–Mo bond in the pentagonal $[\text{Mo}_6\text{O}_{21}]^{6-}$ unit was weakened when MoVO was reduced above MoVO(5.4). The continuous structural change by reduction above MoVO(5.4), suggested by XRD, is thought to be involved in the decrease in strength of the Mo–O–Mo bond in the pentagonal $[\text{Mo}_6\text{O}_{21}]^{6-}$ unit.

In this section, we showed that (1) MoVO has two kinds of lattice oxygen (denoted as α -oxygen and β -oxygen) and (2) the evolution of lattice oxygen with reduction treatment causes a partial structural change in the a – b plane that is involved in the decrease in strength of the Mo–O–Mo bond in the pentagonal $[\text{Mo}_6\text{O}_{21}]^{6-}$ unit.

3.3. Microporosity Changes Caused by Redox Treatment. It has been reported that the heptagonal channel of MoVO works as a micropore with a size of 0.40 nm .^{1,15–17} The change in microporosity of MoVO caused by redox treatment was evaluated by means of molecular adsorption using N_2 , CO_2 , CH_4 , C_2H_6 , and C_3H_8 . The kinetic diameters of N_2 , CO_2 , CH_4 , C_2H_6 , and C_3H_8 have been reported to be 0.36 , 0.33 , 0.38 , 0.40 , and 0.43 nm , respectively.^{15,47} N_2 adsorption was performed at liquid N_2 temperature ($-196\text{ }^\circ\text{C}$), and CO_2 , CH_4 , C_2H_6 , and C_3H_8 adsorptions were performed at room temperature ($25\text{ }^\circ\text{C}$). Micropore volumes were estimated by the DA method for CO_2 , CH_4 , C_2H_6 , and C_3H_8 adsorptions (V_{CO_2} , V_{CH_4} , $V_{\text{C}_2\text{H}_6}$, $V_{\text{C}_3\text{H}_8}$) and by the t -plot method for N_2 adsorption (V_{N_2}). The adsorption isotherms and t -plots are shown in Figures S5–S9. Micropore volumes estimated from molecular adsorptions are shown in Table 2 and Figure 6.

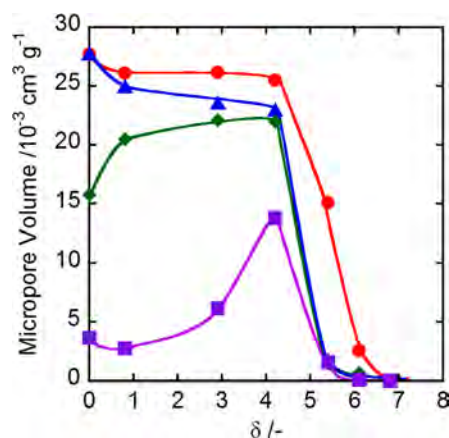


Figure 6. Micropore volumes of MoVO estimated by the Dubinin–Astakhov (DA) method using CO_2 (circle), CH_4 (triangle), C_2H_6 (lozenge), and C_3H_8 (square) plotted against δ .

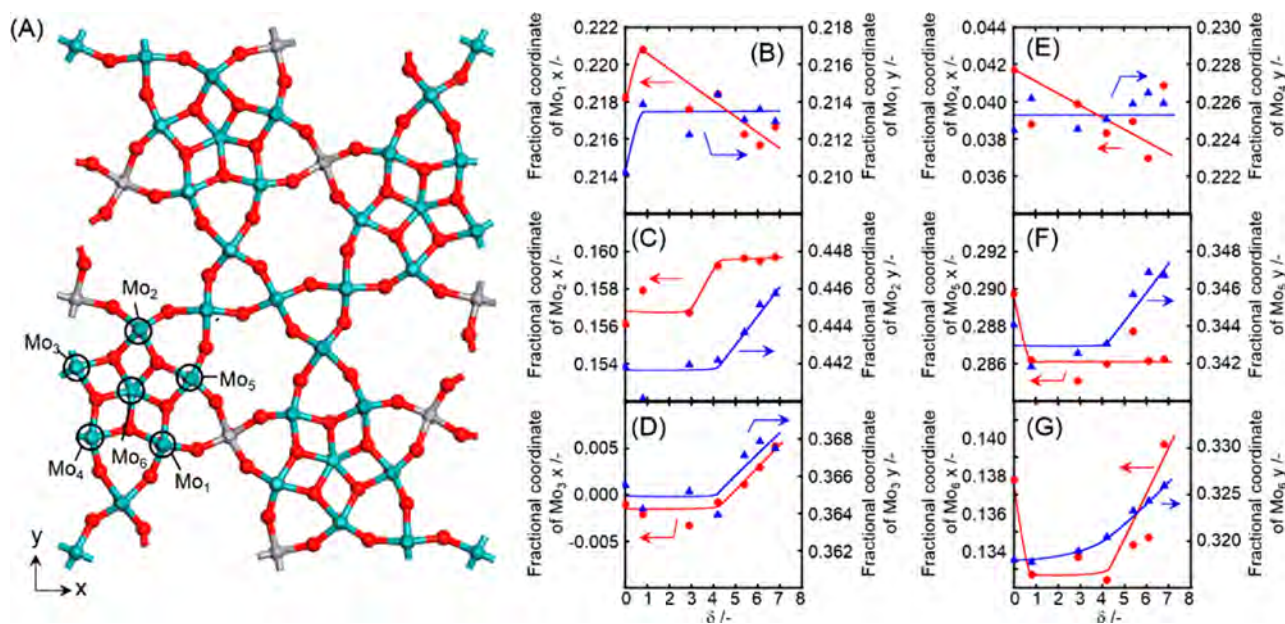


Figure 7. (A) Structural model of MoVO (Mo, light green; V, gray; O, red). Fractional coordinates of (B) Mo₁, (C) Mo₂, (D) Mo₃, (E) Mo₄, (F) Mo₅, and (G) Mo₆ as a function of δ . Atomic numbers are represented in the structural model. Circle, x (a axis); triangle, y (b axis).

External surface areas obtained by N₂ adsorption are also shown in Table 2. External surface areas of MoVO were not changed by redox treatment and were in the range of 5.7–6.5 m² g⁻¹. As observed in our previous study, MoVO(0) showed micropore adsorption.¹⁶ Reduction treatment of MoVO(0) caused small changes in measured micropore volumes, possibly due to the desorption of oxygen incorporated in the heptagonal channel. V_{CO_2} , V_{CH_4} , $V_{\text{C}_2\text{H}_6}$, and V_{N_2} were almost unchanged in the range of MoVO(0.8)–MoVO(4.2) and were 20–25 × 10⁻³ cm³ g⁻¹. V_{N_2} was slightly lower than those volumes and was 13.3–17.6 cm³ g⁻¹. It is well-known that N₂ adsorption at liquid N₂ temperature gives unrealistically small pore volumes due to the diffusional limitations of N₂ into the pore if the pore mouth diameter is small (less than 0.60 nm).^{48,49} Actually, the micropore volume expected from the crystallographic data (23.4 × 10⁻³ cm³ g⁻¹) matches well with V_{CO_2} , V_{CH_4} , and $V_{\text{C}_2\text{H}_6}$ of MoVO(0.8)–MoVO(4.2).² When the catalyst was reduced up to MoVO(5.4), V_{CO_2} became about half of those of MoVO(0.8)–MoVO(4.2) and V_{CH_4} , $V_{\text{C}_2\text{H}_6}$, and V_{N_2} became almost 0. With further reduction above MoVO(6.1), all of the estimated micropore volumes became almost 0. This is due to the decrease in size of the heptagonal channel by the reduction.^{15,17} As discussed in XRD, IR, and Raman analyses, reduction above MoVO(5.4) causes continuous structural change in the a – b plane, which is involved in the decrease in strength of the Mo–O–Mo bond in the pentagonal [Mo₆O₂₁]⁶⁻ unit. This continuous structural change may be related to the decrease in heptagonal channel size. In the case of propane adsorption, $V_{\text{C}_3\text{H}_8}$ increased up to MoVO(4.2) and then decreased with further reduction (Figure 6). The kinetics diameter of C₃H₈ is 0.43 nm and is slightly larger than that of the size of the heptagonal channel (0.40 nm). Since the moderately reduced catalyst is able to adsorb C₃H₈, the size of which is larger than the size of the heptagonal channel, the size of the heptagonal channel was found to be increased by reduction. With further reduction, the heptagonal channel size decreased. As implied in TPR, the evolution of α -oxygen was

completed at MoVO(4.2). In conjunction with TPR and C₃H₈ adsorption, the evolution of α -oxygen is thought to be related to the enlargement of the heptagonal channel. As mentioned in the XRD part, we proposed that α -oxygen is located in the pentamer unit of the structure. Since the evolution of α -oxygen affected the microporosity, we speculated that α -oxygen is the bridging oxygen between the metals in the pentamer unit that faced the heptagonal channel. For reoxidized catalysts, the micropore volumes of MoVO(2.9)-AC estimated by various molecules were almost the same as those of MoVO(0). For MoVO(6.8)-AC, the micropore volumes were drastically increased from MoVO(6.8) and were almost the same as those of MoVO(4.2). This astonishing result indicates that the decreased heptagonal channel size by reduction is restored by the reoxidation most probably due to the reversible structural change.¹⁷ $V_{\text{C}_3\text{H}_8}$ of MoVO(6.8)-AC was close to that of MoVO(4.2) since no α -oxygen came back with reoxidation of MoVO(6.8). These adsorption results together with IR and Raman band shifts and XRD profile changes support the suggestion that evolution of α -oxygen is completed at MoVO(4.2).

In this section, we showed that the partial structural change of the a – b plane strongly affects microporosity. Results of detailed structural analysis are presented in the next section.

3.4. Structural Refinement. As demonstrated above, continuous structural change in the a – b plane suggested by XRD may be strongly related to the microporosity change. In order to understand the relationship between crystal structure and microporosity, Rietveld refinement was carried out. At this time, the crystal structures of the catalysts after redox treatments were refined on the basis of the crystal structure of MoVO(0) obtained by single crystal analysis. Actually, the simulated XRD pattern fitted well with the obtained XRD pattern in MoVO(0) (R_{wp} value = 7.8%), indicating that the crystal structure obtained by single crystal analysis is applicable for Rietveld refinement. An occupancy of oxygen in the unit cell was set on the basis of δ estimated from TPR. At that time, α -oxygen was assumed to be located in the pentamer unit that

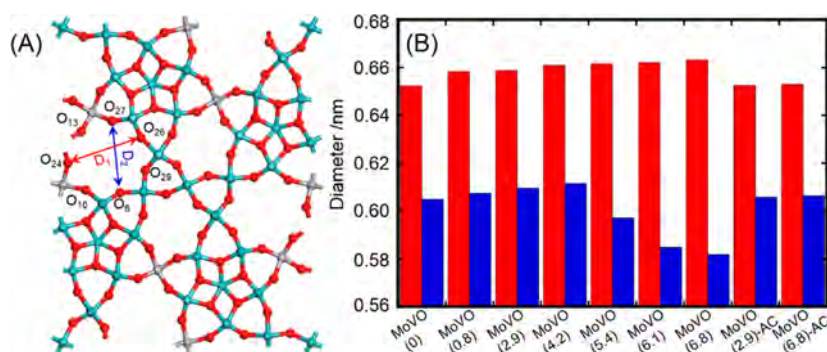


Figure 8. (A) Structural model of MoVO (Mo, light green; V, gray; O, red). (B) Diameters of the heptagonal channel. Diameters were determined on the basis of atomic positions of oxygen. Red bar, D_1 (O_{24} – O_{26} , long axis); blue bar, D_2 (O_6 – O_{27} , short axis).

faced the heptagonal channel, and β -oxygen was assumed to be located in the framework unit in the XRD part. Since the evolution of β -oxygen is involved in the lattice parameter change not only for the a – b plane but also for the c -axis, β -oxygen was assumed to be the axial oxygen bridging to the c direction. An occupancy of the α -oxygen and β -oxygen was determined on the basis of the TPR signal area. In this time, evolved oxygen of MoVO(6.8)-AC was assumed to be all attributed to the β -oxygen. The results of Rietveld refinements for the catalysts are shown in Figures S10–S18. The weighted agreement factors that represent a difference between the observed XRD pattern and simulated pattern obtained from the structural model were in the range of 7.1–8.2%, indicating that the crystal structure was adequately refined for all of the catalysts. We evaluated the detailed structure at each reduction state of MoVO. Figure 7 shows the structural model (A) and structural coordinates in x and y of the pentagonal $[\text{Mo}_6\text{O}_{21}]^{6-}$ unit as a function of δ ((B–G)). The atomic number of oxygen is marked in the structural model.

Mo_1 – Mo_5 are edge-shared octahedra and Mo_6 is the center of the $[\text{MoO}_7]$ pentagonal bipyramid in the pentagonal $[\text{Mo}_6\text{O}_{21}]^{6-}$ unit. The fractional coordinates of Mo_1 , Mo_5 , and Mo_6 were greatly changed between MoVO(0) to MoVO(0.8), suggesting that the desorption of oxygen in the heptagonal channel cause changes in the metal positions. The fractional coordinates of Mo_2 , Mo_3 , Mo_5 , and Mo_6 were substantially increased in the x and y directions (a and b axes, respectively) by reduction above MoVO(5.4). These movements indicate that these metals are close to the heptagonal channel (Figure 7, parts C, D, F, G). On the other hand, the fractional coordinates of Mo_1 and Mo_4 slightly decreased with increase in δ (Figure 7, parts B, E). The different movements of Mo_1 and Mo_4 from those of Mo_2 , Mo_3 , Mo_5 , and Mo_6 expand the pentagonal $[\text{Mo}_6\text{O}_{21}]^{6-}$ unit due to the increase in bond length. This is in good agreement with results of IR and Raman analyses indicating that the strength of the Mo–O–Mo bond in the pentagonal $[\text{Mo}_6\text{O}_{21}]^{6-}$ unit is weakened by reduction above MoVO(5.4). The fractional coordinates of these atoms, of the reoxidized catalysts, were almost the same as those of MoVO(0) (Tables S1, S9, and S10). The expanded pentagonal $[\text{Mo}_6\text{O}_{21}]^{6-}$ unit was found to shrink with reoxidation.

Figure 8 shows the structural model (A) and the diameters of the heptagonal channel in the short axis (D_1) and long axis (D_2) (B) obtained by Rietveld refinement. The diameters of the heptagonal channels were determined on the basis of the atomic positions of oxygen. The atomic number of oxygen is marked in the structural model.

The size of the heptagonal channel was changed by the movement of metals. The diameter in the long axis (D_1) increased with increasing δ due to the lattice expansion (from 0.652 nm for MoVO(0) to 0.663 nm for MoVO(6.8)) and decreased with reoxidation (Figure 8B, red bar). As well as D_1 , the diameter in the short axis (D_2) increased with increasing δ in the range of MoVO(0) (0.605 nm)–MoVO(4.2) (0.612 nm), but it drastically decreased with further reduction and D_2 of MoVO(6.8) was 0.582 nm (Figure 8 (B), blue bar). It was found that the movements of Mo_2 , Mo_3 , Mo_5 , and Mo_6 toward the heptagonal channel decreased D_2 . The decrease of D_2 should be related to the loss of microporosity of the catalysts above MoVO(5.4). Actually, D_2 was increased by reoxidation, which explains the recovery of the microporosity as observed in the adsorption analyses. For enlargement of the heptagonal channel by reduction up to MoVO(4.2), MoVO was found to release α -oxygen, which is assumed to be located at O_{29} , in the early stage of the reduction. The evolution of O_{29} should increase the heptagonal channel size. Therefore, C_3H_8 , the size of which is larger than that of the heptagonal channel, may be able to enter the heptagonal channel due to the generation of a void space by evolution of α -oxygen (O_{29}).

Based on the above results, we propose that the structural change involving the evolution of α -oxygen and the expansion of the pentagonal $[\text{Mo}_6\text{O}_{21}]^{6-}$ unit is strongly related to the microporosity. From the next section, we discuss the relationship between microporosity and catalytic activity for selective oxidation of ethane.

3.5. Selective Oxidation of Ethane. Based on the Rietveld refinement, we proposed that the microporosity of MoVO is strongly related to the structure around the heptagonal channel. We have reported that ethane is converted not on the crystal surface but in the heptagonal channel.^{2,3} This situation suggests that the microporosity change caused by the partial structural change around the heptagonal channel affects the catalytic activity for selective oxidation of ethane. We tested the catalysts for selective oxidation of ethane in order to understand the relevance of crystal structure, microporosity, and catalytic activity for selective oxidation of ethane.

Ethane conversion of the catalysts at 300 °C over the course of the reaction time is shown in Figure 9 (A). Ethane conversion and product selectivity at 10 min and at 69 h from the start of the reaction are shown in Table S20. The products detected were ethene, acetic acid, and CO_x . The initial ethane conversion of MoVO(0) was 13.7% and was slightly increased with increase in reaction time, showing 17.9% ethane conversion at 69 h from the start of the reaction. The product

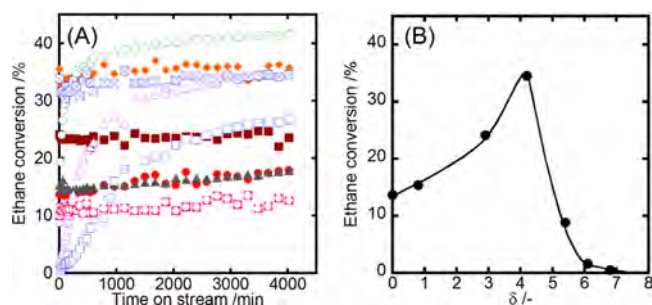


Figure 9. (A) Ethane conversion as a function of reaction time: closed circle, MoVO(0); closed triangle, MoVO(0.8); closed square, MoVO(2.9); closed lozenge, MoVO(4.2); open circle, MoVO(5.4); open triangle, MoVO(6.1); open square, MoVO(6.8); open circle in closed square, MoVO(2.9)-AC; cross mark in open square, MoVO(6.8)-AC. (B) Ethane conversion at 10 min from the start of the reaction as a function of δ . Reaction conditions: catalyst weight, 0.5 g; reaction temperature, 300 °C; reaction gas feed, $C_2H_6/O_2/N_2 = 5/5/40 \text{ mL min}^{-1}$.

selectivity to ethene was almost unchanged during the reaction and was 88.5% at the start of the reaction and 87.1% at 69 h. When the catalyst was slightly reduced, MoVO(0.8) showed 15.4% initial ethane conversion with 87.1% ethene selectivity. The conversion was slightly increased with increase in reaction time and reached 17.9% at 69 h. The selectivity to ethene was almost unchanged during the reaction and was 87.3% at 69 h. With further reduction, ethane conversion was substantially increased. The initial conversion rates of MoVO(2.9) and MoVO(4.2) were 24.1% and 33.0% and the conversion rates at 69 h were 23.6% and 35.7%, respectively. The selectivities to ethene were decreased by reduction and were 79.6% and 76.8% at the initial stage and 82.9% and 81.4% at 69 h for MoVO(2.9) and MoVO(4.2), respectively. These decreases in ethene selectivity were due to the increase in CO_x selectivity. For more reduced catalysts, the initial conversion of MoVO(5.4) was 8.8%, which was far less than that of MoVO(4.2), but the conversion was increased drastically with increase in reaction time and 41.6% conversion was achieved at 69 h. The selectivity to ethene of MoVO(5.4) was higher than that of MoVO(4.2) for all reaction times and was 88.3% at the initial stage and 88.5% at 69 h, due to the decrease in CO_x selectivity. In the case of MoVO(6.1) and MoVO(6.8), the initial ethane conversion rates were both negligible, but their conversion rates were increased with increase in reaction time and the

conversion rates reached 34.5% and 24.6% at 69 h, respectively. The selectivities to ethene were 92.4% and 93.3% at the initial stage and 89.8% and 89.7% at 69 h. For the reoxidized catalysts, the initial conversion of MoVO(2.9)-AC was 10.0%. The conversion was slightly increased with increase in reaction time and was 12.7% at 69 h. The selectivities to ethene were 89.4% at the initial stage and 86.5% at 69 h. For MoVO(6.8)-AC, the initial ethane conversion was 31.2% and that at 69 h was 34.6%, and the selectivities to ethene were 84.4% at the initial stage and 87.1% at 69 h. Surprisingly, the conversion of MoVO(6.8)-AC was about 3-times higher than that of MoVO(2.9)-AC, although both of them were calcined in air under the same conditions after the reduction. As discussed above, the difference between MoVO(2.9)-AC and MoVO(6.8)-AC was only the presence of α -oxygen in the structure. Therefore, the evolution of α -oxygen is one of the main reasons for the increase in catalytic activity for selective oxidation of ethane.

Ethane conversion at 10 min from the start of the reaction as a function of δ is shown in Figure 9B. The initial ethane conversion was increased with increasing δ in the range of MoVO(0)–MoVO(4.2), but the conversion drastically decreased with further reduction. As discussed for the catalytic activity difference between MoVO(2.9)-AC and MoVO(6.8)-AC, the evolution of α -oxygen should strongly contribute to the increase in catalytic activity. Therefore, the increase in catalytic activity in the range of MoVO(0)–MoVO(4.2) should be due to the evolution of α -oxygen. In the case of MoVO(5.4)–MoVO(6.8), structural analysis showed that Mo_2 , Mo_3 , Mo_5 , and Mo_6 in the pentagonal $[Mo_6O_{21}]^{6-}$ unit moved toward the heptagonal channel, resulting in the loss of microporosity. Taking into account the fact that ethane is converted in the heptagonal channel, the drop in the initial ethane conversion with reduction above MoVO(5.4) would be due to the inaccessibility of ethane into the heptagonal channel.

We then investigated the reasons why the ethane conversion of MoVO(5.4), MoVO(6.1), and MoVO(6.8) increased drastically with increase in reaction time despite the fact that only small increases in catalytic activity were found for the other catalysts. Figure S19 and Figure S20 show the results of in situ XRD under 100 mL min^{-1} of 5% H_2/N_2 and 50 mL min^{-1} of air at 400 °C or under 100 mL min^{-1} of 10% C_2H_6/N_2 and 50 mL min^{-1} of air at 300 °C. Measurements were carried out on the (210) plane because this plane was especially active for redox treatment. The gas atmosphere was switched for each, 1 h under the reductive condition and 0.5 h in the

Table 3. Physicochemical Properties of MoVO after Selective Oxidation of Ethane

catalyst	bulk V/Mo ^a	lattice parameter ^b /nm			external surface area ^c /m ² g ⁻¹	micropore volume/10 ⁻³ cm ³ g ⁻¹				
		a	b	c		V _{N₂} ^c	V _{CO₂} ^d	V _{CH₄} ^d	V _{C₂H₆} ^d	V _{C₃H₈} ^d
MoVO(0)	0.39	2.102	2.647	0.4008	3.6	9.0	23.5	20.8	19.3	5.7
MoVO(0.8)	0.39	2.106	2.647	0.4005	3.5	10.7	25.1	22.9	19.9	5.3
MoVO(2.9)	0.39	2.104	2.647	0.4008	3.5	9.5	21.9	18.1	17.1	6.2
MoVO(4.2)	0.39	2.108	2.649	0.4005	4.8	11.9	22.6	23.8	22.5	16.1
MoVO(5.4)	0.39	2.108	2.654	0.4002	4.6	13.8	22.1	17.9	20.4	21.2
MoVO(6.1)	0.39	2.109	2.654	0.4003	5.4	12.2	17.9	15.8	17.0	16.9
MoVO(6.8)	0.39	2.109	2.655	0.4001	4.8	9.2	16.1	13.1	12.3	13.9
MoVO(2.9)-AC	0.38	2.103	2.647	0.4007	4.9	13.9	23.2	21.0	20.2	5.4
MoVO(6.8)-AC	0.39	2.107	2.651	0.4002	4.8	12.0	21.3	23.3	20.5	18.9

^aDetermined by ICP. ^bMeasured by XRD and calculated by Rietveld refinement. ^cMeasured by N_2 adsorption at liquid N_2 temperature and calculated by a t -plot. V_{N_2} represents the micropore volume measured by using N_2 . ^dMicropore volume measured by CO_2 , CH_4 , C_2H_6 , and C_3H_8 adsorption and estimated by the DA method.

oxidative condition, in order to elucidate the partial structural change in the a – b plane. The d value and the peak intensity of (210) increased under 5% H_2/N_2 flow and decreased under air flow. This d value change and intensity change were reversible for the redox treatment, being in agreement with the results of ex situ XRD analysis (Figure 4). The same trend was observed when 10% $\text{C}_2\text{H}_6/\text{N}_2$ was used as a reductive gas instead of 5% H_2/N_2 . The experimental results clearly show that ethane can cause partial structural change in the a – b plane. Therefore, partial structural change of the catalysts may occur during the selective oxidation of ethane. Structural analysis of the catalysts after the reaction was therefore carried out.

Figure S21 shows the XRD, IR, and Raman results, and Table 3 shows the physicochemical properties of the catalysts after selective oxidation of ethane. No elemental composition changes were observed. The external surface areas of the catalysts used were slightly smaller than those before the reaction and were in the range of 3.5–5.4 $\text{m}^2 \text{g}^{-1}$. After the reaction, no peaks related to impurities were observed in XRD, indicating high stability of the catalyst structures under the catalytic test. However, slight changes in peak positions and in peak intensity ratios were observed, particularly in the low angle region ($2\theta = 4$ – 10°). This finding indicates that the structure, especially that in the a – b plane, is changed during selective oxidation of ethane. At the same time, IR or Raman bands attributed to the Mo–O–Mo bond in the pentagonal $[\text{Mo}_6\text{O}_{21}]^{6-}$ unit were shifted and the band positions of the catalysts became almost the same, suggesting that bond lengths in the pentagonal $[\text{Mo}_6\text{O}_{21}]^{6-}$ units were almost the same in all of the catalysts. Rietveld refinement performed on the catalysts after the catalytic test revealed that the lattice parameters of the catalysts were almost the same regardless of the initial reduction states (Table 3). This implies that the amount of β -oxygen was almost the same for all of the catalysts used, because of the evolution of β -oxygen (for MoVO(0), MoVO(0.8), MoVO(2.9), MoVO(2.9)-AC, and MoVO(6.8)-AC) or incorporation of gaseous oxygen into the framework structure as β -oxygen (for MoVO(4.2), MoVO(5.4), MoVO(6.1), and MoVO(6.8)). This can be speculated from the lattice parameter change of the catalysts before the reaction. The structural models obtained by Rietveld refinement indicated that the diameter of the heptagonal channel in the short axis (D_2 in Figure 8A) was increased in MoVO(5.4), MoVO(6.1), and MoVO(6.8) after the reaction. D_2 values of the MoVO(5.4), MoVO(6.1), and MoVO(6.8) catalysts were 0.608, 0.608, and 0.606 nm, respectively (data not shown). By the increase in D_2 , the micropore volumes estimated from adsorption of various molecules of MoVO(5.4), MoVO(6.1), and MoVO(6.8) were significantly increased (Table 3). We concluded that the partial structural change around the heptagonal channel during the catalysis restored the microporosity of MoVO(5.4), MoVO(6.1), and MoVO(6.8), contributing to the increase in catalytic activity. For further confirmation of the partial structural change during the reaction, in situ XRD analysis was carried out. Figures S22, S23, and S24 show the results of in situ XRD analysis for MoVO(0), MoVO(4.2), and MoVO(6.8) at 300 °C under $\text{C}_2\text{H}_6/\text{O}_2/\text{N}_2 = 10/10/80 \text{ mL min}^{-1}$ gas flow. Peak intensities of (020), (120), and (210) are plotted as a function of holding time at 300 °C. Figures S22 and S23 show that the peak intensities of MoVO(0) and MoVO(4.2) were almost unchanged, indicating almost no structural change in the a – b plane during the in situ XRD. However, clear change in peak intensity was observed for

MoVO(6.8) in the early stage of analysis, suggesting partial structural change in the a – b plane as indicated by ex-situ XRD analyses. It is notable that the partial structural change was almost completed at about 360 min after the start of the reaction, although the catalytic activity at 360 min was still very low. Detailed investigation of this difference is now in progress. The experimental results further confirmed that the increase in catalytic activity of the catalysts above MoVO(5.4) during the reaction is surely derived from the structural change in the a – b plane.

Hence, we investigated the active structure for selective oxidation of ethane. As discussed above, the evolution of α -oxygen increases $V_{\text{C}_3\text{H}_8}$. Therefore, if the evolution of α -oxygen contributes to the increase in catalytic activity, a proportional relationship should be found between catalytic activity and $V_{\text{C}_3\text{H}_8}$. Figure S25 shows ethane conversion at 69 h as a function of $V_{\text{C}_2\text{H}_6}$ or $V_{\text{C}_3\text{H}_8}$ obtained after the catalytic test. Although no relationship between ethane conversion and $V_{\text{C}_2\text{H}_6}$ was found, there was a positive correlation between ethane conversion and $V_{\text{C}_3\text{H}_8}$. This implies that the void space produced by the evolution of α -oxygen contributes to the catalysis for selective oxidation of ethane. Figure S26 shows the Arrhenius plot of MoVO(2.9)-AC and MoVO(6.8)-AC. The difference between these two catalysts is only the number of α -oxygen atoms in the structure. The slopes of the lines were almost the same, indicating that the activation energy of ethane was almost the same and was ca. 82 kJ mol^{-1} , being in agreement with our previous report.¹ However, the intercepts were very different. Calculated frequency factors of MoVO(2.9)-AC and MoVO(6.8)-AC were $0.86 \times 10^9 \text{ mmol s}^{-1} \text{ g}_{\text{cat}}^{-1}$ and $2.20 \times 10^9 \text{ mmol s}^{-1} \text{ g}_{\text{cat}}^{-1}$, respectively. The frequency factor of MoVO(6.8)-AC was three times higher than that of MoVO(2.9)-AC. These results indicate that the catalytically active site for ethane activation is the same regardless of the presence of α -oxygen; however, the number of active sites is increased by the evolution of α -oxygen. These results support our proposal that the space produced by the evolution of α -oxygen contributes to the catalysis. Based on these results, the void space generated by evolving α -oxygen should be the active site for the reaction. The space produced by the evolution of α -oxygen may moderately activate molecular oxygen, leading to high catalytic activity for selective oxidation of ethane. Investigation of the active oxygen species is now in progress.

4. CONCLUSION

Redox treatments of orthorhombic $\text{Mo}_{29}\text{V}_{11}\text{O}_{112-\delta}$ catalyst (MoVO) were carried out in order to obtain catalysts with different reduction states. Single crystal analysis combined with Rietveld refinement provided a detailed structural model of MoVO for each reduction state that revealed partial structural change in the a – b plane caused by the redox treatment. The microporosity of MoVO was strongly dependent on the crystal structure in the a – b plane. The change in microporosity significantly affected the catalytic activity for selective oxidation of ethane. Strong dependence was found between the crystal structure, microporosity, and catalytic activity for the selective oxidation of ethane. This work has provided a comprehensive understanding for the catalysis of ethane involving the micropore as the catalysis field and has enabled us to express the catalytic reaction at the molecular level.

■ ASSOCIATED CONTENT

● Supporting Information

Figures showing the crystal image that was used for single crystal analysis, weight losses of MoVO(0), TPR spectra of MoVO(0), UV spectra of MoVO, adsorption isotherms and *t*-plots of MoVO, Rietveld refinement of MoVO, *d* value change and peak intensity change of the (210) plane of MoVO(0) measured by in situ XRD, XRD patterns, IR spectra, and Raman spectra of MoVO after ethane oxidation, change in peak intensities of MoVO(0), MoVO(4.2), and MoVO(6.8) as a function of time under C₂H₆/O₂/N₂ = 10/10/80 mL min⁻¹ at 300 °C measured by in situ XRD, ethane conversion at 69 h as a function of micropore volumes measured by C₃H₈ or C₂H₆ for the catalysts after the reaction, Arrhenius plot for ethane conversion over MoVO(2.9)-AC and MoVO(6.8)-AC and tables of atomic coordinates and occupancy of the framework of MoVO(0), bond distances of MoVO(0), atomic coordinates and occupancy of the framework of MoVO(0.8), atomic coordinates and occupancy of the framework of MoVO(2.9), atomic coordinates and occupancy of the framework of MoVO(4.2), atomic coordinates and occupancy of the framework of MoVO(5.4), atomic coordinates and occupancy of the framework of MoVO(6.1), atomic coordinates and occupancy of the framework of MoVO(6.8), atomic coordinates and occupancy of the framework of MoVO(2.9)-AC, atomic coordinates and occupancy of the framework of MoVO(6.8)-AC, refined parameters and agreement factors of Rietveld refinement for MoVO(0), refined parameters and agreement factors of Rietveld refinement for MoVO(0.8), refined parameters and agreement factors of Rietveld refinement for MoVO(2.9), refined parameters and agreement factors of Rietveld refinement for MoVO(4.2), refined parameters and agreement factors of Rietveld refinement for MoVO(5.4), refined parameters and agreement factors of Rietveld refinement for MoVO(6.1), refined parameters and agreement factors of Rietveld refinement for MoVO(6.8), refined parameters and agreement factors of Rietveld refinement for MoVO(2.9)-AC, refined parameters and agreement factors of Rietveld refinement for MoVO(6.8)-AC, and ethane conversion and product selectivity at the initial stage and at 69 h after the start of the reaction, and cif files for the crystal structures. This material is available free of charge via the Internet at <http://pubs.acs.org>.

■ AUTHOR INFORMATION

Corresponding Authors

*E-mail: ueda@cat.hokudai.ac.jp (W.U.).

*E-mail: [s.ishikawa\(@\)cat.hokudai.ac.jp](mailto:s.ishikawa(@)cat.hokudai.ac.jp) (S.I.).

Author Contributions

The manuscript was written through contributions of all authors. All authors have given approval to the final version of the manuscript.

Notes

The authors declare no competing financial interest.

■ ACKNOWLEDGMENTS

This work was supported by JSPS KAKENHI Grant Number 2324-6135. The synchrotron radiation experiments were performed at the BL40XU of SPring-8 with the approval of the Japan Synchrotron Radiation Research Institute (JASRI) (Proposal Nos. 2011B1181, 2012A1161, and 2014A1316). We

are grateful to Dr. Greg Shaw at Cardiff Catalysis Institute, Cardiff University for careful reading of the manuscript.

■ REFERENCES

- (1) Konya, T.; Katou, T.; Murayama, T.; Ishikawa, S.; Sadakane, M.; Buttrey, D. J.; Ueda, W. An Orthorhombic Mo₃VO_x Catalyst Most Active for Oxidative Dehydrogenation of Ethane among Related Complex Metal Oxides. *Catal. Sci. Technol.* **2013**, *3*, 380–387.
- (2) Ishikawa, S.; Yi, X.; Murayama, T.; Ueda, W. Heptagonal Channel Micropore of Orthorhombic Mo₃VO_x as Catalysis Field for the Selective Oxidation of Ethane. *Appl. Catal. A: Gen.* **2014**, *474*, 10–17.
- (3) Ishikawa, S.; Yi, X.; Murayama, T.; Ueda, W. Catalysis Field in Orthorhombic Mo₃VO_x Oxide Catalyst for the Selective Oxidation of Ethane, Propane and Acrolein. *Catal. Today* **2014**, *238*, 35–40.
- (4) Ishikawa, S.; Murayama, T.; Ohmura, S.; Sadakane, M.; Ueda, W. Synthesis of Novel Orthorhombic Mo and V based Complex Oxides Coordinating Alkylammonium Cation in its Heptagonal Channel and Their Application as a Catalyst. *Chem. Mater.* **2013**, *25*, 2211–2219.
- (5) Gartner, C. A.; Veen, A. C.; Lercher, J. A. Oxidative Dehydrogenation of Ethane: Common Principles and Mechanistic Aspects. *ChemCatChem.* **2013**, *11*, 3196–3217.
- (6) Katou, T.; Vitry, D.; Ueda, W. Structure Dependency of Mo-V-O-based Complex Oxide Catalysts in the Oxidations of Hydrocarbons. *Catal. Today* **2004**, *91–92*, 237–240.
- (7) Ueda, W.; Oshihara, K.; Vitry, D.; Himeno, T.; Kayashima, Y. Hydrothermal Synthesis of Mo-based Oxide Catalysts and Selective Oxidation of Alkanes. *Catal. Surv. Jpn.* **2002**, *6*, 33–44.
- (8) Ueda, W.; Oshihara, K. Selective Oxidation of Light Alkanes over Hydrothermally Synthesized Mo-V-M-O (M = Al, Ga, Bi, Sb, and Te) Oxide Catalysts. *Appl. Catal. A: Gen.* **2000**, *200*, 135–143.
- (9) Chen, C.; Nakatani, K.; Murayama, T.; Ueda, W. Single-Crystalline-Phase Mo₃VO_x: An Efficient Catalyst for the Partial Oxidation of Acrolein to Acrylic acid. *ChemCatChem.* **2013**, *5*, 2869–2873.
- (10) Sadakane, M.; Watanabe, N.; Katou, T.; Nodasaka, Y.; Ueda, W. Crystalline Mo₃VO_x Mixed-Metal-Oxide Catalyst with Trigonal Symmetry. *Angew. Chem., Int. Ed.* **2007**, *46*, 1493–1496.
- (11) Tichy, J. Oxidation of Acrolein to Acrylic acid over Vanadium-Molybdenum Oxide Catalysts. *Appl. Catal. A: Gen.* **1997**, *157*, 363–385.
- (12) Qiu, C.; Chen, C.; Ishikawa, S.; Murayama, T.; Ueda, W. Crystalline Mo-V-W-Mixed Oxide with Orthorhombic and Trigonal Structures as Highly Efficient Oxidation Catalysts of Acrolein to Acrylic acid. *Top. Catal.* **2014**, *57*, 1163–1170.
- (13) Pyrz, W. D.; Blom, D. A.; Sadakane, M.; Kodato, K.; Ueda, W.; Vogt, T.; Buttrey, D. J. Atomic-Scale Investigation of Two-Component MoVO Complex Oxide Catalysts using Aberration-Corrected High-Angle Annular Dark-field Imaging. *Chem. Mater.* **2010**, *22*, 2033–2040.
- (14) Pyrz, W. D.; Blom, D. A.; Sadakane, M.; Kodato, K.; Ueda, W.; Vogt, T.; Buttrey, D. J. Atomic-Level Imaging of Mo-V-O Complex Oxide Phase Intergrowth, Grain Boundaries, and Defects using HAADF-STEM. *Proc. Natl. Acad. Sci. U.S.A.* **2010**, *107*, 6152–6157.
- (15) Ueda, W. Establishment of Crystalline Complex Mo-V-Oxides as Selective Oxidation Catalysts. *J. Jpn. Petrol. Inst.* **2013**, *56*, 122–132.
- (16) Sadakane, M.; Kodato, K.; Kuranishi, T.; Nodasaka, Y.; Sugawara, K.; Sakaguchi, N.; Nagai, T.; Matsui, Y.; Ueda, W. Molybdenum-Vanadium-based Molecular Sieves with Microchannels of Seven-Membered Rings of Corner-Sharing Metal Oxide Octahedra. *Angew. Chem., Int. Ed.* **2008**, *47*, 2493–2496.
- (17) Sadakane, M.; Ohmura, S.; Kodato, K.; Fujisawa, T.; Kato, K.; Shimidzu, K.; Murayama, T.; Ueda, W. Redox Tunable Reversible Molecular Sieves: Orthorhombic Molybdenum Vanadium Oxide. *Chem. Commun.* **2011**, *47*, 10812–10814.
- (18) Ishikawa, S.; Tashiro, M.; Murayama, T.; Ueda, W. Seed-Assisted Synthesis of Crystalline Mo₃VO_x Oxides and Their Crystal Formation Mechanism. *Cryst. Growth Des.* **2014**, *14*, 4553–4561.

- (19) Yasuda, N.; Fukuyama, Y.; Toriumi, K.; Kimura, S.; Takata, M. Submicrometer Single Crystal Diffractometry for Highly Accurate Structure Determination. *AIP Conf. Proc.* **2010**, *1234*, 147–150.
- (20) Yasuda, N.; Murayama, H.; Fukuyama, Y.; Kim, J.; Kimura, S.; Toriumi, K.; Tanaka, Y.; Moritomo, Y.; Kuroiwa, Y.; Kato, K.; et al. X-ray Diffractometry for the Structure Determination of a Submicrometre Single Powder Grain. *J. Synchrotron Radiat.* **2009**, *16*, 352–357.
- (21) Sheldrick, G. M. *SHELX-97*: Program for Crystal Structure Analysis. Universität Göttingen, Germany, 1997.
- (22) Sheldrick, G. M. A Short History of SHELX. *Acta Crystallogr.* **2008**, *A64*, 112–122.
- (23) Sadakane, M.; Yamagata, K.; Kodato, K.; Endo, K.; Toriumi, K.; Ozawa, Y.; Ozeki, T.; Nagai, T.; Matsui, Y.; Sakaguchi, N.; et al. Synthesis of Orthorhombic Mo-V-Sb Oxide Species by Assembly of Pentagonal Mo₆O₂₁ Polyoxometalate Building Blocks. *Angew. Chem., Int. Ed.* **2009**, *48*, 3782–3786.
- (24) DeSanto, P., Jr.; Buttrey, D. J.; Grasselli, R. K.; Pyrz, W. D.; Lugmair, C. G.; Volpe, A. F., Jr.; Vogt, T.; Toby, B. H. Comparison of MoVTaTeO and MoVNbTeO M1 Crystal Chemistry. *Top. Catal.* **2006**, *38*, 31–40.
- (25) Yamazoe, N.; Kihlberg, L. Mo₅O₁₄ - Twinning and Three-Dimensional Structure, Determined from a Partly Tantalum-Substituted Crystal. *Acta Crystallogr.* **1975**, *B31*, 1666–1672.
- (26) Pyrz, W. D.; Blom, D. A.; Shiju, N. R.; Guilants, V. V.; Vogt, T.; Buttrey, D. J. Using Aberration-Corrected STEM Imaging to Explore Chemical and Structural Variations in the M1 Phase of the MoVNbTeO Oxidation Catalyst. *J. Phys. Chem. C* **2008**, *112*, 10043–10049.
- (27) Pyrz, W. D.; Blom, D. A.; Vogt, T.; Buttrey, D. J. Direct Imaging of the MoVTeNbO M1 Phase using an Aberration-Corrected High-Resolution Scanning Transmission Electron Microscope. *Angew. Chem., Int. Ed.* **2008**, *47*, 2788–2791.
- (28) Murayama, H.; Vitry, D.; Ueda, W.; Fuchs, G.; Anne, M.; Dubois, J. L. Structure Characterization of Orthorhombic Phase in MoVTeNbO Catalyst by Powder X-ray Diffraction and XANES. *Appl. Catal. A: Gen.* **2007**, *318*, 137–142.
- (29) Hibst, H.; Rosowski, F.; Cox, G. New Cs-containing Mo-V⁺ based Oxides with the Structure of the M1 phase - Base for New Catalysts for the Direct Alkane Activation. *Catal. Today* **2006**, *117*, 234–241.
- (30) Todea, A. M.; Merca, A.; Bögge, H.; Slageren, J.; Dressel, M.; Engelhardt, L.; Luban, M.; Glaser, T.; Henry, M.; Müller, A. Extending the {(Mo)Mo₃}₁₂M₃₀ Capsule Keplerate Sequence: A {Cr₃₀} Cluster of S = 3/2 Metal centers with a {Na(H₂O)₁₂} Encapsulate. *Angew. Chem., Int. Ed.* **2007**, *46*, 6106–6110.
- (31) Müller, A.; Roy, S. Multifunctional Metal Oxide based Nanoobjects: Spherical Porous Capsules/Artificial Cells and Wheel-shaped Species with Unprecedented Materials Properties. *J. Mater. Chem.* **2005**, *15*, 4673–4677.
- (32) Müller, A.; Roy, S. Linking Giant Molybdenum Oxide based Nano-Objects based on Well-Defined Surfaces in Different Phases. *Eur. J. Inorg. Chem.* **2005**, *18*, 3561–3570.
- (33) Hall, N. Bringing inorganic chemistry to life. *Chem. Commun.* **2003**, *7*, 803–806.
- (34) Müller, A.; Kögerler, P.; Dress, A. W. M. Giant Metal-Oxide-based Spheres and Their Topology: From Pentagonal Building Blocks to Keplerates and Unusual Spin Systems. *Coord. Chem. Rev.* **2001**, *222*, 193–218.
- (35) Miyoshi, S.; Hong, J. O.; Yashiro, K.; Kaimai, A.; Nigara, Y.; Kawamura, K.; Kawada, T.; Mizusaki. Lattice Expansion upon Reduction of Perovskite-Type LaMnO₃ with Oxygen-Deficit Non-stoichiometry. *J. Solid State Ionics* **2003**, *161*, 209–217.
- (36) Ayyub, P.; Palkar, V. R.; Chattopadhyay, S.; Multani, M. Effect of Crystal Size Reduction on Lattice Symmetry and Cooperative Properties. *Phys. Rev. B* **1995**, *51*, 6135–6138.
- (37) Hailstone, R. K.; DiFrancesco, A. G.; Leong, J. G.; Allston, T. D.; Reed, K. J. A Study of Lattice Expansion in CeO₂ Nanoparticles by Transmission Electron Microscopy. *J. Phys. Chem. C* **2009**, *113*, 15155–15159.
- (38) Porter, V. R.; White, W. B.; Roy, R. Optical Spectra of the Intermediate Oxides of Titanium, Vanadium, Molybdenum, and Tungsten. *J. Solid State Chem.* **1972**, *4*, 250–254.
- (39) López, N. J. M.; Botella, P.; Solsona, B.; Oliver, J. M. The Selective Oxidation of Propane on Mo-V-Te-Nb-O Catalysts: The Influence of Te-precursor. *Catal. Today* **2003**, *81*, 87–94.
- (40) Blasco, T.; Concepción, P.; López, N. J. M.; Pariente, J. P. Preparation, Characterization, and Catalytic Properties of VAPO-5 for the Oxydehydrogenation of Propane. *J. Catal.* **1995**, *152*, 1–17.
- (41) Buttrey, D. J. Presented at the 7th World Congress on Oxidation Catalysis. Saint Louis, MO, June 9–12, 2013.
- (42) Vadim, V. G.; Rishabh, B.; Jamal, N. A. S.; Vijay, K. V.; Rajiv, S. S.; Olga, G. P.; Miguel, A. B. Bulk Mixed Mo-V-Te-O Catalysts for Propane Oxidation to Acrylic acid. *Appl. Catal. A: Gen.* **2004**, *274*, 123–132.
- (43) Botella, P.; López, N. J. M.; Solsona, B.; Mifsud, A.; Marquez, F. The Preparation, Characterization, and Catalytic Behavior of MoVTeNbO Catalysts Prepared by Hydrothermal Synthesis. *J. Catal.* **2002**, *209*, 445–455.
- (44) Ivars, F.; Solsona, B.; Castellon, E. R.; López, N. J. M. Selective Propane Oxidation over MoVSbO Catalysts. On the Preparation, Characterization and Catalytic Behavior of M1 phase. *J. Catal.* **2009**, *262*, 35–43.
- (45) Valente, J. S.; Herrera, H. S.; Solórzano, R. Q.; Ángel, P.; Nava, N.; Massó, A.; López, N. J. M. Chemical, Structural, and Morphological Changes of a MoVTeNb Catalyst during Oxidative Dehydrogenation of Ethane. *ACS Catal.* **2014**, *4*, 1292–1301.
- (46) Sadakane, M.; Endo, K.; Kodato, K.; Ishikawa, S.; Murayama, T.; Ueda, W. Assembly of a Pentagonal Polyoxomolybdate Building Block, [Mo₆O₂₁]⁶⁻, into Crystalline MoV Oxides. *Eur. J. Inorg. Chem.* **2013**, *10–11*, 1731–1736.
- (47) Gregg, J. S.; Tayyab, M. M. Test of the Nonane Method for Micropore Evaluation. Use of Nitrogen, n-Hexane and Carbon Tetrachloride as Adsorptives with Ammonium Phosphomolybdate, Phosphotungstate and Silicomolybdate as Absorbents. *J. Chem. Soc., Faraday Trans. 1* **1978**, *74*, 348–358.
- (48) Luo, J.; Zhang, Q.; Martinez, J. M.; Suib, S. L. Adsorptive and Acidic Properties, Reversible Lattice Oxygen Evolution, and Catalytic Mechanism of Cryptomelane-Type Manganese Oxides as Oxidation Catalysts. *J. Am. Chem. Soc.* **2008**, *130*, 3198–3207.
- (49) Martínez, J. G.; Amorós, C. D.; Solano, A. L. Further Evidences of the Usefulness of CO₂ Adsorption to Characterise Microporous Solids. *Stud. Surf. Sci. Catal.* **2000**, *128*, 485–494.
- (50) Contact CrysDATA@FIZ-Karlsruhe.de.



Supercritical antisolvent precipitation of TiO₂ with tailored anatase/rutile composition for applications in redox catalysis and photocatalysis



Raimon P. Marin^a, Satoshi Ishikawa^b, Hasliza Bahruji^a, Greg Shaw^a, Simon A. Kondrat^a, Peter J. Miedziak^a, David J. Morgan^a, Stuart H. Taylor^a, Jonathan K. Bartley^a, Jennifer K. Edwards^a, Michael Bowker^{a,c}, Wataru Ueda^b, Graham J. Hutchings^{a,*}

^a Cardiff Catalysis Institute, School of Chemistry, Cardiff University, Main Building, Park Place, Cardiff CF10 3AT, UK

^b Catalysis Research Centre, Hokkaido University, Kita 21 Nishi 10, Sapporo, Japan

^c Rutherford Appleton Laboratory, UK Catalysis Hub, Research Complex at Harwell (RCaH), Harwell, Oxon OX11 0FA, UK

ARTICLE INFO

Article history:

Received 19 September 2014

Received in revised form 11 February 2015

Accepted 13 February 2015

Available online 1 May 2015

Keywords:

TiO₂

Supercritical CO₂

Photocatalysis

Direct synthesis of hydrogen peroxide

Alcohol oxidation

ABSTRACT

TiO₂ with tailored anatase/rutile composition has been prepared from the supercritical antisolvent (SAS) precipitation of a range of titanium alkoxides. The calcination of the SAS TiO₂ was monitored by *in situ* powder X-ray diffraction to determine the optimal calcination conditions for the formation of a mixed anatase/rutile phase TiO₂. The SAS precipitated material calcined at 450 °C produced a predominantly anatase support while calcination at 750 °C resulted in a 90 wt% anatase and 10 wt% rutile TiO₂. 5 wt% AuPd was added to the SAS TiO₂ using an impregnation technique, with exceptional dispersion of the metals being observed by transmission electron microscopy. Mean metal particle sizes were determined to be below 1 nm for both anatase and anatase/rutile SAS TiO₂ materials. These catalysts were found to be highly active for the selective oxidation of benzyl alcohol and the direct synthesis of hydrogen peroxide. In addition the anatase/rutile SAS TiO₂ was found to have comparable activity to commercial anatase/rutile mixed phase TiO₂ for the photocatalytic splitting of water for hydrogen production.

© 2015 Elsevier B.V. All rights reserved.

1. Introduction

Heterogeneous catalysis is a key tenant of green chemistry and modern life, with direct involvement in the remediation of hazardous compounds, in addition to the manufacture of many bulk and fine chemicals. The use of catalysts in processes is fundamentally green, facilitating the replacement of stoichiometric reagents, enhanced reaction rates and improved atom efficiency.

Heterogeneous photocatalysis has become a promising green technology for contributing to global energy demand and for environmental remediation. Photocatalysis offers a sustainable source of energy by taking full advantage of sunlight to drive chemical reactions using semiconductors to harvest the photon flux from solar energy to generate an electron-hole pair. During light excitation, an electron is promoted into the conduction band of a semiconductor leaving a hole in the valence band. The photogenerated electron migrates to the surface and is trapped by water or

organic substrates. The most promising semiconductor that offers stability, high activity and low toxicity is TiO₂, with a 3.2 eV band gap energy that is able to adsorb photons with the wavelength less than ~380 nm. Fujishima and Honda initiated the interest in photocatalytic water splitting as a sustainable route to produce H₂ [1] with promising activity demonstrated for TiO₂ impregnated with noble metal co-catalysts such as Pd and Pt [2].

Gold dispersed on metal oxide supports has been shown to be effective for the selective oxidation of carbon monoxide [3,4], alcohols [5], alkenes [6,7] and the direct synthesis of hydrogen peroxide [8]. Alloying of gold with palladium and platinum has been shown in multiple studies to enhance activities and selectivities for alcohol oxidations [9–11] and increase hydrogen peroxide yields in the direct synthesis reaction [12–14].

The catalytic properties of these gold and gold alloy supported catalysts have been shown to be highly dependent on the support material and the procedure used to deposit the metal. A multitude of methods, including various wet impregnation [15–17], deposition precipitation [9,18], sol-immobilisation [19], vapour deposition [20] and mechanochemical [21] methods have been shown to give different metal particle sizes, alloy compositions and

* Corresponding author. Tel.: +44 029 2087 4059.
E-mail address: hutch@cf.ac.uk (G.J. Hutchings).

metal–support interactions. Analogous changes in particle composition and morphology can be achieved with different metal oxide and carbon supports [22]. In addition, metal oxide supports themselves can dramatically change activity [23] and reaction selectivity profiles, with the latter shown in a study by Sankar et al. where the undesired production of toluene in the oxidation of benzyl alcohol could be eliminated by using supports with basic sites, such as MgO and ZnO [24].

A multitude of procedures for making metal oxide supports have also been reported [25]. The effect of the different support synthesis methods are often observed as differences in the crystalline phases, morphology, surface area, porosity, crystallite size and the number of defect sites. These support properties can have a dramatic influence on the catalytic properties of noble metal supported catalysts, as observed by Corma *et al.* for Au/CeO₂ catalysed CO oxidation [26,27]. It was found that nanocrystalline CeO₂ greatly enhanced the activity of the catalysts for CO oxidation when compared to CeO₂ comprised of larger crystallites. More recently we have demonstrated that Au and AuPd supported on CeO₂ catalysts prepared by supercritical anti-solvent (SAS) precipitation had exceptional activity for both CO oxidation [28] and the solvent free oxidation of benzyl alcohol [29]. The high activity of these SAS catalysts was attributed to the exceptional dispersion of Au and Pd facilitated by the highly defective CeO₂ produced by the SAS technique.

Further studies into oxidation catalysts synthesised using SAS precipitation, such as vanadium phosphates, Co₃O₄ and CuMnO₄, have shown that poorly crystalline nanocrystalline materials with good redox properties and high activity for a range of reactions [30–32]. Studies have also been performed on the SAS preparation of TiO₂ in both batch and semi-continuous modes using acetylacetonate and alkoxide precursors [33–36]. These studies include the use of supercritical CO₂ to induce hydrolysis of alkoxides [33] and also to facilitate the polymerisation of alkoxides with acetic acid, akin to a sol-gel process [36]. Calcination of these precursors has resulted in various TiO₂ morphologies and significantly different anatase/rutile compositions. However, with the exception of one investigation into CO oxidation using Au/TiO₂ catalysts, prepared by SAS precipitation of titanium acetylacetonate [37], these studies have not explored the potential of the prepared TiO₂ for catalytic applications.

Here we show the SAS preparation of TiO₂ from titanium alkoxides and titanium acetylacetonate, the optimisation of the calcination conditions and a comparison of the resulting materials performance as a catalyst support for the photocatalytic splitting of water, the selective oxidation of benzyl alcohol and the direct synthesis of hydrogen peroxide. We report for the first time the polymerisation of titanium alkoxides with acetic acid in a SAS continuous set up and their use as catalyst support precursors.

2. Experimental

2.1. Preparation of TiO₂ support

Initial studies into the effect of using different titanium alkoxides and titanium acetylacetonate precursors (listed in Table 1) was performed using a small scale SAS reactor, described in detail previously [38]. The following provides a summary of the SAS procedure: A precursor solution was prepared containing 30 mg mL⁻¹ of titanium salt dissolved in 2 vol% H₂O/MeOH and 0.01 g mL⁻¹ acetic acid to prevent alkoxide hydrolysis in solution. This solution was then pumped at 0.5 mL min⁻¹ into a precipitation vessel held at 40 °C, 120 bar. CO₂ (BOC), was pumped concurrently at 12 L min⁻¹. Contact between the precursor solution and the supercritical CO₂ results in rapid extraction of the solvent and precipitation of the

Table 1

Properties of SAS precipitated titanium precursor salts before and after calcination at 450 °C.

Ti precursor	Surface area (m ² g ⁻¹)		Phase ^b	Crystallite size ^c (nm)
	Precipitated	Calcined ^a		
Ti-ethoxide	304	76 (30%)	Anatase	16
Ti-isopropoxide	254	91 (35%)	Anatase (2% rutile)	13
Ti-butoxide	180	54 (25%)	Anatase	21
TiO-acetylacetonate	87	33 (38%)	Anatase (2% rutile)	14
Anatase	–	20	Anatase	61

^a Values in brackets show percentage retention of surface area on calcination.

^b Determined by XRD analysis.

^c Calculated from XRD using the Scherrer equation.

precursor. The precipitation was carried out for an hour, before the system was flushed with CO₂ to remove residual solvent on the precipitate. The apparatus was depressurised and the precipitate recovered, characterised and then calcined to form the TiO₂. The most promising materials were then prepared on a larger scale using apparatus manufactured by Separex using the same temperature and pressure but with higher solvent and CO₂ flow rates to produce a greater quantity of product [31].

2.2. Preparation of catalysts

Supported metal catalysts were then prepared using the SAS precipitated TiO₂ materials as the support. Catalysts were also prepared on P-25 (Degussa) and anatase (Sigma Aldrich 99.8%) standards. 0.5 wt% Pt/TiO₂ photocatalysts were prepared by impregnation with an aqueous solution of 10 mg mL⁻¹ H₂PtCl₆ (Alfa Aesar 99.9%). The resultant slurry was then dried in an oven at 120 °C for 2 h before being calcined at 300 °C for 3 h. 2.5 wt% Au-2.5 wt% Pd/TiO₂ catalysts were used for alcohol oxidation and the direct synthesis of hydrogen peroxide and these were prepared by wet impregnation using HAuCl₄ and PdCl₂ (Alfa Aesar). The resultant slurry was dried at 110 °C for 16 h before being calcined at 400 °C for 2 h.

2.3. Characterisation

The SAS precipitated materials, supports following calcination and final catalysts were characterised using a combination of infrared spectroscopy, X-ray diffraction, thermogravimetric analysis.

Diffuse reflectance infrared Fourier transform spectroscopy (DRIFTS) was carried out using a Bruker Tensor 27 spectrometer equipped with a Harrick praying mantis cell and MCT detector. Surface areas were determined by multi-point N₂ adsorption at 77 K using a Micromeritics Gemini 2360 instrument according to the Brauner Emmet Teller method. Transmission electron microscopy (TEM) was performed using a Jeol 2100 microscope fitted with a LaB₆ filament operating at 200 kV. Samples were prepared by dispersing the powder catalyst in ethanol and dropping the suspension onto a lacey carbon film over a 300 mesh copper grid. Thermal gravimetric analysis (TGA) was performed using a SETARAM Labsys thermogravimetric analyser using 100 μl alumina crucibles.

Powder X-ray diffraction (XRD) was performed using a PANalytical X'Pert Pro diffractometer fitted with a monochromatic Cu K α source ($\lambda = 0.154$ nm) operated at 40 keV and 40 mA. The scans were recorded in the 2θ range 10–80° using a step size of 0.016° and scan step time of 55 s. Anatase (ICDD 03-065-5714) (X_A) and rutile (ICDD 03-065-1118) (X_R) phase composition was determined using the relative intensity ratio method with the following equation. $X_A = 1/(1 + 1.26 (I_R/I_A))$, where I_R is the intensity of the rutile (110) reflection and I_A is the intensity of the anatase (101) reflection.

To study the calcination temperature dependence on rutile formation, SAS prepared TiO₂ precursors, which had been pre-calcined at 400 °C for 2 h, were heated to 750 °C and monitored using an X'pert Pro XRD with an Anton–Parr XRK900 *in situ* cell. Experiments were performed under a flow of 1 mL min⁻¹ air to replicate the conditions in the tube furnace used for the *ex situ* calcination. Two sets of *in situ* XRD experiments were performed. Initial experiments under conditions that replicated the TGA (heating to 750 °C) with diffraction patterns collected every 25 °C from 23–30°, and a heating rate of 10 °C min⁻¹. The second set of isothermal experiments, with 10–80° 2θ scans, were then performed at the various temperatures of 450, 650, 700 and 750 °C. Scans were continuously taken in the isothermal experiments, with each scan taking 30 min (*i.e.* each data point is at 30 min increments). Flow and ramp rates were the same for all experiments.

2.4. Catalyst testing

2.4.1. Photocatalytic water splitting

Liquid phase photocatalytic water splitting experiments were carried out using methanol as sacrificial agent to enhance hydrogen production. The catalyst (0.2 g), methanol (100 μL, Aldrich 99.9%) and water (deionised, 100 mL) were added directly to the stirred reaction vessel. The methanol/water mixture was purged with Ar for 30 min to remove air and the flask illuminated by a 400 W Xe arc lamp (Oriel model 66921). Gas samples were taken every 30 min and analysed using a Varian 3900 GC fitted with a 2 m MS 13X column. Control experiments were carried out under identical conditions, but in the absence of the catalyst no significant hydrogen evolution was observed.

2.4.2. Benzyl alcohol oxidation

Catalyst testing was performed using a stainless steel autoclave (Autoclave Engineers In-line MagneDrive III) with a nominal volume of 100 mL and a maximum working pressure of 140 bar. The vessel was charged with benzyl alcohol (40 mL) and catalyst (25 mg). The autoclave was then purged three times with oxygen before the vessel was pressurised at 10 bar. The pressure was maintained at a constant level throughout the experiment; as the oxygen was consumed in the reaction, it was replenished. The stirrer speed was set at 1500 rpm and the reaction mixture was raised to the required temperature of 140 °C. Samples from the reactor were taken periodically *via* a sampling pipe, ensuring that the volume purged before sampling was higher than the tube volume, and analysed by GC (Varian 3800) using a CP-wax column.

2.4.3. Direct H₂O₂ synthesis

Synthesis of H₂O₂ from H₂ and O₂ was performed using a Parr Instruments stainless steel autoclave with a nominal volume of 100 mL and a maximum working pressure of 140 bar. The reactor was charged with CH₃OH (5.6 g), H₂O (2.9 g) and catalyst (0.01 g). The charged autoclave was then purged three times with 5% H₂/CO₂ (7 bar) before filling with 5% H₂/CO₂ to a pressure of 29 bar at 20 °C. This was followed by the addition of 11 bar of 25% O₂/CO₂. The reactor was then cooled to 2 °C and the reaction started with stirring at 1200 rpm. The reaction was then carried out for 30 min. The amount of hydrogenated H₂O₂ was determined by titrating aliquots with acidified Ce(SO₄)₂ (0.0288 M) in the presence of a ferroin indicator.

2.4.4. H₂O₂ hydrogenation

Hydrogen peroxide hydrogenation was evaluated using the same Parr Instruments stainless steel autoclave. To test each catalyst for H₂O₂ hydrogenation, the autoclave was charged with catalyst (0.01 g) and a solution containing 4 wt% H₂O₂ (5.6 g CH₃OH, 2.22 H₂O and 0.68 g H₂O₂ 50% w/w). The charged autoclave was then purged three times with 5% H₂/CO₂ (7 bar) before filling with

5% H₂/CO₂ to a pressure of 29 bar at 20 °C. The temperature was then allowed to decrease to 2 °C followed by stirring the reaction mixture (1200 rpm) for 30 min. The amount of hydrogenated H₂O₂ was determined by titrating aliquots with acidified Ce(SO₄)₂ (0.0288 M) in the presence of a ferroin indicator.

3. Results and discussion

3.1. Characterisation of SAS precipitated materials

As observed in previous studies, the SAS precipitates were all found to be amorphous, attributable to the fast nucleation rate achieved by SAS [39]. DRIFTS analysis (Fig. 1) of the SAS precursors prepared from the alkoxides had clear $\nu_s(\text{CCO})$ and $\nu_{as}(\text{COO})$ bands at *ca.* 1540 and 1450 cm⁻¹ ($\Delta\nu_{as} - \nu_s$ 90 cm⁻¹), along with a band at 1415 cm⁻¹, that are indicative of chelating bidentate titanium acetate complexes [39]. The bands at *ca.* 1385 and 1050 cm⁻¹ are associated with alkoxides (CH₃ deformation and $\nu(\text{Ti-O-C})$), that in addition to the strong oxo bands below 800 cm⁻¹, suggest that a sol-gel condensate was produced, as seen previously [40]. Similar bands were observed in the acetylacetonate precipitate, although there were bands at 1585 and 1360 cm⁻¹, that can be assigned to the original acetylacetonate ligand rather than the alkoxide [37]. In addition, there are bands associated with hydroxyl groups at *ca.* 3386 and 1630 cm⁻¹ associated with water and evidence of a free carboxylic acid determined from the band at 1720 cm⁻¹ in the isopropoxide sample.

Surface areas of the SAS precipitates (Table 1) were high, which is typical of SAS precipitated materials, due to the high nucleation rates that leads to small (<100 nm) particles [34]. Surface areas of the poly-condensates from the alkoxides were found to be higher than the precipitate from the titanium acetylacetonate, with an observable relationship between the alkoxide chain length and the surface area of the precipitated material. This trend culminates in the highest surface area of 304 m² g⁻¹, being observed for the ethoxide derived precursor. This surface area is comparable to that found by Sui *et al.* in their report of the batch synthesis of TiO₂ using a CO₂ sol-gel procedure, although it is interesting to note that their operating pressure was almost 300 bar higher than in the SAS precipitation methodology [36].

Thermal gravimetric analysis (TGA) was performed on the SAS precipitates to determine an optimal calcination temperature to

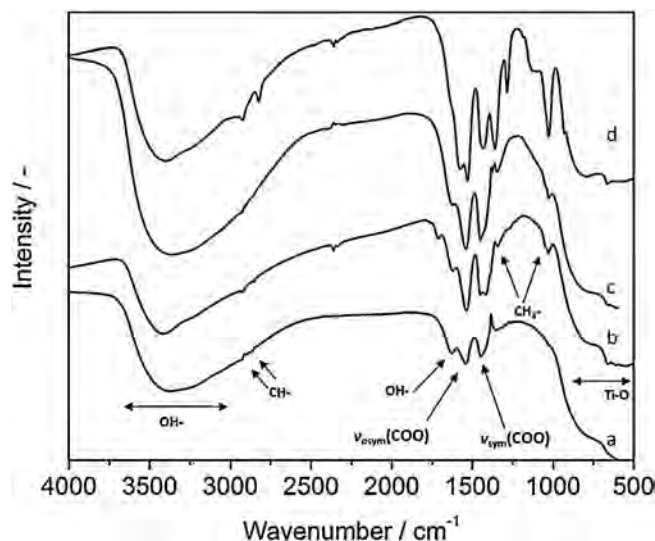


Fig. 1. Diffuse reflectance infrared Fourier transform spectroscopy of SAS precipitates. Precursors used: (a) Ti-ethoxide, (b) Ti-isopropoxide, (c) Ti-butoxide and (d) TiO-acetylacetonate.

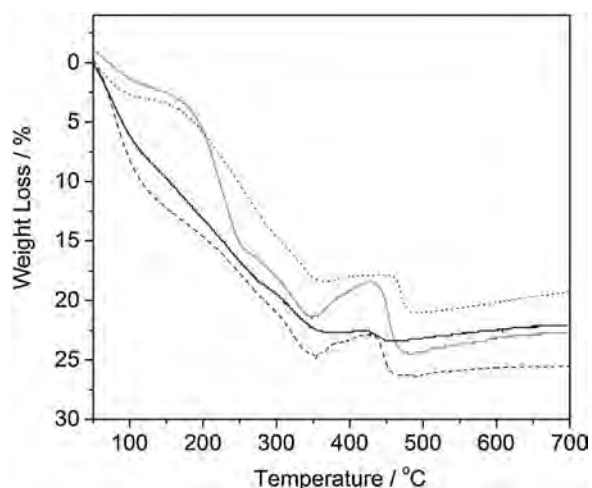


Fig. 2. Thermogravimetric analysis of SAS precipitates. Precursors used: (solid black line) Ti-ethoxide, (dotted line) Ti-isopropoxide, (dashed line) Ti-butoxide and (grey line) TiO-acetylacetonate.

form TiO_2 (Fig. 2). All samples showed a multiple stage decomposition, with an initial mass loss centred around 80°C , that is attributable to the removal of residual solvent observed by DRIFTS. Two further mass losses, centred at 215 and 305°C could be observed prior to a mass gain starting at 350°C that must be associated with an oxidation process. The extent of this mass gain varied considerably between samples, with the ethoxide and isopropoxide samples experiencing a far less significant mass gain compared to the butoxide and acetylacetonate samples. An explanation for this could be that the mass loss events at 215 and 305°C are associated with decomposition of acetate compounds, which are known to cause partial reduction of transition metals [21], with the subsequent mass gain due to the rapid re-oxidation of any reduced species. Finally, a high temperature mass loss was observed, with the extent and temperature depending on the precursor salt used. For the alkoxide derived samples the percentage mass loss of this final step correlated with the size of the alkyl group, the smallest mass loss being associated with the ethoxide precursor and the largest from the butoxide. The mass loss associated with the acetylacetonate precursor was the most significant of all the samples. Clearly the thermal decomposition of the SAS precipitates is highly complex, with the exact nature of many of the individual steps being difficult to assign with confidence. From the perspective of choosing an optimal calcination temperature for TiO_2 formation the onset of final mass loss, which is associated with residual organic compounds, was chosen as the calcination temperature. The highest temperature final mass loss was associated with the titanium isopropoxide derived sample starting at 450°C , consequently all precursors were calcined at this temperature.

3.2. Characterisation of SAS TiO_2

After calcination at 450°C the resultant TiO_2 materials were characterised by XRD to determine the phase composition and crystallite size (Fig. 3 and Table 1). All the samples were found to predominately be anatase, although residual rutile (*ca.* 2 wt) was observed in the isopropoxide and acetylacetonate derived samples, as determined by a relative intensity ratio method detailed in Section 2. The other alkoxide derived TiO_2 materials also contain traces of rutile, but the peak area was so low that it could not be suitably fitted. The prevalence of the metastable anatase phase can be expected given the lower surface free energy and less constrained molecular construction of anatase relative to rutile, which results in this phase being frequently observed as the initial

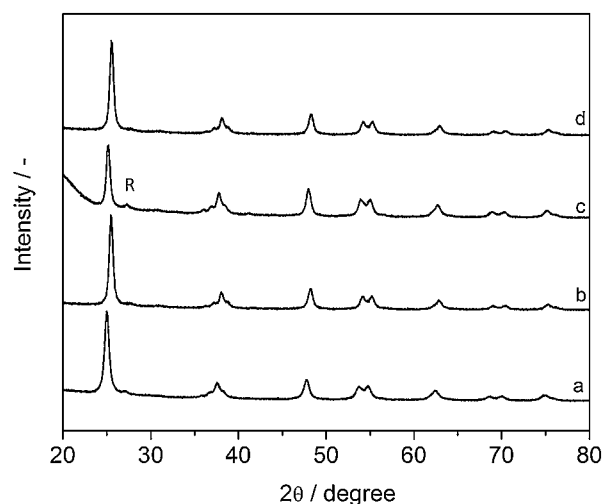


Fig. 3. XRD of SAS precipitates calcined at 450°C for 2 h. Derived from precursors: (a) TiO-acetylacetonate (b) Ti-ethoxide, (c) Ti-isopropoxide, and (d) Ti-butoxide. R indicates (110) rutile reflection.

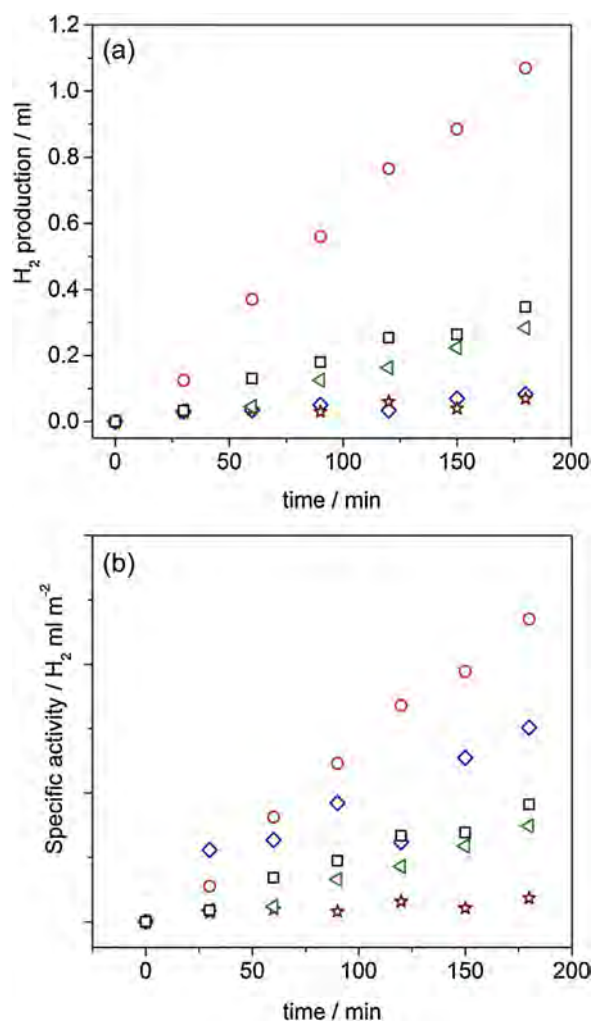


Fig. 4. Photocatalytic reactivity of Pt/ TiO_2 of SAS derived TiO_2 in the water splitting reaction. TiO_2 prepared from SAS precursors with 450°C calcination Δ Ti-ethoxide, \circ Ti-isopropoxide, \star i-butoxide, \diamond TiO-acetylacetonate and \square anatase standard.

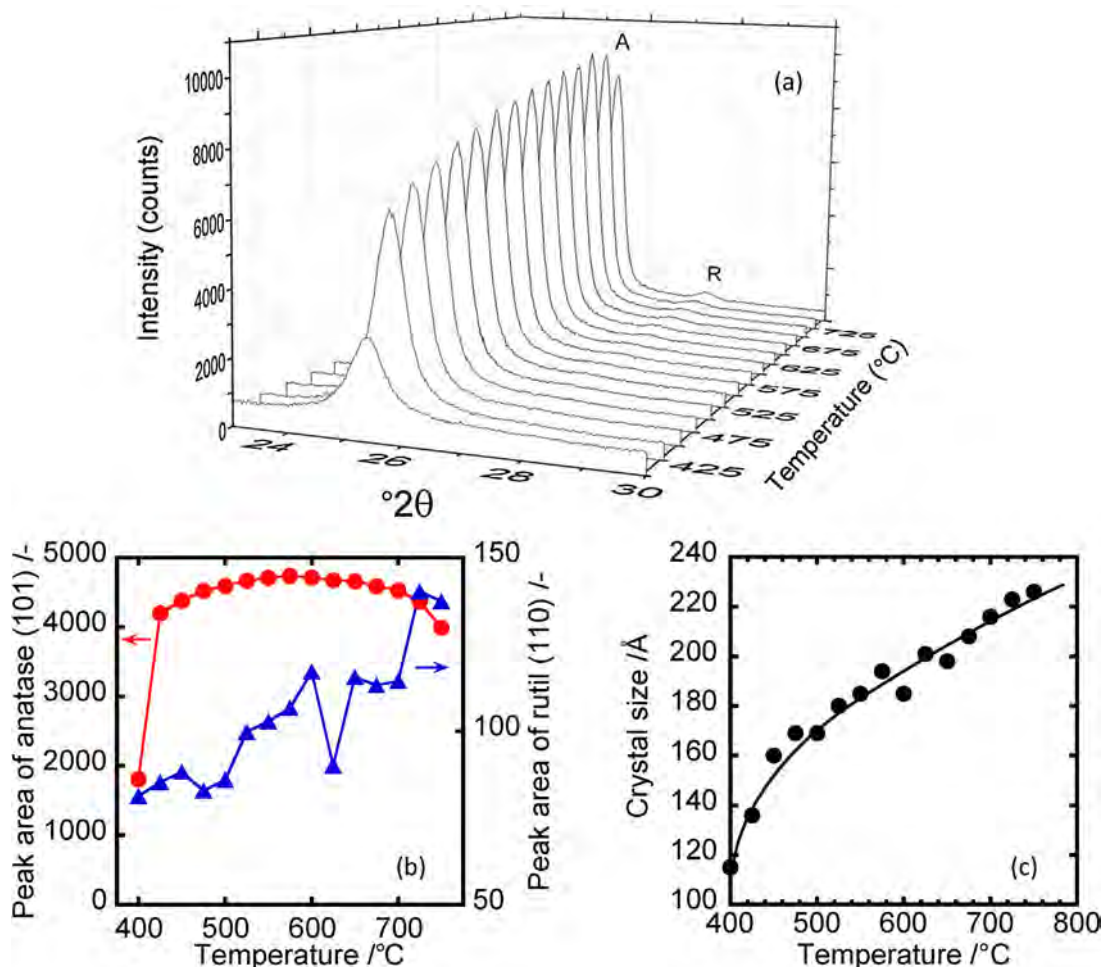


Fig. 5. *In situ* XRD analysis of SAS precipitated Ti-isopropoxide calcined from 400 to 750 $^{\circ}\text{C}$. Ramp rate of 10 $^{\circ}\text{C min}^{-1}$ with scans every 25 $^{\circ}\text{C}$. The sample was held at each desired temperature for 15 min prior to the scan over the range $2\theta = 23\text{--}30^{\circ}$. (a) Diffraction patterns with A denoting anatase (101) and R rutile (110). (b) Peak area analysis of (101) anatase and (110) rutile. (c) Evolution of anatase crystallite size with temperature.

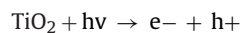
crystalline TiO_2 phase formed [41]. The observed crystallite size for the anatase phases (Table 1) showed that the smallest crystallite size was observed for the isopropoxide and acetylacetonate derived samples. It is notable that the final decomposition temperature observed by TGA (Fig. 2) of these two materials was highest of those investigated. Potentially the slower evolution of the residual organics within these two samples could have slowed TiO_2 crystal growth rates and so yielded smaller crystallite sizes. Surface area of the calcined TiO_2 samples derived from the alkoxides correlate well with observed crystallite sizes from XRD, with higher surface area corresponding to lower crystallite size. The apparent exception is the acetylacetonate derived sample, which has quite a low final surface area. However, this was due to the relatively low surface area of the uncalcined SAS acetylacetonate precursor compared to the alkoxide derived samples. When looking at the percentage retention of surface area after calcination it was observed that the acetylacetonate and isopropoxide derived samples were moderately better than the other two alkoxide samples.

3.3. Photocatalytic activity

The activity of the SAS prepared TiO_2 for photocatalytic water splitting, with methanol as sacrificial agent, was performed and compared to an anatase standard. As discussed in detail in the

experimental section, Pt nanoparticles were dispersed on the TiO_2 to help maintain separation of charge carriers. Fig. 4 shows the volume of hydrogen produced in a 3 h reaction. TiO_2 produced from the SAS isopropoxide precursor produced the most hydrogen followed by the ethoxide derived catalyst and the anatase reference sample, which showed similar activity, whilst the catalysts derived from the butoxide and acetylacetonate salts gave very little hydrogen production (<0.1 mL of hydrogen in 3 h). Degussa P-25 titania (anatase 80% rutile 20%) is a standard semiconductor commonly used in the photocatalytic water splitting reaction, and it has been proposed that its excellent activity is a result of synergistic effects occurring between the anatase and rutile phases [42,43]. The higher activity of the TiO_2 derived from the isopropoxide precursor, relative to the anatase standard, could be associated with the relatively high surface area in conjunction with the presence of small quantities of rutile. The benefit of rutile is that it has a narrow band gap energy (3.0 eV with the conduction band being -0.2 eV below the conduction band of anatase [42]. During light excitation, rutile acts as an electron sink to accept the photogenerated electron from the anatase conduction band, thus increasing the charge carrier lifetime. The charge carrier must then travel to the surface to react, or otherwise undergo recombination. The benefit of a high surface area is that for most of the metal oxides, such as TiO_2 , the surface is covered with hydroxyl groups, which are thought to play a role in

enhancing surface reaction by trapping the photogenerated holes, producing OH^\bullet radicals as shown below [44].



The number of surface hydroxyl groups is proportional to the surface area of the TiO_2 , where the Ti–O dangling bond is compensated by a proton that mostly comes from water molecules during the synthesis, or when annealing at high temperature. Since the surface area of the TiO_2 produced from the SAS method vary in the range $33\text{--}91\text{ m}^2\text{ g}^{-1}$, it is useful to compare the specific activity of the catalysts by normalising the volume of hydrogen produced to the surface area of the TiO_2 as shown in Fig. 4b. TiO_2 produced from isopropoxide and acetylacetonate precursors have the highest surface area normalised H_2 production, consistent with the mixture of anatase and rutile crystalline phases in these catalysts. Despite the higher activity of the rutile containing catalysts it is important to note that their activity was still vastly inferior to the commonly used P-25 titania supported catalysts [42,43].

3.4. Optimisation of SAS prepared TiO_2

Given the reasonable activity for the water splitting reaction of the TiO_2 derived from the isopropoxide precursor, we decided to optimise the calcination procedure of this precursor. The purpose of this was to increase the rutile content, as the phase composition of TiO_2 has significant consequences on the catalytic performance for photocatalysis and many other different reactions. Thermal treatment is the most common method of inducing phase change between anatase and rutile, and so the effect of calcination temperature on the phase composition of the titanium isopropoxide derived sample was investigated. Fig. 5 shows the evolution of the anatase (101) and rutile (110) reflections in an *in situ* XRD study from 400 to 750 °C with a ramp rate of $10^\circ\text{C min}^{-1}$, with a short 2.5 min XRD scan every 25 °C. From this initial experiment it was evident that some crystalline anatase was present at 400 °C, prior to the final mass loss observed at 450 °C by TGA. The peak area of the (101) anatase reflection then dramatically increases up to 450 °C, which correlates with the mass loss observed in the TGA, indicating increasing crystallinity of the anatase phase. The crystallinity then increases at a slower rate, with a maximum (101) peak area observed at 600 °C. Above this temperature the peak area slightly decreases with increasing temperature, with an appreciable rate of change becoming apparent at temperatures above 700 °C. The loss in anatase peak area can be attributed to the growth of the rutile phase, although by 750 °C the size of the characteristic (110) rutile reflection is very small, indicating that only trace amounts of crystalline rutile were present.

As the phase transformation from anatase to rutile is reconstructive the formation is not instantaneous and will be kinetically limited. Therefore, it was not surprising that no appreciable amounts of rutile were observed during the temperature ramp experiment. However, the study does highlight potential temperatures for further investigation. Monitoring the 450 °C calcination temperature would be useful, as there is clearly an increase in the crystallinity of the sample at this temperature, but without further transformation to rutile, whilst experiments at 650, 700 and 750 °C would be expected to show the evolution of rutile at different rates. Consequently, these four temperatures were chosen for iso-thermal *in situ* XRD experiments with the resulting diffraction patterns being shown in Figs. 6 and 7, with the summarised crystallite size and rutile content shown in Fig. 8.

As anticipated from the initial *in situ* XRD experiment, holding the calcination temperature at 450 °C did not result in the growth

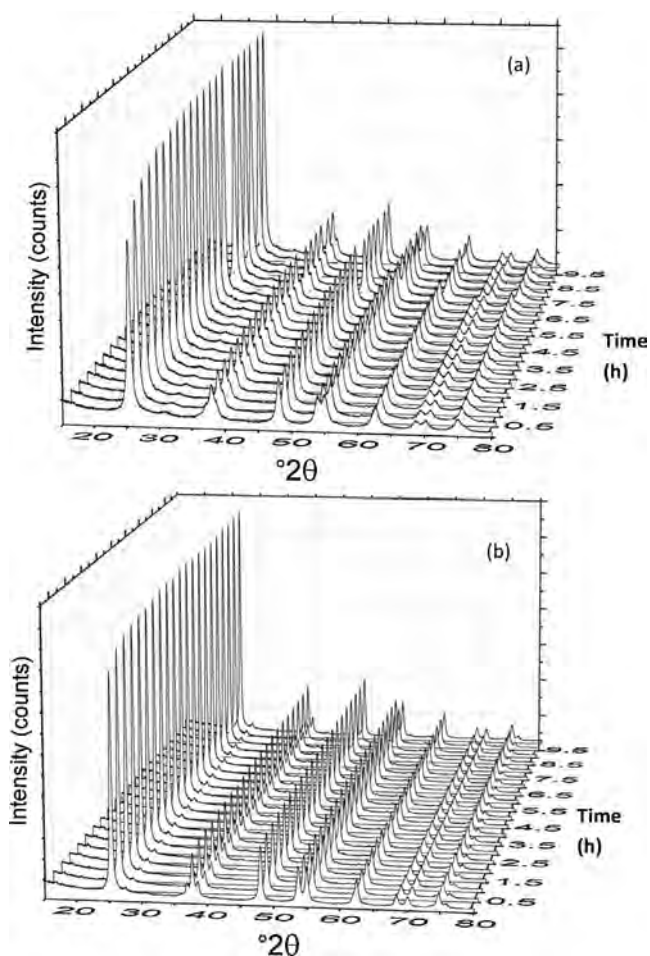


Fig. 6. *In situ* XRD analysis of SAS precipitated Ti-isopropoxide isothermal heat treatment experiments at (a) 450 °C and (b) 650 °C. Scans between 10 and 80° 2θ were taken every 30 min.

of the rutile phase within the 20 h duration of the experiment, with the exception of the small amount of rutile present from the start. Peak area analysis of the anatase (101) reflection showed an increase in crystallinity, with crystallite size growing from an initial 12–16 nm over 5 h, after which the crystallite size stabilised. While it is generally considered that the phase transition temperature for anatase to rutile is 600–700 °C [41], there have been reports of rutile formation at temperatures as low as 465 °C in systems with very small anatase crystallite sizes (4–6 nm) [45]. The relationship between small anatase crystallites and the nucleation of rutile observed, in very pure TiO_2 systems, was attributed to small crystallites having many interfaces for rutile to nucleate on. Potentially this can explain the small amounts of rutile (*ca.* 2%) observed at the start of the reaction, as we have confirmed that there are significant amounts of poorly crystalline TiO_2 initially. However, the anatase crystallites quickly grow to larger sizes that are not conducive to rutile formation at low temperatures.

At 650 and 700 °C it was expected that there would be appreciable growth of rutile over the 20 h calcination period. However, no increase in rutile content from the initial 2% was observed at 650 °C and a modest growth to 6% rutile was seen at 700 °C, during the 20 h experiment. In both cases the crystallite size of anatase stabilises at *ca.* 25 nm after 10 h. This can still be considered in the nanocrystalline region, so it is quite surprising that rutile growth was only observed at the upper end of the temperature range expected for macrocrystalline anatase reconstruction to rutile. Small anatase crystallites thermodynamically have a lower total free energy than

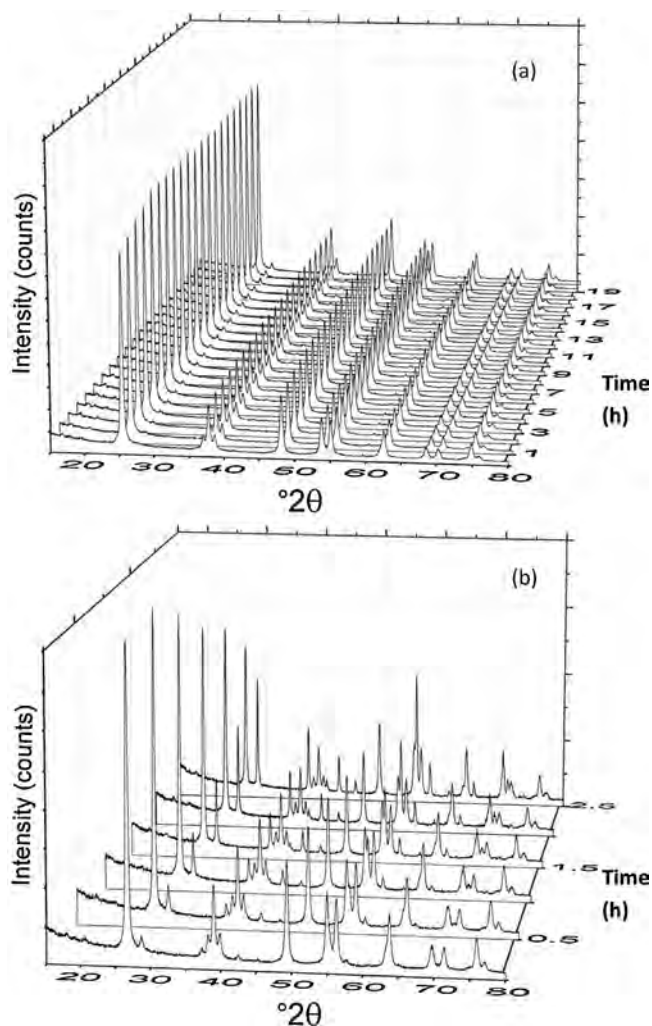


Fig. 7. *In situ* XRD analysis of SAS precipitated Ti-isopropoxide isothermal heat treatment experiments at (a) 700 °C and (b) 750 °C. Scans between 10 and 80° 2 θ were taken every 30 min.

rutile, due to the greater contribution of the low surface energy in nanoparticles relative to macroparticles [46]. This could potentially explain why the anatase derived from SAS precipitation has a relatively high transition temperature. However, this effect was not observed experimentally in the general literature with nanocrystallites being shown to have the opposite effect (*i.e.* enhancing rutile

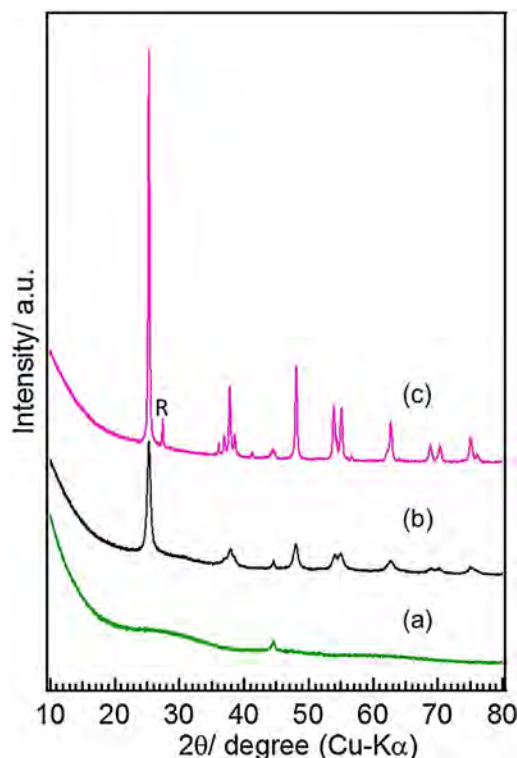


Fig. 9. XRD pattern of (a) Ti-isopropoxide, (b) Ti-isopropoxide *ex situ* calcined 450 °C, and (c) Ti-isopropoxide *ex situ* calcined 750 °C. R denoting rutile (110).

formation) as discussed previously. An alternative rationale for stability of the anatase could be the effect of carbon impurities from the SAS precipitation method, although it has been predicted that carbon doping would in fact enhance phase transformation and not hinder it [41].

In contrast to the slow phase transformation observed at 700 °C, the *in situ* XRD experiment at 750 °C showed a dramatic degree of phase change within 2.5 h, with the phase composition of rutile growing to *ca.* 50%. Most successful photo catalysts reported contain mixtures of anatase and rutile, with rutile compositions of 20–30%. In addition both the selective oxidation of alcohols and the direct synthesis of H₂O₂ generally use Degussa P-25 as the support (which consists of 80% anatase and 20% rutile). Therefore, the SAS prepared materials were calcined at 750 °C for 90 min in an attempt to produce TiO₂ with a desirable rutile content. This material was then doped with 0.5 wt% Pt and tested for the photocatalytic splitting of water and compared with the SAS Ti-isopropoxide derived

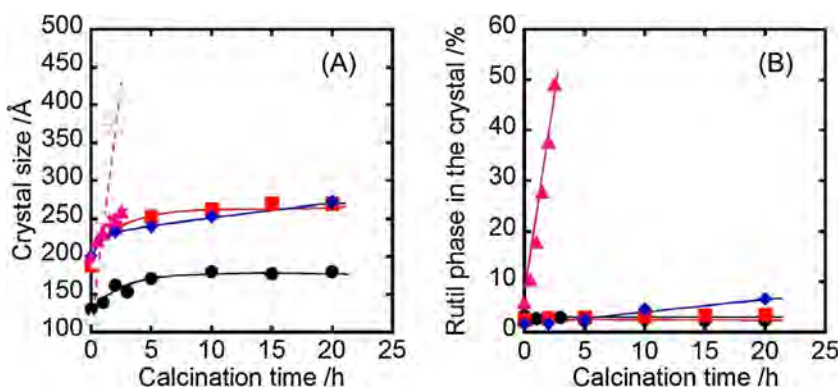


Fig. 8. (A) Crystal size of SAS precipitated Ti-isopropoxide derived TiO₂ obtained by *in situ* XRD and estimated by Sherrer method. Closed circle, 450 °C; closed square, 650 °C; closed lozenge, 700 °C; closed triangle, 750 °C; open triangle, crystal size of rutile phase at 750 °C. (B) Rutile phase content. Closed circle, 450 °C; closed square, 650 °C; closed lozenge, 700 °C; closed triangle, 750 °C.

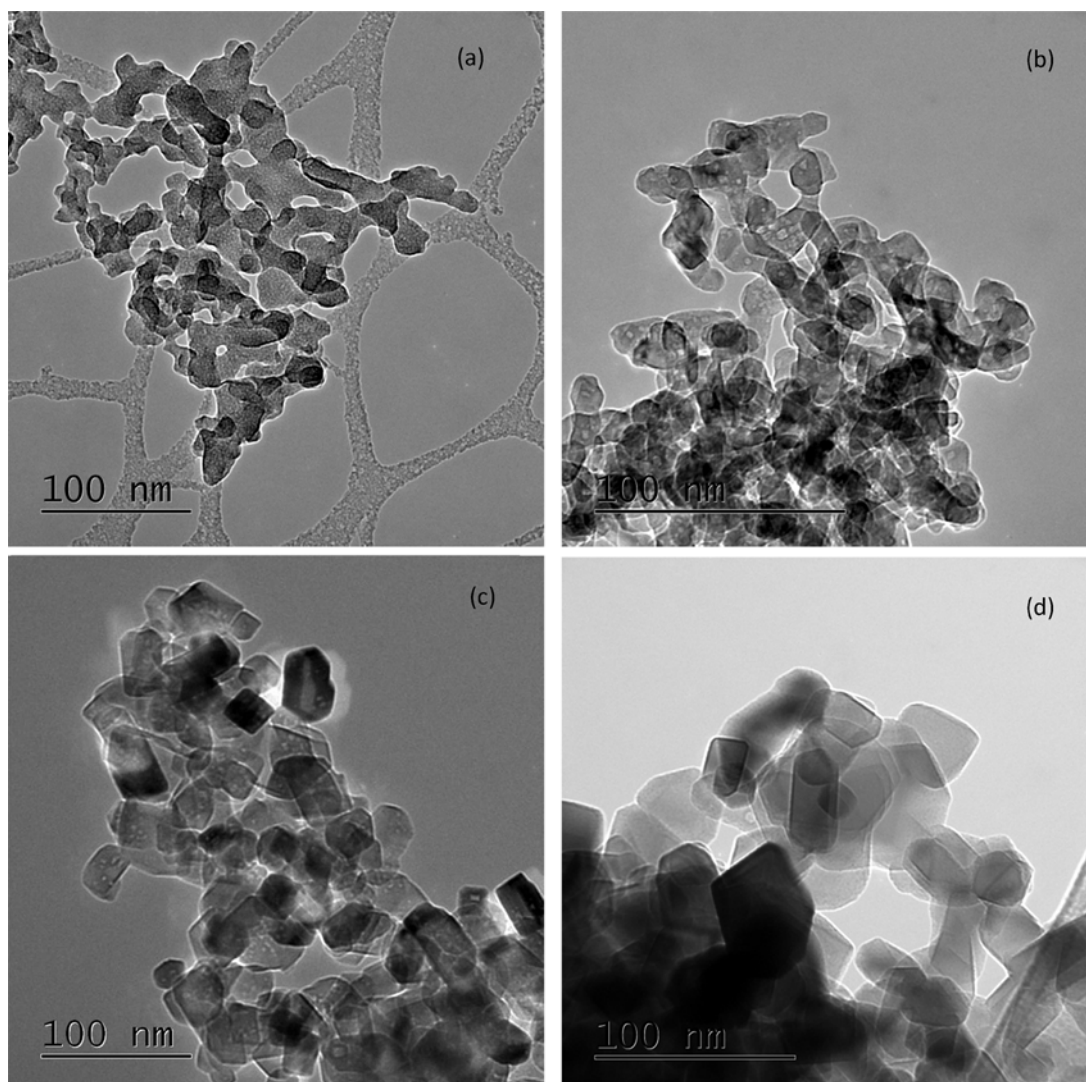


Fig. 10. Representative TEM images of (a) Ti-isopropoxide SAS precipitate and after (b) 450 °C calcination, (c) 650 °C calcination, (d) 750 °C calcination.

material calcined at 450 °C. In addition, the 450 °C and 750 °C calcined SAS Ti-isopropoxide was tested for selective oxidation of benzyl alcohol and the direct synthesis of H_2O_2 , after AuPd impregnation.

3.5. Characterisation of optimised TiO_2 catalysts

Fig. 9 shows the XRD of the TiO_2 prepared from the isopropoxide precursor calcined at 450 and 750 °C. Interestingly, the conditions that gave ca. 30 wt% rutile in the *in situ* XRD cell resulted in only 10 wt% rutile when calcined in a tube furnace. This demonstrates the effect of heat treatment conditions on the phase transformation. The amount and packing of the samples were two differences that have been shown to affect the anatase to rutile phase transformation [41]. Despite the less than expected rutile content, the 750 °C *ex situ* calcined sample still had a fivefold increase in rutile content compared to that found from 450 °C calcination.

TEM of these TiO_2 precursors calcined at 450, 650 and 750 °C along with the uncalcined material was performed to provide information on the morphology of the materials obtained from SAS precipitation (Fig. 10). As predicted from previous SAS studies, the uncalcined isopropoxide precursor comprised of ~50 nm semi-spherical particles that were bridged to form agglomerates. Interestingly this morphology mostly survives the 450 °C

calcination, with no apparent growth in particle size. Another observation is the areas of light contrast observed within the particles, which can be ascribed to voids within the materials. A similar phenomenon was observed for CeO_2 prepared *via* SAS precipitation and was ascribed to densification calcination of the amorphous precursor into the crystalline phase [28]. Calcination at higher temperature (650 and 750 °C) resulted in the formation of slightly larger and more faceted particles, normally associated with TiO_2 . The voids were still found to be present within these more crystalline catalysts, although their frequency decreased with increasing calcination temperature.

Fig. 11 provides representative TEM images of the supports following the addition of the active metal. These catalysts can be compared with gold and palladium supported on P-25 ($\text{AuPd}/\text{TiO}_2(\text{P-25})$), which has been reported multiple times [9,10,12]. $\text{AuPd}/\text{TiO}_2(\text{P-25})$ has been shown to have a bimodal metal particle size distribution, with small particles of 1–8 nm as well as large 40–70 nm particles. In contrast, no particles bigger than 2 nm were observed on the isopropoxide derived TiO_2 calcined at 450 °C ($\text{AuPd}/\text{TiO}_2(\text{isopropoxide-450 °C})$). In fact the majority of particles observed were of a size that was on the limit of accurate quantification for the microscope used, with only a small number of definable particles. As the catalysts were prepared by an impregnation technique, the full 5 wt% metal must have been deposited,

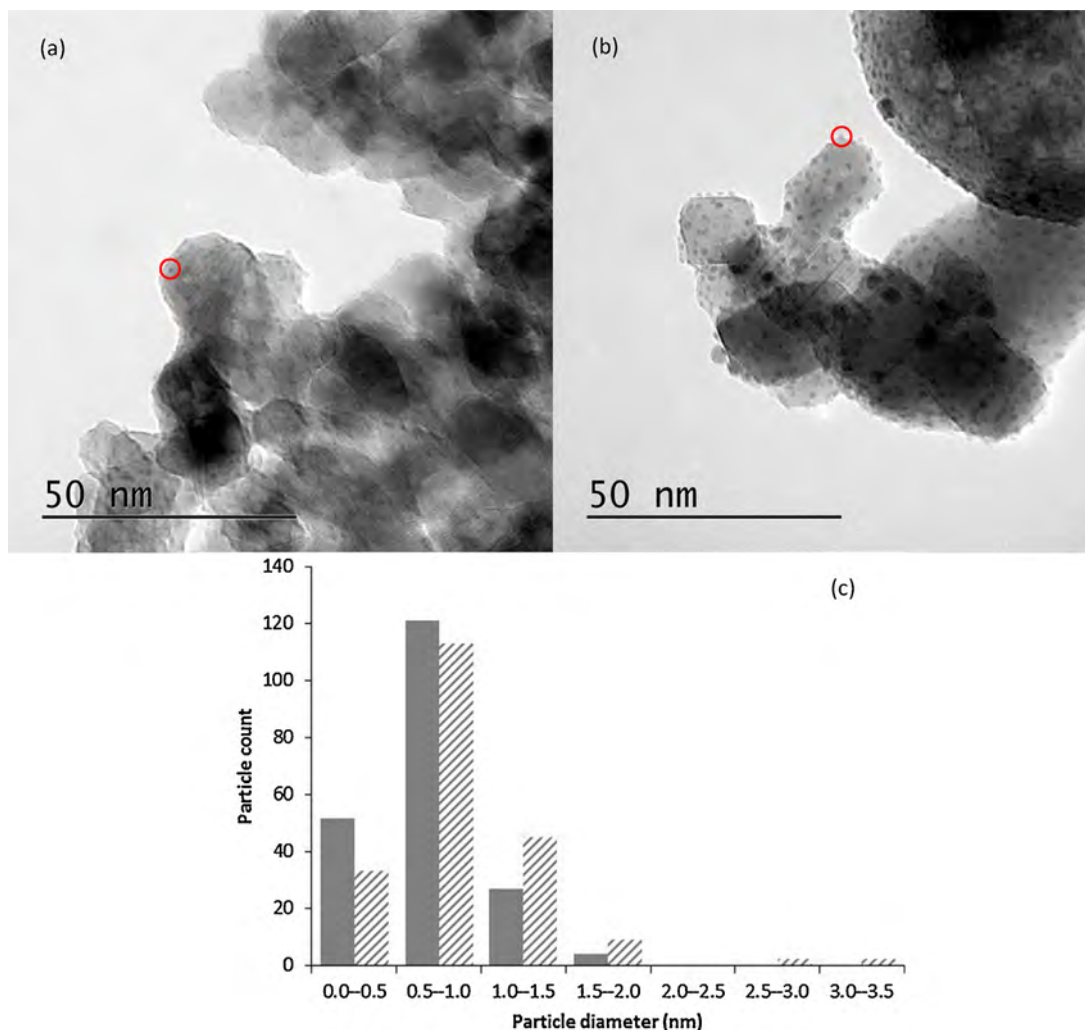


Fig. 11. Representative TEM images of 5 wt% AuPd/TiO₂ prepared from Ti-isopropoxide SAS precipitate calcined at (a) 450 °C, (b) 750 °C calcination. The highlighted areas in red highlight a metal nanoparticle. (c) Particle size distribution of 5 wt% AuPd/TiO₂ 450 °C calcination (grey bar) and 5 wt% AuPd/TiO₂ 750 °C calcination (dashed bar). (For interpretation of the references to color in this figure legend, the reader is referred to the web version of this article.)

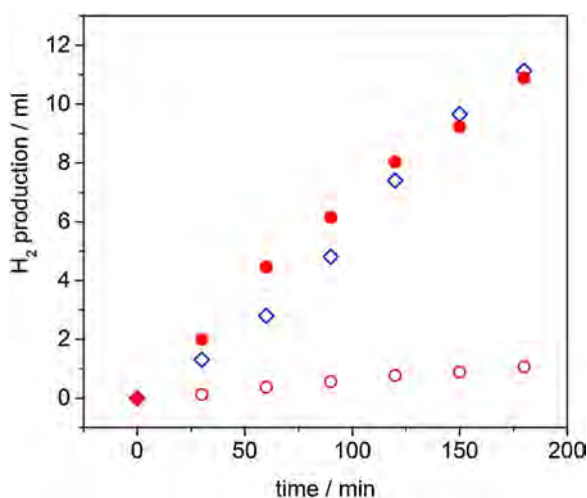


Fig. 12. Photocatalytic reactivity for water splitting with Pt/TiO₂ of Ti-isopropoxide SAS derived TiO₂ calcined at different temperatures and comparable data for a standard Pt/P-25 TiO₂ catalyst. SAS Ti-isopropoxide calcined at 450 °C (○) containing 2 wt% rutile and 750 °C (●) containing 10 wt% rutile. (◇) Catalyst prepared with commercial P-25 containing 20 wt% rutile.

suggesting that a significant proportion of the metal is of a particle size below the detection limit of the TEM. Despite this, a sufficient number of particles could be counted to give a mean particle size of 0.8 nm, although the associated dispersion of metals has previously been reported for SAS prepared CeO₂ where no definable particles could be observed, but EDS analysis confirmed the presence of the metals [29]. The rationale for the high dispersion on the current and previously reported SAS supports is that the process imbues the supports with a large number of surface defects that provide nucleation sites for the impregnated metals. Calcination of the SAS support at 750 °C (AuPd/TiO₂(isopropoxide-750 °C)) resulted in a greater number of larger discernable metal particles (up to 4 nm) than observed in the 450 °C sample. However, the majority of the particles were still sub nanometer, giving a mean particle size of 1 nm. This indicates that there are still a high number of metal nucleation sites, although a smaller number than in the 450 °C calcined support.

XPS characterisation was carried out to analyse the surface composition of the different catalysts and the quantified XPS data is shown in Table 2. The Ti/O ratios for all the catalysts are lower than the expected 0.5 for stoichiometric titania, which is likely to be due to the formation of surface species such as hydroxyl groups formed in wet impregnation of metals. It was noted that the SAS prepared TiO₂ had a greater surface oxygen deficiency than P-25, which could

Table 2
XPS determined atomic concentrations, Pd/Au and Ti/O ratios.

	Element	%At Conc	Pd/Au	Ti/O
AuPd/TiO ₂ (P-25)	Pd 3d	3.11	17.79	0.45
	O 1s	64.57		
	Ti 2p	29.08		
	Cl 2p	3.04		
	Au 4f	0.17		
AuPd/TiO ₂ (isopropoxide-450 °C)	Pd 3d	2.56	11.69	0.42
	O 1s	66.74		
	Ti 2p	28.36		
	Cl 2p	2.14		
	Au 4f	0.21		
AuPd/TiO ₂ (isopropoxide-750 °C)	Pd 3d	4.26	32.27	0.41
	O 1s	65.24		
	Ti 2p	26.93		
	Cl 2p	3.43		
	Au 4f	0.13		

reflect the defective nature of these materials. All Au/Pd catalysts were found to have significantly higher Pd surface concentration relative to Au, suggestive of a core shell morphology. This interpretation is not definitive, as increases in Pd/Au ratios above the nominal Pd/Au molar ratio have previously been shown not to correlate with core-shell morphologies by detailed electron microscopy [47]. Despite all catalysts having a Pd rich surface, the Pd/Au ratio differs significantly between samples with the lowest Pd surface enrichment being observed for AuPd/TiO₂(isopropoxide-450 °C) (Pd/Au of 11.69). The Pd/Au ratio then rises dramatically for AuPd/TiO₂(isopropoxide-750 °C) to 32.27, while AuPd/TiO₂(P-25) ratio lies in-between the SAS prepared materials at 17.79.

3.6. Optimised photocatalyst

Fig. 12 shows the hydrogen production of the Pt/TiO₂ catalyst prepared using the isopropoxide derived catalyst calcined at 450 °C (Pt/TiO₂(isopropoxide-450 °C) and 750 °C (Pt/TiO₂(isopropoxide-750 °C)), compared with a catalyst prepared using P-25 (Pt/TiO₂(P-25)). The dramatically lower activity of the predominantly anatase Pt/TiO₂(isopropoxide-450 °C) relative to Pt/TiO₂(P-25) is clear with an order of magnitude difference in the hydrogen production after 3 h. However, for the Pt/TiO₂(isopropoxide-750 °C) containing 90% anatase and 10% rutile the photocatalytic water splitting activity

increases significantly. The final volume of hydrogen produced from this catalyst was comparable to Pt/TiO₂(P-25). Interestingly the time on line data shows that the initial activity of the SAS derived material was greater than Pt/TiO₂(P-25) although there is deactivation over time. The initial high activity is interesting as the material has a lower rutile content than P-25 (10% vs 20% rutile) and also a lower surface area of 25 m² g⁻¹ compared to the 55 m² g⁻¹ for P-25. Clearly a third factor must be responsible for the high activity of the catalyst. This is most likely to be a more intimate Pt–TiO₂ interaction in the SAS prepared material, due to the high number of nucleation sites present.

3.7. AuPd/TiO₂ catalyst activity for redox reactions

Having demonstrated that the supercritical antisolvent precipitation method can be used to synthesise titania that is effective for photocatalytic water splitting, the most active materials (prepared from the isopropoxide precursor) were also tested as conventional catalyst supports. We have previously reported gold-palladium supported on titania is an effective catalyst for both the oxidation of benzyl alcohol to benzaldehyde and the direct synthesis of hydrogen peroxide [9,10,12]. For comparison AuPd/TiO₂(P-25) was also tested for these reactions. The results of the oxidation of benzyl alcohol are shown in Fig. 13, with AuPd/TiO₂(isopropoxide-450 °C) displaying very similar activity to catalysts supported on commercially sourced P-25, which has been reported to have particularly high turnover numbers for alcohol oxidation reactions [10]. However, isopropoxide-750 °C was, at all points of the reaction, more active than the P-25 supported catalyst. As shown in Fig. 14 the selectivity towards benzaldehyde was very similar for all three catalysts tested. Whilst the activity was similar AuPd/TiO₂(isopropoxide-450 °C) and AuPd/TiO₂(P-25), the particle size distribution was quite different, suggesting that small particle size cannot be the only factor responsible for activity. In addition, it was found that AuPd/TiO₂(isopropoxide-750 °C) had a slightly larger mean particle size than AuPd/TiO₂(isopropoxide-450 °C), but it was significantly more active. Au-Pd alloy morphology could potentially have a significant effect on the activity of the catalysts, with XPS analysis (Table 2) showing that AuPd/TiO₂(isopropoxide-750 °C) had a substantially higher Pd/Au ratio than the other catalysts.

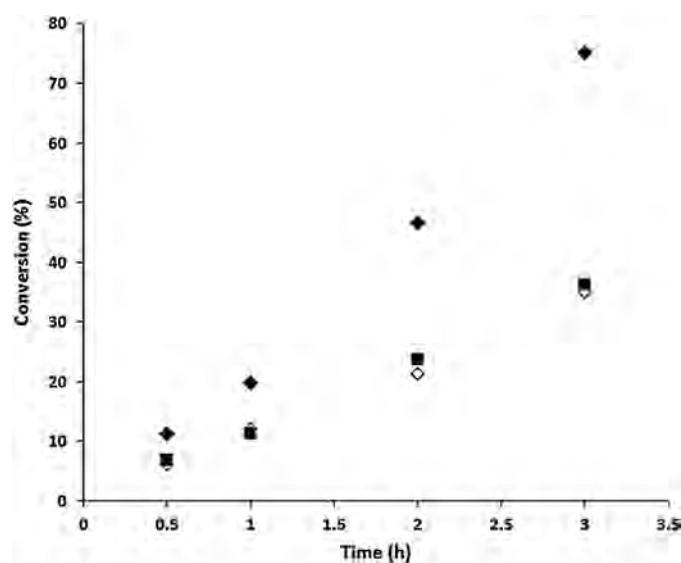


Fig. 13. The conversion of benzyl alcohol AuPd/TiO₂(P-25), squares; AuPd/TiO₂(isopropoxide-450 °C), open diamonds; AuPd/TiO₂(isopropoxide-750 °C), closed diamonds.

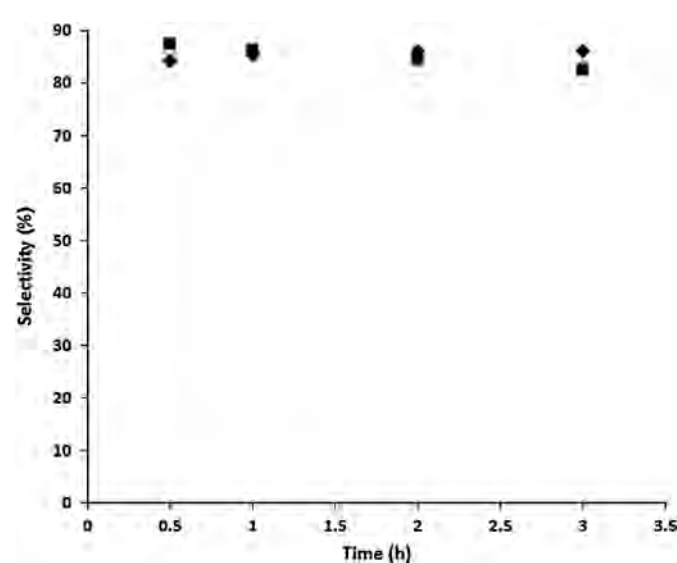


Fig. 14. The selectivity towards benzaldehyde during the oxidation of benzyl alcohol, AuPd/TiO₂(P-25), squares; AuPd/TiO₂(isopropoxide-450 °C), open diamonds; AuPd/TiO₂(isopropoxide-750 °C), closed diamonds.

Table 3
The results of the synthesis and hydrogenation of hydrogen peroxide by gold–palladium supported on various titania.

Catalyst	Calcination temperature (°C)	Calcination time (h)	H ₂ O ₂ productivity (mol kg ⁻¹ h ⁻¹)	H ₂ O ₂ hydrogenation (%)
AuPd/TiO ₂ (P-25)	As received	As received	64	12
AuPd/TiO ₂ (isopropoxide-450 °C)	450	2	135	7
AuPd/TiO ₂ (isopropoxide-750 °C)	750	1.5	108	14

The results of the direct synthesis of hydrogen peroxide are shown in Table 3, with a different trend to the benzyl alcohol oxidation data being observed. We have previously reported that AuPd/TiO₂(P-25) has a hydrogen peroxide product synthesis activity of 64 mol H₂O₂ mol⁻¹ cat h⁻¹, while AuPd/TiO₂(isopropoxide-450 °C) had an improved activity of 135 mol H₂O₂ mol⁻¹ cat h⁻¹. In contrast to the benzyl alcohol data, AuPd/TiO₂(isopropoxide-750 °C) had a lower peroxide productivity (108 mol H₂O₂ mol⁻¹ cat h⁻¹), although this is still higher AuPd/TiO₂(P-25). Small particles are thought to be most active for the reaction and so the trend in productivity correlates well with the particle size distributions observed by TEM analysis. Often more active catalysts which are active for the formation of hydrogen peroxide are usually also active for the over hydrogenation to form water. To try to further understand the observed productivities, hydrogenation tests were carried out as described in Section 2 (Table 3). Under our standard hydrogenation conditions with the that AuPd/TiO₂(P-25) catalyst 12% of the starting H₂O₂ was hydrogenated, whereas only 7% of the H₂O₂ was hydrogenated over that AuPd/TiO₂(isopropoxide-450 °C), which could explain the higher productivity values. The slight reduction in observed peroxide productivity of AuPd/TiO₂(isopropoxide-750 °C) can be related to the higher H₂O₂ hydrogenation of 14%. We have previously shown that acid washing a support can lead to almost complete suppression of the hydrogenation reaction [48], and that the acid washed catalysts exhibit significantly less pure palladium sites. The XPS Pd/Au ratios of the TiO₂ catalysts (Table 2) can act as an indicator of the presence of such hydrogenating palladium species. In this case the Pd/Au ratio correlates with the hydrogenation activity of the catalysts, indicating that there are more palladium rich species on AuPd/TiO₂(P-25) and AuPd/TiO₂(isopropoxide-750 °C) than on AuPd/TiO₂(isopropoxide-450 °C). This could imply that these species are preferentially formed on the rutile phase of titania, however further studies are required to confirm this hypothesis.

4. Conclusion

We have prepared TiO₂ as a support for Pt and AuPd nanoparticles by precipitation with a supercritical CO₂ antisolvent. A range of titanium precursor salts were screened for their physical properties and activity for the photocatalytic splitting of water. The most successful precursor was found to be titanium isopropoxide, which gave the highest surface area and contained a mixture of anatase and rutile phases. Although this material was found to contain rutile after calcination at 450 °C, this made up only ca. 2 wt% of the material. Therefore, we investigated the effect of calcination temperature and duration using *in situ* XRD. It was discovered that, although a small amount of rutile could be produced at low temperature, calcination at 750 °C was required to substantially enhance rutile composition. Supported metal catalysts were prepared with the SAS precipitated titanium isopropoxide calcined at 450 and 750 °C, which contained 2 wt% and 10 wt% rutile respectively. Exceptional dispersion of sub nanometre AuPd was found on the SAS prepared catalyst calcined at 450 °C, and this dispersion was also present on the support calcined at 750 °C. High activity was observed for the 10% rutile containing SAS prepared TiO₂ for the oxidation of benzyl alcohol to benzaldehyde and the photocatalytic splitting of water.

While the predominantly anatase containing SAS prepared TiO₂ was found to be most active for the direct synthesis of hydrogen peroxide.

Acknowledgements

We gratefully acknowledge the UK Technology Strategy Board, the UK Catalysis Hub, the EPSRC EP/K014854/1 and the Japanese Society for the Promotion of Science.

References

- [1] A. Fujishima, K. Honda, *Nature* 238 (1972) 37.
- [2] H. Bahruji, M. Bowker, P.R. Davies, F. Pedrono, *Appl. Catal. B Environ.* 107 (2011) 205–209.
- [3] M. Haruta, T. Kobayashi, H. Sano, N. Yamada, *Chem. Lett.* (1987) 405–408.
- [4] P. Landon, J. Ferguson, B.E. Solsona, T. Garcia, A.F. Carley, A.A. Herzing, C.J. Kiely, S.E. Golunski, G.J. Hutchings, *Chem. Commun.* (2005) 3385–3387.
- [5] A. Corma, M.E. Domine, *Chem. Commun.* (2005) 4042–4044.
- [6] A.K. Sinha, S. Seelan, S. Tsubota, M. Haruta, *Angew. Chem. Int. Ed.* 43 (2004) 1546–1548.
- [7] M.D. Hughes, Y.-J. Xu, P. Jenkins, P. McMorn, P. Landon, D.I. Enache, A.F. Carley, G.A. Attard, G.J. Hutchings, F. King, E.H. Stitt, P. Johnston, K. Griffin, C.J. Kiely, *Nature* 437 (2005) 1132–1135.
- [8] P. Landon, P.J. Collier, A.J. Papworth, C.J. Kiely, G.J. Hutchings, *Chem. Commun.* (2002) 2058–2059.
- [9] P. Miedziak, M. Sankar, N. Dimitratos, J.A. Lopez-Sanchez, A.F. Carley, D.W. Knight, S.H. Taylor, C.J. Kiely, G.J. Hutchings, *Catal. Today* 164 (2011) 315–319.
- [10] D.I. Enache, J.K. Edwards, P. Landon, B. Solsona-Espriu, A.F. Carley, A.A. Herzing, M. Watanabe, C.J. Kiely, D.W. Knight, G.J. Hutchings, *Science* 311 (2006) 362–365.
- [11] Q. He, P.J. Miedziak, L. Kesavan, N. Dimitratos, M. Sankar, J.A. Lopez-Sanchez, M.M. Forde, J.K. Edwards, D.W. Knight, S.H. Taylor, C.J. Kiely, G.J. Hutchings, *Faraday Discuss.* 162 (2013) 365–378.
- [12] J.K. Edwards, B.E. Solsona, P. Landon, A.F. Carley, A. Herzing, C.J. Kiely, G.J. Hutchings, *J. Catal.* 236 (2005) 69–79.
- [13] J.K. Edwards, J. Pritchard, L. Lu, M. Piccinini, G. Shaw, A.F. Carley, D.J. Morgan, C.J. Kiely, G.J. Hutchings, *Angew. Chem. Int. Ed.* 53 (2014) 2381–2384.
- [14] J.K. Edwards, J. Pritchard, P.J. Miedziak, M. Piccinini, A.F. Carley, Q. He, C.J. Kiely, G.J. Hutchings, *Catal. Sci. Technol.* 4 (2014) 3244–3250.
- [15] S.-J. Lee, A. Gavriilidis, *J. Catal.* 206 (2002) 305–313.
- [16] M. Sankar, Q. He, M. Morad, J. Pritchard, S.J. Freakley, J.K. Edwards, S.H. Taylor, D.J. Morgan, A.F. Carley, D.W. Knight, C.J. Kiely, G.J. Hutchings, *ACS Nano* 6 (2012) 6600–6613.
- [17] L. Delannoy, N. El Hassan, A. Musi, N.N.L. To, J.-M. Krafft, C. Louis, *J. Phys. Chem. B* 110 (2006) 22471–22478.
- [18] F.O. Moreau, G.C. Bond, A.O. Taylor, *J. Catal.* 231 (2005) 105–114.
- [19] F. Porta, L. Prati, M. Rossi, S. Coluccia, G. Martra, *Catal. Today* 61 (2000) 165–172.
- [20] M.M. Forde, R.D. Armstrong, R. McVicker, P.P. Wells, N. Dimitratos, Q. He, L. Lu, R.L. Jenkins, C. Hammond, J.A. Lopez-Sanchez, C.J. Kiely, G.J. Hutchings, *Chem. Sci.* 5 (2014) 3603–3616.
- [21] S.A. Kondrat, G. Shaw, S.J. Freakley, Q. He, J. Hampton, J.K. Edwards, P.J. Miedziak, T.E. Davies, A.F. Carley, S.H. Taylor, C.J. Kiely, G.J. Hutchings, *Chem. Sci.* 3 (2012) 2965–2971.
- [22] A.A. Herzing, M. Watanabe, J.K. Edwards, M. Conte, Z.-R. Tang, G.J. Hutchings, C.J. Kiely, *Faraday Discuss.* 138 (2008) 337–351.
- [23] M.M. Schubert, S. Hackenberg, A.C. van Veen, M. Muhler, V. Plzak, R.J. Behm, *J. Catal.* 197 (2001) 113–122.
- [24] M. Sankar, E. Nowicka, R. Tiruvalam, Q. He, S.H. Taylor, C.J. Kiely, D. Bethell, D.W. Knight, G.J. Hutchings, *Chem. Eur. J.* 17 (2011) 6524–6532.
- [25] G. Ertl, H. Knözinger, F. Schüth, J. Weitkamp, *Handbook of heterogeneous catalysis*, 2nd ed., Wiley-VCH, 2008.
- [26] J. Guzman, A. Corma, *Chem. Commun.* (2005) 743–745.
- [27] S. Carrettin, P. Concepcion, A. Corma, J.M. Lopez Nieto, V.F. Puentes, *Angew. Chem. Int. Ed.* 43 (2004) 2538–2540.
- [28] Z.-R. Tang, J.K. Edwards, J.K. Bartley, S.H. Taylor, A.F. Carley, A.A. Herzing, C.J. Kiely, G.J. Hutchings, *J. Catal.* 249 (2007) 208–219.
- [29] P.J. Miedziak, Z. Tang, T.E. Davies, D.I. Enache, J.K. Bartley, A.F. Carley, A.A. Herzing, C.J. Kiely, S.H. Taylor, G.J. Hutchings, *J. Mater. Chem.* 19 (2009) 8619–8627.
- [30] G.J. Hutchings, J.K. Bartley, J.M. Webster, J.A. Lopez-Sanchez, D.J. Gilbert, C.J. Kiely, A.F. Carley, S.M. Howdle, S. Sajip, S. Caldarelli, C. Rhodes, J.C. Volta, M. Poliakoff, *J. Catal.* 197 (2001) 232–235.

- [31] R.P. Marin, S.A. Kondrat, R.K. Pinnell, T.E. Davies, S. Golunski, J.K. Bartley, G.J. Hutchings, S.H. Taylor, *Catal Appl. B* 140–141 (2013) 671–679.
- [32] Z.R. Tang, S.A. Kondrat, C. Dickinson, J.K. Bartley, A.F. Carley, S.H. Taylor, T.E. Davies, M. Allix, M.J. Rosseinsky, J.B. Claridge, Z. Xu, S. Romani, M.J. Crudace, G.J. Hutchings, *Catal. Sci. Technol.* 1 (2011) 64–70.
- [33] M.E. Tadros, C.L.J. Adkins, E.M. Russick, M.P. Youngman, *J. Supercrit. Fluids* 9 (1996) 172–176.
- [34] T. Lu, S. Blackburn, C. Dickinson, M.J. Rosseinsky, G. Hutchings, S. Axon, G.A. Leeke, *Powder Technol.* 188 (2009) 264–271.
- [35] E. Reverchon, G. Caputo, S. Corraera, P. Cesti, *J. Supercrit. Fluids* 26 (2003) 253–261.
- [36] R. Sui, A.S. Rizkalla, P.A. Charpentier, *Langmuir* 21 (2005) 6150–6153.
- [37] Z.-R. Tang, J.K. Bartley, S.H. Taylor, G.J. Hutchings, *Stud. Surf. Sci. Catal.* 162 (2006) 219–226.
- [38] R.P. Marin, S.A. Kondrat, T.E. Davies, D.J. Morgan, D.I. Enache, G.B. Combes, S.H. Taylor, J.K. Bartley, G.J. Hutchings, *Catal. Sci. Technol.* 4 (2014) 1970–1978.
- [39] S.A. Kondrat, S.H. Taylor, *Catalysis* 26 (2014) 218–248.
- [40] R. Sui, A.S. Rizkalla, P.A. Charpentier, *J. Phys. Chem. B* 110 (2006) 16212–16218.
- [41] D.A.H. Hanaor, C.C. Sorrell, *J. Mater. Sci.* 46 (2011) 855–874.
- [42] R.I. Bickley, T. Gonzalez-Carreno, J.S. Lees, L. Palmisano, R.J.D. Tilley, *J. Solid State Chem.* 92 (1991) 178–190.
- [43] J.T. Carneiro, T.J. Savenije, J.A. Moulijn, G. Mul, *J. Phys. Chem. C* 115 (2011) 2211–2217.
- [44] G. Munuera, V. Rives-Arnau, A. Saucedo, *J. Chem. Soc. Faraday Trans. 1: Phys. Chem. Condensed Phases* 75 (1979) 736–747.
- [45] A.A. Gibb, J.F. Banfield, *Am. Miner.* 82 (1997) 717–728.
- [46] H. Zhang, J.F. Banfield, *J. Mater. Chem.* 8 (1998) 2073–2076.
- [47] J.K. Edwards, J. Pritchard, M. Piccinini, G. Shaw, Q. He, A.F. Carley, C.J. Kiely, G.J. Hutchings, *J. Catal.* 292 (2012) 227–238.
- [48] J.K. Edwards, B. Solsona, E.N.N.A.F. Carley, A.A. Herzing, C.J. Kiely, G.J. Hutchings, *Science* (2009) 1037–1041.

Selective Synthesis of Primary Amines by Reductive Amination of Ketones with Ammonia over Supported Pt catalysts

Yoichi Nakamura,^[a] Kenichi Kon,^[a] Abeda Sultana Touchy,^[a] Ken-ichi Shimizu,^{*[a, b]} and Wataru Ueda^[c]

Supported platinum catalysts are studied for the reductive amination of ketones under ammonia and hydrogen. For a model reaction with 2-adamantanone, Pt-loaded MoO_x/TiO₂ (Pt-MoO_x/TiO₂) shows the highest yield of primary amine. The catalyst is effective for the selective transformation of various aliphatic and aromatic ketones to the corresponding primary amines, which demonstrates the first example of the selective synthesis of primary amines by this reaction. The yield of the amine increases with increase in the negative shift of the C=O stretching band in the infrared spectra of adsorbed acetone on the catalysts, suggesting that Lewis acid sites on the support material play an important role in this catalytic system.

Primary amines are important intermediates in the bulk and fine chemical industries.^[1] The reductive amination of carbonyl compounds^[2–6] and borrowing-hydrogen type amination of alcohols^[7–10] can be practical synthetic methods of amines. However, amination of carbonyl compounds by NH₃ generally produces secondary amines,^[11–15] because primary amines are more reactive than NH₃, resulting in the conversion of the primary amines to secondary amines. As for the synthesis of primary amines from aldehydes, a few catalysts such as heterogeneous Ru catalysts^[16,17] and a homogeneous Rh catalyst^[18] are available. The selective synthesis of primary amines by reductive amination of ketones is more challenging. Reductive amination of a ketone with NH₃ and H₂ by Cu^[11] and zeolite^[12]-based heterogeneous catalysts resulted in selective formation of a secondary amine as a major product together with a primary amine as a minor product. Recently reported homogeneous methods for the selective synthesis of primary amines from ketones with NH₃ did not use H₂ but used less atom-efficient reductants such as HCO₂NH₄,^[19] the Hantzsch ester,^[20] silane,^[21] and NaBH₄.^[22] To our knowledge, there are no reports on the selective synthesis of primary amines by the reductive amination of ketones with NH₃ and H₂. During a course of our

efforts on the reductive C–N bond formation reactions by heterogeneous Pt catalysts,^[23,24] we found that Pt and MoO_x co-loaded TiO₂ (Pt-MoO_x/TiO₂) was effective for this catalytic reaction. We report herein the first example of the selective synthesis of primary amines by the reductive amination of ketones under 4 bar NH₃ and 2 bar H₂. We also show the relationship between Lewis acidic nature of the support oxides and the catalytic efficiency.

First, we screened Pt catalysts supported on various support materials (MoO_x/TiO₂, Nb₂O₅, θ-Al₂O₃, ZrO₂, TiO₂, MgO, SiO₂, ZSM-5, C, and CeO₂) for a model reaction of 2-adamantanone (**1a**) in *o*-xylene under 4 bar NH₃ and 2 bar H₂. Table 1 summa-

Table 1. Amination of 2-adamantanone over various catalysts.^[a]

Catalysts	Conv. [%]	Yield [%]		
		2a	3a	4a
Pt-MoO _x /TiO ₂	100	75	7	11
Pt/Nb ₂ O ₅	100	64	6	14
Pt/θ-Al ₂ O ₃	100	62	13	9
Pt/ZrO ₂	100	56	13	15
Pt/TiO ₂	100	54	6	10
Pt/MgO	100	45	43	< 1
Pt/SiO ₂	100	44	6	32
Pt/HZSM-5	100	41	24	10
Pt/C	100	38	6	39
Pt/CeO ₂	100	16	58	< 1

[a] Conversion of **1a** and yields of **2a**, **3a** and **4a** were determined by GC based on **1a**.

izes the yields of the corresponding primary amine (**2a**), alcohol (**3a**), and secondary amine (**4a**) with 0.5 mol% of Pt catalysts. The catalytic tests were performed under the same conditions (0.5 mol% Pt with respect to 2-adamantanone, 100 °C, 20 h). Pt-MoO_x/TiO₂ exhibited the highest yield (75%) of the desired product, 2-adamantylamine (**2a**). Other Pt catalysts exhibited low to moderate yields for 2-adamantylamine (16–64%). The Pt catalysts supported on Lewis acidic oxides (MoO_x/TiO₂, TiO₂, Nb₂O₅, θ-Al₂O₃, ZrO₂)^[24,25] showed higher yields of the primary amine **2a** than the Pt-loaded basic (MgO, CeO₂), neutral (SiO₂, C), and Brønsted acidic (HZSM-5) supports.

[a] Y. Nakamura, Dr. K. Kon, Dr. A. S. Touchy, Dr. K.-i. Shimizu
Catalysis Research Center
Hokkaido University, N-21, W-10, Sapporo (Japan)
E-mail: kshimizu@cat.hokudai.ac.jp

[b] Dr. K.-i. Shimizu
Elements Strategy Initiative for Catalysis and Batteries
Kyoto University, Katsura, Kyoto 615-8520 (Japan)

[c] Prof. Dr. W. Ueda
Kanagawa University
Rokkakubashi 3-27-1, Yokohama (Japan)

For the amination of **1a** with Pt-MoO_x/TiO₂, we established some control experiments. First, the amination of **1a** under 4 bar NH₃ and 1 bar N₂ resulted in no formation of **2a** and 30% yield of the corresponding imine. This suggests that H₂ is necessary for the reduction of the imine to the primary amine. Next, we tested the borrowing-hydrogen type amination of 2-adamantanol under 4 bar NH₃ and 1 bar N₂, which resulted in no formation of **2a**. The amination of **1a** with aqueous NH₃ (4 equiv) under 2 bar H₂ gave lower yield of **2a** (19%) than the standard conditions with gaseous NH₃.

To quantify the degree of Lewis acid-base interaction between the catalyst and a substrate, we performed IR experiments of a model ketone compound, acetone, adsorbed on the Lewis acidic catalysts. As shown in Figure 1, the C=O

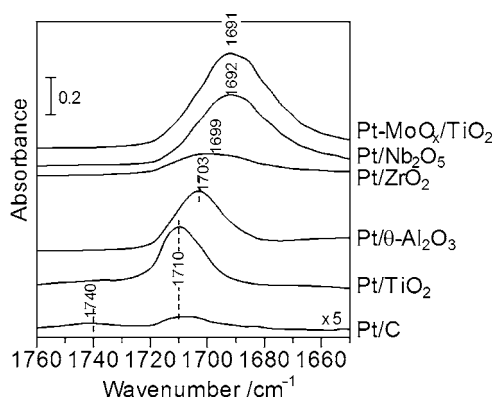


Figure 1. IR spectra of the acetone adsorbed on the catalysts at 40 °C.

stretching band of the acetone adsorbed on Pt-MoO_x/TiO₂, Pt/Nb₂O₅, Pt/ZrO₂, and Pt/θ-Al₂O₃ showed peaks at lower wavenumber than that on the non-Lewis acidic catalyst, Pt/C. This result indicates that the Lewis acid sites on the catalysts interact with carbonyl oxygen of the ketone. Especially, the C=O stretching band for Pt-MoO_x/TiO₂ was centered at the lowest wavenumber (1691 cm⁻¹), which indicates the highest Lewis acidity of the Pt-MoO_x/TiO₂ catalyst. As shown in Figure 2, we examined a correlation between the Lewis acidity of catalysts and the yield of the primary amine **2a** for the reductive amination of 2-adamantanone. There is a fairly good relationship be-

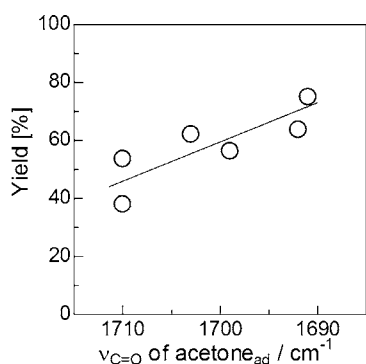
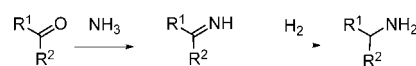


Figure 2. Relationship between the IR band position of the acetone adsorbed on the catalysts (from Figure 1) and the yield of **2a** (from Table 1).

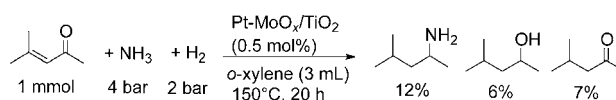
tween the yields of **2a** and the wavenumber of C=O adsorbed acetone on catalysts; the yield linearly increases with decrease of the wavenumber, or in other words, increase in the Lewis acid strength of the catalysts. This suggests that stronger Lewis acidity of the catalyst leads to the higher yield of the primary amine. Previous studies on the reductive amination of carbonyl compounds by heterogeneous catalysts^[13–17] suggested that imines, formed by condensation of a carbonyl compound and NH₃, can be an intermediate, which is hydrogenated to produce the corresponding primary amine (Scheme 1).



Scheme 1.

Assuming this pathway, we can propose two possible roles of the Lewis acid; the acid-base interaction can activate C=O and/or C=N groups and promotes the formation of the imine and/or the reduction of the imine.

Next, we studied the scope and limitation of the present catalytic system. Table 2 shows that the reductive amination of various carbonyl compounds (ketones and benzaldehyde) under 4 bar NH₃ and 2 bar H₂ with 0.5 mol% of Pt-MoO_x/TiO₂ at 80–150 °C. Cyclic and linear aliphatic ketones (entries 1–7) and an aromatic ketone (acetophenone, entry 8) were selectively transformed to the corresponding primary amines (**2**) with moderate to good yields (59–75%). Small amounts of by-products such as secondary amines (**4**), alcohols (**3**) were also observed by the GC analysis. After the reaction of 2-adamantanone (entry 1), the catalyst was easily separated from the reaction mixture by a centrifugation, and the column separation of the mixture gave 2-adamantylamine in 71% of isolated yield. Notably, the primary amines were selectively produced at high conversions (> 90%). We tested the amination of a ketone with C=C group, 4-methyl-3-penten-2-one, but the reaction gave a mixture of the corresponding primary amine, alcohol, and ketone without C=C group (Scheme 2), indicating that hydrogenation of the C=C group is preferential.



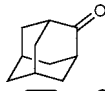
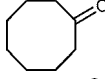
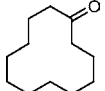
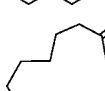
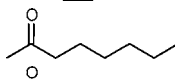
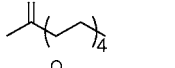
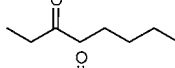
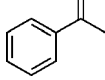
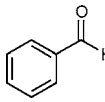
Scheme 2.

Similar to the previous heterogeneous catalysts,^[13–17] the reductive amination of benzaldehyde by Pt-MoO_x/TiO₂ (entry 9) resulted in the selective formation of the secondary amine in 70% yield, while the yield of the primary amine was only 9%.

In conclusion, we reported an unprecedented selective synthesis of primary amines by the reductive amination of ketones with ammonia and hydrogen by the Pt-MoO_x/TiO₂ catalyst. Various aliphatic and aromatic ketones were transformed to the corresponding primary amines. The yield of the primary amine

Table 2. Reductive amination of various ketones and an aldehyde by Pt-MoO_x/TiO₂ catalyst.^[a]

$$\begin{array}{c}
 \text{R}^1 \\
 | \\
 \text{R}^2 - \text{C} = \text{O} \\
 \text{1} \\
 \text{1 mmol}
 \end{array}
 + \text{NH}_3 \quad + \text{H}_2
 \xrightarrow[\text{100}^\circ\text{C, 20 h}]{\text{0.005 mmol Pt, } o\text{-xylene(3 mL)}}
 \begin{array}{c}
 \text{R}^1 \\
 | \\
 \text{R}^2 - \text{C} - \text{NH}_2 \\
 \text{2}
 \end{array}
 \quad
 \begin{array}{c}
 \text{R}^1 \\
 | \\
 \text{R}^2 - \text{C} - \text{OH} \\
 \text{3}
 \end{array}
 \quad
 \begin{array}{c}
 \text{R}^1 \\
 | \\
 \text{R}^2 - \text{C} - \text{N} - \text{R}^1 \\
 | \\
 \text{R}^2 \\
 \text{4}
 \end{array}$$

Entry	Reactants	Conv. [%]	Yield [%]		
			2	3	4
1		100	75 (71) ^[b]	7	11
2 ^[c]		98	70	13	10
3		97	68	4	7
4		95	64	3	<1
5		100	71	10	10
6		98	60	8	14
7		95	77	3	3
8 ^[d]		96	74	<1	6
9		92	9	<1	70

[a] Conversion and yields were determined by GC based on 1. [b] Isolated yield. [c] T = 80 °C. [d] T = 150 °C.

depended on the Lewis acid strength of the support materials, suggesting that Lewis acid sites on the support material could play an important role in this catalytic system.

Experimental Section

Commercially available organic compounds (from Tokyo Chemical Industry and Wako Pure Chemical Industries) were used without further purification. TiO₂ (JRC-TIO-4), MgO (JRC-MGO-3), and CeO₂ (JRC-CEO-3) were supplied by the Catalysis Society of Japan. SiO₂ (Q-10, 300 m²g⁻¹) was supplied from Fuji Silysia Chemical Ltd. HZSM-5 zeolite with a SiO₂/Al₂O₃ ratio of 22.3 was supplied by Tosoh Co. Active carbon (C) was purchased from Kanto Chemical. θ-Al₂O₃ was prepared by calcination of γ-AlOOH (Catapal B Alumina purchased from Sasol) at 1000 °C for 3 h. Nb₂O₅ was prepared by calcination of Nb₂O₅·nH₂O (supplied by CBMM) at 500 °C for 3 h. ZrO₂ was prepared by hydrolysis of zirconium oxynitrate 2-hydrate by an aqueous NH₄OH solution, followed by filtration, washing

with distilled water, drying at 100 °C for 12 h, and by calcination at 500 °C for 3 h.

According to the method in our previous studies,^[23,24] the Pt-MoO_x/TiO₂ catalyst (with Pt loading of 5 wt% and Mo loading of 7 wt%) was prepared by sequential impregnation method. First, the MoO₃-loaded TiO₂ as the support material was prepared as follows; the mixture of TiO₂ (5 g), (NH₄)₆Mo₇O₂₄·4H₂O (0.88 mmol), and citric acid (0.88 mmol) in H₂O (50 mL) was evaporated at 50 °C, followed by drying at 100 °C for 12 h, and by calcination in air at 350 °C for 2 h. The MoO₃-loaded TiO₂ was mixed with an aqueous HNO₃ solution of Pt(NH₃)₂(NO₃)₂, and the mixture was evaporated at 50 °C, followed by drying at 100 °C for 12 h. To prepare the catalyst (Pt-MoO_x/TiO₂) before each catalyst test, this precursor was reduced at 300 °C under the hydrogen flow (0.5 h). Other supported Pt catalysts (with Pt loading of 5 wt%) were prepared by a similar impregnation method using various support materials and the solution of Pt(NH₃)₂(NO₃)₂.

A typical method of catalytic tests is as follows. After the pre-reduction at 300 °C, the Pt-MoO_x/TiO₂ catalyst (19.5 mg, containing 0.005 mmol of Pt) in the closed glass tube with a septum inlet was cooled to room temperature under H₂, followed by injection of the mixtures of substrates (1.0 mmol), dodecane (0.5 mmol) in *o*-xylene (3.0 mL) to the reduced catalysts inside the glass tube through the septum inlet. The septum was removed, and a magnetic stir was put into the glass tube under air. The glass tube was put into the stainless autoclave with a dead space of 33 mL. Subsequently, the autoclave was purged by flushing of NH₃ and was filled with 4 bar NH₃ and 2 bar H₂. The autoclave was heated at 80–150 °C under stirring (300 rpm). Conversion and yields of products were determined by GC (Shimadzu GC-14B) with Ultra ALLOY capillary column UA⁺-1 (Frontier Laboratories Ltd.) using *n*-dodecane as an internal standard. The products were identified by GC-MS (Shimadzu GCMS-QP2010) equipped with the same column as GC. GC yields of primary amines were determined by GC adopting the GC-sensitivity estimated using commercial amines or the amines isolated after the catalytic reactions. For the reaction of 2-adamantanone (Table 2, entry 1), a separate experiment was performed to determine the isolated yield of 2-adamantylamine as follows. After the reaction, the catalyst was removed by filtration and then the reaction mixture was concentrated under vacuum evaporator to remove the volatile compounds. The residue thus obtained was subjected to column chromatography (silica gel 60, Kanto Chemical) with CH₂Cl₂/*n*-hexane (4:1) mixture as the eluting solvent, followed by analyses by ¹H NMR (JEOL ECX-600), ¹³C NMR and GCMS. 2-Adamantylamine (0.71 mmol) was identified by the following data: ¹H NMR (600.17 MHz, CDCl₃ with TMS): δ = 2.98 (s, 1H), 1.97 (d, *J* = 13.1 Hz, 2H), 1.82–1.80 (m, 3H), 1.77–1.74 (m, 3H), 1.70–1.68 (m, 4H), 1.52 (d, *J* = 13.08 Hz, 2H), 1.45 ppm (br s, 2H); ¹³C NMR (150.92 MHz, CDCl₃): δ = 55.43, 38.02, 37.62 (C×2), 35.10 (C×2), 30.71 (C×2), 27.71, 27.50 ppm; GC-MS *m/e* 151.14.

IR spectra were recorded at 40 °C by using a JASCO FT/IR-4200 with an MCT detector. The catalyst disc (30 mg, ϕ = 2 cm) was mounted in the IR cell with CaF₂ windows connected to a flow reaction system. Spectra were measured accumulating 15 scans at a resolution of 4 cm⁻¹. A reference spectrum of the catalyst disc in flowing He was subtracted from each spectrum. Prior to the experi-

ment the catalyst wafer was heated in H₂ flow (20 mL min⁻¹) at 300 °C for 0.5 h, followed by cooling to 40 °C and purging with He. Then, 1 μL of acetone was injected to He flow preheated at 150 °C, which was fed to the IR cell. Then, the IR cell was purged with flowing He (40 mL min⁻¹) for 500 s, and IR measurement was performed. Note that the spectra for Pt-MoO_x/TiO₂, Pt/TiO₂, and Pt/C in Figure 1 were reported in our previous study,^[24] and the spectra for Pt/Nb₂O₅, Pt/ZrO₂ and Pt/θ-Al₂O₃ were newly measured under the same conditions.

Acknowledgements

This work was supported by Grant-in-Aids for Scientific Research B (26289299) from MEXT (Japan), a MEXT program "Elements Strategy Initiative to Form Core Research Center" and a Grant-in-Aid for Scientific Research on Innovative Areas "Nano Informatics" (25106010) from JSPS.

Keywords: amination · ketones · Lewis acid · primary amines

- [1] a) S. Bähn, S. Imm, L. Neubert, M. Zhang, H. Neumann, M. Beller, *ChemCatChem* **2011**, *3*, 1853–1864; b) S. Raoufmoğhaddam, *Org. Biomol. Chem.* **2014**, *12*, 7179–7193.
- [2] A. Baiker, J. Kijenski, *Catal. Rev. Sci. Eng.* **1985**, *27*, 653–697.
- [3] K. S. Hayes, *Appl. Catal. A* **2001**, *221*, 187–195.
- [4] S. Gomez, J. A. Peters, T. Maschmeyer, *Adv. Synth. Catal.* **2002**, *344*, 1037–1057.
- [5] S. Werkmeister, K. Junge, M. Beller, *Green Chem.* **2012**, *14*, 2371–2374.
- [6] S. Ichikawa, T. Seki, T. Ikariya, *Chem. Lett.* **2012**, *41*, 1628–1629.
- [7] C. Gunanathan, D. Milstein, *Angew. Chem. Int. Ed.* **2008**, *47*, 8661–8664; *Angew. Chem.* **2008**, *120*, 8789–8792.
- [8] D. Pinggen, C. Müller, D. Vogt, *Angew. Chem. Int. Ed.* **2010**, *49*, 8130–8133; *Angew. Chem.* **2010**, *122*, 8307–8310.
- [9] S. Imm, S. Bähn, L. Neubert, H. Neumann, M. Beller, *Angew. Chem. Int. Ed.* **2010**, *49*, 8126–8129; *Angew. Chem.* **2010**, *122*, 8303–8306.
- [10] K. Shimizu, K. Kon, W. Onodera, H. Yamazaki, J. N. Kondo, *ACS Catal.* **2013**, *3*, 112–117.
- [11] K. V. R. Chary, K. K. Seela, D. Naresh, P. Ramakanth, *Catal. Commun.* **2005**, *104*, 23–28.
- [12] S. R. Kirumakki, M. Papadaki, K. V. R. Chary, N. Nagaraju, *J. Mol. Catal. A* **2010**, *321*, 15–21.
- [13] F. Qiu, L. Hu, S. Lu, X. Cao, H. Gu, *Chem. Commun.* **2012**, *48*, 9631–9633.
- [14] A. W. Heinen, J. A. Peters, H. van Bekkum, *Eur. J. Org. Chem.* **2000**, 2501–2506.
- [15] J. Bódis, L. Lefferts, T. E. Müller, R. Pestman, J. A. Lercher, *Catal. Lett.* **2008**, *9*, 75–81.
- [16] S. Gomez, J. A. Peters, J. C. van der Waal, W. Zhou, T. Maschmeyer, *Catal. Lett.* **2002**, *84*, 1–5.
- [17] S. Gomez, J. A. Peters, J. C. Vanderwaal, T. Maschmeyer, *Appl. Catal. A* **2003**, *254*, 77–84.
- [18] T. Gross, A. M. Seayad, M. Ahmad, M. Beller, *Org. Lett.* **2002**, *4*, 2055–2058.
- [19] S. Ogo, K. Uehara, T. Abura, S. Fukuzumi, *J. Am. Chem. Soc.* **2004**, *126*, 3020–3021.
- [20] D. Menche, J. Hassfeld, J. Li, G. Menche, A. Ritter, S. Rudolph, *Org. Lett.* **2006**, *8*, 741–744.
- [21] D. Menche, F. Arikian, J. Li, S. Rudolph, *Org. Lett.* **2007**, *9*, 267–270.
- [22] B. Miriyala, S. Bhattacharyya, J. S. Williamson, *Tetrahedron* **2004**, *60*, 1463–1471.
- [23] K. Kon, S. M. A. H. Siddiki, W. Onodera, K. Shimizu, *Chem. Eur. J.* **2014**, *20*, 6264–6267.
- [24] A. S. Touchy, S. M. A. H. Siddiki, K. Kon, K. Shimizu, *ACS Catal.* **2014**, *4*, 3045–3050.
- [25] M. Tamura, K. Shimizu, A. Satsuma, *Appl. Catal. A* **2012**, *433–434*, 135–145.

Received: December 8, 2014

Revised: January 22, 2015

Published online on February 16, 2015

Synthesis of crystalline Mo–V–W–O complex oxides with orthorhombic and trigonal structures and their application as catalysts

Chuntian Qiu¹, Chen Chen¹, Satoshi Ishikawa¹, Zhenxin Zhang¹, Toru Murayama*¹ and Wataru Ueda^{1,2}

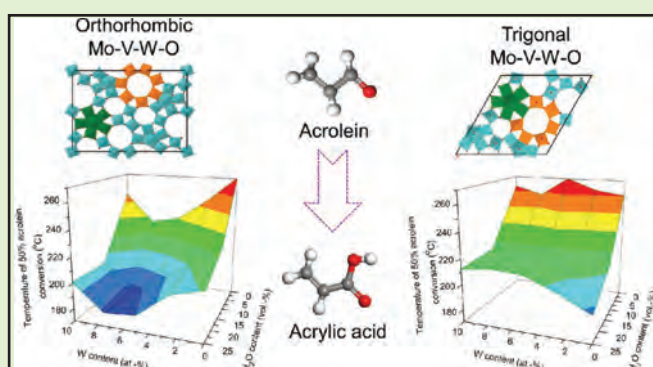
¹Catalysis Research Center, Hokkaido University, N-21, W-10, Sapporo 001-0021, Japan

²Faculty of Engineering, Kanagawa University, 3-27-1, Rokkakubashi, Kanagawa-ku, Yokohama, Kanagawa 221-8686, Japan

Abstract Crystalline Mo–V–W–O complex oxides with the orthorhombic or trigonal structure were synthesized by a hydrothermal method. Those Mo–V–W–O samples with various amounts of tungsten were characterized by inductively coupled plasma atomic emission spectroscopy, TEM, STEM–EDX, X-ray diffraction, Rietveld analysis and a N₂ adsorption method. It was found for the first case that an additional metal such as W can be successfully incorporated into the trigonal Mo–V–O structure by using (CH₃CH₂NH₃)₂Mo₃O₁₀. The alkylammonium cation acted as a structural stabilizer that was requisite for the formation of a trigonal structure when additional metal ions were present. For the orthorhombic Mo–V–W–O structure, introduction of W into the orthorhombic structure caused a rod segregation effect by which nanoscale crystals formed and the external surface area greatly increased. Additionally, these Mo–V–W–O materials were applied as catalysts for the gas phase selective oxidation of acrolein to acrylic acid. The best catalyst was assigned to the orthorhombic Mo–V–O–W7.5, which possessed an ordered arrangement of heptagonal and hexagonal channels and a large external surface area.

Keywords Crystalline Mo–V–W–O, Selective oxidation, Acrolein, Acrylic acid

Cite this article C. Qiu, C. Chen, S. Ishikawa, Z. Zhang, T. Murayama and W. Ueda. *Catal. Struct. React.*, 2015, 1, 71-77



Introduction

Mo–V based complex oxides catalysts have a long history of use in selective oxidation and ammoxidation of light alkanes since the 1960s.^{1–5} Numerous metal components such as Te, Nb, Cu, W and Fe have been applied to optimize the structure and catalytic performance.^{6–8} One of the representative catalysts is MoVTe(Sb)NbO, which was developed by Mitsubishi Chemical Corp. It showed good catalytic performance for oxidation of propane to acrylic acid and ammoxidation of propane to acrylonitrile.^{9,10} Additional metals modified the structure and improved the catalytic activity; however, multiple components increased the complexity of structure and composition.

Recently, we have reported the single crystalline Mo–V–O with an orthorhombic or trigonal structure.^{11–13} These

Mo–V–Os with microporosity were layered in the direction of the *c* axis and contained pentagonal {Mo₆O₂₁} building units and {MO₆} (M = Mo, V) octahedra that were arranged to form heptagonal and hexagonal channels but with different arrangements in the *a*–*b* plane. The simplicity of the component and uniformity of the crystalline structure provide a suitable opportunity to investigate the effects of additional metals and the structure–function relationship.

For molecular sieve type porous materials, the incorporation of a transition metal into the framework could modify properties such as acidity, thermal stability and especially catalytic activity.^{14,15} However, introduction of heteroatom usually affects the normal crystalline growth process, and it is a challenge to introduce a heteroatom metal while maintaining the crystal structure. In this work, we succeeded in introducing tungsten into the framework of the orthorhombic and trigonal structure. We obtained a trigonal structure with an additional metal for the first time by using

*Corresponding author, email: murayama@cat.hokudai.ac.jp

Table 1 Chemical compositions, external surface areas and lattice parameters of Mo–V–W–O

Sample	Composition*/at.-%			External surface area†/m ² g ⁻¹	Lattice parameter/nm		
	Mo	V	W		a	b	c
Amor-MoVO–W0	76.1	23.9	0.0	4.7	0.3998
Amor-MoVO–W2.5	74.0	23.3	2.7	4.7	0.3993
Amor-MoVO–W5.0	70.5	23.6	5.9	4.7	0.3991
Amor-MoVO–W7.5	70.1	21.9	8.0	3.9	0.3990
Amor-MoVO–W10	67.9	21.8	10.3	4.0	0.3989
Orth-MoVO–W0	71.5	28.5	0.0	5.0	2.1279	2.6634	0.4002
Orth-MoVO–W2.5	71.8	25.6	2.6	15.6	2.1205	2.6631	0.3999
Orth-MoVO–W5.0	70.0	25.2	4.8	23.3	2.1203	2.6629	0.3995
Orth-MoVO–W7.5	69.7	23.1	7.2	31.4	2.1183	2.6612	0.3994
Orth-MoVO–W10	68.2	21.6	10.2	35.5	2.1053	2.6592	0.3991
Tri-MoVO–W0	74.8	25.2	0.0	17.4	2.1382	...	0.4030
Tri-MoVO–W2.5	74.9	22.1	3.0	17.5	2.1382	...	0.4022
Tri-MoVO–W5.0	73.2	21.4	5.4	14.4	2.1381	...	0.4018
Tri-MoVO–W7.5	71.6	20.7	7.7	18.3	2.1381	...	0.4014
Tri-MoVO–W10	69.8	20.1	10.1	18.9	2.1380	...	0.4011

* Determined by ICP–AES.

† Measured by N₂ adsorption and determined by *t* plot method.

an organic molybdenum source. Moreover, it was found that the introduction of W into the orthorhombic structure caused crystal splitting that contributed to exposure of more active phase. Activity for oxidation of acrolein to acrylic acid over those M–V–W–Os was further investigated.

Experimental

Synthesis of three distinct Mo–V–O complex oxides

The catalysts were synthesized according to a previous report.^{13,16} For orthorhombic Mo–V–O (denoted as Orth-MoVO–W0), a solution of VOSO₄ (3.28 g, Mitsuwa Chemicals) in deionized water (120 mL) was added to a solution of (NH₄)₆Mo₇O₂₄ (8.82 g, Wako) in deionized water (120 mL) with stirring. The mixture was stirred for 10 min and then transferred into an autoclave with a Teflon inner tube and a Teflon sheet enough length for filling about half of Teflon inner tube space. This sheet is necessary for formation of well crystallized sample, because solids are formed on the sheet. The mixture was purged with N₂ for 10 min (pH = 3.2) and then hydrothermally treated at 175°C for 48 h. The procedure for synthesis of trigonal Mo–V–O (denoted as Tri-MoVO–W0) was the same as that for Orth-MoVO–W0 except that the pH value of the mixture was adjusted to 2.2 with H₂SO₄. As synthesized Orth-MoVO–W0 and Tri-MoVO–W0 were purified by treatment in a solution of oxalic acid (0.4 mol L⁻¹) at 60°C for 30 min to remove amorphous impurities. Amorphous Mo–V–O (denoted as Amor-MoVO–W0) was obtained by the same procedure as that for Orth-MoVO–W0 synthesis but with twofold higher precursor concentrations, without the use of a Teflon sheet, and no N₂ bubbling.

Synthesis of amorphous and orthorhombic Mo–V–W–O complex oxides

Orthorhombic Mo–V–W–O catalysts (denoted as Orth-MoVWO) with various contents of W were synthesized with (NH₄)₆Mo₇O₂₄, VOSO₄ and (NH₄)₆[H₂W₁₂O₄₀].6H₂O under a hydrothermal condition. Firstly, solution A was obtained

with 8.82 g of (NH₄)₆Mo₇O₂₄ and a certain amount of (NH₄)₆[H₂W₁₂O₄₀].6H₂O (with adjustment of W content to 2.5, 5.0, 7.5 and 10 at.-% in the synthesized Mo–V–W–O) being dissolved in 120 mL of deionized water and solution B was obtained with 3.28 g of VOSO₄ being dissolved in another 120 mL of deionized water. Secondly, solution B was poured into solution A under a stirring condition. The obtained mixed solution was introduced into an autoclave with a Teflon sheet in the Teflon inner vessel. The reaction mixture was purged with N₂ for 10 min (pH = 3.2) and then hydrothermally treated at 175°C for 48 h. As synthesized Orth-MoVWO catalysts (denoted as Orth-MoVO–W2.5, Orth-MoVO–W5.0, Orth-MoVO–W7.5 and Orth-MoVO–W10, respectively) were treated with oxalic acid solution (0.4 mol L⁻¹) 2 times at 60°C. The treatment was maintained for 30 min each time.

Amorphous Mo–V–W–O catalysts (denoted as Amor-MoVWO) with various contents of W (denoted as Amor-MoVO–W2.5, Amor-MoVO–W5.0, Amor-MoVO–W7.5 and Amor-MoVO–W10, respectively) were also synthesized with the same precursor at a twofold higher concentration and by the same procedure but without a Teflon sheet.

Synthesis of trigonal Mo–V–W–O complex oxides

A trigonal Mo–V–W–O (denoted as Tri-MoVWO) catalyst was obtained by the same procedure as that for Orth-MoVWO synthesis except that ethylammonium trimolybdate (EATM: (CH₃CH₂NH₃)₂Mo₃O₁₀) was used as an Mo source instead of (NH₄)₆Mo₇O₂₄. The synthesis procedure for EATM was as follows. MoO₃ (0.15 mol, 21.594 g, Kanto) was dissolved in 28.0 mL of 70% ethylamine solution (ethylamine: 0.30 mol, Wako) diluted with 28.0 mL of deionized water. After being completely dissolved, the solution was evaporated under a vacuumed condition at 70°C and then solid powder was obtained. The powder was dried in air at 80°C overnight. As synthesized materials were denoted as Tri-MoVO–W2.5, Tri-MoVO–W5.0, Tri-MoVO–W7.5 and Tri-MoVO–W10, respectively.

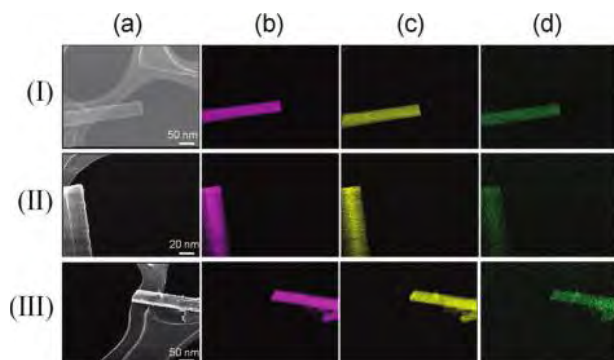


Figure 1 *a* STEM images and element mapping of *b* Mo, *c* V and *d* W of Amor-MoVO–W2.5 (I), Orth-MoVO–W2.5 (II) and Tri-MoVO–W2.5 (III)

Characterization

X-ray diffraction patterns were measured by using an X-ray diffractometer (RINT-Ultima III, Rigaku) with Cu K_{α} to study their crystalline structure. Crystallite size broadening analysis of Rietveld program with Powder Reflex (Material Studio 5.5.3, Accelrys) was utilized to fit the experimental X-ray diffraction (XRD) pattern of Orth-MoVWO. Raman spectra (inVia Reflex Raman spectrometer, RENISHAW) were taken in air on a static sample with Ar laser power. Scanning transmission electron microscopy (STEM) images and metal element mapping of Mo, W and V were obtained on an HD-2000 (HITACHI). Transmission electron microscopy (TEM) images were taken with a 200 kV transmission electron microscope (JEOL JEM-2010F). The chemical composition of the catalysts was determined by the inductively coupled plasma atomic emission spectroscopy (ICP–AES) method with a VISTA–PRO apparatus (Varian). N_2 adsorption–desorption isotherm measurements were carried out on an auto-adsorption system (BELSORP MAX, Nippon BELL) to obtain the external surface area and micropore volume using the t -plot method. Before adsorption measurements, the samples were treated at 400°C for 2 h under air and out gassed at 300°C under vacuum for 2 h.

Gas phase catalytic oxidation

Gas phase catalytic oxidation of acrolein to acrylic acid was performed using a fixed bed stainless tubular reactor at atmospheric pressure. The catalysts (0.25 g) were firstly ground for 5 min, then diluted with 2.5 g Carborundum and pre-treated at 400°C under N_2 of 50 mL min^{-1} for 2 h. Reactant gas was conducted with change in the water content from 0 to 25.2 vol.-% while keeping other feeding gases constant: acrolein = 2.5 mL min^{-1} , O_2 = 8 mL min^{-1} and N_2 balance (total: 107.6 mL min^{-1}). Quantitative analysis was performed using three on-line gas chromatographs with columns of Molecular Sieve 13X, Gaskuropack 54 and Porapak Q. Blank runs showed that no reaction took place without catalysts under the experimental conditions. Carbon balance was always over 95% and selectivity was calculated on the basis of products of sum.

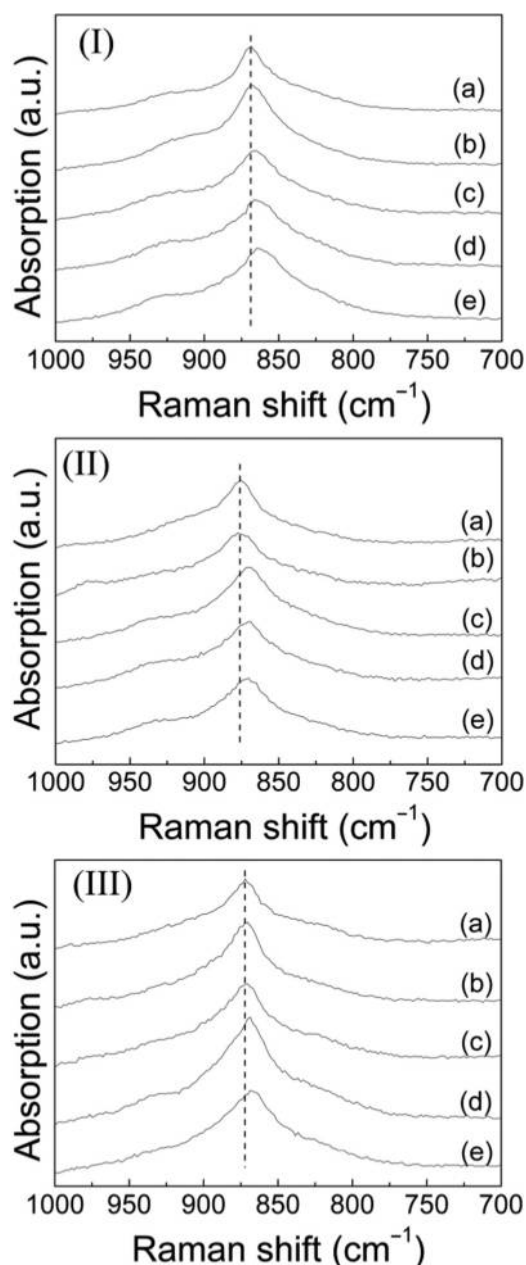


Figure 2 Raman spectra of Amor-MoVWO (I), Orth-MoVWO (II) and Tri-MoVWO (III) with different W contents. *a* W0; *b* W2.5; *c* W5.0; *d* W7.5; *e* W10

Results and discussion

Structural characterization of Mo–V–W–O catalysts

Location of W in Mo–V–W–O

Table 1 shows the chemical compositions of the Mo–V–W–O complex oxides determined by the ICP–AES method. Atomic ratios of tungsten in the Amor-, Orth- and Tri-MoVWO groups were adjusted approximately to 2.5, 5.0, 7.5 and 10 at.-%, respectively. Different Mo and V atomic ratios derived from the distinction of structure requisite. Element mapping of Mo, V and W of Amor-, Orth- and Tri-MoVO–W2.5 showed that metal elements were distributed evenly along the rod shaped materials (Fig. 1). In the Raman spectra (Fig. 2), the main band

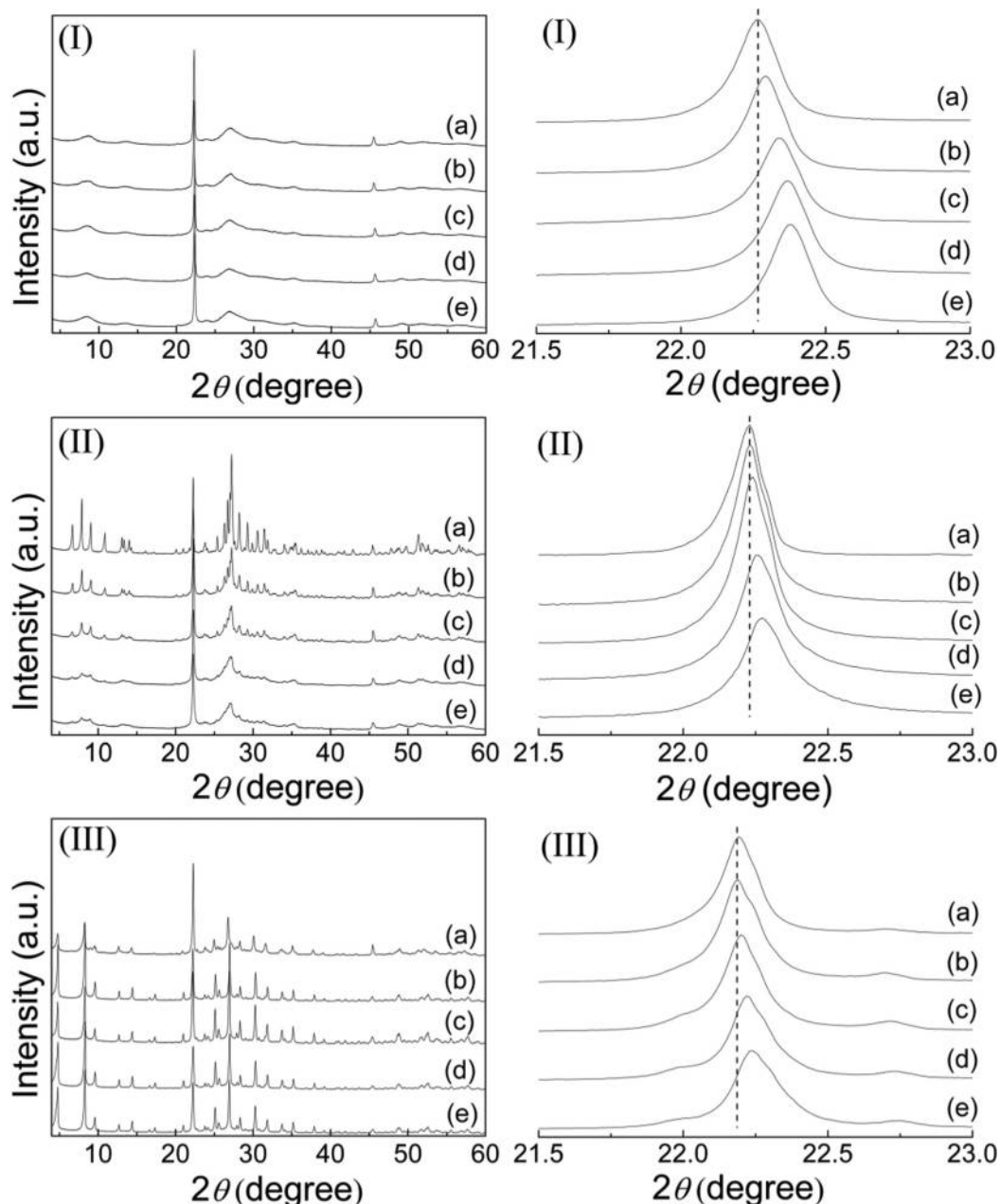


Figure 3 X-ray diffraction patterns of Amor-MoVWO (I), Orth-MoVWO (II) and Tri-MoVWO (III) with different W contents. a W0; b W2.5; c W5.0; d W7.5; e W10

at 872 cm^{-1} that was ascribed to pentagonal units¹⁶ gradually shifted to a low wave number. All of the results indicated that W was successfully introduced into the three different structures.

The crystalline structure of the materials was investigated by XRD characterization (Fig. 3). Diffraction peaks at 22.2° and 45.4° were ascribed to (001) and (002) plane reflections, respectively. Concentrated at the (001) peak, an obvious peak shift in a high angle direction was observed in all of the three different types of Mo–V–W–O, after being calibrated with silicon as an internal standard (Fig. 2). With increasing W content, the lattice parameter decreased gradually (Table 1), implying that lattice contraction happened with the incorporation of W. Based on the above results, W was considered to be incorporated into the framework. Orthorhombic, trigonal and amorphous Mo–V–O contained the same

pentagonal $\{\text{Mo}_6\text{O}_{21}\}$ units and $\{\text{MO}_6\}$ ($M = \text{Mo}, \text{V}$) octahedra. The pentagonal unit was constructed with Mo only and octahedra contained V as well as Mo.^{16,17} It is notable that, as shown in Table 1, with an increase in tungsten content, the ratio of V in Mo–V–W–O decreased gradually, strongly suggesting that tungsten replaced not only Mo but also the V ions. Therefore, there was a high probability that W formed $\{\text{WO}_6\}$ octahedra and acted as linkers connecting $\{\text{Mo}_6\text{O}_{21}\}$ pentagonal units.

Influence of W on Mo–V–O structure

In the XRD pattern of Amor-MoVWO (Fig. 2-I), there were two broad peaks centered at 8° and 27° , implying that Amor-MoVWO was only crystalline along the c axis, while a disordered arrangement of pentagonal $\{\text{Mo}_6\text{O}_{21}\}$ and $\{\text{MO}_6\}$ octahedra was formed in the a – b plane. This is the most

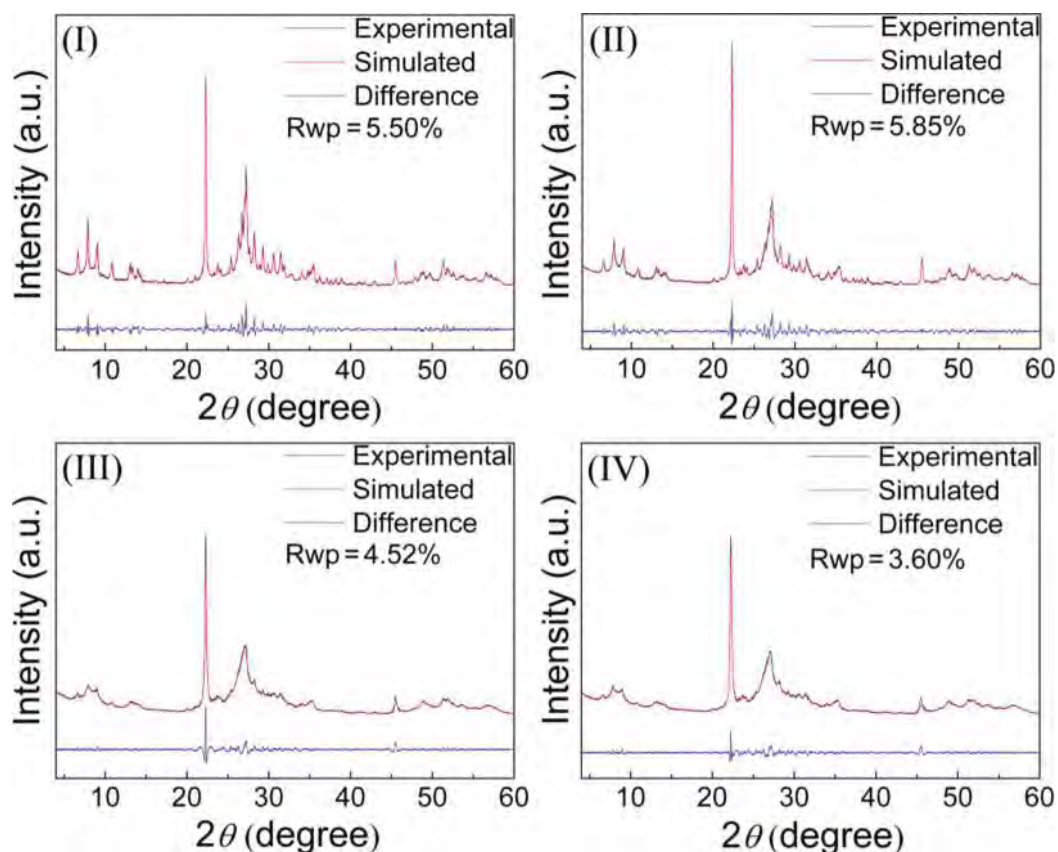


Figure 4 Rietveld analysis of Orth-MoVWO catalysts: Orth-MoVO–W2.5 (I), Orth-MoVO–W5.0 (II), Orth-MoVO–W7.5 (III) and Orth-MoVO–W10 (IV)

distinct difference from the orthorhombic and trigonal structures. With an increase in W content, the XRD patterns of Amor-MoVWO barely changed except for a shift of the (001) peak in a higher angle direction. This revealed that although lattice contraction occurred, the disordered arrangement in the a – b plane was not affected by the introduction of W. Therefore, crystal size (see Fig. S2-I and Table S1 in Supplementary Material on ManeyOnline here <http://dx.doi.org/10.1179/2055075814Y.0000000009>) and external surface area (Table 1) of Amor-MoVWO slightly changed.

In the XRD pattern of Orth-MoVWO (Fig. 3-II), main diffraction peaks corresponding to the orthorhombic structure emerged at 6.6, 7.9, 9.0 and 27.3°, etc., which were ascribed to the planes of (020), (120), (210) and (630), respectively.¹⁸ The emergence of diffraction peaks at a low angle below 10° indicated that Orth-MoVWO was well crystallized along the a and b axes. However, with an increase in W content, the rod segregation effect proceeded. That could be clearly observed from the TEM image (Fig. S1 in Supplementary Material). Orth-MoVWO crystals partially split into smaller rods and those nanoscale rods had sizes of only several tens of nanometers or even smaller (Average crystal size was calculated and is shown in Fig. S2-II and Table S1 in Supplementary Material). For crystalline materials, lattice expansion or contraction usually results in an unstable structure. Lattice contraction occurred with the incorporation of W and that might have caused cleavage of Mo–O and V–O bonds and decrease in the long range order of the a – b plane, thus facilitating dehiscence. The diffraction peaks

(especially below 10°) of Orth-MoVWO decreased and broadened gradually with increasing W content. Rietveld analysis using the crystallite size broadening procedure was carried out and results are shown in Fig. 4. It was confirmed that broadening of diffraction peaks was not caused by the formation of an amorphous phase but by the dehiscence of orthorhombic crystals. Although the addition of W affected the crystallinity of the orthorhombic structure, a decrease in crystal size contributed to a larger external surface area (Table 1) and more active sites were exposed, which is particularly important for the activity of acrolein oxidation to acrylic acid.¹³ When W content rose to 10 at.%, external surface area increased to 35.5 m² g^{−1}, almost 6 times larger than that of the well crystallized Orth-MoVO–W0.

Different from the synthesis process of Amor- and Orth-MoVWO, an organic Mo source (CH₃CH₂NH₃)₂Mo₃O₁₀ (EATM) was used to synthesize Tri-MoVWO (the section on ‘Synthesis of trigonal Mo–V–W–O complex oxides’). As noted above, additional metal ions usually affect the self-assembly process. In the trigonal structure, there is a linker unit of triple-octahedron and the occupancy of this triple-octahedron is only 0.6, while in the orthorhombic structure, the occupancy of quintuple-octahedron (instead of triple-octahedron) is 1.0.^{11,12} This revealed that the trigonal structure is not as stable as the orthorhombic structure. Therefore, simply adding W and other metal precursors into the hydrothermal process only resulted in amorphous phase instead of trigonal structure. The diameter of the heptagonal channel is about 0.4 nm, thus being limited to

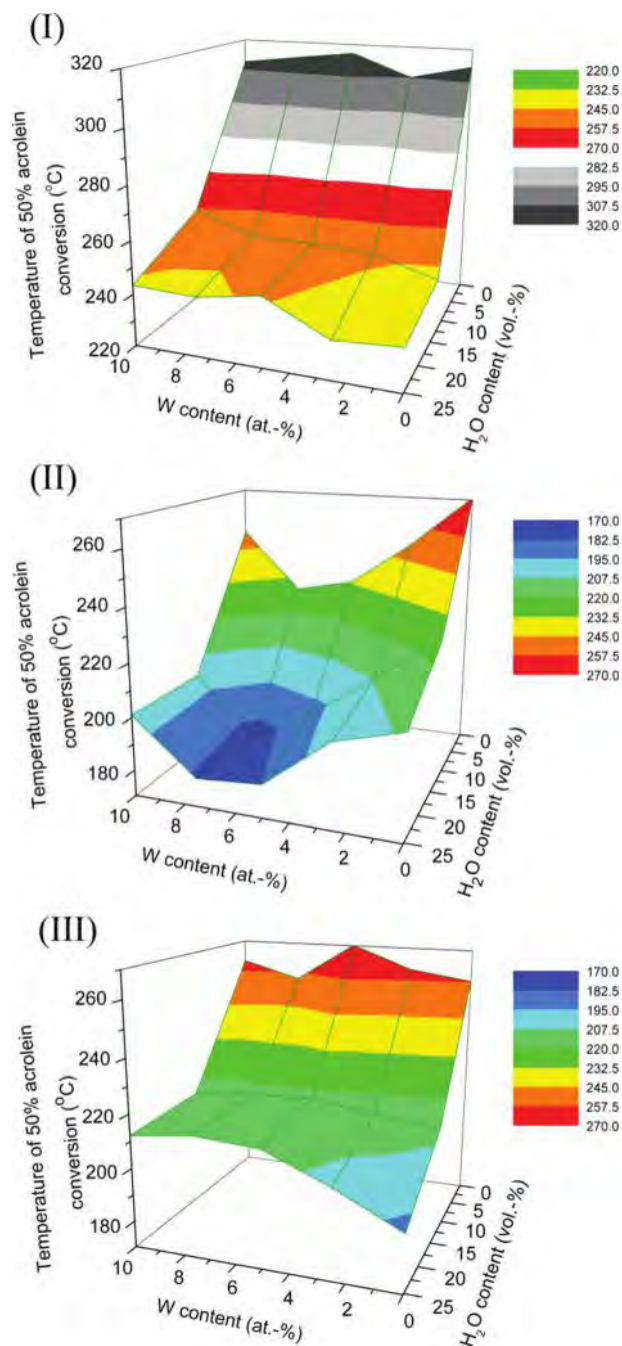


Figure 5 Temperatures of 50% acrolein conversion over Amor-MoVWO (I), Orth-MoVWO (II) and Tri-MoVWO (III) catalysts with different tungsten contents and water partial pressures

counter cation with a small molecular size such as an ammonium cation with a size of 0.28 nm. In the self-assembly process, an ethylamine cation with a larger size than that of an ammonium cation balanced the trigonal framework and played an important role as a structure directing agent and stabilizer for the trigonal structure and it could be easily removed by calcination in air. In the XRD pattern of Tri-MoVWO (Fig. 3-III), peak intensity of W-containing trigonal Mo–V–W–O was higher than that of Tri-MoVO–W₀, suggesting that the use of EATM as Mo source can provide trigonal Mo–V–W–O crystals with better crystallinity (average crystal size shown in Fig. S2-III and

Table S1 in Supplementary Material). Due to the good crystallinity of Tri-MoVWO, only a slight difference in the external surface area of Tri-MoVWO was observed (Table 1).

Catalytic activity for oxidation of acrolein to acrylic acid over Mo–V–W–O

Acrylic acid has become a widely used chemical in recent years because of its extensive applications in super absorbent materials, coatings and additives in textile production.^{19–21} It can be acknowledged that the crystalline structure was maintained and a much larger external surface was achieved for Orth-MoVWO, which was expected to show excellent performance in the selective oxidation of acrolein to acrylic acid.

Catalytic performance without H₂O feeding was investigated in order to eliminate the effect of H₂O (Figs. S3, S4, S5 and S6 in Supplementary Material). Crystalline Mo–V–W–O catalysts had more active sites because the *a*–*b* plane of orthorhombic and trigonal structures was constructed into a high degree of ordered arrangement. Therefore, for acrolein oxidation, crystalline Mo–V–W–O catalysts showed much higher activity than amorphous catalysts did, while selectivity to acrylic acid was almost the same. Figure 5 shows reaction temperatures of 50% acrolein conversion over Amor-, Orth- and Tri-MoVWO catalysts under different H₂O partial pressure and W content conditions. There is no doubt that water acts as an important promoter for the conversion of acrolein. Under the same water feeding condition, Orth- and Tri-MoVWO catalysts always showed higher catalytic activity than that of Amor-MoVWO. Moreover, a positive effect on acrolein conversion was observed when W was incorporated into the orthorhombic structure. However, in the case of trigonal and amorphous structures, W did not show any positive effect because of the slight changes in structure and morphology. The highest catalytic activity was achieved over the Orth-MoVO–W_{7.5} catalyst, which had a crystalline structure and large external surface area. Therefore, crystalline structure is the guarantee for good catalytic performance and external surface area is another important factor for oxidation of acrolein to acrylic acid.

Conclusion

We succeeded in introducing W into the trigonal structure using EATM as Mo source. For Orth-MoVWO, tungsten acted as a structural promoter that resulted in a rod segregation effect and increase in external surface area. Crystalline Orth- and Tri-MoVWO achieved showed very high catalytic activity compared with that of Amor-MoVWO. It was found that crystalline structure and external surface area were responsible for good catalytic activity.

To access the supplementary material for this article please follow www.maneyonline.com/doi/suppl/10.1179/2055075814Y.0000000010.S2

Conflicts of interest

The authors declare that there are no conflicts of interest.

Acknowledgements

This work was supported by JSPS KAKENHI Grant-in-Aid for Young Scientists (24760635).

References

1. X. L. Tu, N. Furuta, Y. Sumida, M. Takahashi and H. Niiduma: 'A new approach to the preparation of MoVNbTe mixed oxide catalysts for the oxidation of propane to acrylic acid', *Catal. Today*, 2006, **117**, (1–3), 259–264.
2. R. N. d'Alnoncourt, L. I. Csepei, M. Havecker, F. Girgsdies, M. E. Schuster, R. Schlögl and A. Trunschke: 'The reaction network in propane oxidation over phase-pure MoVTeNb M1 oxide catalysts', *J. Catal.*, 2014, **311**, 369–385.
3. K. Amakawa, Y. V. Kolen'ko, A. Villa, M. E. Schuster, L. I. Csepei, G. Weinberg, S. Wrabetz, R. N. d'Alnoncourt, F. Girgsdies, L. Prati, R. Schlögl and A. Trunschke: 'Multifunctionality of crystalline MoV(TeNb) M1 oxide catalysts in selective oxidation of propane and benzyl alcohol', *ACS Catal.*, 2013, **3**, (6), 1103–1113.
4. J. M. M. Millet, H. Roussel, A. Pigamo, J. L. Dubois and J. C. Jumas: 'Characterization of tellurium in MoVTeNbO catalysts for propane oxidation or ammoxidation', *Appl. Catal. A-Gen.*, 2002, **232**, (1–2), 77–92.
5. A. Drochner, P. Kampe, N. Menning, N. Blickhan, T. Jekewitz and H. Vogel: 'Acrolein oxidation to acrylic acid on Mo/V/W-mixed oxide catalysts', *Chem. Eng. Technol.*, 2014, **37**, (3), 398–408.
6. G. Mestl, J. L. Margitfalvi, L. Vegvari, G. P. Sziijarto and A. Tompos: 'Combinatorial design and preparation of transition metal doped MoVTe catalysts for oxidation of propane to acrylic acid', *Appl. Catal. A-Gen.*, 2014, **474**, 3–9.
7. Y. Nakazawa, S. Matsumoto, T. Kobayashi and T. Kurakami, Nipponkatakataku Inc.: 'Catalyst and method for producing acrylic acid', US Patent 20130217915 A1, 2013.
8. C. A. Welker-Nieuwoudt, A. Karpov, F. Rosowski, K. J. Mueller-Engel, H. Vogel, A. Drochner, N. Blickhan, N. Duerr, T. Jekewitz, N. Menning, T. Petzold and S. Schmidt: 'Process for heterogeneously catalyzed gas phase partial oxidation of (meth)acrolein to (meth)acrylic acid', Patent 20140018572; 2014.
9. T. Ushikubo, K. Oshima, A. Kayou, M. Vaarkamp and M. Hatano: 'Ammoxidation of propane over catalysts comprising mixed oxides of Mo and V', *J. Catal.*, 1997, **169**, (1), 394–396.
10. H. Tsuji and Y. Koyasu: 'Synthesis of MoVNbTe(Sb)O-x composite oxide catalysts via reduction of polyoxometales in an aqueous medium', *J. Am. Chem. Soc.*, 2002, **124**, (20), 5608–5609.
11. M. Sadakane, N. Watanabe, T. Katou, Y. Nodasaka and W. Ueda: 'Crystalline Mo3VOx mixed-metal-oxide catalyst with trigonal symmetry', *Angew. Chem.-Int. Edit.*, 2007, **46**, (9), 1493–1496.
12. M. Sadakane, K. Kodato, T. Kuranishi, Y. Nodasaka, K. Sugawara, N. Sakaguchi, T. Nagai, Y. Matsui and W. Ueda: 'Molybdenum-vanadium-based molecular sieves with microchannels of seven-membered rings of corner-sharing metal oxide octahedra', *Angew. Chem.-Int. Edit.*, 2008, **47**, (13), 2493–2496.
13. C. Chen, N. Kosuke, T. Murayama and W. Ueda: 'Single-crystalline-phase Mo3VOx: an efficient catalyst for the partial oxidation of acrolein to acrylic acid', *ChemCatChem*, 2013, **5**, (10), 2869–2873.
14. M. Hartmann and L. Kevan: 'Transition-metal ions in aluminophosphate and silicoaluminophosphate molecular sieves: location, interaction with adsorbates and catalytic properties', *Chem. Rev.*, 1999, **99**, (3), 635–663.
15. J. M. Thomas, R. Raja, G. Sankar and R. G. Bell: 'Molecular-sieve catalysts for the selective oxidation of linear alkanes by molecular oxygen', *Nature*, 1999, **398**, (6724), 227–230.
16. T. Konya, T. Katou, T. Murayama, S. Ishikawa, M. Sadakane, D. Buttrey and W. Ueda: 'An orthorhombic Mo3VOx catalyst most active for oxidative dehydrogenation of ethane among related complex metal oxides', *Catal. Sci. Technol.*, 2013, **3**, (2), 380–387.
17. M. Sadakane, K. Yamagata, K. Kodato, K. Endo, K. Toriumi, Y. Ozawa, T. Ozeki, T. Nagai, Y. Matsui, N. Sakaguchi, W. D. Pyrz, D. J. Buttrey, D. A. Blom, T. Vogt and W. Ueda: 'Synthesis of orthorhombic Mo-V-Sb oxide species by assembly of pentagonal Mo(6)O(21) polyoxometalate building blocks', *Angew. Chem.-Int. Edit.*, 2009, **48**, (21), 3782–3786.
18. W. Ueda, D. Vitry, T. Kato, N. Watanabe and Y. Endo: 'Key aspects of crystalline Mo-V-O-based catalysts active in the selective oxidation of propane', *Res. Chem. Intermed.*, 2006, **32**, (3–4), 217–233.
19. E. Saarikoski, H. Rautkoski, M. Rissanen, J. Hartman and J. Seppala: 'Cellulose/acrylic acid copolymer blends for films and coating applications', *J. Appl. Polym. Sci.*, 2014, **131**, (10).
20. M. Y. Zhang, Z. Q. Cheng, M. Z. Liu, Y. Q. Zhang, M. J. Hu and J. F. Li: 'Synthesis and properties of a superabsorbent from an ultravioletirradiated waste nameko mushroom substrate and poly (acrylic acid)', *J. Appl. Polym. Sci.*, 2014, **131**, (13).
21. A. Ben Fradj, R. Lafi, S. Ben Hamouda, L. Gzara, A. H. Hamzaoui and A. Hafiane: 'Effect of chemical parameters on the interaction between cationic dyes and poly(acrylic acid)', *J. Photochem. Photobiol. A-Chem.*, 2014, **284**, 49–54.

CrossMark
click for updatesCite this: *J. Mater. Chem. A*, 2015, 3,
746

Selective carbon dioxide adsorption of ϵ -Keggin-type zirconomolybdate-based purely inorganic 3D frameworks†

Zhenxin Zhang,^a Masahiro Sadakane,^{*bc} Shin-ichiro Noro,^{cde} Toru Murayama,^a Takashi Kamachi,^f Kazunari Yoshizawa^f and Wataru Ueda^{*a}

Polyoxometalate-based 3D frameworks, $\text{Na}_{1.5}\text{H}_{11.4}[\text{ZnMo}_{12}\text{O}_{40}(\text{Zn}_2)] \cdot 5.5\text{H}_2\text{O}$ and $(\text{NH}_4)_{1.5}\text{H}_{8.5}[\text{ZnMo}_{12}\text{O}_{40}(\text{Zn}_2)] \cdot 6\text{H}_2\text{O}$, are synthesized in moderate yields. Rotation of the reactor under hydrothermal conditions is essential to improve the yield. The materials show zeolite-like selective molecule adsorption properties. Depending on the micropore aperture size of the materials, small molecules can be adsorbed in the materials, while large molecules cannot. The enthalpy of adsorption and DFT calculation indicate that the materials strongly interact with CO_2 , but weakly interact with CH_4 , due to electrostatic interactions between the materials and molecules. CO_2/CH_4 co-adsorption experiments show that the materials can selectively adsorb CO_2 , and CO_2 adsorption selectivity of the material with sodium cations is higher than that of the material with ammonium cations. The material with sodium ions can be utilized for gas chromatographic separation of CH_4 and CO_2 .

Received 14th October 2014
Accepted 10th November 2014

DOI: 10.1039/c4ta05496b

www.rsc.org/MaterialsA

CO_2 separation is an important topic from the viewpoints of industrial processes and environmental protection, and many techniques for CO_2 separation have been developed over the past few decades.^{1–5} Generally, there are two kinds of materials for CO_2 separation based on different separation mechanisms. One type of materials for CO_2 separation is based on chemisorption. Such materials include calcium oxide and amine solutions. However, these materials have significant disadvantages such as toxicity, corrosiveness, and high energy for regeneration. The second type of materials is based on physisorption. Such materials include zeolites and metal-organic frameworks (MOFs), and they are considered to have higher application potential because the corresponding processes are environmentally friendly and economically feasible techniques.

Polyoxometalates (POMs) are metal oxide clusters of early transition metals, such as tungsten, molybdenum, vanadium and niobium, which display characteristic redox and acidic

properties, and they therefore have many applications including catalysis, adsorption, separation, electrochemistry, and medicine.^{6–9} In materials chemistry, POMs act as building blocks, and inorganic metal oxides can be synthesized on the basis of connection of POMs with other metal ions.^{10–14} POMs also interact with organic ligands or organic metal complexes to form hybrid materials, including POMOFs^{15–20} and POM-macrocation materials.^{21–29} POM-macrocation materials show interesting adsorption properties.

A novel catalog of POM-based materials has recently been prepared and structurally characterized and is best described to be fully inorganic microporous POM-based metal oxides.^{30,31} Frameworks of the materials are comprised of ϵ -Keggin POM with metal ion linkers (Fig. 1). The materials show zeolite-like properties such as ion exchange, molecule adsorption, and acid catalysis.

An important property of the POM-based microporous material is its high chemical composition diversity, which allows different kinds of elements to be incorporated in the material. The composition of POM units, linker ions, and counterions can be easily changed without altering the basic structure of the material. Several iso-structural materials have been successfully synthesized.³²

Herein, we describe the synthesis of ϵ -Keggin POM-based 3D frameworks composed of $[\text{ZnMo}_{12}\text{O}_{40}]$ and Zn ion linkers with sodium ions or ammonium cations, $\text{Na}_{1.5}\text{H}_{11.4}[\text{ZnMo}_{12}\text{O}_{40}(\text{Zn}_2)] \cdot 5.5\text{H}_2\text{O}$ or $(\text{NH}_4)_{1.5}\text{H}_{8.5}[\text{ZnMo}_{12}\text{O}_{40}(\text{Zn}_2)] \cdot 6\text{H}_2\text{O}$, denoted as Na-Mo-Zn oxide or NH_4 -Mo-Zn oxide, respectively. We demonstrate the adsorption properties of the materials. Small

^aCatalysis Research Center, Hokkaido University, N-21, W-10, Kita-ku, Sapporo 001-0021, Japan. E-mail: ueda@cat.hokudai.ac.jp; Fax: +81-11-706-9163; Tel: +81-11-706-9164

^bDepartment of Applied Chemistry, Graduate School of Engineering, Hiroshima University, 1-4-1 Kagamiyama, Higashi Hiroshima 739-8527, Japan

^cJST, PRESTO, 4-1-8 Honcho, Kawaguchi, Saitama 332-0012, Japan

^dResearch Institute for Electronic Science, Hokkaido University, Sapporo 001-0020, Japan

^eCreative Research Institute (CRIS), Hokkaido University, Sapporo 001-0021, Japan

^fInstitute for Materials Chemistry and Engineering and International Research Center for Molecular Systems, Kyushu University, Fukuoka 819-0395, Japan

† Electronic supplementary information (ESI) available. See DOI: 10.1039/c4ta05496b

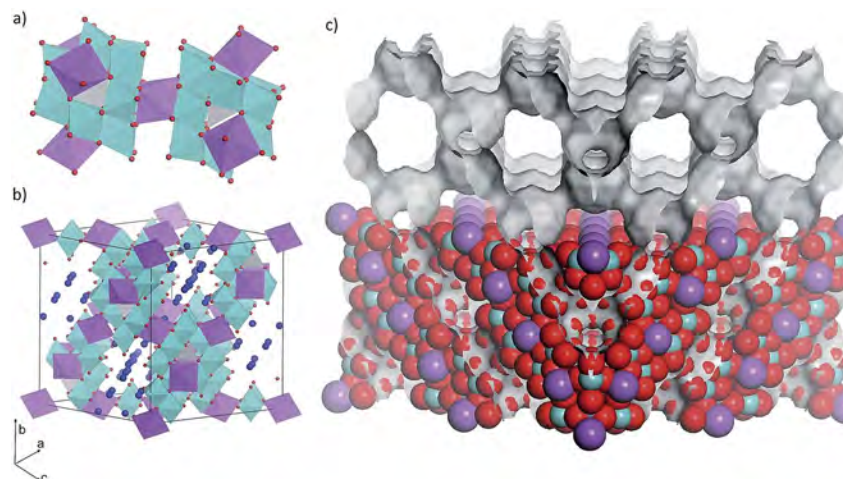


Fig. 1 Polyhedral representations of (a) ϵ -Keggin POM unit and its connection; (b) unit cell of an ϵ -Keggin POM-based framework – gray tetrahedron: central Zn–O tetrahedron, blue octahedron: surrounding Mo–O octahedron, purple octahedron: linker Zn–O octahedron, and deep blue ball: cations and water; and (c) CPK (Corey, Pauling, and Koltun) representation of the material with a Connolly surface (gray curved surface) that shows the micropore system of the material.

molecules such as CO_2 , CH_4 , and C_2H_6 are adsorbed in the materials, while a large molecule such as C_3H_8 is not adsorbed. CO_2/CH_4 co-sorption experiments showed that the materials selectively adsorb CO_2 from a CO_2/CH_4 mixture. CO_2 adsorption in the materials can be tuned by altering counteranions, and CO_2 separation efficiency can be remarkably enhanced by incorporating sodium ions in the material. The Na–Mo–Zn oxide material can be used as a material for gas chromatographic separation of CO_2 and CH_4 .

Experimental

Material synthesis

Synthesis of Na–Mo–Zn oxide. $\text{Na}_2\text{MoO}_4 \cdot 2\text{H}_2\text{O}$ (2.823 g, 11.7 mmol based on Mo) was dissolved in 40 mL of water. Then metal molybdenum (0.2 g, 2.08 mmol) and ZnCl_2 (0.453 g, 3.33 mmol) were added in sequence. The pH value of the precursor solution was adjusted to 4.8 by addition of H_2SO_4 (1 M). The mixture solution was well sealed in an autoclave with a Teflon liner, and the autoclave was fixed in an oven with a mechanical rotation system. Hydrothermal synthesis was performed at 448 K with rotation (1 rpm) for 24 h (see the experimental apparatus in ESI Fig. S1†). After hydrothermal reaction and cooling of the autoclave, the crude solid was transferred to a 100 mL beaker and 60 mL of water was added. For purification and solid recovery, the mixture was centrifuged (1700 rpm, 2 min), and the suspension (containing the product) solution was separated from the precipitate formed at the bottom after centrifugation. Then after addition of 60 mL of water to the precipitate, the solution was centrifuged and the new upper suspension solution was separated. Addition of water, centrifugation, and separation were carried out two more times. The collected suspension (containing the product) was centrifuged (3500 rpm, 120 min), and the solid at the bottom of the centrifugation tube was collected. The collected solid was washed with water by dispersing in 10 mL of water and subsequent centrifugation

(3500 rpm, 120 min). After the washing process was carried out two more times, the obtained solid was dried at 333 K overnight. Then 1.18–1.34 g of Na–Mo–Zn oxide (yield: 57–63% based on Mo) was obtained.

Synthesis of NH_4 –Mo–Zn oxide. $(\text{NH}_4)_6\text{Mo}_7\text{O}_{24} \cdot 4\text{H}_2\text{O}$ (2.060 g, 11.7 mmol based on Mo) was dissolved in 40 mL of water. Then metal molybdenum (0.2 g, 2.08 mmol) and ZnCl_2 (0.453 g, 3.33 mmol) were added in sequence. The pH value of the precursor solution was adjusted to 4.8 by addition of H_2SO_4 (1 M). The mixture solution was well sealed in an autoclave with a Teflon liner, and the autoclave was fixed in an oven with a mechanical rotation system. Hydrothermal synthesis was performed at 448 K with rotation (1 rpm) for 24 h. After the hydrothermal reaction, the purification process was the same as that for Na–Mo–Zn oxide. Then 1.29–1.46 g of NH_4 –Mo–Zn oxide (yield: 62–71% based on Mo) was obtained.

Synthesis of NH_4 –Na–Mo–Zn oxide by ion-exchange of Na–Mo–Zn oxide with NH_4^+ . 0.3 g of Na–Mo–Zn oxide was dispersed into 15 mL of water. Then NH_4Cl (0.065 g, 1.21 mmol) was added. The solution was heated at 353 K for 6 h with stirring. The resulting material was separated by filtration, washed with water 3 times and dried at 333 K overnight.

Elemental analysis: Na–Mo–Zn oxide: calcd for $\text{Na}_{1.5}\text{Zn}_3\text{Mo}_{12}\text{O}_{45.5}\text{H}_{22.4}$: Zn, 9.20; Mo, 53.99; Na, 1.62; H, 1.05, found: Zn, 9.70; Mo, 53.45; Na, 1.39; H, 0.97.

NH_4 –Mo–Zn oxide: calcd for $\text{N}_{1.5}\text{Zn}_3\text{Mo}_{12}\text{O}_{46}\text{H}_{26.5}$: Zn, 9.21; Mo, 54.03; N, 0.99; H, 1.24, found: Zn, 9.25; Mo, 53.95; N, 1.02; H, 1.22.

NH_4 –Na–Mo–Zn oxide: calcd for $\text{N}_{1.4}\text{Na}_{0.1}\text{Zn}_3\text{Mo}_{12}\text{O}_{45.5}\text{H}_{28}$: Zn, 9.23; Mo, 54.17; Na, 0.11, N, 0.92; H, 1.32, found: Zn, 9.61; Mo, 54.24; Na, 0.07; N, 1.20; H, 1.39.

Characterization

Powder X-ray diffraction (XRD) patterns were obtained on RINT2200 (Rigaku) with $\text{Cu K}\alpha$ radiation (tube voltage: 40 kV, tube current: 20 mA). Scanning electron microscopy (SEM)

images were obtained with HD-2000 (HITACHI). Transmission electron microscopy (TEM) images were taken with a 200 kV TEM (JEOL JEM-2100F). Temperature-programmed desorption mass spectrometry (TPD-MS) measurements were carried out from 313 K to 893 K at a heating rate of 10 K min⁻¹ under helium (flow rate: 50 mL min⁻¹). Samples were set up between two layers of quartz wool. A TPD apparatus (BEL Japan, Inc.) equipped with a quadrupole mass spectrometer (M-100QA; Anelva) was used to detect NH₃ ($m/z = 16$) and H₂O ($m/z = 18$). For TPD-MS measurements of the materials after heat treatment, the samples were heated at 473 K under a high vacuum for 2.5 h in a TPD instrument before measurements. After the temperature was decreased to 373 K, TPD measurement was started. Fourier transform infrared (FT-IR) analysis was carried out on a PARAGON 1000, Perkin Elmer. X-ray photoelectron spectroscopy (XPS) was performed on a JPS-9010MC (JEOL). The spectrometer energies were calibrated using the C 1s peak at 284.8 eV. Thermal analysis (TG-DTA) was performed on a Thermo Plus, TG8120 (Rigaku), under N₂ (200 mL min⁻¹). Elemental compositions were determined by an inductive coupling plasma (ICP-AES) method (ICPE-9000, Shimadzu). CHN elemental composition was determined at Instrumental Analysis Division, Equipment Management Center, Creative Research Institution, Hokkaido University.

Sorption experiments

Na–Mo–Zn oxide and NH₄–Mo–Zn oxide were calcined at 473 K for 2.5 h under a vacuum (denoted as Cal–Na–Mo–Zn oxide and Cal–NH₄–Mo–Zn oxide) before all adsorption experiments.

N₂ sorption isotherms were obtained using a BELSORP MAX (BEL Japan Inc.) sorption analyzer at 77 K. Pore size distribution was calculated by the SF method. Molecule (CO₂, CH₄, C₂H₆, and C₃H₈) adsorption was performed on the materials by a BELSORP MAX (BEL Japan Inc.) sorption analyzer. The adsorption temperature was kept at 278, 288, and 298 K using a water bath. Surface areas of the materials were calculated from the CO₂ adsorption isotherm by the BET method, and the cross-sectional area of CO₂ was 0.201 nm².³³

CO₂/CH₄ co-sorption measurements were carried out using a multicomponent gas adsorption apparatus, BELSORP VC (BEL Japan Inc.). In this apparatus, the total adsorbed amount was calculated by a constant volume method, and the composition ratio of CO₂ and CH₄ gases in equilibrium was determined using an Agilent 490 Micro gas chromatographic (GC) system equipped with a thermal conductive detector. From these data, we calculated adsorbed amounts and equilibrium partial pressures for each gas. The initial dosing total pressures were set to 14.5 and 278.7 kPa for Cal–Na–Mo–Zn oxide and 14.5 and 279.9 kPa for Cal–NH₄–Mo–Zn oxide. The initial gas proportion was CO₂ : CH₄ = 40 : 60 (mol). After reaching the equilibrium, a small portion of the gas phase was used for GC analysis, leading to a slight decrease in system total pressure. Then co-sorption measurements were continued by using the residual gas. This process was repeated 5 times for each initial dosing pressure.

The selectivity of CO₂ over CH₄ was calculated by the following equation.

$$S_{\text{CO}_2} = (x_{\text{CO}_2}/y_{\text{CO}_2})/(x_{\text{CH}_4}/y_{\text{CH}_4})$$

y_{CO_2} : mole fraction of component CO₂ in the gas phase;

y_{CH_4} : mole fraction of component CH₄ in the gas phase;

x_{CO_2} : mole fraction of component CO₂ in the adsorbed phase;

x_{CH_4} : mole fraction of component CH₄ in the adsorbed phase.

Calculation of enthalpy of adsorption. Pure gas adsorption of CO₂ and CH₄ was carried out at different temperatures of 278, 288, and 298 K on the materials (Fig. S2–S5†). The isotherms of CO₂ and CH₄ were fitted with several adsorption models (Table S1†), and it was found that the dual-site Langmuir–Freundlich model was the best model, for which the equation is as follows:

$$q = \frac{q_1 b_1 p^{n_1}}{1 + b_1 p^{n_1}} + \frac{q_2 b_2 p^{n_2}}{1 + b_2 p^{n_2}},$$

where q is the adsorbed amount, p is pressure, and q_1 , q_2 , b_1 , b_2 , n_1 , and n_2 are fitting parameters, which are listed in Tables S2–S5.†

The resulting R^2 values of the fitting processes were quite close to 1, indicating that simulated isotherms by using the dual-site Langmuir–Freundlich model fitted the experimental isotherms well.

The enthalpy of adsorption was calculated by the Clausius–Clapeyron equation using the dual-site Langmuir–Freundlich fitting results.

$$\frac{d \ln p}{dT} = \frac{\Delta H}{RT^2},$$

where p is pressure, T is temperature, and ΔH is enthalpy of adsorption.

GC separation of CO₂ and CH₄. GC separation of a gas mixture of CO₂ and CH₄ using a column packed with Na–Mo–Zn oxide was performed with a Shimadzu GC-8A system equipped with a thermal conductivity detector. Na–Mo–Zn oxide was well grounded and screened with a mesh (aperture: 150 μm), and about 20 mL of Na–Mo–Zn oxide was densely packed into a column (length: 1 m, inner diameter: 3 mm). The fresh column of Na–Mo–Zn oxide was treated at 473 K by introducing a carrier gas of He for 2.5 h to remove the original water in the material and open the micropores of the material. The gas mixture (0.1 mL, mole ratio of CO₂ : CH₄ = 1 : 1) was injected, and separation was carried out at 363 K.

Structural determination, computer-based simulation, and DFT calculations

Structural determination of NH₄–Mo–Zn oxide was performed by *ab initio* structural determination with powder diffraction,³⁴ the detailed process of which is shown in the ESI.† Material modeling, X-cell program,³⁵ Pawley refinement, and Rietveld refinement³⁶ were performed with the Materials Studio package (Accelrys Software Inc.). The programs of DICVOL06 (ref. 37) and EdPCR were carried out with the Fullprof package. A charge-flipping algorithm³⁸ was performed with the superflip program in Jana2006, and electron density maps were generated with Chimera 1.8.1.

Monte Carlo simulation was performed to predict the adsorbed structure of the guest molecules in the primitive cell of Ca–Na–Mo–Zn oxide with the adsorption locator program in the Materials Studio package. First, the structure of the material, CO₂, and CH₄ were optimized by using the DMol³ program.^{39,40} We employed the Perdew–Burke–Ernzerhof (PBE) generalized gradient functional and DND basis set. Calculated Mulliken atomic charge was applied for Monte Carlo simulation. Partial atomic charges of CO₂ were C = +0.70e and O = –0.35e,⁴¹ and CH₄ was recognized as an electrostatic neutral molecule.⁴² The guest molecules were introduced into the framework of the material one by one.

Results and discussion

Material synthesis and characterization

The synthesis process for Mo–Zn oxides was carried out mainly according to our previous paper.³² However, the previous process produced Na–Mo–Zn oxide with a low yield (14% based on Mo) with some impurities such as MoO₂, ZnMoO₄ and Mo (Fig. S6†), which might have been caused by an insoluble starting material such as metal Mo and the poorly mixed precursor solution. It was known that mixing of solid precursors during reactions change selectivity of products.^{43,44} Here, we applied the dynamic method for material synthesis, in which the reactors were rotated under hydrothermal conditions (Fig. S1†). In the case of synthesis of Mo–Zn oxides, we found that applying rotation affected the purity and yield of the material. XRD patterns of the crude solids of Na–Mo–Zn oxide and NH₄–Mo–Zn oxide with and without rotation (Fig. S6†) indicated that rotation synthesis suppressed the side-reactions and increased the isolated yields of the materials (about 57–63% based on Mo for Na–Mo–Zn oxide and about 62–71% based on Mo for NH₄–Mo–Zn oxide). We carried out the synthesis many times and found that the reproducibilities of the synthesis of both materials are very good.

Furthermore, it was found that the rotation speed affected the yields of the materials. Low rotation (1 rpm) speed resulted in high isolated yields of both Mo–Zn oxides, and increasing the rotation speed would decrease the yields of products (Fig. S7†). The main impurity in crude solids of the materials from the synthesis with different rotation speeds was metal Mo (Fig. S6†). The amount of metal Mo increased in the crude solid with increase in rotation speed (Fig. S6B†), which illustrated that high rotation speeds hindered Mo consumption. This might ascribe to our rotation apparatus (Fig. S1†), in which a centripetal force would be applied to the solid in the solution to cause non-uniform mixing of the Mo metal in the solution.

By using different Mo sources with different cations (Na₂MoO₄·2H₂O and (NH₄)₆Mo₇O₂₄·4H₂O), materials of Mo–Zn oxide with different counteranions, Na–Mo–Zn oxide and NH₄–Mo–Zn oxide, were prepared. Elemental analysis indicated that the Na : Mo : Zn ratio of Na–Mo–Zn oxide obtained by the dynamic method that we used was the same as that of Na–Mo–Zn oxide obtained by our last non-dynamic method.³² The NH₄ : Mo : Zn ratio of NH₄–Mo–Zn oxide was 1.5 : 12 : 3. XRD patterns and FT-IR spectra (peaks below 1000

cm⁻¹ ascribed to the POM moiety) of both materials were similar to those of Mo–V–Bi oxide and Na–Mo–Zn oxide obtained by our last non-dynamic method (Fig. 2),^{30,32} indicating that the structures of materials synthesized by the dynamic method were similar to the structure of the reported Na–Mo–Zn oxide obtained by our last non-dynamic method. SEM images of the resulting materials showed octahedral morphologies typical of ϵ -Keggin-type heteropolyoxometalate-based framework compounds with sizes of the crystallite being 100–300 nm (Fig. 3a and b).

The structure of NH₄–Mo–Zn oxide was obtained by powder diffraction Rietveld analysis (Fig. S8) (detailed process shown in the ESI) combined with elemental analysis, FT-IR, and XPS analysis (Fig. S9†). The detailed chemical formulae of Na–Mo–Zn oxide and NH₄–Mo–Zn oxide were estimated to be Na_{1.5}H_{11.4}[Zn^{II}Mo^{VI}_{1.1}Mo^V_{10.9}O₄₀{Zn^{II}₂}]·5.5H₂O and (NH₄)_{1.5}H_{8.5}[Zn^{II}Mo^{VI}₄Mo^V₈O₄₀{Zn^{II}₂}]·6H₂O, respectively. The frameworks of

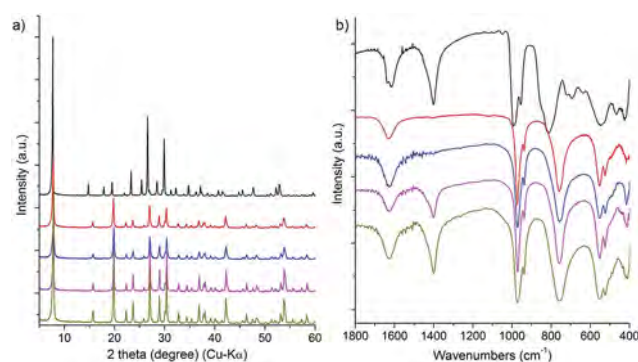


Fig. 2 (a) Powder XRD patterns of POM-based materials – lattice parameter of Na–Mo–Zn oxide: 19.4675 Å and lattice parameter of NH₄–Mo–Zn oxide: 19.4533 Å; and (b) FT-IR spectra of POM-based materials – black: Mo–V–Bi oxide, red: Na–Mo–Zn oxide using a non-dynamic method,³² blue: Na–Mo–Zn oxide using a dynamic method, purple: NH₄–Mo–Zn oxide, and yellow: NH₄–Na–Mo–Zn oxide.

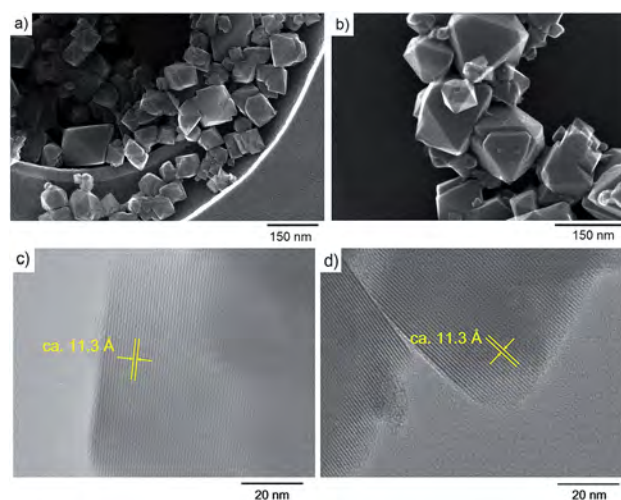


Fig. 3 SEM images of (a) Na–Mo–Zn oxide and (b) NH₄–Mo–Zn oxide and TEM images of (c) Na–Mo–Zn oxide and (d) NH₄–Mo–Zn oxide.

both materials were formed by assembly of ϵ -Keggin-type zirconomolybdate, $[\text{ZnMo}_{12}\text{O}_{40}]$, where one Zn–O tetrahedron was surrounded by 12 Mo–O octahedra. TEM showed that the distance of the (1 1 1) plane was close to each other, indicating that the basic structures of the materials were the same (Fig. 3c and d), and in good agreement with the results of structural analysis.

The difference between the two oxides was the counteranions, because cation species of the starting materials were different. The void space surrounded by the frameworks of Na–Mo–Zn oxide and NH_4 –Mo–Zn oxide was occupied by guest species, including water and sodium ions for Na–Mo–Zn oxide and water and ammonium cations for NH_4 –Mo–Zn oxide, in the as-synthesized materials. FT-IR spectra of the materials showed peak maxima of 1620 cm^{-1} and 1400 cm^{-1} , corresponding to water and ammonium cations in the materials (Fig. 2b). The amounts of sodium and ammonium in the materials of Na–Mo–Zn oxide and NH_4 –Mo–Zn oxide were the same (1.5 per POM unit).

Micropores were constructed by cages and channels, and the cages were connected with the channels in a tetrahedral fashion to build a 3D pore system (Fig. 1c). The numbers of cages and channels per POM were 1 and 2, respectively.

Heat treatment could remove the existing water from Na–Mo–Zn oxide and water and NH_4^+ from NH_4 –Mo–Zn oxide. TPD-MS was applied to investigate desorption of guest molecules from the as-synthesized materials (Fig. S10a and b†). The mass numbers m/z of 16 and 18 corresponded to ammonia and water, respectively. In the case of NH_4 –Mo–Zn oxide, the TPD-MS profile ($m/z = 16$) revealed only one peak with a peak maximum at 600 K, indicating desorption of ammonia at 600 K. Na–Mo–Zn oxide did not contain any ammonia in the structure. After removal of ammonia from NH_4 –Mo–Zn oxide, protons remained in the structure to make charge balance. There were two water desorption peaks, whose peak maxima were at about 400 K and 600 K, in both materials. For Na–Mo–Zn oxide, Na^+ could not be removed by heating and remained in the structure after heating. TG-DTA profiles indicated the weight loss of the materials during heating. The total weight loss of Na–Mo–Zn oxide was 7.5% and that of NH_4 –Mo–Zn oxide was 10.7% (Fig. S10c and d†).

Thermal stability and hydrothermal stability

Thermal stability of the materials was tested. The materials were calcined under N_2 flow (50 mL min^{-1}) for 2 h at 473 K, 523 K, 573 K, and 623 K (NH_4 –Mo–Zn oxide only). The resulting materials were characterized by powder XRD. Na–Mo–Zn oxide was stable at 473 K, and it started to decompose at 523 K as the diffraction peak of (111) decreased dramatically (Fig. S11A†). Compared with Na–Mo–Zn oxide, NH_4 –Mo–Zn oxide was thermally more stable, whose structure did not change at 523 K. Further heating would collapse the structure (Fig. S11B†).

Hydrothermal stability of the materials was also tested. The material (0.15 g) was dispersed in water (20 mL) followed by introducing the mixture into a 50 mL autoclave, and then the autoclave was heated for 24 h at 373 K, 413 K, 448 K, and 503 K in an oven. XRD showed that the peak intensities of both

materials almost did not decrease after hydrothermal treatments, indicating that the crystallinity of the materials did not drastically decrease (Fig. S11C and D†). However, the recovery rate of Na–Mo–Zn oxide decreased with increase in the treatment temperature, demonstrating that the material slowly dissolved in water during the hydrothermal treatment (Fig. S11E†). In the case of NH_4 –Mo–Zn oxide, the recovery rate of the material was higher than that of Na–Mo–Zn oxide. The material was stable under the hydrothermal conditions below 448 K (Fig. S11E†).

Both Mo–Zn oxides were thermally stable at 473 K (Fig. S11†). It was found that calcination at 473 K for 2.5 hours under a high vacuum could remove water and NH_3 without collapse of the structure. The remaining guest molecules, water in the calcined material of Na–Mo–Zn oxide (Cal–Na–Mo–Zn oxide) and NH_4^+ and water in calcined NH_4 –Mo–Zn oxide (Cal– NH_4 –Mo–Zn oxide), were estimated by TPD measurement (Fig. S12†). In the case of Na–Mo–Zn oxide, 63% of the water was removed by heating. Heating of NH_4 –Mo–Zn oxide removed 41% of the water and 65% of NH_3 . The chemical formulae of Cal– NH_4 –Mo–Zn oxide and Cal–Na–Mo–Zn oxide were estimated to be $\text{Na}_{1.5}\text{H}_{11.4}[\text{Zn}^{\text{II}}\text{Mo}^{\text{VI}}_{1.1}\text{Mo}^{\text{V}}_{10.9}\text{O}_{40}\{\text{Zn}^{\text{II}}\}_2] \cdot 2\text{H}_2\text{O}$ and $(\text{NH}_4)_{0.5}\text{H}_{9.6}[\text{Zn}^{\text{II}}\text{Mo}^{\text{VI}}_4\text{Mo}^{\text{V}}_8\text{O}_{40}\{\text{Zn}^{\text{II}}\}_2] \cdot 3.5\text{H}_2\text{O}$, respectively. The amounts of guest species in the two calcined Mo–Zn oxides were similar, 3.5–4 per POM unit (Table S6†).

Adsorption properties

N_2 sorption measurements of both calcined oxides showed a sudden N_2 uptake at very low relative pressure ($p/p_0 = 0.001$), indicating that the materials were microporous materials (Fig. S13a and Table S7†). Pore size distribution calculated by the SF method further demonstrated that both Mo–Zn oxides were microporous materials (Fig. S13b†). The adsorption properties of Cal–Na–Mo–Zn oxide and Cal– NH_4 –Mo–Zn oxide were further studied by small molecule adsorption. The materials selectively adsorbed different kinds of small molecules based on the size of the molecules. Fig. 4 shows the adsorption isotherms of CH_4 , CO_2 , C_2H_6 , and C_3H_8 on the materials at 298 K. The results indicated that the materials adsorbed small molecules including CH_4 , CO_2 and C_2H_6 with kinetic diameters of 0.38, 0.33, and 0.40 nm, respectively, whereas a larger molecule of C_3H_8 with a kinetic diameter of 0.42 nm was not adsorbed by either of the materials.

Surface areas of the materials were calculated by the BET method from CO_2 adsorption isotherms to be $88\text{ m}^2\text{ g}^{-1}$ and $68\text{ m}^2\text{ g}^{-1}$ for Cal–Na–Mo–Zn oxide and Cal– NH_4 –Mo–Zn oxide, respectively. Pore volumes for Cal–Na–Mo–Zn oxide and Cal– NH_4 –Mo–Zn oxide were estimated by the DA method⁴⁵ from CO_2 adsorption isotherms to be $0.039\text{ cm}^3\text{ g}^{-1}$ and $0.033\text{ cm}^3\text{ g}^{-1}$, respectively. For Cal–Na–Mo–Zn oxide, about 1.84 of CO_2 , 0.86 of CH_4 , and 1.04 of C_2H_6 per POM unit were adsorbed. For Cal– NH_4 –Mo–Zn oxide, about 1.44 of CO_2 , 0.89 of CH_4 , and 0.99 of C_2H_6 per POM unit were adsorbed (Table 1).

Moreover, Mo–Zn oxide with NH_4^+ was obtained by an ion-exchange process (NH_4 –Na–Mo–Zn oxide). Here we used a high dosage of NH_4Cl expecting to replace all Na^+ in Na–Mo–Zn

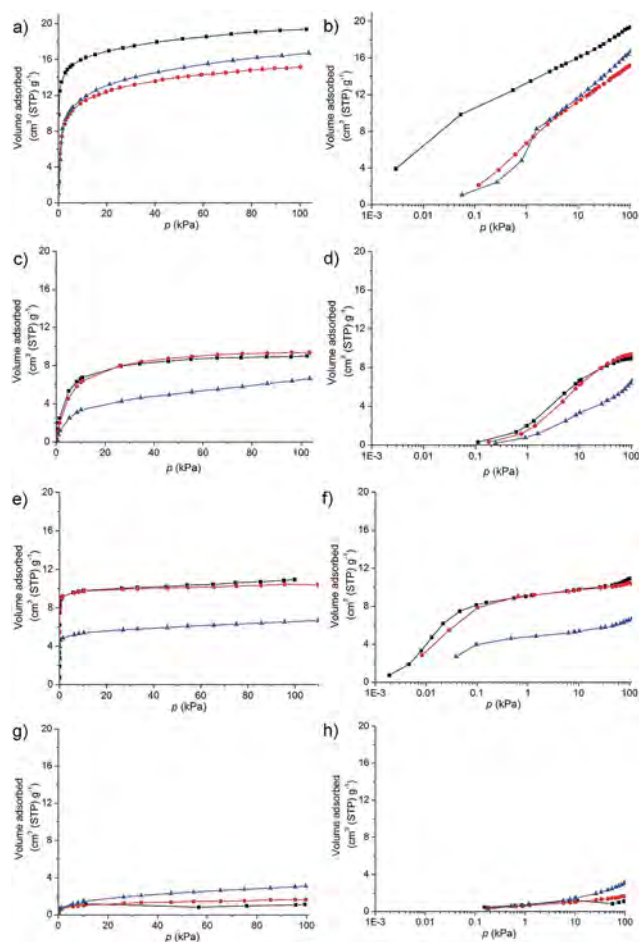


Fig. 4 Adsorption isotherms of (a and b) CO_2 , (c and d) CH_4 , (e and f) C_2H_6 , and (g and h) C_3H_8 at 298 K – black: Cal-Na-Mo-Zn oxide, red: Cal-NH₄-Mo-Zn oxide, and blue: Cal-NH₄-Na-Mo-Zn oxide.

oxide. XRD pattern and FT-IR spectra confirmed that the basic structure of NH₄-Na-Mo-Zn oxide was the same as those of the other two Mo-Zn oxides (Fig. 2). The appearance of an IR band at 1400 cm⁻¹ indicated that NH₄⁺ was successfully introduced into Na-Mo-Zn oxide. Elemental analysis demonstrated that there was still Na⁺ in the material and the chemical formula of as-synthesized NH₄-Na-Mo-Zn oxide was $(\text{NH}_4)_{1.4}\text{Na}_{0.1}\text{H}_{11.4}[\text{ZnMo}_{12}\text{O}_{40}\{\text{Zn}_2\}]\cdot 5.5\text{H}_2\text{O}$. After calcination at 473 K (denoted as Cal-NH₄-Na-Mo-Zn oxide), TPD-MS (Fig. S12d and e†) indicated that the chemical formula of the calcined material

was $(\text{NH}_4)_{1.4}\text{Na}_{0.1}\text{H}_{11.4}[\text{ZnMo}_{12}\text{O}_{40}\{\text{Zn}_2\}]\cdot 3\text{H}_2\text{O}$ and most of the NH₄⁺ remained.

Molecule adsorption was also carried out on Cal-NH₄-Na-Mo-Zn oxide, showing that the material could also adsorb small molecules (Fig. 4). Compared to other two Mo-Zn oxides, the adsorption capacity of Cal-NH₄-Na-Mo-Zn oxide was lower, which might have resulted from remaining NH₄⁺ and water in the Cal-NH₄-Na-Mo-Zn oxide (Table S6†). Therefore, we would like to use Cal-NH₄-Mo-Zn oxide and Cal-Na-Mo-Zn oxide for further experiments.

CO₂ and CH₄ adsorption. CO₂ uptake in both materials sharply increased in the low pressure range (<1 kPa), indicating that both Mo-Zn oxides had strong interactions with CO₂, and both materials showed high CO₂ adsorption capacity (19 cm³(STP) g⁻¹ for Na-Mo-Zn oxide and 15 cm³(STP) g⁻¹ for Cal-NH₄-Mo-Zn oxide at 100 kPa) (Fig. 4a and b). In the case of CH₄ adsorption, the molecule uptake in the low pressure range increased gradually, indicating that the materials showed weaker interaction with CH₄ than that with CO₂ (Fig. 4c and d). Both calcined Mo-Zn oxides adsorbed CO₂ at a low pressure (<1 kPa), whereas they could not adsorb CH₄ at such a low pressure.

The enthalpy of adsorption was calculated using the Clausius-Clapeyron equation, which is shown in Fig. 5. The enthalpies of CO₂ and CH₄ adsorption for Na-Mo-Zn oxide were calculated to be 46–65 kJ mol⁻¹ and 18–30 kJ mol⁻¹, respectively. The enthalpies of CO₂ and CH₄ adsorption for NH₄-Mo-Zn oxide were calculated to be 35–45 kJ mol⁻¹ and 25–30 kJ mol⁻¹, respectively. The enthalpy of CO₂ adsorption in both materials was higher than that of CH₄ adsorption, indicating that the materials strongly interacted with CO₂ but weakly interacted with CH₄.

CO₂ adsorption isotherms of Cal-Na-Mo-Zn oxide and Cal-NH₄-Mo-Zn oxide were different. Cal-Na-Mo-Zn oxide showed much higher adsorption capacity than that of Cal-NH₄-Mo-Zn oxide not only at a high pressure but also at a low pressure (<1 kPa), at which adsorption in micropores occurred (Fig. 4a and b). The enthalpy of CO₂ adsorption (Fig. 5) for Cal-Na-Mo-Zn oxide (46–65 kJ mol⁻¹) appeared to be higher than that of CO₂ for Cal-NH₄-Mo-Zn oxide (35–45 kJ mol⁻¹), indicating that Na⁺ in Cal-Na-Mo-Zn oxide showed stronger interaction with CO₂ than did protons or ammonium cations in Cal-NH₄-Mo-Zn oxide.

On the other hand, adsorption isotherms of CH₄ in Cal-Na-Mo-Zn oxide and Cal-NH₄-Mo-Zn oxide were almost the same. For both calcined Mo-Zn oxides, about 10 cm³ g⁻¹ of gas molecules was adsorbed at 298 K and at 100 kPa. Enthalpies of

Table 1 Numbers of small molecules per POM unit adsorbed in the materials at 100 kPa^a

	POM unit	CO ₂	CH ₄	C ₂ H ₆	C ₃ H ₈
Cal-Na-Mo-Zn oxide	ZnMo ₁₂ O ₄₀	1.84	0.86	1.04	0.11
Cal-NH ₄ -Mo-Zn oxide	ZnMo ₁₂ O ₄₀	1.44	0.89	0.99	0.16
Cal-NH ₄ -Na-Mo-Zn oxide	ZnMo ₁₂ O ₄₀	1.58	0.63	0.63	0.30

^a The values were calculated by the equation: number of molecule adsorbed = $\frac{\text{adsorbed amount (cm}^3 \text{ g}^{-1}) \times \text{molecule weight of the material (g mol}^{-1})}{22400 (\text{cm}^3 \text{ mol}^{-1})}$.

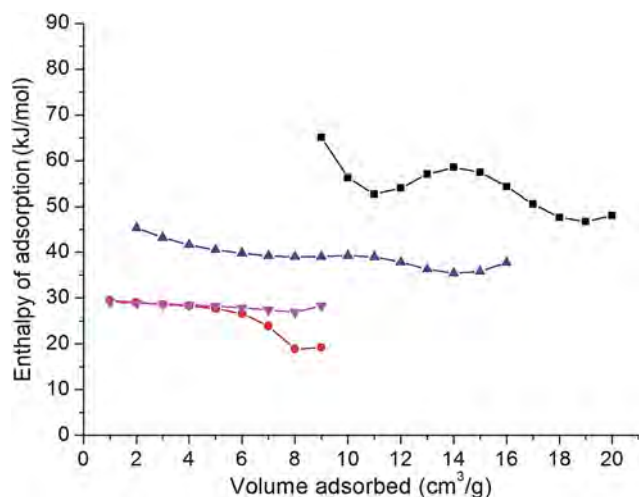


Fig. 5 Enthalpy of CO₂ and CH₄ adsorption for Cal-Na-Mo-Zn oxide and Cal-NH₄-Mo-Zn oxide – black: Cal-Na-Mo-Zn oxide adsorbed CO₂, red: Cal-Na-Mo-Zn oxide adsorbed CH₄, blue: Cal-NH₄-Mo-Zn oxide adsorbed CO₂, and purple: Cal-NH₄-Mo-Zn oxide adsorbed CH₄.

CH₄ adsorption for Cal-Na-Mo-Zn oxide (18–30 kJ mol⁻¹) and Cal-NH₄-Mo-Zn oxide (25–30 kJ mol⁻¹) were almost the same. Therefore, Na⁺ did not affect the adsorption of CH₄ in the materials.

It was reported that the electronic properties of CO₂ and CH₄ caused the different adsorption behaviors. CO₂ has a large quadrupole moment (13.4×10^{-40} cm²), whereas CH₄ is non-polar.⁴⁶ The large amount of CO₂ adsorption and the strong interaction of CO₂ with frameworks were attributed to large quadrupole moment of CO₂ molecules,⁴⁷ which resulted in a relatively strong attraction to the electrostatic field of frameworks.⁴⁸ Cation species would have influence on the adsorption of CO₂. The effect of a cation is complicated. In some reports, it was claimed that the enhancement of CO₂ adsorption after introducing alkaline metal ions is due to increase in the basicity of the material.⁴⁸ In other reports, this was ascribed to alkaline metal ions with high positive atomic partial charge, which strongly interacted with CO₂.⁴⁹

In the present study, partial atomic charges of Na-Mo-Zn oxide and NH₄-Mo-Zn oxide were analyzed by DFT calculations, and the results are shown in Tables S8 and S9.† Frameworks of the materials were covered with oxygen atoms that were all negatively charged. Counteranions such as protons and Na⁺ in the material were positively charged. This framework would display an electrostatic field, and therefore CO₂ would have stronger electrostatic interactions than CH₄ with the framework. Furthermore, the atomic charge of Na⁺ was much higher than that of protons in the material, indicating stronger interactions between Na⁺ and CO₂.

Monte Carlo simulation. A primitive cell of Cal-Na-Mo-Zn oxide contained 2 POM units of [ZnMo₁₂O₄₀] with 2 cages, 23 protons and 3 Na⁺. Assuming that Na⁺ were located in two cages of the material, one cage contains two Na⁺ (cage A) and

another cage contains the other Na⁺ (cage B) (Fig. 6a). Monte Carlo simulation was performed on Cal-Na-Mo-Zn oxide to estimate affinity of CO₂ with Na⁺. CO₂ was loaded one by one during the simulation. It was found that the first CO₂ was located in cage A and the second CO₂ was located in cage B (Fig. 6b and c). In cage A, these two Na ions were bridged by CO₂ in a μ - η^1 - η^1 fashion, as shown in Fig. 6b and c. The distance between the Na⁺ and the carbon atoms of CO₂ was calculated to be 2.35 Å, indicating that CO₂ strongly interacted with Na⁺ in cage A. Adsorption energies estimated by Monte Carlo simulation for CO₂ in cage A (Fig. 6b) and CO₂ in cage B (Fig. 6c) were 53 and 41 kJ mol⁻¹, respectively. The results of calculation were consistent with the observed trend of adsorption enthalpy of CO₂ in the material. In the case of CH₄, it was first filled in cage B, because cage B had more space and CH₄ had weak electrostatic interactions with Na⁺ (Fig. 6d and e). The adsorption energy from Monte Carlo simulation for CH₄ in both sites was 24 kJ mol⁻¹, also indicating that CH₄ would weakly interact with Na⁺.

Co-adsorption and separation experiments. CO₂ exists widely in landfill gas. CO₂ selective adsorption from a CO₂/CH₄ mixture is of great importance for improvement of gas quality. Co-adsorption experiments were carried out on Cal-Na-Mo-Zn

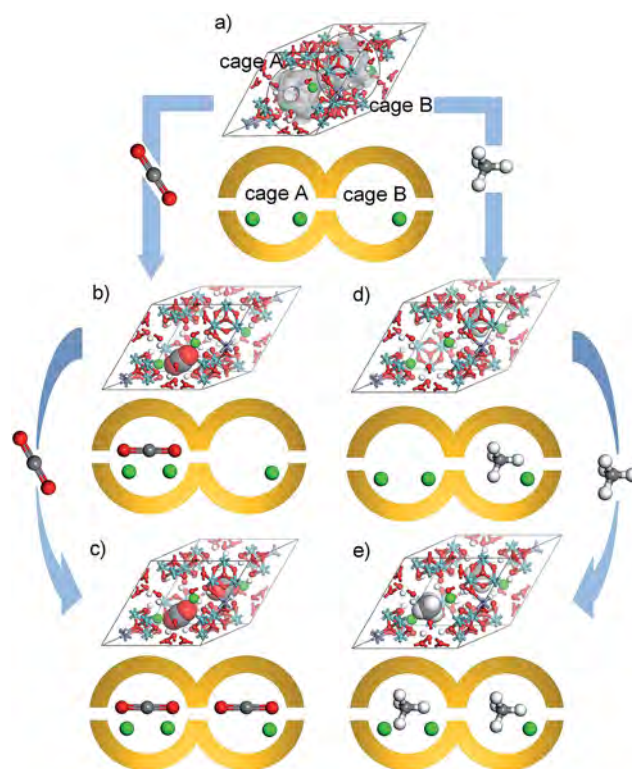


Fig. 6 Representations of adsorbed structures of Cal-Na-Mo-Zn oxide from Monte Carlo simulation – upper: ball-and-stick representations and lower: schematic representations. (a) Primitive cell with cage A and cage B, (b) Cal-Na-Mo-Zn oxide adsorbed first CO₂, (c) Cal-Na-Mo-Zn oxide adsorbed second CO₂, (d) Cal-Na-Mo-Zn oxide adsorbed first CH₄, and (e) Cal-Na-Mo-Zn oxide adsorbed second CH₄ – blue sphere: Mo, purple sphere: Zn, red sphere: O, white sphere: H, gray sphere: C, and green sphere: Na.

oxide and Cal-NH₄-Mo-Zn oxide under both high pressures (125.2 and 127.5 kPa of equilibrium total pressures) and low pressures (1.5 and 1.6 kPa of equilibrium total pressures) at 298 K. The initial ratio of CO₂ and CH₄ was 40 : 60, a typical composition of biogas.⁵⁰ According to the individual adsorption isotherms, in the low pressure range, the materials might show high separation efficiency of CO₂.

Equilibrium total pressure, total adsorbed amount, CO₂ and CH₄ partial pressures, and CO₂ and CH₄ adsorbed amounts are shown in Fig. 7. Under high pressure conditions, both materials adsorbed more CO₂ than CH₄. When the materials continued to be left under mixed gas pressure, they further adsorbed CO₂, while CH₄ desorbed from the materials (Fig. 7a and b), indicating that adsorbed CH₄ was partly replaced by CO₂. Moreover, Cal-Na-Mo-Zn oxide (15 cm³ g⁻¹ at the fifth co-sorption equilibrium) tended to adsorb more CO₂ than did Cal-NH₄-Mo-Zn oxide (11 cm³ g⁻¹ at the fifth co-sorption equilibrium). Under low pressure conditions, the two materials adsorbed similar amounts of CO₂ and CH₄. With prolongation of the adsorption process, Cal-Na-Mo-Zn oxide

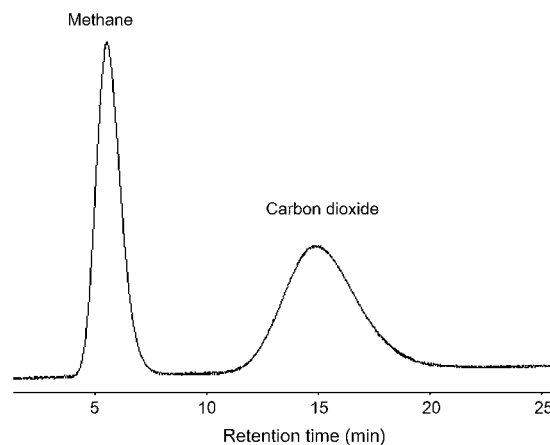


Fig. 8 Gas chromatograms of a gas mixture of CO₂ and CH₄ separated on a column of Cal-Na-Mo-Zn oxide.

further adsorbed CO₂ and concurrently desorbed CH₄, while Cal-NH₄-Mo-Zn oxide adsorbed both CH₄ and CO₂ (Fig. 7c and d).

CO₂ selectivity of the final equilibrium (5th equilibrium data in Fig. 7) for the material was calculated and is summarized in Table 2. Cal-Na-Mo-Zn oxide showed higher selectivity to CO₂ adsorption than that of Cal-NH₄-Mo-Zn oxide under both high and low pressure conditions. Co-sorption experiments demonstrated that Cal-Na-Mo-Zn oxide had better performance of CO₂ separation than that of Cal-NH₄-Mo-Zn oxide.

Table S10† summarizes the performance of different adsorbents, such as zeolites, MOF materials, and other porous materials, for CO₂ selective adsorption from a CO₂/CH₄ mixture. CO₂ selectivity of Cal-Na-Mo-Zn oxide was higher than that of the reported materials in Table S10,† which indicated that Cal-Na-Mo-Zn oxide was a good candidate for CO₂ selective adsorption and separation.

Furthermore, Cal-Na-Mo-Zn oxide was successfully applied to GC separation of CO₂ from a CO₂/CH₄ mixture. The gas mixture (CO₂ : CH₄ = 1 : 1) was injected into a gas chromatograph equipped with a column filled with Na-Mo-Zn oxide. As shown in Fig. 8, CH₄ and CO₂ were separated within a few minutes at 363 K. The peak of CO₂ appeared slower and was broader than that of CH₄, indicating that the material had stronger interactions with CO₂ than with CH₄.

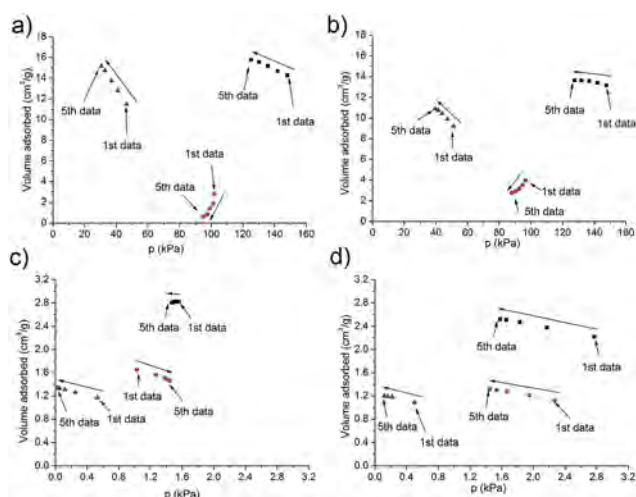


Fig. 7 CO₂/CH₄ co-sorption results of (a) Cal-Na-Mo-Zn oxide at high pressure, (b) Cal-NH₄-Mo-Zn oxide at high pressure, (c) Cal-Na-Mo-Zn oxide at low pressure, and (d) Cal-NH₄-Mo-Zn oxide at low pressure – black square: system total pressure (x-axis) and adsorbed amount (y-axis), red cycle: CH₄ partial pressure (x-axis) and adsorbed amount (y-axis), and blue triangle: CO₂ partial pressure (x-axis) and adsorbed amount (y-axis).

Table 2 CO₂/CH₄ co-sorption in the materials^a

Entry	Material	p_c^b (kPa)	Ratio in gas phase (%)		Ratio in adsorbed phase (%)		CO ₂ selectivity
			CO ₂	CH ₄	CO ₂	CH ₄	
1	Cal-Na-Mo-Zn oxide	1.5	1.70	98.3	47.4	52.6	52
2	Cal-Na-Mo-Zn oxide	125.2	24.4	75.6	96.0	4.0	75
3	Cal-NH ₄ -Mo-Zn oxide	1.6	7.80	92.2	47.7	52.3	11
4	Cal-NH ₄ -Mo-Zn oxide	127.5	31.0	69.0	79.8	20.2	9

^a These are 5th equilibrium data. ^b p_c denotes the equilibrium total pressure.

Conclusion

The materials of Ca–Na–Mo–Zn oxide and Ca–NH₄–Mo–Zn oxide adsorbed small molecules including CO₂, C₂H₆, and CH₄. Both oxides selectively adsorbed CO₂ from the CO₂/CH₄ mixture, because the materials showed higher adsorption capacity of CO₂ than that of CH₄. Ca–Na–Mo–Zn oxide showed stronger interactions with CO₂ than Ca–NH₄–Mo–Zn oxide did, while both oxides showed similar interactions with CH₄. Co-sorption experiments showed that selectivity of CO₂ on Na–Mo–Zn oxide was higher than that on Ca–NH₄–Mo–Zn oxide. Ca–Na–Mo–Zn oxide was applied to GC separation, and CO₂ could be efficiently separated from the CO₂/CH₄ mixture by using the material.

Acknowledgements

This work was financially supported by a Grant-in-Aid for Scientific Research (A) (grant no. 2324-6135) from the Ministry of Education, Culture, Sports, Science, and Technology, Japan. M.S. thanks PRESTO, JST and Nippon Sheet Glass Foundation for Materials Science and Engineering (NSG Foundation) for financial support. S.N. thanks a Grant-in-Aid for Science Research from the Ministry of Education, Culture, Sports, Science and Technology, Japan (grant no. 24550068). K.Y. thanks Grants-in-Aid (grant nos 22245028 and 24109014) for Scientific Research from JSPS and MEXT and the MEXT Projects of “Integrated Research on Chemical Synthesis” and “Elements Strategy Initiative for Catalysts and Batteries”.

Notes and references

- G. Férey, C. Serre, T. Devic, G. Maurin, H. Jobic, P. L. Llewellyn, G. De Weireld, A. Vimont, M. Daturi and J.-S. Chang, *Chem. Soc. Rev.*, 2011, **40**, 550–562.
- K. Sumida, D. L. Rogow, J. a. Mason, T. M. McDonald, E. D. Bloch, Z. R. Herm, T.-H. Bae and J. R. Long, *Chem. Rev.*, 2012, **112**, 724–781.
- N. Du, H. B. Park, M. M. Dal-Cin and M. D. Guiver, *Energy Environ. Sci.*, 2012, **5**, 7306–7322.
- N. A. Khan, Z. Hasan and S. H. Jung, *J. Hazard. Mater.*, 2013, **244–245**, 444–456.
- A. M. Kierzkowska, R. Pacciani and C. R. Müller, *ChemSusChem*, 2013, **6**, 1130–1148.
- Y. Kamiya, M. Sadakane, W. Ueda and J. Reedijk, *Heteropoly Compounds in Comprehensive Inorganic Chemistry II*, ed. K. Poeppelmeier, Elsevier, Oxford, 2013, vol. 7.
- Special thematic issue on polyoxometalates. C. L. Hill, *Chem. Rev.*, 1998, **98**, 1–390.
- Special thematic issue on polyoxometalates. L. Cronin and A. Müller, *Chem. Soc. Rev.*, 2012, **41**, 7325–7648.
- D.-L. Long, R. Tsunashima and L. Cronin, *Angew. Chem., Int. Ed.*, 2010, **49**, 1736–1758.
- M. Sadakane, K. Kodato, T. Kuranishi, Y. Nodasaka, K. Sugawara, N. Sakaguchi, T. Nagai, Y. Matsui and W. Ueda, *Angew. Chem., Int. Ed.*, 2008, **47**, 2493–2496.
- M. Sadakane, K. Yamagata, K. Kodato, K. Endo, K. Toriumi, Y. Ozawa, T. Ozeki, T. Nagai, Y. Matsui, N. Sakaguchi, W. D. Pyrz, D. J. Buttrey, D. A. Blom, T. Vogt and W. Ueda, *Angew. Chem., Int. Ed.*, 2009, **48**, 3782–3786.
- M. Sadakane, N. Watanabe, T. Katou, Y. Nodasaka and W. Ueda, *Angew. Chem., Int. Ed.*, 2007, **46**, 1493–1496.
- S. G. Mitchell, C. Streb, H. N. Miras, T. Boyd, D.-L. Long and L. Cronin, *Nat. Chem.*, 2010, **2**, 308–312.
- D. Liu, Y. Lu, H.-Q. Tan, W.-L. Chen, Z.-M. Zhang, Y.-G. Li and E.-B. Wang, *Chem. Commun.*, 2013, 3673–3675.
- A. Dolbecq, C. Mellot-Draznieks, P. Mialane, J. Marrot, G. Férey and F. Sécheresse, *Eur. J. Inorg. Chem.*, 2005, 3009–3018.
- G. Férey, C. Mellot-Draznieks, C. Serre, F. Millange, J. Dutour, S. Surblé and I. Margiolaki, *Science*, 2005, **309**, 2040–2042.
- L. M. Rodriguez-Albelo, A. Rabdel Ruiz-Salvador, A. Sampieri, D. W. Lewis, A. Gomez, B. Nohra, P. Mialane, J. Marrot, F. Secheresse, C. Mellot-Draznieks, R. N. Biboum, B. Keita, L. Nadjjo and A. Dolbecq, *J. Am. Chem. Soc.*, 2009, **131**, 16078–16087.
- J. Song, Z. Luo, D. K. Britt, H. Furukawa, O. M. Yaghi, K. I. Hardcastle and C. L. Hill, *J. Am. Chem. Soc.*, 2011, **133**, 16839–16846.
- C.-Y. Sun, S.-X. Liu, D.-D. Liang, K.-Z. Shao, Y.-H. Ren and Z.-M. Su, *J. Am. Chem. Soc.*, 2009, **131**, 1883–1888.
- B. Nohra, H. El Moll, L. M. Rodriguez Albelo, P. Mialane, J. Marrot, C. Mellot-Draznieks, M. O’Keeffe, R. N. Biboum, J. Lemaire, B. Keita, L. Nadjjo and A. Dolbecq, *J. Am. Chem. Soc.*, 2011, **133**, 13363–13374.
- H. Tagami, S. Uchida and N. Mizuno, *Angew. Chem., Int. Ed.*, 2009, **48**, 6160–6164.
- S. Uchida, R. Eguchi and N. Mizuno, *Angew. Chem., Int. Ed.*, 2010, **49**, 9930–9934.
- S. Uchida, M. Hashimoto and N. Mizuno, *Angew. Chem., Int. Ed.*, 2002, **6**, 2814–2817.
- R. Eguchi, S. Uchida and N. Mizuno, *Angew. Chem., Int. Ed.*, 2012, **51**, 1635–1639.
- N. Mizuno and S. Uchida, *Chem. Lett.*, 2006, **35**, 688–693.
- S. Uchida, S. Hikichi, T. Akatsuka, T. Tanaka, R. Kawamoto, A. Lesbani, Y. Nakagawa, K. Uehara and N. Mizuno, *Chem. Mater.*, 2007, **19**, 4694–4701.
- R. Eguchi, S. Uchida and N. Mizuno, *J. Phys. Chem. C*, 2012, **116**, 16105–16110.
- Y. Ogasawara, S. Uchida and N. Mizuno, *J. Phys. Chem. C*, 2007, **6**, 8218–8227.
- S. Uchida and N. Mizuno, *J. Am. Chem. Soc.*, 2004, **6**, 1602–1603.
- Z. Zhang, M. Sadakane, T. Murayama, S. Izumi, N. Yasuda, N. Sakaguchi and W. Ueda, *Inorg. Chem.*, 2014, **53**, 903–911.
- Z. Zhang, M. Sadakane, T. Murayama and W. Ueda, *Dalton Trans.*, 2014, 13584–13590.
- Z. Zhang, M. Sadakane, T. Murayama, N. Sakaguchi and W. Ueda, *Inorg. Chem.*, 2014, **53**, 7309–7318.
- A. L. McClellan and H. F. Harnsberger, *J. Colloid Interface Sci.*, 1967, **23**, 577–599.

- 34 *Structure Determination from Powder Diffraction Data*, ed. W. I. F. David, K. Shankland, L. B. McCusker and C. Baerlocher, Oxford University Press, 2006, vol. 47.
- 35 M. A. Neumann, *J. Appl. Crystallogr.*, 2003, **36**, 356–365.
- 36 R. A. Young, *The Rietveld Method*, Oxford University Press, Oxford, 1995.
- 37 A. Boultif and D. Louer, *J. Appl. Crystallogr.*, 2004, **37**, 724–731.
- 38 L. Palatinus and G. Chapuis, *J. Appl. Crystallogr.*, 2007, **40**, 786–790.
- 39 B. Delley, *J. Chem. Phys.*, 2000, **113**, 7759–7764.
- 40 B. Delley, *J. Chem. Phys.*, 1990, **92**, 508–517.
- 41 E. D. Akten, R. Siriwardane and D. S. Sholl, *Energy Fuels*, 2003, **17**, 977–983.
- 42 T. R. Zeitler, M. D. Allendorf and A. Greathouse, *J. Phys. Chem. C*, 2012, **116**, 3492–3502.
- 43 X. Li, Z. Wang, J. Zheng, S. Shao, Y. Wang and Y. Yan, *Chin. J. Catal.*, 2011, **32**, 217–223.
- 44 S. Aguado, J. Gascón, J. C. Jansen and F. Kapteijn, *Microporous Mesoporous Mater.*, 2009, **120**, 170–176.
- 45 M. M. Dubinin, *Prog. Surf. Membr. Sci.*, 1975, **9**, 1–70.
- 46 D. M. D'Alessandro, B. Smit and J. R. Long, *Angew. Chem., Int. Ed.*, 2010, **49**, 6058–6082.
- 47 J. Zhang, N. Burke, S. Zhang, K. Liu and M. Pervukhina, *Chem. Eng. Sci.*, 2014, **113**, 54–61.
- 48 X. Xu, X. Zhao, L. Sun and X. Liu, *J. Nat. Gas Chem.*, 2008, **17**, 391–396.
- 49 A. Zúkal, J. Mayerová and J. Čejka, *Phys. Chem. Chem. Phys.*, 2010, **12**, 5240–5247.
- 50 X. Zhu, K. Li, J.-L. Liu, X.-S. Li and A.-M. Zhu, *Int. J. Hydrogen Energy*, 2014, **39**, 13902–13908.

NOTE

Anti-obesity activities of the yoshinone A and the related marine γ -pyrone compounds

Tomoyuki Koyama¹, Yoshinori Kawazoe², Arihiro Iwasaki³, Osamu Ohno³, Kiyotake Suenaga³ and Daisuke Uemura^{2,4}

The Journal of Antibiotics advance online publication, 2 March 2016; doi:10.1038/ja.2016.19

Marine cyanobacteria are known as important creators of novel natural products. From this valuable source, various bioactive compounds have been found and characterized in terms of their pharmacological and toxicological activities.¹ In the previous work, we have reported on the isolation and structure determination of potent cytotoxic compounds, lyngbyacyclamide A and B;² an inhibitor of osteoclastogenesis, biselyngbyaside;³ and a protein kinase inhibitor, bisebromoamide.⁴ In the recent work, we have reported the new marine γ -pyrones yoshinone A, B1 and B2 from *Leptolyngbya* sp., and determined their planar structures using NMR spectral analysis.⁵ Yoshinone A, as the major compound among them, showed inhibitory activity against the adipogenic differentiation of 3T3-L1 cells with an half maximal inhibitory concentration (IC₅₀) value of 420 nM without cytotoxicity (IC₅₀ > 50 μ M). On the other hand, the yoshinone B1 and B2 showed only limited activity against 3T3-L1 cells, with higher concentrations compared with yoshinone A. Further studies of the structure–activity relationship lead us to conclude that the position of a pyrone ring and an olefin in the side chain will be important for the inhibition of adipogenic differentiation. These γ -pyrones have olefins in their side chain at positions 7 and 6 in the cases of yoshinones A and B1/B2, respectively. To express the effects on adipocyte, the olefin should not be conjugated with γ -pyrone moiety, such as yoshinone A (Figure 1). In the previous studies, kalkipyronone⁶ isolated from cyanobacteria, aureothin,⁷ and actinopyrones A and B⁸ isolated from streptomyces fell into the same 7-en γ -pyrones. Then, we confirmed that kalkipyronone and aureothin showed this activity, with IC₅₀ values of 67.5 and 54.2 nM, respectively. On the basis of these data, we are focusing on the 7-en γ -pyrone (unconjugated type) compounds. These pyrones are expected to be candidates for novel lead compounds for the treatment of obesity and related diseases.⁹ Studies on useful tools that regulate adipocytes will contribute to the prevention and treatment of these diseases. At the present stage of our research,

we have evaluated the anti-obesity activities of the 7-en γ -pyrones using *in vitro* and *in vivo* experiments. In this study, we report on the interesting properties of these pyrones.

Marine cyanobacteria as sources of γ -pyrone compounds have been collected from Ishigaki and Okinawa islands, Japan, and extracted with aqueous methanol. The isolating procedures of the γ -pyrones were performed according to the original reports with minor modifications. Their purity and structures were confirmed by NMR analysis. From the collected cyanobacteria, we noted that got only a trace amount of yoshinone A (<1.0 mg) and 35.7 mg of kalkipyronone, as purified γ -pyrones for the present experiments.

As the *in vitro* experiments, the reducing effects on accumulated triglyceride (TG) in the mature 3T3-L1 adipocyte were investigated with yoshinone A. In Figure 2a, typical images of mature 3T3-L1 adipocytes stained TG with oil red O were shown. As shown in Figure 2b, TG amount in mature 3T3-L1 adipocyte-treated yoshinone A significantly decreased with the dose-dependent manner. On the other hand, a significant increase of lactate (LA) in the culture fluid was observed by yoshinone A treatment of the adipocyte, as shown in Figure 2c. These changes in TG and LA were induced with 0.1–0.01 μ M of yoshinone A with no effect on cell viability. These results revealed that the 7-en γ -pyrones showed TG reduction activities in mature 3T3-L1 adipocyte, in addition to its inhibitory activities on adipose differentiation. As the differentiation ratio in preadipocyte was evaluated with TG amount in the cells, the findings are acceptable for the previous experimental perceptions in 3T3-L1 cells.

In the following experiment, to verify whether or not the LA production is limited in 3T3-L1 cells, we have repeated the experiment with the same conditions using HeLa cells, the most widely used human cultured cells. After treatment with yoshinone A (0, 0.01 and 0.1 μ M) for 48 h, the culture fluids were supplied for HPLC analysis to

¹Department of Food Science and Technology, Graduate School of Marine Science and Technology, Tokyo University of Marine Science and Technology, Tokyo, Japan;

²Research Institute of Natural-Drug Leads, Kanagawa University, Kanagawa, Japan; ³Department of Chemistry, Keio University, Yokohama, Kanagawa, Japan and ⁴Department of Chemistry, Faculty of Science, Kanagawa University, Kanagawa, Japan

Correspondence: Dr T Koyama, Department of Food Science and Technology, Graduate School of Marine Science and Technology, Tokyo University of Marine Science and Technology, 4-5-7 Konan, Minato-ku 108-8477, Tokyo, Japan.

E-mail: ts koyama@kaiyodai.ac.jp

or Professor D Uemura, Department of Chemistry, Faculty of Science, Kanagawa University, 2946 Tsuchiya, Hiratsuka-shi, Kanagawa 259-1293, Japan.

E-mail: uemurad@kanagawa-u.ac.jp

Dedicated to Professor Amos B. Smith, III in celebration of his 50 years of contributions to the chemical sciences.

Received 30 November 2015; revised 20 January 2016; accepted 27 January 2016

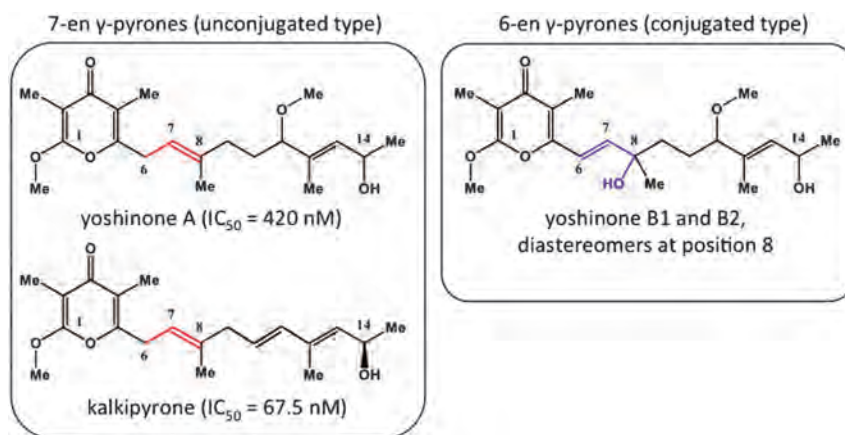


Figure 1 Chemical structures and biological activities of the two types of marine γ -pyrones. The 7-en γ -pyrone is defined as an unconjugated olefin bond (red) at 7 position in the side chain such as yoshinone A and kalkipyronone, and the 6-en γ -pyrone is defined as a conjugated olefin bond (blue) at 6 position in the side chain such as yoshinone B1 and B2. Inhibitory activities against adipogenic differentiation in 3T3-L1 cells were expressed as half maximal inhibitory concentration (IC_{50}) values in the parenthesis. The yoshinone B1 and B2 showed only moderate inhibition even at $5\ \mu\text{M}$.

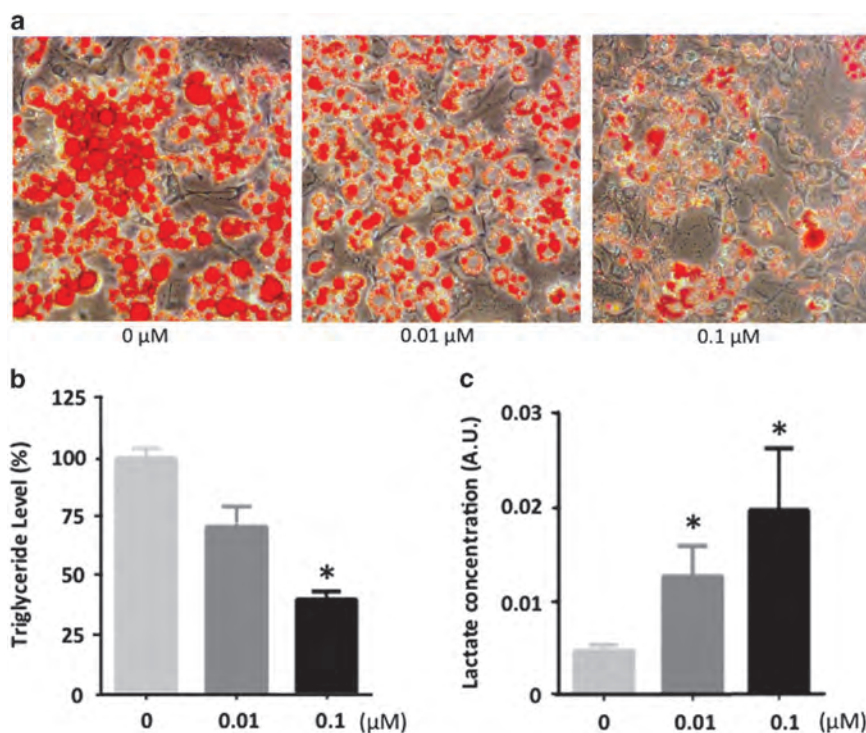


Figure 2 The decrease of accumulated triglyceride in 3T3-L1 cells and enhancement of lactate contents in culture fluid treated with yoshinone A (0, 0.01 and 0.1 μM). The mature 3T3-L1 adipocytes were treated with yoshinone A for 7 days. Typical adipocytes were stained with oil red O (a), the % of triglyceride level in the cells (b) and lactate concentration in the culture fluid after 48 h (c) were shown. Data are presented as the mean \pm s.d. for triplicate samples. * $P < 0.05$ vs control (0 μM).

determined LA and glucose (Glc) concentrations. As shown in Supplementary Figure 1, the enhancement of LA production and Glc consumption were observed clearly with dose-dependent manner of yoshinone A even in HeLa cells without cytotoxicities. These results suggested that yoshinone A induced energy metabolic changes relating to Glc via relatively common pathway in cells. On the basis of these *in vitro* experiments, the induced changes in metabolism will affect the utilization of accumulated TG in mature 3T3-L1 adipocyte with direct or indirect pathway(s). Due to a deficiency of these marine γ -pyrones, further experiments to analyze the mechanism in detail are still needed at this stage.

As with the *in vivo* experiments, kalkipyronone as a 7-en γ -pyrone was provided to the experiment with a small preliminary sample size. To confirm the anti-obesity activity *in vivo*, we performed two experiments as described below.

The IC_{50} value of kalkipyronone was reported as 120 nM in HeLa cells,⁵ but there are no information about the toxicity *in vivo*. In the first experiment using mice, the evaluation for acute toxicity of kalkipyronone with oral administration was determined. Male ddY mice (5 weeks old) were divided into three groups ($n = 3$ each); they received 16.5 and 5.5 mg kg^{-1} per day of kalkipyronone, and vehicle (3% dimethyl sulfoxide solution) orally for 3 days. The physical

measurements, autopsy findings and behavior observations did not indicate a difference among these groups during 7 days from first ingestion. Then, we planned a long-period treatment test in mice with a dosage of 5 mg kg^{-1} per day of kalkipyronone.

For the second experiment *in vivo*, the anti-obesity effects of kalkipyronone *in vivo* were examined by feeding mice a high-fat diet (HFD) for 5 weeks. Mice were fed a normal diet (ND, $n=6$), a HFD ($n=6$) and HFD with oral ingestion of kalkipyronone at a dosage of 5 mg kg^{-1} per day (HFD+KAL, $n=3$) during the experiment. The transitional changes of body weight gain, food intake and water intake of the groups are shown in Supplementary Figure 2. After the experimental period, measured parameters were summarized in Table 1. The body weights of mice in the ND and HFD groups showed significant differences, with the values of 39.5 ± 0.2 and 43.4 ± 0.7 g, respectively. The HFD+KAL group (40.6 ± 2.8 g) exhibited pronounced suppressed body weight gain, but no significant differences, owing to the limited sample size for the experiment. Meanwhile, the weight of adipose tissue was significantly suppressed ($P < 0.05$) with the kalkipyronone treatment: 0.93 ± 0.23 g in the HFD+KAL group vs 1.62 ± 0.15 g in the HFD group. The other tissues' weight did not show significant changes with kalkipyronone treatment (Supplementary Figure 3). These results suggest that oral ingestion of kalkipyronone is effective for suppressing adipose tissue weight gain in mice.

As food intake during the experimental period in the HFD (227.9 ± 19.3 g per head) and HFD+KAL (212.8 ± 31.3 g per head) groups were similar, the suppression of adipose tissue gain was not affected by food consumption or appetite in mice. Another main possible mechanism for anti-obesity is the inhibition of TG absorption in the small intestine. For example, orlistat, a lipase inhibitor in clinical use,¹⁰ suppresses the weight gain *in vivo* to avoid absorption of TG from small intestine. Also, tea polyphenol reduces fat absorption by decreasing emulsification,¹¹ and hot-water extract of *Houttuynia cordata* suppressed adipose tissue weight gain in mice by inhibiting the

absorption of fatty acids and glycerol.¹² These suppressive effects on TG absorption will result in the intact TG undergoing a transition to feces, accompanied increasing fecal TG levels. However, fecal TG in the HFD+KAL group ($43.6 \pm 6.0 \text{ mg g}^{-1}$) was not increased, as compared with that in the HFD group ($41.3 \pm 7.4 \text{ mg g}^{-1}$). Thus, it was suggested that the suppression of adipose tissue gain by kalkipyronone treatment is caused by consumption and/or excretion of absorbed TG in the body.

Some changes in plasma parameters were induced by the treatment of kalkipyronone in mice for 5 weeks. As shown in Table 1, the parameter relating to lipid metabolism (TG, total cholesterol and non-esterified fatty acid) in the HFD+KAL group did not show significant differences against those of the HFD group. On the other hand, the Glc level ($155.1 \pm 28.2 \text{ mg dl}^{-1}$) was relatively higher than that of the HFD group ($135.7 \pm 16.6 \text{ mg dl}^{-1}$), and the plasma LA level ($95.4 \pm 2.4 \text{ mg dl}^{-1}$) in the HFD+KAL group was significantly increased ($P < 0.05$) when compared with that of the HFD group ($68.8 \pm 6.1 \text{ mg dl}^{-1}$). These characteristic changes in plasma LA levels and adipose tissue are supported by the results of the *in vitro* experiments with yoshinone A, as described above. Incidentally, the enhancement of LA production will have the potential for causing the physiological problem by lactic acidosis, but our autopsy studies and behavior observations did not find any abnormal changing and health hazard in the kalkipyronone-treated mice during experiment for 5 weeks. In the near future, further studies including physiological pH monitoring will elucidate that there are no adverse impact by elevated blood lactic level induced by these γ -pyrone treatment in mice.

To summarize, anti-obesity activities of the 7-en γ -pyrone have been shown in experiments in both cultivated cells and in mice. In the mature 3T3-L1 adipocytes, the reducing effects of yoshinone A on accumulated TG amounts accompanied with the enhancement of LA production in the culture fluid were observed *in vitro*. In the HFD feeding mice, the suppressive effects of orally ingested kalkipyronone on adipose tissue weight gain for 5 weeks was accompanied with an enhancement of plasma LA level *in vivo*. On the basis of these preliminary results, it was suggested that the 7-en γ -pyrone expresses an anti-obesity effect *in vivo* with oral administration, and the enhancement of LA production will be a key phenomenon in the reduction of accumulated TG in adipocytes. LA is a major end product of Glc metabolism by the glycolytic system in the cytosol, but, as usual, the citric acid cycle in the mitochondria suppresses LA production by the consumption of Glc metabolites to produce energy. Ubiquinone distributing in the mitochondrial inner membrane has an important role in the mitochondrial respiratory chain, mediating electron transport between NADH and succinate dehydrogenase, and the cytochrome system.¹³ The molecule of ubiquinone contains unconjugated olefin with a quinone ring similar to the 7-en γ -pyrone, such as yoshinone A. We speculate that this unconjugated type of pyrone acts as a mimic of ubiquinone in the mitochondrial membrane to suppress functions, including the citric acid cycle. As a result, yoshinone A induced the accumulation of LA produced as a metabolite from the glycolytic system, and promoted fat utilization by compensating for the deficient energy supplying *in vitro* and *in vivo*. These speculations about bioactivities of the 7-en γ -pyrone have been not yet established due to a lack of supply of these compounds from natural sources. We are currently synthesizing the yoshinopyrones to determine their stereochemistries and to elucidate their detailed activity via further experiments *in vitro* and *in vivo*.

Table 1 Effects of kalkipyronone on high-fat diet received mice for 5 weeks

Measured parameter	Experimental groups		
	ND (n = 6)	HFD (n = 6)	HFD+KAL (n = 3)
Body weight (g)	39.5 ± 0.2	43.4 ± 0.7	40.6 ± 2.8
Food intake (g) ^a	168.2 ± 4.1	227.9 ± 19.3	212.8 ± 31.3
Water intake (g) ^a	205.1 ± 7.1	192.0 ± 9.5	194.3 ± 14.7
Adipose tissue (g)	1.01 ± 0.12	1.62 ± 0.15	$0.93 \pm 0.23^*$
Liver (g)	1.31 ± 0.03	1.41 ± 0.07	1.35 ± 0.11
Hepatic TG (mg g^{-1} liver)	38.2 ± 6.0	41.3 ± 5.7	34.7 ± 5.8
Feces (g) ^b	1.4 ± 0.2	2.5 ± 0.6	1.8 ± 0.2
Fecal TG (mg g^{-1} feces)	9.8 ± 0.2	41.3 ± 7.4	43.6 ± 6.0
Plasma Glc (mg dl^{-1})	133.4 ± 13.7	135.7 ± 16.6	155.1 ± 28.2
Plasma LA (mg dl^{-1})	65.6 ± 6.1	68.8 ± 6.1	$95.4 \pm 2.4^*$
Plasma TG (mg dl^{-1})	134.5 ± 34.5	132.1 ± 25.5	88.0 ± 16.1
Plasma TC (mg dl^{-1})	159.3 ± 18.3	141.2 ± 22.0	130.0 ± 31.5
Plasma NEFA (mEq l^{-1})	0.88 ± 0.17	0.74 ± 0.06	0.70 ± 0.10

Abbreviations: ANOVA, analysis of variance; Glc, glucose; HFD, high-fat diet; HFD+KAL, high-fat diet with kalkipyronone (5 mg kg^{-1} per day per os); LA, lactate; ND, normal diet; NEFA, non-esterified fatty acid; TC, total cholesterol; TG, triglyceride.

^aAccumulated values during experiments.

^bTotal values for 3 days.

* $P < 0.05$ vs HFD.

Data are presented as the mean \pm s.e. and analyzed by ANOVA followed by Dunnett's test.

EXPERIMENTAL PROCEDURE

In vitro experiments in 3T3-L1 adipocyte

The reducing effect of yoshinone A on accumulated TG in adipocytes was evaluated using 3T3-L1 cells after differentiation. The murine preadipocyte 3T3-L1 cells (Riken BRC, Tsukuba, Japan) were cultured in Dulbecco's modified Eagle's medium (Gibco, Thermo Fisher Scientific, Inc., Waltham, MA, USA) supplemented with 10% fetal bovine serum (Gibco) in two 96-well plates at 37 °C, 5% CO₂. Two days after confluence, the differentiation was induced by Dulbecco's modified Eagle's medium containing 10% fetal bovine serum, 0.5 mM of 3-isobutyl-1-methylxanthine, 0.25 μ M of dexamethasone each from Wako Pure Chemical Industries, Ltd. (Osaka, Japan) and 10 μ g ml⁻¹ insulin (Gibco) for 7 days.

The differentiated 3T3-L1 adipocytes in a 96-well plate were treated with 2% Triton-X 100 for 30 min at room temperature followed by sonication. Accumulated TG amounts and cell viability were evaluated referring to the method with by Inuzuka *et al.*⁵

Anti-obesity test in mice

Male ddY mice were obtained from Japan SLC, Inc. (Shizuoka, Japan). They were housed in individual cages under a 12-h/12-h light/dark cycle (lights from 0800 to 2000 hours) in a room with controlled temperature and humidity (25 \pm 1 °C and 60 \pm 5%, respectively). For the experiment, we formulated experimental diets based on the AIN-93M diet.¹⁴ To mimic a westernized diet rich in animal fat, we used HFD-60 (Oriental Yeast Co., Ltd., Tokyo, Japan) including lard as fat (62.2 kcal%) in the experimental HFDs. Male mice (5 weeks old) were fed a ND for 1 week and then divided into the following three groups: ND ($n=6$); HFD ($n=6$); and HFD+KAL ($n=3$). Kalkipyron (5 mg kg⁻¹ per day) was administered orally to the mice fed a HFD (HFD +KAL group). Other mice received vehicle (10 ml kg⁻¹ per day) orally. Body weight, food intake and drinking water were measured every days. After the mice were fed these diets for 5 weeks. The feces were collected for the last 3 days and dried to weigh. The mice were killed by anesthetic overdose with isoflurane. And then, blood was collected from the abdominal vein to prepare plasma, and the epididymal adipose tissue and liver were dissected and weighed. The TG in the liver and feces were extracted with methanol–chloroform solution following homogenization. The plasma TG, total cholesterol, non-esterified fatty acid, Glc and LA levels were measured using the commercially clinical assay kit (Wako Pure Chemical Industries, Ltd.) for each. Data were presented as mean \pm s.e. and analyzed by one-way analysis of variance and the Dunnett's test. Differences between groups were considered to be statistically significant at $P < 0.05$.

Animal studies were performed in accordance with notification number 88 of the Ministry of the Environment, Japan, (2006) and the Guidelines for Animal Experimentation of the Tokyo University of Marine Science and Technology, with the approval of the Animal Care and Use Committee of the Tokyo University of Marine Science and Technology.

CONFLICT OF INTEREST

The authors declare no conflict of interest.

ACKNOWLEDGEMENTS

This study was supported in part by grant-in-aid for Scientific Research from JSPS (25350963 to TK, 24310160 to KS, 24510316 to YK, 25242069 to DU). We are indebted to the Uehara Memorial Foundation (DU) to financial support.

- 1 Nagarajan, M., Maruthanayagam, V. & Sundararaman, M. A review of pharmacological and toxicological potentials of marine cyanobacterial metabolites. *J. Appl. Toxicol.* **32**, 153–185 (2012).
- 2 Maru, N., Ohno, O. & Uemura, D. Lyngbyacyclamide A and B, novel cytotoxic peptides from marine cyanobacteria *Lyngbya* sp. *Tetrahedron Lett.* **51**, 6384–6387 (2010).
- 3 Yonezawa, T. *et al.* Biselyngbyaside, isolated from marine cyanobacteria, inhibits osteoclastogenesis and induces apoptosis in mature osteoclasts. *J. Cell Biochem.* **113**, 440–448 (2012).
- 4 Teruya, T., Sasaki, H., Fukazawa, H. & Suenaga, K. Bisebromoamide, a potent cytotoxic peptide from the marine Cyanobacterium *Lyngbya* sp.: isolation, stereostructure, and biological activity. *Org. Lett.* **11**, 5062–5065 (2009).
- 5 Inuzuka, T. *et al.* An inhibitor of the adipogenic differentiation of 3T3-L1 cells, yoshinone A, and its analogs, isolated from the marine cyanobacterium *Leptolyngbya* sp. *Tetrahedron Lett.* **55**, 6711–6714 (2014).
- 6 Graber, M. A. & Gerwick, W. H. Kalkipyron, a toxic γ -pyrone from an assemblage of the marine cyanobacteria. *Lyngbya majuscula* and *Tolypothrix* sp. *J. Nat. Products* **61**, 677–680 (1998).
- 7 Hirata, Y., Nakata, H., Yamada, K., Okuhara, K. & Naito, T. The structure of aureothin, a nitro compound obtained from *Streptomyces thioluteus*. *Tetrahedron* **14**, 252–274 (1961).
- 8 Yano, K. *et al.* Actinopyrones A, B and C, new physiologically active substances. II. Physico-chemical properties and chemical structures. *J. Antibiotics* **39**, 38–43 (1986).
- 9 Kahn, S. E., Hull, R. L. & Utzschneider, K. M. Mechanisms linking obesity to insulin resistance and type 2 diabetes. *Nature* **444**, 840–846 (2006).
- 10 Heck, A. M., Yanovski, J. A. & Calis, K. A. Orlistat, a new lipase inhibitor for the management of obesity. *Pharmacotherapy* **20**, 270–279 (2000).
- 11 Shishikura, Y., Khokhar, S. & Murray, B.S. Effects of tea polyphenols on emulsification of olive oil in a small intestine model system. *J. Agric. Food Chem.* **54**, 1906–1913 (2006).
- 12 Miyata, M., Koyama, T. & Yazawa, K. Water extract of *Houttuynia cordata* Thunb. leaves exerts anti-obesity effects by inhibiting fatty acid and glycerol absorption. *J. Nutr. Sci. Vitaminol.* **56**, 150–156 (2010).
- 13 Ernster, L. & Dallner, G. Biochemical, physiological and medical aspects of ubiquinone function. *Biochim. Biophys. Acta.* **1271**, 195–204 (1995).
- 14 Reeves, P. G. Components of the AIN-93 diets as improvements in the AIN-76A diet. *J. Nutr.* **127**, 838S–841S (1997).

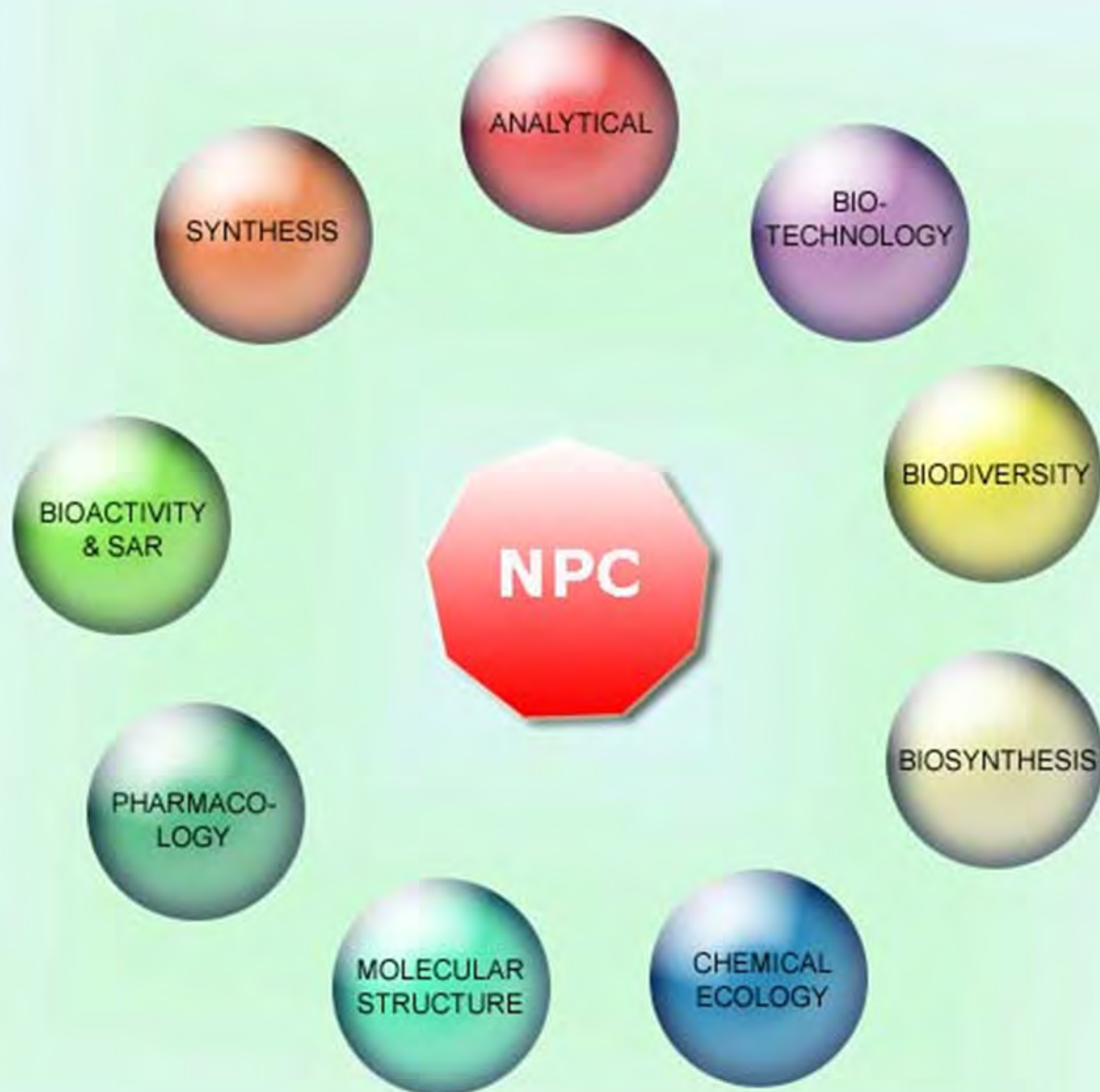


This work is licensed under a Creative Commons Attribution-NonCommercial-ShareAlike 4.0 International License. The images or other third party material in this article are included in the article's Creative Commons license, unless indicated otherwise in the credit line; if the material is not included under the Creative Commons license, users will need to obtain permission from the license holder to reproduce the material. To view a copy of this license, visit <http://creativecommons.org/licenses/by-nc-sa/4.0/>

Supplementary Information accompanies the paper on The Journal of Antibiotics website (<http://www.nature.com/ja>)

NATURAL PRODUCT COMMUNICATIONS

An International Journal for Communications and Reviews Covering all
Aspects of Natural Products Research



Volume 10. Issue 8. Pages 1333-1494. 2015
ISSN 1934-578X (printed); ISSN 1555-9475 (online)
www.naturalproduct.us

EDITOR-IN-CHIEF**DR. PAWAN K AGRAWAL**

Natural Product Inc.
7963, Anderson Park Lane,
Westerville, Ohio 43081, USA
agrawal@naturalproduct.us

EDITORS**PROFESSOR ALEJANDRO F. BARRERO**

Department of Organic Chemistry,
University of Granada,
Campus de Fuente Nueva, s/n, 18071, Granada, Spain
afbarre@ugr.es

PROFESSOR ALESSANDRA BRACA

Dipartimento di Chimica Bioorganica e Biofarmacia,
Universita di Pisa,
via Bonanno 33, 56126 Pisa, Italy
braca@farm.unipi.it

PROFESSOR DE-AN GUO

State Key Laboratory of Natural and Biomimetic Drugs,
School of Pharmaceutical Sciences,
Peking University,
Beijing 100083, China
gda5958@163.com

PROFESSOR YOSHIHIRO MIMAKI

School of Pharmacy,
Tokyo University of Pharmacy and Life Sciences,
Horinouchi 1432-1, Hachioji, Tokyo 192-0392, Japan
mimakiy@ps.toyaku.ac.jp

PROFESSOR STEPHEN G. PYNE

Department of Chemistry
University of Wollongong
Wollongong, New South Wales, 2522, Australia
spyne@uow.edu.au

PROFESSOR MANFRED G. REINECKE

Department of Chemistry,
Texas Christian University,
Forts Worth, TX 76129, USA
m.reinecke@tcu.edu

PROFESSOR WILLIAM N. SETZER

Department of Chemistry
The University of Alabama in Huntsville
Huntsville, AL 35809, USA
wsetzer@chemistry.uah.edu

PROFESSOR YASUHIRO TEZUKA

Faculty of Pharmaceutical Sciences
Hokuriku University
Ho-3 Kanagawa-machi, Kanazawa 920-1181, Japan
y-tezuka@hokuriku-u.ac.jp

PROFESSOR DAVID E. THURSTON

Department of Pharmacy and Forensic Science,
King's College London,
Britannia House, 7 Trinity Street,
London SE1 1DB, UK
david.thurston@kcl.ac.uk

HONORARY EDITOR**PROFESSOR GERALD BLUNDEN**

The School of Pharmacy & Biomedical Sciences,
University of Portsmouth,
Portsmouth, PO1 2DT U.K.
axuf64@dsl.pipex.com

ADVISORY BOARD

Prof. Viqar Uddin Ahmad
Karachi, Pakistan

Prof. Giovanni Appendino
Novara, Italy

Prof. Yoshinori Asakawa
Tokushima, Japan

Prof. Roberto G. S. Berlinck
São Carlos, Brazil

Prof. Anna R. Bilia
Florence, Italy

Prof. Maurizio Bruno
Palermo, Italy

Prof. César A. N. Catalán
Tucumán, Argentina

Prof. Josep Coll
Barcelona, Spain

Prof. Geoffrey Cordell
Chicago, IL, USA

Prof. Fatih Demirci
Eskişehir, Turkey

Prof. Ana Cristina Figueiredo
Lisbon, Portugal

Prof. Cristina Gracia-Viguera
Murcia, Spain

Dr. Christopher Gray
Saint John, NB, Canada

Prof. Dominique Guillaume
Reims, France

Prof. Duvvuru Gunasekar
Tirupati, India

Prof. Hisahiro Hagiwara
Niigata, Japan

Prof. Tsukasa Iwashina
Tsukuba, Japan

Prof. Leopold Jirovetz
Vienna, Austria

Prof. Vladimir I Kalinin
Vladivostok, Russia

Prof. Phan Van Kiem
Hanoi, Vietnam

Prof. Niel A. Koorbanally
Durban, South Africa

Prof. Chiaki Kuroda
Tokyo, Japan

Prof. Hartmut Laatsch
Göttingen, Germany

Prof. Marie Lacaille-Dubois
Dijon, France

Prof. Shoen-Sheng Lee
Taipei, Taiwan

Prof. Imre Mathe
Szeged, Hungary

Prof. M. Soledade C. Pedras
Saskatoon, Canada

Prof. Luc Pieters
Antwerp, Belgium

Prof. Peter Proksch
Düsseldorf, Germany

Prof. Phila Raharivelomanana
Tahiti, French Polynesia

Prof. Luca Rastrelli
Fisciano, Italy

Prof. Stefano Serra
Milano, Italy

Prof. Monique Simmonds
Richmond, UK

Dr. Bikram Singh
Palampur, India

Prof. John L. Sorensen
Manitoba, Canada

Prof. Johannes van Staden
Scottsville, South Africa

Prof. Valentin Stonik
Vladivostok, Russia

Prof. Winston F. Tinto
Barbados, West Indies

Prof. Sylvia Urban
Melbourne, Australia

Prof. Karen Valant-Vetschera
Vienna, Austria

INFORMATION FOR AUTHORS

Full details of how to submit a manuscript for publication in Natural Product Communications are given in Information for Authors on our Web site <http://www.naturalproduct.us>.

Authors may reproduce/republish portions of their published contribution without seeking permission from NPC, provided that any such republication is accompanied by an acknowledgment (original citation)-Reproduced by permission of Natural Product Communications. Any unauthorized reproduction, transmission or storage may result in either civil or criminal liability.

The publication of each of the articles contained herein is protected by copyright. Except as allowed under national "fair use" laws, copying is not permitted by any means or for any purpose, such as for distribution to any third party (whether by sale, loan, gift, or otherwise); as agent (express or implied) of any third party; for purposes of advertising or promotion; or to create collective or derivative works. Such permission requests, or other inquiries, should be addressed to the Natural Product Inc. (NPI). A photocopy license is available from the NPI for institutional subscribers that need to make multiple copies of single articles for internal study or research purposes.

To Subscribe: Natural Product Communications is a journal published monthly. 2015 subscription price: US\$2,595 (Print, ISSN# 1934-578X); US\$2,595 (Web edition, ISSN# 1555-9475); US\$2,995 (Print + single site online); US\$595 (Personal online). Orders should be addressed to Subscription Department, Natural Product Communications, Natural Product Inc., 7963 Anderson Park Lane, Westerville, Ohio 43081, USA. Subscriptions are renewed on an annual basis. Claims for nonreceipt of issues will be honored if made within three months of publication of the issue. All issues are dispatched by airmail throughout the world, excluding the USA and Canada.

Isolation of Monovalerianester A, an Inhibitor of Fat Accumulation, from *Valeriana fauriei*

Keiji Yuki^a, Mariko Ikeda^a, Shosuke Yoshida^a, Osamu Ohno^b, Kiyotake Suenaga^b, Kaoru Yamada^c, Daisuke Uemura^c and Kenji Miyamoto^{a,*}

^aDepartment of Biosciences and Informatics, Keio University, 3-14-1 Hiyoshi, Yokohama, 223-8522, Japan

^bDepartment of Chemistry, Keio University, 3-14-1 Hiyoshi, Yokohama, 223-8522, Japan

^cDepartment of Chemistry, Kanagawa University, 2946 Tsuchiya, Hiratsuka, 256-1293, Japan

kmiyamoto@bio.keio.ac.jp

Received: April 1st, 2015; Accepted: May 1st, 2015

The rhizomes and roots of *Valeriana fauriei* were extracted with 80% aqueous ethanol. This extract was found to exhibit potent inhibitory effects on fat accumulation in 3T3-L1 murine adipocytes. After several steps of chromatographic purification, we succeeded in identifying monovalerianester A as an inhibitor of fat accumulation. Thus, monovalerianester A and the crude extract of the rhizomes and roots of *V. fauriei* may have therapeutic potential for the treatment of obesity.

Keywords: *Valeriana fauriei*, Monovalerianester A, 3T3-L1 murine adipocytes, Inhibitor, Fat accumulation.

Lifestyle-related diseases such as cancer, cardiovascular disease, hypertension, hyperlipidemia, and diabetes are rapidly growing epidemics in developed countries. Obesity is a contributing factor of these diseases [1]. In Japan, the Ministry of Health, Labor and Welfare report that 30% of men and 20% of women are overweight and the number of obese men has increased. Although many anti-obesity initiatives such as aerobic exercise have been proposed, we have focused on finding inhibitors of fat accumulation because they could be applied to the development of anti-obesity drugs.

In our previous study, we screened various sources for inhibitors of fat accumulation. We found that a mushroom, *Coriolus versicolor*, and a plant, *Valeriana fauriei*, exhibited potent inhibition of fat accumulation in 3T3-L1 murine adipocytes. A highly *N*-methylated cyclic heptapeptide, (-)-ternatin, was successfully isolated from *C. versicolor* as a novel inhibitor of fat accumulation [2-4]. *V. fauriei*, a Chinese herbal medicine, is used to treat hysteroepilepsy and cardiac palpitation. The clinical effects are mediated by terpenoid glycosides such as kessoglycol diacetate and kessoglycol β -monoacetate [5, 6]. A novel iridoid glycoside and a sesquiterpenoid isolated from *V. fauriei* showed NGF-potentiating activity [7]. We previously isolated 9-hydroxy-10*E*,12*Z*-octadecadienoic acid (9-HODE) from *V. fauriei* as an inhibitor of fat accumulation [8]. In addition, other active fractions were found in extracts from *V. fauriei*. Here we report the isolation and identification of an inhibitor of fat accumulation other than 9-HODE from *V. fauriei*. To isolate fat accumulation inhibitors, we applied an assay system using 3T3-L1 murine adipocytes, as described previously [2]. To determine the amount of triglycerides in 3T3-L1 cells, LabAssayTM Triglyceride (Wako Pure Chemical Industries, Ltd., Japan) was used. At the same time, Cell Counting Kit-8 (Dojindo Laboratories, Inc., Japan) was used to determine cell viability. To calculate both fat accumulation (FA) and cell viability (CV) rates, the absorbance values of the samples were divided by the value of the control, which was treated only with vehicle.

The rhizomes and roots of *V. fauriei* (2 kg), purchased from Tochimoto Tenkaido Co., Ltd. (Japan), were extracted with 80%

aqueous ethanol for 2 weeks. The concentrated extract (125 g) was partitioned with ethyl acetate and water, and the ethyl acetate layer was then partitioned with 90% aqueous methanol and hexane. Since the 90% aqueous methanol layer showed inhibitory effects on fat accumulation (FA rate, 66%; CV rate, 93%; conc., 100 μ g/mL), it was separated by ODS column chromatography with stepwise elution by 70% aqueous MeOH to MeOH. The 70% aqueous MeOH fraction (FA rate, 69%; CV rate, 112%; conc., 50 μ g/mL) was then subjected to fractionation using silica-gel column chromatography with stepwise elution by CHCl₃/MeOH (100:1, 20:1, 9:1, 2:1, 0:1). The 9:1 CHCl₃/MeOH fraction (FA rate, 9%; CV rate, 33%; conc., 50 μ g/mL) was chromatographed on silica-gel with stepwise elution by *n*-hexane/AcOEt (1:1, 1:9, 1:19, 0:1) and MeOH. The 1:19 *n*-hexane/AcOEt fraction (FA rate, 8%; CV rate, 42%; conc., 25 μ g/mL) and the AcOEt fraction (FA rate, 16%; CV rate, 54%; conc., 25 μ g/mL) were combined and applied to a silica-gel column for chromatography with stepwise elution by CHCl₃/MeOH (9:1, 2:1, 0:1). The 9:1 CHCl₃/MeOH fraction (FA rate, 11%; CV rate, 53%; conc., 12.5 μ g/mL) was finally purified by preparative reversed phase HPLC (50% aqueous MeOH; Cosmosil 5C₁₈-AR-II (Nacalai Tesque Inc., Japan), ϕ 10 \times 250 mm; UV, 220 nm) to yield 0.7 mg of an active compound.

The active compound was analyzed by ¹H and ¹³C NMR (300 MHz, CDCl₃) and electrospray ionization mass spectrometry (ESI-MS) to determine the structure. The spectral data are shown in the experimental section. Based on the spectral data, the active compound was identified as a known iridoid, monovalerianester A (**1**, Figure 1A). Assignment of the ¹H and ¹³C NMR peaks of the active compound was in good agreement with those of monovalerianester A, which have been previously reported [9]. The isolated compound was demonstrated to inhibit fat accumulation in 3T3-L1 murine adipocytes in a dose-dependent manner (Figure 1B). FA rate of 50% (EC₅₀ value) and CV rate of 50% (IC₅₀ value) were determined to be 3.5 μ g/mL (11.1 μ M) and 6.0 μ g/mL (19.1 μ M), respectively. The compound showed potent activity compared with the control compound, (-)-noradrenaline (EC₅₀=260 μ M) [10].

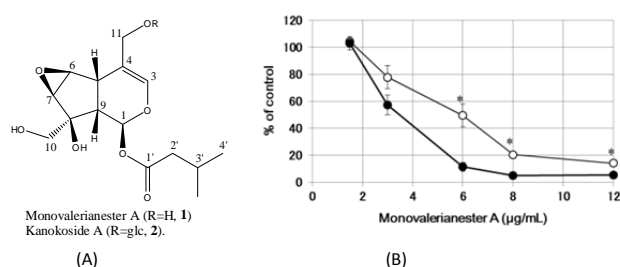


Figure 1: (A) Structures of monovalerianester A (1) and kanokoside A (2). (B) Inhibitory effects of monovalerianester A on fat accumulation in 3T3-L1 cells. 3T3-L1 cells were treated with monovalerianester A and vehicle (control) for 1 week during differentiation. Fat accumulation (solid circles) and cell viability (open circles) were then determined. Data represent the means and standard deviations (SD) of four tests and are shown as a percentage of the control. The mean values were analyzed by t-test. * $p < 0.01$; fat accumulative rates versus cell viability rates.

Monovalerianester A was isolated from *Valeriana officinalis*, a species related to *V. fauriei* [9]. It is the aglycone of kanokoside A (2, Fig. 1), which had been identified from the same plant [11]. No studies have evaluated their biological activities in mammalian cells to assess therapeutic potential. In this study, monovalerianester A was found to inhibit fat accumulation in 3T3-L1 murine adipocytes. This finding generated the possibility that its glycoside, kanokoside A, also possesses such function, and its biological activity may contribute to the anti-obesity effect. In our previous study, 9-hydroxy-10*E*,12*Z*-octadecadienoic acid (9-HODE) was also isolated from the extract of *V. fauriei* using the same bioassay system [8]. Meanwhile, the roots and bulbs of *V. fauriei* have long been used as a traditional herbal medicine, and thus its extract must be safe. Since monovalerianester A, as well as 9-HODE, were shown to suppress fat accumulation selectively, they and the crude extract of the rhizomes and roots of *V. fauriei* may have therapeutic potential for the treatment of obesity.

References

- Mann CC. (2005) Provocative study says obesity may reduce U.S. life expectancy. *Science*, **307**, 1716-1717.
- Shimokawa K, Mashima I, Asai A, Yamada K, Kita M, Uemura D. (2006) (-)-Ternatin, a highly *N*-methylated cyclic heptapeptide that inhibits fat accumulation: Structure and synthesis. *Tetrahedron Letters*, **47**, 4445-4448.
- Shimokawa K, Yamada K, Kita M, Uemura D. (2007) Convergent synthesis and *in vivo* inhibitory effect on fat accumulation of (-)-ternatin, a highly *N*-methylated cyclic peptide. *Bioorganic and Medicinal Chemistry Letters*, **17**, 4447-4449.
- Ito M, Ito J, Kitazawa H, Shimamura K, Fukami T, Tokita S, Shimokawa K, Yamada K, Kanatani A, Uemura D. (2009) (-)-Ternatin inhibits adipogenesis and lipid metabolism in 3T3-L1 cells. *Peptides*, **30**, 1074-1081.
- Sashida Y, Yamasaki K. (1997) *Syoyakugaku* (in Japanese). Nankodo, Tokyo, 258-260.
- Konoshima M, Sawada T, Hata K. (1978) *Syoyakugaku* (in Japanese). Asakura Publishing, Tokyo, 234-236.
- Guo Y, Xu J, Li Y, Watanabe R, Oshima Y, Yamakuni T, Ohizumi Y. (2006) Iridoids and sesquiterpenoids with NGF-potentiating activity from the rhizomes and roots of *Valeriana fauriei*. *Chemical and Pharmaceutical Bulletin*, **54**, 123-125.
- Yuki K, Ikeda M, Miyamoto K, Ohno O, Yamada K, Uemura D. (2012) Isolation of 9-hydroxy-10*E*,12*Z*-octadecadienoic acid, an inhibitor of fat accumulation from *Valeriana fauriei*. *Bioscience, Biotechnology, and Biochemistry*, **76**, 1233-1235.
- Zhou Y, Fang Y, Gong Z, Duan X, Liu Y. (2009) Two new terpenoids from *Valeriana officinalis*. *Chinese Journal of Natural Medicines*, **7**, 270-273.
- Shimokawa K, Iwase Y, Miwa R, Yamada K, Uemura D. (2008) Whole structure-activity relationships of the fat-accumulation inhibitor (-)-Ternatin: Recognition of the importance of each amino acid residue. *Journal of Medicinal Chemistry*, **51**, 5912-5914.
- Endo T, Taguchi H. (1977) The constituents of valerian root. The structures of four new iridoid glycosides, Kanokoside A, B, C, and D from the root of "Hokkaikisso". *Chemical and Pharmaceutical Bulletin*, **25**, 2140-2142.
- Green H, Kehinde O. (1976) Spontaneous heritable changes leading to increased adipose conversion in 3T3 cells. *Cell*, **7**, 105-113.
- Sekiya K, Okuda H, Hotta Y, Arichi S. (1987) Enhancement of adipose differentiation of mouse 3T3-L1 fibroblasts by ginsenosides. *Phytotherapy Research*, **1**, 58-60.
- Russell TR. (1981) [60] Growth and cytodifferentiation of 3T3-L1 preadipocytes into adipocytes. *Methods in Enzymology*, **72**, 720-723.
- Green H, Kehinde O. (1975) An established preadipose cell line and its differentiation in culture II. Factors affecting the adipose conversion. *Cell*, **5**, 19-27.
- Rubin CS, Hirsch A, Fung C, Rosen OM. (1978) Development of hormone receptors and hormonal responsiveness *in vitro*. Insulin receptors and insulin sensitivity in the preadipocyte and adipocyte forms of 3T3-L1 cells. *Journal of Biological Chemistry*, **253**, 7570-7578.

In conclusion, we searched for a new plant component that could inhibit fat accumulation in 3T3-L1 murine adipocytes, and isolated monovalerianester A from the rhizomes and roots of *V. fauriei*. Monovalerianester A was shown to inhibit fat accumulation in a dose-dependent manner. These results suggested that monovalerianester A and the crude extract of the rhizomes and roots of *V. fauriei* may be useful as anti-obesity agents.

Experimental

General: ^1H and ^{13}C NMR spectra were recorded with a JEOL JNM AL300 FT NMR spectrometer. HR-ESI mass spectra were recorded on a Waters LTC premier EX spectrometer.

Measurement of fat accumulation and cell viability: The preadipocyte cell line 3T3-L1, purchased from Human Science Research Resources Bank, Japan Health Sciences Foundation (Osaka, Japan), was cultured in DMEM with 10% FBS in two 96-well plates at 37°C, 5% CO₂ for 4–7 days [12–14]. After the cells reached confluence, the culture buffer was changed to a differentiation buffer (DMEM containing 10% FBS, 1 µM dexamethasone, 0.5 mM IBMX, 90 U/mL penicillin, 90 µg/mL streptomycin, and 10 µg/mL insulin) and the samples were added [15,16]. After 7 days, the differentiated 3T3-L1 adipocytes in a 96-well plate were treated with 2% Triton-X 100 for 30 min at room temperature followed by sonication for 1 min. Fat accumulation was determined by measuring liberated triglyceride using LabAssay™ Triglyceride (Wako Pure Chemical Industries, Ltd., Japan). To determine the cell viability of differentiated 3T3-L1 adipocytes, another 96-well plate was treated with a Cell Counting Kit-8 Test (Dojindo Laboratories, Inc., Japan), and the absorbance at 450 nm was measured. Values are means ± SD for triplicate samples.

Red Maple (<i>Acer rubrum</i>) Aerial Parts as a Source of Bioactive Phenolics Yan Zhang, Hang Ma, Tao Yuan and Navindra P. Seeram	1409
Changes in the Content of the Glycosides, Aglycons and their Possible Precursors of <i>Rhodiola rosea</i> during the Vegetation Period Iman Mirmazloum, Márta Ladányi and Zsuzsanna György	1413
Biocompounds Attenuating the Development of Obesity and Insulin Resistance Produced by a High-fat Sucrose Diet Usune Etxeberria, Ana Laura de la Garza, J. Alfredo Martínez and Fermín I. Milagro	1417
A Novel C21 Cyclopentenone Derivative from <i>Cipadessa cinerascens</i> Jing Zhang, Yao-Wen Chang, Chun-Mao Yuan, Fan Zhang, Ying-Tong Di and Xiao-Jiang Hao	1421
Effects on MC3T3-E1 Cells and <i>In silico</i> Toxicological Study of Two 6-(Propan-2-yl)-4-methyl-morpholine-2,5-diones Marija Vukelić-Nikolić, Ana Kolarević, Katarina Tomović, Denitsa Yancheva, Emiliya Cherneva, Stevo Najman, and Andrija Šmelcerović	1423
Release of Antioxidant Peptides from the Body Wall Proteins of the Sea Cucumber <i>Isostichopus fuscus</i> Arisaí C. Hernández-Sámano and Blanca Hernández-Ledesma	1427
Bioactivity-guided Separation of the Active Compounds in <i>Acacia pennata</i> Responsible for the Prevention of Alzheimer's Disease Pattamapan Lomarat, Sirirat Chancharunee, Natthinee Anantachoke, Worawan Kitphati, Kittisak Sripha and Nuntavan Bunyapraphatsara	1431
Development and Validation of LC-MS/MS Method for Quantitative Determination of Adenosine, Guanosine, Xanthine and Uric acid in Widely Consumed Vegetables in Thailand Narisa Rukdee, Piyanuch Rojsanga and Chutima Matayatsuk Phechkrajang	1435
Chemical Composition of the Essential Oil from <i>Chaerophyllum temulum</i> (Apiaceae) Jelena G. Stamenković, Gordana S. Stojanović, Ivana R. Radojković, Goran M. Petrović and Bojan K. Zlatković	1439
Comparison of Essential Oils Obtained from Different Extraction Techniques as an Aid in Identifying Aroma Significant Compounds of Nutmeg (<i>Myristica fragrans</i>) Suchandra Chatterjee, Sumit Gupta and Prasad. S. Variyar	1443
Chemical Variability of the Essential Oil Isolated from Aerial Parts of <i>Tetraclinis articulata</i> from North-Western Algeria Maghnia Boussaïd, Chahrazed Bekhechi, Fawzia Beddou, Daoudi Chabane Sari, Ange Bighelli, Joseph Casanova and Félix Tomi	1447
Composition and Bioactivities of an (<i>E</i>)-β-Farnesene Chemotype of Chamomile (<i>Matricaria chamomilla</i>) Essential Oil from Nepal Prabodh Satyal, Samon Shrestha and William N. Setzer	1453
Chemical Composition of the Essential Oil from <i>Croton oblongifolius</i> and its Antibacterial Activity against <i>Propionibacterium acnes</i> Sirivan Athikomkulchai, Sarin Tadtong, Nijisiri Ruangrunsi and Tapanee Hongratanaworakit	1459
Composition, <i>in vitro</i> Anti-inflammatory, Antioxidant and Antimicrobial Activities of Essential Oils from Leaf and Twig Parts of <i>Cupressus cashmeriana</i> Yu-Chang Su, Kuan-Ping Hsu, Kuo-Feng Hua and Chen-Lung Ho	1461
Antioxidant and Anticholinesterase Activities of Essential Oils of <i>Cinnamomum griffithii</i> and <i>C. macrocarpum</i> Wan Mohd Nuzul Hakimi Wan Salleh, Farediah Ahmad and Khong Heng Yen	1465
Essential Oil Composition and Antigermination Activity of <i>Artemisia dracunculus</i> (Tarragon) Daniele Fraternali, Guido Flamini and Donata Ricci	1469
<i>In Vitro</i> Activity of Twenty Commercially Available, Plant-Derived Essential Oils against Selected Dermatophyte Species Simona Nardoni, Silvia Giovanelli, Luisa Pistelli, Linda Mugnaini, Greta Profili, Francesca Pisseri and Francesca Mancianti	1473
Intracerebral Distribution of α-Pinene and the Anxiolytic-like Effect in Mice Following Inhaled Administration of Essential Oil from <i>Chamaecyparis obtusa</i> Hikaru Kasuya, Sayuka Iida, Kurumi Ono, Tadaaki Satou and Kazuo Koike	1479
<u>Accounts/Reviews</u>	
A Comprehensive Review of the Cosmeceutical Benefits of <i>Vanda</i> Species (Orchidaceae) Hazrina Hadi, Syarifah Nazira Said Razali and Ammar Ihsan Awadh	1483
Genotoxicity and Antigenotoxicity Studies of Traditional Medicinal Plants: How Informative and Accurate are the Results? Luc Verschaevé	1489

Natural Product Communications

2015

Volume 10, Number 8

Contents

Original Paper

- Isolation of Monovalerianester A, an Inhibitor of Fat Accumulation, from *Valeriana fauriei***
Keiji Yuki, Mariko Ikeda, Shosuke Yoshida, Osamu Ohno, Kiyotake Suenaga, Kaoru Yamada, Daisuke Uemura and Kenji Miyamoto 1333
- Arthropod Deterrents from *Artemisia pallens* (Davana Oil) Components**
Ganga V. Bhagavathy, Glory M Velazquez Nieves, Meiling Z. Webb and Kamlesh R. Chauhan 1335
- Stereoselective Synthesis of 2,15-Dihydroxycalamenene and 2-Methoxycalamenene. Determination of the Configuration of Natural 2,15-Dihydroxycalamenene**
Stefano Serra 1337
- Sesquiterpenes from the Vietnamese Marine Sponge *Dysidea fragilis***
Nguyen Thi Cuc, Hoang Le Tuan Anh, Dan Thi Thuy Hang, Nguyen Xuan Nhiem, Nguyen Hai Dang, Nguyen Hoai Nam, Pham Hai Yen, Do Cong Thung, Vu Kim Thu, Chau Van Minh and Phan Van Kiem 1341
- Vibrational Circular Dichroism Absolute Configuration of 9,12-Cyclomulin-13-ol, a Diterpene from *Azorella* and *Laretia* Species**
Marcelo A. Muñoz, Aurelio San-Martín and Pedro Joseph-Nathan 1343
- Ultrafine Betulin Formulation with Biocompatible Carriers Exhibiting Improved Dissolution Rate**
Svetlana A. Myz, Tatyana P. Shakhtshneider, Mikhail A. Mikhaïlenko, Andrey G. Ogienko, Ekaterina G. Bogdanova, Anna A. Ogienko, Svetlana A. Kuznetsova, Elena V. Boldyreva and Vladimir V. Boldyrev 1345
- Bio-assay Guided Isolation of Anti-cancer Compounds from *Anthocephalus cadamba* Bark**
Deepak Kumar, Chilukuri Tejaswi, Saiprasanna Rasamalla, Sumana Mallick and Bikas C Pal 1349
- Damarane-type Saponins from *Gynostemma longipes* and their Cytotoxic Activity**
Pham Tuan Anh, Pham Thanh Ky, Nguyen Thi Cuc, Nguyen Xuan Nhiem, Pham Hai Yen, Tran Minh Ngoc, Hoang Le Tuan Anh, Bui Huu Tai, Do Thi Trang, Chau Van Minh and Phan Van Kiem 1351
- A New C₂₃ Steroid from the Venom of *Bufo bufo gargarizans***
Shi-Lin Luo, Hai-Yan Tian, Jun-Shan Liu, Ying Wang and Wen-Cai Ye 1353
- (-)-Pentylsedinine, a New Alkaloid from the Leaves of *Lobelia tupa* with Agonist Activity at Nicotinic Acetylcholine Receptor**
Cristian Paz, José Becerra, Mario Silva, Viviana Burgos, Matthias Heydenreich, Bernd Schmidt, Thu Tran and Irina Vetter 1355
- Furoquinoline Alkaloids from the Leaves of *Evodia lepta* as Potential Cholinesterase Inhibitors and their Molecular Docking**
Jirapast Sichaem, Thanawan Rojpitikul, Pattara Sawasdee, Kiattisak Lugsanangarm and Santi Tip-pyang 1359
- Asperginine, an Unprecedented Alkaloid from the Marine-derived Fungus *Aspergillus* sp.**
Pinmei Wang, Shizhe Zhao, Ying Liu, Wanjing Ding, Feng Qiu and Jinzhong Xu 1363
- Effect of Quercetin on Cell Cycle and Cyclin Expression in Ovarian Carcinoma and Osteosarcoma Cell Lines**
Daniela Catanzaro, Eugenio Ragazzi, Caterina Vianello, Laura Caparrotta and Monica Montopoli 1365
- Anti-*Helicobacter pylori* Activity of Four *Alchemilla* Species (Rosaceae)**
Marija Krivokuća, Marjan Niketić, Marina Milenković, Nataša Golić, Carla Masia, Maria Maddalena Scaltrito, Francesca Sisto and Tatjana Kundaković 1369
- Peracylated Glucosyl Kaempferols from *Pasania dodoniifolia* Leaf**
Chi-Chih Chang and Shoei-Sheng Lee 1373
- 6-Methoxyflavonol Glycosides with *In Vitro* Hepatoprotective Activity from *Chenopodium bonus-henricus* Roots**
Zlatina Kokanova-Nedialkova, Magdalena Kondeva-Burdina, Dimitrina Zheleva-Dimitrova, Virginia Tzankova, Stefan Nikolov, Jörg Heilmann and Paraskev T. Nedialkov 1377
- Flavonol Glycosides from the Leaves of *Allium macrostemon***
Risa Nakane and Tsukasa Iwashina 1381
- HPLC Plasma Assay of a Novel Anti-MRSA Compound, Kaempferol-3-O-Alpha-L-(2'',3''-di-p-coumaroyl)rhamnoside, from Sycamore Leaves**
Yiguan Zhang, Frederick Valeriote, Kenneth Swartz, Ben Chen, Mark T. Hamann, Douglas L. Rodenburg, James D. McChesney and Jiajiu Shaw 1383
- Biological Activity of *Dolichandrone serrulata* Flowers and Their Active Components**
Phanida Phanthong, Noppawan Phumala Morales, Sirirat Chancharunee, Supachoke Mangmool, Natthinee Anantachoke and Nuntavan Bunyapraphatsara 1387
- Prenylhydroquinone-Derived Secondary Metabolites from Cultures of the Basidiomycete *Lentinus similis* BCC 52578**
Masahiko Isaka, Somporn Palasarn, Malipan Sappan, Kitlada Srichomthong, Samantha C. Karunaratna and Kevin D. Hyde 1391
- Effects of Thymoquinone on the Pharmacokinetics and Pharmacodynamics of Glibenclamide in a Rat Model**
Ajaz Ahmad, Rao Muzaffar A. Khan, Khalid M. Alkharfy, Mohammad Raish, Fahad I. Al-Jenoobi, and Abdullah M. Al-Mohizea 1395
- Antioxidant and Antiinflammatory Compounds in Nutmeg (*Myristica fragrans*) Pericarp as Determined by *in vitro* Assays**
Chuan-Rui Zhang, Ettannil Jayashree, Paramasivam Suresh Kumar and Muraleedharan G. Nair 1399
- In Vitro* Safety/Protection Assessment of Resveratrol and Pterostilbene in a Human Hepatoma Cell Line (HepG2)**
Germana Lombardi, Samuele Vannini, Francesca Blasi, Maria Carla Marcotullio, Luca Dominici, Milena Villarini, Lina Cossignani and Massimo Moretti 1403

Continued inside backcover

Natural Products | Very Important Paper |

VIP Stereodivergent Synthesis and Stereochemical Reassignment of the C79–C104 Fragment of Symbiodinolide

Hiroyoshi Takamura,^{*,[a]} Takayuki Fujiwara,^[a] Yohei Kawakubo,^[a] Isao Kadota,^[a] and Daisuke Uemura^[b]

Abstract: We have synthesized eight possible diastereoisomers **3a–h** of the C79–C97 fragment of symbiodinolide (**1**) in a stereodivergent manner by utilizing a dithiane addition to the aldehyde as a key step. Comparison of the ¹³C NMR chemical shifts of the natural product **1** and the synthetic products **3a–h** indicated that the relative stereostructure of this fragment in symbiodinolide (**1**) is that represented in **3a** or **f**. We have stereodivergently synthesized eight possible diastereoisomers of the C94–C104 fragment **4a–h**, and we have compared their ¹³C NMR chemical shifts with those of the natural product, which established the relative stereochemistry of this fragment to be that described in diastereo-

isomers **4a** or **e**. By combining the stereostructural outcomes of the C79–C97 and C94–C104 fragments, we have proposed four candidate compounds of the C79–C104 fragment **2a–d**. We also synthesized diastereoisomers **2a** and **b** (**2a** in the preceding article; *Chem. Eur. J.* **2015**, DOI: 10.1002/chem.201503880) by a Julia–Kocienski olefination and diastereoisomers **2c** and **d** by a Wittig reaction. By comparing the ¹³C NMR chemical shifts of natural symbiodinolide (**1**) with those of the synthetic products **2a–d**, we have reassigned the stereostructure of the C79–C104 fragment of natural product **1** to be that depicted in diastereoisomer **2b**.

Introduction

In the preceding article,^[1] we described the stereoselective synthesis of the C79–C104 fragment **2a**, which bears the originally proposed stereochemistry of symbiodinolide (**1**, Figure 1). In addition, we compared the ¹³C NMR chemical shifts of the natural product **1** and the synthetic derivative **2a**, which indicated that the stereostructure of the C91–C99 carbon chain domain of natural product **1** should be reinvestigated. In this article, we report our synthetic approach toward the stereochemical elucidation of the C91–C99 moiety, which led to the stereostructural reassignment of the C79–C104 fragment of symbiodinolide (**1**).

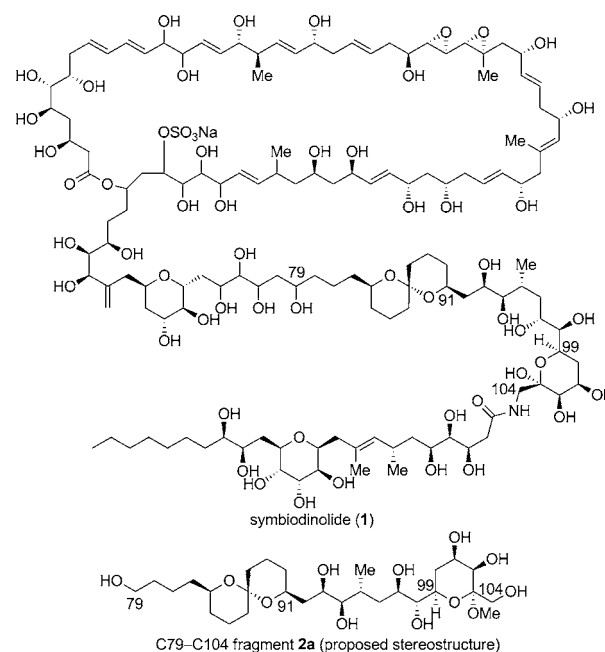


Figure 1. Structures of symbiodinolide (**1**) and the proposed C79–C104 fragment **2a**.

Results and Discussion

Strategy for the stereostructural elucidation of the C79–C104 fragment

In the C91–C99 moiety, there are seven stereogenic centers; therefore, the number of possible diastereoisomers of this

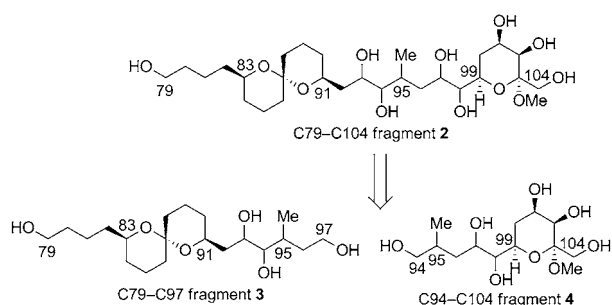
[a] Prof. Dr. H. Takamura, T. Fujiwara, Y. Kawakubo, Prof. Dr. I. Kadota
Department of Chemistry
Graduate School of Natural Science and Technology, Okayama University
3-1-1 Tsushima-naka, Kita-ku, Okayama 700-8530 (Japan)
E-mail: takamura@cc.okayama-u.ac.jp

[b] Prof. Dr. D. Uemura
Department of Chemistry, Faculty of Science, Kanagawa University
2946 Tsuchiya, Hiratsuka 259-1293 (Japan)

Supporting information, containing experimental details, compound data, and copies of NMR spectra of new compounds, and ORCID(s) from the author(s) for this article are available on the WWW under <http://dx.doi.org/10.1002/chem.201503881>.

domain is $2^6=64$.^[2] If we could synthesize all 64 diastereoisomers that correspond to the C79–C104 fragment, we could then compare the NMR data of natural symbiodinolide (1) and the synthesized products and subsequently elucidate the stereostructure of the C79–C104 fragment. This approach toward the configurational determination of this moiety is undoubtedly reliable; however, the supply of 64 possible diastereoisomers by chemical synthesis would require a substantial amount of work. Therefore, with the intention of devising a more efficient and practical method for the structural elucidation of the C79–C104 fragment, we divided the C79–C104 fragment 2 into two fragments: C79–C97 fragment 3 and C94–C104 fragment 4 (Scheme 1). The C79–C97 fragment 3 possesses three undefined stereocenters (C93, C94, and C95); therefore, there are eight possible diastereoisomers of this fragment. We planned to synthesize these eight diastereoisomers in a stereodivergent manner; subsequently, the candidate compound, which possessed the stereochemistry that corresponded to the natural product, would be identified by comparison of the NMR data

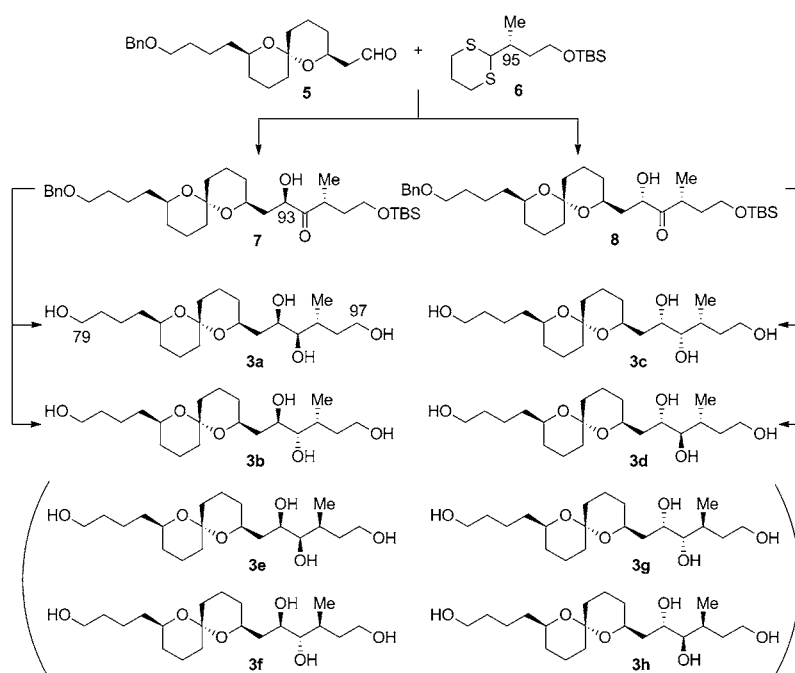
of natural symbiodinolide (1) and the eight diastereoisomers. As three stereogenic centers are involved in the acyclic portion of the C94–C104 fragment 4 (C95, C97, and C98), this fragment also has eight possible diastereoisomers. In a similar way to the strategy proposed for the structural elucidation of fragment 3, comparison of the NMR data of the natural product and the eight synthetic products would lead to the identification of the C94–C104 candidate compound. Because the chiral center at the C95 position is contained in both fragments 3 and 4, the relative stereostructures of these fragments would be connected by the C95 stereochemistry. Finally, we could propose the relative configuration of the C79–C104 fragment 2. At the stage of the structural determination of fragments 3 and 4, we might suggest more than one candidate compound owing to no significant difference between the NMR data for the diastereoisomers. In this case, we would synthesize the possible diastereoisomers of fragment 2, which would come from the combination of the stereostructures of fragments 3 and 4. Hence, comparison of the NMR data of these synthetic products with those of natural symbiodinolide (1) would also establish the stereostructure of fragment 2.



Scheme 1. Strategy for the stereostructural elucidation of the C79–C104 fragment 2.

Stereodivergent synthetic plan for the C79–C97 fragment

Our stereodivergent synthetic plan for the eight possible diastereoisomers of the C79–C97 fragment 3a–h is outlined in Scheme 2.^[3] Two α -hydroxy ketones 7 and 8, which have an epimeric relationship at the C93 position, could be synthesized by the addition of dithiane 6 to aldehyde 5. Diastereoselective reduction of the protected compound of alcohol 7, which is under the control of a Felkin–Anh model^[4] that is effected by the C93 stereogenic center, would afford *syn*-diol 3a. In con-

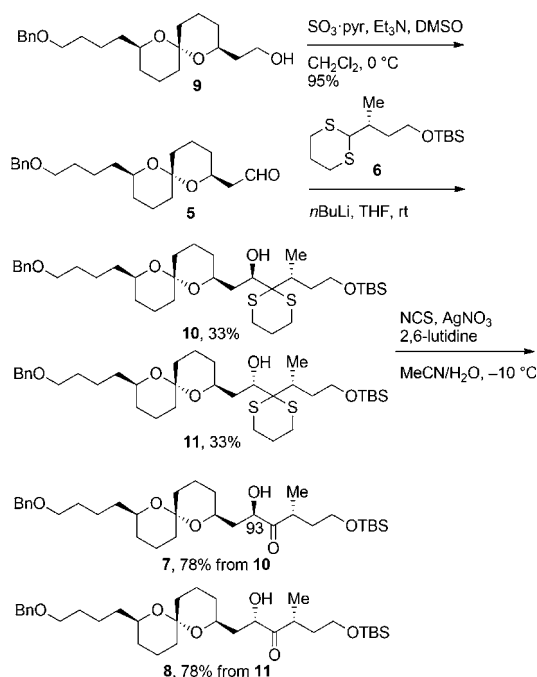


Scheme 2. Stereodivergent synthetic plan for diastereomeric compounds 3a–h. Bn = benzyl, TBS = *tert*-butyldimethylsilyl.

trast, the chelation-controlled diastereoselective reduction of α -hydroxy ketone **7** would provide the *anti*-diol **3b**. In a similar way, *syn*-diol **3c** and *anti*-diol **3d** could be synthesized from the α -hydroxy ketone **8**. The other four possible diastereoisomers **3e–h**, which are the C95 epimers of **3a–d**, could be supplied by using the enantiomer of the dithiane **6** as a coupling precursor.

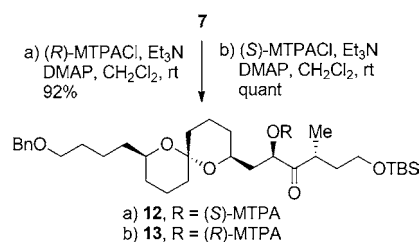
Synthesis of **3a–d**

We first examined the synthesis of the C79–C97 fragment **3a**. Alcohol **9**, which was reported in the preceding paper,^[1] was oxidized with $\text{SO}_3\cdot\text{pyr}$ ^[5] to give aldehyde **5** (Scheme 3). Depro-



Scheme 3. Synthesis of α -hydroxy ketones **7** and **8**. Pyr = pyridine, DMSO = dimethylsulfoxide, THF = tetrahydrofuran, rt = room temperature, NCS = *N*-chlorosuccinimide.

tonation of dithiane **6**^[6] with *n*BuLi and subsequent reaction with the aldehyde **5** furnished the desired two alcohols **10** and **11** both in 33% yield. Hydrolysis of the dithiane moieties of alcohols **10** and **11** with *N*-chlorosuccinimide (NCS)/AgNO₃/2,6-lutidine^[7] provided α -hydroxy ketones **7** and **8**.^[8] The absolute configuration at the C93 position of ketone **7** was determined by the modified Mosher method.^[9] Thus, treatment of α -hydroxy ketone **7** with α -methoxy- β -(trifluoromethyl)phenylacetyl chloride (MTPACl)/Et₃N/4-dimethylaminopyridine (DMAP) yielded MTPA esters **12** and **13** (Scheme 4). The chemical shift differences ($\Delta\delta_{S-R}$) of diastereomeric compounds **12** and **13** in the ¹H NMR data were calculated and the results are summarized in Figure 2. The signs at the left side of the C93 position were positive and those at the right side were negative; therefore, the absolute configuration at the C93 position of α -hydroxy ketone **7** was elucidated.



Scheme 4. Synthesis of MTPA esters **12** and **13** for the stereochemical determination. MTPA = α -methoxy- β -(trifluoromethyl)phenylacetyl, DMAP = 4-dimethylaminopyridine, quant = quantitative.

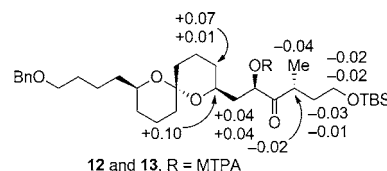
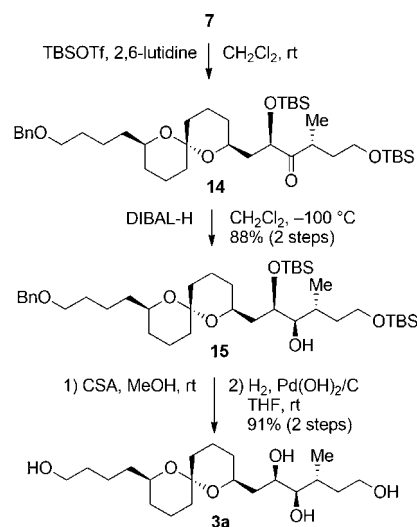


Figure 2. Chemical shift differences ($\Delta\delta_{S-R}$) between diastereomeric compounds **12** and **13**.

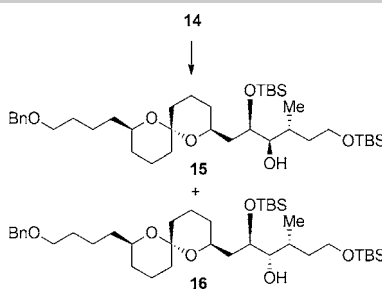
After the alcohol **7** was converted to the *tert*-butyldimethylsilyl (TBS) ether **14**, we examined the diastereoselective reduction of this compound (Scheme 5). As shown in Table 1, the reduction of TBS ether **14** with NaBH₄ proceeded smoothly at



Scheme 5. Synthesis of diastereoisomer **3a**. Tf = trifluoromethanesulfonyl, DIBAL-H = diisobutylaluminum hydride, CSA = camphorsulfonic acid.

–78 to 0 °C; however, the diastereomeric ratio (d.r.) of the desired alcohol **15** and the undesired alcohol **16** was 1.2:1 (entry 1).^[10] Changing the reducing reagent to L-Selectride, which is a more bulky reagent, decreased both of the chemical yield and the d.r., and the starting material **14** was recovered in 69% yield (entry 2). When we treated ketone **14** with diisobutylaluminum hydride (DIBAL-H) at –100 °C, we quantitatively obtained alcohol **15** as a single diastereoisomer (entry 3). The stereochemical outcome of the formation of alcohol **15** could

Table 1. Diastereoselective reduction of ketone 14.

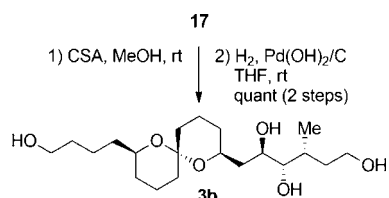


Entry	Conditions	Yield ^[a]	Ratio (15:16) ^[b]
1	NaBH ₄ , MeOH, -78 to 0 °C	quant	1.2:1
2 ^[c]	L-Selectride, CH ₂ Cl ₂ , -78 to 0 °C	25 %	1.3:2
3	DIBAL-H, CH ₂ Cl ₂ , -100 °C	quant	>20:1

[a] Yield of isolated product. [b] Based on the isolation. [c] 69% recovery of starting material 14.

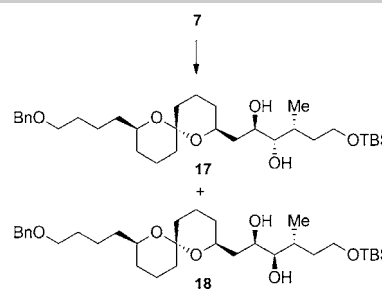
be rationalized by the Felkin–Anh model,^[4] which is induced by the C93 configuration. By using the conditions of entry 3, the alcohol 15 was obtained in 88% yield from α -hydroxy ketone 7 over two steps of TBS protection and DIBAL-H reduction, as described in Scheme 5. Finally, removal of the two TBS moieties of compound 15 with camphorsulfonic acid (CSA) and the benzyl group by hydrogenation conditions furnished the tetraol 3a.

We next investigated the diastereoselective reduction of the α -hydroxy ketone 7, which led to *anti*-diol 17, and the further transformation to the tetraol 3b. As shown in Table 2, the chelation-controlled reduction of ketone 7 with Zn(BH₄)₂^[11] provided the expected *anti*-diol 17 and *syn*-diol 18 in a 1.6:1 d.r. and



Scheme 6. Synthesis of diastereoisomer 3b.

Table 2. Diastereoselective reduction of α -hydroxy ketone 7.

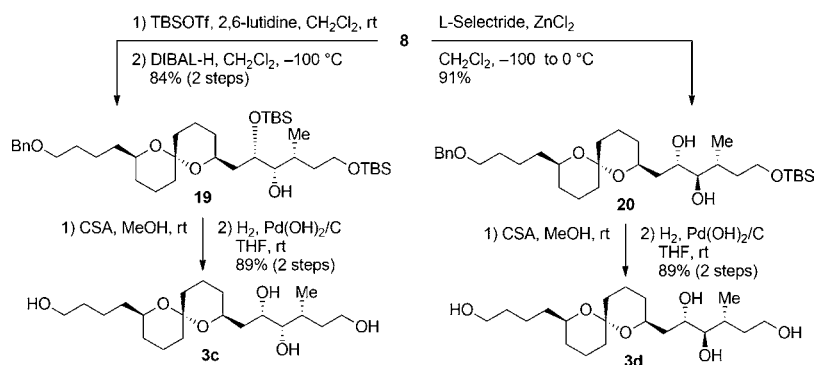


Entry	Conditions	Yield ^[a]	Ratio (17:18) ^[b]
1	Zn(BH ₄) ₂ , Et ₂ O, -78 to 0 °C	87 %	1.6:1
2	L-Selectride, ZnCl ₂ , CH ₂ Cl ₂ , -78 to 0 °C	83 %	9.4:1
3	L-Selectride, ZnCl ₂ , CH ₂ Cl ₂ , -100 to 0 °C	86 %	>20:1

[a] Yield of isolated product. [b] Based on the isolation.

87% combined yield (entry 1). This unsatisfactory result of the diastereoselectivity prompted us to explore the use of a chelating reagent as an additive. After investigation of the reaction conditions, it was proven that the use of L-Selectride as a reducing reagent and ZnCl₂ as a chelating reagent was effective,^[12] and the diol 17 was obtained in 83% yield and 9.4:1 d.r. (entry 2). When the reaction was carried out at -100 to 0 °C, the chemical yield and the d.r. were improved to 86% and >20:1, respectively (entry 3). The TBS and benzyl protective groups of compound 17 were removed to give the tetraol 3b quantitatively over two steps (Scheme 6).^[13]

From the results of the synthesis of diastereomeric compounds 3a and b, we could synthesize the C93,94-*syn*-diol and the corresponding *anti*-diol in a stereoselective manner by the Felkin–Anh controlled reduction of the α -siloxy ketone with DIBAL-H and the chelation-controlled reduction of the α -hydroxy ketone with L-Selectride/ZnCl₂. We envisioned that these reaction conditions could be applied to the synthesis of the other target molecules 3c–h. The stereoselective synthesis of 3c and d is depicted in Scheme 7. Silylation of the α -hydroxy ketone 8 with TBSOTf and subsequent diastereoselective reduction of the resulting α -siloxy ketone with DIBAL-H afforded alcohol 19 as the sole product in 84% yield over two steps.^[10] In parallel, the chelation-controlled reduction of α -hydroxy



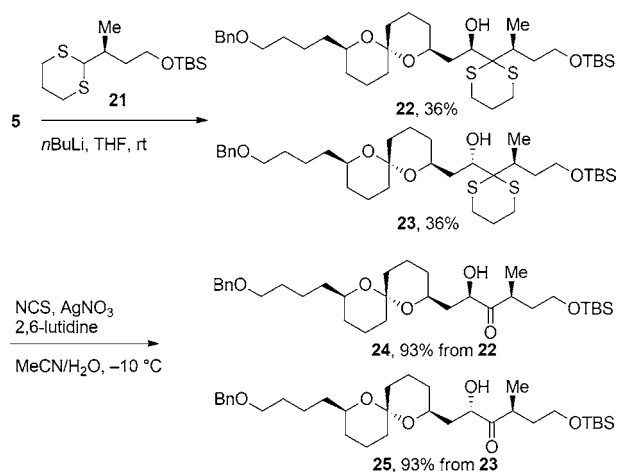
Scheme 7. Synthesis of diastereoisomers 3c and d.

ketone **8** with L-Selectride in the presence of ZnCl_2 ^[12] gave *anti*-diol **20** in 91% yield as a single diastereoisomer. Finally, the tetraols **3c** and **d** were produced by the global deprotection of compounds **19** and **20**, respectively.^[14]

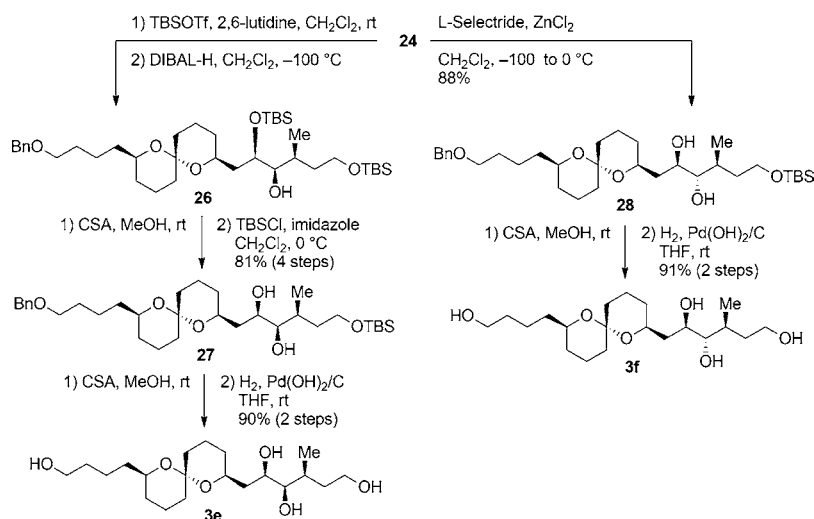
Synthesis of 3 e–h

Having synthesized four diastereoisomers **3a–d** with the (*R*)-configuration at the C95 position, we next tried to synthesize the other four possible diastereoisomers **3e–h**, the C95 epimers of **3a–d**, by using dithiane **21**^[6] and a similar transformation to that used for the synthesis of **3a–d**. Thus, the coupling of the aldehyde **5** and the dithiane **21** by using *n*BuLi gave alcohols **22** and **23** both in 36% yield (Scheme 8). Treatment of alcohols **22** and **23** with NCS/AgNO₃/2,6-lutidine in aqueous MeCN^[7] afforded α -hydroxy ketones **24** and **25**.

The synthetic transformation from ketone **24** to tetraols **3e** and **f** is illustrated in Scheme 9. Protection of α -hydroxy ketone **24** with TBSOTf followed by diastereoselective reduction with DIBAL-H afforded alcohol **26** as a single diastereoisomer.



Scheme 8. Synthesis of α -hydroxy ketones **24** and **25**.



Scheme 9. Synthesis of diastereoisomers **3e** and **f**.

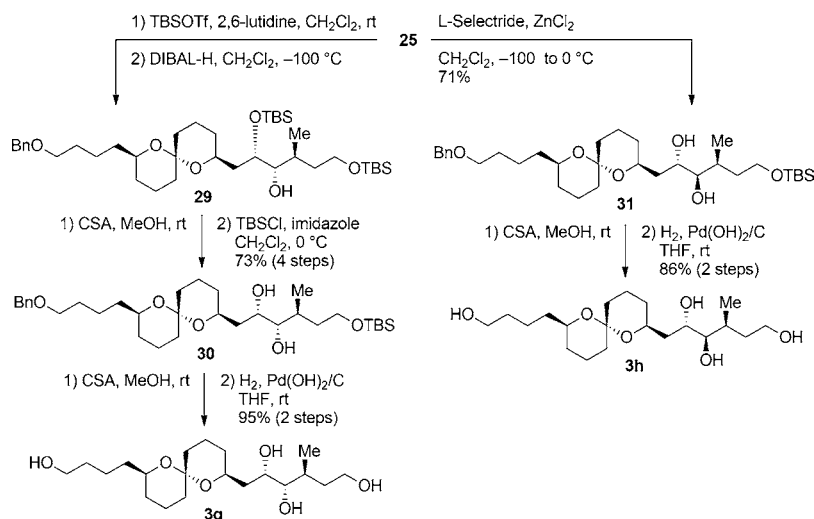
Subsequent removal of the two TBS moieties and selective silylation of the primary alcohol provided diol **27**,^[15,16] which underwent the TBS and benzyl deprotection to furnish the tetraol **3e**. Treatment of the α -hydroxy ketone **24** with L-Selectride/ ZnCl_2 ^[11] afforded *anti*-diol **28** as the sole diastereoisomer in 88% yield.^[10] Removal of the TBS and benzyl protective groups of diol **28** gave the tetraol **3f**. The synthesis of **3g** and **h**, which are the C93-epimers of **3e** and **f**, is shown in Scheme 10. The alcohol **25** was transformed into the diol **30**^[10] by the following four-step sequence: 1) TBS protection, 2) diastereoselective reduction with DIBAL-H, 3) deprotection of the bis-TBS ether, and 4) selective TBS protection of the primary alcohol. Removal of the protective groups of diol **30** afforded the tetraol **3g** in 95% over two steps. The α -hydroxy ketone **25** reacted with L-Selectride/ ZnCl_2 ^[12] to produce *anti*-diol **31**,^[10] which was converted to the tetraol **3h** after deprotection.

Relative configuration of the C79–C97 fragment

With all of the eight possible diastereoisomers of the C79–C97 fragment **3a–h** in hand, we performed 2D NMR analysis on each sample. Figure 3 graphically displays the deviations of the ¹³C NMR chemical shifts at the C91, C93, C94, and C95 positions between symbiodinolide (**1**) and the synthetic **3a–h**.^[17] From these results, it was found that the chemical shift characteristics of the two diastereoisomers **3a** and **f** were more similar to those of the natural product than those of the other six diastereoisomers. Therefore, we judged the relative configuration of the C79–C97 fragment to be that described in either **3a** or **f**.

Synthesis of 4 a–d

There are eight possible diastereoisomers of the C94–C104 fragment, as shown in Figure 4. As in the case of the C79–C97 fragment, we pursued the stereodivergent synthesis of all possible diastereoisomers **4a–h**. The hexaol **4a** was synthesized



Scheme 10. Synthesis of diastereoisomers **3g** and **h**.

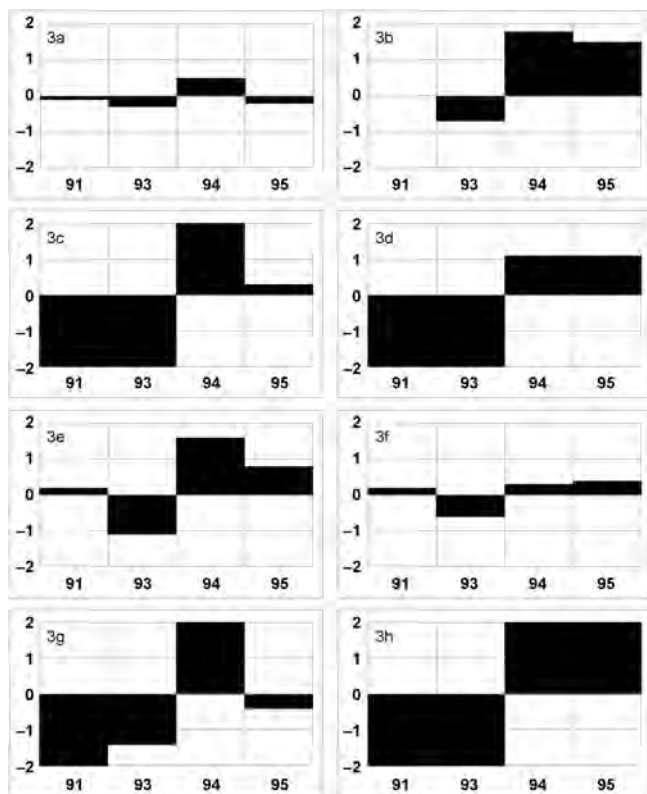


Figure 3. Differences of the ¹³C NMR chemical shifts between natural sym-biodinolide (**1**) and the synthesized products **3a–h** ($\Delta\delta = \delta_1 - \delta_3$ in ppm). The x and y axes represent the carbon number and $\Delta\delta$, respectively.

from compound **32**, which was reported in the preceding article,^[1] through the removal of the *p*-methoxybenzyl (PMB) group by hydrogenation and the acetonide and TBS moieties with CSA in MeOH (Scheme 11). The hexaol **4b**, which is the C97 epimer of **4a**, was synthesized by utilizing the diastereoselective reduction of the α -siloxy ketone. Thus, after alcohol **33**^[1] was silylated to give the corresponding TBS ether, the α -

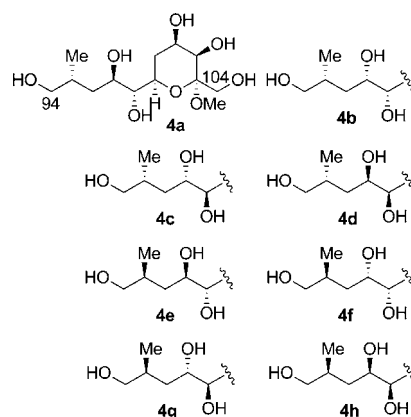
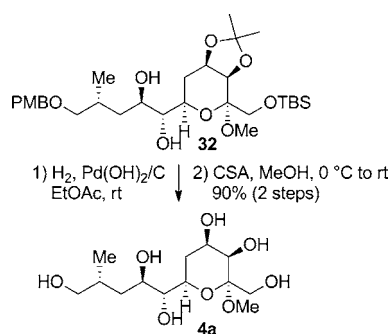
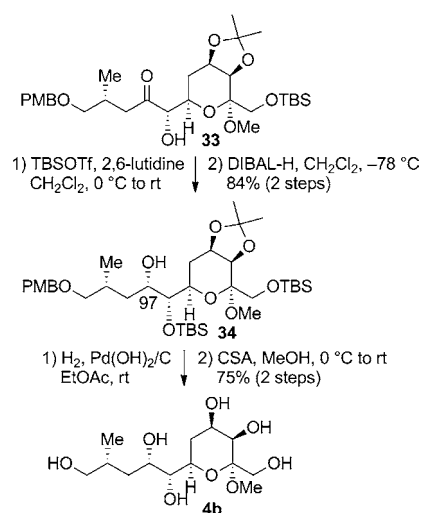


Figure 4. Eight possible diastereoisomers of the C94–C104 fragment **4a–h**.



Scheme 11. Synthesis of diastereoisomer **4a**. PMB = *p*-methoxybenzyl.

siloxy ketone was treated with DIBAL-H, which led to the desired alcohol **34** as a single diastereoisomer in 84% yield over two steps (Scheme 12).^[10] Felkin–Anh controlled,^[4] diastereoselective reduction with DIBAL-H, which was utilized in the synthesis of the C79–C97 fragment, was also effective for the introduction of the stereogenic center at the C97 position. Complete deprotection of alcohol **34** furnished the hexaol **4b** in 75% yield over two steps.



Scheme 12. Synthesis of diastereoisomer **4b**.

We next tried to synthesize the hexaols **4c** and **d**, which are the C98 epimers of **4a** and **b**. As shown in Scheme 13, hydrolysis of the dithiane moiety^[7] of compound **35**^[1] followed by chelation-controlled diastereoselective reduction of the resultant α -hydroxy ketone **36** with Zn(BH₄)₂^[11] provided the desired *anti*-diol **37**.^[18] In contrast, the α -siloxy ketone derived from ketone **36** was reduced with DIBAL-H to yield alcohol **38** as a single diastereoisomer.^[10] Finally, deprotection of compounds **37** and **38** afforded the hexaols **4c** and **d**, respectively.

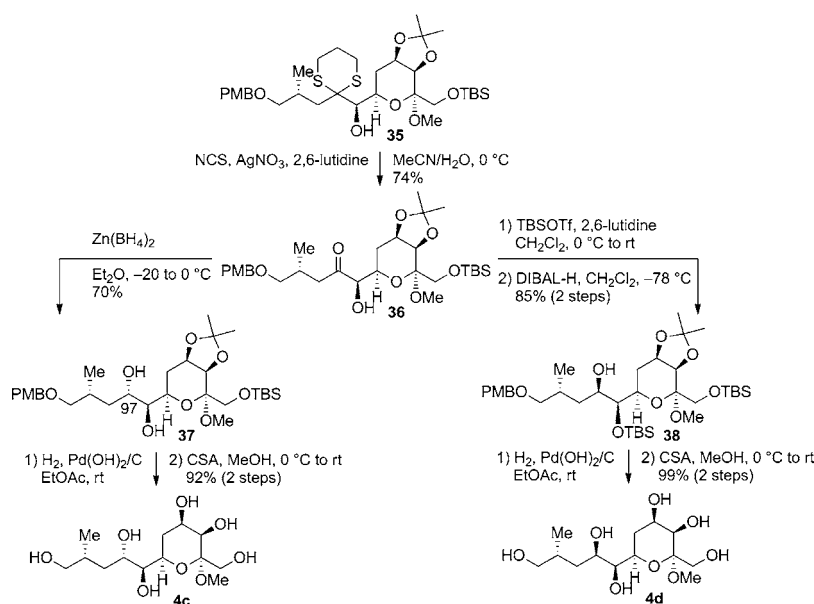
Synthesis of **4e–h**

We next examined the synthesis of hexaols **4e–h**, which are the C95 epimers of **4a–d**. The stereoselective synthesis of **4e** and **f** is described in Scheme 14. Aldehyde **39**^[1] was reacted with the anion prepared from dithiane **40**^[19] to produce alco-

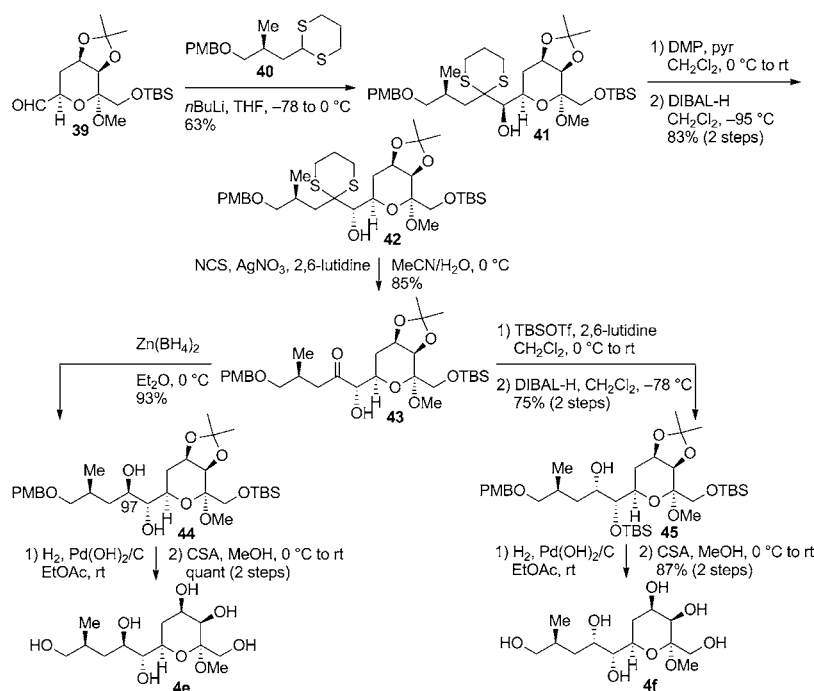
hol **41** as a single diastereoisomer.^[10] Oxidation of alcohol **41** with Dess–Martin periodinane (DMP),^[20] reduction with DIBAL-H, and hydrolysis of the dithiane group^[7] afforded α -hydroxy ketone **43**, which is the common synthetic intermediate toward hexaols **4e** and **f**. The α -hydroxy ketone **43** was derivatized stereodivergently and stereoselectively to diol **44**^[21] by the chelation-controlled reduction with Zn(BH₄)₂^[11] and alcohol **45**^[10] by silylation and subsequent Felkin–Anh type^[4] reduction with DIBAL-H. Global removal of the protective groups of compounds **44** and **45** gave the hexaols **4e** and **f**, respectively. The hexaols **4g** and **h** were synthesized in a similar sequence (Scheme 15); thus, the dithiane **41** was hydrolyzed to give α -hydroxy ketone **46**.^[7] The key synthetic intermediate **46** was transformed to the tetraols **4g** and **h** by the diastereoselective reduction with Zn(BH₄)₂ and DIBAL-H, respectively, and subsequent global deprotection.^[22]

Relative configuration of the C94–C104 fragment

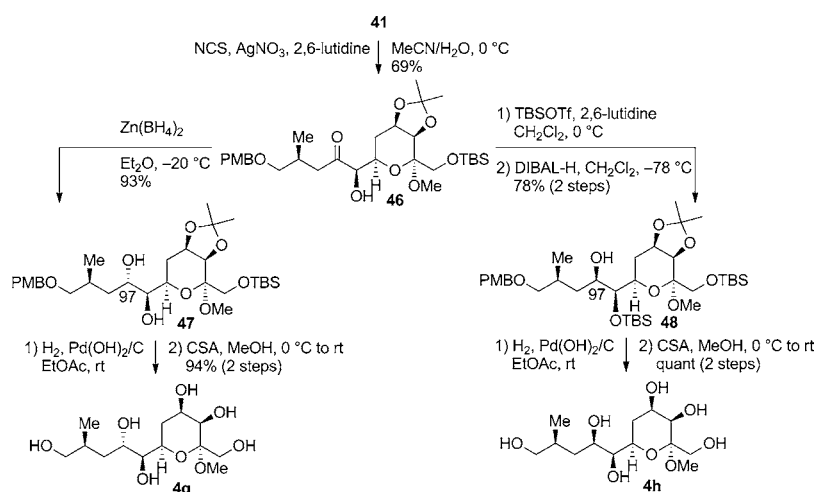
Having completed the stereodivergent synthesis of all of the eight possible diastereoisomers of the C94–C104 fragment **4a–h**, we submitted these synthetic products to 2D NMR analysis and compared their ¹³C NMR characteristics with those of natural symbiodinolide (**1**). Deviations of the ¹³C NMR chemical shifts at the C95, C97, C98, and C99 positions between the natural product and the synthetic diastereoisomers **4a–h** are depicted graphically in Figure 5.^[17] As a result of the comparison among all of the eight diastereoisomers, the chemical shift differences of **4a** and **e** were found to be smaller than those of the other six diastereoisomers. Therefore, we judged the relative stereochemistry of the C94–C104 fragment to be that drawn in either **4a** or **e**.



Scheme 13. Synthesis of diastereoisomers **4c** and **d**.



Scheme 14. Synthesis of diastereoisomers **4e** and **f**. DMP = Dess–Martin periodinane.



Scheme 15. Synthesis of diastereoisomers **4g** and **h**.

Possible stereostructures of the C79–C104 fragment

We could propose the candidate compounds for each C79–C97 fragment (**3a** and **f**) and C94–C104 fragment (**4a** and **e**) by the stereodivergent synthesis of all possible diastereoisomers and subsequent comparison of their ^{13}C NMR chemical shifts with those of the natural product (Scheme 16). Therefore, by connecting the relative configuration of these two fragments through the C95 stereogenic center, we have suggested the possible relative stereostructures of the C79–C104 fragment, as shown in **2a** (**3a+4a**), **2b** (*ent*-**3a+4e**), **2c** (*ent*-**3f+4a**), and **2d** (**3f+4e**). Toward the stereostructural elucidation of the C79–C104 fragment, we next tried to synthesize these four diastereoisomers **2a–d** in a unified manner.^[23]

Synthesis of **2b–d**

We first examined the stereocontrolled synthesis of the alcohol **52** that bears an enantiomeric relationship at the spiroacetal C83–C91 moiety with compounds **3a** and **f**, which are required in the synthesis of compounds **2b** and **c**. We tried to synthesize compound **52** by the Mitsunobu reaction^[24] through stereoinversion of a compound that had been prepared in the preceding paper.^[1] Thus, hydrogenation of alkyne **49**^[1] followed by protection as the *tert*-butyldiphenylsilyl (TBDPS) ether and selective removal of the three TBS groups with CSA afforded triol **50** in 90% yield over three steps (Scheme 17). The stereochemistry at the C83 and C91 positions of compound **50** were inverted under the Mitsunobu conditions^[24] with *p*-nitrobenzo-

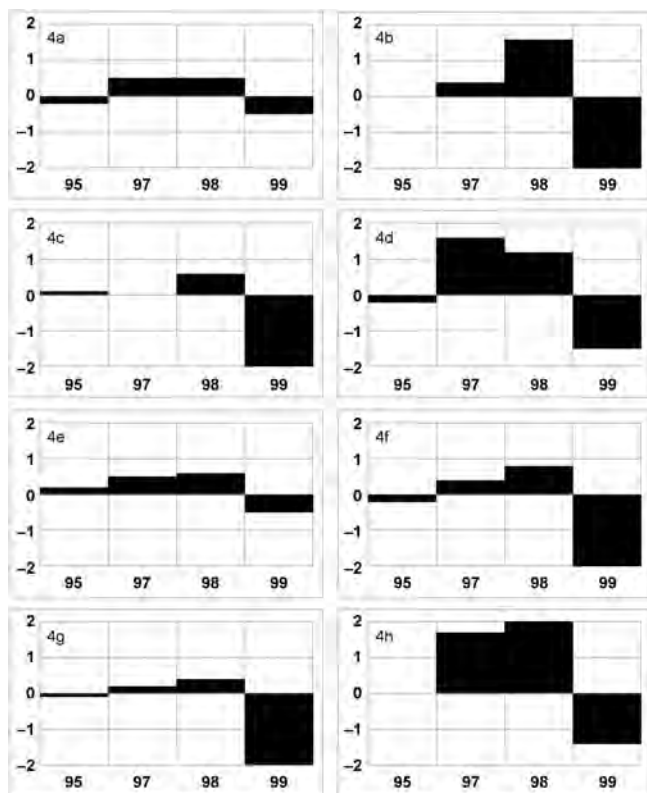
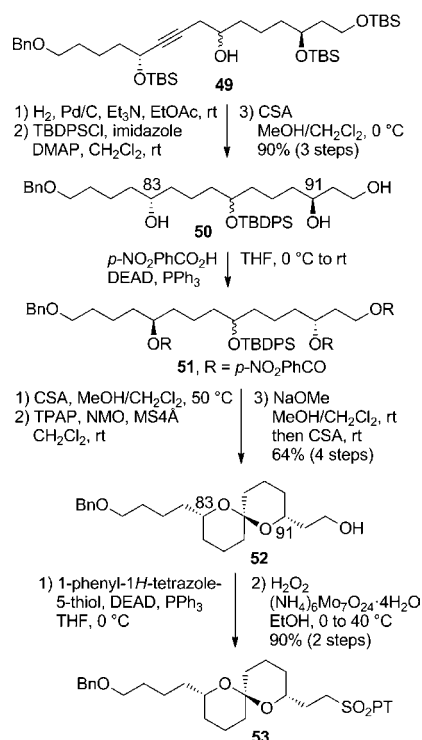


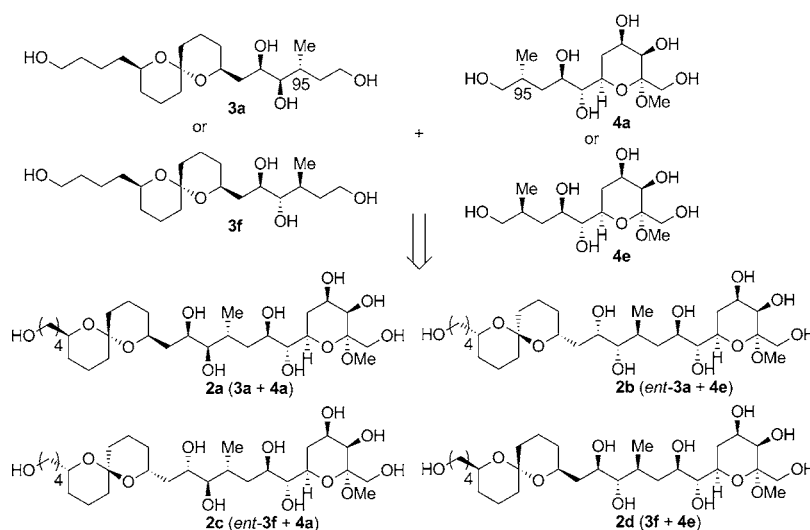
Figure 5. Differences in the ^{13}C NMR chemical shifts of natural symbiodinolide (**1**) and the synthesized products **4a–h** ($\Delta\delta = \delta_1 - \delta_4$ in ppm). The x and y axes represent the carbon number and $\Delta\delta$, respectively.

ic acid/diethyl azodicarboxylate (DEAD)/ PPh_3 ^[25] to provide tris-*p*-nitrobenzoate **51**. Deprotection of the TBDPS ether **51** with CSA and oxidation of the resulting alcohol with tetra-*n*-propylammonium perruthenate (TPAP)^[26] furnished the corresponding ketone. Hydrolysis of the three *p*-nitrobenzoate groups with NaOMe and subsequent spiroacetalization of the resulting trihydroxyketone with CSA were performed in one-



Scheme 17. Synthesis of PT-sulfone **53**. TBDPS = *tert*-butyldiphenylsilyl, DEAD = diethyl azodicarboxylate, TPAP = tetra-*n*-propylammonium perruthenate, NMO = *N*-methylmorpholine oxide, MS = molecular sieves, PT = 1-phenyl-1*H*-tetrazol-5-yl.

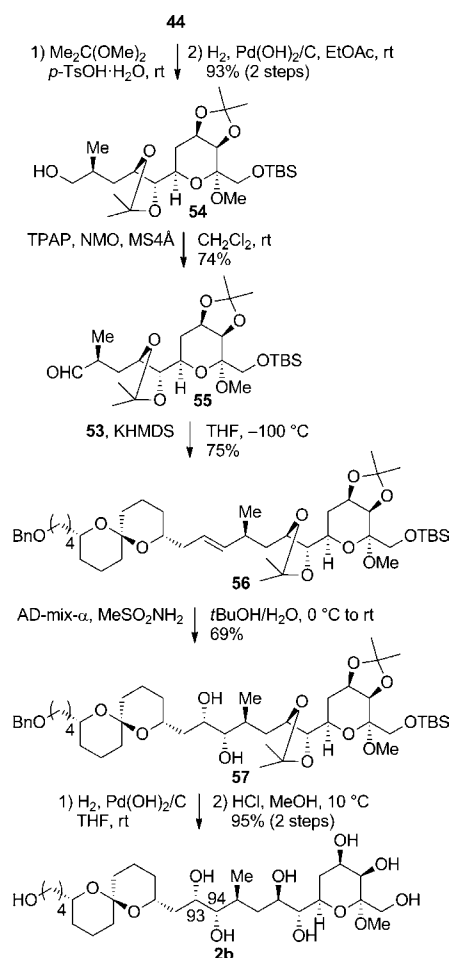
pot to produce the desired product **52** as a single diastereoisomer in 64% yield over four steps. Stereochemical inversion in the Mitsunobu reaction of alcohol **50** to give compound **51** was confirmed at this stage. Thus, the ^1H and ^{13}C NMR data of spiroacetal **52** were identical to those of the enantiomeric alcohol **9**,^[1] and the specific rotation of spiroacetal **52** was $[\alpha]_D^{23} = -52.4$ ($c = 1.02$ in CHCl_3).^[27] The optical purity (> 95%) of compound **52** was determined by derivatization to its (*S*)- and (*R*)-



Scheme 16. Four possible diastereoisomers of the C79–C104 fragment **2a–d**.

MTPA esters and subsequent comparison of their ^1H NMR spectra. The alcohol **52** was transformed to PT-sulfone **53** (PT = 1-phenyl-1*H*-tetrazol-5-yl) by sulfenylation and subsequent oxidation with $\text{H}_2\text{O}_2/\text{Mo}^{\text{VI}}$.^[28]

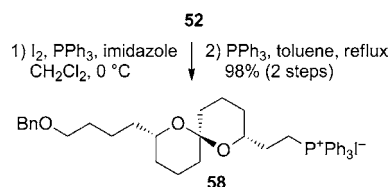
With the coupling precursor **53** in hand, we next tried to synthesize the C93,94-*syn*-diol **2b** by using a similar transformation to that which was used for the synthesis of diastereomeric compound **2a**: a combination of a Julia–Kocienski olefination and a Sharpless asymmetric dihydroxylation.^[1] Acetonide protection of the diol **44** and removal of the PMB moiety gave alcohol **54**, which was oxidized to aldehyde **55** (Scheme 18). The PT-sulfone **53** and the aldehyde **55** were suc-



Scheme 18. Synthesis of diastereoisomer **2b**. KHMDS = potassium hexamethyldisilazide.

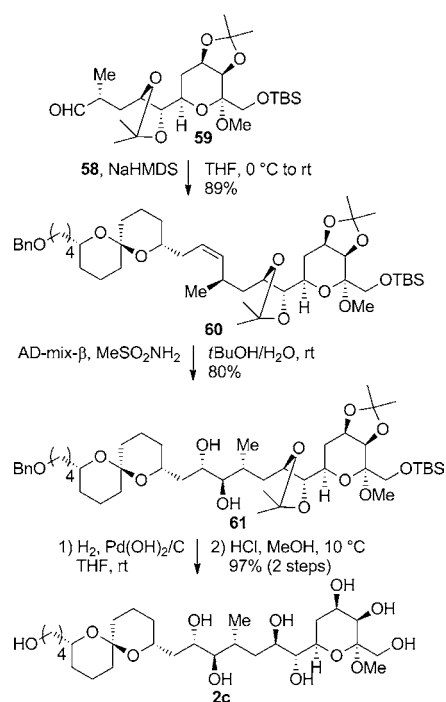
cessfully coupled though a Julia–Kocienski olefination^[29] under the conditions that had been optimized in the synthesis of diastereoisomer **2a**^[1] to give the desired (*E*)-alkene **56** as the sole diastereoisomer in 75% yield. The alkene **56** was subjected to the Sharpless asymmetric dihydroxylation^[30] with AD-mix- α to afford *syn*-diol **57** with the desired stereochemical configuration.^[10] Debenzylation of *syn*-diol **57** by hydrogenation and subsequent removal of the acetonide and TBS moieties with HCl in MeOH furnished diastereoisomer **2b**.

Our final task was the synthesis of diastereoisomers **2c** and **2d** that possess the C93,94-*anti*-configuration, which we planned to introduce by dihydroxylation of the corresponding (*Z*)-alkenes. Phosphonium salt **58**, which is the coupling precursor for the synthesis of **2c**, was prepared from the alcohol **52** by iodination followed by reaction with PPh_3 (Scheme 19). Depro-



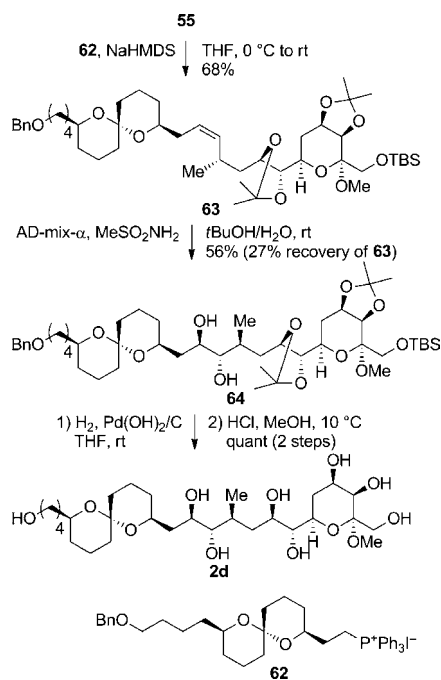
Scheme 19. Synthesis of phosphonium salt **58**.

tonation of the phosphonium salt **58** with sodium hexamethyldisilazide (NaHMDS) and subsequent Wittig reaction with the aldehyde **59** were successfully performed to afford the desired (*Z*)-alkene **60** as a single diastereoisomer in 89% yield (Scheme 20). As a result of detailed investigation on the dihy-



Scheme 20. Synthesis of diastereoisomer **2c**. NaHMDS = sodium hexamethyldisilazide.

droxylation of alkene **60**, it was proven that the dihydroxylation of (*Z*)-alkene **60** with AD-mix- β provided the desired *anti*-diol **61** in 80% yield.^[10,31] Removal of the benzyl, acetonide, and TBS protective groups of compound **61** produced diastereoisomer **2c** in 97% yield over two steps. The stereoselective synthesis of diastereoisomer **2d** is illustrated in Scheme 21. The aldehyde **55** was coupled with phosphonium salt **62**,^[32] which is



Scheme 21. Synthesis of diastereoisomer 2d.

the enantiomer of 58, to furnish (*Z*)-alkene 63 as the sole diastereoisomer in 68% yield. Treatment of the alkene 63 with AD-mix- α afforded the desired *anti*-diol 64 in 56% yield along with 27% recovery of the starting material 63.^[10,33] Complete deprotection of compound 64 produced a quantitative yield of diastereoisomer 2d.

Relative configuration of the C79–C104 fragment

With all of the four suggested diastereoisomers 2a–d in hand,^[23] we next analyzed their 2D NMR spectra carefully and compared their ¹³C NMR chemical shifts with those of natural symbiodinolide (1). As shown in Figure 6, only the diastereoisomer 2b was found to exhibit similar NMR characteristics to those of the natural product.^[17] Significant differences were detected in the ¹³C NMR chemical shifts of diastereoisomers 2a, c, and d, especially in the C91–C99 carbon chain domain. Therefore, we concluded that symbiodinolide (1) has the relative stereostructure in the C79–C104 fragment, as represented in diastereoisomer 2b.

Conclusion

Toward the stereostructural reassignment of the C79–C104 fragment of symbiodinolide (1), which was suggested in the preceding paper,^[1] we have carried out a two-phase approach: 1) stereostructural elucidation of the respective C79–C97 and C94–C104 fragments and 2) stereostructural determination of the C79–C104 fragment by using the results obtained in the first phase. Thus, we first synthesized all of the eight possible diastereoisomers of the C79–C97 fragment 3a–h by using the dithiane addition to an aldehyde and a diastereoselective reduction as the key transformations in the unified route. Comparison of the ¹³C NMR chemical shifts of the natural product 1 and the synthetic derivatives 3a–h led to the proposal of diastereoisomers 3a and f as the candidate compounds for the C79–C97 fragment. Next, all of the eight possible diastereoisomers of the C94–C104 fragment 4a–h were stereodiver-

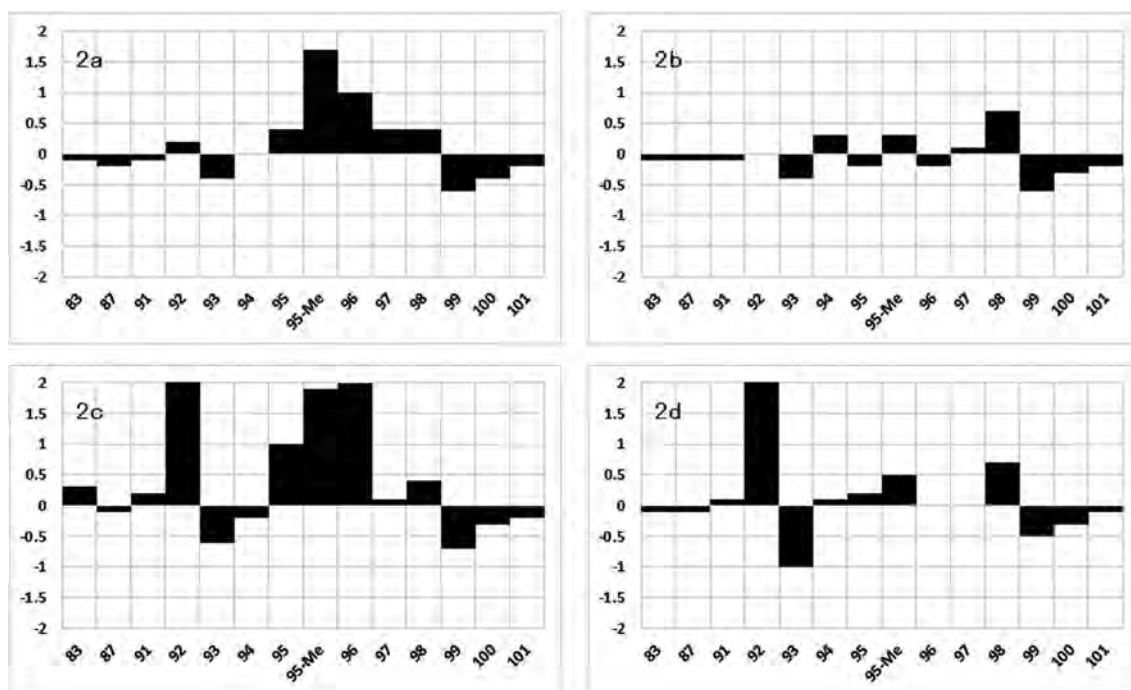


Figure 6. Differences of the ¹³C NMR chemical shifts of natural symbiodinolide (1) and the synthesized products 2a–d ($\Delta\delta = \delta_1 - \delta_2$ in ppm). The x and y axes represent the carbon number and $\Delta\delta$, respectively.

gently synthesized, and comparison of their ^{13}C NMR data with those of the natural product **1** led to the proposal of diastereoisomers **4a** and **e** as the candidate compounds for this fragment. In addition, all four possible diastereoisomers of the C79–C104 fragment **2a–d**, which were raised by the combination of **3a/f** and **4a/e**, were synthesized by the Julia–Kocienski and Wittig olefination and subsequent Sharpless asymmetric dihydroxylation (**2a** in the preceding paper^[1]). Upon comparison of the ^{13}C NMR chemical shifts of the natural product **1** and the synthesized products **2a–d**, we found that only the diastereoisomer **2b** displayed similar NMR characteristics to those of the natural product **1**. Therefore, the relative configuration of the C79–C104 fragment of symbiodinolide (**1**) was re-assigned to be that depicted in diastereoisomer **2b**. Our results obtained in this work indicate that the C91–C99 carbon chain portion of symbiodinolide (**1**) does not possess the zigzag conformation, which was proposed in our original report on the structural determination of this natural product.^[34] As there are seven stereogenic centers in the C91–C99 carbon chain moiety, the number of possible diastereoisomers for this portion is 64. It is noteworthy that the relative stereostructure of the C79–C104 fragment was elucidated by synthesizing only 20 diastereoisomers instead of 64, that is, eight possible diastereoisomers for the C79–C97 fragment, eight possible diastereoisomers for the C94–C104 fragment, and four possible diastereoisomers for the C79–C104 fragment. Further synthetic study toward the complete structural elucidation of symbiodinolide (**1**) is currently underway and will be reported in due course.

Acknowledgements

We are grateful to Division of Instrumental Analysis, Okayama University, for the NMR measurements. We acknowledge JGC-S Scholarship Foundation, The Naito Foundation, The Sumitomo Foundation, and The Uehara Memorial Foundation for their financial supports. This research was supported by a Grant-in-Aid for Scientific Research (No. 24710250) from the Japan Society for the Promotion of Science (JSPS).

Keywords: macrocycles · natural products · polyols · stereodivergent synthesis · structure elucidation

- [1] H. Takamura, T. Fujiwara, Y. Kawakubo, I. Kadota, D. Uemura, *Chem. Eur. J.* **2015**, DOI: 10.1002/chem.201503880.
 [2] As mentioned in the preceding article, we judged that the stereochemical determination of the two cyclic domains (C83–C91 and C99–C103) was reasonable and there is no need to synthesize the stereoisomers of these two portions.
 [3] For selected recent examples on the stereodivergent synthesis of natural products toward the structural elucidation, see: a) T. Kotaki, T. Shinada, K. Kaihara, Y. Ohfuné, H. Numata, *Org. Lett.* **2009**, *11*, 5234–5237; b) B. Sui, E. A.-H. Yeh, D. P. Curran, *J. Org. Chem.* **2010**, *75*, 2942–2954; c) S. Tamura, T. Ohno, Y. Hattori, N. Murakami, *Tetrahedron Lett.* **2010**, *51*, 1523–1525; d) D. Urabe, H. Todoroki, K. Masuda, M. Inoue, *Tetrahedron* **2012**, *68*, 3210–3219; e) H. Takamura, H. Wada, M. Ogino, T. Kikuchi, I. Kadota, D. Uemura, *J. Org. Chem.* **2015**, *80*, 3111–3123.

- [4] a) A. Mengel, O. Reiser, *Chem. Rev.* **1999**, *99*, 1191–1223; b) D. A. Evans, S. J. Siska, V. J. Cee, *Angew. Chem. Int. Ed.* **2003**, *42*, 1761–1765; *Angew. Chem.* **2003**, *115*, 1803–1807.
 [5] J. R. Parikh, W. v. E. Doering, *J. Am. Chem. Soc.* **1967**, *89*, 5505–5507.
 [6] The enantiomer of compound **6** is the known compound. See: J. L.-Y. Cheng, M. A. Brimble, *J. Org. Chem.* **2011**, *76*, 9417–9428.
 [7] a) E. J. Corey, B. W. Erickson, *J. Org. Chem.* **1971**, *36*, 3553–3560; b) A. V. Rama Rao, G. Venkatswamy, S. M. Javeed, V. H. Deshpande, B. Ramamohan Rao, *J. Org. Chem.* **1983**, *48*, 1552–1554.
 [8] We obtained compounds **10** and **11** as an inseparable diastereomeric mixture. The α -hydroxy ketones **7** and **8**, obtained from diastereoisomers **10** and **11**, were separated by silica gel column chromatography.
 [9] I. Ohtani, T. Kusumi, Y. Kashman, H. Kakisawa, *J. Am. Chem. Soc.* **1991**, *113*, 4092–4096.
 [10] For the stereochemical determination, see the Supporting Information.
 [11] a) T. Nakata, T. Tanaka, T. Oishi, *Tetrahedron Lett.* **1983**, *24*, 2653–2656; b) T. Oishi, T. Nakata, *Acc. Chem. Res.* **1984**, *17*, 338–344.
 [12] J. Robertson, W. P. Unsworth, S. G. Lamont, *Tetrahedron* **2010**, *66*, 2363–2372.
 [13] The stereochemistry at the C94 position of compound **17**, which was introduced in the reduction of α -hydroxy ketone **7**, was determined by the difference in ^1H NMR spectra between **3a** and **b**.
 [14] The stereochemistry at the C94 position of compound **20** was determined by the discrepancy in the ^1H NMR spectra of **3c** and **d**.
 [15] Actually, we obtained compounds **22** and **23** as an inseparable diastereomeric mixture, and we proceeded with further transformations with the diastereomeric mixture. In the synthesis of compounds **3e** and **g**, the alcohols **26** and **29** were transformed into diols **27** and **30** because of the chromatographic separation at this stage. In the synthesis of **3f** and **h**, the two diastereoisomers were separated upon formation of a mixture of compounds **28** and **31**.
 [16] The stereochemistries at the C93 and C94 positions of compound **27** were determined because the ^1H NMR spectrum of **3e** was different from those of **3f**, **g**, and **h**.
 [17] See the Supporting Information for details.
 [18] The stereochemistry at the C97 position of diol **37** was determined by the difference in the ^1H NMR spectra between diastereoisomers **4c** and **d**.
 [19] a) R. D. Walkup, P. D. Boatman Jr., R. R. Kane, R. T. Cunningham, *Tetrahedron Lett.* **1991**, *32*, 3937–3940; b) J. B. Shotwell, W. R. Roush, *Org. Lett.* **2004**, *6*, 3865–3868.
 [20] a) D. B. Dess, J. C. Martin, *J. Org. Chem.* **1983**, *48*, 4155–4156; b) D. B. Dess, J. C. Martin, *J. Am. Chem. Soc.* **1991**, *113*, 7277–7287.
 [21] The absolute configuration of the resulting C97 stereogenic center of diol **44** was confirmed by the ^1H NMR spectral difference between diastereoisomers **4e** and **f**.
 [22] For the stereochemical determination at the C97 position of alcohol **48**, see the Supporting Information. The absolute stereochemistry of the C97 stereocenter of diol **47** was confirmed by the discrepancy in ^1H NMR spectra between **4g** and **h**.
 [23] For the synthesis of diastereoisomer **2a**, see ref. [1].
 [24] For reviews on Mitsunobu reaction, see: a) O. Mitsunobu, *Synthesis* **1981**, 1–28; b) K. C. K. Swamy, N. N. B. Kumar, E. Balaraman, K. V. P. P. Kumar, *Chem. Rev.* **2009**, *109*, 2551–2651.
 [25] S. F. Martin, J. A. Dodge, *Tetrahedron Lett.* **1991**, *32*, 3017–3020.
 [26] For a review, see: S. V. Ley, J. Norman, W. P. Griffith, S. P. Marsden, *Synthesis* **1994**, 639–666.
 [27] The alcohol **9**: $[\alpha]_{\text{D}}^{24} = +50.5$ ($c = 1.00$, CHCl_3).
 [28] H. S. Schultz, H. B. Freyermuth, S. R. Buc, *J. Org. Chem.* **1963**, *28*, 1140–1142.
 [29] a) P. R. Blakemore, W. J. Cole, P. J. Kocienski, A. Morley, *Synlett* **1998**, 26–28; b) P. R. Blakemore, *J. Chem. Soc. Perkin Trans. 1* **2002**, 2563–2585; c) C. Aïssa, *Eur. J. Org. Chem.* **2009**, 1831–1844.
 [30] For a review, see: H. C. Kolb, M. S. VanNieuwenhze, K. B. Sharpless, *Chem. Rev.* **1994**, *94*, 2483–2547.
 [31] The *anti*-diol, which is the diastereoisomer of compound **61**, was obtained in 12% yield. When the alkene **60** was treated with AD-mix- α , the diol **61** and its diastereoisomer with the C93,94-*anti*-stereochemistries were obtained in 50 and 17% yields, respectively.

- [32] The phosphonium salt **62** was prepared from the alcohol **9** by the same transformation that was used to convert alcohol **52** into phosphonium salt **58**.
- [33] The *anti*-diol, which is the diastereoisomer of **64**, was obtained in 9% yield. Treatment of the alkene **63** with AD-mix- β gave the diol **64** and its diastereoisomer with the C93,94-*anti*-configurations in 27 and 16% yields, respectively.
- [34] M. Kita, N. Ohishi, K. Konishi, M. Kondo, T. Koyama, M. Kitamura, K. Yamada, D. Uemura, *Tetrahedron* **2007**, *63*, 6241–6251.

Received: September 28, 2015
 Published online on January 7, 2016

Organic Synthesis | Very Important Paper |

VIP Stereoselective Synthesis of the Proposed C79–C104 Fragment of Symbiodinolide

Hiroyoshi Takamura,^{*,[a]} Takayuki Fujiwara,^[a] Yohei Kawakubo,^[a] Isao Kadota,^[a] and Daisuke Uemura^[b]

Abstract: Stereoselective and streamlined synthesis of the proposed C79–C104 fragment **2** of symbiodinolide (**1**), a polyol marine natural product with a molecular weight of 2860, was achieved. In the synthetic route, the proposed C79–C104 fragment **2** was synthesized by utilizing a Julia–Kocienski olefination and subsequent Sharpless asymmetric

dihydroxylation as key transformations in a convergent manner. Detailed comparison of the ¹³C NMR chemical shifts between the natural product and the synthetic C79–C104 fragment **2** revealed that the stereostructure at the C91–C99 carbon chain moiety of symbiodinolide (**1**) should be re-investigated.

Introduction

A variety of biologically active secondary metabolites have been isolated from marine origin.^[1] Among them, polyether and polyol marine natural products, such as brevetoxins, ciguatoxins, halichondrins, and palytoxins, are attractive molecules in natural product, synthetic, and medicinal chemistry due to their extraordinary structures and potent biological activities.^[2] Their structural feature is a long carbon backbone that is highly functionalized by oxygen atoms.

We previously reported the isolation of symbiodinolide (**1**, Figure 1) from the symbiotic marine dinoflagellate *Symbiodinium* sp. in 2007.^[3] Symbiodinolide (**1**) is a 62-membered polyol macrolide with a molecular weight of 2860 and 61 stereogenic centers. This natural product displays voltage-dependent N-type Ca²⁺ channel-opening activity at 7 nM and COX-1 inhibitory effect at 2 μM (65% inhibition). In addition, **1** ruptures the tissue surface of the acoel flatworm *Amphiscolops* sp. at 2.5 μM. The gross structure of **1** was established by extensive 2D NMR analysis^[3] and partial stereochemistries of **1** were elucidated by the degradation of the natural product^[3,4] and chemical synthesis of each fragment^[5] by our group. However, the complete configurational elucidation of **1** remains an unsolved issue because of its huge and complicated molecular structure. In the C91–C99 carbon chain moiety, the stereochemistries were determined by the analysis of ³J_{H,H} coupling con-

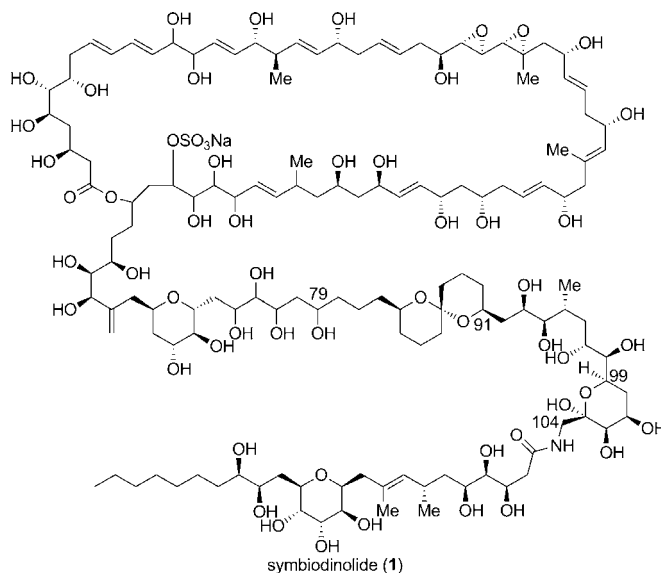


Figure 1. Structure of symbiodinolide (**1**).

stants and NOE observations.^[3] In this article, we first describe the stereoselective synthesis of the C79–C104 fragment **2** possessing the proposed stereostructure. Furthermore, the ¹³C NMR chemical shifts were compared between the natural product and the synthetic product **2**, which indicates that the stereochemical determination of the C91–C99 carbon chain domain of **1** needs to be re-examined.^[6]

Results and Discussion

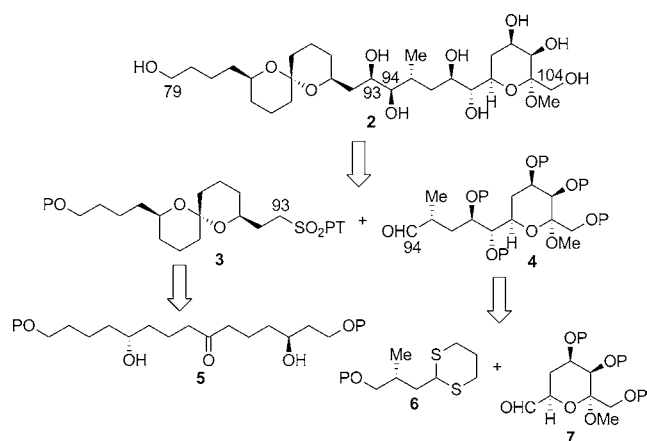
Retrosynthetic analysis of **2**

Our retrosynthetic analysis of the proposed C79–C104 fragment **2** is shown in Scheme 1. We envisioned that the target

[a] Prof. Dr. H. Takamura, T. Fujiwara, Y. Kawakubo, Prof. Dr. I. Kadota
Department of Chemistry, Graduate School of Natural Science
and Technology, Okayama University
3-1-1 Tsushima-naka, Kita-ku, Okayama 700-8530 (Japan)
E-mail: takamura@cc.okayama-u.ac.jp

[b] Prof. Dr. D. Uemura
Department of Chemistry, Faculty of Science, Kanagawa University
2946 Tsuchiya, Hiratsuka 259-1293 (Japan)

Supporting information and ORCID(s) from the author(s) for this article are available on the WWW under <http://dx.doi.org/10.1002/chem.201503880>.

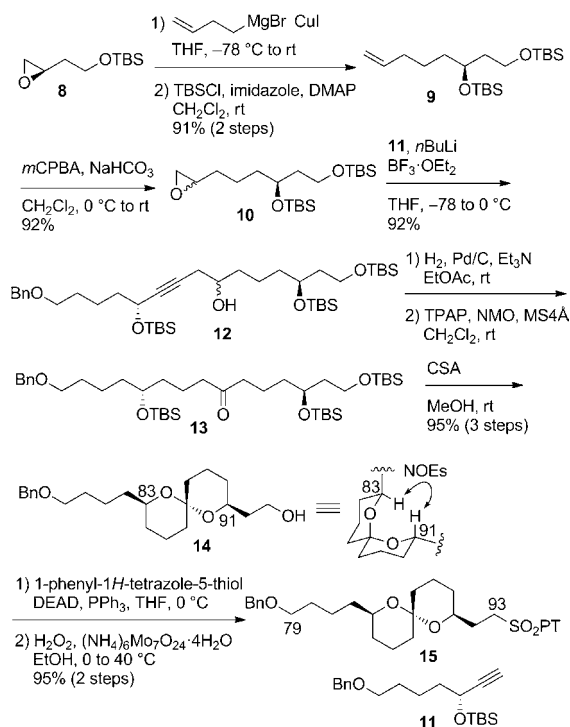


Scheme 1. Retrosynthetic analysis of **2**. P = protective group; PT = 1-phenyl-1*H*-tetrazol-5-yl.

molecule **2** could be synthesized by the Julia–Kocienski olefination^[7] between 1-phenyl-1*H*-tetrazol-5-yl (PT)-sulfone **3** and aldehyde **4** and subsequent stereoselective introduction of the *syn*-diol moiety at the C93- and C94-positions by utilizing Sharpless asymmetric dihydroxylation.^[8] The carbon framework of the coupling precursor **3** could be stereoselectively constructed through the thermodynamically controlled spiroacetalization of dihydroxyketone **5**. On the other hand, tetrahydropyran fragment **4** could be synthesized by the reaction of di-thiane **6** and aldehyde **7**.

Synthesis of PT-sulfone 15

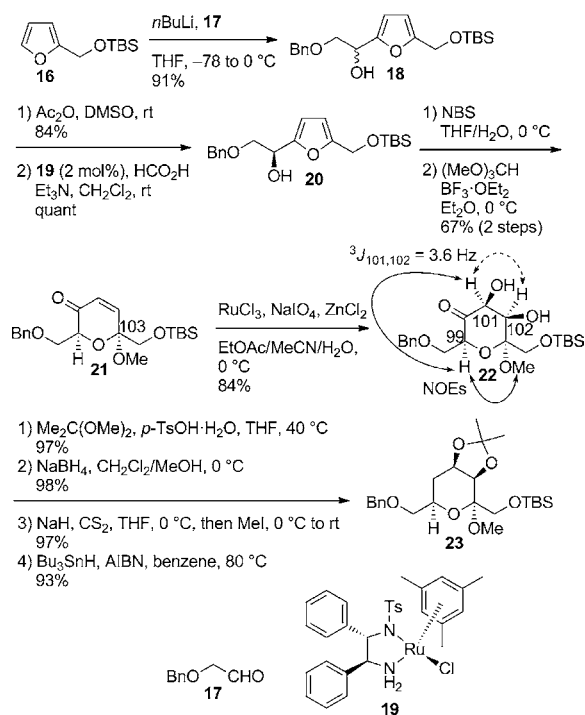
First, we investigated the stereoselective synthesis of the C79–C93 fragment PT-sulfone **15**.^[9] The synthesis commenced from optically pure epoxide **8**, which was prepared from L-aspartic acid by the known procedure (Scheme 2).^[10] The epoxide **8** was treated with 3-butenylmagnesium bromide/CuI^[11] to afford the desired secondary alcohol. The resulting alcohol was protected with TBSCl to provide silyl ether **9**. Alkene **9** was oxidized with *m*CPBA to give terminal epoxide **10** as a 1:1 diastereomeric mixture. The coupling between epoxide **10** and alkyne **11**^[5a,12] with *n*BuLi/BF₃·OEt₂^[13] proceeded smoothly to produce alcohol **12** in 92% yield. Hydrogenation of alkyne **12** followed by tetra-*n*-propylammonium perruthenate (TPAP) oxidation^[14] of the resulting alcohol gave ketone **13**. Global deprotection of the three TBS groups of **13** and spiroacetalization with CSA in MeOH were performed in one-pot to provide alcohol **14** in 95% yield in three steps as a single stereoisomer.^[15] The absolute configuration of **14** was unambiguously established by the NOE correlations between H-83 and H-91. The stereochemical outcome in the spiroacetalization can be rationalized by the thermodynamic stability of **14** due to its double anomeric effect. Treatment of the alcohol **14** with 1-phenyl-1*H*-tetrazole-5-thiol/diethyl azodicarboxylate (DEAD)/PPh₃ and subsequent oxidation of the resulting PT-sulfide with H₂O₂/Mo^{VI}^[16] furnished PT-sulfone **15** in 95% yield in two steps.



Scheme 2. Synthesis of **15**. TBS = *tert*-butyldimethylsilyl, DMAP = 4-dimethylaminopyridine, *m*CPBA = *m*-chloroperbenzoic acid, Bn = benzyl, TPAP = tetra-*n*-propylammonium perruthenate, NMO = *N*-methylmorpholine oxide, MS = molecular sieves, CSA = camphorsulfonic acid, NOE = nuclear Overhauser effect, DEAD = diethyl azodicarboxylate.

Synthesis of aldehyde 29

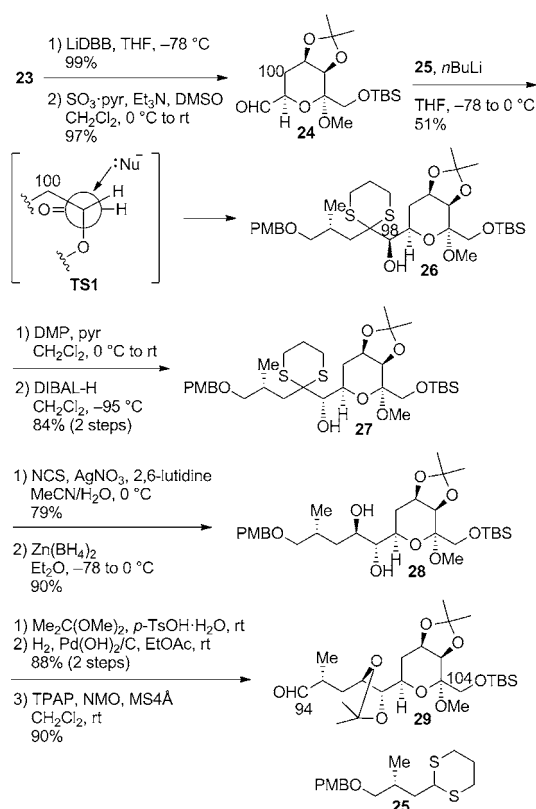
With the coupling precursor **15** in hand, we next examined the stereocontrolled synthesis of the C94–C104 fragment aldehyde **29**,^[17] which is the coupling partner of **15**. We first investigated the stereoselective construction of the tetrahydropyran moiety. Thus, deprotonation of furan **16**^[18] with *n*BuLi and subsequent reaction with aldehyde **17**^[19] gave racemic furyl alcohol **18** (Scheme 3). Oxidation of the alcohol **18** with Ac₂O/DMSO^[20] followed by asymmetric transfer hydrogenation of the resulting furyl ketone by using HCO₂H/Et₃N as the hydrogen source in the presence of 2 mol% of (*S,S*)-ruthenium catalyst **19**^[21] provided optically active furyl alcohol **20** quantitatively as a single stereoisomer.^[22] Achmatowicz rearrangement^[23] of **20** was initiated with NBS in aqueous THF at 0 °C to yield the corresponding hemiacetals as a 1:1 diastereomeric mixture at the C103-position, which were quite unstable and, therefore, reacted immediately with (MeO)₃CH/BF₃·OEt₂ in Et₂O at 0 °C to afford the desired methyl acetal **21** and its 103-epimer in 67 and 10% yields in two steps, respectively. Next, the stereoselective introduction of the vicinal diol moiety at the C101- and C102-positions was examined. We first carried out the OsO₄-catalyzed dihydroxylation of enone **21**; however, unfortunately, the reaction did not proceed at all and the enone **21** was recovered quantitatively. Plietker et al. reported that RuO₄-catalyzed dihydroxylation in the presence of a Lewis acid was efficient for the electron-deficient alkenes.^[24] Therefore, according to their protocol, enone **21** was treated with RuCl₃/NaIO₄ in



Scheme 3. Synthesis of **23**. Ts = toluenesulfonyl, NBS = *N*-bromosuccinimide, AIBN = 2,2'-azobisisobutyronitrile.

the presence of CeCl_3 as a Lewis acid to produce the desired diol **22** in 51% yield. After the detailed investigation, the use of ZnCl_2 as a Lewis acid was found to be effective to furnish **22** in 84% yield as the sole product. The stereostructure of the diol **22** was elucidated by NMR spectroscopy. Thus, the stereochemistry at the C103-position resulting in the transformation from **20** to **21** was verified by the NOE correlations between H-99 and OCH_3 -103. The NOE observations of H-99/H-101 and the small magnitude of the coupling constant ($^3J_{101,102} = 3.6 \text{ Hz}$) confirmed that H-99, H-101, and H-102 were oriented in the *syn* relationship to each other. Although the detailed conformational analysis of **21** was not carried out, the 103-methoxy group seems to sterically prevent the RuO_4 -approaching from the α -face. After the diol **22** was protected with $\text{Me}_2\text{C}(\text{OMe})_2$, the resulting ketone was reduced with NaBH_4 to produce the corresponding β -alcohol, presumably due to the steric repulsion between the acetonide moiety and the reagent. The absolute configuration at the C100-position of the resulting β -alcohol was determined by the $^3J_{99,100}$ coupling constant (5.5 Hz). The hydroxy moiety at the C100-position was removed through a Barton–McCombie deoxygenation^[25] by way of the (*S*)-methyl dithiocarbonate to afford tetrahydropyran **23**.

We next turned our attention to the introduction of the C94–C97 moiety. Thus, deprotection of the benzyl group of **23** with lithium 4,4'-*di-tert*-butylbiphenylide (LiDBB)^[26] followed by Parikh–Doering oxidation^[27] gave aldehyde **24** (Scheme 4). Deprotonation of dithiane **25** with *n*BuLi, which was synthesized from commercially available (*S*)-3-hydroxy-2-methylpropionate by the known procedure,^[28] and addition of the aldehyde **24** led to the formation of alcohol **26** as a single stereoisomer.^[22] The stereoselective addition of the anion, which was formed



Scheme 4. Synthesis of **29**. DBB = 4,4'-*di-tert*-butylbiphenylide, pyr = pyridine, PMB = *p*-methoxybenzyl, DMP = Dess–Martin periodinane, DIBAL-H = diisobutylaluminum hydride, NCS = *N*-chlorosuccinimide.

from **25**, to the aldehyde **24** is understandable by a Felkin–Anh model^[29] as shown in **TS1**. Unfortunately, the stereochemistry at the C98-position was undesired; therefore, the stereoinversion at the C98-position of **26** was performed by Dess–Martin oxidation^[30] and subsequent diastereoselective reduction with DIBAL-H at -95°C to furnish alcohol **27** bearing the desired configuration in 84% yield in two steps as the sole product. After the hydrolysis of the dithiane moiety of **27** with $\text{NCS}/\text{AgNO}_3/2,6$ -lutidine in aqueous MeCN ,^[31] the resulting α -hydroxy ketone was reduced diastereoselectively with $\text{Zn}(\text{BH}_4)_2$ through the chelated transition state^[32] to afford the desired *anti*-diol **28** as a single diastereomer.^[22] Acetonide protection of **28**, removal of the *p*-methoxybenzyl (PMB) group by hydrogenation, and TPAP oxidation^[14] provided the aldehyde **29**.

Synthesis of the proposed C79–C104 fragment 2.

After having synthesized both coupling precursors **15** and **29**, we next focused on the connection of these two fragments by the Julia–Kocienski olefination (Table 1).^[7] When we treated the PT-sulfone **15** with LDA as a base and reacted it with the aldehyde **29**, the (*E*)- and (*Z*)-alkenes **30** and **31** were obtained in 95% combined yield as an inseparable mixture in a 2.8:1 diastereomeric ratio (Table 1, entry 1).^[33] The resulting configurations at the C93- and C94-positions were verified by the $^3J_{93,94}$ coupling constants, respectively (15.3 Hz in **30** and 10.2 Hz in **31**). Although we obtained the desired coupling product **30**,

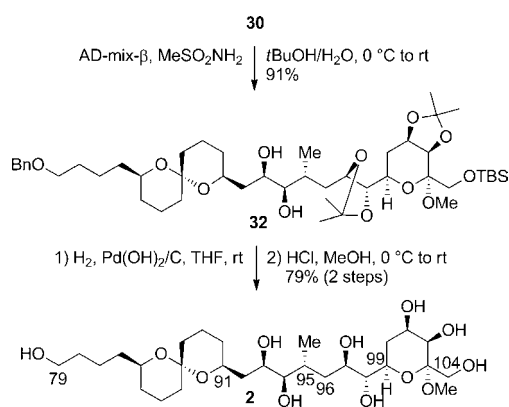
Table 1. Julia–Kocienski olefination between **15** and **29**.

Entry	Conditions ^[a]	Yield [%] ^[b]	Ratio (30 / 31) ^[c]
1	LDA, −78 to 0 °C	95	2.8:1
2	KHMDS, −78 °C	80	8:1
3	KHMDS, −100 °C	70	> 20:1

[a] LDA = lithium diisopropylamide, KHMDS = potassium hexamethyldisilazide. [b] Isolated yield. [c] Determined by analysis of the ¹H NMR spectra.

E/Z selectivity was quite low. When we used KHMDS as the base, the *E/Z* ratio was increased to 8:1 (entry 2). Finally, lowering the reaction temperature to −100 °C, we could obtain the (*E*)-alkene **30** in 70% yield as a single diastereomer (entry 3).

Further transformation from **30** to the target molecule **2** is depicted in Scheme 5. The alkene **30** was exposed to the Sharpless asymmetric dihydroxylation^[8] with AD-mix-β to produce diol **32** possessing the expected and desired stereochemistries.^[22] Finally, deprotection of the benzyl group by hydrogenation followed by simultaneous removal of the acetonide and TBS moieties with HCl in MeOH furnished the proposed C79–C104 fragment **2** in 79% yield in two steps.



Scheme 5. Synthesis of **2**.

Next, we compared the ¹³C NMR data of the synthetic product **2** with those of the corresponding moiety of natural symbiodinolide (**1**).^[34] The ¹³C NMR chemical shifts and their deviations of **1** and **2** are summarized in Table 2. Unexpectedly, the ¹³C NMR chemical shifts of the synthetic **2** did not match those of the natural product. Especially, their chemical shift deviation was critical at the C95–Me group. These findings clearly indicate that the stereostructure at the C91–C99 carbon chain region of symbiodinolide (**1**) should be re-surveyed.^[35]

Table 2. ¹³C NMR chemical shifts and their deviations of natural symbiodinolide (**1**) and the synthetic product **2**.^[a]

Position	1 ^[b]	2 ^[c]	Δ(δ ₁ –δ ₂) ^[d]
83	70.3	70.4	−0.1
87	97.0	97.2	−0.2
91	67.1	67.2	−0.1
92	42.0 ^[e]	41.8	+0.2
93	68.7	69.1	−0.4
94	80.9	80.9	0.0
95	33.5	33.1	+0.4
95-Me	19.0	17.3	+1.7
96	38.7	37.7	+1.0
97	70.5	70.1	+0.4
98	78.5	78.1	+0.4
99	68.8	69.4	−0.6
100	30.7	31.1	−0.4
101	67.1	67.3	−0.2

[a] Chemical shifts are reported in ppm with reference to the internal residual solvent (CD₃OD, δ = 49.0 ppm). [b] Data from ref. [3]. Recorded at 200 MHz. [c] Recorded at 150 MHz. [d] δ₁ and δ₂ are chemical shifts of natural symbiodinolide (**1**) and the synthetic product **2**, respectively. [e] We previously reported the C92 chemical shift (δ = 46.4 ppm) in ref. [3]. In this work, after the careful and detailed reinvestigation of the ¹³C NMR data, we have revised the chemical shift assignment (δ = 42.0 ppm).

Conclusion

Stereoselective and streamlined synthesis of the C79–C104 fragment **2** with the originally assigned stereostructure of symbiodinolide (**1**) was examined. Acid-catalyzed thermodynamically controlled spiroacetalization was used as a key step to afford stereoselectively the coupling precursor **15**. The other coupling precursor **29** was synthesized by utilizing the Achmatowicz reaction for the tetrahydropyran construction and the dithiane addition to the aldehyde for the introduction of the C94–C97 moiety. The PT-sulfone **15** and the aldehyde **29** were coupled by Julia–Kocienski olefination and subsequent Sharpless asymmetric dihydroxylation produced the target molecule **2**. In addition, comparison of the ¹³C NMR chemical shifts between the natural product and synthesized **2** suggests that the relative configuration at the C91–C99 region of symbiodinolide (**1**) needs to be reinvestigated. Further our effort toward the stereostructural elucidation of this moiety of **1** will be reported in the following article.^[36]

Experimental Section

Experimental details, compound data, and copies of NMR spectra of new compounds can be found in the Supporting Information.

Acknowledgements

We are grateful to the Division of Instrumental Analysis, Okayama University, for the NMR measurements. We appreciate the JGC-S Scholarship Foundation, The Naito Foundation, The Sumitomo Foundation, and The Uehara Memorial Foundation for their financial support. This research was supported by

a Grant-in Aid for Scientific Research (no. 24710250) from the Japan Society for the Promotion of Science (JSPS).

Keywords: macrocycles · natural products · polyols · stereoselective synthesis · structure elucidation

- [1] a) D. Uemura in *Bioorganic Marine Chemistry*, Vol. 4 (Ed.: P. J. Scheuer), Springer, Heidelberg, **1991**, pp. 1–31; b) Y. Shimizu, *Chem. Rev.* **1993**, *93*, 1685–1698; c) D. Uemura, *Chem. Rec.* **2006**, *6*, 235–248.
- [2] a) T. Yasumoto, M. Murata, *Chem. Rev.* **1993**, *93*, 1897–1909; b) M. Murata, T. Yasumoto, *Nat. Prod. Rep.* **2000**, *17*, 293–314; c) M. Kita, D. Uemura, *Chem. Rec.* **2010**, *10*, 48–52.
- [3] M. Kita, N. Ohishi, K. Konishi, M. Kondo, T. Koyama, M. Kitamura, K. Yamada, D. Uemura, *Tetrahedron* **2007**, *63*, 6241–6251.
- [4] a) C. Han, D. Uemura, *Tetrahedron Lett.* **2008**, *49*, 6988–6990; b) C. Han, Y. Yamano, M. Kita, H. Takamura, D. Uemura, *Tetrahedron Lett.* **2009**, *50*, 5280–5282; c) C. Han, Y. Yamano, F. Kakiuchi, K. Nakamura, D. Uemura, *Tetrahedron* **2011**, *67*, 9622–9626.
- [5] a) H. Takamura, J. Ando, T. Abe, T. Murata, I. Kadota, D. Uemura, *Tetrahedron Lett.* **2008**, *49*, 4626–4629; b) T. Murata, M. Sano, H. Takamura, I. Kadota, D. Uemura, *J. Org. Chem.* **2009**, *74*, 4797–4803; c) H. Takamura, T. Murata, T. Asai, I. Kadota, D. Uemura, *J. Org. Chem.* **2009**, *74*, 6658–6666; d) H. Takamura, Y. Kadonaga, Y. Yamano, C. Han, Y. Aoyama, I. Kadota, D. Uemura, *Tetrahedron Lett.* **2009**, *50*, 863–866; e) H. Takamura, Y. Kadonaga, Y. Yamano, C. Han, I. Kadota, D. Uemura, *Tetrahedron* **2009**, *65*, 7449–7456; f) H. Takamura, Y. Kadonaga, I. Kadota, D. Uemura, *Tetrahedron Lett.* **2010**, *51*, 2603–2605; g) H. Takamura, Y. Kadonaga, I. Kadota, D. Uemura, *Tetrahedron* **2010**, *66*, 7569–7576; h) H. Takamura, K. Tsuda, Y. Kawakubo, I. Kadota, D. Uemura, *Tetrahedron Lett.* **2012**, *53*, 4317–4319; i) H. Takamura, T. Fujiwara, I. Kadota, D. Uemura, *Beilstein J. Org. Chem.* **2013**, *9*, 1931–1935; j) H. Takamura, H. Wada, M. Ogino, T. Kikuchi, I. Kadota, D. Uemura, *J. Org. Chem.* **2015**, *80*, 3111–3123.
- [6] For reviews on the structural elucidation of natural products by the chemical synthesis, see: a) K. C. Nicolaou, S. A. Snyder, *Angew. Chem. Int. Ed.* **2005**, *44*, 1012–1044; *Angew. Chem.* **2005**, *117*, 1036–1069; b) M. E. Maier, *Nat. Prod. Rep.* **2009**, *26*, 1105–1124; c) T. L. Suyama, W. H. Gerwick, K. L. McPhail, *Bioorg. Med. Chem.* **2011**, *19*, 6675–6701.
- [7] a) P. R. Blakemore, W. J. Cole, P. J. Kociński, A. Morley, *Synlett* **1998**, 26–28; b) P. R. Blakemore, *J. Chem. Soc. Perkin Trans. 1* **2002**, 2563–2585; c) C. Aissa, *Eur. J. Org. Chem.* **2009**, 1831–1844.
- [8] For a review, see: H. C. Kolb, M. S. Van Nieuwenhze, K. B. Sharpless, *Chem. Rev.* **1994**, *94*, 2483–2547.
- [9] For our preliminary communication on the synthesis of the C79–C93 fragment, see ref. [5].
- [10] C. D. Donner, *Tetrahedron Lett.* **2007**, *48*, 8888–8890.
- [11] I. Paterson, E. A. Anderson, S. M. Dalby, J. H. Lim, P. Maltas, O. Loiseleur, J. Genovino, C. Moessner, *Org. Biomol. Chem.* **2012**, *10*, 5861–5872.
- [12] For the preparation of **11**, see the Supporting Information.
- [13] M. Yamaguchi, I. Hirao, *Tetrahedron Lett.* **1983**, *24*, 391–394.
- [14] For a review, see: S. V. Ley, J. Norman, W. P. Griffith, S. P. Marsden, *Synthesis* **1994**, 639–666.
- [15] For reviews on the spiroacetal, see: a) F. Perron, K. F. Albizzati, *Chem. Rev.* **1989**, *89*, 1617–1661; b) J. E. Aho, P. M. Pihko, T. K. Rissa, *Chem. Rev.* **2005**, *105*, 4406–4440.
- [16] H. S. Schultz, H. B. Freyermuth, S. R. Buc, *J. Org. Chem.* **1963**, *28*, 1140–1142.
- [17] For our preliminary communication on the synthesis of the C94–C104 fragment, see ref. [5h].
- [18] S. Celanire, F. Marlin, J. E. Baldwin, R. M. Adlington, *Tetrahedron* **2005**, *61*, 3025–3032.
- [19] N. Nishizono, Y. Akama, M. Agata, M. Sugo, Y. Yamaguchi, K. Oda, *Tetrahedron* **2011**, *67*, 358–363.
- [20] J. D. Albright, L. Goldman, *J. Am. Chem. Soc.* **1965**, *87*, 4214–4216.
- [21] a) A. Fujii, S. Hashiguchi, N. Uematsu, T. Ikariya, R. Noyori, *J. Am. Chem. Soc.* **1996**, *118*, 2521–2522; b) R. Noyori, S. Hashiguchi, *Acc. Chem. Res.* **1997**, *30*, 97–102.
- [22] For the stereochemical determination, see the Supporting Information.
- [23] O. Achmatowicz Jr., P. Bukowski, B. Szechner, Z. Zwierzchowska, A. Zamojski, *Tetrahedron* **1971**, *27*, 1973–1996.
- [24] B. Plietker, M. Niggemann, *J. Org. Chem.* **2005**, *70*, 2402–2405.
- [25] D. H. R. Barton, S. W. McCombie, *J. Chem. Soc. Perkin Trans. 1* **1975**, 1574–1585.
- [26] a) P. K. Freeman, L. L. Hutchinson, *J. Org. Chem.* **1980**, *45*, 1924–1930; b) R. E. Ireland, M. G. Smith, *J. Am. Chem. Soc.* **1988**, *110*, 854–860.
- [27] J. R. Parikh, W. v. E. Doering, *J. Am. Chem. Soc.* **1967**, *89*, 5505–5507.
- [28] a) R. D. Walkup, P. D. Boatman Jr., R. R. Kane, R. T. Cunningham, *Tetrahedron Lett.* **1991**, *32*, 3937–3940; b) J. B. Shotwell, W. R. Roush, *Org. Lett.* **2004**, *6*, 3865–3868.
- [29] a) A. Mengel, O. Reiser, *Chem. Rev.* **1999**, *99*, 1191–1223; b) D. A. Evans, S. J. Siska, V. L. Cee, *Angew. Chem. Int. Ed.* **2003**, *42*, 1761–1765; *Angew. Chem.* **2003**, *115*, 1803–1807.
- [30] a) D. B. Dess, J. C. Martin, *J. Org. Chem.* **1983**, *48*, 4155–4156; b) D. B. Dess, J. C. Martin, *J. Am. Chem. Soc.* **1991**, *113*, 7277–7287.
- [31] a) E. J. Corey, B. W. Erickson, *J. Org. Chem.* **1971**, *36*, 3553–3560; b) A. V. R. Rao, G. Venkatswamy, S. M. Javeed, V. H. Deshpande, B. R. Rao, *J. Org. Chem.* **1983**, *48*, 1552–1554.
- [32] a) T. Nakata, T. Tanaka, T. Oishi, *Tetrahedron Lett.* **1983**, *24*, 2653–2656; b) T. Oishi, T. Nakata, *Acc. Chem. Res.* **1984**, *17*, 338–344.
- [33] We did not observe the epimerization at the C95-position of the aldehyde **29** in our investigation of the Julia–Kociński olefination between **15** and **29**.
- [34] For some examples on comparing the NMR data between model compounds and the natural product toward the structural elucidation, see: a) W. Zheng, J. A. DeMattei, J.-P. Wu, J. J.-W. Duan, L. R. Cook, H. Oinuma, Y. Kishi, *J. Am. Chem. Soc.* **1996**, *118*, 7946–7968; b) T. Oishi, M. Kanemoto, R. Swasono, N. Matsumori, M. Murata, *Org. Lett.* **2008**, *10*, 5203–5206; c) H. Fuwa, K. Ishigai, T. Goto, A. Suzuki, M. Sasaki, *J. Org. Chem.* **2009**, *74*, 4024–4040; d) E. Fleury, M.-I. Lannou, O. Bistri, F. Sautel, G. Massiot, A. Pancrazi, J. Ardisson, *J. Org. Chem.* **2009**, *74*, 7034–7045; e) K. C. Nicolaou, C. F. Gelin, J. H. Seo, Z. Huang, T. Umezawa, *J. Am. Chem. Soc.* **2010**, *132*, 9900–9907.
- [35] The relative configurations of the two cyclic moieties (C83–C91 and C99–C103 domains) were determined by $^3J_{\text{H,H}}$ coupling constants and NOE experiments in ref. [3]. In addition, the ^{13}C NMR chemical shift differences of these two domains between natural **1** and synthetic **2** were not significant. From these two results, we judged that the stereochemical elucidation of these two cyclic domains was reliable.
- [36] H. Takamura, T. Fujiwara, Y. Kawakubo, I. Kadota, D. Uemura, *Chem. Eur. J.* **2015** DOI: 10.1002/chem.201503881, in press.

Received: September 28, 2015
Published online on December 11, 2015



Contents lists available at ScienceDirect

Bioorganic & Medicinal Chemistry Letters

journal homepage: www.elsevier.com/locate/bmcl

Glutathione-triggered activation of the model of pro-oligonucleotide with benzyl protecting groups at the internucleotide linkage



Hisao Saneyoshi*, Kazuhiko Kondo, Naoki Sagawa, Akira Ono*

Department of Material and Life Chemistry, Faculty of Engineering, Kanagawa University, 3-27-1 Rokkakubashi, Kanagawa-ku, Yokohama 221-8686, Japan

ARTICLE INFO

Article history:

Received 15 June 2015

Revised 28 October 2015

Accepted 19 November 2015

Available online 19 November 2015

ABSTRACT

We have examined substituted benzyl protecting groups for the phosphodiester in oligodeoxyribonucleotides. Stability of the protecting groups in buffer and rates of deprotection by glutathione (GSH) were strongly influenced by benzyl ring substituents.

© 2015 Elsevier Ltd. All rights reserved.

Keywords:

Nucleic acid-based therapeutics

Prodrug

Protecting group

Glutathione

Oligonucleotide therapeutics have received considerable attention as next-generation chemotherapy agents.^{1–3} However their delivery into the cell remains a challenge. A primary reason for this is the polyanionic nature of oligonucleotides, limiting their cellular internalization. One possible strategy for improving cellular uptake would be to temporarily mask the negative charges of oligonucleotides with biodegradable phosphate-protecting groups.^{4–9} This pro-oligonucleotide approach has been suggested as a means to enable intracellular delivery, thereby improving the feasibility of oligonucleotide-based therapies.^{10,11} Several potential deprotection triggers for pro-oligonucleotides have been described, including esterases, heat, light, and hypoxia.^{4–9,12–28} For developing pro-oligos to medicines for various diseases in various cells and organs, discovery of new protecting groups which are deprotected by various triggers is still needed.

In this Letter, we focused on the use of intracellular glutathione (GSH) as a deprotection trigger.²⁹ GSH is a ubiquitous bio-thiol with intracellular concentration as high as 10 mM, 10–100 times higher than its concentration outside the cell.^{30,31} Because of this GSH concentration gradient, these pro-oligonucleotides should be stable in the extracellular medium and, after cellular uptake, would be deprotected by the abundant intracellular GSH (Fig. 1).

In 1983, Christadoulou and Reese described the chemical stability and deprotection reactivity of benzyl protecting groups on the phosphotriester in organic solvent. The protecting groups were

cleaved by *p*-thiocresol in the presence of Et₃N. Under these conditions, lability of the protecting groups was dependent on the benzyl substituents, in either the presence or the absence of thiol.³² This previous report led us to examine stability and reactivity of benzyl protecting groups in aqueous solution, with or without GSH. We designed and synthesized several thymidine dimers with benzyl protecting groups on the phosphotriester as model compounds.

Briefly, the 5'-hydroxyl group in thymidine **1** was protected with the 4,4'-dimethoxytrityl (DMTr) group and then reacted with bis(diisopropylamino)chlorophosphine to give nucleoside phosphorodiamidite derivative **3**.²¹ Compound **3** was coupled with a 3'-O-Ac-thymidine derivative to give thymidine dimer phosphoramidite **4**. Non-substituted or substituted benzyl alcohols were coupled with **4** and the resulting phosphite intermediates were oxidized with *t*-butyl hydroperoxide to give phosphotriester derivatives **5–8**. Compounds **5–8** were treated with ammonium hydroxide and, following acid treatment, yielded compounds **9–12** (Scheme 1).

The protected thymidyl-thymidines **9–12** were dissolved at 10 μM in the aqueous buffer and analyzed for stability by HPLC. Removal of benzyl protecting groups in the presence of GSH was similarly monitored (Fig. 2).

HPLC chromatograms of compound **11** with the 2,4-dichlorobenzyl protecting group are shown in Figure 2 as an example. Chromatograms on the left were obtained with a solution of compound **11** in buffer without GSH at time 0 (Fig. 2A) and after incubation for 24 h (Fig. 2B). After 24 h, a peak was observed corresponding to the deprotected product, thymidyl-thymidine (T_pT) (Fig. 2B). Approximately 81% of compound **11** remained at this

* Corresponding authors.

E-mail addresses: saneyoshih@kanagawa-u.ac.jp (H. Saneyoshi), akiraono@kanagawa-u.ac.jp (A. Ono).

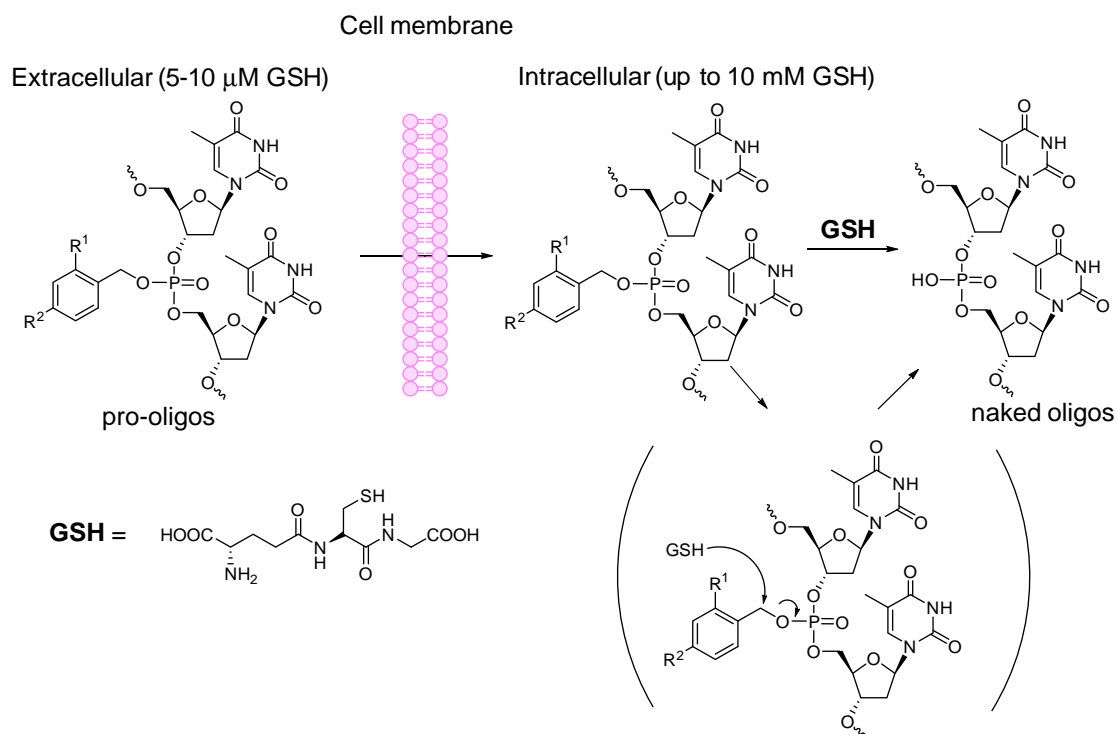
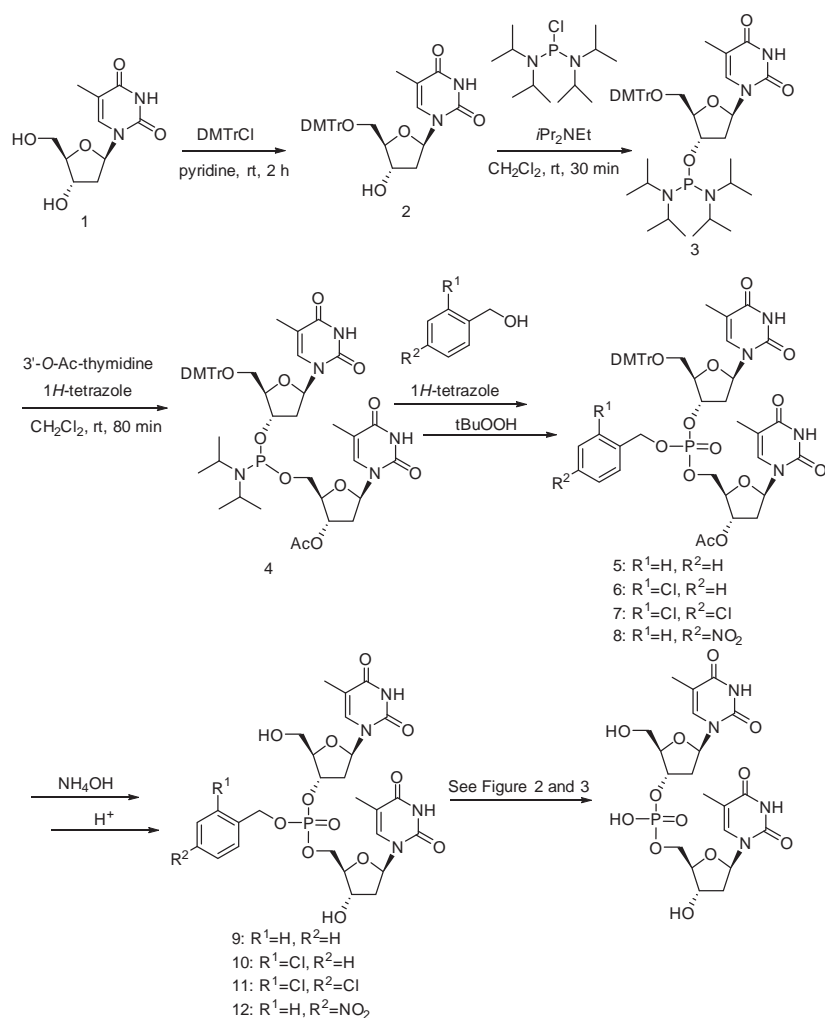


Figure 1. Schematic representation of the expected behavior of GSH-activated pro-oligonucleotides.



Scheme 1. Synthesis of the thymidine dimer with benzyl protecting groups at the internucleotide linkage.

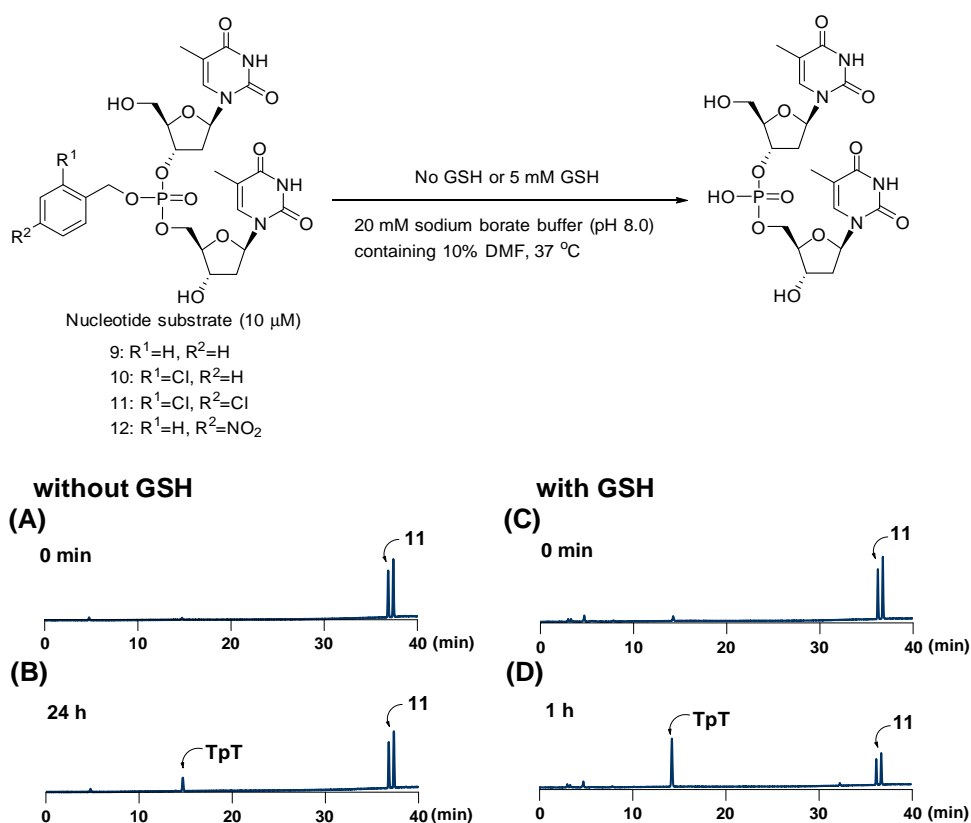


Figure 2. HPLC profiles of **11** in the absence or presence, as indicated, of GSH.

time point, and this value corresponds to the residual ratio. In contrast, chromatograms on the right were obtained with a solution of compound **11** with GSH at time 0 (Fig. 2C) and after 1 h incubation (Fig. 2D). The deprotection rate was markedly accelerated by GSH and the residual ratio of compound **11** was 48%.

Fig. 3 shows plots of residual ratio versus incubation time in solutions of the four different benzyl-protected thymidine dimers without (A) or with (B) GSH.

The compound protected with the unsubstituted benzyl group (red circle, compound **9**) was the least stable ($t_{1/2}$ = 17.8 h) in buffer alone. Those with the 2-chlorobenzyl (yellow circle, compound **10**) and 2,4-dichlorobenzyl (black circle, compound **11**) groups were more stable ($t_{1/2}$ = 92.7 h, 98.0 h). The compound with the 4-nitrobenzyl group (blue circle, compound **12**) was the most stable ($t_{1/2}$ = 696 h). (Fig. 3A).

Deprotection rates of all compounds were accelerated in the presence of GSH (Fig. 3B). The compound with the 4-nitrobenzyl protecting group showed the slowest deprotection rate (**12**: $t_{1/2}$ = 7.8 h), whereas those of the other three were comparable to one another (**9**: $t_{1/2}$ = 1.8 h, **10**: $t_{1/2}$ = 1.3 h, **11**: $t_{1/2}$ = 1.0 h). The deprotection mechanism(s) explaining this difference are not yet clear. However the deprotection pathway in the buffer alone presumes via S_N1 type reaction and introduction of nitro group destabilized benzylic cation, thus deprotection rate via S_N1 type reaction slowed reaction.

Based on the results in aqueous buffer alone, compounds with the substituted benzyl groups were more stable than those with the unsubstituted ring, but their deprotection was, nonetheless, accelerated markedly by GSH. These observations indicate that such substituted benzyl moieties are promising candidates to serve

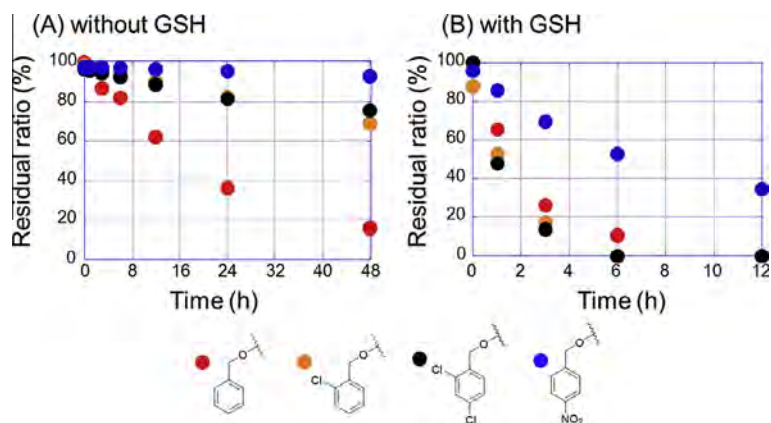


Figure 3. Residual ratio versus incubation time in buffer alone (A) or in the presence of 5 mM GSH (B).

as nonenzymatically degradable protecting groups for pro-oligonucleotides.

In summary, we have compared several benzyl groups for protection of the phosphodiester at the internucleotide linkage in thymidine dimers. By monitoring the deprotection reactions by HPLC, we found that these model pro-oligonucleotides were deprotected with GSH. We further found that stability and deprotection rates were influenced by substituents on the benzene ring.

Acknowledgements

This work was supported by the Strategic Research Base Development Program for Private Universities (Kanagawa University, 2012–2016) from the Ministry of Education, Culture, Sports, Science, and Technology, Japan (A.O.) and Takahashi Industrial and Economic Research Foundation (H.S.).

Supplementary data

Supplementary data associated with this article can be found, in the online version, at <http://dx.doi.org/10.1016/j.bmcl.2015.11.064>.

References and notes

- Dias, N.; Stein, C. A. *Mol. Cancer Ther.* **2002**, *1*, 347.
- Mescalchin, A.; Restle, T. *Molecules* **2011**, *16*, 1271.
- Lee, J.; Yokota, T. *J. Pers. Med.* **2013**, *3*, 144.
- Barber, I.; Rayner, B.; Imbach, J.-L. *Bioorg. Med. Chem. Lett.* **1995**, *5*, 563.
- Iyer, R. P.; Yu, D.; Agrawal, S. *Bioorg. Chem.* **1995**, *23*, 1.
- Iyer, R. P.; Yu, D.; Devlin, T.; Ho, N.-H.; Agrawal, S. *Bioorg. Med. Chem. Lett.* **1996**, *6*, 1917.
- Mignet, N.; Morvan, F.; Rayner, B.; Imbach, J.-L. *Bioorg. Med. Chem. Lett.* **1997**, *7*, 851.
- Tosquellas, G.; Alvarez, K.; Dell'Aquila, C.; Morvan, F.; Vasseur, J.-J.; Imbach, J.-L.; Rayner, B. *Nucleic Acids Res.* **1998**, *26*, 2069.
- Bologna, J.-C.; Morvan, F.; Imbach, J.-L. *Eur. J. Org. Chem.* **1999**, *1999*, 2353.
- Bologna, J. C.; Vives, E.; Imbach, J. L.; Morvan, F. *Antisense Nucleic Acid Drug Dev.* **2002**, *12*, 33.
- Meade, B. R.; Gogoi, K.; Hamil, A. S.; Palm-Apergi, C.; Berg, A. v. d.; Hagopian, J. C.; Springer, A. D.; Eguchi, A.; Kacsinta, A. D.; Dowdy, C. F.; Presente, A.; Lonn, P.; Kaulich, M.; Yoshioka, N.; Gros, E.; Cui, X.-S.; Dowdy, S. F. *Nat. Biotechnol.* **2014**, *32*, 1256.
- Pojjärvi, P.; Heinonen, P.; Virta, P.; Lönnberg, H. *Bioconjugate Chem.* **2005**, *16*, 1564.
- Ora, M.; Taherpour, S.; Linna, R.; Leisvuori, A.; Hietamäki, E.; Poijärvi-Virta, P.; Beigelman, L.; Lönnberg, H. *J. Org. Chem.* **2009**, *74*, 4992.
- Kiuru, E.; Ora, M.; Beigelman, L.; Blatt, L.; Lönnberg, H. *Chem. Biodiversity* **2011**, *8*, 266.
- Kiuru, E.; Ahmed, Z.; Lönnberg, H.; Beigelman, L.; Ora, M. *J. Org. Chem.* **2012**, *78*, 950.
- Wilk, A.; Chmielewski, M. K.; Grajkowski, A.; Phillips, L. R.; Beaucage, S. L. *J. Org. Chem.* **2002**, *67*, 6430.
- Cieślak, J.; Grajkowski, A.; Livengood, V.; Beaucage, S. L. *J. Org. Chem.* **2004**, *69*, 2509.
- Ausín, C.; Grajkowski, A.; Cieślak, J.; Beaucage, S. L. *Org. Lett.* **2005**, *7*, 4201.
- Cieślak, J.; Kauffman, J. S.; Kolodziejcki, M. J.; Lloyd, J. R.; Beaucage, S. L. *Org. Lett.* **2007**, *9*, 671.
- Grajkowski, A.; Ausín, C.; Kauffman, J. S.; Snyder, J.; Hess, S.; Lloyd, J. R.; Beaucage, S. L. *J. Org. Chem.* **2007**, *72*, 805.
- Grajkowski, A.; Cieślak, J.; Kauffman, J. S.; Duff, R. J.; Norris, S.; Freedberg, D. I.; Beaucage, S. L. *Bioconjugate Chem.* **2008**, *19*, 1696.
- Ausín, C.; Kauffman, J. S.; Duff, R. J.; Shivaprasad, S.; Beaucage, S. L. *Tetrahedron* **2010**, *66*, 68.
- Grajkowski, A.; Cieślak, J.; Gapeev, A.; Beaucage, S. L. *New J. Chem.* **2010**, *34*, 880.
- Jain, H. V.; Takeda, K.; Tami, C.; Verthelyi, D.; Beaucage, S. L. *Bioorg. Med. Chem.* **2013**, *21*, 6224.
- Zhang, K.; Taylor, J.-S. *J. Am. Chem. Soc.* **1999**, *121*, 11579.
- Shah, S.; Rangarajan, S.; Friedman, S. H. *Angew. Chem., Int. Ed.* **2005**, *44*, 1328.
- Saneyoshi, H.; Shimamura, K.; Sagawa, N.; Ando, Y.; Tomori, T.; Okamoto, I.; Ono, A. *Bioorg. Med. Chem. Lett.* **2015**, *25*, 2129.
- Zhang, N.; Tan, C.; Cai, P.; Zhang, P.; Zhao, Y.; Jiang, Y. *Chem. Commun.* **2009**, 3216.
- Meister, A.; Anderson, M. E. *Annu. Rev. Biochem.* **1983**, *52*, 711.
- Meister, A. *J. Biol. Chem.* **1988**, *263*, 17205.
- Cacciatore, I.; Cornacchia, C.; Pinnen, F.; Mollica, A.; Di Stefano, A. *Molecules* **2010**, *15*, 1242.
- Christadoulou, C.; Reese, C. B. *Tetrahedron Lett.* **1983**, *24*, 951.

Selective Transport of Mercury(II) Ions across Supported Liquid Membrane with Thymine Derivative as Carrier

Tatsuo Kurokawa,* Manabu Igawa, Akira Ono, and Itaru Okamoto*

Faculty of Engineering, Kanagawa University, 3-27-1 Rokkakubashi, Kanagawa-ku, Yokohama, Kanagawa 221-8686

(E-mail: kuro-kaw@tamacc.chuo-u.ac.jp, itaru.okamoto@riken.jp)

We describe a new highly selective supported liquid membrane (SLM) system made of a polypropylene flat sheet with a thymine derivative in kerosene as the carrier, for the selective transport of mercury ion. When the carrier existed in the membrane, only mercury ions were selectively transported. This SLM selectively separated mercury ions from a mixed solution of mercury and heavy metal ions. The hydrogen ion concentration in the receiving phase is a dominant factor in the mercury ion transport across the SLM.

Mercury is one of the most toxic heavy metals, and mercury ions are highly reactive, e.g., in wastewater from industries. Therefore, an accurate and low-cost detection method and selective separation method need to be developed.

To separate and recover mercury ions, adsorption of the ions to a sorbent^{1–3} or separation by using some type of membranes^{4–10} has been studied. The latter, i.e., the membrane-separation method is advantageous since it enables continuous and low-cost separation. The use of a filtration membrane³ and an ion-exchange membrane^{11–13} has been studied, and these have been practically used for the separation of heavy metal ions. The fundamental research on the separation of mercury ions has been advanced with the development of a liquid membrane,^{7,8} i.e., a supported liquid membrane (SLM).^{9,10} A SLM is a hydrophobic porous membrane support with an organic solvent and a carrier. It is reported that facilitated transport of mercury ions is performed by the SLM with trioctylamine as the carrier and coconut oil as the diluent.^{9,10} However, to our knowledge, there is no report about a membrane that selectively transports only mercury ions from a mixed solution of metal ions.

It is known that thymine, a base in nucleic acids, specifically binds to mercury ions,^{14–17} and it was applied in the study of a mercury-ion probe or sensor.^{15,18–25} Recently, we reported the transport of mercury(II) ions across a polyallylamine membrane fixed with thymine.²⁶ In this study, we synthesized a new thymine derivative (Figure 1) that acts as the carrier of a SLM for selective transport of mercury ions. The thymine derivative (Figure 1) has a long hydrocarbon chain to be dissolved in an organic solvent. The carrier was synthesized in a single step from thymine acetic acid.²⁷

In this study, porous polypropylene membrane (Accurel PP 2E HF (R/P), Membrana) with a thickness of 0.01 cm and a pore size of 0.2 μm was used. To prepare the SLM, a porous polypropylene membrane sheet was cut to dimensions of 3 \times 5 cm for use as the membrane. The thymine derivative was dissolved in acetone, and this acetone solution and kerosene were mixed in the volume ratio of 1:9 (Solution A). The concentration of thymine was 200 μM in Solution A. The porous polypropylene membranes were immersed in 100 mL of Solution A for 24 h. Then, the membranes were used as SLMs.

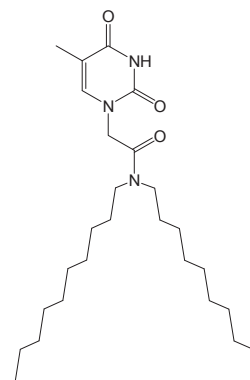


Figure 1. Thymine derivative.

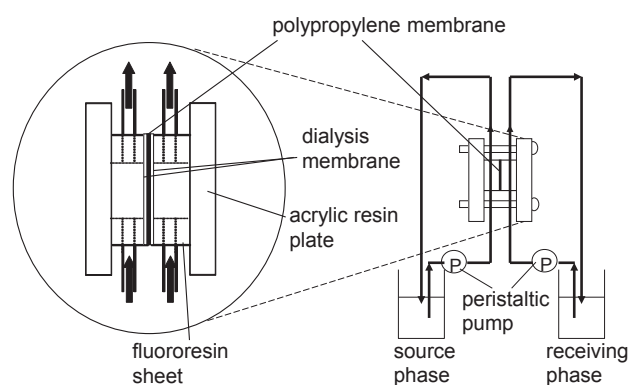


Figure 2. Apparatus for the transport experiment.

To perform the transport experiment, the nitric acid solution (Kanto Chemicals) was used as the receiving-phase solution and was used to prepare the source-phase solution. Mercury(II) nitrate hydrate (Wako), copper(II) nitrate (Wako), and lead(II) nitrate (Wako) were used to prepare the source-phase solution. All the reagents used in this experiment are of analytical grade. The source-phase solution with a volume of 0.2 L and the receiving-phase solution with a volume of 0.1 L were separately circulated to their respective compartments in the cell by using a peristaltic pump (Figure 2). The effective membrane area was 4 cm^2 , and the pumping rate was 5 mL min^{-1} . The SLM was covered on both sides by a dialysis membrane (36/32 dialysis membrane, VISKASE SALES CORP) in order to prevent the elution of the solvent. The transport experiment was conducted for about 24 h, after which aliquots were collected every 60 min from the source phase and the receiving phase. The concentrations of metal ions were determined using inductively coupled plasma atomic emission spectrometry (SPS 1500, SEIKO).

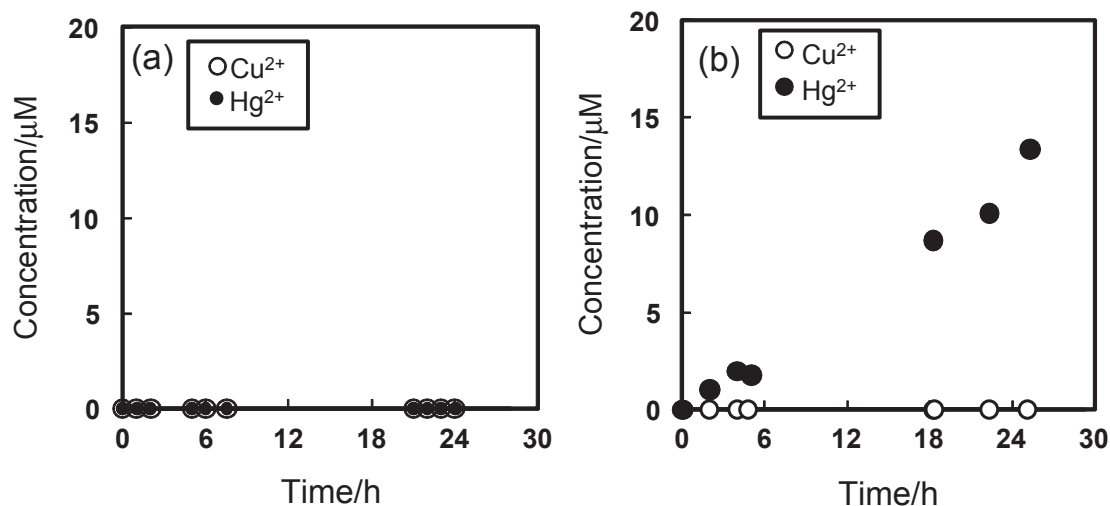


Figure 3. Concentration of metal ions in receiving phase without a carrier (a) and with carrier in supported liquid membrane (b). Source phase (pH 2.5): 1 mM Hg(NO₃)₂, 1 mM Cu(NO₃)₂, 3 mM HNO₃. Receiving phase (pH 2.0): 10 mM HNO₃.

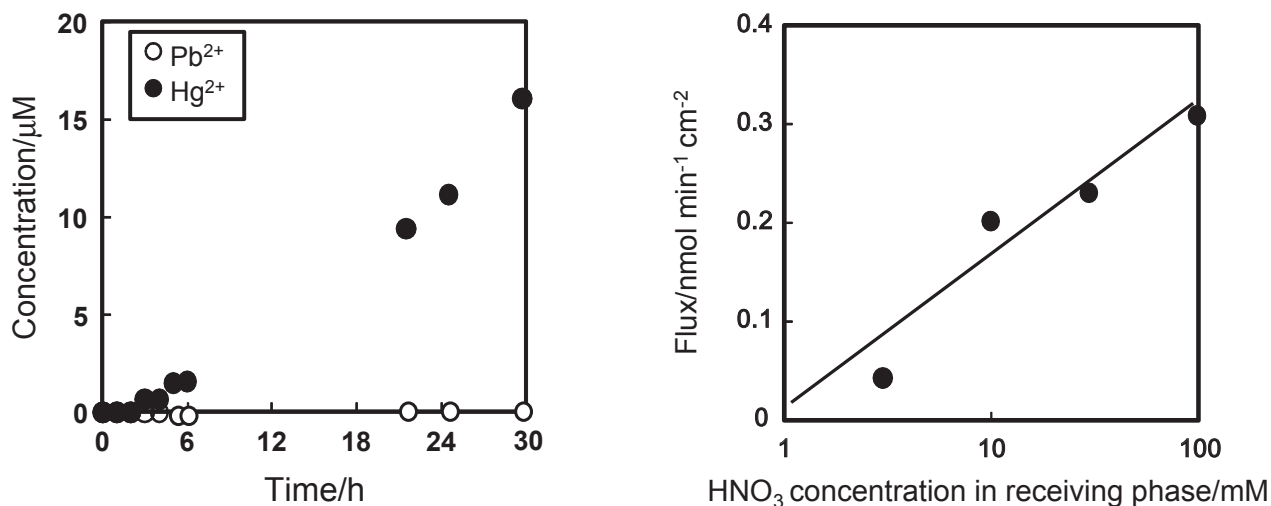


Figure 4. Metal ions concentration in receiving phase. Source phase (pH 2.5): 1 mM Hg(NO₃)₂, 1 mM Pb(NO₃)₂, 3 mM HNO₃. Receiving phase (pH 2.0): 10 mM HNO₃.

Figure 5. Effect of nitric acid concentration in receiving phase on flux. Source phase (pH 2.5): 1 mM Hg(NO₃)₂, 1 mM Cu(NO₃)₂, 3 mM HNO₃. Receiving phase: nitric acid solution.

Figure 3 shows the concentration of the metal ions in the receiving phase without a carrier (a) and with a carrier in the SLM (b). Both metal ions were not transported to the receiving phase without the thymine derivative (Figure 3a). With the thymine derivative, however, mercury ions were selectively transported to the receiving phase, while the copper ions were not (Figure 3b).

Figure 4 shows the concentration of metal ions in the receiving phase. The mercury ions were transported to the receiving phase, while the lead ions were not transported to the receiving phase across the SLM with the thymine derivative.

Figure 5 shows the effect of nitric acid concentration in the receiving phase on the mercury ion flux. The mercury ion flux increased with the concentration of nitric acid in the receiving phase. This result shows that nitric acid promotes the decomposition of the complex into the mercury ion and thymine

derivative at the membrane surface on the receiving phase side and transport mercury ions to the receiving phase (Figure 6). In the decomposition reaction, the proton from nitric acid forms a covalent bond with the thymine derivative instead of the mercury ion (Figure 6).

The mechanism of the mercury-ion transport across the SLM is shown in Figure 6. When the mercury ions distribute in the membrane, each mercury ion binds to two thymine derivatives to form a complex that is the most stable uncharged form in kerosene. The complex diffuses in the membrane and decomposes at the membrane surface on the receiving phase side.

Thus, we show that from the mixed-solution containing copper or lead ions with mercury ions, only mercury ions can be selectively transported across the SLM with the thymine derivative. We conclude that the advantageous selectivity of

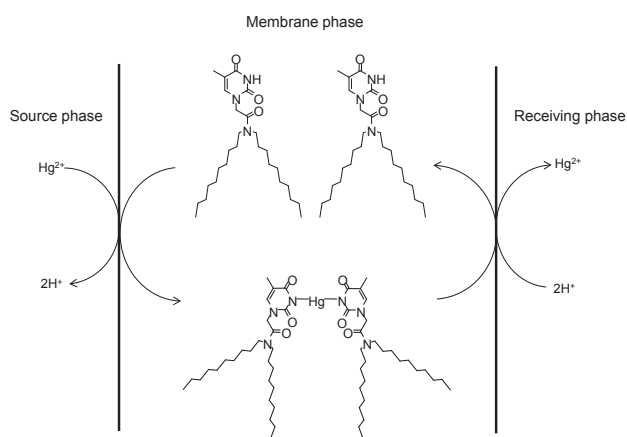


Figure 6. Binding and dissociation between the thymine derivative and mercury ion at the surface of supported liquid membrane for transport of Hg^{2+} .

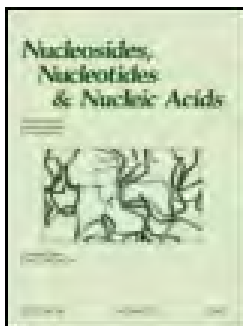
thymine to mercury ions in an aqueous solution makes thymine suitable for the development of a membrane with high selectivity.

This work was partly supported by a Grant-in-Aid for Scientific Research (B) (No. 21350105) and the Science Frontier Project of Kanagawa University “Construction and control of chemical space purposing development of new functionalized molecules and materials” by the Ministry of Education, Culture, Sports, Science and Technology (MEXT), Japan.

Supporting Information is available electronically on J-STAGE.

References and Notes

- X. Liu, C. Qi, T. Bing, X. Cheng, D. Shangguan, *Talanta* **2009**, *78*, 253.
- Y. Takagai, A. Shibata, S. Kiyokawa, T. Takase, *J. Colloid Interface Sci.* **2011**, *353*, 593.
- S. Xu, L. Chen, J. Li, Y. Guan, H. Lu, *J. Hazard. Mater.* **2012**, *237–238*, 347.
- H. Bessbousse, T. Rhlalou, J.-F. Verchère, L. Lebrun, *J. Membr. Sci.* **2008**, *325*, 997.
- C. Sgarlata, G. Arena, E. Longo, D. Zhang, Y. Yang, R. A. Bartsch, *J. Membr. Sci.* **2008**, *323*, 444.
- M. Teng, H. Wang, F. Li, B. Zhang, *J. Colloid Interface Sci.* **2011**, *355*, 23.
- H. Parham, M. Shamsipur, *J. Membr. Sci.* **1994**, *86*, 29.
- A. Safavi, E. Shams, *J. Membr. Sci.* **1998**, *144*, 37.
- K. Chakrabarty, P. Saha, A. K. Ghoshal, *J. Membr. Sci.* **2010**, *350*, 395.
- K. Chakrabarty, P. Saha, A. K. Ghoshal, *J. Membr. Sci.* **2010**, *346*, 37.
- M. Igawa, Y. Narita, H. Okochi, *Bull. Chem. Soc. Jpn.* **2002**, *75*, 2269.
- M. Igawa, S. Akiyama, R. Okada, C. Sugawara, T. Kurokawa, *J. Ion Exch.* **2007**, *18*, 506.
- M. Igawa, H. Kanamori, B. Nanzai, *Chem. Lett.* **2010**, *39*, 996.
- S. Katz, *J. Am. Chem. Soc.* **1952**, *74*, 2238.
- A. Ono, H. Togashi, *Angew. Chem., Int. Ed.* **2004**, *43*, 4300.
- Y. Miyake, H. Togashi, M. Tashiro, H. Yamaguchi, S. Oda, M. Kudo, Y. Tanaka, Y. Kondo, R. Sawa, T. Fujimoto, T. Machinami, A. Ono, *J. Am. Chem. Soc.* **2006**, *128*, 2172.
- Y. Tanaka, S. Oda, H. Yamaguchi, Y. Kondo, C. Kojima, A. Ono, *J. Am. Chem. Soc.* **2007**, *129*, 244.
- A. Okamoto, Y. Ochi, I. Saito, *Bioorg. Med. Chem. Lett.* **2005**, *15*, 4279.
- J.-S. Lee, M. S. Han, C. A. Mirkin, *Angew. Chem.* **2007**, *119*, 4171.
- J. Liu, Y. Lu, *Angew. Chem., Int. Ed.* **2007**, *46*, 7587.
- D. Li, A. Wieckowska, I. Willner, *Angew. Chem., Int. Ed.* **2008**, *47*, 3927.
- M. Hollenstein, C. Hipolito, C. Lam, D. Dietrich, D. M. Perrin, *Angew. Chem., Int. Ed.* **2008**, *47*, 4346.
- B.-C. Ye, B.-C. Yin, *Angew. Chem., Int. Ed.* **2008**, *47*, 8386.
- D.-L. Ma, D. S.-H. Chan, B. Y.-W. Man, C.-H. Leung, *Chem.—Asian J.* **2011**, *6*, 986.
- Z. Wang, D. Zhang, D. Zhu, *Anal. Chim. Acta* **2005**, *549*, 10.
- T. Kurokawa, I. Okamoto, *Membrane* **2014**, *39*, 337.
- Thymine-1-acetic acid (221 mg, 1.2 mmol) was dissolved in 10 mL of anhydrous DMF. Then, 1-(3-dimethylaminopropyl)-3-ethylcarbodiimide hydrochloride (230 mg, 1.2 mmol) and dodecylamine (298 mg, 1.0 mmol) were added and stirred at room temperature for 19 h. After reaction completion, the reaction mixture was diluted with ethyl acetate and the mixture was washed three times with brine. The organic layer was dried with anhydrous MgSO_4 , and the solution was evaporated. The residue was purified by NH-silica gel (FUJI SILYSIA, Chromatorex® NH) column chromatography using hexane and gradually increasing ethyl acetate content up to 50%. The fractions carrying the product were combined and evaporated to yield the product as a colorless solid (425 mg, 0.92 mmol, 92%). $^1\text{H NMR}$ (600 MHz, $\text{DMSO}-d_6$): δ 11.24 (1H, s), 7.37 (1H, s), 4.50 (2H, s), 3.20 (4H, quin, $J = 7.8$ Hz), 1.74 (3H, s), 1.54 (2H, m), 1.42 (2H, quin, $J = 7.4$ Hz), 1.28–1.17 (28H, m), 0.84 (6H, m) (for further information on synthesis and characterization, see Supporting Information).



Exploring a DNA Sequence for the Three-Dimensional Structure Determination of a Silver(I)-Mediated C-C Base Pair in a DNA Duplex By ^1H NMR Spectroscopy

Takenori Dairaku, Kyoko Furuita, Hajime Sato, Yoshinori Kondo, Chojiro Kojima, Akira Ono & Yoshiyuki Tanaka

To cite this article: Takenori Dairaku, Kyoko Furuita, Hajime Sato, Yoshinori Kondo, Chojiro Kojima, Akira Ono & Yoshiyuki Tanaka (2015): Exploring a DNA Sequence for the Three-Dimensional Structure Determination of a Silver(I)-Mediated C-C Base Pair in a DNA Duplex By ^1H NMR Spectroscopy, *Nucleosides, Nucleotides and Nucleic Acids*, DOI: [10.1080/15257770.2015.1088160](https://doi.org/10.1080/15257770.2015.1088160)

To link to this article: <http://dx.doi.org/10.1080/15257770.2015.1088160>



Published online: 17 Nov 2015.



Submit your article to this journal [↗](#)



Article views: 9



View related articles [↗](#)



View Crossmark data [↗](#)

Full Terms & Conditions of access and use can be found at
<http://www.tandfonline.com/action/journalInformation?journalCode=lncn20>

EXPLORING A DNA SEQUENCE FOR THE THREE-DIMENSIONAL STRUCTURE DETERMINATION OF A SILVER(I)-MEDIATED C-C BASE PAIR IN A DNA DUPLEX BY ¹H NMR SPECTROSCOPY

Takenori Dairaku,¹ Kyoko Furuita,² Hajime Sato,³ Yoshinori Kondo,¹ Chojiro Kojima,² Akira Ono,⁴ and Yoshiyuki Tanaka^{1,5}

¹Graduate School of Pharmaceutical Sciences, Tohoku University, Aobayama, Aoba-ku, Sendai, Miyagi, Japan

²Institute for Protein Research, Osaka University, Suita, Osaka, Japan

³Bruker BioSpin K.K., Yokohama, Kanagawa, Japan

⁴Department of Material & Life Chemistry, Kanagawa University, Kanagawa-ku, Yokohama, Kanagawa, Japan

⁵Laboratory of Analytical Chemistry, Faculty of Pharmaceutical Sciences, Tokushima Bunri University, Yamashiro-cho, Tokushima, Japan

□ Recently, we discovered novel silver(I)-mediated cytosine–cytosine base pair (C–Ag^I–C) in DNA duplexes. To understand the properties of these base pairs, we searched for a DNA sequence that can be used in NMR structure determination. After extensive sequence optimizations, a non-symmetric 15-base-paired DNA duplex with a single C–Ag^I–C base pair flanked by 14 A–T base pairs was selected. In spite of its challenging length for NMR measurements (30 independent residues) with small sequence variation, we could assign most non-exchangeable protons (254 out of 270) and imino protons for structure determination.

Keywords metallo-DNA, metallo-base pair, ¹H NMR spectroscopy

INTRODUCTION

DNA molecules containing metal-mediated base pairs (metallo-base pairs) are called as metallo-DNAs. They have been studied extensively because of their potential for use in nanotechnology and molecular devices,^[1–9] for example, metal ion sensor,^[1–6,10,11] metal ion-trapping devices,^[12–17] SNP-detection,^[18–20] molecular magnets,^[21,22] electric nano-wires,^[7,23–28] DNA-based switches,^[8,9,29] and DNA-based logic gates.^[9,30–33]

Received 25 August 2015; accepted 25 August 2015.

Address correspondence to Yoshiyuki Tanaka, Professor, Laboratory of Analytical Chemistry, Faculty of Pharmaceutical Sciences, Tokushima Bunri University, 180 Nishihama-Boji, Yamashiro-cho, Tokushima 770-8514, Japan. E-mail: tanakay@ph.bunri-ac.jp

Color versions of one or more of the figures in the article can be found online at www.tandfonline.com/Incn.

Initially, metallo-base pairs with artificial nucleobases were reported, and their numbers are increasing.^[1–5]

As an alternative strategy for generating metal-mediated base pairs, metallo-base pairs formed with natural nucleobases were searched and several such metal-mediated base pairs were discovered.^[11,34–41] For example, two metallo-base pairs, Hg^{II}-mediated thymine–thymine base pair (T–Hg^{II}–T base pair) and Ag^I-mediated cytosine–cytosine base pair (C–Ag^I–C base pair), have been reported. These metallo-base pairs have already been applied to molecular-devices,^[3] and the Ag^I-cytosine interaction was used to form a silver nanocluster by the reduction of Ag^I ions, which bind to the poly cytosine oligonucleotide.^[42] Moreover, these metallo-base pairs were recognized by DNA polymerase^[43,44] and DNA ligase.^[45]

From the structural point of view, the chemical and three-dimensional (3D) structures of the T–Hg^{II}–T base pair were experimentally determined,^[46–48] and theoretical studies^[49,50] have been conducted. Interestingly, the theoretical investigations based on the 3D structure suggest that a DNA molecule containing T–Hg^{II}–T base pair might be an effective electric nano-wire.^[49,50] In contrast, the structure of the C–Ag^I–C base pair in a DNA duplex has not been determined experimentally, although there have been some structural^[36,37,39,41,51,52]/thermodynamic^[20,53] investigations.

NMR spectroscopy is a suitable method for studying the structural features of the C–Ag^I–C base pair in a DNA duplex. However, before determining the 3D structure, optimal DNA sequence(s) possessing a designated unique secondary structure without any polymorphism need to be identified. In addition, 3D structure determination requires time-consuming ¹H resonance assignments. In this study, to characterize structural features of the C–Ag^I–C base pair within an anti-parallel DNA duplex, we explored DNA sequences suitable for structural characterization of C–Ag^I–C base pair. Subsequently, we recorded the 2D ¹H–¹H NOESY/COSY spectra of the identified DNA duplex with C–Ag^I–C base pair, and then performed resonance assignments based on nuclear Overhauser effect (NOE).

MATERIALS AND METHODS

Sample Preparation

All DNA oligomers, shown in Figures 1b–f, were synthesized using the phosphoramidite method in an automated DNA/RNA synthesizer (ABI model 392). The synthesized DNA oligonucleotides were treated with 28% ammonia aqueous solution at 55°C for 10 hours for deprotection. Each DNA oligomer was purified on a C18 reverse-phase column (Cosmosil 5C18-AR-300; Nacalai Tesque, Japan), with a linear gradient of 5–50% acetonitrile (30 minutes) and 0.1-M triethylammonium acetate (pH 7.0) as a basal buffer.

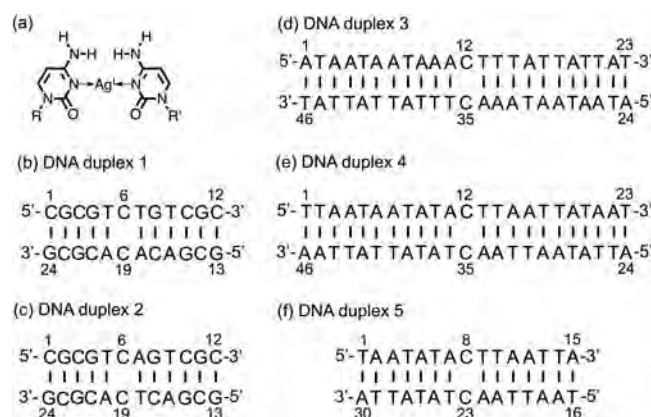


FIGURE 1 (a) Predicted structure of C-Ag⁺-C base pair. R and R' denote DNA backbone. (b)-(f) Sequences of DNA duplexes 1-5 with their residue numbers.

For the exchange of counter cation of phosphate groups of DNA backbone, an anion-exchange column (UNO Q-6; BIO-RAD, USA) was employed. First, a DNA oligomer was adsorbed onto the column, and the column was washed with MILLI-Q water (Millipore, USA) to remove triethylammonium-acetate buffer. Then the DNA oligomer was eluted with 2-M NaCl. Finally, excess NaCl was desalted using a gel filtration column (TSK-GEL G3000PW; TOSO, Japan) with MILLI-Q water as a mobile phase. Each oligomer was quantitated by measuring the ultraviolet (UV) absorbance at 260 nm after digestion with nuclease P1.

NMR Measurements

The sample solutions for Ag⁺-titration experiments with ¹H NMR measurements contained 0.5–2.0-mM DNA duplex, 100-mM NaNO₃, various concentrations of Ag⁺ in water (D₂O:H₂O = 1:9) or D₂O. One-dimensional ¹H NMR spectra of DNA duplexes 1 and 2 were recorded on a JEOL ECA 600 spectrometer at 298 K with 32,768 complex points for a spectral width of 16,534 Hz, and 128 scans were averaged. One-dimensional ¹H NMR spectra of DNA duplexes 3 and 4 were recorded on a JEOL ECA 600 spectrometer at 298 K with 16,384 complex points for a spectral width of 7503 Hz, and 128 scans were averaged.

The sample solutions for ¹H NMR measurements of DNA duplex 5-Ag⁺ complex contained 2.0-mM DNA duplex 5, 100-mM NaNO₃ with or without 2.1-mM AgNO₃. Lyophilized samples were dissolved in water (H₂O:D₂O = 9:1) or D₂O. The NMR sample solutions in Shigemi-tube were heated to 70°C for 15 minutes and slowly cooled down to 25°C. One-dimensional ¹H NMR spectrum of DNA duplex 5-Ag⁺ complex in water (H₂O:D₂O = 9:1) was recorded on a Bruker AVANCE III 950 spectrometer at 298 K

with 22,726 complex points for a spectral width of 22,727 Hz, and eight scans were averaged. Two-dimensional ^1H - ^1H NOESY spectrum of DNA duplex 5-Ag^I complex in water ($\text{H}_2\text{O}:\text{D}_2\text{O} = 9:1$) was recorded on a Bruker AVANCE III 950 spectrometer at a mixing time of 120 milliseconds with 8192×1024 complex points for a spectral width of $22,727 \times 22,831$ Hz at 298 K, and eight scans were averaged. Two-dimensional ^1H - ^1H DQF-COSY spectrum of DNA duplex 5-Ag^I complex in D_2O was recorded on a Bruker AVANCE III 950 spectrometer at 298 K, with 4096×512 complex points for a spectral width of $11432.926 \times 11415.525$ Hz, and 16 scans were averaged. Two-dimensional ^1H - ^1H NOESY spectra of DNA duplex 5-Ag^I complex in D_2O were recorded on a Bruker AVANCE III 950 spectrometer at mixing time of 50 and 120 milliseconds with 4096×512 complex points for a spectral width of $11,432 \times 11,415$ Hz at 298 K, and 16 scans were averaged. NOESY spectrum with a mixing time of 50 milliseconds was used for stereo-specific assignments of H2' and H2'' proton to obtain a better contrast between H1'-H2' and H1'-H2'' cross-peak intensities. Two-dimensional absolute value ^1H - ^1H COSY spectrum of DNA duplex 5-Ag^I complex in D_2O was recorded on a JEOL ECA 600 spectrometer at 298 K with 1280×256 complex points for a spectral width of 6720×5374 Hz, and 256 scans were averaged.

Solution conditions for the respective NMR measurements and their parameters for NMR hardware settings are presented in Figures 2–9 and Figures A1–A10 in Appendix.

RESULTS AND DISCUSSION

First, we synthesized DNA duplexes (Figures 1b–f) to identify an appropriate sequence for the structure determination of C–Ag^I–C base pair. These DNA duplexes were designed to form a DNA duplex with a single C–C mismatch, which will be the C–Ag^I–C base pairing site in the presence of Ag^I ion. For the first trial, we examined whether DNA duplexes 1 and 2 were appropriate for further analyses by performing Ag^I-titration experiments with ^1H NMR spectroscopy.

In Figure 2, NMR signals from methyl protons of thymine residues are displayed as a function of molar ratios of $[\text{Ag}^{\text{I}}]/[\text{duplex}]$. In both sequences, as the concentrations of Ag^I increased, new methyl proton signals appeared (filled circles in Figure 2), indicating the specific binding of an Ag^I ion with the C–C mismatch. Thus, each DNA duplex was converted to a new one containing a C–Ag–C base pair. However, further addition of Ag^I ion results in the generation of further new peaks from an unidentified molecular species above the molar ratio $[\text{Ag}^{\text{I}}]/[\text{duplex}] = 0.6$ or 0.8 (asterisks in Figure 2). Before the C–C mismatch site was occupied with Ag^I, the unidentified molecular species appeared additionally. The 1D ^1H NMR spectra indicated that for DNA duplexes 1 and 2, the molecular species in solution do not converge

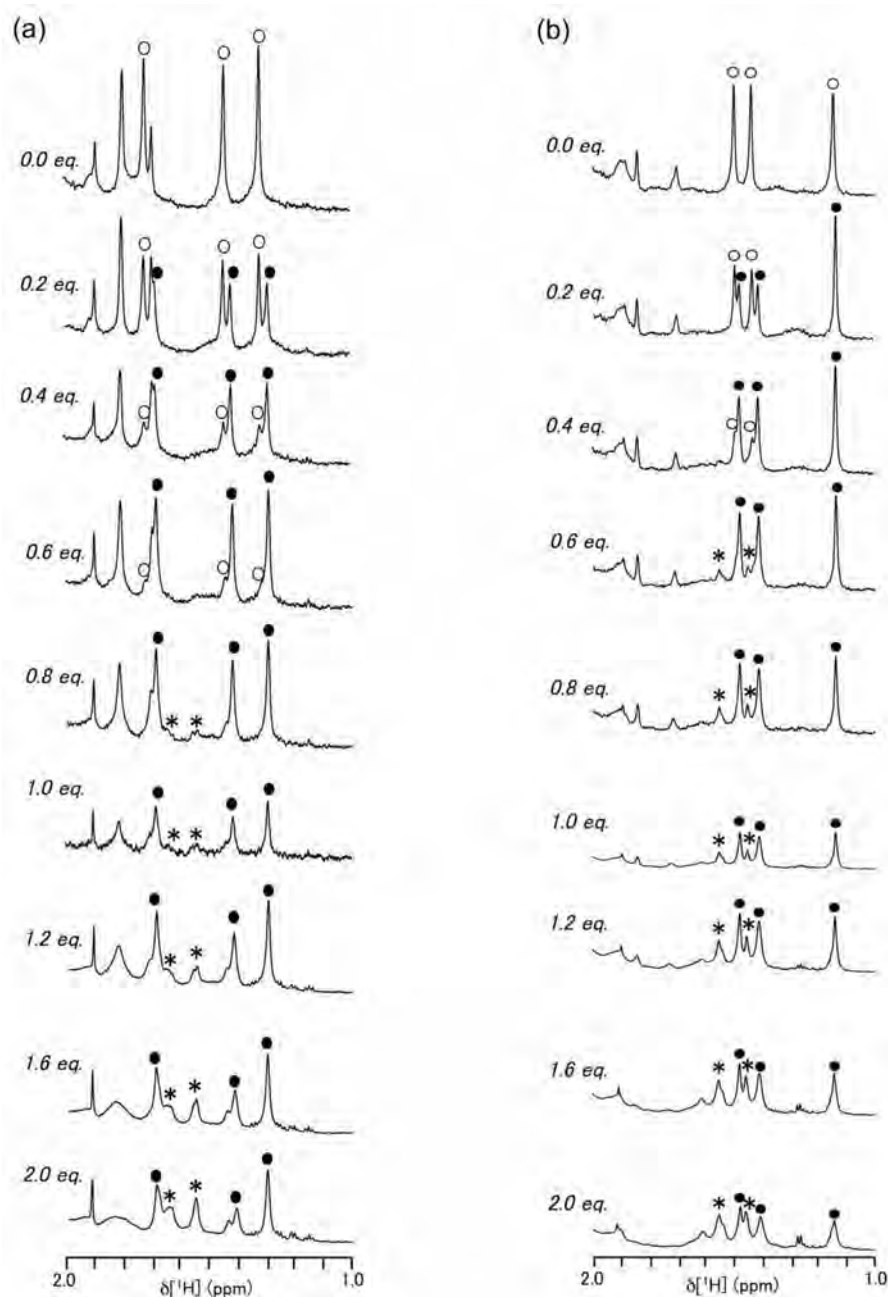


FIGURE 2 Methyl proton region in 1D ^1H NMR spectra of DNA duplexes 1(a) and 2(b). The sample solution for Ag^{I} -titration experiments with ^1H NMR measurements contained 0.5-mM DNA duplex 1 or 2, 100-mM NaNO_3 , various concentrations of Ag^{I} in water ($\text{D}_2\text{O}:\text{H}_2\text{O} = 1:9$). 1D ^1H NMR spectra of DNA duplexes 1 and 2 were recorded on a JEOL ECA 600 spectrometer, at 298 K, with 32,768 complex points for a spectral width of 16,534 Hz, and 128 scans were averaged. Each spectrum was processed with an exponential window function to give a line-broadening of 1.0 Hz. Molar ratios ($[\text{Ag}(\text{I})]/[\text{duplex}]$) are indicated on the left side of each spectrum. Open circles, filled circles, and asterisk indicate signals from Ag^{I} -free, single Ag^{I} -bound, and unknown states respectively.

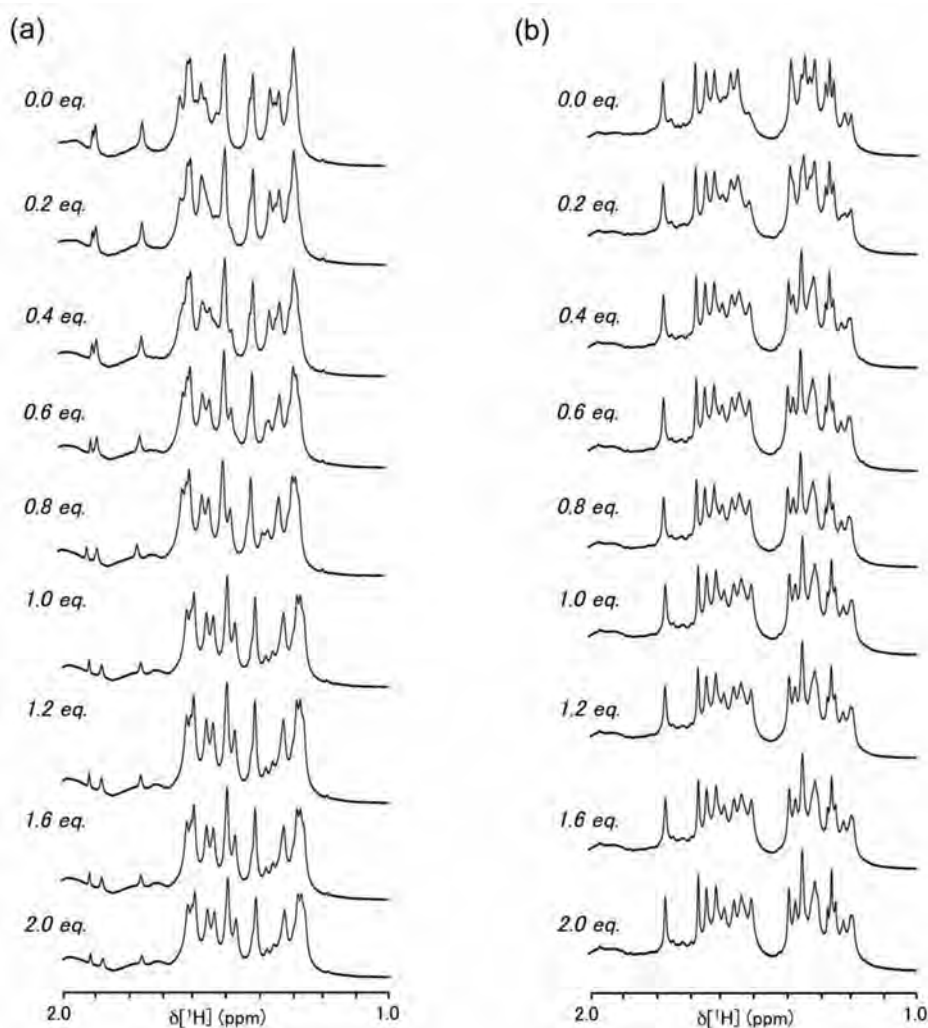


FIGURE 3 Methyl proton region in 1D ^1H NMR spectra of DNA duplexes 3(a) and 4(b). The sample solutions for Ag^{I} -titration experiments with ^1H NMR measurements contained 1.3-mM DNA duplex 3 or 2.0-mM DNA duplex 4, 100-mM NaNO_3 , various concentrations of Ag^{I} in D_2O . 1D ^1H NMR spectra of DNA duplexes 3 and 4 were recorded on a JEOL ECA 600 spectrometer at 298 K, with 16,384 complex points for a spectral width of 7503 Hz, and 128 scans were averaged. Each spectrum was processed with an exponential window function to give a line-broadening of 1.0 Hz.

into a single species under any conditions after the addition of Ag^{I} . Under such conditions, assignment of NMR signals and further structure analysis will be highly difficult, and therefore DNA duplexes 1 and 2 were found to be inappropriate for structure determination.

We then examined the possibility that unassigned signals (asterisks in Figure 2) might arise from the binding of Ag^{I} to cytosine and/or guanine residues in the G-C pairs due to the possible C- Ag^{I} -C base pairing across

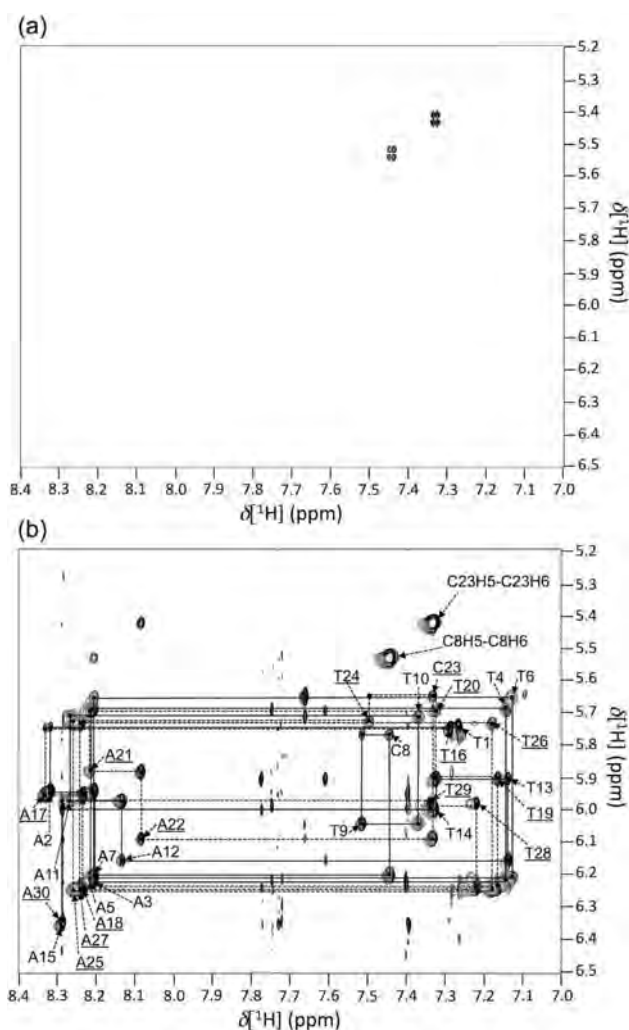


FIGURE 4 (a) H5–H6 cross peaks of residues C8 and C23 in the DQF-COSY spectrum of DNA duplex 5-Ag^I complex. The solution contained 2.0-mM DNA duplex 5, 100-mM NaNO₃ with 2.1-mM AgNO₃ in D₂O (pD 7.1). DQF-COSY spectra were recorded on a Bruker AVANCE III 950 spectrometer at 298 K, with 4096 × 512 complex points for a spectral width of 11432.926 × 11415.525 Hz, and 16 scans were averaged. (b) H8/H6/H2–H1' cross peaks in the NOESY spectrum of DNA duplex 5-Ag^I complex with sequential NOE walks between H8/H6 and H1' (black line: T1–A15; dash line: T16–A30). Intra-residue NOE cross peaks between H8/H6 and H1' are labelled with residue numbers. C8H5–C8H6 and C23H5–C23H6 indicate H5–H6 cross peaks of residues C8 and C23 respectively. The solution contained 2.0-mM DNA duplex 5, 100-mM NaNO₃ with 2.1-mM AgNO₃ in D₂O (pD 7.1). 2D ¹H–¹H NOESY spectra were recorded on a Bruker AVANCE III 950 spectrometer at 298 K (mixing time: 120 milliseconds), with 4096 × 512 complex points for a spectral width of 11,432 × 11,415 Hz, and 16 scans were averaged.

adjacent G-C base pairs or a relatively strong metal cation affinity to guanosine.^[54,55] To verify this, we synthesized DNA duplexes 3 and 4, in which a single C-C mismatch is exclusively flanked by A–T base pairs (Figures 1d and e). DNA duplex 3 was a self-associated (symmetric)-type duplex, and

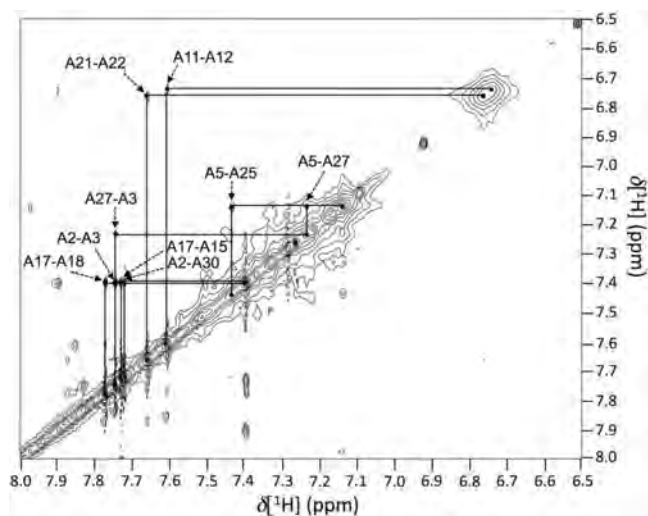


FIGURE 5 H2–H2 cross peaks in the NOESY spectrum of DNA duplex 5- Ag^{I} complex. H2–H2 cross peaks are labelled with residue numbers. The solution contained 2.0-mM DNA duplex 5, 100-mM NaNO_3 with 2.1-mM AgNO_3 in D_2O (pD 7.1). 2D ^1H - ^1H NOESY spectra were recorded on a Bruker AVANCE III 950 spectrometer at 298 K (mixing time: 120 milliseconds), with 4096×512 complex points for a spectral width of $11,432 \times 11,415$ Hz, and 16 scans were averaged.

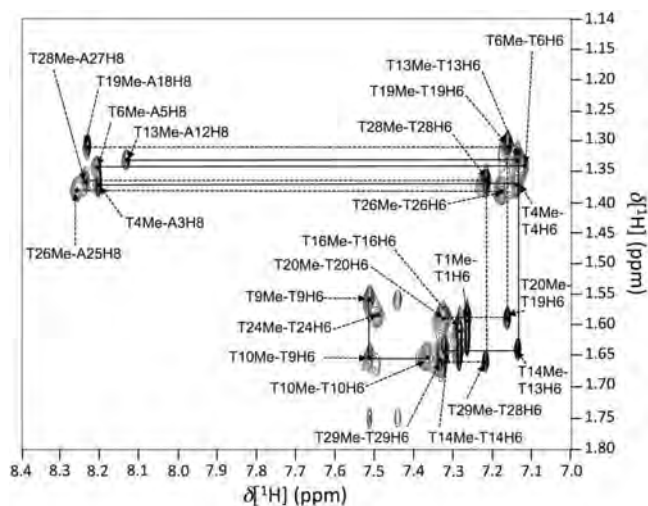


FIGURE 6 H8/H6 methyl proton cross peaks in the NOESY spectrum of DNA duplex 5- Ag^{I} complex. NOE cross peaks between H8/H6 proton and methyl proton are labelled with residue numbers. Black lines and dash lines represent the NOE connectivities derived from the respective DNA strands. The solution contained 2.0-mM DNA duplex 5, 100-mM NaNO_3 with 2.1-mM AgNO_3 in water ($\text{D}_2\text{O}:\text{H}_2\text{O} = 1:9$), pH 6.9. 2D ^1H - ^1H NOESY spectra were recorded on a Bruker AVANCE III 950 spectrometer at 298 K (mixing time: 120 milliseconds), with 8192×1024 complex points for a spectral width of $22,727 \times 22,831$ Hz, and 8 scans were averaged.

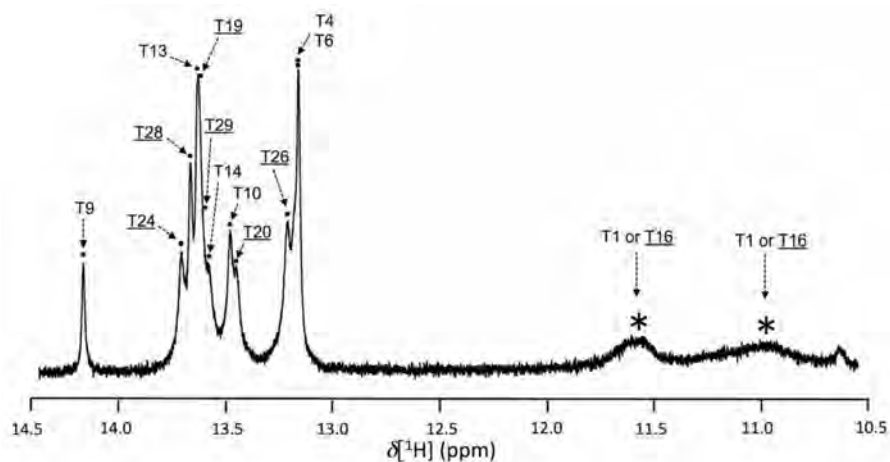


FIGURE 7 Imino proton region in 1D ^1H NMR spectrum of DNA duplex 5- Ag^{I} complex. Imino proton peaks are labelled with residue numbers. Solution contained 2.0-mM DNA duplex 5, 2.1-mM AgNO_3 , 100-mM NaNO_3 in water ($\text{H}_2\text{O}:\text{D}_2\text{O} = 9:1$), pH 6.9. 1D ^1H NMR spectrum was recorded on a Bruker AVANCE III 950 spectrometer, at 298 K, with 22,726 complex points for a spectral width of 22,727 Hz, and 8 scans were averaged.

the signals from the respective cytosine residues in the $\text{C}-\text{Ag}^{\text{I}}-\text{C}$ base pair were averaged. DNA duplex 4 was designed as a non-self-associated (non-symmetric) duplex to allow observation of independent signals from cytidine

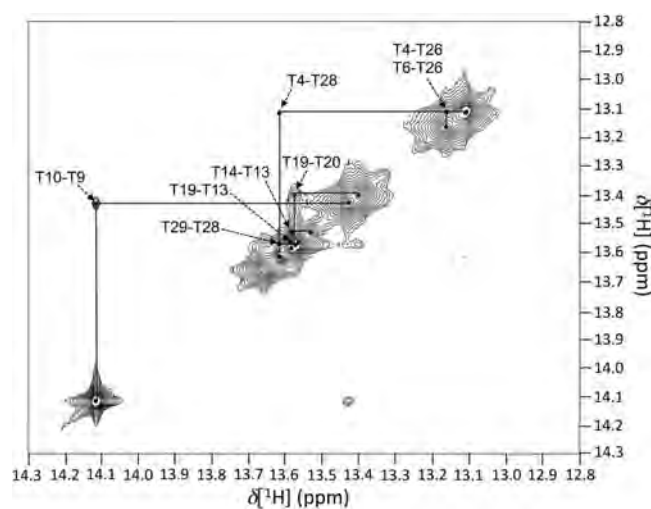


FIGURE 8 Imino proton-imino proton cross peaks in the NOESY spectrum of DNA duplex 5- Ag^{I} complex. Imino proton-imino proton cross peaks are labelled with residue numbers. The solution contained 2.0-mM DNA duplex 5, 100-mM NaNO_3 with 2.1-mM AgNO_3 in water ($\text{D}_2\text{O}:\text{H}_2\text{O} = 1:9$), pH 6.9. 2D $^1\text{H}-^1\text{H}$ NOESY spectra were recorded on a Bruker AVANCE III 950 spectrometer at 298 K (mixing time: 120 milliseconds), with 8192×1024 complex points for a spectral width of $22,727 \times 22,831$ Hz, and 8 scans were averaged.

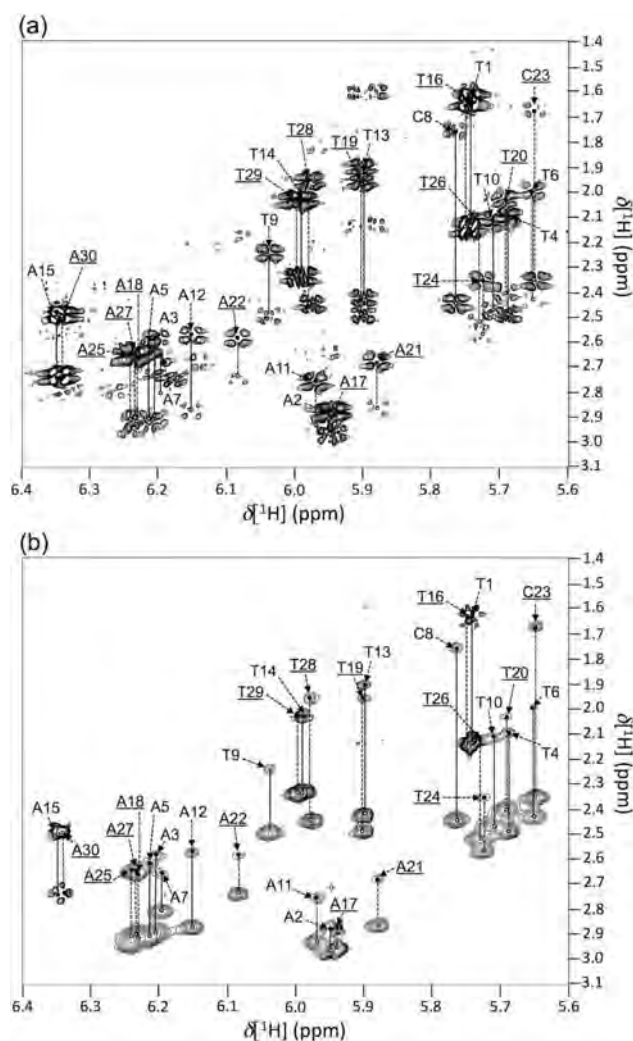


FIGURE 9 (a) Intra-residue H2'/H2''-H1' cross peaks in the DQF-COSY spectrum of DNA duplex 5-Ag^I complex. The solution contained 2.0-mM DNA duplex 5, 100-mM NaNO₃ with 2.1-mM AgNO₃ in D₂O (pD 7.1). DQF-COSY spectra were recorded on a Bruker AVANCE III 950 spectrometer at 298 K, with 4096 × 512 complex points for a spectral width of 11432.926 × 11415.525 Hz, and 16 scans were averaged. (b) Intra-residue NOE cross peaks between H1'/H5-H2'/H2''/methyl protons in the NOESY spectrum of DNA duplex 5-Ag^I complex. Black line: T1-A15, dash line: T16-A30. Intra-residue NOE cross peaks are labelled with residue numbers. Open circles and filled circles indicate H2''-H1' and H2'-H1' cross peaks respectively. The solution contained 2.0-mM DNA duplex 5, 100-mM NaNO₃ with 2.1-mM AgNO₃ in D₂O (pD 7.1). 2D ¹H-¹H NOESY spectra were recorded on a Bruker AVANCE III 950 spectrometer at 298 K (mixing time: 50 milliseconds), with 4096 × 513 complex points for a spectral width of 11,432 × 11,415 Hz, and 16 scans were averaged.

residues of the C-Ag^I-C base pair (C12 and C35) for their structural characterization. We then performed Ag^I-titration experiments of these DNA duplexes, and obtained methyl proton signals as a function of the molar ratio [Ag^I]/[duplex] (Figure 3). Upon addition of Ag^I ion, new signals due

to Ag^I-bound DNA duplexes 3 and 4 appeared, and the shapes of their ¹H NMR spectra gradually changed until the molar ratios, [Ag^I]/[duplex], reached 1.0. Importantly, even at the molar ratios [Ag^I]/[duplex] > 1.0, the spectra did not change for both duplexes, indicating that the species in solutions converged into a singular component. As an initial assumption, the exclusion of any G-C base pair eliminated the secondary Ag^I-binding to DNA duplexes at the C-C mismatch site. Thus, we found appropriate DNA duplexes for the structural characterization of C-Ag^I-C base pair.

For further sequence optimization of 3D structure determination, we explored the possibility of shortening the identified DNA duplexes, since a long DNA sequence makes resonance assignments difficult due to signal overlaps. Shortening of DNA duplex 4 would be more advantageous than that of DNA duplex 3. Since DNA duplex 4 is a non-self-associated type, NMR signals of the respective cytosine bases can be observed independently, and the Ag^I-binding site and the chemical structure of the respective cytosine bases can be explicitly determined. Therefore, the chemical structure of C-Ag^I-C base pair can be determined if its structure is asymmetric.

We next synthesized DNA duplex 5, which lacks four base pairs at each end of DNA duplex 4 (Figure 1f). As a result, DNA duplex 5 also becomes a non-self-associated duplex with a single C-Ag^I-C and 14 A-T base pairs, and 46 independent residues were reduced to 30 independent residues. However, 30 independent residues is still a challenging length for NMR spectroscopy. Furthermore, the exclusion of any G-C base pairs from the sequence limits sequence variations, which may accumulate many NMR signals within a narrow range of chemical shift. Although there exists such a challenging situation for NMR spectroscopy, these sequence requirements must be satisfied for the precise structural characterization of C-Ag^I-C base pair. Therefore, we recorded the NMR spectra of this DNA duplex in the presence of Ag^I ion with an NMR spectrometer with 950 MHz in the ¹H frequency to obtain a better resolution.

For resonance assignment of non-exchangeable protons of the DNA duplex 5-Ag^I complex (Ag^I-DNA complex), we recorded its 2D ¹H-¹H NOESY and DQF-COSY spectra (Figure 4). To identify the H5/H6 resonances of C8 and C23 of C-Ag^I-C base pair in the Ag^I-DNA complex (Figure 1f), we recorded its 2D ¹H-¹H DQF-COSY spectrum. Since cytidine residues were exclusively included at the C-Ag^I-C base pair within the DNA sequence, the H5-H6 cross peaks observed in the DQF-COSY spectrum should correspond to those from the C-Ag^I-C base pair (C8 and C23). As was expected, two H5-H6 cross peaks originated from the C-Ag^I-C base pair (C8 and C23) were identified (Figure 4a). On the other hand, in the absence of Ag^I ion, the H5-H6 cross peaks of C8 and C23 in the COSY spectrum were observed at different chemical shifts (Figure A1 in Appendix). These results indicate that C8 and C23 formed a C-Ag^I-C base pair within DNA duplex 5 in the presence of Ag^I ion.

Next, we assigned the base protons (H8/H6/H2) and anomeric protons (H1') of the Ag^I-DNA complex in the H8/H6/H2-H1' cross section of 2D ¹H-¹H NOESY spectrum with 120-millisecond mixing time (Figure 4b). In the NOESY spectrum (Figure 4b), H5-H6 cross peaks from a C8-Ag^I-C23 base pair were identified in comparison with the same region of the DQF-COSY spectrum (Figure 4a). By using resonance assignments of H5 and H6 in the C8-Ag^I-C23 base pair as a check point, the sequential NOE walks between H8/H6 and H1' were traced through the residues T1-A15 and T16-A30 (Figure 4b). These results indicated that the key NOE data were obtained, which can be used for the ¹H resonance assignment of residual protons and the resulting 3D structure determination, overcoming various challenges. In addition, intra- and inter-residue NOE cross peaks between H2 and H1' were also observed in the same region. From these NOE connectivities, the H2 resonances of adenines, except A5, A7, and A25, were assigned. (Figure A2 in Appendix). Assignment of H2 resonances of A5, A7, and A25 is described below.

Since DNA duplex contains only A-T base pair except for the C-Ag^I-C site, inter-residue NOE cross peaks between H2 protons of neighboring adenine residues were also observed in the H2 to H2 cross section of NOESY spectrum (Figure 5). Intra-strand NOE cross peaks with H2 protons of A-A dinucleotide segments (A2-A3, A11-A12, A17-A18, and A21-A22) were observed in this region. In addition, inter-strand NOE cross peaks with A2-A30, A3-A27, A5-A25, A5-A27, and A15-A17 were also observed in this region. At this point, the H2 resonances of A5 and A25 were assigned.

In order to confirm the assignment of H8/H6 signals, we checked cross section between H8/H6 protons and methyl protons of thymine in the NOESY spectrum of Ag^I-DNA complex. From the spectrum, the intra-residue NOE cross peaks between H6 and methyl protons of thymine bases (H6(T) and Me(T)) were observed and the respective methyl protons generated inter-residue NOE cross peaks with H8 protons of adenine bases (H8(A)) at the 5'-side of the corresponding thymine residues (Figure 6). From these data, A-T dinucleotide segments (A3-T4, A5-T6, A12-T13, A18-T19, A25-T26, and A27-T28) were identified. T-T dinucleotide segments (T9-T10, T13-T14, T19-T20, and T28-T29) in the Ag^I-DNA complex were also identified in a similar way (inter-residue NOE cross peaks between Me(T) and H6(T) at the 5'-side thymine bases of T-T segments instead of those between Me(T) and H8(A) at the 5'-side adenine bases of A-T segments). Notably, these observations are consistent with the assignment of H8/H6 signals based on the sequential NOE walks.

From the inter-strand NOE cross peaks between H2 protons of adenine residues and imino protons of base-paired thymine residues, imino protons except for T1, T16, and T24 were assigned (Figure A3 in Appendix). Then an unassigned imino proton resonance in NOESY spectrum was assigned as H3 of T24, since imino protons of terminal residues (T1 and T16) are often

TABLE 1 Chemical shift table for the Ag^I-DNA complex (T1-A15)^a

	H6/H8 ^b	H2/H5/Me ^c	H1'	H2'	H2''	H3'	H4' ^d	H5'/H5'' ^d	Imino proton
T1	7.25	1.59	5.73	1.61	2.11	4.59	3.96	3.61/3.56	10.92/11.53 ^e
A2	8.30	7.40	5.92	2.85	2.94	5.01	4.39	4.07/4.06	n.a
A3	8.19	7.74	6.20	2.60	2.89	4.99	4.47	4.27/4.25	n.a
T4	7.12	1.36	5.67	2.08	2.46	4.85	4.20	–	13.11
A5	8.19	7.13	6.19	2.56	2.88	4.96	4.36	4.13/4.11	n.a
T6	7.10	1.33	5.63	1.97	2.41	4.84	4.11	3.99/3.97	13.11
A7	8.19	7.25	6.18	2.64	2.79	4.97	4.42	4.09/4.08	n.a
C8	7.42	5.52	5.75	1.74	2.43	4.73	4.08	–	n.a
T9	7.49	1.55	6.01	2.22	2.47	4.85	4.20	4.12/4.08	14.11
T10	7.34	1.64	5.69	2.09	2.45	4.86	4.11	–	13.43
A11	8.25	6.73	5.95	2.74	2.91	5.05	4.41	4.23/4.28	n.a
A12	8.12	7.60	6.13	2.55	2.85	4.97	4.45	4.30/4.28	n.a
T13	7.12	1.32	5.88	1.89	2.40	4.81	4.13	3.99/3.98	13.59
T14	7.31	1.63	5.98	2.01	2.31	4.82	4.04	–	13.53
A15	8.28	7.73	6.33	2.72	2.48	4.73	4.20	4.11/4.09	n.a

Notes. dash (-): not assigned due to signal overlaps. n.a: not applicable (due to the absence of corresponding protons).

^aChemical shifts are given in ppm; ^bchemical shifts for H6 of the pyrimidine residues or H8 of the purine residues; ^cchemical shifts for H2 of adenine, H5 of cytosine, or the methyl proton of thymine; ^dchemical shifts for H4' and H5'/H5'' are tentatively assigned. For H5'/H5'' resonances, stereo-specific assignments were not carried out; ^epossible imino proton signals are listed.

unobservable in NOESY spectra. Furthermore, in the 1D ¹H NMR spectrum of the Ag^I-DNA complex, additional imino proton resonances were also observed (Figure 7). These resonances were tentatively assigned as imino proton resonances from T1 or T16. These assignments were confirmed using imino proton–imino proton NOE cross peaks (Figure 8). From the inter-strand NOE cross peak between imino protons of T24 and H2 protons, the H2 resonance of A7 was assigned (Figure A3 in Appendix). At this stage, all H2 resonances were assigned. In addition, from the intra-residue NOE cross peaks between methyl and imino protons, methyl proton resonances were confirmed (Figure A4 in Appendix). The assignments of H2, H6, and H8 protons of the Ag^I-DNA complex were confirmed by H2–C2, H6–C6, and H8–C8 cross peaks in 2D ¹H–¹³C HSQC spectrum (Figure A5 in Appendix), and H2, H6, and H8 proton resonances in 1D ¹H NMR spectrum (Figure A6 in Appendix).

Stereo-specific assignment of H2' and H2'' were performed using the cross-peak intensities of H2'/H2''–H1' in DQF-COSY and NOESY spectra with 50-milliseconds mixing time (Figure 9). Generally, H2' protons resonate up-field against their geminal H2'' protons. Then, in the case of DQF-COSY spectrum, H2' protons generate stronger cross peaks with their vicinal H1' protons than done by H2'' protons. All adenine and thymine residues except for 3'-terminal residues, A15 and A30, satisfied this tendency, and the stereo-specific assignment of their H2'/H2'' resonances was achieved. In

TABLE 2 Chemical shift table for the Ag^I-DNA complex (T16–A30)^a

	H6/H8 ^b	H2/H5/Me ^c	H1'	H2'	H2''	H3'	H4' ^d	H5'/H5'' ^d	Imino proton
T16	7.27	1.61	5.73	1.63	2.13	4.60	3.98	3.62/3.57	10.92/11.53 ^e
A17	8.31	7.40	5.92	2.86	2.95	5.01	4.25	3.97/3.96	n.a
A18	8.22	7.77	6.22	2.64	2.90	5.00	4.48	4.32/4.31	n.a
T19	7.14	1.29	5.88	1.94	2.46	4.85	4.18	4.07/4.04	13.57
T20	7.30	1.58	5.67	2.01	2.38	4.84	4.07	–	13.40
A21	8.20	6.75	5.86	2.65	2.84	5.02	4.40	4.24/4.22	n.a
A22	8.07	7.65	6.06	2.57	2.72	4.94	4.45	4.32/4.30	n.a
C23	7.31	5.41	5.63	1.65	2.34	4.67	4.19	4.02/4.00	n.a
T24	7.47	1.57	5.70	2.33	2.55	4.88	4.19	–	13.66
A25	8.24	7.42	6.22	2.63	2.92	5.00	4.49	4.27/4.26	n.a
T26	7.16	1.37	5.71	2.10	2.49	4.87	4.22	–	13.16
A27	8.23	7.22	6.22	2.63	2.89	4.98	4.41	4.17/4.15	n.a
T28	7.20	1.36	5.96	1.94	2.42	4.81	4.16	4.01/3.99	13.62
T29	7.32	1.64	5.98	2.02	2.31	4.82	4.04	–	13.58
A30	8.29	7.73	6.34	2.74	2.49	4.73	4.21	4.13/4.09	n.a

Notes. dash (-): not assigned due to signal overlaps; na: not applicable (due to the absence of corresponding protons).

^aChemical shifts are given in ppm; ^bchemical shifts for H6 of the pyrimidine residues or H8 of the purine residues; ^cchemical shifts for H2 of adenine, H5 of cytosine, or the methyl proton of thymine; ^dchemical shifts for H4' and H5'/H5'' are tentatively assigned. For H5'/H5'' resonances, stereo-specific assignments were not carried out; ^epossible imino proton signals are listed.

the case of H2'/H2'' protons of C8 and C23 in C–Ag^I–C base pair, the order of H2'–H1' and H2''–H1' cross-peak intensities of DQF-COSY spectrum was reversed (Figure 9), which may indicate C3'-endo-like puckering, or at least the existence of certain dynamics of sugar puckering. As additional information, H2'/H2''–H1' NOE cross peaks were used for stereo-specific assignment of H2'/H2'' resonances of C8 and C23 (Figure 9). In the same region, H2'' protons usually generate stronger NOE cross peaks with their intra-residue H1' protons than intra-residue H2' protons, irrespective of sugar puckering. From this information, the stereo-specific assignment of H2'/H2'' resonances of C8 and C23 was achieved, and H2' protons were found to resonate up-field against their geminal H2'' protons as expected. We then checked the NOE cross peaks around the C–Ag^I–C base pair since the sugar puckerings of C8 and C23 in the C–Ag^I–C base pair were non-standard. However, volumes of H8/H6–H1' NOE cross peaks were within a variation of their volumes, and we were not able to find any C–Ag^I–C base pair-specific NOE cross peaks. These results indicate that the Ag^I-DNA complex basically takes regular DNA duplex except for the sugar puckerings of C8 and C23.

The H3' resonances were further assigned using the cross peaks with intra-residue H2' in DQF-COSY spectrum (Figure A7 in Appendix). These assignments were also confirmed by H1'–H3' and H6/H8–H3' cross peaks in NOESY spectrum (Figures A8 and A9 in Appendix). In addition, the

assigned H1' resonances were utilized for the tentative assignment of H4' and H5'/H5'' resonances using their NOE cross peaks with intra-residue H1' protons (Figure A10 in Appendix). Thus, we could assign 254 non-exchangeable proton resonances out of 270 expected resonances, as well as 14 imino proton resonances, which are critical information for the 3D structure determination. The resulting resonance assignments are listed in Tables 1 and 2.

CONCLUSIONS

In this study, we extensively explored a DNA sequence for the structure analysis of C–Ag^I–C base pair in a DNA duplex, and identified an appropriate DNA sequence without structural polymorphism. The determined sequence was 15-base-paired DNA duplex with a single C–Ag^I–C base pair flanked by only A–T base pairs. Irrespective of the challenging length of DNA duplex for NMR measurements and the small sequence variation (14 A–T base pairs out of 15 base-paired duplex), we could assign 254 non-exchangeable proton resonances out of 270 expected resonances and all imino proton resonances, which will be the most important bases for 3D structure determination.

FUNDING

This work was performed using the NMR spectrometer under the Cooperative Research Program of the Institute for Protein Research, Osaka University. This work was supported by the Platform for Drug Discovery, Informatics, and Structural Life Science from the Ministry of Education, Culture, Sports, Science and Technology (MEXT), Japan. This work was supported by Grants-in-Aid for Scientific Research (a) 24245037 to Akira Ono and Yoshiyuki Tanaka, (b) 24310163 to Yoshiyuki Tanaka and Chojiro Kojima, (c) 18550146 to Yoshiyuki Tanaka, and Challenging Exploratory Research (15K13734 to Yoshiyuki Tanaka) from MEXT, Japan. Takenori Dairaku and Kyoko Furuita are the recipients of a Research Fellowship for Young Scientists from the Japan Society for the Promotion of Science (JSPS).

REFERENCES

1. Clever, G.H.; Kaul, C.; Carell, T. DNA-metal base pairs. *Angew. Chem. Int. Ed.* **2007**, *46*, 6226–6236.
2. Clever, G.H.; Shionoya, M. Metal-base pairing in DNA. *Coord. Chem. Rev.* **2010**, *254*, 2391–2402.
3. Ono, A.; Torigoe, H.; Tanaka, Y.; Okamoto, I. Binding of metal ions by pyrimidine base pairs in DNA duplexes. *Chem. Soc. Rev.* **2011**, *40*, 5855–5866.
4. Takezawa, Y.; Shionoya, M. Metal-mediated DNA base pairing: Alternatives to hydrogen-bonded Watson-Crick base pairs. *Acc. Chem. Res.* **2012**, *45*, 2066–2076.
5. Scharf, P.; Muller, J. Nucleic acids with metal-mediated base pairs and their applications. *ChemPlusChem.* **2013**, *78*, 20–34.
6. Park, K.S.; Park, H.G. Technological applications arising from the interactions of DNA bases with metal ions. *Curr. Opin. Biotechnol.* **2014**, *28*, 17–24.

7. Wagenknecht, H.-A. Reductive electron transfer and transport of excess electrons in DNA. *Angew. Chem.* **2003**, 115, 3322–3324; *Angew. Chem. Int. Ed.* **2003**, 42, 3204–3206.
8. Liu, X.; Lu C.-H.; Willner, I. Switchable reconfiguration of nucleic acid nanostructures by stimuli-responsive DNA machines. *Acc. Chem. Res.* **2014**, 47, 1673–1680.
9. Wang, F.; Lu C.-H.; Willner, I. From cascaded catalytic nucleic acids to enzyme–DNA nanostructures: Controlling reactivity, sensing, logic operations, and assembly of complex structures. *Chem. Rev.* **2014**, 114, 2881–2941.
10. Ono, A.; Togashi, H. Highly selective oligonucleotide-based sensor for mercury(II) in aqueous solutions. *Angew. Chem. Int. Ed.* **2004**, 43, 4300–4302.
11. Ono, A.; Cao, S.; Togashi, H.; Tashiro, M.; Fujimoto, T.; Machinami, T.; Oda, S.; Miyake, Y.; Okamoto, I.; Tanaka, Y. Specific interactions between silver(I) ions and cytosine–cytosine pairs in DNA duplexes. *Chem. Commun.* **2008**, 4825–4827.
12. Liu, X.J.; Qi, C.; Bing, T.; Cheng, X.H.; Shanguan, D. Specific mercury(II) adsorption by thymine-based sorbent. *Talanta* **2009**, 78, 253–258.
13. Dave, N.; Chan, M.Y.; Huang, P.J.J.; Smith, B.D.; Liu, J.W. Regenerable DNA-functionalized hydrogels for ultrasensitive, instrument-free mercury(II) detection and removal in water. *J. Am. Chem. Soc.* **2010**, 132, 12668–12673.
14. Huang, P.J.J.; Liu, J.W. Immobilization of DNA on magnetic microparticles for mercury enrichment and detection with flow cytometry. *Chem. Eur. J.* **2011**, 17, 5004–5010.
15. Yu, Y.; Zhang, B.W.; Yu, M.; Deng, B.; Li, L.F.; Fan, C.H.; Li, J.Y. High-selective removal of ultra-low level mercury ions from aqueous solution using oligothymonucleic acid functionalized polyethylene film. *Sci. China. Chem.* **2012**, 55, 2202–2208.
16. Wang, Y.S.; Cheng, C.C.; Chen, J.K.; Ko, F.H.; Chang, F.C. Bioinspired supramolecular fibers for mercury ion adsorption. *J. Mater. Chem. A* **2013**, 1, 7745–7750.
17. Kuriyama, M.; Haruta, K.; Dairaku, T.; Kawamura, T.; Kikkawa, S.; Inamoto, K.; Tsukamoto, H.; Kondo, Y.; Torigoe, H.; Okamoto, I.; Ono, A.; Morita, E.H.; Tanaka, Y. Hg²⁺-trapping beads: Hg²⁺-specific recognition through thymine–Hg(II)–thymine base pairing. *Chem. Pharm. Bull.* **2014**, 62, 709–712.
18. Torigoe, H.; Ono, A.; Kozasa, T. Mismatch base pair detection by fluorescence spectral change upon addition of metal cation toward efficient analysis of single nucleotide polymorphism. *Nucleosides Nucleotides Nucl. Acids* **2007**, 26, 1635–1639.
19. Lin, Y.W.; Ho, H.T.; Huang, C.C.; Chang, H.T. Fluorescence detection of single nucleotide polymorphisms using a universal molecular beacon. *Nucleic Acids Res.* **2008**, 36, e123.
20. Torigoe, H.; Miyakawa, Y.; Ono, A.; Kozasa, T. Thermodynamic properties of the specific binding between Ag⁺ ions and C:C mismatched base pairs in duplex DNA. *Nucleosides Nucleotides Nucl. Acids* **2011**, 30, 149–167.
21. Tanaka, K.; Tengeiji, A.; Kato, T.; Toyama, N.; Shionoya, M. A discrete self-assembled metal array in artificial DNA. *Science* **2003**, 299, 1212–1213.
22. Clever, G.H.; Reitmeier, S.J.; Carell, T.; Schiemann, O. Anti-ferromagnetic coupling of stacked Cu^{II}-Salen complexes in DNA. *Angew. Chem. Int. Ed.* **2010**, 49, 4927–4929.
23. Carell, T.; Behrens, C.; Gierlich, J. Electrontransfer through DNA and metal-containing DNA. *Org. Biomol. Chem.* **2003**, 1, 2221–2228.
24. Ito, T.; Nikaido, G.; Nishimoto, S.I. Effects of metal binding to mismatched base pairs on DNA-mediated charge transfer. *J. Inorg. Biochem.* **2007**, 101, 1090–1093.
25. Joseph, J.; Schuster, G.B. Long-distance radical cation hopping in DNA: The effect of thymine–Hg(II)–thymine base pairs. *Org. Lett.* **2007**, 9, 1843–1846.
26. Guo, L.Q.; Yin, N.; Chen, G.N. Photoinduced electron transfer mediated by pi-stacked thymine–Hg²⁺–thymine base pairs. *J. Phys. Chem. C* **2011**, 115, 4837–4842.
27. Isobe, H.; Yamazaki, N.; Asano, A.; Fujino, T.; Nakanishi, W.; Seki, S. Electron mobility in a mercury-mediated duplex of triazole-linked DNA ((TL)DNA). *Chem. Lett.* **2011**, 40, 318–319.
28. Kratochvilova, I.; Golan, M.; Vala, M.; Sperova, M.; Weiter, M.; Pav, O.; Sebera, J.; Rosenberg, I.; Sychrovsky, V.; Tanaka, Y.; Bickelhaupt, F.M. Theoretical and experimental study of charge transfer through DNA: Impact of mercury mediated T–Hg–T base pair. *J. Phys. Chem. B* **2014**, 118, 5374–5381.
29. Porchetta, A.; Vallee-Belisle, A.; Plaxco, K.W.; Ricci, F. Allosterically tunable, DNA-based switches triggered by heavy metals. *J. Am. Chem. Soc.* **2013**, 135, 13238–13241.

30. Freeman, R.; Finder, T.; Willner, I. Multiplexed analysis of Hg²⁺ and Ag⁺ ions by nucleic acid functionalized CdSe/ZnS quantum dots and their use for logic gate operations. *Angw. Chem. Int. Ed.* **2009**, *48*, 7818–7821.
31. Zhang, G.Y.; Lin, W.L.; Yang, W.Q.; Lin, Z.Y.; Guo, L.H.; Qiu, B.; Chen, G.N. Logic gates for multiplexed analysis of Hg²⁺ and Ag⁺. *Analyst* **2012**, *137*, 2687–2691.
32. Bi, S.; Ji, B.; Zhang, Z.P.; Zhu, J.J. Metal ions-triggered ligase activity for rolling circle amplification and its application in molecular logic gate operations. *Chem. Sci.* **2013**, *4*, 1858–1863.
33. Funai, T.; Nakamura, J.; Miyazaki, Y.; Kiri, R.; Nakagawa, O.; Wada, S.; Ono, A.; Urata, H. Regulated incorporation of two different metal ions into programmed sites in a duplex by DNA polymerase catalyzed primer extension. *Angw. Chem. Int. Ed.* **2014**, *53*, 6624–6627.
34. Ono, A.; Togashi, H. Highly selective oligonucleotide-based sensor for mercury(II) in aqueous solutions. *Angw. Chem. Int. Ed.* **2004**, *43*, 4300–4302.
35. Ihara, T.; Ishii, T.; Araki, N.; Wilson, A.W.; Jyo, A. Silver ion unusually stabilizes the structure of a parallel-motif DNA triplex. *J. Am. Chem. Soc.* **2009**, *131*, 3826–3827.
36. Megger, D.A.; Muller, J. Silver(I)-mediated cytosine self-pairing is preferred over Hoogsteen-type base pairs with the artificial nucleobase 1,3-dideaza-6-nitropurine. *Nucleosides Nucleotides Nucleic Acids* **2010**, *29*, 27–38.
37. Ono, T.; Yoshida, K.; Saotome, Y.; Sakabe, R.; Okamoto, I.; Ono, A. Synthesis of covalently linked parallel and antiparallel DNA duplexes containing the metal-mediated base pairs T–Hg(II)–T and C–Ag(I)–C. *Chem. Commun.* **2011**, *47*, 1542–1544.
38. Funai, T.; Miyazaki, Y.; Aotani, M.; Yamaguchi, E.; Nakagawa, O.; Wada, S.; Torigoe, H.; Ono, A.; Urata, H. Ag^I ion-mediated formation of a C–A mispair by DNA polymerases. *Angw. Chem. Int. Ed.* **2012**, *51*, 6464–6466.
39. Day, H.A.; Huguin, C.; Waller, Z.A.E. Silver cations fold i-motif at neutral pH. *Chem. Commun.* **2013**, *49*, 7696–7698.
40. Urata, H.; Yamaguchi, E.; Nakamura, Y.; Wada, S. Pyrimidine-pyrimidine base pairs stabilized by silver(I) ions. *Chem. Commun.* **2011**, *47*, 941–943.
41. Swasey, S.M.; Leal, L.E.; Lopez-Acevedo, O.; Pavlovich, J.; Gwinn, E.G. Silver (I) as DNA glue: Ag⁺-mediated guanine pairing revealed by removing Watson-Crick constraints. *Sci. Rep.* **2015**, *5*, 10163.
42. Ritchie, C.M.; Johnsen, K.R.; Kiser, J.R.; Antoku, Y.; Dickson, R.M.; Petty, J.T. Ag nanocluster formation using a cytosine oligonucleotide template. *J. Phys. Chem. C* **2007**, *111*, 175–181.
43. Urata, H.; Yamaguchi, E.; Funai, T.; Matsumura, Y.; Wada, S. Incorporation of thymine nucleotides by DNA polymerases through T–Hg^{II}–T base pairing. *Angw. Chem. Int. Ed.* **2010**, *49*, 6516–6519.
44. Park, K.S.; Jung, C.; Park, H.G. “Illusionary” polymerase activity triggered by metal ions: Use for molecular logic-gate operations. *Angw. Chem. Int. Ed.* **2010**, *49*, 9757–9760.
45. Bi, S.; Ji, B.; Zhang, Z.P.; Zhu, J.J. Metal ions-triggered ligase activity for rolling circle amplification and its application in molecular logic gate operations. *Chem. Sci.* **2013**, *4*, 1858–1863.
46. Tanaka, Y.; Oda, S.; Yamaguchi, H.; Kondo, Y.; Kojima, C.; Ono, A. ¹⁵N-¹⁵N J-coupling across Hg^{II}: Direct observation of Hg^{II}-mediated T-T base pairs in a DNA duplex. *J. Am. Chem. Soc.* **2007**, *129*, 244–245.
47. Yamaguchi, H.; Sebera, J.; Kondo, J.; Oda, S.; Komuro, T.; Kawamura, T.; Dairaku, T.; Kondo, Y.; Okamoto, I.; Ono, A.; Burda, J.V.; Kojima, C.; Sychrovsky, V.; Tanaka, Y. The structure of metallo-DNA with consecutive thymine-Hg^{II}-thymine base pairs explains positive entropy for the metallo base pair formation. *Nucleic Acids Res.* **2014**, *42*, 4094–4099.
48. Kondo, J.; Yamada, T.; Hirose, C.; Okamoto, I.; Tanaka, Y.; Ono, A. Crystal structure of metallo DNA duplex containing consecutive Watson-Crick-like T–Hg^{II}–T base pairs. *Angw. Chem. Int. Ed.* **2014**, *53*, 1–5.
49. Voityuk, A.A. Electronic coupling mediated by stacked (thymine-Hg-thymine) base pairs. *J. Phys. Chem. B* **2006**, *110*, 21010–21013.
50. Uchiyama, T.; Miura, T.; Takeuchi, H.; Dairaku, T.; Komuro, T.; Kawamura, T.; Kondo, Y.; Benda, L.; Sychrovsky, V.; Bour, P.; Okamoto, I.; Ono, A.; Yanaka, Y. Raman spectroscopic detection of the T–Hg^{II}–T base pair and the ionic characteristics of mercury. *Nucleic Acids Res.* **2012**, *40*, 5766–5774.
51. Wang, Y.; Luan, B.Q.; Yang, Z.; Zhang, X.; Ritzo, B.; Gates, K.; Gu, L.Q. Single molecule investigation of Ag⁺ interactions with single cytosine-, methylcytosine- and hydroxymethylcytosine–cytosine mismatches in a nanopore. *Sci. Rep.* **2014**, *4*, 5883.

52. Wang, Y.; Ritzo, B.; Gu, L.Q. Silver(I) ions modulate the stability of DNA duplexes containing cytosine, methylcytosine and hydroxymethylcytosine at different salt concentrations. *RSC Adv.* **2015**, *5*, 2655–2658.
53. Torigoe, H.; Okamoto, I.; Dairaku, T.; Tanaka, Y.; Ono, A.; Kozasa, T. Thermodynamic and structural properties of the specific binding between Ag^+ ion and C:C mismatched base pair in duplex DNA to form C-Ag-C metal-mediated base pair. *Biochimie* **2012**, *94*, 2431–2440.
54. Kapinos, L.E.; Holý, A.; Günter, J.; Sigel, H. Metal ion-binding properties of 1-methyl-4-aminobenzimidazole (=9-methyl-1,3-dideazaadenine) and 1,4-dimethylbenzimidazole (=6,9-dimethyl-1,3-dideazapurine). Quantification of the steric effect of the 6-amino group on metal ion binding at the N7 site of the adenine residue. *Inorg. Chem.* **2001**, *40*, 2500–2508.
55. Arakawa, H.; Neault, J.F.; Tajmir-Riahi, H.A. Silver(I) complexes with DNA and RNA studied by Fourier transform infrared spectroscopy and capillary electrophoresis. *Biophys. J.* **2001**, *81*, 1580–1587.

APPENDIX

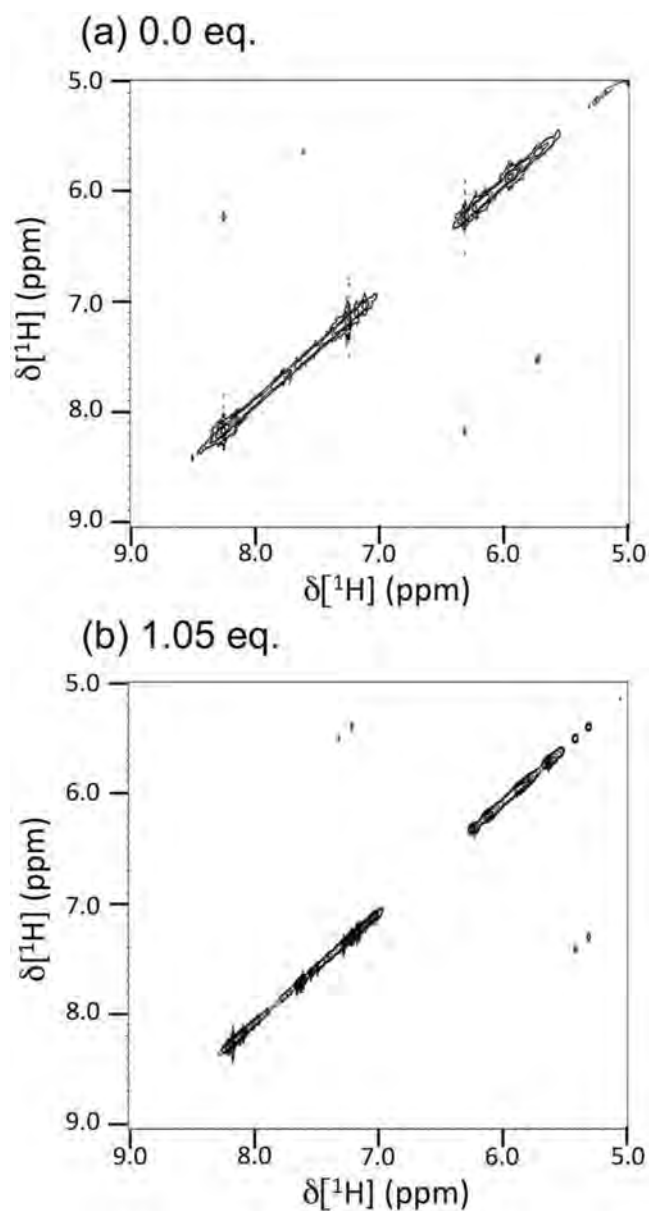


FIGURE A1 H5-H6 cross peaks of residues C8 and C23 in the absolute value ${}^1\text{H}$ - ${}^1\text{H}$ COSY spectra of DNA duplex 5. The solution contained 2.0-mM DNA duplex 5, 100-mM NaNO_3 with/without 2.1-mM AgNO_3 in D_2O (pD 7.1). Absolute value ${}^1\text{H}$ - ${}^1\text{H}$ COSY spectra was recorded on a JEOL ECA 600 spectrometer at 298 K with 1280×256 complex points for a spectral width of 6720×5374 Hz, and 256 scans were averaged.

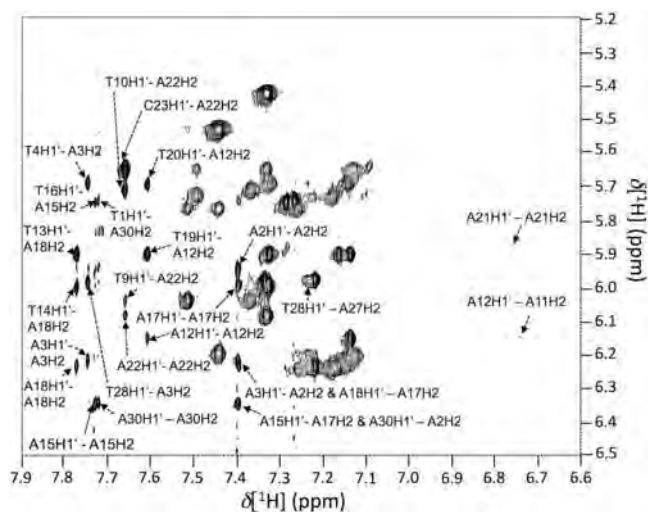


FIGURE A2 H2–H1' cross peaks in the NOESY spectrum of DNA duplex 5-Ag^I complex. The solution contained 2.0-mM DNA duplex 5, 100-mM NaNO₃ with 2.1-mM AgNO₃ in D₂O (pD 7.1). 2D ¹H–¹H NOESY spectra were recorded on a Bruker AVANCE III 950 spectrometer at 298 K (mixing time: 120 milliseconds), with 4096 × 512 complex points for a spectral width of 11,432 × 11,415 Hz, and 16 scans were averaged.

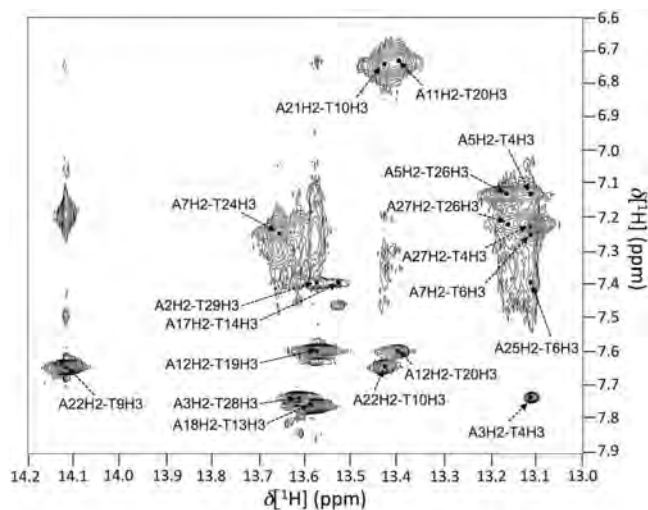


FIGURE A3 H2–imino proton (H3) cross peaks in the NOESY spectrum of DNA duplex 5-Ag^I complex. H2–H3 cross peaks are labelled with residue numbers. The solution contained 2.0-mM DNA duplex 5, 100-mM NaNO₃ with 2.1-mM AgNO₃ in water (D₂O:H₂O = 1:9), pH 6.9. 2D ¹H–¹H NOESY spectra were recorded on a Bruker AVANCE III 950 spectrometer at 298 K (mixing time: 120 milliseconds), with 8192 × 1024 complex points for a spectral width of 22,727 × 22,831 Hz, and 8 scans were averaged.

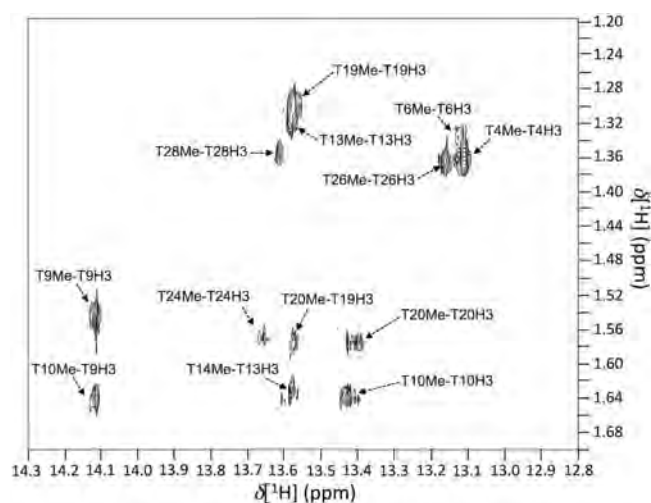


FIGURE A4 Methyl proton–imino proton (H3) cross peaks in the NOESY spectrum of DNA duplex 5- Ag^{I} complex. Methyl proton–H3 cross peaks are labelled with residue numbers. The solution contained 2.0-mM DNA duplex 5, 100-mM NaNO_3 with 2.1-mM AgNO_3 in water ($\text{D}_2\text{O}:\text{H}_2\text{O} = 1:9$), pH 6.9. 2D ^1H – ^1H NOESY spectra were recorded on a Bruker AVANCE III 950 spectrometer at 298 K (mixing time: 120 milliseconds), with 8192×1024 complex points for a spectral width of $22,727 \times 22,831$ Hz, and 8 scans were averaged.

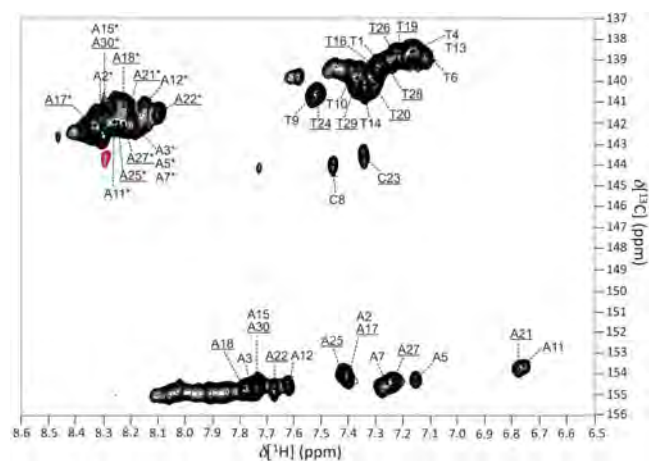


FIGURE A5 H2–C2, H6–C6 and H8–C8 cross peaks in 2D ^1H – ^{13}C HSQC spectrum of DNA duplex 5- Ag^{I} complex. H2–C2 and H6–C6 cross peaks are labelled with residue numbers. H8–C8 cross peaks are labelled with residue numbers and asterisks. The solution contained 2.0-mM DNA duplex 5, 100-mM NaNO_3 with 2.1-mM AgNO_3 in D_2O (pD 7.1). 2D ^1H – ^{13}C HSQC spectrum was recorded on a Bruker AVANCE III 950 spectrometer at 298 K, with 1024×256 complex points for a spectral width of 8152×4050 Hz, and 256 scans were averaged.

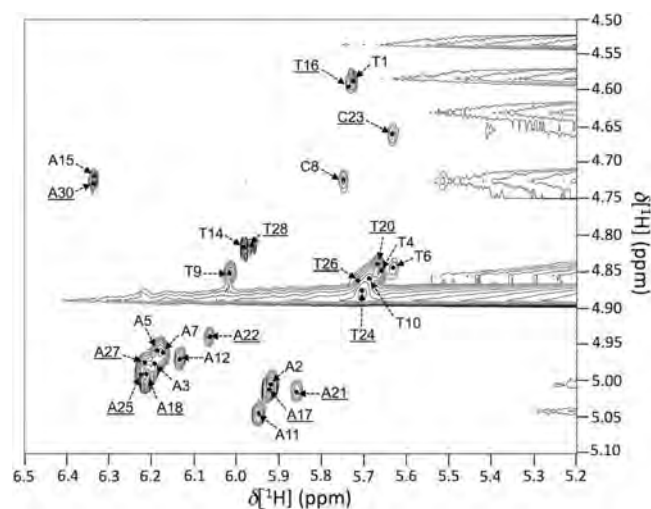


FIGURE A8 H1'–H3' cross peaks in the NOESY spectrum of DNA duplex 5-Ag^I complex. H1'–H3' cross peaks are labelled with residue numbers. The solution contained 2.0-mM DNA duplex 5, 100-mM NaNO₃ with 2.1-mM AgNO₃ in water (D₂O:H₂O = 1:9), pH 6.9. 2D ¹H-¹H NOESY spectra were recorded on a Bruker AVANCE III 950 spectrometer at 298 K (mixing time: 120 milliseconds), with 8192 × 1024 complex points for a spectral width of 22,727 × 22,831 Hz, and 8 scans were averaged.

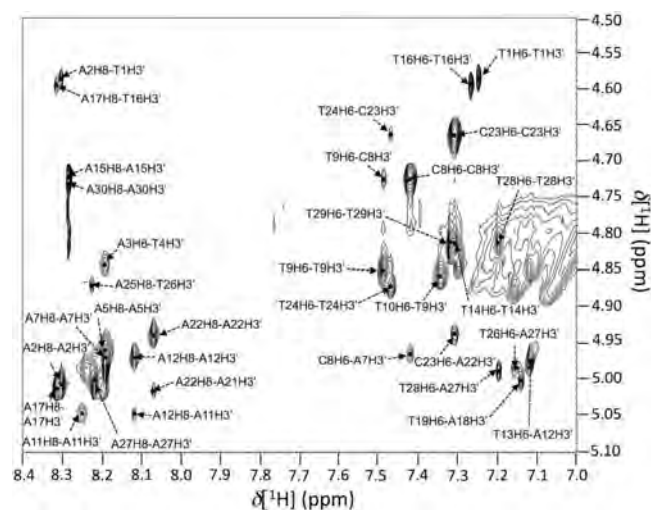


FIGURE A9 H6/H8–H3' cross peaks in the NOESY spectrum of DNA duplex 5-Ag^I complex. H6/H8–H3' cross peaks are labelled with residue numbers. The solution contained 2.0-mM DNA duplex 5, 100-mM NaNO₃ with 2.1-mM AgNO₃ in water (D₂O:H₂O = 1:9), pH 6.9. 2D ¹H-¹H NOESY spectra were recorded on a Bruker AVANCE III 950 spectrometer at 298 K (mixing time: 120 milliseconds), with 8192 × 1024 complex points for a spectral width of 22,727 × 22,831 Hz, and 8 scans were averaged.

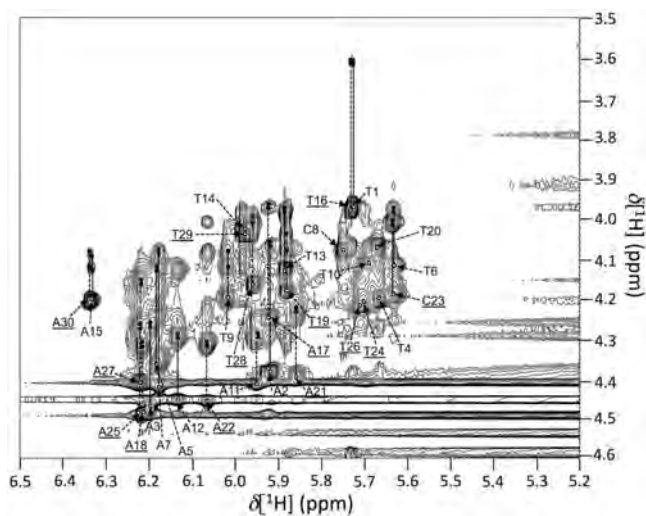
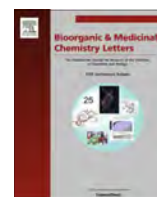


FIGURE A10 H1'-H4'/H5'/H5'' cross peaks in the NOESY spectrum of DNA duplex 5-Ag⁺ complex. Open circles and filled circles indicate H1'-H4' and H1'-H5'/H5'' cross peaks respectively. Intra-residue H1'-H4' and H1'-H5'/H5'' cross peaks are connected with black line (T1-A15) and dotted line (T16-A30). The solution contained 2.0-mM DNA duplex 5, 100-mM NaNO₃ with 2.1-mM AgNO₃ in water (D₂O:H₂O = 1:9), pH 6.9. 2D ¹H-¹H NOESY spectra were recorded on a Bruker AVANCE III 950 spectrometer at 298 K (mixing time: 120 milliseconds), with 8192 × 1024 complex points for a spectral width of 22,727 × 22,831 Hz, and 8 scans were averaged.



Contents lists available at ScienceDirect

Bioorganic & Medicinal Chemistry Letters

journal homepage: www.elsevier.com/locate/bmcl

Bioreductive deprotection of 4-nitrobenzyl group on thymine base in oligonucleotides for the activation of duplex formation



Hisao Saneyoshi*, Yuki Hiyoshi, Koichi Iketani, Kazuhiko Kondo, Akira Ono*

Department of Material and Life Chemistry, Faculty of Engineering, Kanagawa University, 3-27-1 Rokkakubashi, Kanagawa-ku, Yokohama 221-8686, Japan

ARTICLE INFO

Article history:

Received 29 August 2015

Revised 7 October 2015

Accepted 10 October 2015

Available online 22 October 2015

Keywords:

Nucleic acid-based therapeutics

Prodrug

Protecting group

Hypoxia

Hybridization

ABSTRACT

Oligonucleotides containing 4-O-(4-NO₂-benzyl)thymine residues were synthesized to assess potential prodrug-type action against hypoxic cells. These modified oligonucleotides were incapable of stable duplex formation under non-hypoxic conditions. However, following deprotection of the thymine residues under bioreductive conditions, the deprotected oligonucleotides were able to form stable duplexes with target oligonucleotides.

© 2015 Elsevier Ltd. All rights reserved.

Various nucleobase-protecting groups have been used in the chemical synthesis of oligonucleotides.¹ In recent years, the application of protecting groups has expanded to include the control of nucleic acid functions.² For example, in the pioneering work by Kröck and Heckel, 2-nitrobenzyl and its congeners were installed onto thymine residues to generate light-activatable oligonucleotides.³ Their study inspired our use of protected nucleobases to produce hypoxia-activatable oligonucleotides. Hypoxia is a characteristic property of locally advanced solid tumors resulting from the insufficient supply of oxygen from the poorly developed vasculature. Hypoxia induces increased resistance to both chemotherapy and radiation therapy.⁴ Approaches to treating hypoxic tumors with drugs activated under such conditions have been reported.⁵ These prodrugs are typically protected with hypoxia-labile protecting groups that mask binding sites to the target molecules. Under hypoxic conditions, these protecting groups are removed and the drugs are converted into their active forms.

In this report, we describe the synthesis of an oligonucleotide with a hypoxia-labile protecting group on one of the four

nucleobases. Specifically, oligonucleotides containing 4-O-nitrobenzylated thymine residues as the prototype nucleobase were synthesized. The 4-NO₂-benzyl group is frequently used for hypoxia-activated prodrugs or to switch fluorescent probes on and off.^{6–20} In normal cells (non-hypoxic), oligonucleotides containing 4-O-nitrobenzylated thymine residues (pro-oligos) do not hybridize to target RNA sequences (Fig. 1a). In hypoxic tumors, the 4-nitrobenzyl groups are deprotected via reduction of the nitro group to amino (or hydroxyamino) followed by a 1,6-elimination process to expel the active oligos (Fig. 1a and b). Thus, in the hypoxic tumor cell, a pro-oligo will be converted to an active oligonucleotide which hybridizes to the target sequence, thereby inhibiting mRNA translation.

For this study, we synthesized oligonucleotides containing 4-O-(4-NO₂-Bn)thymine residues, which were treated with nitroreductase for conversion into free oligonucleotides. The hybridization properties of the protected and the free oligonucleotides were investigated by thermal denaturation experiments.

Briefly, a protected thymidine **1** was reacted with triisopropylbenzenesulfonyl chloride to produce a 4-O-sulfonylated intermediate, which was subsequently substituted with 4-NO₂ benzyl alcohol to yield 4-benzylated derivative **2**. Acetyl groups in **2** were deprotected with NH₄OH to produce **3** which was treated with 4,4'-dimethoxytrityl chloride to give **4**; then, phosphitylation of the free 3'-hydroxyl group with 2-(cyanoethoxy)-N,N-diisopropylaminochlorophosphine yielded the desired phosphoramidite derivative **5** (Scheme 1). Using the monomer unit **5**, oligonucleotides

* Corresponding authors. Tel.: +81 45 481 5661; fax: +81 45 481 2781.

E-mail addresses: saneyoshih@kanagawa-u.ac.jp (H. Saneyoshi), akiraono@kanagawa-u.ac.jp (A. Ono).

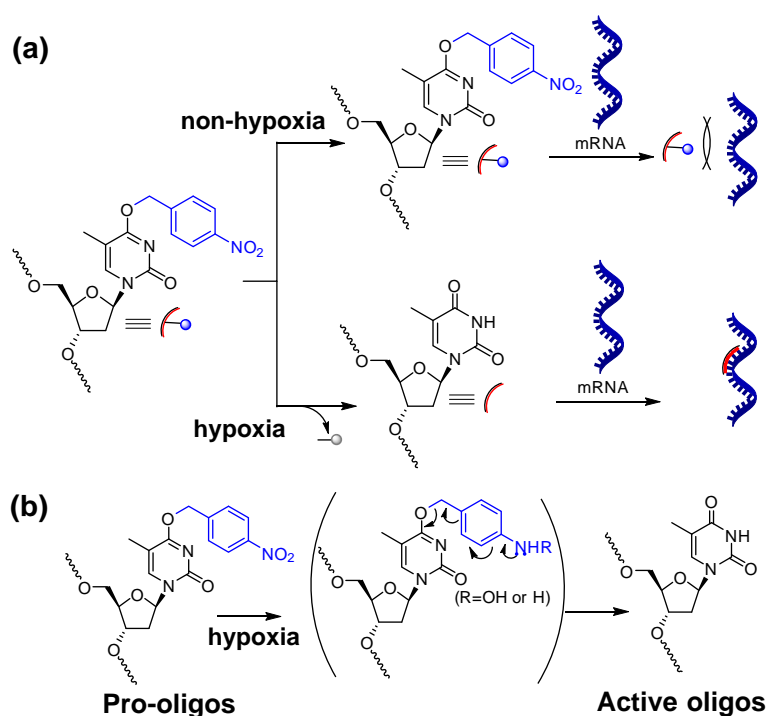
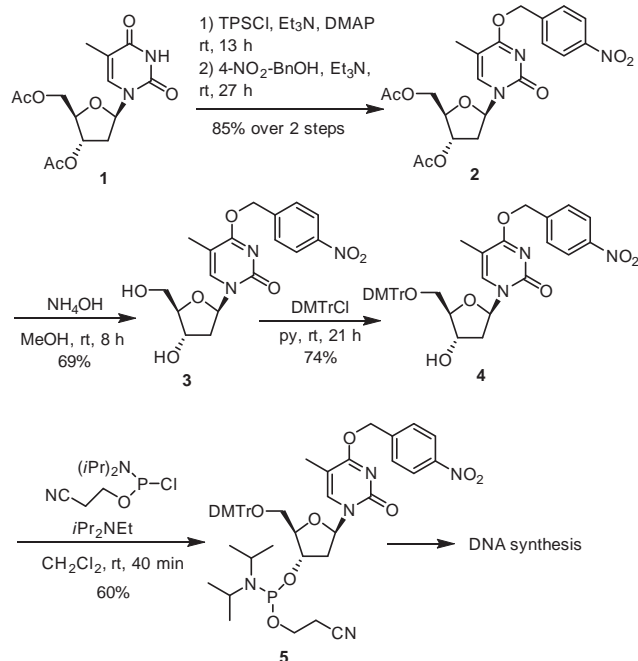


Figure 1. (a) Under non-hypoxic conditions, the pro-oligo does not hybridize to the target RNA. Under hypoxic conditions, the nitrobenzyl groups of the pro-oligo are deprotected and the free oligonucleotide forms a stable complex with the target RNA. (b) Proposed reaction process for the deprotection of 4-nitrobenzyl groups under hypoxic conditions.



Scheme 1. Synthetic route for the phosphoramidite derivative 5.

containing 4-*O*-benzylated thymine residue(s) were synthesized, deprotected, and purified using standard protocols. The purity of synthesized oligonucleotides was determined by HPLC and the structures were confirmed by MALDI-TOF mass spectroscopy (Supporting information).

As a model experiment for the deprotection of 4- NO_2 -benzyl groups in oligodeoxyribonucleotides (ODNs) in hypoxic cells, ODN **1** (5'-TTXIT-3') was treated with nitroreductase (from *Escherichia coli*) in the presence of NADH. Enzymatic reactions were monitored by HPLC. Typical HPLC profiles are shown in Figure 2. Before enzyme addition, a peak corresponding to ODN **1** was observed along with peaks corresponding to the NADH (Fig. 2b, top). After 1 min incubation with the enzyme, the peak corresponding to ODN **1** was diminished and a peak corresponding to a fully deprotected oligonucleotide (retention time 17.2 min) and contamination peak from enzyme sample (19.6 min) were observed (Fig. 2b, middle). The peak (17.2 min) was collected and the structure of the deprotected oligonucleotide was confirmed by MALDI-TOF mass spectroscopy. The other peak (19.6 min) was determined by control injection experiments described in Figure S1. ODN **1** was stable in buffer, with and without NADH or nitroreductase, for at least 1 h. Related HPLC profiles of control experiments are described in the Supplementary data (Fig. S1).

Next, a time course of the deprotection of multiple 4-nitrobenzyl groups in the mixed sequence ODN **5** (5'-CACXGCAXXGGXCAC-3') was similarly analyzed (Fig. S2a). Before enzyme addition, a peak corresponding to ODN **5** was observed along with peak

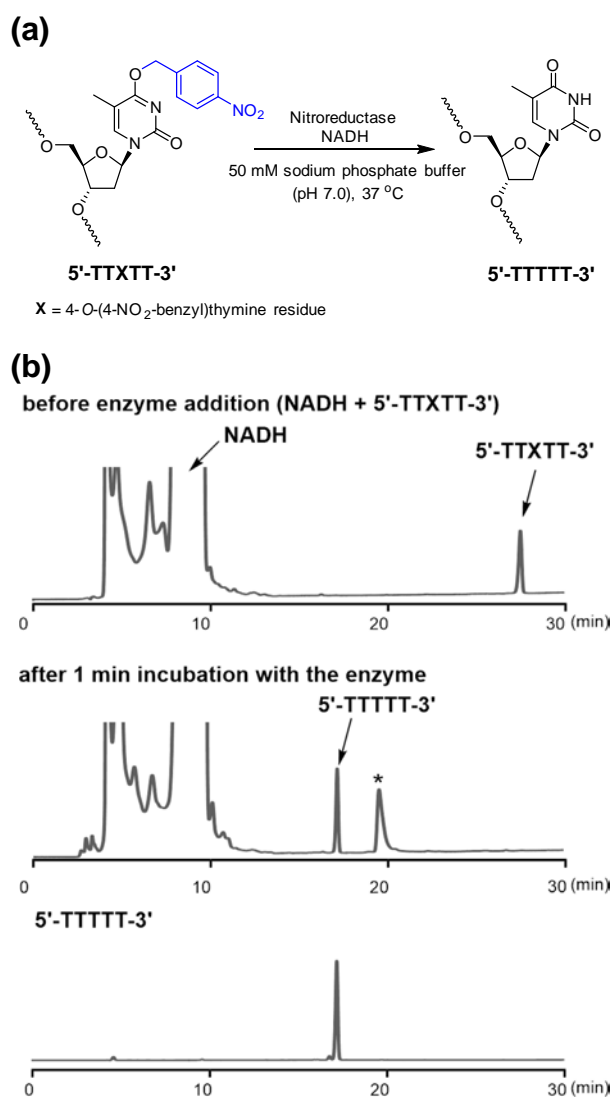


Figure 2. HPLC analysis of the bioreductive deprotection of a 4-NO₂-benzyl group on the thymine base in ODN 1. (a) A schematic representation of enzymatic deprotection of 4-nitrobenzyl group on thymine base in ODN 1. (b) ODN 1 (12 μM) was incubated with nitroreductase (160 μg/mL) and 10 mM NADH in 50 mM sodium phosphate buffer (pH 7.0) at 37 °C. Top, HPLC profile of the solution before addition of the enzyme; middle, HPLC profile after 1 min incubation with the enzyme; bottom, a control oligonucleotide. *Contamination from enzyme sample.

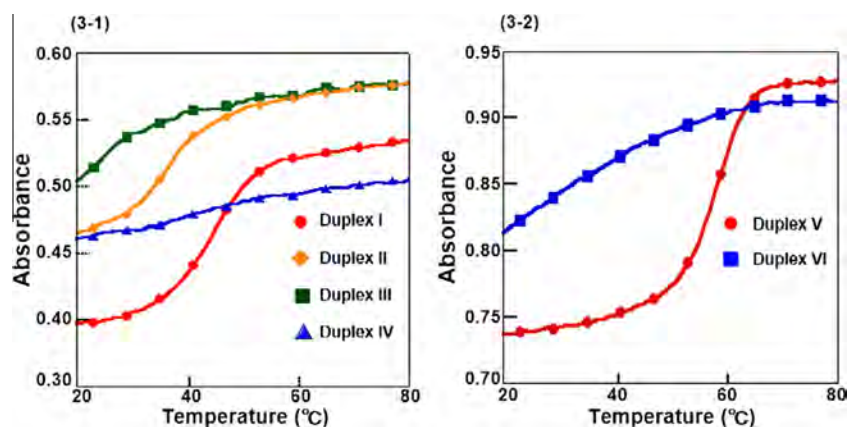


Figure 3. Thermal denaturation profiles of duplexes (I–VI). Conditions: 2 μM each of duplexes I–IV in 10 mM MOPS (pH 7.0), 1 M NaCl; 2 μM each of duplexes V and VI in 10 mM MOPS (pH 7.0), 100 mM NaCl.

corresponding to the NADH. After 5 min incubation with nitroreductase, the ODN 5 peak decreased and several new peaks derived from partially deprotected ODNs (retention time 26.5 min, 24.1 min, 23.4 min, 20.6 min), contamination peak from enzyme sample (19.8 min) and fully deprotected ODN (16.3 min) were observed. After 10 min, the ODN 5 peak was completely diminished and only partially deprotected ODNs and fully deprotected ODN were observed. As time proceeded, partially deprotected products were further deprotected and converted to the fully deprotected ODN (Fig. S2b). This peak was collected and the structure of the deprotected oligonucleotide was confirmed by MALDI-TOF mass spectroscopy.

Hybridization properties of the base-protected ODNs with complementary sequences were investigated by thermal denaturation experiments. Sequences of the duplexes and their melting temperatures (T_m s) are compiled in Table 1. Thermally induced denaturation profiles are shown in Figure 3. A single substitution in the central region decreased the thermal stability of duplex formation (duplex II). Three consecutive substitutions in the central region largely destabilized the thermal stability (duplex III). By distributing the protected thymine residues over the length of the sequence, the duplexes were largely destabilized, thus clear denaturation curves were not observed (duplex IV and VI).

These results demonstrate that oligonucleotides containing 4-O-(4-NO₂-benzyl)thymine residues have potential for use as prodrug-type oligonucleotides under bioreductive conditions. Because 4-O-(4-NO₂-benzyl)thymine residues are stable throughout the processes of oligonucleotide synthesis and deprotection, these residues can be incorporated into oligonucleotides for various applications. Oligonucleotide prodrugs containing 4-NO₂-benzyl groups are expected to be inactive in normal cells because the protected oligonucleotides are unable to hybridize with the target sequences. However, in hypoxic cells such as those present in locally advanced solid tumors, 4-NO₂-benzyl groups become deprotected and the resulting free oligonucleotides form stable complexes with target RNAs.

In summary, the 4-O-(4-NO₂-benzyl)thymine were developed as a novel bioreduction-responsive nucleobase for incorporation in oligonucleotides. This modified thymine base converted to a native thymine base under bioreductive conditions. The methods outlined in this report could be used for the development of oligonucleotide therapeutics with activity towards hypoxic cells.

Table 1
Sequences of the duplexes and their respective melting temperatures. (X = 4-O-(4-NO₂-benzyl)thymine)

Duplex	Sequence	T _m (°C)	ΔT _m (°C)
I	5'-TTTTTTTTTTTTT-3' 3'-AAAAAAAAAAAAA-5'	43.6	–
II	5'-TTTTTXXTTTTT-3' 3'-AAAAAAAAAAAAA-5'	35.2	–8.4
III	5'-TTTTTXXXXTTTT-3' 3'-AAAAAAAAAAAAA-5'	26.0	–17.6
IV	5'-TTTXXTTTXXTTT-3' 3'-AAAAAAAAAAAAA-5'	n.d.	–
V*	5'-CAGTGCATTGGTCAC-3' 3'-GTCACGTAACCCAGTG-5'	57.9	–
VI*	5'-CAGXGCAXXGGXCAC-3' 3'-GTCACGTAACCCAGTG-3'	n.d.	–

* 2 μM each of duplexes V and VI in 10 mM MOPS (pH 7.0), 100 mM NaCl.

Acknowledgments

This work was supported by the Strategic Research Base Development Program for Private Universities (Kanagawa University, 2012–2016), from the Ministry of Education, Culture, Sports, Science, and Technology, Japan (A.O.), and the Takahashi Industrial and Economic Research Foundation (H.S.).

Supplementary data

Supplementary data associated with this article can be found, in the online version, at <http://dx.doi.org/10.1016/j.bmcl.2015.10.025>.

References and notes

1. *Current Protocols in Nucleic Acid Chemistry*; Beaucage, S. L., Bergstrom, D. E., Glick, G. D., Jones, R. A., Eds.; John Wiley & Sons Inc: New York, 2000. and references cited therein.
2. (a) Lindström, U. M.; Kool, E. T. *Nucleic Acids Res.* **2002**, *30*, e101; (b) Ohkubo, A.; Kasuya, R.; Sakamoto, K.; Miyata, K.; Nagasawa, H.; Tshukahara, T.; Maki, Y.; Watanabe, T.; Seio, K.; Sekine, M. *Nucleic Acids Res.* **2008**, *36*, 1952; (c) Liu, Q.; Deiters, A. *Acc. Chem. Res.* **2014**, *47*, 45.
3. Kröck, L.; Heckel, A. *Angew. Chem. Int. Ed.* **2005**, *44*, 471.
4. (a) Höckel, M.; Vaupel, P. *J. Natl. Cancer Inst.* **2001**, *93*, 266; (b) Bertout, J. A.; Patel, S. A.; Simon, M. C. *Nat. Rev. Cancer* **2008**, *8*, 967.
5. Wilson, W. R.; Hay, M. P. *Nat. Rev. Cancer* **2011**, *11*, 393.
6. Lin, T. S.; Wang, L.; Antonini, I.; Cosby, L. A.; Shiba, D. A.; Kirkpatrick, D. L.; Sartorelli, A. C. *J. Med. Chem.* **1986**, *29*, 84.
7. Cazares-Körner, C.; Pires, I. M.; Swallow, I. D.; Grayer, S. C.; O'Connor, L. J.; Olcina, M. M.; Christlieb, M.; Conway, S. J.; Hammond, E. M. *ACS Chem. Biol.* **2013**, *8*, 1451.
8. Cui, L.; Zhong, Y.; Zhu, W.; Xu, Y.; Du, Q.; Wang, X.; Qian, X.; Xiao, Y. *Org. Lett.* **2011**, *13*, 928.
9. Zhu, R.; Liu, M.-C.; Luo, M.-Z.; Penketh, P. G.; Baumann, R. P.; Shyam, K.; Sartorelli, A. C. *J. Med. Chem.* **2011**, *54*, 7720.
10. Hu, L.; Yu, C.; Jiang, Y.; Han, J.; Li, Z.; Browne, P.; Race, P. R.; Knox, R. J.; Searle, P. F.; Hyde, E. I. *J. Med. Chem.* **2003**, *46*, 4818.
11. Zhang, Z.; Tanabe, K.; Hatta, H.; Nishimoto, S.-i. *Org. Biomol. Chem.* **2005**, *3*, 1905.
12. Granchi, C.; Funaioli, T.; Erler, J. T.; Giaccia, A. J.; Macchia, M.; Minutolo, F. *ChemMedChem* **2009**, *4*, 1590.
13. Guo, T.; Cui, L.; Shen, J.; Zhu, W.; Xu, Y.; Qian, X. *Chem. Commun.* **2013**, 10820.
14. Hay, P.; Sykes, B. M.; Denny, W. A.; O'Connor, C. J. *J. Chem. Soc., Perkin Trans. 1* **1999**, 2759.
15. Nakata, E.; Yukimachi, Y.; Kariyazono, H.; Im, S.; Abe, C.; Uto, Y.; Maezawa, H.; Hashimoto, T.; Okamoto, Y.; Hori, H. *Bioorg. Med. Chem.* **2009**, *17*, 6952.
16. Morihito, K.; Kodama, T.; Obika, S. *Chem. Eur. J.* **2011**, *17*, 7918.
17. Yamazoe, S.; McQuade, L. E.; Chen, J. K. *ACS Chem. Biol.* **2014**, *9*, 1985.
18. Wong, R. H. F.; Kwong, T.; Yau, K.-H.; Au-Yeung, H. Y. *Chem. Commun.* **2015**, 4440.
19. Abdi1, K.; Ali Khalaj1, A.; Ostad, S. N.; Khoshayand, M. R. *DARU* **2012**, *20*, 3.
20. Khalaj, A.; Abdi1, K.; Ostad, S. N.; Khoshayand, M. R.; Lamei, N.; Nedaie, H. A. *Chem. Biol. Drug Des.* **2014**, *83*, 183.

ChemComm

Chemical Communications
www.rsc.org/chemcomm



ISSN 1359-7345



FEATURE ARTICLE

Yoshiyuki Tanaka, Akira Ono *et al.*

Structures, physicochemical properties, and applications of
T-Hg^{II}-T, C-Ag^I-C, and other metallo-base-pairs


 Cite this: *Chem. Commun.*, 2015, 51, 17343

Structures, physicochemical properties, and applications of T–Hg^{II}–T, C–Ag^I–C, and other metallo-base-pairs†

 Yoshiyuki Tanaka,^{*ab} Jiro Kondo,^c Vladimír Sychrovský,^d Jakub Šebera,^{de} Takenori Dairaku,^b Hisao Saneyoshi,^f Hidehito Urata,^g Hidetaka Torigoe^h and Akira Ono^{*f}

 Received 1st April 2015,
Accepted 1st October 2015

DOI: 10.1039/c5cc02693h

www.rsc.org/chemcomm

Recently, metal-mediated base-pairs (metallo-base-pairs) have been studied extensively with the aim of exploring novel base-pairs; their structures, physicochemical properties, and applications have been studied. This trend has become more evident after the discovery of Hg^{II}-mediated thymine–thymine (T–Hg^{II}–T) and Ag^I-mediated cytosine–cytosine (C–Ag^I–C) base-pairs. In this article, we focus on the basic science and applications of these metallo-base-pairs, which are composed of natural bases.

Introduction

Studies on metal-mediated base-pairs (metallo-base-pairs) were initiated in the light of materials science and genetic code expansion.^{1,2} K. Tanaka and Shionoya proposed the possibility that Watson–Crick (W–C) base-pairs may be substituted for planar metal chelators.¹ Meggers, Romesberg, and Schultz actually introduced such a metal chelator into DNA duplexes, and they proposed that such a metallo-base-pair would lead to the expansion of the genetic code.² K. Tanaka and Shionoya also introduced their metal chelator into a DNA duplex to generate a molecular magnet,³ and showed that the aligned paramagnetic Cu²⁺ ions in the DNA duplex were ferromagnetically coupled.⁴ Since then, many metallo-base-pairs have been created

through the use of artificial metal chelators, and DNA duplexes including such metallo-base-pairs (metallo-DNAs) have been reported (for their structures and the corresponding references, see Fig. S1 in the ESI†).

As an alternative approach to the creation of novel metallo-base-pairs, it is interesting to examine if natural nucleobases can form metallo-base-pairs. In fact, thymine can specifically bind to Hg²⁺ to form a Hg^{II}-mediated T–T base-pair (T–Hg^{II}–T, Fig. 1).^{5,6} In addition, this Hg²⁺-specific recognition by thymine

^a Faculty of Pharmaceutical Sciences, Tokushima Bunri University, 180 Nishihama-Boji, Yamashirocho, Tokushima, Tokushima 980-8578, Japan. E-mail: tanakay@ph.bunri-u.ac.jp

^b Graduate School of Pharmaceutical Sciences, Tohoku University, 6-3 Aza-Aoba, Aramaki, Aoba-ku, Sendai, Miyagi 980-8578, Japan

^c Department of Materials and Life Sciences, Faculty of Science and Technology, Sophia University, 7-1 Kioi-cho, Chiyoda-ku, Tokyo 102-8554, Japan

^d Institute of Organic Chemistry and Biochemistry, Academy of Sciences of the Czech Republic, v.v.i, Flemingovo náměstí 2, 16610, Praha 6, Czech Republic

^e Institute of Physics, Academy of Sciences of the Czech Republic, v.v.i, Na Slovance 2, CZ-182 21 Prague 8, Czech Republic

^f Department of Material & Life Chemistry, Kanagawa University, 3-27-1 Rokkakubashi, Kanagawa-ku, Yokohama, Kanagawa 221-8686, Japan. E-mail: akiraono@kanagawa-u.ac.jp

^g Osaka University of Pharmaceutical Sciences, 4-20-1 Nasahara, Takatsuki, Osaka 569-1094, Japan

^h Department of Applied Chemistry, Faculty of Science, Tokyo University of Science, 1-3 Kagurazaka, Shinjuku-ku, Tokyo 162-8601, Japan

† Electronic supplementary information (ESI) available: Chemical structures of metallo-base-pairs and their references. See DOI: 10.1039/c5cc02693h

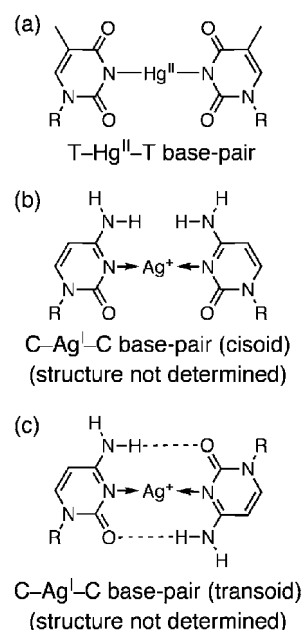


Fig. 1 T–Hg^{II}–T and C–Ag^I–C base-pairs. R denotes ribose.

has been applied to a Hg^{2+} sensor.⁵ Later, it was found that cytosine also binds to Ag^+ to form an Ag^+ -mediated C-C base-pair (C- Ag^+ -C, Fig. 1), and an Ag^+ sensor was developed based on this phenomenon.⁷ Since such natural-nucleobase-based Hg^{2+} and Ag^+ sensors can be prepared from commercially available sources, and because Hg^{2+} is an environmental pollutant, scientists from different fields have joined the research on the metallo-base-pairs to apply them as metal sensors, single-nucleotide-polymorphism (SNP) detectors, heavy-metal trappers, nanomachines, etc.⁸⁻¹⁵

Although many applications of the metallo-base-pairs have been reported (see the review articles⁸⁻¹⁵ and the references cited therein), the basic science of these metallo-base-pairs is also as versatile as their applications, because the resulting structural, thermodynamic, and other fundamental physico-chemical data and parameters are universally applicable to the design and fabrication of molecular devices. In this sense, we would like to review studies on metallo-base-pairs, those composed of natural bases and related unnatural bases whose physicochemical studies were performed. Our review is divided



Yoshiyuki Tanaka

Yoshiyuki Tanaka received his BSc degree in 1991, MSc degree in 1993, and PhD in 1998 from Osaka University. Afterward, he joined AIST-Tsukuba as a post-doctoral fellow. From 2001, he had been working with the Graduate School of Pharmaceutical Sciences, Tohoku University as Research Instructor (2001 and 2002), Assistant Professor (2002–2007) and Associate Professor (2007–2015). Now he became a full Professor of the Laboratory of

Analytical Chemistry at the Faculty of Pharmaceutical Sciences, Tokushima Bunri University. During his scientific carrier, he has received several awards like the “Young Investigator Award” of the “Human Frontier Science Program (HFSPO, Strasbourg)”, 2008. His current research interests are nucleic acids–metal interactions and mechanistic studies on functional RNA/DNA molecules.



Jiro Kondo

Jiro Kondo is an Associate Professor at Sophia University. He obtained his PhD in 2004 from Tokyo Institute of Technology under the supervision of Professor Akio Takénaka. He joined the group of Professor Eric Westhof in Université de Strasbourg as a postdoctoral researcher (2004–2010). In 2010, he moved to Sophia University as an Assistant Professor and is promoted to the current position in 2015. He has received several awards including The IUCr Prize

(2003), The CrSJ Young Scientist Award (2008) and The Young Scientist's Prize of The Commendation for Science and Technology by the Minister of MEXT, Japan (2015). His research interests include nucleic acid crystallography for structure-based drug and material design.



Vladimír Sychrovský

Vladimír Sychrovský received his PhD degree in 1998 from Charles University in Prague, Czech Republic (with Prof. Petr Čárský at J. Heyrovský Institut of Physical Chemistry AS CR). Then he worked in the University of Gothenburg, Sweden with Prof. Dieter Cremer (Postdoctoral) from 1998 to 2000. He became an associated scientist at Heyrovský Institut of Physical Chemistry AS CR during 2000–2004 and has been a senior scien-

tist at Institute of Organic Chemistry and Biochemistry AS CR since 2004. He received Young Investigator Award by the Human Frontier Science Program in 2008 and an award by Daiichi-Sankyo Foundation Of Life-Science in 2011. He became a JSPS fellow since 2012. His research interest is focused on theoretical modeling of general properties of nucleic acids including spectroscopic and charge transport properties and chemical reaction pathways.



Jakub Šebera

Jakub Šebera received his MSc degree from Charles University in Prague in 2003 and PhD degree from Czech Technical University in Prague in 2008 (with Dr Stanislav Zálíš at J. Heyrovský Institut of Physical Chemistry AS CR). Since 2010 he has been working as a post-doctoral fellow in Institute of Physics of the AS CR and the Institute of Organic Chemistry and Biochemistry of the AS CR. In 2014, he became an associated

scientist at Institute of Organic Chemistry and Biochemistry AS CR. His research interests include theoretical modeling of chemically modified nucleic acids, enzymatic DNA repair, and material properties in relation to nanotechnologies.

into the following sections: spectroscopy (Section 1.1), crystallography (Section 1.2), thermodynamics (Section 1.3), theoretical studies (Section 1.4), applications as metal sensors (Section 2.1), Hg^{2+} trapping (Section 2.2), SNP detection (Section 2.3), nanomachines (Section 2.4), conductivity (Section 2.5), and response to enzymes (Section 2.6).

1 Structural and physicochemical studies

1.1 Metallo-base-pairs in solution: spectroscopic studies

One of the advantages of metallo-base-pairs is that programmed metal-ion arrays can be prepared in DNA duplexes in solution.



Takenori Dairaku

Takenori Dairaku received his BSc degree from Oho University in 2009, MSc degree from Tohoku University in 2011, and PhD from Tohoku University in 2015. Afterward, he became a post-doctoral fellow of the Laboratory of Molecular Transformation, Graduate School of Pharmaceutical Sciences, Tohoku University (Professor Yoshinori Kondo's laboratory). Since 2014, he has been a Research Fellow of Japan Society for the Promotion of Science (JSPS Research Fellow).

His current research interests are nucleic acids–metal interactions and development of DNA-based molecular-devices.



Hisao Saneyoshi

Hisao Saneyoshi received his BSc degree from Aoyama Gakuin University in 2001, MSc degree from Tokyo Institute of Technology in 2003, and PhD from Tokyo Institute of Technology in 2006. Afterward, he became a visiting fellow of the Laboratory of Medicinal Chemistry, NCI, NIH (2006–2009). In 2009, he joined Nano Medical Engineering Laboratory, RIKEN as a postdoctoral researcher. In 2013, he moved to the Department of

Material & Life Chemistry, Faculty of Engineering, Kanagawa University as an Assistant Professor. His current research interests are synthesis of chemical probes and bioactive oligonucleotides.



Hidehito Urata

Hidehito Urata is a Professor at Osaka University of Pharmaceutical Sciences. He received his MS (1985) from Osaka University. In 1987, he obtained a position as Assistant Professor at Osaka University of Pharmaceutical Sciences. He received his PhD from Osaka University of Pharmaceutical Sciences in 1995. He was appointed as Lecturer in 2002 and then as Associate Professor in 2004 at the University. He is the recipient of

the Pharmaceutical Society of Japan Award for Young Scientists (1999). In 2006, he was promoted to his current position. His research interests are in the development of functional artificial nucleic acids and recognition of metallo-DNA by DNA polymerases.



Hidetaka Torigoe

Hidetaka Torigoe was born in 1962 in Okayama-ken, Japan and grew up in Kanagawa-ken, Japan. He received his BSc degree in 1985, MSc degree in 1987, and PhD in 1990 from the Faculty of Science, the University of Tokyo under the supervision of Professor Yoji Arata. He joined Jichi Medical School as an assistant professor. In 1991, he moved to the Institute of Physical and Chemical Research (RIKEN) as a research scientist and was

promoted as a senior research scientist in 1999. In 2002, he moved to the Faculty of Science, Tokyo University of Science as a junior associate professor and was promoted as an associate professor in 2005 and a full professor in 2012. His current research interests are triplex and quadruplex nucleic acids, nucleic acids–metal interactions, and nucleic acids–protein interactions.

Thus, properties and structures of metallo-base-pairs in solution are of prime interest. Based on these concepts, chemical structures of metallo-base-pairs as well as 3D structures of two DNA duplexes containing metallo-base-pairs were determined by NMR spectroscopy in solution.^{16–22} One is a Ag^{I} -mediated imidazole–imidazole base-pair ($\text{Im-Ag}^{\text{I}}\text{-Im}$), which employs an artificial nucleobase (imidazole),^{19,21} and the other is a Hg^{II} -mediated T–T base-pair ($\text{T-Hg}^{\text{II}}\text{-T}$), which employs a natural nucleobase (thymine).^{16,17,20,22} In both cases, the chemical structures of these metallo-base-pairs were solidly determined on the basis of N–N and N–Ag *J*-coupling (Fig. 2; details are discussed later).^{16,19} Furthermore, 3D structures of DNA duplexes containing these metallo-base-pairs were determined by NMR spectroscopy (Fig. 2).^{19,21,22} In the case of the T– Hg^{II} –T base-pair, its crystal structure in a DNA duplex

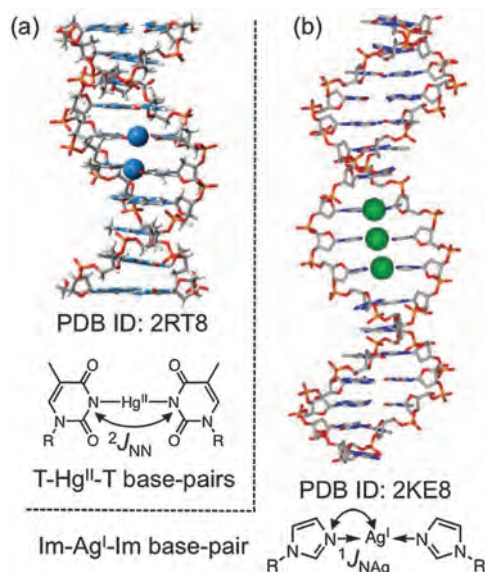


Fig. 2 Three-dimensional structures of metallo-DNA molecules. R denotes ribose.

was also determined (see next section for details).²³ Therefore, currently the T-Hg^{II}-T base-pair is the best benchmark for studying the relationship between the structure and spectroscopic data in solution.

In addition to the abovementioned structural studies, there are many spectroscopic studies of metallo-base-pairs. Especially, the T-Hg^{II}-T base-pair possesses the longest history of all metallo-base-pairs, and it has been extensively studied by Raman,^{20,24,25} IR,²⁵ UV,^{6,26,27} circular dichroism (CD)^{6,26,28,29} and NMR^{6,16,17,27,30,31} spectroscopic techniques from its proposal based on the studies at its early stage (~50 years ago).³² In addition, Hg²⁺-titration studies of poly[d(AT)] using ¹H NMR spectroscopy might be related to T-Hg^{II}-T base-pairing.³³ The U-Hg^{II}-U base-pair (Fig. 3a), the



Akira Ono

Akira Ono was born in 1957 in Saijo-shi, Ehime-ken, Japan. He received his BSc degree in 1981, MSc degree in 1983, and PhD in 1986 from the Faculty of Pharmaceutical Sciences, Hokkaido University under the supervision of Professor Tohru Ueda. Afterward, he joined the Faculty of Pharmaceutical Sciences, Hokkaido University as an assistant professor in Professor T. Ueda's group. In 1993, he moved to the Graduate School of Sciences, Tokyo Metropolitan University as an Associate Professor. In 2005, he moved to the Department of Material & Life Chemistry, Faculty of Engineering, Kanagawa University as a Professor. His current research interests are synthesis of bioactive nucleic acids, nucleic acids-metal interactions, and development of nucleic acids based functional materials.

Akira Ono was born in 1957 in Saijo-shi, Ehime-ken, Japan. He received his BSc degree in 1981, MSc degree in 1983, and PhD in 1986 from the Faculty of Pharmaceutical Sciences, Hokkaido University under the supervision of Professor Tohru Ueda. Afterward, he joined the Faculty of Pharmaceutical Sciences, Hokkaido University as an assistant professor in Professor T. Ueda's group. In 1993, he moved to the Graduate School of Sciences,

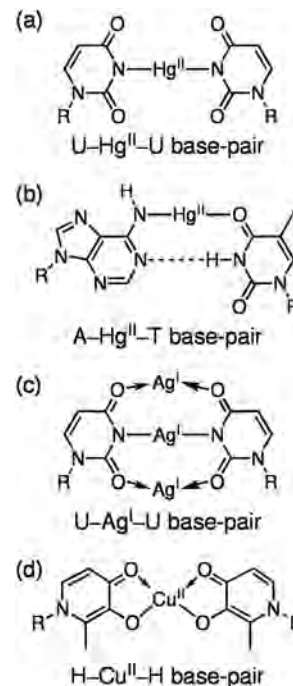


Fig. 3 Structures of metallo-base-pairs studied spectroscopically. R denotes ribose.

RNA analogue of the T-Hg^{II}-T base-pair, was also studied by ¹H NMR spectroscopy.³⁴

Other metallo-base-pairs (A-Hg^{II}-T and C-Ag^I-C) in DNA duplexes were studied by NMR spectroscopy. Extensive ¹⁵N chemical-shift analyses revealed the chemical structure of the A-Hg^{II}-T base-pair (Fig. 3b) in a DNA duplex (the ¹⁵N chemical shifts are discussed later).³⁵⁻³⁸ For the C-Ag^I-C base-pair, a Ag^I-titration study of a single-C-C-mismatch-embedded DNA duplex was performed with ¹H NMR spectroscopy.⁷ Stacking of the C-Ag^I-C base-pair within a DNA duplex was strongly suggested by a slow-exchange phenomenon observed in the ¹H NMR spectra, in which NMR signals from Ag^I-bound and Ag^I-free states were observed independently.⁷ However, the exact base-pairing mode of C-Ag^I-C has not yet been determined. The U-Ag^I-U base-pair (2:3 complex of 1-methyluracil and Ag^I) was also studied by IR and Raman spectroscopy, by using its crystalline sample (Fig. 3c).³⁹ See ref. 18 and references cited therein for other simple Hg^{II}-DNA/nucleoside/nucleotide complexes.

In addition, the possible metallo-base-pairs in a kind of metallated DNA molecule, the so-called M-DNA⁴⁰⁻⁴² were studied. In M-DNA, the penetration of Zn²⁺ into W-C base-pairs to afford metal-mediated base-pairs was suggested by fluorescence and ¹H NMR spectroscopy.⁴⁰⁻⁴² However, the base-pairing pattern has not yet been determined, and several possible models are presented.^{40,43,44}

Based on the similarity between the transoid C-Ag^I-C base-pair⁴⁵⁻⁴⁸ (Fig. 1c) and the hemiprotonated transoid C-C base-pair in an i-motif, an i-motif-type structure composed of transoid C-Ag^I-C base-pairs was proposed on the basis of CD and fluorescence spectroscopy.⁴⁶

In the case of a hydroxypyridone-Cu^{II}-hydroxypyridone base-pair (H-Cu^{II}-H) (Fig. 3d), an average Cu^{II}-Cu^{II} distance

Table 1 ^{13}C chemical shift perturbations upon binding to Hg^{2+} in the T– Hg^{II} –T base-pair^a

Sample (M)/solvent	Metal	Site	C2	C4	C5	5-CH ₃	C6	Ref.
Thymidine (isolated T– Hg^{II} –T)/DMSO	Hg^{2+} (0.5 eq.)	N3	+2.7	+2.4	–0.2	+0.5	0.0	30 and 31
d(TT) (9.1 mM)/H ₂ O (pH 6.0)	Hg^{2+} (10.0 mM)	N3	+2.9 ^b	+2.7 ^b	N.D.	N.D.	N.D.	20
d(GCGCTTTGCGC) ^c (2 mM)/H ₂ O (pH 6.0)	Hg^{2+} (2.0 mM)	N3	N.D.	N.D.	+0.1	+0.9	+0.4	32
d(GCGCTTTGCGC) ^c (2 mM)/H ₂ O (pH 6.0)	Hg^{2+} (2.0 mM)	N3	N.D.	N.D.	+0.9	+1.1	+0.3	32

^a Chemical shift changes are listed in ppm. ^b Average value of two thymine residues is presented. ^c For a DNA oligomer, the chemical shift changes of the underlined residues are indicated. Positive and negative values represent downfield and upfield shifts, respectively. N.D. = not detected.

Table 2 ^{15}N chemical shift perturbations upon binding to metal ions and J -coupling with ^{15}N nuclei^a

Sample (M)/solvent	Metal	Site	N1	N3	NH ₂	N7	N9	$^2J_{\text{NN}}^b$	$^1J_{\text{N-M}}^c$	Ref.
T– Hg^{II} –T										
d(CGCGTTGTCC)-d(GGACTTCGCG) ^b (2.0 mM)/H ₂ O (pH 6)	Hg^{2+} (4.0 mM)	N3	–	+35.3	N.A.	N.A.	N.A.	2.4	N.D.	16
d(CGCGTTGTCC)-d(GGACTTCGCG) ^b (2.0 mM)/H ₂ O (pH 6)	Hg^{2+} (4.0 mM)	N3	–	+29.9	N.A.	N.A.	N.A.		N.D.	16
d(CGCGTTGTCC)-d(GGACTTCGCG) ^b (2.0 mM)/H ₂ O (pH 6)	Hg^{2+} (4.0 mM)	N3	–	+30.3	N.A.	N.A.	N.A.	2.4	N.D.	16
d(CGCGTTGTCC)-d(GGACTTCGCG) ^b (2.0 mM)/H ₂ O (pH 6)	Hg^{2+} (4.0 mM)	N3	–	+30.8	N.A.	N.A.	N.A.		N.D.	16
Im– Ag^{I} –Im										
d(TTAATTT Im Im Im AAATTA) ₂ (0.5–1.4 mM)/ H ₂ O (pH 7.2)	Ag^+ (1.0 eq.)	N3	–3.2	–15.0	N.A.	N.A.	N.A.	N.D.	86	19
d(TTAATTT Im Im Im AAATTA) ₂ (0.5–1.4 mM)/ H ₂ O (pH 7.2)	Ag^+ (1.0 eq.)	N3	–3.3	–14.5	N.A.	N.A.	N.A.	N.D.	86	19
d(TTAATTT Im Im Im AAATTA) ₂ (0.5–1.4 mM)/ H ₂ O (pH 7.2)	Ag^+ (1.0 eq.)	N3	–5.1	–15.9	N.A.	N.A.	N.A.	N.D.	86	19
A– Hg^{II} –T										
d(CGCGAATTCGCG) ₂ ^b (4.8 mM)/H ₂ O (pH 7)	Hg^{II} (28 mM)	N6	+15.3	–3.3	–	–0.5	–3.0	n.a.	N.D.	35
d(CGCGAATTCGCG) ₂ ^b (4.8 mM)/H ₂ O (pH 7)	Hg^{II} (28 mM)	N6	+9.4	+2.4	–	–0.7	–1.0	n.a.	N.D.	35

^a Chemical shift changes and J -coupling constants are reported in ppm and Hz, respectively. For DNA oligomers, the chemical shift changes of the underlined residues are indicated. Positive and negative values represent downfield and upfield shifts, respectively. ^b Two-bond ^{15}N – ^{15}N J -coupling across Hg. ^c One-bond ^{15}N –metal J -coupling, such as $^1J(^{15}\text{N}, ^{107/109}\text{Ag})$ derived from Ag^+ sources in natural abundance ($^{107}\text{Ag}/^{109}\text{Ag} = 51.8:48.2$). N.A. = not applicable; – = not recorded; N.D. = not detected.

of ~ 3.7 Å was determined by EPR spectroscopy for a DNA duplex containing five H– Cu^{II} –H base-pairs.⁴ The Cu^{2+} ions in the H– Cu^{II} –H base-pairs were ferromagnetically coupled⁴ and structural reasons for the ferromagnetic coupling were theoretically studied.⁴⁹

As an overview of this section, characteristic NMR and vibrational spectroscopic features of the metallo-base-pairs are summarised in Tables 1–3. The ^{13}C NMR spectrum of the T– Hg^{II} –T base-pair revealed that the carbonyl-carbon resonances for C4 and C2 shifted downfield by ~ 2.5 ppm upon Hg^{II} -complexation in dimethyl sulfoxide (DMSO) and H₂O (Table 1).^{20,30} More drastic changes in chemical shifts were observed for the ^{15}N resonances of the metal-binding nitrogen atoms, namely, *ca.* +30 ppm (downfield shift) for N3 of the T– Hg^{II} –T base-pair (N3(T))^{16,17} and *ca.* –15 ppm (upfield shift) for N3 of the Im– Ag^{I} –Im base-pair (N3(Im))¹⁹ (Table 2). For the A– Hg^{II} –T base-pair, the Hg^{II} -ligated site was deduced to be N6 (amino nitrogen) and not N1. This deduction is based on careful consideration of the changes in chemical shifts of the N1 atom of the adenosine residue (N1(A)) upon Hg^{2+} -binding, despite the fact that a large change in the chemical shift of N1(A) occurs (+9.4 to +15.3 ppm) (Table 2).^{35–38} As a general rule,¹⁷ the formation of an N–metal coordination bond causes an upfield shift of the ^{15}N resonance (as observed for the Im– Ag^{I} –Im base-pair and similar systems),^{50–54} whereas proton–metal exchange on a nitrogen atom causes a downfield shift (as observed for the T– Hg^{II} –T base-pair).^{16–18} Applying these general trends to the A– Hg^{II} –T base-pair, coordination of N1(A) to Hg^{II} was ruled out, because a downfield shift of N1(A) was observed.

Further details and the background regarding heteronuclear NMR chemical shifts are reviewed in ref. 17 and 18.

Two-bond ^{15}N – ^{15}N J -coupling across Hg^{II} , $^2J(^{15}\text{N}, ^{15}\text{N})$, was observed for the T– Hg^{II} –T base-pair of the DNA duplex with the paired thymine bases ^{15}N -labeled (Table 2).^{16,17} The observation of $^2J(^{15}\text{N}, ^{15}\text{N})$ firmly demonstrates the formation of a $^{15}\text{N}_3(\text{T})$ – Hg^{II} – $^{15}\text{N}_3(\text{T})$ linkage in the T– Hg^{II} –T base-pair. At the same time, the large downfield shift of N3(T) indicates the low covalency (highly ionic nature) of the N3(T)– Hg^{II} bond (high percentage of ionicity and low percentage of covalency).¹⁷ In addition, 1-bond ^{199}Hg – ^{15}N J -coupling, $^1J(^{199}\text{Hg}, ^{15}\text{N}) = 1050$ Hz,¹⁸ was recently reported for the thymidine– Hg^{II} –thymidine complex with its ^{199}Hg NMR chemical shift, $\delta(^{199}\text{Hg}) = -1784$ ppm.^{18,30c} For the Im– Ag^{I} –Im base-pair, 1-bond J -coupling between ^{15}N and $^{107}\text{Ag}/^{109}\text{Ag}$ at natural abundance ($^1J(^{15}\text{N}, ^{107/109}\text{Ag})$) was observed (Table 2).¹⁹ The observation of $^1J(^{15}\text{N}, ^{107/109}\text{Ag})$ confirms the formation of N3(Im)– Ag^{I} linkages in the Im– Ag^{I} –Im base-pair. In a chemical sense, such spectroscopic data, especially J -coupling and chemical shifts of heteronuclei in NMR spectroscopy, provide essential information for the characterisation of metal–nitrogen bonds.

Raman spectroscopy studies were performed on the T– Hg^{II} –T and U– Ag^{I} –U base-pairs.^{20,25,39} Several marker bands for both base-pairs are listed in Table 3. An extraordinarily low-wavenumber-shifted C4=O4 stretching band was observed at 1586/1585 cm^{-1} for the T– Hg^{II} –T base-pair.^{20,25} This extraordinary band was firmly assigned on the basis of an isotope shift of the Raman band by ^{18}O -labeling at the O4 atom. A similar shift to a low wavenumber

Table 3 Marker bands in Raman and IR spectra

Base-pair	Sample/conditions	Raman/cm ⁻¹	IR/cm ⁻¹	Assignment	Ref.
T-Hg ^{II} -T	d(TT)/H ₂ O(pH 6.5)	749	—	Marker band to probe the existence of the imino proton.	20
	d(TT)/D ₂ O(pH 6.5)	736	—		20
	d(TT)/H ₂ O(pH 12.4)	1585	—	C4=O4 stretching (major) [+C2=O2 stretching (minor)]	20
	Hg ₂ [d(TT)] ₂ /H ₂ O(pH 6.5)	1586	—	C4=O4 stretching (major) [+C2=O2 stretching (minor)]	20
	Hg ₂ [¹⁸ O4-d(TT)] ₂ /H ₂ O(pH 6.5)	1570	—	C4= ¹⁸ O4 stretching (major) [+C2=O2 stretching (minor)]	20
	Hg-(1-MeT) ₂ /crystal	1582	1583	C4=O4 stretching (major) [+C2=O2/C5=C6 stret. (minor)]	25
	Hg-(1-MeT) ₂ /crystal	537	537	In-plane ring deformation	25
	Hg-(1-MeT) ₂ /crystal	N.D.	352	In-plane N-Hg-N bending	25
U-Ag ^I -U	Ag ₃ -(1-MeU) ₂ /crystal	1549	1551	C4=O4 stretching (major) [+C2=O2 stretching (minor)]	39
	Ag ₃ -(1-MeU) ₂ /crystal	453	448	In-plane ring/N-Ag-N deformation	39
	Ag ₃ -(1-MeU) ₂ /crystal	362	362	In-plane ring/N-Ag-N deformation	39

d(TT) = thymidyl (3'-5') thymidine; 1-MeT = 1-methylthymine; 1-MeU = 1-methyluridine; N.D. = not detected; — = not recorded.

was observed for the C4=O4 stretching band of the U-Ag^I-U base-pair (Table 3).³⁹ We then identified that a Raman band at 749 cm⁻¹ is the marker band to probe the existence of the imino proton (H3) of thymine (Table 3).²⁰ Disappearance of this band indicates the deprotonation of H3 (imino proton) of thymine (Table 3).²⁰ The Raman/IR bands described above can be used as marker bands to detect T-Hg^{II}-T and U-Ag^I-U base-pairs.

The ionic nature (low covalency) of the N3(T)-Hg^{II} bond was deduced again for the T-Hg^{II}-T base-pair from the low-wavenumber-shifted C4=O4 stretching band at 1586/1585 cm⁻¹, by consideration of an enolate-like resonance contributor (Fig. 4).^{20,25} Both the NMR¹⁷ and vibrational spectroscopic²⁰ data thus corroborate the significant ionic character of the N3(T)-Hg^{II} bond and the cationic nature of Hg^{II}; this was also confirmed theoretically²⁰ (see Section 1.4 for theoretical studies). Usually, spectroscopic parameters acquired from macromolecules, such as DNA oligomers, are not so precisely determined because of low sensitivities/resolutions. However, owing to the site-specific ¹⁵N- and ¹⁸O-labelling of critical atoms and appropriate choices of measurement conditions, the spectroscopic data described above have been precisely determined to reveal the physicochemical properties and even the electronic structures of metallo-base-pairs.

Furthermore, the derived electronic structure suggested the application of the T-Hg^{II}-T base-pair in conductive nanowires. The cationic nature of Hg^{II} in the T-Hg^{II}-T base-pair suggests that the Hg^{II} array may function as an electron acceptor,^{17b} and the Hg^{II} array in a tract of T-Hg^{II}-T base-pairs could provide a route for excess electrons.

In summary, NMR spectroscopy and (partly) Raman spectroscopy provide accurate information about the chemical structures of metallo-base-pairs, since these techniques can provide information on their local geometries around metal centres from NMR signals of the metal cation-binding atoms (or from Raman bands that arise from vibrations around the metal cations). Based on these chemical structures, the 3D structures of metallo-DNAs containing metallo-base-pairs were precisely determined. In addition, the spectroscopic data include plenty of information about the electronic structures of metallo-base-pairs, which will provide guidelines for the fabrication of nanoelectronic devices.

1.2 Metallo-base-pairs in crystals: crystallographic studies

X-ray crystallography is one of the best methods for obtaining accurate 3D structures of metallo-base-pairs and metallo-DNAs that contain them. In 2001, Schultz and coworkers reported the first crystal structure of a nucleic acid duplex containing a metallo-base-pair.⁵⁵ In their previous work,² they found that a 15-nucleotide DNA duplex containing the artificial Cu^{II}-mediated base-pairs with pyridine-2,6-dicarboxylate (Dipic) and pyridine (Py) (Dipic-Cu^{II}-Py) in the middle displayed thermal stability comparable to that of a duplex containing an A-T base-pair instead. A DNA fragment with the sequence d(CGCG(Dipic)AT(Py)CGCG) was crystallised in the presence of 1 equivalent of Cu²⁺, and the crystal structure was determined at a resolution of 1.5 Å. The DNA fragment was crystallised as a Z-form left-handed duplex (Fig. 5a). In the helix, Dipic forms a

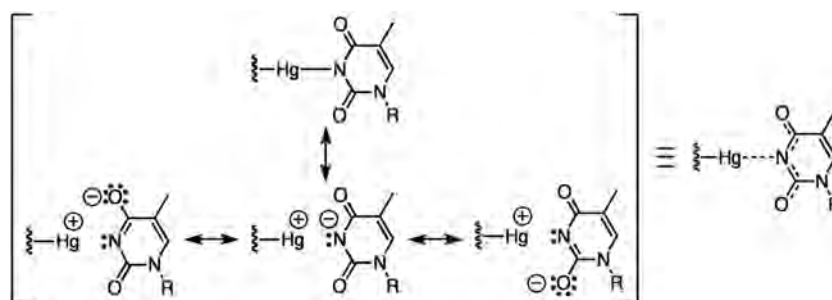


Fig. 4 Resonance contributors for the T-Hg^{II}-T base-pair. R denotes ribose.

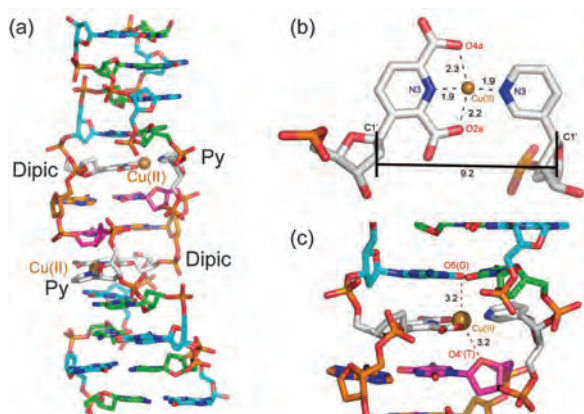


Fig. 5 (a) Overall structure of the Z-form DNA duplex containing Dipic–Cu^{II}–Py base-pairs (PDB ID = 1JES).⁵⁵ (b) Detailed geometry of the Dipic–Cu^{II}–Py base-pair. The C1'–C1' distance (Å) is indicated by a solid line, and distances (Å) between Cu^{II} and four atoms in its proximity are indicated by dashed lines, respectively. (c) Side view of the Dipic–Cu^{II}–Py base-pair. The distances (Å) between Cu^{II} in Dipic–Cu^{II}–Py base-pair and O6(G) and O4(T) atoms in neighbouring base-pairs are indicated by red dashed lines (distances in Å).

Cu^{II}-mediated base-pair with Py (Fig. 5b). In the base-pair, Dipic and Py had anti and syn conformations about the glycosyl bonds, respectively. The Cu²⁺ ion was located between the Dipic and Py bases and had a square-planar coordination geometry. The distances from Cu^{II} to N3(Dipic) and N3(Py) are both 1.9 Å and the N3(Dipic)–Cu^{II}–N3(Py) bond was linear. Cu^{II} was also ligated with O2a(Dipic) and O4a(Dipic), with distances of 2.2 and 2.2–2.3 Å, respectively. In addition to the square-planar coordination, Cu^{II} experienced electrostatic interactions from the axial direction of the square-planar geometry by the deoxyribose O4' atom of the neighbouring T7 residue. The distance from Cu to O4' is 3.0–3.2 Å (Fig. 5c). The axial interaction is possible only in the Z-form conformation. On the opposite side, Cu^{II} was in close proximity (3.1–3.2 Å) to the electron-rich O6(G) atom of the neighbouring residue (Fig. 5c), suggesting the existence of an electrostatic interaction between them. Although the C1'–C1' distance is 9.2–9.4 Å (Fig. 5b), which is 1.3–1.5 Å shorter than those observed in canonical W–C base-pairs (*ca.* 10.7 Å), the overall Z-form conformation was not distorted.

In 2011, another crystal structure of a DNA duplex containing an artificial metallo-base-pair, determined at a resolution of 2.2 Å, was reported by Carell and coworkers.⁵⁶ Two DNA fragments containing salicylic aldehyde (S) were cocrystallised with a DNA polymerase of *Thermococcus kodakaraensis* (KOD XL DNA polymerase) in the presence of Cu²⁺ ions. In the protein–DNA complex, the DNA took a right-handed duplex containing a Cu^{II}-mediated S–S base-pair (S–Cu^{II}–S) at the centre (Fig. 6a). The S base cannot form a pair with itself in the absence of Cu²⁺. However, in the presence of Cu²⁺ and ethylenediamine, the S bases form the S–Cu^{II}–S base-pair (Fig. 6b), just like the authors had designed in their initial concept.^{10,57} The two S bases are reversibly cross-linked by an ethylenediamine bridge, which forms a bisimine system. As observed for the Dipic–Cu^{II}–Py

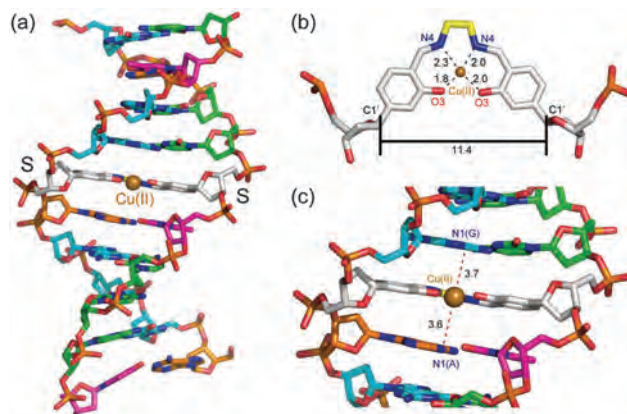


Fig. 6 (a) Overall structure of the B-form DNA duplex containing an S–Cu^{II}–S base-pair (PDB ID = 2XY5).⁵⁶ (b) Detailed geometry of the S–Cu^{II}–S base-pair. The C1'–C1' distance (Å) is represented by a solid line, and critical distances (Å) with Cu^{II} are shown with dashed lines. (c) Side view of the S–Cu^{II}–S base-pair. Axial interactions are represented by red dashed lines (distances in Å).

base-pair discussed earlier, Cu^{II} is located between the two S bases and had a square-planar coordination geometry, being ligated with two O3 and two N4 atoms of the S bases. The distances from Cu^{II} to O3 and N4 are 1.8–2.0 and 2.0–2.3 Å, respectively, (Fig. 6b). In the vertical direction, Cu^{II} experienced electrostatic interactions with the N1(A) and N1(G) atoms of neighbouring residues, with distances of 3.6 and 3.7 Å, respectively (Fig. 6c). The C1'–C1' distance (11.4 Å) is slightly longer than those of canonical W–C base-pairs (Fig. 6b). It is noteworthy that various DNA polymerases incorporate deoxyribosyl salicylic aldehyde with 5'-triphosphate (dSTP) against S residues of the template DNA strand in the presence of Cu²⁺ and ethylenediamine.

An artificial metallo-base-pair was also observed in a crystal structure of a GNA (glycol nucleic acid) duplex determined at a resolution of 1.3 Å by Meggers and coworkers in 2008.⁵⁸ Since GNA has the structurally most simple phosphodiester-containing nucleic acid backbone, GNA is considered to be a promising candidate for an initial genetic molecule of life.⁵⁹ The self-complementary (S)-GNA fragment g(CGATHCG), containing two artificial hydroxypyridone (H) bases, forms a right-handed duplex that is significantly different from the B- and A-form nucleic acid helices (Fig. 7a). In the GNA duplex, Cu²⁺ ions are specifically bound to two H–H mismatches, so that two H–Cu^{II}–H base-pairs are formed. Again, Cu^{II} is located between the two bases and is coordinated, in a square-planar fashion, by four oxygen atoms (Fig. 7b). The distances from Cu^{II} to the O3 and O4 atoms of the H nucleobases are 1.9–2.0 Å (Fig. 7b). Four electrostatic interactions are also observed in the vertical direction: from Cu^{II} to N1(C), O2(C), N7(A), and N9(A), with distances of 3.3, 3.8, 3.6, and 3.4 Å, respectively, (Fig. 7c). The C1'–C1' distance in the H–Cu^{II}–H base-pair (12.7 Å) is 2.0 Å longer than those of standard W–C base-pairs (Fig. 7b), but the Cu^{II}-mediated base-pairs fit well into the overall GNA duplex structure without any severe distortions.

The first metallo-base-pair composed of natural nucleobases was observed in a crystal structure of the duplex form of the

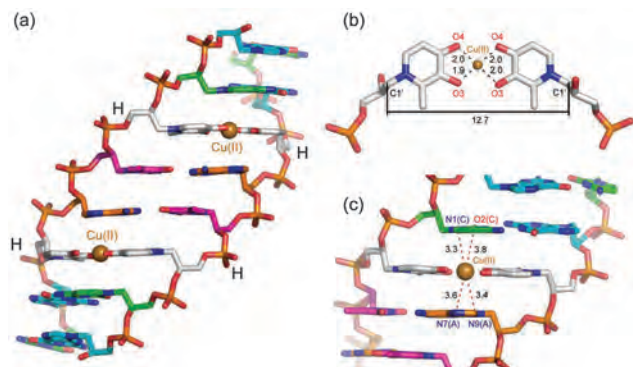


Fig. 7 (a) Overall structure of the GNA (glycol nucleic acid) duplex containing an H-Cu^{II}-H base-pair (PDB ID = 1JAA).⁵⁸ (b) Detailed geometry of the H-Cu^{II}-H base-pair. The C1'-C1' distance (Å) is represented by a solid line, and critical distances (Å) with Cu^{II} are shown with dashed lines. (c) Side view of the H-Cu^{II}-H base-pair. Interactions toward axial directions are represented by red dashed lines (distances in Å).

HIV-1 RNA dimerisation-initiation site, and was reported by Dumas and coworkers in 2003.⁶⁰ In their comprehensive studies of interactions between metal ions and RNA duplexes, an unexpected binding of an Au³⁺ ion with a G-C base-pair was observed in a crystal structure determined at a resolution of 2.3 Å (Fig. 8a). The Au³⁺ ion induced deprotonation at N1(G) and was bound between the W-C edges of G and C to form a Au^{III}-mediated G-C base-pair (G-Au^{III}-C). The distances from Au^{III} to N1(G), N2(G), O2(C), and N3(C) are 1.6–1.7, 2.3–2.4, 2.6, and 2.3–2.4 Å, respectively, (Fig. 8b). Due to the close proximity of Au^{III} and N2(G), Dumas and coworkers suggested that the two hydrogen atoms of the N2 amino group might be pushed away perpendicularly to the plane of the base-pair. The Au³⁺ ion is in close contact with electron-rich N7(G), N1(A), and N6(A) in vertical directions, with distances of 3.4, 3.6–3.8, and 3.6–3.7 Å, respectively, (Fig. 8c). The C1'-C1'

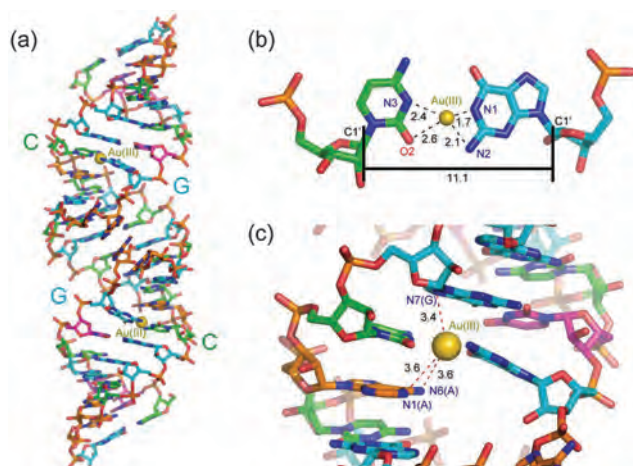


Fig. 8 (a) Overall structure of the duplex form of the HIV-1 RNA dimerisation-initiation site containing C-Au^{III}-G base-pairs (PDB ID = 2OIJ).⁶⁰ (b) Detailed geometry of the C-Au^{III}-G base-pair. The C1'-C1' distance (Å) is represented by a solid line, and critical distances (Å) with Au^{III} are shown with dashed lines. (c) Side view of the C-Au^{III}-G base-pair. Interactions toward axial directions are represented by red dashed lines (distances in Å).

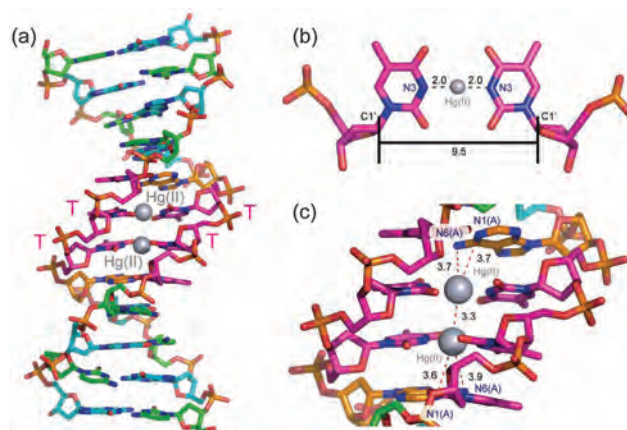


Fig. 9 (a) Overall structure of the B-form DNA duplex containing two consecutive T-Hg^{II}-T base-pairs (PDB ID = 4L24).²³ (b) Detailed geometry of the T-Hg^{II}-T base-pair. The C1'-C1' and N-Hg^{II} distances (Å) are represented by solid and black dashed lines, respectively. (c) Side view of the T-Hg^{II}-T base-pair. A possible metallophilic attraction between Hg^{II}-Hg^{II} and electrostatic interactions are represented by red dashed lines (distances in Å).

distance in the G-C base-pair is enlarged to 10.9–11.1 Å by the Au³⁺-binding (Fig. 8b), but the G-Au^{III}-C base-pair does not distort the A-form RNA duplex. The G-Au^{III}-C base-pair has not been observed in solution so far, and it is unclear whether this metallo-base-pair can stably exist in solution. If it exists, there remain unresolved issues, such as the hybridisation state of N2 (N2 pyramidalisation) and the possibility of an amino-proton-Au³⁺ exchange at N2(G).

Recently, we determined the crystal structure of a B-form DNA duplex containing two contiguous T-Hg^{II}-T base-pairs (metallo-DNA(T-Hg^{II}-T)) at a resolution of 2.7 Å.²³ A pseudo-self-complementary DNA fragment containing two contiguous T-T mismatches took the B-form conformation upon specific binding of Hg²⁺ to the T-T mismatches, thereby forming two contiguous T-Hg^{II}-T base-pairs (Fig. 9a). In the T-Hg^{II}-T base-pair, Hg^{II} was located between two T bases (Fig. 9b). The distance between N3(T) and Hg^{II} was 2.0 Å, which indicates that the N3 atom has lost an imino proton even at neutral pH (the DNA duplex was crystallised at pH 7.0, and the pK_a value at N3(T) is 9.8), which agrees with previous NMR measurements in solution^{6,16,27} (Section 1.1). The local geometries of the metal linkages in the T-Hg^{II}-T base-pairs were basically identical to that observed in the crystal structure of a 2 : 1 complex between 1-methylthymine and Hg^{II}.⁶¹ The propeller-twist angles of the T-Hg^{II}-T base-pairs (−22° and −20°) were remarkably larger than those of canonical W-C base-pairs in the B-form DNA duplex (−1°). This is probably because of no extra bond except for the N3-Hg^{II}-N3 linkage in the T-Hg^{II}-T base-pairs and because of repulsion between carbonyl groups O2 and O4. The C1'-C1' distance was 9.5–9.6 Å (Fig. 9b), which is about 1 Å shorter than those of canonical W-C base-pairs. However, the B-form conformation was not distorted. The distance between two Hg^{II} was 3.3 Å. The relatively short distance between the two Hg²⁺ cations indicates that a metallophilic attraction between Hg^{II} may

exist (Fig. 9c) (see Section 1.4 for metallophilic attraction). Hg^{II} of the tandem T-Hg^{II}-T base-pairs experienced electrostatic interactions with N1(A) and N6(A) atoms of neighbouring A-T base-pairs, with distances of 3.6–3.7 and 3.7–3.9 Å, respectively, (Fig. 9c). In the absence of Hg²⁺, the middle DNA segment that contains T-T mismatches takes an unusual nonhelical conformation containing two contiguous A-T-T triplets. This suggests that the Hg²⁺ ions are necessary for stabilising the B-form conformation, at least in this sequence context. Crystal structures of other types of nucleoside/nucleotide-Hg^{II} complexes are discussed in the review by Y. Tanaka and Ono.^{17b}

The crystallographic structures of metallo-base-pairs and metallo-DNAs provide accurate 3D coordinates of the atoms. Even if the crystal lattice sometimes modulates or alters the molecular structures due to crystal-packing, the crystallographically derived 3D structures can be used as a reliable structural template for designing molecular devices.

1.3 Thermodynamics of metallo-base-pairs

Thermodynamic parameters (ΔG , ΔH , ΔS , and K_d) are useful fundamental physicochemical data. Once they have been determined for a metallo-base-pair of interest, one can theoretically estimate how much metallo-DNA with the designated metallo-base-pair is formed under the given physical and chemical conditions. In addition, thermal denaturation experiments using UV absorbance, and the resulting T_m values, have been used for the detection of the formation of metallo-base-pairs.

Thermal denaturation experiments using UV absorbance showed that the addition of Hg²⁺^{6,62} and Ag⁺^{7,63} significantly stabilised DNA duplexes that contain T-T and C-C mismatches, respectively. However, DNA duplexes in which T-T or C-C mismatches were substituted for other base-pairs/mismatches were not significantly stabilised by the addition of Hg²⁺⁶² and Ag⁺.⁶³ With regard to metal-cation specificities of T-T and C-C mismatches, metal ions other than Hg²⁺ and Ag⁺ (such as Mg²⁺, Ca²⁺, Mn²⁺, Fe²⁺, Fe³⁺, Co²⁺, Ni²⁺, Cu²⁺, Zn²⁺, Ru³⁺, Pd²⁺, Cd²⁺, and Pb²⁺) did not stabilise either DNA duplexes with a T-T mismatch⁶ or a C-C mismatch.⁷ Thus, the combinations of Hg²⁺ with the T-T mismatch and Ag⁺ with the C-C mismatch are highly specific.

Isothermal titration calorimetric (ITC) analyses revealed that the molar ratios between Hg²⁺ and the T-T mismatch⁶² and that between Ag⁺ and the C-C mismatch⁶³ were both 1 : 1 (Table 4). Both binding constants are nearly 10⁶ M⁻¹ (Table 4),^{62,63} which

is significantly larger than those observed for nonspecific metal-ion-DNA interactions. Negative enthalpy changes and positive entropy changes were observed for the binding of the metal ions (Table 4).^{62,63} The observed positive entropy changes may mainly result from the positive dehydration entropy due to the release of structured water molecules surrounding Hg²⁺ and Ag⁺ upon binding to the mismatches. In fact, complete shielding of Hg^{II} from solvent water molecules was observed in 3D structures of DNA duplexes containing T-Hg^{II}-T base-pairs (Fig. 2a and 9c).^{22,23} The observed negative enthalpy change may be mainly driven by the negative binding enthalpy due to the formation of N3-Hg^{II}-N3 and N3-Ag^I-N3 linkages. These conclusions on the T-Hg^{II}-T base-pair were later supported by theoretical calculations of thermodynamic parameters (Table 4), based on a possible reaction scheme proposed for the specific binding of Hg²⁺ to the T-T mismatch.^{22,64} Similar thermodynamic properties were obtained from ITC analyses of the formation of artificial Im-Ag^I-Im base-pairs, *i.e.*, positive entropy and negative enthalpy changes (Table 4).⁶⁵

ITC analyses of the Hg²⁺-binding to the two neighbouring T-T mismatches in a DNA duplex revealed a significantly larger affinity for the binding of the second Hg²⁺ than for the first Hg²⁺ (Table 5).⁶⁶ Positively cooperative binding may be favourable for the alignment of multiple Hg^{II} in a DNA duplex for the application of metallo-base-pairs in nanotechnology. Positively cooperative binding was also deduced from ITC analyses of the binding between Ag⁺ and a DNA duplex containing two neighbouring Im-Im mismatches (Table 5).⁶⁵ By contrast, the cooperative effect was not observed for the binding of Ag⁺ to two neighbouring C-C mismatches (Table 5).⁶⁷ The observed cooperativity of Hg^{II} in T-Hg^{II}-T base-pairs and Ag^I in Im-Ag^I-Im base-pairs may be explained by the attraction between heavy metals (metallophilic attraction)^{68,69} (see the next section for the metallophilic attraction). In relation to the T-Hg^{II}-T base-pair, thermal denaturation experiments of complexation reactions of Hg²⁺/Ag⁺ with 5-substituted uracil/thymine and 2-thiothymine/4-thiothymine within DNA duplexes are reported in ref. 70 and 71.

1.4 Theoretical studies of metallo-base-pairs

Electronic structures of metallo-base-pairs, as deduced from theoretical calculations, can often provide hints on how to tune the properties of metallo-DNAs for use in specific molecular nanodevices. To obtain realistic electronic structures of metallo-base-pairs in nanodevices, reliable 3D structures (models) under working conditions of these nanodevices are required. However, current

Table 4 Experimental and theoretical thermodynamic parameters

Sample (method)	$\Delta H^\circ/\text{kcal mol}^{-1}$	$\Delta S^\circ/\text{cal mol}^{-1} \text{K}^{-1}$	$\Delta G^\circ/\text{kcal mol}^{-1}$	K_a/M^{-1}	n^a	Ref.
T-Hg ^{II} -T (ITC)	-3.85 ± 0.18	13.1 ± 0.65	-7.76 ± 0.19	(4.87 ± 1.35) × 10 ⁵	1.06 ± 0.03	62
T-Hg ^{II} -T (ITC)	-4.76 ± 0.13	10.6 ± 0.84	-7.91 ± 0.12	(6.34 ± 1.17) × 10 ⁵	0.89 ± 0.02	62
T-Hg ^{II} -T (Theory) ^b	-4.04	14.2	-8.27	1.16 × 10 ⁶	1 ^c	22
C-Ag ^I -C (ITC)	-2.37 ± 0.07	18.4 ± 0.7	-7.87 ± 0.15	(5.86 ± 1.29) × 10 ⁵	1.06 ± 0.03	63
C-Ag ^I -C (ITC)	-2.55 ± 0.17	16.5 ± 1.5	-7.45 ± 0.29	(2.92 ± 1.13) × 10 ⁵	1.21 ± 0.07	63
Im-Ag ^I -Im (ITC)	-8.12 ± 1.20 ^d	2.39 ± 0.48 ^d	-8.84 ± 0.24 ^d	(3 ± 1) × 10 ⁶	0.9 ± 0.1	65

^a Stoichiometry of [metal cations]/[binding site]. ^b Theoretical thermodynamic parameters of T-Hg^{II}-T base-pairs taken from ref. 22 (see the ref. 64 for the assumed reaction pathway). ΔG° values are given for 298.15 K. The theoretical K_a was calculated from the theoretical ΔG° . ^c Stoichiometry ($n = 1$) is an assumption. ^d Each value was converted with a conversion factor of $1 J = 0.239 \text{ cal}$.

Table 5 Thermodynamic parameters of tandem T-Hg^{II}-T base-pairs

		T-Hg ^{II} -T	Im-Ag ^I -Im	C-Ag ^I -C
First	<i>n</i>	1.10 ± 0.04	0.98 ± 0.08	1.10 ± 0.10
	<i>K_a</i> /M ⁻¹	(5.85 ± 2.86) × 10 ⁵	(1.5 ± 0.3) × 10 ⁵	(2.74 ± 1.37) × 10 ⁵
	Δ <i>G</i> ^o /kJ mol ⁻¹	-32.8 ± 1.8	-30.7 ± 0.7	-31.0 ± 1.7
	Δ <i>H</i> ^o /kJ mol ⁻¹	-29.0 ± 9.1	-33 ± 0.2	-11.3 ± 8.1
	Δ <i>S</i> ^o /J mol ⁻¹ K ⁻¹	12.9 ± 30.5	-12 ± 4	66.0 ± 21.4
Second	<i>n</i>	1.24 ± 0.10	1.30 ± 0.08	1.10 ± 0.10
	<i>K_a</i> /M ⁻¹	(39.6 ± 20.1) × 10 ⁵	(36 ± 4) × 10 ⁵	(7.19 ± 2.51) × 10 ⁵
	Δ <i>G</i> ^o /kJ mol ⁻¹	-37.7 ± 1.8	-37.4 ± 0.3	-33.4 ± 1.1
	Δ <i>H</i> ^o /kJ mol ⁻¹	-23.6 ± 5.3	-81.3 ± 0.5	-68.0 ± 7.5
	Δ <i>S</i> ^o /J mol ⁻¹ K ⁻¹	47.2 ± 17.8	-148 ± 3	-116 ± 22
	Reference	66	65	67

structural data do not include all of the possibilities, such as sequence/conformational varieties of metallo-DNAs and variations in physical conditions. To overcome this issue, structural interpretation of NMR and optical spectroscopic parameters, employing theoretical methods, has been recognised as a valuable method for the elucidation of 3D structures of not only metallo-base-pairs and metallo-DNAs, but also of any molecule of interest under the given conditions. Therefore, we review theoretical calculations of spectroscopic parameters of T-Hg^{II}-T and related base-pairs. In addition, the metallophilic attraction is discussed as a recent topic in the field of metallo-DNAs.

The formation of the T-Hg^{II}-T base-pair was first demonstrated from the observation of ²*J*(¹⁵N, ¹⁵N) across the metal linkage.¹⁶ The zeroth-order regular approximation density functional theory (ZORA DFT) calculations of ²*J*(¹⁵N, ¹⁵N) later confirmed the existence of the N-Hg^{II}-N linkage in the T-Hg^{II}-T base-pair, and showed agreement between the experimental and calculated ²*J*(¹⁵N, ¹⁵N) values.⁷² DFT calculations of Raman spectra of T-Hg^{II}-T base-pair confirmed the assignment of the C4-O4 stretching vibration of the T-Hg^{II}-T base-pair (Table 3) and unveiled the significant cationic character of Hg^{II} in the T-Hg^{II}-T base-pair.^{20,73} Time-dependent-DFT (TD-DFT) calculations of UV absorption spectra of DNA duplexes containing T-Hg^{II}-T base-pairs elucidated the character of the stacking interaction between consecutive T-Hg^{II}-T base-pairs.⁷⁴

Structural and electronic-structural studies of other metallo-base-pairs were also performed. DFT calculations corroborated the structural studies of Hg^{II}- and Ag^I-mediated base-pairs with azole nucleosides.⁷⁵ The structure, chemical bonding, and formation of a Ag^I-mediated Hoogsteen-type thymine-1,3-dideazaadenine base-pair was studied using the ZORA DFT-D method.⁷⁶ Cu⁺/Ag⁺/Au⁺-mediated base-pairs composed of natural nucleobases and 1-deazaadenine were studied using the B3LYP-D3 DFT method.⁷⁷ The binding of several metal cations to H (hydroxypyridone) and derived nucleobases, as well as the resulting metallo-base-pairs, was calculated using DFT methods.⁷⁸ The DFT calculations further suggested an Ag^I-mediated uracil-uracil base-pair⁷⁹ which took a slightly different structure from the metallo-base-pair of the 2:3 complex between 1-methyluracil and Ag⁺³⁹ (Fig. 3c).

There are several studies on the attraction between heavy metals (metallophilic attraction) in metallo-base-pairs and metallo-DNAs. Heavy-metal cations in metallo-DNAs may exhibit unexpected properties. It was reported that Hg²⁺, Ag⁺, and several other

heavy-metal cations in organometallic compounds do not repel each other, despite their cationic nature, because of the metallophilic attraction between these metals.^{68,69} Stabilisation owing to metallophilicity is assumed to occur for metal-metal contacts ranging from *ca.* 3.2 to 4.0 Å, based on relatively short metal-metal distances in crystals. Metallophilic attraction may therefore be operative in metallo-DNAs, because the separation between consecutive base-pairs in normal nucleic acids falls in this range. Møller-Plesset theory (MP2) and spin-component-scaled MP2 (SCS-MP2) calculations of two U-Hg^{II}-U base-pairs unveiled significant stabilisation owing to metallophilicity.⁸⁰ In particular, the Hg^{II}-Hg^{II} interaction in tandem U-Hg^{II}-U base-pairs contributes 9% to the total stabilisation, despite the significant cationic character of Hg^{II} in U-Hg^{II}-U base-pairs.⁸⁰ The stabilising role of the metallophilic attraction is also seen in the 3D structure of metallo-DNA containing tandem T-Hg^{II}-T base-pairs, showing short Hg-Hg distances in the B-form duplex.^{22,23} Stabilisation owing to metal-metal interactions was also calculated for Ag^I-Ag^I contacts in the thymine-1,3-dideazaadenine base-pair⁷⁶ and for the Im-Ag^I-Im base-pair.²¹ Although direct experimental evidence for the metallophilic attraction is still missing, the experimentally observed contacts (~3.3 Å) between Hg^{II} in metallo-DNA(T-Hg^{II}-T) suggested that its existence is plausible.²³ Theoretical interpretation of UV absorption spectra of two contiguous T-Hg^{II}-T base-pairs unveiled spectral characteristics that are partly induced by metal-metal interactions.⁷⁴ A one-bond ¹⁰⁹Ag-¹⁰⁹Ag *J*-coupling constant (¹*J*(¹⁰⁹Ag, ¹⁰⁹Ag)) of ~1 Hz was calculated for consecutive Im-Ag^I-Im base-pairs using the ZORA DFT method; thus, the measurement of ¹*J*(¹⁰⁹Ag, ¹⁰⁹Ag) provides a possible way to detect the metallophilic attraction, but the *J*-coupling magnitude might be too small for experimental detection.⁸¹

The rational design and optimisation of metallo-DNAs for their use in technological applications could be achieved through knowledge of their 3D structures and properties, as deduced from thermodynamic and spectroscopic parameters (see Sections 1.1 and 1.2 for currently available 3D structures of metallo-DNAs).^{49,82-85} The knowledge of the 3D structure of metallo-DNA containing Im-Ag^I-Im base-pairs allowed for reliable TD-DFT calculations of electronic and optical properties.⁸⁵ The thorough structural characterisation of the T-Hg^{II}-T base-pair, employing spectroscopic data in conjunction with the 3D structure of metallo-DNA(T-Hg^{II}-T), allowed us to calculate the thermodynamic parameters for the T-Hg^{II}-T base-pairing by

using the ONIOM (B3LYP:BP86) method (Table 4).⁶⁴ The calculated thermodynamic parameters were consistent with the experimental parameters (Table 4).⁶²

The use of metallo-DNAs as nanowires in the field of nano-electronics is one of the several promising applications (see Section 2.5 for charge-transport experiments and conductivity measurements). The array of metals embedded in the metallo-DNA scaffold could possess desirable charge-transport properties. DFT calculations of tandem T-Hg^{II}-T base-pairs suggested that the frontier orbitals may enhance the transport of excess electrons rather than holes.⁸⁶ The enhanced conductivity of DNA base-pairs owing to their modification with copper was calculated using the DFT method with Green's function technique.⁸⁷ Theoretical calculations of the electron conductivity of artificial metallo-base-pairs further showed that the electron transport might be controlled by an external magnetic field.⁸⁸ Theoretical DFT calculations indicated that the hole-transport efficiency in a DNA molecule containing a T-Hg^{II}-T base-pair or a T-T mismatch is affected particularly by the spatial overlap between neighbouring base-pairs; this overlap is higher for the Hg^{II}-mediated base-pair.⁸⁹

To summarise, theoretical calculations of metallo-DNA(T-Hg^{II}-T) provided its precise structure, which is consistent with experimental NMR spectroscopic and thermodynamic parameters. The structure and the results of the calculation provided further information on the electronic structures of metallo-DNA(T-Hg^{II}-T)s, whose structures were both spectroscopically and theoretically proven. Thus, based on the agreement between calculations and

experiments, theoretical calculations provided and will continue to provide realistic physicochemical properties of metallo-DNAs. The estimated physicochemical properties will be further used for the optimisation of the properties of metallo-DNAs for their use in technologies such as conductive nanowires.

2 Applications

2.1 Application in metal sensors

The most successful applications of T-Hg^{II}-T and C-Ag^I-C base-pairs are in metal sensors, which are chemical probes for the detection of Hg²⁺ and Ag⁺ ions in aqueous solutions.^{5,7} In 2004, Ono and Togashi reported a fluorescence resonance energy transfer (FRET)-based Hg²⁺ sensor in which the fluorescence is quenched upon the formation of T-Hg^{II}-T base-pairs.⁵ Since then, oligonucleotide-based Hg²⁺ sensors using various mechanisms of detection have been developed. A similar Ag⁺ sensor based on the C-Ag^I-C base-pairing ability of cytosine has also been developed.⁷ For more details on metal sensors, refer to reviews that have been published in recent years;^{11,13,90-94} metal sensors reviewed in those references are summarised in Fig. 10.

2.2 Application in Hg²⁺ trapping

The specific recognition of Hg²⁺ by thymine was applied to Hg²⁺-trapping agents. The Hg²⁺-trapping agents can be classified into two types: thymine/uracil-monomer-based Hg²⁺-trapping agents and

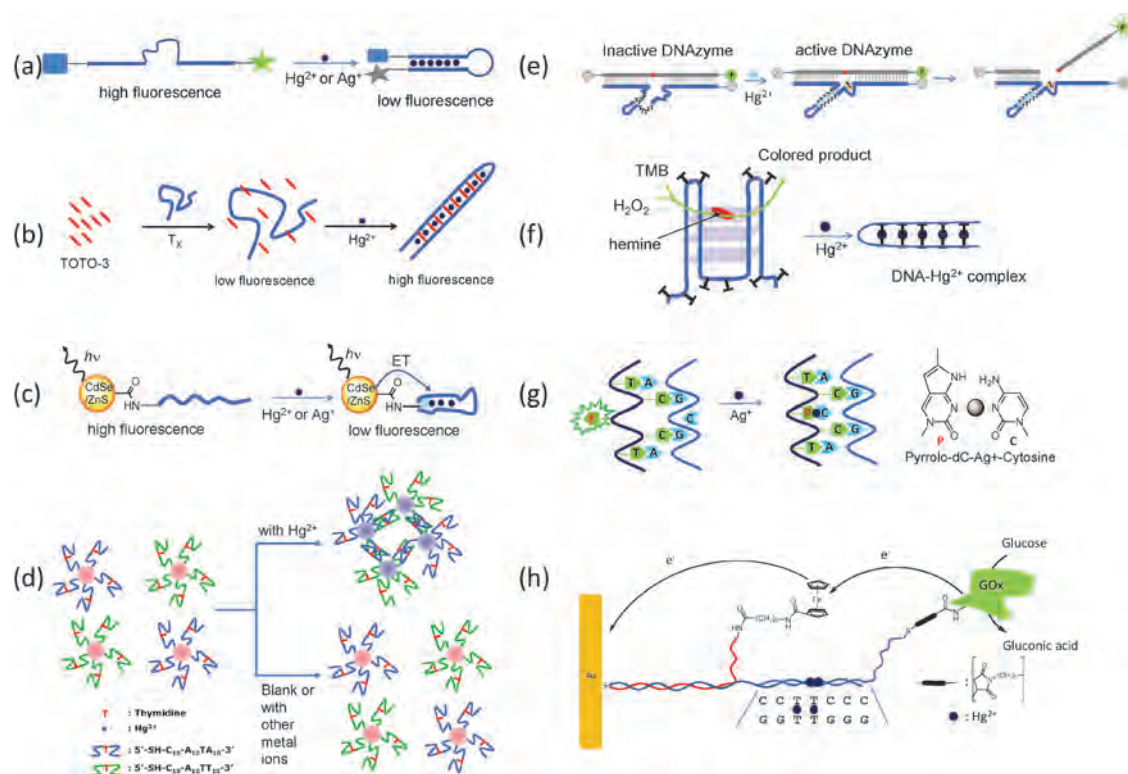


Fig. 10 Sensing mechanisms for the detection of metal ions. (a) Fluorescence-off type.^{5,7} (b) Fluorescence-on type.¹³⁵ (c) Quantum-dot-conjugated oligonucleotides.¹³⁶ (d) Gold-nanoparticle-conjugated oligonucleotides.¹³⁷ (e) DNAzyme.¹⁰⁴ (f) DNAzyme (G-quartet-hemine complex).¹³⁸ (g) Fluorescent nucleobase (pyrrolo-dC).¹³⁹ (h) Electrochemical detection.¹⁴⁰

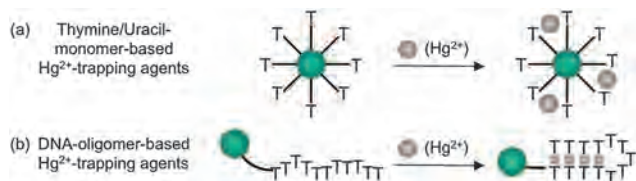


Fig. 11 Two types of Hg^{2+} -trapping agents. (a) Monomer-based (thymine/uracil) agents. (b) DNA-oligomer-based agents.

DNA-oligomer-based agents (Fig. 11). The monomer-based ones include thymine-cross-linked polystyrene beads⁹⁵ and uracil-cross-linked polystyrene fibres,⁹⁶ and DNA-oligomer-based ones include thymidine-rich-DNA-cross-linked polyacrylamide,⁹⁷ T-rich-DNA-cross-linked microparticles,⁹⁸ oligo-T-cross-linked polystyrene beads,^{99,100} and T-rich-DNA-cross-linked silica gel.¹⁰¹

The thymine/uracil-cross-linked polymer has a high density of Hg^{2+} -binding ligands (thymine/uracil) on its polymer surface,^{95,96} although the affinity of Hg^{2+} for each binding site is not so high. On the other hand, the ligand densities are not high for the T-rich-DNA-cross-linked solid support, but the affinity of Hg^{2+} for each binding site is high. Most Hg^{2+} -trapping agents can selectively capture Hg^{2+} in the presence of other cations.^{95–98,100,101} More interestingly, the Hg^{2+} -trapping efficiency of T-rich-DNA-cross-linked polystyrene beads was higher in the presence of other cations, which is favourable for their use under natural conditions.¹⁰⁰ In addition, the Hg^{2+} -trapping agents could be recycled several times.^{95–98,101}

2.3 Detection of single-nucleotide polymorphisms (SNPs)

The specific binding of Hg^{2+} to a T-T mismatch was used for the detection of single-nucleotide polymorphisms (SNPs).¹⁰² For SNP detection, an SNP probe DNA oligomer containing a 19-mer loop sequence, flanked by thymidine heptamers (T_7) at the 5' and 3' sides of the loop, was prepared (Fig. 12). This SNP probe DNA oligomer was further modified with a fluorophore (carboxyfluorescein, Fam) and a quencher (dabcyl, Dab) at the 5' and 3' termini, respectively (Fig. 12). When a target strand is perfectly complementary to the SNP probe DNA oligomer, they strongly hybridise with each other, and fluorescence of Fam was observed irrespective of the presence or absence of Hg^{2+} . By contrast, when a target strand contains a mismatch (SNP) with respect to the probe DNA, the target sequence and the SNP probe do not hybridise strongly. As a result, upon addition of

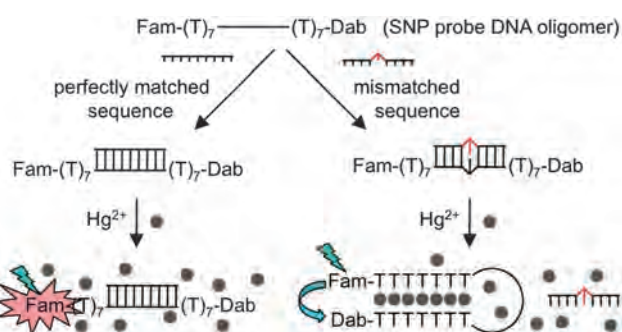


Fig. 12 SNP-detection system using T- Hg^{II} -T base-pairs.

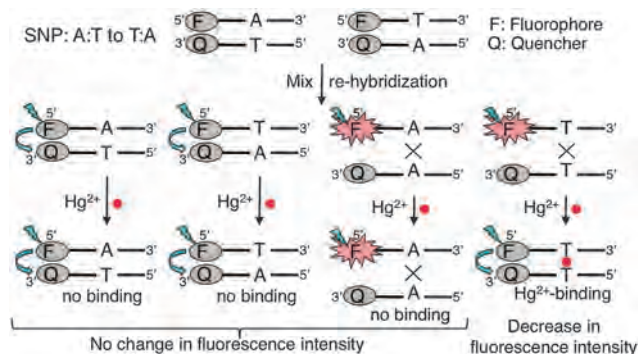


Fig. 13 SNP-detection system using T- Hg^{II} -T base-pairs.

Hg^{2+} , the SNP probe dissociated from the target sequence and folded into a unimolecular hairpin structure through T- Hg^{II} -T base-pairing, resulting in quenching of the Fam fluorescence emission because of the decreased distance between Fam (fluorophore) and Dab (quencher).

Heteroduplex analysis combined with the formation of T- Hg^{II} -T base-pairs was proposed as another approach for high-throughput detection of SNPs.¹⁰³ In the heteroduplex analysis, SNPs were detected on the basis of the mechanism depicted in Fig. 13. Other types of SNPs were detected on the basis of the similar mechanism to that depicted in Fig. 13, except for the use of the formation of C- Ag^{I} -C base-pairs.¹⁰³

2.4 Application in nanomachines

As emerging applications of T- Hg^{II} -T and C- Ag^{I} -C base-pairs, these metallo-base-pairs were applied in nanomachines in the field of nanotechnology.^{14,15} A prototype of such an application is an allosteric DNAzyme that is activated by T- Hg^{II} -T base-pairing, which is also used as a Hg^{2+} sensor with signal amplification (Fig. 10).¹⁰⁴ Nanomachines (DNA machines) were then generated, such as DNA tweezers (automaton/memory devices),¹⁰⁵ DNA walkers,¹⁰⁶ cascade DNAzyme-reaction systems,^{107–109} and logic gates.¹¹⁰

With regard to DNA tweezers, Hg^{2+} closes the DNA tweezer molecule through the hybridisation of an additional DNA strand upon T- Hg^{II} -T base-pairing.¹⁰⁵ It was suggested that these DNA tweezers were able to be used as automaton and memory devices.¹⁰⁵ With regard to the DNA walker, Hg^{2+} altered its hybridisation site on the DNA-rail molecule upon T- Hg^{II} -T base-pairing.¹⁰⁶ For the cascade DNAzyme-reaction systems, artificial signal transduction/amplification systems were built up from two successive DNAzyme reactions.^{107–109} These cascade reaction systems consist of a ligase-like or a nuclease-like DNAzyme for the first step and horseradish-peroxidase-mimicking DNAzymes for the second step.^{107–109} In these systems, $\text{Hg}^{2+}/\text{Ag}^{\text{I}}$ activates the first step (ligase- or nuclease-like DNAzymes) by T- Hg^{II} -T/C- Ag^{I} -C base-pairing.^{107–109} Lastly, logic gates (AND/OR operators) were generated by using T- Hg^{II} -T and/or C- Ag^{I} -C base-pairing (see Section 2.6 for details).¹¹⁰

2.5 Conductivity of metallo-base-pairs

Long metal arrays that can be generated in metallo-DNA duplexes are suggested to be conductive.^{8,10,12,13} For this reason,

the charge-transport ability of metallo-base-pairs was studied in terms of hole-transport ability^{89,111–113} and conductivity.^{114–116} Although the conductivity and electron-transport ability of M-DNA have been reported,^{41,42,114} the structure of the M-DNA molecule has not yet been determined. Therefore, the origin of its conductivity remains unknown. Currently, the conductivities of the T-Hg^{II}-T and H-Cu^{II}-H base-pairs were reported to be similar to those of semiconductors.^{115,116} However, their conductivities are still worth exploring, since T-Hg^{II}-T and H-Cu^{II}-H base-pairs have been chemically and structurally well characterised. The frontier orbital of the stacked H-Cu^{II}-H base-pairs possesses a node between planes of stacked base-pairs,¹¹⁷ whereas the LUMO of the T-Hg^{II}-T base-pair is continuous, covering the tandemly aligned Hg^{II}.⁸⁶ Therefore, we predicted that the T-Hg^{II}-T base-pair should be an electron acceptor;^{17b,22} this was observed experimentally through fluorescence quenching by electron transfer to the T-Hg^{II}-T base-pair.¹¹⁸

The generation of metal arrays in DNA molecules could be an efficient strategy for the conversion of DNA duplexes into conductive DNA nanowires.^{10,13} Currently, 10 contiguous metallo-base-pairs have been generated by using S-Cu^{II}-S base-pairs and mixed S-Cu^{II}-S/T-Hg^{II}-T base-pairs.^{119,120} The number of contiguous metallo-base-pairs for these and other base-pairs is listed in Table 6.^{4,6,19,21,34,119–122} Relatively long tracts of the metallo-base-pairs formed before (Table 6) indicated that tandem alignments of the metallo-base-pairs may also be thermodynamically favourable similarly to the case of T-Hg^{II}-T base-pairs. Therefore, detailed thermodynamic analyses of other so far uncharacterized metallo-base-pairs can be recommended to unveil how favourable these tandem alignments are. In any case, trials to make long tracts of metallo-base-pairs may provide conductive nanowires.

2.6 Response to enzymes

Several artificial base-pairs have been reported to be recognised by DNA polymerases.^{123–127} Can metallo-base-pairs also be recognised? In 2010, DNA polymerases were shown, for the first time, to incorporate metallo-base-pairs in a primer-extension reaction.¹²⁸ In this experiment, dTTP was incorporated into the site opposite to thymine residues in the template

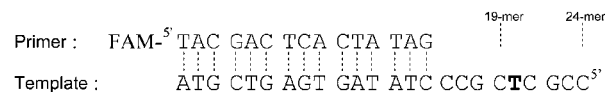


Fig. 14 A template–primer complex for the formation of T-Hg^{II}-T base-pairs by DNA polymerases.

strand by DNA polymerases in the presence of Hg²⁺ ions (Fig. 14).¹²⁸

More precisely, in the presence of dGTP, dCTP, and dTTP, and in the absence of Hg²⁺ ions, the primer-extension reaction with the Klenow fragment (KF) stalled at the 19-mer site just before the thymine residue (20-mer site) in the template strand. However, upon the addition of Hg²⁺ ions (10–100 μM), the enzyme read through the 20-mer site to afford the full-length 24-mer. Without dTTP, the enzyme was unable to read through the 20-mer site even in the presence of Hg²⁺ ions. MALDI-TOF mass analysis of the full-length product demonstrated the incorporation of the thymine base at the 20-mer site (Fig. 15). This reaction is highly specific to Hg²⁺ ions; other metal ions, such as Mn²⁺, Fe²⁺, Fe³⁺, Co²⁺, Cu²⁺, Zn²⁺, Pb²⁺, Ni²⁺, and Au⁺, did not promote the extension. Other polymerases, such as Taq DNA polymerase and KOD Dash DNA polymerase, also catalyse the incorporation of dTTP opposite to thymine in the template in the presence of Hg²⁺ ions.

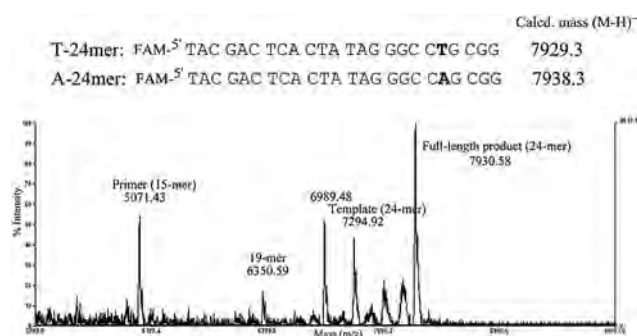


Fig. 15 MALDI-TOF mass spectrum of the primer-extension product (catalysed by DNA polymerases in the presence of Hg²⁺ ions).

Table 6 Metal arrays generated in DNA molecules

Base-pair	Number	$d_{M-M}^a/\text{Å}$	Method	Ref.
S-Cu ^{II} -S/T-Hg ^{II} -T	10		ESI-MS, titration (UV)	119
S-Cu ^{II} -S	10		ESI-MS, titration (UV)	120
U-Hg ^{II} -U	6		NMR, titration (UV/CD), Tm (UV)	34
H-Cu ^{II} -H	5	3.7	ESI-MS, titration (UV/CD), ESR	4
T-Hg ^{II} -T	5		ESI-MS, titration (UV/CD)	6
H-Cu ^{II} -H/Py-Hg ^{II} -Py	3		ESI-MS, titration (UV)	119
Im-Ag ^I -Im	3	3.79–4.51 ^b	NMR (¹ J _{NAg} ^c , ¹⁵ N-CS ^d , NOE-based 3D structure)	19 and 21
T-Hg ^{II} -T	2	4.03–4.15	NMR (¹ J _{NN} ^e , ¹⁵ N-CS ^d , NOE-based 3D structure), titration (UV/CD), Tm (UV)	16, 22 and 27
T-Hg ^{II} -T	2	3.3	Crystal structure	23
Dipic-Cu ^{II} -Py	4		Tm (UV)	121
Dipam-Cu ^{II} -Py	4		Tm (UV)	121
PyPur-Ni ^{II} -PyPur	3		Tm (UV)	122

^a Distance between metal cations. ^b The refined Ag^I-Ag^I distance with theoretical calculations was 3.41–3.68 Å. ^c ¹J(¹⁵N, ^{107/109}Ag). ^d ¹⁵N chemical shift. ^e ¹J(¹⁵N, ¹⁵N).

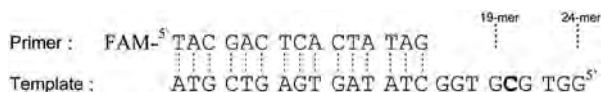


Fig. 16 The template–primer complex for the primer extension catalysed by DNA polymerases in the presence of Ag⁺ ions.

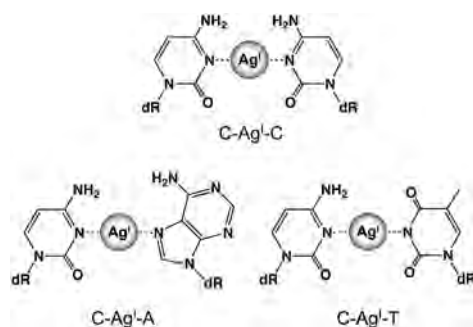


Fig. 17 Ag⁺-mediated base-pairs. The word “dR” denotes deoxyribose.

The logical next question is whether the C–Ag^I–C base-pair can be used as a W–C base-pair analogue in the extension reaction catalysed by DNA polymerases. Primer-extension reactions in the presence of Ag⁺ ions (Fig. 16) showed that KF unexpectedly incorporated dATP instead of dCTP into the site opposite to cytosine in the template to form an Ag^I-mediated C–A base-pair (C–Ag^I–A).¹²⁹ The structure of the C–Ag^I–A base-pair was tentatively assumed to contain an N3(C)–Ag^I–N7(A) linkage (Fig. 17). Extensive studies of the extension reaction in the presence of Ag⁺ ions demonstrated that the C–Ag^I–T base-pair is also formed by DNA polymerases (Fig. 17),¹³⁰ although the Ag^I-mediated enzymatic incorporation of dTTP opposite to cytosine in the template is somewhat dependent on the sequence upstream of the site of incorporation. Under 10 μM deoxynucleoside-5'-triphosphates (dNTPs) and 0.2 units of KF without 3' → 5' exonuclease activity KF(exo-), formation of the C–Ag^I–C base-pair was not observed; hence, of the three Ag^I-mediated base-pairs shown in Fig. 17, the C–Ag^I–C base-pair is the most difficult to be elongated by DNA polymerase.¹³⁰ Under more stringent conditions (20 μM dCTP, 0.8 units of KF(exo-)), however, the enzymatic incorporation of dCTP opposite to cytosine in the template proceeded, depending on the sequence of the template.¹³⁰ It was reported that 5-methyldeoxycytidine triphosphate (m⁵dCTP) shows a higher substrate activity for DNA polymerase than dCTP.¹³¹ The enzymatic formation of the T–Hg^{II}–T and C–Ag^I–T base-pairs is strictly governed by the Hg²⁺ and Ag⁺ ions and is also highly specific for these metal ions. Based on the high specificity and using the primed template shown in Fig. 18, the regulated incorporation of Hg²⁺ and Ag⁺ ions into programmed sites in a duplex by DNA polymerase was achieved.¹³⁰

The formation of T–Hg^{II}–T and C–Ag^I–C base-pairs was exploited for the construction of DNA-based logic gates.¹¹⁰ Primed templates with a T–T or C–C mismatch at the 3' primer terminus were constructed. These primed templates were amplified by the addition of Hg²⁺ and/or Ag⁺ ions. An AND

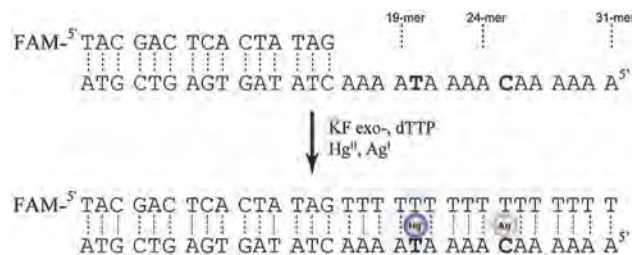


Fig. 18 Regulated incorporation of two different metal ions into programmed sites by DNA polymerases.

gate proceeded with exponential polymerase chain reaction (PCR) amplification (output) when both Hg²⁺ and Ag⁺ ions were added as inputs; the addition of either Hg²⁺ or Ag⁺ ions did not generate output signals. An OR gate proceeded with exponential PCR amplification (output) in the presence of either Hg²⁺ or Ag⁺ ions or in the presence of both ions. In addition, the programmed incorporation of the T–Hg^{II}–T and C–Ag^I–T base-pairs, as described earlier, also behaves like an AND gate.¹³⁰

Some artificial base-pairs have been shown to function as a “third base-pair” in PCR.^{125,126} The development of replicable metallo-base-pairs composed of artificial nucleobases (metal chelators) would provide an alternative approach to the expansion of the genetic alphabet. The Dipic–Cu^{II}–Py base-pair (Fig. 5) was created by Meggers, Romesberg, and Schultz with this concept in mind.^{2,55,132} An actual application in this direction was first reported by Carell and coworkers. They reported a S–Cu^{II}–S base-pair as a base-pair orthogonal to natural ones (Fig. 6 and 19).⁵⁶ Two opposing salicylic aldehyde deoxyribosides (dS) in a duplex form a reversible cross-link through an ethylenediamine bridge; the resulting bridge is stabilised by the coordination of a Cu²⁺ ion. This Cu^{II}-mediated artificial base-pair was recognised by DNA polymerases such as *Bst Pol I*, which selectively incorporated dSTP opposite to a templating dS base in the presence of ethylenediamine and Cu²⁺ ions. Furthermore, natural dNTPs did not compete with dSTP for binding opposite to the templating dS, so that the S–Cu^{II}–S base-pair is fully orthogonal to the canonical base-pairs, even in amplification by PCR.

A metal-mediated hetero-base-pair (metallo-base-pair composed of two different metal chelators) may be advantageous for increasing

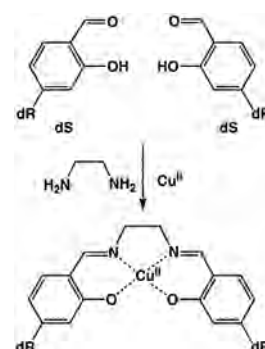


Fig. 19 Formation of the S–Cu^{II}–S base-pair. The word “dR” denotes deoxyribose.

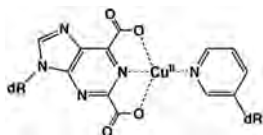


Fig. 20 Pur^{DC}-Cu^{II}-3-Py base-pair. The word "dR" denotes deoxyribose.

the number of codons. Most recently, the Cu^{II}-mediated hetero-base-pair purine-2,6-dicarboxylate-Cu^{II}-3-pyridine (Pur^{DC}-Cu^{II}-3-Py) was reported (Fig. 20).¹³³ Duplexes containing this base-pair were selectively stabilised by the addition of Cu²⁺ or Zn²⁺ ions. Most of the DNA polymerases tested in the study¹³³ incorporated dPur^{DC} triphosphate (dPur^{DC}TP) opposite to 3-Py in the template in the presence of Cu²⁺ ions; some polymerases incorporated dPur^{DC}TP even in the presence of Zn²⁺ ions. Although the enzymatic incorporation of dPur^{DC} opposite to 3-Py in the template in the presence of canonical dNTPs was not described, the introduction of these artificial bases into the sites complementary to the canonical bases caused significant destabilisation of the duplexes. This may suggest that dPur^{DC} and 3-Py do not compete with the natural bases in the DNA-polymerase-catalysed extension reaction.

These results suggest that a metal-mediated base-pair, formed by DNA polymerases, would be useful and widely applicable to molecular devices such as initiators for PCR amplification leading to DNA logic gates, highly sensitive metal-ion sensors,¹³⁴ and a "third base-pair" for expanding the genetic alphabet.

Summary and perspectives

In this feature article, we dealt with both natural-nucleobase-based metallo-base-pairs and artificial metal-chelator-based ones. First, we summarize the current status of natural-nucleobase-based metallo-base-pairs as a starting point of this feature article. We then propose future prospects of the metallo-base-pairs (natural-base-based and artificial metal-chelator-based ones) on the basis of their accumulated fundamental properties.

Since we discovered T-Hg^{II}-T and C-Ag^I-C base-pairs, we have extensively explored their fundamental properties. To date, we determined the chemical structure of the T-Hg^{II}-T base-pair based on the observation of ²J(¹⁵N, ¹⁵N) in ¹⁵N NMR spectra, which is solid evidence for the N3-Hg^{II}-N3 linkage. Additionally, we determined the 3D structures of DNA duplexes including tandem T-Hg^{II}-T base-pairs in solution and in the crystal. Unexpectedly, the ¹⁵N NMR spectra (downfield shift of N3 at the Hg^{II}-ligated site) and the Raman spectra (low-wavenumber shift of the C4=O4 stretching band) indicated the highly ionic nature of the N3-Hg^{II} bond, although it has covalent nature. Theoretical calculations confirmed the low covalency of the N3-Hg^{II} bond (a lowered bond order (0.22) compared to the original N3-H bond (0.50) of thymine) and the resulting highly cationic nature of Hg^{II}. Furthermore, ¹⁵N NMR parameters (²J(¹⁵N, ¹⁵N) and ¹⁵N chemical shifts) derived from T-Hg^{II}-T base-pairs have become standard reference values for NMR parameters for N-metallated compounds. This means that our NMR spectroscopic parameters have influenced

coordination and inorganic chemistry, and they will form the structural/chemical basis for later studies.

We further determined the thermodynamic parameters for T-Hg^{II}-T and C-Ag^I-C base-pairing. In both cases, ITC studies gave negative enthalpy values and positive entropy values for their formation. The positive entropy change was demonstrated to be a dehydration entropy, as the dehydration of Hg²⁺ ions was demonstrated by the 3D structures of metallo(Hg^{II})-DNA duplexes. This is quite a rare case for which the structurally silent entropy parameter was identified from a 3D structure.

The 3D structures further demonstrated the close contact between Hg^{II} in adjacent T-Hg^{II}-T base-pairs in DNA duplexes. This Hg^{II}-Hg^{II} close contact provides evidence for the metallophilic attraction, which was also indicated by our theoretical calculations on tandem T-Hg^{II}-T (U-Hg^{II}-U) base-pairs. Thus, all of the experimental and theoretical data consistently explain the fundamental physicochemical properties of the T-Hg^{II}-T base-pair, and these properties were comprehensively characterised by basic structural, spectroscopic, thermodynamic, and theoretical studies. Therefore, as the next targets, the chemical structures of C-Ag^I-C/C-Ag^I-A/C-Ag^I-T base-pairs and their 3D structures in DNA duplexes should be determined to generate a complete fundamental dataset for metallo-base-pairs composed of natural nucleobases.

As a future prospect, metallo-DNA duplexes with a long tract of metallo-base-pairs may be assumed attractive with regard to the construction of conductive nanowires and semiconductors. Nevertheless, it still remains unclear whether such a long tract of metallo-base-pairs can be generated because growing repulsion among metal cations may be destructive for 3D structures. For this issue, the crystal structure of the metallo(Hg^{II})-DNA duplex unveiled the close distance between Hg²⁺ ions (3.3 Å) of neighbouring T-Hg^{II}-T base-pairs.²³ Furthermore, the positive cooperativity for Hg^{II}-binding to the consecutive T-T mismatches (second *K*_a > first *K*_a, Table 5) indicated that the close contact of Hg²⁺ ions is thermodynamically favourable. Hence, the key issue to be resolved is how to produce a metallo-DNA duplex long enough for the construction of functional nanowires. In addition, their conductivities must be examined. In that regard, theoretical implication of a continuous (node-free) LUMO overlap through adjacent Hg²⁺ ions indicated that an effective route for excess electrons may exist. Both the structural and the electronic properties of metallo(Hg^{II})-DNA thus suggest that realization of a conductive nanowire is possible.

Artificial metal-chelator-based metallo-base-pairs are also interesting candidates of a conductive nanowire. Their several 3D structures are available (Dipic-Cu^{II}-Py,⁵⁵ S-Cu^{II}-S,⁵⁶ H-Cu^{II}-H,⁵⁸ C-Au^{III}-G⁶⁰ and Im-Ag^I-Im^{19,21}), and the electronic properties of the Im-Ag^I-Im base-pair were studied.²¹ It is also noteworthy that the longest metal-arrays were produced using the S-Cu^{II}-S base pair and S-Cu^{II}-S/T-Hg^{II}-T mixed base pairs,^{119,120} In addition, fine-tuning or drastic alteration of the properties of metal-chelator-based metallo-DNA molecules can be freely performed by modifying or altering molecular skeletons. On the other hand, natural nucleobase-based metallo-DNAs may have some limitations for their applications in molecular devices, due to their limited

chemical diversities of nucleobases even if metallo-DNAs with modified nucleobases^{70,71} are taken into consideration. However, extensively accumulated structural/physicochemical data for T-Hg^{II}-T and C-Ag^I-C base-pairs might help us construct molecular devices based on their physicochemical properties.

Therefore, metallo-DNA molecules with other existing metallo-base pairs (artificial metal-chelator-based and natural nucleobases-based ones) need to be characterized both structurally and physicochemically toward their technological applications. We may foresee that the number of structures and spectroscopic/thermodynamic parameters of metallo-DNA molecules will increase due to their necessity for the construction of molecular devices based on the bottom-up approach. Such fundamental achievements will lead to the rational design of a variety of new molecular nanodevices in future.

Acknowledgements

This work was supported by Grants-in-aid for Scientific Research (A) (24245037 to A.O., J.K., H.U., H.T., and Y.T.) and (B) (24310163 to Y.T.) and Challenging Exploratory Research (15K13734 to Y.T.) from the Ministry of Education, Culture, Sports, Science and Technology (MEXT), Japan; a Human Frontier Science Program (HFSP) Young Investigator Grant from HFSP, France (Y.T. and V.S.); and GAČR (P205/10/0228 and 15-21387S to V.S.) from the Czech Republic. T.D. and K.F. are the recipients of a Research Fellowship for Young Scientists from the Japan Society for the Promotion of Science (JSPS). Y.T. and V.S. were further supported by an Invitation Fellowship for Research in Japan (Short-Term) from JSPS.

Notes and references

- K. Tanaka and M. Shionoya, *J. Org. Chem.*, 1999, **64**, 5002–5003.
- E. Meggers, P. L. Holland, W. B. Tolman, F. E. Romesberg and P. G. Schultz, *J. Am. Chem. Soc.*, 2000, **122**, 10714–10715.
- K. Tanaka, A. Tengeji, T. Kato, N. Toyama, M. Shiro and M. Shionoya, *J. Am. Chem. Soc.*, 2002, **124**, 12494–12498.
- K. Tanaka, A. Tengeji, T. Kato, N. Toyama and M. Shionoya, *Science*, 2003, **299**, 1212–1213.
- A. Ono and H. Togashi, *Angew. Chem.*, 2004, **116**, 4400–4402 (*Angew. Chem., Int. Ed.*, 2004, **43**, 4300–4303).
- Y. Miyake, H. Togashi, M. Tashiro, H. Yamaguchi, S. Oda, M. Kudo, Y. Tanaka, Y. Kondo, R. Sawa, T. Fujimoto, T. Machinami and A. Ono, *J. Am. Chem. Soc.*, 2006, **128**, 2172–2173.
- A. Ono, S. Cao, H. Togashi, M. Tashiro, T. Fujimoto, T. Machinami, S. Oda, Y. Miyake, I. Okamoto and Y. Tanaka, *Chem. Commun.*, 2008, 4825–4827.
- T. Carell, C. Behrens and J. Gierlich, *Org. Biomol. Chem.*, 2003, **1**, 2221–2228.
- H.-A. Wagenknecht, *Angew. Chem.*, 2003, **115**, 3322–3324 (*Angew. Chem., Int. Ed.*, 2003, **42**, 3204–3206).
- G. H. Clever, C. Kaul and T. Carell, *Angew. Chem.*, 2007, **119**, 6340–6350 (*Angew. Chem., Int. Ed.*, 2007, **46**, 6226–6236).
- A. Ono, H. Torigoe, Y. Tanaka and I. Okamoto, *Chem. Soc. Rev.*, 2011, **40**, 5855–5866.
- Y. Takezawa and M. Shionoya, *Acc. Chem. Res.*, 2012, **45**, 2066–2076.
- P. Scharf and J. Müller, *ChemPlusChem*, 2013, **78**, 20–34.
- X. Liu, C.-H. Lu and I. Willner, *Acc. Chem. Res.*, 2014, **47**, 1673–1680.
- F. Wang, C.-H. Lu and I. Willner, *Chem. Rev.*, 2014, **114**, 2881–2941.
- Y. Tanaka, S. Oda, H. Yamaguchi, Y. Kondo, C. Kojima and A. Ono, *J. Am. Chem. Soc.*, 2007, **129**, 244–245.
- (a) Y. Tanaka and A. Ono, *Dalton Trans.*, 2008, 4965–4974; (b) Y. Tanaka and A. Ono, in *Metal Complexes – DNA Interactions*, ed. N. Hadjilias and E. Sletten, John Wiley & Sons, 2009, pp. 439–462.
- T. Dairaku, K. Furuita, H. Sato, J. Šebera, D. Yamanaka, H. Otaki, S. Kikkawa, Y. Kondo, R. Katahira, F. M. Bickelhaupt, C. F. Guerra, A. Ono, V. Sychrovský, C. Kojima and Y. Tanaka, *Chem. Commun.*, 2015, **51**, 8488–8491.
- S. Johannsen, N. Megger, D. Böhme, R. K. O. Sigel and J. Müller, *Nat. Chem.*, 2010, **2**, 229–234.
- T. Uchiyama, T. Miura, H. Takeuchi, T. Dairaku, T. Komuro, T. Kawamura, Y. Kondo, L. Benda, V. Sychrovský, P. Bouř, I. Okamoto, A. Ono and Y. Tanaka, *Nucleic Acids Res.*, 2012, **40**, 5766–5774.
- S. Kumbhar, S. Johannsen, R. K. O. Sigel, M. P. Waller and J. Müller, *J. Inorg. Biochem.*, 2013, **127**, 203–210.
- H. Yamaguchi, J. Šebera, J. Kondo, S. Oda, T. Komuro, T. Kawamura, T. Dairaku, Y. Kondo, I. Okamoto, A. Ono, J. V. Burda, C. Kojima, V. Sychrovský and Y. Tanaka, *Nucleic Acids Res.*, 2014, **42**, 4094–4099.
- J. Kondo, T. Yamada, C. Hirose, I. Okamoto, Y. Tanaka and A. Ono, *Angew. Chem.*, 2014, **126**, 2417–2420 (*Angew. Chem., Int. Ed.*, 2014, **53**, 2385–2388).
- R. W. Chrisman, S. Mansy, H. J. Peresie, A. Ranade, T. A. Berg and R. S. Tobias, *Bioinorg. Chem.*, 1977, **7**, 245–266.
- B. Morzyk-Ociepa and D. Michalska, *J. Mol. Struct.*, 2001, **598**, 133–144.
- D. W. Gruenwedel, M. K. Cruikshank and G. M. Smith, *J. Inorg. Biochem.*, 1993, **52**, 251–261.
- Y. Tanaka, H. Yamaguchi, S. Oda, M. Nomura, C. Kojima, Y. Kondo and A. Ono, *Nucleosides, Nucleotides Nucleic Acids*, 2006, **25**, 613–624.
- D. W. Gruenwedel, *J. Inorg. Biochem.*, 1994, **56**, 201–212.
- D. W. Gruenwedel, *Biophys. Chem.*, 1994, **52**, 115.
- (a) E. Buncel, C. Boone, H. Joly, R. Kumar and A. R. Norris, *J. Inorg. Biochem.*, 1985, **25**, 61–73; (b) E. Buncel, C. Boone and H. Joly, *Inorg. Chim. Acta*, 1986, **125**, 167–172; (c) A. R. Norris and R. Kumar, *Inorg. Chim. Acta*, 1984, **93**, 33–35.
- Z. Kuklennyik and L. G. Marzilli, *Inorg. Chem.*, 1996, **35**, 5654–5662.
- (a) S. Katz, *J. Am. Chem. Soc.*, 1952, **74**, 2238–2245; (b) C. A. Thomas, *J. Am. Chem. Soc.*, 1954, **76**, 6032–6034; (c) W. F. Dove and T. Yamane, *Biochim. Biophys. Res. Commun.*, 1960, **3**, 608–612; (d) T. Yamane and N. Davidson, *J. Am. Chem. Soc.*, 1961, **83**, 2599–2607; (e) S. Katz, *Nature*, 1962, **194**, 569; (f) S. Katz, *Nature*, 1962, **195**, 997; (g) T. Yamane and N. Davidson, *Biochim. Biophys. Acta*, 1962, **55**, 780–782; (h) S. Katz, *Biochim. Biophys. Acta*, 1963, **68**, 240.
- P. R. Young, U. S. Nandi and N. R. Kallenbach, *Biochemistry*, 1982, **21**, 62–66.
- S. Johannsen, S. Paulus, N. Düpre, J. Müller and R. K. O. Sigel, *J. Inorg. Biochem.*, 2008, **102**, 1141–1151.
- N. Å. Frøystein and E. Sletten, *J. Am. Chem. Soc.*, 1994, **116**, 3240–3250.
- S. Steinkopf, W. Nerdal, A. Kolstad and E. Sletten, *Acta Chem. Scand.*, 1996, **50**, 775–782.
- E. Sletten and N. Å. Frøystein, in *Metal Ions in Biological Systems*, ed. A. Sigel and H. Sigel, Marcel Dekker, 1996, vol. 32, pp. 397–418.
- E. Sletten and W. Nerdal, in *Metal Ions in Biological Systems*, ed. A. Sigel and H. Sigel, Marcel Dekker, 1997, vol. 34, pp. 479–500.
- B. Morzyk-Ociepa and D. Michalska, *Spectrochim. Acta, Part A*, 2003, **59**, 1247–1254.
- J. S. Lee, L. J. P. Latimer and R. S. Reid, *Biochem. Cell Biol.*, 1993, **71**, 162–168.
- P. Aich, S. L. Labiuk, L. W. Tari, L. J. T. Delbaere, W. J. Roesler, K. J. Falk, R. P. Steer and J. S. Lee, *J. Mol. Biol.*, 1999, **294**, 477–485.
- P. Aich, R. J. S. Skinner, S. D. Wettig, R. P. Steer and J. S. Lee, *J. Biomol. Struct. Dyn.*, 2002, **20**, 93–98.
- E. C. Fusch and B. Lippert, *J. Am. Chem. Soc.*, 1994, **116**, 7204–7209.
- S. S. Alexandre, J. M. Soler, L. Seijo and F. Zamora, *Phys. Rev. B: Condens. Matter Mater. Phys.*, 2006, **73**, 205112.
- D. A. Megger and J. Müller, *Nucleosides, Nucleotides Nucleic Acids*, 2010, **29**, 27–38.
- H. A. Day, C. Huguin and Z. A. E. Waller, *Chem. Commun.*, 2013, **49**, 7696–7698.
- M. Berdakin, V. Steinmetz, P. Maitre and G. A. Pino, *J. Phys. Chem. A*, 2014, **118**, 3804–3809.
- I. Goncharova, *Spectrochim. Acta A*, 2014, **118**, 221–227.
- S. S. Mallajosyula and S. K. Pati, *Angew. Chem.*, 2009, **121**, 5077–5081 (*Angew. Chem., Int. Ed.*, 2009, **48**, 4977–4981).

- 50 G. W. Buchanan and J. B. Stothers, *Can. J. Chem.*, 1982, **60**, 787–791.
- 51 G. W. Buchanan and M. J. Bell, *Can. J. Chem.*, 1983, **61**, 2445–2448.
- 52 Y. Tanaka, C. Kojima, E. H. Morita, Y. Kasai, K. Yamasaki, A. Ono, M. Kainosho and K. Taira, *J. Am. Chem. Soc.*, 2002, **124**, 4595–4601.
- 53 G. Wang, B. L. Gaffney and R. A. Jones, *J. Am. Chem. Soc.*, 2004, **126**, 8908–8909.
- 54 Y. Tanaka and K. Taira, *Chem. Commun.*, 2005, 2069–2079.
- 55 S. Atwell, E. Meggers, G. Spraggon and P. G. Schultz, *J. Am. Chem. Soc.*, 2001, **123**, 12364–12367.
- 56 C. Kaul, M. Müller, M. Wagner, S. Schneider and T. Carell, *Nat. Chem.*, 2011, **3**, 79–8004.
- 57 G. H. Clever, K. Polborn and T. Carell, *Angew. Chem.*, 2005, **117**, 7370–7374 (*Angew. Chem., Int. Ed.*, 2005, **44**, 7204–7208).
- 58 M. K. Schlegel, L.-O. Essen and E. Meggers, *J. Am. Chem. Soc.*, 2008, **130**, 8158–8159.
- 59 L. E. Orgel, *Trends Biochem. Sci.*, 1998, **23**, 491–495.
- 60 E. Ennifar, P. Walter and P. Dumas, *Nucleic Acids Res.*, 2003, **31**, 2671–2682.
- 61 L. D. Kosturko, C. Folzer and R. F. Stewart, *Biochemistry*, 1974, **13**, 3949–3952.
- 62 H. Torigoe, A. Ono and T. Kozasa, *Chem. – Eur. J.*, 2010, **16**, 13218–13225.
- 63 H. Torigoe, I. Okamoto, T. Dairaku, Y. Tanaka, A. Ono and T. Kozasa, *Biochimie*, 2012, **94**, 2431–2440.
- 64 J. Šebera, J. Burda, M. Straka, A. Ono, C. Kojima, Y. Tanaka and V. Sychrovský, *Chem. – Eur. J.*, 2013, **19**, 9884–9894.
- 65 K. Petrovec, B. J. Ravoo and J. Müller, *Chem. Commun.*, 2012, **48**, 11844–11846.
- 66 H. Torigoe, Y. Miyakawa, A. Ono and T. Kozasa, *Thermochim. Acta*, 2012, **532**, 28–35.
- 67 H. Torigoe, Y. Miyakawa, A. Ono and T. Kozasa, *Nucleosides, Nucleotides Nucleic Acids*, 2011, **30**, 149–167.
- 68 P. Pyykkö, *Chem. Rev.*, 1997, **97**, 597–636.
- 69 P. Pyykkö and M. Straka, *Phys. Chem. Chem. Phys.*, 2000, **2**, 2489–2493.
- 70 I. Okamoto, K. Iwamoto, Y. Watanabe, Y. Miyake and A. Ono, *Angew. Chem.*, 2009, **121**, 1676–1679 (*Angew. Chem., Int. Ed.*, 2009, **48**, 1648–8320).
- 71 I. Okamoto, T. Ono, R. Sameshima and A. Ono, *Chem. Commun.*, 2012, **48**, 4347–4349.
- 72 A. Bagno and G. Saielli, *J. Am. Chem. Soc.*, 2007, **129**, 11360–11361.
- 73 L. Benda, M. Straka, V. Sychrovský, P. Bouř and Y. Tanaka, *J. Phys. Chem. A*, 2012, **116**, 8313.
- 74 H. Miyachi, T. Matsui, Y. Shigeta and K. Hirao, *Phys. Chem. Chem. Phys.*, 2010, **12**, 909.
- 75 J. Müller, D. Böhme, P. Lax, M. M. Cerdà and M. Roitzsch, *Chem. – Eur. J.*, 2005, **11**, 6246–6253.
- 76 D. A. Megger, C. Fonseca Guerra, J. Hoffmann, B. Brutschy, F. M. Bickelhaupt and J. Müller, *Chem. – Eur. J.*, 2011, **17**, 6533–6544.
- 77 T. Marino, N. Russo, M. Toscano and M. Pavelka, *Dalton Trans.*, 2012, **41**, 1816–1823.
- 78 T. Matsui, H. Miyachi, Y. Nakanishi, Y. Shigeta, T. Sato, Y. Kitagawa, M. Okumura and K. Hirao, *J. Phys. Chem. B*, 2009, **113**, 12790–12795.
- 79 H. Miyachi, T. Matsui, Y. Shigeta, K. Yamashita and K. Hirao, *Chem. Phys. Lett.*, 2010, **495**, 125–130.
- 80 L. Benda, M. Straka, Y. Tanaka and V. Sychrovský, *Phys. Chem. Chem. Phys.*, 2011, **13**, 100–103.
- 81 M. Kauch and M. Pecul, *ChemPhysChem*, 2012, **13**, 1332–1338; M. Kauch and M. Pecul, *ChemPhysChem*, 2012, **13**, 2627.
- 82 S. S. Mallajosyula and S. K. Pati, *J. Phys. Chem. Lett.*, 2010, **1**, 1881–1894.
- 83 J. Zhao, L. Han, H. Yang, J. Liu and Y. Bu, *ChemPhysChem*, 2012, **13**, 3293–3302.
- 84 P. K. Samanta and S. K. Pati, *Chem. – Eur. J.*, 2014, **20**, 1760–1764.
- 85 P. K. Samanta, A. K. Manna and S. K. Pati, *Chem. – Asian J.*, 2012, **7**, 2718–2728.
- 86 A. A. Voityuk, *J. Phys. Chem. B*, 2006, **110**, 21010–21013.
- 87 H. Liu, G. Q. Li, H. Ai, J. Li and Y. Bu, *J. Phys. Chem. C*, 2011, **115**, 22547–22556.
- 88 Y. Nakanishi, T. Matsui, Y. Kitagawa, Y. Shigeta, T. Saito, Y. Kataoka, T. Kawakami, M. Okumura and K. Yamaguchi, *Bull. Chem. Soc. Jpn.*, 2011, **84**, 366–375.
- 89 I. Kratochvílová, M. Golan, M. Vala, M. Špěrová, M. Weiter, O. Páv, J. Šebera, I. Rosenberg, V. Sychrovský, Y. Tanaka and F. M. Bickelhaupt, *J. Phys. Chem. B*, 2014, **118**, 5374–5381.
- 90 P. D. Selid, H. Y. Xu, E. M. Collins, M. S. Face-Collins and J. X. Zhao, *Sensors*, 2009, **9**, 5446–5459.
- 91 G. Aragay, J. Pons and A. Merkoçi, *Chem. Rev.*, 2011, **111**, 3433–3458.
- 92 D. L. Ma, D. S.-H. Chan, B. Y.-W. Man and C.-H. Leung, *Chem. – Asian J.*, 2011, **6**, 986–1003.
- 93 M. Li, H. Gou, I. Al-Ogaidi and N. Wu, *ACS Sustainable Chem. Eng.*, 2013, **1**, 713–723.
- 94 D.-L. Ma, H.-Z. He, K.-H. Leung, H.-J. Zhong, D. S.-H. Chan and C.-H. Leung, *Chem. Soc. Rev.*, 2013, **42**, 3427–3440.
- 95 X. Liu, C. Qi, T. Bing, X. Cheng and D. Shangguan, *Talanta*, 2009, **78**, 253–258.
- 96 Y. S. Wang, C.-C. Cheng, J.-K. Chen, F.-H. Ko and F.-C. Chang, *J. Mater. Chem. A*, 2013, **1**, 7745–7750.
- 97 N. Dave, M. Y. Chan, P.-J. J. Huang, B. D. Smith and J. Liu, *J. Am. Chem. Soc.*, 2010, **132**, 12668–12673.
- 98 P.-J. J. Huang and J. Liu, *Chem. – Eur. J.*, 2011, **17**, 5004–5010.
- 99 Y. Yu, B. W. Zhang, M. Yu, B. Deng, L. F. Li, C. H. Fan and J. Y. Li, *Sci. China: Chem.*, 2012, **55**, 2202–2208.
- 100 M. Kuriyama, K. Haruta, T. Dairaku, T. Kawamura, S. Kikkawa, K. Inamoto, H. Tsukamoto, Y. Kondo, H. Torigoe, I. Okamoto, A. Ono, E. H. Morita and Y. Tanaka, *Chem. Pharm. Bull.*, 2014, **62**, 709–712.
- 101 D. He, X. He, K. Wang, Y. Zhao and Z. Zou, *Langmuir*, 2013, **29**, 5896–5904.
- 102 Y.-W. Lin, H.-T. Ho, C.-C. Huang and H.-T. Chang, *Nucleic Acids Res.*, 2008, **36**, e123.
- 103 H. Torigoe, A. Ono and T. Kozasa, *Transition Met. Chem.*, 2011, **36**, 131–144.
- 104 J. Liu and Y. Lu, *Angew. Chem.*, 2007, **119**, 7731–7734 (*Angew. Chem., Int. Ed.*, 2007, **46**, 7587–7590).
- 105 Z.-G. Wang, J. Elbaz, F. Remacle, R. D. Levine and I. Willner, *Proc. Natl. Acad. Sci. U. S. A.*, 2010, **107**, 21996–22001.
- 106 Z.-G. Wang, J. Elbaz and I. Willner, *Nano Lett.*, 2011, **11**, 304–309.
- 107 D. Li, A. Wieckowska and I. Willner, *Angew. Chem.*, 2008, **120**, 3991–3995 (*Angew. Chem., Int. Ed.*, 2008, **47**, 3927–3931).
- 108 S. Shimron, J. Elbaz, A. Henning and I. Willner, *Chem. Commun.*, 2010, **46**, 3250–3252.
- 109 F. Wang, R. Orbach and I. Willner, *Chem. – Eur. J.*, 2012, **18**, 16030–16036.
- 110 K. S. Park, C. Jung and H. G. Park, *Angew. Chem.*, 2010, **122**, 9951–9954 (*Angew. Chem., Int. Ed.*, 2010, **49**, 9757–9760).
- 111 T. Ito, G. Nikaido and S. I. Nishimoto, *J. Inorg. Biochem.*, 2007, **101**, 1090–1093.
- 112 J. Joseph and G. B. Schuster, *Org. Lett.*, 2007, **9**, 1843–1846.
- 113 T. Ehrenschwender, W. Schmucker, C. Wellner, T. Augenstein, P. Carl, J. Harmer, F. Breher and H.-A. Wagenknecht, *Chem. – Eur. J.*, 2013, **19**, 12547–12552.
- 114 B. Liu, A. J. Bard, C. Z. Li and H. B. Kraatz, *J. Phys. Chem. B*, 2005, **109**, 5193–5198.
- 115 H. Isobe, N. Yamazaki, A. Asano, T. Fujino, W. Nakanishi and S. Seki, *Chem. Lett.*, 2011, **40**, 318–319.
- 116 S. Liu, G. H. Clever, Y. Takezawa, M. Kaneko, K. Tanaka, X. Guo and M. Shionoya, *Angew. Chem., Int. Ed.*, 2011, **123**, 9048–9052 (*Angew. Chem., Int. Ed.*, 2011, **50**, 8886–8890).
- 117 H. Y. Zhang, A. Calzolari and R. Di Felice, *J. Phys. Chem. B*, 2005, **109**, 15345–15348.
- 118 L. Guo, N. Yin and G. Chen, *J. Phys. Chem. C*, 2011, **115**, 4837–4842.
- 119 K. Tanaka, G. H. Clever, Y. Takezawa, Y. Yamada, C. Kaul, M. Shionoya and T. Carell, *Nat. Nanotechnol.*, 2006, **1**, 190–194 see also: J. Müller, *Nature*, 2006, **444**, 698.
- 120 G. H. Clever and T. Carell, *Angew. Chem.*, 2007, **119**, 254–257 (*Angew. Chem., Int. Ed.*, 2007, **46**, 250–253).
- 121 N. Zimmermann, E. Meggers and P. G. Schultz, *Bioorg. Chem.*, 2004, **32**, 13–25.
- 122 C. Switzer, S. Sinha, P. H. Kim and B. D. Heuberger, *Angew. Chem.*, 2005, **117**, 1553–1556 (*Angew. Chem., Int. Ed.*, 2005, **44**, 1529–1532).
- 123 J. A. Piccirilli, T. Krauch, S. E. Moroney and S. A. Benner, *Nature*, 1990, **343**, 33–37.
- 124 K. M. Guckian, T. R. Krugh and E. T. Kool, *Nat. Struct. Biol.*, 1998, **5**, 954–959.
- 125 I. Hirao, T. Mitsui, M. Kimoto and S. Yokoyama, *J. Am. Chem. Soc.*, 2007, **129**, 15549–15555.
- 126 D. A. Malyshev, Y. J. Seo, P. Ordoukhanian and F. E. Romesberg, *J. Am. Chem. Soc.*, 2009, **131**, 14620–14621.
- 127 N. Minakawa, S. Ogata, M. Takahashi and A. Matsuda, *J. Am. Chem. Soc.*, 2009, **131**, 1644–1645.

- 128 H. Urata, E. Yamaguchi, T. Funai, Y. Matsumura and S.-i. Wada, *Angew. Chem.*, 2010, **122**, 6666–6669 (*Angew. Chem., Int. Ed.*, 2010, **49**, 6516–6519).
- 129 T. Funai, Y. Miyazaki, M. Aotani, E. Yamaguchi, O. Nakagawa, S. Wada, H. Torigoe, A. Ono and H. Urata, *Angew. Chem.*, 2012, **124**, 6570–6572 (*Angew. Chem., Int. Ed.*, 2012, **51**, 6464–6466).
- 130 T. Funai, J. Nakamura, Y. Miyazaki, R. Kiriū, O. Nakagawa, S.-i. Wada, A. Ono and H. Urata, *Angew. Chem.*, 2014, **126**, 6742–6745 (*Angew. Chem., Int. Ed.*, 2014, **53**, 6624–6627).
- 131 T. Tian, S. Peng, H. Xiao, Y. Long, B. Fu, X. Zhang, S. Guo, S. Wang, X. Zhou, S. Liu and X. Zhou, *Chem. Commun.*, 2013, **49**, 10085–10087.
- 132 N. Zimmermann, E. Meggers and P. G. Schultz, *J. Am. Chem. Soc.*, 2002, **124**, 13684–13685.
- 133 E.-K. Kim and C. Switzer, *ChemBioChem*, 2013, **14**, 2403–2407.
- 134 G. Zhu, Y. Li and C.-Y. Zhang, *Chem. Commun.*, 2014, **50**, 572–574.
- 135 C.-K. Chiang, C.-C. Huang, C.-W. Liu and H.-T. Chang, *Anal. Chem.*, 2008, **80**, 3716–3721.
- 136 R. Freeman, T. Finder and I. Willner, *Angew. Chem.*, 2009, **121**, 7958 (*Angew. Chem., Int. Ed.*, 2009, **48**, 7818–7821).
- 137 J.-S. Lee, M. S. Han and C. A. Mirkin, *Angew. Chem.*, 2007, **119**, 4171–4174 (*Angew. Chem., Int. Ed.*, 2007, **46**, 4093–4096).
- 138 T. Li, B. Li, E. Wang and S. Dong, *Chem. Commun.*, 2009, 3551–3553.
- 139 K. S. Park, J. Y. Lee and H. G. Park, *Chem. Commun.*, 2012, **48**, 4549–4551.
- 140 G. Mor-Piperberg, R. Tel-Vered, J. Elbaz and I. Willner, *J. Am. Chem. Soc.*, 2010, **132**, 6878–6879.

High-Resolution Crystal Structure of a Silver(I)–RNA Hybrid Duplex Containing Watson–Crick-like C–Silver(I)–C Metallo-Base Pairs

Jiro Kondo,* Yoshinari Tada, Takenori Dairaku, Hisao Saneyoshi, Itaru Okamoto, Yoshiyuki Tanaka, and Akira Ono

Abstract: Metallo-base pairs have been extensively studied for applications in nucleic acid-based nanodevices and genetic code expansion. Metallo-base pairs composed of natural nucleobases are attractive because nanodevices containing natural metallo-base pairs can be easily prepared from commercially available sources. Previously, we have reported a crystal structure of a DNA duplex containing T–Hg^{II}–T base pairs. Herein, we have determined a high-resolution crystal structure of the second natural metallo-base pair between pyrimidine bases C–Ag^I–C formed in an RNA duplex. One Ag^I occupies the center between two cytosines and forms a C–Ag^I–C base pair through N3–Ag^I–N3 linear coordination. The C–Ag^I–C base pair formation does not disturb the standard A-form conformation of RNA. Since the C–Ag^I–C base pair is structurally similar to the canonical Watson–Crick base pairs, it can be a useful building block for structure-based design and fabrication of nucleic acid-based nanodevices.

Metal-mediated base pairs, which are also called metallo-base pairs, are currently receiving considerable attention because of their potential in nanobiotechnology.^[1] For example, several metallo-base pairs composed of natural and artificial nucleobases have been applied to nucleic acid-based nanodevices, such as metal ion sensors,^[2] electric transport nanowires,^[3] and molecular magnets.^[4] We have been especially focusing on the metallo-base pairs composed

of only natural nucleobases, since nucleic acids containing such base pairs can be easily prepared from commercially available sources. The first metallo-base pair composed of natural nucleobases found in DNA duplex is a T–Hg^{II}–T base pair.^[5] Very recently, more than a half century after discovery of the natural metallo-base pair,^[5a] tertiary structures of DNA duplexes containing the T–Hg^{II}–T base pairs have been finally solved by our X-ray and NMR studies.^[6] The first natural metallo-base pair found in RNA duplex is a G–Au^{III}–C base pair, which was incidentally obtained by heavy metal soaking into crystals of the HIV-1 RNA dimerization-initiation site,^[7] though specificity between Au^{III} and the Watson–Crick G=C base pair is not well understood and occupancy of Au^{III} is only 0.35.

Our discovery of the next metallo-base pair composed of natural nucleobases, a silver-mediated C–C base pair (C–Ag^I–C), expanded the possibilities for application of natural metallo-base pairs to nanobiotechnology.^[8] We have observed by melting temperature analyses that Ag^I significantly stabilizes a DNA duplex d(A₁₀CA₁₀)/d(T₁₀CT₁₀) containing a CC mismatch at the center. However, other metal ions tested (Hg^{II}, Cu^{II}, Ni^{II}, Pd^{II}, Co^{II}, Mn^{II}, Zn^{II}, Pb^{II}, Cd^{II}, Mg^{II}, Ca^{II}, Fe^{II}, Fe^{III}, and Ru^{III}) did not affect the stability of the DNA duplex, suggesting that the CC mismatch selectively captures Ag^I.^[8] The specific binding of Ag^I to the CC mismatch has been confirmed by 1D ¹H NMR spectroscopy, CD spectroscopy, electrospray ionization mass spectroscopy, and isothermal titration calorimetry (ITC).^[8,9] The ITC-derived binding constant of the complex between Ag^I and a DNA duplex containing a CC mismatch is nearly 10⁶ M⁻¹, which is significantly larger than those observed for non-specific interactions between metal ions and DNA (10³–10⁵ M⁻¹).^[9] The 1:1 binding stoichiometry between Ag^I and the CC mismatch was also quantitatively determined by the ITC experiment and 1D ¹H NMR spectroscopy.^[8,9] However, detailed structural information of a nucleic acid duplex containing the C–Ag^I–C base pair has long been missing. Herein, we have successfully determined the crystal structure of an RNA duplex containing the C–Ag^I–C base pairs at a resolution of 1.3 Å. So far, the C–Ag^I–C base pair has been extensively applied for developing several nucleic acid-based nanodevices^[10] and for genetic code expansion^[11] even without its detailed structural information. The present high-resolution crystal structure of the C–Ag^I–C base pair, together with our previously reported crystal and solution structures of the T–Hg^{II}–T base pair^[6] open the possibility of structure-based design of nanodevices containing natural metallo-base pairs.

[*] Dr. J. Kondo

Department of Materials and Life Sciences
 Faculty of Science and Technology, Sophia University
 7-1 Kioi-cho, Chiyoda-ku, Tokyo 102-8554 (Japan)
 E-mail: j.kondo@sophia.ac.jp

Dr. J. Kondo, Y. Tada
 Graduate School of Science and Technology
 Sophia University
 7-1 Kioi-cho, Chiyoda-ku, Tokyo 102-8554 (Japan)

Dr. T. Dairaku, Prof. Y. Tanaka
 Laboratory of Molecular Transformation
 Graduate School of Pharmaceutical Sciences
 Tohoku University
 6-3 Aza-Aoba, Aramaki, Aoba-ku, Sendai 980-8578 (Japan)

Dr. H. Saneyoshi, Dr. I. Okamoto, Prof. A. Ono
 Department of Material and Life Chemistry
 Faculty of Engineering, Kanagawa University
 3-27-1 Rokkakubashi, Kanagawa-ku, Yokohama 221-8686 (Japan)

Prof. Y. Tanaka
 Faculty of Pharmaceutical Sciences
 Tokushima Bunri University
 Yamashiro-cho, 770-8514 Tokushima (Japan)

Supporting information for this article is available on the WWW under <http://dx.doi.org/10.1002/anie.201507894>.

The RNA dodecamer r(GGACU[dC^{Br}]GACUCC) (RNA-C₄C₉; dC^{Br} = 5-bromo-2'-deoxycytosine), designed to form a self-complementary duplex containing two CC mismatches, was chemically synthesized (Gene Design Inc. Japan) and purified by denatured polyacrylamide gel electrophoresis and reverse phase chromatography. A 5-bromo-2'-deoxycytosine is introduced at the sixth position for resolving the phase problem by the anomalous dispersion method. Needle-shaped and rod-shaped single crystals of RNA-C₄C₉ were grown in conditions with and without Ag^I, respectively (RNA-C₄C₉/Ag^I and RNA-C₄C₉ crystals; Supporting Information, Table S1). To confirm whether linearly coordinating Hg^{II} binds to the CC mismatch or not, the RNA was also crystallized in the presence of Hg^{II}, and rod-shaped single crystals were obtained (RNA-C₄C₉/Hg^{II} crystal; Supporting Information, Table S1). These crystal structures are deposited in the Protein Data Bank (PDB) with the ID codes 5AY2, 5AY3, and 5AY4 (Supporting Information, Table S2). Details of materials and methods are found in the Supporting Information.

In the RNA-C₄C₉/Ag^I crystal, an asymmetric unit was composed of two RNA duplexes (Supporting Information, Figure S1a). These duplexes are almost identical to each other (Figure S1b). At the center and both ends of these duplexes, the canonical Watson–Crick G=C and A=U base pairs are formed. At the fourth and ninth positions of these duplexes, Watson–Crick-like C–Ag^I–C metallo-base pairs are formed as expected (Figure 1a,b). The local helical parameters, intra-base pair parameters and pseudorotation phase angles indicate that these RNA duplexes maintain the standard A-form conformation, regardless of C–Ag^I–C formation (Supporting Information, Tables S3, S4).

The $2|F_o| - |F_c|$ electron density maps and the molecular models of the C–Ag^I–C base pairs show that one Ag^I is placed at the center of a CC mismatch (Figure 1c; Supporting Information, Figure S2). The distances between the N3 atoms

of the C₄ and C₉ residues and Ag^I are 2.2–2.3 Å, indicating that N3 coordinates to Ag^I by using its lone pair. The N3–Ag^I–N3 angles are 177–180°. The linear coordination is very similar to that observed in a previously reported NMR structure of a DNA duplex containing a synthetic metallo-base pair, imidazole–Ag^I–imidazole, in which the Ag^I–N3 distances are 2.1 Å.^[12] The propeller twist angles of the C–Ag^I–C base pairs (–29––27°) are remarkably larger than those of the canonical Watson–Crick base pairs in the A-form RNA duplex (–12°) (Figure 1d; Supporting Information, Figure S2, Table S3). The propeller twist along the linear N3–Ag^I–N3 bond apparently occurs owing to the repulsion between amino groups at the fourth positions of cytosines. In fact, the N4–N4 distances (4.9–5.1 Å) are longer than the O2–O2 distances (3.9–4.4 Å). The Ag^I does not make any special interaction with the upper and lower base pairs. The distances of C1'–C1' (9.1–9.6 Å) of the C–Ag^I–C base pairs are about 1 Å shorter than that of the canonical Watson–Crick base pairing (10.7 Å). However, RNA maintains the A-form conformation.

The detailed geometry of the C–Ag^I–C base pair agrees with the previously determined 1:1 binding stoichiometry between Ag^I and the CC mismatch,^[9] and is very similar to that of the T–Hg^{II}–T base pair solved by our X-ray analysis, where one Hg^{II} is placed at the center of a TT mismatch and makes linear coordination to two deprotonated N3 atoms of T residues with 2.0 Å distances (Supporting Information, Figure S3a).^[6] On the other hand, the geometry is completely different from a complex between Ag^I and 1-methylcytosine where two Ag^I ions bridge between two 1-methylcytosines in *trans* geometry through O2–Ag^I–N3 coordinate bonds (Supporting Information, Figure S3b),^[13] and also from a complex between Pt^{II} and cytosine where one Pt^{II} ion makes square planar coordination with two cytosines and two ammonias (Supporting Information, Figure S3c).^[14]

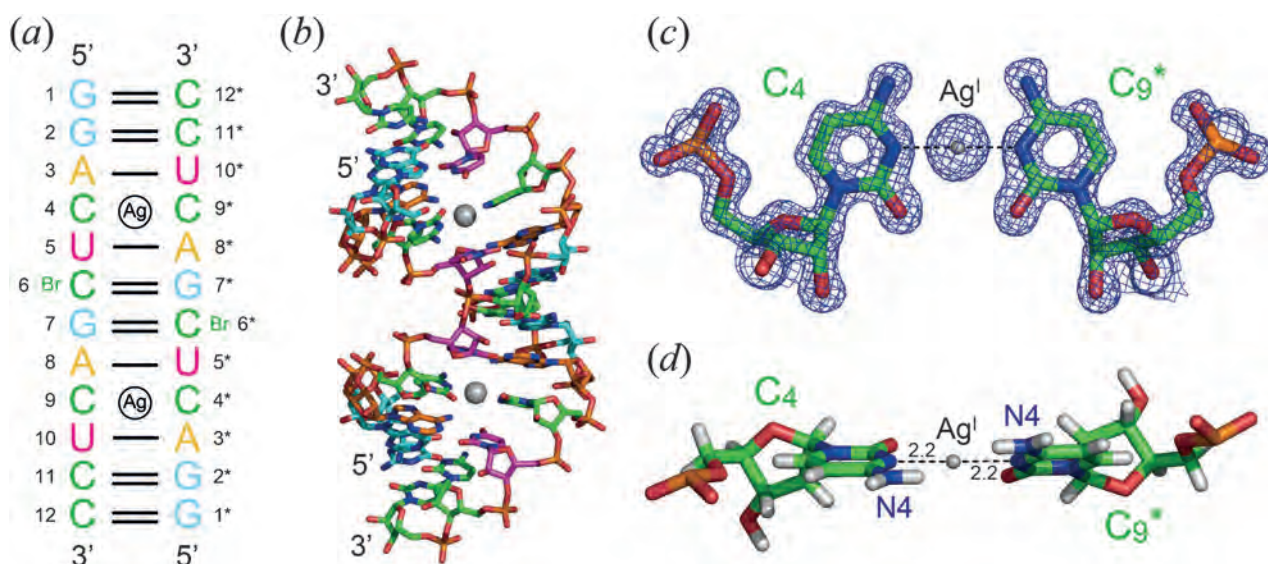


Figure 1. Secondary (a) and crystal structures (b) of the A-form RNA duplex obtained in the presence of Ag^I and local structure of C–Ag^I–C base pair (top view with local $2|F_o| - |F_c|$ (blue: 1.5 σ contour level) map (c), and side view (d). In these figures, Ag^I ions are shown as gray spheres. Coordinate bonds between N3 of C and Ag^I are represented by dashed lines with distances in Å.

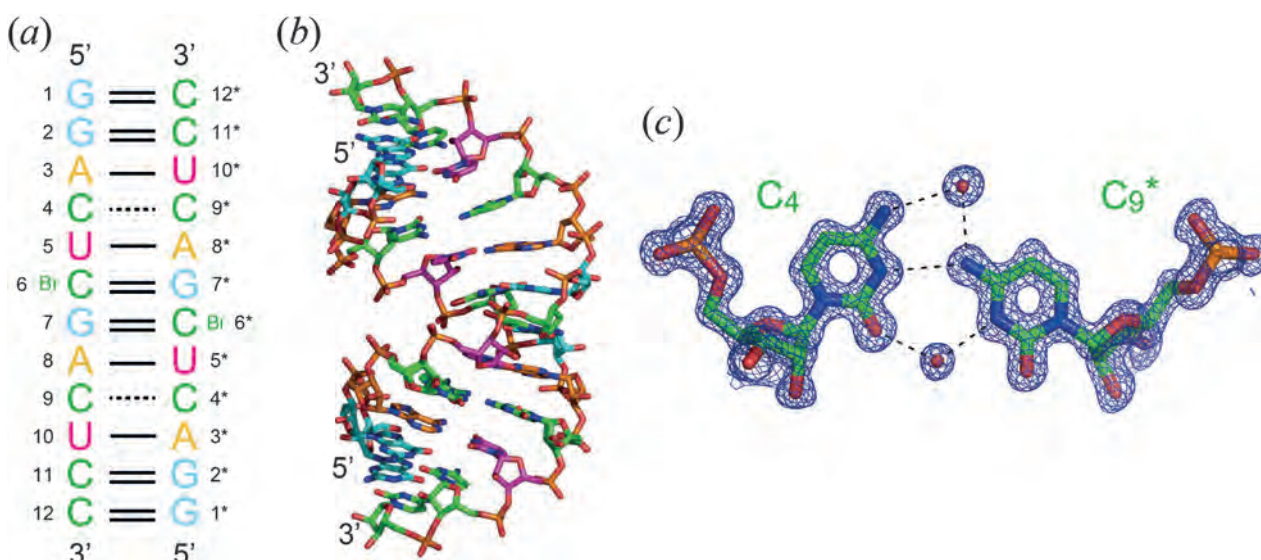


Figure 2. Secondary (a) and crystal structures (b) of the A-form RNA duplex obtained in the absence of Ag^{I} and local structure of water-mediated C–C base pair (top view with local $2|F_o| - |F_c|$ (blue: 1.5 σ contour level) map (c)). Hydrogen bonds are represented by dashed lines.

In the absence of Ag^{I} , RNA- C_4C_9 adopts the A-form double helical structure (Figure 2). The duplex is almost identical to the two duplexes obtained in the presence of Ag^{I} (Supporting Information, Figure S4). In the duplex, two CC mismatches form asymmetrical water-mediated C–C base pairs through one direct hydrogen bond $\text{N3}(\text{C}_4)\cdots\text{H}-\text{N4}(\text{C}_9^*)$, and two water-mediated hydrogen bonds $\text{N4}(\text{C}_4)-\text{H}\cdots\text{O}\cdots\text{H}-\text{N4}(\text{C}_9^*)$ and $\text{O2}(\text{C}_4)\cdots\text{H}-\text{O}-\text{H}\cdots\text{N3}(\text{C}_9^*)$ (Figure 2c; Supporting Information, Figure S5). The base pair is different from the *cis* Watson–Crick C–C⁺ base pair with $\text{O2}(\text{C})\cdots\text{H}-\text{N3}(\text{C}^+)$ and $\text{N3}(\text{C})\cdots\text{H}-\text{N4}(\text{C}^+)$ hydrogen bonds (Supporting Information, Figure S3d).^[15] In the case of the C_4-C_9^* base pair, C_4 stays at its usual position and C_9^* shifts toward the minor groove of the RNA duplex, thereby making a well-ordered C_4-C_9^* base pair. On the other hand, the C_9-C_4^* base pair is disordered between two conformations (Supporting Information, Figure S5b). Since the $\text{C1}'-\text{C1}'$ distances of the two water-mediated C–C base pairs (10.7–10.8 Å) are very similar to those of the Watson–Crick base pairs (10.6 Å in average), the RNA duplex is not distorted at all (Supporting Information, Tables S5, S6).

To confirm the Ag^{I} -selectivity of the CC mismatch, we have also determined a structure of the RNA- $\text{C}_4\text{C}_9/\text{Hg}^{\text{II}}$ crystal obtained in the presence of Hg^{II} . The RNA- $\text{C}_4\text{C}_9/\text{Hg}^{\text{II}}$ crystal is isomorphous with the RNA- C_4C_9 crystal obtained in the absence of Ag^{I} (Supporting Information, Table S2) and RNA duplexes observed in these crystals are identical to each other (Supporting Information, Figure S6). In agreement with our previous result of melting temperature analyses,^[8] Hg^{II} did not bind to the CC mismatches in the RNA- C_4C_9 duplex (Supporting Information, Figure S7). Any strong electron density of Hg^{II} was not observed, meaning that Hg^{II} ions may exist in the crystal lattice but their bindings to the RNA duplex are not specific.

In the past decade, several natural^[8,9,11,16] and artificial^[12,17] Ag^{I} -mediated base pairs have been found and

constructed. However, only one detailed tertiary structure, a DNA duplex containing imidazole- Ag^{I} -imidazole base pairs determined by NMR, has been reported so far.^[12] In the present study, we have successfully determined high resolution crystal structures of RNA duplexes containing CC mismatches in the presence and absence of Ag^{I} and Hg^{II} . These crystal structures revealed the following: i) Ag^{I} specifically binds to the CC mismatch and forms the C– Ag^{I} –C base pair through $\text{N3}-\text{Ag}^{\text{I}}-\text{N3}$ linear coordination; ii) Ag^{I} does not disturb the standard A-form conformation of RNA by forming the C– Ag^{I} –C base pairs; iii) the C– Ag^{I} –C base pair is structurally similar to the canonical Watson–Crick base pairs as well as T– Hg^{II} –T metallo-base pair; iv) the Ag^{I} -selectivity of the CC mismatch was crystallographically confirmed. Now we have detailed structural information of the two Watson–Crick-like metallo-base pairs T– Hg^{II} –T and C– Ag^{I} –C, which are composed of natural nucleobases and have high metal ion selectivity. This information opens the door to the possibility of structure-based design of nucleic acid-based nanodevices containing the natural metallo-base pairs.

Acknowledgements

This work was supported by a Grant-in-Aid for Scientific Research (A) (No. 24245037) and in part by a Strategic Research Foundation Grant-aided Project for Private Universities (No. S1201015) from the Ministry of Education, Culture, Sports, Science and Technology, Japan (MEXT). We thank the Photon Factory for provision of synchrotron radiation facilities (No. 2013G727) and acknowledge the staff of the BL-17A and NW12A beamlines.

Keywords: crystal structure · metallo-base pairs · RNA · silver · X-ray analysis

How to cite: *Angew. Chem. Int. Ed.* **2015**, *54*, 13323–13326
Angew. Chem. **2015**, *127*, 13521–13524

- [1] a) G. H. Clever, C. Kaul, T. Carell, *Angew. Chem. Int. Ed.* **2007**, *46*, 6226–6236; *Angew. Chem.* **2007**, *119*, 6340–6350; b) A. Ono, H. Torigoe, Y. Tanaka, I. Okamoto, *Chem. Soc. Rev.* **2011**, *40*, 5855–5866; c) Y. Takezawa, M. Shionoya, *Acc. Chem. Res.* **2012**, *45*, 2066–2076; d) P. Scharf, J. Müller, *ChemPlusChem* **2013**, *78*, 20–34.
- [2] a) A. Ono, H. Togashi, *Angew. Chem. Int. Ed.* **2004**, *43*, 4300–4302; *Angew. Chem.* **2004**, *116*, 4400–4402; b) E. M. Nolan, S. J. Lippard, *Chem. Rev.* **2008**, *108*, 3443–3480; c) D. L. Ma, D. S. Chan, B. Y. Man, C. H. Leung, *Chem. Asian J.* **2011**, *6*, 986–1003; d) Y. Song, W. Wei, X. Qu, *Adv. Mater.* **2011**, *23*, 4215–4236.
- [3] a) T. Carell, C. Behrens, J. Gierlich, *Org. Biomol. Chem.* **2003**, *1*, 2221–2228; b) T. Ito, G. Nikaido, S. Nishimoto, *J. Inorg. Biochem.* **2007**, *101*, 1090–1093; c) J. Joseph, G. B. Schuster, *Org. Lett.* **2007**, *9*, 1843–1846; d) L. Guo, N. Yin, G. Chen, *J. Phys. Chem. C* **2011**, *115*, 4837–4842; e) H. Isobe, N. Yamazaki, A. Asano, T. Fujino, W. Nakanishi, S. Seki, *Chem. Lett.* **2011**, *40*, 318–319; f) S. Liu, G. H. Clever, Y. Takezawa, M. Kaneko, K. Tanaka, X. Guo, M. Shionoya, *Angew. Chem. Int. Ed.* **2011**, *50*, 8886–8890; *Angew. Chem.* **2011**, *123*, 9048–9052.
- [4] a) K. Tanaka, A. Tengeji, T. Kato, N. Toyama, M. Shionoya, *Science* **2003**, *299*, 1212–1213; b) S. S. Mallajosyula, S. K. Pati, *Angew. Chem. Int. Ed.* **2009**, *48*, 4977–4981; *Angew. Chem.* **2009**, *121*, 5077–5081; c) G. H. Clever, S. J. Reitmeier, T. Carell, O. Schiemann, *Angew. Chem. Int. Ed.* **2010**, *49*, 4927–4929; *Angew. Chem.* **2010**, *122*, 5047–5049.
- [5] a) S. Katz, *Nature* **1962**, *195*, 997–998; b) S. Katz, *Biochim. Biophys. Acta Spec. Sect. Nucleic Acids Relat. Subj.* **1963**, *68*, 240–253; c) Z. Kuklenyik, L. G. Marzilli, *Inorg. Chem.* **1996**, *35*, 5654–5662; d) Y. Miyake, H. Togashi, M. Tashiro, H. Yamaguchi, S. Oda, M. Kudo, Y. Tanaka, Y. Kondo, R. Sawa, T. Fujimoto, T. Machinami, A. Ono, *J. Am. Chem. Soc.* **2006**, *128*, 2172–2173; e) Y. Tanaka, S. Oda, H. Yamaguchi, Y. Kondo, C. Kojima, A. Ono, *J. Am. Chem. Soc.* **2007**, *129*, 244–245.
- [6] a) J. Kondo, T. Yamada, C. Hirose, I. Okamoto, Y. Tanaka, A. Ono, *Angew. Chem. Int. Ed.* **2014**, *53*, 2385–2388; *Angew. Chem.* **2014**, *126*, 2417–2420; b) H. Yamaguchi, J. Šebera, J. Kondo, S. Oda, T. Komuro, T. Kawamura, T. Dairaku, Y. Kondo, I. Okamoto, A. Ono, J. V. Burda, C. Kojima, V. Sychrovský, Y. Tanaka, *Nucleic Acids Res.* **2014**, *42*, 4094–4099.
- [7] E. Ennifar, P. Walter, P. Dumas, *Nucleic Acids Res.* **2003**, *31*, 2671–2682.
- [8] A. Ono, S. Cao, H. Togashi, M. Tashiro, T. Fujimoto, T. Machinami, S. Oda, Y. Miyake, I. Okamoto, Y. Tanaka, *Chem. Commun.* **2008**, 4825–4827.
- [9] a) H. Torigoe, I. Okamoto, T. Dairaku, Y. Tanaka, A. Ono, T. Kozasa, *Biochimie* **2012**, *94*, 2431–2440; b) H. Torigoe, Y. Miyakawa, A. Ono, T. Kozasa, *Nucleosides Nucleotides Nucleic Acids* **2011**, *30*, 149–167.
- [10] a) T. Li, L. Shi, E. Wang, S. Dong, *Chem. Eur. J.* **2009**, *15*, 3347–3350; b) S. Shimron, J. Elbaz, A. Henning, I. Willner, *Chem. Commun.* **2010**, 46, 3250–3252; c) Y. Wang, J. Li, H. Wang, J. Jin, J. Liu, K. Wang, W. Tan, R. Yang, *Anal. Chem.* **2010**, *82*, 6607–6612; d) C. Zhao, K. Qu, Y. Song, C. Xu, J. Ren, X. Qu, *Chem. Eur. J.* **2010**, *16*, 8147–8154; e) D. Q. Feng, G. Liu, W. Zheng, J. Liu, T. Chen, D. Li, *Chem. Commun.* **2011**, 47, 8557–8559; f) H. Gong, X. Li, *Analyst* **2011**, *136*, 2242–2246; g) W. Y. Xie, W. T. Huang, N. B. Li, H. Q. Luo, *Analyst* **2011**, *136*, 4130–4133; h) W. Y. Xie, W. T. Huang, N. B. Li, H. Q. Luo, *Chem. Commun.* **2012**, *48*, 82–84; i) J. Ding, W. Qin, Y. Zhang, X. Wang, *Biosens. Bioelectron.* **2013**, *45*, 148–151; j) Q. Yang, F. Li, Y. Huang, H. Xu, L. Tang, L. Wang, C. Fan, *Analyst* **2013**, *138*, 2057–2060; k) G. Xu, G. Wang, X. He, Y. Zhu, L. Chen, X. Zhang, *Analyst* **2013**, *138*, 6900–6906; l) W. Guo, X. J. Qi, R. Orbach, C. H. Lu, L. Freage, I. Mironi-Harpaz, D. Seliktar, H. H. Yang, I. Willner, *Chem. Commun.* **2014**, *50*, 4065–4068; m) Y. Wei, B. Li, X. Wang, Y. Duan, *Biosens. Bioelectron.* **2014**, *58*, 276–281; n) P. Miao, K. Han, B. Wang, G. Luo, P. Wang, M. Chen, Y. Tang, *Sci. Rep.* **2015**, *5*, 9161; o) A. L. Sun, K. Deng, W. L. Fu, *Biosens. Bioelectron.* **2015**, *74*, 66–70; p) M. Lu, L. Xu, X. Zhang, R. Xiao, Y. Wang, *Biosens. Bioelectron.* **2015**, *73*, 195–201.
- [11] a) K. S. Park, C. Jung, H. G. Park, *Angew. Chem. Int. Ed.* **2010**, *49*, 9757–9760; *Angew. Chem.* **2010**, *122*, 9951–9954; b) T. Funai, Y. Miyazaki, M. Aotani, E. Yamaguchi, O. Nakagawa, S. Wada, H. Torigoe, A. Ono, H. Urata, *Angew. Chem. Int. Ed.* **2012**, *51*, 6464–6466; *Angew. Chem.* **2012**, *124*, 6570–6572; c) T. Funai, J. Nakamura, Y. Miyazaki, R. Kiriu, O. Nakagawa, S. Wada, A. Ono, H. Urata, *Angew. Chem. Int. Ed.* **2014**, *53*, 6624–6627; *Angew. Chem.* **2014**, *126*, 6742–6745.
- [12] a) S. Johannsen, N. Megger, D. Böhme, R. K. O. Sigel, J. Müller, *Nat. Chem.* **2010**, *2*, 229–234; b) S. Kumbhar, S. Johannsen, R. K. O. Sigel, M. P. Waller, J. Müller, *J. Inorg. Biochem.* **2013**, *127*, 203–210.
- [13] a) T. J. Kistenmacher, M. Rossi, L. G. Marzilli, *Inorg. Chem.* **1979**, *18*, 240–244; b) L. G. Marzilli, T. J. Kistenmacher, M. Rossi, *J. Am. Chem. Soc.* **1977**, *99*, 2797–2798.
- [14] A. Khutia, P. J. Sanz Miguel, B. Lippert, *Chem. Eur. J.* **2011**, *17*, 4195–4204.
- [15] a) N. B. Leontis, J. Stombaugh, E. Westhof, *Nucleic Acids Res.* **2002**, *30*, 3497–3531; b) P. Auffinger, Y. Hashem, *Bioinformatics* **2007**, *23*, 1035–1037.
- [16] a) T. Ono, K. Yoshida, Y. Saotome, R. Sakabe, I. Okamoto, A. Ono, *Chem. Commun.* **2011**, 47, 1542–1544; b) D. A. Megger, J. Müller, *Nucleosides Nucleotides Nucleic Acids* **2010**, *29*, 27–38; c) T. Ihara, T. Ishii, N. Araki, A. W. Wilson, A. Jyo, *J. Am. Chem. Soc.* **2009**, *131*, 3826–3827; d) H. Urata, E. Yamaguchi, Y. Nakamura, S. Wada, *Chem. Commun.* **2011**, 47, 941–943; e) I. Okamoto, K. Iwamoto, Y. Watanabe, Y. Miyake, A. Ono, *Angew. Chem. Int. Ed.* **2009**, *48*, 1648–1651; *Angew. Chem.* **2009**, *121*, 1676–1679; f) I. Okamoto, T. Ono, R. Sameshima, A. Ono, *Chem. Commun.* **2012**, *48*, 4347–4349; g) H. A. Day, C. Huguin, Z. A. E. Waller, *Chem. Commun.* **2013**, *49*, 7696–7698.
- [17] a) K. Tanaka, Y. Yamada, M. Shionoya, *J. Am. Chem. Soc.* **2002**, *124*, 8802–8803; b) N. Zimmermann, E. Meggers, P. G. Schultz, *J. Am. Chem. Soc.* **2002**, *124*, 13684–13685; c) D. A. Megger, C. F. Guerra, J. Hoffmann, B. Brutschy, F. M. Bickelhaupt, J. Müller, *Chem. Eur. J.* **2011**, *17*, 6533–6544; d) D. Böhme, N. Düpre, D. A. Megger, J. Müller, *Inorg. Chem.* **2007**, *46*, 10114–10119; e) D. Shin, C. Switzer, *Chem. Commun.* **2007**, 4401–4403; f) B. D. Heuberger, D. Shin, C. Switzer, *Org. Lett.* **2008**, *10*, 1091–1094; g) K. Petrovec, B. J. Ravoo, J. Müller, *Chem. Commun.* **2012**, *48*, 11844–11846; h) K. S. Park, J. Y. Lee, H. G. Park, *Chem. Commun.* **2012**, *48*, 4549–4551; i) I. Sinha, J. Kösters, A. Hepp, J. Müller, *Dalton Trans.* **2013**, *42*, 16080–16089; j) H. Mei, I. Röhl, F. Seela, *J. Org. Chem.* **2013**, *78*, 9457–9463; k) S. Hensel, N. Megger, K. Schweizer, J. Müller, *Beilstein J. Org. Chem.* **2014**, *10*, 2139–2144; l) T. Richters, O. Krug, J. Kösters, A. Hepp, J. Müller, *Chem. Eur. J.* **2014**, *20*, 7811–7818; m) T. Richters, J. Müller, *Eur. J. Inorg. Chem.* **2014**, 437–441; n) H. Mei, H. Yang, I. Röhl, F. Seela, *ChemPlusChem* **2014**, *79*, 914–918; o) H. Mei, S. A. Ingale, F. Seela, *Chem. Eur. J.* **2014**, *20*, 16248–16257; p) I. Sinha, C. F. Guerra, J. Müller, *Angew. Chem. Int. Ed.* **2015**, *54*, 3603–3606; *Angew. Chem.* **2015**, *127*, 3674–3677.

Received: August 24, 2015

Published online: October 8, 2015



Cite this: *Chem. Commun.*, 2015, 51, 8488

Received 23rd March 2015,
Accepted 10th April 2015

DOI: 10.1039/c5cc02423d

www.rsc.org/chemcomm

Direct detection of the mercury–nitrogen bond in the thymine–Hg^{II}–thymine base-pair with ¹⁹⁹Hg NMR spectroscopy†

Takenori Dairaku,^{‡a} Kyoko Furuita,^{‡b} Hajime Sato,^{‡c} Jakub Šebera,^{‡de} Daichi Yamanaka,^a Hiroyuki Otaki,^a Shoko Kikkawa,^a Yoshinori Kondo,^a Ritsuko Katahira,^b F. Matthias Bickelhaupt,^{fg} Célia Fonseca Guerra,^f Akira Ono,^h Vladimír Sychrovský,^{*d} Chojiro Kojima^{*b} and Yoshiyuki Tanaka^{*ai}

We have observed the 1-bond ¹⁹⁹Hg–¹⁵N J-coupling (¹J(¹⁹⁹Hg,¹⁵N) = 1050 Hz) within the Hg^{II}-mediated thymine–thymine base pair (T–Hg^{II}–T). This strikingly large ¹J(¹⁹⁹Hg,¹⁵N) is the first one for canonical sp²-nitrogen atoms, which can be a sensitive structure-probe of N-mercured compounds and a direct evidence for N-mercuration.

Mercury-199 NMR spectroscopy is used to probe coordination modes, coordinating elements, and the nature of metals in biomolecules.¹ Within the ¹⁹⁹Hg NMR data, those for N–Hg bonds are of particular importance as metals in proteins and in DNA/RNA molecules frequently interact with nitrogen atoms. Moreover, the N–Hg^{II} bond formation in the Hg^{II}-mediated thymine–thymine base pair (T–Hg^{II}–T) corresponds to an irregular “deprotonative” N-mercuration in water of a bulk proton source.^{2–7} In addition, extraordinary thermal stability with a positive reaction entropy was observed for N–Hg^{II}–N bonding in a DNA duplex.^{8–12}

The stability of the Hg–DNA complex can be explained partly owing to the metallophilic attraction between Hg atoms in consecutive T–Hg^{II}–T base pairs, and the metallophilic attraction itself is a recent hot topic of inorganic chemistry.^{13–17}

Despite such biological/chemical importance, N–Hg^{II} bonds remained uncharacterized. Particularly, the measurements of ¹J(¹⁹⁹Hg,¹⁵N) is challenging, owing to the large chemical shift anisotropy (CSA) of ¹⁹⁹Hg and low natural abundance of ¹⁵N.¹⁸ The only |¹J(¹⁹⁹Hg,¹⁵N)| value of a linear two-coordinate complex was recorded for (Me₃Si)₂N–Hg^{II}–N(SiMe₃)₂.¹⁹ The |¹J(¹⁹⁹Hg,¹⁵N)| values for other coordination modes of ¹⁹⁹Hg are also limited to Hg^{II}–CyDTA (*trans*-1,2-diaminocyclohexane-*NNN'*-tetraacetate)²⁰ and Hg^{II}–(NHMe₂)₂Cl₂²¹ complexes (Tables S1 and S2 in ESI†). However, in all cases, some of important parameters such as structure, ¹⁵N or ¹⁹⁹Hg NMR chemical shifts ($\delta(^{15}\text{N})$ or $\delta(^{199}\text{Hg})$), 2-bond ¹⁵N–¹⁵N J-couplings across Hg^{II}, (²J(¹⁵N,¹⁵N)) or hybridization state of nitrogen atoms always remained unknown. Therefore, a complete ¹⁹⁹Hg/¹⁵N NMR J/ δ dataset for a structurally well-defined compound has never been recorded so far.

In this sense, the T–Hg^{II}–T base pair (Fig. 1) provides an excellent platform for studying ¹J(¹⁹⁹Hg,¹⁵N), as its chemical and 3-dimensional (3D) structures have been solidly determined^{3,6,7,12,22} and historically accumulated data^{2–4,23,24} are available. Regarding the NMR parameters of the T–Hg^{II}–T base pair, the ¹⁹⁹Hg chemical shift $\delta(^{199}\text{Hg})$,²³ the 2-bond ¹⁵N–¹⁵N J-coupling across Hg^{II}, ²J(¹⁵N,¹⁵N)⁶ and $\delta(^{15}\text{N})$ ⁶ were previously determined. Hence, the only missing NMR parameter for characterizing the unique physicochemical properties of the N–Hg^{II} bond is ¹J(¹⁹⁹Hg,¹⁵N). Once it is measured for T–Hg^{II}–T, the T–Hg^{II}–T system will provide a complete J/ δ dataset for ¹⁹⁹Hg/¹⁵N with a reliable structure, and the ¹J(¹⁹⁹Hg,¹⁵N) value may provide a key concept for constructing molecular devices^{8,25–44} from Hg^{II}–DNA complexes.

To measure ¹J(¹⁹⁹Hg,¹⁵N) in T–Hg^{II}–T, its highly soluble ¹⁵N-labeled complex is crucial for ¹⁹⁹Hg/¹⁵N signal detection. In addition, Hg^{II}–ligand exchanges must be suppressed to avoid the disappearance of ¹J(¹⁹⁹Hg,¹⁵N) owing to exchange broadening. Considering these facts, we determined the ¹J(¹⁹⁹Hg,¹⁵N) value by using a thymidine–Hg^{II}–thymidine complex (T–Hg^{II}–T).

^a Graduate School of Pharmaceutical Sciences, Tohoku University, 6-3 Aza-Aoba, Aramaki, Aoba-ku, Sendai, Miyagi 980-8578, Japan.

E-mail: tanaka@mail.pharm.tohoku.ac.jp

^b Institute for Protein Research, Osaka University, 3-2 Yamadaoka, Suita, Osaka 565-0871, Japan. E-mail: kojima@protein.osaka-u.ac.jp

^c Application, Bruker BioSpin K.K., 3-9 Moriya-cho, Kanagawa-ku, Yokohama, Kanagawa 221-0022, Japan

^d Institute of Organic Chemistry and Biochemistry, Academy of Sciences of the Czech Republic, v.v.i., Flemingovo náměstí 2, 16610, Praha 6, Czech Republic. E-mail: vladimir.sychrovsky@uochb.cas.cz

^e Institute of Physics, Academy of Sciences of the Czech Republic, v.v.i., Na Slovance 2, CZ-182 21 Prague 8, Czech Republic

^f Department of Theoretical Chemistry and Amsterdam Center for Multiscale Modeling (ACMM), VU University Amsterdam, De Boelelaan 1083, NL-1081 HV Amsterdam, The Netherlands

^g Institute for Molecules and Materials (IMM), Radboud University Nijmegen, Heyendaalseweg 135, NL-6525 AJ Nijmegen, The Netherlands

^h Department of Material & Life Chemistry, Kanagawa University, 3-27-1 Rokkakubashi, Kanagawa-ku, Yokohama, Kanagawa 221-8686, Japan

ⁱ Faculty of Pharmaceutical Sciences, Tokushima Bunri University, Yamashiro-cho, Tokushima 770-8514, Japan. E-mail: tanakay@ph.bunri-u.ac.jp

† Electronic supplementary information (ESI) available: Additional information as noted in text. See DOI: 10.1039/c5cc02423d

‡ These authors contributed equally to this work.

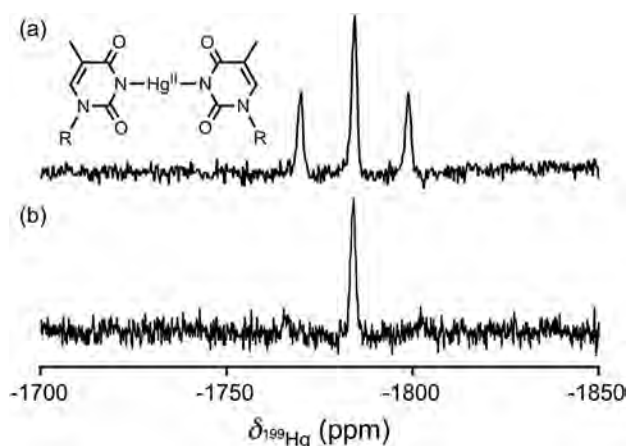


Fig. 1 One-dimensional ^{199}Hg NMR spectrum (71.667 MHz for ^{199}Hg frequency) of the thymidine- Hg^{II} -thymidine complex (25 mM) in DMSO-d_6 under natural abundance ^{199}Hg (16.84%). (a) The 1D ^{199}Hg NMR spectrum without ^{15}N -decoupling. (b) The 1D ^{199}Hg NMR spectrum with ^{15}N -decoupling. The ^{199}Hg NMR chemical shifts are displayed with respect to dimethylmercury (0 ppm) using 1 M HgCl_2 in DMSO-d_6 as a secondary reference (-1501 ppm).⁵⁵ The chemical structure of the T- Hg^{II} -T is depicted above the spectrum, with “R” denoting ribose.

To confirm if the splitting of the ^{199}Hg resonance is $^1J(^{199}\text{Hg},^{15}\text{N})$, we monitored the disappearance of the splitting upon ^{15}N -decoupling using a special NMR probe for detecting ^{15}N -heteronucleus correlations. Lastly, the derived $^1J(^{199}\text{Hg},^{15}\text{N})$ value was also investigated theoretically with relativistic density functional theory (DFT) including spin-orbit coupling effects.

In this study, we used ^{15}N -labeled thymidine to produce ^{15}N -labeled T- Hg^{II} -T. To suppress the exchange of Hg^{II} ligands, we prepared a sample that contained T- Hg^{II} -T exclusively, without any anion (competitive Hg^{II} -ligands against thymine). Such sample was prepared by the reaction [thymidine + $\text{HgO} \rightarrow \text{T-Hg}^{\text{II}}\text{-T} + \text{H}_2\text{O}$] followed by H_2O evaporation.²⁴ The resulting pure ^{15}N -labeled T- Hg^{II} -T was subjected to ^{199}Hg NMR measurements in dimethyl sulfoxide- d_6 (DMSO-d_6) (Fig. 1). The ^{199}Hg NMR signal was successfully observed as a triplet resonance at $\delta(^{199}\text{Hg}) = -1784$ ppm, with the absolute 1J -value $|^1J(^{199}\text{Hg},^{15}\text{N})| = 1050$ Hz (Fig. 1 and Table 1). The observed $\delta(^{199}\text{Hg})$ value was the same as that observed previously in T- Hg^{II} -T,²³ which ensured successful sampling.

The ^{199}Hg NMR spectrum under ^{15}N -decoupling and ^{15}N NMR spectrum were recorded to exclude the possibility that the observed splitting of the ^{199}Hg signal might arise from a structural polymorphism. Notably, the splitting disappeared upon the ^{15}N -decoupling (Fig. 1b). It should be further noted that this ^{15}N -decoupled ^{199}Hg NMR spectrum can't be recorded with conventionally available probes. This measurement became possible only by using the special probe, which can perform a ^{15}N - ^{199}Hg double resonance spectroscopy. In addition, the splitting of the ^{15}N resonance (1050 Hz) was observed as satellite peaks at $\delta(^{15}\text{N}) = 184$ ppm in the 1-dimensional ^{15}N NMR spectrum (Fig. S1 in ESI†). Thus, the splitting of the ^{199}Hg resonance shown in Fig. 1a should be interpreted as $^1J(^{199}\text{Hg},^{15}\text{N})$.

The $|^1J(^{199}\text{Hg},^{15}\text{N})|$ value of 1050 Hz for T- Hg^{II} -T was strikingly larger than the 1J -coupling of $(\text{Me}_3\text{Si})_2\text{N-Hg}^{\text{II}}\text{-N}(\text{SiMe}_3)_2$ (316.2 Hz),¹⁹

Table 1 Experimental and theoretical ^{199}Hg NMR parameters

Ligand	Method	N-hybrid ^a	$ ^1J_{\text{HgN}} ^b$	$\delta(^{199}\text{Hg})^c$
Thymine ^d	Experiment	sp^2	1050	-1784
	Theory ^e	sp^2	931 ^f	-1848
$\text{N}(\text{SiMe}_3)_2$ ^g	Experiment	sp^2 -like ^h	316.2 ⁱ	-992 ^j
	Theory ^e	sp^2 -like ^h	278.4 ^f	-827

^a Hybridization state of nitrogen atoms. ^b The “absolute” 1-bond ^{199}Hg - ^{15}N - J -coupling, $|^1J(^{199}\text{Hg},^{15}\text{N})|$, in Hz. ^c ^{199}Hg NMR chemical shift in ppm with respect to dimethylmercury (0 ppm). ^d The T- Hg^{II} -T complex. ^e The theoretical calculation (ZORA-SO-B3LYP/TZ2P) in this work. The average values of $^1J(^{199}\text{Hg},^{15}\text{N})$ and $\delta(^{199}\text{Hg})$ were calculated for rotational conformers of thymidine- Hg^{II} -thymidine, because the energy barrier for rotation around the N- Hg^{II} -N axis was smaller than 1.1 kcal mol⁻¹. The calculated $\delta(^{199}\text{Hg})$ and $^1J_{\text{HgN}}$ values were therefore averaged over respective rotamers (Table S5 in ESI). ^f The “-” sign was calculated for J -coupling (Table S4 in ESI). ^g The $(\text{Me}_3\text{Si})_2\text{N-Hg}^{\text{II}}\text{-N}(\text{SiMe}_3)_2$ complex. ^h See Supporting discussion (ESI) for details. ⁱ Ref. 19. ^j Ref. 53. For chemical shift referencing see the footnote to Table S1 in ESI. It should be noted that ^{15}N ⁶ and ^1H ⁵⁴ chemical shift perturbations for the thymidine- Hg^{II} -thymidine complexation were coherent with those observed for the formation of the T- Hg^{II} -T base-pairs in a DNA duplex (Table S1 in ESI).

Hg^{II} -CyDTA complexes (365.7–395.5 Hz),²⁰ and $\text{Hg}^{\text{II}}\text{-(NHMe}_2)_2\text{Cl}_2$ (14.7 Hz)²¹ (Table 1 and Tables S1 and S2 in ESI†). Thus, the observed $|^1J(^{199}\text{Hg},^{15}\text{N})|$ value for T- Hg^{II} -T is the largest of all 1J -values reported to date.

Here we investigate the correlation between $|^1J(^{199}\text{Hg},^{15}\text{N})|$ value and N-hybridization state. Within the compounds whose $|^1J(^{199}\text{Hg},^{15}\text{N})|$ were reported, T- Hg^{II} -T and $(\text{Me}_3\text{Si})_2\text{N-Hg}^{\text{II}}\text{-N}(\text{SiMe}_3)_2$ possess the linear two-coordinate structure, and their $|^1J(^{199}\text{Hg},^{15}\text{N})|$ values can be compared. Regarding the N-hybridization state of $(\text{Me}_3\text{Si})_2\text{N-Hg}^{\text{II}}\text{-N}(\text{SiMe}_3)_2$, an sp^2 -like planar structure of the nitrogen atoms was suggested from the electron diffraction study,¹⁹ which is further supported by Bent's rule⁴⁵ (see Supporting discussion in ESI† for Bent's rule). Therefore, the Hg^{II} -bound nitrogen atoms in both samples belong to the sp^2 category basically, and the current data of $|^1J(^{199}\text{Hg},^{15}\text{N})|$ are insufficient for us to correlate between $|^1J(^{199}\text{Hg},^{15}\text{N})|$ and N-hybridization, due to the lack of the 1J -values for N(sp)- Hg^{II} and N(sp³)- Hg^{II} bonds.

As a further investigation, $|^1J(^{199}\text{Hg},^{15}\text{N})|$ values for the “sp² nitrogen” in T- Hg^{II} -T and “sp²-like nitrogen” in $(\text{Me}_3\text{Si})_2\text{N-Hg}^{\text{II}}\text{-N}(\text{SiMe}_3)_2$ were strikingly different (Table 1). However, this may be because the sp^2 -like N-hybridization in $(\text{Me}_3\text{Si})_2\text{N-Hg}^{\text{II}}\text{-N}(\text{SiMe}_3)_2$ might be different from the “canonical sp^2 nitrogen” in T- Hg^{II} -T. This possibility was also inferred from $^{14}/^{15}\text{N}$ NMR spectroscopic data,⁴⁶ where the ^{14}N NMR chemical shift for the $\text{Si}_2\text{N-Hg}^{\text{II}}\text{-NSi}_2$ linkage showed a rather sp^3 -like value ($\delta(^{14}\text{N}) = 66.2$ ppm,⁴⁶ Table S1 in ESI†). By contrast, $\delta(^{15}\text{N})$ for Hg^{II} -linked N3 in T- Hg^{II} -T is 184 ppm, and the value is located within the empirical range for an sp^2 -hybridized nitrogen (Fig. S1 and Table S1 in ESI†). From these facts, the N-hybridization state of $(\text{Me}_3\text{Si})_2\text{N-Hg}^{\text{II}}\text{-N}(\text{SiMe}_3)_2$ can't be unambiguously assigned (see also Supporting discussion in ESI† for details). However, on the basis of the investigations mentioned above, the $|^1J(^{199}\text{Hg},^{15}\text{N})|$ value might be a sensitive NMR parameter for detecting differences in the fine electronic structures of T- Hg^{II} -T and $(\text{Me}_3\text{Si})_2\text{N-Hg}^{\text{II}}\text{-N}(\text{SiMe}_3)_2$.

We then quantum chemically computed $|^1J(^{199}\text{Hg}, ^{15}\text{N})| = 931$ Hz and $\delta(^{199}\text{Hg}) = -1848$ ppm for T-Hg^{II}-T using DFT including relativistic corrections from the zeroth-order regular approximation (ZORA) with spin-orbit (SO) coupling, as implemented in the ADF program^{47–49} (see Table 1 and Tables S3–S5 in ESI†). The theoretical $|^1J(^{199}\text{Hg}, ^{15}\text{N})|$ and $\delta(^{199}\text{Hg})$ values agree well with the experimental data (Table 1). With reference to the theoretical values given by Bagno and Saielli ($|^1J(^{199}\text{Hg}, ^{15}\text{N})| = 670$ Hz, $\delta(^{199}\text{Hg}) = -1727$ ppm),⁵⁰ the theoretical $|^1J(^{199}\text{Hg}, ^{15}\text{N})|$ value was refined by using the complex where it was actually recorded (Table S3 in ESI†). The $|^1J(^{199}\text{Hg}, ^{15}\text{N})|$ value of 278.4 Hz calculated for (Me₃Si)₂N-Hg^{II}-N(SiMe₃)₂ also agreed satisfactorily with experiment (316.2 Hz).¹⁹ The signs of $^1J(^{199}\text{Hg}, ^{15}\text{N})$ for T-Hg^{II}-T and (Me₃Si)₂N-Hg^{II}-N(SiMe₃)₂ were both “–” theoretically (Table S4 in ESI†).

In order to investigate the correlation between $|^1J(^{199}\text{Hg}, ^{15}\text{N})|$ values and N-hybridization states theoretically, we further analyzed the theoretical $^1J(^{199}\text{Hg}, ^{15}\text{N})$. The calculated $^1J(^{199}\text{Hg}, ^{15}\text{N})$ values were dependent on the “Fermi Contact” + “Spin Dipole coupling” (FC + SD) term (Table S4 in ESI†). With the dominance of this FC term, one may find the correlation between the N-hybridization and $|^1J(^{199}\text{Hg}, ^{15}\text{N})|$ in the future, although it should be experimentally explored.

Empirically, the $\delta(^{199}\text{Hg})$ values are clustered in terms of linked elements, hybridization states, and other factors of Hg^{II}-linked atoms (Table S2 in ESI†). Such phenomena were explained on the basis of the empirical correlation of $\delta(^{199}\text{Hg})$ with the ionicity of the X-Hg^{II} bond (high ionicity → up-field shift of $\delta(^{199}\text{Hg})$),⁵¹ Unfortunately, owing to both a paucity of experimental $\delta(^{199}\text{Hg})$ values for a linear two-coordinate N-Hg^{II}-N linkage and the uncertain N-hybridization state in (Me₃Si)₂N-Hg^{II}-N(SiMe₃)₂, the correlation between $\delta(^{199}\text{Hg})$ and the N-hybridization state of Hg^{II}-linked nitrogen also remains obscure. Nevertheless, the highly up-field-shifted $\delta(^{199}\text{Hg})$ value for T-Hg^{II}-T among those of N-mercurated compounds suggests that N(sp²)-Hg^{II}-N(sp²) covalent linkages possess significant ionic character, which agrees with our previous studies (Table 1 and Tables S1 and S2 in ESI†).^{7,52} This observation suggests that $\delta(^{199}\text{Hg})$ values can be used as a sensitive indicator for probing the Hg^{II} coordination environment not only in C-mercurated complexes but also in N-mercurated complexes, including metalloproteins¹ and metallo-DNA/RNA.

Accordingly, ¹⁹⁹Hg NMR parameters, especially $^1J(^{199}\text{Hg}, ^{15}\text{N})$, are sensitive parameters for characterizing the electronic structures of N-mercurated complexes and their N-Hg^{II} bonds as well as their Hg atoms. Hence, the $^1J(^{199}\text{Hg}, ^{15}\text{N})$ value could be a key parameter for predicting the physicochemical properties of N-mercurated complexes and making them into molecular devices, based on a bottom-up approach.

The $|^1J(^{199}\text{Hg}, ^{15}\text{N})|$ value of 1050 Hz has been reported for canonical sp²-hybridized nitrogen for the first time. From this result, the T-Hg^{II}-T system provides a comprehensive and reliable ¹⁹⁹Hg/¹⁵N NMR dataset for probing the Hg^{II} environment in N-mercurated compounds. This newly observed $^1J(^{199}\text{Hg}, ^{15}\text{N})$ coupling can be used for detecting N-Hg bond formations and precisely characterizing these bonds.

This work was performed using the NMR spectrometer under the Cooperative Research Program of the Institute for Protein

Research, Osaka University. This work was supported by the Platform for Drug Discovery, Informatics, and Structural Life Science from the Ministry of Education, Culture, Sports, Science and Technology (MEXT), Japan. This work was supported by grants-in-aid for Scientific Research (A) (24245037 to A.O. and Y.T.), (B) (24310163 to Y.T. and C.K.), (C) (18550146 to Y.T.) from MEXT, Japan; a Human Frontier Science Program (HFSP) Young Investigator Grant from HFSP, France (Y.T. and V.S.); and GAČR (P205/10/0228 and 16-12465S to V.S.) from the Czech Republic. T.D. and K.F. are the recipients of a Research Fellowship for Young Scientists from the Japan Society for the Promotion of Science (JSPS). Y.T. and V.S. were further supported by an Invitation Fellowship for Research in Japan (Short-Term) from JSPS. F.M.B. and C.F.G. were supported by the National Research School Combination – Catalysis (NRSC-C) and the Netherlands Organization for Scientific Research (NWO-CW and NWO-EW).

Notes and references

- 1 L. M. Utschig, J. W. Bryson and T. V. O'Halloran, *Science*, 1995, **268**, 380–385.
- 2 S. Katz, *Biochim. Biophys. Acta*, 1963, **68**, 240–253; references cited therein.
- 3 L. D. Kosturko, C. Folzer and R. F. Stewart, *Biochemistry*, 1974, **13**, 3949–3952.
- 4 Z. Kuklenyik and L. G. Marzilli, *Inorg. Chem.*, 1996, **35**, 5654–5662.
- 5 Y. Miyake, H. Togashi, M. Tashiro, H. Yamaguchi, S. Oda, M. Kudo, Y. Tanaka, Y. Kondo, R. Sawa, T. Fujimoto, T. Machinami and A. Ono, *J. Am. Chem. Soc.*, 2006, **128**, 2172–2173.
- 6 Y. Tanaka, S. Oda, H. Yamaguchi, Y. Kondo, C. Kojima and A. Ono, *J. Am. Chem. Soc.*, 2007, **129**, 244–245.
- 7 T. Uchiyama, T. Miura, H. Takeuchi, T. Dairaku, T. Komuro, T. Kawamura, Y. Kondo, L. Benda, V. Sychrovský, P. Bouř, I. Okamoto, A. Ono and Y. Tanaka, *Nucleic Acids Res.*, 2012, **40**, 5766–5774.
- 8 A. Ono and H. Togashi, *Angew. Chem.*, 2004, **116**, 4400–4402 (*Angew. Chem., Int. Ed.*, 2004, **43**, 4300–4302).
- 9 H. Torigoe, A. Ono and T. Kozasa, *Chem. – Eur. J.*, 2010, **16**, 13218–13225.
- 10 H. Torigoe, Y. Miyakawa, A. Ono and T. Kozasa, *Thermochim. Acta*, 2012, **532**, 28–35.
- 11 J. Šebera, J. Burda, M. Straka, A. Ono, C. Kojima, Y. Tanaka and V. Sychrovský, *Chem. – Eur. J.*, 2013, **19**, 9884–9894.
- 12 H. Yamaguchi, J. Šebera, J. Kondo, S. Oda, T. Komuro, T. Kawamura, T. Daraku, Y. Kondo, I. Okamoto, A. Ono, J. V. Burda, C. Kojima, V. Sychrovský and Y. Tanaka, *Nucleic Acids Res.*, 2014, **42**, 4094–4099.
- 13 P. Pyykkö, *Chem. Rev.*, 1997, **97**, 597–636.
- 14 F.-A. Polonius and J. Müller, *Angew. Chem.*, 2007, **119**, 5698–5701 (*Angew. Chem., Int. Ed.*, 2007, **46**, 5602–5604).
- 15 L. Benda, M. Straka, Y. Tanaka and V. Sychrovský, *Phys. Chem. Chem. Phys.*, 2011, **13**, 100–103.
- 16 L. Benda, M. Straka, V. Sychrovský, P. Bouř and Y. Tanaka, *J. Phys. Chem. A*, 2012, **116**, 8313–8320.
- 17 S. Kumbhar, S. Johannsen, R. K. O. Sigel, M. P. Waller and J. Müller, *J. Inorg. Biochem.*, 2013, **127**, 203–210.
- 18 J. Mason and R. J. Goodfellow, in *Multinuclear NMR*, ed. J. Mason, Plenum Press, New York, 1987, ch. 12 & 21.
- 19 P. Bernatowicz, S. Szymański and B. Wrackmeyer, *J. Phys. Chem. A*, 2001, **105**, 6414–6419.
- 20 E. H. Curzon, N. Herron and P. Moore, *J. Chem. Soc., Dalton Trans.*, 1980, 721–725.
- 21 S. S. Al-Showiman, *Inorg. Chim. Acta*, 1988, **141**, 263–274.
- 22 J. Kondo, T. Yamada, C. Hirose, I. Okamoto, Y. Tanaka and A. Ono, *Angew. Chem.*, 2014, **126**, 2417–2420 (*Angew. Chem., Int. Ed.*, 2014, **53**, 2385–2388).
- 23 A. R. Norris and R. Kumar, *Inorg. Chim. Acta*, 1984, **93**, 33–35.
- 24 E. Buncel, C. Boone, H. Joly, R. Kumar and A. R. Norris, *J. Inorg. Biochem.*, 1985, **25**, 61–73.
- 25 K. Tanaka and M. Shionoya, *J. Org. Chem.*, 1999, **64**, 5002–5003.
- 26 H. Weizman and Y. Tor, *J. Am. Chem. Soc.*, 2001, **123**, 3375–3376.

- 27 C. Switzer, S. Sinha, P. H. Kim and B. D. Heuberger, *Angew. Chem.*, 2005, **117**, 1553–1556 (*Angew. Chem., Int. Ed.*, 2005, **44**, 1529–1532).
- 28 K. Tanaka, G. H. Clever, Y. Takezawa, Y. Yamada, C. Kaul, M. Shionoya and T. Carell, *Nat. Nanotechnol.*, 2006, **1**, U190–U195.
- 29 G. H. Clever, C. Kaul and T. Carell, *Angew. Chem.*, 2007, **119**, 6340–6350 (*Angew. Chem., Int. Ed.*, 2007, **46**, 6226–6236).
- 30 J. Müller, *Eur. J. Inorg. Chem.*, 2008, 3749–3763.
- 31 A. Ono, S. Cao, H. Togashi, M. Tashiro, T. Fujimoto, T. Machinami, S. Oda, Y. Miyake, I. Okamoto and Y. Tanaka, *Chem. Commun.*, 2008, 4825–4827.
- 32 S. Johannsen, N. Megger, D. Böhme, R. K. O. Sigel and J. Müller, *Nat. Chem.*, 2010, **2**, 229–234.
- 33 A. Ono, H. Torigoe, Y. Tanaka and I. Okamoto, *Chem. Soc. Rev.*, 2011, **40**, 5855–5866.
- 34 E. Meggers, P. L. Holland, W. B. Tolman, F. E. Romesberg and P. G. Schultz, *J. Am. Chem. Soc.*, 2000, **122**, 10714–10715.
- 35 S. Atwell, E. Meggers, G. Spraggon and P. G. Schultz, *J. Am. Chem. Soc.*, 2001, **123**, 12364–12367.
- 36 E. Meggers, *Curr. Opin. Chem. Biol.*, 2007, **11**, 287–292.
- 37 M. K. Schlegel, L.-O. Essen and E. Meggers, *J. Am. Chem. Soc.*, 2008, **130**, 8158–8159.
- 38 K. Tanaka, A. Tengeiji, T. Kato, N. Toyama and M. Shionoya, *Science*, 2003, **299**, 1212–1213.
- 39 G. H. Clever, S. J. Reitmeier, T. Carell and O. Schiemann, *Angew. Chem.*, 2010, **122**, 5047–5049 (*Angew. Chem., Int. Ed.*, 2010, **49**, 4927–4929).
- 40 T. Carell, C. Behrens and J. Gierlich, *Org. Biomol. Chem.*, 2003, **1**, 2221–2228.
- 41 T. Ito, G. Nikaido and S. I. Nishimoto, *J. Inorg. Biochem.*, 2007, **101**, 1090–1093.
- 42 J. Joseph and G. B. Schuster, *Org. Lett.*, 2007, **9**, 1843–1846.
- 43 L. Q. Guo, N. Yin and G. N. Chen, *J. Phys. Chem. C*, 2011, **115**, 4837–4842.
- 44 H. Isobe, N. Yamazaki, A. Asano, T. Fujino, W. Nakanishi and S. Seki, *Chem. Lett.*, 2011, **40**, 318–319.
- 45 H. A. Bent, *Chem. Rev.*, 1961, **61**, 275–311.
- 46 O. Just, D. A. Gaul and W. S. Rees, Jr., *Polyhedron*, 2001, **20**, 815–821.
- 47 G. te Velde, F. M. Bickelhaupt, E. J. Baerends, C. Fonseca Guerra, S. J. A. van Gisbergen, J. G. Snijders and T. Ziegler, *J. Comput. Chem.*, 2001, **22**, 931–967.
- 48 M. Swart, C. Fonseca Guerra and F. M. Bickelhaupt, *J. Am. Chem. Soc.*, 2004, **126**, 16718–16719.
- 49 J. M. Fonville, M. Swart, Z. Vokacova, V. Sychrovský, J. E. Šponer, J. Šponer, C. W. Hilbers, F. M. Bickelhaupt and S. S. Wijmenga, *Chem. – Eur. J.*, 2012, **18**, 12372–12387.
- 50 A. Bagno and G. Saielli, *J. Am. Chem. Soc.*, 2007, **129**, 11360–11361.
- 51 D. Rehder, *Coord. Chem. Rev.*, 1991, **110**, 161–210.
- 52 Y. Tanaka and A. Ono, *Dalton Trans.*, 2008, 4965–4974.
- 53 A. E. Wetherby, Jr., S. D. Benson and C. S. Weinert, *Inorg. Chim. Acta*, 2007, **360**, 1977–1986.
- 54 Y. Tanaka, H. Yamaguchi, S. Oda, M. Nomura, C. Kojima, Y. Kondo and A. Ono, *Nucleosides, Nucleotides Nucleic Acids*, 2006, **25**, 613–624.
- 55 S. S. Lemos, D. U. Martins, V. M. Deflon and J. Elena, *J. Organomet. Chem.*, 2009, **694**, 253–258.



Contents lists available at ScienceDirect

Bioorganic & Medicinal Chemistry Letters

journal homepage: www.elsevier.com/locate/bmcl

Development of a photolabile protecting group for phosphodiester in oligonucleotides



Hisao Saneyoshi*, Kanami Shimamura, Naoki Sagawa, Yuki Ando, Takahito Tomori, Itaru Okamoto, Akira Ono*

Department of Material and Life Chemistry, Faculty of Engineering, Kanagawa University, 3-27-1 Rokkakubashi, Kanagawa-ku, Yokohama 221-8686, Japan

ARTICLE INFO

Article history:

Received 23 January 2015

Revised 20 March 2015

Accepted 25 March 2015

Available online 31 March 2015

Keywords:

Nucleic acid-based therapeutics

Prodrug

Protecting group

ABSTRACT

A photolabile protecting group, consisting of an *o*-nitrobenzyl group and a 3-(2'-hydroxy-3',6'-dimethylphenyl)-2,2-dimethylpropyl moiety, was developed for phosphodiester in oligodeoxyribonucleotides. Deprotection was triggered by photoirradiation and subsequent spontaneous cyclization to release the naked oligonucleotide.

© 2015 Elsevier Ltd. All rights reserved.

Oligonucleotide-based therapies promise to be highly specific tools for the treatment of numerous human diseases. However, the multi-anionic nature of oligonucleotides prohibits cellular internalization.^{1,2} In addition, oligonucleotides are sensitive to extra- and intracellular nucleolytic enzymes.³ To circumvent these drawbacks, prodrug approaches (pro-oligonucleotides) have received considerable attention.^{4–6} In the past two decades several protecting groups for masking phosphodiester have been reported. Deprotection can be initiated by several triggers, including exposure to esterases,^{4,7–18} thermolytic triggers,^{19–26} hypoxia,²⁷ and light,^{28–30} to generate biologically active oligonucleotides after cellular uptake of pro-oligonucleotides.

This study describes the development of a new protecting group for use with phosphodiester in oligonucleotides. The structure of the protecting group and its expected deprotection pathway are shown in [Scheme 1](#). The protecting group is composed of a trigger group (R) and a 3-(2'-hydroxy-3',6'-dimethylphenyl)-2,2-dimethylpropyl skeleton. Depending on the specific structure the R residue, several functions can act as triggers, including light, enzymes, hypoxia, and heat. The trigger reaction releases R to generate a free phenolic hydroxyl group that spontaneously cyclizes to produce a deprotected phosphodiester group. Note that the presence of methyl groups on the skeleton can accelerate the cyclization reaction.^{31–33} Cheruvallath and colleagues³⁴ used the same skeleton structure to connect synthetic oligonucleotides to a solid

support. In their procedure, the synthesized oligonucleotides were released by treatment with concd NH₄OH at 55 °C. Since the leaving ability of a phosphodiester group is considerably greater than that of a phosphomonoester group, our protecting group was expected to undergo deprotection in neutral solutions, such as cytoplasm.

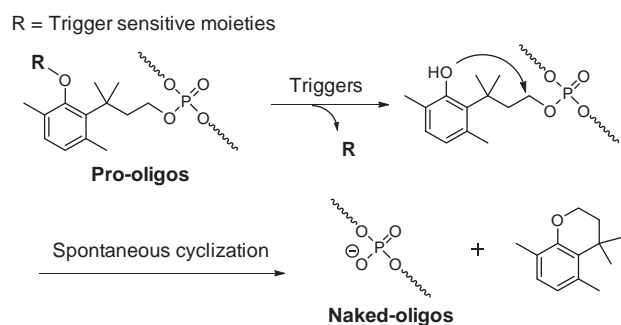
In this study, a photolabile *o*-NO₂-benzyl group was used as a trigger-sensitive moiety (R). *o*-NO₂-benzyl group has been used for protection and caging of oligonucleotides^{35–37} and the photolysis of *o*-NO₂-benzyl groups proceeds in neutral solutions without any additional reagents, allowing us to monitor the formation of intermediates.

The synthesis of a phosphoramidite unit **6** is shown in [Scheme 2](#). Briefly, 3,6-dimethylphenol **1** was treated with methyl 3,3-dimethyl acrylate in the presence of methanesulfonic acid. The resulting lactone derivative **2** was reduced by lithium aluminum hydride to give 2-(4-hydroxy-2-methylbutan-2-yl)-3,6-dimethylphenol **3**.³⁸ Compound **3** was treated with *o*-NO₂ benzyl bromide in the presence of K₂CO₃ to give **4**. Compound **4** was assembled with 5'-O-(4,4'-dimethoxytrityl)-3'-O-bis(*N,N*-diisopropylamino)phosphinyl-2'-deoxythymidine **5**²³ in the presence of 1-*H*-tetrazole to give the desired phosphoramidite unit **6**. Using monomer unit **6**, oligodeoxyribonucleotides having the protecting group (Pro-ODN) were synthesized using a standard protocol, as described in the [Supplementary material](#).

A methanolic solution of Pro-ODN **1** was irradiated with a super high-pressure UV lamp at 0 °C for 5 min. The resulting solution was stored at an appropriate temperature until HPLC analysis ([Fig. 1](#)). Two peaks corresponding to diastereomers of Pro-ODN **1** were

* Corresponding authors. Tel.: +81 45 481 5661; fax: +81 45 491 7915.

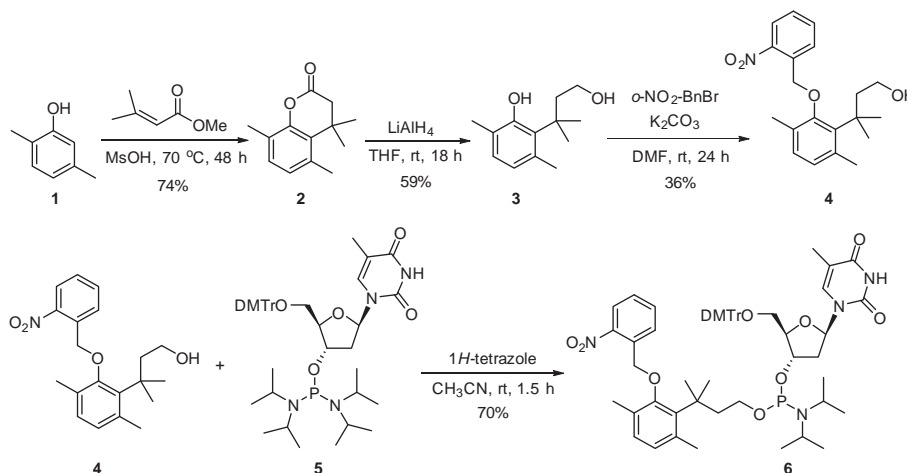
E-mail addresses: saneyoshih@kanagawa-u.ac.jp (H. Saneyoshi), akiraono@kanagawa-u.ac.jp (A. Ono).



Scheme 1. The molecular structure of the present photolabile protecting group and its expected deprotection pathway.

observed prior to irradiation (Fig. 1a). After irradiation, the peaks corresponding to Pro-ODN **1** disappeared and were replaced with peaks corresponding to a phenolic intermediate, Pro-ODN **1'** and a small amount of full deprotected product, ODN **1** (Fig. 1b). In this HPLC profile, 14% of ODN **1'** was converted to ODN **1**. Pro-ODN **1'** was relatively stable in methanol at 4 °C. Thus, 59% of Pro-ODN **1'** was remained after 48 h (Fig. 1c, left). The cyclization rate increased at 37 °C and Pro-ODN **1'** was converted to a ODN **1** after 4 h in 66% yield (Fig. 1c, right). Pro-ODN **1'** was fully deprotected after 24 h (Fig. S1).

The deprotection reaction was then performed in a buffer solution instead of MeOH (Fig. 2) using Pro-ODN **2**, which contains two protecting groups. As similar to the Pro-ODN **1**, first deprotection of *o*-nitrobenzyl groups proceed smoothly in 5 min photo-



Scheme 2. Synthesis of a phosphoramidite building block with a new protecting group for oligonucleotides.

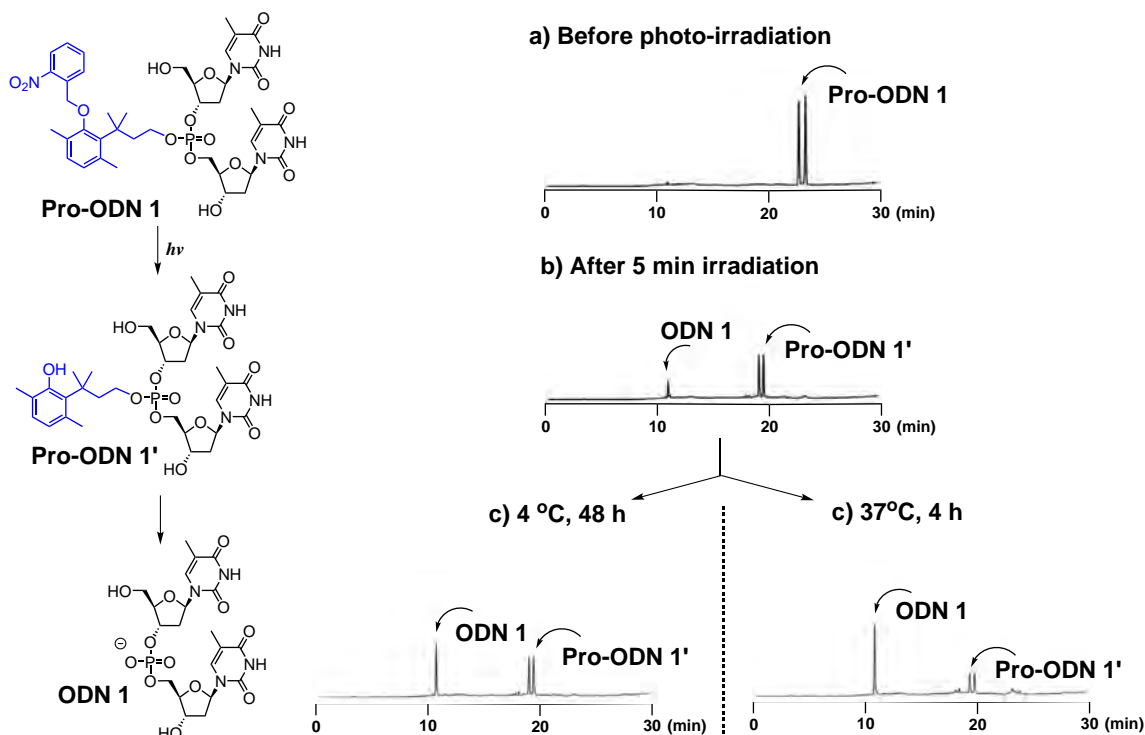


Figure 1. Reverse-phase HPLC chromatograms of (a) Pro-ODN **1** (b) after 5 min of photoirradiation and (c) after prolonged incubation (left, 4 °C, 48 h; right, 37 °C, 4 h).

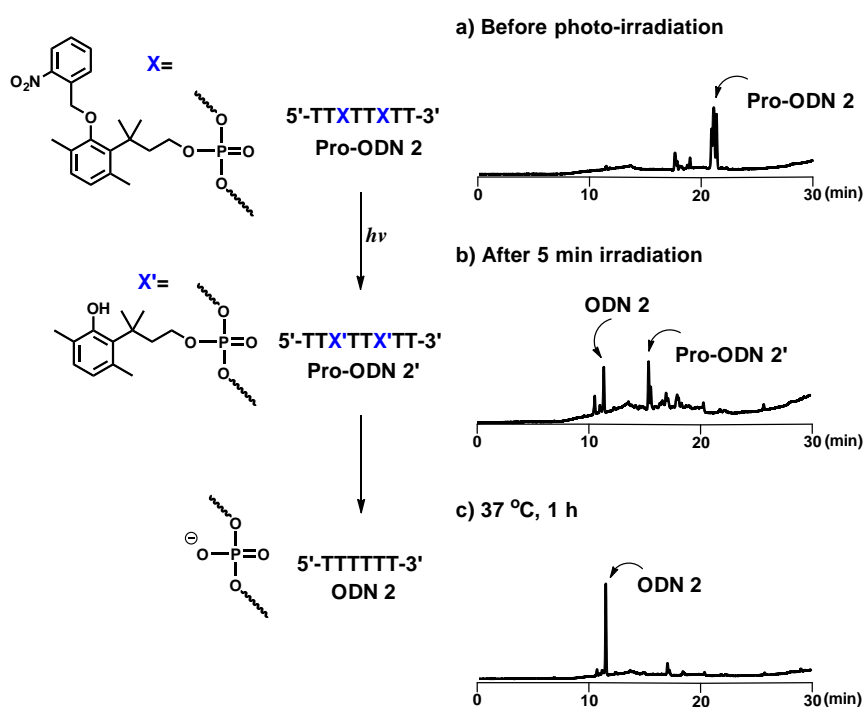


Figure 2. Reverse-phase HPLC chromatograms of (a) Pro-ODN **2** (b) after 5 min of photoirradiation and (c) after incubation at 37 °C for 1 h. A solution containing 28 μM Pro-ODN **2** in 50 mM Tris–HCl (pH 7.0) was used.

irradiation to give the phenolic intermediate, Pro-ODN **2'** and fully deprotected product, ODN **2** (Fig. 2b). In the aqueous solution, Pro-ODN **2'** was fully converted to fully deprotected ODN **2** after 1 h at 37 °C (Fig. 2c).

In conclusion, oligonucleotides were synthesized with new protecting groups on their phosphodiester moieties. Deprotection was initiated by photoirradiation (5 min) and the deprotection reaction was monitored by HPLC. The analyses indicated that phenolic intermediates were initially generated and degraded to yield fully deprotected ODN. Our results indicate that other trigger-sensitive moieties may be employed instead of *o*-NO₂-benzyl groups to fabricate novel protecting groups. For example, the *o*-NO₂-benzyl group can be replaced with other photosensitive groups for excitation at longer wavelengths (including two-photon excitation to avoid biological damage and enhance light permeability). In addition, replacement of the *o*-NO₂-benzyl with acyl, nitrobenzenesulfonyl, or glycoside groups will allow for diverse designs of biolabile protecting groups for phosphodiester in DNA/RNA.

Acknowledgments

This work was supported by the Strategic Research Base Development Program for Private Universities (Kanagawa University, 2012–2016) from the Ministry of Education, Culture, Sports, Science, and Technology, Japan.

Supplementary data

Supplementary data associated with this article can be found, in the online version, at <http://dx.doi.org/10.1016/j.bmcl.2015.03.064>.

References and notes

- Shoji, Y.; Akhtar, S.; Periasamy, A.; Herman, B.; Juliano, R. L. *Nucleic Acids Res.* **1991**, *19*, 5543.
- Gewirtz, A. M.; Stein, C. A.; Glazer, P. M. *Proc. Natl. Acad. Sci. U.S.A.* **1996**, *93*, 3161.
- Dias, N.; Stein, C. A. *Mol. Cancer Ther.* **2002**, *1*, 347.
- Krise, J. P.; Stella, V. J. *Adv. Drug Delivery Rev.* **1996**, *19*, 287.
- Bologna, J.-C.; Vives, E.; Imbach, J.-L.; Morvan, F. *Antisense Nucleic Acid Drug Dev.* **2002**, *12*, 33.
- Hecker, S. J.; Erion, M. D. *J. Med. Chem.* **2008**, *51*, 2328.
- Périgaud, C.; Gosselin, G.; Lefebvre, I.; Girardet, J.-L.; Benzaria, S.; Barber, I.; Imbach, J.-L. *Bioorg. Med. Chem. Lett.* **1993**, *3*, 2521.
- Iyer, R. P.; Yu, D.; Agrawal, S. *Bioorg. Med. Chem. Lett.* **1994**, *4*, 2471.
- Barber, I.; Rayner, B.; Imbach, J.-L. *Bioorg. Med. Chem. Lett.* **1995**, *5*, 563.
- Iyer, R. P.; Yu, D.; Agrawal, S. *Bioorg. Chem.* **1995**, *23*, 1.
- Iyer, R. P.; Yu, D.; Devlin, T.; Ho, N.-H.; Agrawal, S. *Bioorg. Med. Chem. Lett.* **1996**, *6*, 1917.
- Mignet, N.; Morvan, F.; Rayner, B.; Imbach, J.-L. *Bioorg. Med. Chem. Lett.* **1997**, *7*, 851.
- Tosquellas, G.; Alvarez, K.; Dell'Aquila, C.; Morvan, F.; Vasseur, J.-J.; Imbach, J.-L.; Rayner, B. *Nucleic Acids Res.* **1998**, *26*, 2069.
- Bologna, J.-C.; Morvan, F.; Imbach, J.-L. *Eur. J. Org. Chem.* **1999**, 1999, 2353.
- Pojjärvi, P.; Heinson, P.; Virta, P.; Lönnberg, H. *Bioconjugate Chem.* **2005**, *16*, 1564.
- Ora, M.; Taherpour, S.; Linna, R.; Leisvuori, A.; Hietamäki, E.; Poijjärvi-Virta, P.; Beigelman, L.; Lönnberg, H. *J. Org. Chem.* **2009**, *74*, 4992.
- Kiuru, E.; Ora, M.; Beigelman, L.; Blatt, L.; Lönnberg, H. *Chem. Biodivers.* **2011**, *8*, 266.
- Kiuru, E.; Ahmed, Z.; Lönnberg, H.; Beigelman, L.; Ora, M. *J. Org. Chem.* **2012**, *78*, 950.
- Wilk, A.; Chmielewski, M. K.; Grajkowski, A.; Phillips, L. R.; Beaucage, S. L. *J. Org. Chem.* **2002**, *67*, 6430.
- Cieślak, J.; Grajkowski, A.; Livengood, V.; Beaucage, S. L. *J. Org. Chem.* **2004**, *69*, 2509.
- Ausín, C.; Grajkowski, A.; Cieślak, J.; Beaucage, S. L. *Org. Lett.* **2005**, *7*, 4201.
- Grajkowski, A.; Ausín, C.; Kauffman, J. S.; Snyder, J.; Hess, S.; Lloyd, J. R.; Beaucage, S. L. *J. Org. Chem.* **2007**, *72*, 805.
- Grajkowski, A.; Cieślak, J.; Kauffman, J. S.; Duff, R. J.; Norris, S.; Freedberg, D. I.; Beaucage, S. L. *Bioconjugate Chem.* **2008**, *19*, 1696.
- Ausín, C.; Kauffman, J. S.; Duff, R. J.; Shivaprasad, S.; Beaucage, S. L. *Tetrahedron* **2010**, *66*, 68.
- Grajkowski, A.; Cieślak, J.; Gapeev, A.; Beaucage, S. L. *New J. Chem.* **2010**, *34*, 880.
- Jain, H. V.; Takeda, K.; Tami, C.; Verthelyi, D.; Beaucage, S. L. *Bioorg. Med. Chem.* **2013**, *21*, 6224.
- Zhang, N.; Tan, C.; Cai, P.; Zhang, P.; Zhao, Y.; Jiang, Y. *Chem. Commun.* **2009**, 3216.
- Zhang, K.; Taylor, J.-S. *J. Am. Chem. Soc.* **1999**, *121*, 11579.
- Shah, S.; Rangarajan, S.; Friedman, S. H. *Angew. Chem., Int. Ed.* **2005**, *44*, 1328.
- Tang, X.; Dmochowski, I. J. *Mol. Biosyst.* **2007**, *3*, 100.
- Shan, D.; Nicolaou, M. G.; Borchardt, R. T.; Wang, B. *J. Pharm. Sci.* **1997**, *86*, 765.
- Levine, M. N.; Raines, R. T. *Chem. Sci.* **2012**, *3*, 2412.
- Jung, M. E.; Piizzi, G. *Chem. Rev.* **2005**, *105*, 1735.

34. Cheruvallath, Z. S.; Cole, D. L.; Ravikumar, V. T. *Bioorg. Med. Chem. Lett.* **2003**, *13*, 281.
35. Ohtsuka, E.; Tanaka, S.; Ikehara, M. *Nucleic Acids Res.* **1974**, *1*, 1351.
36. Chaulk, S. G.; MacMillan, A. M. *Nucleic Acids Res.* **1998**, *26*, 3173.
37. Kröck, L.; Heckel, A. *Angew. Chem., Int. Ed.* **2005**, *44*, 471.
38. Greenwald, R. B.; Choe, Y. H.; Conover, C. D.; Shum, K.; Wu, D.; Royzen, M. J. *Med. Chem.* **2000**, *43*, 475.

DOI:10.1002/ejic.201500955

Isolation of a Tetranuclear Intermediate Complex in the Synthesis of Paddlewheel-Type Dirhodium Tetraacetate

Yusuke Kataoka,^{*[a]} Natsumi Yano,^[a] Tatsuya Kawamoto,^[b] and Makoto Handa^{*[a]}

Keywords: Rhodium / Reaction intermediates / X-ray diffraction / Electronic structure / Density functional calculations

To investigate the detailed mechanism of formation of the paddlewheel-type dirhodium tetraacetate $[\text{Rh}_2(\text{O}_2\text{CCH}_3)_4(\text{L})_2]$ ($[\mathbf{1}-(\text{L})_2]$; L = axial-coordinated solvent ligand), we performed a step-by-step synthesis. The isolated red intermediate complex $[\text{Rh}_4(\mu\text{-Cl})_4(\text{O}_2\text{CCH}_3)_4(\text{L})_4]$ ($[\mathbf{2}-(\text{L})_4]$) was characterized by means of single-crystal X-ray diffraction, ^1H NMR spectroscopy, infrared spectroscopy, and elemental analysis.

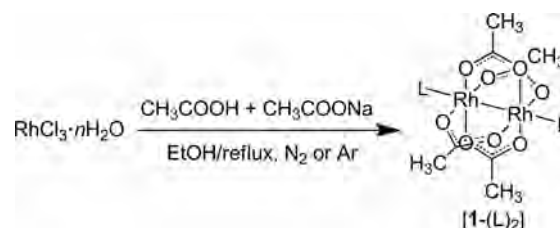
The crystal structure of $[\mathbf{2}-(\text{MeOH})_4]$, which was crystallized from MeOH solution, has a unique twisted-box $\text{Rh}_4(\mu\text{-Cl})_4$ core coordinated by four μ -carboxylato bridging ligands and four MeOH molecules as axially coordinated solvent molecules. The electronic structure and absorption properties of $[\mathbf{2}-(\text{MeOH})_4]$ in MeOH were also carefully investigated both experimentally and theoretically.

Introduction

Paddlewheel-type dirhodium tetracarboxylate complexes^[1] that contain an Rh–Rh single bond have been extensively studied because of their interesting structures and attractive properties, such as catalytic abilities,^[2] their potential utilities in photodynamic therapy, or as antitumor agents.^[3] These rich functional properties are derived from the molecular orbital (MO) interactions of the dirhodium unit, which includes degenerate σ -, π -, and δ -bonding orbitals and δ^* - and π^* -antibonding orbitals because of the presence of 14 d-electrons.^[4] The most basic complex of this type is dirhodium tetraacetate, $[\text{Rh}_2(\text{O}_2\text{CCH}_3)_4(\text{L})_2]$ ($[\mathbf{1}-(\text{L})_2]$; L = axial-coordinated solvent), for which basic information, such as its electrochemical and photophysical properties, is already available.^[5] Currently, $[\mathbf{1}-(\text{L})_2]$ is regarded as an important starting material for the synthesis of not only paddlewheel-type dirhodium(II) complexes bridged by carboxylato,^[6] amidato,^[7] and amidinato^[8] ligands but also (porous) coordination polymers^[9] and extended metal-atom chains.^[10]

It is well known that the most efficient and general synthetic method for $[\mathbf{1}-(\text{L})_2]$ is heating $\text{RhCl}_3 \cdot n\text{H}_2\text{O}$ to reflux under an inert gas, such as N_2 or Ar, in a mixture of sodium acetate, acetic acid, and ethanol (EtOH), as depicted in Scheme 1.^[11] The red reaction solution gradually turns into

a dark green solution after having become a dark red solution, and a green solid precipitate of $[\mathbf{1}-(\text{L})_2]$ is obtained after 1 h of heating under reflux conditions. In this reaction, it has been deduced that EtOH serves as the reducing agent. However, the details of this mechanism remain unknown, and the reaction intermediate in the synthesis of $[\mathbf{1}-(\text{L})_2]$ has never been isolated. To clarify the mechanistic details for the synthesis of $[\mathbf{1}-(\text{L})_2]$, the intermediate complex in the formation of $[\mathbf{1}-(\text{L})_2]$ must be isolated.



Scheme 1. General reaction scheme of dirhodium tetraacetate $[\mathbf{1}-(\text{L})_2]$; L = EtOH or H_2O .

Herein, we report the first isolation of the intermediate in the synthesis of dirhodium tetraacetate. The intermediate complex, $[\text{Rh}_4(\mu\text{-Cl})_4(\mu\text{-O}_2\text{CCH}_3)_4(\text{L})_4]$ $[\mathbf{2}-(\text{L})_4]$, which was isolated by a step-by-step synthetic procedure, was characterized by means of elemental analysis, ^1H NMR spectroscopy, infrared spectroscopy, and single-crystal X-ray diffraction analysis. In addition, we investigated the electronic structure and absorption properties of $[\mathbf{2}-(\text{L})_4]$ by both experimental techniques and density functional theory (DFT) calculations, because $[\mathbf{2}-(\text{L})_4]$ is considered to be a promising precursor for novel dirhodium complexes and coordination polymers. The overall mechanism for the synthesis of $[\mathbf{1}-(\text{L})_2]$ is also investigated and discussed in detail.

[a] Department of Chemistry, Interdisciplinary Graduate School of Science and Engineering, Shimane University, 1060 Nishikawatsu, Matsue 690-8504, Japan
E-mail: kataoka@riko.shimane-u.ac.jp
<http://www.shimane-u.ac.jp/en/>

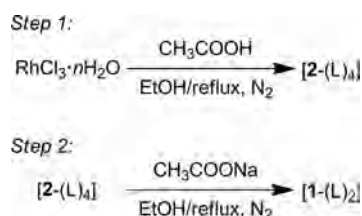
[b] Department of Chemistry, Faculty of Science, Kanagawa University, 2946 Tsuchiya, Hiratsuka 259-1293, Japan

Supporting information for this article is available on the WWW under <http://dx.doi.org/10.1002/ejic.201500955>.

Results and Discussion

Synthesis and Characterization of [2-(L)₄]

To investigate the mechanism of the formation of [1-(L)₂] in detail, we herein performed a step-by-step synthesis. The exact strategy used in this study is shown in Scheme 2.



Scheme 2. Step-by-step synthetic procedure used in this study; L = EtOH or H₂O.

The initial step (Step 1), which consists of a reaction of RhCl₃·3H₂O and CH₃COOH in EtOH (i.e., without the addition of CH₃COONa), gave a dark red hygroscopic product [2-(EtOH)₄]. In this case, although L = EtOH immediately after completion of the synthesis, EtOH was gradually exchanged for H₂O in air. Drying under vacuum at 343 K for 1 h gave the desolvated product [2] (yield 37.7%).

Single crystals of [2-(MeOH)₄] suitable for X-ray diffraction were obtained by means of slow concentration of the MeOH solution at 298 K. The crystal structure of [2-(MeOH)₄] was determined by single-crystal X-ray diffraction at 150 K. Compound [2-(MeOH)₄] crystallizes in the tetragonal space group *I*₄/a. The structure (ORTEP view) of [2-(MeOH)₄] is shown in Figure 1, and selected geometrical parameters are summarized in Table S1 of the Supporting Information. The two Rh₂ units, each of which is bridged by two μ-carboxylato ligands, are connected by four μ-Cl ligands. Each axis of the Rh–Rh bonds in the Rh₄(μ-Cl)₄ core is perpendicularly arranged, and thus the Rh₄(μ-Cl)₄ core takes on a unique twisted box shape. Interestingly, the Rh–Rh bond in [2-(MeOH)₄] (2.538 Å) is

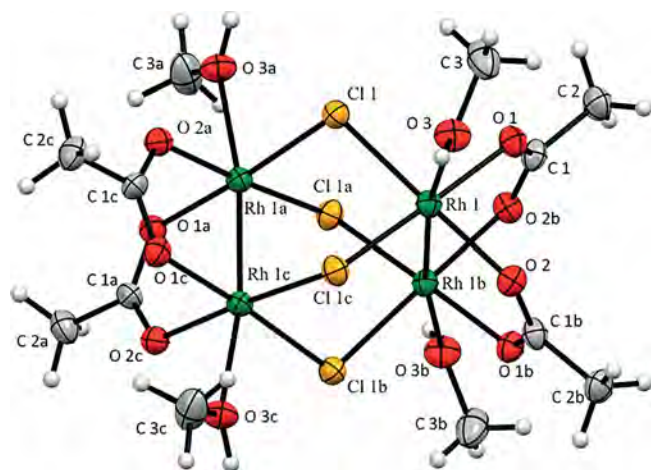


Figure 1. ORTEP view of [2-(MeOH)₄] determined by single-crystal X-ray diffraction at 150 K. Ellipsoids are drawn at the 50% probability level.

longer than those found in typical paddlewheel-type dirhodium complexes with single Rh–Rh bonds (2.37–2.45 Å)^[1b] because of the orientation of the coordinating mode and the bulkiness of μ-Cl ions. We predicted that there would be no direct bonds between Rh₂ and Rh₂ units but that strong MO interactions in the Rh–Cl bond and weak orbital interactions between Rh₂ and Rh₂ units through μ-Cl ions would be present, because the color of [2-(MeOH)₄] (dark red) is different from that of [1-(MeOH)₂] (dark green). Indeed, the Rh–Cl bonds (2.315 Å) of [2-(MeOH)₄] are shorter than typical Rh–Cl bonds. Notably, the overall structure of [2-(MeOH)₄] is unexpectedly similar to that of [Rh₄(μ-Cl)₄(O₂C*n*Pr)₄(CH₃CN)₄] (Rh–Rh 2.555 Å), which was synthesized by the reaction of trialkylchlorosilane with [Rh₂(O₂C*n*Pr)₄].^[12]

As depicted in Figure 2, the ¹H NMR spectrum of desolvated [2] in [D₆]DMSO shows only one singlet resonance at δ = 1.94 ppm, which corresponds to the C–H atom of the methyl group in the μ-acetato ligand. This signal is shifted considerably downfield relative to that of [1] in [D₆]DMSO (δ = 1.79 ppm) because of the electron-withdrawing effects of the μ-Cl ions in [2].

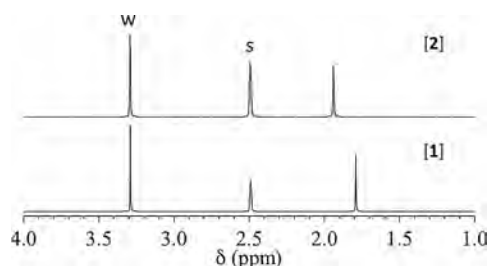


Figure 2. ¹H NMR spectra of desolvated [1] and [2] in [D₆]DMSO. Here S and W indicate solvent (DMSO) and water, respectively.

The symmetric [*v*_{sym}(COO⁻)] and asymmetric [*v*_{asym}(COO⁻)] stretching modes of desolvated [2] in the infrared spectrum (KBr disk) were also analyzed (see Figure 3). The values of *v*_{sym}(COO⁻), *v*_{asym}(COO⁻), and their separation [i.e., Δ*v*(COO⁻) = *v*_{asym}(COO⁻) – *v*_{sym}(COO⁻)] of [2] are 1443, 1553, and 110 cm⁻¹, respectively. The Δ*v*(COO⁻) of [2] is smaller than those of typical Rh^{II}₂ complexes, such as [1-(H₂O)₂] (150 cm⁻¹).

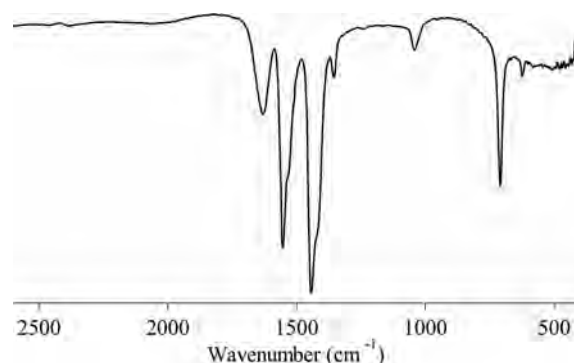


Figure 3. Infrared spectrum of [2].

Reactivity of [2] and Overall Mechanism for the Synthesis of [1]

Subsequently, to investigate the reactivity of [2], a reaction of [2] and NaOAc in EtOH was performed (Step 2 in Scheme 2). Under reflux conditions, the dark red solution gradually became green. Eventually, a small amount of deep green powder precipitated from the reaction solution. The ^1H NMR ($\delta = 1.79$ ppm in $[\text{D}_6]\text{DMSO}$) and ESI-MS (m/z found 464.8549) spectra revealed that this deep green product can be identified as [1]. The reaction yield from [2] to [1] was only 38.7%. This result is not in conflict with the synthetic yield (typically approximately 25–30%) for [1]. It should also be noted (a) that the reaction from [2] to [1] does not occur at room temperature, and (b) that, whereas [2] is stable in the solid state, it gradually decomposes to metallic rhodium in EtOH.

Next, to clarify the overall reaction mechanism of the synthesis of [1], we also attempted the reaction of $\text{RhCl}_3 \cdot 3\text{H}_2\text{O}$ with NaOAc in EtOH (without the addition of HOAc). Surprisingly, this reaction directly gave [1]. However, the yield of [1] in this reaction was quite small (only 4.4%), and the main product of this reaction was actually rhodium black (i.e., rhodium oxide). Therefore, this result suggests that, to achieve the efficient production of [1], the synthesis should proceed through [2].

Optimized Geometry and Electronic Structure of [2-(MeOH)₄] in MeOH

To investigate the molecular geometry and electronic structure of [2-(MeOH)₄] in the solvent medium, we initially performed a geometry optimization of [2-(MeOH)₄] in MeOH by using DFT calculations [rB3LYP/LANL08(f) & cc-pVDZ] with a polarizable continuum model (PCM).^[13] Table S1 in the Supporting Information lists the selected geometrical parameters with X-ray structure data of [2-(MeOH)₄]. The optimized geometry of [2-(MeOH)₄] contains a unique twisted $\text{Rh}_4(\mu\text{-Cl})_4$ box core as observed experimentally, and its structural parameters are in general agreement with the corresponding experimental values. For example, the Rh–Rh and Rh–Cl bond lengths of the optimized structure of [2-(MeOH)₄] are 2.563 and 2.407 Å, respectively, which represent differences of only 0.025 and 0.092 Å, respectively, relative to the experimental values.

Next, the electronic structure of [2-(MeOH)₄] in MeOH was analyzed in detail. Selected MO diagrams and their energies are shown in Figure 4. Here, the HOMO and LUMO are the highest occupied MO and lowest unoccupied MO, respectively. In the occupied MO spaces, unstable MOs from the HOMO to HOMO–13 are mainly localized on the two Rh_2 moieties (i.e., d-orbital interactions between two Rh ions) with small orbital contributions from the Cl ions. The HOMO and HOMO–3 are assigned as the $\pi^*_a(\text{Rh}_2)$ orbitals and are both equivalently localized on two Rh_2 units. Here, the $\pi^*_a(\text{Rh}_2)$ orbitals in the HOMO formed antibonding orbital interactions with the p-orbitals of the Cl ions, whereas the $\pi^*_a(\text{Rh}_2)$ orbitals in HOMO–3 have no

remarkable orbital interactions with surrounding ligands. Thus, the energy of the HOMO is higher than that of HOMO–3. In HOMO–1 and HOMO–2, the MOs are heavily localized on one side of the Rh_2 units in [2-(MeOH)₄] and are commonly identified as $\pi^*_b(\text{Rh}_2)$ orbitals. The MO energies of these two MOs are closely degenerate. The primary MO contributors in the degenerate HOMO–4 and HOMO–5 are commonly the $\delta^*(\text{Rh}_2)$ orbitals. Strong $\sigma(\text{Rh}_2)$ orbital interactions in the Rh_2 units are observed in HOMO–6 and HOMO–8. Here, whereas $\sigma(\text{Rh}_2)$ orbitals in HOMO–6 and HOMO–8 engage in antibonding orbital interactions between $\sigma(\text{Rh}_2)$ and p(O) in MeOH, only HOMO–6 exhibits antibonding orbital interactions between $\sigma(\text{Rh}_2)$ and p(Cl) orbitals. Therefore, the MO energies of HOMO–6 are slightly higher relative to those of HOMO–8. The dominant MO contributions of HOMO–7 and HOMO–9 are the $\delta(\text{Rh}_2)$ orbitals. Here, whereas HOMO–7 has antibonding orbital interactions between $\delta(\text{Rh}_2)$ and the p-orbitals of surrounding atoms, HOMO–9 exhibits bonding orbital interactions between $\delta(\text{Rh}_2)$ and p(Cl) orbitals. HOMO–10 and HOMO–11 are mainly localized on the $\pi_a(\text{Rh}_2)$ orbitals. The stable d–d orbital interactions of [2-(MeOH)₄] consist of $\pi_b(\text{Rh}_2)$ orbitals, which are observed at HOMO–12 and HOMO–13, and

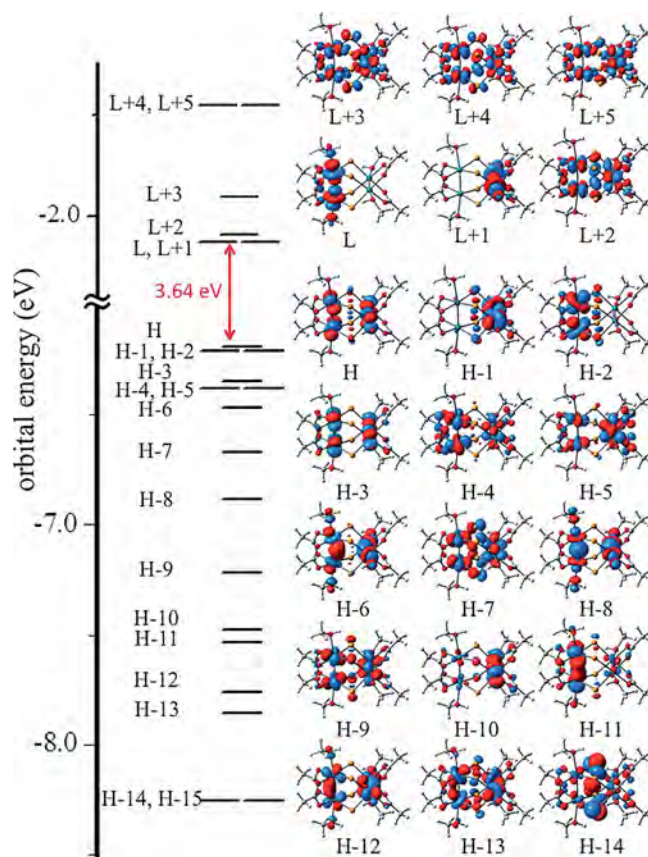


Figure 4. Selected MO diagrams and their MO energies of [2-(MeOH)₄] in MeOH calculated by B3LYP [basis: LANL08(f) for Pt and aug-cc-pVDZ for others] with the PCM method. HOMO and LUMO are abbreviated as H and L, respectively, with diagrams.

only HOMO–13 engages in bonding orbital interactions with p(Cl) orbitals. The main orbitals that contribute to HOMO–14 and HOMO–15 are p(Cl) orbitals.

In contrast, the unoccupied MOs from the LUMO to LUMO+5 are also mainly attributed to the d-orbital characteristics of the Rh₂ units. The degenerate LUMO and LUMO+1 are localized on the σ*(Rh₂) units and exhibit antibonding orbital interactions with p(O) in MeOH. The energy difference between the HOMO and LUMO (i.e., the HOMO–LUMO gap) of [2-(MeOH)₄] is 3.64 eV. This value is smaller than that of [1-(H₂O)₂] (3.98 eV). LUMO+1 and LUMO+2 include antibonding orbital interactions between p(O) in O₂CCH₃ ligands and δ*(Rh₂), which are ascribed to the d(x²-y²) characteristics of the Rh ions. The most unstable d-orbital interactions in [2-(MeOH)₄] are observed in the degenerate LUMO+4 and LUMO+5. Their MOs are assigned as δ'(Rh₂), which are also the result of the d(x²-y²) characteristics of the Rh ions.

Absorption Spectral Feature of [2-(MeOH)₄] in MeOH

The UV/Vis spectrum of [2-(MeOH)₄] in MeOH is shown in Figure 5a. A low-lying band (694 nm) and an intense band (315 nm) are observed in the visible and UV regions, respectively. In addition, a gently sloping shoulder band is observed at 400–555 nm. Relative to the absorption spectrum of [1-(MeOH)₂], the wavelengths of the absorption bands of [2-(MeOH)₄] are shifted towards the low-energy region (i.e., the absorption band was redshifted).

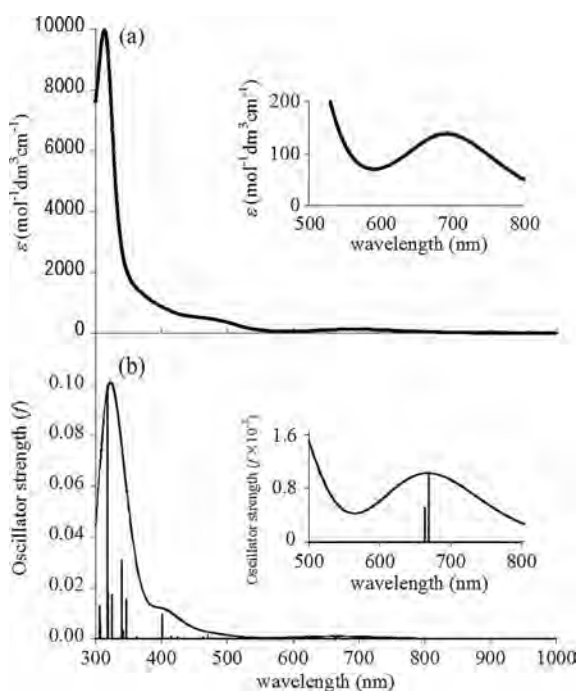


Figure 5. (a) Experimental and (b) theoretical absorption spectra of [2-(MeOH)₄] in MeOH.

To assign the detailed excitation characteristics of [2-(MeOH)₄] in MeOH, time-dependent DFT (TD-DFT) calculations were performed. Our calculated results, includ-

ing excitation energies [nm], oscillator strengths (*f*), and excitation characteristics, are summarized in Table S2 of the Supporting Information, and the simulated spectrum of [2-(MeOH)₄] in MeOH is shown in Figure 5b. The shape of the simulated spectrum is in good agreement with that of the observed spectrum. The experimentally observed low-lying band at 694 nm comprises three different excitations (S₀→S₁: 668.8 nm; S₀→S₃: 664.0 nm; and S₀→S₄: 664.0 nm) and is thus identified as the spin-allowed d–d transition, which is mainly associated with excitation from π*(Rh₂) to σ*(Rh₂) (i.e., excitation from the HOMO, HOMO–1, HOMO–2, and HOMO–3 to the LUMO and LUMO+1). Substantial oscillator strength is theoretically observed for the S₀→S₄₀ and S₄₁ excitations (both at 346.6 nm), and we concluded that these excitations correspond to the dominant component of the experimentally observed shoulder band at 400–550 nm. The main excitation characteristics of this shoulder band are the δ(Rh₂)→σ*(Rh₂) and σ(Rh₂)→σ*(Rh₂) transitions. In addition, at wavelengths below 400 nm, several intense excitations were predicted, and the simulated spectrum, which takes these excitations into account, is in good agreement with the experimental spectrum. The most intense excitation is observed at the S₀→S₅₅ excitation, which includes the characteristics of δ(Rh₂)→δ'(Rh₂) excitation characters (HOMO–5→LUMO+5 and HOMO–4→LUMO+4) as dominant components.

Conclusion

In this study, the red intermediate complex [2-(L)₄], which is an intermediate in the synthesis of [1-(L)₂], was isolated by a step-by-step synthetic procedure and characterized by means of elemental analysis, ¹H NMR spectroscopy, infrared spectroscopy, and single-crystal X-ray diffraction analysis. This characterization revealed that [2-(L)₄] has an Rh₄(μ-Cl)₄ core with a unique twisted box shape, which is coordinated by four μ-carboxylato bridging ligands. The reaction of [2-(L)₄] and NaOAc in EtOH afforded [1-(L)₂]. Although the reaction of RhCl₃·3H₂O and NaOAc in EtOH directly gave [1-(L)₂] as one of the products, its yield was very low (4.4%). Therefore, the synthesis that involves [2-(L)₄] as an intermediate is suggested to be a reasonable method for the preparation of [1-(L)₂]. The electronic structure and absorption spectral features of [2-(MeOH)₄] were also closely investigated by means of absorption spectrum and TD-DFT calculations. The results of these analyses indicate that (1) the unstable occupied MOs and stable unoccupied MOs of [2-(MeOH)₄] are mainly localized on the two Rh₂ units, (2) strong orbital interactions between Rh₂ units and Cl ions are present, and (3) the absorption spectral features are dominated by d–d excitations at the two Rh₂ units. We suggest that [2-(MeOH)₄] might also be a promising catalyst for several reactions and could be a building block for supramolecular complexes and coordination polymers, because the electronic structure feature of [2-(MeOH)₄] is similar to that of [1-(L)₂].

Experimental Section

General Information: All reagents and solvents were purchased from commercial sources and were used without further purification. Complex [2] was synthesized according to a literature procedure.^[11] All reactions were carried out under N₂. ¹H NMR spectra were recorded with a JEOL-ECS 500SS spectrometer operating at 500.0 MHz. Chemical shifts (δ) were referenced to residual DMSO ($\delta = 2.49$ ppm). UV/Vis absorption spectra were measured in MeOH with a JASCO V-670 spectrometer. Elemental analyses for carbon and hydrogen were conducted with a Yanaco CHN CORDER MT-6 installed at Shimane University.

Synthesis of [Rh₄(μ -Cl)₄(O₂CCH₃)₄] ([2]): A mixture of RhCl₃·3H₂O (500.0 mg, 1.90 mmol), CH₃COOH (25 mL, 43.7 mmol), and EtOH (25 mL) was heated to reflux at 353 K under N₂ for 1 h. After cooling to room temperature, the obtained deep red solution was filtered through a Celite column and then concentrated under vacuum to give a dark red powder. The obtained powder was redissolved in a small portion of EtOH and poured onto a silica gel column and eluted with CHCl₃/EtOH (9:1, v/v). The first fraction was collected, concentrated under vacuum, and dried under reduced pressure at 343 K to give a dark red powder of [2]. Yield 141.3 mg (37.7% based on RhCl₃·3H₂O). C₈H₁₂O₈Rh₄ (441.99): calcd. C 12.17, H 1.53; found C 12.35, H 1.87. ¹H NMR ([D₆]DMSO, 298 K): $\delta = 1.94$ (s, 12 H) ppm. UV/Vis (CH₃OH): λ_{max} (ϵ) = 694 (139), 450–550 (br., 511 at 460 nm), 315 nm (9983 mol⁻¹ dm³ cm⁻¹). IR data (KBr disk): $\tilde{\nu} = 1631$ (m), 1553 (s), 1443 (s), 1354 (vw), 1041 (w), 709 (m), 624 (vw) cm⁻¹.

Reaction of [2] and NaOAc: A mixture of [2] (150.0 mg, 0.190 mmol), NaOAc (500.0 mg, 6.10 mmol), and EtOH (40 mL) was heated to reflux under N₂ for 1 h. After cooling to room temperature, the obtained green solution was concentrated under vacuum to give a dark green powder. The obtained powder was redissolved in a small portion of CH₃CN and poured onto a silica gel column and eluted with CH₃CN/CHCl₃ (2:3, v/v). The first fraction was collected, water was added (5 mL), then it was concentrated under vacuum and dried under reduced pressure at 353 K to give a dark green powder of [1]. Yield 65.3 mg (38.7% based on [2]). ¹H NMR ([D₆]DMSO, 298 K): $\delta = 1.79$ (s, 12 H) ppm. HRMS (ESI-TOF): *m/z* calcd. 464.8534 [M + Na], found 464.8549.

Crystal-Structure Determination and Refinement: Single crystals of [2-(MeOH)₄] suitable for X-ray diffraction analysis were obtained as described in the text above. A single crystal was attached to a Cryoloop using paraffin oil (Hampton Research). Diffraction data were collected at 150 K with a Rigaku Mercury 70 CCD system equipped with an Mo rotating-anode X-ray generator with monochromated Mo-K α radiation ($\lambda = 0.71075$ Å). Diffraction data were processed using CrystalClear-SM (Rigaku). The structure was solved by direct methods (SIR-2004) and refined using the full-matrix least-squares technique (*F*²) with SHELXL97 as part of the CrystalStructure 4.1 software. Non-hydrogen atoms were refined with anisotropic displacement parameters, and all hydrogen atoms were located at the calculated positions and refined with a riding model. The residual electron density in the void spaces of the final refined structure was evaluated using the PLATON SQUEEZE program. Crystal data of [2-(MeOH)₄]: C₁₂H₂₈Cl₄O₁₂Rh₄ (917.78), *T* = 150 K, tetragonal, space group *I*₄/a (no. 88), *a* = *b* = 18.071(7), *c* = 10.456(4) Å, $\alpha = \beta = \gamma = 90^\circ$, *V* = 3415(2) Å³, *D*_{calcd.} = 1.785 g cm⁻³, *Z* = 4, *R*₁(all) = 0.0708, *R*₁(*I* > 2 σ) = 0.0610, *wR*₂(all) = 0.1543, *wR*₂ (*I* > 2 σ) = 0.1478, *GoF* = 1.136, 7480 total reflections. CCDC-1419392 {for [2-(MeOH)₄]} contains the supplementary crystallographic data for this paper. These data can be

obtained free of charge from The Cambridge Crystallographic Data Centre via www.ccdc.cam.ac.uk/data_request/cif.

Density Functional Theory Calculations: All density functional theory (DFT) calculations were performed using the Gaussian 09 C.01 program package.^[13] The hybrid DFT functional rB3LYP was used with the effective-core-potential (ECP) basis set for the Rh atoms, Dunning's augmented correlation-consistent double- ζ basis set (aug-cc-pVDZ) for O and Cl atoms, and the correlation-consistent double- ζ basis set for the other atoms. The solvent effect of the MeOH ($\epsilon = 32.613$) was considered by the polarizable continuum model (PCM). Full optimization of the geometry without symmetry constraints was performed in DMF for the singlet ground state (*S*₀), and the resulting geometry was confirmed to be at a potential energy minimum by vibrational frequency analysis (no imaginary frequencies). The spin-allowed *S*₀→*S*_{*n*} excitations were calculated using the time-dependent DFT (TD-DFT) method. MOs were drawn using the GaussView 5.0 visualizer.

Acknowledgments

This work was supported by Grants-in-Aid for Scientific Research (KAKENHI) (no. 15H00877, 15K17897, and 25620145) and the Strategic Research Base Development Program for Private Universities of the Ministry of Education, Culture, Sports and Technology (MEXT), Japan. Y. K. acknowledges the SEI Group CSR Foundation, the JAPAN PRIZE Foundation, and the Electronic Technology Research Foundation of Chugoku.

- [1] a) F. A. Cotton, B. G. Deboer, M. D. LaPrade, J. R. Pipal, D. A. Ucko, *Acta Crystallogr., Sect. B* **1971**, *27*, 1664; b) H. T. Chifotides, K. R. Dunber, in *Multiple Bonds between Metal Atoms* (Eds.: F. A. Cotton, C. A. Murillo, R. A. Walton), Springer Science and Business Media, Inc., New York, **2005**, pp. 465–589.
- [2] a) J. Hansen, H. M. L. Davies, *Coord. Chem. Rev.* **2008**, *252*, 545; b) M. C. Pirrung, H. Liu, A. T. Morehead Jr., *J. Am. Chem. Soc.* **2002**, *124*, 1014–1023; c) Y. Kataoka, K. Sato, Y. Miyazaki, Y. Suzuki, H. Tanaka, Y. Kitagawa, T. Kawakami, M. Okumura, W. Mori, *Chem. Lett.* **2010**, *39*, 358–359.
- [3] a) R. A. Howard, T. G. Spring, J. L. Bear, *Cancer Res.* **1976**, *36*, 4402–4405; b) H. T. Chifotides, K. R. Dunber, *Acc. Chem. Res.* **2005**, *38*, 146–156; c) P. K.-L. Fu, P. M. Bradley, C. Turro, *Inorg. Chem.* **2001**, *40*, 2476–2477; d) Z. Majer, S. Bösze, I. Szabó, V. G. Mihucz, A. Gaál, G. Szilvágý, G. Pepponi, F. Meirer, P. Wobruschek, N. Szoboszlai, D. Ingerle, C. Strelie, *Microchem. J.* **2015**, *120*, 51–57.
- [4] a) J. G. Norman Jr., H. J. Kolari, *J. Am. Chem. Soc.* **1978**, *100*, 791; b) Y. Kataoka, Y. Kitagawa, T. Saito, Y. Nakanishi, T. Matsui, K. Sato, Y. Miyazaki, T. Kawakami, M. Okumura, W. Mori, K. Yamaguchi, *Bull. Chem. Soc. Jpn.* **2010**, *83*, 1481–1488.
- [5] a) P. M. Bradley, B. E. Bursten, C. Turro, *Inorg. Chem.* **2001**, *40*, 1376–1379; b) Y. Kataoka, Y. Kitagawa, T. Saito, Y. Nakanishi, K. Sato, Y. Miyazaki, T. Kawakami, M. Okumura, W. Mori, K. Yamaguchi, *Supramol. Chem.* **2011**, *23*, 329–336.
- [6] a) E. B. Boyar, S. D. Robinson, *Coord. Chem. Rev.* **1983**, *50*, 109–208; b) L. H. Tong, S. Clifford, A. Gomila, S. Duval, L. Guénée, A. F. Williams, *Chem. Commun.* **2012**, *48*, 9891–9893.
- [7] a) M. Q. Ahsan, I. Bernal, J. L. Bear, *Inorg. Chem.* **1986**, *25*, 260–265; b) Y. Fuma, M. Ebihara, S. Kutsumizu, T. Kawamura, *J. Am. Chem. Soc.* **2004**, *126*, 12238–12239.
- [8] a) J. L. Bear, C. L. Yao, R. S. Lifsey, J. D. Korp, K. M. Kadish, *Inorg. Chem.* **1991**, *30*, 336–340; b) F. P. Pruchnik, H. Pruchnik, Z. Kochel, *Polyhedron* **2009**, *28*, 769–774.

- [9] a) S. Naito, T. Tanibe, E. Saito, T. Miyao, W. Mori, *Chem. Lett.* **2001**, 30, 1178–1179; b) S. Takamizawa, E. Nakata, H. Yokoyama, K. Mochizuki, W. Mori, *Angew. Chem. Int. Ed.* **2003**, 42, 4331–4334; *Angew. Chem.* **2003**, 115, 4467; c) M. Handa, M. Watanabe, D. Yoshioka, S. Kawabata, R. Nukada, M. Mikuriya, H. Azuma, K. Kasuga, *Bull. Chem. Soc. Jpn.* **1999**, 72, 2681–2686; d) F. A. Cotton, Y. Kim, *J. Am. Chem. Soc.* **1993**, 115, 8511–8512; e) H. Miyasaka, C. S. C.-Fernández, R. Clérac, K. R. Dunbar, *Angew. Chem. Int. Ed.* **2000**, 39, 3831–3835; *Angew. Chem.* **2000**, 112, 3989.
- [10] J.-T. Sheu, C.-C. Lin, I. Chao, C.-C. Wang, S.-M. Peng, *Chem. Commun.* **1996**, 3, 315–316.
- [11] P. Legzdins, R. W. Mitchell, G. L. Rempel, J. D. Ruddick, G. Wilkinson, *J. Chem. Soc. A* **1970**, 3322–3326.
- [12] Z. Yang, H. Oki, M. Ebihara, T. Kawamura, *J. Chem. Soc., Dalton Trans.* **1998**, 14, 2277–2278.
- [13] M. J. Frisch, G. W. Trucks, H. B. Schlegel, G. E. Scuseria, M. A. Robb, J. R. Cheeseman, G. Scalmani, V. Barone, B. Mennucci, G. A. Petersson, H. Nakatsuji, M. Caricato, X. Li, H. P. Hratchian, A. F. Izmaylov, J. Bloino, G. Zheng, J. L. Sonnenberg, M. Hada, M. Ehara, K. Toyota, R. Fukuda, J. Hasegawa, M. Ishida, T. Nakajima, Y. Honda, O. Kitao, H. Nakai, T. Vreven, J. A. Montgomery Jr., J. E. Peralta, F. Ogliaro, M. Bearpark, J. J. Heyd, E. Brothers, K. N. Kudin, V. N. Staroverov, R. Kobayashi, J. Normand, K. Raghavachari, A. Rendell, J. C. Burant, S. S. Iyengar, J. Tomasi, M. Cossi, N. Rega, J. M. Millam, M. Klene, J. E. Knox, J. B. Cross, V. Bakken, C. Adamo, J. Jaramillo, R. Gomperts, R. E. Stratmann, O. Yazyev, A. J. Austin, R. Cammi, C. Pomelli, J. W. Ochterski, R. L. Martin, K. Morokuma, V. G. Zakrzewski, G. A. Voth, P. Salvador, J. J. Dannenberg, S. Dapprich, A. D. Daniels, Ö. Farkas, J. B. Foresman, J. V. Ortiz, J. Cioslowski, D. J. Fox, *Gaussian 09*, revision C.01, Gaussian, Inc., Wallingford, CT, USA, **2009**.

Received: August 21, 2015

Published Online: November 10, 2015



Preparation, structure, and dynamic and electrochemical behaviors of dinuclear rhodium(I) complexes with bridging formamidinato ligands



Yuki Ide ^a, Takahisa Ikeue ^{a,*}, Yusuke Kataoka ^a, Ryoko Inoue ^a, Mikio Nakamura ^{b,**},
Daisuke Yoshioka ^c, Masahiro Mikuriya ^c, Tatsuya Kawamoto ^d, Makoto Handa ^{a,***}

^a Department of Chemistry, Graduate School of Science and Engineering, Shimane University, 1060 Nishikawatsu, Matsue 690-8504, Japan

^b Department of Chemistry, Faculty of Science, Toho University, Funabashi 274-8510, Japan

^c Department of Applied Chemistry for Environment and Research Center for Coordination Molecule-based Devices, School of Science and Technology, Kwansai Gakuin University, 2-1 Gakuen, Sanda 669-1337, Japan

^d Department of Chemistry, Faculty of Science, Kanagawa University, Hiratsuka, Kanagawa 259-1293, Japan

ARTICLE INFO

Article history:

Received 27 August 2015

Received in revised form

16 October 2015

Accepted 4 December 2015

Available online 15 December 2015

Keywords:

Dirhodium(I) complexes

Formamidinato ligand

Crystal structures

Dynamic NMR

Cyclic voltammogram

ABSTRACT

Dinuclear rhodium(I) complexes, [Rh(4-Me-pf)(cod)]₂ (**1**), [Rh(3,5-Me₂-pf)(cod)]₂ (**2**), [Rh(4-Me-pf)(nbd)]₂ (**3**), [Rh(3,5-Me₂-pf)(nbd)]₂ (**4**), and [Rh(2,6-F₂-pf)(nbd)]₂ (**5**), have been synthesized and characterized by X-ray structure analysis, ¹H, ¹³C, and ¹⁹F NMR, UV–vis, ESI-TOF-MS, and elemental analysis. In these complexes, two rhodium atoms are bridged by two formamidinato ligands and each rhodium atom is coordinated by one chelating cod or nbd ligand to form an approximately square planar coordination structure with two nitrogen atoms and two double bonds. The Rh–Rh distances are in the range of 3.2668 to 2.9726 Å, suggesting a direct bonding interaction between two rhodium atoms. Variable temperature NMR studies in CD₂Cl₂ solution have revealed that **1–5** exhibit a novel dynamic behavior, that is, an interconversion between two enantiomers. The activation parameters for racemization have been determined by the line shape analyses of the ¹H and ¹⁹F NMR spectra taken at various temperatures. Variable temperature NMR studies have also revealed that the rotation rates of the four aryl groups around N–C(aryl) bonds are extremely different in each complex. The cyclic voltammetry study has shown that the oxidation potentials corresponding to Rh³⁺/Rh²⁺ are 0.41 V in the cod complexes (**1** and **2**) while those in the nbd complexes (**3–5**) have shown negative shift by ca. 0.2 V. The reasons for the difference in dynamic behaviors and redox properties among these complexes have been discussed.

© 2015 Elsevier B.V. All rights reserved.

1. Introduction

A wide variety of studies have been done on the binuclear transition metal complexes, which include i) theoretical, spectroscopic, and magnetic studies to reveal metal–metal interactions, ii) structural modeling of biological molecules, and iii) catalytic activities for various reactions [1–11]. The aim of these explorations has been the use of transition metal ions such as rhodium and

iridium ions with bridging ligands to improve the stability and reactivity of the binuclear transition metal complexes. Since the first reports on binuclear chloride-bridged rhodium(I) complexes [Rh(μ-Cl)(cod)]₂ and [Rh(μ-Cl)(nbd)]₂ carrying 1,5-cyclooctadiene (cod) and 2,5-norbornadiene (nbd) as diene ligands [12–14], a number of analogous rhodium(I) complexes such as [Rh(L)(cod)]₂ (L = carboxylato, pyrazolato, and pyridine-2-olato) [7–9,15–19] and [Rh(L)(nbd)]₂ (L = carboxylato, pyrazolato, and pyridine-2-olato) have been investigated [8,9,20–22]. Some of these complexes have exhibited catalytic activities in the reactions such as hydroformylation, hydrogenation, and polymerization [7–9,23–27]. More recently, *N,N'*-bis(alkylphenyl or alkoxyphenyl)formamidinato anions (R_m-pf[−]) have been extensively used as bridging ligands in transition metal chemistry [28–38], particularly in the preparation of binuclear paddle–wheel complexes [M₂(R_m-pf)₄]^{0,1+,2+} (M = Rhodium or Iridium ion) [39–45]. For example,

Abbreviations: 4-Me-pf, *N,N'*-bis(4-methylphenyl)formamidinato; 3,5-Me₂-pf, *N,N'*-bis(3,5-dimethylphenyl)formamidinato; 2,6-F₂-pf, *N,N'*-bis(2,6-difluorophenyl)formamidinato; cod, 1,5-cyclooctadiene; nbd, 2,5-norbornadiene.

* Corresponding author.

** Corresponding author.

*** Corresponding author.

E-mail address: ikeue@riko.shimane-u.ac.jp (T. Ikeue).

<http://dx.doi.org/10.1016/j.jorganchem.2015.12.018>

0022-328X/© 2015 Elsevier B.V. All rights reserved.

binuclear rhodium(II) complex $[\text{Rh}_2(\text{R}_m\text{-pf})_4]$ was prepared by the reaction of dirhodium(II) mixed ligand complex $\text{Rh}_2(\text{R}_m\text{-pf})_2(\text{O}_2\text{CCF}_3)_2$ with molten $\text{H}(\text{R}_m\text{-pf})$ [46,47]. During the surveillance of the literature, we have found several papers reported by Piraino et al. [36,37,46–48] on the characterization and electrochemical studies of formamidinate-bridged rhodium(I) dimers, $[\text{Rh}(4\text{-Me-pf})(\text{cod})]_2$ (**1**) and $[\text{Rh}(4\text{-Me-pf})(\text{nbd})]_2$ (**3**). We were very much interested in these complexes as potent reducing agents. We have considered that the catalytic activity of these complexes can be finely tuned by the introduction of various substituents at the nitrogen and carbon atoms of the bridged ligands. Furthermore, the Rh–Rh catalytic center can be modulated sterically and electronically by the nature of diene ligands. Thus, the elucidation of the structural, spectroscopic, and redox properties of $[\text{Rh}(\text{R}_m\text{-pf})(\text{L})]_2$ ($\text{L} = \text{carboxylato}$, pyrazolato, and pyridine-2-olato) is essential for the development of efficient catalysts. In this paper, we will report the syntheses, molecular structures, dynamic behavior, and redox properties of various formamidinate bridged binuclear complexes such as $[\text{Rh}(4\text{-Me-pf})(\text{cod})]_2$ (**1**), $[\text{Rh}(3,5\text{-Me}_2\text{-pf})(\text{cod})]_2$ (**2**), $[\text{Rh}(4\text{-Me-pf})(\text{nbd})]_2$ (**3**), $[\text{Rh}(3,5\text{-Me}_2\text{-pf})(\text{nbd})]_2$ (**4**), and $[\text{Rh}(2,6\text{-F}_2\text{-pf})(\text{nbd})]_2$ (**5**) as shown in Scheme 1.

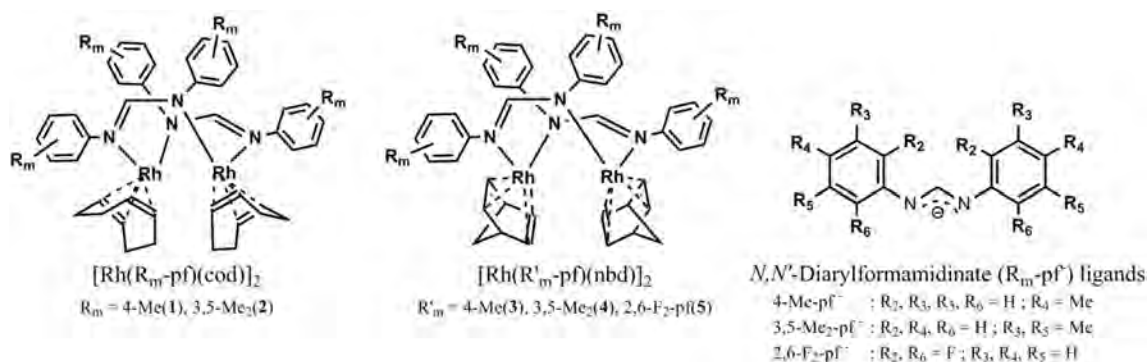
2. Experimental

2.1. Synthesis

$[\text{Rh}(\mu\text{-Cl})(\text{cod})]_2$ and $[\text{Rh}(\mu\text{-Cl})(\text{nbd})]_2$ were prepared by the methods of Giordano et al. and Abel et al., respectively [12–14]. The formamidinate ligands were prepared using the modified method in literature [49]. $[\text{Rh}(4\text{-Me-pf})(\text{cod})]_2$ (**1**) and $[\text{Rh}(3,5\text{-Me}_2\text{-pf})(\text{cod})]_2$ (**2**) were obtained by the reaction of $[\text{Rh}(\mu\text{-Cl})(\text{cod})]_2$ with $\text{H}(\text{R}_m\text{-pf})$ ($\text{R}_m = 4\text{-Me}$ and $3,5\text{-Me}_2$) in toluene (Scheme 2), according to the method developed by Piraino et al. [48]. $[\text{Rh}(4\text{-Me-pf})(\text{nbd})]_2$ (**3**), $[\text{Rh}(3,5\text{-Me}_2\text{-pf})(\text{nbd})]_2$ (**4**), and $[\text{Rh}(2,6\text{-F}_2\text{-pf})(\text{nbd})]_2$ (**5**) were similarly obtained by the reaction of $[\text{Rh}(\mu\text{-Cl})(\text{nbd})]_2$ with $\text{H}(\text{R}_m'\text{-pf})$ ($\text{R}_m' = 4\text{-Me}$, $3,5\text{-Me}_2$, and $2,6\text{-F}_2$) in toluene (Scheme 3) [48].

2.1.1. Typical procedure

In the preparation of **1–5**, we have slightly modified the method developed by Piraino et al. [48] and obtained the complexes in better yield. As shown in Schemes 2 and 3, a toluene solution containing KOBu^t (2.10 mmol) and the formamidinate ligands (2.10 mmol) was stirred for 12 h at room temperature, to which $[\text{Rh}(\mu\text{-Cl})(\text{cod})]_2$ or $[\text{Rh}(\mu\text{-Cl})(\text{nbd})]_2$ (1.00 mmol) was added. The mixture was stirred for 6 h at room temperature. After condensation of the solution, *n*-hexane was added to the concentrated solution. The solution was kept at room temperature for a few days.



Scheme 1. Structural scheme of *N,N'*-diarylformamidinate ligands, $[\text{Rh}(\text{R}_m\text{-pf})(\text{cod})]_2$ (**1–2**), and $[\text{Rh}(\text{R}_m'\text{-pf})(\text{nbd})]_2$ (**3–5**).

Orange colored single crystals were obtained from the solution. These crystals were filtered, washed with hexane, and dried under vacuum. Analytically pure samples were obtained by recrystallization from $\text{CH}_2\text{Cl}_2/n\text{-hexane}$.

2.1.2. $[\text{Rh}(4\text{-Me-pf})(\text{cod})]_2$ (**1**)

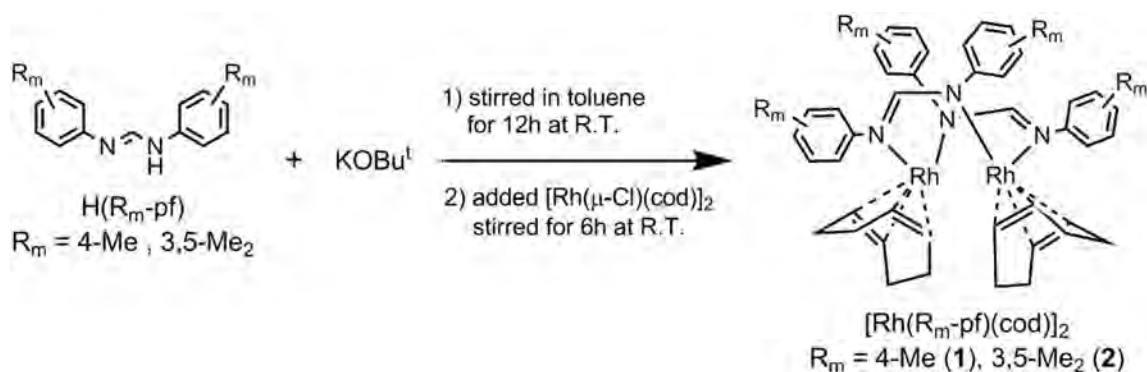
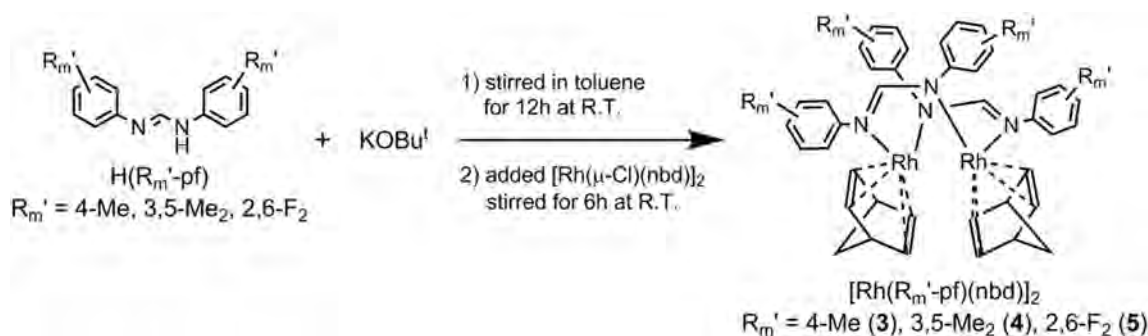
This complex was originally prepared and characterized by Piraino et al. [48]. We have added full ^1H NMR data together with the assignments. UV–vis, IR, Reflectance, and HR-MS (ESI-TOF) data are also listed below. **1** was isolated in 80.2% yield (697 mg, 0.802 mmol). Anal. Calcd. for $\text{C}_{46}\text{H}_{54}\text{N}_4\text{Rh}_2$: C, 63.60; H, 6.27; N, 6.45%. Found: C, 63.41; H, 6.18; N, 6.29%. ^1H NMR (CD_2Cl_2 , 500 MHz, 298 K): $\delta = 1.79$ (*cod*-CH₂, 4H, m), 1.91 (*cod*-CH₂, 4H, m), 2.29 (*p*-CH₃, 12H, s), 2.54 (*cod*-CH₂, 4H, m), 2.91 (*cod*-CH₂, 4H, br), 3.82 (*cod*-CH, 4H, br), 4.35 (*cod*-CH, 4H, br), 7.02 (*m*-H, 8H, d, $J = 8.0$ Hz), 7.18 (*o*-H, 8H, br), and 7.19 ppm (CH, 2H, t, $J_{\text{Rh-H}} = 1.7$ Hz). ^{13}C NMR (CD_2Cl_2 , 125 MHz, 298 K): $\delta = 20.8$ (*p*-CH₃, q, $J_{\text{C-H}} = 126$ Hz), 31.0 (*cod*-CH₂, t, $J_{\text{C-H}} = 127$ Hz), 31.4 (*cod*-CH₂, t, $J_{\text{C-H}} = 127$ Hz), 76.1 (*cod*-CH, br), 84.7 (*cod*-CH, br), 125.0 (*o*-C, d, $J_{\text{C-H}} = 160$ Hz), 129.1 (*m*-C, d, $J_{\text{C-H}} = 156$ Hz), 132.4 (*p*-C, s), 150.3 (*ipso*-C, s), and 165.0 ppm (CH, d, $J_{\text{C-H}} = 169$ Hz). UV–vis (CHCl_3): $\lambda_{\text{max}}(\epsilon: 10^4 \text{ mol}^{-1}\text{dm}^3 \text{ cm}^{-1}) = 241$ (5.4, sh), 276 (8.2), 355 (1.7, sh), and 455 nm (0.7). Reflectance: $\lambda_{\text{max}} = 296, 340, 379$, and 460 nm. IR (KBr): $\nu_{\text{N-C-N}} = 1561$ and $\nu_{\text{C-H}} = 2829\text{--}3014 \text{ cm}^{-1}$. HR-MS (ESI-TOF): Calcd. for $[\text{M}]^+$: 868.2453; Found: 868.2450 *m/z*.

2.1.3. $[\text{Rh}(3,5\text{-Me}_2\text{-pf})(\text{cod})]_2$ (**2**)

2 was isolated in 82.3% (761 mg, 0.823 mmol). Anal. Calcd. for $\text{C}_{50}\text{H}_{62}\text{N}_4\text{Rh}_2$: C, 64.93; H, 6.76; N, 6.06%. Found: C, 64.81; H, 6.54; N, 6.02%. ^1H NMR (CD_2Cl_2 , 500 MHz, 298 K): $\delta = 1.83$ (*cod*-CH₂, 4H, br), 1.92 (*cod*-CH₂, 4H, br), 2.30 (*m*-CH₃, 24H, s), 2.61 (*cod*-CH₂, 4H, br), 2.92 (*cod*-CH₂, 4H, br), 3.90 (*cod*-CH, 4H, br), 4.35 (*cod*-CH, 4H, br), 6.68 (*p*-H, 4H, s), 7.05 (*o*-H, 8H, br), and 7.21 ppm (CH, 2H, t, $J_{\text{Rh-H}} = 2.0$ Hz). ^{13}C NMR (CD_2Cl_2 , 125 MHz, 298 K): $\delta = 21.6$ (*m*-CH₃, q, $J_{\text{C-H}} = 126$ Hz), 31.2 (*cod*-CH₂, t, $J_{\text{C-H}} = 131$ Hz), 31.4 (*cod*-CH₂, t, $J_{\text{C-H}} = 126$ Hz), 76.5 (*cod*-CH, br), 84.4 (*cod*-CH, br), 123.2 (*o*-C, d, $J_{\text{C-H}} = 163$ Hz), 124.5 (*p*-C, d, $J_{\text{C-H}} = 167$ Hz), 137.7 (*m*-C, s), 152.7 (*ipso*-C, s), and 164.6 ppm (CH, d, $J_{\text{C-H}} = 170$ Hz). UV–vis (CHCl_3): $\lambda_{\text{max}}(\epsilon: 10^4 \text{ mol}^{-1}\text{dm}^3 \text{ cm}^{-1}) = 308$ (2.1), 357 (1.0, sh), and 461 nm (0.4). Reflectance: $\lambda_{\text{max}} = 310$ and 479 nm. IR (KBr): $\nu_{\text{N-C-N}} = 1550$ and $\nu_{\text{C-H}} = 2825\text{--}3018 \text{ cm}^{-1}$. HR-MS (ESI-TOF): Calcd. for $[\text{M}]^+$: 924.3079; Found: 924.3094 *m/z*.

2.1.4. $[\text{Rh}(4\text{-Me-pf})(\text{nbd})]_2$ (**3**)

This complex was originally prepared and characterized by Piraino et al. [48]. We have added full ^1H NMR data together with the assignments. UV–vis, IR, Reflectance, and HR-MS (ESI-TOF) data are also listed below. **3** was isolated in 60.2% (504 mg, 0.602 mmol).

Scheme 2. Synthetic scheme of $[\text{Rh}(\text{R}_m\text{-pf})(\text{cod})]_2$ (1–2).Scheme 3. Synthetic scheme of $[\text{Rh}(\text{R}_m'\text{-pf})(\text{nbd})]_2$ (3–5).

Anal. Calcd. for $\text{C}_{44}\text{H}_{46}\text{N}_4\text{Rh}_2$: C, 63.16; H, 5.54; N, 6.70%. Found: C, 63.52; H, 5.23; N, 6.81%. ^1H NMR (CD_2Cl_2 , 500 MHz, 298 K): $\delta = 1.35$ (*nbd*- CH_2 , 4H, t, $J = 1.6$ Hz), 2.28 (*p*- CH_3 , 12H, s), 3.86 (*nbd*- $\text{CH}=\text{CH}$, 4H, t, $J = 4.0$ Hz), 4.04 (*nbd*-CH, 2H, br), 4.12 (*nbd*- $\text{CH}=\text{CH}$, 4H, t, $J = 3.4$ Hz), 4.24 (*nbd*-CH, 2H, br), 7.01 (*m*-H, 8H, d, $J = 8.3$ Hz), 7.02 (CH, 2H, br), and 7.12 ppm (*o*-H, 8H, d, $J = 7.7$ Hz). ^{13}C NMR (CD_2Cl_2 , 125 MHz, 298 K): $\delta = 20.8$ (*p*- CH_3 , q, $J_{\text{C-H}} = 126$ Hz), 50.9 (*nbd*-CH, d, $J_{\text{C-H}} = 151$ Hz), 51.5 (*nbd*-CH, d, $J_{\text{C-H}} = 151$ Hz), 52.9 (*nbd*- $\text{CH}=\text{CH}$, d, $J_{\text{C-H}} = 177$ Hz), 58.3 (*nbd*- $\text{CH}=\text{CH}$, d, $J_{\text{C-H}} = 170$ Hz), 61.9 (*nbd*- CH_2 , t, $J_{\text{C-H}} = 131$ Hz), 124.4 (*o*-C, d, $J_{\text{C-H}} = 158$ Hz), 129.1 (*m*-C, d, $J_{\text{C-H}} = 157$ Hz), 132.0 (*p*-C, s), 149.4 (*ipso*-C, s), and 162.3 ppm (CH, d, $J_{\text{C-H}} = 170$ Hz). UV–vis (CHCl_3): $\lambda_{\text{max}}(\epsilon: 10^4 \text{ mol}^{-1}\text{dm}^3 \text{ cm}^{-1}) = 243$ (3.6), 308 (4.3), 369 (2.0), 470 (0.8), and 525 nm (0.5). Reflectance: $\lambda_{\text{max}} = 316, 365, 475$, and 523 nm. IR (KBr): $\nu_{\text{N-C-N}} = 1554$ and $\nu_{\text{C-H}} = 2856\text{--}2992 \text{ cm}^{-1}$. HR-MS (ESI-TOF): Calcd. for $[\text{M}]^+$: 836.1827; Found: 836.1827 *m/z*.

2.1.5. $[\text{Rh}(3,5\text{-Me}_2\text{-pf})(\text{nbd})]_2$ (4)

4 was isolated in 44.9% (401 mg, 0.449 mmol). Anal. Calcd. for $\text{C}_{48}\text{H}_{54}\text{N}_4\text{Rh}_2$: C, 64.58; H, 6.10; N, 6.28%. Found: C, 64.55; H, 5.99; N, 6.20%. ^1H NMR (CD_2Cl_2 , 500 MHz, 298 K): $\delta = 1.37$ (*nbd*- CH_2 , 4H, t, $J = 1.4$ Hz), 2.29 (*m*- CH_3 , 24H, s), 3.95 (*nbd*- $\text{CH}=\text{CH}$, 4H, t, $J = 3.7$ Hz), 4.11 (*nbd*- $\text{CH}=\text{CH}$, 4H, t, $J = 3.4$ Hz), 4.12 (*nbd*-CH, 2H, br), 4.25 (*nbd*-CH, 2H, br), 6.64 (*p*-H, 4H, s), 6.95 (*o*-H, 8H, s), and 7.00 ppm (CH, 2H, br). ^{13}C NMR (CD_2Cl_2 , 125 MHz, 298 K): $\delta = 21.5$ (*m*- CH_3 , q, $J_{\text{C-H}} = 126$ Hz), 50.9 (*nbd*-CH, d, $J_{\text{C-H}} = 151$ Hz), 51.4 (*nbd*-CH, d, $J_{\text{C-H}} = 143$ Hz), 52.6 (*nbd*- $\text{CH}=\text{CH}$, d, $J_{\text{C-H}} = 163$ Hz), 58.3 (*nbd*- $\text{CH}=\text{CH}$, d, $J_{\text{C-H}} = 172$ Hz), 61.9 (*nbd*- CH_2 , t, $J_{\text{C-H}} = 132$ Hz), 122.7 (*o*-C, d, $J_{\text{C-H}} = 155$ Hz), 124.4 (*p*-C, d, $J_{\text{C-H}} = 156$ Hz), 137.8 (*m*-C, s), 151.7 (*ipso*-C, s), and 162.1 ppm (CH, d, $J_{\text{C-H}} = 166$ Hz). UV–vis (CHCl_3): $\lambda_{\text{max}}(\epsilon: 10^4 \text{ mol}^{-1}\text{dm}^3 \text{ cm}^{-1}) = 309$ (8.1), 369 (4.0), 469 (1.4), and 527 nm (1.0). Reflectance: $\lambda_{\text{max}} = 299, 366, 481$ and 528(sh) nm. IR (KBr): $\nu_{\text{N-C-N}} = 1546$ and $\nu_{\text{C-H}} = 2858\text{--}2916 \text{ cm}^{-1}$.

HR-MS (ESI-TOF): Calcd. for $[\text{M}]^+$: 892.2453; Found: 892.2454 *m/z*.

2.1.6. $[\text{Rh}(2,6\text{-F}_2\text{-pf})(\text{nbd})]_2$ (5)

5 was isolated in 38.8% (359 mg, 0.388 mmol). Anal. Calcd. for $\text{C}_{40}\text{H}_{30}\text{F}_8\text{N}_4\text{Rh}_2$: C, 51.97; H, 3.27; N, 6.06%. Found: C, 52.17; H, 3.31; N, 6.09%. ^1H NMR (CD_2Cl_2 , 500 MHz, 298 K): $\delta = 1.27$ (*nbd*- CH_2 , 4H, br), 3.57 (*nbd*- $\text{CH}=\text{CH}$, 4H, br), 3.71 (*nbd*-CH, 2H, br), 4.20 (*nbd*-CH, 2H, br), 4.39 (*nbd*- $\text{CH}=\text{CH}$, 4H, br), 6.85 (*m*-H, 8H, m), 6.97 (*p*-H, 4H, m), and 7.04 ppm (CH, 2H, br). ^{13}C NMR (CD_2Cl_2 , 125 MHz, 298 K): $\delta = 50.6$ (*nbd*-CH, d, $J_{\text{C-H}} = 152$ Hz), 53.4 (*nbd*- $\text{CH}=\text{CH}$, d, $J_{\text{C-H}} = 174$ Hz), 57.5 (*nbd*- $\text{CH}=\text{CH}$, d, $J_{\text{C-H}} = 174$ Hz), 61.8 (*nbd*- CH_2 , t, $J_{\text{C-H}} = 265$ Hz), 111.6 (*p*-C, m), 125.0 (*m*-C, m), 128.9 (*ipso*-C, s), 159.4 (*o*-C, d, $J_{\text{C-F}} = 248$ Hz), and 169.5 ppm (CH, d, $J_{\text{C-H}} = 173$ Hz). ^{19}F NMR (CD_2Cl_2 , 470 MHz, 298 K): $\delta = -121.2$ ppm (*o*-F, br). UV–vis (CHCl_3): $\lambda_{\text{max}}(\epsilon: 10^4 \text{ mol}^{-1}\text{dm}^3 \text{ cm}^{-1}) = 254$ (3.1), 298 (2.7), 395 (0.5), 435 (0.5), and 529 nm (0.8). Reflectance: $\lambda_{\text{max}} = 322, 431$, and 534 nm. IR (KBr): $\nu_{\text{N-C-N}} = 1560$ and $\nu_{\text{C-H}} = 2858\text{--}3067 \text{ cm}^{-1}$. HR-MS (ESI-TOF): Calcd. for $[\text{M}]^+$: 924.0447; Found: 924.0454 *m/z*.

2.2. Measurements

Elemental Analyses for carbon, hydrogen, and nitrogen were conducted using a Yanako CHN CORDER MT-6. UV–Vis absorption spectra were recorded in CHCl_3 solution on a Shimadzu UV-3100 spectrometer. Reflectance spectra were recorded on a Shimadzu ISR-3100 spectrometer. IR spectra were recorded on a JASCO FT/IR-350 spectrometer. ^1H , ^{13}C , and ^{19}F NMR spectra were recorded on a JEOL delta SCX-500 spectrometer operating at 500.1 MHz for ^1H . Chemical shifts for ^1H and ^{13}C signals were referenced to CH_2Cl_2 ($\delta = 5.32$ and 53.8 ppm for ^1H and ^{13}C signals, respectively). Chemical shifts of ^{19}F NMR spectra were referenced to hexafluorobenzene ($\delta = -164.9$ ppm). Computer simulation was performed with gNMR software purchased from Adept Scientific,

Amor Way, Letchworth Herts SG6 1 ZA, UK. Mass spectra were recorded on a Bruker microTOF using positive mode ESI-TOF method for acetonitrile solutions by using sodium formate as reference. Cyclic voltammograms were measured in CH₂Cl₂ solutions containing tetra-*n*-butylammonium hexafluorophosphate (TBAPF₆) on BAS ALS-DY2325 Electrochemical Analyzer. A glassy carbon disk (3.0 mm radius), a platinum wire, and a saturated calomel electrode (SCE) were used as working, counter, and reference electrodes, respectively.

2.3. X-ray crystal structure analysis

Crystals suitable for X-ray structure analysis were obtained from CH₂Cl₂/*n*-hexane mixed-solvent solutions for **1–3**, **5** and from benzene/*n*-hexane mixed-solvent solutions for **4**. Crystal intensity data for **1**, **2**, and **4** were collected at 90 K with a Bruker CCD X-ray diffractometer (SMART APEX) using graphite-monochromated Mo-*K*_α radiation (λ = 0.71073 Å). The structure was solved by direct methods, and refined by full-matrix least-squares methods. All non-hydrogen atoms were refined with anisotropic thermal parameters. The hydrogen atoms were inserted at their calculated positions and fixed there. All of the calculations were carried out on a Windows 7 Core i5 computer utilizing the SHELXTL software package and SHELXL-2014/7. X-ray measurements of the single crystal for **3** was done with Rigaku VariMax Saturn-724 (1.2 kW Mo rotating anode) at 90 K. Single crystal for X-ray analysis was obtained by the diffusion method. X-ray diffraction data was processed using Crystal Clear 1.6.3 followed by CrystalStructure Ver. 4.0.1. Structure was solved from the processed data using SIR 2004, and then refined by Shelxl64 (Shelx-2013). Final structures were validated by Platon CIF check. The crystal intensity data for **5** were collected at 90 K with a Rigaku AFC10 diffractometer with a Saturn CCD system equipped with a MicroMax-007 HF/VariMax rotating-anode X-ray generator with confocal monochromated Mo *K*_α radiation (λ = 0.71075). Their structures were solved by direct methods (SHELXS97 for **5**) and refined on F² using full-matrix least squares technique using the SHELXL program.

Crystallographic data for complex **1–5** reported in this paper have been deposited with the Cambridge Crystallographic Data Centre, CCDC nos. 999583, 1416893, 1420843, 1416894, and 1420703. Copies of the information may be obtained free of charge from: The Director, CCDC, 12 Union Road, Cambridge, CB2 1EZ, UK (fax: +44-1223-336033; e-mail: deposit@ccdc.cam.ac.uk or via http://www.ccdc.cam.ac.uk/data_request/cif). Crystal data and details concerning the data collection are given in Table 1 for **1–5**. All non-hydrogen atoms were refined anisotropically. Hydrogen atoms were located in the calculated positions and refined by using a riding model. Selected bond distances and angles are listed in Table 2, Table S1, and Table S2, respectively.

3. Result and discussion

3.1. Molecular structures

X-ray crystal structures of [Rh(4-Me-pf)(cod)]₂ (**1**) and [Rh(3,5-Me₂-pf)(cod)]₂ (**2**) shown in Fig. 1(a) and (b), respectively, agree with the binuclear nature. Each molecule has two formamidinate ligands bridging the two rhodium atoms. Each rhodium atom is bonded to two nitrogen atoms of different formamidinate ligands and to the double bond centers of a 1,5-cyclooctadiene(cod) ring to form an approximately square planar coordination structure. Dihedral angles, torsion angles, and selected distances (the average of Rh–C and Rh–N distances) of **1** and **2** are shown in Table 2. Close inspection of the data has revealed, however, that the rhodium atoms in **1** and **2** are displaced from the center of the square by

0.143 Å and 0.185 Å, respectively. The slight deviation of the metal atom from the center of the square toward the other metal atom suggests an intermetallic interaction between rhodium(I) centers [50]. The dihedral angles between the square-planar coordination planes are 54.2° and 51.9° for **1** and **2**, respectively, which are smaller than the corresponding angle observed for structurally similar [Rh(O₂C₈H₁₅)(cod)]₂ (58.1°) by ca. 5° [7]. The torsion angles N(1)–Rh(1)–Rh(1A)–N(2A) in **1** and **2** are 29.3(1)° and 27.6(1)°, respectively. The angles are larger than the corresponding angle 16.7°(2) of lantern type Rh(II) complex [Rh₂(4-Me-pf)₄] by 12.6° and 10.9°, respectively [46]. The average Rh–N distances for **1** and **2** are 2.108 Å and 2.116 Å, respectively, which are slightly longer than those for [Rh(μ-pyrazolato)(cod)]₂, i.e. 2.07–2.08 Å [18,19]. The average Rh–C distances for **1** and **2** are 2.130 Å and 2.125 Å, respectively, which are again longer than those for [Rh(L)(cod)]₂ (L = carboxylato, pyrazolato, and pyridine-2-olato), i.e. 2.08–2.09 Å [7–9,15–19]. The Rh··Rh distances of **1** and **2** are 3.2666(8) and 3.1282(6) Å, respectively. It should be noted that the Rh··Rh distance of **2** is the shortest among all the analogous complexes [Rh(L)(cod)]₂ (L = carboxylato, pyrazolato, and pyridine-2-olato) reported previously; they are in the range of 3.15–3.48 Å as listed in Table 3 [7–9,15–19]. Alvarez et al. have pointed out on the basis of the ab initio theoretical studies that the mutual arrangement between two coordination planes around the two d⁸ metal atoms in dimeric complexes [M(μ-X)L₂]₂ (X = S, N, P, Cl, Br etc.; L = cod, nbd, CO, C₂H₄ etc.) tends to change from the coplanar to the bent structure due to the attractive M··M interaction [11,51,52]. Correspondingly, the Rh··Rh length has shown a decrease from 3.525 to 3.168 Å in the case of [Rh(μ-Cl)(CO)₂]₂. Thus, the Rh··Rh lengths of 3.2666(8) and 3.1282(6) Å for **1** and **2**, respectively, should be the indication of direct metal–metal interaction between the rhodium atoms.

The X-ray crystal structures of [Rh(4-Me-pf)(nbd)]₂ (**3**), [Rh(3,5-Me₂-pf)(nbd)]₂ (**4**), and [Rh(2,6-F₂-pf)(nbd)]₂ (**5**) are shown in Fig. 2(a)–(c), respectively. Dihedral angles, torsion angles, and selected distances (the average of Rh–C and Rh–N distances) of **3–5** are shown in Table 2. As in the case of **1** and **2**, the rhodium atoms of **3–5** are displaced from their coordination planes; the displaced lengths are 0.102 and 0.155 Å for **3**, 0.143 and 0.124 Å for **4**, and 0.074 and 0.106 Å for **5**. Thus, the displacement lengths in **5** are shorter than those in the other two nbd complexes. The dihedral angle between two square planar coordination planes is 44.8° in **3**, 44.2° in **4**, and 44.9° in **5**. These values are smaller than those in **1** and **2** by ca. 10°. The results might be the indication that the steric repulsion between two diene ligands decreases as the ligand changes from cod to nbd. In fact, while the shortest distances between cod ligands in **1** and **2** are 3.632(5) and 3.600(4) Å for C21–C23A and C20–C22A, respectively, those between nbd ligands in **3**, **4**, and **5** are 3.42(1), 3.367(6), and 3.366(6) Å for C1–C9, C35–C42, and C28–C38, respectively. The average Rh–N distances for **3**, **4**, and **5** are 2.109 Å, 2.093 Å, and 2.118 Å respectively, these distances agree with for those of **1** and **2** (2.108 and 2.116 Å, respectively). The average Rh–C distances for **3**, **4**, and **5** are 2.131 Å, 2.104 Å, and 2.118 Å respectively, agree well with precedent for those of [Rh(L)(nbd)]₂ (L = pyrazolato and carboxylato) [20–23].

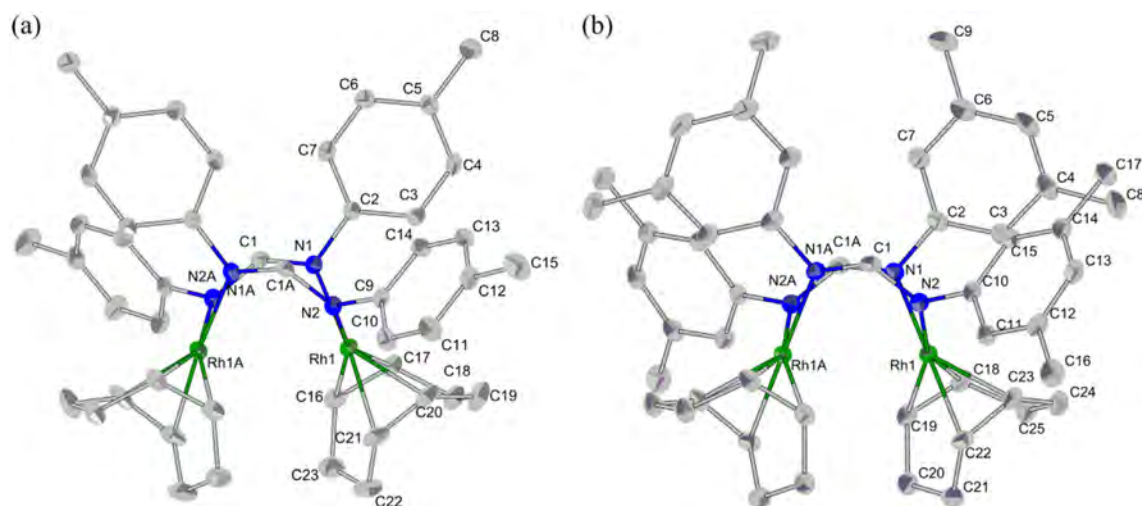
Correspondingly, the Rh··Rh distances are 3.0205(11), 2.9724(9), and 3.0906(14) Å for **3**, **4**, and **5**, respectively, which are significantly shorter than 3.2666(8) for **1** and 3.1282(6) Å for **2** (Table 3). In both cod and nbd complexes, the Rh··Rh distances of **2** and **4** are shorter than those of **1** and **3**. The results suggest that the formamidinate ligands with electron-releasing substituents tend to shorten the Rh··Rh distance. Furthermore, the data in Table 3 indicate that the Rh··Rh distance in **4** is the shortest among all the analogous nbd complexes reported previously. The results are indicative of a strong direct metal–metal interaction between two Rh atoms in **4**. As for the other structural parameters, while the

Table 1
Crystal data and data collection details for 1–5.

Compounds	[Rh(4-Me-pf) (cod)] ₂ (1)	[Rh(3,5-Me ₂ -pf) (cod)] ₂ (2)	[Rh(4-Me-pf) (nbd)] ₂ (3)	[Rh(3,5-Me ₂ -pf) (nbd)] ₂ · 1.5C ₆ H ₆ (4)	[Rh(2,6-F ₂ -pf) (nbd)] ₂ (5)
Empirical formula	C ₄₆ H ₅₄ N ₄ Rh ₂	C ₅₀ H ₆₂ N ₄ Rh ₂	C ₄₄ H ₄₆ N ₄ Rh ₂	C ₅₇ H ₆₃ N ₄ Rh ₂	C ₄₀ H ₃₀ F ₈ N ₄ Rh ₂
Formula weight	868.75	924.86	868.69	1009.93	924.50
Temperature (K)	90 (2)	90 (2)	90 (2)	90 (2)	90 (2)
Wave length (Å)	0.71073	0.71073	0.71075	0.71073	0.71075
Crystal system	Monoclinic	Monoclinic	Tetragonal	Triclinic	Triclinic
Space group	C2/c	C2/c	P $\bar{4}$ 2 ₁ c	P $\bar{1}$	P $\bar{1}$
a (Å)	21.958 (3)	19.958 (4)	21.549 (5)	9.904 (3)	8.655 (4)
b (Å)	12.1009 (18)	13.155 (3)	21.549 (5)	15.500 (4)	10.653 (5)
c (Å)	15.797 (2)	16.446 (3)	16.044 (4)	16.426 (5)	19.204 (9)
A (°)	90	90	90	81.380 (5)	91.132 (7)
B (°)	112.285 (3)	106.609 (3)	90	75.503 (5)	99.723 (8)
γ (°)	90	90	90	75.165 (5)	96.616 (9)
Volume (Å ³)	3884.0 (10)	4137.7 (14)	7450 (4)	2350.0 (11)	1732.0 (14)
Z	4	4	8	2	2
Density (Calculated) (g cm ⁻³)	1.486	1.485	1.492	1.427	1.773
Absorption coefficient (mm ⁻¹)	0.888	0.838	0.923	0.745	1.033
F (000)	1792	1920	3424	1046	920
Crystal size (mm)	0.15 × 0.15 × 0.10	0.42 × 0.26 × 0.15	0.13 × 0.05 × 0.04	0.40 × 0.30 × 0.20	0.09 × 0.07 × 0.02
θ Range for data collection (°)	1.96 to 28.51	1.88 to 28.55	1.89 to 28.00	1.79 to 28.55	3.21 to 26.50
Index ranges	-27 ≤ h ≤ 25, -15 ≤ k ≤ 15, -20 ≤ l ≤ 16	-23 ≤ h ≤ 25, -7 ≤ k ≤ 16, -21 ≤ l ≤ 21	-28 ≤ h ≤ 28, -28 ≤ k ≤ 28, -21 ≤ l ≤ 21	-12 ≤ h ≤ 13, -20 ≤ k ≤ 16, -21 ≤ l ≤ 20	-10 ≤ h ≤ 9, -13 ≤ k ≤ 10, -24 ≤ l ≤ 24
Reflections collected	11657	12230	125277	14487	13163
Independent reflections	4504 [R _{int} = 0.0228]	4786 [R _{int} = 0.0264]	9009 [R _{int} = 0.0957]	10422 [R _{int} = 0.0242]	6970 [R _{int} = 0.0308]
Maximum and minimum transmission	0.915 and 0.878	0.885 and 0.720	0.964 and 0.856	0.865 and 0.755	0.980 and 0.857
Refinement method	Full-matrix least-squares on F ²	Full-matrix least-squares on F ²			
Data/restraints/parameters	4504/0/237	4786/0/257	9009/84/479	10422/0/576	6970/0/487
Goodness-of-fit on F ²	1.244	0.981	1.201	0.986	1.055
Final R indices (I > 2σ(I))	R ₁ = 0.0344, wR ₂ = 0.0735	R ₁ = 0.0345, wR ₂ = 0.0866	R ₁ = 0.0539, wR ₂ = 0.1126	R ₁ = 0.0465, wR ₂ = 0.1195	R ₁ = 0.0374, wR ₂ = 0.0794
R indices (all data)	R ₁ = 0.0389, wR ₂ = 0.0750	R ₁ = 0.0414, wR ₂ = 0.0887	R ₁ = 0.0541, wR ₂ = 0.1127	R ₁ = 0.0582, wR ₂ = 0.1246	R ₁ = 0.0501, wR ₂ = 0.0859
Largest peak and hole (e Å ⁻³)	+0.673 and -0.712	+2.263 and -0.697	+0.614 and -1.076	+2.246 and -2.091	+0.874 and -0.517

Table 2Selected bond distances (Å), bond angles (°), dihedral angles (°), and torsion angles (°) for **1–5** with their estimated standard deviations in parentheses.

Compounds	[Rh(4-Me-pf)(cod)] ₂ (1)	[Rh(3,5-Me ₂ -pf)(cod)] ₂ (2)	[Rh(4-Me-pf)(nbd)] ₂ (3)	[Rh(3,5-Me ₂ -pf)(nbd)] ₂ · 1.5C ₆ H ₆ (4)	[Rh(2,6-F ₂ -pf)(nbd)] ₂ (5)
Rh··Rh distance (Å)	3.2666 (8)	3.1282 (6)	3.0205 (11)	2.9724 (9)	3.0906 (14)
Average Rh–N distances (Å)	2.108	2.116	2.109	2.093	2.118
Average Rh–C distances (Å)	2.130	2.125	2.131	2.104	2.118
N–C(methine) distances (Å)	N(1)–C(1) 1.321(3) N(2)–C(1A) 1.320(4) N(2A)–C(1) 1.320(4)	N(1)–C(1) 1.313(3) N(2)–C(1A) 1.321(3) N(2A)–C(1) 1.321(3)	N(1)–C(22) 1.318(9) N(2)–C(22) 1.328(9) N(3)–C(37) 1.329(10) N(4)–C(37) 1.330(10)	N(1)–C(1) 1.308(4) N(2)–C(1) 1.324(4) N(3)–C(18) 1.310(5) N(4)–C(18) 1.312(4)	N(1)–C(1) 1.320(4) N(2)–C(1) 1.307(5) N(3)–C(14) 1.317(5) N(4)–C(14) 1.313(5)
Distances of Rh ion from square ligand plane (Å)	0.143	0.185	0.102(Rh1), 0.155(Rh2)	0.143(Rh1), 0.124(Rh2)	0.074(Rh1), 0.106(Rh2)
Distances of Rh-centroid (C=C) (avg.) (Å)	2.012	2.007	2.013	1.985	2.000
Dihedral angle between Rh(1)–Rh(2) square planes (°)	54.2	51.9	44.8	44.2	44.9
Torsion angle of N(1)–Rh(1)–Rh(1A)–N(2A) (°)	29.3 (1)	27.6 (1)	–	–	–
Torsion angle of N(1)–Rh(1)–Rh(2)–N(2) (°)	–	–	29.0 (3)	31.5 (1)	28.3 (1)
Torsion angle of N(3)–Rh(1)–Rh(2)–N(4) (°)	–	–	30.2(3)	29.8(1)	25.3(1)

**Fig. 1.** ORTEP drawing of (a) **1** and (b) **2**, showing the thermal ellipsoids at 50% probability level. Hydrogen atoms are omitted for clarity. Symmetry code: (A) $-x, y, -z + 1/2$ for **1** and $-x + 1, y, -z + 1/2$ for **2**.**Table 3**Rh··Rh distances (Å) in complexes of the type [Rh(L)(cod)]₂ and [Rh(L)(nbd)]₂ (L = formamidinate, carboxylate, pyroazole, and 2-hydroxypyridine).

Compounds	Rh··Rh (Å)	Reference
[Rh(4-Me-pf)(cod)] ₂ (1)	3.2666 (8)	This work
[Rh(3,5-Me ₂ -pf)(cod)] ₂ (2)	3.1282 (6)	This work
[Rh(O ₂ CH)(cod)] ₂	3.3868 (8)	[15]
[Rh(O ₂ CCF ₃)(cod)] ₂	3.4844 (6)	[16]
[Rh(O ₂ C ₈ H ₁₅)(cod)] ₂	3.3390 (4)	[7]
[Rh(O ₂ C-1-Adamantyl)(cod)] ₂	3.3026 (3)	[9]
[Rh(O ₂ CCH ₂ Ph)(cod)] ₂	3.3868 (4)	[9]
[Rh(pz ^{FC})(cod)] ₂	3.189 (1)	[19]
[Rh(pz ^{ph-o-ph})(cod)] ₂	3.219 (3)	[18]
[Rh(pz ^{ph-o-Bup})(cod)] ₂	3.2339 (9)	[18]
[Rh(mhp)(cod)] ₂	3.267 (1)	[17]
[Rh(4-Me-pf)(nbd)] ₂ (3)	3.0205 (11)	This work
[Rh(3,5-Me ₂ -pf)(nbd)] ₂ (4)	2.9724 (9)	This work
[Rh(2,6-F ₂ -pf)(nbd)] ₂ (5)	3.0906 (14)	This work
[Rh(O ₂ CCH ₃)(nbd)] ₂	3.1050 (7)	[21]
[Rh(O ₂ CC(CH ₃) ₃)(nbd)] ₂	3.107 (2)	[22]
[Rh(O ₂ CCH ₂ C(CH ₃) ₃)(nbd)] ₂	3.0636 (2)	[9]
[Rh(bupz)(nbd)] ₂	3.098 (2)	[20]
[Rh(mbupz)(nbd)] ₂	3.071 (2)	[20]

torsion angles N(1)–Rh(1)–Rh(2)–N(2) and N(3)–Rh(1)–Rh(2)–N(4) in **3** and **4** are slightly greater than those in **1** and **2**, the torsion angles in **5** are closer to those in **1** and **2** rather than in **3** and **4** (Table 2).

3.2. Temperature dependent NMR spectra

Fig. 3 shows the ¹H NMR spectra of the cod complex [Rh(4-Me-pf)(cod)]₂ (**1**) taken in CD₂Cl₂ solution at (a) 298 K, (b) 273 K, (c) 253 K, (d) 243 K, and (e) 213 K. The corresponding spectra of [Rh(3,5-Me₂-pf)(cod)]₂ (**2**) are given in Fig. S1. As shown in Fig. 3(a), while the aliphatic and olefinic protons of the cod ligands showed four and two signals, the *p*-methyl protons exhibited a single sharp signal at 2.29 ppm. In the aromatic region, the *m*-protons gave a relatively sharp doublet at 7.02 ppm while the *o*-protons showed a very broad signal centered at 7.2 ppm. The methine protons of the formamidinate ligands exhibited a sharp triplet at 7.19 ppm due to the coupling ($J = 1.7$ Hz) with magnetically equivalent two rhodium atoms ($I = 1/2$) [15,45]. As the temperature was lowered, all these signals except methine signal further broadened and split into several lines as shown in

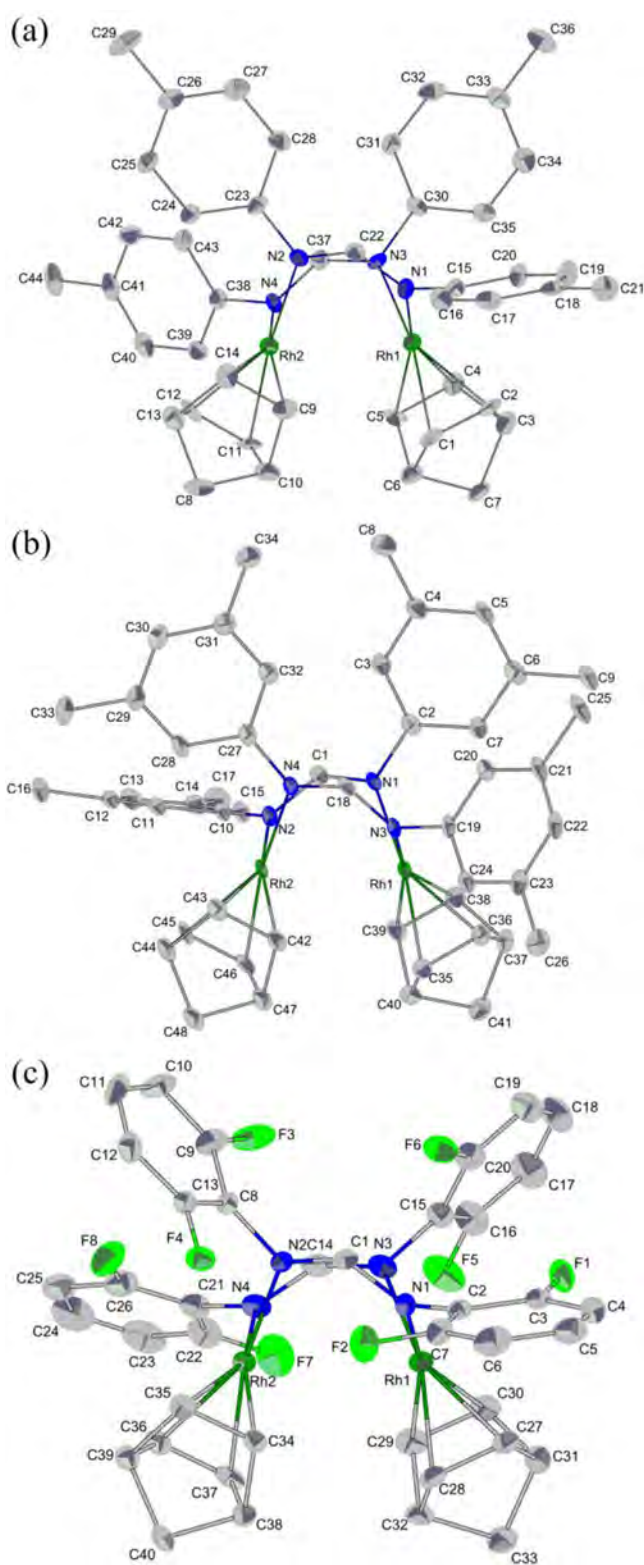


Fig. 2. ORTEP drawing of (a) **3**, (b) **4**, and (c) **5**, showing the thermal ellipsoids at 50% probability level. Hydrogen atoms are omitted for clarity.

Fig. 3(b)–(e). At 213 K, two signals were observed for the *p*-methyl, eight signals for the aliphatic, and four signals for the olefinic protons. While the *ortho* protons exhibited clearly resolved three doublets at 7.53, 6.87, and 6.38 ppm with 2:1:1 ratio, the *meta* protons showed a broad singlet at 7.04 ppm. The formamidinate

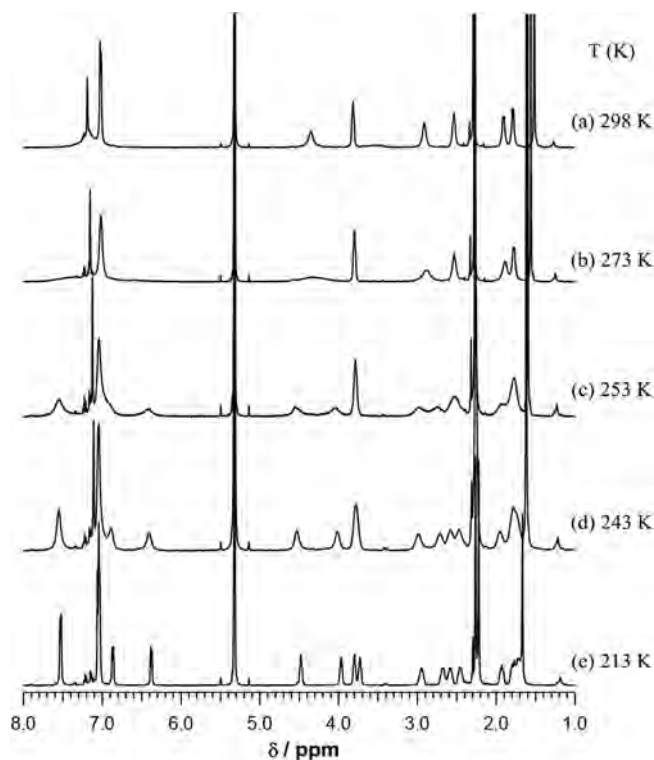


Fig. 3. ^1H NMR spectra of **1** taken in CD_2Cl_2 solution at (a) 298 K, (b) 273 K, (c) 253 K, (d) 243 K, and (e) 213 K.

methine protons maintained a sharp singlet at 7.06 ppm even at 213 K.

Obviously, some dynamic processes are taking place in this complex. In order to explain the change in signal numbers depending on the temperature, we have assumed that both the racemization between enantiomers (**A** and **B** in Fig. 4) and the rotation of aryl groups around the C(aryl)-N bonds (α and β in Fig. 4) are fast on the ^1H NMR timescale at 298 K. We have also assumed that the rotation of the coordinated cod ligands is slow even at 298 K. Under these assumptions, the four *p*-tolyl groups are equivalent at 298 K giving a singlet for the *p*-methyl, a doublet for the *ortho* and *meta* protons. The aliphatic and olefinic protons should give four and two signals, respectively, being consistent with the observed signal numbers. Thus, the complex **1** exists as a racemic mixture **A** and **B**, which are rapidly interconverting on the ^1H NMR timescale at 298 K. As the temperature is lowered, the racemization process is slowed down and is frozen on the ^1H NMR timescale at 213 K. In such a situation, the *p*-methyl, aliphatic, and olefinic protons should give two, eight, and four signals, respectively, which is also consistent with the observed signal numbers. Discrepancy of the signal numbers was recognized, however, in the *ortho* signals; the *ortho* protons showed three doublets in a 2:1:1 ratio instead of the expected two signals with equal intensity. The results indicate that the rotation about N–C(tolyl) bonds in one of the two kinds of *p*-tolyl rings, α or β in Fig. 4, is frozen on the ^1H NMR timescale at lower temperature, which will be discussed later.

Fig. 5 shows the ^1H NMR spectra of the nbd complex $[\text{Rh}(\text{4-Me-pf})(\text{nbd})_2]$ (**3**) taken in CD_2Cl_2 solution at (a) 298 K (b) 263 K, (c) 233 K, (d) 213 K and (e) 183 K. The corresponding spectra of $[\text{Rh}(\text{3,5-Me}_2\text{-pf})(\text{nbd})_2]$ (**4**) are given in Fig. S2. As shown in Fig. 5, the temperature dependence of **3** is essentially the same as that of the cod complex **1**. However, there are some differences in the signal widths. In contrast to the case of **1**, **3** exhibited sharp and well-resolved signals for the olefinic and *ortho* protons even at

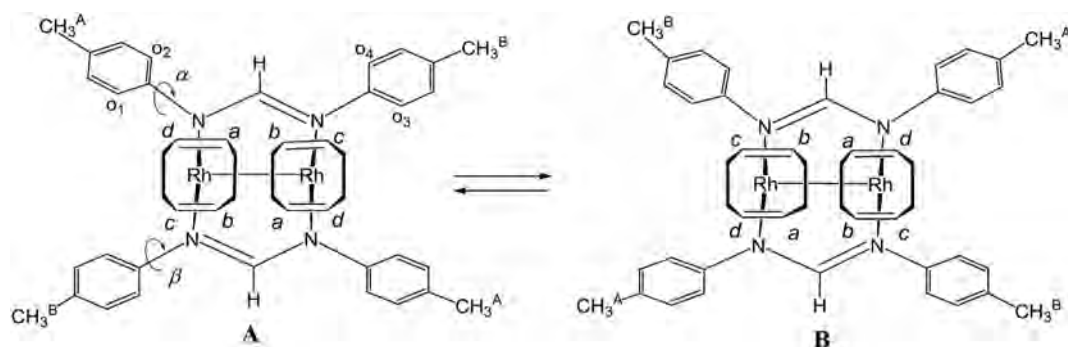


Fig. 4. Racemization between enantiomers **A** and **B** in **1**. (note): CH_3^{A} exchanges its site with CH_3^{B} . Similarly, the olefinic protons *a*, *b*, *c*, and *d* exchange their sites with those of *b*, *a*, *d*, and *c*, respectively. Symbols α and β with curved arrow indicate the rotation of the aryl groups about the N–C(aryl) bonds. The *ortho* protons are labeled as o^1 – o^4 .

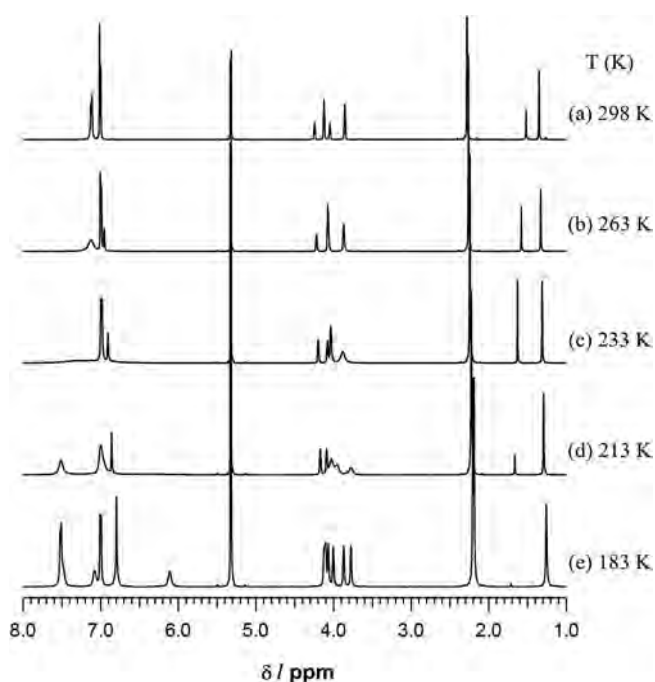


Fig. 5. ^1H NMR spectra of **3** taken in CD_2Cl_2 solution at (a) 298 K, (b) 263 K, (c) 233 K, (d) 213 K, and (e) 183 K.

298 K as shown in Fig. 5(a). The results suggest that the rate for racemization in **3** is much faster than that in **1** at 298 K. It should also be noted that the rotation of the coordinated nbd ligands is slow on the ^1H NMR timescale even at 298 K since the bridgehead methine protons showed two signals at 4.05 and 4.24 ppm. At 183 K, the *p*-methyl and olefinic protons showed two and four signals, respectively, as in the case of **1**. The bridged methylene protons of the nbd ligand maintained a broad singlet though they should give an AB quartet in principle. Probably, the difference in chemical shifts is too small to show an AB quartet. As for the aromatic protons, not only the *ortho* but also the *meta* protons gave three separated signals in a 2:1:1 ratio; 7.53, 7.48, and 6.12 ppm for the *ortho* and 7.00, 7.08, and 6.82 ppm for the *meta* protons. The results again indicate that the rotation about N–C(tolyl) bonds in one of the two kinds of *p*-tolyl rings is frozen at 183 K in **3** and **4**.

Fig. S3 shows the temperature dependent ^1H NMR spectra of $[\text{Rh}(2,6\text{-F}_2\text{-pf})(\text{nbd})_2]$ (**5**). As a whole, the spectral change in **5** is similar to those in **3** and **4**. Notable difference was observed, however, in the bridged methylene protons of the nbd ligands. While the methylene protons in **3** and **4** maintained a broad singlet

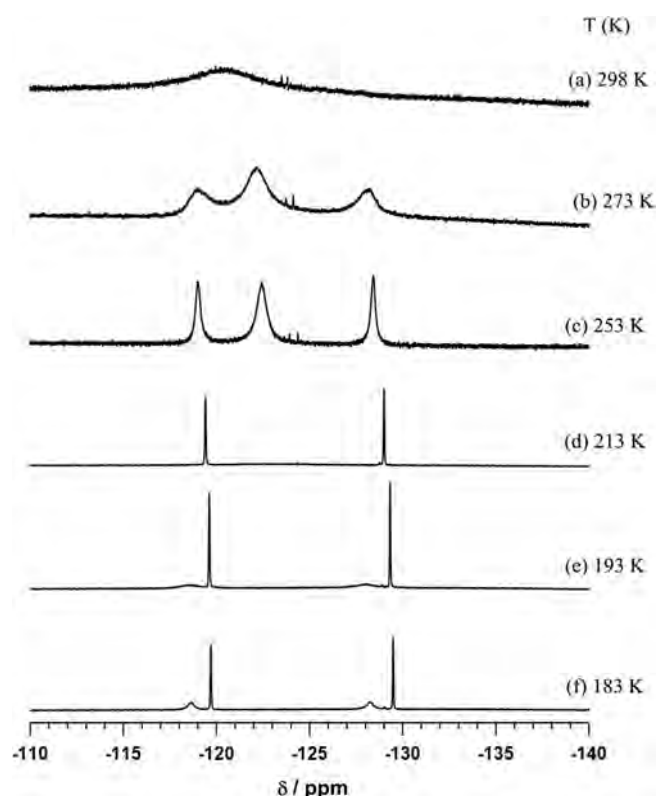


Fig. 6. ^{19}F NMR spectra of **5** taken in CD_2Cl_2 solution with C_6F_6 at (a) 298 K, (b) 273 K, (c) 253 K, (d) 213 K, (e) 193 K, and (f) 183 K. Chemical shifts are referenced to C_6F_6 .

even at 183 K, those of **5** showed a clear AB quartet with $J = 8.0$ Hz. Similarly, while the *meta* protons showed a doublet of doublets at 298 K, they gave three multiplets at 193 K centered at 6.78, 6.89, and 7.01 ppm in a 1:2:1 ratio. Thus, the rotation of one of the two kinds of 2,6-difluorophenyl rings is frozen on the ^1H NMR timescale as in the case of **1–4**.

Fig. 6 shows the temperature dependent ^{19}F NMR spectra taken in CD_2Cl_2 solution with C_6F_6 at (a) 298 K, (b) 273 K, (c) 253 K, (d) 213 K, (e) 193 K, and (f) 183 K. A very broad unsymmetrical signal centered at -121 ppm at 298 K split into three signals as shown in Fig. 6(a)–(c). The signal in the middle, *i.e.* -122 ppm at 253 K, broadened at lower temperature and split into two signals below 213 K. In contrast, the two other signals sharpened as the temperature was lowered as shown in Fig. 6(d)–(e). Thus, two sharp signals and two broad signals coexisted at 183 K as shown in Fig. 6(f). The observation of four separate signals at 183 K indicates

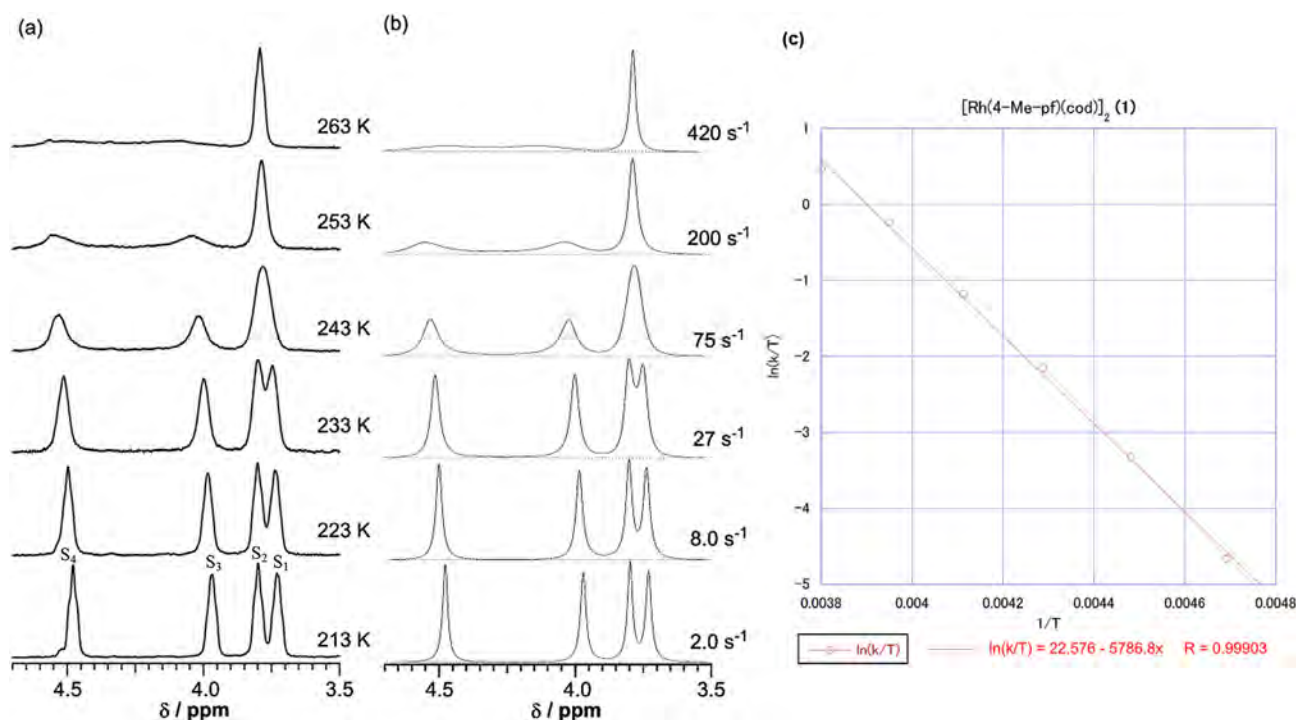


Fig. 7. (a) Temperature dependent ^1H NMR spectra of the olefinic protons in **1** in CD_2Cl_2 solution. (b) Calculated spectra corresponding to the observed ones. (c) Eyring's plots.

Table 4
Activation parameters for dynamic processes.

Compounds	Racemization				Aryl rotation			
	Probes	ΔH^\ddagger kJ mol $^{-1}$	ΔS^\ddagger J mol $^{-1}$	$\Delta G^\ddagger_{298\text{K}}$ kJ mol $^{-1}$	Probes	ΔH^\ddagger kJ mol $^{-1}$	ΔS^\ddagger J mol $^{-1}$	$\Delta G^\ddagger_{298\text{K}}$ kJ mol $^{-1}$
1	alkenyl(^1H)	48.1	−9.8	51.1	<i>ortho</i> (^1H) ^a	n.d.	n.d.	n.d.
	<i>p</i> -Me(^1H)	48.1	−5.0	51.2				
2	alkenyl(^1H)	54.7	+5.2	53.2	<i>ortho</i> (^1H) ^a	n.d.	n.d.	n.d.
3	alkenyl(^1H)	46.2	+9.3	43.4	<i>ortho</i> (^1H) ^b	35.1 ^b	−19.2 ^b	40.8 ^b
	<i>p</i> -Me(^1H)	45.9	+6.0	44.1				
4	alkenyl(^1H)	50.5	+19.5	44.7	3,5-Me ₂ (^1H)	39.4 ^b	−16.1 ^b	44.2 ^b
5	alkenyl(^1H)	42.5	−26.3	50.3	2,6-fluoro(^{19}F)	33.2 ^c	−7.5 ^c	35.4 ^c
	methylene(^1H)	42.7	−23.4	49.7				

^a Determination of the activation parameters for rotation is difficult because $k_{\text{rot(s)}}$ is much smaller than k_{rac} in cod complexes.

^b Activation parameters for rotation of the slowly rotating aryl groups.

^c Activation parameters for rotation of the rapidly rotating aryl groups.

that the rotation of four aryl rings are slowed down in **5** on the ^{19}F NMR timescale, which should be ascribed to the increase in barriers to rotation and/or the increase in chemical shift differences between two interconverting fluorine atoms.

3.3. Activation parameters for racemization

The rate constants for racemization between **A** and **B** in Fig. 4 were determined by the line shape analysis of the olefinic proton signals. As shown in Fig. 4, the olefinic protons *a*, *b*, *c*, and *d* exchange their sites with *b*, *a*, *d*, and *c*, respectively. Fig. 7(a) shows the temperature dependent ^1H NMR spectra of the olefinic proton region in **1**. Close inspection of the spectral change reveals that the mutual exchange takes place between two downfield shifted signals (s_1 and s_2) and two upfield shifted signals (s_3 and s_4). The theoretical spectrum with rate constant k_{rac} was obtained by taking the mutual exchanges, $s_1 \rightleftharpoons s_2$ and $s_3 \rightleftharpoons s_4$, into consideration. The rate constant for racemization was determined at each temperature by the comparison of the observed spectra given in Fig. 7(a) with the theoretical ones given in Fig. 7(b). The activation parameters

were determined from the Eyring's plots shown in Fig. 7(c), and they were listed in Table 4. The rate constants can also be determined by the line shape analysis of the *p*-methyl signals as shown in Fig. S4. The activation parameters obtained from two different probes, *i.e.* olefinic and *p*-methyl protons, showed a reasonable agreement. Similar analyses were performed for complexes **2**–**5** as shown in Figs. S5–S8, respectively.

The data in Table 4 indicate that the activation free energy for racemization decreases by 7–9 kJ/mol as the diene ligand changes from cod to nbd. The results suggest that the transition state for racemization might be sterically more hindered in the cod complexes than in the nbd complexes due to the bulkier nature of cod as compared with nbd ligand. Activation parameters of **5** are characterized by somehow larger negative values in activation entropy, which could be ascribed to the conformational restriction at the transition state due to the presence of the 2,6-difluoro groups.

3.4. Activation parameters for aryl rotation

As mentioned in the previous section, the rates for rotation of

aryl groups around N–C(aryl) bonds are quite different among four aryl groups. Two of them rotate rapidly as compared with the other two. Thus, the variable temperature NMR spectra of these complexes are quite complicated because they include dynamic processes such as racemization, rotation of slowly rotating aryl groups, and rotation of rapidly rotating aryl groups; the rate constants for these processes are given as k_{rac} , $k_{\text{rot(slow)}}$, and $k_{\text{rot(rapid)}}$, respectively. Since the *ortho* proton signals of rapidly rotating aryl groups never split into two parts even at 183 K in **1–4**, it is reasonable to assume that $k_{\text{rot(rapid)}}$ is much larger than k_{rac} , i.e. $k_{\text{rot(rapid)}} \gg k_{\text{rac}}$.

A priori, there are three cases on the relationships between k_{rac} and $k_{\text{rot(slow)}}$. They are, i) *case(1)*: $k_{\text{rac}} \gg k_{\text{rot(slow)}}$, ii) *case(2)*: $k_{\text{rac}} \ll k_{\text{rot(slow)}}$, and iii) *case(3)*: $k_{\text{rac}} \sim k_{\text{rot(slow)}}$. In *case(1)*, a broad *ortho* signal should split directly into three signals in a 2:1:1 ratio as the temperature is lowered. This is because the *ortho* protons of the slowly rotating aryl groups can be nonequivalent only when the racemization process is slowed down. It is therefore impossible to determine the $k_{\text{rot(slow)}}$ values from the line shape analysis. In *case(2)*, a broad *ortho* signal should split into two signals with equal intensities at low temperature where the racemization is slowed down. As the temperature is further lowered, one of the *ortho* signals should split into two to give three signals in a 2:1:1 ratio. Since the spectral change occurs step by step, we can easily determine both k_{rac} and $k_{\text{rot(slow)}}$ values. In *case(3)*, the line shape of the *ortho* signals should be affected by both k_{rac} and $k_{\text{rot(slow)}}$ values. It is therefore possible to know $k_{\text{rot(slow)}}$ since the k_{rac} values have been determined independently from the line shape analysis of the olefinic proton signals.

As shown in Fig. 3, a broad *ortho* signal of **1** (δ 7.18) at 298 K started to split into three signals below 253 K, suggesting that $k_{\text{rac}} > k_{\text{rot(slow)}}$. Because the *ortho* protons of the rapidly rotating aryl group exhibit a sharp doublet even at 183 K, the rate constants for rotation $k_{\text{rot(rapid)}}$ should be much larger than k_{rac} . As shown in Fig. 4, racemization process induces site exchange such as o1 \rightleftharpoons o3 and o2 \rightleftharpoons o4 with the rate constant equal to k_{rac} . Similarly, the rotation around C–N(aryl) bonds signified as α and β in Fig. 4 induces site exchange such as o1 \rightleftharpoons o2 and o3 \rightleftharpoons o4 with the rate constants equal to $k_{\text{rot(rapid)}}$ and $k_{\text{rot(slow)}}$, respectively. Here, we assumed that the rotation α is much faster than rotation β . In the line shape analysis of the *ortho* proton signals, we used k_{rac} values that have been determined from the line shape analysis of the olefinic proton signals. The $k_{\text{rot(rapid)}}$ value is tentatively fixed at a very large value, $1.0 \times 10^6 \text{ s}^{-1}$, in the temperature range examined. Thus, the line shape of the *ortho* proton signals can be a function of $k_{\text{rot(slow)}}$.

Fig. S9 shows the observed and calculated spectra of the *ortho* proton signals of **1**. A precise simulation was difficult because of the presence of the *meta* and methine signals in the same region. However, the observed spectrum seems to be correctly reproduced by the theoretical one calculated using the already-determined k_{rac} and tentatively fixed $k_{\text{rot(rapid)}} = 1.0 \times 10^6 \text{ s}^{-1}$. In other words, the best-fit spectrum was obtained without using $k_{\text{rot(slow)}}$. The result suggests that complex **1** belongs to *case(1)* where k_{rac} is much larger than $k_{\text{rot(slow)}}$. Thus, it is impossible to determine $k_{\text{rot(slow)}}$ in this complex. The temperature dependent *ortho* proton signals of **2** exhibited a similar behavior as shown in Fig. S10. On the basis of these results, it is concluded that the rate constants of the three dynamic processes in the cod complexes **1** and **2** have the following relationship, $k_{\text{rot(rapid)}} \gg k_{\text{rac}} \gg k_{\text{rot(slow)}}$, and that the activation parameters for rotation of four aryl groups are difficult to determine.

Fig. S11(a) shows the NMR spectra of the *ortho* proton signals of the nbd complex **3** taken at 223 K. The rate constant for racemization was determined to be 230 s^{-1} from the line shape analysis of the alkenyl proton signals shown in Fig. S6. Unlike the case in cod

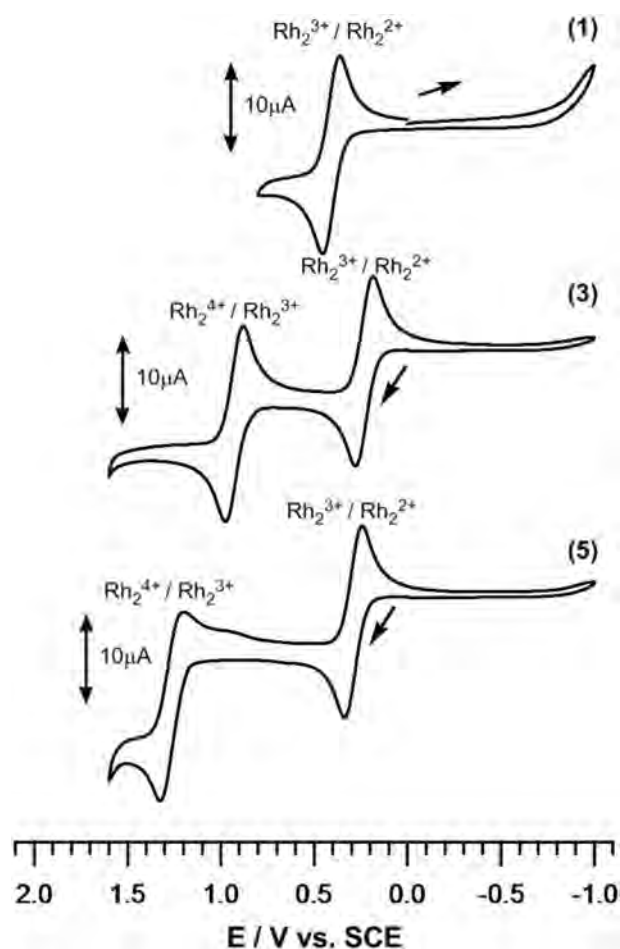


Fig. 8. Cyclic voltammograms of **1**, **3**, and **5** ($1.0 \times 10^{-3} \text{ M}$) at a scan rate of 0.05 V s^{-1} in CH_2Cl_2 solutions containing 0.1 M TBAPF_6 .

Table 5
Half-wave potentials $E_{1/2}$ (V vs. SCE) of complexes **1–5** in CH_2Cl_2 , 0.1 M TBAPF_6 .

Compounds	$E_{1/2}$ (V)	
	$\text{Rh}_2^{4+}/\text{Rh}_2^{3+}$	$\text{Rh}_2^{3+}/\text{Rh}_2^{2+}$
[Rh(4-Me-pf)(cod)] ₂ (1)	–	+0.41
[Rh(3,5-Me ₂ -pf)(cod)] ₂ (2)	–	+0.47
[Rh(4-Me-pf)(nbd)] ₂ (3)	+0.98	+0.23
[Rh(3,5-Me ₂ -pf)(nbd)] ₂ (4)	+0.86	+0.17
[Rh(2,6-F ₂ -pf)(nbd)] ₂ (5)	+1.26	+0.29

complexes, the calculated spectrum with $k_{\text{rac}} = 230 \text{ s}^{-1}$ and $k_{\text{rot(rapid)}} = 1.0 \times 10^5 \text{ s}^{-1}$ was completely different from the observed one as shown in Fig. S11(b). The result suggests that complex **3** belongs to *case(3)* where k_{rac} is comparable to $k_{\text{rot(slow)}}$. Thus, the theoretical spectra were drawn by using various $k_{\text{rot(slow)}}$ values as shown in Fig. S11(c)–(e). The best-fit spectrum was obtained with $k_{\text{rot(slow)}} = 3000 \text{ s}^{-1}$. By applying the same method, we were able to estimate the $k_{\text{rot(slow)}}$ values at several temperatures as shown in Fig. S12. The $k_{\text{rot(slow)}}$ values in complex **4** were similarly obtained by the simulation of the 3,5-methyl signals as shown in Fig. S13. The activation parameters for rotation of the slowly rotating aryl groups in **3** and **4** are listed in Table 4.

Fig. 6 shows the temperature dependent ^{19}F NMR spectra of **5**. A broad fluorine signal at 298 K split into three signals at 273 K, indicating clearly that **5** belongs to *case(1)* where k_{rac} is much larger than $k_{\text{rot(slow)}}$. As shown in Fig. 6(c)–(f), a broad signal in the middle

split into two signals while the other two signals assigned to slowly rotating aryl groups were quite sharp. Thus, it is possible to treat the temperature dependent ^{19}F NMR signals of rapidly rotating aryl groups as a function of $k_{\text{rot}(\text{rapid})}$. Fig. S14 shows the observed and calculated spectra of the *ortho* fluorine signals, from which the $k_{\text{rot}(\text{rapid})}$ values were determined at several temperatures. The activation parameters for rotation of rapidly rotating aryl groups are also listed in Table 4.

In order to obtain the $k_{\text{rot}(\text{slow})}$ values in **5**, the spectral change at higher temperature range was analyzed. Fig. S15 shows the computer simulation of the *ortho* fluorine signals at 253 K. The observed spectrum was correctly reproduced by the introduction of the k_{rac} and $k_{\text{rot}(\text{rapid})}$ values determined from the line shape analysis of the olefinic proton and fluorine signals given in Fig. S8 and Fig. S14, respectively. Thus, the rate constants of the three dynamic processes in **5** have the following relationship, $k_{\text{rot}(\text{rapid})} \gg k_{\text{rac}} \gg k_{\text{rot}(\text{slow})}$, and that the activation parameters for rotation of slowly rotating aryl groups are difficult to determine.

The data in Table 4 indicate that the difference in activation free energies for rotation between two aryl groups in **5** is much larger than 15 kJ mol^{-1} at 298 K. Thus, the ratio of the rate constants $k_{\text{rot}(\text{rapid})}/k_{\text{rot}(\text{slow})}$ is at least 420. Such a large difference in rotation rates could be ascribed to the difference in steric environment of the aryl groups; one of the aryl groups binds to the imino nitrogen while the other binds to the amino nitrogen. The aryl group bonding to the imino nitrogen would suffer a larger steric repulsion at the transition state for rotation where the phenyl and the $\text{Rh}-\text{N}=\text{C}$ plains are coplanar due to the shorter $\text{N}-\text{C}(\text{aryl})$ bond.

3.5. Electrochemistry

The cyclic voltammograms of **1** and **3** and those of **2**, **4**, and **5** are given in Fig. 8 and Fig. S16, respectively. Table 5 lists the electrochemical data of **1**–**5**. As shown in Fig. 8, the cod complexes **1** and **2** exhibited only one chemically reversible redox process $\text{Rh}_2^{3+}/\text{Rh}_2^{2+}$ at $E_{1/2} = 0.41 \text{ V}$ versus SCE. The sweep up to 1.7 V is shown in Fig. S17, which showed a broad peak around 0 V ascribed to the decomposition of the complex. Thus, electrochemical feature of **1** is essentially the same as that reported by P. Zanella et al. [36].

In contrast, the nbd complexes **3**–**5** showed two chemically reversible redox processes; the $E_{1/2}$ values are 0.23 and 0.98 V for **3**, 0.17 and 0.86 V for **4**, and 0.29 and 1.26 V for **5**. The first and second oxidation potentials correspond to the $\text{Rh}_2^{3+}/\text{Rh}_2^{2+}$ and $\text{Rh}_2^{4+}/\text{Rh}_2^{3+}$ redox processes, respectively. Thus, the nbd complexes **3**–**5** are more easily oxidized than the corresponding cod complexes **1** and **2**. Similar electrochemical results have been described for the dinuclear rhodium(I) complexes $[\text{Rh}(\mu\text{-pz}^{\text{Fc}})(\text{cod})]_2$, $[\text{Rh}(\mu\text{-pz}^{\text{Fc}})(\text{nbd})]_2$, and $[\text{Rh}(\mu\text{-pz}^{\text{But}})(\text{nbd})]_2$ containing pyrazolato ligands [19]. The difference in redox behaviors between cod and nbd complexes is related with the $\text{Rh}\cdots\text{Rh}$ distances due to the bulkier nature of cod as compared with nbd ligand. As mentioned, the $\text{Rh}\cdots\text{Rh}$ distances of **3** (3.0224 Å) and **4** (2.9726 Å) are significantly shorter than those of **1** (3.2668 Å) and **2** (3.1282 Å). In the case of **5**, the first and second oxidation potentials were observed at 0.29 and 1.26 V, respectively. Thus, the difference in second oxidation potentials between **4** and **5** reached as much as 0.7 V. The large positive shifts of the second oxidation potential in **5** is ascribed to the electron withdrawing nature of 2,6-difluorophenyl group. It should be noted that, in spite of the large positive shift, the CV spectrum of **5** exhibits a clear reversible process, suggesting that the Rh_2^{4+} species is stable enough during the CV measurement. More detailed redox features of the nbd complexes including the spectroscopic studies of the Rh_2^{4+} species are now in progress in this research group.

4. Conclusion

A series of dinuclear rhodium(I) complexes $[\text{Rh}(\text{R}_m\text{-pf})(\text{L})]_2$ were synthesized and their molecular structures were determined by X-ray crystallographic analysis. The $\text{Rh}\cdots\text{Rh}$ distance decreased by ca. 0.2 Å as the ligand L was changed from 1,5-cyclooctadiene(cod) to 2,5-norbornadiene(nbd). Similar decrease was observed in $\text{Rh}\cdots\text{Rh}$ distance of the nbd complexes as the N-aryl substituent of the formamidinate ligand was changed from 2,6-difluorophenyl (3.091 Å) to 4-methylphenyl (3.0224 Å), and then to 3,5-dimethylphenyl (2.9726 Å) group. Thus, the electron donating group strengthens the $\text{Rh}\cdots\text{Rh}$ interaction. The structural results are connected to the redox properties because the first oxidation potential of the nbd complex decreased on going from 2,6-difluorophenyl (+0.29 V) to 4-methylphenyl (+0.23 V), and then to 3,5-dimethylphenyl (+0.17 V) group. These complexes commonly exhibited a novel dynamic behavior associated with a racemization process as was revealed from the temperature dependent NMR spectra. The activation free energies determined by the line shape analysis were in the range of 43.4–53.2 kJ mol^{-1} at 298 K. Interestingly, the rotation rates of the N-aryl groups are quite different in each complex; two of them rotate rapidly while the other two rotate slowly. We have assumed that the aryl groups attached to the amino nitrogen rotate more rapidly than those attached to the imino nitrogen atoms.

Acknowledgments

The present work was partially supported by Grants-in-Aid for Scientific Research Nos. and 26410080 from the Ministry of Education, Culture, Sports, Science and Technology and Technology and the Support Project to Assist Private Universities in Developing Bases for Research. The X-ray diffraction experiment was performed at Advanced Research Support Center, Ehime University. The authors are grateful to Dr. Mori (Ehime University) for the crystallographic analysis. The authors are grateful to Ms. Michiko Egawa (Shimane University) for her measurements of elemental analysis.

Appendix A. Supplementary data

Supplementary data related to this article can be found at <http://dx.doi.org/10.1016/j.jorganchem.2015.12.018>.

References

- [1] F.A. Cotton, T.R. Felthouse, S. Klein, *Inorg. Chem.* 20 (1981) 3037.
- [2] B.E. Bursten, F.A. Cotton, *Inorg. Chem.* 20 (1981) 3042.
- [3] R.H. Beer, W.B. Tolman, S.G. Bott, S.J. Lippard, *Inorg. Chem.* 30 (1991) 2082.
- [4] M.J. Chen, H.M. Feder, *Inorg. Chem.* 18 (1979) 1864.
- [5] F.A. Cotton, K.R. Dunbar, C.T. Eagle, *Inorg. Chem.* 26 (1987) 4127.
- [6] A. Kina, K. Ueyama, T. Hayashi, *Org. Lett.* 7 (2005) 5889.
- [7] W.M. Alley, C.W. Girard, S. Özkaz, R.G. Finke, *Inorg. Chem.* 48 (2009) 1114.
- [8] I.D. Kostas, K.A. Vallianatou, P. Kyritsis, J. Zednik, J. Vohlidal, *Inorg. Chim. Acta* 357 (2004) 3084.
- [9] J. Zednik, J. Sedláček, J. Svoboda, J. Vohlidal, D. Bondarev, I. Cisarova, *Collect. Czech. Chem. Commun.* 73 (2008) 1205.
- [10] F.A. Cotton, C. Lin, C.A. Murillo, *Inorg. Chem.* 39 (2000) 4574.
- [11] G. Auillon, A. Lledós, S. Alvarez, *Inorg. Chem.* 39 (2000) 906.
- [12] J.A. Ibers, R.G. Snyder, *Acta Cryst.* 15 (1962) 923.
- [13] G. Giordano, R.H. Crabtree, *Inorg. Synth.* 19 (1979) 218.
- [14] E.W. Abel, M.A. Bennett, G. Wilkinson, *J. Chem. Soc.* (1959) 3178.
- [15] R. Fornika, E. Dinjus, H. Görls, W. Leitner, *J. Organomet. Chem.* 511 (1996) 145.
- [16] F.A. Cotton, E.V. Dikarev, M.A. Petrukhina, *J. Chem. Soc. Dalton Trans.* (2000) 4241.
- [17] G.S. Rodman, K.R. Mann, *Inorg. Chem.* 27 (1988) 3338.
- [18] M. Cano, J.V. Heras, M. Maeso, M. Alvaro, R. Fernandez, E. Pinilla, J.A. Campo, A. Monge, *J. Organomet. Chem.* 534 (1997) 159.
- [19] J.A. Campo, M. Cano, J.V. Heras, E. Pinilla, M. Ruiz-Bermejo, R. Torres, *J. Organomet. Chem.* 582 (1999) 173.

- [20] C. López, J.A. Jiménez, R.M. Claramunt, M. Cano, J.V. Heras, J.A. Campo, E. Pinilla, A. Monge, *J. Organomet. Chem.* 511 (1996) 115.
- [21] A.H. Reis Jr., C. Willi, S. Siegel, B. Tani, *Inorg. Chem.* 18 (1979) 1859.
- [22] W.R. Cullen, S.J. Rettig, E.B. Wickenheiser, *Can. J. Chem.* 72 (1994) 1294.
- [23] O. Trhlíkova, J. Zedník, H. Balcar, J. Brus, J. Sedláček, *J. Mol. Catal. A Chem.* 378 (2013) 57.
- [24] I.D. Kostas, *Inorg. Chim. Acta* 355 (2003) 424.
- [25] E. Leitmannová, J. Svoboda, J. Sedláček, J. Vohlídál, P. Kacer, L. Cervený, *Appl. Catal. A Gen.* 372 (2010) 34.
- [26] B. Breit, *Acc. Chem. Res.* 36 (2003) 264.
- [27] F. Ungvary, *Coord. Chem. Rev.* 249 (2005) 2946.
- [28] A.A. Mohamed, *Coord. Chem. Rev.* 254 (2010) 1918.
- [29] F.A. Cotton, R. Poli, *Inorg. Chim. Acta* 122 (1986) 243.
- [30] F.A. Cotton, J.H. Matonic, C.A. Murillo, *Inorg. Chem.* 35 (1996) 498.
- [31] Y.-S. Yen, C.-W. Yeh, J.-D. Chen, J.-C. Wang, *J. Clust. Sci.* 19 (2008) 109.
- [32] F.A. Cotton, S.C. Haefner, J.H. Matonic, X. Wang, C.A. Murillo, *Polyhedron* 16 (1997) 541.
- [33] H.E. Abdou, A.A. Mohamed, J.P. Fackler Jr., *J. Clust. Sci.* 18 (2007) 630.
- [34] S. Radak, Y. Ni, G. Xu, K.L. Shaffer, T. Ren, *Inorg. Chim. Acta* 321 (2001) 200.
- [35] S.J. Archibald, N.W. Alcock, D.H. Busch, D.R. Whitcomb, *Inorg. Chem.* 38 (1999) 5571.
- [36] P. Zanello, F. Laschi, A. Cinquantini, P. Piraino, *Inorg. Chim. Acta* 155 (1989) 49.
- [37] P. Piraino, G. Bruno, F. Nicolo, F. Faraone, S.L. Schiavo, *Inorg. Chem.* 24 (1985) 4760.
- [38] K.V. Catalan, D.J. Mindiola, D.L. Ward, K.R. Dunbar, *Inorg. Chem.* 36 (1997) 2458.
- [39] F.A. Cotton, C. Lin, C.A. Murillo, *Acc. Chem. Res.* 34 (2001) 759.
- [40] F.A. Cotton, C. Lin, C.A. Murillo, *Inorg. Chem.* 39 (2000) 4574.
- [41] Y. Harada, T. Ikeue, Y. Ide, Y. Kimura, I. Hirimitsu, D. Yoshioka, M. Mikuriya, Y. Kataoka, M. Handa, *Inorg. Chim. Acta* 424 (2015) 186.
- [42] W. Chen, T. Ren, *J. Clust. Sci.* 19 (2008) 99.
- [43] R. Clérac, F.A. Cotton, K.R. Dunbar, C.A. Murillo, X. Wang, *Inorg. Chem.* 40 (2001) 420.
- [44] J.L. Bear, C.-L. Yao, R.S. Lifsey, J.D. Korp, K.M. Kadish, *Inorg. Chem.* 30 (1991) 336.
- [45] T. Ren, C. Lin, E.J. Valente, J.D. Zubkowski, *Inorg. Chim. Acta* 297 (2000) 283.
- [46] P. Piraino, G. Bruno, S.L. Schiavo, F. Laschi, P. Zanello, *Inorg. Chem.* 26 (1987) 2205.
- [47] P. Piraino, G. Bruno, G. Tresoldi, S.L. Schiavo, P. Zanello, *Inorg. Chem.* 26 (1987) 91.
- [48] P. Piraino, G. Tresoldi, F. Faraone, *J. Organomet. Chem.* 224 (1982) 305.
- [49] R.M. Roberts, *J. Org. Chem.* 14 (1949) 277.
- [50] R. Fandos, C. Hernández, A. Otero, A. Rodríguez, M.J. Ruiz, J.L.G. Fierro, P. Terreros, *Organometallics* 18 (1999) 2718.
- [51] G. Aullón, S. Alvarez, *Inorg. Chem.* 35 (1996) 3137.
- [52] G. Aullón, G. Ujaque, A. Lledós, S. Alvarez, P. Alemany, *Inorg. Chem.* 37 (1998) 804.

Aggregation of Dinuclear Cations $[(\text{Au}(\text{PR}_3))_2(\mu\text{-OH})]^+$ into Dimers Induced by Polyoxometalate (POM) Template Effects

Takuya Yoshida,^[a,b,c] Eri Nagashima,^[a] Hidekazu Arai,^[a] Satoshi Matsunaga,^[a] and Kenji Nomiya*^[a]

Keywords: Auophilicity; Gold; Polyoxometalates; Cluster compounds; Phosphane ligands

Abstract. Intercluster compounds, $[(\text{Au}(\text{P}(p\text{-XPh})_3))_2(\mu\text{-OH})]_2[\alpha\text{-SiMo}_{12}\text{O}_{40}(\text{Au}(\text{P}(p\text{-XPh})_3))_2]_n\text{EtOH}$ [$X = \text{F}$ (**1**), Cl (**2**)] were synthesized by polyoxometalate (POM)-mediated clusterization, and were unequivocally characterized by X-ray crystallography, elemental analysis, thermogravimetric and differential thermal analysis (TG/DTA), Fourier transform infrared (FT-IR), solid-state cross-polarization magic-angle-spinning (CPMAS) ^{31}P nuclear magnetic resonance (NMR), and solution (^1H , $^{31}\text{P}\{^1\text{H}\}$) NMR spectroscopy. The “dimer-of-dinuclear phosphane-gold(I) cation”, i.e., $[(\text{Au}(\text{P}(p\text{-XPh})_3))_2(\mu\text{-OH})]_2^{2+}$ was formed by the self-assembly of dinuclear phosphane-gold(I) cations, i.e., $[(\text{Au}(\text{P}(p\text{-XPh})_3))_2(\mu\text{-OH})]^+$, through inter-cat-

ionic auophilic interactions as the crossed-edge arrangement (or tetrahedral Au_4 structure) for **1**, while as the parallel-edge arrangement (or rectangular Au_4 structure) for **2**. The latter arrangement was first attained only by assistance of the POM. The POM anions in **1** and **2** contained two mononuclear phosphane-gold(I) cations, i.e., $[\text{Au}(\text{P}(p\text{-XPh})_3)]^+$, linked to the OMo_2 oxygen atoms of edge-sharing MoO_6 octahedra. In the solution $^{31}\text{P}\{^1\text{H}\}$ NMR of **1** and **2**, we observed single signals due to the rapid exchange of the phosphane-gold(I) units. This shows that the OMo_2 oxygen atoms of edge-sharing MoO_6 octahedra in the Keggin POM act as multi-centered active binding sites for the formation of $[(\text{Au}(\text{P}(p\text{-XPh})_3))_2(\mu\text{-OH})]_2^{2+}$.

Introduction

Polyoxometalates (POMs) are molecular metal-oxide clusters, which have attracted considerable attention in the fields of catalysis, medicine, surface science, and materials science, since POMs are often considered to be molecular analogues of metal oxides in terms of structural analogy.^[1] The metal-organic-POM hybrid materials have been designed and prepared, which are interesting from a research perspective with respect to crystal growth, crystal engineering, structure, sorption properties, and so on.^[2] In many hybrid compounds consisting of metal cluster cations and POM anions, POMs have been combined with separately prepared metal cluster cations.^[2a–2c]

Recently, we unexpectedly discovered a clusterization of mononuclear phosphane-gold(I) cations, $[\text{Au}(\text{PR}_3)]^+$ during the course of carboxylate elimination from a monomeric phosphane-gold(I) carboxylate, $[\text{Au}(\text{RS-pyrrid})(\text{PPh}_3)]$ (*RS*-Hpyrrid =

RS-2-pyrrolidone-5-carboxylic acid)^[3] in the presence of free-acid form of Keggin POM, $\text{H}_3[\alpha\text{-PW}_{12}\text{O}_{40}] \cdot 7\text{H}_2\text{O}$.^[4a] This reaction resulted in the formation of tetrakis(triphenylphosphane-gold(I))oxonium cations, $[(\text{Au}(\text{PPh}_3))_4(\mu_4\text{-O})]^{2+}$ as countercations of POM anions. In the formation of the tetragold(I) cluster cations, we demonstrated that the POM surface oxygen atoms act as a template in the clusterization of phosphane-gold(I) cations.^[4b] In addition, we also discovered that the formation of various phosphane-gold(I) cluster cations was strongly dependent on the bulkiness, acidity and charge density of the POMs, and substituent on the aryl group of the phosphane ligands; for example, $[(\text{Au}(\text{PPh}_3))_4(\mu_4\text{-O})]^{2+}[(\text{Au}(\text{PPh}_3))_3(\mu_3\text{-O})][\alpha\text{-PW}_{12}\text{O}_{40}]$, $[(\text{Au}(\text{P}(p\text{-RPh})_3))_2(\mu\text{-OH})]_2[\alpha\text{-PM}_{12}\text{O}_{40}]_2$ ($R = \text{Me}$, $M = \text{W}$; $R = \text{Me}$, $M = \text{Mo}$; $R = \text{F}$, $M = \text{Mo}$), $[(\text{Au}(\text{P}(m\text{-FPh})_3))_4(\mu_4\text{-O})]_2[(\text{Au}(\text{P}(m\text{-FPh})_3))_2(\mu\text{-OH})]_2[\alpha\text{-PM}_{12}\text{O}_{40}]$, and so on have been prepared.^[4b–4e] The POM-mediated clusterization of phosphane-gold(I) cations provides effective synthetic routes for novel phosphane-gold(I) cluster cations by a combination of the phosphane-gold(I) carboxylate and different POMs. In fact, the previously described heptagold(I) cluster cation has been synthesized only by the POM-mediated clusterization method.^[4c] Also, the POM anion as a counterion of tetragold(I) cluster cation can be exchanged with the BF_4^- anion, resulting in a formation of the previously reported tetragold(I) cluster cation by the Schmidbaur research group.^[4a]

The field of element-centered gold clusters $[\text{E}(\text{AuL})_n]^{m+}$ ($E =$ group 13–17 elements) has been extensively studied by the Schmidbaur^[5a,5b] and Laguna^[5c] research groups. Many phosphane-gold(I) cluster cations have been stabilized by auophilic

* Prof. Dr. K. Nomiya
E-Mail: nomiya@kanagawa-u.ac.jp

[a] Department of Chemistry
Kanagawa University
Tsuchiya 2946
Hiratsuka, Kanagawa 259–1293, Japan

[b] Research Center for Gold Chemistry
Tokyo Metropolitan University
Minami-osawa 1–1
Hachioji, Tokyo 192–0397, Japan

[c] Department of Applied Chemistry
Tokyo Metropolitan University
Minami-osawa 1–1
Hachioji, Tokyo 192–0397, Japan

Supporting information for this article is available on the WWW under <http://dx.doi.org/10.1002/zaac.201500176> or from the author.

interactions in the solid state.^[6] For example, oxygen-centered trigold(I) cluster cations, $[\{Au(PR_3)\}_3(\mu_3-O)]^+$ have been reported to exhibit different forms of structural dimerization by inter-cationic aurophilic interactions depending upon the bulkiness of the phosphane ligands, i.e., trinuclear units are aggregated through crossed edges ($R = Me$) or parallel edges ($R = Ph$, etc.), resulting in hexagold(I) dioxonium cations as dimer of trinuclear clusters, $[\{Au(PR_3)\}_3(\mu_3-O)]_2^{2+}$.^[6a–6d] The carbon-centered hexagold(I) cluster cation, $[\{Au(PPh_3)\}_6(\mu_6-C)]^{2+}$ has several intra-cationic aurophilic interactions with hypercoordinated carbon atom.^[6e,6f] In the case of our phosphanegold(I) clusters, the heptagold(I) cluster cation, $[\{Au(PPh_3)\}_4(\mu_4-O)\{Au(PPh_3)\}_3(\mu_3-O)]^{3+}$ was regarded as an assembly of the tetranuclear unit, $[\{Au(PPh_3)\}_4(\mu_4-O)]^{2+}$ and the trinuclear unit, $[\{Au(PPh_3)\}_3(\mu_3-O)]^+$ induced by inter-cationic aurophilic interactions.^[4c] The tetragold(I) cluster cation as a counterion of POM anion, $[\{Au(PPh_3)\}_4(\mu_4-O)]^+$ has a trigonal-pyramidal structure (C_{3v} symmetry) with intra-cationic aurophilic interactions,^[4a,4b] while that as a counterion of BF_4^- anion has a tetrahedral structure (T_d symmetry).^[6g] The tetragold(I) cluster cation has a different arrangement depending upon the counterions. Recently, the hydroxido-bridged gold(I) complex, $[\{Au(NHC)\}_2(\mu-OH)]BF_4$ (NHC = *N*-heterocyclic carbene) has been reported.^[6h] Because the Au–Au distance is long (3.746 Å), aurophilic interaction does not appear in this complex. Very recently, the hydroxido-bridged phosphanegold(I) clusters, $[\{Au(PR_3)\}_2(\mu-OH)]_2(OTf)_2$ ($R = Ph$, *o*-MePh) has also been synthesized.^[6i] In contrast with the NHC–Au complex, the two monomer units, $[\{Au(PR_3)\}_2(\mu-OH)]^+$ were aggregated by inter-cationic aurophilic interactions. In addition, the hydrogen bond between the $\mu-OH$ group and OTf^- anion plays an important role for the formation of the structure.

Several phosphanegold(I) complexes have been known to serve as effective homogeneous catalysts for organic synthesis.^[7] For example, $[\{Au(PPh_3)\}_3(\mu_3-O)]BF_4$ ^[6a,6b] has been used as an effective catalyst for a Claisen rearrangement of propargyl vinyl ethers.^[7a–7d] Conceivably, the oxonium cation, $[\{Au(PR_3)\}_3(\mu_3-O)]^+$ is the source of the catalytically active species $[Au(PR_3)]^+$.^[7d] Very recently, a rearrangement of propargylic *gem*-diesters catalyzed by the monomeric phosphanegold(I) cation with Keggin POM anion, $H_{4-n}[Au(PPh_3)(NCCH_3)]_n[\alpha-SiW_{12}O_{40}]$ ($n = 1–4$) has been reported.^[7e] The hybrid compounds between POM anions and phosphanegold(I) cations constitute a new family of efficient and recyclable catalysts.

The oxygen-centered tetragold(I) cluster cation has been formed by utilizing the POM surface oxygen atoms, i.e., the OW_2 oxygen atoms of edge-sharing WO_6 octahedra.^[4a,4b] However, a role of POM for the formation of $[\{Au(PR_3)\}_2(\mu-OH)]_2^{2+}$ is still unclear.^[4d] In this work, we examined the POM-mediated clusterization using the Keggin molybdo-POM of heteroatom Si with higher negative charge (4–), $H_4[\alpha-SiMo_{12}O_{40}] \cdot 12H_2O$, and the phosphanegold(I) carboxylate precursor with the *para* *X*-substituted triarylphosphane ligand ($X = F, Cl$), $[Au(RS-pyrrld)\{P(p-XPh)_3\}]$.

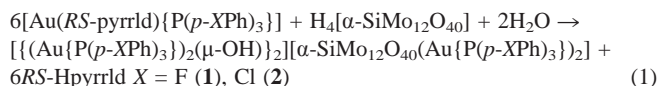
In this paper, we report the synthesis and compositional and structural characterization of two novel intercluster compounds, i.e., $[\{Au\{P(p-XPh)_3\}_2(\mu-OH)\}_2][\alpha-SiMo_{12}O_{40}(Au\{P(p-XPh)_3\}_2)_nEtOH]$ [$X = F$ (**1**), Cl (**2**)], which are composed of $[\{Au\{P(p-XPh)_3\}_2(\mu-OH)\}_2]^{2+}$ and a POM anion with two mononuclear phosphanegold(I) cations linked to the OMO_2 oxygen atoms of edge-sharing MoO_6 octahedra. The mononuclear phosphanegold(I) cations linked to the POM indicate a transient state in the formation of the phosphanegold(I) cluster cations.^[4b] Thus, the formation of $[\{Au(PR_3)\}_2(\mu-OH)]_2^{2+}$ may occur in the POM surface oxygen atoms.

Results and Discussion

Synthesis and Compositional Characterization

Intercluster compounds between $[\{Au\{P(p-XPh)_3\}_2(\mu-OH)\}_2]^{2+}$ and the Keggin POM anions containing mononuclear phosphanegold(I) cations were obtained for **1** in a 73.4% (0.181 g scale) yield, and for **2** in a 38.7% (0.102 g scale) yield. These compounds were prepared by reactions between $[Au(RS-pyrrld)\{P(p-XPh)_3\}]$ [$X = F$ (**1**), Cl (**2**)] in CH_2Cl_2 and the Keggin POM, $H_4[\alpha-SiMo_{12}O_{40}] \cdot 12H_2O$ in mixed $EtOH-H_2O$ solvent. Their crystallizations were carried out by slow evaporation or liquid-liquid diffusion at room temperature. Characterizations were performed by X-ray crystallography, CHN elemental analysis, TG/DTA, FT-IR analysis, solid-state CPMA S ^{31}P NMR, and solution (1H , $^{31}P\{^1H\}$) NMR spectroscopy.

The formation of **1** and **2** is represented in Equation (1):



X-ray crystallography of **1** and **2** showed the formation of discrete intercluster compounds between $[\{Au\{P(p-XPh)_3\}_2(\mu-OH)\}_2]^{2+}$ and Keggin POM anions containing two mononuclear phosphanegold(I) cations, $[\alpha-SiMo_{12}O_{40}(Au\{P(p-XPh)_3\}_2)]^{2-}$ [$X = F$ (**1**), Cl (**2**)] (see Section “Molecular Structures of **1** and **2**”).

The solid-state FT-IR spectra of **1** and **2** showed characteristic vibrational bands based on the coordinating phosphane ligands. The FT-IR spectra also showed prominent vibrational bands due to the Keggin molybdo-POM with the heteroatom Si (956, 906, 876, and 795 cm^{-1} for **1**; 955, 906, 876, and 795 cm^{-1} for **2**).^[8] The carbonyl vibrational bands of the anionic *RS*-pyrrld ligand in $[Au(RS-pyrrld)\{P(p-XPh)_3\}]$ disappeared, suggesting the elimination of the carboxylate ligand. Elimination of this ligand was also confirmed by 1H NMR spectroscopy.

Molecular Structures of **1** and **2**

Single-crystal X-ray analysis revealed that **1** crystallizes in the monoclinic $C2/c$ space group and is composed of one $[\{Au\{P(p-FPh)_3\}_2(\mu-OH)\}_2]^{2+}$ counteranion, one Keggin

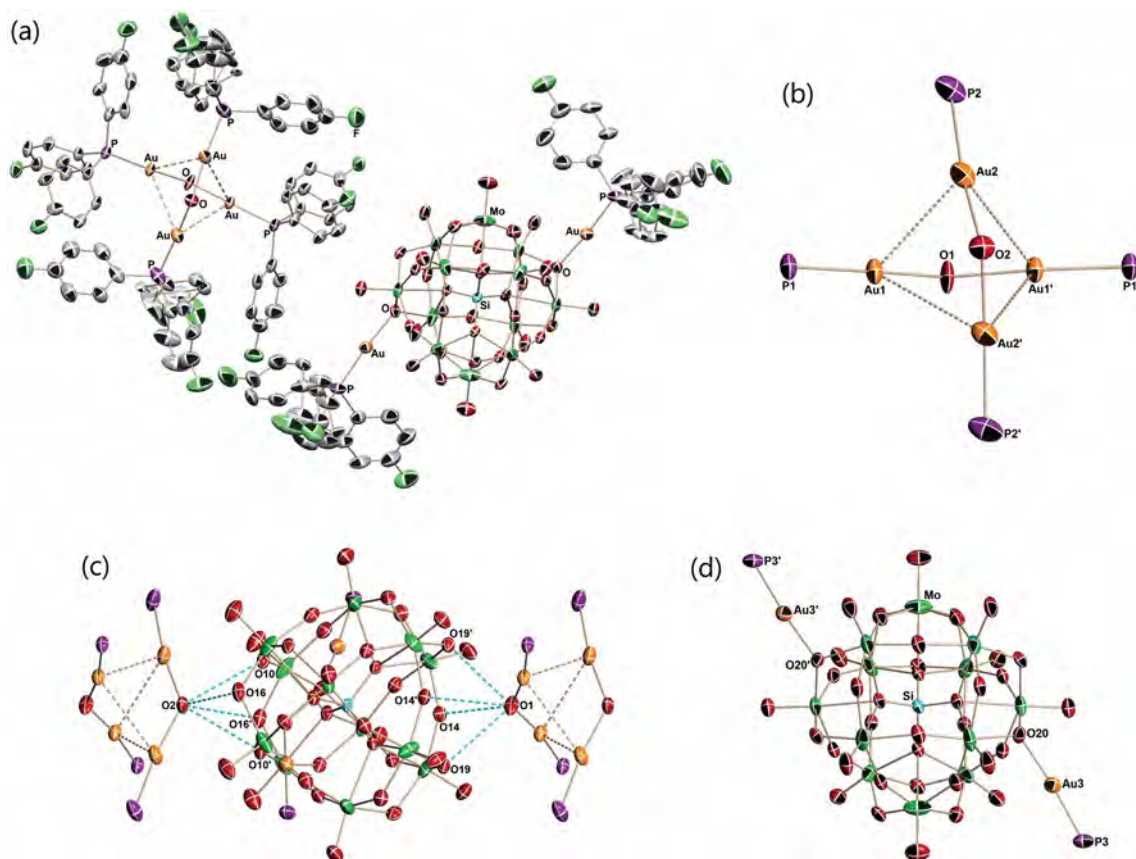


Figure 1. (a) Molecular structure of $[\{(Au\{P(p-FPh)_3\})_2(\mu-OH)\}_2][\alpha-SiMo_{12}O_{40}(Au\{P(p-FPh)_3\})_2]$ (**1**), (b) the partial structure of $[\{(Au\{P(p-FPh)_3\})_2(\mu-OH)\}_2]^{2+}$ in a crossed-edge arrangement or tetrahedral Au_4 structure, (c) the interactions between $[\{(Au\{P(p-FPh)_3\})_2(\mu-OH)\}_2]^{2+}$ and the POM anions, and (d) the partial structure of the mononuclear phosphane-gold(I) cations linked to the POM in **1**.

POM anion, $[\alpha-SiMo_{12}O_{40}]^{4-}$, two mononuclear phosphane-gold(I) cations, $[Au\{P(p-FPh)_3\}]^+$ linked to the OMo_2 oxygen atoms of the edge-sharing MoO_6 octahedra of the POM, and four CH_2Cl_2 molecules as crystallization solvents (Figure 1a).

The counteranion $[\{(Au\{P(p-FPh)_3\})_2(\mu-OH)\}_2]^{2+}$ in **1** can be regarded as the dimerization of dinuclear phosphane-gold(I) cations, $[(Au\{P(p-FPh)_3\})_2(\mu-OH)]^+$. The dinuclear phosphane-gold(I) cations consists of two mononuclear phosphane-gold(I) cations, i.e., $[Au\{P(p-FPh)_3\}]^+$ linked by a $\mu-OH$ group and is triangular in shape. Two dinuclear phosphane-gold(I) cations dimerize to form $[\{(Au\{P(p-FPh)_3\})_2(\mu-OH)\}_2]^{2+}$ by inter-cationic aurophilic interactions ($Au1-Au2$: 3.1742 Å, $Au1-Au2'$: 3.3470 Å) in a crossed-edge arrangement (or tetrahedral Au_4 structure), leading to a tetrahedral array of the four gold(I) atoms (Figure 1b). The counteranion $[\{(Au\{P(p-FPh)_3\})_2(\mu-OH)\}_2]^{2+}$ with a parallel-edge arrangement (or rectangular Au_4 structure) has already been reported.^[44] Also, the halide-bridged phosphane-gold(I) clusters, $[\{(Au\{P(p-FPh)_3\})_2(\mu-X)\}_2]^{2+}$ ($X = Cl, Br, I$) has been synthesized as a crossed-edge arrangement with large anion such as SbF_6^- .^[6j,6k] The inter-cationic aurophilic interactions we observed were longer than those of the previously reported for $[\{(Au\{P(p-MePh)_3\})_2(\mu-OH)\}_2]^{2+}$ ($Au1-Au1'$: 2.991 Å) with

a crossed-edge arrangement.^[44] The $Au-O-Au$ angles are 139.3° ($Au1-O1-Au1'$) and 134.6° ($Au2-O2-Au2'$), and these angles are wider than that in $[\{(Au\{P(p-MePh)_3\})_2(\mu-OH)\}_2]^{2+}$ ($Au1-O1-Au1'$: 116.1°).^[44] The $\mu-OH$ groups in $[\{(Au\{P(p-FPh)_3\})_2(\mu-OH)\}_2]^{2+}$ interact with the OMo_2 oxygen atoms of the edge- and corner-sharing MoO_6 octahedra of the Keggin POMs ($O1-O14$: 3.190, $O1-O19$: 3.103, $O2-O10$: 3.167, $O2-O16$: 3.133 Å) (Figure 1c).

Two mononuclear phosphane-gold(I) cations link to the OMo_2 oxygen atoms of the edge-sharing MoO_6 octahedra of the Keggin POM (Figure 1d). It should be noted that the OM_2 oxygen atoms of the edge-sharing MO_6 octahedra in the Keggin POM ($M = W, Mo$) act as a multi-centered active binding site.^[4b,9] Two aryl groups of the phosphane-gold(I) unit showed flipping disorder concerted with the disorder of the CH_2Cl_2 solvent molecule.

Single-crystal X-ray analysis revealed that **2** crystallizes in the triclinic $P\bar{1}$ space group and is composed of one $[\{(Au\{P(p-ClPh)_3\})_2(\mu-OH)\}_2]^{2+}$ counteranion, one Keggin POM anion, $[\alpha-SiMo_{12}O_{40}]^{4-}$, two mononuclear phosphane-gold(I) cations, $[Au\{P(p-ClPh)_3\}]^+$ linked to the OMo_2 oxygen atoms of the edge-sharing MoO_6 octahedra of the POM, and nine CH_2Cl_2 molecules as crystallization solvents (Figure 2a).

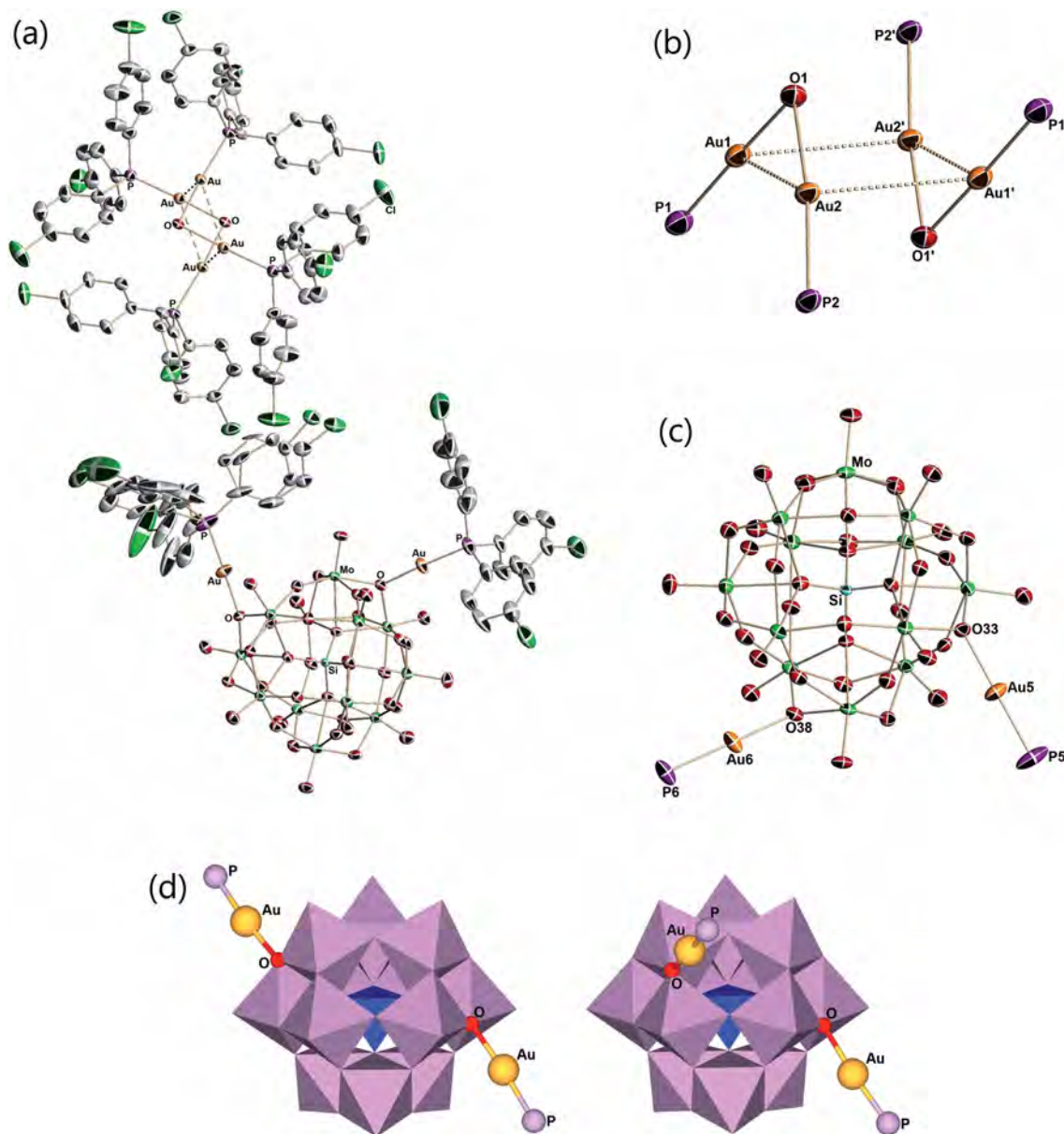


Figure 2. (a) Molecular structure of $[\{(Au\{P(p\text{-ClPh})_3\})_2(\mu\text{-OH})\}_2][\alpha\text{-SiMo}_{12}\text{O}_{40}(Au\{P(p\text{-ClPh})_3\})_2]\cdot\text{EtOH}$ (**2**), (b) the partial structure of $[\{(Au\{P(p\text{-ClPh})_3\})_2(\mu\text{-OH})\}_2]^{2+}$ in a parallel-edge arrangement or rectangular Au_4 structure, (c) the partial structure of the mononuclear phosphane-gold(I) cations linked to the POM in **2**, and (d) polyhedral representation of the polyoxoanion moieties of **1** (left) and **2** (right).

As to **2**, the dinuclear phosphane-gold(I) cation consists of two mononuclear phosphane-gold(I) cations, $[Au\{P(p\text{-ClPh})_3\}]^+$ linked by a $\mu\text{-OH}$ group, and the two dinuclear phosphane-gold(I) cations dimerized by inter-cationic aurophilic interactions ($Au1\text{--}Au2'$: 3.2297, $Au3\text{--}Au4'$: 3.1933 Å) forming $[\{(Au\{P(p\text{-ClPh})_3\})_2(\mu\text{-OH})\}_2]^{2+}$ (Figure 2b). Unlike **1**, the dinuclear phosphane-gold(I) cations of **2** dimerized in a parallel-edge arrangement, leading to a rectangular array of the four gold(I) atoms. The interactions of F–H for **1** in the crystal structures were quite different from those of Cl–H for **2**, i.e., the number of F–H interactions consists of 11 types, which were larger than 5 types of Cl–H interactions. These interactions might bring about the structural difference of $[\{(Au\{P(p\text{-XPh})_3\})_2(\mu\text{-OH})\}_2]^{2+}$ of **1** and **2**. The Au–O–Au angles are

92.22° ($Au1\text{--}O1\text{--}Au2$) and 90.95° ($Au3\text{--}O2\text{--}Au4$), and these angles are narrower than those in **1** (139.3 , 134.6°). Because of these narrow angles, the intra-cationic aurophilic interactions of the dinuclear phosphane-gold(I) cation are short ($Au1\text{--}Au2$: 3.0038, $Au3\text{--}Au4$: 2.9758 Å). The counteranion $[\{(Au\{P(p\text{-ClPh})_3\})_2(\mu\text{-OH})\}_2]^{2+}$ with a parallel-edge arrangement in **2** is similar to that of the previously reported $[\{(Au\{P(p\text{-FPh})_3\})_2(\mu\text{-OH})\}_2]^{2+}$ with $[\alpha\text{-PMo}_{12}\text{O}_{40}]^{3-}$.^[4d] The gold(I) atoms in $[\{(Au\{P(p\text{-ClPh})_3\})_2(\mu\text{-OH})\}_2]^{2+}$ interact with the OMo_2 oxygen atoms of the edge-sharing MoO_6 octahedra and the terminal oxygen atom of the Keggin POMs ($Au1\text{--}O7$: 3.159, $Au1\text{--}O28$: 3.116, $Au3\text{--}O37$: 3.061 Å). The hydroxido-bridged phosphane-gold(I) cluster with a parallel-edge arrangement in **2** is a second example by assistance of

the POM anion, after our first example,^[4d] both of which have never been synthesized without the POM anions. The structure of a parallel-edge arrangement of $[\{Au(PR_3)_2(\mu-X)\}_2]^{2+}$ without the POM has been reported only for the thiolato-bridged cations, $[\{Au(PR^1)_2(\mu-SR^2)\}_2]^{2+}$ ($R^1 = Ph, Me$; $R^2 = CMe_3, 2-H_2NC_6H_4, CH_2CMe_3, 4-MeC_6H_4, 2,3,4,6-tetraacetyl-1-thio-D-glucopyranosato$).^[10]

Two mononuclear phosphanegold(I) cations link to the OMo_2 oxygen atoms of edge-sharing MoO_6 octahedra of the Keggin POM. However, the OMo_2 oxygen atoms linked to mononuclear phosphanegold(I) cations in **2** are different from those of **1** (Figure 2c, d). Two aryl groups in the POM moiety were disordered, also in concert with the CH_2Cl_2 disorder.

Both compounds **1** and **2** were composed of the POM anion with 4- charge, i.e., $[\alpha-SiMo_{12}O_{40}]^{4-}$, the two mononuclear phosphanegold(I) cations, i.e., $[Au\{P(p-XPh)_3\}]^+$, and one $[\{Au\{P(p-XPh)_3\}_2(\mu-OH)\}_2]^{2+}$ countercation. From the viewpoint of the $[\{Au\{P(p-XPh)_3\}_2(\mu-OH)\}_2]^{2+}$ countercation with larger size and the two mononuclear phosphanegold(I) cations with smaller size, in comparison with the size of the Keggin POM anion, the charge balance among these cations and anions resulted in that the two mononuclear phosphanegold(I) cations were linked to the POM anion. These features are consistent with the X-ray molecular structure.

Solid-State CPMAS ^{31}P and Solution $^{31}P\{^1H\}$ NMR

The solid-state CPMAS ^{31}P NMR spectrum of **1** (Figure 3a) showed two signals at $\delta = 21.1$ and 23.1 ppm originating from the inequivalent phosphane groups. It is likely that the signal at $\delta = 21.1$ ppm is assignable to $[\{Au\{P(p-FPh)_3\}_2(\mu-OH)\}_2]^{2+}$, and the signal at $\delta = 23.1$ ppm is assignable to the

two mononuclear phosphanegold(I) cations linked to the OMo_2 oxygen atoms of the edge-sharing MoO_6 octahedra of the POM. On the other hand, the solid-state CPMAS ^{31}P NMR spectrum of **2** (Figure 3b) showed one broad signal at $\delta = 25.5$ ppm, which will be due to the overlap of the signals based on $[\{Au\{P(p-ClPh)_3\}_2(\mu-OH)\}_2]^{2+}$ and the mononuclear phosphanegold(I) cations linked to the POM.

The solution $^{31}P\{^1H\}$ NMR spectra of **1** and **2** in $[D_6]DMSO$ (Figure 3c, d) showed single sharp signals at $\delta = 23.23$ ppm for **1** and 24.07 ppm for **2**. These signals shifted to a higher field from the monomeric phosphanegold(I) carboxylate. In general, the $^{31}P\{^1H\}$ NMR signals of oxygen-centered phosphanegold(I) clusters are observed in the higher field in comparison with that of the monomeric phosphanegold(I) carboxylates, $[Au(RS-pyrrld)(PR_3)]$.^[4] The single signals observed in solution $^{31}P\{^1H\}$ NMR of **1** and **2** are explained by the rapid exchange among $[\{Au\{P(p-XPh)_3\}_2(\mu-OH)\}_2]^{2+}$ and the mononuclear phosphanegold(I) cations linked to the POM.^[4b] Because Keggin molybdo-POMs are unstable in DMSO, minor peaks at $\delta = 41.06$ and 41.71 ppm assignable to $[Au\{P(p-XPh)_3\}_2]^+$ ^[11] were also observed, resulting from decomposition of **1** and **2** in the $[D_6]DMSO$ solution. Thus, dissolution of these compounds leads to a complete disintegration of the structures equilibrating all $[Au\{P(p-XPh)_3\}]^+$ units.

Conclusions

Crystalline samples of novel intercluster compounds, $[\{Au\{P(p-XPh)_3\}_2(\mu-OH)\}_2][\alpha-SiMo_{12}O_{40}(Au\{P(p-XPh)_3\}_2)]$ [$X = F$ (**1**), Cl (**2**)] were obtained by slow evaporation or the liquid-liquid diffusion method. Two types of $[\{Au\{P(p-$

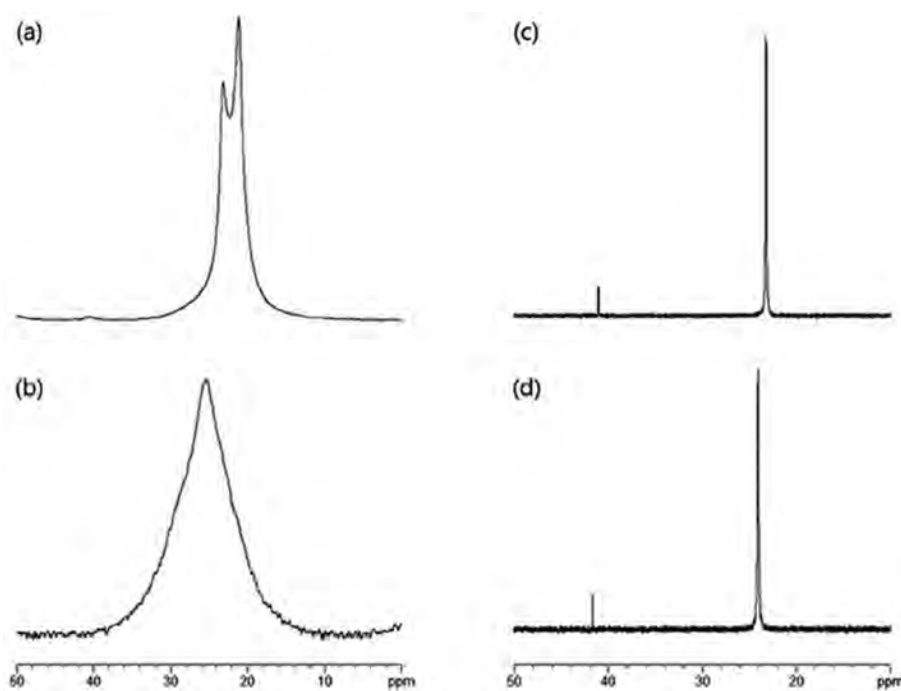


Figure 3. Solid-state CPMAS ^{31}P NMR spectra of (a) **1** and (b) **2**, and solution $^{31}P\{^1H\}$ NMR spectra in $[D_6]DMSO$ of (c) **1** and (d) **2**.

$(XPh)_3\})_2(\mu-OH)_2]^{2+}$ indicate different dimerization arrangements depending upon the substituent on the aryl group of the triarylphosphanes, i.e., a crossed-edge arrangement or tetrahedral Au_4 structure (**1**) and a parallel-edge arrangement or rectangular Au_4 structure (**2**). The mononuclear phosphanegold(I) cations linked to the POM anion reveal that the OMO_2 oxygen atoms of edge-sharing MoO_6 octahedra in the POM act as multi-centered active binding sites for the formation of $[(Au\{P(p-XPh)_3\})_2(\mu-OH)_2]^{2+}$. This fact also shows that the POM's surface oxygen atoms have different affinity to gold atoms. Formation of the present $[(Au\{P(p-XPh)_3\})_2(\mu-OH)_2]^{2+}$, as well as the previous tetragold(I) cluster cations, is strongly dependent on the POM. A mechanisms of formation of the phosphanegold(I) clusters utilizing the mononuclear phosphanegold(I) cations linked to the POM is studied in full progress. Also, the catalytic activities of our compounds are studied and their details will be reported in due course.

Experimental Section

General: The following reactants were used as received: EtOH, CH_2Cl_2 , Et_2O (all from Wako), and $[D_6]DMSO$ (Isotec). With respect to the Keggin POM, $H_4[\alpha-SiMo_{12}O_{40}] \cdot 12H_2O$ was prepared according to the ether extraction method,^[12] and was identified by TG/DTA and FT-IR analysis. The precursors, $[Au(RS-pyrrld)\{P(p-XPh)_3\}]$ ($X = F, Cl$) were synthesized using $P(p-XPh)_3$ ($X = F, Cl$), according to the previously reported procedure for preparation of the monomeric phosphanegold(I) carboxylate,^[13,4d] and characterized by CHN elemental analysis, TG/DTA, FT-IR analysis, and solution (1H , $^{13}C\{^1H\}$, $^{31}P\{^1H\}$) NMR spectroscopy.

Solid-state CPMAS ^{31}P NMR (121.00 MHz) spectra were recorded in 6-mm-outer-diameter rotors with a Jeol JNM-ECP 300 FT-NMR spectrometer with a Jeol ECP-300 NMR spectroscopic data processing system. The spectra were referenced to an external standard of $(NH_4)_2HPO_4$ ($\delta = 1.60$ ppm). 1H NMR (500.00 MHz) and $^{31}P\{^1H\}$ NMR (202.00 MHz) spectra in a $[D_6]DMSO$ solution were recorded in 5-mm-outer-diameter tubes with a Jeol JNM-ECP 500 FT-NMR spectrometer with a Jeol ECP-500 NMR spectroscopic data processing system. The 1H NMR spectra were referenced to an internal standard of tetramethylsilane ($SiMe_4$). The $^{31}P\{^1H\}$ NMR spectra were referenced to an external standard of 25% H_3PO_4 in H_2O in a sealed capillary. The $^{31}P\{^1H\}$ NMR spectroscopic data, with the usual 85% H_3PO_4 reference, were shifted to +0.544 ppm from our data. IR spectra were recorded with a Jasco 4100 FT-IR spectrometer in KBr disks at room temperature. CHN elemental analyses were performed using a Perkin-Elmer 2400 Series II CHNS/O Elemental Analyzer (Kanagawa University). TG/DTA analyses were acquired with a Rigaku Thermo Plus 2 series TG 8120 instrument.

$[(Au\{P(p-FPh)_3\})_2(\mu-OH)_2][\alpha-SiMo_{12}O_{40}(Au\{P(p-FPh)_3\})_2]$ (**1**): A solution of $[Au(RS-pyrrld)\{P(p-FPh)_3\}]$ (0.192 g, 0.300 mmol) dissolved in CH_2Cl_2 (25 mL) was slowly added to a yellow clear solution of $H_4[\alpha-SiMo_{12}O_{40}] \cdot 12H_2O$ (0.101 g, 0.050 mmol) dissolved in 15 mL of an EtOH- H_2O (5:1, v/v) mixed solvent. After stirring for 1 h at room temperature, the reaction solution was filtered through a folded filter paper (Whatman No. 5). The resulting yellow clear filtrate was slowly evaporated at room temperature in the dark. After 3 d, yellow needle crystals formed were collected on a membrane filter (JG 0.2 μm), washed with EtOH (20 mL \times 2) and Et_2O (20 mL \times 2), and dried in vacuo for 2 h. Yield: 0.181 g (73.4%). The crystalline samples

were soluble in DMSO, but insoluble in H_2O , EtOH and Et_2O . **Solid-state CPMAS ^{31}P NMR** (room temp.): $\delta = 21.1, 23.1$ ppm. **$^{31}P\{^1H\}$ NMR** (26.3 °C, $[D_6]DMSO$): $\delta = 23.23$ (main), 41.06 (minor) ppm. **1H NMR** (25.7 °C, $[D_6]DMSO$): $\delta = 7.38$ –7.64 (m, *Aryl*) ppm. **IR** (KBr): $\tilde{\nu} = 1590$ (s), 1496 (s), 1396 (w), 1302 (vw), 1278 (vw), 1238 (m), 1161 (m), 1104 (w), 1013 (vw), 990 (vw), 956 (m), 906 (vs), 876 (w), 828 (m), 795 (s), 709 (vw), 641 (vw), 619 (vw), 534 (m), 451 (w), 411 (vw) cm^{-1} . $C_{108}H_{74}O_{42}F_{18}Si_1P_6Mo_{12}Au_6$: calcd. C 26.30, H 1.51%; found: C 26.36, H 1.02%. TG/DTA under atmospheric conditions: no weight loss was observed at below 204.0 °C. The sample dried in vacuo for 2 h was used for CHN elemental analysis, TG/DTA, FT-IR and NMR, while the crystal used for X-ray crystallography was taken straight from mother liquor without drying.

$[(Au\{P(p-ClPh)_3\})_2(\mu-OH)_2][\alpha-SiMo_{12}O_{40}(Au\{P(p-ClPh)_3\})_2] \cdot EtOH$ (**2**): $[Au(RS-pyrrld)\{P(p-ClPh)_3\}]$ (0.207 g, 0.300 mmol) was dissolved in CH_2Cl_2 (15 mL). A yellow clear solution of $H_4[\alpha-SiMo_{12}O_{40}] \cdot 12H_2O$ (0.101 g, 0.050 mmol) dissolved in 15 mL of an EtOH- H_2O (5:1, v/v) mixed solvent was slowly added along an interior wall of a round-bottomed flask containing a colorless clear solution of the gold(I) complex. The round-bottomed flask containing two layers, i.e., the gold(I) complex solution in the lower layer and the POM solution in the upper layer, was sealed and left in the dark at room temperature. After 5 d, orange plate crystals and a by-product of pale-yellow white powder had formed. The orange plate crystals were separated by decantation several times with EtOH added. The residual crystals were collected with a membrane filter (JG 0.2 μm), washed with EtOH (20 mL \times 2) and Et_2O (20 mL \times 2), and dried in vacuo for 2 h. Yield: 0.102 g (38.7%). The crystalline samples were soluble in DMSO, but insoluble in H_2O , EtOH and Et_2O . **Solid-state CPMAS ^{31}P NMR** (room temp.): $\delta = 25.5$ ppm. **$^{31}P\{^1H\}$ NMR** (26.7 °C, $[D_6]DMSO$): $\delta = 24.07$ (main), 41.71 (minor) ppm. **1H NMR** (25.8 °C, $[D_6]DMSO$): $\delta = 1.09$ (t, $J = 6.9$ Hz, CH_3CH_2OH solvent molecule), 7.51–7.61 (m, *Aryl*) ppm. **IR** (KBr): $\tilde{\nu} = 1576$ (m), 1561 (w), 1480 (s), 1389 (m), 1301 (vw), 1269 (vw), 1183 (vw), 1141 (vw), 1088 (vs), 1012 (m), 991 (vw), 955 (s), 906 (vs), 876 (w), 795 (vs), 751 (s), 705 (w), 631 (w), 569 (m), 535 (w), 496 (m), 454 (vw) cm^{-1} . $C_{110}H_{80}O_{43}Si_1P_6Cl_{18}Mo_{12}Au_6$: calcd. C 25.05, H 1.53%; found: C 25.13, H 1.72%. TG/DTA under atmospheric conditions: a weight loss of 0.72% because of desorption of EtOH was observed at temperature less than 232.0 °C; calcd. 0.87% for one EtOH molecule. The sample dried in vacuo for 2 h was used for CHN elemental analysis, TG/DTA, FT-IR and NMR, while the crystal used for X-ray crystallography was taken straight from mother liquor without drying.

X-ray Crystallography: Single crystals with dimensions of $0.30 \times 0.06 \times 0.01$ mm³ for **1** and $0.22 \times 0.14 \times 0.08$ mm³ for **2** were mounted on cryoloops using liquid paraffin and then cooled by a stream of cooled N_2 gas. Data collection was performed with a Rigaku VariMax with a Saturn CCD diffractometer at 120 K for **1** and a Bruker SMART APEX CCD diffractometer at 100 K for **2**. Intensity data were automatically collected to capture the Lorentz and polarization effects during integration. The structure was solved by direct methods (program SHELXS-97)^[13a] followed by subsequent difference Fourier calculations and were refined by a full-matrix, least-squares procedure on F^2 (program SHELXL-97).^[13b] Absorption correction was performed using SADABS (empirical absorption correction).^[13c] The compositions and formulae for the POMs were determined by CHN elemental analysis, TG/DTA and 1H NMR spectroscopy. Many solvent molecules in the crystals were eliminated by drying in vacuo before characterization such as CHN elemental analysis, TG/DTA, FT-IR and NMR, while the crystals used for X-ray crystallography were taken straight from mother liquor. Thus, the solvent molecules were not necessarily

Table 1. Crystallographic data for **1** and **2**.

	1	2
Formula	C ₁₁₂ H ₈₂ Au ₆ Cl ₈ F ₁₈ Mo ₁₂ O ₄₂ P ₆ Si	C ₁₁₇ H ₉₂ Au ₆ Cl ₃₆ Mo ₁₂ O ₄₂ P ₆ Si
Formula weight	5272.37	5993.09
Color, shape	yellow, needle	orange, plate
Crystal system	monoclinic	triclinic
Space group	C2/c	P $\bar{1}$
T /K	120	100
a /Å	27.245(5)	17.2349(14)
b /Å	14.747(3)	17.2715(14)
c /Å	34.924(7)	31.040(3)
a /°		95.3260(10)
β /°	93.15(3)	101.8900(10)
γ /°		108.2240(10)
V /Å ³	14011(5)	8464.3(12)
Z	4	2
D _{calc} /g·cm ⁻³	2.500	2.351
F(000)	9880	5648
GOF	1.146	1.033
R ₁ [I > 2.00σ(I)]	0.0636	0.0502
R (all data)	0.0716	0.0722
wR ₂ (all data)	0.1448	0.1443

consistent between X-ray analysis and other characterization. Most atoms in the main part of the structure were refined anisotropically, while the rest (as disordered crystallization solvents) were refined isotropically. The restraint command “isor” and “simu” were employed to keep thermal parameters reasonable except the crystallization solvents. This command led to the restraint number 18 for **1** and 12 for **2**. Details of the crystallographic data for **1** and **2** are listed in Table 1. The polyhedral representations in Figure 2 and solid-state packing of **1** and **2** (Figures S5, S6) were drawn using the VESTA 3 series.^[13d]

Crystallographic data (excluding structure factors) for the structures in this paper have been deposited with the Cambridge Crystallographic Data Centre, CCDC, 12 Union Road, Cambridge CB21EZ, UK. Copies of the data can be obtained free of charge on quoting the depository numbers CCDC-1026053 (code: ty004rc2c, **1**) and CCDC-1026054 (code: ty052sp-1, **2**) (Fax: +44-1223-336-033; E-Mail: deposit@ccdc.cam.ac.uk, http://www.ccdc.cam.ac.uk)

Supporting Information (see footnote on the first page of this article): FT-IR spectra, TG/DTA data, and solid-state packing of **1** and **2**.

Acknowledgements

This work was supported by JSPS KAKENHI, grant number 22550065 and by the Strategic Research Base Development Program for Private Universities of the Ministry of Education, Culture, Sports, Science and Technology of Japan.

References

- [1] a) M. T. Pope, *Heteropoly and Isopoly Oxometalates*, Springer-Verlag, New York, **1983**; b) V. W. Day, W. G. Klemperer, *Science* **1985**, *228*, 533–541; c) M. T. Pope, A. Müller, *Angew. Chem. Int. Ed. Engl.* **1991**, *30*, 34–48; d) C. L. Hill, C. M. Prosser-McCartha, *Coord. Chem. Rev.* **1995**, *143*, 407–455; e) T. Okuhara, N. Mizuno, M. Misono, *Adv. Catal.* **1996**, *41*, 113–252; A series of 34 recent papers in a volume devoted to *Polyoxometalates in Catalysis*: f) C. L. Hill, *J. Mol. Catal. A* **1996**, *114*, 1; g) A series of 14 recent papers in a volume devoted to *Polyoxometalates*: C. L. Hill, *Chem. Rev.* **1998**, *98*, 1–2; h) R. Neumann, *Prog. Inorg. Chem.* **1998**, *47*, 317–370; i) M. T. Pope, A. Müller, *Polyoxometalate Chemistry from Topology via Self-Assembly to Applications*, Kluwer Academic Publishers, Netherlands, **2001**; j) T. Yamase, M. T. Pope, *Polyoxometalate Chemistry for Nano-Composite Design*, Kluwer Academic Publishers, Netherlands, **2002**; k) M. T. Pope, in *Comprehensive Coordination Chemistry II* (Ed.: A. G. Wedd), Elsevier Science, New York, **2004**, vol. 4, pp. 635–678; l) C. L. Hill, in *Comprehensive Coordination Chemistry II* (Ed.: A. G. Wedd), Elsevier Science, New York, **2004**, vol. 4, pp. 679–759; m) A series of 29 recent papers in a volume devoted to *Polyoxometalates in Catalysis*: C. L. Hill, *J. Mol. Catal. A* **2007**, *262*, 1; n) A. Proust, R. Thouvenot, P. Gouzerh, *Chem. Commun.* **2008**, 1837–1852; o) B. Hasenknopf, K. Micoine, E. Lacôte, S. Thorimbert, M. Malacria, R. Thouvenot, *Eur. J. Inorg. Chem.* **2008**, 5001–5013; p) D. Laurencin, R. Thouvenot, K. Boubekeur, F. Villain, R. Villanneau, M.-M. Rohmer, M. Bénard, A. Proust, *Organometallics* **2009**, *28*, 3140–3151; q) D.-L. Long, R. Tsunashima, L. Cronin, *Angew. Chem. Int. Ed.* **2010**, *49*, 1736–1758; r) K. Nomiya, Y. Sakai, S. Matsunaga, *Eur. J. Inorg. Chem.* **2011**, 179–196; s) N. V. Izarova, M. T. Pope, U. Kortz, *Angew. Chem. Int. Ed.* **2012**, *51*, 9492–9510.
- [2] a) M. Schulz-Dobrick, M. Jansen, *Eur. J. Inorg. Chem.* **2006**, 4498–4502; b) M. Schulz-Dobrick, M. Jansen, *Z. Anorg. Allg. Chem.* **2007**, *633*, 2326–2331; c) S. Uchida, N. Mizuno, *Coord. Chem. Rev.* **2007**, *251*, 2537–2546; d) M.-P. Santoni, G. S. Hanan, B. Hasenknopf, *Coord. Chem. Rev.* **2014**, *281*, 64–85.
- [3] R. Noguchi, A. Hara, A. Sugie, K. Nomiya, *Inorg. Chem. Commun.* **2006**, *9*, 355–359. The representation of H₂pyrrld is changed to Hpyrrld; thus, the formulation of [Au(RS-Hpyrrld)(PPh₃)] used so far is also changed to [Au(RS-pyrrld)(PPh₃)].
- [4] a) K. Nomiya, T. Yoshida, Y. Sakai, A. Nanba, S. Tsuruta, *Inorg. Chem.* **2010**, *49*, 8247–8254; b) T. Yoshida, S. Matsunaga, K. Nomiya, *Chem. Lett.* **2013**, *42*, 1487–1489; c) T. Yoshida, K. Nomiya, S. Matsunaga, *Dalton Trans.* **2012**, *41*, 10085–10090; d) T. Yoshida, S. Matsunaga, K. Nomiya, *Dalton Trans.* **2013**, *42*, 11418–11425; e) T. Yoshida, Y. Yasuda, E. Nagashima, H. Arai, S. Matsunaga, K. Nomiya, *Inorganics* **2014**, *2*, 660–673.
- [5] a) H. Schmidbaur, *Chem. Soc. Rev.* **1995**, *24*, 391–400; b) H. Schmidbaur, A. Schier, *Chem. Soc. Rev.* **2008**, *37*, 1931–1951; c) M. C. Gimeno, A. Laguna, *Chem. Soc. Rev.* **2008**, *37*, 1952–1966.
- [6] a) A. N. Nesmeyanov, E. G. Perevalova, Y. T. Struchkov, M. Y. Antipin, K. I. Grandberg, V. P. Dyadchenko, *J. Organomet. Chem.* **1980**, *201*, 343–349; b) Y. Yang, V. Ramamoorthy, P. R. Sharp, *Inorg. Chem.* **1993**, *32*, 1946–1950; c) K. Angermaier, H.

- Schmidbaur, *Inorg. Chem.* **1994**, *33*, 2069–2070; d) S.-C. Chung, S. Krüger, H. Schmidbaur, N. Rösch, *Inorg. Chem.* **1996**, *35*, 5387–5392; e) F. Scherbaum, A. Grohmann, B. Huber, C. Krüger, H. Schmidbaur, *Angew. Chem. Int. Ed. Engl.* **1988**, *27*, 1544–1546; f) F. Scherbaum, A. Grohmann, G. Müller, H. Schmidbaur, *Angew. Chem. Int. Ed. Engl.* **1989**, *28*, 463–465; g) H. Schmidbaur, S. Hofreiter, M. Paul, *Nature* **1995**, *377*, 503–504; h) S. Gaillard, J. Bosson, R. S. Ramón, P. Nun, A. M. Z. Slawin, S. P. Nolan, *Chem. Eur. J.* **2010**, *16*, 13729–13740; i) Y. Tang, B. Yu, *RSC Adv.* **2012**, *2*, 12686–12689; j) A. Hamel, N. W. Mitzel, H. Schmidbaur, *J. Am. Chem. Soc.* **2001**, *123*, 5106; k) H. Schmidbaur, A. Hamel, N. W. Mitzel, A. Schier, S. Nogai, *Proc. Natl. Acad. Sci. USA* **2002**, *99*, 4916.
- [7] a) A. S. K. Hashmi, *Chem. Rev.* **2007**, *107*, 3180–3211; b) E. Jiménez-Núñez, A. M. Echavarren, *Chem. Rev.* **2008**, *108*, 3326–3350; c) D. J. Gorin, B. D. Sherry, F. D. Toste, *Chem. Rev.* **2008**, *108*, 3351–3378; d) H. Schmidbaur, A. Schier, *Z. Naturforsch.* **2011**, *66b*, 329–350; e) D. Hueber, M. Hoffmann, B. Louis, P. Pale, A. Blanc, *Chem. Eur. J.* **2014**, *20*, 3903–3907.
- [8] C. Rocchiccioli-Deltcheff, M. Fournier, R. Franck, R. Thouvenot, *Inorg. Chem.* **1983**, *22*, 207–216.
- [9] a) M. Filowitz, R. K. C. Ho, W. G. Klemperer, W. Shum, *Inorg. Chem.* **1979**, *18*, 93–103; b) W. H. Knoth, R. L. Harlow, *J. Am. Chem. Soc.* **1981**, *103*, 4265–4266.
- [10] a) S. Wang, J. P. Fackler Jr., *Inorg. Chem.* **1990**, *29*, 4404–4407; b) A. Sladek, H. Schmidbaur, *Chem. Ber.* **1995**, *128*, 907–909; c) J. M. López-de-Luzuriaga, A. Sladek, W. Schneider, H. Schmidbaur, *Chem. Ber./Recueil* **1997**, *130*, 641–646; d) J. Chen, T. Jiang, G. Wei, A. A. Mohamed, C. Homrighausen, J. A. Krause Bauer, A. E. Bruce, M. R. M. Bruce, *J. Am. Chem. Soc.* **1999**, *121*, 9225–9226; e) A. A. Mohamed, J. Chen, A. E. Bruce, M. R. M. Bruce, J. A. Krause Bauer, D. T. Hill, *Inorg. Chem.* **2003**, *42*, 2203–2205; f) A. Battisti, O. Bellina, P. Diversi, S. Losi, F. Marchetti, P. Zanella, *Eur. J. Inorg. Chem.* **2007**, 865–875.
- [11] a) R. V. Parish, O. Parry, C. A. McAuliffe, *J. Chem. Soc., Dalton Trans.* **1981**, 2098–2104; b) R. E. M. Brooner, T. J. Brown, R. A. Widenhofer, *Chem. Eur. J.* **2013**, *19*, 8276–8284.
- [12] E. O. North, W. Haney, *Inorg. Synth.* **1939**, *1*, 127–129.
- [13] a) G. M. Sheldrick, *Acta Crystallogr., Sect. A* **1990**, *46*, 467–473; b) G. M. Sheldrick, *SHELXL-97*, Program for Crystal Structure Refinement, University of Göttingen, Göttingen, Germany, **1997**; c) G. M. Sheldrick, *SADABS*, Program for Area Detector Adsorption Correction, University of Göttingen, Göttingen, Germany, **1996**; d) K. Momma, F. Izumi, *J. Appl. Crystallogr.* **2011**, *44*, 1272–1276.

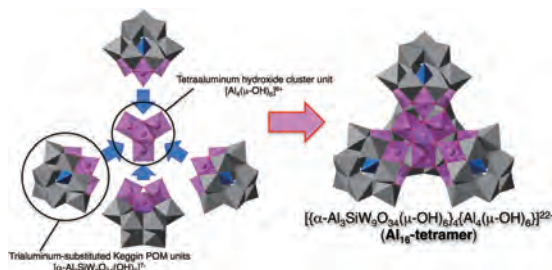
Received: March 31, 2015
Published Online: June 1, 2015

**Al₁₆-hydroxide Cluster-containing Tetrameric Polyoxometalate,
[[α -Al₃SiW₉O₃₄(μ -OH)₆]₄{Al₄(μ -OH)₆}]²²⁻**

Yusuke Inoue, Satoshi Matsunaga, and Kenji Nomiya*

Department of Chemistry, Faculty of Science, Kanagawa University, 2946 Tsuchiya, Hiratsuka, Kanagawa 259-1293

(E-mail: nomiya@kanagawa-u.ac.jp)



A novel Al₁₆-hydroxide cluster-containing polyoxometalate (POM) tetramer, [[α -Al₃SiW₉O₃₄(μ -OH)₆]₄{Al₄(μ -OH)₆}]²²⁻ (Al₁₆-tetramer), was obtained as a potassium salt and characterized by single-crystal X-ray diffraction, FTIR, elemental analysis (H, Al, K, Cl, Na, Si, and W), TG/DTA, and (²⁹Si, ¹⁸³W) NMR. The Al₁₆-tetramer adopts a nanosized structure containing an Al₁₆-hydroxide cluster and maintains its structure in solution. Therefore, the Al₁₆-tetramer is a model compound for aluminum-containing clusters.

REPRINTED FROM

**Chemistry
Letters**

Vol.44 No.12 2015 p.1649–1651

CMLTAG
December 5, 2015

The Chemical Society of Japan

Al₁₆-hydroxide Cluster-containing Tetrameric Polyoxometalate, [[α -Al₃SiW₉O₃₄(μ -OH)₆]₄{Al₄(μ -OH)₆}]²²⁻

Yusuke Inoue, Satoshi Matsunaga, and Kenji Nomiya*

Department of Chemistry, Faculty of Science, Kanagawa University, 2946 Tsuchiya, Hiratsuka, Kanagawa 259-1293

(E-mail: nomiya@kanagawa-u.ac.jp)

A novel Al₁₆-hydroxide cluster-containing polyoxometalate tetramer, [[α -Al₃SiW₉O₃₄(μ -OH)₆]₄{Al₄(μ -OH)₆}]²²⁻ (**Al₁₆-tetramer**), was obtained as a potassium salt and characterized by single-crystal X-ray diffraction, FTIR, elemental analysis, TG/DTA, and (²⁹Si, ¹⁸³W)NMR. The **Al₁₆-tetramer** adopts a nanosized structure containing an Al₁₆-hydroxide cluster, and maintains its structure in solution. Therefore, the **Al₁₆-tetramer** is a model compound for aluminum-containing clusters.

Polyoxometalates (POMs) are discrete metal oxide clusters that are of current interest as soluble metal oxides, and for their applications in catalysis, medicine, and materials science.¹ The W or Mo atoms in POMs can be substituted with other metal ions (M) and the formation of M–O–M linkages on the heterometal sites of POMs can lead to the construction of a nanosized inorganic architecture with a well-defined structure.²

On the other hand, the Al³⁺ ion exists in a wide and dynamic range of hydroxide cluster species in aqueous solution.³ The complex solution speciation of Al³⁺ hydroxide clusters can provide not only a clear understanding of aluminum in natural water systems, but also a basis for commercial applications. Although many studies on Al³⁺ hydroxide clusters in aqueous solution have been reported, the number of solid-state studies of Al³⁺ clusters is limited.³ The synthetic and structural studies of Al-substituted POMs can provide valuable molecular models of Al-hydroxide clusters. In addition, the Al–OH–Al bonds of Al-substituted POMs can be extended to the synthesis of POM-based nanosized inorganic molecules with higher nuclearity and molecular weights. Although several Al-substituted POMs have been reported so far, fully structurally characterized Al-substituted POMs are limited.⁴

In this paper, we report a novel Al₁₆-hydroxide cluster-containing POM tetramer, [[α -Al₃SiW₉O₃₄(μ -OH)₆]₄{Al₄(μ -OH)₆}]²²⁻ (**Al₁₆-tetramer**), which was characterized by single-crystal X-ray diffraction, FTIR (Figure S1), elemental analysis (H, Al, K, Cl, Na, Si, and W), TG/DTA (Figure S2), and (²⁹Si, ¹⁸³W)NMR.

Four equivalents of AlCl₃·6H₂O were added in small portions to a solution of trilacunary Keggin silicotungstate, Na₁₀[A- α -SiW₉O₃₄]·18H₂O,⁵ while maintaining the pH value at 6.5 with 1 M KOH_(aq). The solution was then heated to 80 °C for 30 min. After cooling to room temperature, saturated KCl_(aq) was added to the solution, and colorless plate crystals were obtained with a yield of 10.6% based on Na₁₀[A- α -SiW₉O₃₄]·18H₂O after 1 day (see Supporting Information). The addition of an Al source results in a decrease in the pH of the solution. When AlCl₃ was added to the solution in one portion, the pH value of the solution dropped to ca. 3 and a tetraaluminum-substituted open-Dawson structural POM, [Al₄(μ -OH)₆{ α , α -Si₂W₁₈O₆₆}]¹⁰⁻ (**Al₄-open**),⁶ was obtained instead of the **Al₁₆-tetramer**. In the synthesis of

Al₄-open, the Al source, i.e., AlCl₃·6H₂O or Al(NO₃)₃·9H₂O, was added “in one portion” to the solution of Na₁₀[A- α -SiW₉O₃₄]·18H₂O, followed by stirring the solution at 80 °C for 30 min. Therefore, the reaction condition of **Al₄-open** was more acidic than that of **Al₁₆-tetramer**. This fact suggested that careful addition of AlCl₃·6H₂O and control of the pH value of the solution are crucial for the formation of the **Al₁₆-tetramer**. The formula of the potassium salt of the **Al₁₆-tetramer**, K₂₂[[α -Al₃SiW₉O₃₄(μ -OH)₆]₄{Al₄(μ -OH)₆}]·3KCl·69H₂O, was determined by elemental analysis (H, Al, K, Cl, Na, Si, and W), TG/DTA, and X-ray crystallography.

X-ray crystallography revealed that in the formation of the tetrapod-shaped POM tetramer [[α -Al₃SiW₉O₃₄(μ -OH)₆]₄{Al₄(μ -OH)₆}]²²⁻, the four trialuminum-substituted Keggin POM units, [α -Al₃SiW₉O₃₄(μ -OH)₆]⁷⁻, were linked to the tetraaluminum hydroxide cluster unit [Al₄(μ -OH)₆]⁶⁺ via Al–

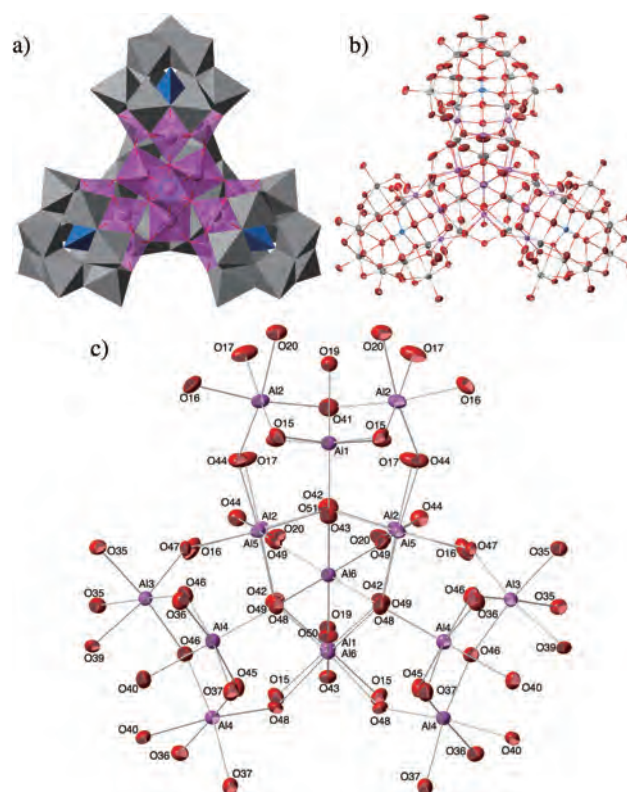


Figure 1. (a) Molecular structure of the polyoxoanion, [[α -Al₃SiW₉O₃₄(μ -OH)₆]₄{Al₄(μ -OH)₆}]²²⁻ of the **Al₁₆-tetramer**, in polyhedral representation; (b) its thermal ellipsoid plot. (c) The partial structure around the Al₁₆ hydroxide cluster unit. Color code: Al, pink; W, gray; Si, blue; O, red.

O–Al bonds (Figures 1a and 1b). The center-to-terminal distance was found to be about 1.1 nm, and therefore, the polyoxoanion **Al₁₆-tetramer** has a nanosized structure with *T_d* symmetry.

The central {Al₄(μ-OH)₆} unit was composed of four AlO₆ octahedra connected to each other by corner-sharing Al–O–Al bonds, and displayed *T_d* symmetry (Figure 1c). A tetranuclear aluminum hydroxide cluster similar to the central {Al₄(μ-OH)₆} unit in the **Al₁₆-tetramer** has been reported for [Al₄(OH)₆(H₂O)₁₂][Al(H₂O)₆]₂Br₁₂ by Sun et al.⁷ [Al₄(OH)₆(H₂O)₁₂]⁶⁺ was capped with 12 terminal water molecules. The **Al₁₆-tetramer** is regarded as a structure in which the twelve coordinated water molecules of [Al₄(OH)₆(H₂O)₁₂]⁶⁺ are substituted by the twelve terminal oxygen atoms of the four tri-Al-substituted Keggin POM units. Therefore, the **Al₁₆-tetramer** is a model compound for [Al₄(OH)₆(H₂O)₁₂]⁶⁺ capped with tri-Al-substituted Keggin POM units as an inorganic ligand. Bond valence sum (BVS) calculations revealed that all the thirty oxygen atoms of the Al–O–Al bonds are protonated, and are ascribed to the OH[−] groups (the BVS value; O41, 1.040; O42, 1.030; O43, 0.938; O44, 0.967; O45, 1.026; O46, 1.046; O47, 0.971; O48, 0.963; O49, 0.931; O50, 0.931; O51, 0.964; Table S1).

The structure of the **Al₁₆-tetramer** was similar to those of the Nb₁₆-containing Keggin POM tetramers, [(α-Nb₃XW₉O₄₀)₄{Nb₄(μ-O)₆}]^{20−} (X = Si^{2c} and Ge^{2d}) reported by Hill et al. and Xu et al., respectively. As with the **Al₁₆-tetramer**, the structures of [(α-Nb₃XW₉O₄₀)₄{Nb₄(μ-O)₆}]^{20−} were described as tetramers consisting of the four triniobium-substituted Keggin POM units [α-Nb₃XW₉O₄₀]^{7−}, linked by tetranioobium oxide cluster unit [Nb₄(μ-O)₆]⁸⁺. In contrast to the **Al₁₆-tetramer**, all the oxygen atoms of [(α-Nb₃XW₉O₄₀)₄{Nb₄(μ-O)₆}]^{20−} were not protonated and were ascribed to the O^{2−} atoms. In addition, the syntheses of [(α-Nb₃XW₉O₄₀)₄{Nb₄(μ-O)₆}]^{20−} were carried out under highly acidic conditions (ca. pH 0.3). The addition of a base (pH > 5) led to disassembly from tetramer to triniobium-substituted Keggin monomers. On the other hand, the **Al₁₆-tetramer** was synthesized under near-neutral conditions (pH 6.5). These facts suggest that the monomer–tetramer conversion of the **Al₁₆-tetramer** may show the opposite behavior of its Nb analogues. The detailed study of the monomer–tetramer conversion of the **Al₁₆-tetramer** is in progress and will be reported in due course.

The solution ²⁹Si NMR spectrum of the **Al₁₆-tetramer** in D₂O showed only one resonance peak, at −81.181 ppm (Figure 2a). The ¹⁸³W NMR spectrum of the **Al₁₆-tetramer** in D₂O (Figure 2b) showed a two-line spectrum at −93.959 (2W) and −160.654 (1W) ppm in a 2:1 integration ratio. These spectra are consistent with the molecular structure of the **Al₁₆-tetramer**, suggesting that it is a single species that maintains its structure in solution. The tetraaluminum-substituted open-Dawson structural POM (**Al₄-open**), synthesized by a similar method, showed a single peak (−82.55 ppm) in the ²⁹Si NMR spectrum and a five-line spectrum (−79.67, −83.33, −149.84, −175.17, and −197.67 ppm) in the ¹⁸³W NMR spectrum.⁶ In addition, we have synthesized the trialuminum(III)-substituted monomer, [α-Al₃SiW₉O₃₄(μ-OH)₃(H₂O)₃]^{4−} (**Al₃-monomer**), and dimer, [{α-Al₃SiW₉O₃₄(μ-OH)₃]₂(μ-OH)₃]^{4−} (**Al₆-dimer**), and also measured their ²⁹Si and ¹⁸³W NMR spectra as a preliminary experiment.⁸ Although the solution ²⁹Si and ¹⁸³W NMR spectra of **Al₁₆-tetramer**, **Al₃-monomer**, and **Al₆-dimer** gave identical

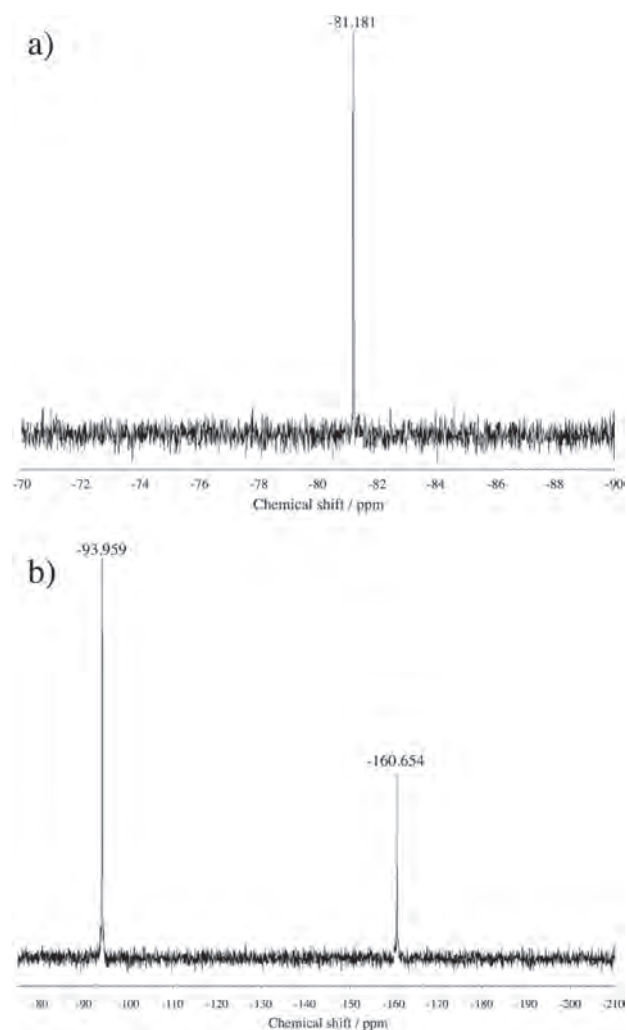


Figure 2. (a) Solution ²⁹Si NMR spectrum and (b) solution ¹⁸³W NMR spectrum of the **Al₁₆-tetramer** dissolved in D₂O.

NMR patterns, i.e., single ²⁹Si signal and two ¹⁸³W signals with the integration ratio of 2:1, the chemical shifts of **Al₁₆-tetramer** were different from those of **Al₃-monomer** (−80.76 ppm for ²⁹Si NMR; −111.00, −153.11 ppm for ¹⁸³W NMR) and **Al₆-dimer** (−81.42 ppm for ²⁹Si NMR; −90.19, −159.78 ppm for ¹⁸³W NMR). Therefore, the **Al₁₆-tetramer** was clearly distinguishable from **Al₄-open**, **Al₃-monomer**, and **Al₆-dimer** by ²⁹Si and ¹⁸³W NMR.

In conclusion, we successfully synthesized the novel Al₁₆-hydroxide cluster-containing POM tetramer, [{α-Al₃SiW₉O₃₄(μ-OH)₆]₄{Al₄(μ-OH)₆}]^{22−} (**Al₁₆-tetramer**). X-ray crystallography revealed that the **Al₁₆-tetramer** has a nanosized structure containing an Al₁₆-hydroxide cluster. In addition, ²⁹Si and ¹⁸³W NMR revealed that the **Al₁₆-tetramer** maintains its structure in solution. Crystal structure and spectroscopic analyses of the aluminum-hydroxide clusters are very important for a clear understanding of the formation and evolution processes of aluminum species. The **Al₁₆-tetramer** is a “stable” model compound for the above-mentioned [Al₄(OH)₆(H₂O)₁₂]⁶⁺ cluster, with a well-defined structure that contributes to the understanding of its properties and reactivity.

This study was supported by JSPS KAKENHI, Grant number 22550065, by the Strategic Research Base Development Program for Private Universities of the Ministry of Education, Culture, Sports, Science and Technology of Japan, and also by a grant from Research Institute for Integrated Science, Kanagawa University (No. RIIS201505).

Supporting Information is available electronically on J-STAGE.

References and Notes

- 1 a) M. T. Pope, A. Müller, *Angew. Chem., Int. Ed. Engl.* **1991**, *30*, 34. b) M. T. Pope, *Heteropoly and Isopoly Oxometalates*, Springer-Verlag, New York, **1983**. c) V. W. Day, W. G. Klemperer, *Science* **1985**, *228*, 533. d) C. L. Hill, *Chem. Rev.* **1998**, *98*, 1. e) A series of 34 recent papers in a volume devoted to Polyoxoanions in Catalysis ed. by C. L. Hill: *J. Mol. Catal. A: Chem.* **1996**, *114*, Issues 1–3, pp. 1–371. f) *Polyoxometalate Chemistry from Topology via Self-Assembly to Applications*, ed. by M. T. Pope, A. Müller, Kluwer Academic Publishers, Netherlands, **2001**. doi:10.1007/0-306-47625-8. g) *Polyoxometalate Chemistry for Nano-Composite Design*, ed. by T. Yamase, M. T. Pope, Kluwer Academic Publishers, Netherlands, **2002**. doi:10.1007/b105365. h) A series of 32 recent papers in a volume devoted to Polyoxometalates in Catalysis ed. by C. L. Hill: *J. Mol. Catal. A: Chem.* **2007**, *262*, Issues 1–2, pp. 1–242. i) D.-L. Long, R. Tsunashima, L. Cronin, *Angew. Chem., Int. Ed.* **2010**, *49*, 1736.
- 2 a) S.-T. Zheng, G.-Y. Yang, *Chem. Soc. Rev.* **2012**, *41*, 7623. b) K. Nomiya, Y. Sakai, S. Matsunaga, *Eur. J. Inorg. Chem.* **2011**, 179. c) G.-S. Kim, H. Zeng, D. VanDerveer, C. L. Hill, *Angew. Chem., Int. Ed.* **1999**, *38*, 3205. d) S.-J. Li, S.-X. Liu, C.-C. Li, F.-J. Ma, D.-D. Liang, W. Zhang, R.-K. Tan, Y.-Y. Zhang, L. Xu, *Chem.—Eur. J.* **2010**, *16*, 13435. e) K.-Y. Wang, B. S. Bassil, Z.-G. Lin, A. Haider, J. Cao, H. Stephan, K. Viehweger, U. Kortz, *Dalton Trans.* **2014**, *43*, 16143.
- 3 a) P. A. Jordan, N. J. Clayden, S. L. Heath, G. R. Moore, A. K. Powell, A. Tapparo, *Coord. Chem. Rev.* **1996**, *149*, 281. b) W. H. Casey, *Chem. Rev.* **2006**, *106*, 1. c) Z. L. Mensinger, W. Wang, D. A. Keszler, D. W. Johnson, *Chem. Soc. Rev.* **2012**, *41*, 1019.
- 4 a) Q. H. Yang, D. F. Zhou, H. C. Dai, J. F. Liu, Y. Xing, Y. H. Lin, H. Q. Jia, *Polyhedron* **1997**, *16*, 3985. b) Y. Kikukawa, S. Yamaguchi, Y. Nakagawa, K. Uehara, S. Uchida, K. Yamaguchi, N. Mizuno, *J. Am. Chem. Soc.* **2008**, *130*, 15872. c) C. N. Kato, Y. Katayama, M. Nagami, M. Kato, M. Yamasaki, *Dalton Trans.* **2010**, *39*, 11469. d) Y. Kikukawa, K. Yamaguchi, M. Hibino, N. Mizuno, *Inorg. Chem.* **2011**, *50*, 12411. e) M. Carraro, B. S. Bassil, A. Sorarù, S. Berardi, A. Suchopar, U. Kortz, M. Bonchio, *Chem. Commun.* **2013**, *49*, 7914. f) C. N. Kato, Y. Makino, W. Unno, H. Uno, *Dalton Trans.* **2013**, *42*, 1129. g) C. N. Kato, T. Kashiwagi, W. Unno, M. Nakagawa, H. Uno, *Inorg. Chem.* **2014**, *53*, 4824.
- 5 A. Tézé, G. Hervé in *Inorganic Syntheses*, ed. by A. P. Ginsberg, John Wiley & Sons, New York, **1990**, Vol. 27, pp. 85–96. doi:10.1002/9780470132586.ch16.
- 6 S. Matsunaga, Y. Inoue, T. Otaki, H. Osada, K. Nomiya, submitted for publication.
- 7 Z. Sun, H. Wang, H. Feng, Y. Zhang, S. Du, *Inorg. Chem.* **2011**, *50*, 9238.
- 8 S. Matsunaga, Y. Inoue, H. Osada, K. Nomiya, unpublished work. The detailed study of **Al₃-monomer** and **Al₆-dimer** including the monomer–tetramer conversion of the **Al₁₆-tetramer** is in progress and will be reported in due course.

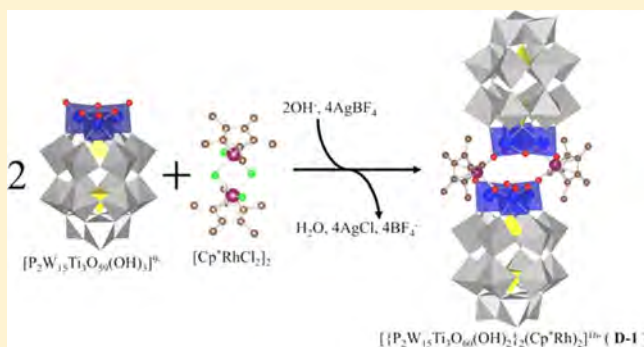
Synthesis and Molecular Structure of a Water-Soluble, Dimeric Tri-Titanium(IV)-Substituted Wells–Dawson Polyoxometalate Containing Two Bridging (C₅Me₅)Rh²⁺ Groups

Yusuke Matsuki, Takahiro Hoshino, Shoko Takaku, Satoshi Matsunaga, and Kenji Nomiya*

Department of Chemistry, Faculty of Science, Kanagawa University, Hiratsuka, Kanagawa 259-1293, Japan

Supporting Information

ABSTRACT: A novel trititanium(IV)-substituted Wells–Dawson polyoxometalate (POM)-based organometallic complex, i.e., a dimeric POM containing two bridging Cp*Rh²⁺ groups (Cp* = C₅Me₅) or $[\{\alpha\text{-P}_2\text{W}_{15}\text{Ti}_3\text{O}_{60}(\text{OH})_2\}_2(\text{Cp}^*\text{Rh})_2]^{16-}$ (**D-1**) with C_i symmetry, was synthesized in an analytically pure form by a 1:2 molar ratio reaction of the organometallic precursor $[\text{Cp}^*\text{RhCl}_2]_2$ with the separately prepared, monomeric trititanium(IV)-substituted Wells–Dawson POM, “[P₂W₁₅Ti₃O₅₉(OH)₃]⁹⁻” (**M-1**). The crystalline sample (NaK-**D-1**) of the water-soluble, mixed sodium/potassium salt of **D-1** was obtained in the 14.7% yield, which has been characterized by complete elemental analysis, TG/DTA, FTIR, single-crystal X-ray structure analysis, and solution (¹⁸³W, ³¹P, ¹H and ¹³C{¹H}) NMR spectroscopy. Single-crystal X-ray structure analysis revealed that the two species of the protonated Wells–Dawson subunits, “[P₂W₁₅Ti₃O₆₀(OH)₂]¹⁰⁻” were bridged by the two Cp*Rh²⁺ groups, resulting in the an overall C_i symmetry. The Cp*Rh²⁺ groups were linked to the two terminal oxygen atoms of the titanium(IV) sites and one edge-sharing oxygen atom of the surface Ti–O–Ti bond. The ¹⁸³W NMR of **D-1** dissolved in D₂O showed that its solution structure was represented as a dimeric POM with a formula of $[\{\alpha\text{-P}_2\text{W}_{15}\text{Ti}_3\text{O}_{60}(\text{OH})_3\}_2(\text{Cp}^*\text{Rh}(\text{OH}))_2]^{16-}$ (**D-2**) with C_i (or S₂) symmetry. A trititanium(IV)-substituted Wells–Dawson POM-supported organometallic complex has never been reported so far, and thus **D-1** in the solid state and **D-2** in solution are the first example of this type of complex.



INTRODUCTION

Polyoxometalates (POMs) are discrete metal-oxide clusters that are of current interest as soluble metal oxides. The coordination chemistry of POMs with transition metal cations (TMC) has been particularly well documented in the past few decades.¹ In fact, POM-supported organometallic and transition-metal complexes have been intensively studied² from the viewpoint of molecular modeling of the metal-oxide-supported transition metal catalysts. The Keggin and Wells–Dawson POMs contain four different oxygen atoms: edge-sharing oxygen (OM₂), corner-sharing oxygen (OM₂), terminal oxygen (OM), and the interior oxygen atoms attached to the heteroatom (OM₃), which show subtly different reactivities. The edge-sharing oxygen atoms are more nucleophilic than the other oxygen atoms.³ Nevertheless, the relatively lower reactivities of the bridging and the terminal oxygen atoms in a large number of POMs prevent the formation of TMC derivatives.

To improve the nucleophilicity of the surface oxygen atoms in POM, there are two synthetic routes: (i) the use of lacunary species of POMs in which the most nucleophilic oxygen atoms constitute the vacant sites and (ii) the increase of the overall negative charge of the POMs.⁴ The former has been realized, for example, as the monolacunary Keggin and Wells–Dawson

POM-based $[\text{Ru}(\text{arene})]^{2+}$ complexes,^{4,5a,b} while the latter pathway can be achieved, for example, by replacement of one or several Mo^{VI} and W^{VI} centers by cations with a lower charge (V^V, Nb^V, Ti^{IV}, ...).⁶ In fact, tri-M(V)-substituted Wells–Dawson POM-supported organometallic complexes (M = Nb^V, V^V) have been formed by covalently binding cationic organometallic species utilizing the surface, three extra negative charge of the tri-M-substituted Wells–Dawson POM anion $[\text{P}_2\text{W}_{15}\text{M}_3\text{O}_{62}]^{9-}$, compared with the parent anion $[\text{P}_2\text{W}_{18}\text{O}_{62}]^{6-}$. For the case of M = Nb^V, $[(\text{Cp}^*\text{Rh})\text{P}_2\text{W}_{15}\text{Nb}_3\text{O}_{62}]^{7-}$,^{6b-d} $[\{(\text{C}_6\text{H}_6)\text{Ru}\}\text{P}_2\text{W}_{15}\text{Nb}_3\text{O}_{62}]^{7-}$,^{6b,c} $[\{(\text{cod})\text{Y}\}\text{P}_2\text{W}_{15}\text{Nb}_3\text{O}_{62}]^{8-}$ (Y = Rh^I, Ir^I),^{6e-h} and $[\{Z\}\text{P}_2\text{W}_{15}\text{Nb}_3\text{O}_{62}]^{8-}$ (Z = Re(CO)₃⁺, Ir(CO)₂⁺, Rh(CO)₂⁺) have been reported,⁶ⁱ and for the case of M = V^V, $[(\text{CpTi})\text{P}_2\text{W}_{15}\text{V}_3\text{O}_{62}]^{6-}$,^{6j} $[(\text{Cp}^*\text{Rh})_2\text{P}_2\text{W}_{15}\text{V}_3\text{O}_{62}]^{5-}$,^{6k} $[(\text{Cp}^*\text{Rh})\text{P}_2\text{W}_{16}\text{V}_2\text{O}_{62}]^{6-}$,^{6l} $[\{(\text{cod})\text{Pt}\}\text{P}_2\text{W}_{15}\text{V}_3\text{O}_{62}]^{7-}$,^{6m} and $[\{(\text{C}_6\text{H}_6)\text{Ru}\}\text{P}_2\text{W}_{15}\text{V}_3\text{O}_{62}]^{7-}$ ⁶ⁿ have been reported. These complexes are monomeric forms with the compositional 1:1 or 1:2- ratio of the Wells–Dawson POM and an organometallic fragment. On the other hand, only a few dimeric complexes with the 2:1 or

Received: May 28, 2015

Published: November 13, 2015

2:2 ratio of Keggin POM and an organometallic fragment such as $[(\text{PNbW}_{11}\text{O}_{40})_2\text{ZrCp}_2]^{6-6\circ}$ and $[\alpha\text{-PW}_{11}\text{Al}(\text{OH})\text{-O}_{39}\text{ZrCp}_2]^{6-6\text{p}}$ have been reported.

As for the trititanium(IV)-substituted Wells–Dawson POM, it has been reported as two stable tetrapod-shape tetramers by the reactions of the trilacunary Wells–Dawson POM $[\text{B-P}_2\text{W}_{15}\text{O}_{56}]^{12-}$ with Ti^{IV} ,⁷ but not as the monomeric form $[\text{P}_2\text{W}_{15}\text{Ti}_3\text{O}_{62}]^{12-}$. One of the tetramers, $[\{\text{P}_2\text{W}_{15}\text{Ti}_3\text{O}_{57.5}(\text{OH})_3\}_4\text{Cl}\}^{25-}$ (here called the non-Ti(OH)₃-bridging tetramer, i.e., the tetramer without the bridging Ti(OH)₃ groups), is composed of four Wells–Dawson units, linked through intermolecular Ti–O–Ti bonds, and one encapsulated Cl^- ion.^{7d} The other tetramer, $[\{\text{P}_2\text{W}_{15}\text{Ti}_3\text{O}_{59}(\text{OH})_3\}_4\{\mu_3\text{-Ti}(\text{H}_2\text{O})_3\}_4\text{Cl}\}^{21-}$ (**Tb-1**; called the Ti(OH)₃-bridging tetramer, i.e., the tetramer with bridging Ti(OH)₃ groups), is composed of four Wells–Dawson units, four $\mu_3\text{-Ti}(\text{H}_2\text{O})_3$ groups, and one encapsulated anion such as Cl^- , Br^- , I^- , or NO_3^- .^{7e–g} These Wells–Dawson POM-based tetrapod-shaped tetramers are actually generated by self-assembly due to the rapid formation of Ti–O–Ti bonds among the monomers $[\text{P}_2\text{W}_{15}\text{Ti}_3\text{O}_{62}]^{12-}$. Nevertheless, the monomeric form of the trititanium(IV)-substituted Wells–Dawson POM has never been obtained so far by the reaction of the trilacunary Wells–Dawson POM $[\text{P}_2\text{W}_{15}\text{O}_{56}]^{12-}$ with Ti^{IV} . Thus, the organometallic complexes supported on the trititanium(IV)-substituted Wells–Dawson POM have been scarcely reported. The single crystal of the dimeric complex of the dititanium(IV)-substituted Wells–Dawson POM units bridged by two $[\text{Ti}(\text{ox})_2]$ groups or $[(\text{P}_2\text{W}_{16}\text{Ti}_2\text{O}_{62})_2\{\text{Ti}(\text{ox})_2\}_2]^{20-}$ has been structurally characterized,^{7b} but it was not reproduced in our hands, which is probably at most a minor, less soluble product of the reaction of the trilacunary Wells–Dawson POM with $\text{K}_2[\text{Ti}(\text{ox})_2]$ as the Ti source.^{7c}

Recently, we found that the monomeric species of the trititanium(IV)-substituted Wells–Dawson POM was *in situ*-generated by hydrolysis of the Ti(OH)₃-bridging tetramer (**Tb-1**),⁷ⁱ but not of the non-Ti(OH)₃-bridging tetramer. In our preliminary experiments, we isolated the solid, monomeric form, $[\text{P}_2\text{W}_{15}\text{Ti}_3\text{O}_{59}(\text{OH})_3]^{9-}$ (**M-1**), as a water-soluble sodium salt of the protonated form of the Ti–O–Ti sites (**Na-M-1**), which has been always contaminated with soluble titanium(IV) compounds. **Na-M-1** has never been transformed to an organic solvent-soluble form such as Bu_4N^+ salt. Moreover, **Na-M-1** was readily returned to the tetrameric species under acidic and neutral conditions, and therefore, it is stable only under basic conditions. Thus, its use as a POM support for formation of the organometallic complexes was seriously restricted. Nevertheless, in this work, using **Na-M-1** obtained by a hydrolysis of **Tb-1** by aqueous NaOH, we examined the reaction in water with the *in situ*-generated, chloride-free $[\text{Cp}^*\text{Rh}]^{2+}$ ($\text{Cp}^* = \text{C}_5\text{H}_5$) species under several conditions. We first obtained the analytically pure compound of the trititanium(IV)-substituted Wells–Dawson POM-based organometallic complex, $[\{\text{P}_2\text{W}_{15}\text{Ti}_3\text{O}_{60}(\text{OH})_2\}_2(\text{Cp}^*\text{Rh})_2]^{16-}$ (**D-1**), as crystals of the mixed sodium/potassium salt and also successfully determined the molecular structure.

Herein, we report full details of the synthesis of the crystalline sample of the water-soluble sodium/potassium salt (**NaK-D-1**) of the dimeric complex consisting of a 2:2-ratio of **M-1** and the $\text{Cp}^*\text{Rh}^{2+}$ group and characterization by complete elemental analysis including oxygen, thermogravimetric (TG) and differential thermal analyses (DTA), FTIR, X-ray crystallography, and solution (^{183}W , ^{31}P , ^1H , and $^{13}\text{C}\{^1\text{H}\}$)

NMR spectroscopy. The solid-state and solution structures of this POM were elucidated.

EXPERIMENTAL SECTION

Materials. The following were used as received: KCl, NaOAc, 0.1 M NaOH aq., 1 M NaOH aq., AgBF_4 , Me_2CO , MeOH, EtOH, and Et_2O (Wako); D_2O (Isotec); and $\text{RhCl}_3\cdot 3\text{H}_2\text{O}$, Cp^*H , and DSS (Aldrich). The trilacunary Wells–Dawson POM, $\text{Na}_{12}[\text{P}_2\text{W}_{15}\text{O}_{56}]\cdot 23\text{H}_2\text{O}$, was prepared according to the literature⁷ⁱ and characterized by TG/DTA, FT-IR, and ^{31}P NMR in D_2O . The Ti(OH)₃-bridging Wells–Dawson tetramer with an encapsulated Cl^- ion, $\text{Na}_{19}\text{H}_2[\{\alpha\text{-}1,2,3\text{-P}_2\text{W}_{15}\text{Ti}_3\text{O}_{59}(\text{OH})_3\}_4\{\mu_3\text{-Ti}(\text{H}_2\text{O})_3\}_4\text{Cl}\}\cdot 124\text{H}_2\text{O}$ (**Na-Tb-1**), was prepared according to the literature^{7e,g,i,j} and characterized by TG/DTA, FT-IR, and solution (^{183}W and ^{31}P) NMR in D_2O . The precursor $[\text{Cp}^*\text{RhCl}_2]_2$ was prepared according to literature methods⁸ and identified with elemental analysis, TG/DTA, FT-IR, and ^1H and $^{13}\text{C}\{^1\text{H}\}$ NMR in $\text{DMSO-}d_6$.

Instrumentation/Analytical Procedures. A complete elemental analysis was carried out by Mikroanalytisches Labor Pascher (Remagen, Germany). A sample was dried at room temperature under 10^{-3} to 10^{-4} Torr overnight before analysis. CHN elemental analyses were carried out with a PerkinElmer 2400 CHNS Elemental Analyzer II (Kanagawa University). Infrared spectra were recorded on a JASCO 4100 FTIR spectrometer in KBr disks at room temperature. TG and DTA were acquired using a Rigaku Thermo Plus 2 series TG/DTA TG 8120 instrument. The ^{31}P NMR (160 MHz) and ^1H NMR (400 MHz) spectra in a D_2O solution were recorded in 5 mm outer diameter tubes on a JEOL JNM-ECA 400 FT-NMR spectrometer and a JEOL ECA-400 NMR data processing system. $^{13}\text{C}\{^1\text{H}\}$ NMR (99 MHz) spectra in a D_2O solution were recorded in 5 mm outer diameter tubes on a JEOL JNM-ECA 400 FT-NMR spectrometer and a JEOL ECA-400 NMR data processing system. The ^{31}P NMR spectra were referenced to an external standard of 25% H_3PO_4 in H_2O in a sealed capillary. The ^{31}P NMR signals with the usual 85% H_3PO_4 are shifted to +0.544 ppm from our data with 25% H_3PO_4 . The ^1H NMR and $^{13}\text{C}\{^1\text{H}\}$ NMR spectra in D_2O were referenced to an internal standard of DSS. The ^{183}W NMR (16.0 MHz) spectra were recorded in 10 mm outer diameter tubes, on a JEOL JNM-ECS 400 FT-NMR spectrometer equipped with a JEOL NM-40T10L low-frequency tunable probe and a JEOL ECS-400 NMR data-processing system. These spectra were referenced to an external standard (saturated $\text{Na}_2\text{WO}_4\text{-D}_2\text{O}$ solution) by the substitution method. Chemical shifts were reported on the δ scale with resonances upfield of Na_2WO_4 (δ 0) as negative. The ^{183}W NMR signals were shifted to -0.787 ppm by using a 2 M Na_2WO_4 solution as a reference instead of the saturated Na_2WO_4 solution.

Preparation of the Precursor “ $\text{Na}_9[\text{P}_2\text{W}_{15}\text{Ti}_3\text{O}_{59}(\text{OH})_3]\cdot \text{TiO}_2\cdot 25\text{H}_2\text{O}$ ” (Na-M-1**) via *in Situ* Generated **Tb-1** Formation.** TiCl_4 (2.5 mL, 22.8 mmol) was dissolved in cooled water (ca. 0 °C, 240 mL). To the solution was added $\text{Na}_{12}[\text{P}_2\text{W}_{15}\text{O}_{56}]\cdot 23\text{H}_2\text{O}$ (20 g, 4.54 mmol). The solution was stirred for 30 min in a water bath at 80 °C. The pH was adjusted to 9.0 by using 1 M aqueous NaOH. The solution was stirred for 30 min in a water bath at 60 °C, followed by stirring for 1 day at an ambient temperature. The white solid formed was filtered off by a membrane filter (JG 0.2 μm). After stirring the filtrate for 1 h in an ice bath, NaOAc (80 g, 0.98 mol) was added. The white powder formed was collected with a glass filter (P40). The contaminated NaOAc was removed by washing the white powder with the cooled MeOH (60 mL). The final white powder was collected with a glass filter (P40), washed with Me_2CO (20 mL) and Et_2O (20 mL), and dried *in vacuo* for 2 h. The white powder was obtained in a yield of 12.8 g {78.4% relative to $\text{Na}_{12}[\text{P}_2\text{W}_{15}\text{O}_{56}]\cdot 23\text{H}_2\text{O}$ }, which was very soluble in water, but insoluble in Me_2CO , MeCN, MeOH, EtOH, and Et_2O .

TG/DTA under air flow: a weight loss of 9.73% at below 296.8 °C was observed with an endothermic peak at 79.0 °C; calcd 9.59% for $x = 25$ in “ $\text{Na}_9[\text{P}_2\text{W}_{15}\text{Ti}_3\text{O}_{59}(\text{OH})_3]\cdot \text{TiO}_2\cdot x\text{H}_2\text{O}$ ”. IR (KBr) (polyoxometalate region): 1626 (w), 1086 (m), 1053 (vw), 1013 (vw), 941

(s), 912 (s), 789 (vs), 743 (vs), 599 (m), 563 (m), 526 (m), 463 (w) cm^{-1} . ^{31}P NMR [23.6 °C, D_2O]: $\delta = -4.94, -14.59$ ppm.

The water-soluble, sodium salts of the monomeric, trititanium(IV)-substituted Wells–Dawson POM (**M-1**) as powder samples have been prepared by three independent workers (see syntheses 1–3 in the Supporting Information) and characterized by FT-IR; TG/DTA; complete elemental analysis based on H, Cl, Na, Cs, O, P, W, and Ti analyses; solution ^{31}P and solid-state CPMAS ^{31}P NMR; and ^{183}W NMR (Supporting Information). Although their compounds were the monomeric species of the trititanium(IV)-substituted Wells–Dawson POM, the complete elemental analyses showed that all of the compounds were contaminated with titanium(IV) compounds, i.e., “water-soluble titanium(IV) species.” At present, we have never obtained the monomeric species without contamination of titanium(IV) species (Supporting Information).

Preparation of $\text{Na}_4\text{K}_{12}[\{\alpha\text{-P}_2\text{W}_{15}\text{Ti}_3\text{O}_{60}(\text{OH})_2\}_2(\text{Cp}^*\text{Rh})_2\}\cdot 25\text{H}_2\text{O}$ (NaK-D-1**).** The monomeric trititanium(IV)-substituted Wells–Dawson POM as the sodium salt, “ $\text{Na}_9[\text{P}_2\text{W}_{15}\text{Ti}_3\text{O}_{59}(\text{OH})_3]\cdot \text{TiO}_2\cdot 25\text{H}_2\text{O}$ ” (**Na-M-1**: 2.82 g, 0.60 mmol), was dissolved in water (10 mL). To the solution was added 0.1 M NaOH aq. (3 mL) for 2 h and stirred for 30 min at an ambient temperature (solution A). Separately, AgBF_4 (0.234 g, 12.0 mmol) was dissolved in MeOH (40 mL), whereinto $[\text{Cp}^*\text{RhCl}_2]_2$ (0.186 g, 0.30 mmol) was added. AgCl formed was filtered off through a membrane filter (JG 0.2 μm). Water (40 mL) was added to the filtrate, and MeOH was removed by a rotary evaporator at 40 °C (the resulting solution B). Solution B was added to solution A in one portion, followed by stirring for 1 h in a water-bath at 90 °C. The yellow-orange powder of the sodium salt (**Na-D-1**) was formed by reprecipitation by EtOH (75 mL). The yellow-orange precipitate formed was collected on a membrane filter (JG 0.2 μm), washed with Et₂O (60 mL), and dried *in vacuo* for 2 h. At this stage, **Na-D-1** was obtained in a yield of 2.72 g.

Crystallization. The yellow-orange powder (0.60 g) of **Na-D-1** was dissolved in water (40 mL). KCl (0.48 g, 6.4 mmol) was added to the yellow-orange solution, followed by stirring for 1 min in a water-bath at 50 °C. The 50 mL vial containing the resulting yellow-orange solution (ca. 40 mL) was sealed with a screw cap. One day later, on standing, a mixture of the yellow-orange powder and the orange block crystals of the sodium/potassium salts was deposited. The yellow-orange powder was removed by dissolving the mixture in water for 3 min with stirring in a water-bath at 50 °C. Undissolved orange block crystals were collected by a membrane filter (JG 0.2 μm), washed with EtOH (30 mL), and dried *in vacuo* for 2 h. The crystalline sample of $\text{Na}_4\text{K}_{12}[\{\alpha\text{-P}_2\text{W}_{15}\text{Ti}_3\text{O}_{60}(\text{OH})_2\}_2(\text{Cp}^*\text{Rh})_2\}\cdot 25\text{H}_2\text{O}$ (**NaK-D-1**) obtained in a yield of 0.087 g {14.7% relative to “ $\text{Na}_9[\text{P}_2\text{W}_{15}\text{Ti}_3\text{O}_{59}(\text{OH})_3]\cdot \text{TiO}_2\cdot 25\text{H}_2\text{O}$ ”} was soluble in hot water, but insoluble in MeOH, MeCN, EtOH, and Et₂O. Anal. Calcd for $\text{C}_{20}\text{H}_{4.8}\text{Na}_4\text{K}_{12}\text{O}_{131}\text{P}_4\text{Rh}_2\text{Ti}_6\text{W}_{30}$ or $\text{Na}_4\text{K}_{12}[\{\alpha\text{-P}_2\text{W}_{15}\text{Ti}_3\text{O}_{60}(\text{OH})_2\}_2(\text{Cp}^*\text{Rh})_2\}\cdot 7\text{H}_2\text{O}$: C, 2.65; H, 0.53; K, 5.17; Na, 1.01; O, 23.09; P, 1.36; Rh, 2.27; Ti, 3.16; W, 60.75%. Found: C, 3.02; H, 0.54; K, 5.33; Na, 0.83; O, 23.00; P, 1.37; Rh, 2.21; Ti, 3.22; W, 60.20%; total 99.72%. A weight loss of 3.41% (weakly solvated or adsorbed water) was observed during the course of drying at room temperature at 10^{-3} to 10^{-4} Torr overnight before the analysis, suggesting the presence of 18 water molecules (calcd 3.45%). TG/DTA under air flow: a weight loss of 4.82% at below 260.1 °C was observed without a clear endothermic peak; calcd 4.79% for $x = 25$ in $\text{Na}_4\text{K}_{12}[\{\alpha\text{-P}_2\text{W}_{15}\text{Ti}_3\text{O}_{60}(\text{OH})_2\}_2(\text{Cp}^*\text{Rh})_2\}\cdot x\text{H}_2\text{O}$. IR (KBr) (polyoxometalate region): 1620 (w), 1476 (vw), 1452 (vw), 1378 (vw), 1085 (s), 1051 (w), 1011 (w), 938 (s), 913 (s), 751 (vs), 599 (m), 563 (m), 521 (m), 463 (m) cm^{-1} . ^{31}P NMR [23.9 °C, D_2O]: $\delta = -5.16, -14.57$ ppm. ^1H NMR [24.0 °C, D_2O]: $\delta = 1.92$ ppm. $^{13}\text{C}\{^1\text{H}\}$ NMR [24.0 °C, D_2O]: $\delta = 11.36, 96.13$ ppm. ^{183}W NMR [D_2O , RT, substitution method]: $\delta = -153.14$ (1W), -159.28 (2W), -185.39 (2W), -189.93 (2W), -203.13 (2W), -232.23 (2W), -234.71 (2W), -235.72 (2W) ppm.

The workup of ^{183}W NMR measurement is as follows, in which the cation of **NaK-D-1** was exchanged using a cation exchange resin in an Na^+ form in order to obtain the highly concentrated solution. The sodium potassium salt (**NaK-D-1**: 0.87 g) was suspended in 2.8 mL of

D_2O , to which a cation exchange resin in an Na^+ form (2 g) was added, followed by stirring for 30 min. After the resin was filtered off through a glass filter (P40), the orange filtrate was used for ^{183}W NMR measurement at room temperature (Figure 3a). ^{31}P NMR of this solution (Supporting Information, control experiments #2) was the same as that of **NaK-D-1** in D_2O (Figure 5a), indicating that the cation exchange workup did not give any effects on the dimeric POM structure in solution.

It should be noted that the powder sample of **Na-D-1** was contaminated with titanium(IV) compounds, while the crystalline sample (**NaK-D-1**) of the mixed sodium/potassium salt of **D-1** was obtained as an analytically pure form without contamination of any titanium(IV) compounds.

X-ray Crystallography. Orange block crystals of **NaK-D-1** (0.21 \times 0.09 \times 0.08 mm) were surrounded by liquid paraffin (Paraton-N) to prevent their degradation. The data collection was done by a Bruker SMART APEX CCD diffractometer at 100 K in the range of $1.72^\circ < \theta < 27.50^\circ$. The intensity data were automatically corrected for Lorentz and polarization effects during integration. The structure was solved by direct methods (program SHELXS-97),^{10a} followed by subsequent difference Fourier calculation, and refined by a full-matrix least-squares procedure on F^2 (program SHELXS-97).^{10b} Absorption correction was performed with SADABS (empirical absorption correction).^{10c} The composition and the formula of the POM containing many counteranions and many hydrated water molecules were determined by complete elemental analysis and TG/DTA analysis. In X-ray crystallography, the polyoxoanion **D-1**, eight potassium cations, and 52 hydrated water molecules per formula unit were identified in the crystal structure, but the location of the four sodium and the four potassium cations per formula unit were not determined as a result of the disorder. Most atoms in the main part of the structure were refined anisotropically, while the rest (as disordered C atoms of Cp* and crystallization solvents) was refined isotropically. Refinements of the positions of many counterions and many solvent molecules in the POM are limited because of their disorder. We can reveal only the molecular structure of the POM, but not the crystal structure. These features are very common in the POM crystallography.

Crystal data for **NaK-D-1**: $\text{C}_{20}\text{H}_4\text{K}_8\text{O}_{176}\text{P}_4\text{Rh}_2\text{Ti}_6\text{W}_{30}$; $M = 9531.84$; triclinic, space group $P\bar{1}$; $a = 14.3212(14)$, $b = 15.4969(15)$, $c = 21.536(2)$ Å, $\alpha = 105.7400(10)$, $\beta = 90.6940(10)$, $\gamma = 90.5890(10)^\circ$, $V = 4599.5(8)$ Å³, $Z = 1$, $D_c = 3.441$ g cm^{-3} , $\mu(\text{Mo-K}\alpha) = 19.418$ mm⁻¹. $R_1 = 0.0539$, $wR_2 = 0.1185$ (for all data). $R_{\text{int}} = 0.0387$, $R_1 = 0.0433$, $wR_2 = 0.1128$, GOF = 1.019 (54 500 total reflections, 20 878 unique reflections where $I > 2\sigma(I)$).

The CCDC-1055696 contains the supplementary crystallographic data for **NaK-D-1** in this paper. These data can be obtained free of charge from The Cambridge Crystallographic Data Centre via www.ccdc.cam.ac.uk/data_request/cif.

RESULTS AND DISCUSSION

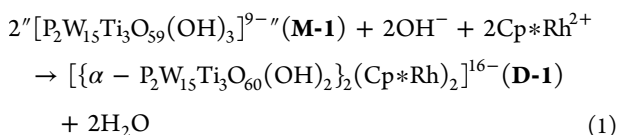
Synthesis and Compositional Characterization.

Trititanium(IV)-substituted Wells–Dawson POM monomer (**M-1**) was obtained as a water-soluble sodium salt (**Na-M-1**) by *in situ* hydrolysis of the $\text{Ti}(\text{H}_2\text{O})_3$ -bridging tetramer (**Na-Tb-1**) by aqueous NaOH. A crystalline solid was obtained, but the crystal data were poor, although they suggested the monomeric nature of **M-1**. This compound in solution was readily converted to the tetramers under acidic/neutral aqueous conditions; i.e., it was stable only under basic conditions (pH 9–11). This compound cannot be converted to an organic solvent-soluble form such as Bu_4N^+ salt. These features are quite unusual in the common POM-support chemistry, seriously restricting formation of the Ti_3 -POM-based organometallic complexes. Further, it was found by the complete elemental analysis that the monomeric Ti_3 -Wells–Dawson POM (**M-1**) was always contaminated with “water-soluble titanium(IV) species” (Supporting Information), and it has

never been obtained in a form without a contaminating ion of titanium(IV) species. The anion–cation charge-balance based on the complete elemental analysis data also suggested that this compound contained protonation of the surface Ti–O–Ti sites in the **M-1**.

The solution ^{31}P NMR in D_2O showed a two-line spectrum at -4.94 and -14.59 ppm (Figure 5b), which was quite different from those of the $\text{Ti}(\text{H}_2\text{O})_3$ -bridging tetramer (**Na-Tb-1**) at -7.04 and -13.77 ppm^{7e} and the non- $\text{Ti}(\text{H}_2\text{O})_3$ -bridging tetramer at -7.59 and -13.97 ppm,^{7d} both with the encapsulated Cl^- ion.

The POM-supported organometallic complex, i.e., the 2:2-type dimer (**D-1**), was formed by a 1:1-molar ratio reaction under 1 h of stirring at 90°C of “[$\text{P}_2\text{W}_{15}\text{Ti}_3\text{O}_{59}(\text{OH})_3$] $^{9-}$ ” (**M-1**) with the separately *in situ*-derived chloride-free [Cp^*Rh] $^{2+}$ in water. The POM-supported organometallic complexes reported previously have been formed by mixing at room temperature,⁶ whereas the formation of **D-1** requires conditions of stirring for 1 h at 90°C . The formation of polyoxoanion **D-1** can be represented in eq 1.



A crystalline sample of the 2:2 ratio complex (**NaK-D-1**) of the trititanium(IV)-substituted Wells–Dawson POM and $\text{Cp}^*\text{Rh}^{2+}$, i.e., $\text{Na}_4\text{K}_{12}[\{\alpha - \text{P}_2\text{W}_{15}\text{Ti}_3\text{O}_{60}(\text{OH})_2\}_2(\text{Cp}^*\text{Rh})_2] \cdot 25\text{H}_2\text{O}$, was obtained, which was characterized by complete elemental analysis based on C, H, K, Na, O, P, Rh, Ti, and W analyses; FTIR; TG/DTA; X-ray crystallography; and (^{183}W , ^{31}P , ^1H and $^{13}\text{C}\{^1\text{H}\}$) NMR in a D_2O .

The complete elemental analysis of **NaK-D-1** was carried out using the sample dried at room temperature under a vacuum of 10^{-3} to 10^{-4} Torr overnight. The total of the found values of nine elements was 99.72%, indicating that the obtained compound was very pure. The data we found were in accord with the calculated values for the formula with four sodium and 12 potassium cations, two Cp^*Rh groups, two diprotonated trititanium(IV)-substituted Wells–Dawson POMs, and seven hydrated water molecules. The weight loss of 3.41% observed during the course of drying at 10^{-3} to 10^{-4} Torr overnight at room temperature, before the analysis, corresponded to 18 water molecules (calcd 3.45%).

The number of water molecules, i.e., 25, in the formula of **NaK-D-1** was determined by the elemental analysis data (as seven hydrated water molecules plus 18 water molecules), which was also completely consistent with the TG/DTA measurements under air flow. In the TG/DTA, a weight loss of 4.82% observed at below 260.1°C for **NaK-D-1** corresponded to ca. 25 water molecules (calc. 4.79%).

The solid FTIR spectrum (Figure 1a) of **NaK-D-1** measured in a KBr disk showed prominent bands at 1085, 1051, 1011, 938, 913, and 751 cm^{-1} . The spectrum showed the characteristic band of the Wells–Dawson-type “[$\alpha - \text{P}_2\text{W}_{18}\text{O}_{62}$] $^{6-}$ ” POM framework in the polyoxometalate region ($1200\text{--}400\text{ cm}^{-1}$) at 1090, 957, 916, and 789 cm^{-1} . The Ti–O–Ti vibration bands of the inter-Wells–Dawson POM subunits were not observed at around 660 cm^{-1} . The presence of the $\text{Cp}^*\text{Rh}^{2+}$ groups was confirmed by the IR band at 1476, 1452, and 1378 cm^{-1} . The solid IR spectrum of **Na-M-1** showed that it was the monomeric species, because of no vibrational bands due to

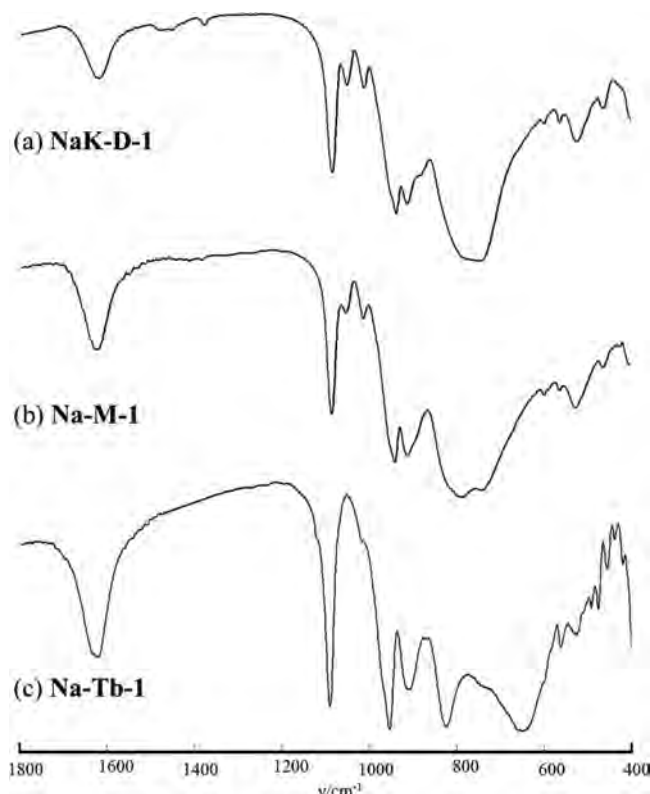


Figure 1. FTIR spectra in the polyoxoanion region ($1800\text{--}400\text{ cm}^{-1}$), measured in KBr disks, of (a) $\text{Na}_4\text{K}_{12}[\{\alpha - \text{P}_2\text{W}_{15}\text{Ti}_3\text{O}_{60}(\text{OH})_2\}_2(\text{Cp}^*\text{Rh})_2] \cdot 25\text{H}_2\text{O}$ (**NaK-D-1**), (b) “ $\text{Na}_9[\alpha - \text{P}_2\text{W}_{15}\text{Ti}_3\text{O}_{59}(\text{OH})_3] \cdot \text{TiO}_2 \cdot 25\text{H}_2\text{O}$ ” (**Na-M-1**), and (c) the $\text{Ti}(\text{H}_2\text{O})_3$ -bridging tetramer (**Na-Tb-1**).

the intermolecular Ti–O–Ti bonds around 660 cm^{-1} (Figure 1b), which have been shown in the tetramer, **Na-Tb-1** (Figure 1c).

Molecular Structure of D-1 in NaK-D-1. The molecular structure of polyoxoanion **D-1**, its polyhedral representation, and the partial structure around the Rh and Ti_3 centers are shown in Figure 2a–c, respectively. Selected bond lengths (Å) and angles (deg) around the Rh and Ti_3 centers in the **D-1** are given in Table 1, while the other bond lengths (Å) in **D-1** (Table S1) and the bond valence sum (BVS) calculations of the W, Ti, O, and P atoms (Table S2) are deposited in the Supporting Information.

X-ray crystallography of **D-1** revealed that the two organometallic fragments were sandwiched between two trititanium(IV)-substituted Wells–Dawson POM units [$\alpha - \text{P}_2\text{W}_{15}\text{Ti}_3\text{O}_{60}(\text{OH})_2$] $^{10-}$, resulting in C_i symmetry. The [Cp^*Rh] $^{2+}$ groups are coordinated to two oxygen atoms (O3, O20) of one of the Wells–Dawson units and to one oxygen atom (O1) of the second subunit [Rh–O average 2.121 Å] (Figure 2b and c). Each Rh center was bound to the terminal oxygen atoms of the Ti sites (O1, O3) and the edge-sharing (O20) of the Ti–O–Ti linkage. No example has been reported for the Wells–Dawson Ti_3 -substituted POM-based bridging organometallic complexes. In the trititanium(IV)-substituted Wells–Dawson unit in **D-1**, the W–O bond lengths were in the normal range:^{1a} W–Ot (terminal) [$1.711(8)\text{--}1.735(8)\text{ Å}$; average 1.723 Å], W–Oc (corner-sharing) [$1.790(7)\text{--}2.056(8)\text{ Å}$; average 1.903 Å], W–Oe (edge-sharing) [$1.899(8)\text{--}1.962(8)\text{ Å}$; average 1.927 Å], and W–Oa (coordinating to P atom) [$2.335(8)\text{--}2.386(8)\text{ Å}$; average 2.352 Å] (Table S1).

The values of the bond valence sum (BVS) calculations (Table S2) for **D-1**, which were calculated based on the observed bond lengths, were in the range of 6.081–6.287 (average 6.148) for 15 W atoms, 4.825–4.924 (average 4.874) for two P atoms, 4.163–4.225 (average 4.185) for three Ti atoms, and 1.456–2.175 (average 1.865) for 60 O atoms, excluding O19 and O21; these values were within reasonable agreement with the formal valences of W^{6+} , P^{5+} , Ti^{4+} , and O^{2-} , respectively (Table S2). The calculated BVS values of O19 and O21 at the two edge-sharing Ti–O–Ti bonds were 1.167 and 1.197, respectively, suggesting that each of the two edge-sharing oxygen atoms of the substituted-titanium(IV) site was protonated.

(^{183}W , ^{31}P , 1H , and $^{13}C\{^1H\}$) NMR Characterization. The ^{183}W NMR spectrum of **D-1** dissolved in D_2O showed an eight line ^{183}W NMR spectrum at -153.14 , -159.28 , -185.39 , -189.93 , -203.13 , -232.23 , -234.71 , -235.72 ppm with a relative intensity ratio of 1:2:2:2:2:2:2:2 (Figure 3a). This

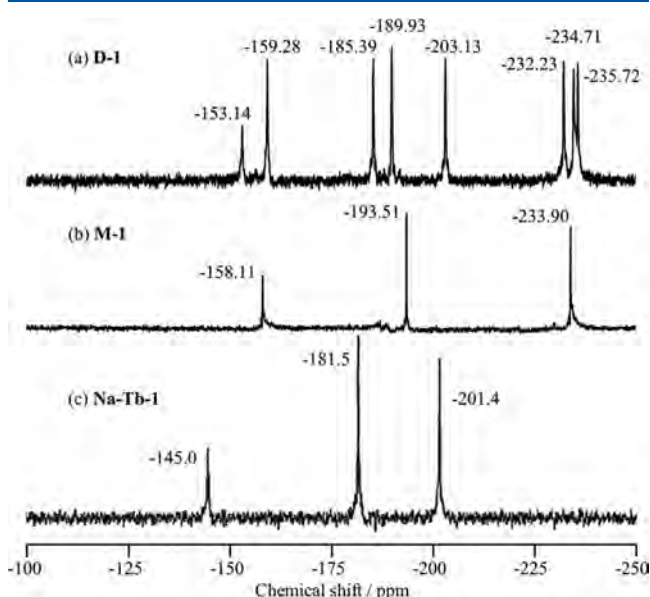


Figure 3. ^{183}W NMR spectra of (a) **D-1**; (b) the monomer (**M-1**) showing a three line ^{183}W NMR at -158.11 (1W), -193.51 (2W, $J_{P-W} = 1.9$ Hz), -233.90 (2W, $J_{P-W} = 1.7$ Hz) ppm (Supporting Information); and (c) the $Ti(H_2O)_3$ -bridging tetramer (**Na-Tb-1**) showing a three line ^{183}W NMR at -145.0 (3W \times 4), -181.5 (6W \times 4), and -201.4 (6W \times 4) dissolved in D_2O .

spectrum is in contrast to those of the monomer (**M-1**) showing a three line ^{183}W NMR at -158.11 (1W), -193.51 (2W, $J_{P-W} = 1.9$ Hz), and -233.90 (2W, $J_{P-W} = 1.7$ Hz) ppm (Supporting Information, Figure 3b) and of the $Ti(H_2O)_3$ -bridging tetramer (**Na-Tb-1**) showing a three line ^{183}W NMR at -145.0 (3W \times 4), -181.5 (6W \times 4), and -201.4 (6W \times 4) (Figure 3c).^{7e} The eight line ^{183}W NMR spectrum (Figure 3a) indicates that the POM in D_2O is a dimer based on C_i (or S_2) symmetry, but not a monomer. If the solid-state structure or the integrity **NaK-D-1** with C_i symmetry is preserved in solution, it should show a 15 line spectrum. The formula of the dimeric POM dissolved in D_2O can be represented as $[\{\alpha-P_2W_{15}Ti_3O_{60}(OH)_3\}_2\{Cp^*Rh(OH)\}_2]^{16-}$ (**D-2**). Polyhedral representation of the dimeric POM **D-2** with C_i symmetry (Figure 4) is consistent with a species showing the eight line ^{183}W NMR spectrum with a relative intensity ratio of

1:2:2:2:2:2:2:2 of **D-1** dissolved in D_2O (Figure 3a). Thus, the solid-state structure or its integrity of **D-1** in **NaK-D-1** is not preserved in aqueous solution, while the dimeric nature is kept as **D-2** in the solution.

The dimeric POM **D-2** will result from hydrolysis of the Cp^*Rh moieties resulting in breaking of the Rh–O20 bond, by nucleophilic attack of the water molecule in the $[\{\alpha-P_2W_{15}Ti_3O_{60}(OH)_2\}_2(Cp^*Rh)_2]^{16-}$ (**D-1**), subsequent deprotonation of the coordinated water molecule of the once formed, $[Cp^*Rh(H_2O)]^{2+}$ unit, and the resulting in protonation of the surface oxygen atom of one Ti–O–Ti site or formation of $[\{\alpha-P_2W_{15}Ti_3O_{60}(OH)_3\}]^{9-}$.

The two species **D-1** and **D-2** are quite different, although both are represented as the compounds with the same C_i (or S_2) symmetry (Figure 4).

If there is a fast dynamic process leading to an average higher symmetry in solution than that observed in the solid state, there may be no difference between **D-1** and **D-2**. However, the dynamic process containing hopping of the Cp^*Rh group should be accompanied by a rapid deprotonation–protonation process of the Ti–O–Ti sites. As a matter of fact, deprotonation of Ti–(OH)–Ti sites is not easy to attain at room temperature. In fact, formation of **D-1** with unusual bonding behaviors requires heating **M-1** at $90^\circ C$. That is to say, **D-1** cannot be synthesized at room temperature due to the presence of protonation of three $\mu-O$ sites of **M-1**. Thus, the possibility of the dynamic process will be low.

On the other hand, if present, the monomeric POM, or the 1:1 anion, can be described as formulas such as $[\{\alpha-P_2W_{15}Ti_3O_{60}(OH)_2\}\{Cp^*Rh(H_2O)_n\}]^{8-}$ ($n = 1, 2$), $[\{\alpha-P_2W_{15}Ti_3O_{60}(OH)_3\}\{Cp^*Rh(OH)\}]^{8-}$, and $[\{\alpha-P_2W_{15}Ti_3O_{60}(OH)_3\}\{Cp^*Rh(OH)(H_2O)\}]^{8-}$ and so on, all showing a 15 line ^{183}W NMR spectrum because of no symmetry element present.

Thus, all of ^{31}P , 1H , and $^{13}C\{^1H\}$ NMR spectra of **NaK-D-1** in D_2O should be understood on the basis of **D-2** present in solution as shown by ^{183}W NMR.

The ^{31}P NMR spectrum of **NaK-D-1** dissolved in D_2O (Figure 5a) showed a two-line spectrum at -5.16 and -14.57 ppm, indicating that the two Wells–Dawson subunits in **D-2** were equivalent in D_2O . The lower-field signal at -5.16 ppm was assigned to the P atom closest to the titanium(IV)-substituted side. Compared with the ^{31}P NMR of **Na-M-1** in D_2O at -4.94 and -14.59 ppm (Figure 5b), the lower-field signal at -4.94 ppm was shifted to much a higher field, whereas the higher-field signal at -14.59 ppm was only little shifted to a lower field. In addition to two main signals at -4.94 and -14.59 ppm, ^{31}P NMR of **Na-M-1** in D_2O (Figure 5b) also contained very broad, minor peaks at around -6.2 and -14.2 ppm, which are not due to the $Ti(H_2O)_3$ -bridging and non- $Ti(H_2O)_3$ -bridging tetramers but may be due to other oligomeric species containing Wells–Dawson units, although they were not identified at present.

The 1H NMR spectrum of **NaK-D-1** in D_2O (Figure 6a) showed a single peak at 1.92 ppm due to the methyl groups of two Cp^* groups of **D-2**, which was significantly shifted from that of the *in situ*-generated " $Cp^*Rh(BF_4)_2$ " or " $[Cp^*Rh(H_2O)_3](BF_4)_2$ " at 1.67 ppm. Therefore, the two Cp^*Rh fragments in **D-2** were equivalent in D_2O . The $^{13}C\{^1H\}$ NMR (Figure 7a) showed a two-line spectrum at 11.36 and 96.13 ppm due to the Cp^* group, both being somewhat shifted from that of the *in situ*-generated " $Cp^*Rh(BF_4)_2$ " (Figure 7b) at 10.79 and 96.94 ($J_{Rh-C} = 9.9$ Hz) ppm due to coupling with

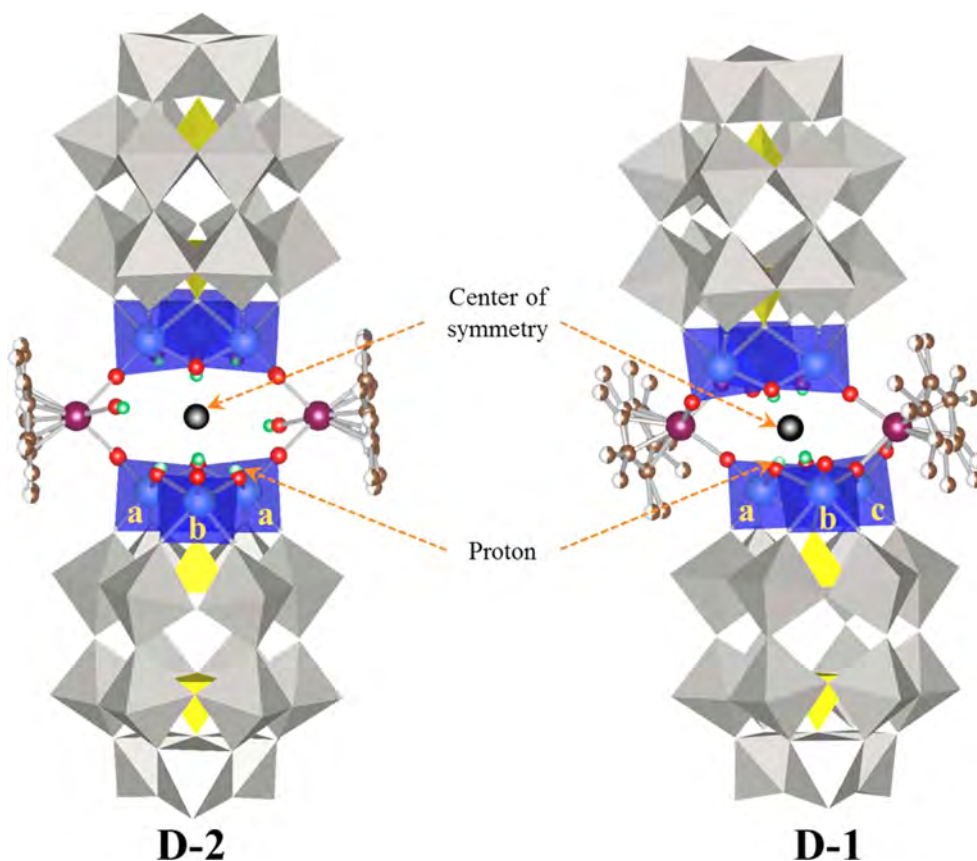


Figure 4. Polyhedral representation of the dimeric POM $[\{\alpha\text{-P}_2\text{W}_{15}\text{Ti}_3\text{O}_{60}(\text{OH})_3\}_2\{\text{Cp}^*\text{Rh}(\text{OH})\}_2]^{16-}$ (**D-2**) with C_i symmetry, which is consistent with a species showing an eight line ^{183}W NMR spectrum with a relative intensity ratio of 1:2:2:2:2:2:2:2 of **D-1** dissolved in D_2O (Figure 3a). The **D-2** with a formula of $[\{\alpha\text{-P}_2\text{W}_{15}\text{Ti}_3\text{O}_{60}(\text{OH})_3\}_2\{\text{Cp}^*\text{Rh}(\text{OH})\}_2]^{16-}$ is different from the **D-1** with a formula of $[\{\alpha\text{-P}_2\text{W}_{15}\text{Ti}_3\text{O}_{60}(\text{OH})_2\}_2(\text{Cp}^*\text{Rh})_2]^{16-}$. In **D-2**, two Ti octahedra (designated as a) in the cap site are equivalent, but they are inequivalent with the one Ti octahedron (designated as b), whereas in **D-1**, three Ti octahedra (designated as a, b, and c) are inequivalent with each other. In **D-2**, the three bridging oxygen ($\mu\text{-O}$) sites in the Ti–O–Ti bonds are protonated, while in **D-1** the two bridging oxygen sites are protonated. In **D-2**, one Cp^*Rh group is bonding to two terminal oxygen atoms of the two POM units, while in **D-1**, it is bonding to three oxygen atoms (two are the terminal oxygen atoms and one is the bridging oxygen) of the two POM units.

^{103}Rh nuclei. Therefore, the two Cp^*Rh fragments in **D-2** were equivalent, and **D-2** is relatively stable in D_2O .

As to stability of **D-2** in solution, the resistant nature of **D-2** to Cl^- ions or no reactivity of **D-2** with Cl^- ions was confirmed by control experiments #2, while the *in situ*-generated " $\text{Cp}^*\text{Rh}(\text{BF}_4)_2$ " in water or " $[\text{Cp}^*\text{Rh}(\text{H}_2\text{O})_3](\text{BF}_4)_2$ " readily reacted with Cl^- ions to form the water-insoluble $[\text{Cp}^*\text{RhCl}_2]_2$ (Supporting Information, control experiments #1). These results suggest that the reactivity of the $[\text{Cp}^*\text{Rh}(\text{OH})]^+$ moiety in the dimer **D-2** with Cl^- ions is much lower than that of the $[\text{Cp}^*\text{Rh}(\text{H}_2\text{O})_3]^{2+}$ moiety in the " $\text{Cp}^*\text{Rh}(\text{BF}_4)_2$ " with Cl^- ions. The monomeric POM or the 1:1 anion, which can be described as, for example, $[\{\alpha\text{-P}_2\text{W}_{15}\text{Ti}_3\text{O}_{60}(\text{OH})_2\}\{\text{Cp}^*\text{Rh}(\text{H}_2\text{O})_n\}]^{8-}$ ($n = 1, 2$) and $[\{\alpha\text{-P}_2\text{W}_{15}\text{Ti}_3\text{O}_{60}(\text{OH})_3\}\{\text{Cp}^*\text{Rh}(\text{OH})(\text{H}_2\text{O})\}]^{8-}$, if present, will readily react with Cl^- ions.

The dissociation process of the dimeric POM (**D-2**: the 2:2 anion) to the monomer (the 1:1 anion) is not contained in the aqueous solution, as shown by the observed eight line ^{183}W NMR spectrum and the two control experiments #1 and #2 (Supporting Information).

Thus, the solution (^{183}W , ^{31}P , ^1H , and $^{13}\text{C}\{^1\text{H}\}$) NMR of **D-1** in D_2O shows that the dimeric nature of **D-2** is preserved in aqueous solution.

CONCLUSION

In summary, we successfully synthesized a novel trititanium(IV)-substituted Wells–Dawson POM-based organometallic complex containing the two bridging Cp^*Rh groups, $[\{\alpha\text{-P}_2\text{W}_{15}\text{Ti}_3\text{O}_{60}(\text{OH})_2\}_2(\text{Cp}^*\text{Rh})_2]^{16-}$ (**NaK-D-1**), as the crystalline sample of the mixed sodium/potassium salt, using the separately prepared powder sample of the trititanium(IV)-substituted Wells–Dawson POM support (**Na-M-1**) as the sodium salt that has been isolated by a hydrolysis of the $\text{Ti}(\text{H}_2\text{O})_3$ -bridging tetramer (**Na-Tb-1**) with aqueous NaOH . The monomeric species **Na-M-1** showed quite unusual behaviors, in comparison with the so far well-studied, trimetal ($\text{M} = \text{Nb}^{\text{V}}, \text{V}^{\text{V}}$)-substituted Wells–Dawson POMs and seriously restricted its utilization as the POM-support for organometallics: (1) **Na-M-1** was obtained only in the form always contaminated with titanium(IV) compounds, but not without contamination of titanium(IV) species (see Supporting Information). (2) It was stable only in a basic solution (pH 9–11) and readily converted to the tetrameric species under acidic/neutral aqueous conditions. (3) It cannot be changed to the organic solvent-soluble forms such as Bu_4N^+ salt. (4) The surface oxygen atoms in the Ti–O–Ti sites of **Na-M-1** were protonated.

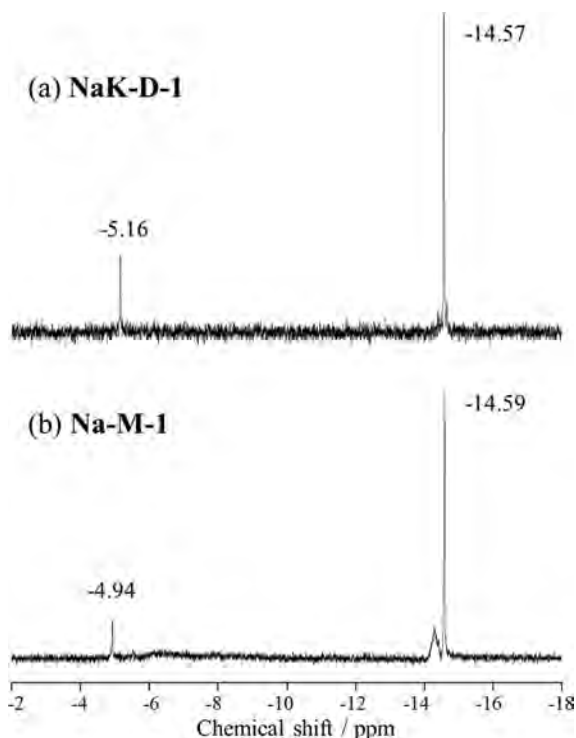


Figure 5. ^{31}P NMR spectra of (a) $\text{Na}_4\text{K}_{12}[\{\alpha\text{-P}_2\text{W}_{15}\text{Ti}_3\text{O}_{60}(\text{OH})_2\}_2(\text{Cp}^*\text{Rh})_2]\cdot 25\text{H}_2\text{O}$ (**NaK-D-1**) and (b) $^{\text{Na}}_9[\alpha\text{-P}_2\text{W}_{15}\text{Ti}_3\text{O}_{59}(\text{OH})_3]\cdot \text{TiO}_2\cdot 25\text{H}_2\text{O}$ (**Na-M-1**) dissolved in D_2O .

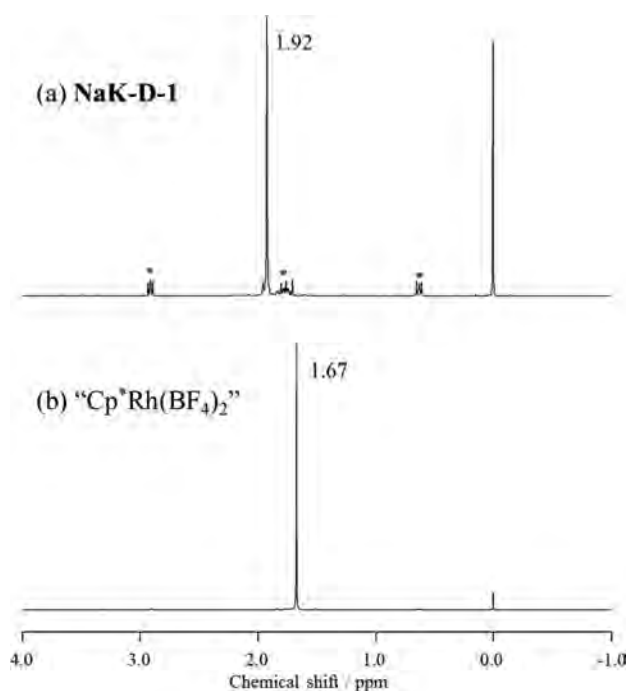


Figure 6. ^1H NMR spectra of (a) $\text{Na}_4\text{K}_{12}[\{\alpha\text{-P}_2\text{W}_{15}\text{Ti}_3\text{O}_{60}(\text{OH})_2\}_2(\text{Cp}^*\text{Rh})_2]\cdot 25\text{H}_2\text{O}$ (**NaK-D-1**) dissolved in D_2O and (b) $^{\text{Cp}^*}\text{Rh}(\text{BF}_4)_2$ derived from $[\text{Cp}^*\text{RhCl}_2]_2$ and AgBF_4 in D_2O . The signals denoted by asterisks are due to DSS as an internal standard.

Nevertheless, the finally formed **NaK-D-1** was obtained as an analytically pure, crystalline compound without contamination of titanium(IV) compounds. This complex (**NaK-D-1**) was

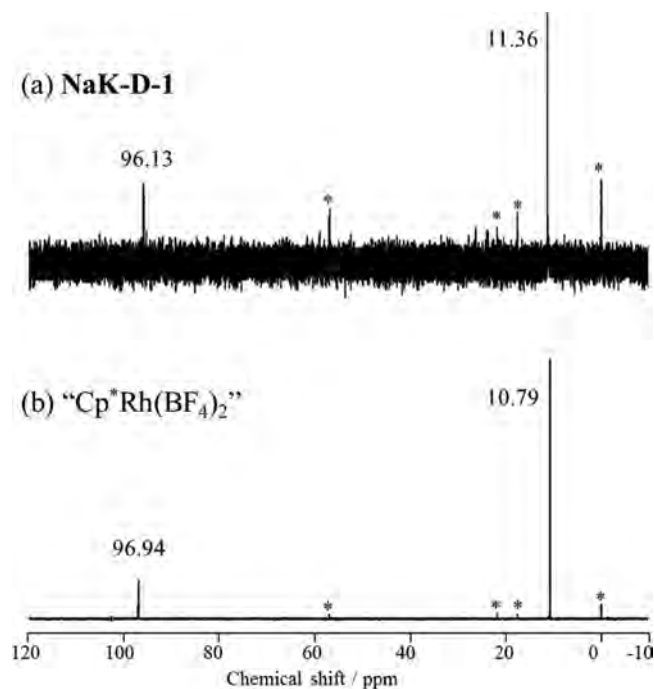


Figure 7. $^{13}\text{C}\{^1\text{H}\}$ NMR spectra of (a) $\text{Na}_4\text{K}_{12}[\{\alpha\text{-P}_2\text{W}_{15}\text{Ti}_3\text{O}_{60}(\text{OH})_2\}_2(\text{Cp}^*\text{Rh})_2]\cdot 25\text{H}_2\text{O}$ (**NaK-D-1**) dissolved in D_2O and (b) $^{\text{Cp}^*}\text{Rh}(\text{BF}_4)_2$ derived from $[\text{Cp}^*\text{RhCl}_2]_2$ and AgBF_4 in D_2O . The signals denoted by asterisks are due to DSS as an internal standard.

water-soluble and stable in water. Since the trititanium(IV)-substituted Wells–Dawson POM-supported organometallic complexes have never been reported so far, **D-1** is the first example of this type of complex. The surface Ti–O–Ti sites of the precursor **M-1** were protonated, and they were not completely deprotonated in the synthesis of **D-1**, even under alkali conditions. The unique, Cp^*Rh -bridging dimeric structure of **D-1** will be attributed to the intrinsic protonation of the surface Ti–O–Ti sites of the POM support **M-1**. The eight line ^{183}W NMR spectrum of **D-1** dissolved in D_2O showed that the solid-state structure or its integrity of **D-1** in **NaK-D-1** is not preserved in aqueous solution, while the dimeric nature is kept in D_2O by the form of $[\{\alpha\text{-P}_2\text{W}_{15}\text{Ti}_3\text{O}_{60}(\text{OH})_2\}_2\{\text{Cp}^*\text{Rh}(\text{OH})\}_2]^{16-}$ with C_i symmetry (**D-2**). Analogous Ti_3 -substituted Wells–Dawson POM-based organometallic complexes as homogeneous catalyst precursors can be also expected using the organometallic precursors such as $\{(\text{arene})\text{Ru}\}^{2+}$ and $\{(\text{COD})\text{Pt}\}^{2+}$.

■ ASSOCIATED CONTENT

Supporting Information

The Supporting Information is available free of charge on the ACS Publications website at DOI: 10.1021/acs.inorgchem.5b01206.

Reaction of *in situ*-generated $^{\text{Cp}^*}\text{Rh}(\text{BF}_4)_2$ in water or $[\text{Cp}^*\text{Rh}(\text{H}_2\text{O})_3](\text{BF}_4)_2$ with Cl^- ion (control experiments #1), Cl^- ion resistant nature of **D-1** or actually **D-2** (control experiments #2), TG/DTA curve of **D-1** (Figure S1), syntheses 1–3 and characterization of the monomeric trititanium(IV)-substituted Wells–Dawson POMs (**M-1**), trimetal-substituted Well–Dawson POMs, and their ^{31}P and ^{183}W NMR (Table S1), selected bond lengths (Å) around the atom (P, W) center for $[\{\alpha\text{-}$

$P_2W_{15}Ti_3O_{60}(OH)_2\{Cp^*Rh\}_2\}^{16-}$ (D-1) in NaK-D-1 (Table S2), and bond valence sum (BVS) calculations of W, Ti, P, and O atoms for $\{\alpha-P_2W_{15}Ti_3O_{60}(OH)_2\{Cp^*Rh\}_2\}^{16-}$ (D-1) in NaK-D-1 (Table S3) (PDF)
Crystallographic data (CIF)

AUTHOR INFORMATION

Corresponding Author

*Phone: 81-463-59-4111. Fax: 81-463-58-9684. E-mail: nomiya@kanagawa-u.ac.jp.

Notes

The authors declare no competing financial interest.

ACKNOWLEDGMENTS

This work was supported by JSPS KAKENHI Grant number 22550065 and also by the Strategic Research Base Development Program for Private University of the Ministry of Education, Culture, Sports, Science and Technology of Japan.

REFERENCES

- (1) (a) Pope, M. T. *Heteropoly and Isopoly Oxometalates*; Springer-Verlag: New York, 1983. (b) Day, V. W.; Klemperer, W. G. *Science* **1985**, *228*, 533–541. (c) Pope, M. T.; Müller, A. *Angew. Chem., Int. Ed. Engl.* **1991**, *30*, 34–48. (d) Hill, C. L.; Prosser-McCartha, C. M. *Coord. Chem. Rev.* **1995**, *143*, 407–455. (e) Okuhara, T.; Mizuno, N.; Misono, M. *Adv. Catal.* **1996**, *41*, 113–252. (f) A series of 34 papers in a volume devoted to polyoxoanions in catalysis: Hill, C. L. *J. Mol. Catal. A: Chem.* **1996**, *114*, 1–371. (g) Hill, C. L. *Chem. Rev.* **1998**, *98*, 1–390. (h) Neumann, R. *Prog. Inorg. Chem.* **1998**, *47*, 317–370. (i) *Polyoxometalate Chemistry from Topology via Self-Assembly to Applications*; Pope, M. T., Müller, A., Eds.; Kluwer Academic Publishers: Dordrecht, The Netherlands, 2001. (j) *Polyoxometalate Chemistry for Nano-Composite Design*; Yamase, T., Pope, M. T., Eds.; Kluwer Academic Publishers: Dordrecht, The Netherlands, 2002. (k) Pope, M. T. In *Comprehensive Coordination Chemistry II*; Wedd, A. G., Ed.; Elsevier Science: New York, 2004; Vol. 4, pp 635–678. (l) Hill, C. L. In *Comprehensive Coordination Chemistry II*; Wedd, A. G., Ed.; Elsevier Science: New York, 2004; Vol. 4, pp 679–759. (m) A series of 32 recent papers in a volume devoted to polyoxometalates in catalysis: Hill, C. L. *J. Mol. Catal. A: Chem.* **2007**, *262*, 1–242. (n) Proust, A.; Thouvenot, R.; Gouzerh, P. *Chem. Commun.* **2008**, 1837–1852. (o) Hasenknopf, B.; Micoine, K.; Lacôte, E.; Thorimbert, S.; Malacria, M.; Thouvenot, R. *Eur. J. Inorg. Chem.* **2008**, *2008*, 5001–5013. (p) Laurencin, D.; Thouvenot, R.; Boubekeur, K.; Villain, F.; Villanneau, R.; Rohmer, M.-M.; Benard, M.; Proust, A. *Organometallics* **2009**, *28*, 3140–3151. (q) Long, D.-L.; Tsunashima, R.; Cronin, L. *Angew. Chem., Int. Ed.* **2010**, *49*, 1736–1758. (r) Pradeep, C. P.; Long, D.-L.; Cronin, L. *Dalton Trans.* **2010**, *39*, 9443–9457.
 - (2) (a) Dolbecq, A.; Dumas, E.; Mayer, C. R.; Mialane, P. *Chem. Rev.* **2010**, *110*, 6009–6048. (b) Putaj, P.; Lefebvre, F. *Coord. Chem. Rev.* **2011**, *255*, 1642–1685.
 - (3) (a) Knoth, W. H.; Harlow, R. L. *J. Am. Chem. Soc.* **1981**, *103*, 1865–1867. (b) Filowitz, M.; Ho, R. K. C.; Klemperer, W. G.; Shum, W. *Inorg. Chem.* **1979**, *18*, 93–103.
 - (4) Artero, V.; Laurencin, D.; Villanneau, R.; Thouvenot, R.; Herson, P.; Gouzerh, P.; Proust, A. *Inorg. Chem.* **2005**, *44*, 2826–2835.
 - (5) (a) Nomiyama, K.; Hayashi, K.; Kasahara, Y.; Iida, T.; Nagaoka, Y.; Yamamoto, H.; Ueno, T.; Sakai, Y. *Bull. Chem. Soc. Jpn.* **2007**, *80*, 724–731. (b) Sakai, Y.; Shinohara, A.; Hayashi, K.; Nomiyama, K. *Eur. J. Inorg. Chem.* **2006**, *2006*, 163–171.
 - (6) (a) Abramov, P. A.; Sokolov, M. N.; Virovets, A. V.; Floquet, S.; Haouas, M.; Taulelle, F.; Cadot, E.; Vicent, C.; Fedin, V. P. *Dalton Trans.* **2015**, *44*, 2234–2239. (b) Pohl, M.; Lin, Y.; Weakley, T. J. R.; Nomiyama, K.; Kaneko, M.; Weiner, H.; Finke, R. G. *Inorg. Chem.* **1995**, *34*, 767–777. (c) Edlund, D. J.; Saxton, R. J.; Lyon, D. K.; Finke, R. G. *Organometallics* **1988**, *7*, 1692–1704. (d) Nomiyama, K.; Nozaki, C.; Kaneko, M.; Finke, R. G.; Pohl, M. *J. Organomet. Chem.* **1995**, *505*, 23–28. (e) Pohl, M.; Lyon, D. K.; Mizuno, N.; Nomiyama, K.; Finke, R. G. *Inorg. Chem.* **1995**, *34*, 1413–1429. (f) Nomiyama, K.; Pohl, M.; Mizuno, N.; Lyon, D. K.; Finke, R. G. *Inorg. Synth.* **1997**, *31*, 186–201. (g) Pohl, M.; Finke, R. G. *Organometallics* **1993**, *12*, 1453–1457. (h) Weiner, H.; Aiken, J. D., III; Finke, R. G. *Inorg. Chem.* **1996**, *35*, 7905–7913. (i) Nagata, T.; Pohl, M.; Weiner, H.; Finke, R. G. *Inorg. Chem.* **1997**, *36*, 1366–1377. (j) Rapko, B. M.; Pohl, M.; Finke, R. G. *Inorg. Chem.* **1994**, *33*, 3625–3634. (k) Nomiyama, K.; Hasegawa, T. *Chem. Lett.* **2000**, 410–411. (l) Nomiyama, K.; Sakai, Y.; Hasegawa, T. *J. Chem. Soc., Dalton Trans.* **2002**, 252–258. (m) Nomiyama, K.; Torii, H.; Kato, C. N.; Sado, Y. *Chem. Lett.* **2003**, *32*, 664–665. (n) Nomiyama, K.; Kasahara, Y.; Sado, Y.; Shinohara, A. *Inorg. Chim. Acta* **2007**, *360*, 2313–2320. (o) Radkov, E. V.; Young, V. G., Jr.; Beer, R. H. *J. Am. Chem. Soc.* **1999**, *121*, 8953–8954. (p) Nozaki, C. N.; Makino, Y.; Unno, W.; Uno, H. *Dalton Trans.* **2013**, *42*, 1129–1135.
 - (7) (a) Nomiyama, K.; Sakai, Y.; Matsunaga, S. *Eur. J. Inorg. Chem.* **2011**, *2011*, 179–196. (b) Crano, N. J.; Chambers, R. C.; Lynch, V. M.; Fox, M. A. *J. Mol. Catal. A: Chem.* **1996**, *114*, 65–75. (c) Nomiyama, K.; Arai, Y.; Shimizu, Y.; Takahashi, M.; Takayama, T.; Weiner, H.; Nagata, T.; Widergren, J. A.; Finke, R. G. *Inorg. Chim. Acta* **2000**, *300–302*, 285–304. (d) Sakai, Y.; Yoza, K.; Kato, C. N.; Nomiyama, K. *Dalton Trans.* **2003**, 3581–3586. (e) Sakai, Y.; Yoza, K.; Kato, C. N.; Nomiyama, K. *Chem. - Eur. J.* **2003**, *9*, 4077–4083. (f) Kortz, U.; Hamzeh, S. S.; Nasser, A. *Chem. - Eur. J.* **2003**, *9*, 2945–2952. (g) Sakai, Y.; Yoshida, S.; Hasegawa, T.; Murakami, H.; Nomiyama, K. *Bull. Chem. Soc. Jpn.* **2007**, *80*, 1965–1974. (h) Murakami, H.; Hayashi, K.; Tsukada, I.; Hasegawa, T.; Yoshida, S.; Miyano, R.; Kato, C. N.; Nomiyama, K. *Bull. Chem. Soc. Jpn.* **2007**, *80*, 2161–2169. (i) Sakai, Y.; Ohta, S.; Shintoyo, Y.; Yoshida, S.; Taguchi, Y.; Matsuki, Y.; Matsunaga, S.; Nomiyama, K. *Inorg. Chem.* **2011**, *50*, 6575–6583. (j) Sakai, Y.; Kitakoga, Y.; Hayashi, K.; Yoza, K.; Nomiyama, K. *Eur. J. Inorg. Chem.* **2004**, *2004*, 4646–4652.
 - (8) (a) Kang, J. W.; Moseley, K.; Maitlis, P. M. *J. Am. Chem. Soc.* **1969**, *91*, 5970–5977. (b) White, C.; Yates, A.; Maitlis, P. M. *Inorg. Synth.* **1992**, *29*, 228–234.
 - (9) Note: we also obtained the powder and crystalline samples of the mixed sodium/cesium salt (NaCs-D-1). The complete elemental analysis of the powder sample of NaCs-D-1 showed that it was contaminated with titanium(IV) compounds, whereas X-ray crystallography revealed that its crystalline sample was not contaminated with titanium(IV) compounds. However, crystallization of NaCs-D-1 was scarcely reproducible. On the other hand, the present mixed NaK salt (NaK-D-1) was readily crystallized, and crystallization was reproducible by several independent workers.
 - (10) (a) Sheldrick, G. M. *Acta Crystallogr., Sect. A: Found. Crystallogr.* **1990**, *46*, 467–473. (b) Sheldrick, G. M. *SHELXL-97, Program for Crystal Structure Refinement*; University of Göttingen: Göttingen, Germany, 1997. (c) Sheldrick, G. M. *SADABS*; University of Göttingen: Göttingen, Germany, 1996.



Efficient decomposition of a new fluorochemical surfactant: Perfluoroalkane disulfonate to fluoride ions in subcritical and supercritical water



Hisao Hori*, Hiroki Saito, Hidenori Sakai, Toshiyuki Kitahara, Takehiko Sakamoto

Department of Chemistry, Faculty of Science, Kanagawa University, 2946 Tsuchiya, Hiratsuka 259-1293, Japan

ARTICLE INFO

Article history:

Received 10 March 2014
Received in revised form 30 May 2014
Accepted 10 June 2014
Available online 8 July 2014

Handling Editor: I. Cousins

Keywords:

Fluorine
Surfactant
Alternative
Iron

ABSTRACT

Decomposition of ${}^{-}\text{O}_3\text{SC}_3\text{F}_6\text{SO}_3{}^{-}$ in subcritical and supercritical water was investigated, and the results were compared with the results for $\text{C}_3\text{F}_7\text{SO}_3{}^{-}$. This is the first report on the decomposition of perfluoroalkane disulfonates, which are being introduced in electronics industry as greener alternatives to environmentally persistent and bioaccumulative perfluoroalkyl surfactants. Addition of zerovalent iron to the reaction system dramatically increased the yield of F^{-} in the reaction solution: when the reaction of ${}^{-}\text{O}_3\text{SC}_3\text{F}_6\text{SO}_3{}^{-}$ was carried out in subcritical water at 350 °C for 6 h, the F^{-} yield was 70%, which was 23 times the yield without zerovalent iron. Prolonged reaction increased the F^{-} formation: after 18 h, the F^{-} yield from the reaction of ${}^{-}\text{O}_3\text{SC}_3\text{F}_6\text{SO}_3{}^{-}$ reached 81%, which was 2.1 times the F^{-} yield from the reaction of $\text{C}_3\text{F}_7\text{SO}_3{}^{-}$. Although the reactivity of FeO toward these substrates was lower than zerovalent iron in subcritical water, the reactivity was enhanced when the reaction temperature was elevated to supercritical state, at which temperature FeO underwent *in situ* disproportionation to form zerovalent iron, which acted as the reducing agent. When the reaction of ${}^{-}\text{O}_3\text{SC}_3\text{F}_6\text{SO}_3{}^{-}$ was carried out in the presence of FeO in supercritical water at 380 °C for 18 h, the F^{-} yield reached 92%, which was the highest yield among tested.

© 2014 Elsevier Ltd. All rights reserved.

1. Introduction

Perfluoroalkyl surfactants such as perfluoroalkane sulfonates ($\text{C}_n\text{F}_{2n+1}\text{SO}_3{}^{-}$) and their derivatives have been used in surface treatment agents, emulsifying agents in polymer synthesis, fire-fighting foams, and so on because of their high surface-active effect, high thermal and chemical stability, and high light transparency. After it became clear that some of them, particularly, perfluorooctane sulfonate ($\text{C}_8\text{F}_{17}\text{SO}_3{}^{-}$, PFOS) persists and bioaccumulates in the environment (Giesy and Kannan, 2002; Ahrens, 2011), international legal measures regarding the production, use, and import and export of PFOS were implemented (UNEP, 2009), and efforts to develop greener alternatives are advancing (UNEP, 2011).

Perfluoroalkane disulfonates (${}^{-}\text{O}_3\text{SC}_n\text{F}_{2n}\text{SO}_3{}^{-}$) are among the alternatives developed, and are being introduced in electronics industry (Rahman et al., 2007). If these new surfactants are to be widely used, waste treatment techniques will have to be established for them. Although they are likely to decompose more easily than corresponding perfluoroalkane sulfonates because the former

have two $\text{SO}_3{}^{-}$ groups, no one has confirmed that they do in fact decompose more easily. If they could be decomposed to F^{-} ions by means of environmentally benign techniques, the well-established protocol for treatment of F^{-} ions could be used, whereby Ca^{2+} is added to the system to form environmentally harmless CaF_2 , which is a raw material for hydrofluoric acid. Thus, the development of such a method would allow the recycling of fluorine, the global demand for which is increasing.

Reaction in subcritical or supercritical water is recognized as an innovative and environmentally benign waste-treatment technique, owing to the high diffusivity and low viscosity of these media, as well as their ability to hydrolyze many organic compounds (Jessop and Leitner, 1999). Subcritical water is defined as hot water at sufficient pressure to maintain the liquid state, and supercritical water is defined as water at temperatures and pressures higher than the critical point (374 °C, 22.1 MPa). Recently, such water was used for pilot- and practical-plant-scale decomposition of trinitrotoluene (Hawthorne et al., 2000) and polychlorinated biphenyls (Kawasaki et al., 2006). We previously reported that PFOS is not decomposed in pure subcritical water at around 350 °C, whereas PFOS can be decomposed by the use of zerovalent iron as a reducing agent in the medium (Hori et al., 2006).

* Corresponding author. Tel.: +81 463 59 4111; fax: +81 463 58 9688.

E-mail address: h-hori@kanagawa-u.ac.jp (H. Hori).

Herein we report on the decomposition of a typical perfluoroalkane disulfonate, ${}^{-}\text{O}_3\text{SC}_3\text{F}_6\text{SO}_3{}^{-}$, in subcritical and supercritical water, in the presence of an oxidizing agent (O_2) or an iron-based reducing agent (zerovalent iron or FeO), and the results are compared with results for a perfluoroalkane sulfonate, $\text{C}_3\text{F}_7\text{SO}_3{}^{-}$, which is also used as a PFOS alternative surfactant. An effective methodology for the decomposition of the perfluoroalkane disulfonate to F^{-} ions is presented.

2. Experimental

2.1. Materials

Dipotassium 1,1,2,2,3,3-hexafluoropropane-1,3-disulfonate $\text{KO}_3\text{SC}_3\text{F}_6\text{SO}_3\text{K}$ (>99%) and potassium heptafluoropropane sulfonate $\text{C}_3\text{F}_7\text{SO}_3\text{K}$ (>99%) were obtained from Mitsubishi Material Electric Chemicals (Akita, Japan). Zerovalent iron (>99.9%, <53 μm), FeO (>99.9%, <180 μm), and Fe_3O_4 (>99.9%, <150 μm) powders were purchased from Kojundo Chemical Laboratory (Saitama, Japan) and used as received. Argon (99.99%), O_2 (99.999%), and CO_2 (0.995%)/ N_2 gases were purchased from Taiyo Nippon Sanso (Tokyo, Japan). Other reagents were of high purity and were obtained from Wako Pure Chemical Industries (Osaka, Japan).

2.2. Reaction procedures

Reactions were carried out in a stainless steel high-pressure reactor fitted with a gold vessel to prevent contamination from the reactor material. The internal volume of the reactor was 31 mL. In a typical run using zerovalent iron, an argon-saturated aqueous (Milli-Q) solution (10 mL) of ${}^{-}\text{O}_3\text{SC}_3\text{F}_6\text{SO}_3{}^{-}$ (14.7 μmol ; 1.47 mM) and zerovalent iron (9.60 mmol) was introduced into the gold vessel, and the reactor was pressurized to 0.60 MPa with argon and sealed. The reactor was placed in an oven, and the reactor temperature was raised to the desired value (200–380 $^{\circ}\text{C}$) and then held constant for a specified time (e.g., 6 h), after which the reactor was quickly cooled to room temperature. We also conducted control experiments in the absence of zerovalent iron, with FeO or Fe_3O_4 , under O_2 instead of argon, and with $\text{C}_3\text{F}_7\text{SO}_3{}^{-}$.

2.3. Analysis

An ion-chromatography system (IC-2001, Tosoh Corp., Tokyo, Japan) was used to measure the F^{-} and SO_4^{2-} concentrations. The separation column was a TSKgel Super IC-Anion column (4.6 mm i.d., 15 cm length, Tosoh Corp.) and the mobile phase was an aqueous solution containing $\text{Na}_2\text{B}_4\text{O}_7$ (6 mM), H_3BO_3 (15 mM), and NaHCO_3 (0.2 mM). The concentrations of ${}^{-}\text{O}_3\text{SC}_3\text{F}_6\text{SO}_3{}^{-}$ and $\text{C}_3\text{F}_7\text{SO}_3{}^{-}$ were quantified by means of an ion-chromatography system (IC-2010, Tosoh). The separation column was a Tosoh TSKgel Super Anion HS column (4.6 mm i.d., 10 cm length) and the mobile phase was an aqueous solution containing acetonitrile (39%), NaHCO_3 (7 mM), and Na_2CO_3 (7 mM).

A liquid chromatography–mass spectrometry (LC–MS) system (LCMS-2010 EV, Shimadzu, Kyoto, Japan) with a separation column (TSKgel ODS-80TSQA) was used to identify the intermediates in the reaction solutions. The mobile phase was a mixture (50:50, v/v) of methanol and aqueous $\text{CH}_3\text{COONH}_4$ (1 mM, adjusted to pH 4.0 with acetic acid), and the flow rate was 0.2 mL min^{-1} . The total fluorine content in several reaction solutions was quantified by combustion-ion chromatography at Nissan Arc (Yokosuka, Japan). The instrument consisted of a combustion unit (AQF-100, Dia Instruments, Chigasaki, Japan; matrix combustion temperature,

1100 $^{\circ}\text{C}$) and an ion chromatograph unit (Dionex ICS-3000, Thermo Fisher Scientific, Waltham, MA, USA).

The products in the gas phase were analyzed by gas chromatography–mass spectrometry (instrument: QP2010 SE, Shimadzu, Kyoto, Japan) with a fused silica capillary column (Rt-Q-BOND, Restek, Bellefonte, PA, USA). The carrier gas was helium and the oven temperature was held constant at 30 $^{\circ}\text{C}$. A gas chromatograph (GC 323, GL Sciences, Tokyo, Japan) with a thermal conductivity detector was also used. The column was packed with active carbon (60/80 mesh) and the carrier gas was argon. Changes in iron-based reducing agents that occurred during the reactions were determined by X-ray diffractometry (XRD) with Cu $\text{K}\alpha$ radiation (Multiflex, Rigaku, Tokyo, Japan). X-ray photoelectron spectroscopy (XPS) measurements were also carried out at Nissan Arc with a Quantum-2000 instrument (Physical Electronics, Eden Prairie, MN, USA) with Al $\text{K}\alpha$ radiation.

3. Results and discussion

3.1. Reactions in subcritical water

The results for reactions of ${}^{-}\text{O}_3\text{SC}_3\text{F}_6\text{SO}_3{}^{-}$ and $\text{C}_3\text{F}_7\text{SO}_3{}^{-}$ in subcritical water at 350 $^{\circ}\text{C}$ and at a constant reaction time of 6 h are summarized in Table 1. We observed F^{-} and SO_4^{2-} as products in the reaction solutions and CO_2 as a product in the gas phase. The detection of CO_2 after reactions including the reactions in the absence of oxidizing agent (O_2) is not surprising because there are several examples in the decomposition of hazardous compounds in subcritical and supercritical water, even though no oxidizing agent was added (Tester et al., 1993; Foy et al., 1996). When the initial amount of ${}^{-}\text{O}_3\text{SC}_3\text{F}_6\text{SO}_3{}^{-}$ was 14.6 μmol (i.e., the concentration in the initial aqueous solution was 1.46 mM) and the reaction was carried out under argon without any additive (entry 1), most (99%) of the initial substrate remained after the reaction, and the yield of F^{-} [(moles of F^{-} formed)/(moles of fluorine content in initial substrate, i.e., moles of initial ${}^{-}\text{O}_3\text{SC}_3\text{F}_6\text{SO}_3{}^{-}$ \times 6)] was 3%. This observation indicates that ${}^{-}\text{O}_3\text{SC}_3\text{F}_6\text{SO}_3{}^{-}$ was stable in pure subcritical water. In an attempt to facilitate the decomposition of ${}^{-}\text{O}_3\text{SC}_3\text{F}_6\text{SO}_3{}^{-}$, we first examined the possibility of using O_2 to induce oxidative decomposition. However, introduction of 0.60 MPa (5.10 mmol) of O_2 did not enhance the decomposition of ${}^{-}\text{O}_3\text{SC}_3\text{F}_6\text{SO}_3{}^{-}$ (entry 2).

Next, we investigated the decomposition of ${}^{-}\text{O}_3\text{SC}_3\text{F}_6\text{SO}_3{}^{-}$ in the presence of zerovalent iron. Addition of the zerovalent iron dramatically accelerated the decomposition of the substrate to F^{-} ions: when the reaction was carried out in the presence of zerovalent iron (9.60 mmol) under an argon atmosphere, the amount of the ${}^{-}\text{O}_3\text{SC}_3\text{F}_6\text{SO}_3{}^{-}$ substrate completely disappeared from the reaction solution (entry 3). Simultaneously, the F^{-} yield reached 70% (entry 3), which was 23 times the yield without iron (entry 1). Addition of FeO also enhanced the decomposition of the substrate, although the enhancement was not as great as that observed with zerovalent iron: the proportion of remaining ${}^{-}\text{O}_3\text{SC}_3\text{F}_6\text{SO}_3{}^{-}$ was 38%, and the F^{-} yield was 54% (entry 5). On the other hand, when the reaction was carried out in the presence of zerovalent iron or FeO under O_2 , the F^{-} yield was lower than that under argon (compare entries 3 and 4; 5 and 6). This result indicates that the presence of O_2 decreases the decomposition of the substrate to F^{-} induced by zerovalent iron or FeO.

We also carried out the reaction using $\text{C}_3\text{F}_7\text{SO}_3{}^{-}$. Similar to the results observed for ${}^{-}\text{O}_3\text{SC}_3\text{F}_6\text{SO}_3{}^{-}$, $\text{C}_3\text{F}_7\text{SO}_3{}^{-}$ was stable in pure subcritical water: 97% of the initial substrate remained (entry 7), and the reactivity was almost uninfluenced by addition of O_2 (entry 8). The decomposition of $\text{C}_3\text{F}_7\text{SO}_3{}^{-}$ was enhanced by addition of zerovalent iron: the proportion of remaining substrate

Table 1
Decomposition of ${}^{-}\text{O}_3\text{SC}_3\text{F}_6\text{SO}_3^{-}$ and $\text{C}_3\text{F}_7\text{SO}_3^{-}$ in subcritical water under various reaction conditions.^a

| Entry | Substrate (initial amount, μmol) | Gas | Reducing agent | Reaction pressure (MPa) | Remaining substrate (μmol) (%) ^b | F ⁻ (μmol) (yield, %) ^c | CO ₂ in the gas phase (μmol) | SO ₄ ²⁻ (μmol) |
|-------|---|----------------|----------------|-------------------------|--|--|--|---|
| 1 | ${}^{-}\text{O}_3\text{SC}_3\text{F}_6\text{SO}_3^{-}$ (14.6) | Ar | None | 17.8 | 14.5 [99] | 2.63 [3] | 1.62 | 1.10 |
| 2 | ${}^{-}\text{O}_3\text{SC}_3\text{F}_6\text{SO}_3^{-}$ (14.9) | O ₂ | None | 17.2 | 14.2 [95] | 2.23 [2] | 3.74 | 1.49 |
| 3 | ${}^{-}\text{O}_3\text{SC}_3\text{F}_6\text{SO}_3^{-}$ (14.7) | Ar | Fe | 17.4 | n.d. ^d [0] | 61.9 ± 2.4 [70 ± 3] | 4.58 ± 0.16 | Trace |
| 4 | ${}^{-}\text{O}_3\text{SC}_3\text{F}_6\text{SO}_3^{-}$ (14.9) | O ₂ | Fe | 17.3 | n.d. [0] | 49.6 [55] | 13.9 | 4.94 |
| 5 | ${}^{-}\text{O}_3\text{SC}_3\text{F}_6\text{SO}_3^{-}$ (14.9) | Ar | FeO | 17.5 | 5.68 ± 0.08 [38 ± 1] | 48.2 ± 2.8 [54 ± 3] | 1.35 ± 0.33 | 1.71 ± 0.06 |
| 6 | ${}^{-}\text{O}_3\text{SC}_3\text{F}_6\text{SO}_3^{-}$ (14.9) | O ₂ | FeO | 17.0 | 10.1 [68] | 1.87 [2] | 0.61 | 8.21 |
| 7 | $\text{C}_3\text{F}_7\text{SO}_3^{-}$ (14.9) | Ar | None | 17.5 | 14.5 [97] | 0.42 [0] | 1.46 | 0.37 |
| 8 | $\text{C}_3\text{F}_7\text{SO}_3^{-}$ (14.9) | O ₂ | None | 16.9 | 14.5 [97] | 0.52 [0] | 4.62 | 0.31 |
| 9 | $\text{C}_3\text{F}_7\text{SO}_3^{-}$ (14.7) | Ar | Fe | 16.8 | 2.79 [19] | 23.9 [23] | n.d. | 1.12 |
| 10 | $\text{C}_3\text{F}_7\text{SO}_3^{-}$ (14.9) | Ar | FeO | 17.4 | 13.2 [89] | 14.9 [14] | 0.32 | 1.31 |

^a An aqueous solution (10 mL) of the substrate and additive (Fe or FeO; 9.60 mmol) were introduced to the reactor, which was pressurized with argon or oxygen (0.60 MPa) and then heated at 350 °C for 6 h.

^b Remaining substrate (%) = [(moles of remaining substrate)/(moles of initial substrate)] × 100.

^c F⁻ yield (%) = [(moles of F⁻ formed)/(moles of fluorine content in initial substrate)] × 100.

^d n.d. = Not detected.

decreased to 19%, and the F⁻ yield increased to 23% (entry 9). Although addition of zerovalent iron accelerated the decomposition of $\text{C}_3\text{F}_7\text{SO}_3^{-}$ to F⁻ ions, the F⁻ yield from the reaction of $\text{C}_3\text{F}_7\text{SO}_3^{-}$ was considerably lower than the F⁻ yield from the reaction of ${}^{-}\text{O}_3\text{SC}_3\text{F}_6\text{SO}_3^{-}$ (70%, entry 3). Addition of FeO also enhanced the decomposition of $\text{C}_3\text{F}_7\text{SO}_3^{-}$ somewhat: the proportion of remaining substrate was 89% and the F⁻ yield was 14% (entry 10).

3.2. Decomposition in the presence of zerovalent iron

Because zerovalent iron gave the highest F⁻ yields among tested, we further investigated the decomposition of ${}^{-}\text{O}_3\text{SC}_3\text{F}_6\text{SO}_3^{-}$ and $\text{C}_3\text{F}_7\text{SO}_3^{-}$ with zerovalent iron in detail by varying other reaction conditions. The reaction-time dependences of the decomposition of ${}^{-}\text{O}_3\text{SC}_3\text{F}_6\text{SO}_3^{-}$ and $\text{C}_3\text{F}_7\text{SO}_3^{-}$ in the presence of zerovalent iron at 350 °C are shown in Fig. 1a and b, respectively. The ${}^{-}\text{O}_3\text{SC}_3\text{F}_6\text{SO}_3^{-}$ substrate disappeared from the reaction solution within 1 h, and the decrease in the amount of substrate was accompanied by an increase in the amount of F⁻ and CO₂ (Fig. 1a). After disappearance of the substrate, the amounts of F⁻ and CO₂ continued to increase. This result suggests that some reaction intermediate(s) produced F⁻ and CO₂ during this period. After 18 h, the amount of F⁻ reached 71.7 μmol (81% yield), which indicates that the fluorine content in ${}^{-}\text{O}_3\text{SC}_3\text{F}_6\text{SO}_3^{-}$ was successfully decomposed to F⁻ ions.

The decomposition of $\text{C}_3\text{F}_7\text{SO}_3^{-}$ proceeded much slower than the decomposition of ${}^{-}\text{O}_3\text{SC}_3\text{F}_6\text{SO}_3^{-}$: 52% of the initial amount of $\text{C}_3\text{F}_7\text{SO}_3^{-}$ remained after 1 h (Fig. 1b) (the corresponding value for ${}^{-}\text{O}_3\text{SC}_3\text{F}_6\text{SO}_3^{-}$ was 0%), and 12% of the initial amount still remained after prolonged reaction (18 h). The amount of F⁻ increased to 39.7 μmol (39% yield) after 18 h. However, the yield was almost half of the F⁻ yield from the reaction of ${}^{-}\text{O}_3\text{SC}_3\text{F}_6\text{SO}_3^{-}$ (81%). Note that the decrease in $\text{C}_3\text{F}_7\text{SO}_3^{-}$ did not follow pseudo-first-order kinetics, but followed pseudo-second-order kinetics with a rate constant of $(4.8 \pm 0.5) \times 10^2 \text{ M}^{-1} \text{ h}^{-1}$ (Fig. 2).

We also investigated the temperature dependences of the reactions of these substrates at a constant reaction time of 6 h (Fig. 1c and d). At 200 °C, almost no decomposition of ${}^{-}\text{O}_3\text{SC}_3\text{F}_6\text{SO}_3^{-}$ was observed (Fig. 1c). Substrate decomposition was observed above 200 °C and the substrate completely disappeared from the reaction solution at 300 °C, while F⁻ formation increased with increasing temperature. At 380 °C, the temperature at which the water reached the supercritical state, the amount of F⁻ reached 67.5 μmol (77% yield). We further prolonged the reaction time to 18 h at 380 °C, expecting that F⁻ formation further increased. However, contrary to our expectation, the amount of F⁻ (64.3 μmol ; 73% yield) did not increase, suggesting that part of F⁻ ions were strongly bound on the iron surface after prolonged reaction time. Consistently, the XPS spectrum for the F(1s) region of the recovered iron powder after the reaction for 18 h showed a dominant peak around 684 eV, which can be assigned to negatively charged mono-valent fluorine, F⁻ (Fig. 3). This observation clearly indicates that F⁻ ions are present not only in the reaction solution but also on the iron surface. If species containing fluorine-carbon bonds (i.e., organofluorine component) are present on the surface, the peak corresponding to fluorine bonded to carbon (F-C) should appear around 689 eV. The absence of the F-C peak in the XPS spectrum indicates that the fluorine component of the substrate was completely decomposed to F⁻ ions on the iron surface after prolonged reaction time.

Furthermore, we quantified the total fluorine content in the reaction solution after the reaction at 380 °C for 18 h by combustion-ion chromatography. The total fluorine content (i.e., the amount of fluorine atoms) was 64 μmol , which was the same as the F⁻ amount in the reaction solution. This observation indicates that the reaction solution after prolonged reaction time does not include organofluorine component virtually, and consistent with the results of the XPS measurement.

The temperature dependence of the reaction of $\text{C}_3\text{F}_7\text{SO}_3^{-}$ is shown in Fig. 1d. This substrate was less reactive than ${}^{-}\text{O}_3\text{SC}_3\text{F}_6\text{SO}_3^{-}$

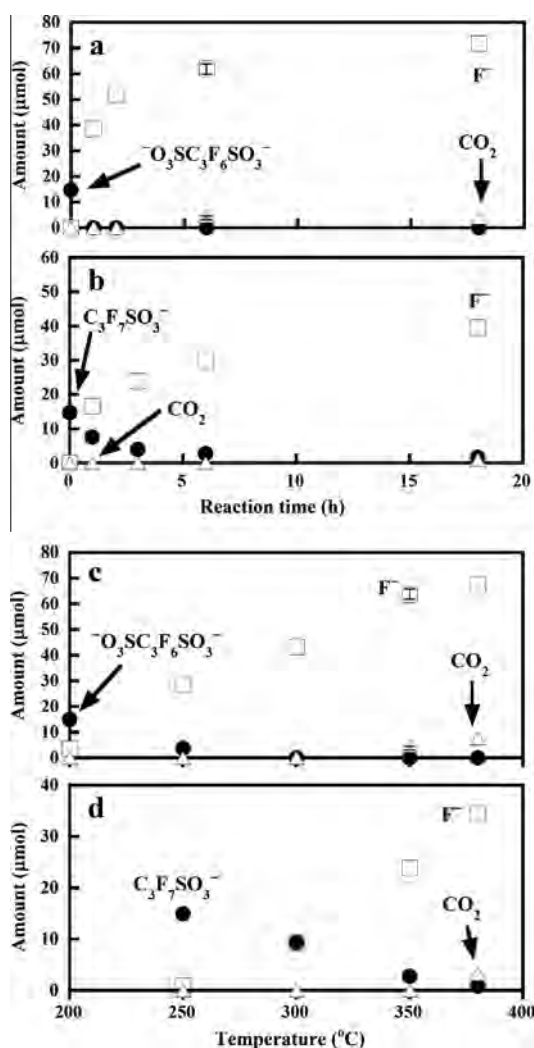


Fig. 1. Reaction-time dependences of the decomposition of (a) $\text{O}_3\text{SC}_3\text{F}_6\text{SO}_3^-$ and (b) $\text{C}_3\text{F}_7\text{SO}_3^-$ in the presence of zerovalent iron at 350 °C and temperature dependences of the decomposition of (c) $\text{O}_3\text{SC}_3\text{F}_6\text{SO}_3^-$ and (d) $\text{C}_3\text{F}_7\text{SO}_3^-$ in the presence of zerovalent iron. For the measurements of (a) and (b), an aqueous solution (10 mL) of $\text{O}_3\text{SC}_3\text{F}_6\text{SO}_3^-$ or $\text{C}_3\text{F}_7\text{SO}_3^-$ (14.7 μmol ; 1.47 mM) and zerovalent iron powder (9.60 mmol) were introduced into the reactor, which was pressurized with argon (0.60 MPa) and heated at 350 °C for 1–18 h. For the measurements of (c) and (d), an aqueous solution (10 mL) of $\text{O}_3\text{SC}_3\text{F}_6\text{SO}_3^-$ or $\text{C}_3\text{F}_7\text{SO}_3^-$ (14.7 μmol ; 1.47 mM) and zerovalent iron powder (9.60 mmol) were introduced into the reactor, which was pressurized with argon (0.60 MPa) and (c) heated at 200–380 °C or (d) heated at 250–380 °C for 6 h.

SO_3^- : almost no decomposition was observed at 250 °C. When the reaction was carried out at 380 °C, the amount of remaining substrate was 0.84 μmol (6%) and the amount of F^- was 34.6 μmol (34% yield): the yield was 0.44 times the F^- yield of $\text{O}_3\text{SC}_3\text{F}_6\text{SO}_3^-$.

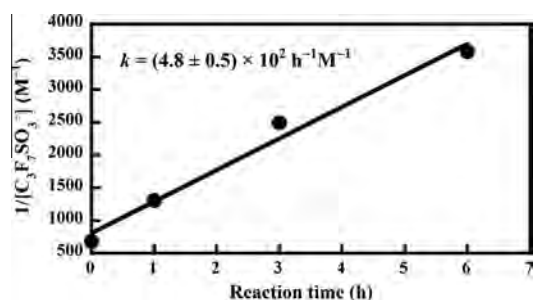


Fig. 2. Pseudo-second-order plot of the concentration of $\text{C}_3\text{F}_7\text{SO}_3^-$ vs. reaction time. The reaction conditions were the same as those described in Fig. 1b.

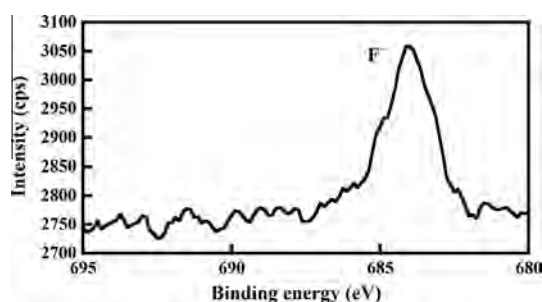


Fig. 3. XPS spectrum [F(1s) region] of the recovered iron powder after reaction at 380 °C for 18 h. An aqueous solution (10 mL) of $\text{O}_3\text{SC}_3\text{F}_6\text{SO}_3^-$ (14.7 μmol ; 1.47 mM) and zerovalent iron powder (9.60 mmol) were introduced into the reactor, which was pressurized with argon (0.60 MPa) and heated, after which the solid was recovered.

To detect reaction intermediates, we analyzed reaction solutions by LC–MS. When $\text{O}_3\text{SC}_3\text{F}_6\text{SO}_3^-$ was decomposed in the presence of zerovalent iron, the total-ion mass chromatograms of several reaction solutions showed two peaks: one peak that yielded signals at m/z 231, which corresponds to $\text{HC}_3\text{F}_6\text{SO}_3^-$, and one peak that yielded signals at m/z 181, which corresponds to $\text{HC}_2\text{F}_4\text{SO}_3^-$. The presence of $\text{HC}_3\text{F}_6\text{SO}_3^-$ indicates that the decomposition of $\text{O}_3\text{SC}_3\text{F}_6\text{SO}_3^-$ proceeded through cleavage of the S–C bond. The reaction-time dependence at 350 °C of the LC–MS peak intensity for $\text{HC}_3\text{F}_6\text{SO}_3^-$ and $\text{HC}_2\text{F}_4\text{SO}_3^-$ is shown in Fig. 4. The peak intensity of $\text{HC}_3\text{F}_6\text{SO}_3^-$ increased during the initial stage of the reaction (≤ 1 h) and then decreased, indicating that the formed $\text{HC}_3\text{F}_6\text{SO}_3^-$ decomposed under these reaction conditions. While the peak intensity of $\text{HC}_3\text{F}_6\text{SO}_3^-$ was decreased, the peak intensity of $\text{HC}_2\text{F}_4\text{SO}_3^-$ increased up to 6 h and then slightly decreased. When the reaction temperature was elevated to 380 °C, the reaction solution after 6 h or 18 h did not show these peaks. These observations indicate that one pathway of the decomposition of $\text{O}_3\text{SC}_3\text{F}_6\text{SO}_3^-$ in the presence of zerovalent iron proceeded via formation of $\text{HC}_3\text{F}_6\text{SO}_3^-$ and $\text{HC}_2\text{F}_4\text{SO}_3^-$.

3.3. Decomposition in the presence of FeO

As described above, zerovalent iron induced efficient decomposition of $\text{O}_3\text{SC}_3\text{F}_6\text{SO}_3^-$ in subcritical and supercritical water. However, the iron reacted not only with the substrate but also with subcritical and supercritical water to form H_2 and Fe_3O_4 (Eq. (1)).



Consistently, when the reaction of $\text{O}_3\text{SC}_3\text{F}_6\text{SO}_3^-$ in the presence of zerovalent iron was carried out at 350 °C for 6 h, H_2 made up 42.4% of the total gas after the reaction (corresponding to 3.21 mmol of H_2), and the XRD pattern of the recovered iron powder showed peaks that were assigned to Fe_3O_4 (Fig. 5b). According to Eq. (1), the amount of H_2 indicates that 2.41 mmol of the zerovalent iron was consumed by the reaction with H_2O . This value was much larger than the initial amount of $\text{O}_3\text{SC}_3\text{F}_6\text{SO}_3^-$ (14.7 μmol). In addition, the reactivity of Fe_3O_4 toward the substrate was low: for example, when we carried out the reaction of $\text{O}_3\text{SC}_3\text{F}_6\text{SO}_3^-$ (14.9 μmol) in the presence of Fe_3O_4 (9.60 mmol) at 350 °C for 18 h, the proportion of remaining substrate was 74% and the yield of F^- was 20%.

Iron(II) oxide undergoes disproportionation to zerovalent iron and Fe_3O_4 at higher temperatures (>257 °C) (Broussard, 1969; Stølen et al., 1995):



If the disproportionation did occur in subcritical or supercritical water, zerovalent iron would form *in situ*, and the formed iron might be preferentially consumed by reaction with the substrate

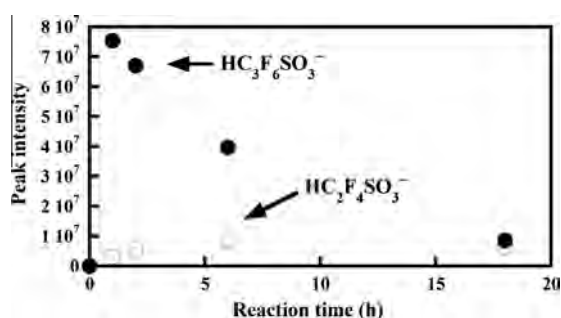


Fig. 4. Reaction-time dependence of the intensity of the LC-MS peaks for $\text{HC}_3\text{F}_6\text{SO}_3^-$ and $\text{HC}_2\text{F}_4\text{SO}_3^-$. The reaction conditions were the same as those described in Fig. 1a.

than with water. To test this possibility, we carried out the reactions of ${}^-\text{O}_3\text{SC}_3\text{F}_6\text{SO}_3^-$ and $\text{C}_3\text{F}_7\text{SO}_3^-$ in the presence of FeO, despite the facts that their reactivity at 350 °C for 6 h was lower than those of zerovalent iron (compare entries 3 and 5; 9 and 10 in Table 1).

The reaction-time dependences of the decomposition of ${}^-\text{O}_3\text{SC}_3\text{F}_6\text{SO}_3^-$ and $\text{C}_3\text{F}_7\text{SO}_3^-$ in the presence of FeO at 350 °C are shown in Fig. 6a and b, respectively. The amount of ${}^-\text{O}_3\text{SC}_3\text{F}_6\text{SO}_3^-$ decreased and the amounts of F^- and CO_2 increased with increasing reaction time (Fig. 6a). After 18 h, the amount of the substrate was

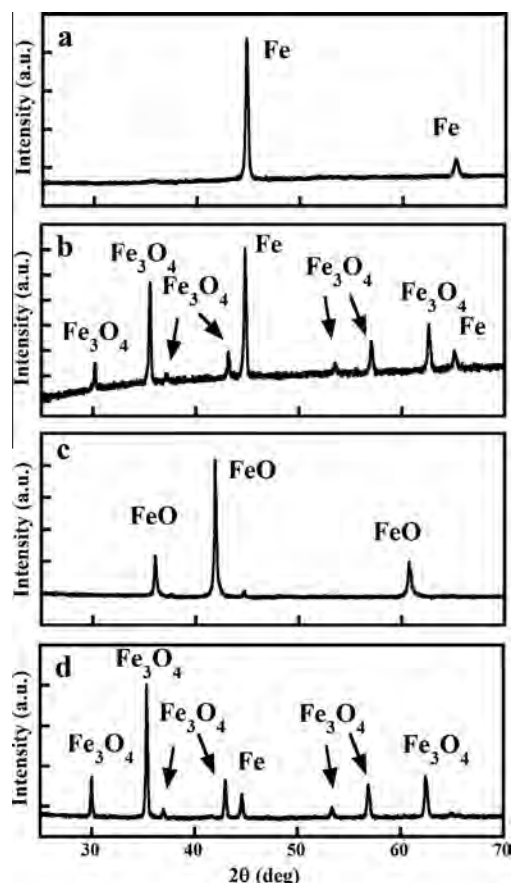


Fig. 5. XRD patterns of the zerovalent iron powder (a) before and (b) after reaction at 350 °C and of the FeO powder (c) before and (d) after reaction at 380 °C. For the measurement of pattern (b), an aqueous solution (10 mL) of ${}^-\text{O}_3\text{SC}_3\text{F}_6\text{SO}_3^-$ (14.7 μmol ; 1.47 mM) and zerovalent iron powder (9.60 mmol) were introduced into the reactor, which was pressurized with argon (0.60 MPa) and heated at 350 °C for 6 h, after which the solid was recovered. For the measurement of pattern (d), an aqueous solution (10 mL) of ${}^-\text{O}_3\text{SC}_3\text{F}_6\text{SO}_3^-$ (14.9 μmol ; 1.49 mM) and FeO powder (9.60 mmol) were introduced into the reactor, which was pressurized with argon (0.60 MPa) and heated at 380 °C for 6 h, after which the solid was recovered.

2.17 μmol (the proportion of remaining substrate was 15%) and the amount of F^- reached 58.0 μmol (65% yield). The decomposition of $\text{C}_3\text{F}_7\text{SO}_3^-$ was much slower than that of ${}^-\text{O}_3\text{SC}_3\text{F}_6\text{SO}_3^-$. After 18 h, the remaining amount of the substrate was 12.7 μmol (85% of the initial amount remained) and the amount of F^- was 20.1 μmol (19% yield) (Fig. 6b). These results indicate that FeO was less reactive than zerovalent iron at 350 °C, even though the reaction time was extended to 18 h.

However, the advantage of FeO over zerovalent iron was observed when the reaction temperature was elevated to supercritical state. The temperature dependence of the decomposition of ${}^-\text{O}_3\text{SC}_3\text{F}_6\text{SO}_3^-$ in the presence of FeO at a constant reaction time of 6 h is shown in Fig. 6c. When the reaction of ${}^-\text{O}_3\text{SC}_3\text{F}_6\text{SO}_3^-$ was carried out in the presence of FeO at 380 °C, ${}^-\text{O}_3\text{SC}_3\text{F}_6\text{SO}_3^-$ completely disappeared from the reaction solution and the amount of F^- reached 79.5 μmol (89% yield) (Fig. 6c). This yield was higher than the F^- yield when zerovalent iron was used (77%). After 18 h, the F^- amount reached 82.0 μmol (92% yield). This yield

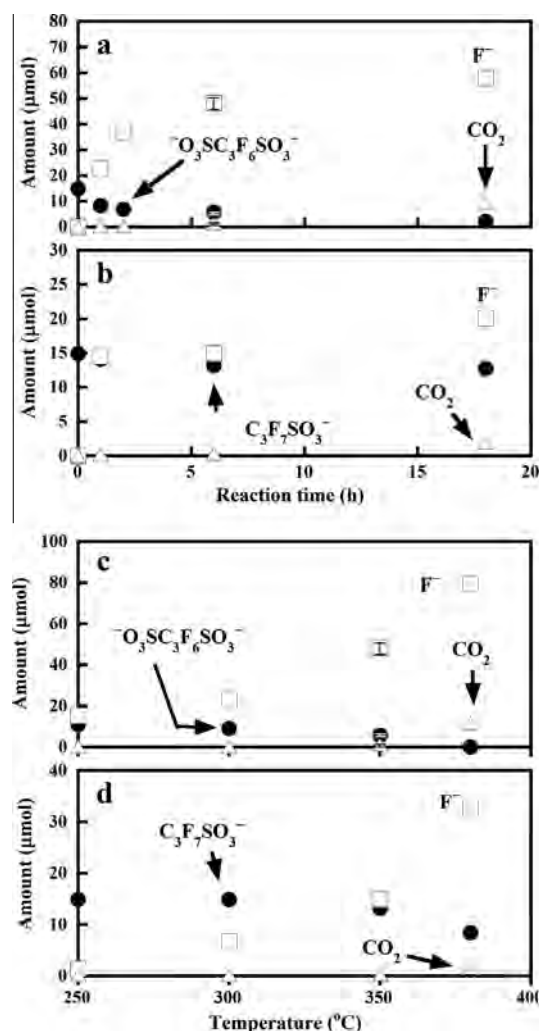


Fig. 6. Reaction-time dependences of the decomposition of (a) ${}^-\text{O}_3\text{SC}_3\text{F}_6\text{SO}_3^-$ and (b) $\text{C}_3\text{F}_7\text{SO}_3^-$ in the presence of FeO at 350 °C and temperature dependences of the decomposition of (c) ${}^-\text{O}_3\text{SC}_3\text{F}_6\text{SO}_3^-$ and (d) $\text{C}_3\text{F}_7\text{SO}_3^-$ in the presence of FeO. For the measurements of (a) and (b), an aqueous solution (10 mL) of ${}^-\text{O}_3\text{SC}_3\text{F}_6\text{SO}_3^-$ or $\text{C}_3\text{F}_7\text{SO}_3^-$ (14.9 μmol ; 1.49 mM) and FeO powder (9.60 mmol) were introduced into the reactor, which was pressurized with argon (0.60 MPa) and heated at 350 °C for 1–18 h. For the measurements of (c) and (d), an aqueous solution (10 mL) of ${}^-\text{O}_3\text{SC}_3\text{F}_6\text{SO}_3^-$ or $\text{C}_3\text{F}_7\text{SO}_3^-$ (14.9 μmol ; 1.49 mM) and FeO powder (9.60 mmol) were introduced into the reactor, which was pressurized with argon (0.60 MPa) and heated at 250–380 °C for 6 h.

was much higher than the F^- yield that zerovalent iron was used (73%), and was the highest F^- yield among tested, while the substrate was completely disappeared from the reaction solution. The total fluorine content in the reaction solution was $84\ \mu\text{mol}$, which was almost the same as the F^- amount in the reaction solution ($82.0\ \mu\text{mol}$), indicating that the reaction solution after prolonged reaction time (18 h) does not include organofluorine component virtually.

The XRD patterns of the FeO powder before and after reaction of ${}^{-}\text{O}_3\text{SC}_3\text{F}_6\text{SO}_3^-$ at $380\ ^\circ\text{C}$ are shown in Fig. 5c and d, respectively. After the reaction for 6 h, the recovered FeO powder from the reaction mixture showed only peaks assignable to zerovalent iron and Fe_3O_4 (Fig. 5d), indicating that the disproportionation of FeO to zerovalent iron and Fe_3O_4 did occur, and the zerovalent iron that formed *in situ* acted as the real reducing agent for the decomposition of the substrate, because Fe_3O_4 showed low reactivity toward the substrate (as described above).

The temperature dependence of the decomposition of $\text{C}_3\text{F}_7\text{SO}_3^-$ in the presence of FeO is shown in Fig. 6d. When the reaction was carried out at $380\ ^\circ\text{C}$ for 6 h, the amount of the substrate was $8.42\ \mu\text{mol}$ (the proportion of remaining substrate was 57%) and the amount of F^- was $32.7\ \mu\text{mol}$ (31% yield): the remaining substrate was higher than that of zerovalent iron (6%), whereas the F^- yield was almost the same as that when zerovalent iron was used (34%). After 18 h, the amount of the substrate decreased to $4.46\ \mu\text{mol}$ (the proportion of remaining substrate was 30%) and the F^- amount reached $60.4\ \mu\text{mol}$ (58% yield). This F^- yield was 0.63 times the F^- yield of ${}^{-}\text{O}_3\text{SC}_3\text{F}_6\text{SO}_3^-$ in the presence of FeO at $380\ ^\circ\text{C}$ for 18 h.

4. Conclusion

Decomposition of ${}^{-}\text{O}_3\text{SC}_3\text{F}_6\text{SO}_3^-$ and $\text{C}_3\text{F}_7\text{SO}_3^-$ in pure subcritical water was negligible, as was decomposition in subcritical water in the presence of O_2 . Addition of zerovalent iron accelerated the decomposition of these substrates to F^- . Although the reactivity of FeO was lower than zerovalent iron in subcritical water at $350\ ^\circ\text{C}$, the reactivity was dramatically enhanced when the reaction temperature was elevated to supercritical state, at which temperature *in situ* disproportionation of FeO to zerovalent iron and Fe_3O_4 did occur. The perfluoroalkane disulfonate ${}^{-}\text{O}_3\text{SC}_3\text{F}_6\text{SO}_3^-$ decomposed more efficiently than $\text{C}_3\text{F}_7\text{SO}_3^-$ in the presence of zerovalent iron or FeO.

Acknowledgement

This work was supported in part by a Grant-in-Aid for Scientific Research from the Japan Society for the Promotion of Sciences (JSPS).

References

- Ahrens, L., 2011. Polyfluoroalkyl compounds in the aquatic environment: a review of their occurrence and fate. *J. Environ. Monit.* 13, 20–31.
- Broussard, L., 1969. Disproportionation of wüstite. *J. Phys. Chem.* 73, 1848–1854.
- Foy, B.R., Waldthausen, K., Sedillo, M.A., Buelow, S.J., 1996. Hydrothermal processing of chlorinated hydrocarbons in a titanium reactor. *Environ. Sci. Technol.* 30, 2790–2799.
- Giesy, J.P., Kannan, K., 2002. Perfluorochemical surfactants in the environment. *Environ. Sci. Technol.* 36, 146A–152A.
- Hawthorne, S.B., Lagadec, A.J.M., Kalderis, D., Lilke, A.V., Miller, D.J., 2000. Pilot-scale destruction of TNT, RDX, and HMX on contaminated soils using supercritical water. *Environ. Sci. Technol.* 34, 3224–3228.
- Hori, H., Nagaoka, Y., Yamamoto, A., Sano, T., Yamashita, N., Taniyasu, S., Kutsuna, S., Osaka, I., Arakawa, R., 2006. Efficient decomposition of environmentally persistent perfluorooctanesulfonate and related fluorochemicals using zerovalent iron in subcritical water. *Environ. Sci. Technol.* 40, 1049–1054.
- Jessop, P.G., Leitner, W. (Eds.), 1999. *Chemical Synthesis Using Supercritical Fluids*. Wiley-VCH, Weinheim, Germany.
- Kawasaki, S.-I., Oe, T., Anjoh, N., Nakamori, T., Suzuki, A., Arai, K., 2006. Practical supercritical water reactor for destruction of high concentration polychlorinated biphenyls (PCB) and dioxin waste. *Process Saf. Environ. Prot.* 84, 317–324.
- Rahman, M.D., Houlihan, F.M., Padmanaban, M., Lee, S., Dammel, R.R., Rentkiewicz, D., Anyadiegwu, C., 2007. Photoactive Compounds, PCT International Patent Application, WO2007/007175 A2.
- Stølen, S., Glöcker, R., Grønvold, F., 1995. Nearly stoichiometric iron monoxide formed as a metastable intermediate in a two-stage disproportionation of quenched wüstite. *Thermodynamic and kinetic aspects. Thermochim. Acta* 256, 91–106.
- Tester, J.W., Holgate, H.R., Armellini, F.J., Webley, P.A., Killilea, W.R., Hong, G.T., Barner, H.E., 1993. Supercritical water oxidation technology. In: Tedder, D.W., Pohland, F.G. (Eds.), *Emerging Technologies in Hazardous Waste Management III*, ACS Symposium Series 518. American Chemical Society, Washington, DC, pp. 35–76.
- UNEP, 2009. Fourth Meeting of the Conference of the Parties of the Stockholm Convention, United Nations Environment Programme, Geneva. <<http://chm.pops.int/Convention/COPs/Meetings/COP4/tabid/404/mctl/ViewDetails/EventModID/870/EventID/23/xmid/1673/language/en-US/Default.aspx>>, 4–8 May 2009.
- UNEP, 2011. Guidance on alternatives to perfluorooctane sulfonic acid and its derivatives. In: Report of the Persistent Organic Pollutants Review Committee on the Work of its Sixth Meeting, United Nations Environment Programme. <<http://chm.pops.int/TheConvention/POPsReviewCommittee/Guidance/tabid/345/Default.aspx>>.

Hydrogen Peroxide Induced Efficient Mineralization of Poly(vinylidene fluoride) and Related Copolymers in Subcritical Water

Hisao Hori,^{*,†} Hirotaka Tanaka,[†] Kengo Watanabe,[†] Takahiro Tsuge,[†] Takehiko Sakamoto,[†] Abdellatif Manseri,[‡] and Bruno Ameduri[‡]

[†]Department of Chemistry, Faculty of Science, Kanagawa University, 2946 Tsuchiya, Hiratsuka, Kanagawa 259-1293, Japan

[‡]Ingenierie et Architectures Macromoléculaires, Institut Charles Gerhardt UMR 5253, École Nationale Supérieure de Chimie de Montpellier, 8 Rue École Normale, 34296 Montpellier Cedex 1, France

Supporting Information

ABSTRACT: Decompositions of poly(vinylidene fluoride) (PVDF), poly(vinylidene fluoride-co-chlorotrifluoroethylene) copolymer (poly(VDF-co-CTFE)), and poly(vinylidene fluoride-co-hexafluoropropylene) copolymer (poly(VDF-co-HFP)) in subcritical water were investigated with the aim of developing a technique to recover the fluorine component. By use of H₂O₂, these (co)polymers can be efficiently mineralized at a relatively low temperature (300 °C). When PVDF was heated with 3.0 M H₂O₂ for 6 h, which corresponds to 31 times the molar amount of fluorine and 32 times the molar amount of carbon in the polymer, both F⁻ and CO₂ yields reached 98%. Poly(VDF-co-CTFE) copolymer was also mineralized under the same reaction conditions (the yields of F⁻, CO₂, and Cl⁻ were 98, 95, and 97%, respectively). Poly(VDF-co-HFP) copolymer was more readily decomposed than poly(VDF-co-CTFE), leading to almost complete mineralization (F⁻ yield, 96%; CO₂ yield, 92%) with 2.0 M H₂O₂. Addition of stoichiometric Ca(OH)₂ to the reactions formed CaF₂ well-identified by X-ray diffraction spectrometry.

INTRODUCTION

Fluoropolymers, olefinic polymers in which some or all of the hydrogen atoms are replaced by fluorine atoms, are used in many industrial applications owing to their high chemical and thermal stability and other specific characteristics.^{1–8} Among these polymers, poly(tetrafluoroethylene) (PTFE, -(CF₂CF₂)_n-) is most frequently used.^{1–6} However, PTFE cannot be processed by melt molding, a conventional technique for fabricating thermoplastic polymers, because the viscosity of the PTFE melt (10⁹–10¹¹ Pa s) is about 6 orders of magnitude higher than that of common thermoplastic polymers.^{4,6} To overcome this limitation, poly(vinylidene fluoride) (PVDF, -(CF₂CH₂)_n-) has been developed and introduced in industry.^{1–7} Besides PVDF, poly(chlorotrifluoroethylene) (PCTFE, -(CF₂CFCl)_n-) is also a melt processable commercially available fluoropolymer endowed with many properties for various applications (gas barrier packaging, coatings, liners for protections) while CTFE copolymers can be involved in paints and materials for energy applications (e.g., fuel cell membranes and polymer electrolyte for lithium ion batteries).⁸ PVDF shows a high resistance to temperature, chemicals, ignition, mechanical stresses, and UV irradiation so that it has been used for various applications including chemical process equipment, electrical equipment, and especially energy-related applications such as lithium ion battery electrode binders.^{1–7} Recently, the production of PVDF reached the largest volume of fluoropolymer after PTFE.^{5,7} Furthermore, several copolymers based on VDF and other monomers, which enhanced the properties such as the softness and impact resistance, have been developed. Wider use of PVDF and related copolymers will require the establishment of waste

treatment. These (co)polymers can be incinerated. However, incineration requires high temperatures to break the strong C–F bonds, and the released hydrogen fluoride gas can damage the firebrick of an incinerator. Thus, in many cases, the wastes of these (co)polymers are disposed of in landfills. If the (co)polymers could be decomposed to F⁻ ions (i.e., undergo mineralization) by means of environmentally benign techniques, the well-established protocol for treatment of F⁻ ions could be used, whereby Ca²⁺ is added to the system to form CaF₂, which is a raw material for hydrofluoric acid. Thus, the development of such a method would allow the recycling of fluorine, the global demand for which is increasing.

Several studies reported the degradation of PVDF^{9–17} and related copolymers,^{10–12} as well as that of PCTFE.^{11,18} However, most previous reports, including studies related to batteries' performance,^{13–16} examined the thermal stability or aging characteristics of the (co)polymers and did not focus on their decomposition to obtain F⁻ ions for waste treatment. Only our previous study reported that PVDF can be efficiently decomposed into F⁻ and CO₂ in supercritical water at 380 °C in the presence of an ca. 5.8-fold molar excess of O₂ relative to fluorine content in PVDF.¹⁷

Reactions in subcritical or supercritical water are recognized as an innovative and environmentally benign waste-treatment technique, owing to the high diffusivity and low viscosity of these media, as well as their ability to hydrolyze many organic

Received: May 7, 2015

Revised: July 25, 2015

Accepted: August 18, 2015

Published: August 18, 2015

compounds.¹⁹ Subcritical water is defined as hot water with sufficient pressure to maintain the liquid state, while supercritical water is defined as water at temperatures and pressures higher than the critical point, 374 °C and 22.1 MPa. Recently, supercritical water was used for pilot and practical plant-scale decomposition of trinitrotoluene²⁰ and polychlorinated biphenyls.²¹ Subcritical water was widely used for the hydrothermal biomass treatment²² and also used for decomposition of a perfluoroalkyl sulfonic acid membrane.²³

Although PVDF is efficiently mineralized in supercritical water at 380 °C in the presence of an O₂ excess, a technique that can work under mild conditions (lower temperature and pressure) is more preferable for real-world industrial processes. The present study reports an effective method for complete mineralization of PVDF and poly(vinylidene fluoride-co-chlorotrifluoroethylene) copolymer (poly(VDF-co-CTFE), $-\text{[(CH}_2\text{CF}_2)_m(\text{CF}_2\text{CFCl})_n]_p-$) and poly(vinylidene fluoride-co-hexafluoropropylene) copolymer (poly(VDF-co-HFP), $-\text{[(CH}_2\text{CF}_2)_m(\text{CF}_2\text{CFCF}_3)_n]_p-$) in subcritical water at relatively low temperature (~300 °C) by use of H₂O₂. Furthermore, the formation of CaF₂ upon addition of a stoichiometric amount of Ca(OH)₂ to the reaction system is reported.

EXPERIMENTAL SECTION

Materials. Powdered PVDF and 1,1,2,2-tetrafluoroethane (F₂HCCHF₂) were purchased from SynQuest Laboratories (Alachua, FL). The weight-average molecular weight of the PVDF was 6.47×10^5 with a polydispersity of 2.52 (relative to polystyrene as a standard). Poly(VDF-co-CTFE) copolymer with a 67.0/33.0 VDF/CTFE molar ratio and poly(VDF-co-HFP) copolymer with a 95.3/4.7 VDF/HFP molar ratio were obtained from Elf Atochem (France), prepared by emulsion-free radical copolymerization of VDF and CTFE or HFP. The weight-average molecular weights of poly(VDF-co-CTFE) and poly(VDF-co-HFP) relative to poly(methyl methacrylate) in DMF were 3.5×10^5 with a polydispersity of 2.9 and 4.5×10^5 with a polydispersity of 3.2, respectively. Combustion ion chromatography revealed that the fluorine contents in PVDF, poly(VDF-co-CTFE) copolymer, and poly(VDF-co-HFP) copolymer were 60.7, 51.5, and 59.4 wt %, respectively, and the chlorine content in poly(VDF-co-CTFE) copolymer was 14.5 wt %. These analytical values were used to calculate the F⁻ yields (and Cl⁻ yields when poly(VDF-co-CTFE) was used) of the reactions. Argon (99.99%) and CO₂ (0.995%)/N₂ gases were purchased from Taiyo Nippon Sanso (Tokyo, Japan). Malonic acid (>98%), 1,3,5-trifluorobenzene, and other reagents were obtained from Wako Pure Chemical Industries (Osaka, Japan).

Reaction Procedures. Reactions were carried out in a stainless steel high-pressure reactor fitted with a gold vessel to prevent contamination from the reactor material. The internal volume of the reactor was 31 mL. In a typical run, an aqueous solution of H₂O₂ (0.1–5.0 M, 10 mL) and the powdered (co)polymer (PVDF or copolymers, 30 mg) were introduced into the reactor, which was then pressurized to 0.60 MPa with argon, sealed, and heated to the desired temperature with a rate of ca. 10 °C min⁻¹. After a specified time passed, the reactor was quickly cooled to room temperature, and the reaction solution was subjected to ion chromatography. The gas phase was collected with a sampling bag and subjected to gas chromatography (GC) and gas chromatography–mass spectrometry (GC/MS). Reactions involving a stoichiometric

amount of Ca(OH)₂ (the molar amount was half the molar amount of fluorine atoms in the (co)polymer) were also performed. The white precipitate that formed during these reactions was collected by centrifugation, washed with pure water, dried in vacuo overnight, and then subjected to X-ray diffraction (XRD) analysis.

Analysis. The fluorine content in the (co)polymers was quantified by combustion ion chromatography at Nissan Arc (Yokosuka, Japan) by means of an instrument consisting of a combustion unit (AQF-100, Mitsubishi Chemical Analytec, Chigasaki, Japan; matrix combustion temperature, 1100 °C) and an ion chromatograph unit (Dionex ICS-3000, Thermo Fisher Scientific, Waltham, MA).

The F⁻ concentrations were measured with an ion-chromatography system (IC-2001, Tosoh, Tokyo, Japan) consisting of an automatic sample injector (30 μL injection volume), a degasser, a pump, a guard column (TSKguard column Super IC-A, 4.6 mm i.d., 1.0 cm length, Tosoh), a separation column (TSKgel Super IC-Anion, 4.6 mm i.d., 15 cm length, Tosoh), a column oven (40 °C), and a conductivity detector with a suppressor device. The mobile phase was an aqueous solution containing Na₂B₄O₇ (6 mM), H₃BO₃ (15 mM), and NaHCO₃ (0.2 mM); and the flow rate was 0.8 mL min⁻¹. An ion-chromatography system (IC-2001) with a separation column (TSKgel Super IC-AP, 4.6 mm id, 7.5 cm length, Tosoh) was also used to quantify malonic acid and Cl⁻. The mobile phase was an aqueous solution containing NaHCO₃ (1.7 mM), Na₂CO₃ (1.8 mM), and acetonitrile (23 vol %). A GC system (GC 323, GL Sciences) consisting of an injector (150 °C), a column oven (110 °C), and a thermal conductivity detector (130 °C) was used to quantify CO₂. The column was an active carbon column (60/80 mesh, 2.17 mm i.d., 2 m length), and the carrier gas was argon. The products in the gas phase were also analyzed with a GC/MS (QP2010 SE, Shimadzu, Kyoto, Japan) system with a fused-silica capillary column (Rt-Q-BOND, Restek, Bellefonte, PA). The carrier gas was helium, and the injection temperature was held constant at 120 °C. The sample gas was transferred into the GC/MS system in split mode (ratio, 20/1), and analyses were conducted in full-scan mode (*m/z* 2.0–200). The oven temperature was kept at 30 °C for 5 min, raised to 200 °C at a rate of 20 °C min⁻¹, and held at that temperature for 20 min. XRD patterns of the collected precipitates were measured with Cu Kα radiation (Multiflex, Rigaku, Tokyo, Japan).

RESULTS AND DISCUSSION

Decomposition of PVDF. H₂O₂ concentration dependences of the F⁻ amount in the reaction solution and the CO₂ amount in the gas phase formed after the reactions at 300 °C for 6 h are shown in Figure 1. When the reaction was carried out in the absence of H₂O₂, a solid residue (18 mg) formed and little CO₂ formed in the gas phase. Simultaneously, 511 μmol of F⁻ formed in the reaction solution (Table 1, entry 1), which corresponds to a yield [(moles of F⁻ formed, i.e., 511 μmol)/(moles of fluorine in the polymer, i.e., 959 μmol)] of 53%. We previously reported that the reaction of PVDF in pure supercritical water (without any additive, that is, in the presence of argon) at 380 °C resulted in a carbon-rich solid residue (for example, a solid after 6 h reaction consisted of 79.6 wt % carbon) and little formation of CO₂; meanwhile, F⁻ clearly formed in the reaction solution.¹⁷ The results observed here indicate that a similar phenomenon occurred, that is, the decomposition of PVDF mainly proceeded via a dehydro-

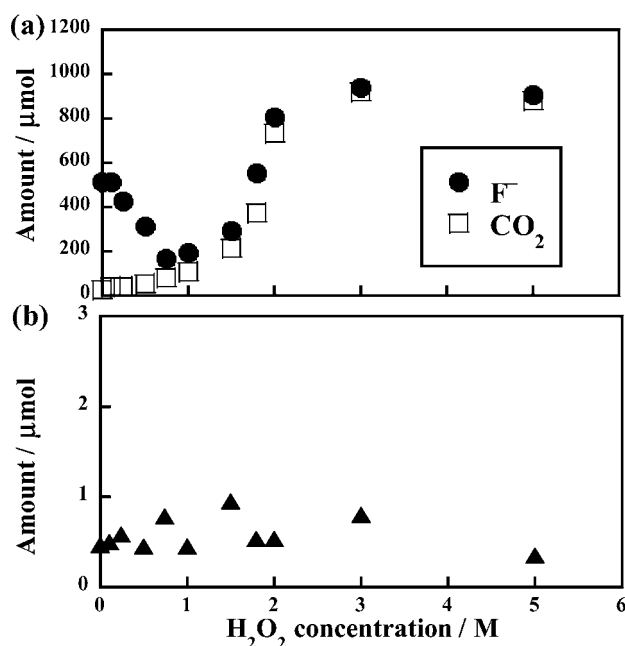
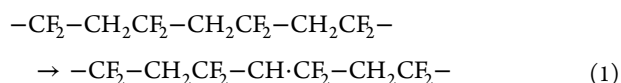


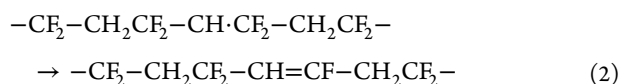
Figure 1. H₂O₂ concentration dependence of PVDF decomposition in subcritical water at 300 °C: detected amounts of (a) F⁻ and CO₂ and (b) malonic acid. PVDF (30 mg; fluorine content, 959 μmol; carbon content, 937 μmol) and an aqueous H₂O₂ solution (10 mL) were introduced into the reactor, which was pressurized with argon (0.60 MPa) and heated at 300 °C for 6 h.

fluorination mechanism (Scheme 1a), as has been reported for the thermolysis of PVDF.^{9–11}

First, C–H scission occurs in a –CH₂– group:



The scission leads to the formation of a C=C bond in the polymer chain, eq 2, and HF formation.



Further loss of HF along the polymer chain results in the formation of carbon-rich residue.

In the absence of H₂O₂, a small amount of 1,3,5-trifluorobenzene (0.20 μmol) was also detected, similar to the previous result.¹⁷ The formation of 1,3,5-trifluorobenzene can be explained by chain scission during the dehydrofluorination processes (Scheme 1a).

We measured the carbon ratio of the residue obtained at 300 °C. The carbon ratio was 47.1 wt %, which was higher than the carbon ratio of the initial polymer (37.5 wt %). This result supports the conclusion that the decomposition of PVDF in the absence of H₂O₂ proceeds via dehydrofluorination mechanism. From these data, the carbon recovery for the present reaction was calculated to be 79%, according to the equation [(moles of carbon in the products, i.e., residue + CO₂ + malonic acid + 1,3,5-trifluorobenzene)/(moles of carbon in the initial PVDF)].

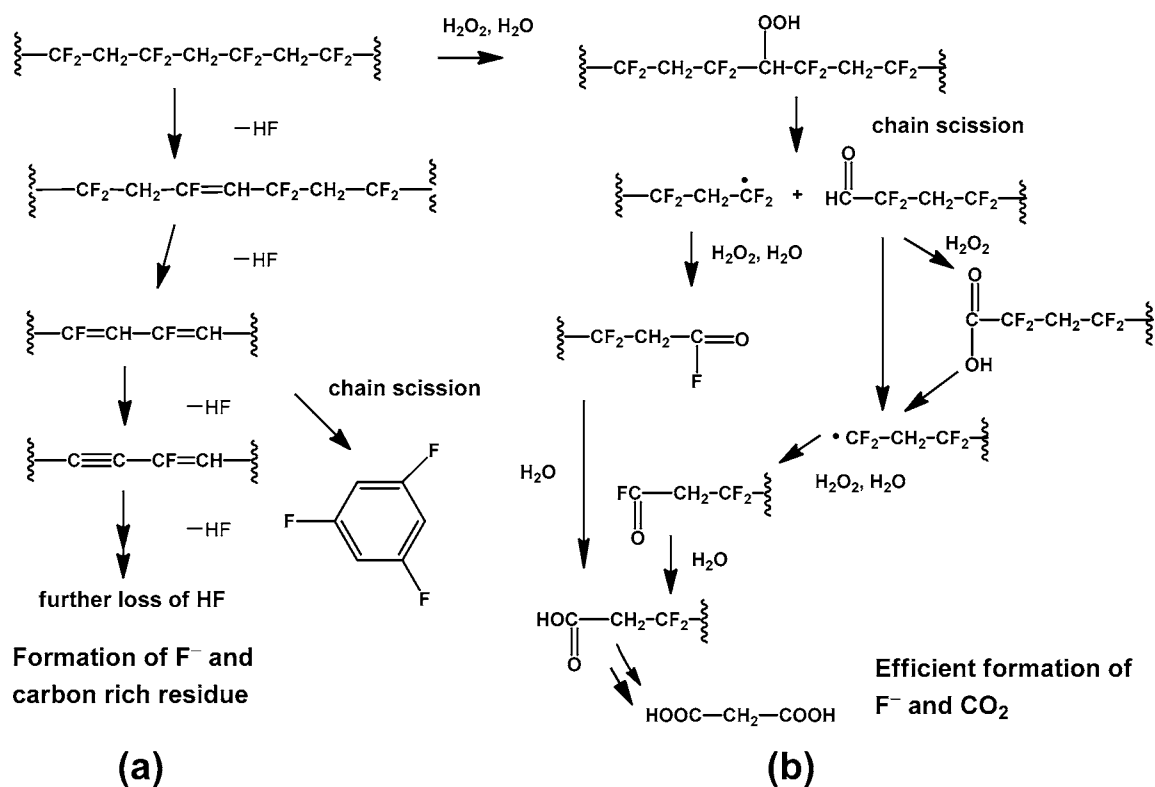
To our surprise, when the reaction was carried out in the presence of H₂O₂, the F⁻ amount showed a unique dependence on the H₂O₂ concentration (Figure 1a). The F⁻ amount decreased with increasing H₂O₂ concentration to 0.75 M, then turned to increase around 1.0 M, and tended to saturate above 3.0 M. The solid residue observed in the absence of H₂O₂ disappeared when the H₂O₂ concentration increased above 2.0 M. When the H₂O₂ concentration was 3.0 M (that is, 30 mmol in the initial reaction solution), which corresponds to a 31-fold molar excess relative to the fluorine content of the polymer (959 μmol), the F⁻ amount reached 943 μmol (98% yield, Table 1, entry 2). Meanwhile, the CO₂ amount gradually increased with increasing H₂O₂ concentration, increased sharply above 1.0 M, and finally tended to saturate around 3.0 M. When 3.0 M of H₂O₂ was used, the CO₂ amount reached 917 μmol, which corresponds to a CO₂ yield [(moles of CO₂ formed, i.e., 917 μmol)/(moles of carbon in the polymer, i.e., 937 μmol)] of 98% (Table 1, entry 2). These results indicate that virtually complete mineralization of fluorine and carbon in PVDF was achieved at a relatively low temperature (300 °C) by use of a 31-fold and a 32-fold molar excess of H₂O₂ with respect to the fluorine and the carbon in the polymer, respectively. Not only F⁻ but also malonic acid was detected in the reaction solution, although the amount (0.3–1.0 μmol) was 2–3 orders of magnitude lower than the F⁻ amount (Figure 1b).

As described above, PVDF was efficiently mineralized in the presence of excess H₂O₂. In such conditions, we propose the reaction mechanism outlined in Scheme 1b.

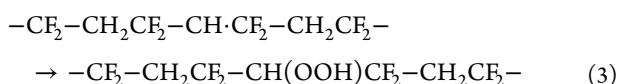
Table 1. Decomposition of PVDF and Related Copolymers in Subcritical Water^a

| entry | (co)polymer | initial H ₂ O ₂ conc. (M) | reaction press. (MPa) | F ⁻ (μmol) [yield (%)] ^b | CO ₂ (μmol) [yield (%)] ^c | malonic acid (μmol) | Cl ⁻ (μmol) [yield (%)] ^d | F ₂ HCCHF ₂ (μmol) |
|-------|-------------------|---|-----------------------|--|---|------------------------|---|--|
| 1 | PVDF | none | 10.1 | 511 [53] | 27 [3] | 0.4 | – | n.d. |
| 2 | PVDF | 3.0 | 11.1 | 943 ± 9 ^e [98 ± 1] | 917 ± 21 ^e [98 ± 2] | 0.8 ± 0.1 ^e | – | n.d. |
| 3 | poly(VDF-co-CTFE) | none | 9.8 | 9 [1] | 2 [0] | 0.2 | 15 [12] | n.d. |
| 4 | poly(VDF-co-CTFE) | 3.0 | 11.4 | 796 [98] | 700 [95] | n.d. | 119 [97] | 0.5 |
| 5 | poly(VDF-co-HFP) | none | 8.8 | 91 [10] | 8 [1] | 0.4 | – | n.d. |
| 6 | poly(VDF-co-HFP) | 2.0 | 10.0 | 897 [96] | 832 [92] | 5.7 | – | n.d. |

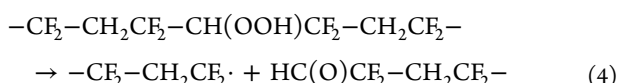
^aThe (co)polymer (30 mg) and an aqueous solution of H₂O₂ (10 mL) were introduced into the reactor, which was pressurized with argon and then heated at 300 °C for 6 h. For the reactions in the absence of H₂O₂, pure water was used instead of an aqueous solution of H₂O₂. ^bF⁻ yield (%) = [(moles of F⁻ formed)/(moles of fluorine in the (co)polymer)] × 100. ^cCO₂ yield (%) = [(moles of CO₂ formed)/(moles of carbon in the (co)polymer)] × 100. ^dCl⁻ yield (%) = [(moles of Cl⁻ formed)/(moles of chlorine in the copolymer)] × 100. ^eThese values were obtained from two reactions under the same reaction conditions.

Scheme 1. Proposed Mechanism for the Decomposition of PVDF (a) in the Absence of H₂O₂ and (b) in the Presence of a Large Excess of H₂O₂ (≥3.0 M)

The first step is an abstraction of a hydrogen atom from a $-\text{CH}_2-$ group, eq 1. The resulting radical reacts with H_2O_2 in the presence of water to produce a hydroperoxide:



This product is unstable and can cause scission of the main chain, which results in a $-\text{CF}_2\cdot$ terminal radical and an aldehyde:



The $-\text{CF}_2\cdot$ radical can be transformed into an acid fluoride end-group ($-\text{COF}$) in the presence of H_2O_2 , and the aldehyde can either undergo a direct cleavage of the C–C bond to form a terminal $-\text{CF}_2\cdot$ radical or can be oxidized into a carboxylic acid, which is subsequently cleaved as shown in Scheme 1b. The acid fluoride is hydrolyzed to the corresponding carboxylic acid. This sequence of steps leads to mineralization of PVDF. The formation of a carboxylic acid end-group and subsequent C–C bond cleavage can shorten the polymer chain stepwise, resulting in the formation of malonic acid as a final product.

As described above, when a small amount of H_2O_2 was introduced into the reaction system (≤ 0.75 M), the F^- amount decreased. This observation suggests that the decomposition of PVDF via dehydrofluorination mechanism was suppressed in the presence of a small H_2O_2 amount: the presence of H_2O_2 around the $-\text{CH}_2-$ group may inhibit the C=C bond formation in the polymer chain (eq 2), at which conditions the H_2O_2 amount is not enough to generate a hydroperoxide group in the polymer chain.

Temperature dependence of PVDF decomposition in the presence of 2.0 M of H_2O_2 at constant reaction time of 6 h is shown in Figure 2a. At 200 °C, almost no decomposition of the polymer occurred. Both F^- and CO_2 clearly formed during the reaction at 250 °C, at which conditions the water is in a subcritical state, and the F^- and CO_2 amounts increased further with increasing reaction temperature. At 300 °C, the F^- amount reached 809 μmol (yield, 84%) while that of CO_2 was 732 μmol (yield, 78%). We extended the reaction time in the presence of 2.0 M H_2O_2 at 300 °C (Figure 2b). The prolonged reaction time increased the mineralization further. After 12 h, the F^- and CO_2 amounts reached 914 μmol (yield, 95%) and 846 μmol (yield, 90%), respectively. This means that most of the fluorine and carbon in the polymer also mineralized by use of 2.0 M of H_2O_2 , a 21-fold molar excess relative to fluorine or carbon in the initial polymer, by extending the reaction time to 12 h.

Decomposition of Poly(VDF-co-CTFE) Copolymer.

H_2O_2 concentration dependences of the amounts of major products and minor products after the reactions at 300 °C for 6 h are shown in panels a and b of Figure 3, respectively. Not only F^- but also Cl^- formed in the reaction solution, and CO_2 formed in the gas phase as major products (Figure 3a). As minor products, F_2HCCHF_2 in the gas phase and malonic acid in the reaction solution, the amounts of which were 3 orders of magnitude lower than those of F^- and CO_2 , were detected (Figure 3b).

The reactivity of poly(VDF-co-CTFE) copolymer was markedly different from that of PVDF. PVDF clearly formed F^- in the absence of H_2O_2 (the F^- yield was 53%; Table 1, entry 1), whereas poly(VDF-co-CTFE) copolymer released a few F^- ions (9 μmol , which corresponds to a yield of 1%; Table 1, entry 3). This result suggests that poly(VDF-co-CTFE)

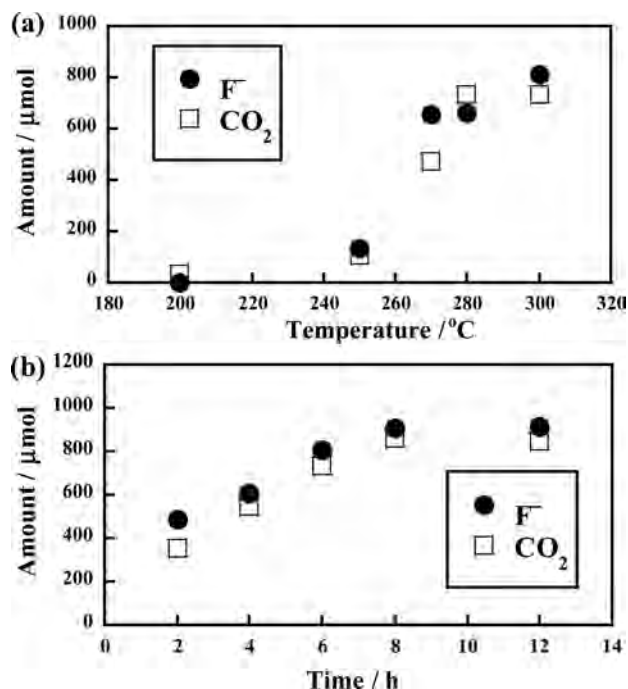


Figure 2. (a) Temperature dependence of PVDF decomposition in the presence of H₂O₂ and (b) time dependence of PVDF decomposition in subcritical water in the presence of H₂O₂. For the measurements shown in panel a, PVDF (30 mg) and an aqueous H₂O₂ solution (2.0 M, 10 mL) were introduced into the reactor, which was pressurized with argon (0.60 MPa) and heated at 200–300 °C for 6 h. For the measurements shown in panel b, PVDF (30 mg) and an aqueous H₂O₂ solution (2.0 M, 10 mL) were introduced into the reactor, which was pressurized with argon (0.60 MPa) and heated at 300 °C for 2–12 h. Besides F⁻, a trace of malonic acid was detected in the solutions after the reactions described in panel a (0.1–0.6 μmol) and panel b (0.3–0.5 μmol).

copolymer cannot decompose via dehydrofluorination mechanism, as proposed in the decomposition of PVDF in the absence of H₂O₂ (Scheme 1a).

Whereas the amount of F⁻ formed from PVDF showed a “V-shape” dependence on the H₂O₂ concentration (Figure 1a), the amounts of F⁻ and CO₂ from poly(VDF-*co*-CTFE) copolymer were monotonically increased with increasing H₂O₂ concentration (Figure 3a). Furthermore, a small amount of F₂HCCHF₂ was detected during the decomposition of poly(VDF-*co*-CTFE) copolymer with higher H₂O₂ concentrations (≥2.0 M) (Figure 3b). When the reaction was carried out in the presence of 3.0 M H₂O₂, the amounts of F⁻, CO₂, and Cl⁻ reached 796, 700, and 119 μmol, which correspond to yields of 98, 95, and 97%, respectively (Table 1, entry 4), where the Cl⁻ yield (%) was calculated by the equation (moles of Cl⁻ formed, i.e., 119 μmol)/(moles of chlorine in the copolymer, i.e., 123 μmol) × 100. That is, virtually complete mineralization was achieved with 30 mmol of H₂O₂, which is 37 times the molar amount of fluorine and 41 times the molar amount of carbon in the copolymer.

Temperature dependence of the decomposition of poly(VDF-*co*-CTFE) copolymer in the presence of 2.0 M H₂O₂ at constant reaction time of 6 h is displayed in Figure 4. The formation of F⁻ and Cl⁻ was prominent when the reaction was carried out at 300 °C. However, while F⁻ and Cl⁻ amounts increased monotonically with increasing temperature, that of CO₂ showed only a slight increase above 300 °C (Figure 4a),

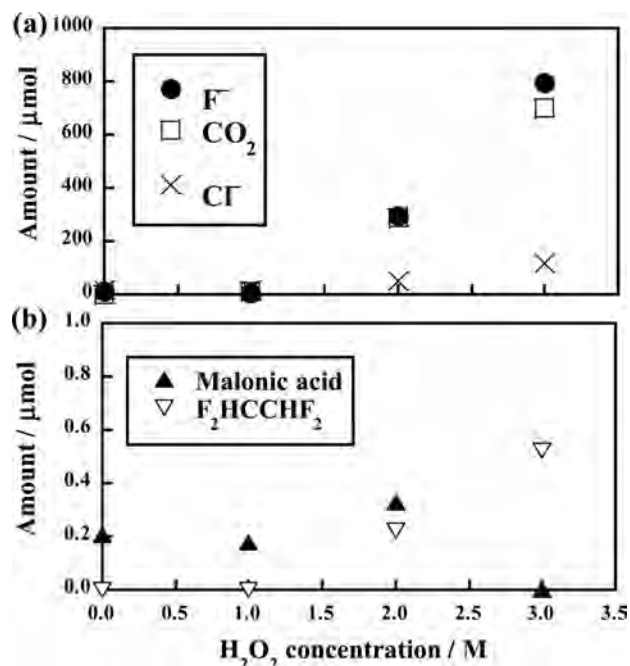


Figure 3. H₂O₂ concentration dependence of decomposition of poly(VDF-*co*-CTFE) copolymer in subcritical water at 300 °C: detected amounts of (a) F⁻, Cl⁻, and CO₂ and (b) malonic acid and F₂HCCHF₂. The copolymer (30 mg; fluorine content, 813 μmol; carbon content, 737 μmol; chlorine content, 123 μmol) and an aqueous H₂O₂ solution (10 mL) were introduced into the reactor, which was pressurized with argon (0.60 MPa) and heated at 300 °C for 6 h.

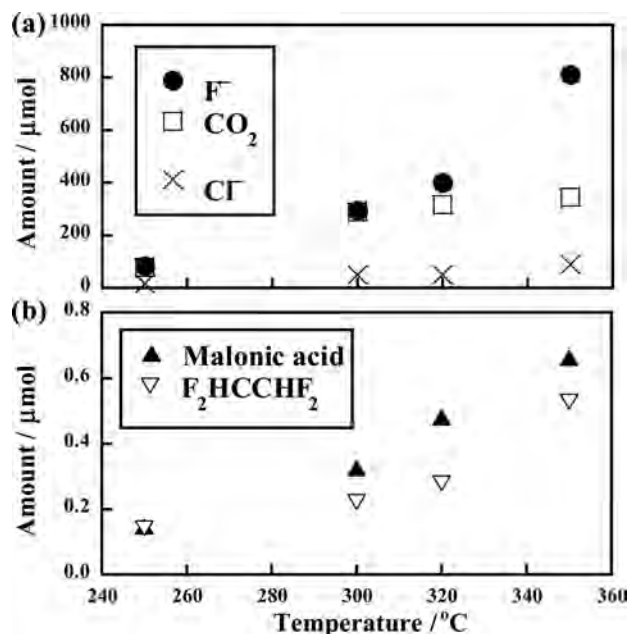


Figure 4. Temperature dependence of decomposition of poly(VDF-*co*-CTFE) copolymer in the presence of 2.0 M of H₂O₂: detected amounts of (a) F⁻, Cl⁻, and CO₂ and (b) malonic acid and F₂HCCHF₂. The copolymer (30 mg) and an aqueous H₂O₂ solution (10 mL) were introduced into the reactor, which was pressurized with argon (0.60 MPa) and heated at 250–350 °C for 6 h.

although the amounts of the minor products, malonic acid and F₂HCCHF₂, increased at these temperatures (Figure 4b). When the reaction was carried out at 350 °C, while the fluorine

content was completely converted to F^- (yield, 100%), the amounts of Cl^- (88.4 μmol) and CO_2 (345 μmol) resulted in lower yields, 72 and 47%, respectively, and the color of the reaction solution was slightly black. These results indicate that the H_2O_2 concentration of 2.0 M (that is, 20 mmol in the 10 mL reaction solution) was insufficient to induce the complete mineralization at 350 $^\circ\text{C}$, suggesting that some decomposition pathway(s) which does not lead to mineralization of the carbon and chlorine of the copolymer to CO_2 and Cl^- , for example, the dehydrofluorination, which forms $C=C$ bonds in the polymer chain, allowing incorporation of the chlorine atoms, may participate at 350 $^\circ\text{C}$.

Figure 5 exhibits the time dependence of the decomposition of poly(VDF-co-CTFE) copolymer in the presence of 2.0 M

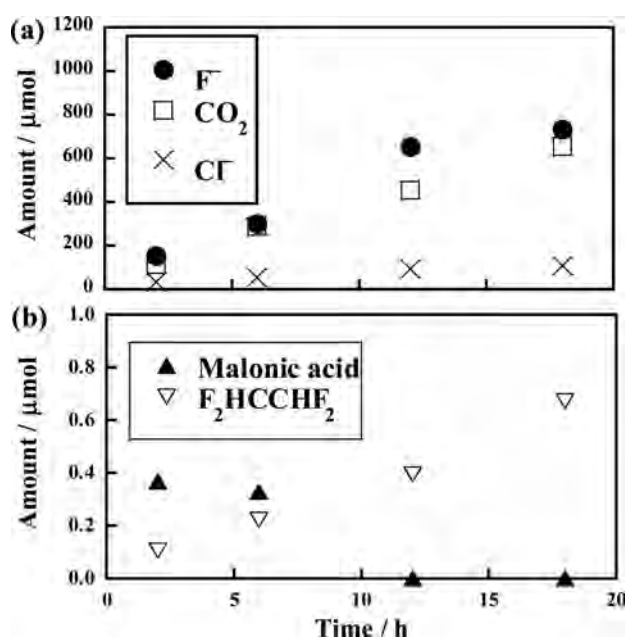


Figure 5. Time dependence of decomposition of poly(VDF-co-CTFE) copolymer in subcritical water in the presence of H_2O_2 at 300 $^\circ\text{C}$: detected amounts of (a) F^- , Cl^- , and CO_2 and (b) malonic acid and F_2HCCHF_2 . Poly(VDF-co-CTFE) (30 mg) copolymer and an aqueous H_2O_2 solution (2.0 M, 10 mL) were introduced into the reactor, which was pressurized with argon (0.60 MPa) and heated for 2–18 h.

H_2O_2 at 300 $^\circ\text{C}$. The F^- , CO_2 , and Cl^- amounts increased monotonically with increasing reaction time (Figure 5a). After 18 h, the F^- , CO_2 , and Cl^- contents reached 732, 651, and 104 μmol , which correspond to yields of 90, 88, and 85%, respectively, indicating that most of the fluorine, carbon, and chlorine in the initial copolymer mineralized. When the F^- yield is compared with the Cl^- yield, both values were similar at each reaction time. This result indicates that the abstraction of chlorine atoms from the polymer chain did not proceed prior to the abstraction of the fluorine atoms and the $-CH_2CF_2-$ unit in the polymer chain may decompose preferentially. As for the minor products, the amount of malonic acid decreased with increasing reaction time (Figure 5b), which indicates that malonic acid was an intermediate product in the decomposition of the copolymer. In contrast, the amount of F_2HCCHF_2 increased with increasing reaction time, indicating that F_2HCCHF_2 is a final product under these reaction conditions.

Decomposition of Poly(VDF-co-HFP) Copolymer.

Compared to poly(VDF-co-CTFE), poly(VDF-co-HFP) copolymer was more readily decomposed by H_2O_2 . Figure 6a

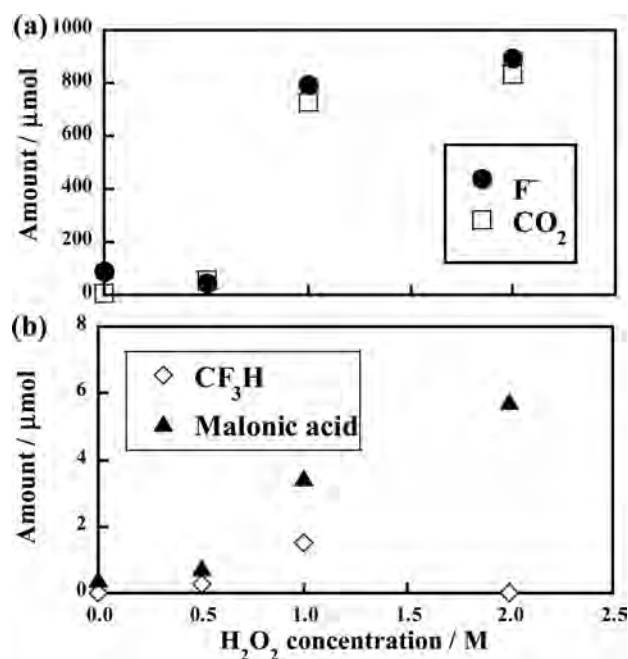


Figure 6. H_2O_2 concentration dependence of decomposition of poly(VDF-co-HFP) copolymer in subcritical water at 300 $^\circ\text{C}$: detected amounts of (a) F^- and CO_2 and (b) malonic acid and CF_3H . The copolymer (30 mg; fluorine content, 938 μmol ; carbon content, 902 μmol) and an aqueous H_2O_2 solution (10 mL) were introduced into the reactor, which was pressurized with argon (0.60 MPa) and heated at 300 $^\circ\text{C}$ for 6 h.

shows H_2O_2 concentration dependences of the amounts of F^- and CO_2 after the reactions at 300 $^\circ\text{C}$ for 6 h. When the reaction was carried out in the absence of H_2O_2 , the amounts of F^- and CO_2 were 91 μmol (yield, 10%) and 8 μmol (yield, 1%), respectively (Table 1, entry 5). Although F^- formed clearly in the absence of H_2O_2 , the yield was considerably lower than that of PVDF (53%, Table 1, entry 1). This result suggests that the decomposition of the copolymer via dehydrofluorination mechanism was limited, although 95% of the polymer chain consisted of $-CH_2CF_2-$ unit. When 0.5 M H_2O_2 was added, the F^- amount decreased to 46 μmol (yield, 5%), whereas that of CO_2 increased up to 54 μmol (yield, 6%). This tendency is similar to the decomposition of PVDF (Figure 1a). Further increase in the H_2O_2 concentration enhanced the formation of F^- and CO_2 . When the reaction was carried out in the presence of 2.0 M H_2O_2 (20 mmol), the F^- and CO_2 contents reached 897 μmol (yield, 96%) and 832 μmol (yield, 92%), respectively (Table 1, entry 6). Therefore, almost complete mineralization of the copolymer was achieved with 20 mmol H_2O_2 , the molar amount of which was 21 times that of fluorine and 22 times that of carbon in the copolymer. When the reaction was carried out in the presence of medium H_2O_2 concentration (0.5 or 1.0 M), a small amount of CF_3H was detected in the gas phase (Figure 6b). Simultaneously, a small amount of malonic acid was detected in the reaction solution. We previously reported that CF_3H was detected during the decomposition of perfluoroalkyl sulfonic acid membrane polymer bearing CF_3 group in the pendant chain of the polymer in

subcritical water and demonstrated that water was the source of hydrogen in the CF_3H by means of a reaction using D_2O .²³ Similarly, the CF_3H in the present study may form by a reaction of the CF_3 radical derived from the copolymer and water. However, CF_3H disappeared with increasing H_2O_2 concentration to 2.0 M. In the gas phase, F_2HCCHF_2 , which appeared during the reaction of poly(VDF-co-CTFE) copolymer, was quasi not detected or only trace amounts (10^{-8} mol) were noted in the presence of H_2O_2 .

Temperature dependence of the decomposition of poly(VDF-co-HFP) copolymer in the presence of 2.0 M H_2O_2 at constant reaction time of 6 h is displayed in Figure 7. The main

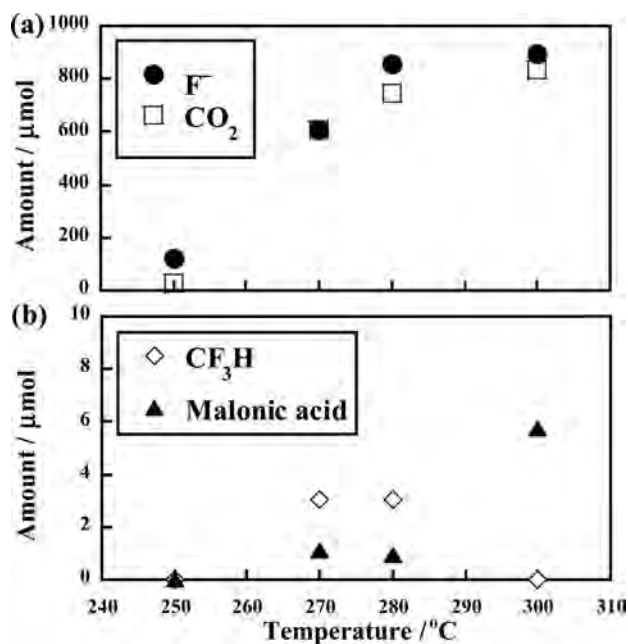


Figure 7. Temperature dependence of decomposition of poly(VDF-co-HFP) copolymer in subcritical water in the presence of 2.0 M of H_2O_2 : detected amounts of (a) F^- and CO_2 and (b) malonic acid and CF_3H . The copolymer (30 mg) and an aqueous H_2O_2 solution (2.0 M, 10 mL) were introduced into the reactor, which was pressurized with argon (0.60 MPa) and heated at 250–300 $^{\circ}\text{C}$ for 6 h.

products, F^- and CO_2 , formed efficiently above 270 $^{\circ}\text{C}$ (Figure 7a), and CF_3H and malonic acid were also detected at 270 and 280 $^{\circ}\text{C}$ as minor products. When the reaction temperature was increased to 300 $^{\circ}\text{C}$, CF_3H disappeared and almost complete mineralization (F^- yield, 96%; CO_2 yield, 92%) was achieved.

The time dependence of the decomposition of poly(VDF-co-HFP) copolymer in the presence of 2.0 M H_2O_2 at 300 $^{\circ}\text{C}$ is shown in Figure 8. The amounts of F^- and CO_2 reached 670 μmol (yield, 71%) and 598 μmol (66%) even after a short reaction time of 1 h, and the amounts almost saturated after 4 h (Figure 8a). After 4 h, the F^- and CO_2 amounts reached 906 μmol (yield, 97%) and 825 μmol (yield, 91%), respectively, reflecting that the fluorine and carbon in the copolymer were efficiently mineralized. In addition, CF_3H disappeared after 6 h (Figure 8b).

CaF_2 Formation. To determine whether CaF_2 formed in such a reaction system, the (co)polymer decomposition reactions were performed in the presence of $\text{Ca}(\text{OH})_2$. When PVDF (30 mg, fluorine content, 959 μmol) and a stoichiometric amount of $\text{Ca}(\text{OH})_2$ (481 μmol) were heated at 300 $^{\circ}\text{C}$ for 12 h in the presence of 2.0 M H_2O_2 (20 mmol, 10

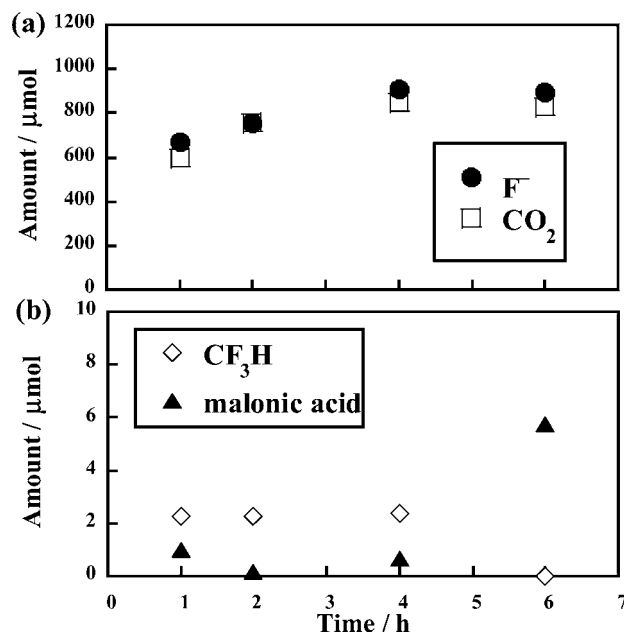


Figure 8. Time dependence of decomposition of poly(VDF-co-HFP) copolymer in subcritical water in the presence of H_2O_2 at 300 $^{\circ}\text{C}$: detected amounts of (a) F^- and CO_2 and (b) malonic acid and CF_3H . The copolymer (30 mg) and an aqueous H_2O_2 solution (2.0 M, 10 mL) were introduced into the reactor, which was pressurized with argon (0.60 MPa) and heated at 300 $^{\circ}\text{C}$ for 1–6 h.

mL), a white precipitate was obtained. After purification by simple washing with pure water, the XRD pattern of the precipitate showed only peaks assigned to CaF_2 (Figure S-1 in Supporting Information). The molar amount of the collected CaF_2 was 370 μmol , which corresponds to 740 μmol of fluorine atoms. That is, 77% of the fluorine atoms in PVDF were recovered in the collected CaF_2 . When a reaction in the absence of H_2O_2 was carried out under the same reaction conditions as mentioned above, a black precipitate (51 mg), which seems to be a mixture containing carbon, was obtained instead of the white precipitate. This result indicates that H_2O_2 is required for the efficient CaF_2 formation.

In a similar manner, when poly(VDF-co-CTFE) copolymer (30 mg) was reacted in the presence of a stoichiometric amount of $\text{Ca}(\text{OH})_2$ (409 μmol) and H_2O_2 (3.0 M, 30 mmol) at 300 $^{\circ}\text{C}$ for 6 h, CaF_2 (237 μmol , 58% yield) was obtained (Figure S-2 in Supporting Information). Finally, the reaction of poly(VDF-co-HFP) copolymer (30 mg) in the presence of $\text{Ca}(\text{OH})_2$ (476 μmol) and 2.0 M H_2O_2 (20 mmol, 10 mL) was carried out at 300 $^{\circ}\text{C}$ for 6 h, and CaF_2 was obtained (375 μmol , 80% yield); the XRD pattern is shown in Figure S-3 in Supporting Information. The lower CaF_2 yield (58%) observed for poly(VDF-co-CTFE) copolymer compared to that of other (co)polymers may be ascribed to Ca^{2+} reacting with not only F^- but also with Cl^- , although CaCl_2 was removed from the reaction mixture by washing with pure water.

CONCLUSION

Decompositions of PVDF, poly(VDF-co-CTFE), and poly(VDF-co-HFP) copolymers in subcritical water were investigated. Addition of H_2O_2 into the reaction system led to an efficient mineralization of these (co)polymers that released to F^- and CO_2 (and also Cl^- if poly(VDF-co-CTFE) copolymer) at a relatively low temperature (300 $^{\circ}\text{C}$). When PVDF was

heated in subcritical water at 300 °C for 6 h in the presence of 3.0 M H₂O₂, which corresponds to 31 times the fluorine molar amount and 32 times the carbon molar amount in this polymer, both the F⁻ and CO₂ yields reached 98%. That result indicates a complete mineralization of this polymer. Poly(VDF-co-CTFE) copolymer was also efficiently mineralized at 300 °C for 6 h by use of 3.0 M H₂O₂, which corresponds to 37 times the fluorine molar amount and 41 times the carbon molar amount in the copolymer, leading to F⁻, CO₂, and Cl⁻ yields of 98, 95, and 97%, respectively. Poly(VDF-co-HFP) copolymer was readily decomposed faster in the presence of H₂O₂ than poly(VDF-co-CTFE) copolymer: almost complete mineralization of the copolymer (F⁻ and CO₂ yields were 96 and 92%, respectively) was achieved after a reaction at 300 °C in the presence of 2.0 M H₂O₂ for 6 h, which is 21 times the fluorine molar amount and 22 times the carbon molar amount in the copolymer. The H₂O₂ concentration dependence of the formation of F⁻ was different in these (co)polymers: the F⁻ amount from PVDF for 6 h showed a “V-shape” dependence on the H₂O₂ concentration, whereas the F⁻ amount from poly(VDF-co-CTFE) copolymer was monotonically increased with increasing H₂O₂ concentration. This difference suggests that PVDF can decompose via dehydrofluorination mechanism in the absence of H₂O₂, whereas poly(VDF-co-CTFE) copolymer cannot. The behavior of poly(VDF-co-HFP) copolymer was similar to that of PVDF, although the amount of F⁻ formed in the absence of H₂O₂ was considerably lower than that of PVDF.

Addition of stoichiometric Ca(OH)₂ into the reaction system resulted in the formation of CaF₂ with yields of 77, 58, and 80% for PVDF and poly(VDF-co-CTFE) and poly(VDF-co-HFP) copolymers, respectively.

■ ASSOCIATED CONTENT

■ Supporting Information

The Supporting Information is available free of charge on the ACS Publications website at DOI: 10.1021/acs.iecr.5b01716.

XRD patterns of the precipitates obtained from the reactions of PVDF, poly(VDF-co-CTFE), and poly(VDF-co-HFP) copolymers in the presence of H₂O₂ and Ca(OH)₂ (PDF)

■ AUTHOR INFORMATION

Corresponding Author

*Tel: (+81)-463-59-4111. Fax: (+81)-463-58-9688. E-mail: h-hori@kanagawa-u.ac.jp.

Notes

The authors declare no competing financial interest.

■ ACKNOWLEDGMENTS

This work was supported by a grant from the Japan Society for the Promotion of Science (15H02841). The authors also thank the Elf Atochem company (Pierre Benite, France) for free gifts of poly(VDF-co-CTFE) and poly(VDF-co-HFP) copolymers.

■ REFERENCES

- (1) Seiler, D. A. PVDF in the Chemical Process Industry. In *Modern Fluoropolymers: High Performance Polymers for Diverse Applications*; Scheirs, J., Ed.; John Wiley & Sons: New York, 1997; pp 487–506.
- (2) *Fluoropolymers: Synthesis and Applications*; Hougham, G., Cassidy, P. E., Johns, K., Davidson, T., Eds.; Plenum: New York, 1999; Vol. 1 and 2.
- (3) Humphrey, J. S.; Amin-Sanayei, R. Vinyl Fluoride Polymers. In *Encyclopedia of Polymer Science and Technology*, 3rd Ed; Mark, H. F., Ed.; John Wiley & Sons: New York, 2004; Vol. 4, pp 510–533.
- (4) Drobny, J. G. *Technology of Fluoropolymers*, 2nd ed; CRC Press: Boca Raton, FL, 2009.
- (5) Ameduri, B.; Boutevin, B. *Well-Architected Fluoropolymers: Synthesis, Properties and Applications*; Elsevier: Oxford, UK, 2004.
- (6) *Handbook of Fluoropolymer Science and Technology*; Smith, D. W., Iacono, S. T., Iyer, S. S., Eds.; Wiley: New York, 2014.
- (7) Ameduri, B. From vinylidene fluoride (VDF) to the applications of VDF-containing polymers and copolymers: recent developments and future trends. *Chem. Rev.* **2009**, *109*, 6632.
- (8) Boschet, F.; Ameduri, B. (Co)polymers of chlorotrifluoroethylene: synthesis, properties, and applications. *Chem. Rev.* **2014**, *114*, 927.
- (9) Hirschler, M. M. Effect of oxygen on the thermal decomposition of poly(vinylidene fluoride). *Eur. Polym. J.* **1982**, *18*, 463.
- (10) Loginova, N. N.; Madorskaya, L. Y.; Podlesskaya, N. K. Relations between the thermal stability of partially fluorinated polymers and their structure. *Polym. Sci. U.S.S.R.* **1983**, *25*, 2995.
- (11) Zulfiqar, S.; Zulfiqar, M.; Rizvi, M.; Munir, A.; McNeill, I. C. Study of the thermal degradation of polychlorotrifluoroethylene, poly(vinylidene fluoride) and copolymers of chlorotrifluoroethylene and vinylidene fluoride. *Polym. Degrad. Stab.* **1994**, *43*, 423.
- (12) Zulfiqar, S.; Rizvi, M.; Munir, A.; Ghaffar, A.; McNeill, I. C. Thermal degradation studies of copolymers of chlorotrifluoroethylene and methyl methacrylate. *Polym. Degrad. Stab.* **1996**, *52*, 341.
- (13) Younesi, R.; Hahlin, M.; Treskow, M.; Scheers, J.; Johansson, P.; Edström, K. Ether based electrolyte, LiB(CN)₄ salt and binder degradation in the Li–O₂ battery studied by hard X-ray photoelectron spectroscopy (HAXPS). *J. Phys. Chem. C* **2012**, *116*, 18597.
- (14) Komaba, S.; Yabuuchi, N.; Ozeki, T.; Han, Z. J.; Shimomura, K.; Yui, H.; Katayama, Y.; Miura, T. Comparative study of sodium polyacrylate and poly(vinylidene fluoride) as binders for high capacity Si–graphite composite negative electrodes in Li-ion batteries. *J. Phys. Chem. C* **2012**, *116*, 1380.
- (15) Yu, J.; Huang, X.; Wu, C.; Jiang, P. Permittivity, thermal conductivity and thermal stability of poly(vinylidene fluoride)/graphene nanocomposites. *IEEE Trans. Dielectr. Electr. Insul.* **2011**, *18*, 478.
- (16) Hassoun, J.; Reale, P.; Panero, S.; Scrosati, B.; Wachtler, M.; Fleischhammer, M.; Kasper, M.; Wohlfahrt-Mehrens, M. Determination of the safety level of an advanced lithium ion battery having a nanostructured Sn-C anode, a high voltage LiNi_{0.5}Mn_{1.5}O₄ cathode, and a polyvinylidene fluoride-based gel electrode. *Electrochim. Acta* **2010**, *55*, 4194.
- (17) Hori, H.; Sakamoto, T.; Ohmura, K.; Yoshikawa, H.; Seit, T.; Fujita, T.; Morizawa, Y. Efficient-oxygen induced mineralization of melt-processable fluoropolymers in subcritical and supercritical water. *Ind. Eng. Chem. Res.* **2014**, *53*, 6934.
- (18) Myers, A. L.; Jobst, K. J.; Mabury, S. A.; Reiner, E. J. Using mass detect plots as a discovery tool to identify novel fluoropolymer thermal decomposition products. *J. Mass Spectrom.* **2014**, *49*, 291.
- (19) *Chemical Synthesis Using Supercritical Fluids*; Jessop, P. G., Leitner, W., Eds.; Wiley-VCH: Weinheim, Germany, 1999.
- (20) Hawthorne, S. B.; Lagadec, A. J. M.; Kaleris, D.; Lilke, A. V.; Miller, D. J. Pilot-scale destruction of TNT, RDX, and HMX on contaminated soils using supercritical water. *Environ. Sci. Technol.* **2000**, *34*, 3224.
- (21) Kawasaki, S.-I.; Oe, T.; Anjoh, N.; Nakamori, T.; Suzuki, A.; Arai, K. Practical supercritical water reactor for destruction of high concentration polychlorinated biphenyls (PCB) and dioxin waste streams. *Process Saf. Environ. Prot.* **2006**, *84*, 317.
- (22) Möller, M.; Nilges, P.; Harnisch, F.; Schröder, U. Subcritical water as reaction environment: fundamentals of hydrothermal biomass transformation. *ChemSusChem* **2011**, *4*, 566.
- (23) Hori, H.; Murayama, M.; Sano, T.; Kutsuna, S. Decomposition of perfluorinated ion-exchange membrane to fluoride ions by using

zerovalent metals in subcritical water. *Ind. Eng. Chem. Res.* **2010**, *49*, 464.



Efficient oxygen-induced decomposition of triphenylsulfonium trifluoromethanesulfonate to fluoride ions in subcritical water



Hisao Hori*, Hiroaki Yokota

Department of Chemistry, Faculty of Science, Kanagawa University, 2946 Tsuchiya, Hiratsuka 259-1293, Japan

ARTICLE INFO

Article history:

Received 19 March 2015

Received in revised form 29 May 2015

Accepted 12 June 2015

Available online 23 June 2015

Keywords:

Recovery
Supercritical water
Iron
Mineralization
PFOS

ABSTRACT

Decomposition of $[(C_6H_5)_3S][CF_3SO_3]$ in subcritical water, specifically, in the presence of either an iron-based reducing agent (zerovalent iron or FeO) or an oxidizing agent (O_2), was investigated with the aim of developing a technique to recover the fluorine component from the liquid waste. This is the first report on the decomposition of salts consisting of perfluoroalkanesulfonates and organic cations, which are widely used in the electronics industry as photoacid generators. The highest F^- yield was achieved by the reaction in the presence of O_2 at a temperature close to the critical point: when the reaction was carried out at 372 °C for 6 h, the F^- yield reached 93.6%, indicating that almost all the fluorine atoms in the anionic moiety, $CF_3SO_3^-$, were transformed into F^- ions. In addition, the formation of CHF_3 and benzene was suppressed by the use of O_2 . Whereas the $CF_3SO_3^-$ in $[(C_6H_5)_3S][CF_3SO_3]$ was efficiently decomposed to F^- ions in the presence of O_2 , the $CF_3SO_3^-$ in the corresponding potassium salt, CF_3SO_3K , was less reactive: the F^- yield of the reaction in the presence of O_2 at 373 °C for 6 h was only 57.1%, indicating that the cation in these salts affects the reactivity of the anion.

© 2015 Elsevier B.V. All rights reserved.

1. Introduction

Perfluoroalkanesulfonates ($C_nF_{2n+1}SO_3^-$) and their derivatives are widely used in industry because of their high thermal and chemical stability, high surface-active effect, high transparency, and so forth. Among these compounds, salts with organic cations are vital to the electronics industry, and they are used as photoacid generators in photolithography and other photochemical processes [1]. After it became clear that perfluorooctanesulfonate ($C_8F_{17}SO_3^-$, PFOS) persists and bioaccumulates in the environment [2,3], international regulations on the production, use, and import and export of PFOS were implemented [4], and efforts to develop greener alternatives are advancing [5]. The main strategy for the design of alternatives is to shorten the perfluoroalkyl chain, because compounds with shorter chains are less bioaccumulative. Triphenylsulfonium perfluoroalkanesulfonates with short perfluoroalkyl groups, that is, $[(C_6H_5)_3S][C_nF_{2n+1}SO_3]$ ($n = 1-4$), are representative of the greener photoacid generators that have been introduced in industry [6], even though the surface active effect of these chemicals is considerably lower than that of PFOS. The liquid waste containing these chemicals can be incinerated. However,

high temperatures are necessary to break the strong C–F bonds, and incineration results in the formation of hydrogen fluoride gas, which can seriously damage the firebrick of an incinerator. If these chemicals could be decomposed to F^- ions by means of environmentally benign techniques, the well-established protocol for treatment of F^- ions could be used, whereby Ca^{2+} is added to the system to form environmentally harmless CaF_2 , which is a raw material for hydrofluoric acid. Thus, the development of decomposition techniques that work under mild conditions would allow the recycling of fluorine, the global demand for which is increasing.

Reaction in subcritical or supercritical water is an innovative and environmentally benign waste-treatment technique, owing to the high diffusivity and low viscosity of these media, as well as their ability to hydrolyze many types of organic compounds [7]. Subcritical water is defined as hot water at sufficient pressure to maintain the liquid state, and supercritical water is defined as water at temperatures and pressures higher than the critical point (374 °C, 22.1 MPa). Recently, subcritical or supercritical water was used for pilot-plant- and practical-plant-scale decomposition of trinitrotoluene [8] and polychlorinated biphenyls [9]. We previously reported that although PFOS (potassium salt) is not decomposed in pure subcritical water around 350 °C, it can be decomposed by zerovalent iron in the same medium [10]. Decomposition of the cationic moiety of triphenylsulfonium perfluoroalkanesulfonates induced by UV-light irradiation was

* Corresponding author. Tel.: +81 463 59 4111; fax: +81 463 58 9688.
E-mail address: h-hori@kanagawa-u.ac.jp (H. Hori).

described in several reports to explain the photoacid generation mechanism [1,6]. However, there was no report focused on the decomposition of the anionic moiety of these chemicals to obtain F^- ions for waste treatment.

Herein we report on the decomposition of triphenylsulfonium trifluoromethanesulfonate, $[(C_6H_5)_3S][CF_3SO_3]$ (**1**), a typical triphenylsulfonium perfluoroalkanesulfonate, in subcritical water in the presence of an iron-based reducing agent (zerovalent iron or FeO) or an oxidizing agent (O_2). In addition, the reactivity of **1** is compared with that of CF_3SO_3K (**2**). This is the first report not only on the decomposition of salts consisting of perfluoroalkanesulfonates and organic cations in subcritical water, but also on a technique aimed at waste treatment that successfully achieves the efficient formation of F^- ions.

2. Experimental

2.1. Materials

Triphenylsulfonium trifluoromethanesulfonate (**1**, >98%) and potassium trifluoromethanesulfonate (**2**, >97%) were purchased from Wako Pure Chemical Industries (Osaka, Japan). Powdered zerovalent iron (>99.9%, <53 μm) and FeO (>99.9%, <53 μm) were purchased from Kojundo Chemical Laboratory (Saitama, Japan) and used as received. Argon (99.99%), O_2 (99.999%), CO_2 (0.995%)/ N_2 , CHF_3 (0.971%/ N_2), and benzene (C_6H_6 , 487 ppm/ N_2) gases were purchased from Taiyo Nippon Sanso (Tokyo, Japan). Other reagents were of high purity and were obtained from Wako Pure Chemical Industries.

2.2. Reaction procedures

Reactions were carried out in a stainless steel high-pressure reactor fitted with a gold vessel to prevent contamination from the reactor material. The internal volume of the reactor was 31 mL. In a typical run using zerovalent iron, an argon-saturated aqueous (Milli-Q) solution (10 mL) of **1** (9.94 μmol , 0.99 mM) and zerovalent iron (9.60 mmol) was introduced into the gold vessel, and the reactor was pressurized to 0.60 MPa with argon and sealed. The reactor was placed in an oven, and the reactor temperature was raised to the desired value (in the range from 76 to 373 $^\circ C$) and then held constant for a specified time (e.g., 6 h), after which the reactor was quickly cooled to room temperature. We also conducted reactions in the absence of zerovalent iron, reactions with FeO, reactions under O_2 instead of argon (in the absence of zerovalent iron), and reactions with **2**.

2.3. Analysis

An ion-chromatography system (IC-2001, Tosoh, Tokyo, Japan) consisting of an automatic sample injector (30- μL injection volume), a degasser, a pump, a guard column (TSKguard column Super IC-A, 4.6-mm i.d., 1.0-cm length, Tosoh), a separation column (TSKgel Super IC-Anion, 4.6-mm i.d., 15-cm length, Tosoh), a column oven (40 $^\circ C$), and a conductivity detector with a suppressor device was used to quantify the F^- and SO_4^{2-} concentrations in the reaction solution. The mobile phase was an aqueous solution containing $Na_2B_4O_7$ (6 mM), H_3BO_3 (15 mM), and $NaHCO_3$ (0.2 mM). The concentrations of $CF_3SO_3^-$ (anionic moiety of **1** and **2**) were quantified by means of an ion-exclusion chromatography system consisting of an automatic sample injector (5.0- μL injection volume), a guard column (TSKgel OApak-P, 7.8-mm i.d., 1.0-cm length, Tosoh), a separation column (TSKgel OApak-A, 7.8-mm i.d., 30-cm length, Tosoh), a pump, a column oven (40 $^\circ C$), and a conductivity detector. The mobile phase was phthalic acid (10 mM). The concentrations of

$[(C_6H_6)_3S]^+$ (the cationic moiety of **1**) were quantified by HPLC (Agilent 1120, Agilent Technologies, Palo Alto, CA, USA) with UV detection (235 nm). The mobile phase was a 70:30 (v/v) mixture of aqueous NaH_2PO_4 (20 mM, adjusted to pH 3.0 with H_3PO_4) and methanol, the separation column was a Tosoh TSKgel ODS-100Z (4.6-mm i.d., 15-cm length), and the injection volume was 10 μL .

A Shimadzu TOC-LCSH analyzer (Shimadzu, Kyoto, Japan) was used to quantify the total organic carbon content in a reaction solution obtained after most of the fluorine content in **1** was decomposed to F^- ions (that is, the fluorine atoms in $CF_3SO_3^-$ were almost completely transformed into F^-).

The gas-phase products were analyzed by gas chromatography–mass spectrometry on an instrument (QP2010 SE, Shimadzu) equipped with a fused silica capillary column (Rt-Q-BOND, Restek, Bellefonte, PA, USA). The carrier gas was helium, and the injection temperature was held constant at 120 $^\circ C$. The sample gas was introduced into the instrument in split mode (ratio, 20/1) and analyses were conducted in full-scan mode (m/z 2.0–200). The oven temperature was kept at 30 $^\circ C$ for 5 min, raised to 200 $^\circ C$ at a rate of 20 $^\circ C min^{-1}$, and held at that temperature for 20 min.

3. Results and discussion

3.1. Reactions in the presence of iron-based reducing agents

Initially, we carried out the reactions of **1** in the presence of zerovalent iron because we previously observed that PFOS is efficiently decomposed to F^- ions by zerovalent iron in subcritical water. Plots of the temperature dependences of the amounts of $CF_3SO_3^-$ and F^- in the reaction solution at a constant reaction time of 6 h (Fig. 1) revealed that the amount of $CF_3SO_3^-$ showed no sign of decreasing at temperatures below 245 $^\circ C$, reflecting the high thermal and chemical stability of $CF_3SO_3^-$. When the reaction temperature increased to 294 $^\circ C$, at around which temperature the characteristics of subcritical water, that is, high ionic dissociation constant ($\sim 10^{-11}$) and low dielectric constant (~ 22) are prominent [11], obvious consumption of $CF_3SO_3^-$ and formation of F^- were observed. $CF_3SO_3^-$ completely disappeared from the reaction solution at 343 $^\circ C$, and the amount of F^- continued to increase with increasing temperature. When the reaction was carried out at 373 $^\circ C$, the amount of F^- reached 22.2 μmol , corresponding to a yield of 74.4% (Table 1, entry 4). In addition to F^- ions, trace

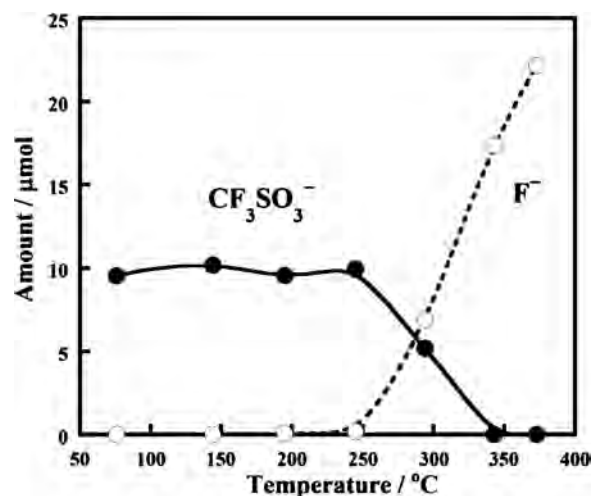


Fig. 1. Reaction-temperature dependence of the amounts of $CF_3SO_3^-$ and F^- in the reaction solution after the reaction of **1** in the presence of zerovalent iron. An aqueous solution (10 mL) of **1** (9.94 μmol , 0.99 mM) and zerovalent iron powder (9.60 mmol) were introduced into the reactor, which was pressurized with argon (0.60 MPa) and heated at 76–373 $^\circ C$ for 6 h.

Table 1
Decomposition of **1** in subcritical water under various reaction conditions.^a

| Entry | Added gas ^b | Reducing agent ^c | Temp. (°C) | Press. (MPa) | Remaining CF ₃ SO ₃ ⁻ (μmol)
[ratio (%)] | F ⁻ (μmol)
[yield (%)] ^d | CO ₂ (μmol) | CHF ₃ (μmol) | C ₆ H ₆ (μmol) |
|-------|------------------------|-----------------------------|------------|--------------|--|---|------------------------|-------------------------|--------------------------------------|
| 1 | Ar | Fe | 343 | 15.8 | n.d. ^e [0] | 17.4 [58.4] | 1.91 | 2.43 | 3.78 |
| 2 | Ar | None | 344 | 15.4 | 8.80 [88.5] | 3.16 [10.6] | 3.95 | n.d. | 1.18 |
| 3 | O ₂ | None | 343 | 15.5 | 6.71 [67.5] | 7.00 [23.5] | 43.4 | n.d. | 0.60 |
| 4 | Ar | Fe | 373 | 22.8 | n.d. | 22.2 [74.4] | 4.57 | 2.43 | 3.92 |
| 5 | Ar | FeO | 372 | 21.5 | n.d. | 15.9 [53.3] | 4.71 | 1.92 | 1.94 |
| 6 | O ₂ | None | 372 | 21.6 | n.d. | 27.9 [93.6] | 41.2 | n.d. | 1.03 |

^a Initial amount of **1**, 9.94 μmol; reaction solution volume, 10 mL; reaction time, 6 h.

^b 4.99 mmol.

^c 9.60 mmol.

^d F⁻ yield (%) = [(moles of F⁻ formed)/(moles of fluorine content in initial **1** = moles of initial **1** × 3)] × 100.

^e n.d. = not detected.

amounts (~0.20 μmol) of SO₄²⁻ were detected in the reaction solutions above 245 °C.

Plots of the temperature dependences of the amounts of gaseous products (Fig. 2) revealed that benzene and CO₂ were detected even at the low temperatures of 76 and 144 °C, at which temperatures the amount of CF₃SO₃⁻ showed no sign of decreasing (Fig. 1). This fact indicates that the cationic moiety, [(C₆H₆)₃S]⁺, decomposed at these temperatures. Consistently, the amount of [(C₆H₆)₃S]⁺ in the reaction solution was very low (0.01 μmol) even at 76 °C, and the cation completely disappeared above 144 °C. Increasing the reaction temperature further resulted in not only the formation of benzene and CO₂ but also the formation of CHF₃ (Fig. 2). The amount of CHF₃ formed increased sharply at above around 300 °C, at which temperature CF₃SO₃⁻ consumption and F⁻ formation occurred efficiently (Fig. 1). These results clearly indicate that [(C₆H₆)₃S]⁺ decomposed more readily than CF₃SO₃⁻.

To examine the effect of CO₂ on the reactivity of CF₃SO₃⁻, the reaction in the presence of a large amount of CO₂ (49.9 μmol) was carried out. After the reaction at 294 °C, 72.8% of the initial CF₃SO₃⁻ remained and the F⁻ yield was 9.6%, whereas the corresponding values obtained from the reaction in the absence of CO₂ was 52.1 and 23.1%, respectively (from the data in Fig. 1). These results indicate that the presence of a large amount of CO₂ inhibits the decomposition of CF₃SO₃⁻.

The results for reactions of **1** in subcritical water at 343–344 °C and a constant reaction time of 6 h are summarized in Table 1 (entries 1–3). When the reaction was carried out under argon without zerovalent iron (entry 2), 88.5% of the CF₃SO₃⁻ in the

initial **1** remained after the reaction, and the F⁻ yield was only 10.6%. In contrast, when the reaction was carried out in the presence of zerovalent iron (9.60 mmol) under argon, CF₃SO₃⁻ disappeared from the reaction solution, and the F⁻ yield reached 58.4% (entry 1), which is 5.5 times the yield without iron (entry 2).

As described above, CF₃SO₃⁻ was efficiently decomposed to F⁻ ions in the presence of zerovalent iron, and the highest F⁻ yield, 74.4%, was obtained by reaction at 373 °C for 6 h (Table 1, entry 4). In an attempt to increase the F⁻ yield further, we examined the decomposition of **1** in the presence of FeO, because FeO undergoes disproportionation to zerovalent iron and Fe₃O₄ at temperatures of >257 °C [12,13]. We speculated that zerovalent iron formed in situ might be more reactive than zerovalent iron added at the beginning of the reaction, as has been demonstrated in the decomposition of fluorinated ionic liquid anions [14]. However, when the reaction was carried out in the presence of FeO under argon at 372 °C for 6 h, the F⁻ yield (53.3%, entry 5 in Table 1) was lower than the yield obtained by use of zerovalent iron (74.4%, entry 4).

3.2. Reactions in the presence of O₂

At 343 °C, the addition of O₂ also enhanced the decomposition of CF₃SO₃⁻, although the CF₃SO₃⁻ consumption and F⁻ formation were not as great as those observed in the presence of zerovalent iron at this temperature: when the reaction was carried out under O₂ (4.99 mmol), 67.5% of the CF₃SO₃⁻ remained after the reaction, and the F⁻ yield was 23.5% (Table 1, entry 3). Note a large amount of CO₂ formed during the reaction in the presence of O₂, suggesting that O₂ efficiently induced oxidative decomposition of [(C₆H₆)₃S]⁺. We examined the reaction of **1** in the presence of O₂ at 372 °C, despite the fact that the reactivity of **1** at 343 °C in the presence of O₂ was lower than that in the presence of zerovalent iron. To our surprise, elevating the temperature by 29 °C dramatically increased the reactivity of **1**. When the reaction of **1** was carried out at 372 °C in the presence of O₂, CF₃SO₃⁻ was no longer present in the reaction solution after 0.5 h. Plots of the reaction-time dependences of the amounts of products in the reaction solution and in the gas phase (Fig. 3a and b, respectively) revealed that large amounts of F⁻ and SO₄²⁻ had already formed after 0.5 h, and the amounts remained nearly constant as the reaction time was increased. These results indicate that the decomposition of CF₃SO₃⁻ in **1** was complete within 0.5 h. After 6 h, the amount of F⁻ was 27.9 μmol, which corresponds to a yield of 93.6% (Table 1, entry 6). That is, almost all the fluorine in **1** (=fluorine atoms in CF₃SO₃⁻) was transformed into F⁻ ions. The amount of SO₄²⁻ after 6 h was 16.8 μmol, which indicates that 84.5% of the sulfur content in the initial **1** was transformed into SO₄²⁻. In the gas phase, a large amount of CO₂ was detected, CHF₃ was not detected, and the formation of benzene was suppressed (Fig. 3b). The amount of CO₂ in the gas phase was 1 order of magnitude

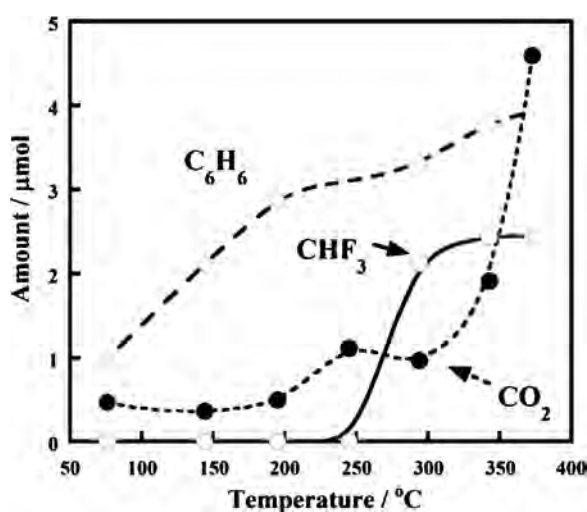


Fig. 2. Reaction-temperature dependence of the amounts of benzene, CO₂ and CHF₃ in the gas phase after the reaction of **1** in the presence of zerovalent iron. The reaction conditions were the same as those described in the caption of Fig. 1.

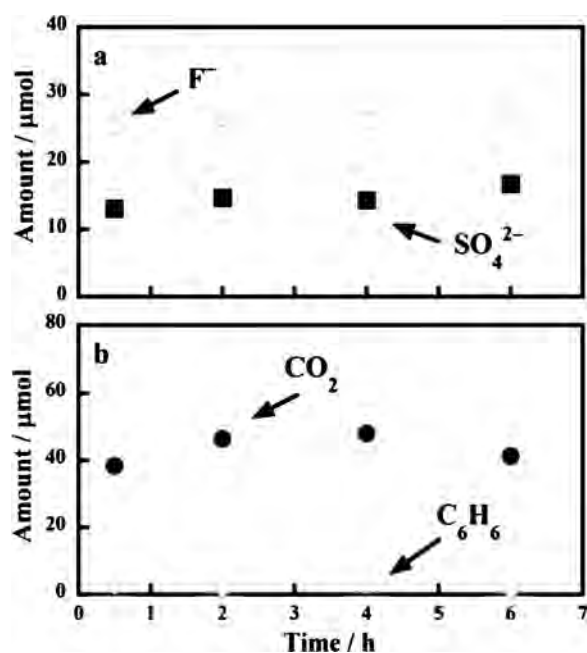


Fig. 3. Reaction-time dependence of the decomposition of **1** in the presence of O_2 at 372 °C: (a) amounts of F^- and SO_4^{2-} in the reaction solution and (b) amounts of CO_2 and C_6H_6 in the gas phase. An aqueous solution (10 mL) of **1** (9.94 μmol , 0.99 mM) was introduced into the reactor, which was pressurized with O_2 (0.60 MPa, 4.99 mmol) and heated for 0.5–6 h. After each reaction, $CF_3SO_3^-$ was not detected in the reaction solution, and CHF_3 was not detected in the gas phase.

higher than the amount formed by the reaction in the presence of zerovalent iron (compare entries 4 and 6 in Table 1). The disappearance of CHF_3 is advantageous because it is a greenhouse gas with a high global-warming potential [15].

We measured total organic carbon in the reaction solution after the reaction in the presence of O_2 for 6 h at 372 °C, under which conditions 93.6% of the fluorine content in the initial **1** was transformed to F^- ions, as described above. The total organic carbon content was measured to be 19.8 μmol . This value and the carbon content in the initial **1** (189 μmol ; calculated from the number of moles of initial **1** \times 19) indicate that 10.5% of the carbon content in the initial **1** remained in the reaction solution, although the fluorine content in the initial **1** was almost completely transformed to F^- ions.

Under this reaction condition, no product other than CO_2 (41.2 μmol) and benzene (1.03 μmol) was detected in the gas phase (Table 1, entry 6). From these data, the total carbon content after the reaction (i.e., the sum of moles of total organic carbon in the reaction solution and moles of carbon in CO_2 and benzene in the gas phase) was calculated to be 67.2 μmol , whereas the carbon content in the initial **1** was 189 μmol . That is, the carbon recovery was 35.6%. After the reaction, the pH value of the reaction solution was 2.6, which indicates that some portion of the formed CO_2 remained in the reaction solution. Furthermore, a solid residue (\sim 1.0 mg), which was tightly attached on the bottom and wall of the gold vessel in the reactor, was present after the reaction. These

Table 2
Decomposition of **2** in subcritical water under various reaction conditions.^a

| Entry | Added gas | Reducing agent | Temp. (°C) | Press. (MPa) | Remaining $CF_3SO_3^-$ (μmol) [ratio (%)] | F^- (μmol) [yield (%)] | CO_2 (μmol) | CHF_3 (μmol) |
|-------|-----------|----------------|------------|--------------|--|---------------------------------------|----------------------------|-----------------------------|
| 1 | Ar | Fe | 343 | 15.5 | 8.55 [84.7] | 4.12 [13.6] | 3.58 | 0.32 |
| 2 | Ar | None | 343 | 15.4 | 9.48 [93.9] | 0.29 [1.0] | Trace | n.d. |
| 3 | O_2 | None | 343 | 15.4 | 9.91 [98.1] | 0.19 [0.6] | Trace | n.d. |
| 4 | Ar | Fe | 373 | 22.1 | 4.80 [47.5] | 5.96 [19.7] | 5.82 | n.d. |
| 5 | O_2 | None | 373 | 21.6 | 2.31 [22.9] | 17.3 [57.1] | 17.4 | n.d. |

^a Initial amount of **2**, 10.1 μmol ; reaction solution volume, 10 mL; reaction time, 6 h.

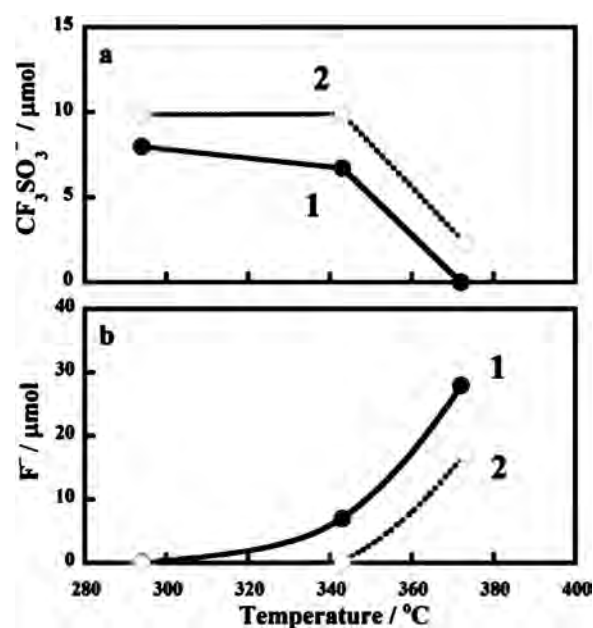


Fig. 4. Reaction-temperature dependence of the decomposition of **1** and **2** in the presence of O_2 : (a) amount of $CF_3SO_3^-$ and (b) amount of F^- in the reaction solution. An aqueous solution (10 mL) of **1** (9.94 μmol , 0.99 mM) or **2** (10.1 μmol ; 1.01 mM) was introduced into the reactor, which was pressurized with O_2 (0.60 MPa, 4.99 mmol) and heated at the desired temperature for 6 h.

results suggest that the most of the rest of carbon atoms were present in the solid residue.

3.3. Effect of the cation on decomposition of the anion

We also carried out reactions of **2**, which has a potassium ion instead of the organic cation in **1**, and the results revealed that the reactivity of $CF_3SO_3^-$ in **2** was lower than that in **1** under all of the tested reaction condition. For example, when the reaction of **2** was carried out at 343 °C for 6 h in subcritical water under argon without any additive, 93.9% of the initial $CF_3SO_3^-$ remained and only a small amount of F^- formed (1.0% yield; Table 2, entry 2). In contrast, when **1** was subjected to the same reaction conditions, 88.5% of the $CF_3SO_3^-$ remained after the reaction, and the F^- yield was 10.6% (Table 1, entry 2). When the reaction of **2** was carried out in the presence of O_2 at 343 °C for 6 h, almost no decomposition of $CF_3SO_3^-$ occurred (Table 2, entry 3), whereas when **1** was used, 67.5% of the $CF_3SO_3^-$ remained, and the F^- yield was 23.5% (Table 1, entry 3). Although the decomposition of $CF_3SO_3^-$ in **2** was somewhat increased by addition of zerovalent iron (Table 2, entry 1), the F^- yield (13.6%) was considerably lower than that for **1** under the same conditions (58.4%, entry 1 in Table 1).

Comparison of the plots of the temperature dependences of the decompositions of **2** and **1** in subcritical water at 373 °C in the presence of O_2 (Fig. 4) revealed that compared to the reaction of **1**, the reaction of **2** consumed less $CF_3SO_3^-$ (Fig. 4a) and generated less F^- at each temperature (Fig. 4b). When the reaction of **2** was carried out at 373 °C for 6 h, 22.9% of the initial $CF_3SO_3^-$ remained,

and the F⁻ yield was 57.1% (Table 2, entry 5). In contrast, when **1** was used, almost complete decomposition of CF₃SO₃⁻ to F⁻ ions was achieved (Table 1, entry 6). These results clearly indicate that the cation affected the reactivity of the anion.

4. Conclusions

We investigated the decomposition of **1** in subcritical water in the presence of an iron-based reducing agent (zerovalent iron or FeO) or an oxidizing agent (O₂). Addition of zerovalent iron enhanced the decomposition of the anionic moiety (CF₃SO₃⁻): when the reaction was carried out in the presence of zerovalent iron at 373 °C for 6 h, the F⁻ yield reached 74.4%. Simultaneously, CHF₃ and benzene were produced in the gas phase. The oxidative decomposition of **1** in the presence of O₂ increased the extent of decomposition of CF₃SO₃⁻: when the reaction was carried out in the presence of O₂ at 372 °C for 6 h, the F⁻ yield reached 93.6%, indicating that almost all the fluorine atoms in CF₃SO₃⁻ had been transformed into F⁻ ions. Furthermore, the formation of CHF₃ and benzene was suppressed by the use of O₂. Although the CF₃SO₃⁻ in **1** was almost completely decomposed to F⁻ ions in the presence of O₂, the CF₃SO₃⁻ in potassium salt **2** was more stable: the F⁻ yield was only 57.1% after reaction in the presence of O₂ at 373 °C for 6 h. This observation clearly indicates that the cation affected the reactivity of the anion.

Acknowledgment

This work was supported by grants from the Japan Society from the Promotion of Science (nos. 24310061 and 15H02841).

References

- [1] A.R. Pawloski, P.F. Nealey, W. Conley, J. Photopolym. Sci. Technol. 15 (2002) 731–739.
- [2] J.P. Giesy, K. Kannan, Environ. Sci. Technol. 36 (2002) 146A–152A.
- [3] L. Ahrens, J. Environ. Monitor 13 (2011) 20–31.
- [4] UNEP, Fourth Meeting of the Conference of the Parties of the Stockholm Convention, Geneva, 4–8 May 2009, United Nations Environment Programme, 2009 <http://chm.pops.int/Convention/COPs/Meetings/COP4/tabid/404/mct/ViewDetails/EventModID/870/EventID/23/xmid/1673/language/en-US/Default.aspx/>.
- [5] UNEP, Report of the Persistent Organic Pollutants Review Committee on the Work of its Sixth Meeting, United Nations Environment Programme, 2011 <http://chm.pops.int/TheConvention/POPsReviewCommittee/Guidance/tabid/345/Default.aspx/>.
- [6] R.R. Dammel, G. Pawlowski, A. Romano, F.M. Houlihan, W.K. Kim, R. Sakamuri, D. Abdallah, M. Padmanaban, M. Rahman, D. McKenzie, J. Photopolym. Sci. Technol. 18 (2005) 593–602.
- [7] P.G. Jessop, W. Leitner (Eds.), Chemical Synthesis Using Supercritical Fluids, Wiley-VCH, Weinheim, 1999.
- [8] S.B. Hawthorne, A.J.M. Lagadec, D. Kalderis, A.V. Lilke, D.J. Miller, Environ. Sci. Technol. 34 (2000) 3224–3228.
- [9] S.I. Kawasaki, T. Oe, N. Anjoh, T. Nakamori, A. Suzuki, K. Arai, Process Saf. Environ. Prot. 84 (2006) 317–324.
- [10] H. Hori, Y. Nagaoka, A. Yamamoto, T. Sano, N. Yamashita, S. Taniyasu, S. Kutsuna, I. Osaka, R. Arakawa, Environ. Sci. Technol. 40 (2006) 1049–1054.
- [11] J.W. Tester, H.R. Holgate, F.J. Armellini, P.A. Webley, W.R. Killilea, G.T. Hong, H.E. Barner, in: D.W. Tedder, F.G. Pohland (Eds.), Emerging Technologies in Hazardous Waste Management III, ACS Symposium Series 518, American Chemical Society, 1993, pp. 35–76.
- [12] L. Broussard, J. Phys. Chem. 73 (1969) 1848–1854.
- [13] S. Stølen, R. Glöcker, F. Grønvold, Thermochim. Acta 256 (1995) 91–106.
- [14] H. Hori, Y. Noda, A. Takahashi, T. Sakamoto, Ind. Eng. Chem. Res. 52 (2013) 13622–13628.
- [15] IPCC, Fifth Assessment Report: Climate Change 2013: Working Group I: The Physical Science Basis, Intergovernmental Panel on Climate Change, Geneva, Switzerland, 2013, <http://www.climatechange2013.org/>.



Contents lists available at ScienceDirect

Separation and Purification Technology

journal homepage: www.elsevier.com/locate/seppur

Efficient photochemical recovery of rhenium from aqueous solutions



Hisao Hori^{a,*}, Yuta Yoshimura^a, Takafumi Otsu^a, Kotomi Kume^a, Yuki Mitsumori^a, Shuzo Kutsuna^b, Kazuhide Koike^b

^a Department of Chemistry, Faculty of Science, Kanagawa University, 2946 Tsuchiya, Hiratsuka, Kanagawa 259-1293, Japan

^b National Institute of Advanced Industrial Science and Technology (AIST), AIST Tsukuba West, 16-1 Onogawa, Tsukuba 305-8569, Japan

ARTICLE INFO

Article history:

Received 7 February 2015

Received in revised form 28 September 2015

Accepted 5 October 2015

Available online 9 October 2015

Keywords:

Perrhenate
Hydrometallurgy
Acetone
Precipitate
Reduction

ABSTRACT

Recovery of rhenium from aqueous solutions by photoinduced-electron transfer from an electron donor to excited-state ReO_4^- is reported for the first time. Specifically, irradiation of aqueous ReO_4^- in the presence of 2-propanol as the electron donor efficiently decreased the ReO_4^- concentration in the solution and resulted in formation of a precipitate consisting of amorphous ReO_2 and ReO_3 and formation of acetone by oxidation of 2-propanol. After 19 h of irradiation, ReO_4^- had completely disappeared, and 89.1% of the initial rhenium content was recovered in the collected precipitate. Although an induction period prior to the decrease in the ReO_4^- concentration was observed, the induction period could be eliminated by introduction of acetone to the reaction system, which afforded 94.7% recovery of rhenium within 6 h of irradiation. The acceleration of the reaction induced by acetone could be explained by an increase in the light absorption of ReO_4^- via precomplexation with acetone, which resulted in an increase in the emission intensity from the excited rhenium species.

© 2015 Elsevier B.V. All rights reserved.

1. Introduction

Rhenium, which is a minor metal in the Earth's crust and has a high melting point (3180 °C, second only to that of tungsten), has vital applications in industry. Rhenium used in superalloys for turbine blades for aircraft and thermal power plants accounts for 70% of total rhenium consumption, and rhenium in petroleum reforming catalysts for the production of lead-free high-octane gasoline accounts for 20% [1]. The rest is used in electronic parts such as electrical contacts, electron targets, and heating elements. The utility of rhenium for these applications arises from its high heat resistance, high corrosion resistance, and high hardness [2]. In addition, some rhenium compounds have unique catalytic activities: for example, rhenium oxides catalyze the selective oxidation of methanol to methylal (dimethoxymethane) [3], and rhenium diimine complexes catalyze CO_2 reduction to CO under visible-light irradiation [4]. Increases in aircraft production (approximately 36,770 new airplanes will be built from 2014 to 2033, owing to mainly the rapid growth of low-cost carriers [5]) and new applications of rhenium can be expected to increase the global demand for this metal.

Molybdenum and copper ores are the sole economically viable mineral sources of rhenium, which is obtained as a by-product of

the metallurgical processing of these ores; specifically, the rhenium component is oxidized to volatile Re_2O_7 in the flue dusts and then collected in aqueous solution in the form of perrhenate ion (ReO_4^-) [6–10]. In addition, during processing of secondary raw materials (spent catalysts and alloys), the rhenium content is also transformed into ReO_4^- in aqueous solutions [7,11–13]. The recovery of ReO_4^- from aqueous solutions is difficult because of its low concentration and high solubility at all pH values. Reported techniques for effectively recovering rhenium (present as ReO_4^-) from aqueous solutions include adsorption on ion exchange resins [7,9,13,14], solvent extraction with amines [15–17], precipitation through the formation of a less-water-soluble zinc complex [12], adsorption on activated carbon [18], and adsorption on biomaterials such as algae [19]. Among these techniques, ion exchange and solvent extraction have been extensively studied and have been introduced in real-world industrial processes [10,16]. However, these techniques require additional steps to separate the collected ReO_4^- from resins or solvent, as well as recrystallization to precipitate a salt (typically NH_4ReO_4 , generated by addition of NH_4OH), and the mother liquor generally contains a non-negligible amount of ReO_4^- (4–35 g/L as NH_4ReO_4) [12]. Finally, the collected precipitate is heated at 700–800 °C in the presence of hydrogen gas to produce metallic rhenium.

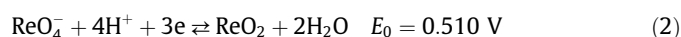
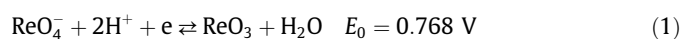
The emission of light from the excited state of ReO_4^- has never been reported, although the anion is known to have an absorption maximum around 249 nm in water [20], and emissions from

* Corresponding author.

E-mail address: h-hori@kanagawa-u.ac.jp (H. Hori).

tetravalent ReCl_6^{2-} and ReBr_6^{2-} have been reported [21]. We speculated that if aqueous ReO_4^- could emit with a lifetime at least on the order of nanoseconds, photoinduced electron transfer from an electron donor to the excited state of the anion might result in the formation and precipitate of an insoluble reduced rhenium species (such as ReO_3), which could easily be separated from the aqueous solution (Scheme 1).

Such a reaction scheme would eliminate the need for further separation and recrystallization steps. With this idea in mind, we investigated the photochemical reactions of ReO_4^- in the presence of several electron donors. The overall reduction reactions of ReO_4^- may be represented by Eqs. (1) and (2) (E_0 : standard reduction potentials) [22], if the products are ReO_3 and ReO_2 .



Herein, we report an effective method for photochemical recovery of rhenium from aqueous solutions of ReO_4^- , although the optimum scheme ended up being somewhat different from the scheme that we initially envisioned.

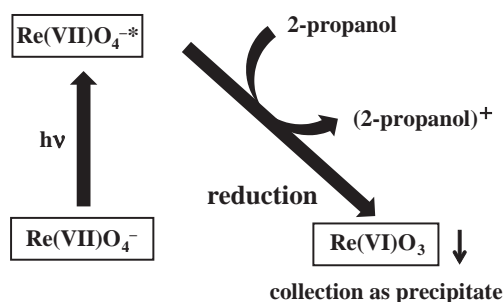
2. Experimental

2.1. Materials

Potassium perrhenate (99.99%) and rhenium (IV) oxide (ReO_2 , 99.7%) were purchased from Sigma–Aldrich (St. Louis, MO, USA). Other reagents were obtained from Wako Pure Chemical Industries (Osaka, Japan). Argon (99.99%) was purchased from Taiyo Nippon Sanso (Tokyo, Japan).

2.2. Photochemical procedures

A cylindrical Pyrex photochemical cell (22-mL volume) equipped with a quartz window and a rubber septum was used for the photochemical reactions. The ionic strength of the reaction solution was maintained by the addition of NaClO_4 . In a typical run with 2-propanol as the electron donor, the cell was charged with an aqueous solution (10 mL) containing ReO_4^- (103.7 μmol ; 10.37 mM, as the potassium salt), 2-propanol (0.50 M), NaClO_4 (0.10 M) and a poly(tetrafluoroethylene) stir bar. The pH of the solution was 5.2. The solution was saturated with argon gas, and the cell was sealed with a rubber septum, placed in a water bath, and irradiated with UV–visible light (220–460 nm) from a 200 W xenon–mercury lamp (L2001-01L; San-Ei Electric, Osaka, Japan) while stirring. The light from the lamp was introduced into an optical-quartz glass fiber, passed to a quartz cell containing pure water to cut the infrared light, and then introduced into the cell.



Scheme 1. Postulated reaction scheme for photochemical recovery of rhenium from aqueous solution.

The irradiance at the center of the light spot on the sample was 98 mW cm^{-2} , as measured with a UV detector (UVD-S254, Ushio, Tokyo, Japan; sensitive wavelength, 220–310 nm). The reaction temperature was kept constant at 20 °C. After a specified time passed, the cell was placed in an argon-filled globe bag and opened, and the reaction mixture was centrifuged to separate the reaction solution and the precipitate. The supernatant was subjected to ion chromatography, inductively coupled plasma atomic emission spectroscopy (ICP-AES), and headspace gas chromatography–mass spectrometry (GC/MS). The collected precipitate was washed with pure (Milli-Q) water under an argon atmosphere, dried under vacuum overnight, and subjected to X-ray diffractometry (XRD), X-ray photoelectron spectroscopy (XPS), transmission electron microscopy, and ICP-AES. The XRD, XPS, and transmission electron microscopy measurements were performed in the absence of air whenever possible.

2.3. Analysis

The ReO_4^- concentrations in the reaction solutions were quantified with an ion-chromatography system (IC-2001, Tosoh, Tokyo, Japan) consisting of an automatic sample injector (30- μL injection volume), a degasser, a pump, a separation column (TSKgel IC-Anion-PW_{XL}, 4.6 mm i.d., 3.5-cm length, Tosoh), a column oven (40 °C), and a conductivity detector equipped with a suppressor device. The mobile phase was an aqueous solution containing NaHCO_3 (1.7 mM), Na_2CO_3 (1.8 mM), and acetonitrile (20 vol.%); and the flow rate was 0.8 mL min^{-1} . The detection limit for ReO_4^- was 78 $\mu\text{g L}^{-1}$, calculated from a signal-to-noise ratio of 3. The total rhenium concentrations in the reaction solutions were quantified by ICP-AES (SPS-3500, SII Nanotechnology, Tokyo, Japan).

To elucidate the fate of 2-propanol, we analyzed the reaction solutions with a headspace GC/MS system consisting of an automatic headspace sampler (HP7694, Agilent Technologies, Palo Alto, CA, USA) and a GC/MS instrument (GC6890N, Agilent) equipped with a fused-silica capillary column (PorabOND-Q, Agilent). The carrier gas was helium, and the flow rate was 1.0 mL min^{-1} . The sample solution was heated at 80 °C for 1 h in the headspace sampler, and an aliquot of the gas phase (1.0 mL) was introduced into the GC/MS system in split mode (ratio, 30/1). The oven temperature was kept at 50 °C for 2 min, raised to 200 °C at a rate of 10 °C min^{-1} , and held at that temperature for 5 min. Analyses were conducted in full-scan mode (m/z 10–100).

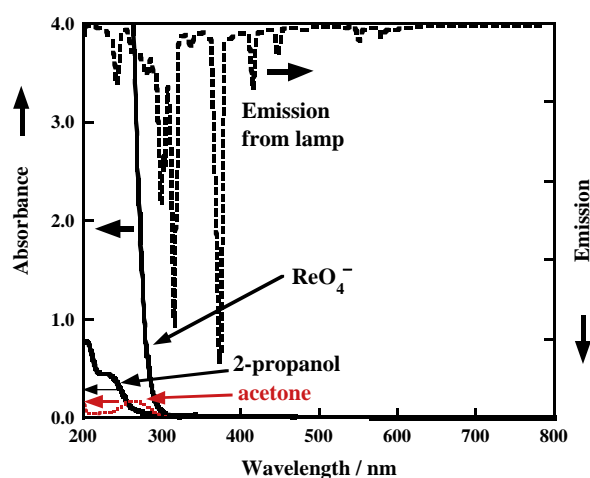


Fig. 1. Wavelength distribution for the absorptions of ReO_4^- (10.37 mM in water), 2-propanol (0.50 M in water) and acetone (9.0 mM in water) and the emission from the xenon–mercury lamp. The path length for the measurement of the absorption spectra was 1.0 cm. Effect of acetone on the reaction is discussed in Section 3.5.

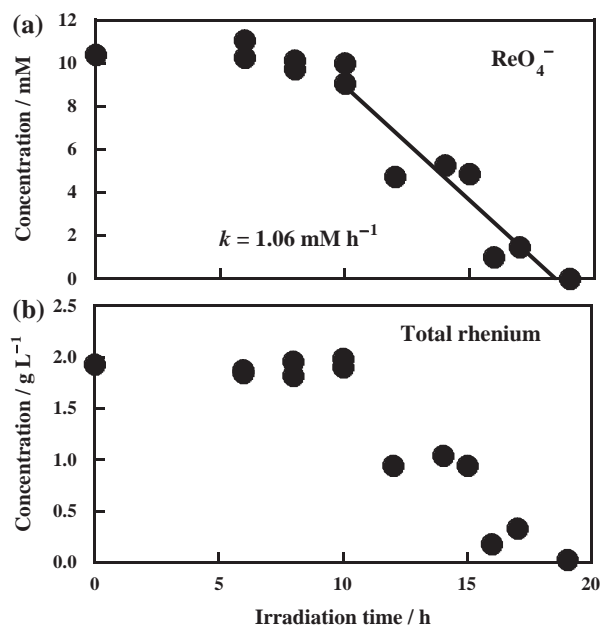


Fig. 2. Irradiation-time dependence of (a) ReO_4^- concentration and (b) total rhenium concentration in the reaction solution. An aqueous solution (10 mL) containing ReO_4^- (10.37 mM), 2-propanol (0.50 M), and NaClO_4 (0.10 M) was irradiated with a xenon–mercury lamp under argon.

The XPS and XRD measurements of the collected precipitate were carried out at Nissan Arc (Yokosuka, Japan) with, respectively, a Quantum-2000 instrument with Al $K\alpha$ radiation (Physical Electronics, Eden Prairie, MN, USA) and a SmartLab 9kW instrument with Cu $K\alpha$ radiation (Rigaku, Tokyo, Japan). The rhenium content in the precipitate was quantified by ICP-AES after dissolution of the precipitate in aqua regia. The surface of the precipitate particles was observed by transmission electron microscopy at Nissan Arc with a Tecnai G2 F20 instrument (FEI, Hillsboro, OR, USA).

Emission lifetime and time-resolved spectra were measured with a Temprow Type-AKK1 fluorescence lifetime spectrofluorometer (Horiba, Kyoto, Japan) by means of a time-correlated single-photon counting method. As the excitation light source, the third-harmonic wave of a Tsunami Ti:sapphire laser with a Spitfire Regenerative Amplifier (266 nm and 1 kHz repetition rate, Spectra-Physics, Santa Clara, CA, USA) and a Horiba NanoLED-265 (266 nm and 1 MHz repetition rate) were employed for the emission decay and time-resolved emission spectral measurements, respectively. The aqueous ReO_4^- solution (1.0 mM, potassium salt) was sealed

in a $1.0 \times 1.0 \times 4.0$ cm quartz cell after argon had been bubbled through the solution for 20 min, and the measurement was conducted at 298 K.

3. Results and discussion

3.1. Photochemical reactions of ReO_4^-

In our reaction conditions, an aqueous solution containing ReO_4^- and 2-propanol was irradiated with UV–visible light from a xenon–mercury lamp through a water filter. The wavelength distributions of the absorptions of ReO_4^- and 2-propanol (at the concentrations used for subsequent photochemical reactions) and the emission from the lamp are shown in Fig. 1. Under these conditions, the lamp emits mainly 220–460-nm light. Because ReO_4^- strongly absorbs light from the deep-UV region to 310 nm (the absorbance at 255 nm exceeds 4) and 2-propanol absorbs only weakly at this region (the absorbance of 2-propanol at 255 nm is 0.16), ReO_4^- was the predominant absorbing species under our reaction conditions.

Investigation of the irradiation-time dependence of the concentration of ReO_4^- in the presence of 2-propanol (Fig. 2(a)) revealed that the ReO_4^- concentration in the reaction solution showed no sign of decreasing until approximately 10 h after the start of irradiation, which seemed to indicate that ReO_4^- was not reactive under these conditions. However, to our surprise, the concentration of ReO_4^- began to decrease monotonously after 10 h, with a zero-order rate constant of 1.06 mM h^{-1} , and a dark purple precipitate formed simultaneously. After 19 h, the concentration of ReO_4^- decreased to below the detection limit of the ion chromatography. We also monitored the total rhenium concentration in the reaction solution to examine the possibility that some rhenium-containing species other than ReO_4^- remained in the reaction solution (Fig. 2(b)), and we found that the irradiation-time dependence of the total rhenium concentration was similar to that of the ReO_4^- concentration (Fig. 2(a)). After 19 h, the total rhenium concentration decreased to 0.03 g L^{-1} (the initial concentration was 1.93 g L^{-1}); that is, 98.4% of the rhenium initially present in the solution had been removed.

We next carried out photochemical reactions of ReO_4^- (10.37 mM) with various combinations of light irradiation and electron donors (Table 1). Virtually no reaction occurred in the absence of either light irradiation or 2-propanol (entries 1 and 2, respectively). In contrast, reaction in the presence of both light irradiation and 2-propanol (entry 3) efficiently decreased the concentration of ReO_4^- , clearly indicating that the combination of light irradiation and 2-propanol was required for removal of ReO_4^- .

Table 1
Effects of reaction conditions on remaining ReO_4^- and total rhenium.^a

| Entry | Initial ReO_4^- (mM) | Light | Electron donor ^b | Remaining ReO_4^- (mM) [ratio (%)] | Remaining total rhenium (g L^{-1}) |
|-------|-------------------------------|---------|-----------------------------|---|---|
| 1 | 10.37 | Absent | 2-Propanol | 10.37 [100] | 1.86 |
| 2 | 10.37 | Present | Absent | 10.10 [97.4] | 1.87 |
| 3 | 10.37 | Present | 2-Propanol | n.d. ^c [0] | 0.03 |
| 4 | 10.37 | Present | 1-Propanol | 10.37 [100] | – ^d |
| 5 | 10.37 | Present | 1-Butanol | 10.37 [100] | – ^d |
| 6 | 10.37 | Present | 2-Butanol | 9.80 [94.5] | – ^d |
| 7 | 10.37 | Present | Glycerin | 10.21 [98.5] | – ^d |
| 8 | 10.37 | Present | Sucrose | 10.27 [99.0] | – ^d |
| 9 | 10.37 | Present | Triethanolamine | 6.68 [64.4] | – ^d |
| 10 | 5.18 | Present | 2-Propanol | n.d. ^c [0] | 5×10^{-3} |
| 11 | 2.59 | Present | 2-Propanol | n.d. ^c [0] | 3×10^{-3} |

^a Reaction time = 19 h.

^b Initial concentration = 0.50 M.

^c n.d. = not detected.

^d Not measured.

We also attempted to remove ReO_4^- by using several other electron donors (1-propanol, 1-butanol, 2-butanol, glycerin, sucrose, and triethanolamine; entries 4–9). With these electron donors, almost no precipitate formed, although when triethanolamine was used, the ReO_4^- concentration decreased to 64.4% of the initial concentration after 19 h, and the solution turned violet (entry 9). These results suggest that a unique interaction occurs between ReO_4^- and 2-propanol and causes the decrease in the ReO_4^- concentration and the formation of the precipitate.

Photochemical removal of ReO_4^- using 2-propanol was also effective at lower initial ReO_4^- concentrations (5.18 and 2.59 mM, entries 10 and 11); after 19 h, the ReO_4^- concentration was below the detection limit.

In the above reactions using 2-propanol (0.50 M) and ReO_4^- (10.37 mM), the pH value of the initial reaction solution (before light irradiation) was 5.2. When the initial pH value was changed to 10.9 by use of NaOH, the ReO_4^- concentration after 19 h irradiation was decreased to 0.46 mM, which corresponds to 4.4% of the initial concentration (10.37 mM). This result indicates that ReO_4^- was efficiently removed from the basic solution, although the remaining ReO_4^- ratio was somewhat higher than that obtained at pH of 5.2 (the remaining ratio of ReO_4^- was 0%).

3.2. Fate of 2-propanol

We expected that in the present reaction system, ReO_4^- would be reduced to ReO_3 while 2-propanol was oxidized (Scheme 1). To elucidate the fate of 2-propanol during the reaction, we analyzed the reaction solutions by headspace GC/MS, which revealed the presence of acetone. A plot of the irradiation-time dependence of the acetone concentration (Fig. 3) showed that acetone formed after 6 h and the acetone concentration increased monotonously with increasing irradiation time (rate constant, 0.62 mM h^{-1}) while the concentration of ReO_4^- decreased (Fig. 2(a)). After 19 h, at which point ReO_4^- had disappeared from the reaction solution (Fig. 2(a)), the acetone concentration was 8.90 mM. These results clearly indicate that ReO_4^- reduction was accompanied by 2-propanol oxidation to acetone.

3.3. Consecutive reaction of ReO_4^-

After the ReO_4^- had completely disappeared (Fig. 2(a)), the resulting solution was still reactive, and additional runs were

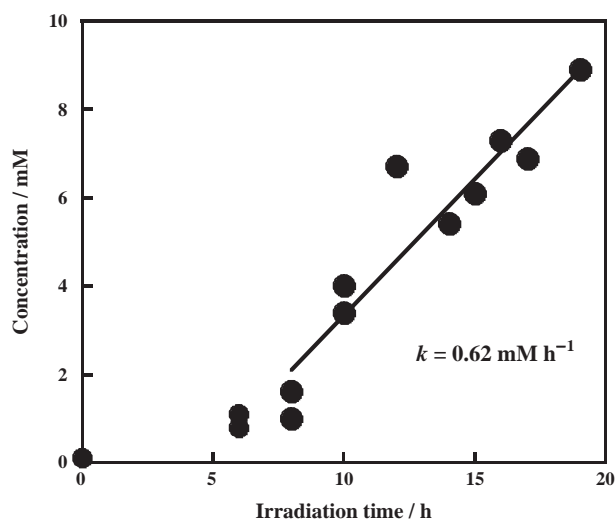


Fig. 3. Irradiation-time dependence of acetone concentration in the reaction solution. The experimental conditions are described in the caption of Fig. 2.

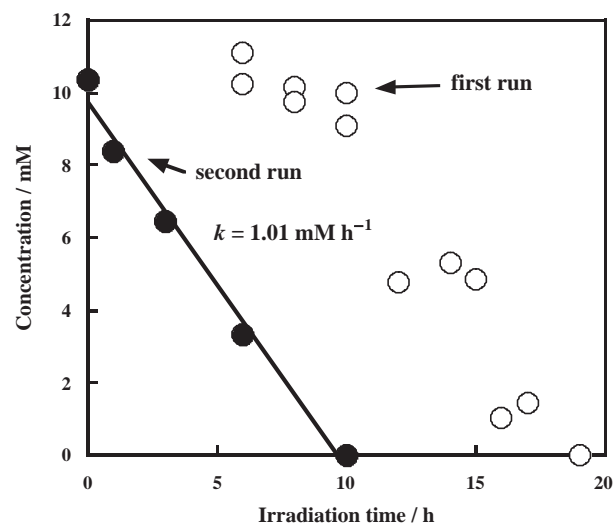


Fig. 4. Comparison of the irradiation-time dependences of ReO_4^- concentration during the first and second runs. For the second run, an additional $103.7 \mu\text{mol}$ of ReO_4^- (potassium salt) was introduced to the reaction mixture after 19 h of irradiation at which point the initial charge of ReO_4^- had completely disappeared. The data for the first run are the same as those in Fig. 2(a).

therefore possible. When an additional $103.7 \mu\text{mol}$ of ReO_4^- (potassium salt) was introduced to the reaction mixture (without removal of precipitate formed during the initial 19 h irradiation period), the concentration of ReO_4^- , which was 10.37 mM at the start of the second run, again decreased monotonously upon irradiation (rate constant, 1.01 mM h^{-1}), falling below the detection limit after 10 h of irradiation (Fig. 4, second run). Note that an induction period prior to the decrease in ReO_4^- , which was observed in the first run, was not observed in the second run. The rate constant for the decrease in ReO_4^- concentration during the second run (1.01 mM h^{-1}) was similar to that observed after the induction period in the first run (1.06 mM h^{-1}).

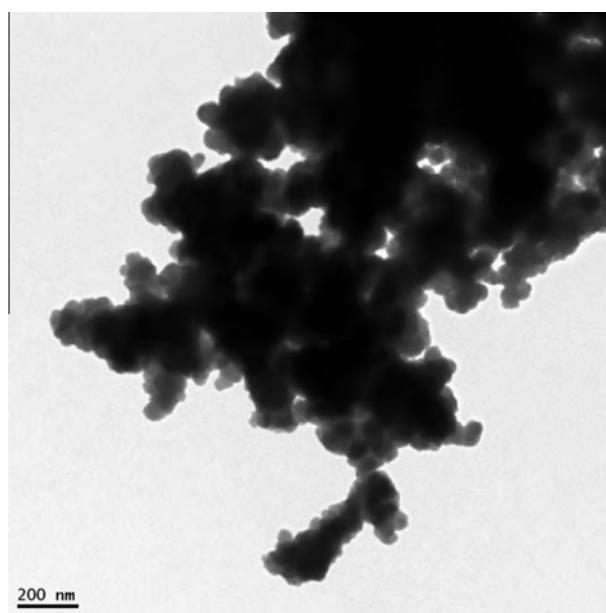


Fig. 5. Transmission electron microscopy image of the precipitate collected after the photochemical reaction of ReO_4^- in the presence of 2-propanol for 19 h. The reaction conditions are described in the caption of Fig. 2.

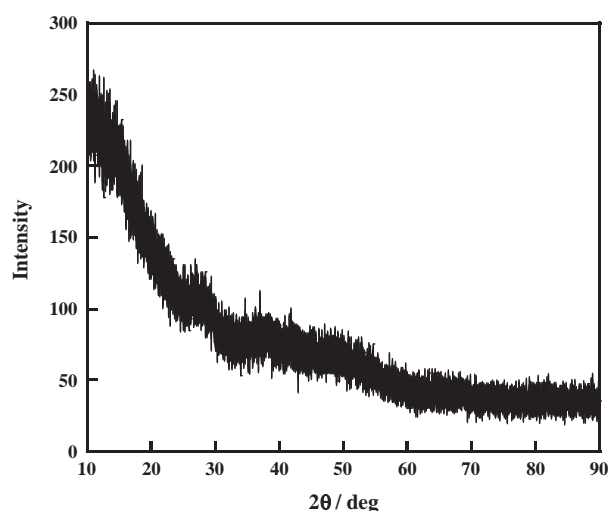


Fig. 6. XRD pattern of the precipitate collected after the photochemical reaction of ReO_4^- in the presence of 2-propanol for 19 h. The reaction conditions are described in the caption of Fig. 2.

3.4. Characterization of the precipitate

The precipitate formed after the photochemical reaction in the presence of 2-propanol for 19 h was washed with pure water under argon, dried under vacuum, and then characterized. The weight of the collected precipitate (27.0 mg) and the proportion of rhenium (63.7 wt%, as quantified by ICP-AES) indicate that 89.1% of the rhenium content in the initial ReO_4^- was recovered in the collected precipitate after 19 h of reaction. The precipitate consisted of aggregated particles of a few micrometers, and the primary particle size was approximately 100 nm (Fig. 5). The absence of any diffraction peaks in the XRD pattern of the precipitate indicates that the precipitate is amorphous (Fig. 6). XPS measurement revealed that the precipitate, which we initially assumed to be Re(VI)O_3 (Scheme 1), consisted of Re(IV) and Re(VI) in an approximately 10:3 molar ratio (Fig. 7). Furthermore, the atomic ratio of rhenium-bound oxygen to rhenium was estimated to be 2.4. These results indicate that the particle surface consisted of an approximately 10:3 mixture of ReO_2 and ReO_3 ; that is, most of the ReO_4^- was reduced to ReO_2 .

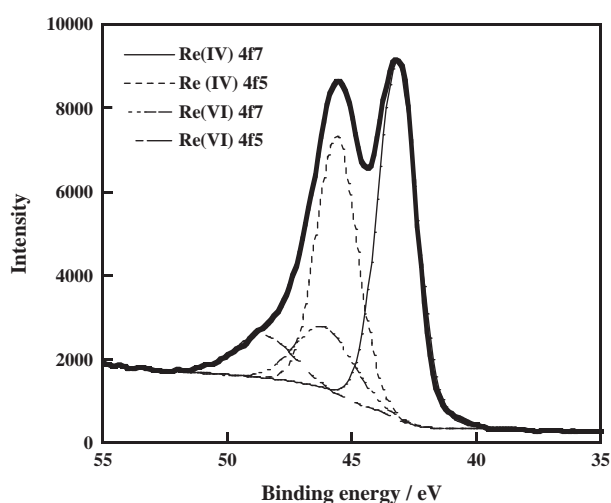


Fig. 7. XPS spectrum [Re(4f) region] of the precipitate collected after the photochemical reaction of ReO_4^- in the presence of 2-propanol for 19 h. The reaction conditions are described in the caption of Fig. 2.

3.5. Reactions in the presence of added acetone

As described above, the concentration of ReO_4^- did not decrease until 10 h after the start of irradiation (Fig. 2(a)); that is, there was an induction period. Because induction periods are undesirable in real-world applications, we tried to shorten the induction period by various methods. As shown in Fig. 4, if additional ReO_4^- was introduced to the reaction mixture after the initial charge of ReO_4^- had been completely consumed, induction period did not appear in the second run. The only difference in initial conditions between the first and the second runs was that acetone and a precipitate including ReO_2 and ReO_3 were present in the second run. To determine how the presence of the precipitate affected the induction period, we carried out a reaction in the presence of finely powdered ReO_2 (22 mg) in addition to the usual aqueous solution containing ReO_4^- , 2-propanol, and NaClO_4 (the concentrations were the same as those described in the caption of Fig. 2). After irradiation for 6 h, the concentration of ReO_4^- had not decreased at all, suggesting that it was not the precipitate but acetone that was responsible for initiating the decrease in the ReO_4^- concentration. To confirm this, we carried out photochemical reactions of ReO_4^- and 2-propanol in the presence of acetone at several concentrations (Fig. 8). As expected, the induction period became shorter as the initial acetone concentration was increased. At an acetone concentration of 9.02 mM, which is comparable to the initial ReO_4^- concentration (10.37 mM), there was no induction period, and the concentration of ReO_4^- fell below the detection limit within 6 h of the start of irradiation. Because acetone absorbs light very little compared with ReO_4^- (Fig. 1), ReO_4^- is the predominant absorbing species even though acetone is present. Increasing the initial acetone concentration further (to 12.0 mM) did not have a noticeable effect on the time profile of the ReO_4^- concentration. These results suggest that some interaction, such as precomplexation between ReO_4^- (or its excited state) and acetone, initiated the decrease in the ReO_4^- concentration. When the reaction was carried out in the presence of 9.02 mM of acetone for 6 h, the weight (28.7 mg) and the proportion of rhenium (63.7 wt%) of the collected precipitate indicate that 94.7% of the rhenium content in the initial ReO_4^- was recovered in the collected precipitate. We also carried out a photochemical reaction in the presence of acetone without 2-propanol. Under these conditions, 99.8% of the initial ReO_4^- remained after 6 h of irradiation, and no precipitate formed.

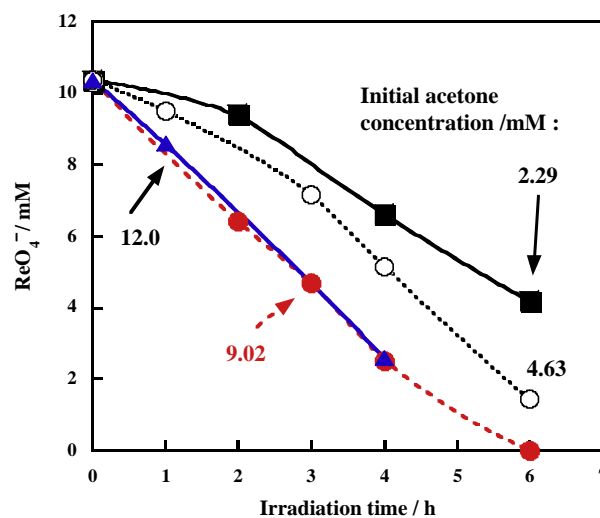


Fig. 8. Irradiation-time dependences of ReO_4^- concentration in reaction solutions containing acetone at initial acetone concentrations of 2.29, 4.63, 9.02, and 12.0 mM. The reaction conditions are described in the caption of Fig. 2, except that the reactions were performed with added acetone.

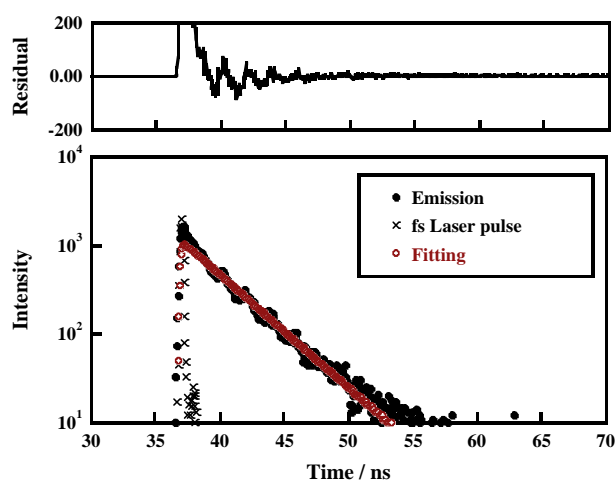


Fig. 9. Emission decay profile of ReO_4^- in water (1.0 mM).

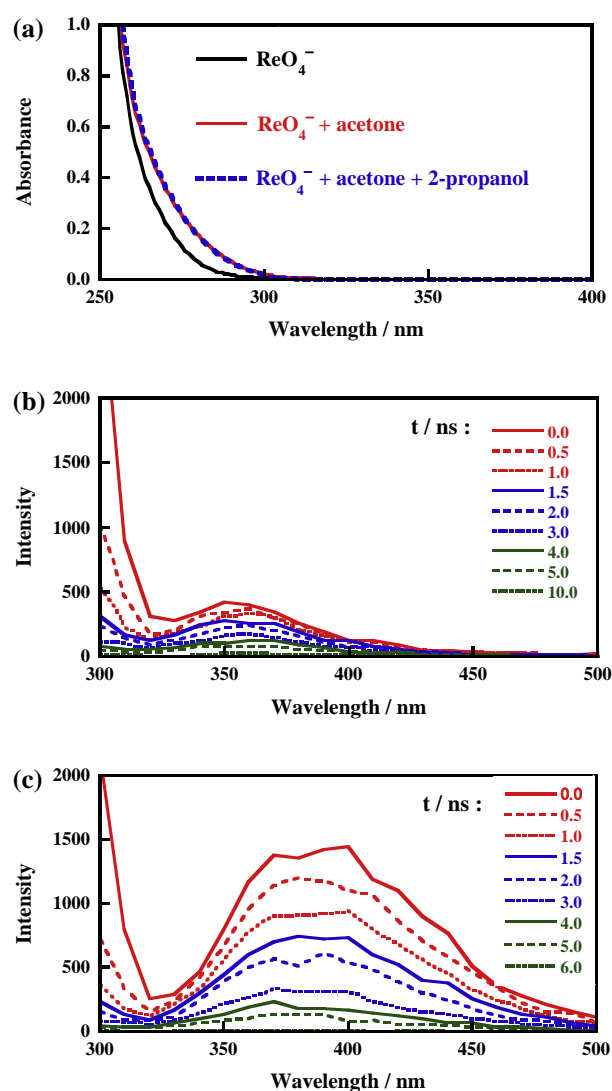


Fig. 10. (a) UV absorption spectra of an aqueous solution involving ReO_4^- (1.0 mM), an aqueous solution involving ReO_4^- (1.0 mM) and acetone (9.0 mM), and an aqueous solution involving ReO_4^- (1.0 mM), acetone (9.0 mM) and 2-propanol (0.50 M); (b) time-resolved emission spectra of aqueous solution involving ReO_4^- (1.0 mM); (c) time-resolved emission spectra of aqueous solution involving ReO_4^- (1.0 mM) and acetone (9.0 mM). In panel b and panel c, 't' means time after laser irradiation.

These results indicate that acetone acted not as an electron donor to ReO_4^- but rather as a promotor for decreasing the ReO_4^- concentration.

3.6. Emission behavior of ReO_4^- and role of acetone

Finally, we investigated the emission behavior of ReO_4^- in pure water because emission from the excited state of ReO_4^- is a prerequisite for the photochemical reaction that occurred in this system. The emission decay profile of ReO_4^- is shown in Fig. 9. As expected, ReO_4^- showed an emission, and its lifetime was measured to be 3.4 ns. The time-resolved emission spectra of ReO_4^- (Fig. 10(b)) clearly show an emission maximum around 350 nm. These results are consistent with a reaction mechanism involving reduction of ReO_4^- initiated by photoinduced electron transfer to the excited state of ReO_4^- .

As described above, addition of acetone, which concentration was comparable to the initial ReO_4^- , efficiently accelerated the decrease in the ReO_4^- concentration. To clarify the role of acetone in the photochemical reaction, we measured the UV absorption spectra of the aqueous solutions involving ReO_4^- , ReO_4^- and acetone, and ReO_4^- and acetone and 2-propanol (Fig. 10(a)). Significant difference was observed between the spectrum involving ReO_4^- and the spectrum involving ReO_4^- and acetone, that is, red-shift (4–9 nm) and increase in the absorbance occurred by addition of acetone. On the other hand, the spectrum of the solution involving ReO_4^- and acetone was almost the same as that involving ReO_4^- , acetone and 2-propanol. These results strongly suggest the presence of precomplexation between ReO_4^- and acetone. Addition of acetone also affected the emission behavior of ReO_4^- . The time-resolved emission spectra of the aqueous solution involving ReO_4^- (1.0 mM) and acetone (9.0 mM) are shown in Fig. 10(c). It is clear that not only each emission maximum was red-shifted (~ 20 nm), but also the emission intensity was greatly increased in the presence of acetone (compare Fig. 10(c) and (b)). In this manner, addition of acetone causes an increase in the light absorption of ReO_4^- , which results in an increase in the emission intensity from the excited species. In other words, the concentration of excited ReO_4^- increases when acetone is present. This phenomenon may be one reason why addition of acetone accelerated the photochemical reduction of ReO_4^- to ReO_3 and ReO_2 in the presence of 2-propanol.

4. Conclusion

Recovery of rhenium from aqueous solutions by means of photoinduced electron transfer from an electron donor to excited ReO_4^- was investigated. When ReO_4^- was irradiated in the presence of 2-propanol, the concentration of ReO_4^- efficiently decreased: after 19 h, ReO_4^- completely disappeared from the reaction solution, and acetone formed as an oxidation product of 2-propanol. The disappearance of ReO_4^- was accompanied by the formation of a precipitate involving amorphous ReO_2 and ReO_3 (in 10:3 ratio on the surface) with aggregated particle size of a few micrometers and the primary particle size of approximately 100 nm. After reaction for 19 h, 89.1% of the rhenium content in the initial ReO_4^- was recovered in the collected precipitate. Other electron donors, 1-propanol, 1-butanol, 2-butanol, glycerin, sucrose, and triethanolamine, caused almost no precipitation.

Although an induction period prior to the decrease in the ReO_4^- concentration was observed, the induction period could be eliminated by introducing acetone to the initial reaction solution: when the initial acetone concentration was comparable to the initial ReO_4^- concentration, ReO_4^- completely disappeared from the reaction solution after 6 h of irradiation, and 94.7% of the rhenium content in the initial ReO_4^- was recovered in the collected precipitate.

These results indicate that acetone promoted the decrease in the ReO_4^- concentration. The acceleration of the reaction induced by acetone can be explained by an increase in the light absorption of ReO_4^- via precomplexation with acetone, which increases the emission intensity from the excited species.

The effects of coexisting chemicals on the reaction system are being investigated in our laboratory.

Acknowledgement

This work was supported in part by a Grant-in-Aid for Scientific Research from the Japan Society for the Promotion of Science (15K12248).

References

- [1] Mineral Commodity Summaries 2014, U.S. Geological Survey, Reston, 2014, <<http://minerals.usgs.gov/minerals/pubs/mcs/2014/mcs2014.pdf>> (accessed 02.02.15).
- [2] I.L. Shabalin, *Ultra-High Temperature Materials I: Carbon (Graphene/Graphite) and Refractory Metals*, Springer, Dordrecht, 2014.
- [3] Y. Yuan, Y. Iwasawa, Performance and characterization of supported rhenium oxide catalysts for selective oxidation of methanol to methylal, *J. Phys. Chem. B* 106 (2002) 4441–4449.
- [4] H. Takeda, K. Koike, T. Morimoto, H. Inumaru, O. Ishitani, Photochemistry and photocatalysis of rhenium (I) diimine complexes, *Adv. Inorg. Chem.* 63 (2011) 137–186.
- [5] Long-term forecast, Boeing Company, Arlington, <<http://www.boeing.com/boeing/commercial/cmo/>> (accessed 02.02.15).
- [6] J.D. Lessard, D.G. Gribbin, L.N. Shekhter, Recovery of rhenium from molybdenum and copper concentrates during the looping sulfide oxidation process, *Int. J. Refract. Met. Hard Mater.* 44 (2014) 1–6.
- [7] E.E. Ergozin, T.K. Chkalov, T.V. Kovrigina, K.T. Serikbaeva, A.I. Nikitina, Recovery of perrhenate ions with a macrocellular anion exchanger based on epoxidized monoethanolamine vinyl ether, allyl glycidyl ether, and polyethyleneimine, *Russ. J. Appl. Chem.* 86 (2013) 1545–1548.
- [8] S.H. Joo, Y.U. Kim, J.G. Kang, H.S. Yoon, D.S. Kim, S.M. Shin, Recovery of molybdenum and rhenium using selective precipitation method from molybdenite roasting dust in alkali leaching solution, *Mater. Trans.* 53 (2012) 2038–2042.
- [9] N. Nebeker, J.B. Hiskey, Recovery of rhenium from copper leach solution by ion exchange, *Hydrometallurgy* 125–126 (2012) 64–68.
- [10] Z.S. Abisheva, A.N. Zagorodnyaya, N.S. Beckturganov, Review of technologies for rhenium recovery from mineral raw materials in Kazakhstan, *Hydrometallurgy* 109 (2011) 1–8.
- [11] S.R. Izatt, R.L. Bruening, N.E. Izatt, Metal separations and recovery in the mining industry, *JOM* 64 (2012) 1279–1284.
- [12] A.N. Zagorodnyaya, Z.S. Abisheva, Rhenium recovery from ammonia solutions, *Hydrometallurgy* 65 (2002) 69–76.
- [13] A.G. Kholmogorov, O.N. Kononova, S.V. Kachin, S.N. Ilyichev, V.V. Kryuchokov, O.P. Kalyakina, G.L. Pashkov, Ion exchange recovery and concentration of rhenium from salt solutions, *Hydrometallurgy* 51 (1999) 19–35.
- [14] M. Jia, H. Cui, W. Jin, L. Zhu, Y. Liu, J. Chen, Adsorption and separation of rhenium (VII) using N-methylimidazolium functionalized strong basic anion exchange resin, *J. Chem. Technol. Biotechnol.* 88 (2013) 437–443.
- [15] J. Kang, Y.U. Kim, S.H. Joo, H.S. Yoon, J.R. Kumar, K.H. Park, P.K. Parhi, S.M. Shin, Behavior of extraction, stripping, and separation possibilities of rhenium and molybdenum from molybdenite roasting dust leaching solution using amine based extractant tri-octyl amine (TOA), *Mater. Trans.* 54 (2013) 1209–1212.
- [16] A.G. Kasikov, A.M. Petrova, Recovery of rhenium (VII) with triisooctylamine from sulfuric acid solutions, *Russ. J. Appl. Chem.* 79 (2006) 914–919.
- [17] T. Ogata, K. Takeshita, K. Tsuda, A. Mori, Solvent extraction of perrhenate ions with podand-type nitrogen donor ligands, *Sep. Purif. Technol.* 68 (2009) 288–290.
- [18] S.Y. Seo, W.S. Choi, T.J. Yang, M.J. Kim, T. Tran, Recovery of rhenium and molybdenum from a roaster fume scrubbing liquor by adsorption using activated carbon, *Hydrometallurgy* 129–130 (2012) 145–150.
- [19] Y. Xiong, J. Xu, W. Shan, Z. Lou, D. Fang, S. Zang, G. Han, A new approach for rhenium (VII) recovery by using modified algae *Laminaria japonica* absorbent, *Bioresour. Technol.* 127 (2013) 464–472.
- [20] P. Mullen, K. Schwochau, C.K. Jørgensen, Vacuo ultraviolet spectra of permanganate, perrhenate and perrhenate, *Chem. Phys. Lett.* 3 (1969) 49–51.
- [21] A.W. Maverick, M.D. Lord, Q. Yao, L.J. Henderson, Photophysics and photochemistry of hexachlororhenate(IV) and hexabromorhenate(IV), *Inorg. Chem.* 30 (1991) 553–558.
- [22] W.M. Haynes (Ed.), *CRC Handbook of Chemistry*, CRC Press, Boca Raton, 2011.

有機フッ素化合物の国際規制動向と分解無害化・再資源化反応の開発

International Regulatory Trend and Development of Decomposition Techniques for Environmentally Persistent Organofluorine Compounds



堀 久男

神奈川大学理学部 化学科

〒259-1293

神奈川県平塚市土屋 2946

Hisao HORI

Department of Chemistry, Faculty of Science,
Kanagawa University

2946 Tsuchiya, Hiratsuka 259-1293, Japan

論文要旨：有機フッ素化合物は熱的、化学的に安定で、高い界面活性作用や低粘性、低屈折率等の優れた性質を持つ。このため様々な産業あるいは消費者向けの用途があり、新材料の研究も盛んである。一方で環境中に残留しやすく、廃棄物の分解処理も困難、さらにPFOSやPFOAと呼ばれる一部の化合物やその関連物質には生体蓄積性があるという側面もある。本稿ではこのような有機フッ素化合物の製造や使用に係る世界の規制動向と、最近我々が取り組んでいる先端フッ素材料に関する分解・再資源化反応の研究成果について報告する。

Abstract: Organofluorine compounds have been widely used in industrial and consumer applications, owing to their specific characters such as high thermal and chemical stability. After it became clear that some of them, particularly, perfluorooctanesulfonate (PFOS) and perfluorooctanoic acid (PFOA), bioaccumulate in the environment, international legal measures regarding the production, use, and import and export of several organofluorine compounds are being implemented. Hence, it is desirable to develop effective methodologies for decomposing these compounds to environmentally harmless species under mild conditions. If they could be decomposed to F^- ions by means of environmentally benign techniques, the well-established protocol for the treatment of F^- ions could be used: Ca^{2+} is added to the system to form CaF_2 , which is a raw material for hydrofluoric acid. Thus, the development of such techniques would allow for the recycling of fluorine resource, the global demand for which is increasing. We describe herein the international regulatory trend for organofluorine compounds. We also describe our developed methodologies for efficient decomposition of cutting-edge fluorinated materials (ionic liquid and polymers) to F^- ions.

Key words: regulation, fluorine, decomposition, waste treatment, recovery

1 はじめに

炭素原子とフッ素原子から形成される有機フッ素化合物は耐熱性、耐薬品性、界面活性等の優れた性質を持ち、我々の生活にも欠かすことのできない化学物質である。その種類は低分子化合物から高分子化合物まで多岐にわたる。分子量が数百程度の化合物は界面活性剤や表面処

理剤に、数万以上の化合物、すなわちフッ素ポリマーはパッキン等の汎用品は勿論のこと、イオン交換膜、光ファイバー、レジスト等の先端材料として利用されている¹⁾。このように他の材料では実現できない高い機能を持つ一方で、環境残留性や一部の物質が示す生体蓄積性、廃棄物の分解処理が困難であること、さらには原料(螢石)の入手難といった側面が近年になって顕在化しつつある。

連絡者：堀 久男
E-mail : h-hori@kanagawa-u.ac.jp

2 規制の経緯

有機フッ素化合物の中でも炭素数が8程度のペルフルオロカルボン酸類 (PFCA 類, 一般式 $C_nF_{2n+1}COOH$, $n = 1, 2, 3, \dots$) やペルフルオロアルキルスルホン酸類 (PFAS 類, $C_nF_{2n+1}SO_3H$), およびそれらの塩類や誘導体は反射防止剤, 表面処理剤, 乳化剤, はっ水剤等の構成成分あるいはそれらの中間原料として用いられてきた。ところが2000年頃から一部の化合物が環境水中や野生生物中に存在していることが明らかとなった^{2, 3)}。その典型がペルフルオロオクタンスルホン酸 ($C_8F_{17}SO_3H$) とペルフルオロオクタン酸 ($C_7F_{15}COOH$) であり, それぞれ PFOS, PFOA と呼ばれている。PFOS は従来, Perfluorooctanesulfonate の略, つまり陰イオン ($C_8F_{17}SO_3^-$) の部分を意味していた (酸も塩も水中では完全に解離するのでどちらも PFOS である)。これは環境分析の文献を中心とした表現で, PFOS の定量分析はこの陰イオンの部分の量に基づくため, このような表現になる。最近のストックホルム条約の資料では酸 (Perfluorooctanesulfonic acid) を PFOS と表現している。これは製造の記述には酸と塩を区別する必要があるためであろう。本原稿では特に断らない限り, 従来通り PFOS を酸と塩の両方を含めた意味で表すことにする。

PFOS 問題は2000年5月16日に当時世界で PFOS を最も多く製造していた企業が, 生体蓄積性の懸念から2003年以降その製造を中止すると発表したことに始まる⁴⁾。その決定の判断材料となった内容 (同社がミシガン州立大学へ委託した研究) が2001年になって学術誌に公表され²⁾, 人工物質である PFOS が, 産業活動がない極地にまで分布していることが明らかとなった。環境分析の研究が進むにつれて2004年までには PFOS のみならず PFOA, さらにペルフルオロノナン酸 ($C_8F_{17}COOH$, PFNA), ペルフルオロデカン酸 ($C_9F_{19}COOH$), ペルフルオロウンデカン酸 ($C_{10}F_{21}COOH$) といったペルフルオロアルキル基が長い PFCA 類 (長鎖 PFCA 類) が北極圏の野生動物に PFOA 以上に蓄積していることも分かった⁵⁾ (Fig. 1)。

このような状況を受けて米国環境保護局 (USEPA) は2000年10月18日に PFOS およびその関連物質を significant new use rule (SNUR, 重要新規利用規制) に指定することを提案した⁶⁾。SNUR とは有害性がまだ解明されていない一方で, 人や環境にリスクをもたらす恐れや相当量の環境への排出, もしくは人への暴露の恐れがあると判断された化学物質の製造や輸入を制限する規則である。PFOS および関連物質についての SNUR の適用は2002年4月10日に13物質⁷⁾, さらに2003年

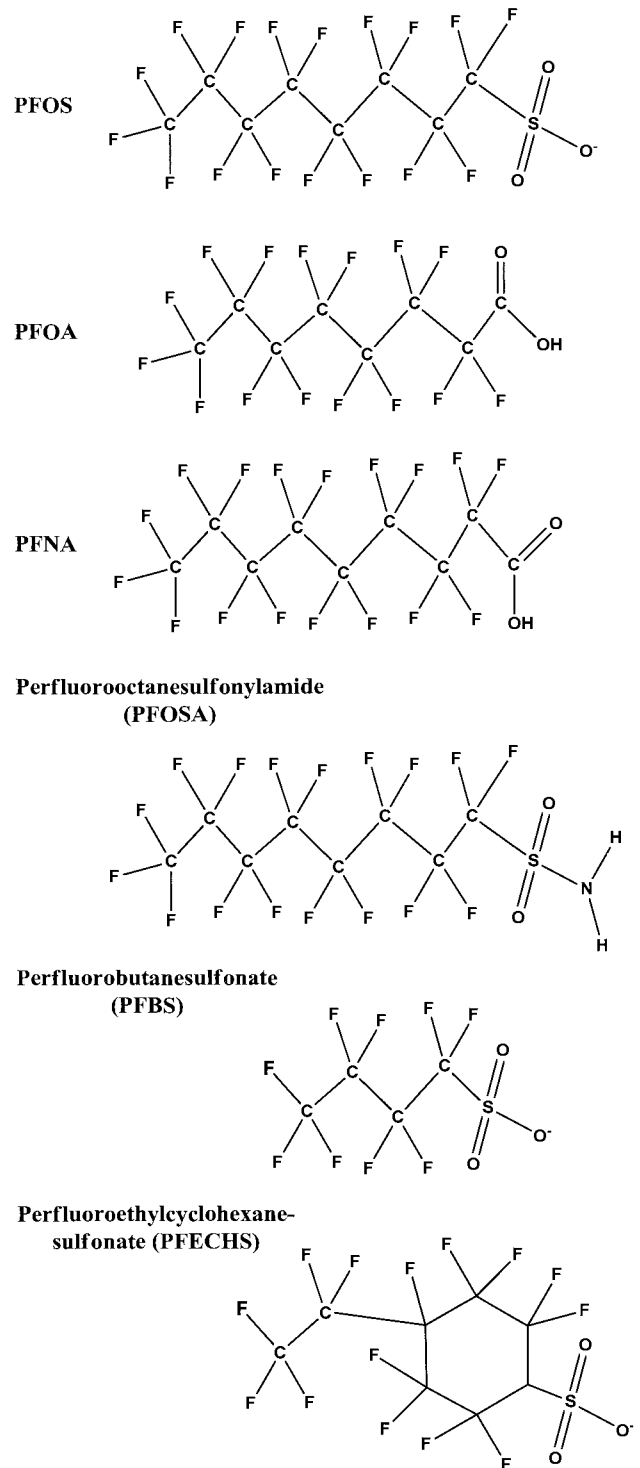


Fig. 1 環境水中で検出されている有機フッ素化合物 (PFNA のような長鎖 PFCA 類はそれ自体が使用されるだけでなく, テロメリゼーション反応で合成される PFOA に混入している場合もある。PFOSA は PFOS 前駆体の一種, PFBS は典型的な PFOS 代替品, PFECHS は PFOS 関連物質である)

1月8日に75物質について開始された⁸⁾。これにより米国ではこれらの物質の製造・輸入が許可制となった。但し半導体レジストや写真フィルム, 航空機用油圧作動

油等の既存の用途は適用除外とされた。我が国でもPFOSは2002年12月に化学物質の審査および製造等の規制に関する法律（化審法）で指定化学物質（後の名称は第二種監視化学物質）となっている。

USEPAはさらに2006年3月にペルフルオロアルキルスルホン酸類183物質をSNURに指定することを提案し、2007年11月8日からその適用が開始された⁹⁾。これについても既存の産業用途については適用が除外された。追加された物質は主に炭素数が5よりも大きなペルフルオロアルキル基がSO₂基に結合したものであった。同じ頃、EUでは国別にリスク評価を進めており、例えば英国では英国環境庁が2004年5月にPFOSの環境リスク評価書の草案を公開した¹⁰⁾。さらに同国の環境・食糧・地方事業省が2004年8月3日にPFOSリスク削減計画の最終報告書を発表した¹¹⁾。2006年6月にはドイツが¹²⁾、2007年6月には英国¹³⁾が飲料水ガイドライン（0.3 μg/L）を設定している。

EUは域内各国でのリスク評価の結果を受けて2006年12月12日に2006/122/EC指令を發布した¹⁴⁾。これはPFOS濃度が0.005%以上の物質もしくは調製品、0.1%以上の半製品や成型品、1 μg/m²以上のコーティング製品の販売を2008年6月27日以降禁止するという内容である。このEU指令が記述した「PFOS」は一般式C₈F₁₇SO₂Y（Y=OH、金属塩（O-M⁺）、ハロゲン化物、アミド、その他ポリマーを含む誘導体）で表される全物質である。化学出身の人間なら酸であるC₈F₁₇SO₃HをC₈F₁₇SO₂Y（Y=OH）と書くことには違和感を持つのではないだろうか。こういうことからこの規制は化学以外の専門家が主導したことが想像される。なお、この規制には必須な用途に関する除外規定があり、フトリソグラフィ用フォトレジストや反射防止膜、フィルム、紙、あるいはプリント基板用の写真コーティング、メッキ浴ミスト防止剤、航空機用油圧作動油には適用されなかった。また、消火剤についても2006年12月27日より前に販売されたものは2011年6月27日までは使用できることになっていた。

2005年6月には残留性有機汚染物質に関するストックホルム条約（POPs条約）での規制の検討が開始され（スウェーデンが附属書A物質、つまり製造、使用、輸出入の禁止を提案した）、紆余曲折を経て2009年5月の第4回締約国会議において、PFOSおよびその原料であるペルフルオロオクタンスルホンフルオリド（C₈F₁₇SO₂F、PFOSF）の附属書B物質（製造、使用、輸出入の制限）への追加が決定した¹⁵⁾。これにより国際的な規制が本格的に行われることになった。ただし代替困難な用途（半導体用途、フォトマスク、金属メッキ、

泡消火剤）は適用除外とされた。この決定を受けて我が国では2009年10月にPFOSおよびPFOSFの化審法第一種特定化学物質（原則として製造、輸入が禁止）への指定が決定し、2010年4月1日に施行された。この場合も当時代替物がなかったエッチング、半導体レジスト製造、業務用写真フィルムについては例外的に使用の継続が認められた。これに先立ちPFOSは2008年11月に化学物質排出把握管理促進法（化管法）の第一種指定化学物質に指定され、2010年度分より環境中への排出量および移動量が国に届け出されることになっていた。2009年4月には水道水に係る要検討項目に指定されている。

PFOSが第一種特定化学物質に指定されたことを受けて2010年9月には環境省が廃棄物処理に関するガイドラインを発表し、分解処理後の排水中のPFOS濃度を2 μg/L以下、焼却温度を1100℃にするよう定めた¹⁶⁾（焼却温度は2011年3月に850℃まで緩和された¹⁷⁾）。このような記述をするとPFOSはまだ日本で使用されているのかと思われるかも知れないが、現実には2010年までに供給が止まっており、廃棄物の大半はストックされている泡消火剤である¹⁸⁾。EUのPFOS規制は2007年6月に発効したREACH規則に引き継がれ、2011年3月には調製品中のPFOS濃度の規制値が0.001%に引き下げられている¹⁹⁾。

一方末端がカルボン酸であるPFOAの規制についてはPFOSとは異なる展開があった。USEPAは2003年4月にPFOAの予備リスクアセスメント結果を公表した²⁰⁾。2004年6月17日および2005年2月5日にはカナダ環境省が紙や繊維の加工に用いられていた合計4種類のフッ素化テロマー物質（PFCA類の前駆体）の製造、販売、使用、販売目的の提供を2年の期限付きで禁止した（2006年6月に更新）²¹⁾。さらに2005年1月4日にはUSEPAがリスクアセスメントの草案を公表したが、正式版が発行されない状況の中、USEPAは2006年1月に世界の主要フッ素企業8社に対し、PFOAおよび長鎖ペルフルオロカルボン酸類および前駆体の工場排出やフッ素製品中の残留を2015年までにゼロにする自主削減プログラム（PFOA Stewardship program）に参加するよう提案した（2006年3月までに全社が同意）²²⁾。2006年11月にはUSEPAと米国のフッ素企業が工場近郊の飲料水について、浄化あるいは代替水源に責任を持つレベルとして0.5 μg/Lという数値を設定することで合意した²³⁾。2006年12月にはノースカロライナ州が地下水中の暫定許容濃度を2 μg/Lに設定し²⁴⁾、2009年1月にはUSEPAの水質局が暫定的な健康基準値として0.4 μg/Lを設定する等²⁵⁾、水質に関連する基準値がで

きた。つまり PFOA は規制の導入に先立って企業が自主的に削減を進めた側面が強い。USEPA は 2013 年 10 月にカーペット用途に限定してペルフルオロアルキル基の炭素が 7 以上 20 以下の PFCA 類 (原文は carboxylate なので塩も含む、もちろん PFOA も含まれる) の SNUR 適用を決定した (同年 12 月開始)²⁶⁾。さらに PFOA Stewardship program の終了に合わせ、このプログラムが対象とした物質が審査なしに市場へ再導入されることを防ぐため、2015 年 1 月に様々な PFOA 関連物質の SNUR 適用を決定した (開始は同年 12 月)²⁷⁾。対象物質はフッ素化されたアクリル共重合体、アルキルポリフルオロオクチル基等を持つシロキサン、部分的にフッ素化されたアルコール、フッ素化された酸のアルキルエステル等であるが、具体的な構造は米国官報上で秘密 (claimed confidential) になっている。劣化して PFOA あるいは長鎖 PFCA 類を発生しそうなものが対象なので炭素数が 7 以上のペルフルオロアルキル基を持つ物質と考えられる。

EU においては水道水の PFOA 基準値が 2006 年 6 月にドイツ¹²⁾、2007 年 6 月には英国¹³⁾ で PFOS と同時に 0.3 µg/L に設定される等の動きがあった後、2013 年 7 月に PFOA およびそのアンモニウム塩 (C₇F₁₅COONH₄, APFO) が REACH 規則の高懸念物質 (very high concern, SVHC) に指定され、2014 年 10 月には PFOA とその塩類、さらには C₇F₁₅ および C₈F₁₇ 構造を有する物質を 2 ppb 以上含む製品の製造や販売を禁止する提案がなされた²⁸⁾。これに対してフッ素産業界の国際組織 FluoroCouncil は 2015 年 2 月にこの規制値は代替品である短鎖化合物の製造に支障が出るという意見を表明している²⁹⁾。

2015 年 10 月には EU によりストックホルム条約の検討委員会 (POPRC11) において PFOA とその塩類、さらには関連物質 (環境中で PFOA になる可能性がある物質) を、附属書 A 物質、B 物質、あるいは C 物質 (非意図的生成物の排出削減、廃絶) へ指定することが提案されている³⁰⁾。

我が国においては、PFOA は 2002 年 12 月に PFOS と同時に化審法の指定化学物質 (後の名称は第二種監視化学物質) となった。APFO はそれ以前から「ペンタデカフルオロオクタン酸アンモニウム」として化管法の第二種指定化学物質になっていたが、2008 年 3 月に「アンモニウムペルフルオロオクタノアート (別名パーフルオロオクタン酸アンモニウム塩)」の名称で化審法第二種監視化学物質になった (ルはおかしいが 3 月 21 日付告示でこう記載されている)。また炭素数 14~17 の長鎖 PFCA 類は、2007 年 5 月に第一種監視化学物質 (2011

年以降の名称は監視化学物質) になった。PFOA は 2009 年 4 月には PFOS と共に水道水に係る要検討項目に指定されているが、製造や使用に関する本格的な規制の導入は本稿の執筆時点 (2015 年 11 月) では開始されていない。

これまでの経緯を見ると規制の検討はまず PFOS、次に PFOA、さらに長鎖 PFCA 類や分解して PFOA あるいは長鎖 PFCA 類を生成する可能性がある物質 (前駆体) へと拡大したことが分かる。産業界ではこのような動きに対応して代替物への切り替えを進めているが、ストックホルム条約の検討委員会 (POPRC6) は 2011 年 11 月に「PFOS およびその塩」の代替品に関するガイダンスを発行した³¹⁾。それによると代替品として最初に普及したのはペルフルオロアルキル基の炭素数が 8 のフルオロテロマー類 (C₈F₁₇CH₂CH₂ 構造を持つ物質で末端は OH や PO₄H⁻ 基など) であった。しかしこれは PFOA 前駆体の範疇に入るため PFOA Stewardship program の開始後、ユーザーは再度代替品を探す必要に迫られた。その後普及している代替物の中心は生体蓄積性がより低い短鎖 PFAS 類 (例えばペルフルオロブタンスルホン酸, C₄F₉SO₃H, PFBS) や短鎖 PFCA 類 (例えばペルフルオロヘキサン酸, C₅F₁₁COOH) である。

現在、リスクの検討はこれらの短鎖化合物に移りつつある。USEPA は短鎖フルオロテロマー類について審査している³²⁾。PFBS の利用が始まったのは PFOS 問題が顕在化した後であるが、近年ラブラトル海や大西洋の海水中で PFOS や PFOA と同等の濃度の PFBS が検出されている^{33, 34)}。PFOS や PFOA が 60 年以上使用されて蓄積された結果がこの海洋中の濃度であるとする、使用が始まってからそれほど年数が経っていない PFBS の濃度がそれらと同程度ということは不思議であるが、PFBS が水圏中で移動しやすいことを反映していると思われる。環境水中では環状の不思議な化合物も検出されている (Fig. 1)³⁵⁾。

3 有機フッ素化合物の分解・無害化、再資源化反応の開発

上述のように有機フッ素化合物の環境影響が懸念されつつある。その環境リスクの低減のためには有害性の度合いに応じて排水や廃棄物の無害化を行う必要があるが、炭素・フッ素結合は炭素が形成する共有結合では最強なため容易に分解しない。焼却は可能であるものの、高温が必要であるだけでなく、生成するフッ化水素ガスによる焼却炉材の劣化が著しい。これらの物質をフッ化物イオン (F⁻) まで分解できれば、既存の処理技術によりフッ化カルシウム (CaF₂) に変換できる。CaF₂ の

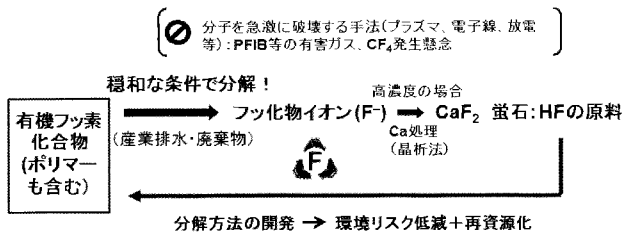


Fig. 2 有機フッ素化合物の分解・再資源化スキーム

鉱物は螢石で、硫酸処理によりフッ素ポリマーを含む全ての有機フッ素化合物の原料であるフッ化水素酸になるため、産出が特定国に偏在し、入手に制約が多いフッ素資源の循環利用にも寄与できる (Fig. 2)。この場合、穏和な条件でF⁻まで分解することが重要である。これまでも電子線照射やプラズマ、放電等の高エネルギー的な手法を使えばフッ素ポリマーさえも分解することは知られていた。しかしその場合、毒性が非常に高いペルフルオロイソブチレン (CF₃C(CF₃)CF₂, PFIB) や温暖化係数が二酸化炭素の数千倍のテトラフルオロメタン (CF₄) 等の有害ガスの発生が懸念されている。

我々は、PFAS類およびPFCA類、さらにはそれらの関連物質について、ヘテロポリ酸光触媒³⁶⁾、ペルオキソ二硫酸イオン (S₂O₈²⁻) + 光照射³⁷⁻³⁹⁾、金属粉 + 亜臨界水⁴⁰⁻⁴²⁾、鉄イオン光触媒⁴³⁾、S₂O₈²⁻ + 温水^{44, 45)}、酸素ガス + 亜臨界水⁴⁶⁾、S₂O₈²⁻ + 超音波照射⁴⁷⁾、酸化タングステン光触媒 + S₂O₈²⁻⁴⁸⁾等の手法によりF⁻までの分解、すなわち無機化を達成してきた。近年はこれらの知見を基に、対象物質を環境中二次生成物⁴⁸⁾、新規フッ素系界面活性剤^{49, 50)}、フッ素系イオン交換膜⁵¹⁾、フッ素系イオン液体⁵²⁾、レジスト用光酸発生剤⁵³⁾、さらにはポリフッ化ビニリデン (PVDF, -(CH₂CF₂)_n-, VDF: フッ化ビニリデン) 等のフッ素ポリマー^{54, 55)}まで拡大している。以下に最近の成果について紹介したい。

4 フッ素系イオン液体の分解反応

フッ素系イオン液体とは、陰イオンと陽イオンからなる塩類でありながら常温付近で液体の物質(イオン液体)のうち、陰イオンがペルフルオロアルキル基から成り立っている化合物である。これらは安定であることが特徴のイオン液体の中でも特に不燃性や耐薬品性、さらには電気化学特性に優れている。このためリチウム二次電池等の様々なエネルギーデバイスにおいて電解質材料として導入されつつある。しかしながら分解処理方法は未だに確立されておらず、現状ではオガ屑と混合し、少しずつ焼却するとか、中和して排水するといった方法しかない。本研究ではフッ素系イオン液体の陰イオンとして使用されるビス (ペルフルオロアルカンスルホニル) イ

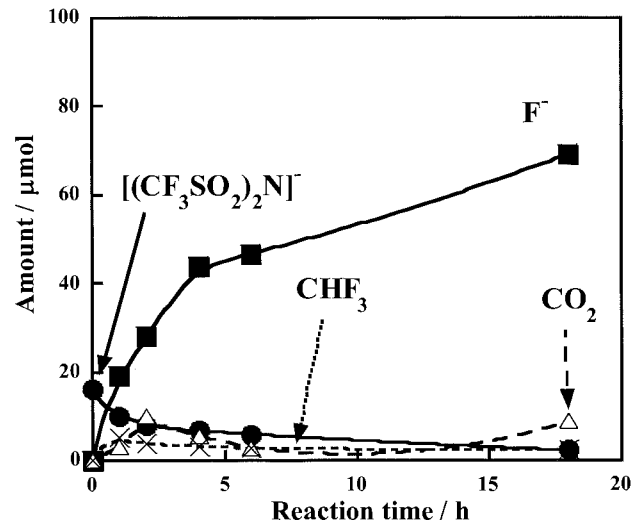


Fig. 3 FeO を還元剤として用いた [(CF₃SO₂)₂N]⁻の亜臨界水分解 (345 °C) : 基質および生成物の物質量の時間依存性⁵²⁾。● : [(CF₃SO₂)₂N]⁻, ■ : F⁻, × : CHF₃, △ : CO₂

ミド類 (C_nF_{2n+1}SO₂)₂N⁻について、高温高压の水 (亜臨界水, 超臨界水) 中で分解することを検討した。その結果、(CF₃SO₂)₂N⁻の場合、酸化鉄 (II) (FeO) を還元剤として用いることでF⁻を最高で86%の収率で得ることができた (Fig. 3)⁵²⁾。反応初期には温暖化係数が高いCF₃Hが検出されたが、長時間反応させることで消失した。この反応では反応中にFeOが不均化して発生するゼロ価鉄が高活性な還元剤として作用していることが分かった。

5 熱可塑性フッ素ポリマーの分解・再資源化反応

現在まで最も多く使用されているフッ素ポリマーはポリテトラフルオロエチレン (PTFE, -(CF₂CF₂)_n-) であり、フッ素ポリマーの全需要の6割強を占めている。PTFEは熱可塑性ポリマーに分類されるものの、高温で溶融させた場合の粘度 (10⁹~10¹¹ Pa s) は通常の熱可塑性ポリマーのそれらよりも約6桁高いため溶融成形ができない。このためCH₂基を導入する等、骨格を変えて溶融成形を可能にした新しいポリマーが開発され、普及しつつある。そのようなフッ素ポリマーを産業界では「熱可塑性フッ素ポリマー」と呼んでいる。熱可塑性フッ素ポリマーはエネルギーデバイス (リチウムイオン電池の電極材料, 電解膜材料, 水素機器シール材等), 化学プラント (配管, ライニング等), 半導体製造装置 (ラインチューブ等) をはじめとする様々な産業用途へ導入が進んでいるが、廃棄物の大半は埋め立て処分されている。

我々は代表的な熱可塑性フッ素ポリマーであるPVDFおよびエチレン-テトラフルオロエチレン共重合体 (ETFE, -(CH₂CH₂)_m(CF₂CF₂)_n-) について、様々な酸

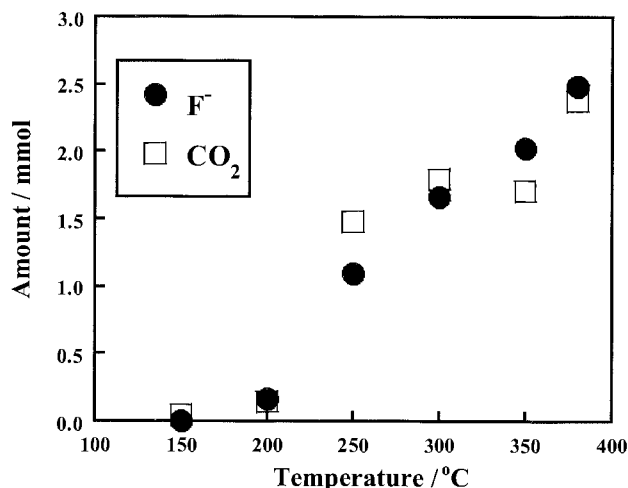


Fig. 4 O₂を酸化剤として用いたETFEの亜臨界水および超臨界水分解（反応時間：6 h）：生成物の物質量の温度依存性（380℃のみ超臨界水状態である）⁵⁴⁾

化剤や還元剤を添加した亜臨界水あるいは超臨界水反応で分解することを試みた。その結果、酸素ガスを共存させた超臨界水反応によりこれらのポリマーのフッ素成分および炭素成分をF⁻およびCO₂まで完全に分解することに成功した (Fig. 4)⁵⁴⁾。さらに反応系にあらかじめ化学量論量の水酸化カルシウムを添加することで純粋なCaF₂を得ることができた。アルゴンガスを共存させた場合、PVDFとETFEでは反応性に顕著な違いが見られた。すなわちPVDFではF⁻が生成すると同時に炭素を多く含む残渣が発生したのに対し、ETFEでは分解自体が進行しなかった。この現象はPVDFではHF脱離機構による分解が起こるのに対し、ETFEでは起こらないことを意味する。より低温で分解する反応条件を探索した結果、酸化剤として過酸化水素水を用いることで300℃の亜臨界水中でPVDF、VDF-クロロトリフルオロエチレン共重合体およびVDF-ヘキサフルオロプロピレン共重合体をF⁻およびCO₂まで（塩素原子を含む場合にはCl⁻まで）完全に分解し、CaF₂を得ることに成功した⁵⁵⁾。

6 おわりに

以上有機フッ素化合物の規制動向と分解、再資源化反応について紹介した。既に炭素数が7あるいは8程度のペルフルオロアルキル基を持つ化合物は、少なくともEU等への輸出品の製造工程では非常に使いにくい状況になっており、世界における環境リスクの評価は代替品である短鎖化合物にシフトしている。短鎖になると生体蓄積性は低下するが、ペルフルオロアルキル基に特有な性能も低下してしまう。また水溶性が増加して環境水中へ流失しやすくなる。有機フッ素化合物の環境リスクの

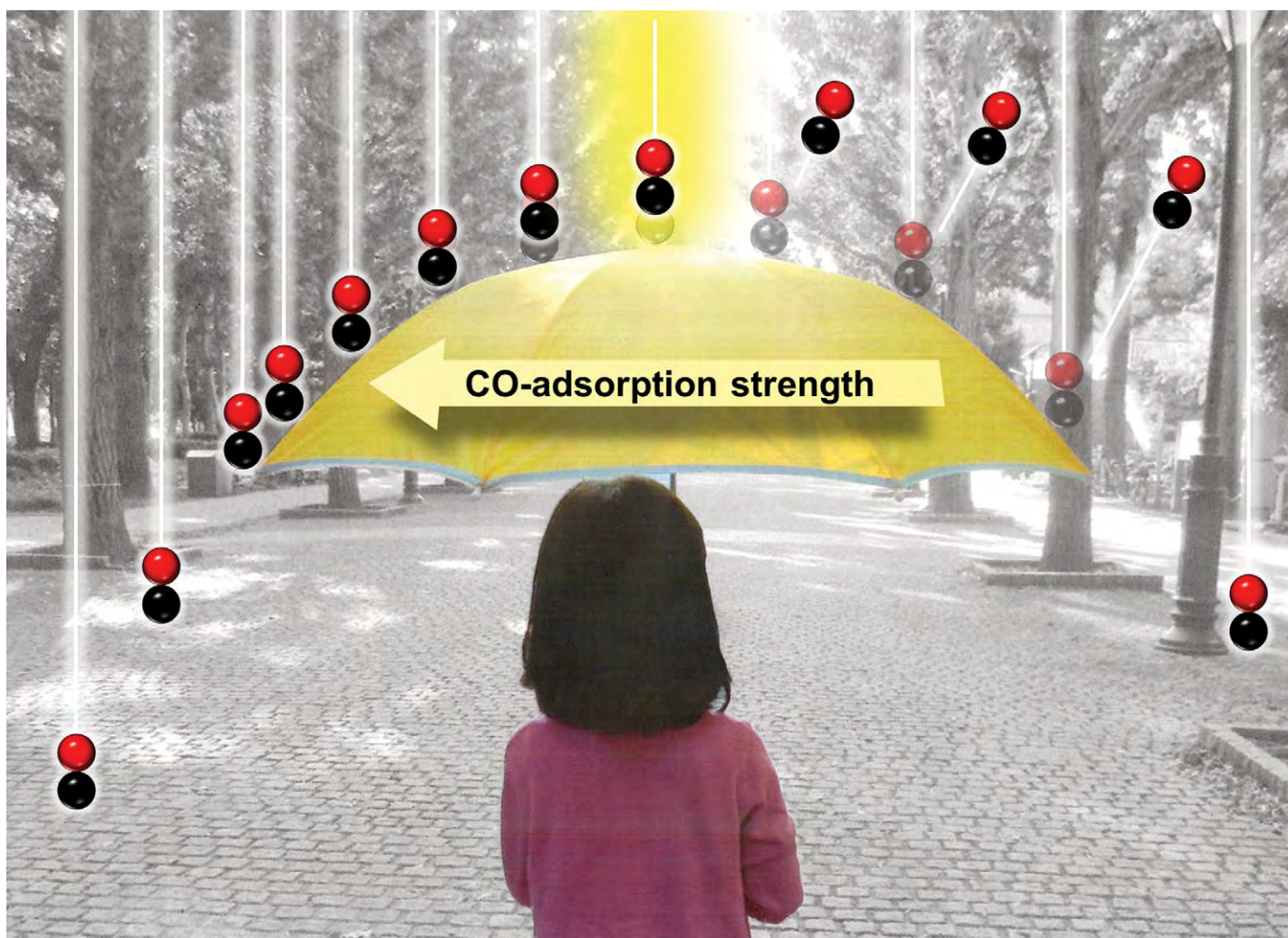
低減のためには使用サイトでの回収および廃棄物の分解・無害化方法の開発と共に、新しい材料の開発段階でその分解挙動を予測し、廃棄物処理方法まで考慮することが重要と思われる。

文献

- 1) フッ素樹脂の最新動向, 澤田英夫監修, シーエムシー (2013).
- 2) J. P. Giesy, K. Kannan, *Environ. Sci. Technol.*, **35**, 1339-1342 (2001).
- 3) J. P. Giesy, K. Kannan, *Environ. Sci. Technol.*, **35**, 146A-152A (2002).
- 4) R. Renner, *Environ. Sci. Technol.*, **35**, 154A-160A (2001).
- 5) J. W. Martin, M. M. Smithwick, B. M. Braue, P. F. Hoekstra, D. C. G. Muir, S. A. Mabury, *Environ. Sci. Technol.*, **38**, 373-380 (2004).
- 6) USEPA, Perfluorooctyl Sulfonates; Proposed Significant New Use Rule, Federal Register, October 18, **65** (202), 62319-62333 (2000). 米国官報 (Federal Register) は米国政府出版局のサイト <http://www.gpo.gov/fdsys/browse/collection.action?collectionCode=FR> で発行日を指定することで見ることができる。このサイトには学術雑誌のように巻、号、ページから書誌に入る仕組みがないため本稿では発行日も記載した。
- 7) USEPA, Perfluoroalkyl Sulfonates; Significant New Use Rule, Federal Register, March 11, **67** (47), 11007-11013 (2002).
- 8) USEPA, Perfluoroalkyl Sulfonates; Significant New Use Rule, Federal Register, December 9, **67** (236), 72854-72867 (2002).
- 9) USEPA, Perfluoroalkyl Sulfonates; Significant New Use Rule, Federal Register, October 9, **72** (194), 57222-57235 (2007).
- 10) Environment Agency for England and Wales, Draft Environmental Risk Evaluation Report: Perfluorooctanesulfonate (PFOS) (2004).
- 11) Department for Environment, Food and Rural Affairs and the Environment Agency for England and Wales, Perfluorooctane Sulfonate, Risk Reduction Strategy and Analysis of Advantages and Drawbacks, Final Report (2004).
- 12) Statement by the Drinking Water Commission of the German Ministry of Health at the Federal Environment Agency, June 21 (revised July 13) (2006).
- 13) UK Drinking Water Inspectorate, Guidance on the Water Supply (Water Quality) Regulations 2000/2001 Specific to PFOS (Perfluorooctane Sulfonate) and PFOA (Perfluorooctanoic Acid) Concentrations in Drinking Water, 1 June (2007).
- 14) DIRECTIVE 2006/122/EC of the European Parliament and of the Council of 12 December 2006, Official Journal of the European Union, L 372/32-34, 27 December (2006).
- 15) Report of the Conference of the Parties of the Stock-

- holm Convention on Persistent Organic Pollutants on the work of its fourth meeting, UNEP/POPS/COP.4/38, 8 May (2009).
- 16) PFOS 含有廃棄物の処理に関する技術的留意事項, 環境省廃棄物・リサイクル対策部, 平成 22 年 9 月.
 - 17) PFOS 含有廃棄物の処理に関する技術的留意事項, 環境省廃棄物・リサイクル対策部, 平成 23 年 3 月, <https://www.env.go.jp/recycle/misc/pfos/tptc.pdf>.
 - 18) 平成 22 年度環境省 POPs 廃棄物適正処理等検討会 (第 2 回) 資料, 平成 22 年 9 月.
 - 19) Commission Regulation (EU) No 207/2011 of 2 March 2011 amending Regulation (EC) No 1907/2006 of the European Parliament and of the Council on the Registration, Evaluation, Authorisation and Restriction of Chemicals (REACH) as regards Annex XVII (Diphenylether, pentabromo derivative and PFOS), Official Journal of the European Union, L58/27-28, 3 March (2011).
 - 20) USEPA, Preliminary Risk Assessment of the Developmental Toxicity Associated with Exposure to Perfluorooctanoic Acid (PFOA) and its Salts. OPPT, Risk Assessment Division, April 10 (2003).
 - 21) Department of the Environment and Department of Health, Order Adding Toxic Substances to Schedule 1 to the Canadian Environmental Protection Act, 1999, Canada Gazette, Official Newspaper of the Government of Canada, June 17, 140, No. 24 (2006).
 - 22) USEPA, 2010/2015 PFOA Stewardship Program, <http://www2.epa.gov/assessing-and-managing-chemicals-under-tsca/20102015-pfoa-stewardship-program>. Last updated on October 14 (2015).
 - 23) USEPA, EPA Reaches Agreement with DuPont to Protect Drinking Water Near W. Va. Plant. News Releases from Region 3, Release Date: November 21 (2006), <http://yosemite.epa.gov/opa/admpress.nsf/90829d899627a1d98525735900400c2b/d71a299a96058ad58525722d00542655?opendocument>.
 - 24) Division of Water Resources, North Carolina Department of Environmental Quality, Interim Maximum Allowable Concentrations (IMACs), http://portal.ncdenr.org/c/document_library/get_file?uuid=2380a642-0f7e-42e2-8e59-1c32087724af&groupId=38364. Last updated on April 1 (2013).
 - 25) USEPA, Provisional Health Advisories for Perfluorooctanoic Acid (PFOA) and Perfluorooctane Sulfonate (PFOS), January 8 (2009), <http://www2.epa.gov/sites/production/files/2015-09/documents/pfoa-pfos-provisional.pdf>.
 - 26) USEPA, Perfluoroalkyl Sulfonates and Long-Chain Perfluoroalkyl Carboxylate Chemical Substances; Final Significant New Use Rule, Federal Register, October 22, 78 (204), 62443-62451 (2013).
 - 27) USEPA, Significant New Use Rule on Certain Chemical Substances, Federal Register, October 2, 80 (191), 59593-59610 (2015).
 - 28) European Chemicals Agency (ECHA). Annex XV Restriction Report. Proposal for a restriction-Perfluorooctanoic acid (PFOA), PFOA salts and PFOA-related substances, 17 October (2014), <http://echa.europa.eu/documents/10162/e9cddee6-3164-473d-b590-8fcf-9caa50e7>.
 - 29) The Global Industry Council for FluoroTechnology (FluoroCouncil), Re: Annex XV Restriction Report: Proposal for a Restriction for Perfluorooctanoic acid (PFOA), PFOA salts and PFOA-related substances (17 October 2014), 18 February (2015).
 - 30) Stockholm Convention on Persistent Organic Pollutants, Persistent Organic Pollutants Review Committee Eleventh meeting, Rome, 19-23 October, UNEP/POPS/POPRC.11/5 (2015), <http://chm.pops.int/TheConvention/ThePOPs/ChemicalsProposedforListing/tabid/2510/Default.aspx>.
 - 31) Report of the Persistent Organic Pollutants Review Committee on the work of its sixth meeting. Guidance on alternatives to perfluorooctane sulfonic acid and its derivatives, UNEP/POPS/POPRC.6/13/ADD.3/Rev. 1, 8 November (2011).
 - 32) USEPA, New Chemicals Program Review of Alternatives for PFOA and Related Chemicals, <http://www2.epa.gov/assessing-and-managing-chemicals-under-tsca/new-chemicals-program-review-alternatives-pfoa-and-related-chemicals>. Last updated October 25 (2015).
 - 33) N. Yamashita, S. Taniyasu, G. Petrick, S. Wei, T. Gamo, P. K. S. Lam, K. Kannan, *Chemosphere*, **70**, 1247-1255 (2008).
 - 34) J. P. Benskin, D. C. G. Muir, B. F. Scott, C. Spencer, A. O. De Silva, H. Kylin, J. W. Martin, A. Morris, R. Lohmann, G. Tomy, B. Rosenberg, S. Taniyasu, N. Yamashita, *Environ. Sci. Technol.*, **46**, 5815-5823 (2012).
 - 35) A. O. De Silva, C. Spencer, B. F. Scott, S. Backus, D. C. G. Muir, *Environ. Sci. Technol.*, **45**, 8060-8066 (2011).
 - 36) H. Hori, E. Hayakawa, H. Einaga, S. Kutsuna, K. Koike, T. Ibusuki, H. Kitagawa, R. Arakawa, *Environ. Sci. Technol.*, **38**, 6118-6124 (2004).
 - 37) H. Hori, A. Yamamoto, E. Hayakawa, S. Taniyasu, N. Yamashita, S. Kutsuna, H. Kitagawa, R. Arakawa, *Environ. Sci. Technol.*, **39**, 2383-2388 (2005).
 - 38) H. Hori, A. Yamamoto, K. Koike, S. Kutsuna, I. Osaka, R. Arakawa, *Water Res.*, **41**, 2962-2968 (2007).
 - 39) H. Hori, A. Yamamoto, S. Kutsuna, *Environ. Sci. Technol.*, **39**, 7692-7697 (2005).
 - 40) H. Hori, Y. Nagaoka, A. Yamamoto, T. Sano, N. Yamashita, S. Taniyasu, S. Kutsuna, I. Osaka, R. Arakawa, *Environ. Sci. Technol.*, **40**, 1049-1054 (2006).
 - 41) H. Hori, Y. Nagaoka, T. Sano, S. Kutsuna, *Chemosphere*, **70**, 800-806 (2008).
 - 42) H. Hori, T. Sakamoto, Y. Kimura, A. Takai, *Catal. Today*, **196**, 132-136 (2012).
 - 43) H. Hori, A. Yamamoto, K. Koike, S. Kutsuna, I. Osaka, R. Arakawa, *Chemosphere*, **68**, 572-578 (2007).
 - 44) H. Hori, Y. Nagaoka, M. Murayama, S. Kutsuna, *Environ. Sci. Technol.*, **42**, 7438-7443 (2008).

- 45) H. Hori, M. Murayama, N. Inoue, K. Ishida, S. Kutsuna, *Catal. Today*, **151**, 131-136 (2010).
- 46) H. Hori, M. Murayama, S. Kutsuna, *Chemosphere*, **77**, 1400-1405 (2009).
- 47) H. Hori, Y. Nagano, M. Murayama, K. Koike, S. Kutsuna, *J. Fluorine Chem.*, **141**, 5-10 (2012).
- 48) H. Hori, A. Ishiguro, K. Nakajima, T. Sano, S. Kutsuna, K. Koike, *Chemosphere*, **93**, 2657-2922 (2013).
- 49) H. Hori, H. Saito, H. Sakai, T. Kitahara, T. Sakamoto, *Chemosphere*, **129**, 27-32 (2015).
- 50) Y. Patil, H. Hori, H. Tanaka, T. Sakamoto, B. Ameduri, *Chem Commun.*, **49**, 6662-6664 (2013).
- 51) H. Hori, M. Murayama, T. Sano, S. Kutsuna, *Ind. Eng. Chem. Res.*, **49**, 464-471 (2010).
- 52) H. Hori, Y. Noda, A. Takahashi, T. Sakamoto, *Ind. Eng. Chem. Res.*, **52**, 13622-13628 (2013).
- 53) H. Hori, H. Yokota, *J. Fluorine Chem.*, **178**, 1-5 (2015).
- 54) H. Hori, T. Sakamoto, K. Ohmura, H. Yoshikawa, T. Seita, T. Fujita, Y. Morizawa, *Ind. Eng. Chem. Res.*, **53**, 6934-6940 (2014).
- 55) H. Hori, H. Tanaka, K. Watanabe, T. Tsuge, T. Sakamoto, A. Manseri, B. Ameduri, *Ind. Eng. Chem. Res.*, **54**, 8650-8658 (2015).



Showcasing research from the laboratory of Dr Abe and Dr Ramesh at the National Institute for Materials Science, Japan.

Title: Correlation between the surface electronic structure and CO-oxidation activity of Pt alloys

CO adsorption rules the catalysis: a quantitative relation has been established between the catalytic CO purification and the CO adsorption to platinum and its alloys: Pt_3T (T = Pt, Ti, Hf, Ta). The CO-purification activity of the catalysts shows an "umbrella-shaped" dependence on the CO-adsorption strength.

As featured in:



See Hideki Abe,
Gubbala V. Ramesh *et al.*,
Phys. Chem. Chem. Phys.,
2015, 17, 4879.



www.rsc.org/pccp

Registered charity number: 207890

Correlation between the surface electronic structure and CO-oxidation activity of Pt alloys†

Cite this: *Phys. Chem. Chem. Phys.*,
2015, 17, 4879

Hideki Abe,^{*ab} Hideki Yoshikawa,^a Naoto Umezawa,^{ab} Ya Xu,^a
Govindachetty Saravanan,^{ac} Gubbala V. Ramesh,^{*a} Toyokazu Tanabe,^a
Rajesh Kodiyath,^a Shigenori Ueda,^d Nobuaki Sekido,^a Yoko Yamabe-Mitarai,^a
Masahiko Shimoda,^a Takahisa Ohno,^a Futoshi Matsumoto^e and Takayuki Komatsu^f

The surface electronic structure and CO-oxidation activity of Pt and Pt alloys, Pt₃T (T = Ti, Hf, Ta, Pt), were investigated. At temperatures below 538 K, the CO-oxidation activities of Pt and Pt₃T increased in the order Pt < Pt₃Ti < Pt₃Hf < Pt₃Ta. The center-of-gravity of the Pt d-band (the d-band center) of Pt and Pt₃T was theoretically calculated to follow the trend Pt₃Ti < Pt₃Ta < Pt₃Hf < Pt. The CO-oxidation activity showed a volcano-type dependence on the d-band center, where Pt₃Ta exhibited a maximum in activity. Theoretical calculations demonstrated that the adsorption energy of CO on the catalyst surface monotonically decreases with the lowering of the d-band center because of diminished hybridization of the surface d-band and the lowest-unoccupied molecular orbital (LUMO) of CO. The observed volcano-type correlation between the d-band center and the CO oxidation activity is rationalized in terms of the CO adsorption energy, which counterbalances the surface coverage by CO and the rate of CO oxidation.

Received 31st July 2014,
Accepted 11th September 2014

DOI: 10.1039/c4cp03406f

www.rsc.org/pccp

1. Introduction

The development of environmental-remediation technologies is of paramount importance to balance the growth in the economy and the natural environment. One of the key objectives of the current environmental-purification technologies is the reduction of expensive precious-group metals (PGMs: Pt, Pd and Rh) in automobile catalysts.^{1,2} There have been numerous approaches to alloy PGMs and more abundant metals such as Ni or Co to achieve high performance and low material costs (alloy catalysts).^{3–7} However, it still remains a challenge to adequately design alloy catalysts for exhaust purification, because of the lack of understanding of

the correlation between the catalytic activity and experimentally measurable or theoretically calculable parameters of the alloys, such as the center-of-gravity of the Pt d-band (the d-band center).^{8–14} Furthermore, surface segregation, which readily occurs on alloy surfaces in harsh conditions including high-temperature exhausts, makes it difficult to interrelate the apparent activity with the electronic and/or atomic structure of unperturbed surfaces.¹⁵ To evaluate an inherent alloying effect on the exhaust-purification activity of alloy catalysts, it is required to investigate thermally stable alloys with high melting points (>2000 K), such as early-d-Pt alloys (Pt-T: T = early d-metals), because their high ordering enthalpies can inhibit surface segregation and segregation-induced changes on the electronic or atomic structure of the surface.^{16–18}

Here we report that a simple correlation can be established between the apparent exhaust-purification activity and the surface electronic structure of early-d-Pt alloys, Pt₃T (T = Ti, Ta or Hf). X-ray photoemission spectroscopy using synchrotron radiation (Hard X-ray Photoemission Spectroscopy: HX-PES) demonstrated that the surface of Pt₃T was free from segregation when exposed to a simulated exhaust (a 2 : 1 mixture of carbon monoxide (CO) and O₂ gases, 10 kPa) at temperatures below 598 K. At temperatures lower than 538 K, the catalytic activity of Pt and Pt₃T for the oxidation of CO increased in the order Pt < Pt₃Ti < Pt₃Hf < Pt₃Ta. This trend leads to a volcano-type dependence of the CO oxidation activity on the theoretically calculated center-of-gravity of the Pt d-band (the d-band center) which increases in the order Pt < Pt₃Hf < Pt₃Ta < Pt₃Ti. Theoretical calculations have further demonstrated that the

^a National Institute for Materials Science, 1-1 Namiki, Tsukuba, Ibaraki 305-0044, Japan. E-mail: ABE.Hideki@nims.go.jp, GUBBALA.Venkataramesh@nims.go.jp; Fax: +81-29-859-2301; Tel: +81-29-860-4806

^b Precursory Research for Embryonic Science and Technology (PRESTO), Japan Science and Technology Agency (JST), 4-1-8 Honcho Kawaguchi, Saitama, 332-0012, Japan

^c CSIR-National Environmental Engineering Research Institute (CSIR-NEERI), Environmental Materials Division, Nehru Marg, Nagpur 440020, India

^d NIMS Beamline Station at SPring-8, 1-1-1 Kouto, Sayo, Hyogo 679-5148, Japan

^e Department of Material and Life Chemistry, Faculty of Engineering, Kanagawa University, 3-27-1, Rokkakubashi, Kanagawa-ku, Yokohama 221-8686, Japan

^f Department of Chemistry and Materials Science, Tokyo Institute of Technology, 2-12-1-E1-10 Ookayama, Meguro-ku, Tokyo 185-8550, Japan

† Electronic supplementary information (ESI) available: HX-PES profiles in the O1s and Pt 4p_{3/2} regions for the surfaces of Pt₃Ti, Pt₃Ta and Pt₃Hf that were heated at different temperatures in the reactant gas. See DOI: 10.1039/c4cp03406f

adsorption energy of CO on the catalyst surface decreases monotonically with the lowering of the d-band center because of diminished hybridization of the surface d-band and the lowest-unoccupied molecular orbital (LUMO) of CO. The observed volcano-type correlation between the d-band center and the CO oxidation activity is accounted for in terms of the CO adsorption energy which counterbalances the surface coverage by CO and the rate of CO oxidation. This established correlation allows us to understand and even predict the exhaust-purification activity of unknown Pt-based alloys by theoretically calculating and/or experimentally determining the d-band center, which will be a guiding principle in the quest for efficient alloy catalysts for exhaust purification.

2. Experimental section

2.1 Sample preparation

Polycrystalline samples of intermetallic Pt₃T (T = Ti, Ta, and Hf) were synthesized in a pure Ar atmosphere (99.9999%) using an arc furnace. Prior to the synthesis, the arc furnace was evacuated to a vacuum level with a pressure lower than 10⁻³ Pa and backfilled with pure Ar. All starting materials were purchased from Furuya Kinzoku Co. An aliquot of 1 g of Pt powder (99.9%) was pelletized with a stainless-steel die and melted in the arc furnace into an ingot. Titanium (sponge, 99%) and Ta (wire, 99%) metals were used as received. As-purchased Hf metal (chunk, 98%) was first melted in the arc furnace to remove surface oxides. The ingots of Pt and the other metals were weighed such that the molar ratio was Pt:T = 3:1 and melted together in the arc furnace. The ingot obtained, with a combined weight of approximately 3 g, was cut into two halves with a diamond saw. One of the halves was ground using an agate mortar for powder X-ray diffraction (pXRD), Brunauer–Emmett–Teller (BET) surface area measurements and catalytic CO oxidation measurements. Slices that were 0.5 mm thick were cut from the other half and polished to a mirror finish for hard X-ray photoemission spectroscopy (HX-PES) measurements.

2.2 Characterization

pXRD (RIGAKU RINT 2000, Cu-K α radiation, $\lambda = 1.541 \text{ \AA}$) was used to examine the powdered samples of the Pt₃T alloys. The specific surface area of each sample was determined using the BET method. A Micromeritics ASAP 2020 was used to collect a partial adsorption isotherm at liquid-nitrogen temperature (77 K) using krypton as the adsorption gas. HX-PES was performed at room temperature in ultra-high vacuum using synchrotron radiation (5.95 keV, SPring-8, beamline BLXU15) and an electron energy analyzer (VG SCIENTA R4000).¹⁹ A 0.3 mm-thick Pt plate (99.9%, Furuya Kinzoku Co.), a 0.3 mm-thick Ti plate (99.9%, Nilaco Co.) and slices of Ta and Hf taken from button-shaped ingots prepared in the arc furnace were used as references for HX-PES. All samples for HX-PES were fixed using carbon adhesives to grounded Cu sample holders. The HX-PES data were referenced to the Fermi edge of an Au film that was electrically connected to the samples *via* the sample holder.

2.3 Catalytic measurements

A fixed-bed flow micro-reactor (Ohkura Riken) equipped with a gas chromatograph (GL Sciences) was used to evaluate the catalytic activities of the samples for the oxidation of CO.²⁰ An aliquot of 150 mg of Pt or Pt₃T powder was introduced into the micro-reactor and subjected to a constant flow (100 ml min⁻¹) of a reactant gas that consisted of CO, O₂ and He at a molar ratio of 2:1:97 (Sumitomo Seika Chemicals). The BET surface areas of the powders were determined prior to the catalytic measurements. The composition of the outlet gas from the micro-reactor was analyzed at different sample temperatures ranging from 473 to 573 K.

2.4 Theoretical calculations

Theoretical calculations of the electronic structures of the catalyst were performed using density-functional theory. The exchange–correlation energy functional was represented by the Perdew–Bruke–Ernzerhof²¹ generalized gradient approximation. Projector-augmented wave pseudopotentials were employed as implemented in the VASP code.^{22,23} The valence configurations of the pseudo-potentials were 5d⁹6s¹ for Pt, 3p⁶3d³4s¹ for Ti, 5p⁶5d³6s² for Ta and 5p⁶5d²6s² for Hf. The energy cutoff for the plane-wave basis set expansion was set at 500 eV. Monkhorst–Pack *k*-point sets of 12 \times 12 \times 12 and 10 \times 10 \times 10 were used for the 1-atom and 4-atom unit cells for Pt and Pt₃Ti, respectively, whereas an 8 \times 8 \times 8 set was used for the 16-atom unit cells of Pt₃Ta and Pt₃Hf. The optimized lattice constants were as follows: $a = 3.98 \text{ \AA}$ for Pt; $a = 3.95 \text{ \AA}$ for Pt₃Ti; $a = 4.93 \text{ \AA}$, $b = 5.61 \text{ \AA}$, $c = 9.40 \text{ \AA}$, $\beta = 100.56^\circ$ for Pt₃Ta; and $a = 5.71 \text{ \AA}$, $b = 5.71 \text{ \AA}$, $c = 9.32 \text{ \AA}$, $\gamma = 119.99^\circ$ for Pt₃Hf, which are consistent with reported experimental crystallographic parameters.^{24–26}

The unit cells were extended for the creation of slab models of the Pt(111), Pt₃Ti(111), Pt₃Ta(001) and Pt₃Hf(001) surfaces. The Pt(111) slab model consisted of 15 layers of Pt planes, including 120 atoms in total, and a vacuum of the same thickness as the Pt slab. The 7–9th layers were fixed during the surface relaxations to represent the bulk region. The 120-atom slab model of Pt₃Ti(111) was created in the same manner as that of Pt(111). The Pt₃Ta(001) slab model consisted of 12 layers of Pt₃Ta planes, including a total of 96 atoms, and a vacuum of the same thickness as the Pt₃Ta slab. The 5–8th layers were fixed during the surface relaxations. A similar model was constructed for the Pt₃Hf(001) surface. For the surface calculations, the *k*-point sampling was set at 2 \times 2 \times 1. The atomic positions of the slab modes were fully relaxed except for the fixed layers. The total density of states (DOS) was plotted with a smearing factor of 0.05 eV. The d-band centers were evaluated by applying the following formula to the calculated DOS:

$$\text{d-band center} = \frac{\int E \text{DOS}(E) dE}{\int \text{DOS}(E) dE}$$

where DOS(*E*) is the density of states of the occupied d-states.

For the calculation of the CO adsorption energy on each surface, a CO molecule was placed above a Pt atom with the C–Pt distance fixed at 1.94 \AA (Fig. S1, ESI[†]).²⁷ The total energy of

a single CO molecule, $E_{\text{tot}}(\text{CO})$, was also computed using the same size supercell to evaluate the CO adsorption energy according to

$$E_{\text{ads}} = E_{\text{tot}}(\text{CO-Metal}) - E_{\text{tot}}(\text{Metal}) - E_{\text{tot}}(\text{CO}),$$

where $E_{\text{tot}}(\text{CO-Metal})$ and $E_{\text{tot}}(\text{Metal})$ are the total energies of the slabs with or without a CO molecule on the surface, respectively.

3. Results and discussion

Fig. 1 presents the structural models for Pt and Pt₃T: Pt, *Fm* $\bar{3}$ *m*, $a = 3.9200$ Å; Pt₃Ti, Cu₃Au type, *Pm* $\bar{3}$ *m*, $a = 3.9040$ Å; Pt₃Ta, Pt₃Nb type, *P2*₁*m*, $a = 4.8690$ Å, $b = 5.5370$ Å, $c = 9.2690$ Å, $\beta = 100.62^\circ$; and Pt₃Hf, Ni₃Ti type, *P6*₃/*mmc*, $a = 5.6360$ Å, $c = 9.2080$ Å, $\beta = 120^\circ$.^{24–26} The Pt and/or Pt₁₂Ti cubo-octahedron depicted by the stick-and-ball model and grey polyhedra in Fig. 1a share the six square planes of the neighboring polyhedra in forming the framework of Pt and/or Pt₃Ti. The crystal structures of Pt₃Ta and Pt₃Hf, unlike that of either Pt or Pt₃Ti, are constructed from two types of Pt₁₂T polyhedra with different configurations (Fig. 1b and c). One of the two types of Pt₁₂T polyhedra is isomorphic to the Pt₁₂Ti cubo-octahedron. The other type of Pt₁₂T polyhedron, which is depicted by a stick-and-ball model and white polyhedra, is a structural derivative

obtained by rotating one of the eight Pt triangles of a Pt₁₂T cubo-octahedron by 180°. The monoclinic structure of Pt₃Ta is constructed by face- and edge-sharing of the Pt₁₂T cubo-octahedron and its structural derivative. The hexagonal structure of Pt₃Hf is also constructed by face- and edge-sharing of the two types of Pt₁₂T polyhedra, but in a different sequence (Fig. 1c).

Fig. 2 shows the pXRD profiles for Pt₃T, together with the diffraction patterns simulated using the reported crystallographic parameters. The pXRD profiles for Pt₃Ti, Pt₃Ta and Pt₃Hf are consistent with the simulated patterns. The synthesized samples of Pt₃T were single-phase ordered alloys with the desired compositions and crystal structures.

Fig. 3 shows the HX-PES profiles for the core levels of the T elements in Pt₃T. The Ti 2p levels of Pt₃Ti were shifted by 1.0 eV toward high binding energies relative to those of pure Ti (Fig. 3a). Similar shifts were observed for the other Pt₃T (Fig. 3b and c). Both the Ta 4f levels of Pt₃Ta and the Hf 4f levels of Pt₃Hf were shifted by 1.5 eV toward high binding energies relative to those of the corresponding pure metals (Table 1).

The HX-PES profiles for the Pt 4f levels of pure Pt and Pt₃T are presented in Fig. 4. The Pt 4f_{7/2} and 4f_{5/2} levels were, in descending order, Pt, Pt₃Ti, Pt₃Ta and Pt₃Hf, where the amplitude of the spin-orbit splitting was 3.35 ± 0.20 eV irrespective of the identity of T (Table 2). In summary, the synthesized Pt₃T samples were ordered alloys that exhibited different crystal

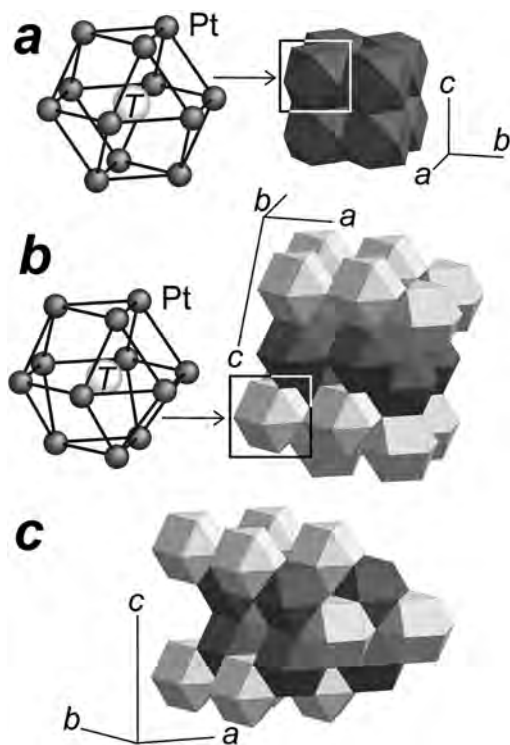


Fig. 1 Crystal structures of Pt and Pt₃T. (a) Ball-and-stick model for a Pt₁₂T cubo-octahedron (left) and the crystal structures of Pt and Pt₃Ti as a polygonal model (right). The grey polyhedra correspond to the Pt₁₂T and/or Pt₁₂T cubo-octahedra. (b) Ball-and-stick model for a structural derivative of the Pt₁₂T cubo-octahedron (left) and a polygonal model for Pt₃Ta (right). The grey and white polyhedra correspond to the cubo-octahedral Pt₁₂T and its structural derivative, respectively. (c) Polygonal model for Pt₃Hf.

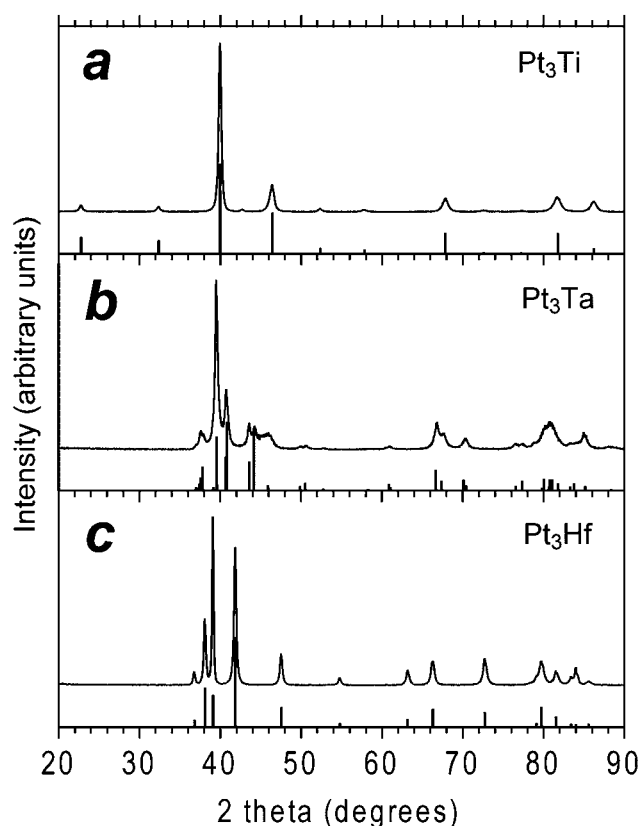


Fig. 2 pXRD profiles for Pt₃Ti (a), Pt₃Ta (b) and Pt₃Hf (c). Simulated diffraction patterns are indicated as solid bars.

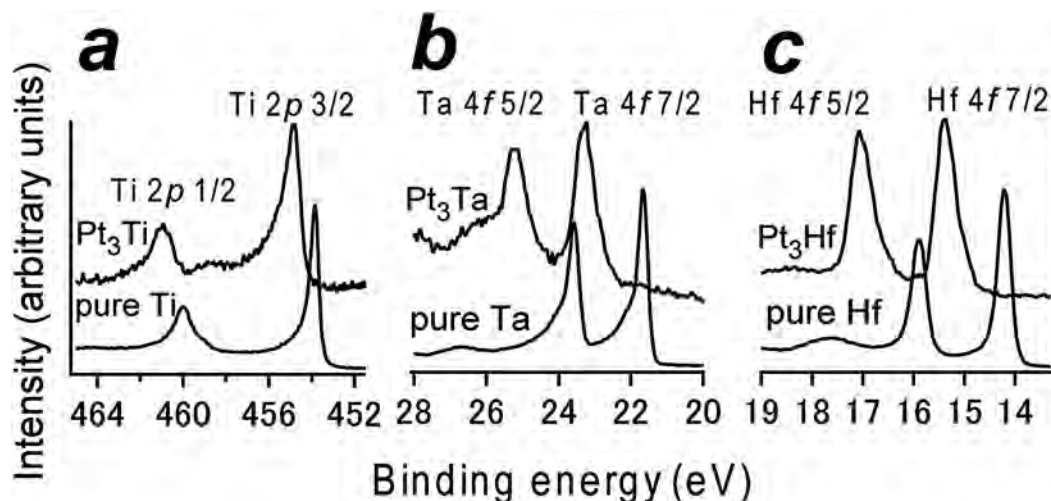


Fig. 3 HX-PES profiles for the core levels of the T elements in Pt_3T . (a) Ti 2p levels of Pt_3Ti and pure Ti. (b) Ta 4f levels of Pt_3Ta and pure Ta. (c) Hf 4f levels of Pt_3Hf and pure Hf.

Table 1 Core levels of the T elements in Pt_3T

| Material | Binding energy (eV) | Binding energy (eV) | Spin-orbit splitting Δ^a (eV) |
|------------------------|------------------------------------|------------------------------------|--------------------------------------|
| Pt_3Ti | Ti 2p _{3/2} | Ti 2p _{1/2} | 6.10 |
| | 454.82 ± 0.20 (455.2) ^b | 460.92 ± 0.20 (461.3) ^b | |
| Ti | 453.82 ± 0.20 (454.0) ^c | 460.02 ± 0.20 (460.0) ^c | 6.20 |
| | | | |
| Pt_3Ta | Ta 4f _{7/2} | Ta 4f _{5/2} | 2.05 |
| | 23.22 ± 0.20 | 25.27 ± 0.20 | |
| Ta | 21.67 ± 0.20 (21.7) ^d | 23.57 ± 0.20 (23.7) ^d | 1.90 |
| | | | |
| Pt_3Hf | Hf 4f _{7/2} | Hf 4f _{5/2} | 1.70 |
| | 15.37 ± 0.20 | 17.07 ± 0.20 | |
| Hf | 14.22 ± 0.20 (14.31) ^e | 15.87 ± 0.20 (15.98) ^e | 1.65 (1.67) ^e |

Note: literature values are indicated in parentheses. ^a Δ : spin-orbit splitting. ^b Ref. 28–30. ^c Ref. 31 and 32. ^d Ref. 33 and 34. ^e Ref. 35.

Table 2 Pt core levels of pure Pt and Pt_3T

| Material | Pt 4f _{7/2} binding energy (eV) | Pt 4f _{5/2} binding energy (eV) | Spin-orbit splitting Δ^a (eV) |
|------------------------|--|--|--------------------------------------|
| Pt | 70.97 ± 0.20 (71.30) ^b | 74.32 ± 0.20 (74.23) ^b | 3.35 |
| Pt_3Ti | 71.37 ± 0.20 (71.3) ^c | 74.72 ± 0.20 (74.65) ^c | 3.35 |
| Pt_3Ta | 71.52 ± 0.20 | 74.82 ± 0.20 | 3.30 |
| Pt_3Hf | 71.62 ± 0.20 | 74.92 ± 0.20 | 3.30 |

^a Δ : spin-orbit splitting. ^b Ref. 36. ^c Ref. 28–30.

for 1 hour in a fixed-bed flow micro-reactor at a temperature of 548, 598 or 823 K. After exposure to the reactant gas, the Pt_3T samples were transferred to the UHV chamber for HX-PES measurements.

The left panel of Fig. 5a shows Pt 4f profiles for the Pt_3Ti surfaces subjected to different atmospheres. Both of the Pt 4f profiles for the Pt_3Ti surfaces heated at 548 K (light-blue profile) or 598 K (green profile) were identical to that for the as-prepared Pt_3Ti surface (blue profile). The Pt 4f emission peaks for the Pt_3Ti surface heated at 823 K (red profile), however, exhibited large shoulders at 71.02 ± 0.20 and 74.36 ± 0.20 eV. These values were consistent with the Pt 4f emission peaks for the pure Pt surface at 70.97 ± 0.20 and 74.32 ± 0.20 eV, respectively (black profile). The Pt_3Ti surface, when heated to 823 K in the reactant gas mixture, precipitated pure Pt.

The right panel of Fig. 5a shows the Ti 2p profile for the Pt_3Ti surfaces. The Ti 2p_{3/2} (454.87 ± 0.20 eV) and Ti 2p_{1/2} (460.97 ± 0.20 eV) levels of the as-prepared surface were consistent with those of the surfaces heated at 548 K or 598 K, though an additional peak was observed at 458.85 ± 0.20 eV for the heated surfaces. This peak was attributed to the adsorption of oxygen onto the surface of Ti to form a suboxide, TiO_{2-x} ($x > 0$).^{28–30,37} For the sample heated at 823 K, the Ti emission peaks for Pt_3Ti and TiO_x ($x < 2$) nearly vanished. Two peaks appeared at 459.25 ± 0.20 and 465.00 ± 0.20 eV instead, corresponding to the Ti 2p_{3/2} and Ti 2p_{1/2} emissions,

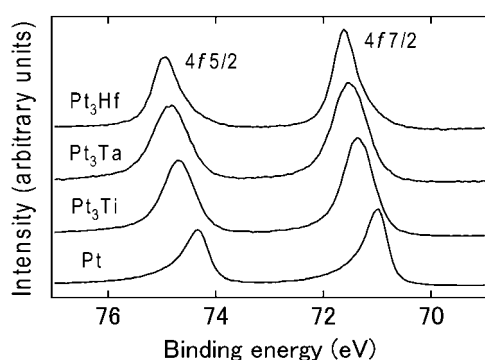


Fig. 4 HX-PES profiles for the Pt core levels of pure Pt and Pt_3T .

structures and electronic structures from those of the constituent elements.

Prior to the catalytic testing, the chemical stability of each Pt_3T surface was examined at elevated temperatures in a reactant gas that consisted of CO, O₂ and He at a molar ratio of 2 : 1 : 97. Each Pt_3T surface was exposed to the reactant gas

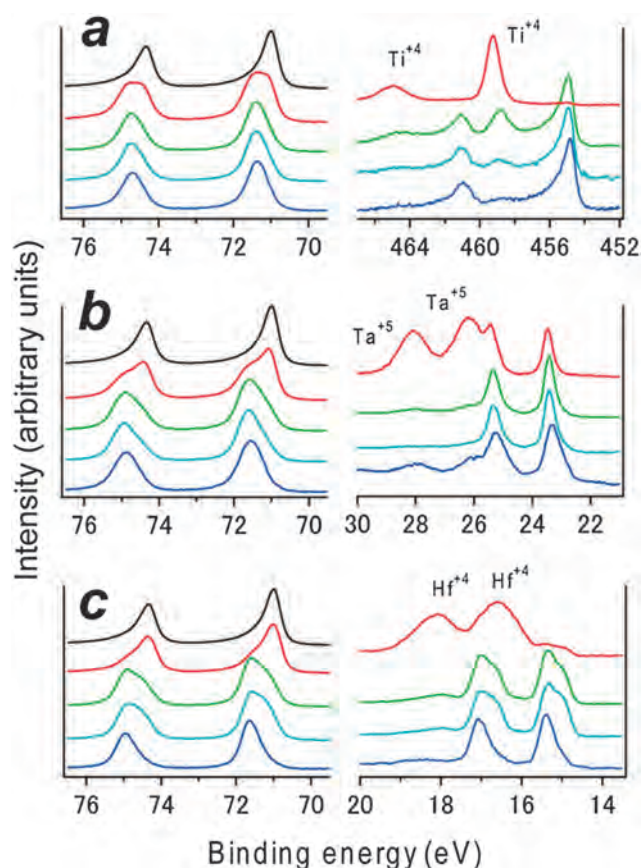


Fig. 5 HX-PES profiles for the Pt_3T surfaces subjected to different atmospheres. (a) Pt 4f (left) and Ti 2p levels (right) of the Pt_3Ti surface. (b) Pt 4f (left) and Ta 4f levels (right) of the Pt_3Ta surface. (c) Pt 4f (left) and Hf 4f levels (right) of the Pt_3Hf surface. Colored profiles correspond to the as-prepared surfaces (blue) and to the surfaces heated in the reactant gas at 548 K (light blue), 598 K (green) or 823 K (red). Black profiles indicated in the left panels from a through c correspond to the Pt 4f levels of the pure Pt surface.

respectively, from titanium dioxide, Ti^{4+}O_2 .^{31,32} The Pt_3Ti surface retained its chemical composition when heated in the reactant gas at temperatures below 598 K but was decomposed at 823 K into pure Pt and TiO_2 .

The left and right panels of Fig. 5b show the Pt 4f and Ta 4f profiles, respectively, for the Pt_3Ta surfaces. The Pt 4f profiles for the Pt_3Ta surfaces heated at 548 or 598 K were virtually identical to that of the as-prepared surface (left panel) and the Ta 4f profiles for the Pt_3Ta surfaces heated at 548 or 598 K were similar to that for the as-prepared surface (right panel). A shoulder at 26.0 eV and a weak peak at 28.0 eV on the Ta 4f profile for the as-prepared Pt_3Ta surface (blue profile in the right panel) correspond to a surface contamination that was removed by heating in the reactant gas. The Pt_3Ta surface retained the chemical composition of the as-prepared surface when heated to temperatures ranging from 548 to 598 K. At a temperature of 823 K, the emission peaks that correspond to pure Pt (red profile in the left panel) and $\text{Ta}^{5+}_2\text{O}_5$ (red profile in the right panel) became clearly visible.^{33,34} At 823 K, the Pt_3Ta surface decomposed into pure Pt and Ta_2O_5 , similar to the behavior of the Pt_3Ti surface.

The left and right panels of Fig. 5c show the Pt 4f and Hf 4f profiles for the Pt_3Hf surface. The Pt emission peaks for the surfaces heated to 548 K or 598 K, 71.60 ± 0.20 and 74.90 ± 0.20 eV, respectively, were consistent with those observed for the as-prepared Pt_3Hf surface, at 71.62 ± 0.20 and 74.92 ± 0.20 eV, respectively (left panel). The Hf emission peaks for the surfaces heated at 548 K or 598 K, 15.35 ± 0.20 and 17.00 ± 0.20 eV, respectively, were also consistent with those for the as-prepared Pt_3Hf surface, 15.37 ± 0.20 and 17.07 ± 0.20 eV, respectively (right panel).

The Pt 4f and Hf 4f emission peaks for the Pt_3Hf surfaces heated at 548 or 598 K, unlike those for the as-prepared surface, exhibited shoulders at lower binding energies. The binding energies for the shoulders of the Pt 4f emission peaks were revealed by deconvolution to be at 71.15 ± 0.20 and 74.46 ± 0.20 eV. These values were not consistent with the Pt 4f levels of the pure Pt surface, 70.97 ± 0.20 and 74.32 ± 0.20 eV. The binding energies for the shoulders of the Hf 4f emission peaks, 14.98 ± 0.20 and 16.66 ± 0.20 eV, were also inconsistent with the values for HfO_2 (16.60 ± 0.20 and 18.10 ± 0.20 eV), Pt_3Hf (15.37 ± 0.20 and 17.07 ± 0.20 eV) or pure Hf (14.22 ± 0.20 and 15.87 ± 0.20 eV).³⁵

Morant *et al.* reported that a suboxide of Hf, HfO_{2-x} ($x > 0$), was formed on a Hf surface at room temperature at an early stage of adsorption of oxygen ($\leq 5 \text{ L}$).³⁵ The reported binding energies for the Hf 4f emissions from HfO_{2-x} , 15.1 and 16.8 eV, are similar to the values for the shoulders of the Hf 4f emissions from Pt_3Hf surfaces heated at 548 or 598 K, 14.98 ± 0.20 and 16.66 ± 0.20 eV, respectively. The observed shoulders of the Hf 4f peaks for the Pt_3Hf surfaces heated at 548 or 598 K are assigned to a suboxide of the surface Hf that may accompany a core-level shift for the surface Pt.

The Pt 4f profile for the Pt_3Hf surface heated at 823 K (red profile in the left panel of Fig. 5c) was different from that for the surface heated at either 548 or 598 K and was similar to that for the pure Pt surface. The Hf 4f profile for the surface heated at 823 K (red profile in the right panel of Fig. 5c) showed two peaks that corresponded to Hf^{4+}O_2 at 16.60 ± 0.20 and 18.10 ± 0.20 eV. The Pt_3Hf surface retained the chemical composition of the as-prepared surface when heated to temperatures ranging from 548 to 598 K but decomposed into pure Pt and HfO_2 when heated at 823 K.

Summarizing the HX-PES data in the core-level region, we conclude that the Pt_3T surfaces retain their chemical compositions when exposed to the O_2 -containing reactant gas, as long as the temperature is lower than 598 K. When the temperature exceeds 823 K, the Pt_3T surfaces decompose into pure Pt and a transition-metal oxide of T in its highest available oxidation state. Indeed, the O1s emission peaks for the Pt_3T surfaces heated at 823 K were more intense than those for the surfaces heated below 598 K (see Fig. S2, ESI†). Catalytic tests were performed at temperatures below 598 K to establish a reliable correlation between the catalytic activity and the surface electronic structure of Pt_3T .

Fig. 6 shows the temperature dependence of the catalytic activities of Pt and Pt_3T toward the oxidation of CO. The specific CO oxidation activity of Pt increased monotonically

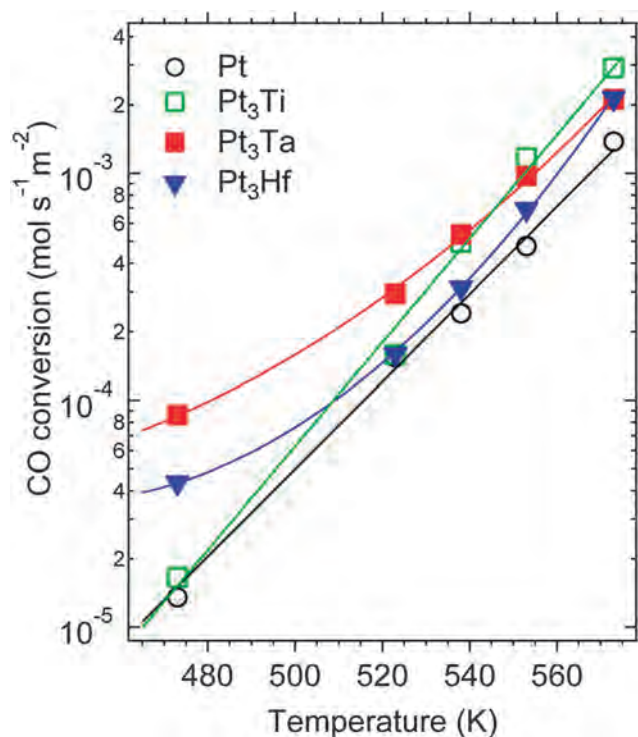


Fig. 6 Catalytic CO oxidation over the Pt and Pt₃T surfaces. The specific activities for CO oxidation over Pt (○), Pt₃Ti (□), Pt₃Ta (■) and Pt₃Hf (▼) are plotted as functions of temperature.

with increasing temperature (open circles in Fig. 6). The specific CO oxidation activities of Pt at 473 and 573 K were 1.35×10^{-5} and 1.38×10^{-3} mol s⁻¹ m⁻², respectively. The specific CO oxidation activity of Pt₃Ti also increased with increasing temperature but at a higher rate. The specific activity of Pt₃Ti at 473 K was 1.66×10^{-5} mol s⁻¹ m⁻², which was higher than the value of Pt at the same temperature. At 573 K, however, the specific activity of Pt₃Ti was 2.91×10^{-3} mol s⁻¹ m⁻², which was double that observed for Pt. Pt₃Ta showed the highest specific CO oxidation activity at low temperatures. The specific activity of Pt₃Ta at 473 K, 8.62×10^{-5} mol s⁻¹ m⁻², was 5-fold higher than the values for Pt or Pt₃Ti. The specific activity of Pt₃Hf at each temperature was between those of Pt₃Ta and Pt. The specific CO oxidation activities of Pt and Pt₃T were Pt < Pt₃Ti < Pt₃Hf < Pt₃Ta at temperatures below 538 K and Pt < Pt₃Hf < Pt₃Ta < Pt₃Ti above 538 K.

Fig. 7 shows the HX-PES profiles for the pure Pt and the as-prepared Pt₃T surfaces in the valence region, together with the calculated DOS for Pt and T. Both the HX-PES and the DOS profiles for pure Pt exhibit a large peak immediately below the Fermi level, assigned to the Pt 5d orbital (Fig. 7a). In contrast, the HX-PES profile for Pt₃Ti exhibits no corresponding peak below the Fermi level (Fig. 7b). Theoretical calculations have shown that the Pt 5d and Ti 3d orbitals are hybridized to split into anti-bonding and bonding states located above and below the Fermi level.³⁸ The valence band of Pt₃Ti is a bonding state of Pt and Ti that consists mostly of the Pt 5d state with a small Ti 3d component. As with Pt₃Ti, neither Pt₃Ta (Fig. 7c) nor

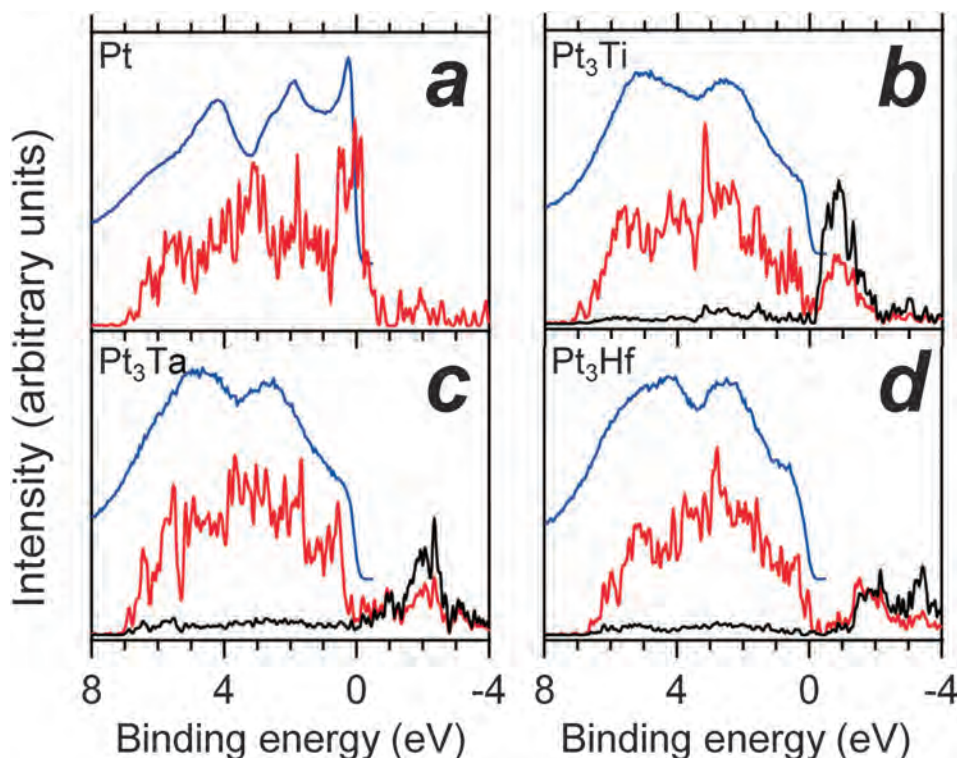


Fig. 7 HX-PES profiles and calculated density-of-states (DOS) for Pt and Pt₃T in the valence region. (a) Pt. (b) Pt₃Ti. (c) Pt₃Ta. (d) Pt₃Hf. The blue, red and black profiles correspond to the experimental HX-PES data and the DOS components of Pt and T, respectively.

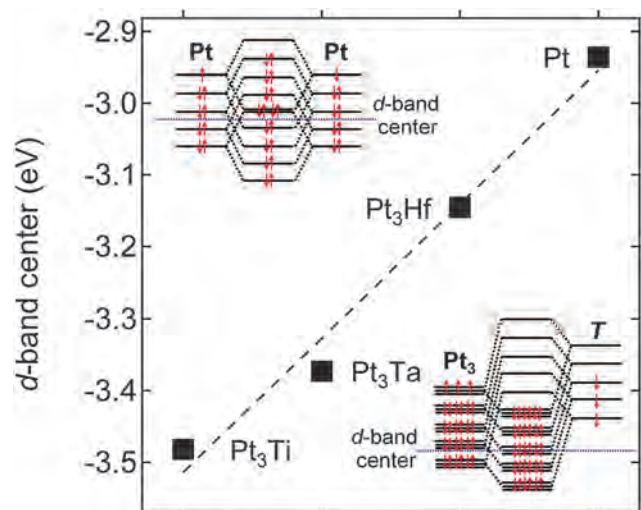


Fig. 8 Calculated d-band centers for Pt and Pt_3T . Insets show schematic energy diagrams for Pt (top left) and Pt_3T (bottom right).

Pt_3Hf (Fig. 7d) shows any predominant peaks immediately below the Fermi level in the HX-PES or DOS profiles: the Ta 5d orbital and the Hf 5d orbital are hybridized with the Pt 5d orbital and split into anti-bonding and bonding states.

The calculated gravity centers of the filled Pt d-band (d-band center) for Pt and Pt_3T were ordered as $\text{Pt}_3\text{Ti} < \text{Pt}_3\text{Ta} < \text{Pt}_3\text{Hf} < \text{Pt}$ (Fig. 8). Pure Pt has the highest energy d-band center because the d-band in pure Pt is mostly filled by electron pairs, as shown in the top-left inset. In Pt_3T , however, few electrons are donated by the T element, and only the bonding states are occupied, which results in a downshift in the d-band center (bottom-right inset). The energy level of the d-band center of Pt_3T is determined by the energy gap between the d-orbitals of Pt and T: a smaller energy gap results in a lower d-band center due to a larger energy splitting. The energy levels of the d-orbitals were calculated as -5.52 eV (Pt), -4.12 eV (Ti), -3.55 eV (Ta), and -2.64 eV (Hf). These values are consistent with the trend presented in Fig. 8.

The CO oxidation activities at the lowest temperature in the measurement range, 473 K, were plotted against the calculated d-band centers (Fig. 9). The CO oxidation activity exhibited a volcano-type dependence on the d-band center with Pt_3Ta at the top. The CO oxidation activities of Pt_3Ti and Pt_3Hf were higher than that of pure Pt, but lower than that of Pt_3Ta .

Fig. 10 shows the theoretically calculated CO adsorption energy on the catalyst surface of Pt and Pt_3T . The amplitude of CO adsorption energy decreases monotonically as the d-band center decreases. The CO adsorption energy on the Pt_3Ti surface is 30% lower than that on the pure Pt surface. This trend is attributed to poor electron back-donation from the Pt_3T surfaces to CO ad molecules, which is caused by the increased energy gap between the d-band center and the lowest unoccupied $2\pi^*$ molecular orbital (LUMO) of the CO ad molecules.^{27,39,40}

The volcano-type correlation established in this work may be assigned to a downshift in the d-band center of Pt_3T relative to that of Pt, which is accompanied by a weakening of the CO

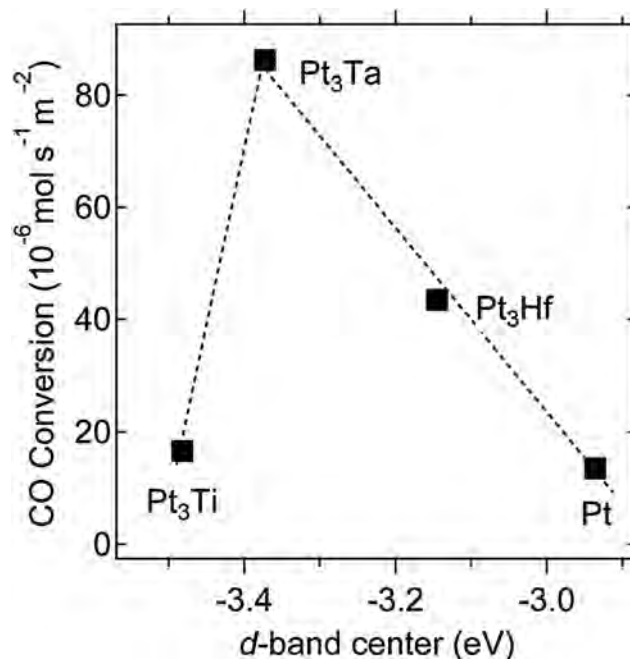


Fig. 9 Correlation between the CO oxidation activity and the d-band center. Specific CO oxidation activities of Pt and Pt_3T at 473 K are plotted as a function of the d-band center.

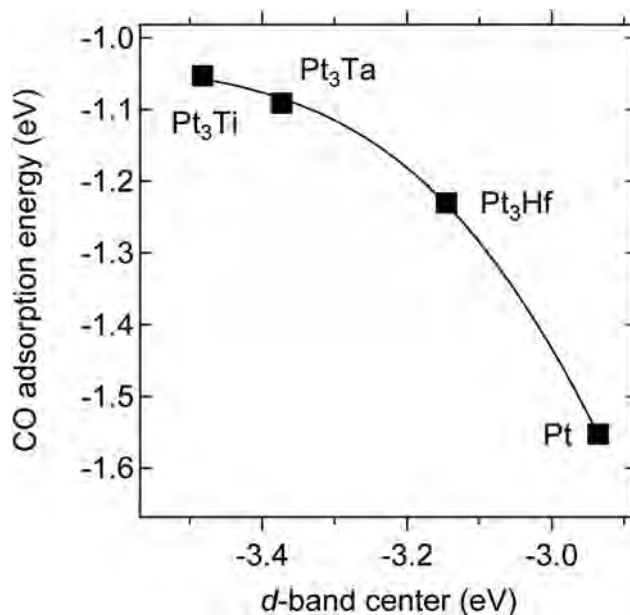


Fig. 10 Correlation between the CO adsorption energy and the d-band center.

adsorption. The CO adsorption onto the Pt surface is so strong that the catalysis is blocked by the CO adlayer. In contrast, CO oxidation is poorly promoted by Pt_3Ti at low temperatures because CO ad molecules readily desorb from the surface.^{41–45} Pt_3Ta , which exhibits an intermediate d-band center, achieves the highest CO oxidation activity because of an optimum balance in the adsorption and desorption of CO.

4. Conclusions

In conclusion, we have demonstrated that ordered early d-metal alloys, Pt₃T (T = Ti, Ta and Hf), exhibit catalytic activities that are superior to that of pure Pt for the oxidation of CO. The specific CO oxidation activities of Pt and Pt₃T showed a volcano-type correlation with the d-band center of the catalyst. The observed volcano-type correlation has been interpreted as a result of the weakening of CO adsorption onto the catalyst surface caused by a downshift in the d-band center of Pt₃T relative to that of Pt.

The outstanding issues and potential limitations to be addressed include the chemical composition of the catalyst surface at work, the surface dynamics of the reaction intermediates and how the atomic arrangement on the surface affects the apparent activity. The Pt₃Ta catalyst, which exhibited a very high CO oxidation activity, should be synthesized in the form of nanoparticles for practical use. These issues are challenging, yet worthy of effort, because the high activity and the reduced precious-metal content of alloy catalysts will strongly promote the future development of such metal catalysts for environmental and/or energy applications.

Acknowledgements

This work was supported by the JST PRESTO program. We gratefully acknowledge the Toyota Motor Corporation for financial support. The HX-PES measurements were performed under the approval of the NIMS Beamline Station (Proposal No. 2009B4608 and 2010A4609). The authors are grateful to HiSOR, Hiroshima University, and JAEA/SPring-8 for the development of HX-PES at BL15XU of SPring-8.

References

- X. Xie, Y. Li, Z. Q. Liu, M. Haruta and W. Shen, *Nature*, 2009, **458**, 746–749.
- C. H. Kim, G. Qi and W. L. Dahlberg, *Science*, 2010, **327**, 1624–1627.
- S. Zhou, B. Varughese, B. Eichhorn, G. Jackson and K. McIlwrath, *Angew. Chem., Int. Ed.*, 2005, **44**, 4539–4543.
- Y. Kang and C. Murray, *J. Am. Chem. Soc.*, 2010, **132**, 7568–7569.
- J. L. Zhang, M. B. Vukmirovic, Y. Xu, M. Mavrikakis and R. R. Adzic, *Angew. Chem., Int. Ed.*, 2005, **44**, 2132–2145.
- V. R. Stamenkovic, B. S. Mun, K. J. J. Mayrhofer, P. N. Ross and N. M. Marković, *J. Am. Chem. Soc.*, 2006, **128**, 8813–8819.
- T. Komatsu and A. Tamura, *J. Catal.*, 2008, **258**, 306–314.
- E. Nikolla, J. Schwank and S. Linic, *J. Am. Chem. Soc.*, 2009, **131**, 2747–2754.
- T. Hofmann, T. H. Yu, M. Folse, L. Weinhardt, M. Bar, Y. Zhang, B. V. Merinov, D. J. Myers, W. A. Goddard III and C. Heske, *J. Phys. Chem. C*, 2012, **116**, 24016–24026.
- F. Abild-Pedersen, A. Nilsson and J. K. Nørskov, *J. Phys. Chem. C*, 2013, **117**, 6914–6915, and references therein.
- V. R. Stamenkovic, B. S. Mun, M. Arenz, K. J. J. Mayrhofer, C. A. Lucas, G. F. Wang, P. N. Ross and N. M. Marković, *Nat. Mater.*, 2007, **6**, 241–247.
- B. Hammer and J. K. Nørskov, *Nature*, 1995, **376**, 238–240.
- Y. Morikawa, J. J. Mortensen, B. Hammer and J. K. Nørskov, *Surf. Sci.*, 1997, **386**, 67–72.
- B. Hammer and J. K. Nørskov, *Theory of adsorption and surface reactions*, Kluwer Academic Publishers, 1997.
- C. A. Menning and J. G. G. Chen, *J. Chem. Phys.*, 2009, **130**, 174709.
- G. Saravanan, H. Abe, Y. Xu, N. Sekido, H. Hirata, S. Matsumoto, H. Yoshikawa and Y. Yamabe-Mitarai, *Langmuir*, 2010, **26**, 11446–11451.
- H. Abe, F. Matsumoto, L. R. Alden, S. C. Warren, D. H. Abruña and F. J. DiSalvo, *J. Am. Chem. Soc.*, 2008, **130**, 5452–5458.
- T. Ghosh, B. M. Leonard, Q. Zhou and F. J. DiSalvo, *Chem. Mater.*, 2010, **22**, 2190–2202.
- T. Ohsawa, Y. Adachi, I. Sakaguchi, K. Matsumoto, H. Haneda, S. Ueda, H. Yoshikawa, K. Kobayashi and N. Ohashi, *Chem. Mater.*, 2009, **21**, 144–150.
- D. H. Chun, Y. Xu, M. Demura, K. Kishida, D. M. Wee and T. Hirano, *J. Catal.*, 2006, **243**, 99–107.
- P. J. Perdew, K. Burke and M. Ernzerhof, *Phys. Rev. Lett.*, 1996, **77**, 3865–3868.
- G. Kresse and J. Furthmüller, *Phys. Rev. B: Condens. Matter Mater. Phys.*, 1996, **54**, 11169–11186.
- G. Kresse and J. Hafner, *Phys. Rev. B: Condens. Matter Mater. Phys.*, 1993, **47**, 558–561.
- Pearson's Handbook of Crystallographic Data for Intermetallic Phases*, ed. P. L. Villars and L. D. Calvert, American Society for Metals, Metals Park, OH, 1985, vol. 3, pp. 3044, 3058, 3059.
- B. C. Giessen, R. H. Kane and N. J. Grant, *Trans. Metall. Soc. AIME*, 1965, **233**, 855–864.
- A. E. Dwight and P. A. Beck, *Trans. Metall. Soc. AIME*, 1959, **215**, 976–979.
- B. Hammer, Y. Morikawa and J. K. Nørskov, *Phys. Rev. Lett.*, 1996, **76**, 2141–2144.
- A. Dauscher, L. Hilaire, J. C. Spirlet, W. Müller and G. Maire, *Surf. Sci.*, 1988, **204**, 161–173.
- G. N. Derry and P. N. Ross, *Solid State Commun.*, 1984, **52**, 151–154.
- W. Chen, L. Severin, M. Göthelid, M. Hammer, S. Cameron and J. Paul, *Phys. Rev. B: Condens. Matter Mater. Phys.*, 1994, **50**, 5620–5627.
- A. R. Burke, C. R. Brown, W. C. Bowling, J. E. Glaub, D. Kapsch, C. M. Love, R. B. Whitaker and W. E. Moddeman, *Surf. Interface Anal.*, 1988, **11**, 353–358.
- R. P. Netterfield, P. J. Marin, C. G. Pacey, W. G. Sainty, D. R. McKenzie and G. Auchterlonie, *J. Appl. Phys.*, 1989, **66**, 1805–1809.
- J. D. Rogers, V. S. Sundaram, G. G. Kleiman, C. G. C. Castro, R. A. Douglas and A. C. Peterlevitz, *J. Phys. F: Met. Phys.*, 1982, **12**, 2097–2102.
- S. F. Ho, S. Contarini and J. W. Rabalais, *J. Phys. Chem.*, 1987, **91**, 4779–4788.

- 35 C. Morant, L. Galán and J. M. Sanz, *Surf. Interface Anal.*, 1990, **16**, 304–308.
- 36 P. Légaré, G. Lindauer, L. Hilaire, G. Maire, J. J. Ehrhardt, J. Jupille, A. C. Cassuto, C. Guillot and J. Lecante, *Surf. Sci.*, 1988, **198**, 69–78.
- 37 J. Paul, S. D. Cameron, D. J. Dwyer and F. M. Hoffmann, *Surf. Sci.*, 1986, **177**, 121–138.
- 38 W. Chen, E. Chulkov and J. Paul, *Phys. Scr.*, 1996, **54**, 392–396.
- 39 J. A. Rodriguez and D. W. Goodman, *Science*, 1992, **257**, 897–903.
- 40 J. A. Rodriguez, C. M. Truong and D. W. Goodman, *J. Chem. Phys.*, 1992, **96**, 7814–7825.
- 41 P. N. Ross, *J. Vac. Sci. Technol., A*, 1992, **10**, 2546–2550.
- 42 P. N. Ross, *Electrochim. Acta*, 1991, **36**, 2053–2062.
- 43 U. Bardi, D. Dahlgren and P. N. Ross, *J. Catal.*, 1986, **100**, 196–209.
- 44 U. Bardi, G. A. Somorjai and P. N. Ross, *J. Catal.*, 1984, **85**, 272–276.
- 45 T. Jiang, D. J. Mowbray, S. Dobrin, H. Falsig, B. Hvolbæk, T. Bligaard and J. K. Nørskov, *J. Phys. Chem. C*, 2009, **113**, 10548–10553.



Photocatalytic decomposition of various organic compounds over WO₃-supported ordered intermetallic PtPb co-catalysts



Takao Gunji^a, Arockiam John Jeevagan^a, Masanari Hashimoto^a, Toshiaki Nozawa^a, Toyokazu Tanabe^a, Shingo Kaneko^b, Masahiro Miyauchi^c, Futoshi Matsumoto^{a,*}

^a Department of Material and Life Chemistry, Kanagawa University, 3-27-1, Rokkakubashi, Kanagawa-ku, Yokohama, Kanagawa 221-8686, Japan

^b Research Institute for Engineering, Kanagawa University, 3-27-1, Rokkakubashi, Kanagawa-ku, Yokohama, Kanagawa 221-8686, Japan

^c Department of Metallurgy and Ceramic Science, Graduate School of Science and Engineering, Tokyo Institute of Technology, 2-12-1 Ookayama, Meguro-ku, Tokyo 152-8552, Japan

ARTICLE INFO

Article history:

Received 2 June 2015

Received in revised form 5 August 2015

Accepted 9 August 2015

Available online 11 August 2015

Keywords:

Photocatalyst

Intermetallic PtPb co-catalyst

Visible light

Quantum efficiency

Reaction mechanism

ABSTRACT

This study investigates the photocatalytic decomposition of acetic acid and its reaction mechanism over WO₃-supported ordered intermetallic PtPb nanoparticle (NiAs-type structure, P63/mmc, $a = 0.4259$ nm; $c = 0.5267$ nm) (PtPb NPs/WO₃) co-catalysts under an oxygen-rich atmosphere and visible light. We rationally designed and synthesized the ordered intermetallic nanoparticle on WO₃ co-catalysts by a photodeposition and polyol method. Remarkably enhanced activities were observed for the synthesized PtPb NPs/WO₃ catalyst toward the decomposition of organic compounds compared to pure WO₃ and WO₃-supported individual Pt co-catalysts.

© 2015 Elsevier B.V. All rights reserved.

1. Introduction

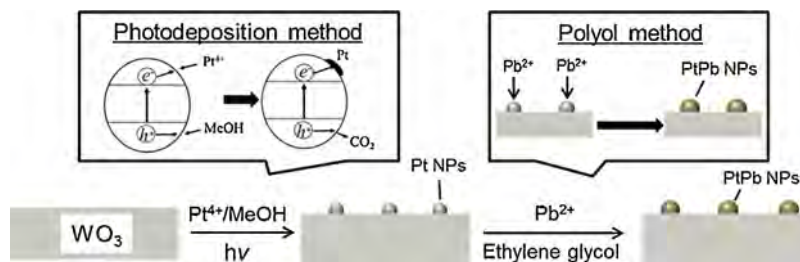
In recent years, semiconductor photocatalysts such as TiO₂ and WO₃ have gained attention for applications in environmental remediation [1], H₂ evolution [2], water splitting [3], and CO₂ reduction [4]. Photocatalysts that are active in the visible light region can be very useful as they efficiently decompose harmful organic compounds such as acetic acid (AcOH), acetaldehyde, and formaldehyde under indoor light or sun-light [5,6]. In particular, WO₃ has attracted considerable interest because of its visible light-responsive properties and deeper holes in its valence band. However, WO₃ by itself cannot be used as a photocatalyst because of its lower conduction band (CB) edge. The CB level of WO₃ (+0.50 V vs. NHE) is slightly negative compared with the potential for the multi-electron reduction of oxygen (O₂/H₂O₂ = 0.68 V vs. NHE) [7]. The oxygen in WO₃ lacks the ability to scavenge CB electrons that causes the recombination rate of electrons and holes to increase, resulting in a significant decline in photocatalytic activity. Therefore, in order to improve the photocatalytic efficiency of WO₃ for decomposing organic compounds, WO₃ requires

a co-catalyst on its surface to facilitate oxygen reduction reactions (ORR). Recently, Abe et al. reported that Pt nanoparticle-loaded (1 wt.%) WO₃ (Pt NPs/WO₃) photocatalysts effectively decomposed organic compounds under visible light and full arc in an oxygen-rich atmosphere [8]. This indicated that the surface of the Pt NPs facilitates oxygen reduction on WO₃. We have previously reported that ordered intermetallic PtPb NPs exhibit efficient electrocatalytic activity for the oxidation of formic acid, methanol (MeOH), and ethanol [9]. In our recent study, we demonstrated that ordered intermetallic PtPb NPs on TiO₂ electrochemically accelerated ORR in acidic media [10]. In addition, we found that H₂PtCl₆·6H₂O and Pb(CH₃COO)₂ can be co-reduced using sodium borohydride to precipitate PtPb NPs (average particles size: 9.5 nm) over the WO₃ support (PtPb NPs/WO₃). PtPb NPs/WO₃ showed substantial photocatalytic activity toward the decomposition of AcOH in aqueous solutions [11]. However, its photocatalytic activity was not sufficient with this method because the nanoparticle size was not controlled and the details of the photocatalytic reaction mechanism of PtPb NPs/WO₃ were not disclosed.

The investigations suggested that the construction of ordered intermetallic PtPb NPs as co-catalysts for photocatalysis on WO₃ could potentially increase the photocatalytic activity. Herein, we report the synthesis of PtPb NPs/WO₃ via a photodeposition and polyol method to control the particle size and demonstrate

* Corresponding author. Fax: +81 45 413 9770.

E-mail address: fmatsumoto@kanagawa-u.ac.jp (F. Matsumoto).



Scheme 1. Schematic representation of Pt NPs and ordered intermetallic PtPb NPs loading on WO_3 using two step synthesis method.

enhanced photocatalytic activity toward the decomposition of various organic compounds. The product is compared to pure WO_3 and Pt NPs/ WO_3 toward the photocatalytic decomposition of various organic compounds. In addition, we discuss how co-catalysts contribute in enhancing the decomposition of organic compounds under visible light irradiation.

2. Experimental

2.1. Preparation of PtPb loaded WO_3 photocatalyst

A two-step synthesis method for the formation of WO_3 -supported ordered intermetallic PtPb NPs is shown in Scheme 1. Pt (1 wt.%) NPs/ WO_3 was used as a starting material for the synthesis of ordered intermetallic PtPb NPs/ WO_3 . In the first step, Pt NPs/ WO_3 was synthesized through a photodeposition method reported by Abe et al. [8]. In the second step, the synthesized Pt NPs/ WO_3 (0.4 g) was dispersed in ethylene glycol (50 mL) in the presence of $\text{Pb}(\text{CH}_3\text{COO})_2$ (0.03 mmol), and then potassium hydroxide (1 mg) was added to the mixture. The mixture was sonicated for 20 min in a bath-type sonicator. The mixture was then refluxed for 6 min under a microwave (Focused microwave instrument, CEM) power of 300 W. After cooling, the PtPb NPs/ WO_3 was collected by centrifugation, washed with ethanol, and finally dried under vacuum.

2.2. Characterization

X-ray photoelectron spectroscopy (XPS) measurements (JEOL, JP-9010 MC) were performed to examine the chemical states (Pt 4f and Pb 4f) of the catalyst. MgK α as X-ray source with anodic voltage (10 kV) and current (10 mA) were used for XPS measurements. All XPS spectra of the samples were obtained with a take-off angle at 45° with respect to the specimens by using the pass energies of 100 eV and 200 eV for narrow and survey scans, respectively. We used a 200 kV transmission electron microscope (TEM and/or STEM, JEM-2100F, JEOL) equipped with two aberration correctors (CEOS GmbH) for the image- and probe-forming lens systems and an X-ray energy-dispersive spectrometer (JED-2300T, JEOL) for compositional analysis. Both the aberration correctors were optimized to realize the point-to-point resolutions of TEM and scanning transmission electron microscopy (STEM) as 1.3 and 1.1 Å, respectively. A probe convergence angle of 29 mrad and a high-angle annular-dark-field (HAADF) detector with an inner angle greater than 100 mrad were used for HAADF-STEM observation. The samples for TEM were prepared by dropping a methanol suspension of the sample powder onto a commercial TEM grid coated with a collodion film. The sample was thoroughly dried in vacuum prior to observation. The UV–vis experiments were conducted on a UV-2600 (Shimadzu) double beam spectrometer with an integration sphere diffuse reflectance attachment. The powder samples were measured from 300 to 800 nm. Powder X-ray diffraction (pXRD) was performed using CuK α radiation (Rigaku RINT-Ultima III; $\lambda = 0.1548$ nm) with an increment of 0.02° in a range of

diffraction angles from 20 to 80°. An obliquely finished Si crystal (non-reflection Si plate) was used as a sample holder to minimize the background.

2.3. Evaluation of the decomposition rate of AcOH with Pt NPs/ WO_3 and PtPb NPs/ WO_3

The photocatalytic decomposition of AcOH was carried out in a circulation system made of Pyrex, in which a suspension of the photocatalyst powder (200 mg) in an aerated aqueous AcOH solution (5 vol%, 300 mL) was continuously stirred using a magnetic stirrer. A 300 W Xe lamp was used as the light source. The components were analyzed in the gas phase by gas chromatography (GC-8A, Shimadzu) equipped with a 2 m Porapak-Q column, a 2 m molecular sieve 3 \times column, and a flame ionisation detector while using Ar as the carrier gas. The sample was illuminated with a 300 W Xe lamp (PE-300BF, BA-X300ES, Hayashi Tokei Works Co., Ltd., Japan) in conjunction with an optical fiber coupler, UV cut-off filter (L-42, HOYA Co., Ltd., Japan), and an IR cut-off filter (MR5090/CM). A spectro-radiometer (USR-45D, Ushio Co.) measured the visible light intensity, which was adjusted to 20 mW cm⁻².

3. Results and discussion

Fig. 1 shows the XPS profiles for the (A) W 4f and (B) Pt 4f regions of (a) PtPb NPs/ WO_3 and (b) WO_3 , respectively. Fig. 1A shows the XPS profiles in the W 4f region for bulk WO_3 and PtPb NPs/ WO_3 as references. Spectra (a) and (b) shown in Fig. 1A show two peaks, 37.8 and 35.6 eV, assigned to W⁶⁺. This result was significantly different from our previous study using sodium borohydride as a reducing agent [11]. The spectra suggest that the oxidation state of W does not change from the original state of WO_3 after reduction by ethylene glycol. The XPS profiles shown in Fig. 1B represent the Pt 4f regions for the (a) ordered intermetallic PtPb, (c) reference bulk PtPb, and (d) bulk Pt NPs. The Pt 4f peaks in the bulk PtPb spectra were shifted to a higher binding energy level (by +0.3 eV) than that of bulk Pt. The Pt 4f peaks in PtPb NPs/ WO_3 corresponded to Pt 4f in the bulk PtPb peaks. This indicated that the Pb ions were reduced on the Pt NP sites of WO_3 and could form intermetallic compounds with the same chemical composition as bulk PtPb.

Fig. 2 shows the diffuse reflectance UV–vis absorption spectra for pure WO_3 , Pt NPs/ WO_3 and PtPb NPs/ WO_3 . The absorption edges of the synthesized Pt NPs/ WO_3 and PtPb NPs/ WO_3 sample are closely matched with pure WO_3 . This result indicates that Pt NPs/ WO_3 and PtPb NPs/ WO_3 samples had ability to absorb visible light as like pure WO_3 .

Fig. 3 shows the pXRD patterns of PtPb NPs/ WO_3 (Pt loading on WO_3 : 1 wt.% and 4 wt.%). It is clear that, when the amount of PtPb is 1 wt.%, no distinct peaks of PtPb in the PtPb NPs/ WO_3 sample was found because of the PtPb NPs peak on PtPb NPs/ WO_3 was much small in low loading amount (1 wt.%). However, we observed corresponding PtPb peak in PtPb NPs/ WO_3 on high loading amount (4 wt.%) of PtPb NPs.

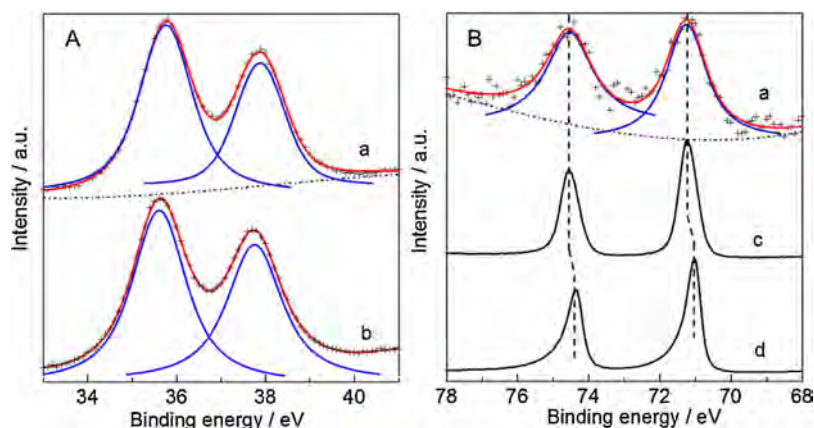


Fig. 1. XPS profiles in the (A) W 4f and (B) Pt 4f regions for (a) PtPb NPs/WO₃ (Pt loading: 1 wt.%), (b) WO₃, (c) bulk PtPb, and (d) bulk Pt.

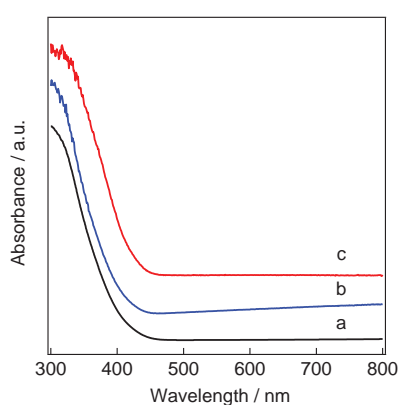


Fig. 2. Diffuse reflectance UV-vis absorption spectra of (a) pure WO₃, (b) Pt NPs/WO₃ and (c) PtPb NPs/WO₃ (b, c: Pt loading on WO₃: 1 wt.%).

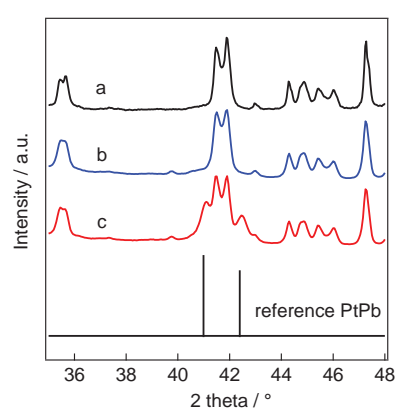


Fig. 3. pXRD diffractograms of (a) pure WO₃, (b) PtPb NPs/WO₃ (Pt loading on WO₃: 1 wt.%) and (c) PtPb NPs/WO₃ (Pt loading on WO₃: 4 wt.%).

Fig. 4A shows a transmission electron microscopy (TEM) image of PtPb NPs/WO₃. The PtPb NPs attached to WO₃ appear as dark spots. The TEM images revealed that the average particle diameter of the ordered intermetallic PtPb NPs on the WO₃ surface was

5.6 nm, which was larger than the photodeposited Pt NPs (average diameter: 3.8 nm for photodeposited Pt NPs) on the WO₃ surface (see Fig. S1). Furthermore, this result implies that the Pb ions may site-selectively react with the Pt NPs immobilized on the WO₃ sur-

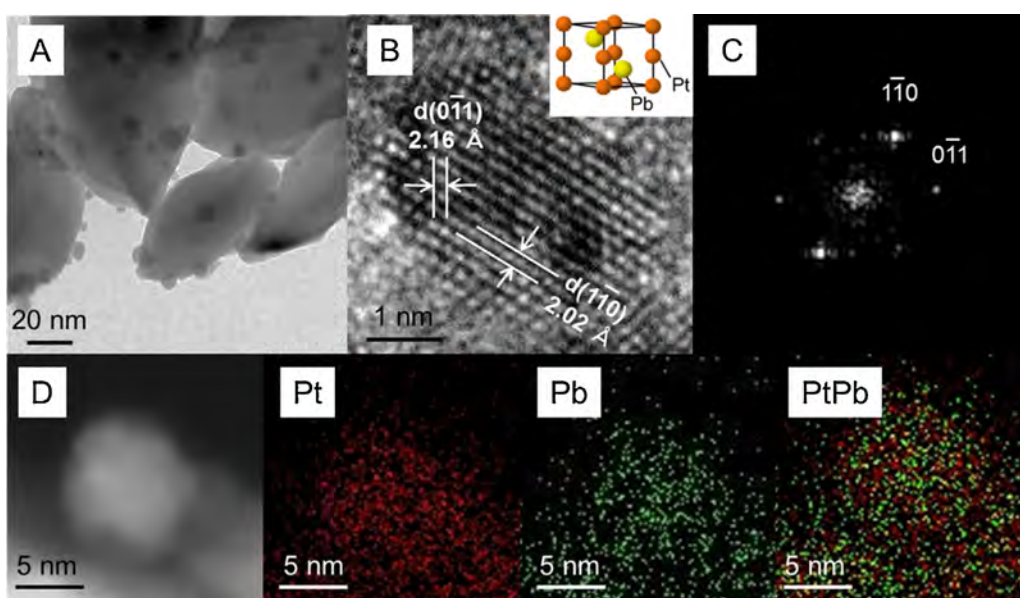


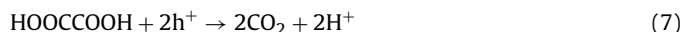
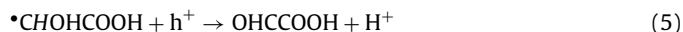
Fig. 4. (A) TEM and (B) HR-TEM images of PtPb NPs/WO₃ (Pt loading: 1 wt.%). (C) FFT pattern obtained from (B). (D) HAADF-STEM image of PtPb NPs/WO₃ and corresponding mapping images. Inset shows the simulated atomically ordered intermetallic PtPb.

face. A high-resolution TEM (HR-TEM) image and its corresponding fast-Fourier transformation (FFT) pattern for the PtPb NPs in PtPb NPs/WO₃ are shown in Fig. 4B and C. The PtPb phase clearly shows two kinds of lattice fringes in which the PtPb NPs have atomically ordered structures on the WO₃ surface. The *d* lattice fringes of the NPs shown in the HR-TEM image are 0.216 and 0.202 nm (Fig. 4B), respectively. This is quite similar to that of the (1 1 0) and (0 1 1) phase of an ordered intermetallic PtPb phase (Fig. 4C). Fig. 4D shows a scanning transmission electron microscopy (STEM) image and compositional mapping with an HAADF-STEM of the PtPb NPs. From the data, it was determined that the Pt and Pb atoms were uniformly dispersed in the particles and that the Pt and Pb molar ratio was 67:33. As shown in Figs. 1–4, Pb precipitation on Pt NPs can site-selectively occur to form individually isolated PtPb NPs on the WO₃ supports. Thus, we succeeded in forming ordered intermetallic compounds of PtPb NPs by photodeposition and polyol methods.

The photocatalytic activity of WO₃, Pt NPs/WO₃, and PtPb NPs/WO₃ was examined for the decomposition of AcOH. The CO₂ evolution during decomposition of AcOH over the WO₃ (black), Pt NPs/WO₃ (blue), and PtPb NPs/WO₃ (red) photocatalysts under visible light irradiation is shown in Fig. 5A. WO₃ shows poor CO₂ generation without Pt or PtPb co-catalysts. Conversely, the photocatalytic activity of WO₃ was enhanced significantly when loaded with Pt NPs. Furthermore, the highest yield of CO₂ evolution was observed with PtPb NPs/WO₃. The amount of CO₂ generation at 5 h for PtPb NPs/WO₃ was 6.4 times more than that for Pt NPs/WO₃. In addition, the CO₂-generation rate at 0–5 h with the PtPb NPs/WO₃ (575.2 μmol h⁻¹) was much higher than that of the Pt NPs/WO₃ (66.5 μmol h⁻¹) and WO₃ (19.6 μmol h⁻¹). Furthermore, the apparent quantum efficiency (QE) of PtPb NPs/WO₃ for CO₂ generation from AcOH was 23%, whereas that of Pt (1 wt.%) NPs/WO₃ was 7.3% (Fig. 5A inset). The apparent QE of Pt NPs/WO₃ and PtPb NPs/WO₃ were determined as four- and two-electron reactions, respectively (see Supplementary material, for the detail of QE). The QE was calculated using the rate-limiting light amount. The QE of PtPb NPs/WO₃ was much higher than that of Pt NPs/WO₃ despite its two-electron reaction. Abe et al. also reported that the apparent QE for the decomposition of AcOH with Pt NPs/WO₃ was approximately 10% [6,8]. In addition, the PtPb NPs in PtPb NPs/WO₃ were stable even after 5 h of measurements and the photocatalytic activity did not change even after reuse (see Supplementary material, STEM and STEM-EDS mapping profiles and XPS after the reaction of PtPb NPs/WO₃ (Figs. S2 and 3). Fig. S4 shows stability tests for the photocatalytic activity of AcOH decomposition with PtPb NPs/WO₃).

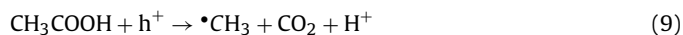
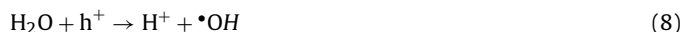
The ordered intermetallic PtPb NPs/WO₃ exhibited enhanced photocatalytic activity toward AcOH decomposition. This can be explained by the difference in the decomposition mechanism of AcOH between the Pt and PtPb NPs. In considering the AcOH decomposition reaction mechanism, we have determined the amount of H₂O₂ produced from ORR by the co-catalyst. The redox reactions co-instantaneously proceed in the photocatalytic reaction. When using WO₃ as a supporting material to decompose AcOH, multi-electron reduction reaction of oxygen (O₂/H₂O₂ = 0.68 V, O₂/H₂O = 1.23 V vs. NHE) proceeds on the reduction sites because the single-oxygen reduction reaction (O₂/HO₂⁻ = -0.13 V, O₂/O₂⁻ = -0.56 V vs. NHE) was more negative than the CB level of pure WO₃ (+0.5 V vs. NHE). H₂O₂ was produced as a product of the two-electron reduction of oxygen on the Pt and/or PtPb NP co-catalysts. When Pt NPs are used as the co-catalyst on WO₃ for decomposing AcOH, CO₂ was not produced in a short timeframe (within 30 min); in such a reaction, H₂O₂ was generated on the reduction sites (see Supplementary material, decomposition of AcOH over Pt NPs/WO₃, Fig. S5). In addition, CO₂ and H₂O₂ were the only reaction products observed. These results indicate that CO₂ was not directly produced when AcOH was decomposed with the

Pt NP co-catalysts. Accordingly, the following reaction mechanism is proposed:



CO₂ was formed through several oxidation reactions when using Pt NPs as co-catalysts. The α-carbon of AcOH was oxidized from the methyl group to the carboxyl group (Eqs. (2)–(6)). H₂O₂ evolution from the reduction reactions in a short timeframe suggests that the oxidation reactions also proceeded. However, CO₂ generation was not observed during this timeframe because of the sequential oxidation of the methyl group. Glycolic acid (Eq. (3)) and glyoxylic acid (Eq. (5)) could not be analyzed because of chemisorption onto the Pt co-catalyst. Eventually, CO₂ was generated through the oxidation of oxalic acid (Eqs. (6) and (7)). In fact, no C–C bond could be cleaved until the formation of oxalic acid.

Decomposition of AcOH on the Pt and PtPb NP co-catalysts proceeds via different mechanisms. In contrast to the Pt NPs, the PtPb NPs generate CO₂ in a short period (within 10 min) (see Supplementary material, decomposition of AcOH over PtPb NPs/WO₃, Fig. S6). In addition, other products were analyzed for considering the reaction mechanism with the PtPb NP co-catalysts. MeOH and ethane were analyzed using PtPb NPs as co-catalysts for AcOH decomposition (Fig. 5C and D). Accordingly, we propose the following reaction mechanism:



Unlike the Pt NPs co-catalysts, CO₂ formed during AcOH decomposition with PtPb NPs because C–C bonds were cleaved in the initial process (Eq. (9)). Pb might act as a surface modifier to mediate interactions between the co-catalyst and AcOH and accelerate the photochemical cleavage of C–C bonds. Evidently, CO₂ was detected when H₂O₂ was formed on the reduction sites. Methane radicals were formed as radical intermediates because MeOH and ethane were produced. In order to cleavage C–C bond, radical intermediate has to be stably-formed on catalyst. Pb atom in ordered intermetallic PtPb was strongly contributed a stabilization of methane radical when compared with pure Pt co-catalyst. Formaldehyde and formic acid were not detected because the decomposition of AcOH proceeded rapidly than that of MeOH.

The PtPb NPs are thought to work as co-catalysts for reduction of O₂ and oxidative decomposition of AcOH on the surface on WO₃ based on our previous works and present results [10]. Although the PtPb NPs are formed in the reduction sites because the Pt NPs were formed by the electron excited by absorbing visible light and the PtPb NPs was formed by reacting Pb atoms with the Pt NPs, the surface of PtPb NPs would become both sites where electrons and holes

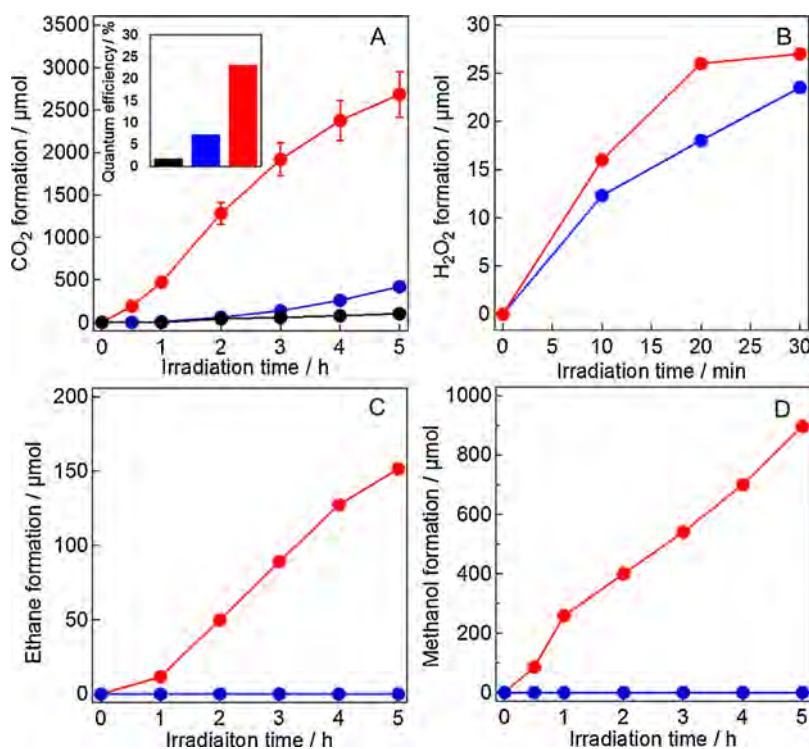


Fig. 5. Time course of (A) CO₂, (B) H₂O₂, (C) ethane and (D) methanol evolution during the decomposition of AcOH over WO₃ (black), Pt NPs/WO₃ (blue) (Pt loading: 1 wt.%) and PtPb NPs/WO₃ (red) (Pt loading: 1 wt.%) photocatalysts suspended in an aqueous AcOH solution in the presence of O₂ under visible light irradiation ($\lambda > 420$ nm). Inset (A): Quantum efficiency of the corresponding decomposition of AcOH. (For interpretation of the references to color in this figure legend, the reader is referred to the web version of this article.)

formed by absorbing visible light are consumed. On the surface of WO₃ which does not exhibit preferential orientation (Fig. 1A) and has low degree of the crystallinity, it could be considered that the reduction and oxidation sites are fixed on the WO₃ surface and shift the position depending on the situation. The photochemical cleavage of CC bonds which is characteristic phenomena in the PtPb NPs/WO₃ is produced by catalytic activity of the PtPb NPs. When Pb ions are reduced with polyol, the question whether Pb atoms are deposited on only the Pt NPs or not is significantly important for the interpretation of the reaction mechanism. We confirmed that Pb ions were not reduced by an individual action of polyol and Pb ions were reduced catalytically on the Pt surfaces by polyol. However, the possibility that cluster of Pb is deposited on the WO₃ surface cannot be denied. The Pb cluster would become Pb oxide cluster in the photocatalytic activity tests. We positively formed

the PbO₂ NPs on the WO₃ surfaces with Pb ions and holes formed by absorbing visible light on the WO₃ to check the contribution of PbO₂ NPs to the photochemical cleavage of CC bonds. The Pt NPs/PbO₂ NPs/WO₃ could not exhibit the photo-chemical cleavage of CC bonds. We concluded that origin of the photochemical cleavage of CC bonds is the surface of PtPb NPs and is not the surface of PbO₂ NPs.

Fig. 6A and B shows the oxidation of formaldehyde and MeOH with various photocatalysts (see Supplementary material, decomposition of formaldehyde and MeOH over Pt NPs/WO₃, Fig. S7). When using WO₃ without Pt or PtPb NP co-catalysts, the decomposition of formaldehyde and MeOH did not proceed. In contrast, CO₂ was produced in the decomposition of formaldehyde and MeOH with the co-catalysts. The CO₂-generation rate in the oxidation of formaldehyde with PtPb NPs/WO₃ at 0–5 h was 12.6 times higher

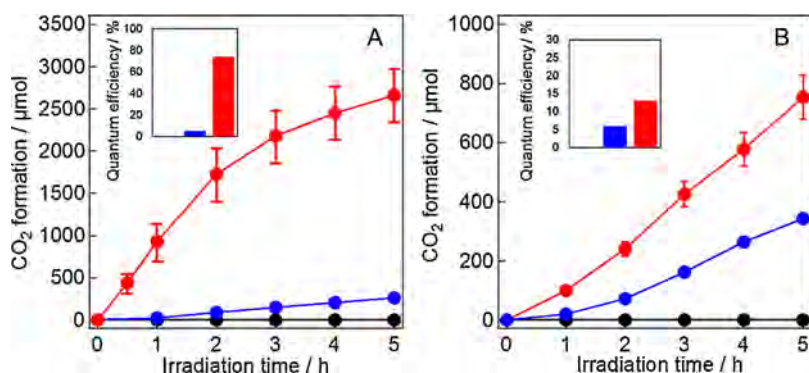


Fig. 6. Time course of CO₂ evolution during the decomposition of (A) formaldehyde and (B) MeOH over WO₃ (black), Pt NPs/WO₃ (blue) (Pt loading: 1 wt.%) and PtPb NPs/WO₃ (red) (Pt loading: 1 wt.%) photocatalysts suspended in an aqueous formaldehyde or MeOH solution in the presence of O₂ under visible light irradiation ($\lambda > 420$ nm). Inset: Quantum efficiency of the corresponding decomposition of formaldehyde or MeOH. (For interpretation of the references to color in this figure legend, the reader is referred to the web version of this article.)

than that with Pt NPs/WO₃ (Fig. 6A). For MeOH oxidation, the CO₂-generation rate with PtPb NPs/WO₃ at 0–5 h was 11.3 times higher than that with Pt NPs/WO₃ (Fig. 6B). In addition, the apparent QEs of formaldehyde and MeOH with PtPb NPs/WO₃ for CO₂ generation were 74% and 13%, respectively. The apparent QEs for formaldehyde and MeOH generation were calculated as four- and six-electron reactions, respectively.

Hongsen et al. propound the electrochemical reaction mechanism of oxidation for formaldehyde and/or MeOH over ordered intermetallic PtPb and pure Pt [12]. They suggest that formaldehyde and MeOH electrooxidations on PtPb and Pt produce different adsorbed substances as intermediates. When PtPb NPs are used as electrocatalysts for the oxidation of formaldehyde and MeOH, the oxidation pathway via CO_{ads} is precluded at all potentials. However, when Pt NPs are used as electrocatalysts, adsorbed CO is formed on the Pt surface from the dehydrogenation of formaldehyde and MeOH. Therefore, the enhanced photocatalytic performance of PtPb NPs/WO₃ was shown by the formation of ordered intermetallic compounds; PtPb NPs/WO₃ was more tolerant than Pt NPs CO poisoning when formaldehyde and/or MeOH were decomposed by the photocatalysts. These results show that the photocatalytic reaction mechanism for the decomposition of organic compounds was strongly dependent on the co-catalyst. Furthermore, it is probable that the oxidation of organic compounds in the photocatalytic decomposition occurred on the co-catalyst.

4. Conclusion

We have successfully synthesized WO₃-supported PtPb NPs using a photodeposition and polyol method. The XPS and TEM/STEM characterizations demonstrated that ordered intermetallic PtPb co-catalyst NPs were formed on the WO₃ surface. Furthermore, we demonstrated effective decomposition of various organic compounds over PtPb NPs/WO₃ compared with bare WO₃ and pure Pt NPs/WO₃. PtPb NPs/WO₃ exhibited enhanced photocatalytic activity toward various organic compounds. The reaction mechanism of the photocatalytic decomposition of various organic compounds was investigated. Higher photocatalytic activity was dependent on the co-catalyst. Both co-catalysts (Pt and PtPb NPs) showed different organic compound decomposition products (or chemisorbed species) and proceeded via different reaction pathways.

Acknowledgements

This work was financially supported by the Strategic Research Base Development Program for Private Universities of the Ministry of Education, Culture, Sports, Science and Technology of Japan.

A part of this work was supported by National Institute for Materials Science (NIMS) microstructural characterization platform as a program of “Nanotechnology Platform” of the Ministry of Education, Culture, Sports, Science and Technology (MEXT), Japan.

Appendix A. Supplementary data

Supplementary data associated with this article can be found, in the online version, at <http://dx.doi.org/10.1016/j.apcatb.2015.08.016>.

References

- [1] (a) M.R. Hoffmann, S.T. Martin, W. Choi, D.W. Bahnemann, *Chem. Rev.* 95 (1995) 69–96;
(b) A. Fujishima, T.N. Rao, D.A.J. Tryk, *Photochem. Photobiol. C* 1 (2000) 1–12;
(c) H. Kisch, *Angew. Chem. Int. Ed.* 52 (2013) 812–847.
- [2] A. Tanaka, K. Hashimoto, H.J. Kominami, *J. Am. Chem. Soc.* 136 (2014) 586–589.
- [3] (a) K. Maeda, K.J. Domen, *Phys. Chem. Lett.* 1 (2010) 2655;
(b) E. Thimsen, F. Leformal, M. Graetzel, S.C. Warren, *Nano Lett.* 11 (2011) 35–43.
- [4] K. Mori, H. Yamashita, M. Anpo, *RSC Adv.* 2 (2012) 3165–3172.
- [5] T. Arai, M. Horiuchi, M. Yanagida, T. Gunji, H. Sugihara, K. Sayama, *J. Phys. Chem. C* 113 (2009) 6602–6609.
- [6] T. Arai, M. Horiguchi, M. Yanagida, T. Gunji, H. Sugihara, K. Sayama, *Chem. Commun.* 43 (2008) 5565–5567.
- [7] H.P. Maruska, A.K. Ghosh, *Sol. Energy* 20 (1978) 443–458.
- [8] R. Abe, H. Takami, N. Murakami, B.J. Ohtani, *J. Am. Chem. Soc.* 130 (2008) 7780–7781.
- [9] (a) F. Matsumoto, *Electrochemistry* 80 (2012) 132;
(b) F. Matsumoto, C. Roychowdhury, F.J. DiSalvo, H. Abruña, *Electrochem. Soc.* 155 (2008) B148–B154;
(c) T. Gunji, T. Tanabe, A.J. Jeevagan, S. Usui, T. Tsuda, S. Kaneko, G. Saravanan, H. Abe, F. Matsumoto, *J. Power Sources* 273 (2015) 990–998.
- [10] T. Gunji, G. Saravanan, T. Tanabe, T. Tsuda, M. Miyauchi, G. Kobayashi, H. Abe, F. Matsumoto, *Catal. Sci. Technol.* 4 (2014) 1436–1445.
- [11] T. Gunji, T. Tsuda, A.J. Jeevagan, M. Hashimoto, T. Tanabe, S. Kaneko, M. Miyauchi, G. Saravanan, H. Abe, F. Matsumoto, *Catal. Commun.* 56 (2014) 96–100.
- [12] W. Hongsen, A. Laif, F.J. DiSalvo, H.D. Abruña, *Phys. Chem. Chem. Phys.* 10 (2008) 3739–3751.

マグネトロンスパッタ法により作製した リン酸リチウムオキシナイトライド固体電解質薄膜の イオン伝導性に及ぼす導入ガス中窒素濃度の影響

金子 信悟^{a,b}, 横溝美衣子^c, 望月 康正^b, 嵐田 敏彦^d,
笹元 貴弘^d, 田邊 豊和^{b,c}, 松本 太^{b,c,*}

^a 神奈川大学 工学研究所 (〒 221-8686 神奈川県横浜市神奈川区六角橋 3-27-1)

^b 神奈川大学 リチウム電池オープンラボ (〒 221-8686 神奈川県横浜市神奈川区六角橋 3-27-1)

^c 神奈川大学 工学部 (〒 221-8686 神奈川県横浜市神奈川区六角橋 3-27-1)

^d (株)協同インターナショナル 川崎テクノセンター (〒 215-0005 神奈川県川崎市麻生区千代ヶ丘 8-5-1)

Influence of N₂ Concentration in the Induction Gases on the Ionic Conductivity of Lithium Phosphorus Oxynitride Solid Electrolyte Thin Film Prepared by Magnetron Sputtering

Shingo KANEKO^{a,b}, Miiko YOKOMIZO^c, Yasumasa MOCHIZUKI^b,
Toshihiko ARASHIDA^d, Takahiro SASAMOTO^d, Toyokazu TANABE^{b,c}
and Futoshi MATSUMOTO^{b,c,*}

^a Research Institute for Engineering, Kanagawa University (3-27-1, Rokkakubashi, Kanagawa-ku, Yokohama-shi, Kanagawa 221-8686)

^b Lithium Battery Open-laboratory, Kanagawa University (3-27-1, Rokkakubashi, Kanagawa-ku, Yokohama-shi, Kanagawa 221-8686)

^c Faculty of Engineering, Kanagawa University (3-27-1, Rokkakubashi, Kanagawa-ku, Yokohama-shi, Kanagawa 221-8686)

^d Kawasaki Techno Center, Kyodo International Inc. (8-5-1, Chiyogaoka, Asao-ku, Kawasaki-shi, Kanagawa 215-0005)

Amorphous lithium phosphorus oxynitride (LiPON) thin films were deposited on SUS plates from a Li₃PO₄ target using RF magnetron sputtering with induction gas having various N₂ concentrations. The ionic conductivity of the amorphous LiPON films was approximately $7.6 \times 10^{-6} \text{ S} \cdot \text{cm}^{-1}$ at 75% N₂ concentration, at which both doubly and triply phosphorus-coordinated nitrogen units would be linked to the Li₃PO₄ structure.

Keywords : Lithium-ion Secondary Battery, Amorphous Solid Electrolyte, LiPON, Sputtering Pressure, Higher Order Structure

1. 緒 言

リチウムイオン二次電池 (LIBs) は, その高いエネルギー密度と起電力のため電気自動車や携帯電話など幅広い分野に用いられている。しかし LIBs の構成部材には, 可燃性有機電解液, 酸素を放出する可能性のある正極材料が存在することから, 高電位・高レートでの充放電中の発熱や電極間の内部短絡, あるいは衝撃による液漏れの際に発火する危険性がある。このため, 発火・引火の危険性が無い安全な LIBs 技術の開発が求められている。現在までに安全性を高める方法として様々な方法が検討されているが, その一つとして, 可燃性有機電解液を使用せず, 内部に液体成分を含まない全固体電池^{1,2)}の開発がある。

有望な全固体電池の確立には良質な固体電解質の確立が急

務であり, その固体電解質には高いイオン伝導性, 電気化学的安定性(電位窓が広い), 熱的・化学的な安定性などの性能が求められるが, これら全てを満たす材料は見られていない。結晶性電解質として報告された Thio-LISICON (Lithium superionic conductor)³⁾は室温で $10^{-3} \text{ S} \cdot \text{cm}^{-1}$ 以上のイオン伝導度を示し, 輸率もほぼ1である。さらに, 最近報告された Li₁₀GeP₂S₁₂ は有機性電解液を超える $1.2 \times 10^{-2} \text{ S} \cdot \text{cm}^{-1}$ のイオン伝導度を誇る⁴⁾。しかし硫化物系は水分に対して不安定であり, 人体に有害な H₂S を生成する可能性があるため生産工程や安全性に問題がある。比較的安全な LISICON 型: γ -Li₃PO₄ 型骨格を基礎とする酸化物固溶体³⁾, ペロブスカイト型 La_{0.51}Li_{0.34}TiO_{2.94}, NASICON 型 Li_{1.3}Al_{0.3}Ti_{1.7}(PO₄)₃, ガーネット型 Li₇La₃Zr₂O₁₂⁵⁾などの酸化物系は安定性に優れるが, 通常 1000℃以上で焼結しなければ高いイオン伝導度($10^{-6} \text{ S} \cdot \text{cm}^{-1}$ 程度)を得ることはできず, 現状, 工業的に用途拡大は困難ともいえる。

* E-mail : fmatsumoto@kanagawa-u.ac.jp

これまで我々のグループでは、発火の危険性がある有機電解液を用いない全固体薄膜型 LIBs の開発に向けて、アモルファス状態でも優れたイオン伝導性を示すことが報告されているリン酸リチウムオキシナイトライド(LiPON)^{6,7)}に着目し、マグネトロンスパッタ法を用いた LiPON 薄膜の作製方法について検討している。本稿では、特に、既報の室温付近での LiPON のイオン伝導度($2.0 \sim 4.0 \mu\text{S}\cdot\text{cm}^{-1}$)^{7~12)}のさらなる向上を図るべく、マグネトロンスパッタ時の導入ガス中の有効窒素濃度の検討ならびにイオン伝導性の優劣を左右する LiPON 構造の解析を行った結果について報告する。

2. 実験操作

2.1 LiPON 薄膜の作製とイオン伝導度測定

基板には SUS コイン(タクミ技研製φ 16 mm スペーサー SUS316L)を採用し、電極層の形成前に機械研磨を施すことにより、走査型プローブ顕微鏡(日本電子製, JSPM-4200)観察に基づく算術平均粗さ 50 nm 程度まで表面を平滑化して用いた。この基板に RF マグネトロン式スパッタリング装置(神港精機製 4300 型)により図 1a に示すような形で電極層を成膜した。LiPON 層の成膜には、 Li_3PO_4 をターゲットとして用い、スパッタ時に導入する Ar を N_2 で一部置換(N_2 : 10, 25, 50, 75, 100 vol%)したガス雰囲気中(ガス流量 50 sccm), 真空度: 2×10^{-1} Pa, チャンバー内温度 $20 \sim 30$ °C, 出力 150 W で 10 時間のスパッタを実施した。イオン伝導度の測定には交流インピーダンス法を用いた。固体電解質の場合、通常の電気化学測定とは異なり、参照電極のない二極式の対称セルで測定を行うことが一般的である。本研究では、SUS コイン上に Pt 電極と電解質を積層した電極試験片 Pt/LiPON/Pt/Ti/SUS (図 1b)を測定セル(HS セル 宝泉製)にセットし、周波数応答解析装置(Bio-Logic 製 VMP3)を用いて、周波数範囲: 10 mHz ~ 500 kHz, 印可電圧: 2 mV で交流インピーダンスを測定し、得られた結果を EC-LAB (Bio-Logic)で解

析することによりイオン伝導度を算出した。なお、本稿に登場する全ての電極試験片は、2.2 で述べる膜厚評価に基づき、SUS コイン上に形成した Pt (表層側), LiPON, Pt, Ti 層(SUS コイン側)の膜厚が、それぞれほぼ 100, 1000, 300, 50 nm となるように規定して用いた。

2.2 LiPON 薄膜評価法

作製した電極片の各層の膜厚は、クロスセクションポリリッシャーを用いてサンプルを加工し、その断面を切り出すことによって評価した。装置には電界放出形走査型電子顕微鏡(FE-SEM: 日立製 SU-8010)を用いた。LiPON の結晶構造は、薄膜アタッチメント付き X 線回折装置(薄膜 XRD: リガク製 UltimaIII)を用いて平行ビーム法により評価した。また、X 線光電子分光法(XPS)により成膜した固体電解質を測定し、検出した各スペクトルについて数値解析ソフト Igor を用いてフィッティングすることにより構成元素の化学状態を分析した。この結果をイオン伝導度の結果と照合し、イオン伝導発現の機構についても考察した。XRD, XPS の評価には、Si<100> ウェハ上にて 2.1 と同条件で成膜した LiPON 薄膜を用いた。

3. 実験結果及び考察

図 1c にスパッタリング時の導入ガス中の窒素濃度 50 vol% でスパッタリングにより成膜した薄膜層の X 線回折図形を示す。成膜後無処理のサンプルでは特にピークは検出されず、 $10 \sim 30$ 度付近にアモルファス状の生成物の存在を示唆する勾配が見られた。このサンプルの交流インピーダンス測定結果から算出したイオン伝導度は約 $2.2 \times 10^{-6} \text{S}\cdot\text{cm}^{-1}$ であり、これまでに報告されている室温付近での LiPON 層のイオン伝導度($2.0 \sim 4.0 \mu\text{S}\cdot\text{cm}^{-1}$)^{7~12)}と同程度の値となることがわかった。このサンプルを大気雰囲気下で加熱したところ、図 1c に示すように、 450 °C で 5 時間熱処理した場合にターゲットに用いた Li_3PO_4 に対応する回折パターンが見られた。

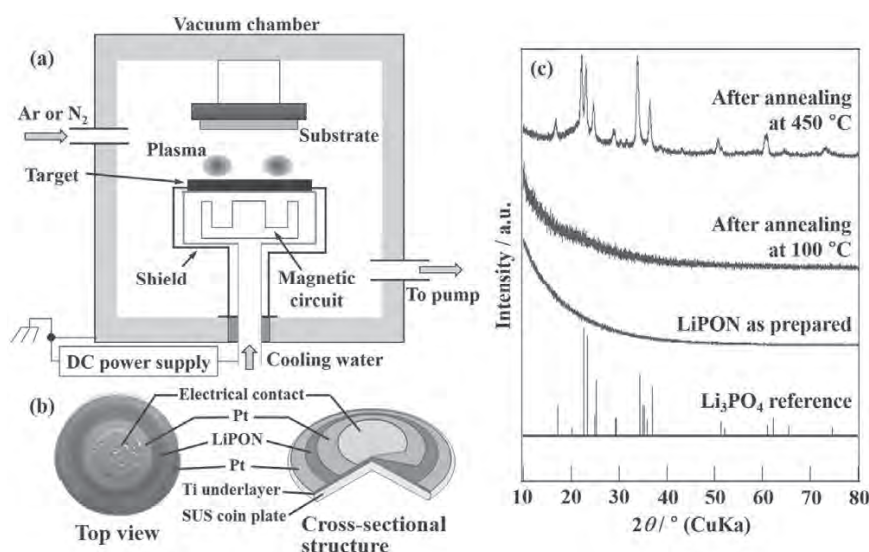


Fig. 1 Fabrication of the thin film of LiPON solid electrolyte and its crystallographic data. a) Schematic illustration of RF magnetron sputtering system, b) photograph (top view) and cross-sectional structure of a tested electrode with a LiPON layer, c) XRD pattern of a LiPON thin film synthesized on a Si wafer before and after annealing at 100 and 450 °C for 5 h.

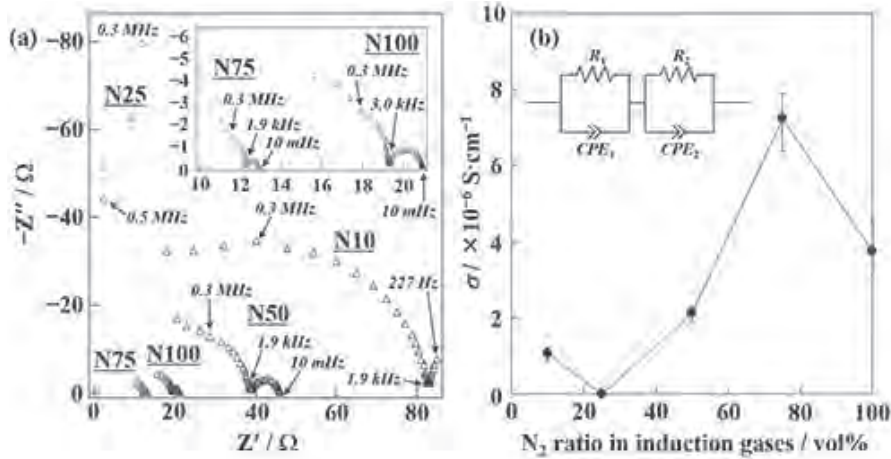


Fig. 2 AC impedance data of LiPON thin films prepared using N_2 concentration from 10 vol% to 100 vol% as a ratio to Ar in the induction gases. Cole-Cole plot a) and ionic conductivity plot b) of LiPON thin films obtained by changing N_2 ratio in the induction gases. The inset in Fig. 2b represents the electrical equivalent circuit fitted to the spectra in Fig. 2a.

また 450°C での熱処理後のサンプルのイオン伝導度は、 Li_3PO_4 に典型的なレベルである $10^{-8}\text{S}\cdot\text{cm}^{-1}$ 以下 ($5.6 \times 10^{-9}\text{S}\cdot\text{cm}^{-1}$) までの急激な低下を示した⁷⁾。これは、熱処理中に LiPON 構造中の N が O で置換されたことにより、 Li_3PO_4 の結晶化が進行したためであると考えられる。以上のことから、スパッタリングによって得られたサンプルはアモルファス状の LiPON であることを確認した。

図 2a に、スパッタリング時の導入ガス中の窒素濃度を 10, 25, 50, 75, 100 vol% (図中、N10 ~ N100 と表記) と変化させ成膜した、LiPON 層を Pt 層で挟んだ積層電極片の交流インピーダンス測定結果としての Cole-Cole プロットを示す。なお、以後登場する全ての LiPON 層については、熱処理を行わず、スパッタ後のアモルファス状のまま評価に供している。測定点が高周波数側で散逸し解析不能と判断した導入ガス中の窒素濃度 25 vol% の系を除き、いずれの系のスペクトルも高周波数側の比較的大きい不完全な円弧と低周波数側の小さな円弧のセットを描き、低周波数側の円弧の末端が実数軸上に収束する共通点をもつ (10 vol% の系も $120\ \Omega$ 付近で収束する) ことがわかった。本研究の電極のスペクトルは導入ガス中の窒素割合が高くなるにつれて高周波数側に縮む傾向を示し、特に、全体として抵抗値が小さい系であるほど、高周波数側の円弧は半分以上が欠けたような不明確な形状になった。これは、導入ガス中の窒素濃度が高くなるにつれて LiPON バルク中のイオン伝導が複雑な素過程を経るようになり、複数の緩和時間を持つためであると考えられる。さらに高周波数域からの測定を行えば明確なプロットを観測できる可能性があるが、現状ではこれが限界である。他方、低周波数側の円弧はスペクトルが全体として高周波数寄りにあるほど直径の小さい半円となる傾向を示した。本研究では、高周波数側の円弧が不完全でも実数軸に収束した位置までを固体電解質 LiPON のバルク抵抗値とみなし、この値と仮定した等価回路を用いてフィッティングすることによってイオン伝導度を算出した (図 2b)。図 2b の等価回路において、 R_1 および CPE_1 は、バルク応答の抵抗ならびに定位相成分 (Constant

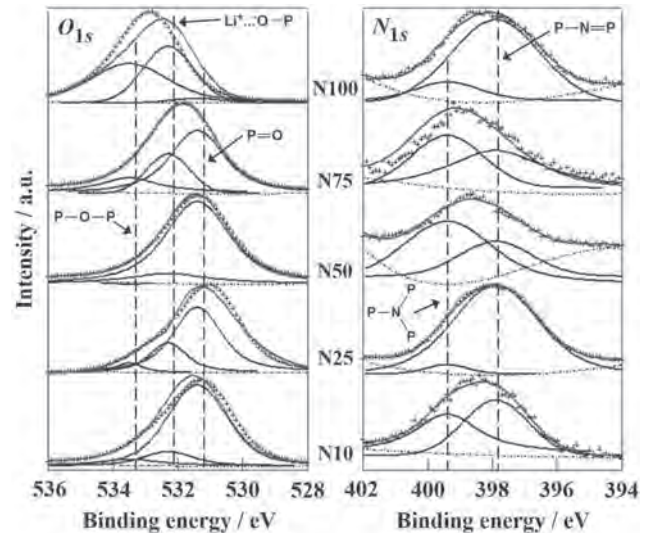


Fig. 3 O_{1s} and N_{1s} XPS spectra of LiPON thin films deposited at N_2 concentration from 10% to 100% as a ratio to Ar in the induction gases.

Phase Element, CPE) を表し、一方、Pt 電極 - LiPON 電解質界面 (表層側ならびに SUS 基板側) 間の抵抗ならびに定位相成分が、それぞれ R_2 および CPE_2 として並列で表される。図 2b に示されるように、インピーダンス測定から求めた LiPON のイオン伝導度は、導入ガス中の窒素濃度の変化に応じて変動し、窒素濃度 50 vol% までは既報^{7)~12)} と同程度かそれ以下、50 vol% より高濃度では既報を超える値に大別された。特に導入ガス中の窒素濃度が 75 vol% まで及ぶと、50 vol% までのイオン伝導度に比べて標準偏差が大きくなるものの、本研究で最大となる約 $7.6 \times 10^{-6}\text{S}\cdot\text{cm}^{-1}$ のイオン伝導度を示し、既報の値を上回ることがわかった。

図 3 に、導入ガス中の窒素濃度を変えて作製された LiPON 薄膜の XPS 測定結果を示す。10 vol% (N10) の窒素濃度で作製されたサンプルの O_{1s} スペクトルでは、1つの非対称なピークが 531 eV 付近に観察され、導入ガス中に占める窒素量が増加するにつれて高エネルギー側へのシフトを示した。このピー

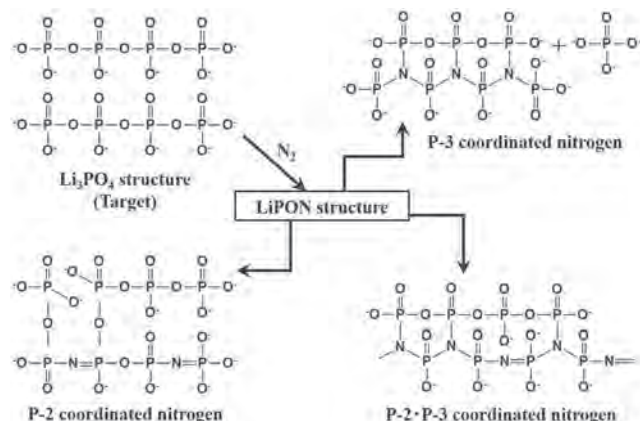


Fig. 4 Expected structural models of nitrated Li_3PO_4 main structure incorporating P-N=P and P-N<(P)₂ units resulting from the reaction of ambient phosphate chains with N.

はフィッティングにより P-O-P (533.5 eV), $\text{Li}^+\dots\text{O}^-$ (532.3 eV), P=O (531.4 eV) の 3 つの化学状態に帰属することができ¹³⁾, 窒素濃度の変化に応じて O の化学状態が明確に異なることがわかった。また N_{1s} でも 1 つの非対称なピークが見られ, 各濃度ともに N 元素のドーピングを示す P-N<(P)₂ (399.9 eV), P-N=P (397.9 eV) の 2 つの状態をもつことが明らかになった。このような種々の結合様態を持つ LiPON のイオン伝導は, 図 2b で示されるように導入ガス中の窒素濃度に依存して顕著に変化する。そこで, XPS スペクトルの各化学状態に対応するピークの積分値から各結合の存在比を算出し, この比を基に構造とイオン伝導の関係について考察を行った。

図 4 には, 本研究で提案される Li_3PO_4 中に N がドーピングされた場合に形成する主要構造を示す。N 元素が Li_3PO_4 構造中にドーピングされた場合, P-O-P 結合の O 元素と置換される。もし LiPON 中に P-N=P 構造単位が生成した場合, N^{3-} の有効イオン半径 (1.32 Å) は O^{2-} (1.24 Å) よりも大きいため P=O は P-O⁻へと転換し, 構造内にひずみを生じる。このとき 2 つの P-N=P 部位が生成すると 1 つの P-O 結合が構造から切断される (以下, P-2 配位型と呼ぶ)^{11),12),14)~16)}。P-2 配位型では単結合と二重結合が共役的に配置されることになるため, 電子は非局在化し, Li^+ は一次ないし二次元的に移動しやすくなるものと思われる。これに対し, P-N<(P)₂ 構造単位が形成される場合には, N が構造上近接する他の主鎖構造中の P とも結合して高次構造を形成するため, P-2 配位型に比べて著しい構造ひずみを生じる。このとき 2 つの P-N<(P)₂ 単位が生成すると 2 つ以上の P-O 結合が失われることになる (以下, P-3 配位型と呼ぶ)。それゆえ, P-3 配位型による静電的エネルギーの低下に対する寄与は P-2 配位型に比べて大きくなり, Li^+ の移動度を高めることにつながると考えられる。本研究の LiPON 薄膜のイオン伝導度は, 10 vol% から 25 vol% まで導入ガス中の窒素濃度を増やすと一度解析不能なレベルまで低下し, それ以後は増加傾向を示し, 75 vol% で極大域値となる (図 2b)。この挙動は, 図 3 の異なる窒素濃度で製膜された LiPON 層の N_{1s} スペクトルで示される P-3 配位型構造の形成度合いと

良く一致した。しかし LiPON 構造中には P-2 型配位も混在するため, 窒素濃度 75 vol% でのスパッタリングの場合などでは P-2 および P-3 型の両者が調和したネットワーク (P-2・P-3 配位混成型) 構造を形成しうる。以上のことから, LiPON の Li^+ の伝導機構においては, 一次ないし二次移動として P-2 型を利用した移動, そして高次移動として他の主鎖構造との間での架橋を介する三次元的な移動によってイオン伝導性の優劣が支配されていると考察した。

4. 結 言

スパッタリング中の導入ガス中の窒素濃度を変化させて LiPON 薄膜を作製し, そのイオン伝導度と XPS 構造解析から以下の点が明らかとなった。

- (1) 得られた LiPON 薄膜はアモルファス構造を有しており, その状態で $10^{-6} \text{ S}\cdot\text{cm}^{-1}$ レベルのイオン伝導度を発揮した。
- (2) LiPON 薄膜のイオン伝導度は, 窒素濃度を 10 vol% から 25 vol% まで上げると一度低下するが, 75 vol% まで増加させると本研究で検討した限り最大レベルとなる約 $7.6 \times 10^{-6} \text{ S}\cdot\text{cm}^{-1}$ にまで達した。
- (3) P-3 配位型からのイオン伝導性の改善は P-2 配位型からの影響に比べて顕著であり, 高いイオン伝導性は P-2, P-3 配位型の調和の結果として発現した。

(Received May 13, 2015 ; Accepted August 17, 2015)

文 献

- 1) R. Kanno ; GS Yuasa Tech. Rep., 3, 1 (2006).
- 2) J. B. Bates ; *Electron. Eng.*, 69, 63 (1997).
- 3) 工藤徹一, 日比野光宏, 本間 格 ; リチウムイオン電池の科学, p. 192 (内田老鶴圃, 2010).
- 4) N. Kamaya, K. Homma, Y. Yamakawa, M. Hirayama, R. Kanno, M. Yonemura, T. Kamiyama, Y. Kato, S. Hama, K. Kawamoto, A. Mitsui ; *Nat. Mater.*, 10, 682 (2011).
- 5) 金村聖志ら ; 高性能リチウムイオン電池開発最前線, p. 260 (NTS, 2013).
- 6) T. Lapp, S. Skaarup, R. A. Hooper ; *Solid State Ionics*, 11, 97 (1983).
- 7) J. B. Bates, N. J. Dudney, G. R. Gruzalski, R. A. Zuhr, A. Choudhury, C. F. Luck ; *J. Power Sources*, 43-44, 103 (1993).
- 8) B. Kim, Y. S. Cho, J.-G. Lee, K.-H. Joo, K.-O. Jung, J. Oh, B. Park, H.-J. Sohn, T. Kang, J. Cho, Y.-S. Park, J. Y. Oh ; *J. Power Sources*, 109, 214 (2002).
- 9) J. Schwenzel, V. Thangadurai, W. Weppner ; *J. Power Sources*, 154, 232 (2006).
- 10) Y. Hamon, A. Douard, F. Sabary, C. Marcel, P. Vinatier, B. Pecquenard, A. Levasseur ; *Solid State Ionics*, 177, 257 (2006).
- 11) Z. Hu, D. Li, K. Xie ; *Bull. Mater. Sci.*, 31, 681 (2008).
- 12) N. Suzuki, S. Shirai, N. Takahashi, T. Inaba, T. Shiga ; *Solid State Ionics*, 191, 49 (2011).
- 13) N. Mascaraque, J. L. G. Fierro, A. Durán, F. Muñoz ; *Solid State Ionics*, 233, 73 (2013).
- 14) B. C. Bunker, D. R. Tallant, C. A. Luck, R. J. Kirkpatrick, G. L. Turner, M. R. Reidmeyer ; *J. Am. Ceram. Soc.*, 70, 675 (1987).
- 15) Y. G. Kim, H. N. G. Wadley ; *J. Vac. Sci. Technol.*, A26, 174 (2008).
- 16) Z. Hu, K. Xie, D. Wei, N. Ullah ; *J. Mater. Sci.*, 46, 7588 (2011).

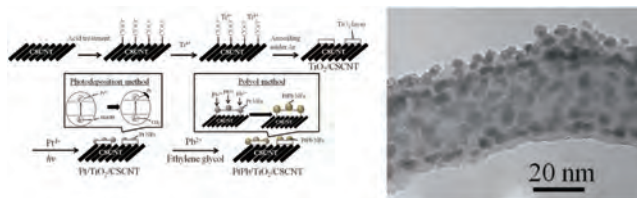
Preparation of a PtPb/TiO₂/Cup-stacked Carbon Nanotube Composite for Enhancement of the Electrocatalytic Reaction of the Oxygen Reduction Reaction

Fuma Ando,¹ Takao Gunji,¹ Hikaru Fujima,¹ Tsuyoshi Takeda,² Toyokazu Tanabe,¹ Shingo Kaneko,¹ and Futoshi Matsumoto*¹

¹Department of Material and Life Chemistry, Kanagawa University, 3-27-1 Rokkakubashi, Yokohama, Kanagawa 221-8686

²Sankei Giken Kogyo Co., Ltd., 2-5-1 Akabane Minami, Kita-ku, Tokyo 115-8588

(E-mail: ft101828zr@kanagawa-u.ac.jp)



PtPb ordered intermetallic nanoparticles (NPs) were deposited on titanium oxide (TiO₂)/cup-stacked carbon nanotubes (CSCNT) to improve the activity of the electrochemical oxygen reduction reaction (ORR). The PtPb NPs/TiO₂/CSCNTs were prepared by the step-by-step preparation method, first annealing under an inert atmosphere with Ti-alkoxide to obtain TiO₂, then Pt NP photodeposition and finally microwave synthesis to prepare ordered intermetallic PtPb NPs on TiO₂.

REPRINTED FROM

**Chemistry
Letters**

Vol.44 No.12 2015 p.1741–1743

CMLTAG
December 5, 2015

The Chemical Society of Japan

Preparation of a PtPb/TiO₂/Cup-stacked Carbon Nanotube Composite for Enhancement of the Electrocatalytic Reaction of the Oxygen Reduction Reaction

Fuma Ando,¹ Takao Gunji,¹ Hikaru Fujima,¹ Tsuyoshi Takeda,² Toyokazu Tanabe,¹ Shingo Kaneko,¹ and Futoshi Matsumoto*¹

¹Department of Material and Life Chemistry, Kanagawa University, 3-27-1 Rokkakubashi, Yokohama, Kanagawa 221-8686

²Sankei Giken Kogyo Co., Ltd., 2-5-1 Akabane Minami, Kita-ku, Tokyo 115-8588

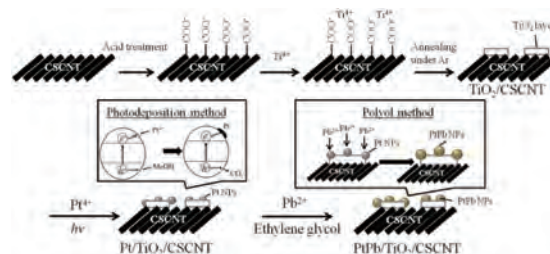
(E-mail: ft101828zr@kanagawa-u.ac.jp)

PtPb ordered intermetallic nanoparticles (NPs) were deposited on titanium oxide (TiO₂)/cup-stacked carbon nanotubes (CSCNT) to improve the activity of the electrochemical oxygen reduction reaction (ORR). The use of CSCNTs as a support material resulted in high loading of PtPb NPs/TiO₂. The PtPb NPs/TiO₂/CSCNTs were prepared by the step-by-step preparation method, viz. first annealing under an inert atmosphere with Ti-alkoxide to obtain TiO₂, then Pt NP photodeposition, and finally microwave synthesis to prepare ordered intermetallic PtPb NPs on TiO₂ via reaction of Pb²⁺ with Pt/TiO₂. The new particles enhanced ORR electrocatalytic activity.

Problems associated with the consumption of fossil fuels, including air pollution caused by carbon dioxide (CO₂), nitrogen oxide (NO_x), and sulfur dioxide (SO₂), are damaging the environment and human health.¹ To save limited natural resources and sustain life, the development of new energy sources and improvements in the efficiency of energy generation, conversion, and storage have become crucial issues.² Fuel cells are thought to be a promising technology to directly convert chemical energy into electricity via electrochemical reactions. Recently, there has been increased interest in polymer electrolyte membrane fuel cells (PEMFCs). PEMFCs have energy conversion efficiencies as high as 80%. However, the durability of PEMFCs has been recently recognized as one of the most important issues that must be addressed before the commercialization of PEMFCs.³ Pt surface area loss due to carbon corrosion and Pt dissolution from the carbon support and/or aggregation on the carbon support are considered some of the major problems to address.⁴ Carbon black (CB) is normally used as a support material for the Pt catalyst to maximize the mass activity of the catalyst. However, the oxidized sites of CB accelerate the degradation of the support material for Pt NPs. CB will oxidize at the edge sites because polar functional groups can form at those sites. The polar functional groups will be further oxidized and will eventually corrode away. Recently, carbon nanotubes (CNTs) have been proposed as promising support materials for Pt NPs because the CNT supports exhibit high conductivity and mass transport capability as well as high chemical stability. However, there are no novel binding sites for adsorbing Pt ions on the CNT surfaces, although the surfaces of CNT are composed of non-oxidized graphitic carbon. Usually, functional groups are generated on the external walls to make the binding sites for the Pt source using harsh oxidative treatments, such as refluxing in HNO₃ or H₂SO₄-HNO₃.⁵ However, the treated CNT surfaces will suffer from serious carbon corrosion under conditions such as low pH, high potential, high humidity, and high temperature (ca. 80 °C). A new methodology for the deposition of catalyst NPs on CNT surfaces should be developed that satisfies the requirements of both high NP dispersion and chemical stability. Recently, nanocrystalline TiO₂ as a catalyst support has received increasing attention due to its inherent stability in the electrochemical environment, its commercial availability, and its enhancement of electrocatalytic activity due to its corrosion resistance and the synergistic effect between NPs and TiO₂.⁶ For example, a novel electrocatalyst based on mesoporous TiO₂-supported Pt NPs was reported by Shen et al.⁷ It showed high

stability under accelerated stress test conditions and an activity comparable to that of the commercial Pt/C catalyst.⁷ Manzo-Robledo et al. reported a Pd/TiO₂-C electrode that exhibits higher methanol-oxidation kinetics compared to a Pd/C electrode.⁸ Based on these studies, we considered the preparation of PtPb/TiO₂ on cup-stacked carbon nanotubes (CSCNTs) to enhance the oxygen reduction reaction (ORR). CSCNTs are tubular carbon nanostructures with a stacked cup arrangement of graphene layers. Therefore, the edges of the graphene layers are densely exposed on the surface of the CSCNTs. The graphene edges are used as scaffolds to thoroughly coat the CSCNT surface with TiO₂ layers. The PtPb ordered intermetallic NP electrocatalyst was selectively deposited on the TiO₂ layers. The CSCNT functions as an electron conducting path. The surface of the CSCNT that cannot be covered with TiO₂ can be transformed into the surface of a multiwalled carbon nanotube through a high-temperature treatment after the formation of TiO₂/CSCNT.⁹ Recently, we reported that PtPb/TiO₂ showed enhancement of electrocatalytic activity for the ORR.¹⁰ The nature of the support, the composition of catalytic sites, the sites' interaction with the support, and the electronic structure of the catalytic sites all most likely influenced the observed electrochemical behavior. In this study, PtPb NPs were chemically deposited on small, thin TiO₂ layers that were prepared on CSCNTs. Scheme 1 depicts the step-by-step preparation method of PtPb NPs/TiO₂/CSCNT by annealing under an inert atmosphere with Ti-alkoxide to obtain TiO₂, photodeposition for Pt NPs, and microwave synthesis to prepare ordered intermetallic PtPb NPs on TiO₂ via the reaction of Pb²⁺ with Pt/TiO₂. A commercially available CSCNT (50 nmφ, Sankei Giken Kogyo Co., Ltd., Japan) was treated with an acidic solution of H₂SO₄ (6 M) and HNO₃ (6 M) at 90 °C for 6 h to introduce carboxylic acid functional groups on the CSCNT surfaces, followed by washing with water and drying overnight at 110 °C. The purchased CSCNTs have the following characteristics: average length of 2.0 μm, BET surface area of 99 m² g⁻¹, volume resistivity of 0.05 Ω cm (30 MPa), and G/D Raman peak ratio of 0.85. A Ti precursor solution was prepared by dissolving Titanium(IV) isopropoxide (TTIP, 0.2 g) in isopropanol (100 mL).

Functionalized carbon was added to the solution under vigorous stirring. Deionized water (1.0 mL) was used to accelerate the reaction of TTIP. After further stirring for 6 h, the resulting mixture was collected and dried overnight under vacuum, followed by heat treatment at 450 °C for 1 h under Ar atmosphere to yield CSCNT-



Scheme 1. Schematic representation of the step-by-step method to prepare ordered intermetallic PtPb NPs/TiO₂/CSCNT.

supported TiO₂ (TiO₂/CSCNT).¹¹ Pt NPs were photochemically deposited on TiO₂/CSCNT. Next, 0.25 mmol of H₂[PtCl₆], which was used as the Pt source, and 50 mg of TiO₂/CSCNT were dissolved in 50 vol % aqueous methanol solution (100 mL). This solution was stirred for 12 h under irradiation with a UV lamp (Xe lamp, 300 W). The PtPb/TiO₂/CSCNTs were prepared using the polyol method. The Pt NPs/TiO₂/CSCNTs (0.030 g) and Pb(CH₃COO)₂·3H₂O (0.022 mmol) were dissolved in 50 mL of ethylene glycol. The mixture was bath-sonicated and then treated in a flask under reflux for 1 min with 300 W microwave radiation. The mixture in the flask was cooled to room temperature with water. The mixture was again treated under microwave radiation (focused microwave instrument, CEM) at 300 W for 9 min. After the mixture cooled, the PtPb NPs/TiO₂/CSCNT was collected by centrifugation, washed sequentially with methanol, and dried under vacuum. Transmission electron microscope (TEM) and scanning transmission electron microscope (STEM) images were obtained using a JEOL 2100-F microscope with a 200 kV operating voltage. The composition of the PtPb NPs/TiO₂/CSCNT was analyzed using an energy-dispersion spectroscopic (EDS) analyzer (Oxford link system), which was coupled to the TEM. The TEM sample was prepared by dropping a suspension of the sample powder in methanol onto a copper microgrid, followed by thoroughly drying under vacuum prior to observation. The chemical composition of the samples and loading weight of Pt and PtPb on CB or TiO₂/CSCNT were determined using inductively coupled plasma-mass spectrometry (ICP-MS, PE-3300 DV, Perkin-Elmer). The loading weight of TiO₂ on TiO₂/CSCNT was estimated by thermogravimetry (Thermo plus EVO TG8120, Rigaku) under air. An aliquot of 1 mg of PtPb NPs/TiO₂/CSCNT (or commercially available Pt NPs/CB (10 wt % Pt, E-TEK) or prepared PtPb NPs/CB) was suspended in a solution of 995 μL of distilled water and 250 μL of isopropanol. Additionally, 5 μL of a 5% w/w Nafion® solution (EW: 1100, Aldrich) in alcohol was added to this suspension. The resulting suspension was bath-sonicated for 1 h. The suspension was coated onto a 5-mm-diameter glassy carbon (GC) electrode. The ORR activities of PtPb NPs/TiO₂/CSCNT and Pt NPs/CB were subsequently examined in O₂-saturated 0.1 M HClO₄ aqueous solution using a three-electrode cell with an Ag/AgCl (3 M NaCl) reference electrode. The electrochemical tests were performed at room temperature (23 ± 1 °C), at a sweep rate of 10 mV s⁻¹ and a rotation speed of 2000 rpm.

Figure 1 shows low-resolution TEM images of (a) CSCNT and (b) TiO₂-coated CSCNT. From TEM image (a) at high magnification, the stacking morphology of truncated conical sheets at an angle to the fiber axis can be seen; because of this angle, a large portion of the graphene edges are exposed and opened at the apparent tube surface as well as at the inner hollow core. After the TiO₂ coating treatment, the CSCNT surface does not reveal a stacking morphology due to the coated material. X-ray powder diffraction (XRD) analysis with the treated CSCNT sample indicated the formation of TiO₂ by matching the obtained XRD patterns with the standard TiO₂ pattern (not shown here). To confirm the TiO₂ distribution on CSCNT, a STEM image and its compositional mappings (Figure 2) were obtained using TiO₂/CSCNT. Small white spots in the STEM image correspond to TiO₂. The small spots, having diameters less than 10 nm, were heterogeneously dispersed on the surfaces. Red, orange, and green colors, indicating the existence of C, O, and Ti atoms, respectively, always overlap in the compositional mappings obtained from TiO₂/CSCNT.

Figure 3 shows a low-resolution TEM image of Pt NPs/TiO₂/CSCNT. Pt NPs appeared as dark spots uniformly dispersed on the CB. The size distribution of the Pt NPs was evaluated using approximately 100 particles in the TEM images. The average diameter of the Pt NPs was calculated as 2.5 nm, and the Pt NPs exhibited a narrow particle-size distribution. Uniformly dispersed deposition of Pt NPs on un-

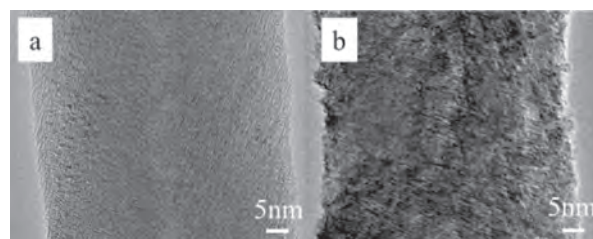


Figure 1. Low-resolution TEM image of (a) CSCNT and (b) TiO₂/CSCNT.

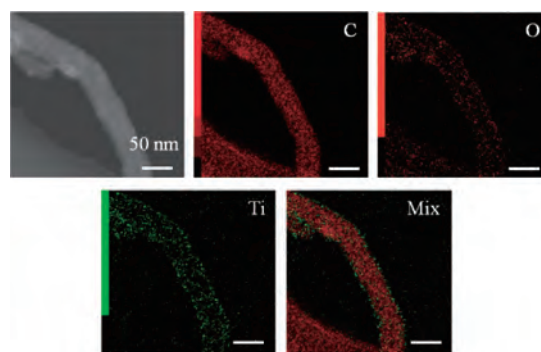


Figure 2. Scanning transmission electron microscope (STEM) image of the TiO₂/CSCNT (TiO₂ loading weight on TiO₂/CSCNT: 10 wt %) and the corresponding compositional mapping images.

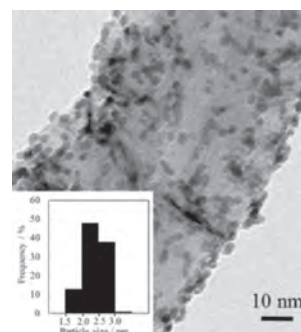


Figure 3. Low-resolution TEM image of Pt/TiO₂/CSCNT and its particle size distribution histogram.

treated CSCNTs or multiwalled CNTs using a Pt ion precursor and reducing agent could not be achieved. After converting Pt NPs to PtPb NPs by reacting Pb ions with Pt NPs and a polyol, a STEM image and its compositional mapping of PtPb/TiO₂/CSCNT was obtained to confirm the mixture of Pt and Pb atoms in the NPs (Figure 4). The atomic ratio of Pt:Pb was fairly consistent with the desired value of a PtPb ordered intermetallic phase, 54 ± 2:46 ± 2.0. In the mapping image, Pb atoms could be observed only in PtPb NPs, not on CSCNT surfaces; that is, Pb NPs were not formed on CSCNTs in the microwave reaction, indicating the selective reaction of Pb atoms with Pt NPs on the TiO₂/CSCNT surfaces, as both Bauer and the current authors have previously reported.^{12,13} The average diameter of the PtPb NPs prepared on TiO₂ was calculated to be 4.5 nm from the TEM images. Some PtPb NPs seemed to sit outside the TiO₂ islands. However, it is possible that the majority of PtPb NPs sit on the TiO₂, although this cannot be proven by TEM images. As will be discussed below, the deposition of PtPb on TiO₂ prevents Pb atoms on the PtPb

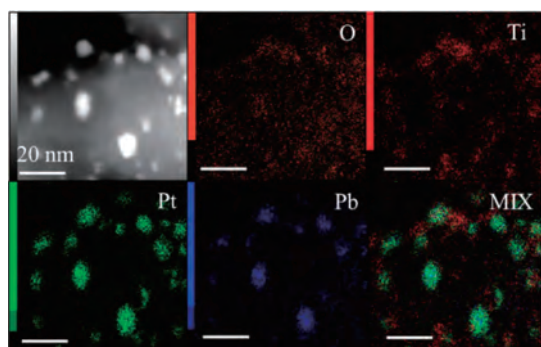


Figure 4. Scanning transmission electron microscope (STEM) image of the PtPb/TiO₂/CSCNT (PtPb loading weight on PtPb/TiO₂/CSCNT: 10 wt %) and the corresponding compositional mapping images.

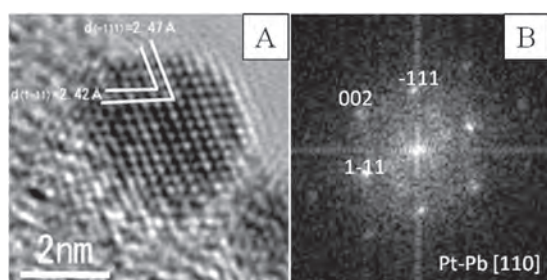


Figure 5. High-resolution transmission electron microscope (TEM) image of PtPb NPs on TiO₂/CSCNT and FFT pattern obtained from the TEM image.

NPs from electrochemical dissolution, which in turn stabilizes the high ORR activity on PtPb NPs/TiO₂/CSCNT.

Figure 5A displays a high-resolution TEM (HR-TEM) image of the PtPb NPs, and Figure 5B shows the corresponding fast Fourier-transform (FFT) patterns obtained from Figure 5A. Together, these images indicate that the NPs are single crystalline. The *d* lattice spacing of the NPs presented in the HR-TEM image are 0.242 and 0.247 nm, which closely match those of the (111) and (111) planes, respectively for PtPb ordered intermetallic compounds (0.242 nm for the (111) plane and 0.246 nm for the (111) plane, ICDD PDF File #06-0374). The FFT image shown in Figure 5B demonstrates that the Pt and Pb atoms were arranged in crystal structures corresponding to structurally modified PtPb ordered intermetallic phases.

Figure 6 compares the linear sweep voltammograms (LSVs) for the ORR recorded after 100 potential cycles with (a) PtPb NPs/TiO₂/CSCNT, (b) Pt/TiO₂/CSCNT, (c) Pt/CB, (d) PtPb/CB, and (e) PtPb/TiO₂ in O₂-saturated 0.1 M HClO₄ solution. Here, CB-supported Pt NPs (c) were used as the control. The ORR curve (a) obtained with PtPb NPs/TiO₂/CSCNT is shifted in the positive direction, owing to the formation of PtPb ordered intermetallic phase and the interaction between NPs and TiO₂ when compared with curve (b) with Pt/TiO₂/CSCNT and with curve (c) with Pt/CB. After 100 cycles, curve (d), obtained with PtPb/CB, indicates degradation of ORR activity because Pb atoms dissolve from the PtPb NPs surface on CB. The TiO₂ support material on CSCNT would prevent the Pb atoms on the PtPb NP surface from electrochemical dissolution. As shown in curve (e), PtPb supported on TiO₂ (average particle size: 50 nm) did not show enhancement of ORR activity. The reason for low ORR activity at PtPb/TiO₂ might be the high electron resistance of the TiO₂ support powder. The electronic interaction between PtPb and TiO₂ could not

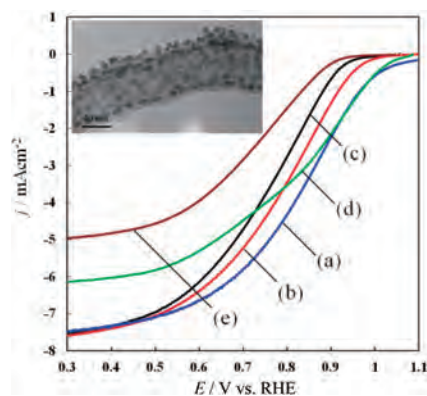


Figure 6. Linear sweep voltammograms (LSVs) after 100 potential cycles from 0.3 to 1.1 V on (a) PtPb NPs/TiO₂/CSCNT, (b) Pt/TiO₂/CSCNT, (c) Pt/CB, (d) PtPb/CB, and (e) PtPb/TiO₂ in O₂-saturated 0.1 M HClO₄ aqueous solution at 10 mV s⁻¹. Inset: a TEM image of PtPb/TiO₂/CSCNT used to obtain the LSVs.

be confirmed with the PtPb/TiO₂ sample. Therefore, the CSCNT-supported PtPb/TiO₂ sample was prepared and examined for enhancement of ORR activity in this study.

In this study, we proposed a preparation method for a catalyst with high catalytic activity for the ORR. The deliberate formation of PtPb on TiO₂ to make the most of the electric interaction between PtPb NPs and TiO₂ was confirmed with XRD, XPS, TEM, and STEM, from the viewpoint of crystallinity, size, degree of dispersion, and the electronic states of the NPs. The unique catalytic property of PtPb ordered intermetallic NPs and the strong interaction between PtPb NPs and TiO₂ layers successfully afforded enhancement of ORR in acidic aqueous solutions. The improved ORR performance of PtPb NPs/TiO₂/CSCNT is not an effect of the CSCNT support material. Rather, the higher performance is due to the interaction between PtPb NPs and TiO₂. The CSCNTs can provide a large amount of structure to PtPb NPs on TiO₂ on the CSCNT surface. In future work, the tolerance of PtPb/TiO₂/CSCNT during ORR cycles under a high oxidation atmosphere will be examined.

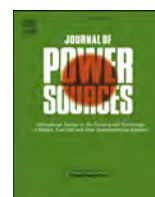
References

- G. A. Meehl, W. M. Washington, W. D. Collins, J. M. Arblaster, A. Hu, L. E. Buja, W. G. Strand, H. Teng, *Science* **2005**, *307*, 1769.
- M. P. Walsh, *J. Power Sources* **1990**, *29*, 13.
- J. Xie, D. L. Wood, III, D. M. Wayne, T. A. Zawodzinski, P. Atanassov, R. L. Borup, *J. Electrochem. Soc.* **2005**, *152*, A104.
- S. D. Knights, K. M. Colbow, J. St-Pierre, D. P. Wilkinson, *J. Power Sources* **2004**, *127*, 127.
- L.-M. Ang, T. S. A. Hor, G.-Q. Xu, C. Tung, S. Zhao, J. L. S. Wang, *Chem. Mater.* **1999**, *11*, 2115.
- B. Ruiz-Camacho, H. H. R. Santoyo, J. M. Medina-Flores, O. Álvarez-Martínez, *Electrochim. Acta* **2014**, *120*, 344.
- D. Huang, B. Zhang, J. Bai, Y. Zhang, G. Wittstock, M. Wang, Y. Shen, *Electrochim. Acta* **2014**, *130*, 97.
- L. A. Estudillo-Wong, A. M. Vargas-Gómez, E. M. Arce-Estrada, A. Manzo-Robledo, *Electrochim. Acta* **2013**, *112*, 164.
- H. Shioyama, *AIST Today* **2005**, *5-1*, 21.
- T. Gunji, G. Saravanan, T. Tanabe, T. Tsuda, M. Miyauchi, G. Kobayashi, H. Abe, F. Matsumoto, *Catal. Sci. Technol.* **2014**, *4*, 1436.
- S. Beak, D. Jung, K. S. Nahm, P. Kim, *Catal. Lett.* **2010**, *134*, 288.
- J. C. Bauer, X. Chen, Q. Liu, T.-H. Phan, R. E. Schaak, *J. Mater. Chem.* **2008**, *18*, 275.
- A. J. Jeevagan, T. Gunji, N. Sawano, G. Saravanan, T. Kojima, S. Kaneko, G. Kobayashi, F. Matsumoto, *ECS Trans.* **2014**, *58*, 25.



Contents lists available at ScienceDirect

Journal of Power Sources

journal homepage: www.elsevier.com/locate/jpowsour

Improving cycling performance of Li-rich layered cathode materials through combination of Al₂O₃-based surface modification and stepwise precycling



Genki Kobayashi ^{a,b,*}, Yuta Irii ^b, Futoshi Matsumoto ^b, Atsushi Ito ^c, Yasuhiko Ohsawa ^c, Shinji Yamamoto ^c, Yitao Cui ^{d,1}, Jin-Young Son ^d, Yuichi Sato ^e

^a Research Center of Integrative Molecular Systems (CIMoS), Institute for Molecular Science, 38 Nishigonaka, Myodaiji, Okazaki, Aichi 444-8585, Japan

^b Department of Material and Life Chemistry, Faculty of Engineering, Kanagawa University, 3-27-1 Rokkakubashi, Kanagawa-ku, Yokohama 221-8686, Japan

^c Nissan Research Center, Nissan Motor Co., Ltd., 1 Natsushima, Yokosuka, Kanagawa 237-8523, Japan

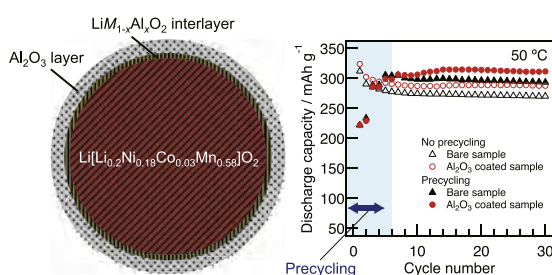
^d Japan Synchrotron Radiation Research Institute/SPring-8, 1-1-1 Kouto, Sayo, Hyogo 679-5198, Japan

^e Research Institute for Engineering, Kanagawa University, 3-27-1 Rokkakubashi, Kanagawa-ku, Yokohama 221-8686, Japan

HIGHLIGHTS

- Al₂O₃-coated Li[Li_{0.2}Ni_{0.18}Co_{0.03}Mn_{0.58}]O₂ was synthesized and investigated.
- The surface-modification layer is composed of Li–Al oxides and Al oxides.
- An interlayer formed between the modification layer and Li[Li_{0.2}Ni_{0.18}Co_{0.03}Mn_{0.58}]O₂ particles.
- A discharge capacity >310 mA h⁻¹ and excellent cycling stability at 50 °C are achieved.

GRAPHICAL ABSTRACT



ARTICLE INFO

Article history:

Received 10 July 2015

Received in revised form

24 September 2015

Accepted 4 November 2015

Available online xxx

Keywords:

Lithium secondary battery

Surface modification

Li-rich layered oxide

Hard X-ray photoelectron spectroscopy

ABSTRACT

Controlling a cathode/electrolyte interface by modifying the surface of a cathode material with metal oxides or phosphates is a concept being explored as a possible strategy for improving the electrochemical performance of such materials. This study therefore looks at the crystal structure and chemical bonding state from bulk to surface of Al₂O₃-coated Li[Li_{0.2}Ni_{0.18}Co_{0.03}Mn_{0.58}]O₂ and explores the influence that surface modification has on the electrochemical performance. Investigation by X-ray diffraction, hard X-ray photoelectron spectroscopy (HAXPES) and galvanostatic charge/discharge reaction reveals that the surface-modification layer is composed of Li–Al oxides and Al oxides, with a LiM_{1-x}Al_xO₂ (M = transition metal) interlayer formed between the modification layer and Li[Li_{0.2}Ni_{0.18}Co_{0.03}Mn_{0.58}]O₂ particles. The cycling performance of the Li-rich layered oxide is enhanced by its surface modification with Al₂O₃, achieving a discharge capacity of more than 310 mA h⁻¹ and excellent cycling stability at 50 °C when combined with a more gradual Li-insertion/de-insertion process (i.e., stepwise precycling treatment).

© 2015 Elsevier B.V. All rights reserved.

* Corresponding author. Research Center of Integrative Molecular Systems (CIMoS), Institute for Molecular Science, 38 Nishigonaka, Myodaiji, Okazaki, Aichi 444-8585, Japan.

E-mail address: gkobayashi@ims.ac.jp (G. Kobayashi).

¹ Present address: Synchrotron Radiation Research Organization, The University of Tokyo, 7-3-1 Hongo, Bunkyo-ku, Tokyo 113-8656, Japan.

1. Introduction

There is currently a demand for greater energy density in lithium secondary batteries that is being driven by their increasing use in portable energy storage devices, large-scale batteries for automobiles and power storage units. In order to meet these needs, it is essential to develop high-capacity cathode materials that are cheap, safe and exhibit good cycling performance. Recently, Li-rich layered oxides with a chemical formula of $x\text{Li}_2\text{MnO}_3-(1-x)\text{LiMO}_2$ ($M = \text{Ni, Co, Mn}$) have attracted considerable attention as a promising cathode material for next-generation lithium-ion batteries. These materials offer several advantages over conventional cathode materials such as LiCoO_2 , including: a capacity as high as $\sim 250 \text{ mA h g}^{-1}$, low cost, structural stability, and high capacity retention at high voltages [1–9]. The high capacity of these materials has been attributed to their charge/discharge reaction mechanism, which differs from conventional cathode materials in which Li^+ extraction during charging causes oxidation of the transition metal. Instead, the delithiation of Li-rich layered oxides during the initial charging process is accompanied not only by an increase in the valency of the transition metal ions, but also by the oxidation of O^{2-} . This results in irreversible oxygen loss [10,11] at the surface and/or O^- formation in the lattice [5,12,13]. Furthermore, it has been found that the specific charge reaction of Li-rich layered oxides induces a structural rearrangement [14,15], which in turn lowers the valency of some manganese ions from Mn^{4+} to Mn^{3+} [10,11,16] and results in the formation of a by-product [17] due to the oxygen-reductive reaction during the 1st discharge. Note that although Mn^{3+} in layered rock-salt-type oxides is electrochemically inactive, the structural rearrangement that occurs during the 1st charge/discharge process makes these ions active and means that the $\text{Mn}^{3+}/\text{Mn}^{4+}$ redox reaction contributes to the charge/discharge capacity from the 2nd cycle onwards. However, there is also an irreversible oxygen loss during the 1st cycle that creates microcracks at the cathode surface in conjunction with lattice distortion, thereby producing a large irreversible capacity and subsequent lowering of the cycling performance [18]. There is therefore clearly a trade-off between the activation of the manganese redox reaction after the 1st cycle and the cycling performance, which ultimately results in deterioration in crystallinity at the cathode surface due to oxygen extraction.

In previous studies, we were able to improve the cycling performance of Li-rich layered oxides, $x\text{Li}_2\text{MnO}_3-y\text{LiNi}_{1/2}\text{Mn}_{1/2}\text{O}_2-z\text{LiNi}_{1/3}\text{Co}_{1/3}\text{Mn}_{1/3}\text{O}_2$ ($x + y + z = 1$), and increase their discharge capacity through a stepwise precycling treatment. In this, the Li^+ extraction/insertion and redox reaction of the oxide ions during charge/discharge were slowed by maintaining an upper potential limit of more than 4.5 V [18,19]. The main effect of this stepwise precycling treatment is that it inhibits the formation of microcracks at the surface of the material particles, while also preventing lattice distortion during the 1st charge to 4.8 V. Indeed, no microcracks or amorphous regions were observed in the treated samples, not even after 50 charge/discharge cycles [18].

The surface modification of cathode materials with other metal oxides or phosphates is a proven technique for preventing any loss in surface crystallinity during the charge/discharge reaction [20–26]. The main role of this surface modification layer is to protect the surface structure of the cathode material from side reactions with the electrolyte, though in the case of Li-rich layered oxides, this layer may also restrict the loss of oxygen from the lattice that would otherwise reduce the irreversible capacity of the cathode. Herein, we report a method for further improving the cycling performance of cathodes based on Li-rich layered oxides

through a combination of both stepwise precycling and surface modification with Al_2O_3 .

2. Experimental

Samples of $\text{Li}[\text{Li}_{0.2}\text{Ni}_{0.18}\text{Co}_{0.03}\text{Mn}_{0.58}]\text{O}_2$ were synthesized by mixing a Ni–Mn–Co precursor with $\text{LiOH}\cdot\text{H}_2\text{O}$. The precursor was prepared in advance through coprecipitation using $\text{Ni}(\text{NO}_3)_2\cdot 6\text{H}_2\text{O}$, $\text{Co}(\text{NO}_3)_2\cdot 6\text{H}_2\text{O}$ and $\text{Mn}(\text{NO}_3)_2\cdot 4\text{H}_2\text{O}$ as the starting materials, and $2 \text{ mol L}^{-1} \text{ Na}_2\text{CO}_3$ and $0.2 \text{ mol L}^{-1} \text{ NH}_4\text{OH}$ solutions as the precipitation agents. For this, the stoichiometric starting materials were first dissolved in distilled water to form a 2-mol L^{-1} solution, and then the precipitation agents were added drop-by-drop to obtain a composite carbonate precursor. This was dried at 120°C for 5 h, sintered at 500°C for 5 h, ground, and then mixed with $\text{LiOH}\cdot\text{H}_2\text{O}$. This mixture was pressed into pellets, and finally sintered at 900°C in air for 12 h. The resulting pristine $\text{Li}[\text{Li}_{0.2}\text{Ni}_{0.18}\text{Co}_{0.03}\text{Mn}_{0.58}]\text{O}_2$ powder was subjected to surface modification with Al_2O_3 through a wet-coating process, in which $\text{Al}(\text{NO}_3)_3\cdot 9\text{H}_2\text{O}$ was dissolved in deionized water with a pH of ~ 7 , though this increased to ~ 9 following the addition of the Li-rich layered oxide powder. After being filtered, the precursor was dried at 120°C overnight, and then sintered at 450°C in air for 3 h.

Synchrotron X-ray diffraction patterns of the samples were obtained using the BLO2B2 beam line at SPring-8, Japan. A Debye–Scherrer diffraction camera was used for the measurements, which were performed at room temperature using specimens sealed in a glass capillary (diameter: 0.2 or 0.3 mm) under vacuum. Diffraction data were collected in steps of 0.01° from 3.0° to 70° , with the wavelength of the incident beam having been calibrated in advance using a NIST SRM Ceria 640b CeO_2 standard and fixed at 0.6 \AA . The lattice parameters and structures of the samples were determined by X-ray Rietveld analysis, which was performed using the RIETAN-FP program [27].

A spherical aberration (Cs)-corrected scanning tunneling electron microscope (STEM) was used to determine the distribution of Al_2O_3 on the $\text{Li}[\text{Li}_{0.2}\text{Ni}_{0.18}\text{Co}_{0.03}\text{Mn}_{0.58}]\text{O}_2$ particles. Samples for this were prepared by embedding in epoxy resin to improve ease of handling, followed by mechanical grinding and Ar ion milling. A Mo grid was used as the sample holder for the Cs-STEM imaging.

High-angle annular dark-field (HAADF)-STEM imaging and energy-dispersive X-ray spectroscopy (EDX) were performed on a 2-wt% Al_2O_3 -coated $\text{Li}[\text{Li}_{0.2}\text{Ni}_{0.18}\text{Co}_{0.03}\text{Mn}_{0.58}]\text{O}_2$ sample using a JEM-ARM200F system (JEOL) equipped with a “JEOL Centurio” silicon drift detector (100 mm^2) and EDX analysis station. For Cs-STEM observations, an accelerating voltage of 200 V, beam diameter of $\sim 0.2 \text{ nm}$ and energy resolution of $\sim 0.5 \text{ eV}$ (full width at half maximum (FWHM)) were used.

Hard X-ray photoelectron spectroscopy (HAXPES) measurements were performed using a VG SCIENTA R-4000 hemispherical electron-energy analyzer at the BL46XU beam line at SPring-8, Japan [28,29]. The excitation energy was set to 7939.05 eV and the analyzer was at an acceptance angle of $\pm 7.5^\circ$ from the sample. By measuring the Fermi edge of gold, the energy resolution for the HAXPES measurements was found to be $\sim 235 \text{ meV}$. To inhibit peak shift attributable to the charging effect in the sample, sheet electrodes containing a conductive additive (carbon) were cut and placed on a sample stage. Using an Ar glove box, this was inserted into a transfer vessel, which was then connected to the HAXPES preparation chamber to reduce the pressure to less than $3 \times 10^{-4} \text{ Pa}$. All HAXPES measurements were performed at room temperature under a pressure of less than $5 \times 10^{-6} \text{ Pa}$. The escape depth was controlled by varying the take-off angle (TOA) of the

photoelectrons relative to the sample surface, as shown in Fig. S1. The excitation energy was set to 7939.05 eV and the energy resolution for the HAXPES measurements was confirmed to be ~235 meV by fitting the gold Fermi level.

Galvanostatic charging/discharging of bare and 2-wt%-Al₂O₃-coated Li[Li_{0.2}Ni_{0.18}Co_{0.03}Mn_{0.58}]O₂ samples was performed using 2032-type coin cells at 25 and 50 °C. These cells consisted of a Li metal anode and 1 M LiPF₆ in ethylene carbonate/dimethyl carbonate (ratio of 1:2) as the electrolyte. The working electrode was made from a mixture of the test sample/conductive carbon/polyvinylidene fluoride (85:10:5). The mass of active material loaded in the sheet electrodes is approximately 4 mg (1.99 mg cm⁻²). The charging rate was set to C/10 over a potential range of 2.0–4.8 V. Stepwise precycling treatment was performed by increasing the upper potential limit from 4.5 to 4.8 V by 0.1 V every two cycles, as reported previously [18,19].

3. Results and discussions

In the synchrotron X-ray diffraction (SXRD) profiles of the bare and 2-wt%-Al₂O₃-coated Li[Li_{0.2}Ni_{0.18}Co_{0.03}Mn_{0.58}]O₂ samples shown in Fig. 1(a), the diffraction peaks can be indexed to a conventional, layered rock-salt-type structure with a space group of *R3m*. The exceptions to this are the superlattice peaks [8,30,31] observed at 8–10°. No extra peaks corresponding to impurity phases are observed in the case of the surface-modified sample, which indicates that the surface-modification process did not result in decomposition of the sample or produce any change in its structural symmetry. The inset transmission electron microscopy

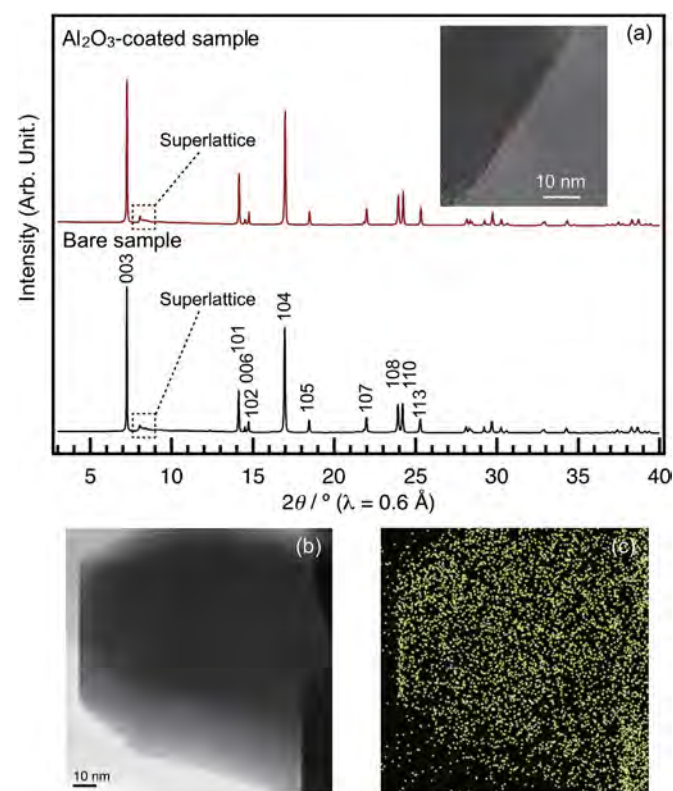


Fig. 1. (a) SXRD profiles of bare and Al₂O₃-coated Li[Li_{0.2}Ni_{0.18}Co_{0.03}Mn_{0.58}]O₂ samples. Inset shows a TEM image of the Al₂O₃-coated sample. (b) STEM image and (c) elemental map showing the uniform coating of Al₂O₃ over the sample particles.

(TEM) image in Fig. 1(a) shows that a continuous amorphous layer is formed on the surface of the highly crystalline Li[Li_{0.2}Ni_{0.18}Co_{0.03}Mn_{0.58}]O₂ particles to a thickness of ~3 nm. The elemental mapping shown in Fig. 1(b) and (c) confirms that Al is uniformly dispersed on the particles. The structural parameters of both samples are determined by Rietveld analysis, which is performed using the RIETAN-FP program [27]. The refinement parameters and fitting profiles in Tables 1a and b and Fig. 2, respectively, show that the *a*-axis shrank and the *c*-axis expand after surface modification with Al₂O₃. This change in the lattice corresponds to the early stage of Li⁺ deintercalation from the Li-rich layered oxide [15] during charging, thereby indicating that the Al₂O₃-modified surface reacts with Li⁺ on the surface of the cathode material. HAADF-STEM imaging and linear elemental analysis performed using EDX (Fig. 3) reveal that Al ions are present on the surface of the Li[Li_{0.2}Ni_{0.18}Co_{0.03}Mn_{0.58}]O₂ particles to a depth of ~10 nm into the bulk after surface-modification.

The chemical bonding state of Al in the Al₂O₃-coated Li[Li_{0.2}Ni_{0.18}Co_{0.03}Mn_{0.58}]O₂ sample is examined nondestructively using HAXPES [28,29], which allows for detection at greater depths and over a wider range of energies than conventional photoelectron spectroscopy techniques based on vacuum-ultraviolet and soft X-rays [32]. The detection depth of the sample can be determined by varying the TOA, with a TOA of 80° related to the chemical bonding state of the bulk at a depth of ~33 nm or more. Conversely, surface-sensitive information (i.e., a depth of ~10 nm or more) can be obtained using a TOA of 15°. Because Li-rich layered oxides are insulating materials, sheet electrodes containing a conductive additive (carbon) are needed to inhibit peak shift caused by charging effects. Fig. 4(a) and (b) show the HAXPES Al 1s spectra for Al₂O₃-coated Li[Li_{0.2}Ni_{0.18}Co_{0.03}Mn_{0.58}]O₂ at TOA angles of 80° and 15°, respectively. Note that Al-doped Li[Li_{0.2}Ni_{0.18}Al_{0.03}Mn_{0.58}]O₂ is used as a reference to detect the bonding state of Al in the lattice of the Li-rich layered oxide, as shown in Fig. 4(c). The Al 1s peak for the Al₂O₃-coated Li[Li_{0.2}Ni_{0.18}Co_{0.03}Mn_{0.58}]O₂ sample appears at a lower binding energy than in the case of α-Al₂O₃ (1562.3 eV, see Fig. S2(a)); but more importantly, the main spectrum of the Al-doped Li[Li_{0.2}Ni_{0.18}Al_{0.03}Mn_{0.58}]O₂ indicates that the binding energy of Al in the bulk is 1560.1 eV (Fig. 4(c)). It can therefore be assumed that the coating layer consists mainly of Al oxides and Li(M_{1-x}Al_x)O₂ (M = Ni, Co, and/or Mn). To clarify this, curve fittings of the Al 1s spectra are carried out for the Al₂O₃-coated and Al-doped samples. The FWHM values for the peaks of Al 1s of LiM_{1-x}Al_xO₂ are fixed at the same value (1.25 eV) as the main peak of the Al-doped sample, whereas those of the other peaks detected in the high-energy range are fixed at the same value (1.66 eV) as the α-Al₂O₃ sample (Fig. S2). Other parameters such as the intensity and peak positions are allowed to vary. The peak with the lowest Al 1s binding energy is observed at approximately the same binding

Table 1a
Rietveld refinement results for the X-ray diffraction patterns of bare Li[Li_{0.2}Ni_{0.18}Co_{0.03}Mn_{0.58}]O₂.

| Atom | Site | g | x | y | z | B/Å ² |
|-------|------|--------------------------|---|---|-----------|---------------------|
| Li(1) | 3a | 1-g _{Ni(1)} | 0 | 0 | 0 | =B _{Ni(1)} |
| Ni(1) | 3a | 0.0244 | 0 | 0 | 0 | 1.084(10) |
| Li(2) | 3b | 1.2-g _{Li(1)} | 0 | 0 | 0.5 | =B _{Ni(2)} |
| Ni(2) | 3b | 0.183-g _{Ni(1)} | 0 | 0 | 0.5 | 0.396(3) |
| Co(1) | 3b | 0.0033 | 0 | 0 | 0.5 | =B _{Ni(2)} |
| Mn(1) | 3b | 0.584 | 0 | 0 | 0.5 | =B _{Ni(2)} |
| O(1) | 6c | 1 | 0 | 0 | 0.2419(2) | 0.836(3) |

Unit cell: Rhombohedral *R*-3*m*, *a* = 2.85907(6), *c* = 14.2534(2).

*R*_{wp} = 4.70, *R*_p = 3.605, *R*_e = 4.00, *S* = *R*_{wp}/*R*_e = 1.174, *R*₁ = 1.68, *R*_F = 0.61.

Table 1bRietveld refinement results for the X-ray diffraction patterns of 2-wt%-Al₂O₃-coated Li[Li_{0.2}Ni_{0.18}Co_{0.03}Mn_{0.58}]O₂.

| Atom | Site | g | x | y | z | B/Å ² |
|-------|------|--------------------------|---|---|-----------|---------------------|
| Li(1) | 3a | 1-g _{Ni(1)} | 0 | 0 | 0 | =B _{Ni(1)} |
| Ni(1) | 3a | 0.150(2) | 0 | 0 | 0 | 1.144(11) |
| Li(2) | 3b | 1.2-g _{Li(1)} | 0 | 0 | 0.5 | =B _{Ni(2)} |
| Ni(2) | 3b | 0.183-g _{Ni(1)} | 0 | 0 | 0.5 | 0.366(3) |
| Co(1) | 3b | 0.0033 | 0 | 0 | 0.5 | =B _{Ni(2)} |
| Mn(1) | 3b | 0.584 | 0 | 0 | 0.5 | =B _{Ni(2)} |
| O(1) | 6c | 1 | 0 | 0 | 0.2418(4) | 0.959(2) |

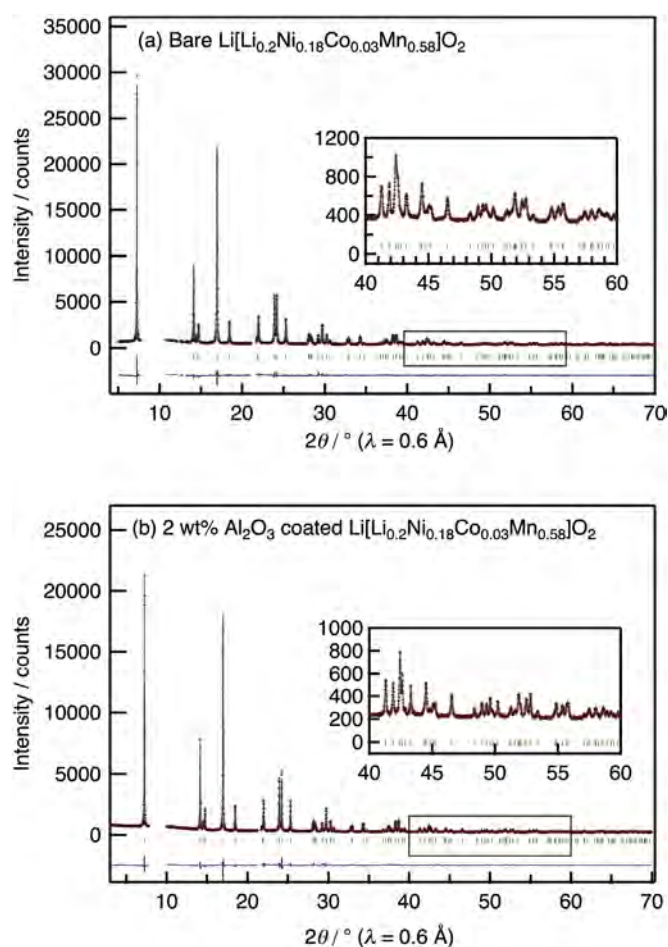
Unit cell: Rhombohedral *R*-3*m*, *a* = 2.85841(2), *c* = 14.26688(10).*R*_{wp} = 4.54, *R*_p = 3.45, *R*_e = 4.81, *S* = *R*_{wp}/*R*_e = 0.9445, *R*_i = 2.97, *R*_f = 1.59.

Fig. 2. Synchrotron X-ray Rietveld refinement profiles of (a) bare and (b) 2-wt%-Al₂O₃-coated Li[Li_{0.2}Ni_{0.18}Co_{0.03}Mn_{0.58}]O₂ samples. The final observed, calculated, and residual differences are indicated by red crosses, a cyan line, and blue line, respectively. The green tick marks indicate the positions of the Bragg reflections. (For interpretation of the references to colour in this figure legend, the reader is referred to the web version of this article.)

energy as the Al-doped sample, and the fact that the intensity of this peak increases when the TOA is 15° (surface-sensitive measurement) indicates that Al ions in the lattice are localized in a region extending no more than 10 nm from the surface. The second peak, which is observed at 1561 eV, is attributed to Li–Al oxides on the basis of the fact that the Al 2s peak of LiAlO₂ occurs at 118.7 eV [21,22], with the corresponding Al 1s line occurring at 1560.6 eV. The peak at 1561.9 eV could also be related to one of the Al oxides though, as the binding energy of α -Al₂O₃ is very similar (1562.3 eV)

(see Fig. S2(a)). The peak at 1563.3 eV, on the other hand, is most likely the result of Al–F or Al–O–F bonds given that the Al 2p lines of AlF₃, (Al–O–F), and Al(OH)_xF_{3–x} occur at 76.6, 75.8, and 76.0 eV, respectively, with the corresponding to the binding energy of Al 1s lines at 1563.4, 1562.6, and 1562.8 eV [21,22]. This fluoride-containing component is believed to be formed by a reaction between polyvinylidene difluoride and the cathode materials during the 120 °C vacuum drying process used to make the sheet electrodes. These results indicate that the surface-modification layer is composed of Li–Al oxides and Al oxides, and that a LiM_{1–x}Al_xO₂ interlayer is formed between the modification layer and the Li-rich layered oxide, as illustrated in Fig. 5. It is known that doping cathode materials with Al improves their electrode performance because it increases their structural and thermal stability, with the dissolution of Mn in the electrolyte at high temperatures (≥ 50 °C) known to be inhibited by doping Al into the spinel structure (i.e., by the formation of Li[Li_{0.1}Al_{0.1}Mn_{1.8}]O₄) [33]. Similarly, layered rock-salt-type Li[Ni_{0.8}Co_{0.15}Al_{0.05}]O₂ has been commercially successful as a cathode material because of the improvement in structural stability that Al doping brings. The LiM_{1–x}Al_xO₂ interlayer created in this study is therefore expected to enhance the cycling performance of Li-rich layered oxides.

Fig. 6(a) shows the cycling performance of bare and 2-wt%-Al₂O₃-coated Li[Li_{0.2}Ni_{0.18}Co_{0.03}Mn_{0.58}]O₂ samples before and after stepwise precycling treatment at 25 °C. We see from this that the initial discharge capacity of the bare cathode material without precycling is 245 mA h g^{–1}, and that its capacity retention rate is 89% after 30 cycles. In contrast, the surface-modified sample achieves a discharge capacity of more than 270 mA h g^{–1}, and its capacity does not deteriorate even after 30 cycles. Thus, its electrochemical performance is almost the same as that of the sample subjected to only precycling, yet precycling treatment of the surface-modified sample does not improve its electrochemical properties. Generally, high temperatures tend to bring about an increase in charge/discharge capacity, but a decrease in capacity retention due to side reactions of the electrolyte such as metal dissolution. As shown in Fig. 6(b), the surface-modified sample exhibits an initial discharge capacity of more than 310 mA h g^{–1} without precycling treatment, but has a low cycling stability at 50 °C. On the other hand, the sample subjected to both surface modification and precycling exhibits not only high discharge capacity, but also excellent cycling performance. This means that high electrochemical performance at high temperatures requires both surface modification and precycling treatment.

The charge/discharge profiles of the two samples at 25 and 50 °C are compared in Fig. 6(c)–(f), from which it is evident that the bare and surface-modified samples not subjected to precycling treatment exhibit a plateau at ~ 4.5 V in the 1st charging curve. This can be mainly attributed to lithium extraction that is accompanied by partial oxidation of the oxide ions, resulting in an irreversible oxygen loss from the lattice (Fig. 6(c) and (e)) [10,11]. The characteristic reaction of Li-rich layered oxides during their initial charging process often leads to the formation of microcracks and amorphous domains on the surface, which in turn triggers a large irreversible capacity loss during the 1st cycle that subsequently leads to capacity fading [1]. Compared to the bare sample, the surface-modified sample demonstrates only a small 1st charge capacity, but a large 1st discharge capacity. This low irreversible capacity indicates that the surface-modification layer inhibits the electrochemical inactivation of the cathode material, and that this is accompanied by an extreme release of oxygen and electrolyte side reactions during the 1st charging process. There are also differences in the shapes of the discharge curves after the 30th cycle, with an increase in discharge capacity after the surface-modification process being observed for voltages lower than 3.5 V (Fig. 6(c)). In the

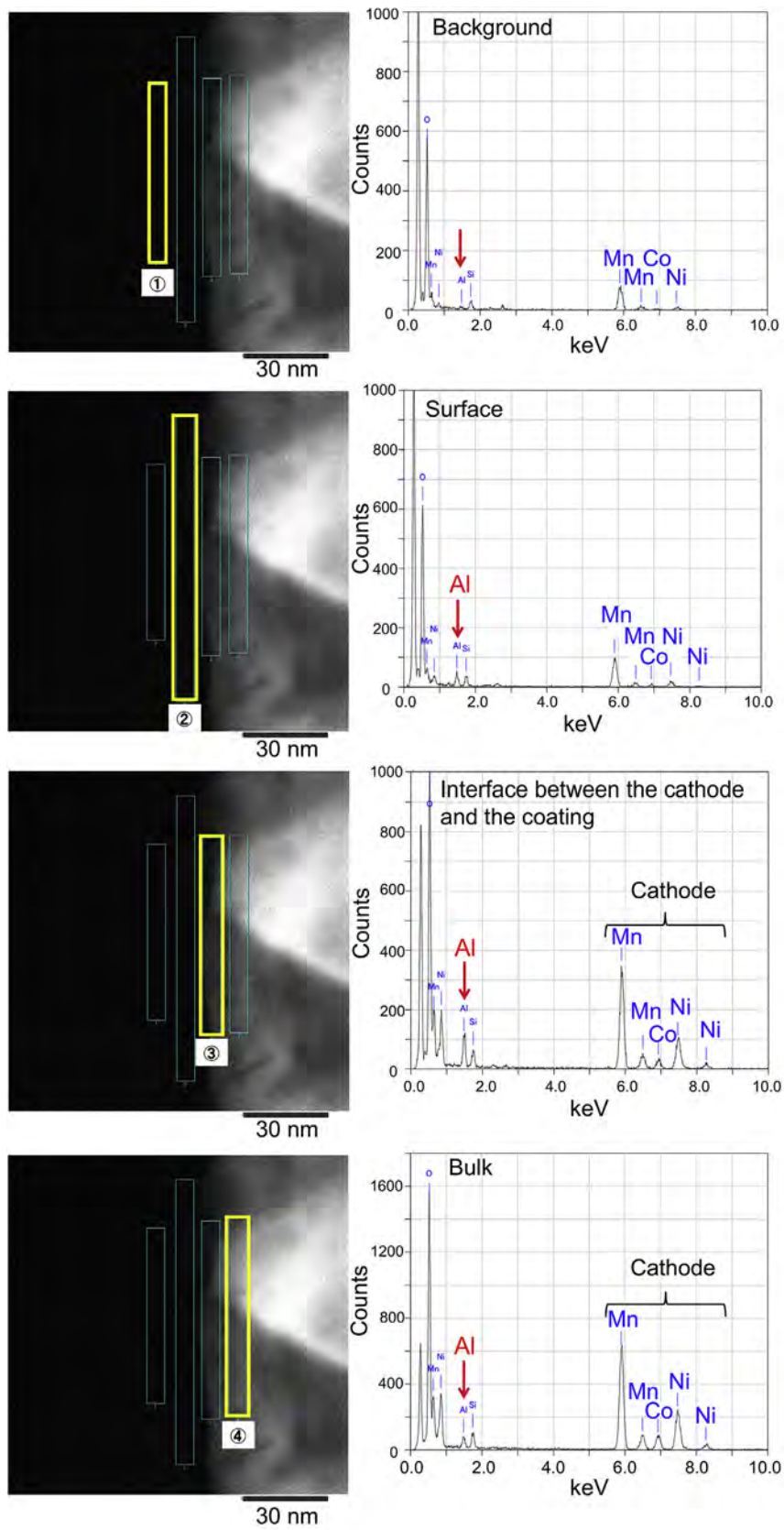


Fig. 3. HAADF-STEM images and related EDX results for 2-wt%-Al₂O₃-coated Li[Li_{0.2}Ni_{0.18}Co_{0.03}Mn_{0.58}]O₂.

case of Li-rich layered oxides, it has been suggested that some tetravalent manganese ions are reduced to a trivalent state by the

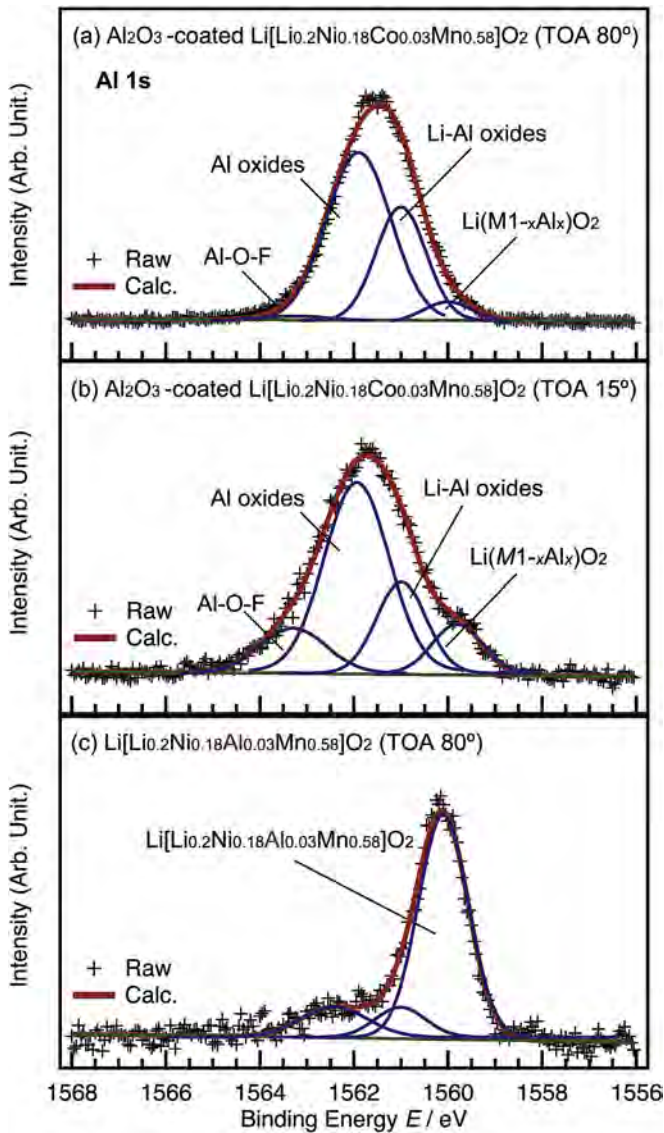


Fig. 4. Al 1s HAXPES spectra of Al_2O_3 -coated $\text{Li}[\text{Li}_{0.2}\text{Ni}_{0.18}\text{Co}_{0.03}\text{Mn}_{0.58}]\text{O}_2$ and $\text{Li}[\text{Li}_{0.2}\text{Ni}_{0.18}\text{Al}_{0.03}\text{Mn}_{0.58}]\text{O}_2$ samples obtained at TOA values of: (a) 80° , (b) 15° , and (c) 80° . Fitted curves and their components are shown by the red and blue lines, respectively. (For interpretation of the references to colour in this figure legend, the reader is referred to the web version of this article.)

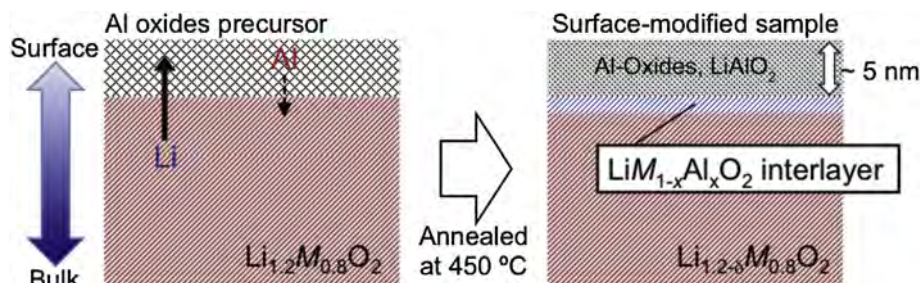


Fig. 5. Schematic of the structure of 2-wt%- Al_2O_3 -coated $\text{Li}[\text{Li}_{0.2}\text{Ni}_{0.18}\text{Co}_{0.03}\text{Mn}_{0.58}]\text{O}_2$.

irreversible oxygen release that occurs during the 1st charging process and the subsequent reinsertion of Li during the discharge reaction, which results in an increase in capacity at voltages lower

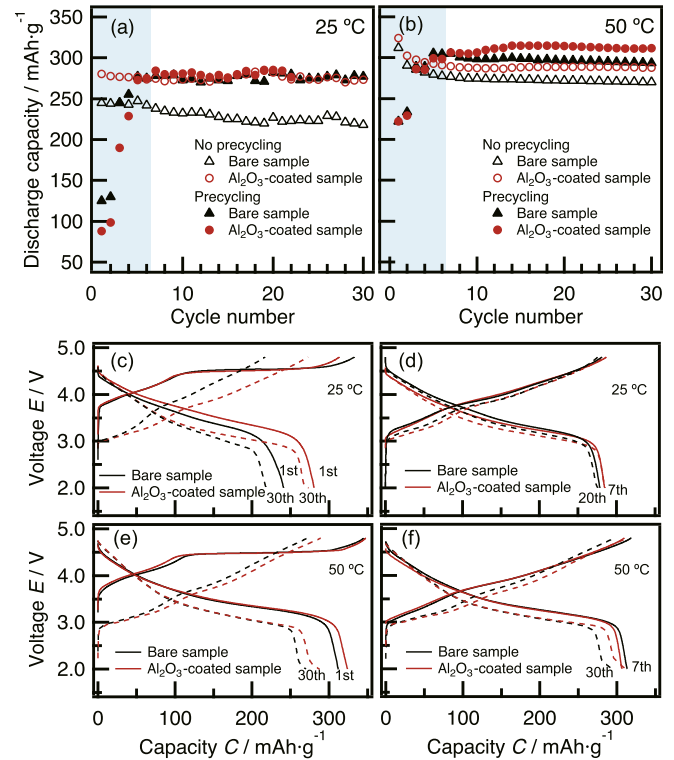


Fig. 6. Cycling performance and charge/discharge curves of bare and Al_2O_3 -coated $\text{Li}[\text{Li}_{0.2}\text{Ni}_{0.18}\text{Co}_{0.03}\text{Mn}_{0.58}]\text{O}_2$ samples at: (a) 25°C , (b) 50°C , (c) with no treatment at 25°C , (d) after stepwise precycling at 25°C , (e) with no treatment at 50°C , and (f) after stepwise precycling at 50°C .

than 3.5 V [10,11,16]. If so, then this $\text{Mn}^{3+}/\text{Mn}^{4+}$ redox reaction likely contributes to the charge/discharge capacity of the surface-modified sample. In contrast, no significant difference is observed in the charge/discharge curves of the precycled samples (Fig. 6(d)). With the measurements performed at 50°C , the initial charge capacity of the bare and surface-modified samples increases to close to the theoretical capacity, with the discharge capacity also increasing to more than 310 mA h g^{-1} (Fig. 6(e)). However, capacity fading is also observed in the surface-modified sample after a few cycles at 50°C , as is the case with the bare sample. It would therefore seem that the extraction of a greater amount of Li and the oxidation of a greater number of oxygen ions from the crystal

structure during the 1st charging process at 50°C induces an irreversible structural rearrangement, which could include the migration of transition metal ions to lithium sites, a phase

transition to a spinel-like structure and/or the formation of inactive amorphous domains [14,15,18]. Consequently, surface modification with Al₂O₃ is insufficient to maintain the primary electrochemical performance at 50 °C. Fig. 6(f) shows the charge/discharge curves of samples subjected to stepwise precycling, and though these are obtained immediately after stepwise precycling, there is little difference between the bare and the surface-modified samples. The notable exception is the fact that the discharge capacity of the surface-modified sample after 30 cycles is greater than that of the bare sample.

4. Conclusion

This study has confirmed that a LiM_{1-x}Al_xO₂ interlayer is formed between an Al₂O₃ modification layer and Li[Li_{0.2}Ni_{0.18}Co_{0.03}Mn_{0.58}]O₂ particles. At room temperature, surface modification with Al₂O₃ results in almost the same degree of improvement in cycling performance as stepwise precycling treatment. Stepwise precycling of the surface-modified sample does not result in any further improvement in performance at room temperature; however, a synergistic effect of combining Al₂O₃ surface modification and precycling is present at 50 °C. The surface-modified sample subjected to precycling exhibited a capacity of more than 310 mA h g⁻¹ and excellent cycling performance, this being despite the fact that the charge/discharge reaction at 50 °C readily degrades performance. These results therefore clearly demonstrate that combining Al₂O₃ surface-modification and stepwise precycling is an effective approach to inhibiting the deterioration in electrochemical performance of Li-rich layered oxides at high temperatures.

Acknowledgments

Synchrotron experiments were performed as a project approved by the Japan Synchrotron Radiation Research Institute (JASRI) (Proposal Nos. 2011B1883, 2012A1622, 2012B1903, and 2013A1834).

Appendix A. Supplementary data

Supplementary data related to this article can be found at <http://dx.doi.org/10.1016/j.jpowsour.2015.11.014>.

References

- [1] Z. Lu, J.R. Dahn, *J. Electrochem. Soc.* 149 (2002) A1454.
- [2] S.-H. Kang, Y.K. Sun, K. Amine, *Electrochem. Solid-State Lett.* 6 (2003) A183.
- [3] S.-H. Kang, K. Amine, *J. Power Sources* 124 (2003) 533.
- [4] C.S. Johnson, J.S. Kim, C. Lefief, N. Li, J.T. Vaughey, M.M. Thackeray, *Electrochem. Commun.* 6 (2004) 1085.
- [5] Y.-S. Hong, Y.J. Park, K.S. Ryu, S.H. Chang, M.G. Kim, *J. Mater. Chem.* 14 (2004) 1424.
- [6] M.M. Thackeray, C.S. Johnson, J.T. Vaughey, N. Li, S.A. Hackney, *J. Mater. Chem.* 15 (2005) 2257.
- [7] D.A.R. Barkhouse, J.R. Dahn, *J. Electrochem. Soc.* 152 (2005) A746.
- [8] M.M. Thackeray, S.H. Kang, C.S. Johnson, J.T. Vaughey, S.A. Hackney, *Electrochem. Commun.* 8 (2006) 1531.
- [9] C.S. Johnson, N. Li, C. Lefief, J.T. Vaughey, M.M. Thackeray, *Chem. Mater.* 20 (2008) 6095.
- [10] Z. Lu, J.R. Dahn, *J. Electrochem. Soc.* 149 (2002) A815.
- [11] A.R. Armstrong, M. Holzapfel, P. Novák, C.S. Johnson, S.-H. Kang, M.M. Thackeray, P.G. Bruce, *J. Am. Chem. Soc.* 128 (2006) 8694.
- [12] M. Sathiyaa, K. Ramesha, G. Rousse, D. Foix, D. Gonbeau, A.S. Prakash, M.L. Doublet, K. Hemalatha, J.M. Tarascon, *Chem. Mater.* 25 (2013) 1121.
- [13] M. Sathiyaa, G. Rousse, K. Ramesha, C.P. Laisa, H. Vezin, M.T. Sougrati, M.L. Doublet, D. Foix, D. Gonbeau, W. Walker, A.S. Prakash, M. Ben Hassine, L. Dupont, J.M. Tarascon, *Nat. Mater.* 12 (2013) 827.
- [14] M. Jiang, B. Key, Y.S. Meng, C.P. Grey, *Chem. Mater.* 21 (2009) 2733.
- [15] N. Tran, L. Croguennec, M. Ménétrier, F. Weill, P. Biensan, C. Jordy, C. Delmas, *Chem. Mater.* 20 (2008) 4815.
- [16] A. Ito, Y. Sato, T. Sanada, M. Hatano, H. Horie, Y. Ohsawa, *J. Power Sources* 196 (2011) 6828.
- [17] N. Yabuuchi, K. Yoshii, S.-T. Myung, I. Nakai, S. Komaba, *J. Am. Chem. Soc.* 133 (2011) 4404.
- [18] A. Ito, D. Li, Y. Sato, M. Arao, M. Watanabe, M. Hatano, H. Horie, Y. Ohsawa, *J. Power Sources* 195 (2010) 567.
- [19] A. Ito, D. Li, Y. Ohsawa, Y. Sato, *J. Power Sources* 183 (2008) 344.
- [20] J. Cho, Y.J. Kim, T.-J. Kim, B. Park, *Angew. Chem. Int. Ed.* 40 (2001) 3367.
- [21] A.T. Appapillai, A.N. Mansour, J. Cho, Y. Shao-Horn, *Chem. Mater.* 19 (2007) 5748.
- [22] Y.-C. Lu, A.N. Mansour, N. Yabuuchi, Y. Shao-Horn, *Chem. Mater.* 21 (2009) 4408.
- [23] Q.Y. Wang, J. Liu, A.V. Murugan, A. Manthiram, *J. Mater. Chem.* 19 (2009) 4965.
- [24] J. Liu, A. Manthiram, *Chem. Mater.* 21 (2009) 1695.
- [25] J. Liu, A. Manthiram, *J. Mater. Chem.* 20 (2010) 3961.
- [26] M.-S. Park, J.-W. Lee, W. Choi, D. Im, S.-G. Doo, K.-S. Park, *J. Mater. Chem.* 20 (2010) 7208.
- [27] F. Izumi, K. Momma, *Solid State Phenom.* 130 (2007) 15.
- [28] Y.-T. Cui, G.-L. Li, H. Oji, J.-Y. Son, *J. Phys. Conf. Ser.* 502 (2014) 012007.
- [29] H. Oji, T. Matsumoto, Y.-T. Cui, J.-Y. Son, *J. Phys. Conf. Ser.* 502 (2014) 012005.
- [30] M.M. Thackeray, S.-H. Kang, C.S. Johnson, J.T. Vaughey, R. Benedek, S.A. Hackney, *J. Mater. Chem.* 17 (2007) 3112.
- [31] J. Bréger, M. Jiang, N. Dupré, Y.S. Meng, Y. Shao-Horn, G. Ceder, C.P. Grey, *J. Solid State Chem.* 178 (2005) 2575.
- [32] K. Kobayashi, *Nucl. Instr. Meth. Phys. Res.* 601 (2009) 32.
- [33] Y.-S. Lee, M. Yoshio, *Electrochem. Solid-State Lett.* 4 (2001) A85.

The application of a water-based hybrid polymer binder to a high-voltage and high-capacity Li-rich solid-solution cathode and its performance in Li-ion batteries

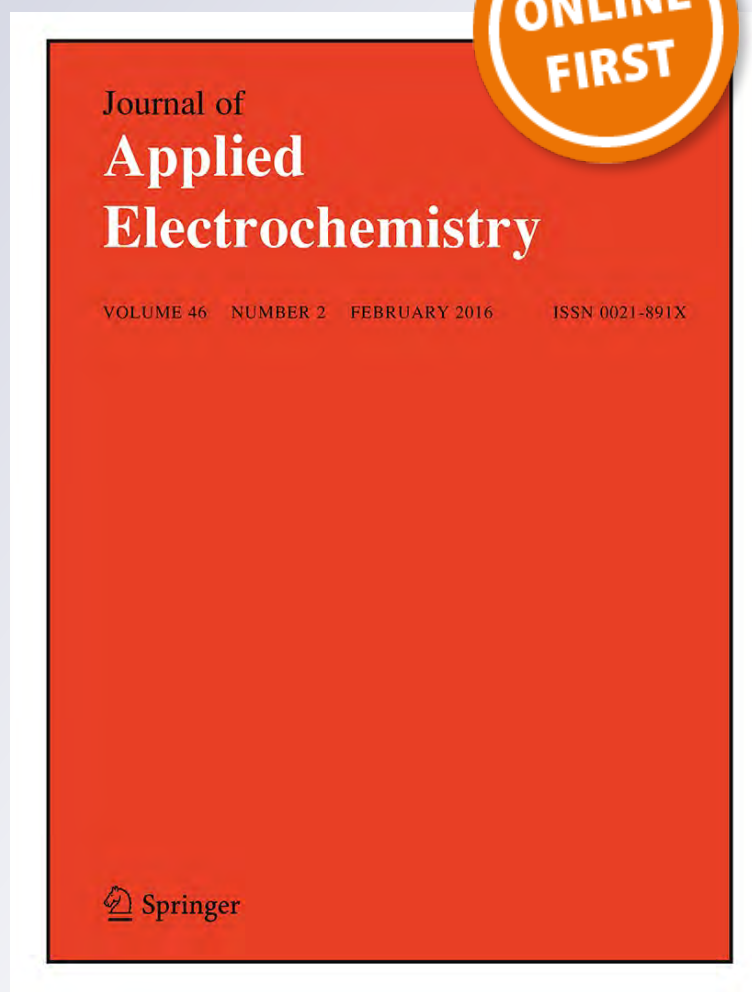
Kouhei Notake, Takao Gunji, Hayato Kokubun, Shinya Kosemura, Yasumasa Mochizuki, Toyokazu Tanabe, Shingo Kaneko, Shinsaku Ugawa, et al.

Journal of Applied Electrochemistry

ISSN 0021-891X

J Appl Electrochem

DOI 10.1007/s10800-016-0930-8



Your article is protected by copyright and all rights are held exclusively by Springer Science +Business Media Dordrecht. This e-offprint is for personal use only and shall not be self-archived in electronic repositories. If you wish to self-archive your article, please use the accepted manuscript version for posting on your own website. You may further deposit the accepted manuscript version in any repository, provided it is only made publicly available 12 months after official publication or later and provided acknowledgement is given to the original source of publication and a link is inserted to the published article on Springer's website. The link must be accompanied by the following text: "The final publication is available at link.springer.com".

The application of a water-based hybrid polymer binder to a high-voltage and high-capacity Li-rich solid-solution cathode and its performance in Li-ion batteries

Kouhei Notake¹ · Takao Gunji¹ · Hayato Kokubun¹ · Shinya Kosemura¹ · Yasumasa Mochizuki² · Toyokazu Tanabe^{1,2} · Shingo Kaneko³ · Shinsaku Ugawa⁴ · Hojin Lee⁴ · Futoshi Matsumoto^{1,2}

Received: 22 September 2015 / Accepted: 16 January 2016
© Springer Science+Business Media Dordrecht 2016

Abstract Uniform cathode films were prepared with a Li-rich solid-solution ($\text{Li}[\text{Li}_{0.2}\text{Ni}_{0.18}\text{Co}_{0.03}\text{Mn}_{0.58}]\text{O}_2$) cathode material and a water-based hybrid polymer binder (TRD202A, JSR, Japan) composed of acrylic polymer and fluoropolymer, carboxymethyl cellulose, and conducting carbon additive. The films exhibited stable charge/discharge cycling performances (average discharge capacity: 260 mAh g^{-1}) when cycled between 4.8 and 2.0 V for 80 cycles. After 80 cycles in the

chemical environment of Li-ion cells, a cathode film prepared with the water-based hybrid polymer binder showed longer-term reliability as well as higher electrochemical resistance when compared with a cathode film using the conventional polyvinylidene difluoride binder. Additionally, even without electrochemical pretreatment, the Al_2O_3 coating on the cathode surfaces improved the cycling stability by preventing the cathode surface from making direct contact with H_2O .

✉ Futoshi Matsumoto
ft101828zr@kanagawa-u.ac.jp

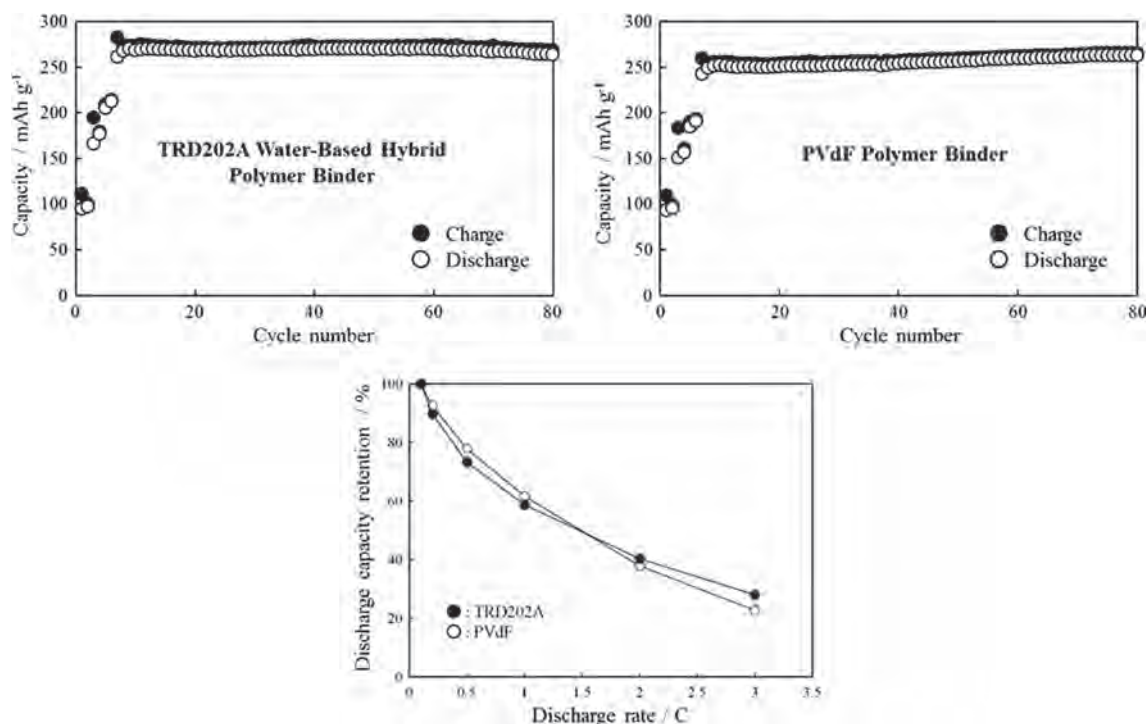
¹ Faculty of Engineering, Kanagawa University, 3-27-1 Rokkakubashi, Kanagawa-ku, Yokohama, Kanagawa 221-8686, Japan

² LIB Open-Library, Kanagawa University, 3-27-1 Rokkakubashi, Kanagawa-ku, Yokohama-shi, Kanagawa 221-8686, Japan

³ Research Institute for Engineering, Kanagawa University, 3-27-1 Rokkakubashi, Kanagawa-ku, Yokohama-shi, Kanagawa 221-8686, Japan

⁴ JSR Corporation, 100 Kawajiri-cho, Yokkaichi, Mie 510-8552, Japan

Graphical Abstract



Keywords Lithium ion battery · Water-based binder · High-capacity cathode material · Li-rich solid-solution

1 Introduction

Recently, water-soluble and aqueous polymers (water-based polymers) have attracted much attention as binders for lithium ion batteries (LIBs) because of the need for low-cost materials and environmentally compatible electrode fabrication processes [1–8]. For example, *N*-methyl-2-pyrrolidone (NMP), which is listed as a carcinogenic chemical with reproductive toxicity [1, 9, 10] is often used as a solvent to prepare a slurry (cathode material particle/conducting carbon additive/conventional polyvinylidene difluoride (PVdF) binder/NMP solvent) employed in the fabrication process of electrode films on current collectors; this slurry should be recycled without releasing it to the atmospheric environment. Therefore, switching from a nonaqueous-based fabrication process to an aqueous-based process has been widely investigated. In graphite anodes, styrene butadiene rubber has already been employed in some commercially available Li-ion batteries [11, 12]. Furthermore, for cathodes, the employment of water-soluble or aqueous binders is under investigation. Some companies have produced prototype models using water-soluble and aqueous binders, and they have reported their battery test results [13, 14]. The hurdles in developing water-soluble and aqueous polymer binders for

use in cathodes in LIBs are still high; improvements are necessary to increase the resistance to electrochemical oxidation and dissolution of metal oxide surfaces in water. In order to overcome these problems, a variety of polymer materials have been applied in the fabrication of cathodes with water-based slurries [3, 7, 15–18]. For example, carboxymethyl cellulose (CMC) is attracting interest as a binder in LIBs, and because the price of CMC is much lower (\$1.1/lb, when compared with one of the prices of PVdF at \$5.5/lb [1, 19]), it is expected to decrease the cost of LIBs by replacing conventional organic solvent-based binders. Several interesting papers have already been published [20–22] demonstrating that CMC binder can be applied as a cathode binder. However, the oxidation of CMC is initiated at voltages over 4.5 V, and it does not exhibit the strong adhesion properties necessary for forming stable cathode films to withstand long-term charge/discharge cycles. New binders exhibiting strong adhesion properties and high resistance to electrochemical oxidation should be developed as quickly as possible to respond to industrial demand.

In recent years, Li-rich solid-solution layered cathode materials comprising layered LiMO₂ (M: transition metals) and Li₂MnO₃ have attracted much interest because some materials exhibit capacities as high as 250 mAh g⁻¹ in the voltage range of 2.0 and 4.8 V [23–28]. These materials are charged to above 4.5 V (vs. Li/Li⁺) to fully activate the Li₂MnO₃ component, and after activation, the cathodes are charged to 4.5 V to reach discharge capacities over 250

mAh g⁻¹ [29–31]. To use these promising high-voltage and high-capacity cathodes in the next-generation Li-ion batteries prepared in environmentally compatible electrode fabrication processes with a water-based binder, water-based binders having high resistances to electrochemical oxidation during charging process should be developed. In this study, an aqueous hybrid polymer (TRD202A, JSR), which was composed of acrylic polymer and fluoropolymer, was selected as a binder for the Li-rich solid-solution layered cathode material Li[Ni_{0.18}Li_{0.20}Co_{0.03}Mn_{0.58}]O₂. A cathode prepared with Li[Ni_{0.18}Li_{0.20}Co_{0.03}Mn_{0.58}]O₂ particles, TRD202A binder, CMC, and conductive carbon additive was tested and analyzed for charge/discharge capacity, cycle stability, rate performance, mechanical resistance, resistance of electrochemical oxidation, and changes of the surface composition and structure after water-treatment used for preparing water-based slurry. The water-based TRD202A cathode binder is a water-based emulsion and is designed with a unique hybrid polymer developed from acrylic polymer and fluoropolymer to satisfy both the requirements of high adhesion and chemical and electrochemical resistances. Wu and co-workers have already reported an application of the TRD202 binder in a Li-rich solid-solution cathode. They mentioned that the TRD202A binder can be used for high-voltage cathodes in the voltage range of 2–4.6 V [13], and its thermal stability is equivalent to that of PVdF. Proisini has also examined polyvinyl acetate as a binder for the high-voltage cathode material LiNi_{0.5}Mn_{1.5}O₄ and reported the results of cycling and rate tests [14].

However, they have not examined the water-based binders for charge/discharge capacities, long cycle stability, rate performance, mechanical resistance, resistance of electrochemical oxidation, or changes of the surface composition and structure after water-treatment used for preparing the water-based slurry. We have examined in depth the above points with the Li-rich solid-solution cathode (3/5)Li₂MnO₃·(1/5)Li[Ni_{0.5}Mn_{0.5}]O₂·(1/5)Li[Ni_{1/3}Co_{1/3}Mn_{1/3}]O₂. The composition studied here can be alternately expressed as Li[Ni_{0.18}Li_{0.20}Co_{0.03}Mn_{0.58}]O₂ in the standard notation for such layered compositions. The notation of Li[Ni_{0.18}Li_{0.20}Co_{0.03}Mn_{0.58}]O₂ will be used for the rest of this paper. We reported that a Li[Ni_{0.18}Li_{0.20}Co_{0.03}Mn_{0.58}]O₂ cathode exhibited stable charge/discharge capacities following an electrochemical pretreatment used to stabilize the charge/discharge capacities [32]. The electrochemical pretreatment applied to stabilize the charge/discharge capacity of the Li-rich solid-solution cathode materials was developed by Ito and Sato [33]. As shown in this paper and reported by other groups [31–33], the Li[Ni_{0.18}Li_{0.20}Co_{0.03}Mn_{0.58}]O₂ cathodes require a high voltage of 4.8 V in the charging process, and its charge/discharge performances are stable for long cycles. Its stable charge/discharge

performances are reliable for the performance tests of the water-based TRD202A binder with a high-voltage Li-rich solid-solution layered cathode material; namely, the TRD202A binder was blamed for the performance degradation of the cathode prepared with that binder. The results of the cathode performance tests with TRD202A-based cathodes are compared with those obtained with conventional PVdF-based cathodes in this paper. The relative merits of the TRD202A and PVdF binders are discussed with respect to the charge/discharge capacities, long cycling stability, rate performance, mechanical resistance, resistance of electrochemical oxidation, and changes of the surface composition and structure after water-treatment for the preparation of a water-based slurry.

2 Experimental

2.1 Preparation of the cathode material and Al₂O₃-coated cathode material

The Li[Ni_{0.18}Li_{0.20}Co_{0.03}Mn_{0.58}]O₂ cathode material examined in this study was synthesized using a co-precipitation procedure using the following commercial reactants: nickel sulfate hexahydrate (NiSO₄·6H₂O, 99 %, Kano Chemical Co., Inc., Japan), manganese sulfate monohydrate (MnSO₄·H₂O, 99 %, Kano Chemical Co., Inc., Japan), cobalt sulfate heptahydrate (CoSO₄·7H₂O, 99 %, Wako Pure Chemical Industries, Ltd, Japan), and sodium carbonate (Na₂CO₃, 99.8 %, Wako Pure Chemical Industries, Ltd, Japan). All of the reactants were used without further purification. In order to obtain a target composition of the synthesized cathode of Ni:Co:Mn = 0.18:0.03:0.58 (atomic ratio), 46 mmol NiSO₄·6H₂O, 147 mmol MnSO₄·H₂O, and 7.0 mmol CoSO₄·7H₂O were dissolved in 100 mL H₂O. The total concentration of the transition metal ions in the solution was adjusted to 2 M. Further, 2 M Na₂CO₃ and 1.4 wt% NH₄OH aqueous solutions were prepared. Next, 80 mL of the 2 M Na₂CO₃ solution was injected at a speed of 0.5 cm³ s⁻¹ into the transition metal ion solution at 60 °C. During the whole synthesis, the pH was kept at 7.5 with pH meter by injecting the NH₄OH solution. The carbonates of Ni, Mn, and Co precipitated out of the transition metal ions and sodium carbonate mixture solution. The precipitates of the transition metal carbonate were recovered by filtration. They were dried under vacuum at 100 °C for 5 h after they were washed several times with hot water until the filtrate exhibited neutral pH during the washing process. Afterward, to compensate for any possible losses, the transition metal carbonate was mixed with an excess (7.0 %) of lithium carbonate (Li₂CO₃, 98 %, Kano Chemical Co., Inc., Japan) using a wet planetary ball-milling machine with a Teflon jar (672 mL) containing Teflon balls (diameter 1.5 cm, 88 balls) and acetone (80 mL)

under ambient conditions at a speed of 300 rpm for 3 h. After ball milling, the mixture was dried at 120 °C for 5 h. A pellet (diameter: 2 mm) of the dried mixture was formed using 30 kN of pressure. The pellet was then sintered at 900 °C for 12 h in air, quenched with liquid N₂, and ground with a mortar to obtain the particles used to prepare the cathode films on an Al current collector.

A 45-mm aluminum nitrate aqueous solution was prepared with aluminum nitrate nonahydrate (Al(NO₃)₃·9H₂O, 98 %, Kano Chemical. Co., Inc., Japan) to prepare the Al₂O₃-cated Li[Ni_{0.18}Li_{0.20}Co_{0.03}Mn_{0.58}]O₂ sample. The solution was adjusted to a neutral pH with an NH₃ aqueous solution. Then, 2.5 g Li[Ni_{0.18}Li_{0.20}Co_{0.03}Mn_{0.58}]O₂ was added to 20 mL of the Al(NO₃)₃ solution and mixed with a stirrer for 3 h. After filtering and drying the Li[Ni_{0.18}Li_{0.20}Co_{0.03}Mn_{0.58}]O₂ dispersion, the Li[Ni_{0.18}Li_{0.20}Co_{0.03}Mn_{0.58}]O₂ sample was annealed in air at 900 °C for 3 h.

2.2 Characterization of synthesized cathode materials

Powder X-ray diffractometry (*p*XRD) was performed using CuK_α radiation (Rigaku RINT-UltimaIII; $\lambda = 0.1548$ nm) at an increment of 0.02° at diffraction angles ranging from 20° to 80°. An obliquely finished Si crystal (nonreflective Si plate) was used as the sample holder to minimize the background noise. The average sizes and shapes of the cathode particles were evaluated with a field-emission scanning electron microscope (FE-SEM, S-4000, Hitachi). For the cross-sectional images of the cathode layer on the Cu current collector with the FE-SEM, a cross-section polisher (JEOL) was used with the following conditions: accelerating voltage, 5 kV; Ar flow rate, 8.5 m³/min. The Li:Ni:Co:Mn elemental ratio for the synthesized cathode materials and the loading of Al₂O₃ on the cathode material were determined by ICP-MS using an Agilent, 7700 × spectrometer. X-ray photoelectron spectroscopy (XPS) measurements (JEOL, JP-9010 MC) were performed to examine the chemical states (Al 2*p*) of the cathode material. A MgK α X-ray source with an anodic voltage (10 kV) at a current of (10 mA) was used for XPS measurements. All XPS spectra of the samples were obtained with a take-off angle of 45° with respect to the specimens by using the pass energies of 100 and 200 eV for narrow and survey scans, respectively. A 200 kV transmission electron microscope (TEM and/or STEM, JEM-2100F, JEOL) equipped with two aberration correctors (CEOS GmbH) for the image- and probe-forming lens systems and an X-ray energy-dispersive spectrometer (JED-2300T, JEOL) were used for compositional analysis. Both aberration correctors were optimized to realize the point-to-point resolutions of TEM and scanning transmission electron microscopy (STEM) as 1.3 and 1.1 Å, respectively. A probe convergence angle of 29 mrad and a

high-angle annular-dark-field (HAADF) detector with an inner angle greater than 100 mrad were used for HAADF-STEM observation. HAADF-STEM was used to perform microscopic observation of the morphologies and particle sizes of the materials. The samples for the HAADF-STEM analysis were prepared by dropping a methanol suspension of the sample powder onto a commercial TEM grid coated with a polymer film. The sample was thoroughly dried in a vacuum prior to observation. The adhesion of the cathode films to the Al current collector was investigated using tack testing with a Tackiness tester (TAC1000) from Rhesca Corporation with the following conditions: approaching speed (30 mm/min), pressurization (100 gf), duration (10 s), and speed of pulling (600 mm/min). The cathode samples (2 cm²) were adhered to glass slides with double-coated adhesive tape (Nitto Denko, No. 515, Japan). The adhesive tape was attached to the tip of a metal probe (diameter: 2 mm). The tip of the probe faced the surface of the cathode samples and the adhesive tip of the probe made contact with the cathode surface. The probe was separated from the sample at the specified speed. The adhesive force of the cathode films on the Al current collector was evaluated by measuring the pulling force at the time when the cathode films separated from the Al current collector. The samples after charge/discharge cycles were rinsed with dimethyl carbonate (DMC) and then dried under vacuum before performing the tackiness test.

2.3 Cell preparation and electrochemical tests

A total of 910 mg of accurately weighed Li[Ni_{0.18}Li_{0.20}Co_{0.03}Mn_{0.58}]O₂ active material, 50 mg of acetylene black (AB, DENKA BLACK, DENKI KAGAKU GOGYO, Japan), 10 mg of CMC (CMC, Polyscience Inc, cat.#6139), and 30 mg of water-soluble binder (TRD202A, JRS) were mixed in Milli-Pore water (>18 M Ω) with planetary mixing equipment (Mazerustar, KK-250S, KURABO, Japan) until they formed a homogenous mixture; the mixture had a suitable viscosity for coating the cathode films to preserve the wt% of the cathode material:TRD202A:AB:CMC = 91:3:5:1 in the prepared cathode films. The mixture was coated using a doctor-blade (100 μ m gap) coater on Al current collector. The mixture thin film/Al was dried at 130 °C for 5 h in a vacuum drying oven. The loading of the cathode materials on the Al current collector was 2.0–3.0 mg cm⁻². The resulting cathode/Al contained a 200 mm² stainless steel mesh as the current collector under 300 kg cm⁻² pressure. For comparison, polyvinylidene difluoride (PVdF, KF9130, Kureha, Japan) was used as a binder as received without any further treatment. The wt% of the cathode films was cathode material:PVDF:AB = 91:4:5:1. Electrochemical tests were performed using a CR2032 coin-type cell. The test cell was composed of a

cathode and a lithium metal anode separated by a porous polypropylene film (Celgard 3401). The electrolyte used in the tests was a 1 M LiPF_6 -ethylene carbonate (EC)/DMC mixture (1:2 by vol., Ube Chemicals, Japan). The charge/discharge cycling was performed using a multichannel battery tester (model BTS2004, Nagano Corp., Japan). All the tests were performed at room temperature. A constant-current/constant-voltage (CC-CV) mode was used for the cycling tests. The charge/discharge cycling tests that followed the pretreatment process were performed at a charge/discharge current density of $0.07\text{--}0.09\text{ mA cm}^{-2}$ with a cutoff voltage of $2.0\text{--}4.8\text{ V}$ (vs. Li/Li^+). In CV mode in the charging process, a voltage of 4.8 V was held constant for 5 h. In the pretreatment, the discharge voltage limit was fixed at 2.0 V , and the charge voltage limit was increased 0.1 V stepwise from 4.5 to 4.8 V every two cycles to stabilize the charge/discharge capacities in the following charge/discharge tests. The charge/discharge capacities observed during the pre-cycling process are hereafter included with the results of the charge/discharge cycle tests in all of the figures and in the discussion section. In the voltammetric experiments used to estimate the oxidation potential of the TRD202A and PVdF binders, binder-coated glassy carbon disk (GC, diameter: 0.3 cm) electrodes were used with a Li metal counter/reference electrode (electrode area: 0.1 cm^2) and a 1 M LiPF_6 -EC/DMC mixture at 1 mV s^{-1} . The electrochemical measurements were carried out using a Bio-Logic SAS workstation (Model, VMP3). The binder-coated GC electrodes were prepared by pasting a slurry of the binder/AB/NMP (1:1:7 wt ratio) on the GC electrode surfaces and drying the electrodes under vacuum at $90\text{ }^\circ\text{C}$.

3 Results and discussion

3.1 Characterization of as-prepared and water-treated $\text{Li}[\text{Ni}_{0.18}\text{Li}_{0.2}\text{Co}_{0.03}\text{Mn}_{0.58}]\text{O}_2$ cathode materials

Figure 1 shows an SEM image of the as-prepared $\text{Li}[\text{Ni}_{0.18}\text{Li}_{0.2}\text{Co}_{0.03}\text{Mn}_{0.58}]\text{O}_2$ cathode material particles. The cathode particles appear as agglomerates of particles with $30\text{--}200\text{ nm}$ diameters. The distribution of size of the cathode particles was evaluated on the basis of approximately 100 particles in the SEM images. The average diameter of the as-prepared cathode particles was calculated as 100 nm . They exhibited a narrow particle size distribution (inset of Fig. 1). A cross-sectional SEM image of the cathode film prepared with a water-based slurry of $\text{Li}[\text{Ni}_{0.18}\text{Li}_{0.2}\text{Co}_{0.03}\text{Mn}_{0.58}]\text{O}_2$ particle/AB/CMC/TRD202A is shown in Fig. 2. From the cross-sectional image, the cathode particles are illustrated as having several micron diameters, even though the as-prepared

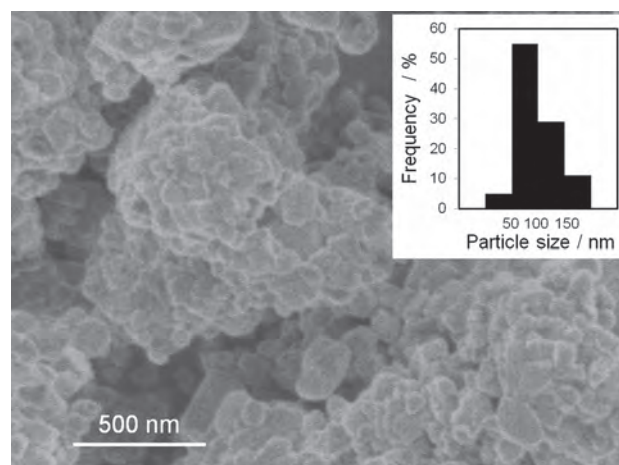


Fig. 1 An SEM image of the as-prepared $\text{Li}[\text{Ni}_{0.18}\text{Li}_{0.2}\text{Co}_{0.03}\text{Mn}_{0.58}]\text{O}_2$ particles and their particle size distribution histograms

cathode particles have $30\text{--}200\text{ nm}$ diameters. It can be considered that the as-prepared cathode particles agglutinate strongly to form the agglomerations having several micron diameters. The SEM-EDS mapping profile of the C, Mn, Ni, and Co elements exhibits uniform dispersion of the elements in the prepared cathode films with the TRD202A binder and does not exhibit segregation of the binder or the cathode particles in the cathode films. Secondary particles of the cathode materials are efficiently bounded by a small amount of TRD202A binder in the prepared cathode films.

Figure 3 shows the XRD patterns (A) observed with the as-prepared $\text{Li}[\text{Ni}_{0.18}\text{Li}_{0.2}\text{Co}_{0.03}\text{Mn}_{0.58}]\text{O}_2$ cathode material powder (a) and with the cathode films prepared with the TRD202A (b) and PVdF (c) binders. The three results shown in Fig. 3 have similar peak patterns, which can be indexed as the layered rock salt-type symmetry (R3-m). No impurity phase was found, and a peak shift due to the difference in the preparation processes between the two binders was not observed. Broad peaks detected in the range of $22\text{--}25^\circ$ show that these materials have a super lattice structure, in which Li^+ ions order themselves in the transition metal layer. A difference in the observed peak patterns between the as-prepared (a) and filmed $\text{Li}[\text{Ni}_{0.18}\text{Li}_{0.2}\text{Co}_{0.03}\text{Mn}_{0.58}]\text{O}_2$ (b, c) is noted from the peak intensity; for example, in the as-prepared particle sample, the [003] peak is the highest and the [104] peak is the next highest; conversely, in the TRD202A- and PVdF-based cathode films, the highest peak is the [104] peak. Apart from that, there is also a difference in the peak intensity at approximately $64^\circ\text{--}66^\circ$. The reason for the difference in the peak intensity may be because of the prominent orientation of the cathode particles on the Al current collector. The peak shift was compared for the three peak patterns (a–c) with the magnified [104] peak as the typical peak (Fig. 3b). The filmed cathode particles used with the

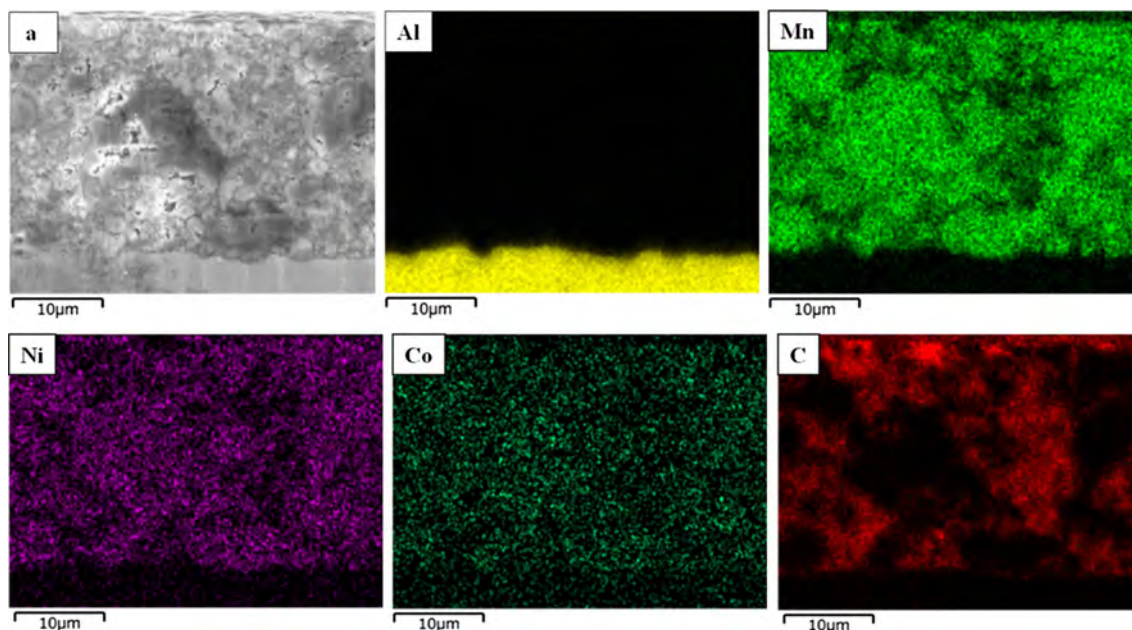


Fig. 2 a A cross-sectional SEM image and element (Mn, Ni, Co, Al, C) mapping of a $\text{Li}[\text{Li}_{0.2}\text{Ni}_{0.18}\text{Co}_{0.03}\text{Mn}_{0.58}]\text{O}_2$ cathode film prepared with TRD202A binder on an Al current collector

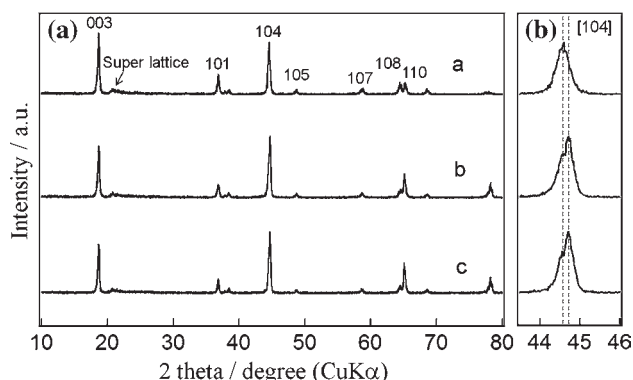


Fig. 3 a XRD diffractograms of (a) as-prepared $\text{Li}[\text{Li}_{0.2}\text{Ni}_{0.18}\text{Co}_{0.03}\text{Mn}_{0.58}]\text{O}_2$ and $\text{Li}[\text{Li}_{0.2}\text{Ni}_{0.18}\text{Co}_{0.03}\text{Mn}_{0.58}]\text{O}_2$ films prepared with (b) TRD202A and (c) PVdF binders, and b a comparison of the XRD diffractograms with a magnified (104) peak as a typical peak

TRD202A and PVdF binders exhibited new peaks at approximately $44^\circ\text{--}45^\circ$ when compared with the as-prepared cathode particles. The new peaks could not be assigned to any peak patterns typically seen for transition metal oxides and lithium oxides. However, aside from the difference in the peak sizes at approximately $44^\circ\text{--}45^\circ$, it is noted that cathode particles that were treated with both water and organic solvent also exhibited the peaks that were located at the same degree. Therefore, the large change in the crystal structure of the cathode particles does not occur as a result of their exposure to water during the water-based slurry preparation process. The Li:Ni:Mn:Co elemental ratio of the synthesized cathode particles was

Table 1 The surface compositions of the as-prepared and water-treated cathode particles with ICP-MS and STEM-EDX

| | | Atomic % | | | |
|----------------------------------|---------|----------|------|-----|-----|
| | | O | Mn | Ni | Co |
| ICP-MS data | | 71.7 | 20.8 | 6.4 | 1.1 |
| As-prepared sample | Bulk | 75.9 | 18.0 | 5.0 | 1.1 |
| | Surface | 75.8 | 17.9 | 5.3 | 1.0 |
| Sample dispersed in water slurry | Bulk | 75.3 | 18.4 | 5.2 | 1.1 |
| | Surface | 77.4 | 17.0 | 3.7 | 1.9 |

determined to be 1.2: 0.18: 0.03: 0.58 using an ICP spectrometer, and the values are listed for comparison with the STEM-EDS data in Table 1. The mol% of oxygen atoms in the as-prepared sample corresponds to the resulting surplus when subtracting the total of mol% among metals such as Li, Mn, Ni, and Co from 100 %.

Figure 4 shows low-resolution (right side) and high-resolution (left side) TEM images of the as-prepared $\text{Li}[\text{Ni}_{0.18}\text{Li}_{0.2}\text{Co}_{0.03}\text{Mn}_{0.58}]\text{O}_2$ particles (a) and $\text{Li}[\text{Ni}_{0.18}\text{Li}_{0.2}\text{Co}_{0.03}\text{Mn}_{0.58}]\text{O}_2$ particles (b) recovered from the cathode film that was prepared with the TRD202A binder and was exposed to water. The as-prepared $\text{Li}[\text{Ni}_{0.18}\text{Li}_{0.2}\text{Co}_{0.03}\text{Mn}_{0.58}]\text{O}_2$ particles (a) exhibit a single-crystal composition. The d lattice spacing of the particles presented in the HR-TEM image is 0.475 nm, which closely matches those of the [003] plane, for $\text{Li}[\text{Ni}_{0.18}\text{Li}_{0.2}\text{Co}_{0.03}\text{Mn}_{0.58}]\text{O}_2$ particle (0.475 nm for the [003] plane [34]). The lattice fringe observed on the as-prepared $\text{Li}[\text{Ni}_{0.18}\text{Li}_{0.2}\text{Co}_{0.03}\text{Mn}_{0.58}]\text{O}_2$

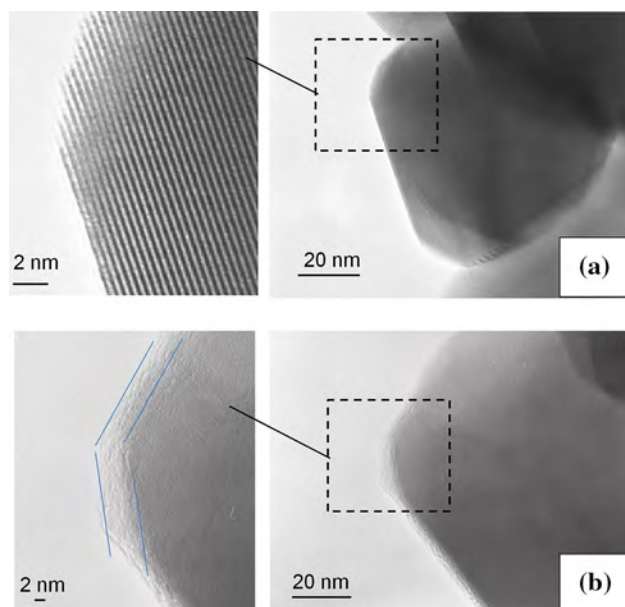


Fig. 4 Surface TEM images of as-prepared $\text{Li}[\text{Ni}_{0.18}\text{Li}_{0.2}\text{Co}_{0.03}\text{Mn}_{0.58}]\text{O}_2$ particles (a) and $\text{Li}[\text{Ni}_{0.18}\text{Li}_{0.2}\text{Co}_{0.03}\text{Mn}_{0.58}]\text{O}_2$ particles (b) treated with TRD202A/CMC/AB/ H_2O slurries

particles can be seen even at the surface of the particles. Furthermore, in the TEM images observed for the water-treated $\text{Li}[\text{Ni}_{0.18}\text{Li}_{0.2}\text{Co}_{0.03}\text{Mn}_{0.58}]\text{O}_2$ particles (b), the lattice fringe, which was observed in the as-prepared $\text{Li}[\text{Ni}_{0.18}\text{Li}_{0.2}\text{Co}_{0.03}\text{Mn}_{0.58}]\text{O}_2$ particles, has the same d spacings as the inner part of the water-treated cathode particles. Fragmented clear lattice fringes could be observed near the surface of the cathode particles, and disordered layers were clearly observed on the water-treated particle surfaces. The average thickness of the surface layer was 3.4 nm. The surface and bulk compositions of the as-prepared and water-treated $\text{Li}[\text{Ni}_{0.18}\text{Li}_{0.2}\text{Co}_{0.03}\text{Mn}_{0.58}]\text{O}_2$ particles that were analyzed with STEM-EDX are summarized in Table 1. The surface composition of the water-treated sample differs from the inner compositions and the surface composition of the as-prepared sample even when the as-prepared sample exhibits the same values both on the surface and in the inner part of the particle, and the compositions of the as-prepared sample nearly coincided with the inner part of the water-treated sample. The results indicate that the surface of the $\text{Li}[\text{Ni}_{0.18}\text{Li}_{0.2}\text{Co}_{0.03}\text{Mn}_{0.58}]\text{O}_2$ particles dissolved during water-treatment used to prepare the water-based slurry with $\text{Li}[\text{Ni}_{0.18}\text{Li}_{0.2}\text{Co}_{0.03}\text{Mn}_{0.58}]\text{O}_2/\text{AB}/\text{binder}/\text{H}_2\text{O}$, and the dissolved metals were deposited on the surface of the $\text{Li}[\text{Ni}_{0.18}\text{Li}_{0.2}\text{Co}_{0.03}\text{Mn}_{0.58}]\text{O}_2$ particles. To date, it has been reported that the change of the surface structure and composition of the cathode particles affect the value of the charge/discharge capacities and the cathode stability [31, 32, 35, 36]. It is uncertain whether the formation of the surface layer during the water-treatment used for the incorporation of

a water-soluble binder influences the performance of the cathodes; this is discussed in the next section. The differences in the composition of the cathode samples resulting from the ICP-MS and STEM-EDX analyses are clearly shown in Table 1. This difference may come from the nonuniformity of the composition in the sample particles or from uncertainties inherent in the STEM-EDX and ICP-MS procedures. Re-examination of the compositional analysis of the cathode samples is under investigation.

3.2 Cycle and rate performance of the $\text{Li}[\text{Ni}_{0.18}\text{Li}_{0.2}\text{Co}_{0.03}\text{Mn}_{0.58}]\text{O}_2$ cathode prepared with TRD202A and PVdF binders

Figure 5 shows the results of charge/discharge cycle tests obtained from the TRD202A- and PVdF-based $\text{Li}[\text{Ni}_{0.18}\text{Li}_{0.2}\text{Co}_{0.03}\text{Mn}_{0.58}]\text{O}_2$ cathode films at room temperature and at a 0.1 C charge/discharge rate. The charge/discharge capacities observed during the pre-cycling process are hereafter included with the results of charge/discharge cycling tests in these figures. For both the TRD202A- and the PVdF-based cathodes, stable average discharge capacities of approximately 275 mAh g^{-1} were observed after pretreatment until the 80th cycle. Figure 6 shows every tenth charge/discharge cycle curve of the TRD202A (a)- and PVdF (b)-based $\text{Li}[\text{Ni}_{0.18}\text{Li}_{0.2}\text{Co}_{0.03}\text{Mn}_{0.58}]\text{O}_2$ cathodes using a 0.1 C rate between 2.0 and 4.8 V. The two cathodes exhibit similar voltage fade behaviors observed from the charge/discharge cycles, which is a negative characteristic of Li-rich solid-solution cathode materials and should be improved to develop high energy-density Li-ion batteries for everyday use [37, 38]. The degree of voltage fade during the charge/discharge cycles is similar for the TRD202A- and PVdF-based $\text{Li}[\text{Ni}_{0.18}\text{Li}_{0.2}\text{Co}_{0.03}\text{Mn}_{0.58}]\text{O}_2$ cathodes. The use of the TRD202A binder in the preparation of the cathode does not enhance the voltage fade and does not change the charge and discharge curves for any of the cycles. The rate performance is a very important aspect for the application of $\text{Li}[\text{Ni}_{0.18}\text{Li}_{0.2}\text{Co}_{0.03}\text{Mn}_{0.58}]\text{O}_2$ cathodes [39, 40]. Figure 7 shows the rate capabilities of TRD202A- and PVdF-based $\text{Li}[\text{Ni}_{0.18}\text{Li}_{0.2}\text{Co}_{0.03}\text{Mn}_{0.58}]\text{O}_2$ cathodes at room temperature. All cells were charged at the same current with a 0.1 C rate to ensure identical initial conditions for each discharge. The discharge current is at 0.1, 0.2, 0.5, 1, 2, and 3 C. This figure shows that the $\text{Li}[\text{Ni}_{0.18}\text{Li}_{0.2}\text{Co}_{0.03}\text{Mn}_{0.58}]\text{O}_2$ cathodes prepared with TRD202A and PVdF binders exhibit comparable discharge capacities even at high rate currents. It is clear from this result that the TRD202A binder also does not negatively influence the rate performance.

In Fig. 8, the stability of the TRD202A- and PVdF-based $\text{Li}[\text{Ni}_{0.18}\text{Li}_{0.2}\text{Co}_{0.03}\text{Mn}_{0.58}]\text{O}_2$ cathodes under a fully charged condition to 4.8 V was examined. After

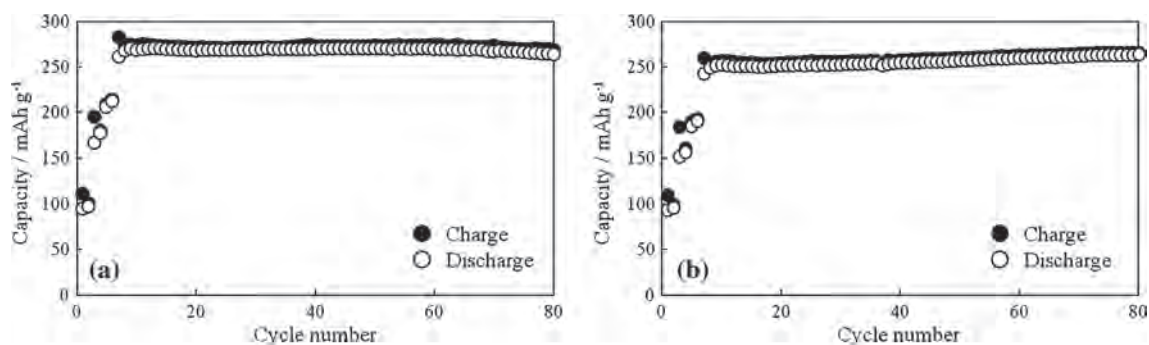


Fig. 5 Cycling performance obtained for the $\text{Li}[\text{Ni}_{0.18}\text{Li}_{0.20}\text{Co}_{0.03}\text{Mn}_{0.58}]\text{O}_2$ electrodes prepared with **a** TRD202A and **b** PVdF binders on an Al current collector

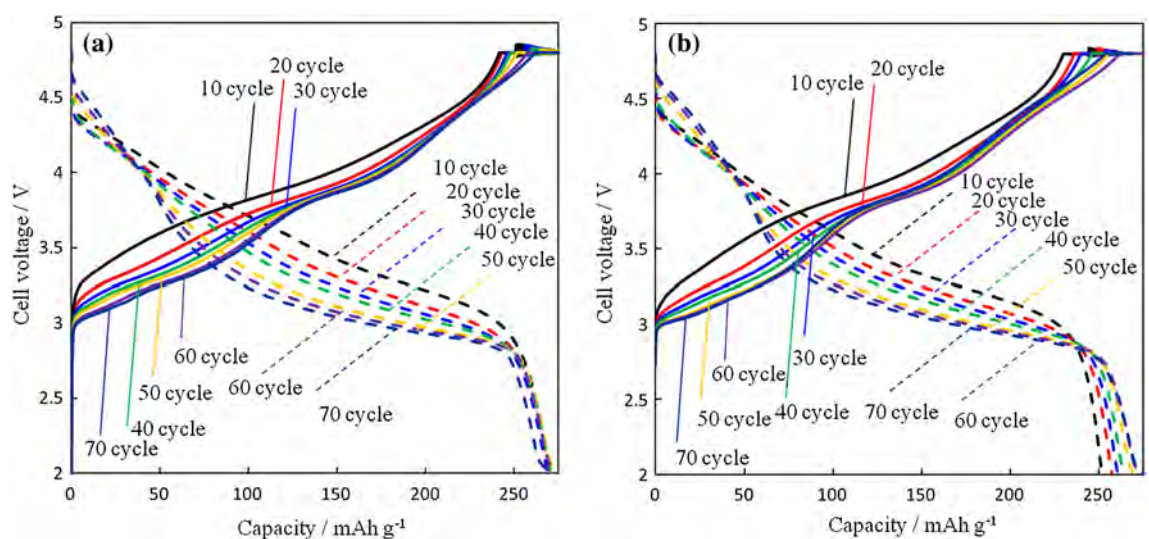


Fig. 6 Charge and discharge curves measured for the $\text{Li}[\text{Ni}_{0.18}\text{Li}_{0.20}\text{Co}_{0.03}\text{Mn}_{0.58}]\text{O}_2$ cathodes prepared with the **a** TRD202A and **b** PVdF binders on Al current collectors

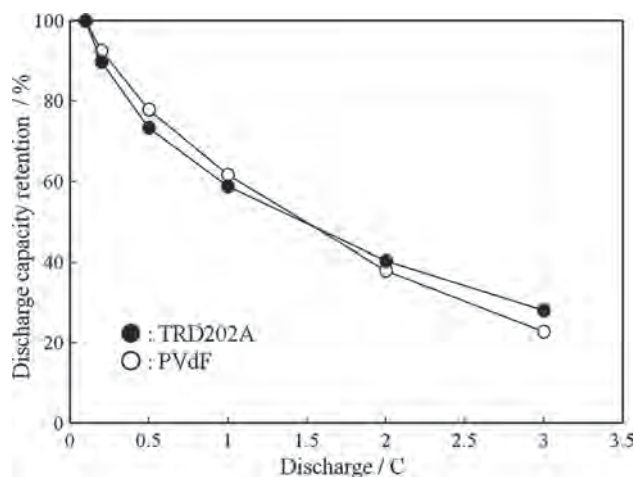


Fig. 7 The rate performances of $\text{Li}[\text{Ni}_{0.18}\text{Li}_{0.20}\text{Co}_{0.03}\text{Mn}_{0.58}]\text{O}_2$ cathodes prepared with the TRD202A and PVdF binders

pretreatment was performed for new coin cells prepared with TRD202A- and PVdF-based $\text{Li}[\text{Ni}_{0.18}\text{Li}_{0.20}\text{Co}_{0.03}\text{Mn}_{0.58}]\text{O}_2$ cathodes, the cells were charged to 4.8 V and left in open-circuit conditions at room temperature (25 °C) for 28 days. After 28 days, the cells were discharged to estimate the discharge capacities. The result are shown for the discharge curves obtained before and after 28 days with TRD202A- and PVdF-based $\text{Li}[\text{Ni}_{0.18}\text{Li}_{0.20}\text{Co}_{0.03}\text{Mn}_{0.58}]\text{O}_2$ cathodes. The resistances of the binders to electrochemical oxidation under the full-charge conditions were compared for the TRD202A and PVdF binders. The capacity of the cell prepared with a PVdF-based $\text{Li}[\text{Ni}_{0.18}\text{Li}_{0.20}\text{Co}_{0.03}\text{Mn}_{0.58}]\text{O}_2$ cathode faded to 12.7 % over 28 days in open-circuit conditions. The capacity faded 10.0 % in the TRD202A-based $\text{Li}[\text{Ni}_{0.18}\text{Li}_{0.20}\text{Co}_{0.03}\text{Mn}_{0.58}]\text{O}_2$ cathode, which is smaller than that of the cathode made with the PVdF binder. In the subsequent charge/discharge cycles at 0.1 C, both the

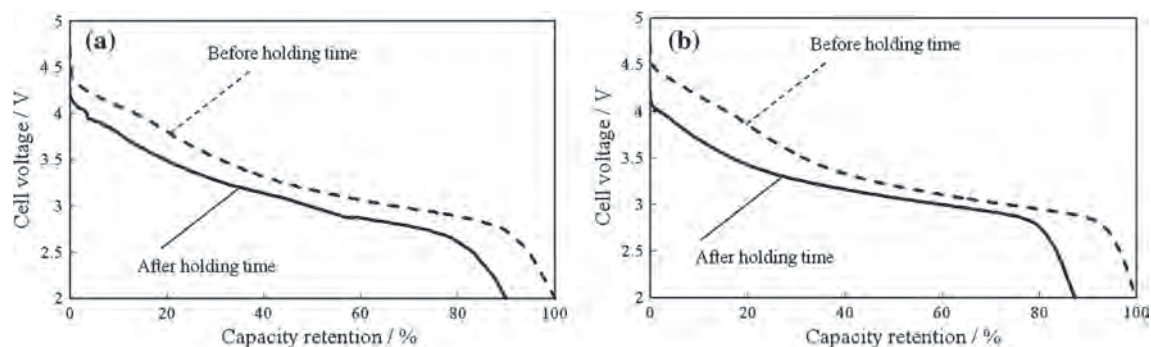


Fig. 8 The discharge curves measured from $\text{Li}[\text{Ni}_{0.18}\text{Li}_{0.20}\text{Co}_{0.03}\text{Mn}_{0.58}]\text{O}_2$ cathodes prepared with the **a** TRD202A and **b** PVdF binders before and after holding under full-charge condition for 28 days at 25 °C

TRD202A- and the PVdF-based $\text{Li}[\text{Ni}_{0.18}\text{Li}_{0.20}\text{Co}_{0.03}\text{Mn}_{0.58}]\text{O}_2$ cathodes exhibited a recovery of the charge/discharge capacities to the values observed before the 28-day open-circuit test. The TRD202A-based $\text{Li}[\text{Ni}_{0.18}\text{Li}_{0.20}\text{Co}_{0.03}\text{Mn}_{0.58}]\text{O}_2$ cathodes had lower self-discharge rates than those of PVdF-based $\text{Li}[\text{Ni}_{0.18}\text{Li}_{0.20}\text{Co}_{0.03}\text{Mn}_{0.58}]\text{O}_2$ cathodes. In addition, TRD202A and PVdF binders had comparable resistances to electrochemical oxidation when a potential difference of 4.8 V (vs. Li/Li^+) was applied to the cathodes. It is assumed that TRD202 and PVdF cannot be oxidized at an electrode potential less than 4.8 V and do not suffer serious damage from the electrochemical oxidation at this potential. To get more information on the oxidation potential of the TRD202A and PVdF binders, linear-potential sweep voltammetry was applied to the TRD202A- and PVdF-coated GC electrodes in a 1 M $\text{LiPF}_6\text{-EC}/\text{DMC}$ mixture under a dry Ar atmosphere. As a reference, the oxidation potential of CMC was also measured with the CMC/AB-coated electrode. As seen from Fig. 9, the TRD202A (a) and PVdF (b) binders start to oxidize at approximately 5.5 V. Also from these voltammograms, the electrochemical resistivity of the TRD202A binder to oxidation can be confirmed. CMC (c) is oxidized at approximately 4.8 V, which corresponds to the cutoff potential in the charge process. The CMC, which is one of the components in the cathode films, may be oxidized when the high voltage of approximately 4.8 V is applied. CMC was added to the cathode slurry to improve the viscosity of the slurry and does not act as a binder between the cathode active material and conductive additive. If the CMC molecules are oxidized in the cathode film at approximately 4.8 V, the oxidation reaction would not cause serious damage such as the decomposition of the electron pathway or the detachment of the cathode material particles from the cathode films. Adhesion of the cathode films before and after charge/discharge cycles with TRD202A and PVdF was also compared with a tackiness tester. The tackiness strengths of the cathode films before and after 70 charge/discharge cycles are

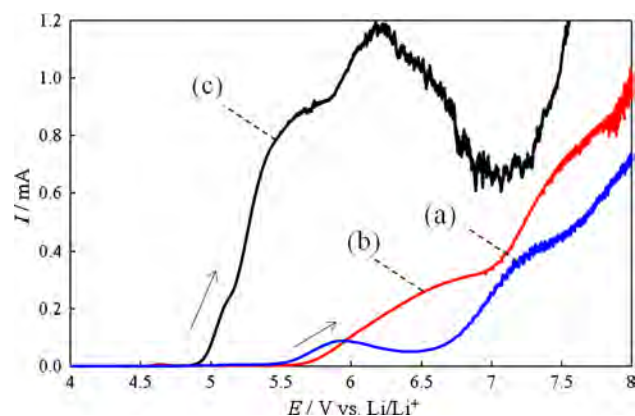


Fig. 9 Linear sweep voltammograms of **a** TRD202A/AB-, **b** PVdF/AB-, and **c** CMC/AB-coated GC electrodes in a 1 M $\text{LiPF}_6\text{-EC}/\text{DMC}$ solution in an Ar-saturated atmosphere for the evaluation of the oxidation potential of the binders. The potential sweep rate: 1 mV s^{-1}

examined. Although the tackiness strengths obtained for the TRD202A- and PVdF-based cathode films were nearly similar before charge/discharge cycles, after 70 cycles, the TRD202A-based cathode film exhibited a fluctuation in a narrow range, while the strength of the PVdF-based cathode decreased to less than half. The tests of the tackiness strength before and after multiple charge/discharge cycles revealed a clear difference in the TRD202A and PVdF binders. The results clearly demonstrate the distinction characteristics of the TRD202A as a binder for maintaining the electrode structure for the high charge/discharge performance of high-voltage cathodes.

3.3 Characterization and cycle performance of Al_2O_3 -coated $\text{Li}[\text{Ni}_{0.18}\text{Li}_{0.20}\text{Co}_{0.03}\text{Mn}_{0.58}]\text{O}_2$ cathode

Figures 10a, b are TEM images obtained from Al_2O_3 -coated $\text{Li}[\text{Ni}_{0.18}\text{Li}_{0.20}\text{Co}_{0.03}\text{Mn}_{0.58}]\text{O}_2$ cathode materials. The surface layer seen in both figures has a different d lattice spacings compared to the bulk layer. The average

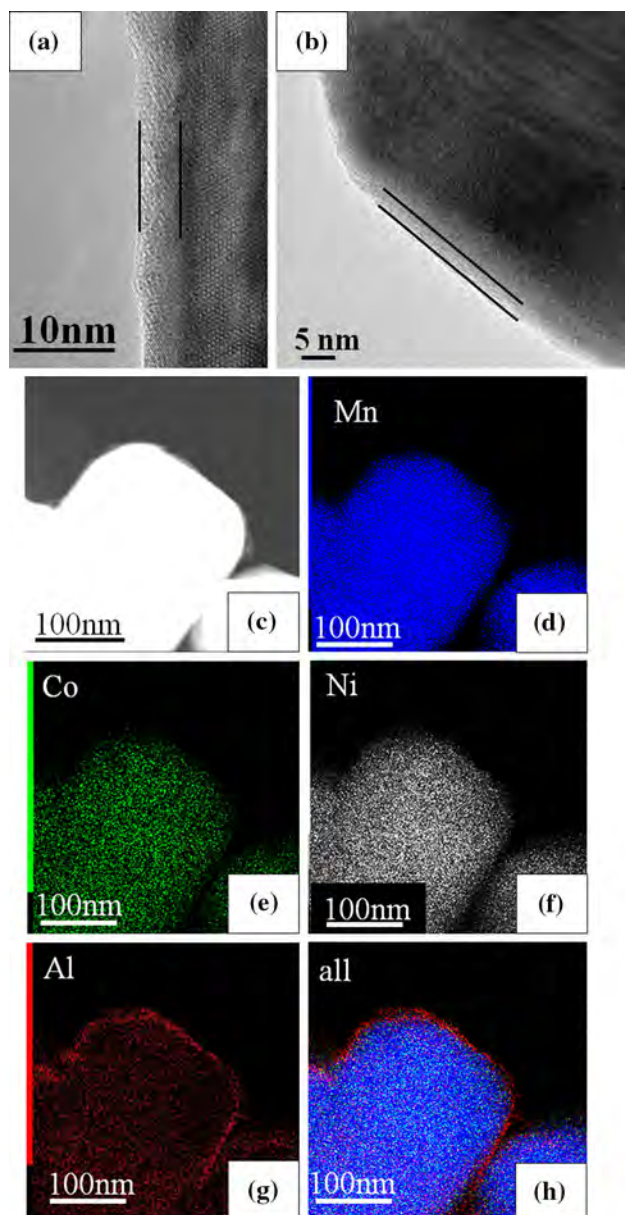


Fig. 10 TEM images (a, b), an STEM (c) image, and STEM-EDS mapping profile (d–h) images of the Al_2O_3 -coated $\text{Li}[\text{Ni}_{0.18}\text{Li}_{0.2}\text{Co}_{0.03}\text{Mn}_{0.58}]\text{O}_2$ particles

thickness is 4.0 nm. The $\text{Li}[\text{Ni}_{0.18}\text{Li}_{0.2}\text{Co}_{0.03}\text{Mn}_{0.58}]\text{O}_2$ particles are nearly fully covered with an Al_2O_3 layer having 3–5 nm in thickness. To confirm the Al_2O_3 -coating on the cathode particle surface, an STEM image (c) and its compositional mappings (d–h) were obtained using the Al_2O_3 -coated $\text{Li}[\text{Ni}_{0.18}\text{Li}_{0.2}\text{Co}_{0.03}\text{Mn}_{0.58}]\text{O}_2$ particles. In image (c), a thin Al_2O_3 -layer can be seen on the cathode particle surface. Blue, green, white, and red, indicate the existence of Mn(d), Co(e), Ni(f), and Al(g) atoms, respectively. The signals of Mn, Co, and Ni always overlap in the compositional mappings obtained from the Al_2O_3 -coated $\text{Li}[\text{Ni}_{0.18}\text{Li}_{0.2}\text{Co}_{0.03}\text{Mn}_{0.58}]\text{O}_2$ particles. The Al

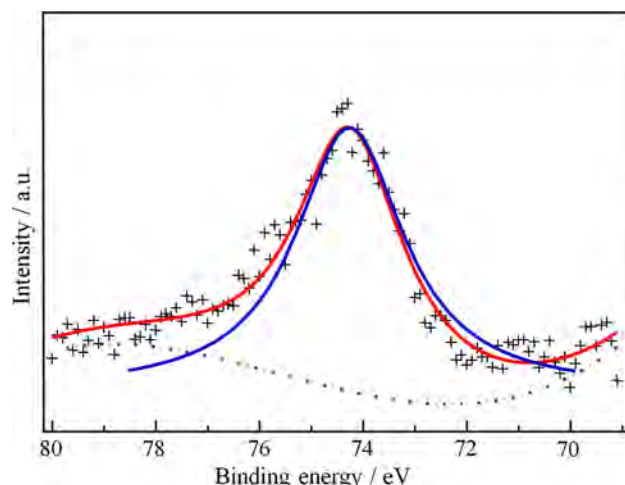


Fig. 11 XPS spectra (red lines) and fitted curves (blue lines) in the Al $2p_{3/2}$ region of the Al_2O_3 -coated $\text{Li}[\text{Ni}_{0.18}\text{Li}_{0.2}\text{Co}_{0.03}\text{Mn}_{0.58}]\text{O}_2$ cathodes

signals can be seen nearly entirely throughout the cathode surfaces in the overlapping of the Mn, Co, Ni, and Al signals in image (h).

A p XRD measurement of the Al_2O_3 -coated $\text{Li}[\text{Ni}_{0.18}\text{Li}_{0.2}\text{Co}_{0.03}\text{Mn}_{0.58}]\text{O}_2$ particles was attempted to confirm the formation of an Al_2O_3 -layer on the particle surface, although the localization of Al atoms throughout the particle surface was confirmed from the STEM compositional mappings of Fig. 11h. However, peaks originating from Al_2O_3 were not detected in the p XRD pattern obtained; therefore, the electron states of the Al atoms of the Al_2O_3 layers were evaluated with XPS. Figure 11 shows the XPS spectra (red lines) and fitted curves (blue lines) for the Al $2p_{3/2}$ of Al_2O_3 -coated $\text{Li}[\text{Ni}_{0.18}\text{Li}_{0.2}\text{Co}_{0.03}\text{Mn}_{0.58}]\text{O}_2$ cathodes to confirm the formation of an Al_2O_3 layer on the cathode particles. The Al $2p_{3/2}$ peak observed from the cathode particles was located at 74.27 eV, which shifted 1.27 eV higher relative to the corresponding peak for Al metal. The observed value of 74.27 eV is consistent with values reported in other papers [36], indicating that Al_2O_3 layers were formed on the cathode surface. The TEM/STEM and XPS characterization results clearly indicate that the formation of Al_2O_3 layers can be achieved on the surface of $\text{Li}[\text{Ni}_{0.18}\text{Li}_{0.2}\text{Co}_{0.03}\text{Mn}_{0.58}]\text{O}_2$ particles.

In Fig. 12, the results of the charge/discharge cycling test obtained without the pretreatment of $\text{Li}[\text{Ni}_{0.18}\text{Li}_{0.2}\text{Co}_{0.03}\text{Mn}_{0.58}]\text{O}_2$ at room temperature are shown. These cathodes were prepared with the TRD202A and PVdF binders. A stable average discharge capacity of 260 mAh g^{-1} was observed for the PVdF-based $\text{Li}[\text{Ni}_{0.18}\text{Li}_{0.2}\text{Co}_{0.03}\text{Mn}_{0.58}]\text{O}_2$ cathode even without pretreatment, while the TRD202A-based $\text{Li}[\text{Ni}_{0.18}\text{Li}_{0.2}\text{Co}_{0.03}\text{Mn}_{0.58}]\text{O}_2$ cathode, which was not electrochemically treated, exhibited a gradual degradation of the discharge capacity from 260 to

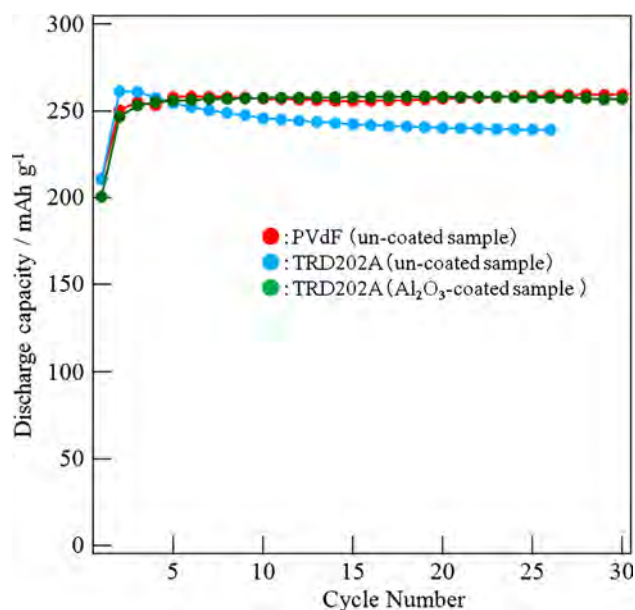


Fig. 12 Cycling performance obtained for nonelectrochemically treated Al_2O_3 -coated and un-coated $\text{Li}[\text{Ni}_{0.18}\text{Li}_{0.20}\text{Co}_{0.03}\text{Mn}_{0.58}]\text{O}_2$ electrodes prepared with TRD202A and un-coated $\text{Li}[\text{Ni}_{0.18}\text{Li}_{0.20}\text{Co}_{0.03}\text{Mn}_{0.58}]\text{O}_2$ electrodes prepared with PVdF binders

240 mAh g^{-1} at the 30th cycle. The reason for the difference in behavior between the two cathodes without electrochemical pretreatment is due to changes in the surface composition of the $\text{Li}[\text{Ni}_{0.18}\text{Li}_{0.20}\text{Co}_{0.03}\text{Mn}_{0.58}]\text{O}_2$ particles that occurred when exposing the cathodes' surface particles to water during the preparation of the water-based slurry, as shown in Table 1 and discussed above. The water-treated cathode particles need the electrochemical treatment to exhibit stable charge/discharge capacities. An Al_2O_3 -coated $\text{Li}[\text{Ni}_{0.18}\text{Li}_{0.20}\text{Co}_{0.03}\text{Mn}_{0.58}]\text{O}_2$ cathode prepared with the TRD202A binder shows a stable discharge capacity of 260 mAh g^{-1} during 30 cycles even without electrochemical pretreatment. The results show that coating Al_2O_3 on the $\text{Li}[\text{Ni}_{0.18}\text{Li}_{0.20}\text{Co}_{0.03}\text{Mn}_{0.58}]\text{O}_2$ particles were effective for improving the cycle performance even without electrochemical pretreatment. The Al_2O_3 layer coated on the cathode particles prevents direct contact between the cathode particle surface and water when the slurry of cathode material/TRD202A/CMC/AB is prepared with water. The effectiveness of Al_2O_3 as a coating material to improve the stability of the cycle performance has already been reported in many papers [36, 41–43]. It is understood that the Li^+ ion can pass through the Al_2O_3 layers on the cathode material surface [44, 45]. Fully coating the cathode surface with Al_2O_3 does not appear to prevent Li^+ ions from reaching the cathode material nor the diffusion of Li^+ ions from the cathode material through the Al_2O_3 layers. This result demonstrates the best way to use the cathode materials with a water-soluble binder.

4 Conclusions

The characteristics of a water-based hybrid polymer binder, TRD202A, composed of acrylic polymer and fluoropolymer, were examined for applications in high-voltage cathodes. The charge/discharge capacities, cycle stability, rate performance, mechanical resistance, resistance of electrochemical oxidation, changes of the surface composition and structure were studied after water-treatment during the preparation of a water-based slurry. The TRD202A binder exhibited equivalent charge/discharge capacities, cycle stability, rate performance, and resistance to electrochemical oxidation when compared with the conventional PVdF binder, while exhibiting a higher mechanical resistance. From these results, the TRD202A binder was identified as a promising water-based binder that satisfies many necessary characteristics for the development of high-performance and environmentally friendly cathodes. Fortunately, the $\text{Li}[\text{Ni}_{0.18}\text{Li}_{0.20}\text{Co}_{0.03}\text{Mn}_{0.58}]\text{O}_2$ cathode materials were not influenced by the water-treatment process when the water-based slurry of $\text{Li}[\text{Ni}_{0.18}\text{Li}_{0.20}\text{Co}_{0.03}\text{Mn}_{0.58}]\text{O}_2$ cathode material/TRD202A/CMC/AB was prepared for the fabrication of cathode films. However, some Li-rich solid-solution cathode materials having different compositions of Li, Mn, Ni, and Co ions exhibited gradual decreases in the discharge capacity. On the surface of a $\text{Li}[\text{Ni}_{0.18}\text{Li}_{0.20}\text{Co}_{0.03}\text{Mn}_{0.58}]\text{O}_2$ cathode material treated with water, unknown transition metal oxide layers, which formed by the dissolution of the surface of the cathode particles, covered the surface of the $\text{Li}[\text{Ni}_{0.18}\text{Li}_{0.20}\text{Co}_{0.03}\text{Mn}_{0.58}]\text{O}_2$ cathode material; as a result, the unknown layers prevented the surface of the $\text{Li}[\text{Ni}_{0.18}\text{Li}_{0.20}\text{Co}_{0.03}\text{Mn}_{0.58}]\text{O}_2$ cathode material from dissolving further. The protective layers can enhance the stability of the charge/discharge performance even after water-treatment of the cathode particles. As shown in this paper, to realize stable charge/discharge performances at all compositions, a water-stable surface layer, such as Al_2O_3 or carbon, should be formed on the cathode particles. In our next work, we will try to identify protective surface layers for a variety of Li-rich solid-solution cathode materials having different compositions of Li, Mn, Ni, and Co ions.

References

1. Wood III DL, Li J, Daniel C (2015) *J Power Sources* 275:234–242
2. Yuca N, Zhao H, Song X, Dogdu MF, Yuan W, Fu Y, Battaglia VS, Xiao X, Liu G (2014) *ACS Appl Mater Interfaces* 6:17111–17118
3. Yabuuchi N, Kinoshita Y, Misaki K, Natsuyama T, Komaba S (2015) *J Electrochem Soc* 162:A538–A544

4. He M, Yuan L-X, Zhang W-X, Hu X-L, Huang Y-H (2011) *J Phys Chem C* 115:15703–15709
5. Mancini M, Nobili F, Tossici R, Mehrens MW, Marassi R (2011) *J Power Sources* 196:9665–9671
6. Komaba S, Yabuuchi N, Ozeki T, Han Z-J, Shimomura K, Yui H, Katayama Y, Miura T (2012) *J Phys Chem C* 116:1380–1389
7. Sun M, Zhong H, Jiao S, Shao H, Zhang L (2014) *Electrochim Acta* 127:239–244
8. Klamor S, Schröder M, Brunklaus G, Niehoff P, Berkemeier F, Schappacher FM, Winter M (2015) *Phys Chem Chem Phys* 175:632–5641
9. Solomon GM, Morse EP, Garbo MJ, Milton DK (1996) *J Occup Environ Med* 38:705–713
10. Pinter T, Hof F (2011) *Chem Commun* 47:12688–12690
11. Buqa H, Holzapfel M, Krumeich F, Veit C, Novák P (2006) *J Power Sources* 161:617–622
12. Lee J-H, Lee S, Paik U, Choi Y-M (2005) *J Power Sources* 147:249–255
13. Wu Q, Ha S, Prakash J, Dees DW, Lu W (2013) *Electrochim Acta* 114:1–6
14. Prosini PP, Carewska M, Masci A (2015) *Solid State Ionics* 274:88–93
15. Oiu L, Shao Z, Wang D, Wang F, Wang J (2014) *Carbohydr Polym* 112:532–538
16. Prosini PP, Cento C, Carewska M, Masci A (2015) *Solid State Ionics* 274:34–39
17. Doberdò I, Löffler N, Laszczynski N, Cericola D, Penazzi N, Bodoardo S, Kim G-T, Passerini S (2014) *J Power Sources* 248:1000–1006
18. Soeda K, Yamagata M, Ishikawa M (2015) *ECS Trans* 64:13–22
19. Courtel FM, Niketic S, Duguay D, Lebdeh YA, Davidson IJ (2011) *J Power Sources* 196:2128–2134
20. Wang Z, Dupré N, Gaillot A-C, Lestriez B, Martin J-F, Daniel L, Patoux S, Guyomard D (2012) *Electrochim Acta* 62:77–83
21. Li J, Klopsch R, Nowak S, Kunze M, Winter M, Passerini S (2011) *J Power Sources* 196:7687–7691
22. Qiu L, Shao Z, Wang D, Wang W, Wang F, Wang J (2014) *Carbohydr Polym* 111:588–591
23. Thackeray MM, Kang S-H, Johnson CS, Vaughey JT, Benedek R, Hackney SA (2007) *J Mater Chem* 17:3112–3125
24. Armstrong AR, Holzapfel M, Novak P, Johnson CC, Kang S-H, Thackeray MM, Bruce PG (2006) *J Am Chem Soc* 128:8694–8698
25. Numata K, Sakaki C, Yamanaka S (1997) *Chem Lett* 8:725–726
26. Lu Z, Dahn JR (2002) *J Electrochem Soc* 149:A815–A822
27. Lu Z, Dahn JR (2002) *J Electrochem Soc* 149:A778–A791
28. Jarvis KA, Deng Z, Allard LF, Manthiram A, Ferreira PJ (2011) *Chem Mater* 23:3614–3621
29. Oh P, Myeong S, Cho W, Lee M-J, Ko M, Jeong HY (2014) *J Cho Nano Lett* 14:5965–5972
30. Yu H, Zhou H (2013) *J Phys Chem Lett* 4:1268–1280
31. Zhang K, Han X, Hu Z, Zhang X, Tao Z (2015) *J. Chem. Chem Soc Rev* 44:699–728
32. Ito A, Li DC, Sato Y, Arao M, Watanabe M, Hatano M, Horie H, Ohsawa Y (2010) *J Power Sources* 195:567–573
33. Watanabe A, Matsumoto F, Fukunishi M, Kobayashi G, Ito A, Hatano M, Ohsawa Y, Sato Y (2012) *Electrochemistry* 80:561–565
34. Ito A, Li D, Ohsawa Y, Sato Y (2008) *J Power Sources* 183:344–346
35. Huang X, Qiao Q, Sun Y, Li F, Wang Y, Ye SJ (2015) *Soild Satate Electrochem* 19:805–812
36. Kaneko S, Xia B, Zhang Q, Fang G, Liu W, Sun H, Matsumoto F, Sato Y, Zheng J, Li D (2014) *Electrochemistry* 82:438–443
37. Zhang X, Belharouak I, Li L, Lei Y, Elam JW, Nie A, Chen X, Yassar RS, Axeibaum RL (2013) *Adv Energy Mater* 3:1299–1307
38. Peralta D, Colin J-F, Boulineau A, Simonin L, Fabre F, Bouvet J, Feydi P, Chakir M, Chapuis M, Patoux S (2015) *J Power Sources* 280:687–694
39. Vu A, Walker LK, Barenō J, Burrell AK, Bloom I (2015) *J Power Sources* 280:155–158
40. Martha SK, Nanda J, Veith GM, Dudney N (2012) *J Power Sources* 199:220–226
41. Song B, Liu H, Liu Z, Xiao P, Lai MO, Lu L (2013) *Sci Rep* 3:3094
42. Pol VG, Li Y, Dogan F, Secor E, Thackeray MM, Abraham DP (2014) *J Power Sources* 258:46–53
43. Zou GS, Yang XK, Wang XY, Ge L, Shu HB, Bai YS, Wu C, Guo HP, Hu L, Yi X (2014) *J. Soild State Electrochem* 18:1789–1797
44. Xu M, Chen ZY, Li LJ, Zhu HL, Zhao QF, Xu L, Peng NF, Gong L (2015) *J Power Sources* 281:444–454
45. Choi M, Ham G, Jin B-S, Lee S-M, Lee YM, Wang G, Kim H-S (2014) *J Alloy Compd* 606:110–117

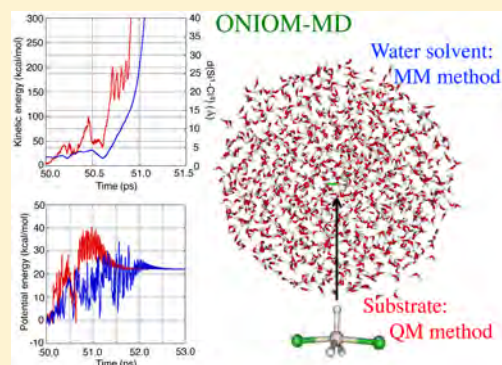
Quantum Mechanical and Molecular Dynamics Studies of the Reaction Mechanism of the Nucleophilic Substitution at the Si Atom

Toshiaki Matsubara* and Tomoyoshi Ito

Department of Chemistry, Faculty of Science, Kanagawa University, 2946, Tsuchiya, Hiratsuka, Kanagawa 259-1293, Japan

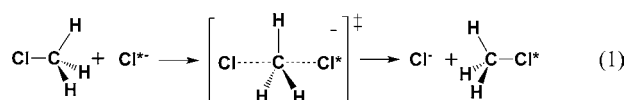
Supporting Information

ABSTRACT: The mechanism of the nucleophilic substitution at the Si atom, $\text{SiH}_3\text{Cl} + \text{Cl}^{*-} \rightarrow \text{SiH}_3\text{Cl}^* + \text{Cl}^-$, is examined by both quantum mechanical (QM) and molecular dynamics (MD) methods. This reaction proceeds by two steps with the inversion or retention of the configuration passing through an intermediate with the trigonal bipyramid (TBP) structure, although the conventional $\text{S}_{\text{N}}2$ reaction at the C atom proceeds by one step with the inversion of the configuration passing through a transition state with the TBP structure. We followed by the QM calculations all the possible paths of the substitution reaction that undergo the TBP intermediates with the cis and trans forms produced by the frontside and backside attacks of Cl^- . As a result, it was thought that TBP_{cis1} produced with a high probability is readily transformed to the energetically more stable $\text{TBP}_{\text{trans}}$. This fact was also shown by the MD simulations. In order to obtain more information concerning the trajectory of Cl^- on the dissociation from $\text{TBP}_{\text{trans}}$, which we cannot clarify on the basis of the energy profile determined by the QM method, the MD simulations with and without the water solvent were conducted and analyzed in detail. The QM-MD simulations without the water solvent revealed that the dissociation of Cl^- from $\text{TBP}_{\text{trans}}$ occurs without passing through TBP_{cis1} . The ONIOM-MD simulations with the water solvent further suggested that the thermal fluctuation of the water solvent significantly affects the oscillation of the kinetic and potential energies of the substrate to facilitate the isomerization of the TBP intermediate from the cis form to the trans form and the subsequent dissociation of Cl^- from $\text{TBP}_{\text{trans}}$.



INTRODUCTION

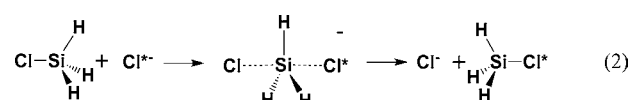
The substitution reaction as well as the elimination reaction are of primary importance in organic syntheses¹ and are therefore widely utilized in the field of the chemical industry. Also, the substitution reaction constantly occurs everywhere in vivo, which is essentially concerned with the important process in the organism.^{2,3} For example, it is well-known that an alkylation of a part of DNA by the substitution reaction leads to cancer.^{4,5} The $\text{S}_{\text{N}}2$ reaction is a type of mechanism of the nucleophilic substitution, and an archetypal model of this reaction is as follows, i.e., the reaction of chloromethane with the chloride anion.



In this reaction, the chloride anion preferentially attacks the central carbon from the backside, and both the association of incoming chloride anion and the dissociation of leaving chlorine synchronously occur with the inversion of configuration through the transition state with a trigonal bipyramid structure. The $\text{S}_{\text{N}}2$ reaction thus proceeds by one step in the case of carbon.

However, when we replace the C atom by the Si atom, the substitution reaction proceeds by two steps, since the trigonal

bipyramid structure exists not as a transition state but as an equilibrium structure as follows.



Due to the great interest in the stability of the trigonal bipyramidal structure, various studies concerning the 5-coordinate cluster of Si has been conducted in both experimental and theoretical aspects.^{6–17} In recent years, the energy profiles of eq 2 were calculated by the density functional and perturbation theory methods.^{18–20} The calculations showed that the potential energy surface from the reactant to the trigonal bipyramid intermediate is downhill and that from the trigonal bipyramid intermediate to the product is uphill. The potential energy profile of the substitution reaction thus drastically changes when we exchange the C atom for the Si atom. The large energy barrier existing in the case of the C atom disappears in the case of the Si atom. A. P. Bento and F. M. Bickelhaupt attributed this drastic change in the energy profile to the change in the steric repulsion between the spectator H atoms and the reacting

Received: March 4, 2016

Revised: April 1, 2016

Cl atoms.¹⁸ Namely, the congestion of the atoms around the central Si atom is significantly reduced due to the larger size of the Si atom in the third period. In fact, when the H atoms are replaced by the more bulky OMe groups, the energy barrier reappears, since the 5-coordinate intermediate destabilizes in energy due to the increase in the steric repulsion between the OMe groups and the reacting Cl atoms and becomes a transition state.

The frontside attack as well as backside attack are possible in the case of Si.^{19,20} In the case of the frontside attack, the 5-coordinate intermediate has a cis form and the substitution reaction proceeds with the retention of the configuration. Thus, the chloride anion can attack the central Si atom from any side without energy barrier. Since the edge attack also exists besides the face attack (Figure 1),^{11,12,21,22} four paths, paths a–d, to form the 5-coordinate intermediate are considered as presented in Figure 2. In the formed 5-coordinate intermediate

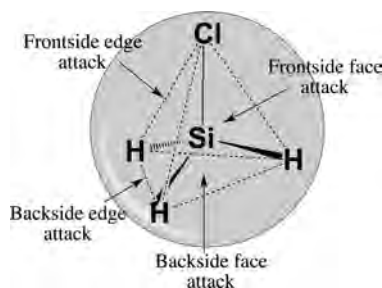


Figure 1. Pattern of the attack of Cl^- to SiH_3Cl .

TBP_{cis1} with the cis form, the rearrangement of the position of Cl can occur by two ways, i.e., a Berry pseudorotation (BPR)²³ and an intramolecular migration (IM). The two Cl at the equatorial and axial positions in TBP_{cis1} switch each other by BPR forming $\text{TBP}_{\text{cis1}'}$, and the Cl trans to H in TBP_{cis1} migrates to the position trans to Cl by IM isomerizing to $\text{TBP}_{\text{trans}}$ with the trans form. Accordingly, three substitution reaction paths have been considered so far,^{11,12} i.e., the first one follows: $\text{TBP}_{\text{trans}}$ is generated by the backside face attack of Cl^- , and the axial Cl in $\text{TBP}_{\text{trans}}$ dissociates. The second one follows: TBP_{cis1} is generated by the frontside face attack of Cl^- , and after the subsequent switch between the axial and equatorial Cl by BPR, the axial Cl in $\text{TBP}_{\text{cis1}'}$ dissociates. The third one follows here: $\text{TBP}_{\text{cis1}'}$ is generated by the frontside edge attack of Cl^- , and the axial Cl in $\text{TBP}_{\text{cis1}'}$ dissociates. The substitution reaction path passing through TBP_{cis2} does not practically exist as mentioned in the Results and Discussion section. These possible routes of the substitution reaction are systematically described in Figure 2. Although the most favorable path has not been clarified so far, it is reasonable to think on the basis of our calculation results that even if a cis form is generated first, it is transformed to the energetically most stable intermediate $\text{TBP}_{\text{trans}}$ with the trans form by IM before the Cl^- dissociation, and then the Cl^- dissociation occurs in $\text{TBP}_{\text{trans}}$. We will discuss the preference of the path for the formation of the 5-coordinate intermediate in the first section of the Results and Discussion section.

For the dissociation of Cl^- from the 5-coordinate intermediate $\text{TBP}_{\text{trans}}$, two paths, paths e and f, are thought. In path e, the Cl^- dissociation occurs after the transformation

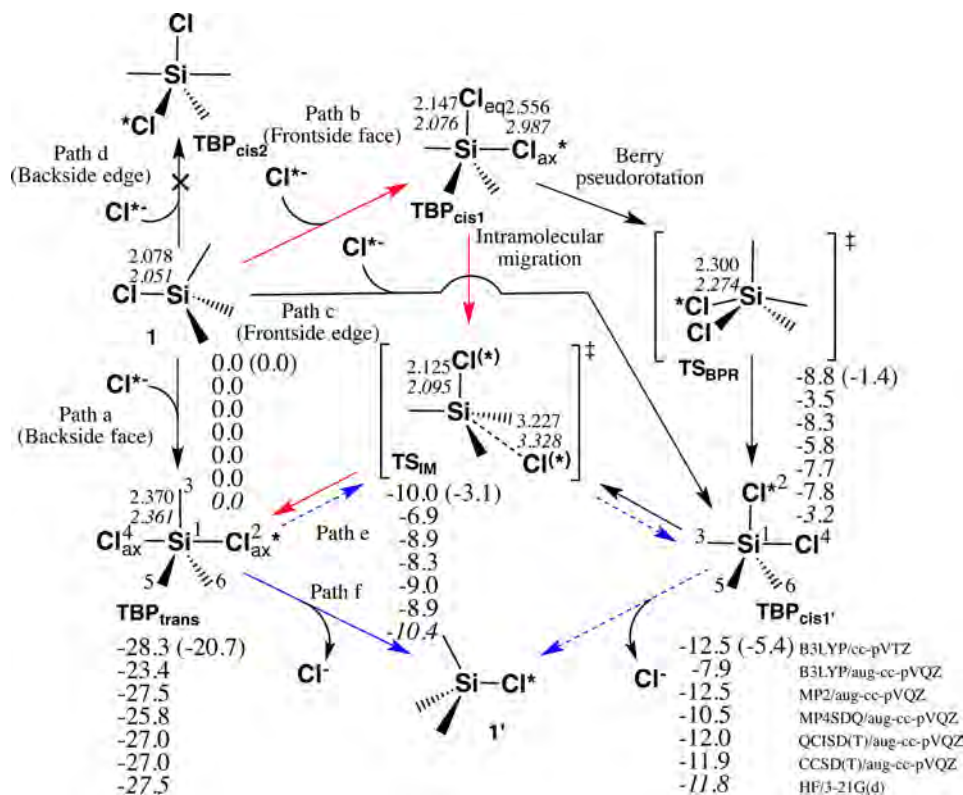


Figure 2. Reaction scheme of the nucleophilic substitution, $\text{SiH}_3\text{Cl} + \text{Cl}^* \rightarrow \text{SiH}_3\text{Cl}^* + \text{Cl}^-$. Bond distances (Å) of the optimized structures at the B3LYP/cc-pVTZ level and the relative energies (kcal/mol) at the B3LYP/cc-pVTZ, B3LYP/aug-cc-pVQZ, MP2/aug-cc-pVQZ, MP4SDQ/aug-cc-pVQZ, QCISD(T)/aug-cc-pVQZ, and the CCSD(T)/aug-cc-pVQZ levels are also displayed together. Numbers in italic type are the bond distances, and the relative energies at the HF/3-21G(d) level and the numbers in parentheses are the Gibbs free energies at the B3LYP/cc-pVTZ level.

to $\text{TBP}_{\text{cis1}'}$, and on the other hand, in path f, the Cl^- dissociation occurs in $\text{TBP}_{\text{trans}}$ without the transformation to $\text{TBP}_{\text{cis1}'}$. We have to answer the question which path is more favorable in order to clarify the entire mechanism of the substitution reaction. It is however impossible to find the answer to this question on the basis of the potential energy profile calculated by the usual quantum mechanical method, because both the transition state to form $\text{TBP}_{\text{cis1}'}$ and the intermediates $\text{TBP}_{\text{cis1}'}$ involved in path e are more stable in energy than the product $\mathbf{1}'$ as mentioned in the Results and Discussion section. We therefore conducted a quantum mechanical molecular dynamics simulation taking account of the thermal motion that is thought to be one of the effective tools to obtain such information concerning the reaction path. We also have a great interest in the solvent effect in this Cl^- dissociation process, because an environmental effect caused by the thermal motion, which we have reported as a dynamical environmental effect,^{24,25} is expected to promote the dissociation of Cl^- that requires a large thermal energy. In fact, we have found that the thermal fluctuation of the water molecules of the solvent significantly affects the kinetic and potential energies of the substrate in this study. In order to take account of the water solvent in the present reaction system, we used the ONIOM-molecular dynamics method.²⁶

In the present study, we examine the reaction mechanism of the nucleophilic substitution, $\text{SiH}_3\text{Cl} + \text{Cl}^{*-} \rightarrow \text{SiH}_3\text{Cl}^* + \text{Cl}^-$, as follows. First, we search the reaction paths at the various levels of the quantum mechanical (QM) method. Second, we analyze the reaction paths taking account of the thermal motion by means of the QM-molecular dynamics (MD) method, and third, we shed light on the solvent effect on the reaction using ONIOM-molecular dynamics (MD) method. Here, we used water as a solvent. Following the explanation of the computational details, we will discuss these three things in turn. Conclusions are summarized in the final section.

COMPUTATIONAL DETAILS

Quantum Mechanical (QM) Calculation. All the quantum mechanical (QM) calculations were performed using the GAUSSIAN03 program package.²⁷ The geometry optimizations were carried out by the density functional theory (DFT) at the B3LYP level, which consists of a hybrid Becke + Hartree–Fock exchange and Lee–Yang–Parr correlation functional with non-local corrections,^{28–30} using the basis set cc-pVTZ. We confirmed that the geometries and energies calculated by this level are in good agreement with those reported previously.^{18,19} The equilibrium and transition state structures were identified by the number of imaginary frequencies calculated from the analytical Hessian matrix. The reaction coordinates were followed from the transition state to the reactant and the product by the intrinsic reaction coordinate (IRC) technique.³¹ We furthermore performed the B3LYP, MP2, MP4SDQ, QCISD(T), and CCSD(T) single-point calculations with the aug-cc-pVQZ basis set at the B3LYP/cc-pVTZ optimized geometry to obtain a more reliable energetics. We also confirmed that the HF/3-21G(d) level we adopted for the molecular dynamics simulations reproduces the geometries and the energetics calculated by these post-Hartree–Fock levels very well. The Gibbs free energies were calculated at the B3LYP/cc-pVTZ level with a scale factor of 0.9614³² for calculated vibrational frequencies at the temperature of 298.15 K. The atomic charge was obtained by the natural bond orbital (NBO) analysis.³³ The basis set superposition error (BSSE) included in the interaction (INT) energies between SiH_3Cl and Cl^- was corrected by the counterpoise method.^{34,35}

Table 1. Comparison of the Distance, Population, Interaction (INT) Energy, and the Energy Decomposition Analysis (EDA) among the Si–Cl Bonds of $\text{TBP}_{\text{trans}}$ and TBP_{cis1}

| | $\text{TBP}_{\text{trans}}$ | | TBP_{cis1} | |
|------------------------------------|-----------------------------|---------------------|----------------------------|---------------------|
| | Si–Cl _{ax} | Si–Cl _{ax} | Si–Cl _{ax} | Si–Cl _{eq} |
| Distance (Å) ^a | 2.370 | 2.556 | 2.147 | |
| Population (e) ^a | 0.181 | 0.149 | 0.306 | |
| INT energy (kcal/mol) ^a | 50.3 | 24.6 | 80.2 | |
| EDA ^b (kcal/mol) | | | | |
| ES | −83.0 | −51.3 | −125.4 | |
| EX | 77.5 | 59.3 | 135.5 | |
| PL | −16.4 | −9.8 | −70.1 | |
| CT | −29.4 | −21.2 | −54.1 | |
| MIX | 7.4 | 5.8 | 43.1 | |
| total | −43.9 | −17.2 | −70.9 | |

^aCalculations were performed at the B3LYP/cc-pVTZ level. Counterpoise corrections are included for the INT energies. See the Computational Details section for the detail. ^bEDA were performed at the HF/6-31G level.

In order to analyze the component of the INT energies, we performed the energy decomposition analysis (EDA)³⁶ at the HF/6-31G level using the GAMESS program.³⁷

QM- and ONIOM-Molecular Dynamics (MD) Simulations. For the molecular dynamics (MD) simulations, we used the QM- and ONIOM-molecular dynamics (MD) methods.²⁶ The direct MD simulations were performed for the two intermediates of the substitution reaction, $\text{TBP}_{\text{trans}}$ and $\text{TBP}_{\text{cis1}'}$, with and without the water solvent calculating the energy and its gradient by the QM or the ONIOM method on the fly. The time evolution of the nuclei was performed using the Beeman algorithm³⁸ with a time step of 1 fs under the constant temperature through the use of Berendsen's velocity scaling algorithm.³⁹ The MD simulations of the intermediates, $\text{TBP}_{\text{trans}}$ and $\text{TBP}_{\text{cis1}'}$, without the water solvent were performed by the QM-MD method, where the energy was calculated at the HF level of theory with the basis set 3-21G(d) for all the atoms, because the HF/3-21G(d) level was confirmed to be good enough to describe the geometries and the energetics of the present substitution reaction (see Figure 2). On the other hand, the MD simulations of the intermediates, $\text{TBP}_{\text{trans}}$ and $\text{TBP}_{\text{cis1}'}$, with the water solvent were carried out by the ONIOM-MD method. To mimic the water solvent, 1055 water molecules are randomly placed inside the spherical space with the radius of 20 Å, where the substrate, $\text{TBP}_{\text{trans}}$ or $\text{TBP}_{\text{cis1}'}$, is centered. No periodic or constrained spherical boundary conditions were used during the MD simulations. All the water molecules were involved in the outer part of the ONIOM method and treated by the molecular mechanics (MM) method with the TIP3P⁴⁰ force field parameters. The van der Waals parameters reported by Rappe et al.⁴¹ were used for the Si, Cl, and H atoms of the substrate $\text{TBP}_{\text{trans}}$ or $\text{TBP}_{\text{cis1}'}$. The stretching, bending, and torsional contributions involving Si are set to zero. The substrates $\text{TBP}_{\text{trans}}$ and $\text{TBP}_{\text{cis1}'}$ were included in the inner part and treated by the QM method at the HF/3-21G(d) level.

In the present study, the optimized structure is used as the initial geometry of the MD simulation, and the potential energies relative to that of the optimized structure are presented. The geometry optimizations for the system with the water solvent were performed by the ONIOM-MD method by solving the Newton's equation of motion at zero Kelvin. The nuclei with initial velocities of zero start to move on the potential energy

surface downward. The nuclei slowly come close to the minimum of the potential energy surface with the velocities always staying small by the velocity scaling of the Berendsen thermostat and finally stop at the minimum with the velocities of zero. The energy of the entire system as well as the temperature is almost constant during the MD simulation as shown by Figure S2. We monitored the water solvent during the ONIOM-MD simulations and confirmed that there is no significant change in the structure of the water solvent, which is explicitly shown by the change in the ONIOM energy of the entire system (Figure S2B). The data collected every 10 fs from 10 to 100 ps were used to calculate the average and the standard deviation of the geometric parameter and energy, because the potential energy of the entire system as well as the temperature becomes almost constant after 10 ps. The standard deviation (fluctuation) σ is defined as follows.

$$\sigma = \sqrt{\frac{1}{n} \sum_{i=1}^n (X_i - \bar{X})^2} \quad (3)$$

RESULTS AND DISCUSSION

Quantum Mechanical (QM) Calculations of the Intermediates and the Transition States. As mentioned in the Introduction, SiH_3Cl interacts with Cl^- to form $\text{SiH}_3\text{Cl}_2^-$, which is an equilibrium structure. The nucleophilic substitution of SiH_3C with Cl^- therefore undergoes an intermediate $\text{SiH}_3\text{Cl}_2^-$ and proceeds by an associative mechanism consisting of two steps, the association of Cl^- and the dissociation of the other Cl^- . Both cis and trans isomers can be formed for the intermediate $\text{SiH}_3\text{Cl}_2^-$, since Cl^- can attack the Si atom from both frontside and backside, as shown in Figure 1. We have confirmed that this formation of the trigonal bipyramidal intermediate $\text{SiH}_3\text{Cl}_2^-$ is energetically downhill and proceeds without energy barrier. In the case of C, the trigonal bipyramid CH_3Cl_2^- is a transition state of the $\text{S}_{\text{N}}2$ substitution reaction (see Figure S1).

When Cl^- facially attacks the Si atom from the backside as the $\text{S}_{\text{N}}2$ substitution reaction in the case of C, the trans form of the intermediate $\text{SiH}_3\text{Cl}_2^-$ is formed as presented in path a in Figure 2. The substitution reaction is then completed by the

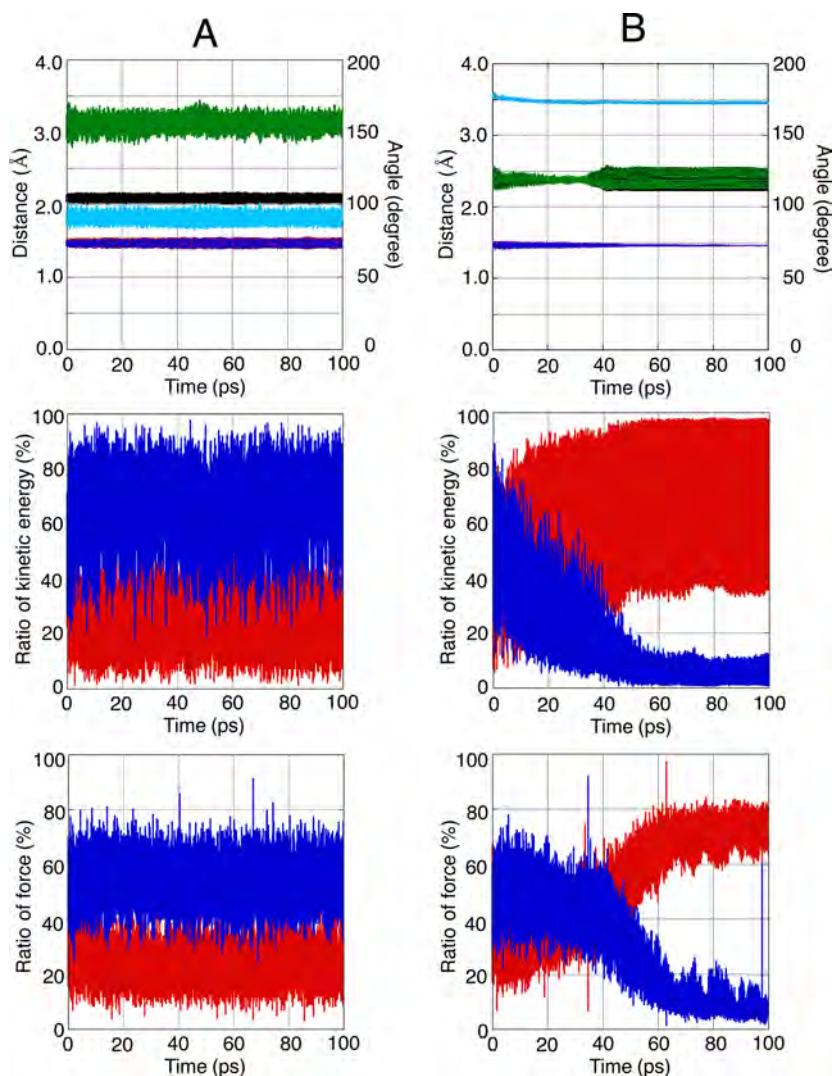


Figure 3. Changes in the geometric parameters and in the ratio of the kinetic energy and the force in the substrate TBP_{cis} (A) and $\text{TBP}_{\text{trans}}$ (B) in the QM-MD simulations in the gas phase at 300 K. In the geometric parameters, the following colors are relevant: black, $d(\text{Si}^1-\text{Cl}^2)$; orange, $d(\text{Si}^1-\text{H}^3)$; green, $d(\text{Si}^1-\text{Cl}^4)$; red, $d(\text{Si}^1-\text{H}^5)$; blue, $d(\text{Si}^1-\text{H}^6)$; pale blue, $\angle\text{Cl}^2-\text{Si}^1-\text{Cl}^4$. In the ratio of the kinetic energy, the following colors apply: blue, three H; red, two Cl. In the ratio of the force, the following colors apply: blue, three H; red, two Cl.

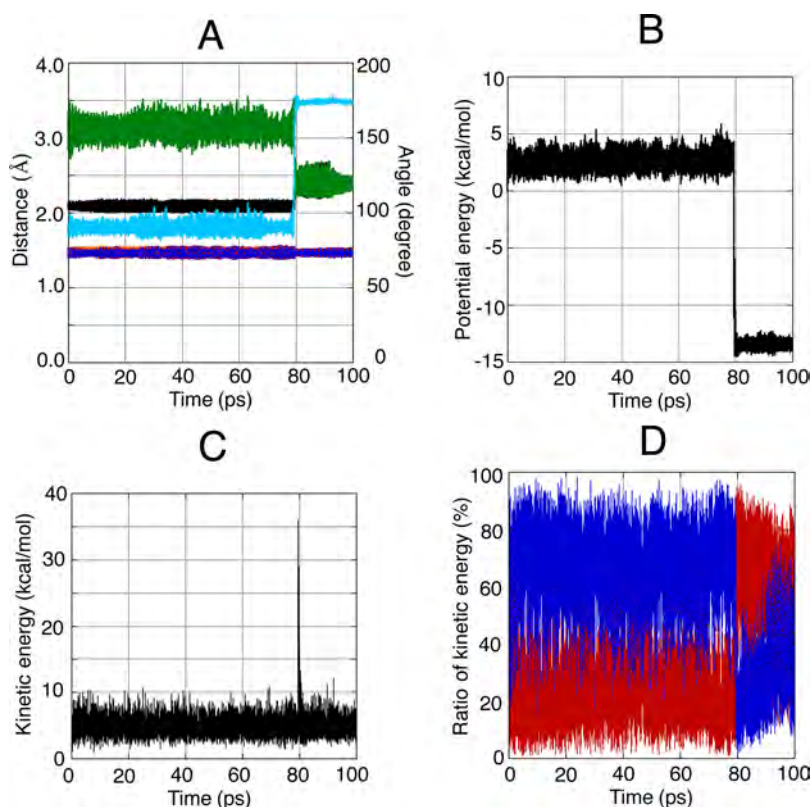


Figure 4. Changes in the geometric parameters (A), potential energy (B), kinetic energy (C), and the ratio of the kinetic energy (D) of the substrate in the QM-MD simulation of the isomerization from TBP_{cis1} to $\text{TBP}_{\text{trans}}$ in the gas phase at 400 K. In part A, the following colors apply: black, $d(\text{Si}^1-\text{Cl}^2)$; orange, $d(\text{Si}^1-\text{H}^3)$; green, $d(\text{Si}^1-\text{Cl}^4)$; red, $d(\text{Si}^1-\text{H}^5)$; blue, $d(\text{Si}^1-\text{H}^6)$; pale blue, $\angle\text{Cl}^2-\text{Si}^1-\text{Cl}^4$. In part D, the following colors apply: blue, three H; red, two Cl.

dissociation of the other Cl^- with the inversion of the structure. On the other hand, when Cl^- facially attacks the Si atom from the frontside, the cis form of the intermediate $\text{SiH}_3\text{Cl}_2^-$ is formed (path b in Figure 2) and the incoming Cl^- occupies the axial position. In this case, the two Cl need to switch their position to complete the substitution reaction, because it is considered that the Cl not at the equatorial position but at the axial position dissociates. As presented in Table 1, the bond distance is longer by 0.409 Å for the $\text{Si}-\text{Cl}_{\text{ax}}$ than for the $\text{Si}-\text{Cl}_{\text{eq}}$, and the bond population is also consistently smaller for the $\text{Si}-\text{Cl}_{\text{ax}}$ than for the $\text{Si}-\text{Cl}_{\text{eq}}$ in TBP_{cis1} , suggesting that the bond energy is smaller for the $\text{Si}-\text{Cl}_{\text{ax}}$ than for the $\text{Si}-\text{Cl}_{\text{eq}}$. Actually, the calculated interaction energy was much smaller for the $\text{Si}-\text{Cl}_{\text{ax}}$ than for the $\text{Si}-\text{Cl}_{\text{eq}}$. This is due to the small polarization and charge transfer energies for the $\text{Si}-\text{Cl}_{\text{ax}}$ compared to those for the $\text{Si}-\text{Cl}_{\text{eq}}$, as revealed by the energy decomposition analysis (EDA). As a pathway of the switching between two Cl at the axial and equatorial positions, the Berry pseudorotation (BPR)¹⁹ is well-known (vide infra).

The incoming Cl^- can also attack the Si atom on the edge as displayed in Figure 1, although its probability is low. If the Cl^- attacks from the frontside, the cis form $\text{TBP}_{\text{cis1}'}$ is produced (path c in Figure 2). Since the incoming Cl^- occupies the equatorial position and the leaving Cl^- occupies the axial position in this case, the switch of the position between the two Cl at the equatorial and axial positions is not needed to complete the substitution reaction. On the other hand, if the Cl^- attacks from the backside (path d in Figure 2), the other cis form TBP_{cis2} , where both Cl species occupy the equatorial position, is produced. However, the geometry optimization of

TBP_{cis2} revealed that TBP_{cis2} does not exist as an equilibrium structure.

After the association of Cl^- to SiH_3Cl to form the 5-coordinate complex $\text{SiH}_3\text{Cl}_2^-$, a switch of the position between two Cl or an isomerization would occur as summarized in Figure 2. A switch of the position between two Cl in the cis form occurs by BPR. TBP_{cis1} formed by the frontside face attack is transformed to $\text{TBP}_{\text{cis1}'}$ through the transition state TS_{BPR} , which has a square pyramidal structure. This step is energetically neutral, and the energy barrier was 4–5 kcal/mol at the various level. The other BPR from $\text{TBP}_{\text{trans}}$ to TBP_{cis2} is impossible, because TBP_{cis2} does not exist as mentioned above. From $\text{TBP}_{\text{cis1}'}$, the isomerization to $\text{TBP}_{\text{trans}}$ is possible by the intramolecular migration (IM) of Cl through the transition state TBP_{IM} . The Cl at the position trans to H migrates to the position trans to Cl without the dissociation. The energy barrier of this migration is very small, because the trans form $\text{TBP}_{\text{trans}}$ is much more stable in energy than the cis form $\text{TBP}_{\text{cis1}'}$.

On the basis of these results, the most probable path of the substitution reaction would be considered, as displayed by the red and blue arrows in Figure 2. First, the cis form TBP_{cis1} would be formed by the association of Cl^- , because the probability of the frontside face attack is predominantly high. The cis form TBP_{cis1} would be then converted to the trans form $\text{TBP}_{\text{trans}}$ by IM of Cl with the very small energy barrier. Accordingly, the dissociation of Cl^- would take place from $\text{TBP}_{\text{trans}}$ by path e or f. In path e, the reaction undergoes $\text{TBP}_{\text{cis1}'}$ before reaching $1'$. However, we cannot know which path is more favorable from the energy profile obtained by the quantum chemical calculations, because both TS_{IM} and $\text{TBP}_{\text{cis1}'}$ involved in path e are

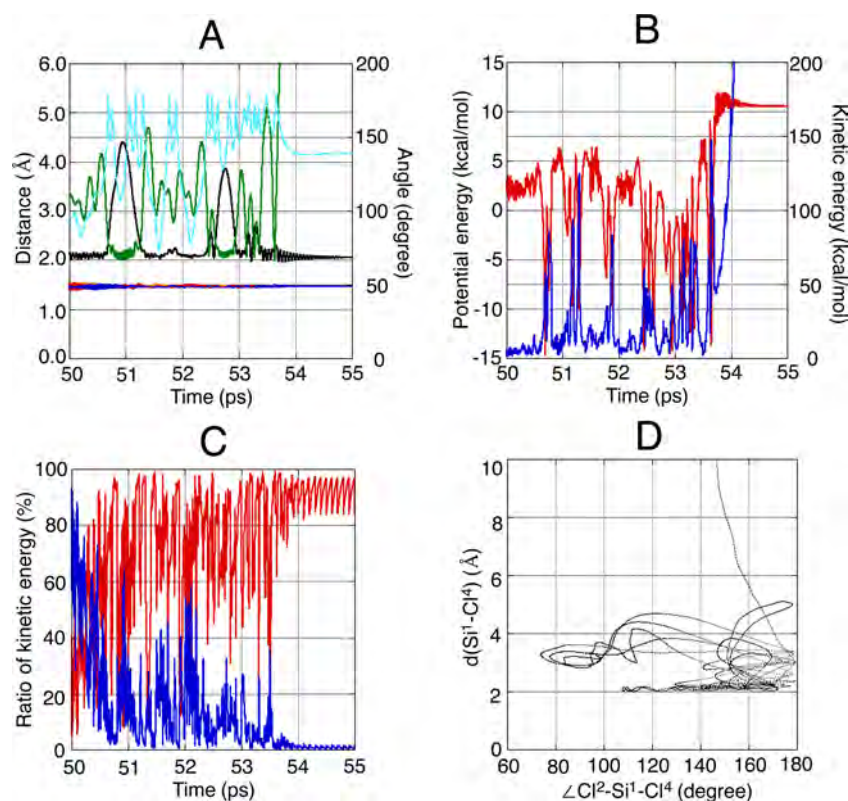


Figure 5. Changes in the geometric parameters (A), and in the potential energy and kinetic energy (B), and the ratio of the kinetic energy (C) of the substrate and the plot of $d(\text{Si}^1-\text{Cl}^4)$ vs $\angle\text{Cl}^2-\text{Si}^1-\text{Cl}^4$ (D) in the QM-MD simulation of the dissociation of Cl^- starting from TBP_{cis1} in the gas phase. See the text for the detail of the MD simulation. In part A, the following colors apply: black, $d(\text{Si}^1-\text{Cl}^2)$; orange, $d(\text{Si}^1-\text{H}^3)$; green, $d(\text{Si}^1-\text{Cl}^4)$; red, $d(\text{Si}^1-\text{H}^5)$; blue, $d(\text{Si}^1-\text{H}^6)$; pale blue, $\angle\text{Cl}^2-\text{Si}^1-\text{Cl}^4$. In part B, the following colors apply: blue, kinetic energy; red, potential energy. In part C, the following colors apply: blue, three H; red, two Cl.

lower in energy than $\mathbf{1}'$. We therefore performed the molecular dynamics simulations to obtain the information about the preference of the reaction path.

QM-Molecular Dynamics (MD) Simulations in the Gas Phase. We performed the QM-MD simulations at 300 K in the gas phase for the 5-coordinate intermediate TBP_{cis1} and $\text{TBP}_{\text{trans}}$, which is involved in the dissociation process of Cl^- . Both temperature and potential energy become constant immediately after starting the MD simulation (Figure S2). The changes in the geometric parameters and the distribution of the kinetic energy and the force are presented in Figure 3. There is no distinctive change in the oscillation in the case of the cis form TBP_{cis1} . In contrast, in the case of the trans form $\text{TBP}_{\text{trans}}$, one can find an obvious change in the oscillation of each geometric parameter during the MD simulation. We have obtained the same feature of the oscillation in every MD simulation of $\text{TBP}_{\text{trans}}$ in the gas phase. When the vibration of the entire molecule starts, the $\text{Cl}^2-\text{Si}^1-\text{Cl}^4$ axis, which is originally linear, bends by 7.3° , and the rotation of the entire molecule around the $\text{Cl}^2-\text{Si}^1-\text{Cl}^4$ axis also starts. This rotation around the axial axis never takes place in the case of the cis form TBP_{cis1} . The rotation velocity becomes constant after 40 ps, which is 0.5 times per ps. The magnitude of the vibration of each bond also changes after 40 ps, i.e., that of two Si-Cl bonds becomes larger, and in contrast that of three Si-H bonds becomes smaller. The stretching of two Si-Cl bonds occurs alternately in $\text{TBP}_{\text{trans}}$.

The distribution of the kinetic energy and the force in the entire molecule strongly depend on the geometric formation of

the trigonal bipyramid $\text{SiH}_3\text{Cl}_2^-$. The sum of the kinetic energy of three H is larger than that of two Cl in the cis form throughout the MD simulation. This order is however reversed, and the kinetic energy of two Cl finally becomes much larger than that of three H in the trans form. The same tendencies for the kinetic energy in the cis and trans forms were found also for the force. In the trans form, the force of three H becomes small and that of two Cl becomes large after 40 ps, because a lot of kinetic energy distributed to the vibration of the three Si-H bonds is transferred to the vibration of the two Si-Cl bonds.

When the temperature of TBP_{cis1} is raised from 300 to 400 K, the isomerization from TBP_{cis1} to $\text{TBP}_{\text{trans}}$ through TS_{IM} readily occurs as presented in Figure 4. By this increase in the temperature, the magnitude of the fluctuation of the potential energy of the entire molecule increased from 0.5 to 0.7 kcal/mol. Since the magnitude of the oscillation of the potential energy at 400 K becomes almost equal to the energy barrier of 1.4 kcal/mol for the isomerization, the probability of the occurrence of the isomerization becomes high. It should be noted here that the magnitude of the oscillation of the Si- Cl_{ax} stretching and the $\text{Cl}_{\text{eq}}-\text{Si}-\text{Cl}_{\text{ax}}$ bending becomes small just before the isomerization at around 80 ps. This fact would indicate that the kinetic energy of the Cl_{ax} that largely moves in the isomerization is consumed for its movement. The thermal energy of about 16 kcal/mol emitted during the isomerization is mainly transformed to the kinetic energy of the migrating Cl. The order of the magnitude of the kinetic energies of the three H and the two Cl is switched just when the transformation from TBP_{cis1} to $\text{TBP}_{\text{trans}}$ takes place at around 80 ps. As mentioned

above, the kinetic energy of two Cl is smaller than that of three H in TBP_{cis1} , but is larger than that of three H in $\text{TBP}_{\text{trans}}$.

Even if we further raise the temperature of the entire molecule, it is hard to simulate the dissociation of Cl^- from the 5-coordinate intermediate. However, as we have already reported for the enzymatic reaction,⁴² the reaction proceeds when a thermal energy is provided for an appropriate local unit that significantly contributes to the normal mode corresponding to the reaction coordinate. We therefore selected the Cl^4 that largely moves in both isomerization and dissociation and intentionally increased the kinetic energy of the Cl^4 increasing the velocity of the Cl^4 by 1.01 times in the Berendsen's velocity scaling when 50 ps passed starting from the intermediate TBP_{cis1} at 300 K. Thereby, the probability of the occurrence of the Cl^- dissociation increases, since the thermal energy is efficiently provided for the normal mode that corresponds to the Cl^- dissociation.

After starting the supply of the kinetic energy to the Cl^4 , the cis form is immediately transformed to the trans form as presented in Figure 5A. The formed trans form is converted to the cis form two times before and after 52 ps. The dissociation of Cl^- finally occurs at around 53.7 ps in the trans form. The changes in the kinetic and potential energies are presented together in Figure 5B. Most of the kinetic energy of the entire molecule comes from the kinetic energy of the Cl^4 . The kinetic energy provided to the Cl^4 is slightly transmitted to the Si^1 and the Cl^2 , but is not at all to the H^3 , H^5 , and H^6 . Just after the kinetic energy increases, the potential energy also increases, and

the trans form is converted to the cis form two times before the dissociation of the Cl^- . However, the dissociation of Cl^- never occurs in the cis form, because the kinetic energy of two Cl is remarkably decreased in the cis form (Figure 5C), and in addition, the cis form cannot keep the supplied kinetic energy (Figure S3B,D). Thus, the dissociation of Cl^- occurs from the trans form without passing through the cis form, although the $\text{Si}-\text{Cl}_{\text{ax}}$ bond in TBP_{cis1} is much weaker than the $\text{Si}-\text{Cl}_{\text{ax}}$ bond in $\text{TBP}_{\text{trans}}$. During the dissociation of Cl^- from the trans form, the angle $\angle\text{Cl}^2-\text{Si}^1-\text{Cl}^4$ is reduced as shown by Figure 5D, because the dissociating Cl^- is able to escape from the strong attraction of Si. Before the Cl^- dissociation, the Si^1-Cl^2 and Si^1-Cl^4 bonds stretch alternately, and the Si^1-Cl^2 bond shortens when the Cl^4 dissociates (Figure S3C).

ONIOM-Molecular Dynamics (MD) Simulations in the Water Solvent. In order to examine the effect of the water solvent on the Cl^- dissociation process after the formation of the 5-coordinate intermediate, we performed the ONIOM-MD simulations for $\text{TBP}_{\text{trans}}$ and TBP_{cis1} in the water solvent. The oscillation of the geometric parameters of $\text{TBP}_{\text{trans}}$ at 300 K is displayed in Figure 6A. It is obvious that the oscillation of all the geometric parameters is affected by the thermal motion of the surrounding water molecules of the solvent, and its magnitude becomes large compared to that in the gas phase. We have reported this effect of the thermal motion of the environment for the organometallic reactions.^{24,25} Especially, the magnitude of the vibration of the two $\text{Si}-\text{Cl}$ bonds further enlarges at intervals of 20 ps. The rotation of the entire

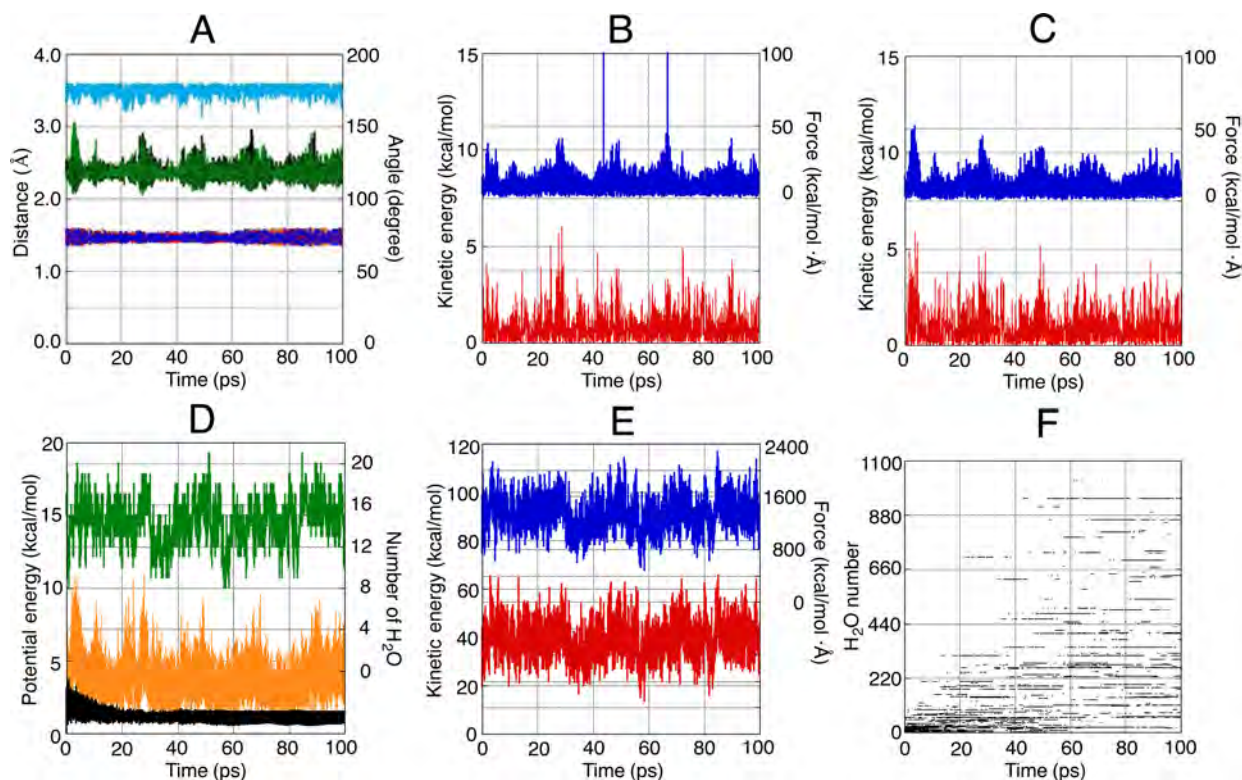


Figure 6. Changes in the geometric parameters of the substrate (A), kinetic energy and force of Cl^2 (B) and Cl^4 (C), potential energy of the substrate and number of water molecules existing in the area within the radius of 5 Å from Si^1 (D), kinetic energy and force of the water molecules existing in the area within the radius of 5 Å from Si^1 (E), and the number for the water molecules existing in the area within the radius of 5 Å from Si^1 (F) in the ONIOM-MD simulation of $\text{TBP}_{\text{trans}}$ in the water solvent at 300 K. In part A, the following colors apply: black, $d(\text{Si}^1-\text{Cl}^2)$; orange, $d(\text{Si}^1-\text{H}^3)$; green, $d(\text{Si}^1-\text{Cl}^4)$; red, $d(\text{Si}^1-\text{H}^5)$; blue, $d(\text{Si}^1-\text{H}^6)$; pale blue, $\angle\text{Cl}^2-\text{Si}^1-\text{Cl}^4$. In parts B, C, and E, the following colors apply: blue, force; red, kinetic energy. In part D, the following colors apply: orange, potential energy of the substrate; green, number of water molecules existing in the area within the radius of 5 Å from Si^1 . The change in the potential energy of the substrate in the gas phase (black) is also presented together.

molecule around the $\text{Cl}^2\text{-Si}^1\text{-Cl}^4$ axis that was found in the gas phase does not occur in the water solvent. As shown by Figure 6B,C, the kinetic energy and the force of the Cl^2 and the Cl^4 are also significantly affected by the thermal motion of the surrounding water molecules of the solvent. These changes in the kinetic energy and the force of two Cl would cause the changes in the vibration of two Si-Cl bonds, as shown by the fact that the trend in the change coincides each other.

The oscillation of the potential energy of the entire molecule is also remarkably influenced by the thermal motion of the surrounding water molecules (Figure 6D). Both the average and the fluctuation of the potential energy become much larger than those for the gas phase. This dynamical environmental effect of the water molecules of the solvent would promote the reaction. In fact, the isomerization from TBP_{cis1} to $\text{TBP}_{\text{trans}}$ that never occurs at 300 K in the gas phase during the simulation readily occurs even at low temperature in the water solvent as mentioned below. The oscillation of the potential energy of the substrate in the water solvent further enlarges at intervals of 20 ps, with this feature being the same as that found for the vibration of the Si-Cl bonds.

In order to clarify the reason why this feature of the oscillation appears, we focused on the number of water molecules existing around the substrate. The number of water molecules existing in the area within the radius of 5 Å from the Si^1 is shown in Figure 6D. The number of water molecules largely fluctuates, suggesting that the local density of the water molecule significantly changes. Figure 6F shows that the water molecules that are in the area of 5 Å radius from the Si^1

frequently switch with other water molecules that are in the outer area and never stay in the same area for a long time at 300 K. It is thought that this movement of the water molecules would cause the change in the density of a local area. The condition with a high density would make the substrate unstable in energy. In fact, when the density of the water molecule increases at intervals of 20 ps, the potential energy of the substrate also increases. The fluctuation of the density of the surrounding water molecules would play an important role in the occurrence of the reaction of the substrate. In the crowded condition at intervals of 20 ps, the kinetic energy and the force of the surrounding water molecules also similarly increase as shown by Figure 6E.

TBP_{cis1} was immediately converted to $\text{TBP}_{\text{trans}}$ in the water solvent at 300 K. This fact would be reasonably explained by the effect of the water solvent mentioned above. Since the potential energy of the substrate largely fluctuates in the water solvent, the isomerization reaction can easily proceed by jumping over the small energy barrier of 1.4 kcal/mol. We therefore intentionally lowered the temperature up to 100 K in order to simulate the isomerization reaction properly. Figure 7A shows that the isomerization takes place at around 65 ps. The corresponding geometric parameters change at that moment. The potential energy is lowered by about 15 kcal/mol by this isomerization from TBP_{cis1} to $\text{TBP}_{\text{trans}}$ (Figure 7B). The generated thermal energy is released outside mainly via the Cl^4 atom as indicated by Figure 7C. No obvious change in the kinetic energy and the force was found at around 65 ps for the atoms other than the Cl^4 . The decay of the potential energy of

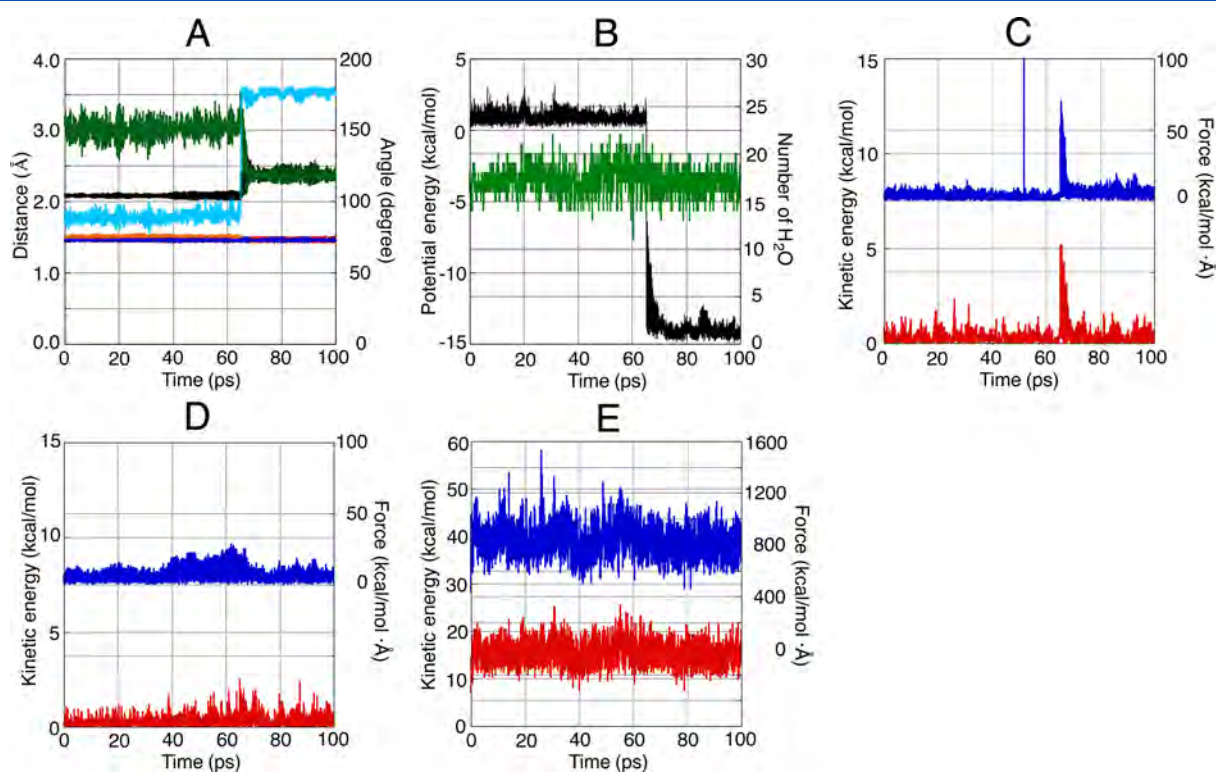


Figure 7. Changes in the geometric parameters of the substrate (A), potential energy of the substrate and number of water molecules existing in the area within the radius of 5 Å from Si^1 (B), kinetic energy and force of Cl^4 (C) and Cl^2 (D), and the kinetic energy and force of the water molecules existing in the area within the radius of 5 Å from Si^1 (E) in the ONIOM-MD simulation of the isomerization from TBP_{cis} to $\text{TBP}_{\text{trans}}$ in the water solvent at 100 K. In part A, the following colors apply: black, $d(\text{Si}^1\text{-Cl}^2)$; orange, $d(\text{Si}^1\text{-H}^3)$; green, $d(\text{Si}^1\text{-Cl}^4)$; red, $d(\text{Si}^1\text{-H}^5)$; blue, $d(\text{Si}^1\text{-H}^6)$; pale blue, $\angle\text{Cl}^2\text{-Si}^1\text{-Cl}^4$. In part B, the following colors apply: black, potential energy of the substrate; green, number of water molecules existing in the area within the radius of 5 Å from Si^1 . In parts C, D, and E, the following colors apply: blue, force; red, kinetic energy.

the substrate after the isomerization is slow compared to the case of the gas phase (see Figure 4B), because the kinetic energy of the Cl^4 remains for a while due to the presence of the surrounding water molecules.

As we expected, the number of water molecules existing in the area within the radius of 5 Å from the Si^1 increased just before the isomerization (Figure 7B). This indicates that the fluctuation of the density of the surrounding water molecule of the solvent plays an important role in the occurrence of the reaction. The increase in the density of the surrounding water molecule would make the substrate active and promote the isomerization reaction. Figure 7D shows that the kinetic energy and the force of the Cl^2 increase when the density of the surrounding water molecule increases. The migration of Cl^4 cis to Cl^2 would be induced by an active motion of Cl^2 . When the density of the surrounding water molecule becomes high, the kinetic energy and the force of those water molecules also become large (Figure 7E), as mentioned above.

Even in the water solvent, it is difficult to simulate the dissociation of Cl^- from the 5-coordinate intermediate by an usual manner. We therefore intentionally increased the kinetic energy of the Cl^4 increasing the velocity of the Cl^4 by 1.01 times in the Berendsen's velocity scaling, as mentioned in the previous section. The simulation was performed starting from the intermediate TBP_{cis1} at 300 K, and the kinetic energy of the Cl^4 was increased after 50 ps. At that moment, TBP_{cis1} is already transformed to $\text{TBP}_{\text{trans}}$. The dissociation of Cl^-

immediately occurs after 50 ps (at around 50.7 ps), as shown in Figure 8A. The dissociation of Cl^- occurs in $\text{TBP}_{\text{trans}}$ also in the water solvent, although the kinetic energy is not localized on the two Cl of $\text{TBP}_{\text{trans}}$ in the water solvent. The angle $\angle\text{Cl}^2-\text{Si}^1-\text{Cl}^4$ largely decreases during the Cl^- dissociation in order to escape from the strong attraction of Si^1 , which is similar to the case of the gas phase. However, $\text{TBP}_{\text{trans}}$ never passes through $\text{TBP}_{\text{cis1}'}$. The water molecules of the solvent would come into the space made by the elongation of the Si^1-Cl^4 bond and break the Si^1-Cl^4 bond before reaching $\text{TBP}_{\text{cis1}'}$. When we perform the same MD simulation from 50 ps without the water solvent, it takes a longer time to complete the dissociation of Cl^- as shown by Figure 9A. This suggests that the thermal motion of the water molecules of the solvent promotes the dissociation of Cl^- .

In our final details, we focus on the changes in the potential and kinetic energies of the substrate and the water molecules of the solvent existing in the area within the radius of 5 Å from the substrate just before the dissociation of Cl^- . The changes in the potential energies of the substrate with and without the water solvent are presented in Figure 8B. The potential energy of the substrate $\text{TBP}_{\text{trans}}$ gradually increases until reaching the potential energy of the product I' without the water solvent. On the other hand, with the water solvent, the potential energy of the substrate suddenly increases to more than 30 kcal/mol just before the Cl^- dissociation, which is much larger than the potential energy of the product I' . This suggests that $\text{TBP}_{\text{trans}}$

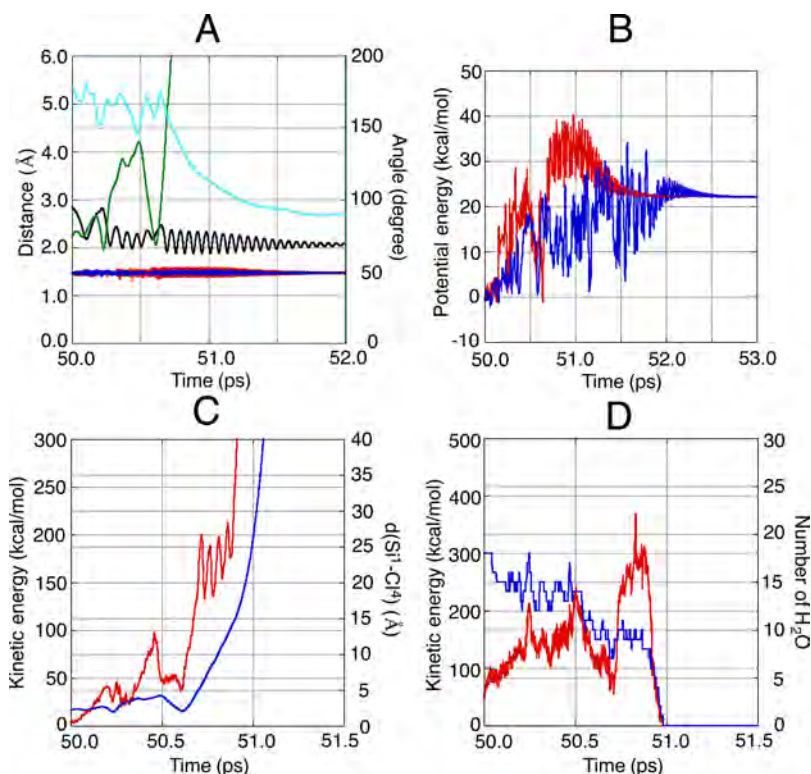


Figure 8. Changes in the geometric parameters of the substrate (A), potential energy of the substrate (B), kinetic energy of the substrate and distance $d(\text{Si}^1-\text{Cl}^4)$ (C), and the kinetic energy of the water molecules and number of water molecules existing in the area within the radius of 5 Å from Cl^4 (D) in the ONIOM-MD simulation of the dissociation of Cl^- starting from $\text{TBP}_{\text{trans}}$ in the water solvent. See the text for the detail of the MD simulation. In part A, the following colors apply: black, $d(\text{Si}^1-\text{Cl}^2)$; orange, $d(\text{Si}^1-\text{H}^3)$; green, $d(\text{Si}^1-\text{Cl}^4)$; red, $d(\text{Si}^1-\text{H}^5)$; blue, $d(\text{Si}^1-\text{H}^6)$; pale blue, $\angle\text{Cl}^2-\text{Si}^1-\text{Cl}^4$. In part B, the change in the potential energy of the substrate without the water solvent (blue) is also presented together. In part C, the following colors apply: red, kinetic energy of the substrate; blue, distance $d(\text{Si}^1-\text{Cl}^4)$. In part D, the following colors apply: red, kinetic energy of the water molecules existing in the area within the radius of 5 Å from Cl^4 ; blue, number of water molecules existing in the area within the radius of 5 Å from Cl^4 .

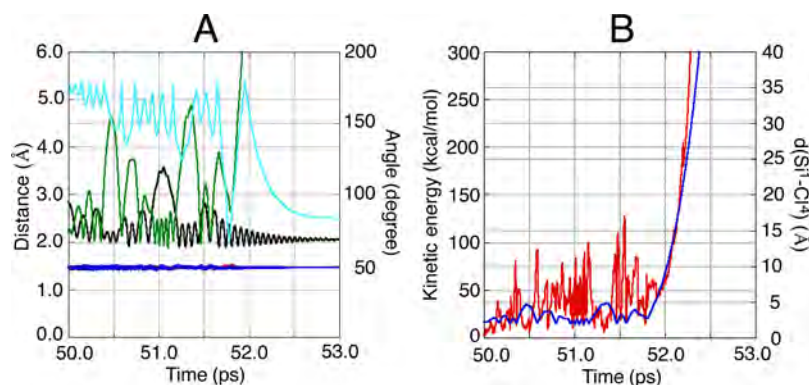


Figure 9. Changes in the geometric parameters of the substrate (A) and the kinetic energy of the substrate and the distance $d(\text{Si}^1-\text{Cl}^4)$ (B) in the QM-MD simulation of the dissociation of Cl^- starting from $\text{TBP}_{\text{trans}}$ without the water solvent. See the text for the detail of the MD simulation. In part A, the following colors apply: black, $d(\text{Si}^1-\text{Cl}^2)$; orange, $d(\text{Si}^1-\text{H}^3)$; green, $d(\text{Si}^1-\text{Cl}^4)$; red, $d(\text{Si}^1-\text{H}^5)$; blue, $d(\text{Si}^1-\text{H}^6)$; pale blue, $d(\text{Cl}^2-\text{Si}^1-\text{Cl}^4)$. In part B, the following colors apply: red, kinetic energy of the substrate; blue, distance $d(\text{Si}^1-\text{Cl}^4)$.

can obtain a larger thermal energy and the Cl^- dissociation is more facile in the water solvent. The kinetic energy of $\text{TBP}_{\text{trans}}$ in the water solvent also remarkably increases just before the Cl^- dissociation (Figure 8C), although there is no such increase in the kinetic energy of $\text{TBP}_{\text{trans}}$ without the water solvent (Figure 9B). At that moment, the number of water molecules existing in the area within the radius of 5 Å from the Cl^4 becomes constant despite the rise in temperature of the entire system, and the kinetic energy of those water molecules also significantly increases (Figure 8D). Thus, the thermal energies of the substrate and an area around the substrate are increased and retained in a certain time just before the Cl^- dissociation by the thermal fluctuation of the surrounding water molecules of the solvent, which promotes the dissociation of Cl^- .

CONCLUDING REMARKS

It is known that the nucleophilic substitution at the Si atom proceeds by two steps with the inversion or retention of the configuration passing through an intermediate with the trigonal bipyramid (TBP) structure, although the conventional $\text{S}_{\text{N}}2$ reaction at the C atom proceeds by one step with the inversion of the configuration passing through a transition state with the TBP structure. In the present study, we examined in detail the mechanism of $\text{SiH}_3\text{Cl} + \text{Cl}^{*-} \rightarrow \text{SiH}_3\text{Cl}^* + \text{Cl}^-$ as a model reaction by means of both quantum mechanical (QM) and molecular dynamics (MD) methods. Since both frontside and backside attacks of Cl^- are possible, there exist three paths, paths a–c, to generate the 5-coordinate intermediates. Path d by the backside edge attack of Cl^- is absent, because the 5-coordinate intermediate $\text{TBP}_{\text{cis}2}$ does not exist as an equilibrium structure. It is intuitively thought that the reaction would take path b by the frontside face attack of Cl^- that has a high probability due to the large area of Cl^- attack. The generated 5-coordinate intermediate $\text{TBP}_{\text{cis}1}$ would be immediately transformed to the energetically more stable $\text{TBP}_{\text{trans}}$. As for the dissociation of Cl^- from the $\text{TBP}_{\text{trans}}$, we conducted the MD simulations in order to obtain more information concerning the trajectory of Cl^- . The QM-MD simulations in the gas phase for the TBP intermediate with the cis form showed that the cis form is immediately transformed to the trans form, and then the dissociation of Cl^- from $\text{TBP}_{\text{trans}}$ occurs without passing through $\text{TBP}_{\text{cis}1'}$, although the $\text{Si}-\text{Cl}_{\text{ax}}$ bond in $\text{TBP}_{\text{cis}1'}$ is much weaker than the $\text{Si}-\text{Cl}_{\text{ax}}$ bond in $\text{TBP}_{\text{trans}}$. For the TBP intermediates in the water solvent,

we performed the ONIOM-MD simulations. As a result, it was found that $\text{TBP}_{\text{cis}1}$ is more readily transformed to $\text{TBP}_{\text{trans}}$ in the water solvent and the generated $\text{TBP}_{\text{trans}}$ similarly never passes through $\text{TBP}_{\text{cis}1'}$ in the Cl^- dissociation. The ONIOM-MD simulations also suggested that the thermal fluctuation of the water solvent significantly affects the oscillation of the kinetic and potential energies of the substrate to facilitate the isomerization of the TBP intermediate from the cis form to the trans form and the subsequent dissociation of Cl^- from $\text{TBP}_{\text{trans}}$.

ASSOCIATED CONTENT

Supporting Information

The Supporting Information is available free of charge on the ACS Publications website at DOI: 10.1021/acs.jpca.6b02308.

Additional figures showing potential energy profiles, changes in the temperature and the potential energy, and changes in the distance $d(\text{Si}^1-\text{Cl}^4)$ with the kinetic energy of the substrate, among other data; and listings giving the optimized Cartesian coordinates of equilibrium structures and transition states at the B3LYP/cc-pVTZ level.(PDF)

AUTHOR INFORMATION

Corresponding Author

*Phone: +81-463-59-4111. E-mail: matsubara@kanagawa-u.ac.jp.

Notes

The authors declare no competing financial interest.

ACKNOWLEDGMENTS

A part of the computations was performed at the Research Center for Computational Science, Okazaki, Japan.

REFERENCES

- (1) McMurry, J. *Organic Chemistry*, 7th ed.; Thomson: California, 2008.
- (2) McKee, T.; McKee, J. R. *Biochemistry: The Molecular Basis of Life*, 4th ed.; Oxford University Press: Oxford, 2008.
- (3) Bruice, P. Y. *Organic Chemistry*, 5th ed.; Prentice Hall: New Jersey, 2006.
- (4) Vollhardt, K. P. C.; Schore, N. E. *Organic Chemistry: Structure and Function*, 6th ed.; W. H. Freeman: New York, 2011.
- (5) Sorrell, T. N. *Organic Chemistry*, 2nd ed.; University Science Books: California, 2005.

- (6) Deiters, J. A.; Holmes, R. R.; Holmes, J. M. Fluorine and chlorine apicophilicities in five-coordinated phosphorus and silicon compounds via molecular orbital calculations. A model for nucleophilic substitution. *J. Am. Chem. Soc.* **1988**, *110*, 7672–7681.
- (7) Corriu, R. J. P.; Dabosi, G.; Martineau, M. Stereochemical proof of the existence of nucleophilic activation at a silicon atom in nucleophilic substitution reactions. Substitution of the Si-Cl-bond with retention of configuration. *J. Organomet. Chem.* **1978**, *154*, 33–43.
- (8) Holmes, R. R. The stereochemistry of nucleophilic substitution of tetracoordinate silicon. *Chem. Rev.* **1990**, *90*, 17–31.
- (9) Sheldon, J. C.; Hayes, R. N.; Bowie, J. H. Do barriers exist for nucleophilic substitution at tetravalent silicon in the gas phase? An ab initio and ion cyclotron resonance study. *J. Am. Chem. Soc.* **1984**, *106*, 7711–7715.
- (10) Damrauer, R.; Burggraf, L. W.; Davis, L. P.; Gordon, M. S. Gas-phase and computational studies of pentacoordinate silicon. *J. Am. Chem. Soc.* **1988**, *110*, 6601–6606.
- (11) Deiters, J. A.; Holmes, R. R. Pathways for nucleophilic substitution at silicon. A molecular orbital approach. *J. Am. Chem. Soc.* **1987**, *109*, 1686–1692.
- (12) Deiters, J. A.; Holmes, R. R. Effect of entering and leaving groups on nucleophilic substitution reactions at silicon. A molecular orbital approach. *J. Am. Chem. Soc.* **1987**, *109*, 1692–1696.
- (13) Windus, T. L.; Gordon, M. S.; Davis, L. P.; Burggraf, L. W. Theoretical Study of Pseudorotation of Pentacoordinated Silicon Anions: $\text{SiH}_5\text{-X}_n^-$ ($\text{X} = \text{F}, \text{Cl}$). *J. Am. Chem. Soc.* **1994**, *116*, 3568–3579.
- (14) Corriu, R. J. P.; Guerin, C.; Henner, B. J. L.; Man, W. W. C. W. Pentacoordinated silicon anions: reactivity toward strong nucleophiles. *Organometallics* **1988**, *7*, 237–238.
- (15) Tamao, K.; Hayashi, T.; Ito, Y.; Shiro, M. Electronic and steric effects in pentacoordinate anionic diorganotrifluorosilicates: x-ray structures and carbon-13 NMR studies for evaluation of charge distribution in aryl groups on silicon. *Organometallics* **1992**, *11*, 182–191.
- (16) Chuit, C.; Corriu, R. J. P.; Reye, C.; Young, J. C. Reactivity of penta- and hexacoordinate silicon compounds and their role as reaction intermediates. *Chem. Rev.* **1993**, *93*, 1371–1448.
- (17) Pierrefixe, S. C. A. H.; Guerra, C. F.; Bickelhaupt, F. M. Hypervalent Silicon versus Carbon: Ball-in-a-Box Model. *Chem. - Eur. J.* **2008**, *14*, 819–828.
- (18) Bento, A. P.; Bickelhaupt, F. M. Nucleophilic Substitution at Silicon ($\text{S}_{\text{N}}2@(\text{Si})$) via a Central Reaction Barrier. *J. Org. Chem.* **2007**, *72*, 2201–2207.
- (19) Bento, A. P.; Bickelhaupt, F. M. Frontside versus Backside $\text{S}_{\text{N}}2$ Substitution at Group 14 Atoms: Origin of Reaction Barriers and Reasons for Their Absence. *Chem. - Asian J.* **2008**, *3*, 1783–1792.
- (20) Yang, Z.-Z.; Ding, Y.-L.; Zhao, D.-X. Theoretical Analysis of Gas-Phase Front-Side Attack Identity $\text{S}_{\text{N}}2(\text{C})$ and $\text{S}_{\text{N}}2(\text{Si})$ Reactions with Retention of Configuration. *J. Phys. Chem. A* **2009**, *113*, 5432–5445.
- (21) Corriu, R. J. P.; Guerin, C. Nucleophilic displacement at silicon stereochemistry and mechanistic implications. *J. Organomet. Chem.* **1980**, *198*, 231–320.
- (22) Bassindale, A. R.; Taylor, P. G. *The Chemistry of Organic Silicon Compounds*; Patai, S., Rappoport, Z., Eds.; Wiley: New York, 1989; Vol. 1.
- (23) Berry, R. S. Correlation of Rates of Intramolecular Tunneling Processes, with Application to Some Group V Compounds. *J. Chem. Phys.* **1960**, *32*, 933–938.
- (24) Matsubara, T. Application of the ONIOM-Molecular Dynamics Method to the Organometallic Reaction $\text{Cis}-(\text{H})_2\text{Pt}(\text{PR}_3)_2 \rightarrow \text{H}_2 + \text{Pt}(\text{PR}_3)_2$ ($\text{R} = \text{H}, \text{Me}, \text{Ph}, \text{and t-Bu}$). An Insight into the Dynamical Environmental Effects. *J. Phys. Chem. A* **2008**, *112*, 9886–9894.
- (25) Matsubara, T. Dynamical Behavior of the H_2 Molecule of the $\text{PtH}(\text{H}_2)[\text{P}(\text{t-Bu})_3]_2^+$ Complex. A Theory of Chemical Reactivity. *J. Phys. Chem. A* **2009**, *113*, 3227–3236.
- (26) Matsubara, T.; Dupuis, M.; Aida, M. The ONIOM molecular dynamics method for biochemical applications: Cytidine deaminase. *Chem. Phys. Lett.* **2007**, *437*, 138–142.
- (27) Frisch, M. J.; Trucks, G. W.; Schlegel, H. B.; Scuseria, G. E.; Robb, M. A.; Cheeseman, J. R.; Montgomery, J. A., Jr.; Vreven, T.; Kudin, K. N.; Burant, J. C.; et al. *Gaussian 03, revision E.01*; Gaussian, Inc.: Wallingford, CT, 2004.
- (28) Becke, A. D. Density-Functional Exchange-Energy Approximation with Correct Asymptotic Behavior. *Phys. Rev. A: At, Mol, Opt. Phys.* **1988**, *38*, 3098–3100.
- (29) Lee, C.; Yang, W.; Parr, R. G. Development of the Colle-Salvetti Correlation-Energy Formula into a Functional of the Electron Density. *Phys. Rev. B: Condens. Matter Mater. Phys.* **1988**, *37*, 785–789.
- (30) Becke, D. Density-Functional Thermochemistry. III. The Role of Exact Exchange. *J. Chem. Phys.* **1993**, *98*, 5648–5652.
- (31) Fukui, K.; Kato, S.; Fujimoto, H. Constituent Analysis of the Potential Gradient along a Reaction Coordinate. Method and an Application to Methane + Tritium Reaction. *J. Am. Chem. Soc.* **1975**, *97*, 1–7.
- (32) Scott, A. P.; Radom, L. Harmonic Vibrational Frequencies: An Evaluation of Hartree-Fock, Mller-Plesset, Quadratic Configuration Interaction, Density Functional Theory, and Semiempirical Scale Factors. *J. Phys. Chem.* **1996**, *100*, 16502–16513.
- (33) Glendening, E. D.; Reed, A. E.; Carpenter, J. E.; Weinhold, F. *NBO Version 3.1*.
- (34) Boys, S. F.; Bernardi, F. The calculation of small molecular interactions by the differences of separate total energies. Some procedures with reduced errors. *Mol. Phys.* **1970**, *19*, 553–566.
- (35) Simon, S.; Duran, M.; Dannenberg, J. J. How does basis set superposition error change the potential surfaces for hydrogen-bonded dimers? *J. Chem. Phys.* **1996**, *105*, 11024–11031.
- (36) Kitaura, K.; Morokuma, K. A new energy decomposition scheme for molecular interactions within the Hartree-Fock approximation. *Int. J. Quantum Chem.* **1976**, *10*, 325–340.
- (37) Schmidt, M. W.; Baldridge, K. K.; Boatz, J. A.; Elbert, S. T.; Gordon, M. S.; Jensen, J. J.; Koseki, S.; Matsunaga, N.; Nguyen, K. A.; Su, S.; Windus, T. L.; Dupuis, M.; Montgomery, J. A. General Atomic and Molecular Electronic Structure System. *J. Comput. Chem.* **1993**, *14*, 1347–1363.
- (38) Beeman, D. Some multistep methods for use in molecular dynamics calculations. *J. Comput. Phys.* **1976**, *20*, 130–139.
- (39) Berendsen, H. J. C.; Postma, J. P. M.; van Gunsteren, W. F.; DiNola, A.; Haak, J. R. Molecular dynamics with coupling to an external bath. *J. Chem. Phys.* **1984**, *81*, 3684–3690.
- (40) Jorgensen, W. L.; Chandrasekhar, J.; Madura, J. D.; Impey, R. W.; Klein, M. L. Comparison of simple potential functions for simulating liquid water. *J. Chem. Phys.* **1983**, *79*, 926–935.
- (41) Rappe, A. K.; Casewit, C. J.; Colwell, K. S.; Goddard, W. A.; Skiff, W. M. UFF, a full periodic table force field for molecular mechanics and molecular dynamics simulations. *J. Am. Chem. Soc.* **1992**, *114*, 10024–10035.
- (42) Matsubara, T.; Dupuis, M.; Aida, M. Ab Initio ONIOM-Molecular Dynamics (MD) Study on the Deamination Reaction by Cytidine Deaminase. *J. Phys. Chem. B* **2007**, *111*, 9965–9974.

Photocatalytic Activity of Pd-Au Alloy Nanoparticle Co-catalyst/TiO₂ for Acetic Acid Decomposition

Arockiam John Jeevagan¹, Takao Gunji¹, Toyokazu Tanabe¹,
Shingo Kaneko² and Futoshi Matsumoto¹

¹Department of Material and Life Chemistry, Kanagawa University, 3-27-1,
Rokkakubashi, Kanagawa, Yokohama, Kanagawa 221-8686, Japan

²Research Institute for Engineering, Kanagawa University,

3-27-1, Rokkakubashi, Kanagawa, Yokohama, Kanagawa 221-8686, Japan

Abstract

A comparison of the photocatalytic activity on acetic acid (AcOH) decomposition with Pt nanoparticle (NP)-deposited, Pd NP-deposited and Pd-Au alloy NP-deposited TiO₂ will be reported in this paper. Pd and Au atoms were co-deposited on the TiO₂ surfaces via reductions of the photo-excited electrons under light irradiation. The composition, particle size, distribution and structures of the synthesized NPs were characterized by X-ray diffraction (XRD), transmission electron microscope (TEM) and X-ray photoelectron spectroscopy (XPS). The photocatalytic experiments revealed that the CO₂ elimination rate in the decomposition of AcOH was enhanced on Pd-Au-deposited TiO₂ compared to the photocatalysts of pure TiO₂, Pt- and Pd-deposited TiO₂.

Introduction

The remediation of environmental pollution using photocatalysts is a promising solution to the increasing demand for energy and the associated environmental concerns (1). Particularly, photocatalytic degradation of organic compounds using titanium dioxide (TiO₂) as a photocatalyst is a powerful tool, which is often applied in the purification of water and wastewater (2, 3). Because of its eccentric physical and chemical behaviors, easy availability and nontoxicity, TiO₂ acts as a significant photocatalyst and has been widely investigated in energy and environmental fields (4, 5). However, its poor quantum efficiency, which is due to the rapid recombination rate of photogenerated electron-hole pairs, still limits the widespread use of TiO₂ in practical applications. Suppressing the recombination of charge carriers and extending the optical absorption edge will be essential for the enrichment of its photocatalytic activity. Hence, various strategies have been used to improve the photocatalytic performance of TiO₂, including textural modification, transitional or rare earth metal doping and noble metal particle deposition (6). In particular, modifying the surface of the photocatalysts with noble metals is a feasible approach to enhancing the photocatalytic activity. These small metal particles accelerate the separation of photogenerated charge carriers.

To date, several methods have been employed to synthesize supported metal catalysts. Among these methods, the photo-deposition method is considered an effective method for the synthesis of supported metal catalysts. This process is effective due to its ability to design nano-sized metals with well-controlled sizes on solid supports. It has been reported that under light irradiation, the semiconductor material TiO₂ leads to charge separation, in which electrons are

promoted to the conduction band and holes are left in the valence band (7-9). Hence, a mixture of semiconductor materials and metal precursor ions irradiated under light irradiation initiates reduction by the conduction band electrons, which leads to the formation of metal nanoparticles (NPs) (10).

Palladium (Pd) has attracted great attention due to its wide application in catalytic processes and in promoting O₂ to scavenge photo-generated electrons, and Pd significantly inhibits the photocatalytic deactivation (11). Moreover, Pd loaded TiO₂ has been used in gas-phase photocatalysis and decomposition of organic compounds (11, 12). In addition, it has been reported that metallic Au acts as an excellent electronic conductor and facilitates the rapid transfer of photoelectrons on TiO₂. Moreover, the combination of Pd and Au alloy exhibited an obvious synergetic effect and greatly enhanced their catalytic activities and selectivity (13-16). Furthermore, bimetallic alloy nanoparticles (NPs) have attracted significant interest due to their large surface area and abundant active sites exposed on branched surfaces (17-19). Recently, it has been shown that Pd-Au/TiO₂ catalysts were prepared by the photo-assisted deposition method and used for direct synthesis of H₂O₂ (20); a Pd-Au/TiO₂ nanotube film was also used for the photocatalytic degradation of malathion (21), and Pd-Au NP-decorated TiO₂ nanofibers were used for the decomposition of formic acid and high-yield hydrogen production (22).

Herein, we have attempted to synthesize a TiO₂-supported Pd-Au alloy NP photocatalyst (Pd-Au/TiO₂) by the photo-assisted deposition method and have examined the application of such a system to the photocatalytic decomposition of acetic acid (AcOH). The designed photocatalyst system was characterized by *p*XRD, TEM and XPS. AcOH decomposition is important in waste water treatment and in the production of hydrocarbons in the “photo-Kolbe” reaction (23). In addition, the application of AcOH as a model compound is reasonable, as it is among the final by-products of photocatalytic degradation of most organic compounds in water, where various aliphatic acids, including AcOH, are also present. Hence, we have used the present Pd-Au NP catalysts in the decomposition of AcOH. The Pd-Au co-catalyst NP/TiO₂ system showed enhanced photocatalytic activity toward AcOH decomposition compared to pure TiO₂ and Pd- and Pt-deposited TiO₂.

Experimental

Materials

TiO₂ (P25, average primary particle size: 21 nm) was purchased from Nippon Aerosil Co. Ltd, Japan. PdCl₂ was purchased from Wako pure chemicals (99%). HAuCl₄·3H₂O was purchased from Sigma-Aldrich and was used without further purification. All other chemicals were used as analytical grade reagents without further purification.

Preparation of co-catalysts on TiO₂

The Pd-Au/TiO₂ and Pd/TiO₂ photocatalysts were synthesized by the previously reported procedure with slight modifications (20). 500 mg of metal oxide was dissolved in H₂O (20 mL) and stirred for 15 minutes. Then, 8.3 mL of a diluted HCl aqueous PdCl₂ (5.7 mM) and HAuCl₄·3H₂O (5.7 mM) solution was added to the metal oxide suspension. The mixture was stirred for 20 minutes under Ar atmosphere. After that, the suspension was transferred to the quartz cell and irradiated with light using a 200 W high-pressure Hg lamp with stirring for 3 h. The synthesized sample was centrifuged, washed repeatedly with millipore water and dried

under 383 K for 8 h. The photodeposition of Pd on the TiO₂ was also carried out by the same method using an aqueous solution of Pd precursors containing TiO₂ particles.

Characterization

High resolution XRD measurements were carried out using the high brilliance synchrotron radiation at BL15XU ($\lambda = 0.65297 \text{ \AA}$) of SPring-8 at the Japan Synchrotron Radiation Research Institute. The size and distribution of the synthesized NPs on the TiO₂ surfaces were characterized using a transmission electron microscope (TEM, JEOL 2100-F) with an operating voltage of 200 kV. The samples for TEM measurements were prepared by dropping a methanol suspension of the catalyst powder onto a copper grid (150 mesh). X-ray photoelectron spectroscopy (XPS) measurements were applied to the synthesized samples to identify the chemical states of the Pd and Au atoms on the catalysts using an XPS spectrometer (JPS-9010, JEOL), where MgK α was used as the X-ray source with anodic voltage (10 kV) and current (10 mA). The absorbance spectra were recorded in a UV-Vis diffuse reflectance spectrophotometer (UV-2600, Shimadzu). The metal contents of the products were determined using inductively coupled plasma-mass spectrometry (ICP-MS, Agilent, 7700x).

Photocatalytic measurements

The photocatalytic decomposition of AcOH was performed at room temperature with a circulation system made of Pyrex, in which a suspension of the photocatalyst powder (0.30 g) in an aerated, aqueous AcOH solution (5 vol%, 50 mL) was continuously stirred using a magnetic stirrer. A 300 W Xe lamp was used as the light source. The sample was illuminated with a 300 W Xe lamp (PE-300BF, BA-X300ES, Hayashi Tokei Works Co. Ltd, Japan) in conjunction with an optical fiber coupler and a cold mirror unit (MR5090/CM, Eagle Co., Ltd). The components in the gas phase were analyzed by a gas chromatograph (GC-8A, Shimadzu) equipped with a 2 m Porapak-Q column, a 2 m molecular sieve 3X column, and a flame ionization detector while using Ar as the carrier gas.

Results and discussion

Fig. 1 shows a high resolution powder XRD pattern using high brilliance synchrotron radiation for PdAu/TiO₂, where reference data of pure Au (24) and Pd (25) are also shown. Using synchrotron radiation, a number of weak peaks were clearly observed and can be assigned because of the high intensity used compared to conventional Lab. XRD. The high resolution XRD pattern shows weak peaks assigned to the Pd-Au alloy besides the TiO₂ support. The Pd-Au alloy peaks are situated between the reference peaks of Au and Pd. The composition of the Pd-Au alloy particles on TiO₂ can be estimated using Vegard's law, which describes the linear relationship between the crystal lattice parameter and the composition of a solid solution alloy. According to the law, the lattice constant of a binary Pd-Au solid solution system varies linearly with composition, as shown in Fig. 2. Using the linear relation, the estimated composition of the Pd-Au alloy particles on TiO₂ is 76.1% Au and 23.9% Pd, where 4.034 \AA was used as the lattice constant and was calculated from the Pd-Au alloy peaks of the high resolution XRD pattern (Fig. 1).

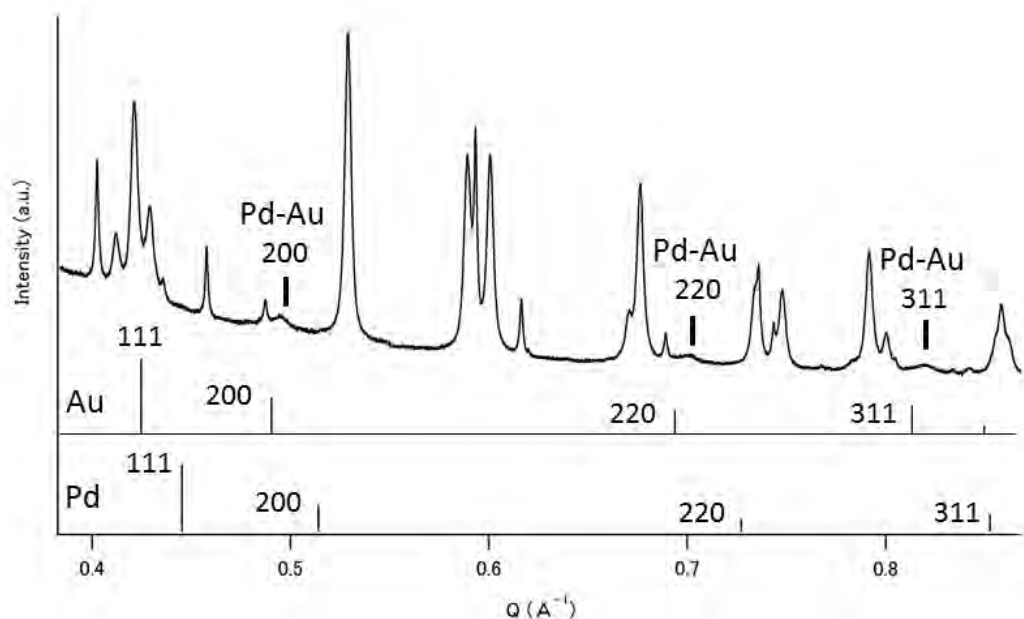


Figure 1. Powder XRD pattern using high brilliance synchrotron radiation for Pd-Au/TiO₂. Reference data of Au and Pd are also shown for comparison.

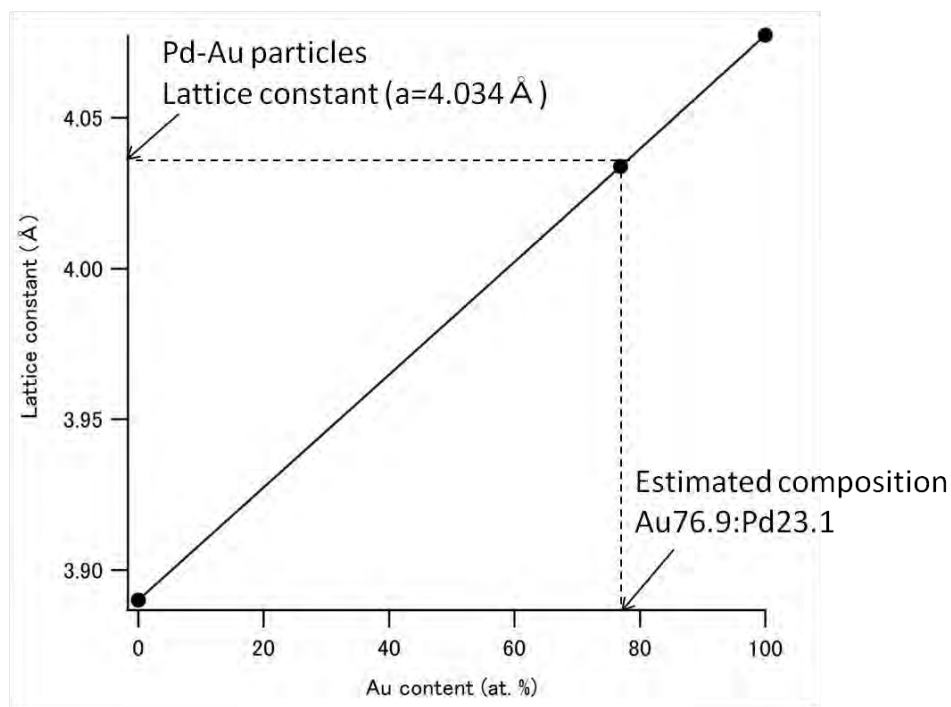


Figure 2. Vegard's law plot of the lattice parameters of a Pd-Au alloy system as a function of Au content.

Pd and PdAu deposition on TiO₂ was verified by TEM analysis, which yields valuable, direct information on the dimension and the distribution of Pd and Pd-Au NPs on the TiO₂ surface. Figure 3 shows TEM images of the Pd/TiO₂ (a) and the Pd-Au/TiO₂ (b) photocatalyst systems.

As observed in Fig. 3 (a) and (b), the average diameters of the Pd and Pd-Au NPs are 3.20 ± 0.20 and 3.40 ± 0.20 nm, respectively. Pd and Au were well-dispersed on the TiO₂ surface.

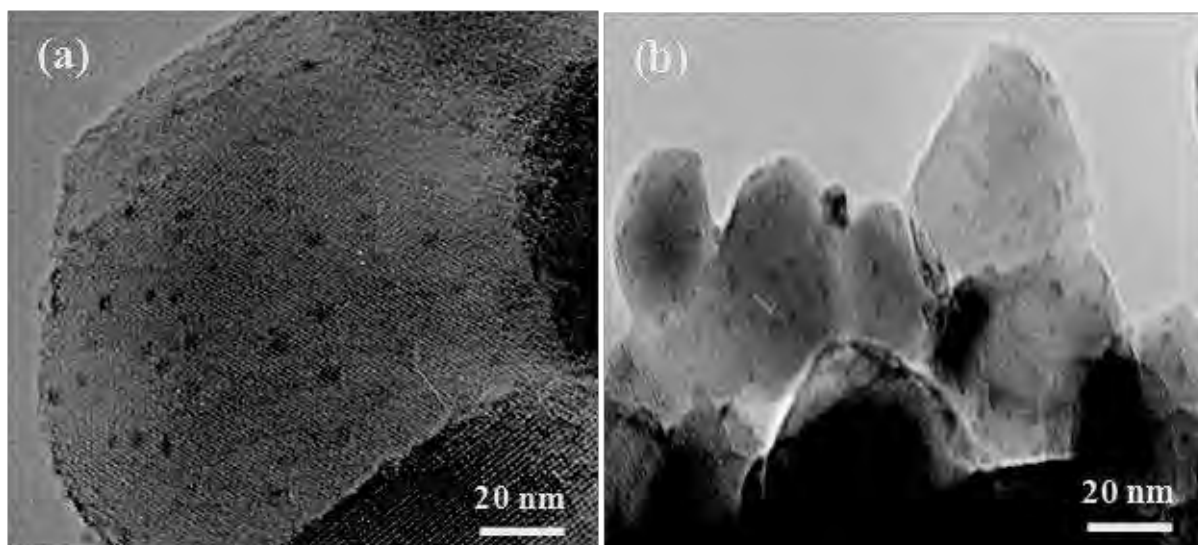


Figure 3. TEM images of (a) Pd/TiO₂ and (b) Pd-Au/TiO₂ photocatalysts.

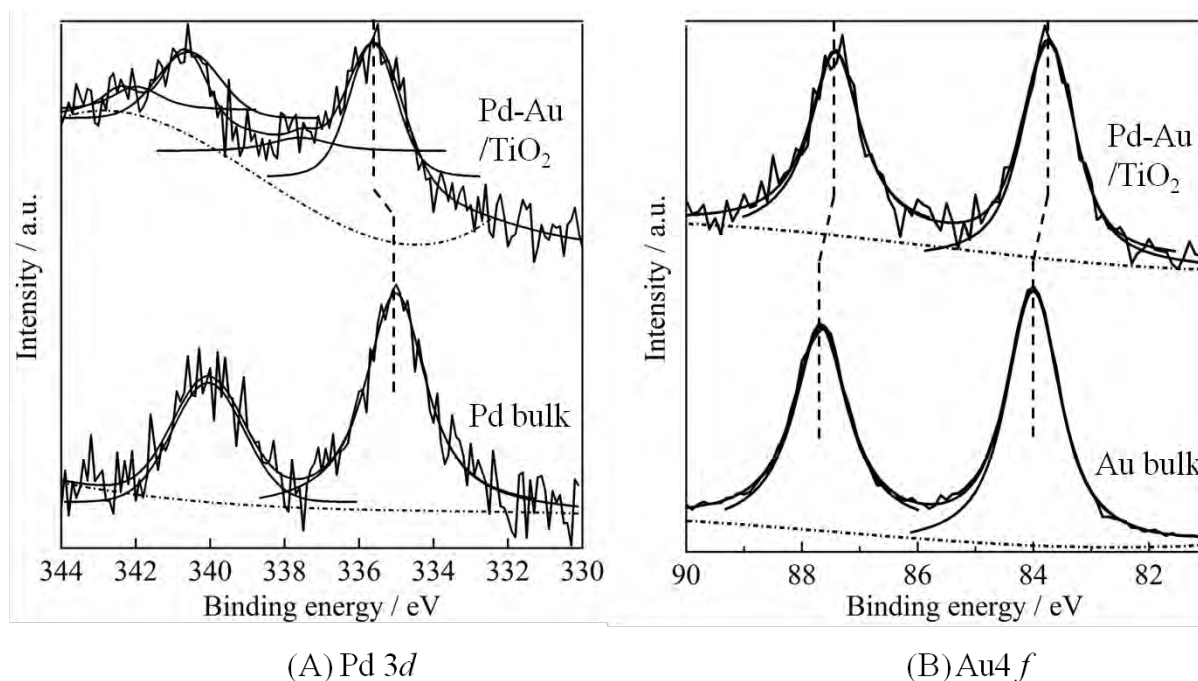


Figure 4. XPS profiles of the (A) Pd 3*d* and (B) Au 4*f* regions of Pd-Au/TiO₂ and Pd and Au bulks.

The XPS profiles of the Pd 3*d* (a) and Au 4*f* (b) regions of Pd-Au/TiO₂, as well as the Pd and Au bulks, are shown in Fig. 4. As shown in Fig. 4a, the Pd 3*d*_{5/2} and 3*d*_{3/2} peaks in the spectrum of the Pd-Au/TiO₂ catalysts are located at 336.19 ± 0.10 and 340.58 ± 0.10 eV, respectively,

exhibiting shifts toward the higher binding energy region compared to metallic Pd⁰. In contrast, the Au 4f_{7/2} and Au 4f_{5/2} peaks in the spectrum of the Pd-Au/TiO₂ photocatalyst are located at 87.43 ± 0.10 and 83.74 ± 0.10 eV, respectively (Fig. 4b), exhibiting shifts toward the lower binding energy region compared to metallic Au⁰. The shifts of the binding energy for Au and Pd in the Pd-Au/TiO₂ catalyst could be attributed to the charge transfer effect between them due to the formation of the Pd-Au alloy.

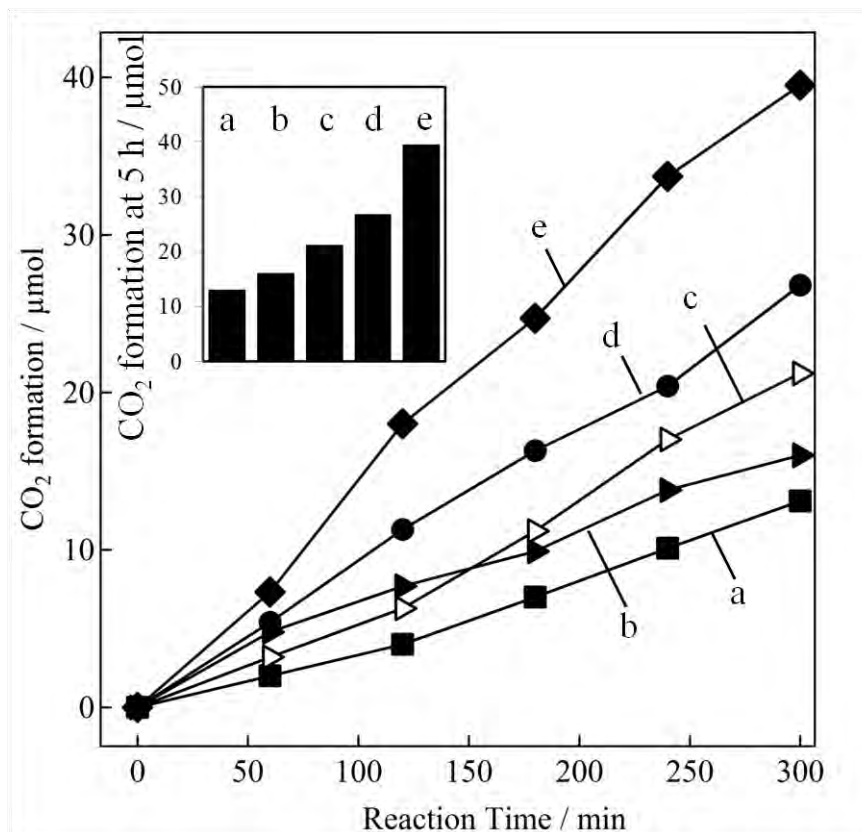


Figure 5. Time courses of CO₂ evolution during the decomposition of AcOH over (a) pure TiO₂, (b) Au/TiO₂, (c) Pd/TiO₂, (d) Pt/TiO₂ and (e) Pd-Au/TiO₂ photocatalysts suspended in aqueous AcOH in the presence of O₂ under full arc ($\lambda > 380$ nm). NP loading on TiO₂: 1.0 wt %.

The activity tests for photocatalytic AcOH decomposition on the prepared samples were carried out under UV-Vis light irradiation. Fig. 5 shows the amount of CO₂ production over different photocatalysts as a function of irradiation time. The pure TiO₂ sample shows a low CO₂ evolution rate (a, average rate: 2.49 $\mu\text{mol h}^{-1}$ between 0 and 300 min of irradiation time). The average CO₂ generation rates of the Au/TiO₂ (b), Pd/TiO₂ (c) and Pt/TiO₂ (d) photocatalysts were approximately 3.37, 4.06 and 5.32 $\mu\text{mol h}^{-1}$, respectively. Among the tested samples, the Pd-Au alloy NPs deposited on TiO₂ (d) shows the highest CO₂ generation rate of 8.18 $\mu\text{mol h}^{-1}$. The CO₂ generation rate of the Pd-Au NPs deposited on TiO₂ was approximately 2 times higher than that of the Pd NPs deposited on TiO₂. In addition, the Pd-Au/TiO₂ composites exhibited higher efficiency for the decomposition of AcOH than the benchmarked Pt/TiO₂. The higher photocatalytic activity of the composites could be attributed to the efficient oxidative decomposition of AcOH and/or reduction of O₂ on the Pd-Au NPs surface.

Conclusions

In summary, to accelerate the decomposition of AcOH, the bimetallic co-catalyst Pd–Au alloy was applied to the TiO₂ surface. Although it has been reported that many bimetallic alloy surfaces exhibit higher catalytic activities in homogeneous and heterogeneous chemical reactions, few publications have employed bimetallic alloy NPs as co-catalysts in photocatalysis reactions. In the present study, the Pd-Au alloy NPs were synthesized on TiO₂ photocatalyst surfaces by a co-photodeposition of Pd and Au with the assistance of UV light. On the basis of *p*XRD, TEM and XPS data, the formation of Pd-Au alloy NPs on a TiO₂ surface was confirmed. The photodeposited Pd-Au/TiO₂ exhibited a higher generation rate of CO₂ from the AcOH decomposition than the pure TiO₂, Pd/TiO₂, Au/TiO₂ or benchmarked Pt/TiO₂ photocatalysts.

Acknowledgments

This work was financially supported by the Strategic Research Base Development Program for Private Universities of the Ministry of Education, Culture, Sports, Science and Technology of Japan. The High resolution *p*XRD measurements were performed under the approval of the NIMS Beamline Station (Proposal 2014A4907). The authors are grateful to Dr. Masahisa Tanaka, National Institute for Materials Science, for the support of the XRD measurements.

References

1. P.V. Kamat, *Chem. Rev.*, **93**, 267 (1993).
2. S. Jin and F. Shiraishi, *Chem. Eng. J.*, **97**, 203 (2004).
3. S. Devipriya and S. Yesodhanan, *Sol. Energy Mater. Sol. Cells*, **309**, 348(2005).
4. A.L. Linsebigler, L. Guanquan and J.T. Yates, *Chem. Rev.*, **95**, 735 (1995).
5. M.S. Chen and D.W. Goodman, *Science*, **306**, 252 (2004).
6. K. Woan, G. Pyrgiotakis and W. Sigmund, *Adv. Mater.*, **21**, 2233 (2009).
7. M.A. El-Sayed, *Acc. Chem. Res.*, **34**, 257 (2001).
8. D. Astruc, F. Lu and J.R. Aranzas, *Angew. Chem. Int. Ed.*, **44**, 7852 (2005).
9. P. Pichat and M.A. Fox, in *Photoinduced Electron Transfer*, ed, M.A. Fox and M. Chanon, Elsevier, Amsterdam (1998).
10. K. Mori, K. Furubayashi, S. Okada and H. Yamashita, *RSC Adv.*, **2**, 1047 (2012).
11. S.L. Lee, J. Scott, K. Chiang and R. Amal, *J. Nanopart. Res.*, **11**, 209 (2009).
12. Z. Wu, Z. Sheng, Y. Liu, H. Wang, N. Tang and J. Wang, *J. Hazard. Mater.*, **164**, 542(2009).
13. J.K. Edwards, A. Thomas, A.F. Carley, A.A. Herzing, C.J. Kely and G.J. Hutchings, *Green Chem.*, **10**, 388 (2008).
14. X. Zhou, Y. Huang, W. Xing, C. Liu, J. Liao and T. Lu, *Chem. Commun.*, 3540 (2008).
15. A. Ayati, A. Ahmadpour, F.F. Bomoharam, B. Tanheai, M. Manttari and M. Sillanpaa, *Chemosphere*, **107**, 163 (2014).
16. A. Cybula, J.B. Priebe, M.M. Pohl, J.W. Sobezak, M. Schneider, A.Z. Jurek, A. Bruckner and A. Zaleska, *Appl. Catal. B: Environmental*, **152**, 202 (2014).
17. Z. Peng and H. Yang, *J. Am. Chem. Soc.*, **131**,7542 (2009).
18. S. Guo, S. Dong and E. Wang, *ACS Nano*, **4**, 547 (2009).

19. M. Hosgeini, T. Banakar, R. Cousin, A. Aboukais, B.L. Su, G. De Weireld and S. Siffert, *Appl. Catal. B: Environmental*, **111**, 218 (2012).
20. K. Mori, T. Araki, T. Takashi, S. Shironita and H. Yamashita, *Photochem. Photobiol. Sci.*, **8**, 652 (2009).
21. H. Yu, X. Wang, H. Sun and M. Huo, *J. Hazard. Mater.* **164**, 542 (2009).
22. Z. Zhang, S-W. Cao, Y. Liao and C. Xue, *Appl. Catal. B: Environmental*, **162**, 204 (2015).
23. B. Kraeutler and A.J. Bard, *J. Am. Chem. Soc.*, **99**, 7729 (1977).
24. W. Jr. Sluserk, B. Lalevic and N. Fuschillo, *J. Appl. Phys.*, **44**, 2891 (1973).
25. M. Ellner, *J. Less-Common Met.*, **78**, 21(1981).

Enhanced Oxygen Reduction Reactions and Stable Long-term Activity on TiO₂-supported Dealloyed PtCu Nanoparticles in Acidic Aqueous Solutions

Takao Gunji¹, Kengo Sasaki¹, Arockiam John Jeevagan¹, Shingo Kaneko²,
Toyokazu Tanabe¹, Futoshi Matsumoto¹

¹Department of Material and Life Chemistry, Kanagawa University, 3-27-1,
Rokkakubashi, Kanagawa, Yokohama, Kanagawa 221-8686, Japan

²Research Institute for Engineering, Kanagawa University,
3-27-1, Rokkakubashi, Kanagawa-ku, Yokohama, Kanagawa 221-8686, Japan

Abstract

Dealloyed PtCu nanoparticles (NPs) were prepared on titanium oxide (TiO₂) surfaces with chemical reduction of Pt and Cu ion precursors using a reducing agent in an organic solvent containing TiO₂, which was followed by an electrochemical dealloying process of potential cycling (-0.2~1.2 V *vs.* RHE). Dealloyed PtCu NPs/TiO₂ shows higher and substantial electrocatalytic activities towards oxygen reduction reactions (ORR) compared to conventional carbon black-supported Pt NPs (Pt NPs/CB). The current densities at 0.9 V (*vs.* RHE) were -4.0 and -2.0 mAcm⁻² on dealloyed PtCu NPs/TiO₂ and Pt NPs/CB, respectively.

Introduction

Current problems arising from the depletion of fossil fuels and air pollution following their combustion have captured the attention of scientists and policy makers world-wide.¹ The development of new energy sources and improvements in energy efficiency, generation, conversion and storage have become some of the most pressing issues confronting today's scientific community.² The use of fuel cells that directly convert chemical energy into electricity by using electrochemical reactions, which can reach efficiencies as high as 90%, has been presented as one of the most promising technologies.³ Recently, there has been an increased interest in polymer electrolyte membrane (PEM) fuel cells that use hydrogen gas (H₂) fuels and oxidants of oxygen gas (O₂). However, in these technologies, expensive electrocatalysts containing platinum (Pt) are required to produce fuel cells that satisfy demand from both an economic and environmental point of view. To spread the application of PEM to various areas, the oxidation reaction of H₂ and reduction reaction of O₂ (ORR) at the anode and cathode, respectively, have to be accelerated while at the same time decreasing the amount of Pt that is used as an electrocatalyst. Specifically, in order to accelerate the ORR kinetics to reach a practical usable level in fuel cells, the development of cathode ORR catalysts that can address cost and durability issues as well as sluggish ORR kinetics is needed. The partial^{4,5} and complete^{6,7} replacement of Pt metal and core-shell structures^{8,9} has attracted considerable interest on ORR. Many studies of enhancements to ORR have been reported.^{9,10} Alternately, dealloying, the selective dissolution of elemental components from Pt-based alloys, is currently being used to tailor the morphology and composition gradient of Pt-based alloy nanoparticles (NPs) for catalytic applications.^{11,12} It has been reported that the selective dissolution of the less-noble component from the NPs typically

results in an enhancement of the electrocatalytic reaction.¹³⁻¹⁵ For example, Strasser has demonstrated that electrochemical dealloying of non-noble base metals from base-metal-rich Pt bimetallics significantly alters the surface catalytic rates for ORR with Pt_{0.25}Cu_{0.75} alloy NPs.¹⁵ He explains the reason for the electrocatalytic enhancement with geometric effects and hypothesizes that the dealloying creates favorable structural arrangements of Pt atoms at the particle surface, such as additional active crystallographic facets or more favorable Pt-Pt interatomic distances for ORR. We directed our attention to the favorable structural arrangements of Pt atoms and hypothesize that dealloying of less-noble metals from Pt-based ordered intermetallic phases, such as PtPb and PtBi, which, in contrast to disordered alloys have definite compositions and structures, can produce unique and uniform crystallographic structures that can enhance ORR on the NP surfaces. In addition, we have recently reported that PtPb NPs with immobilized titanium oxide (TiO₂) showed substantial electrocatalytic activity for ORR.¹⁶ The nature of the support as well as the NP interactions with the support and the electronic structure of catalytic sites may all influence the observed accelerated electrochemical behavior. The synergistic effects of the favorable structural arrangements of Pt atoms by dealloying and the electronic interactions^{17,18} between dealloyed NPs and TiO₂ are expected to produce superior ORR activity. In this study, dealloyed NPs/TiO₂ were prepared with the PtCu ordered intermetallic NPs, followed by dealloying of Cu atoms from the PtCu ordered intermetallic NPs. The electrocatalytic performance of dealloyed NPs/TiO₂ for ORR was examined with respect to its activity and stability.

Experimental

1. Synthesis of PtCu ordered intermetallic NPs

Dichloro(1,5-cyclooctadiene)platinum(II) (Pt(COD)Cl₂, 0.0151 mmol, Sigma-Aldrich), Cu₁₀H₁₄CuO₄ (0.0227 mmol, Sigama-Aldrich) and TiO₂ (ST01, Ishihara Sangyo Kaisha,Ltd.) or Vulcan carbon black(CB, XC-72R, E-TEK) (0.020 g) were dissolved in a two-neck flask containing 15 mL of distilled tetrahydrofuran (THF) under a dry Ar atmosphere. Then, the mixture was stirred for 30 min. Again under a dry Ar atmosphere, 0.72 mmol of the reducing agent triethylborohydride was added into 20 mL of distilled THF. The reducing agent solution was then transferred into a syringe. The reducing agent solution was injected through the septum into the two-neck flask containing the stirred precursor solution, followed by stirring for 18 hrs. After stirring overnight, the solvent was distilled off at a reduced pressure to leave a dark-brown precipitate. The PtCu NPs/CB or PtCu NPs/TiO₂ were collected by centrifugation, washed sequentially with EtOH and water and finally dried under vacuum. The products were air-stable black powders.

2. Characterization of synthesized PtCu ordered intermetallic NPs on TiO₂

Powder X-ray diffractometry (*p*XRD) experiments were performed using CuK_α radiation (Rigaku RINT- UltimaIII; $\lambda = 0.1548$ nm) in increments of 0.02 degrees from 20 to 80 degrees. An obliquely finished Si crystal (non-reflection Si plate) was used as a sample holder to minimize the background. A 200 kV transmission electron microscope (TEM, JEM-2100F, JEOL) was used for evaluating the dispersion of NPs on TiO₂ and CB. The samples for the TEM experiments were prepared by dropping a methanol suspension of the sample powder onto a commercial TEM grid coated with a polymer film. The sample was dried thoroughly under a vacuum before observation. The loadings of Pt on the synthesized Pt NPs/WO₃ and PtPb NPs/WO₃ were estimated through

inductively coupled plasma-mass spectrometry (ICP-MS, Agilent, 7700x). X-ray photoelectron spectroscopy (XPS) measurements (JEOL, JP-9010 MC) were performed to examine the chemical states (Pt 4*f* and Cu 2*p*) of the catalyst. MgK α was used as the X-ray source with an anodic voltage (10 kV) and current (10 mA). All of the XPS spectra for the samples were obtained with a take-off angle at 45° relative to the specimens.

3. Electrochemistry

An aliquot of 1 mg NPs/CB or NPs/TiO₂ was suspended in a solution of 995 μ L of distilled water and 250 μ L of isopropyl alcohol. Additionally, 5 μ L of a 5% w/w Nafion[®] solution (EW: 1,100, Aldrich) in alcohol was added to this suspension. The resulting suspension was sonicated for 1 hr. The suspension was coated onto a 5-mm-diameter GC electrode. The ORR activities of Pt NPs/CB, Pt NPs/TiO₂, dealloyed- PtCu NPs/CB and PtCu NPs/TiO₂ were subsequently examined in O₂-saturated 0.1 M HClO₄ using a three-electrode cell with an Ag/AgCl (3 M NaCl) reference electrode and a salt bridge of NaClO₄. The electrochemical tests were performed at room temperature (23 \pm 1°C), at a sweep rate of 10 mVs⁻¹ and a rotation speed of 2000 rpm. The geometric area of the GC electrode was used to calculate the current density of ORR. The electrode potential measured with the Ag/AgCl reference electrode was converted to the value referred to reversible hydrogen electrode (RHE) in voltammograms. Pt NPs/CB (20 wt% Pt loading, E-TEK) was used as a control.

Results and discussion

Figure 1 shows the *p*XRD profiles for (a) as-prepared PtCu NPs/CB, (b) as-prepared PtCu NPs/TiO₂ and (c) TiO₂. The simulated *p*XRD patterns for the PtCu (hexagonal, P63/mmc, $a = b = 0.426$ nm, $c = 0.548$ nm) and Pt phase (face-centered cubic (fcc), Fm-3 m, $a = 0.3925$ nm) are indicated by the solid bars below the graph. The *p*XRD profile (a) exhibits two peaks at 25.0° and 43.5° that correspond to the (0 0 2) and (1 0 1) reflections of carbon, respectively. The peaks corresponding to the (2 0 0) and (2 2 0) reflections of pure PtCu (Fm-3 m, $a = 0.3925$ nm) indicated in the simulated *p*XRD peak pattern at the bottom of the figure can be seen at approximately 46.3° and 70.5°. The (1 1 1) peak observed around 41° for pure PtCu overlaps the (1 0 1) peak of carbon. The formation of PtCu ordered intermetallic phases on CB can be confirmed from the *p*XRD profile. In profile (b), the (1 1 1) peak that can be indexed to the hexagonal type structure of PtCu ordered intermetallic structure can be seen at 41.3°. All other peaks in profile (b) match the characteristic peaks for TiO₂ (c). The peak at 41.3° does not clearly match the simulated (1 1 1) peak of Pt. The formation of pure PtCu ordered intermetallic NPs on TiO₂ is barely confirmed from these results.

Figure 2 (A) and (B) show the TEM images obtained with (A) as-prepared PtCu NPs/CB and (B) PtCu NPs/TiO₂. PtCu NPs appear as dark spots that are uniformly dispersed on the CB and TiO₂. The distributions of the size of the PtCu NPs on CB and TiO₂ were evaluated on the basis of approximately 100 particles in the TEM images. The average diameters of the Pt NPs on CB and TiO₂ were calculated as 2.1 and 2.5 nm, respectively, and they exhibit a narrow particle-size distribution. ICP-MS showed that the average mole ratios of Pt to Cu for as-prepared PtCu NPs was Pt:Cu= 48-51:52-49 on TiO₂ and CB. The loadings Pt on as-prepared PtCu NPs/TiO₂ and PtCu NPs/CB were estimated to be 9.1% and 8.8%, respectively.

Figure 3 shows cyclic voltammograms for ORR obtained with PtCu NPs/CB(A) and PtCu NPs/TiO₂(B) at 0, 25, 50 and 100 cycles in a 0.1 M HClO₄ aqueous solution in the

potential region of 0.4-1.1 V (*vs.* RHE). For both of the NPs, the ORR curves shifted to the positive direction with the potential cycles, indicating the enhancement of the ORR. The ORR acceleration might be due to activation of the NP surfaces caused by electrochemical dealloying of Cu atoms from the NP surfaces during potential cycles. After 100 cycles, stable ORR curves could be observed on both of the NP surfaces.

Figure 4 shows linear-sweep voltammograms for ORR obtained with Pt NPs/CB (a), PtCu NPs/CB (b, after 100 cycles in 0.1 M HClO₄ aqueous solution), Pt NPs/TiO₂ (c) and PtCu NPs/TiO₂ (d, after 100 cycles in 0.1 M HClO₄ aqueous solution) in an oxygen-saturated 0.1 M HClO₄ solution. Here, CB-supported Pt NPs (a) were used as a control. The current densities at 0.9 V (*vs.* RHE) were -4.0, -3.9, -1.2 and -2.0 mAcm⁻² on dealloyed- PtCu NPs/TiO₂ and PtCu NPs/CB, Pt NPs/TiO₂ and Pt NPs/CB, respectively. Our results clearly indicate that the Pt atomic arrangement in the dealloyed PtCu NPs on CB and TiO₂ supports significantly enhances the ORR activity. Although the difference in the ORR activity between the dealloyed PtCu NPs on TiO₂ and CB cannot be recognized at 0.9 V, the ORR current density measured over 0.9 V with dealloyed PtCu NPs on TiO₂ is higher than the one observed with dealloyed PtCu NPs on CB. It has been reported that Pt NPs/TiO₂ enhance ORR in acidic solutions^{17,18}. Our Pt NPs/TiO₂ exhibited less ORR activity than conventional Pt NPs/CB. It is possible that the reason for the decrease in ORR activity of our sample is because of high resistivity in the TiO₂ particles (particle size < 25 nm) on which the dealloyed NPs are immobilized. The dealloyed PtCu NPs immobilized on high resistivity TiO₂ particles showed the highest ORR activity. This result indicates that if the resistivity of the TiO₂ support is reduced by thin TiO₂ layers immobilized on CB, the dealloyed PtCu NPs on TiO₂ will exhibit higher ORR activity. Strasser has reported that electrochemical dealloyed Pt_{0.25}Cu_{0.75} alloy NPs/CB show -3.1 mAcm⁻² for ORR in O₂-saturated 0.1 M HClO₄ aqueous solution.¹⁵ Our dealloyed NPs produced with a PtCu ordered intermetallic phase on TiO₂ show a significant enhancement in the ORR. The surface compositions of as-prepared and dealloyed PtCu NPs were evaluated with the results of XPS measurements. As mentioned above, the average mole ratios of Pt to Cu for as-prepared PtCu NPs was consistent with the desired value for a PtCu ordered intermetallic phase, Pt:Cu= 51.2:48.8. As predicted from the voltammograms, the mole ratios of Pt to Cu for dealloyed PtCu NPs after potential cycling for ORR increases to Pt:Cu= 78.2:21.8.

Figure 5 shows the changes in current densities for ORR at 0.9 V with potential cycling between 1.1 and 0.4 V on (a) Pt NPs/CB, (b) Pt NPs/TiO₂ (c) PtCu NPs/CB and (d) PtCu NPs/TiO₂ in O₂-saturated 0.1 M HClO₄ aqueous solutions. The electrodes that were treated with potential cycling in Fig. 3 were used in these experiments for evaluation of the durability of the NPs. The ORR current density of Pt NPs/CB decreased steeply with an increase in the ORR cycles. PtCu NPs/CB also exhibited a slow decrease in the ORR current. On the other hand, TiO₂-supported Pt and PtCu NPs maintained stable ORR current densities even after 500 cycles, indicating that these stable ORR current performances arise from the interactions between the TiO₂ support and the NPs during ORR.

Conclusions

Pt_xCu_y ordered intermetallic NPs have previously been used to form unique surface structures by the alloying of Cu atoms from the surface for enhancing ORR in acidic aqueous solutions^{15,19}. The dealloyed surface of Pt_xCu_y ordered intermetallic NPs have exhibited higher ORR activity than a conventional Pt NPs^{15,19}. However, stable ORR

activities on a dealloyed Pt_xCu_y surface have not been reported as far as we know. In this study, in order to improve the stability of the activity with high ORR activity, PtCu ordered intermetallic NPs were selected as an ordered structure in which less-noble metals were dealloyed from the NP surfaces to form Pt-rich dealloyed surfaces showing high ORR activity. In addition, the NPs were immobilized on TiO₂ supports to enable a strong electronic interaction^{17,18} between dealloyed NPs and TiO₂. Dealloyed PtCu NPs/TiO₂ showed higher and substantial electrocatalytic activity towards ORR when compared to conventional CB-supported Pt NPs. The current densities at 0.9 V (vs. RHE) were -4.0 and -2.0 mAcm⁻² on dealloyed PtCu NPs/TiO₂ and Pt NPs/CB, respectively. The activity and its stability are better than the results previously reported with PtCu NPs/CB¹⁹ and Pt_{0.25}Cu_{0.75} NPs/CB.¹⁵ The strong electronic interactions between dealloyed PtCu NPs and the TiO₂ support was confirmed to induce higher electrocatalytic activity and a substantial improvement in performance of dealloyed PtCu NPs/TiO₂ in ORR. The voltammograms obtained using a dealloyed PtCu NPs/TiO₂-fixed glassy carbon (GC) electrode for ORR contain some resistances because dealloyed PtCu NPs were deposited on high resistivity TiO₂ particles. In the future work, dealloyed PtCu NPs will be chemically deposited on small, thin TiO₂ particles that are prepared on CB or carbon nanotube to obtain ORR voltammograms that do not show resistance of TiO₂.

Acknowledgement

This work was financially supported by the Strategic Research Base Development Program for Private Universities of the Ministry of Education, Culture, Sports, Science and Technology of Japan.

References

1. M. Z. Jacobson, W. G. Colella and D. M. Golden, *Science*, **308**, 1901 (2005).
2. M. Granovskii, I. Dincer and M. A. Rosen, *J. Power Sources*, **157**, 411 (2006).
3. K. Sopian and W. R. W. Daud, *Renewable Energy*, **31**, 719 (2006).
4. J. Kim and Y. Lee, S. Sun, *J. Am. Chem. Soc.*, **132**, 4996 (2010).
5. Y. Kang and C.B. Murray, *J. Am. Chem. Soc.*, 7568 (2010).
6. Z. Yang, Z. Yao, G. Li, G. Fang, H. Nie, Z. Liu, X. Zhou, X. Chen and S. Huang, *ACS Nano*, **6**, 205 (2012).
7. J.L. Fernandez, D.A. Waish and A.J. Bard, *J. Am. Chem. Soc.*, **127**, 357 (2005).
8. X. Sun, D. Li, Y. Ding, W. Zhu, S. Guo, Z.L. Wang and S. Sun, *J. Am. Chem. Soc.*, **131**, 17298(2009).
9. S. Zhang, X. Zhang, G. Jiang, H. Zhu, S. Guo, D. Su, G. Lu and S. Sun, *J. Am. Chem. Soc.*, **136**, 7734 (2014).
10. J.X. Wang, H. Inada, L. Wu, Y. Zhu, Y.M. Choi, P. Liu, W.-P. Zhou and R.R. Adzic, *J. Am. Chem. Soc.*, **131**, 17298 (2009).
11. X. Li, Q. Chen, I. McCue, J. Snyder, P. Crozier, J. Erlebacher and K. Sieradzki, *Nano Lett.*, **14**, 2569 (2014).
12. D. Wang, Y. Yu, H.L. Xin, R. Hovden, P. Ercius, J.A. Mundy, H. Chen, J.H. Richard, D.A. Muller, F.J. DiSalvo and H.D. Abruna, *Nano Lett.*, **12**, 5230 (2012).
13. C. Du, M. Chen, W. Wang and G. Yin, *ACS Appl. Mater. Interface*, **3**, 3105 (2011).
14. J. Yu, Y. Ding, C. Xu, A. Inoue, T. Sakurai, and M. Chen, *Chem. Mater.*, **20**, 4548 (2008).
15. S. Koh and P. Strasser, *J. Am. Chem. Soc.*, **129**, 12624 (2007).

16. T. Gunji, G. Saravanan, T. Tanabe, T. Tsuda, M. Miyauchi, G. Kobayashi, H. Abe and F. Matsumoto, *Catalysis Science and Technology*, **4**, 1436 (2014).
17. J. Shim, C.-R. Lee, H.-K. Lee, J.-S. Lee and E.J. Cairns, *J. Power Sources*, **102**,172 (2001).
18. A. Kumar and V. Ramani, *ACS Catal.*, **4**, 1516 (2014).
19. H.-H. Li, C.-H. Cui, S. Zhao, H.-B. Yao, M.-R. Gao, F.-J. Fan and S.-H. Yu, *Adv. Energy Mater.*, **2**, 1182 (2012).

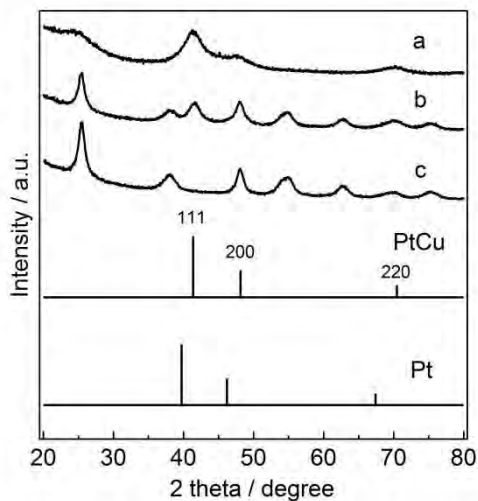


Figure 1. *p*XRD profiles of (a) PtCu/CB, (b) PtCu/TiO₂ and (c) TiO₂.

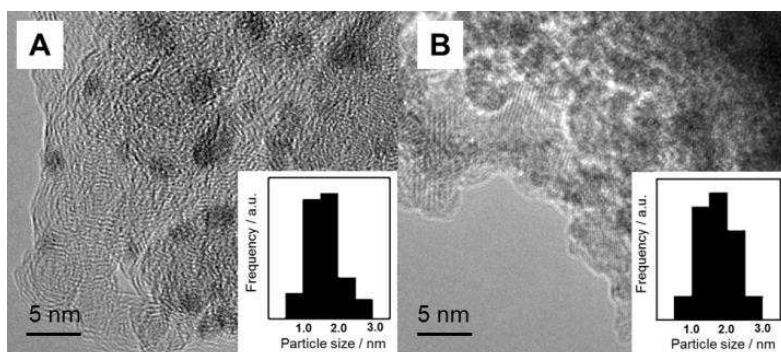


Figure 2. TEM images of (a) PtCu/CB and (b) PtCu/TiO₂. Inset: particle size distribution evaluated with the TEM images.

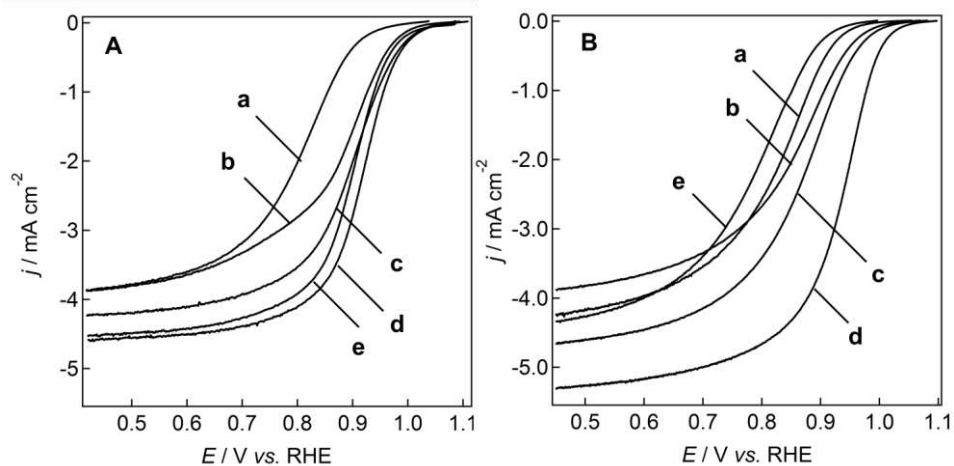


Figure 3. Cyclic voltammograms for ORR obtained with (A) PtCu NPs/CB and (B) PtCu NPs/TiO₂ at (a) 0, (b) 25, (c) 50 and (d) 100 cycles in O₂-saturated 0.1 M HClO₄ aqueous solution at 2000 rpm and 10 mV s⁻¹.

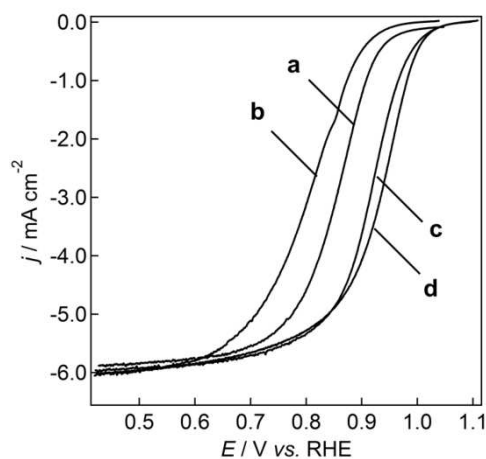


Figure 4. Comparison of ORR polarization curves obtained with catalyst-coated GC electrodes after 100 cycles in O₂-saturated 0.1 M HClO₄ aqueous solution at 2000 rpm and 10 mVs⁻¹. (a) Pt NPs/CB, (b) Pt NPs/TiO₂ (c) PtCu NPs/CB and (d) PtCu NPs/TiO₂.

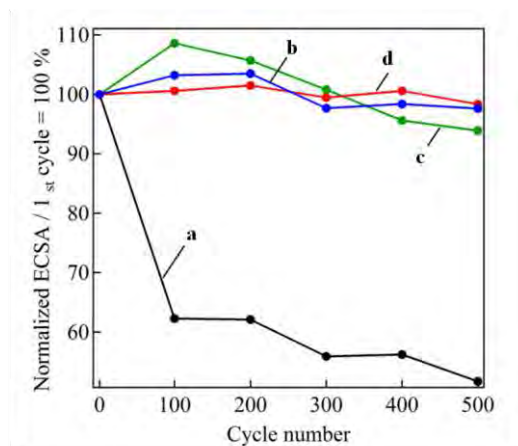


Figure 5. Change in the ORR current densities at 0.9 V with potential cycles after 100 cycles with (a) Pt NPs/CB, (b) Pt NPs/TiO₂ (c) PtCu NPs/CB and (d) PtCu NPs/TiO₂ in O₂-saturated 0.1 M HClO₄ aqueous solutions.

Development of Moving Micro-Machines That Use Hydrogen Peroxide and Glucose as Fuels

Takuya Kuzuoka¹, Tomohiro Kouno¹, Tomohiro Koyama¹, Yuji Morita¹,
Keitaro Yamazaki¹, Takao Gunji¹, Toyokazu Tanabe¹, Shingo Kaneko²,
Ben Nanzai¹, Futoshi Matsumoto¹

¹Department of Materials and Life Chemistry, Kanagawa University, 3-27-1,
Rokkakubashi, Kanagawa-ku, Yokohama, Kanagawa 221-8686, Japan

²Research Institute for Engineering, Kanagawa University,
3-27-1, Rokkakubashi, Kanagawa-ku, Yokohama, Kanagawa 221-8686, Japan

Abstract

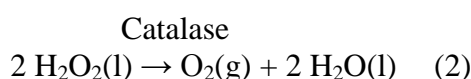
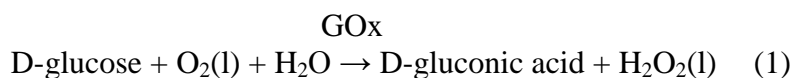
We developed micro-machines constructed using metal or polymer materials that move by converting the chemical energy of hydrogen peroxide (H₂O₂) and glucose to the mechanical energy of dioxygen (O₂) bubble impulses. The conversion process is based on electrochemical and enzymatic reactions. The micro-machines with enzymatic reactions exhibited a higher moving speed than the conventional micro-machines with electrochemical reactions. Our originally designed Au/Pt/cationic polymer/glucose oxidase (GOx)/catalase type micro-machines could move using glucose as fuel. However, the speed of movement achieved using glucose is much smaller compared with other micro-machines that move using H₂O₂ as fuel.

Introduction

Recently, micro- and nano-machines with components at or near the micro- and nano-meter scale have attracted significant attention. This research area has the potential for micro- and nano-machines to be applied as useful tools in various aspects of our daily life such as drug delivery systems, actuators, micro- and nano-robots (1-3). One promising application is the fabrication of micro- and nano-robots that can independently move and work by continuously consuming energy. However, this application still faces the issue of which energy sources to use and how to continuously supply the energy to the micro- and nano-machines. To our knowledge, Ismagilov was the first to report a system in which plates moved under the impulse of dioxygen (O₂) bubbles that were generated using platinum-catalyzed decomposition of hydrogen peroxide [2H₂O₂ (l) + O₂ (g) → 2H₂O(l)] (4). After his initial research, a significant amount of research was reported (5-7). For example, Wang and co-workers suggested a widely accepted bipolar electrochemical mechanism (“self-electrophoresis”) to achieve self-propulsion of bimetallic catalytic nanomotors with a bi-segmented nanowire to induce electromigration of protons from one end of the metal to another in an electrical double layer, which surrounds the nanowire (8). The Ozin group fabricated the catalytic conical tube microjet engines that operate based on the impulse of O₂ bubbles (the bubble-driven mechanism) (9), which is similar to the work of Ismagilov. In addition, Wang has fabricated the catalytic conical tube microjet engines (a hollow body type) by sequentially depositing platinum and gold on an etched silver wire template, followed by template dicing and dissolution (5).

In this study, to examine unsolved problems of the developed machines and motors we fabricated four types of micro-machines, as shown in Fig. 1. The unsolved problems include movement speed, toxicity of metals used as materials for the machines and

energy sources used by the machines to move or work (most of the developed machines can move when H_2O_2 is dissolved in the test solution where the machines are immersed in), when the application of micro-machines to human bodies is considered. Fabrication of an Au/Pt (outside wall: Au, inside wall: Pt) metal type micro-machine [Fig. 1-(a)] and its movement have been reported by Wang (5). We also attempted to prepare an Au/Pt metal type micro-machine to compare the movement rate with other three micro-machines that we originally prepared. The Au/Pt metal type micro-machine operates according to the electrochemical reaction of hydrogen peroxide (H_2O_2) on the Pt and Au metal surfaces. Specifically, H_2O_2 is reduced on Au metal surfaces to H_2O . Furthermore, the continuous formation of O_2 bubbles on Pt, which is the driving force of the micro-machines, occurs by oxidation of H_2O_2 on Pt metal surfaces. The second type of micro-machine based on Pt/Au/thiol/catalase [Fig. 1-(b)] is similar to the Au/Pt metal type (a). Specifically, the continuous formation of O_2 bubbles by oxidation of H_2O_2 on catalase molecules, which are attached on the Au inside wall in the hollow body of the micro-machine, can move the micro-machine. Thiol compounds that adsorb on the Au surface and a glutaraldehyde linker that reacts with the adsorbed thiol compounds fix the catalase molecules on the Au surface of the inside wall. The next micro-machine type [Fig. 1-(c)], the polymer hollow-type body design, was considered to lighten the hollow-type body to improve its movement rate and because the nano- and micro-meter sized Au and Pt metals are toxic to human bodies. The walls of the polymer hollow-type body are composed of two types of polymer layers. The inside wall is the photoresist polymer layer A that contains a compound with amino groups. The polymer layer B in the outside wall is composed of only the photoresist polymer. Amino groups that exist on the polymer layer A were used to fix catalase on the inside wall surface in the polymer hollow-type body with a glutaraldehyde linker. The Au/Pt/cationic polymer/glucose oxidase (GOx)/catalase type micro-machine [Fig. 1-(d)] uses glucose as a fuel to move in glucose solutions. The following serial reactions (eq. 1 and 2) form O_2 bubbles to move the micro-machine via redox reactions of glucose in the test solution.



We used the layer-by-layer (LbL) method to fix a large number of GOx and catalase molecules on the inside wall of the micro-machine. The LbL assembly consists of the sequentially adsorbed complementary multivalent molecules on the surface, which occurs by either electrostatic or non-electrostatic interactions (10). In the Au/Pt/cationic polymer/GOx/catalase type micro-machine, which was based on the electrostatic interactions between the cationic polymer and enzyme molecules (GOx or catalase), the alternating multilayers of the cationic polymer layer and the enzyme layer were accumulated on the Pt inside wall, as shown in Fig. 1-(d).

The objectives of the present study are to select materials to construct various types of micro-machines, to optimize preparation conditions (concentrations of chemicals and reaction times when micro-machines are constructed) and to compare the movement rates and the paths traced by moving micro-machines among four micro-machine types. In addition, the movement of the Au/Pt/cationic polymer/GOx/catalase type micro-machine,

which was designed as a micro-machine for moving in human blood using glucose as fuel, is demonstrated in this paper.

Experimental

1. Preparation of micro-machine shapes

A silver (Ag) wire (0.5 mm diameter, Nilaco, Japan) was dipped in a 25 wt% nitric acid aqueous solution for 5 s and was then removed from the nitric acid solution. The dipping and pulling process was repeated until the tips of the Ag wires were sharp and pointy due to acid etching. First, platinum (Pt) and then gold (Au) (or Au and, then, Pt) were deposited on the etched Ag wire using Pt and Au electrodeposition baths (PTP-6 for Pt deposition and Eco-gold for Au deposition, Nissin Kasei Co., Ltd., Japan). For the electrodeposition of Pt and Au on the Ag wire, a constant current density of 0.5 Adm^{-2} was used. After the deposition of Pt and Au (or Au and then Pt), the deposited Au/Pt/Ag wires were cut into 500 μm long segments with a cutter using a microscope. The 500 μm long Au/Pt/Ag wires were immersed again in a 25 wt% nitric acid aqueous solution for 1 day to dissolve the Ag cores. Finally, the hollow bodies composed of a Pt inside wall and an Au outside wall (or vice versa) were obtained [Fig. 2-(a) and (b)]. As seen in Fig. 2-b, the Pt and Au layers are deposited on the inside and outside walls of the hollow bodies, respectively. In the catalase-fixed hollow bodies, an Au layer was formed as the inside wall to fix the catalase molecules using thiol compounds that spontaneously adsorb on Au surfaces.

To prepare the hollow bodies with polymer materials, first, the etched Ag wires were dipped into a photoresist (FPPR-200, Fuji Chemicals Industrial Co., Ltd. Japan) solution containing 1,10-diaminodecane (1 wt%, Wako, Japan). Then, the wires were dried under air to form polymer layer A, which contains amino groups of 1,10-diaminodecane. In the next step, the polymer-layer-coated Ag wires were dipped into a 1,10-diaminodecane-free photoresist solution to form polymer layer B on top of polymer layer A and were then dried under air. In each step, the photoresist layers were baked at a low temperature to evaporate residual solvent. The photoresist layer-coated Ag wires were exposed to ultraviolet light through a metal mask (Fig. 2-c). The ultraviolet light-exposed resist areas were removed by rinsing with a rinsing solvent (FPPR-D, Fuji Chemicals Industrial Co., Ltd. Japan); then, the 500 μm long photoresist layers were left on the Ag wire surfaces (Fig. 2-d). The photoresist polymers/Ag wires were immersed again in a 25 wt% nitric acid aqueous solution for 1 day to dissolve the Ag cores. The polymer hollow bodies were formed (Fig. 2-e and f). The photograph (f) indicates hollow body formation using polymer materials.

2. Modification of the hollow body micro-machines

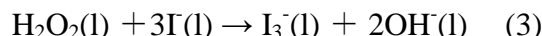
The Pt/Au metal hollow bodies (outside: Pt, inside: Au) were immersed into a 0.024 wt% 11-amino-1-undecanethiol (11A1UT, Wako, Japan)/ethanol solution for 24 h to adsorb 11-amino-1-undecanethiol to the Au surface. For comparison, a modification of 2-aminoethanethiol and 7-amino-1-heptanethiol (Wako, Japan) was also examined as a starting material for fixing catalase on the Au surfaces. After rinsing it with ethanol, a 1% glutaraldehyde aqueous solution was reacted for 2 h with 11A1UT-adsorbed Pt/Au to modify the amino groups of the 11A1UT molecules. The modified ends of the 11A1UT molecules that were adsorbed on the Au surfaces were reacted for 1 h with the amino groups existing on the surface of catalase molecules, resulting in the fixation of catalase molecules on the Au inside wall of the Pt/Au hollow bodies.

In the polymer-type hollow bodies, the amino groups existing on the inside walls, which were composed of polymer layer A and an amino group, were used to fix the catalase molecules. Similar to the case of modification with 11A1UT, glutaraldehyde was used as a linker to bind catalase molecules to polymer layer A.

Fabrication of the Au/Pt/cationic polymer/GOx/catalase type micro-machines was performed using the layer-by-layer method with the cationic polymers (polyethyleneimine (PEI, Wako, Japan), polyallylamine (PAMN, Nittobo Medical Co., Ltd., Japan), and polyacrylamide (PAMD, Wako, Japan) to assemble the GOx and catalase layers on the Pt inside layer of the Au/Pt hollow bodies. In total, 50 mg mL⁻¹ of the GOx and catalase phosphoric buffer aqueous solutions (pH 7.4) were prepared. The cationic polymer solutions of PEI, PAMN and PAMD were prepared by dissolving 50 mg of cationic polymers in 1 mL of water. The Au/Pt hollow bodies were immersed in the cationic polymer solutions for 5 min. After the Au/Pt hollow bodies were removed from the cationic polymer solutions, the Au/Pt hollow bodies were immersed in the GOx solution for 5 min and were then removed from the solution. The process of dipping into the cationic polymer or GOx solutions was repeated 10 times to form a GOx/cationic polymer multilayer on the Pt inside wall. A catalase/cationic polymer multilayer was formed on the GOx/cationic polymer multilayer on the Pt surface by repeating the catalase and cationic polymer adsorption process 10 times.

3. Movement evaluation of the micro-machines

For the movement tests, the prepared micro-machines were placed in 9 cm diameter petri dishes filled with 3 wt% H₂O₂ (Kanto Chemical Co. Inc., Japan) or 1 M D(+)-glucose (Junsei Chemical Co., Ltd., Japan) aqueous solutions. The petri dishes were placed on a vibration-isolation table to prevent micro-machines from moving due to vibrations of the test solutions. The paths traced by the moving micro-machines were recorded using a digital camera for 30 min. A poly(oxyethylene)octylphenyl ether surfactant (TritonX-100, Dow Chemicals) was added to the test solution (1 wt% Triton X-100 solution) for the movement test of the Au/Pt metal type micro-machines to remove the O₂ bubbles from the surface of the hollow metal bodies. To compare the H₂O₂ amount formed during the reaction of glucose and molecular dioxygen (O₂) on the GOx fixed on the inside wall of the micro-machines, a quantitative analysis of H₂O₂ formed in the micro-machines, where only the GOx molecules were fixed on the inside wall of the micro-machines, was performed based on the following reaction (3):



The I₃⁻ concentration was determined using the absorption coefficient (2.6×10⁴ M⁻¹ cm⁻¹ at 350 nm) of I₃⁻. From the I₃⁻ concentration, the H₂O₂ concentration was estimated based on an assumption that all H₂O₂ formed in the test solution react with I⁻ ions.

Results and discussion

The selection of the thiol compounds used for the Pt/Au/thiol/catalase type micro-machine and the optimization of the modification time of the thiol compounds on the Au inside wall were examined with 2-aminoethanethiol, 7-amino-1-heptanethiol and 11A1UT, with a modification time of 3-24 h. The optimized conditions were determined using the average movement speed of the fabricated micro-machines in H₂O₂ solutions for 5 min. 11A1UT and a 24 h modification time for 11A1UT were selected. The compounds with amino groups (2-aminoethanethiol, 1,10-diaminodecan, 3-

phenylpropylamine, n-dodecylamine) that were mixed in polymer layer A on the inside wall of the polymer/catalase type micro-machine were also examined, and 1,10-diaminodecan was chosen for the movement speed evaluation of the Au/Pt/cationic polymer/GOx/catalase micro-machines. Figure 3 shows the paths traced by the Au/Pt metal type moving micro-machines, which were recorded for 1 min using a digital camera. To confirm that the Au/Pt metal type micro-machines move due to electrochemical reaction of H_2O_2 on the Pt inside and Au outside walls and to examine the effectiveness of the addition of Triton X-100 surfactant to the H_2O_2 test aqueous solutions on the movement speed of micro-machines, the mobility of the Au hollow type and Au/Pt type micro-machines was evaluated in the H_2O_2 and H_2O_2 -free solutions and the H_2O_2 solution in the presence or absence of the Triton X-100 surfactant. From Fig. 3, it is clear that the conditions that exhibited the largest movement distance in 1 min were a combination of the Au/Pt type micro-machine, the H_2O_2 solution and the addition of surfactant to the test solution, which indicates the necessity to move the micro-machines faster.

Figure 4 shows the comparison of the movement distances for 1 min of (a) a conventional Au/Pt metal type, (b) a Pt/Au/thiol/catalase type and (c) a polymer/catalase type micro-machine in 30 wt% H_2O_2 aqueous solutions. All three micro-machine types randomly moved in the H_2O_2 test solution. Although there was a small difference in the paths traced by the moving micro-machines, the paths of the Pt/Au/thiol/catalase type and polymer/catalase type micro-machines in H_2O_2 solutions draw circles compared with the Au/Pt type micro-machine. Even the O_2 bubble formation from the inside walls of the Pt/Au/thiol/catalase type and polymer/catalase type micro-machines with enzyme reactions realizes a circular orbital. From the results in Fig. 4, it is clear that the micro-machines can go in straight lines in test solutions by improving bubble formation uniformity in the inside walls. Regarding the movement distance in 1 min, the Pt/Au/thiol/catalase type micro-machine moved the longest distance among the three micro-machine types. The micro-machine type that moved the second longest distance is the polymer/catalase type micro-machine. It is found that the use of enzymatic reaction to move the micro-machines is the best choice. The polymer/catalase type micro-machine would move a longer distance by increasing the amount of catalase fixed on inside walls of the polymer/catalase type micro-machine by optimizing the polymer material and the compounds contained on the sidewall of the polymer layer A. In subsequent experiments, the movement direction control of micro-machines was examined, as shown in Fig. 5. In Fig. 5, the concentrated H_2O_2 solutions were injected into the H_2O_2 -free aqueous solutions to make the H_2O_2 concentration gradient in the test solutions. The Pt/Au/thiol/catalase type micro-machine could climb up the H_2O_2 concentration gradient from a low concentration area to a high concentration area. The Pt/Au/thiol type micro-machine that was not modified by catalase, which was a blank sample, did not move in the concentrated H_2O_2 solution injection point direction. The difference in behavior of the Pt/Au/thiol/catalase and Pt/Au/thiol type micro-machines clearly suggests the capability to control the movement direction of the Pt/Au/thiol/catalase type micro-machine.

Finally, the preparation of a micro-machine that can move using glucose as a fuel was tested by our enzymatic reaction-based micro-machine design. As mentioned in the introduction, the sequential GOx and catalase reactions use glucose molecules as fuel to generate impulses of dioxygen (O_2) bubbles in the inside walls of the micro-machine, and the LbL method was applied to fix GOx and catalase on the inside walls. The comparison of the H_2O_2 amount formed in the multilayer GOx and cationic polymer layers on the inside walls of the Pt, Au and Ag hollow body types of the micro-machine to determine

the best cationic polymer and material to use as the inside wall is shown in Fig. 6. The dotted line in Fig. 6 corresponds to the H_2O_2 amount consumed by the Pt/Au/thiol/catalase hollow body in 5 min. Specifically, the amount of H_2O_2 of $0.9 \mu\text{mol}$ is the H_2O_2 amount required for a hollow body to move. Thus, this amount should be formed in the inside walls by the reaction between GOx and glucose. The combination of the cationic polymer and the inside wall material, where an amount of more than $0.9 \mu\text{mol}$ of H_2O_2 can be formed, was examined. From the nine combinations of cationic polymers and metals, only the combination of PAM and Pt produced more than $0.9 \mu\text{mol}$ of H_2O_2 in 5 min. In addition, because the combination of PAM and Au did not form a large amount of H_2O_2 compared with PAM and Pt, the Au metal was used as the outside wall material to inhibit bubble formation on the outside wall surface. Using the LbL method, the Au/Pt hollow body that was modified with PAM and GOx was sequentially modified with PAM and catalase to form the multilayer of cationic polymer and catalase layers on the multilayer of PAM/GOx. The mobility of the Au/Pt/cationic polymer/GOx/catalase type micro-machine with H_2O_2 as a fuel was confirmed. The Au/Pt/cationic polymer/GOx/catalase type micro-machines moved using H_2O_2 , with a movement rate comparable with that of the Pt/Au/thiol/catalase type micro-machine. The two results [1) that the Au/Pt hollow body modified with PAM and GOx could form the necessary amount of H_2O_2 via the enzymatic reaction between glucose and O_2 to move the micro-machine and 2) that the Pt/Au/cationic polymer/GOx/catalase type micro-machine could move with H_2O_2] indicate that the Au/Pt/cationic polymer/GOx/catalase type micro-machine can move using glucose molecules dissolved in the test solution as a fuel. Unfortunately, the movement examination of the Au/Pt/cationic polymer/GOx/catalase type micro-machine did not show any dynamic movement compared with the Pt/Au/thiol/catalase type micro-machine. However, the Au/Pt/cationic polymer/GOx/catalase type micro-machine demonstrated movement in the glucose solution in the absence of H_2O_2 . Figure 7 is the movement rate summary of the four micro-machines examined in this study. The Au/Pt/cationic polymer/GOx/catalase type micro-machine exhibited the lowest performance among the four examined micro-machines. Although the functions of GOx and catalase in cationic polymer/GOx/catalase multilayers were confirmed to generate movement similar to that of the Pt/Au/thiol/catalase type micro-machine, we believe that the unexpected result occurred because the sequential reaction of GOx and catalase [eq. (1) and (2)] did not effectively collaborate to form a large amount of O_2 bubbles in the inside walls of the Au/Pt/cationic polymer/GOx/catalase type micro-machine. The optimization of amount of GOx and catalase fixed on the inside walls and the order of the GOx and catalase layers in the multilayers (e.g., cationic polymer/GOx/cationic polymer/catalase/cationic polymer), will be examined as the next step of our research.

Conclusions

In this study, the three types of micro-machines were prepared with a mild method using Ag wire, metal deposition and dissolution of core Ag wire to fabricate hollow body type micro-machines. The Pt/Au/thiol/catalase and polymer/catalase type micro-machines exhibited higher movement rates compared with a conventional Au/Pt type micro-machine. The use of an enzymatic reaction to decompose H_2O_2 to O_2 was effective for the preparation of hollow body type micro-machines. The enzymatic reaction type micro-machine was applied to examine the movement of the hollow type micro-machine in a glucose solution in the absence of H_2O_2 . Micro-machine movement using glucose was

confirmed. However, the movement speed was much lower than that of the other three micro-machines. The design modification of the GOx and catalase layers in the hollow body type micro-machine will be examined in detail in subsequent studies.

References

1. S.M. Oja, M. Wood, B. Zhang, *Anal. Chem.*, **85**, 473 (2013).
2. A. Rajendran, M. Endo, K. Hidaka, H. Sugiyama, *J. Am. Chem. Soc.*, **135**, 1117 (2013).
3. G. Bottari, O. Trukhina, M. Ince, T. Torres, *Coord. Chem. Rev.*, **256**, 2453 (2012).
4. R.F. Ismagilov, A. Schwartz, N. Bowden, G.M. Whitesides, *Angew. Chem. Int. Ed.*, **41**, 652 (2002).
5. K.M. Manesh, M. Cardona, R. Yuan, M. Clark, D. Kagan, S. Balasubramanian, J. Wang, *ACS Nano*, **4**, 1799 (2010).
6. J. Wang, *ACS Nano*, **3**, 4 (2009).
7. Y. Hong, M. Diaz, U.M.C-Figueroa, A. Sen, *Adv. Funct. Mater.*, **20**, 1568 (2010).
8. Y. Wang, R.M. Hernandez, D.J. Bartlett, J.M. Bingham, T.R. Kline, A. Sen, T.E. Mallouk, *Langmuir*, **22**, 10451 (2006).
9. S. Fournier-Bidoz, A.C. Arsenault, I. Manners, G.A. Ozin, *Chem. Commun.*, **4**, 441 (2005).
10. J. Borges, J. mano, *Chem. Rev.*, **114**, 8883 (2014).

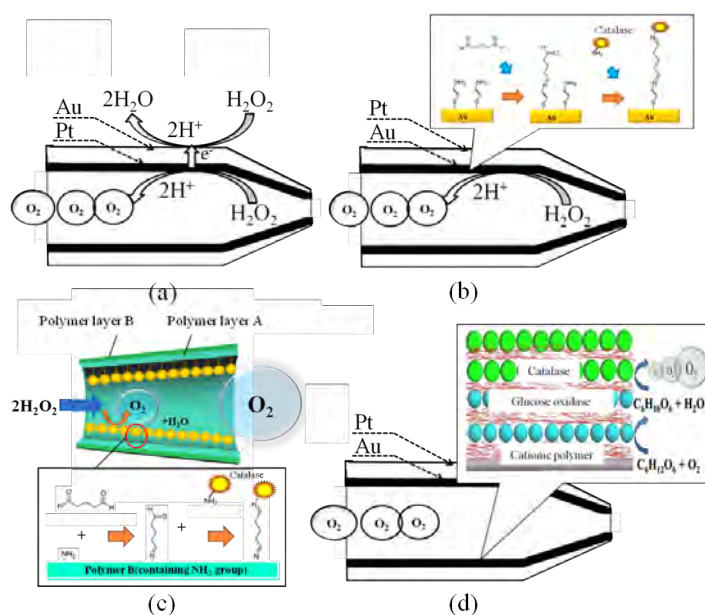


Fig. 1 Schematic depictions of four-types of micro-machines fabricated in this study. The (a) Au/Pt metal, (b) Pt/Au/thiol/catalase, (c) Polymer/catalase, and (d) Au/Pt/cationic polymer/GOx/catalase types.

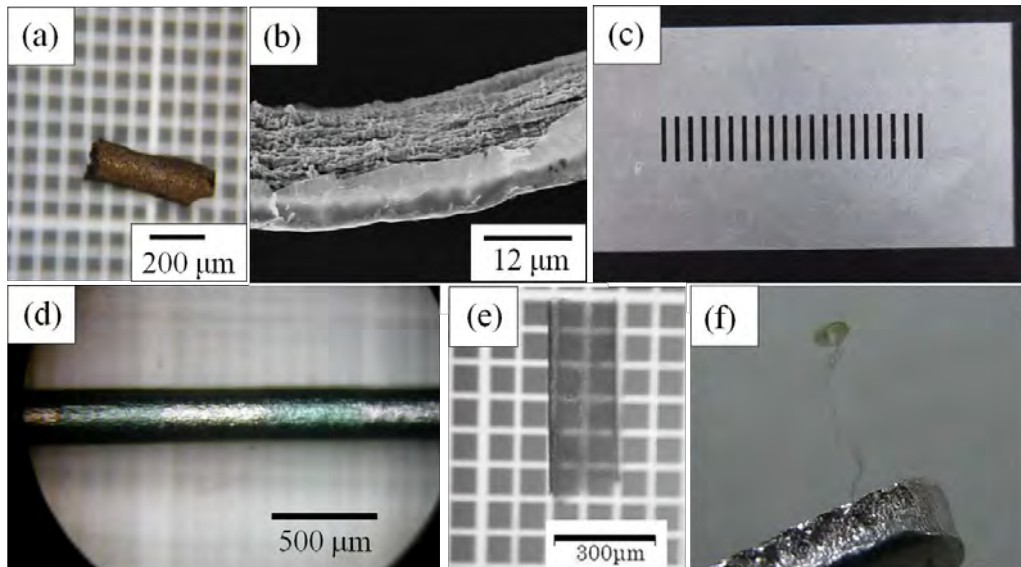


Fig. 2 Photographs of the micro-machine: The (a, b) Pt/Au/thiol/catalase and (e, f) Polymer/catalase types. (b, f): a cross-sectional image of the Pt/Au/thiol/catalase type micro-machine. (c) A metal mask with 500 μm gaps for preparing a thin resist layer (length: 500 μm) on an Ag wire. (d) A photograph of an Ag wire with thin 500 μm long resist layers.

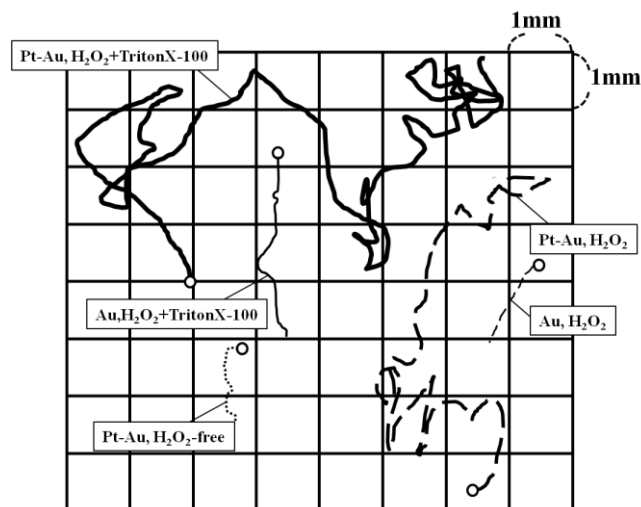


Fig. 3 One minute time courses of the fabricated Au/Pt and Au metal type micro-machines under various conditions. The circle (O) is the starting point for each micro-machine. The concentration of H_2O_2 in the test solution is 30 wt%.

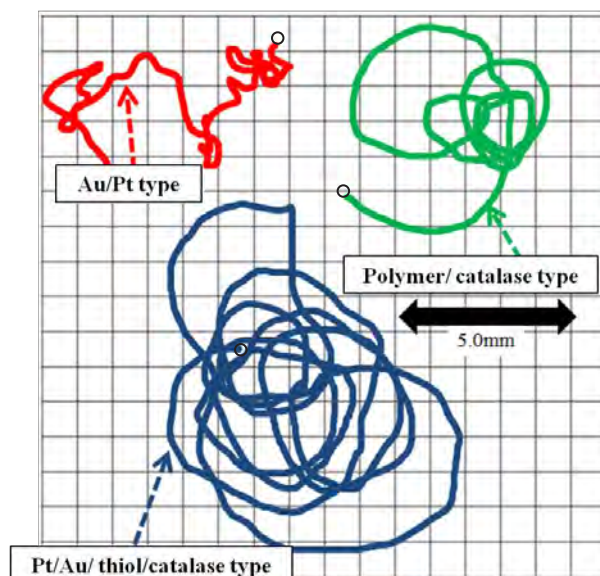


Fig. 4 One minute time courses of the fabricated (a) Au/Pt metal, (b) Pt/Au/thiol/catalase, and (c) Polymer/catalase type micro-machines in a 30 wt% H_2O_2 aqueous solution. The circle (O) is the starting point for each micro-machine.

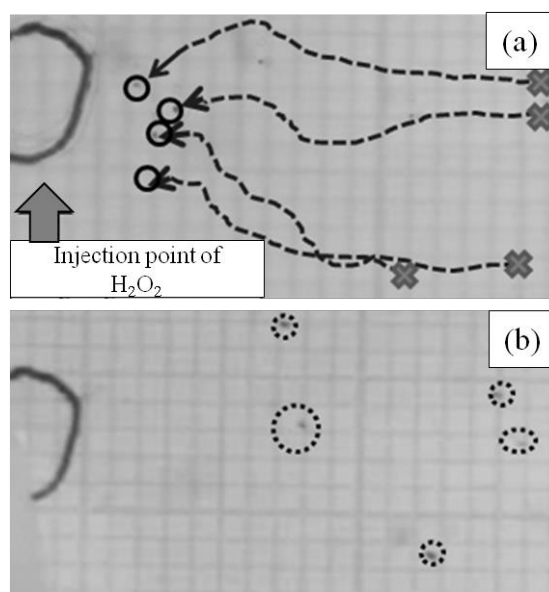


Fig. 5 Photographs indicating the time courses of the fabricated Pt/Au/thiol/catalase type micro-machines after injecting H_2O_2 solution at the injection point. Examination with the (a) Pt/Au/thiol/catalase and (b) Pt/Au/thiol micro-machines. X and O are the starting points and positions after 1 min for each micro-machine, respectively.

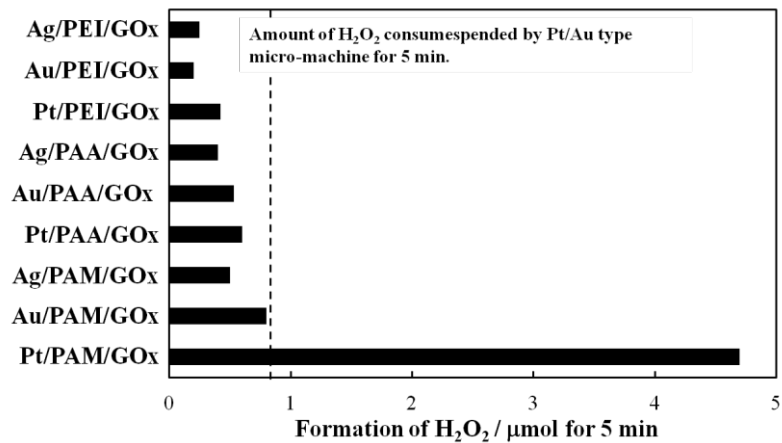


Fig. 6 Amount of H₂O₂ formed on the micro-machine in which glucose oxidase was fixed with PEI, PAA and PAM cationic polymers. The inside walls were prepared using Ag, Au and Pt metals. The concentration of glucose is 0.1 M in aqueous solutions.

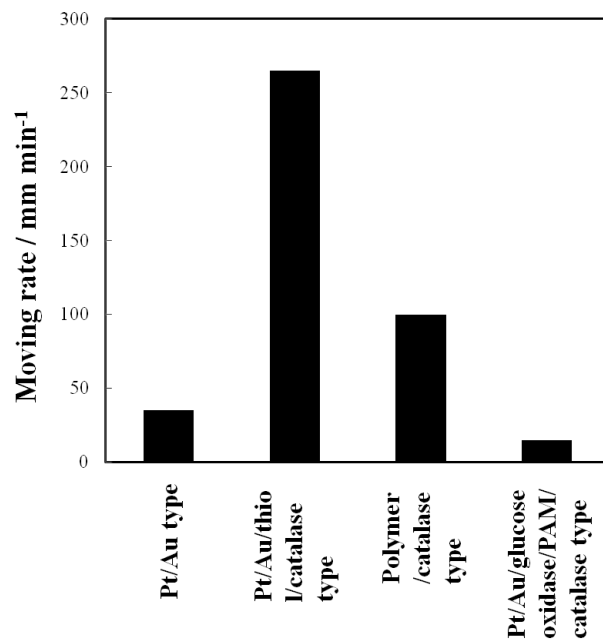


Fig. 7 Movement rate summary of the Au/Pt, Pt/Au/thiol/catalase, Polymer/catalase and Au/Pt/PAM/GOx/catalase type micro-machines in a 30 wt% H₂O₂ aqueous solution.

Preparation of Ordered Intermetallic PtBi co-Catalyst Nanoparticles/WO₃ and its Photocatalytic Activity towards the Decomposition of Acetic Acid

Takao Gunji¹, Masanari Hashimoto¹, Toyokazu Tanabe¹,
Shingo Kaneko² and Futoshi Matsumoto*¹

¹Department of Material and Life Chemistry, Kanagawa University, 3-27-1,
Rokkakubashi, Kanagawa, Yokohama, Kanagawa 221-8686, Japan

²Research Institute for Engineering, Kanagawa University,
3-27-1, Rokkakubashi, Kanagawa-ku, Yokohama, Kanagawa 221-8686, Japan

Abstract

The ordered intermetallic PtBi, which has a NiAs type structure (NiAs-type structure; P63/mmc, $a = b = 0.431$ nm; $c = 0.549$ nm), was prepared on the surface of tungsten oxide (WO₃) using the photodeposition method and polyol method. The prepared ordered intermetallic PtBi nanoparticles (NPs) used as co-catalyst showed much higher photocatalytic activity towards the decomposition of acetic acid (AcOH) under visible light irradiation ($\lambda > 420$ nm) than that observed with photodeposited Pt NPs/WO₃.

Introduction

The photocatalyst tungsten oxide (WO₃) has been intensively investigated for use in environmental remediation because of its highly efficient adsorption of visible light and its valence band potential that is similar to that of TiO₂. However, WO₃ cannot be used as a photocatalyst for the photodecomposition of volatile organic compounds without a co-catalyst because its conduction level (+0.5 V vs. NHE) is slightly negative when compared with that for the two electron reduction reaction (+0.68 V vs. NHE).¹ Co-catalyst loaded WO₃ photocatalyst surfaces such as Pt² and Pd³ have proved to be an effective approach to promote charge separation and transfer, suppress charge recombination and facilitate the multi oxygen reduction reaction. As a result, it exhibits a higher photocatalytic activity for the decomposition of organic compounds under visible light irradiation.^{2,3}

Recently, we reported that ordered intermetallic compound PtPb nanoparticles (NPs) used as a co-catalyst for the WO₃ photocatalyst effectively decompose various organic compounds such as acetic acid (AcOH) and formaldehyde.⁴ To explain this observed enhancement of photocatalytic reactions, we suggest that because the ordered intermetallic compound PtPb can also electrochemically oxidize formic acid, methanol and ethanol on the WO₃ photocatalyst,^{5,6} the PtPb NPs work as a co-catalyst for the oxidation reaction. However, the Pb atoms contained in the ordered intermetallic PtPb NPs are well-known to be poisonous to human health, damaging the nervous system and causing brain disorders. Although the PtPb NPs exhibit attractive behavior for photodecomposition, its employment for environmental conservation cannot be permitted. An alternative to PtPb NPs that exhibits similar or higher photodecomposition activities for organic compounds under visible light irradiation should be identified and developed.

PtBi ordered intermetallic NPs have attracted much interest as an alternative to PtPb because it exhibits electrochemical behavior close to that of PtPb NPs but is low-toxic. PtBi has a NiAs type structure, which is the same crystal structure as the ordered intermetallic PtPb.⁷ As shown in the case of PtPb NPs, carbon-supported ordered intermetallic PtBi exhibits much enhanced electrocatalytic activity towards the oxidation reaction of formic acid and alcohols when compared to pure Pt.^{8,9} Herein, to find new co-catalyst exhibiting high photocatalytic activity towards the decomposition of AcOH, we examined the application of ordered intermetallic PtBi as a co-catalyst of WO₃ photocatalysis for the photodecomposition of AcOH. The ordered intermetallic PtBi was prepared by our original two-step preparation method with photodeposition and the polyol method. The amount of CO₂ formed during the photodecomposition of AcOH with PtBi NPs/WO₃ was compared to that of pure WO₃ and Pt NPs/WO₃.

Experimental

Figure 1 shows a schematic diagram of the preparation of PtBi NPs/WO₃. In the first step, WO₃ photocatalyst-supported Pt NPs were prepared using the photodeposition method. 0.02 mmol of H₂PtCl₆•6H₂O, which was used as a Pt source, and 400 mg of WO₃ powder were dispersed in a 5 vol% methanol aqueous solution. This slurry was stirred for 3 h under irradiation with visible light ($\lambda > 420$ nm: Xe lamp, 300 W). In the second step, ordered intermetallic PtBi was prepared using the polyol method. The synthesized WO₃ photocatalyst-supported Pt NPs (Pt NPs/WO₃) were used as a starting material. 0.01 mmol of Bi(NO₃)₃•5H₂O, which was used as a Bi precursor, and 200 mg of Pt NPs/WO₃ were dispersed in 50 mL of ethylene glycol, which was used as a solvent and reducing agent. The mixture was then sonicated in a bath-type ultrasonicator and treated in the flask with a reflux set for 15 min under 300 W microwave radiation. After the mixture cooled, the PtBi NPs/WO₃ was collected via centrifugation, washed sequentially with methanol and dried under vacuum.

A 200 kV transmission electron microscope (TEM and/or STEM, JEM-2100F, JEOL, Japan) equipped with two aberration correctors (CEOS GmbH) for the image- and probe-forming lens systems and an X-ray energy-dispersive spectrometer (STEM-EDS, JED-2300T, JEOL, Japan) was used for compositional analysis. X-ray photoelectron spectroscopy (XPS, JP-9010 MC, JEOL, Japan) measurements were performed to examine the chemical states (Pt 4f and W 4f) of the catalyst. MgK α was used as the X-ray source with an anodic voltage (10 kV) and current (10 mA). All of the XPS spectra for the samples were obtained with a take-off angle of 45° relative to the specimens.

The photocatalytic decomposition of AcOH was carried out in a circulation system made of Pyrex, in which a suspension of the photocatalyst powder (200 mg) in an aerated aqueous AcOH solution (5 vol%, 300 mL) was continuously stirred using a magnetic stirrer. A 300 W Xe lamp was used as the light source. The components were analyzed in the gas phase by gas chromatography (GC-8A, Shimadzu, Japan) equipped with a 2 m Porapak-Q column, a 2 m molecular sieve 3X column, and a flame ionization detector while using Ar as the carrier gas. The sample was illuminated with a 300 W Xe lamp (PE-300BF, BA-X300ES, Hayashi Tokei Works Co., Ltd., Japan) in conjunction with an optical fiber coupler, UV cut-off filter (L-42, HOYA Co., Ltd., Japan), and cold mirror unit (MR5090/CM, Eagle Co., Ltd). A spectro-radiometer (USR-45D, Ushio Co., Japan) was used to measure the visible light intensity, which was adjusted to 20 mW cm⁻².

Results and discussion

Figure 2 shows the TEM images of Pt NPs/WO₃ (A) and PtBi NPs/WO₃ (B) and the STEM image of the prepared PtBi NPs and their STEM-EDS mapping profiles. The PtBi NPs were deposited on the surface of the WO₃ photocatalyst. The PtBi NPs on the WO₃ photocatalyst were slightly larger than those of the WO₃-supported pure Pt NPs because Bi was selectively reacted on the Pt NPs on the WO₃ surface. The images in the lower part of Fig. 2 represent a STEM image and compositional mapping with a HAADF-STEM to demonstrate that the Pt and Bi atoms are uniformly dispersed in a particle of PtBi NPs. The Pt and Bi mole ratio was calculated to be 62.2 : 37.8 % based on the EDS analysis. These results indicate that the PtBi NPs on the WO₃ surface completely formed an ordered intermetallic compound by the photodeposition and polyol methods. Figure 3 shows the XPS profile in the (A) W 4*f* and (B) Pt 4*f* regions for (a) PtBi NPs/WO₃ (Pt loading: 1 wt. %), (b) WO₃ and (c) bulk Pt. The oxidation state of W is maintained before and after the preparation of the PtBi NPs on the WO₃ surfaces. The Pt 4*f* peak in the PtBi NPs/WO₃ exhibited a 0.5 eV shift to a higher binding energy compared with that of the pure bulk Pt. This shift indicates the formation of an intermetallic phase of PtBi.

Figure 4 presents the plots of CO₂ generation during the liquid-phase decomposition of AcOH over the (a) WO₃, (b) Pt NPs/WO₃ and (c) PtBi NPs/WO₃ under visible light irradiation ($\lambda > 420$ nm). The rates of CO₂ generation over the bare WO₃, Pt NPs/WO₃ and PtBi NPs/WO₃ were estimated with the slope of the CO₂ formation vs. time in the time range of 0 to 300 min. The CO₂ generation rates are 19.6, 66.5 and 464.0 $\mu\text{mol}\cdot\text{h}^{-1}$ on the WO₃, Pt NPs/WO₃ and PtBi NPs/WO₃, respectively. The PtBi NPs/WO₃ exhibited much enhanced photocatalytic activity towards the decomposition of AcOH. In addition, the apparent QEs of AcOH with PtBi NPs/WO₃ for CO₂ generation were *ca.* 18 %. The apparent QEs for AcOH generation were calculated as two-electron reactions.⁴ This result indicates that the surfaces of the PtBi NPs work more efficiently for the decomposition of AcOH as a co-catalyst, not only enhancing the oxygen reduction reaction but also the oxidation reaction of AcOH. We have reported that a high activity towards the photocatalytic decomposition of AcOH can be observed on the PtPb ordered intermetallic NPs used as a co-catalyst.⁴ Unfortunately, the CO₂ generation during the photocatalytic decomposition of AcOH over PtBi NPs/WO₃ exhibited a slightly lower photocatalytic activity compare with when PtPb was used as a co-catalyst (575.2 $\mu\text{mol}\cdot\text{h}^{-1}$).⁴ From these results, it can be understood that the oxidation of organic compounds in the photocatalytic decomposition occurred on the co-catalyst of the ordered intermetallic compound surface. In addition, the ordered intermetallic PtBi enhanced the photocatalytic decomposition towards the electro-oxidation of not only AcOH but also formic acid, methanol and ethanol. The mechanism of the photo-oxidation reaction and the reason for the difference in the reaction activity between the PtPb and PtBi NPs as co-catalysts will be discussed in our next paper.

Conclusions

The WO₃-supported ordered intermetallic PtBi NPs was prepared using a two-step synthesis method incorporating the photodeposition and polyol methods. The physical characterization, such as STEM and STEM-EDS, demonstrates that ordered intermetallic PtBi co-catalyst NPs were formed on the WO₃ surface. Furthermore, the decomposition rate of AcOH over PtBi NPs/WO₃ was enhanced compared with those over bare WO₃ and pure Pt NPs/WO₃. The comparison of the photocatalytic activity towards the decomposition of AcOH between Pt NPs/WO₃ and PtBi NPs/WO₃ suggests the efficiency

of ordered intermetallic PtBi NPs as a co-catalyst for the oxidation reaction. A new non-toxic ordered intermetallic PtBi co-catalyst exhibiting a higher photodecomposition activity for AcOH is proposed in this study.

Acknowledgement

This work was financially supported by the Strategic Research Base Development Program for Private Universities of the Ministry of Education, Culture, Sports, Science and Technology of Japan. A part of this work was supported by the National Institute for Materials Science (NIMS) microstructural characterization platform as a program of the "Nanotechnology Platform" of the Ministry of Education, Culture, Sports, Science and Technology (MEXT), Japan.

References

1. H. P. Maruska and A. K. Ghosh, *Sol. Energy*, **20**, 443 (1978).
2. R. Abe, H. Takami, N. Murakami and B. Ohtani, *J. Am. Chem. Soc.*, **130**, 7780 (2008).
3. T. Arai, M. Horiguchi, M. Yanagida, T. Gunji, H. Sugihara and K. Sayama, *Chem. Commun.*, 5567(2008).
4. T. Gunji, A. J. Jeevagan, M. Hashimoto, T. Nozawa, T. Tanabe, S. Kaneko, M. Miyauchi and F. Matsumoto, *Appl. Catal. B: Environ.*, **181**, 475 (2016).
5. T. Gunji, T. Tanabe, A. J. Jeevagan, S. Usui, T. Tsuda, S. Kaneko, G. Saravanan, H. Abe and F. Matsumoto, *J. Power Sources*, **273**, 990 (2015).
6. F. Matsumoto, C. Roychowdhury, F.J. DiSalvo and H.D. Abruña, *J. Electrochem. Soc.*, **155**(2), B148 (2008).
7. J. C. Bauer, X. Chen, Q. Liu, T-H. Phana and R. E. Schaak, *J. Mater. Chem.*, **18**, 275 (2008).
8. W. Hongsen, A. Laif, F. J. DiSalvo and H. D. Abruña, *Phy. Chem. Chem. Phy*, **10**, 3739 (2008).
9. F. Matsumoto, *Electrochemistry*, **80**(3), 132 (2012).

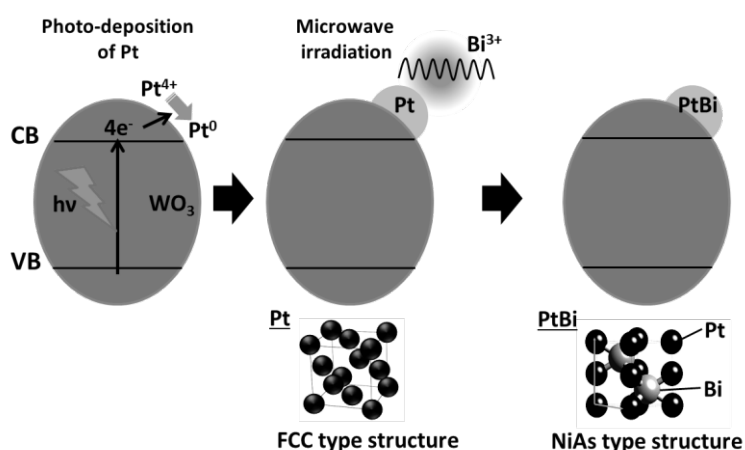


Figure 1. Schematic representation of Pt NPs and ordered intermetallic PtBi NPs loaded on WO₃ using two-step preparation method.

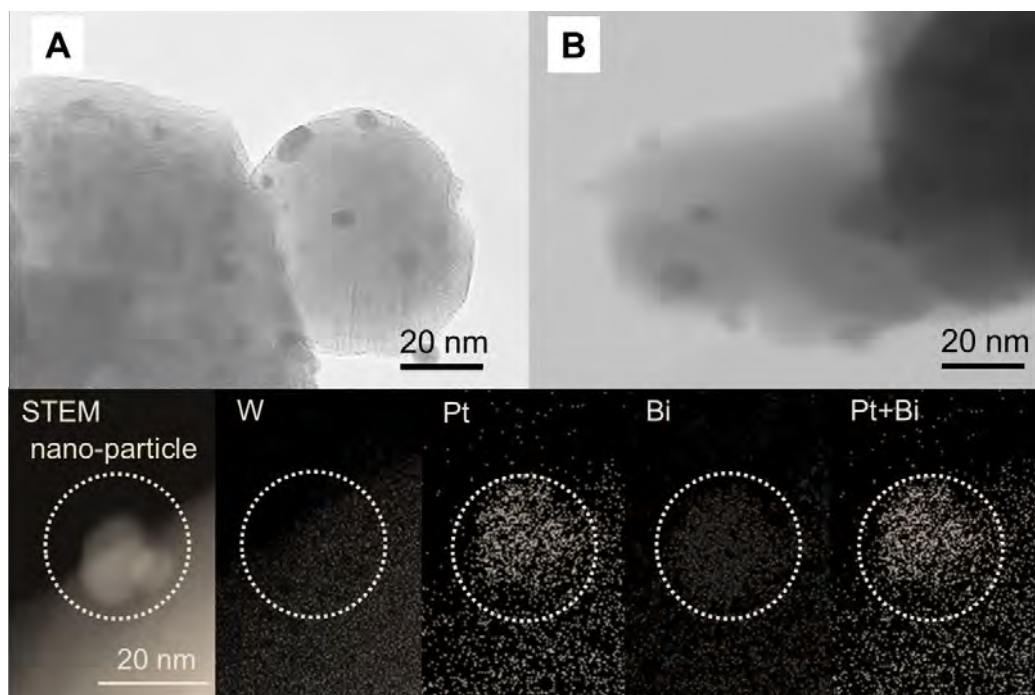


Figure 2. TEM images of (A) Pt NPs/ WO_3 and (B) PtBi NPs/ WO_3 . Lower images: HAADF-STEM image of PtBi NPs/ WO_3 and corresponding mapping images.

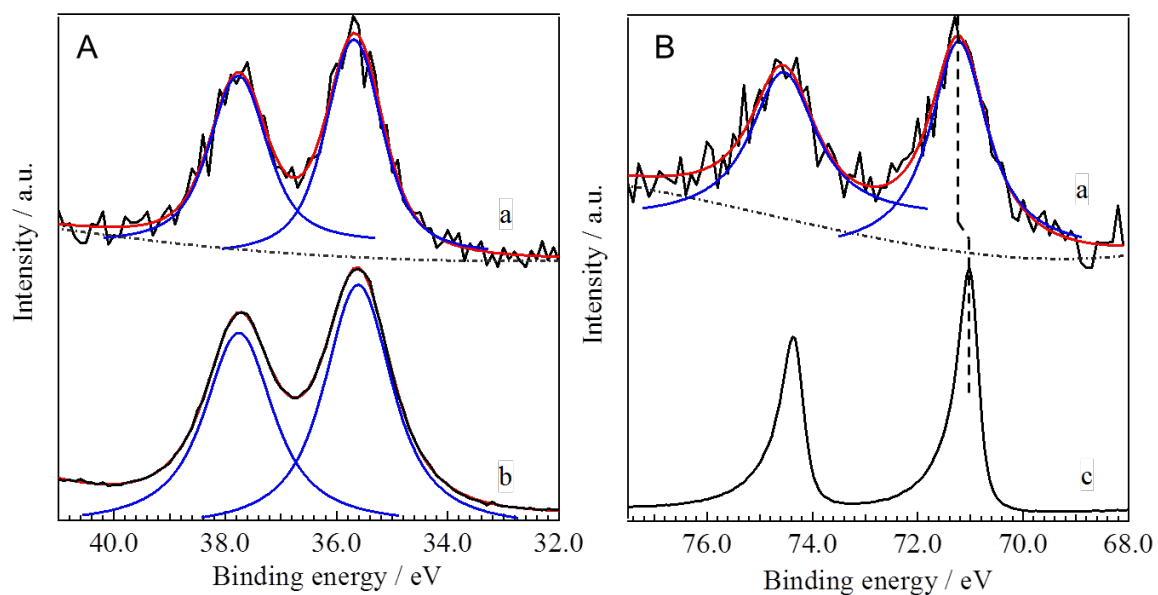


Figure 3. XPS profiles in the (A) W 4*f* and (B) Pt 4*f* regions for (a) PtBi NPs/ WO_3 (Pt loading: 1 wt. %), (b) WO_3 and (c) bulk Pt.

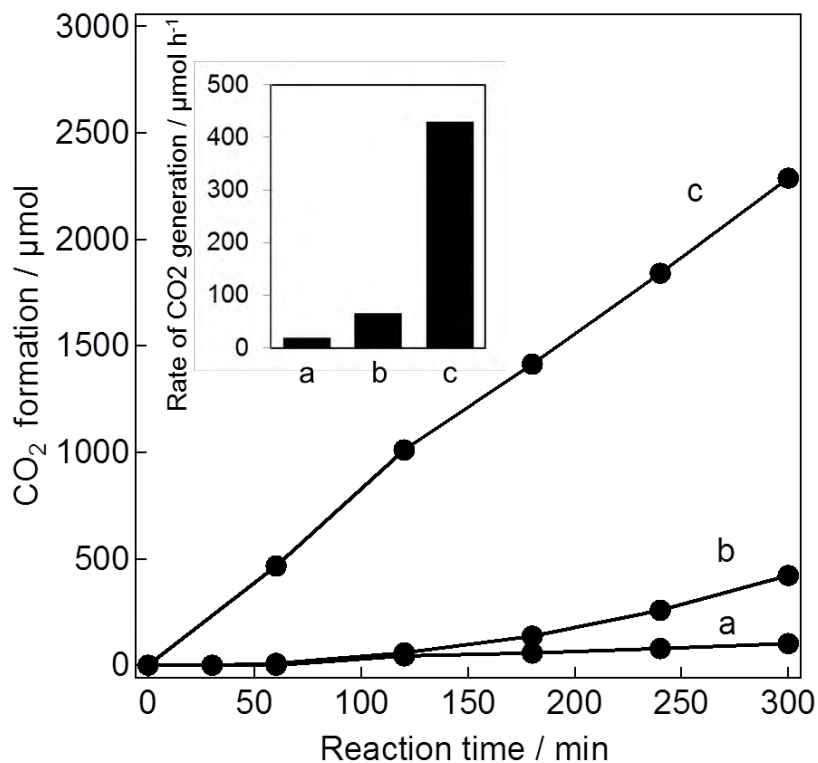


Figure 4. Time courses of the CO₂ evolution during the decomposition of AcOH in an aqueous AcOH solution in the presence of O₂ under visible light irradiation over (a) bare WO₃, (b) Pt NPs/WO₃, and (c) PtBi NPs/WO₃. Insets summarize the CO₂ generation rate with all the photocatalysts.

The Effect of Brighteners on the Fabrication of Electroplated Bright Aluminum Films Using an AlCl_3 -EMIC-Toluene Bath

Kazuma Uehara¹, Takao Gunji¹, Toyokazu Tanabe¹,
Shingo Kaneko², Futoshi Matsumoto¹

¹Department of Materials and Life Chemistry, Kanagawa University, 3-27-1,
Rokkakubashi, Kanagawa-ku, Yokohama, Kanagawa 221-8686, Japan

²Research Institute for Engineering, Kanagawa University,
3-27-1, Rokkakubashi, Kanagawa-ku, Yokohama, Kanagawa 221-8686, Japan

Abstract

The effect of brighteners such as 4-pyridinecarboxylic acid hydrazide (4-PCAH), 3-pyridinecarboxylic acid hydrazide (3-PCAH), 2-pyridinecarboxylic acid hydrazide (2-PCAH) and conventional 1,10-phenanthroline (PH) on the electrodeposition efficiency and brightness of aluminum (Al) was investigated. Electrodeposited Al films were prepared with constant currents in an aluminum chloride (AlCl_3)-ethyl-3-methylimidazolium chloride (EMIC)-toluene bath, and the results were compared using a scanning electron microscope (SEM) and UV-vis spectrometer. Among the four brighteners used in this study, 4-PCAH exhibited the highest brightness on the electrodeposited Al surfaces.

Introduction

Aluminum (Al) is the second most abundant metallic element in the Earth's crust after silicon. Al has been widely used as a coating material because of its ability to resist corrosion that results from the phenomenon of passivation and to reflect high visible light. Some of the many uses of Al include applications in transportation, packaging, construction, and consumer durables. Thin layers of Al are usually deposited onto flat surfaces by physical vapor deposition (1), chemical vapor deposition (2) or a hot-dip coating process (3). Specifically, electrochemical deposition of Al at ambient temperature has attracted much interest for applications in corrosion-resistive coatings (4), decorative coatings (5), electro-refining processes (7) and Al-ion batteries (7). This is because the deposition processes do not require expensive equipment, the size of the Al films can be easily scaled up or scaled down, and Al films of uniform thickness can be prepared on the surface of various shapes. However, as demonstrated by the Pourbaix diagram of Al (8), the reduction of protons preferentially occurs in aqueous solutions at any pH, making Al electrodeposition infeasible. Aprotic electrolytes such as inorganic molten salts (9), organic molten salts (i.e., ionic liquids) (10), and molecular organic solvents (11) have been applied for Al electrodeposition. There have been many published papers in which various electrolytes and conditions were used (12-14). Of the aprotic electrolytes, ionic liquids composed solely of ions with melting points below 100°C are being increasingly employed as replacements for organic solvents in metal research where electrodeposition in aqueous solutions is infeasible (15, 16). Numerous ionic liquid electrolytic systems for use in Al electrodeposition have been investigated (17-20). These studies aimed to form smooth Al films that exhibited high visible light reflectivity on the surface. It was reported that trace amount of brighteners such as 1,10-phenanthroline (PH) (21, 22) and

nicotinic acid (23) were added to the ionic liquid electrolytes to obtain a smooth surface of the Al films. However, electrodeposition of bright Al has been unsuccessful even with the addition of such electrolyte additives. We found that nicotinic acid hydrazine can function as a brightener for the preparation of bright Al films. In this study, we report the effectiveness of 4-pyridinecarboxylic acid hydrazide (4-PCAH) in smoothing deposited Al surfaces in terms of brightness, surface roughness and film thickness compared with Al films prepared with 3-pyridinecarboxylic acid hydrazide (3-PCAH), 2-pyridinecarboxylic acid hydrazide (2-PCAH) and PH. The Al films prepared with the mixture of ionic liquid/organic solvent containing 4-PCAH had brighter surfaces and generated films between 20-100 μm in thickness.

Experimental

(1) Preparation of electrolytic baths

Electrolytic baths was prepared in an argon-filled glove box (Miwa, MDB-1KXV) by the stepwise addition of anhydrous AlCl_3 grains (0.19 mol, Fluka, crystallized, 99%; used as received) to EMIC (9.5×10^{-2} mol, Wako Pure Chemical, 99%; used as received) at 25°C . Toluene (0.87 mol) was added to the electrolyte bath, and 1.8×10^{-3} mol of the brighteners was then added to the AlCl_3 /EMIC/toluene bath at 25°C . The temperature of the baths and agitation speed of the stirrer tips during the mixing process were controlled using a hot magnetic stirrer (As-one, TJA-550) at 25°C and 100 rpm. 4-PCAH (98+%, Alfa Aesar), 3-PCAH, 2-PCAH and PH (98+%, Wako) were used as a brightener without further purification.

(2) Electrodeposition of aluminum films

A 50 mL glass beaker was used as an electrolytic cell. The temperature of the baths and agitation speed of the stirrer tips were controlled during electrodeposition processes by a hot magnetic stirrer (As-one, TJA-550) at 25°C and 100 rpm. The surfaces of Cu plates were polished and washed to remove surface impurities and to flatten the surfaces of plates used as working electrodes. Al sheets (99.999%, 5 cm x 5 cm) and Al wire (1 mm diameter, 3 cm length) were used as counter and reference electrodes, respectively. Portions of the Cu plates were covered with PTFE tape such that only a 10 mm x 10 mm area was exposed. The distance between the Cu plates and the Al counter electrodes was 10 mm. The electrochemical deposition of Al was carried out with an electrochemical analyzer (Hokuto Denko, HZ-5000).

(3) Characterization of the prepared aluminum films

The surfaces and cross sections of the prepared Al films were observed using a field emission type SEM (FE-SEM, SU-8010, Hitachi). Cross sections of the prepared Al film samples were made by milling the samples with sandpaper after embedding the samples in a conductive polymer (Technovit 5000, Kulzer). A UV-vis spectrometer (UV-2600, Shimadzu) was used to evaluate the reflectivity of the deposited Al films.

Results and discussion

Figure 1 shows photographs of the Al films obtained by electrodeposition of Al from (A) EMIC/ AlCl_3 /toluene/4-PCAH, (B) EMIC/ AlCl_3 /toluene/3-PCAH, (C) EMIC/ AlCl_3 /toluene/2-PCAH and (D) EMIC/ AlCl_3 /toluene/PH baths. In these baths, a constant current of 8 mAcm^{-2} (A-D) was used for Al electrodeposition. In order to recognize the differences in brightness of the Al surfaces, the characters "KU KU UNIV"

were reflected onto the Al film surfaces. Whether or not the reflected characters could be observed was used as an index for surface brightness, i.e., surface smoothness. The Al films obtained with the EMIC/ AlCl_3 /toluene/4-PCAH bath exhibited the highest brightness among the four brighteners, though the brightness began to degrade as the deposition time increased. In contrast, the Al films obtained with the EMIC/ AlCl_3 /toluene/PH bath and deposition times of 10 and 30 min barely reflected the characters. For deposition times that exceeded 2 h (Fig. 2-(d)), dull characters could barely be observed on the partial area. PH has been reported as a representative brightener for Al electrodeposition in several papers.^{21,22} 4-PCAH, which was applied as a Al deposition brightener for the first time, demonstrated a remarkable improvement in the brightness of the Al surfaces when compared to brightness levels obtained with EMIC/ AlCl_3 /toluene/3-PCAH, EMIC/ AlCl_3 /toluene/2-PCAH and EMIC/ AlCl_3 /toluene/PH baths. Al electrodeposition using the EMIC/ AlCl_3 /toluene/4-PCAH bath over 2 h with 4 and 12 mAcm^{-2} , and the EMIC/ AlCl_3 /toluene/PH bath with 4 mAcm^{-2} resulted in brightness degradation. Employment of a 12 mAcm^{-2} current in the EMIC/ AlCl_3 /toluene/PH bath naturally led to the same brightness level as Al films prepared with an 8 mAcm^{-2} current in the EMIC/ AlCl_3 /toluene/PH bath (results not shown).

The surface SEM images of the deposited Al films (Fig. 2-(1)) revealed that the Al surfaces obtained with the (a) EMIC/ AlCl_3 /toluene/4-PCAH and (b) EMIC/ AlCl_3 /toluene/3-PCAH baths were smooth. On the other hand, the surface images of films obtained with the (c) EMIC/ AlCl_3 /toluene/2-PCAH and (d) EMIC/ AlCl_3 /toluene/PH baths exhibited grains that were several micrometers in size. The grain sizes were closely related to the surface roughness, and the Al films obtained with EMIC/ AlCl_3 /toluene/3-PCAH, EMIC/ AlCl_3 /toluene/2-PCAH and EMIC/ AlCl_3 /toluene/PH baths had much larger grains than those resulting from deposition in the EMIC/ AlCl_3 /toluene/4-PCAH bath. Cross-sectional SEM images (Fig. 2-(2)) confirmed that all Al films obtained in this study were composed of dense Al layers. Figure 3 shows the dependence of film thickness on deposition time. The thickness of the Al films was extracted from the cross-sectional SEM images. The estimated thickness has the errors of 8-12%. The dotted lines represent theoretical thicknesses that were calculated using charge flows for electrodeposition and density of Al metal. The downward deviation of data points from the lines corresponds to the decrease in current efficiency. All Al films prepared in this study had current efficiencies of almost 100%.

Figure 4 shows reflectance spectra of the Al films obtained with AlCl_3 -EMIC-toluene-4-PCAH (b), AlCl_3 -EMIC-toluene-3-PCAH (c), AlCl_3 -EMIC-toluene-2-PCAH (d) and AlCl_3 -EMIC-toluene-PH (e) baths. Spectrum (a) was obtained using commercial Al foil (A1N80H-H18, Mitsubishi Aluminum, Japan). The Al films were prepared with a deposition time of 2 h and constant current of 8 mAcm^{-2} . The Al film obtained with AlCl_3 -EMIC-toluene-4-PCAH (b) exhibited reflectivity similar to that observed with Al foil, followed by the Al film obtained with AlCl_3 -EMIC-toluene-PH (e). The 4-PCAH, 3-PCAH and 2-PCAH brighteners are positional isomers, and studies to investigate their differences in reflectivity yielded interesting results, highlighting the importance of adsorption of brighteners on Al surfaces.

Conclusions

In this study, we demonstrated that the addition of 4-PCAH to EMIC/ AlCl_3 /toluene baths improved the brightness of deposited Al films. The Al films clearly reflected characters on their surfaces such that they could be read. The reflectivity of Al surfaces prepared with EMIC/ AlCl_3 /toluene/4-PCAH was 84% at 450 nm, which to our knowledge is the highest value reported to date. Although the EMIC/ AlCl_3 /toluene/4-PCAH, /3-PCAH, /2-PCAH and /PH baths exhibited current efficiencies close to 100%, both the grain size and surface smoothness of the prepared Al films differed significantly. Importantly, the fact that different structural isomers produced Al surfaces with different surface roughness and reflectivity suggests that the position of hydrazine on the pyridine ring affects the surface roughness of Al films; the highest reflectivity was observed for Al surfaces prepared with 4-PCAH, which has N atoms in the pyridine ring and hydrazine in the *para* position. We propose that the pyridine N atoms of 4-PCAH adsorbed to the surface of Al allowing hydrazine to partially coordinate with Al^{3+} ions; alternatively, the hydrazine N atoms could have adsorbed on the Al surface allowing pyridine to partially coordinate with the Al ions. The mechanism used to flatten the Al surfaces deposited with 4-PCAH will be discussed in our next paper.

References

1. HANDBOOK of Deposition Technologies for Films and Coatings, 2nd Edition, Noyes Publications, Park Ridge, New Jersey (1994).
2. T. Kobayashi, A. Sekiguchi, N. Akiyama, N. Hosokawa and T. Asamaki, *J. Vac. Sci. & Technol.*, **A10**, 525 (1992).
3. S. Shawki and Z.A. Hamid, *Surf. Interface Anal.*, **35**, 943 (2003).
4. M. Campo, M. Carboneras, M.D. Lopez, B. Torres, P. Rodrigo, E. Otero and J. Rams, *Surf. Coat. Technol.*, **203**, 3224 (2009).
5. T. Tokunaga, K. Matsuura and M. Ohno, *J. Alloys Compd.*, **601**, 179 (2014).
6. M. Jia, Z.L. Tian, Y.Q. Lai, F.Y. Liu, J. Li and Y.X. Liu, *Acta Metall. Sin.*, **47**, 727 (2011).
7. N. Jayaprakash, S. K. Das and L. A. Archer, *Chem. Commun.*, **47**, 12610 (2011).
8. M. Pourbaix, *Atlas of Electrochemical Equilibria in Aqueous Solutions*, NACE, Houston (1966).
9. M. Jafarian, M.G. Mahjani, F. Gobal and I. Danaee, *J. Appl. Electrochem.*, **36**, 1169 (2006).
10. N. Koura, Y. Tashiro, M. Futamura, F. Matsumoto and Y. Idemoto, *J. Surf. Finish. Soc. Jpn.*, **52**, 791 (2001).
11. W. Simka, D. Puszczuk and G. Nawrat, *Electrochim. Acta*, **54**, 5307 (2009).
12. J.-K. Chang, S.-Y. Chen, W.-T. Tsai, M.-J. Deng and I.-W. Sun, *Electrochem. Commun.*, **9**, 1602 (2007).
13. S.Z.E. Abedin, P. Giridhar, P. Schwab and F. Endres, *Electrochem. Commun.*, **12**, 1084 (2010).
14. W.H. Huang, M.L. Wang, H.W. Wang and N.H. Ma, *Surf. Coat. Technol.*, **213**, 264 (2012).
15. F. Endres, *ChemPhysChem*, **3**, 144 (2002).
16. A.P. Abbott and K.J. McKenzie, *Phys. Chem. Chem. Phys.*, **8**, 4265 (2006).
17. A.P. Abbott, R.C. Harris, Y.-T. Hsieh, K.S. Ryder and I.-W. Sun, *Phys. Chem. Chem. Phys.*, **16**, 14675 (2014).
18. J. Tang and K. Azumi, *Electrochim. Acta*, **56**, 1130 (2011).

19. P. Giridhar, S.Z.E. Abedin and F. Endres, *Electrochim. Acta*, **70**, 210 (2012).
20. D. Pradhan, D. Mantha and R.G. Reddy, *Electrochim. Acta*, **54**, 6661 (2009).
21. A. Endo, M. Miyake and T. Hirato, *Electrochim. Acta*, **137**, 470 (2014).
22. L. Barchi, U. Bardi, S. Caporali, M. Fantini, A. Scrivani and A. Scrivani, *Prog Org Coat*, **67**, 146 (2010).
23. F. Endres, M. Bukowski, R. Hempelmann and H. Natter, *Angew. Chem.*, 115 (2003) 3550, *Int. Ed.*, **42**, 3428 (2003).

Table 1 Bath composition and deposition conditions for Al electrodeposition

| | |
|--------------------------------------|---------------------------------|
| 1-ethyl-3-methylimidazolium chloride | 14.3 mol% |
| AlCl ₃ | 28.6 mol% |
| Toluene | 57.1 mol% |
| Additive | 1.8 x 10 ⁻³ mol |
| Temperature | 25 ° C |
| Current density | -4.0 ~ -10.0 mAcm ⁻² |

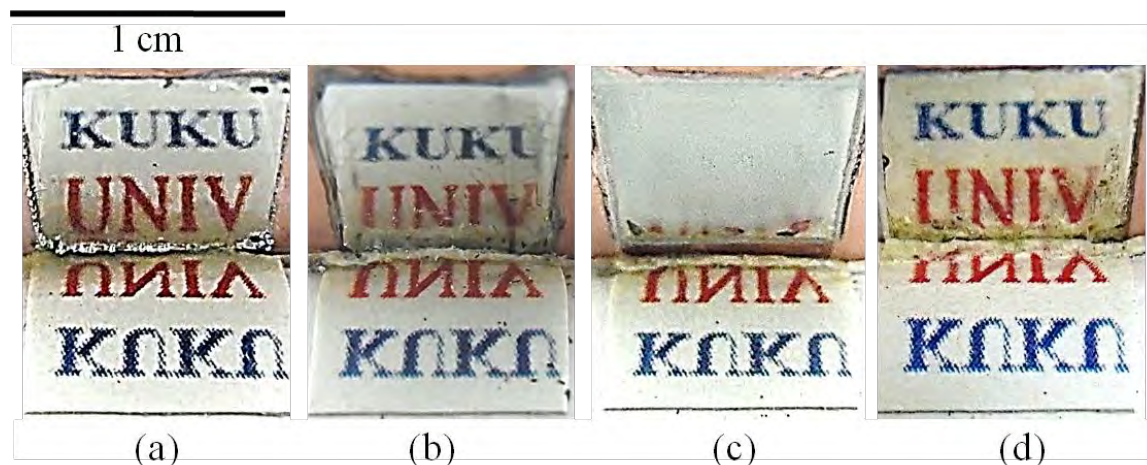


Fig. 1 Micrographs of the Al film surfaces obtained on a Cu substrate by coulometric electrodeposition in (a) AlCl₃-EMIC-toluene-4-PCAH, (b) AlCl₃-EMIC-toluene-3-PCAH, (c) AlCl₃-EMIC-toluene-2-PCAH and (d) AlCl₃-EMIC-toluene-PH baths. Deposition time: 2 h; constant current: 8 mAcm⁻².

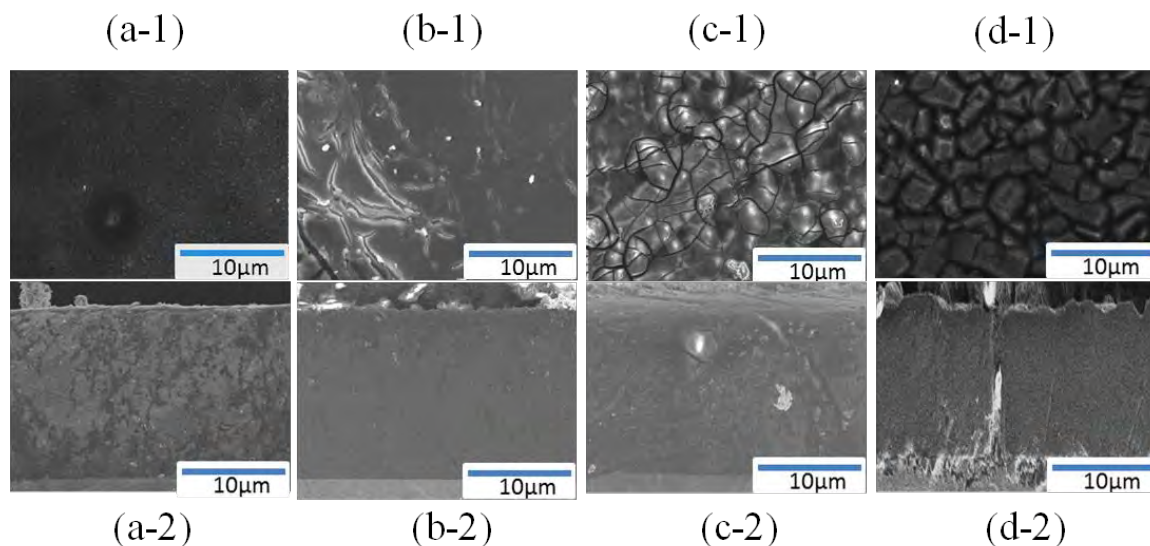


Fig. 2 SEM images of the surface (1) and cross sections (2) of the Al films electrodeposited in (a) AlCl_3 -EMIC-toluene-4-PCAH, (b) AlCl_3 -EMIC-toluene-3-PCAH, (c) AlCl_3 -EMIC-toluene-2-PCAH and (d) AlCl_3 -EMIC-toluene-PH baths. Deposition time: 2 h. Constant current: 8 mAcm^{-2} .

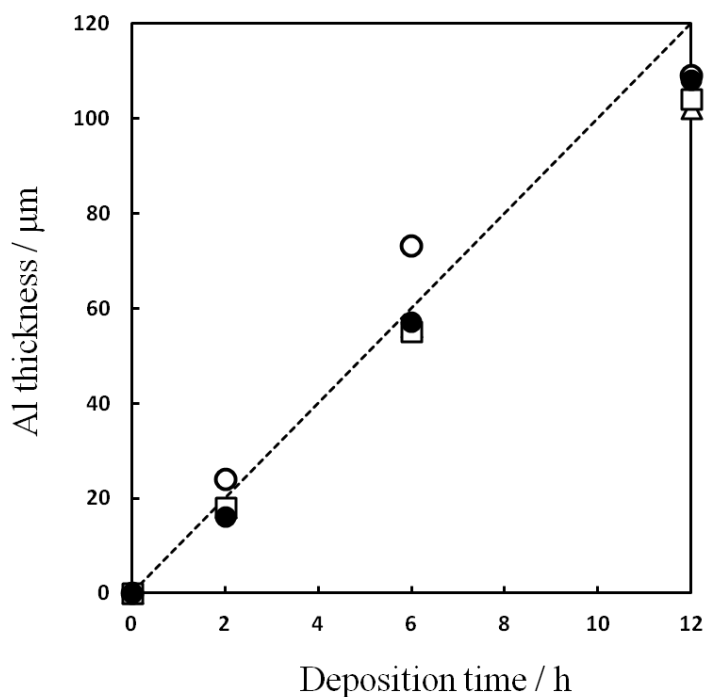


Fig. 3 Relationship between the thickness of the deposited Al and deposition time. Electrochemical deposition baths: (○) AlCl_3 -EMIC-toluene-4-PCAH, (●) AlCl_3 -EMIC-toluene-3-PCAH, (□) AlCl_3 -EMIC-toluene-2-PCAH and (△) AlCl_3 -EMIC-toluene-PH baths. Constant current: 8 mAcm^{-2} .

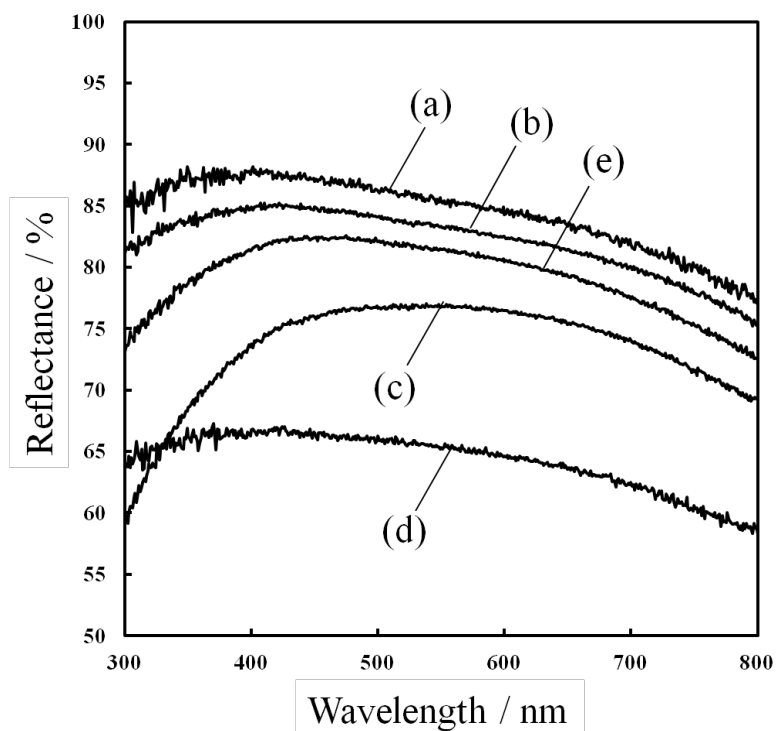


Fig. 4 Reflectance spectra of Al deposition films in AlCl_3 -EMIC-toluene-4-PCAH (b), AlCl_3 -EMIC-toluene-3-PCAH (c), AlCl_3 -EMIC-toluene-2-PCAH (d) and AlCl_3 -EMIC-toluene-PH (e) baths. Spectrum (a) was obtained using commercial Al foil.

■原 著■ 2014 年度神奈川大学総合理学研究所共同研究助成論文

ヒスチジンを中心とした塩基性アミノ酸を配位子とする ポリマー性銀 (I) 錯体の合成、構造解析及び抗菌活性

力石紀子¹ 野宮健司^{1,2} 松永 諭¹ 両角宗一郎¹ 高山晃彦¹
高木由貴¹ 井上ちさと¹ 柳田貢助¹ 吉川理絵¹

Synthesis, Structure and Antimicrobial Activity of Silver(I) Coordination
Polymers with Histidine and Other Basic Amino Acid Ligands

Noriko Chikaraishi Kasuga¹, Kenji Nomiya^{1,2}, Satoshi Matsunaga¹,
Soichiro Morozumi¹, Akihiko Takayama¹, Yoshitaka Takagi¹, Chisato Inoue¹,
Kousuke Yanagita¹ and Rie Yoshikawa¹

¹ Department of Chemistry, Faculty of Science, Kanagawa University, Hiratsuka City, Kanagawa 259-1293, Japan

² To whom correspondence should be addressed. E-mail: nomiya@kanagawa-u.ac.jp

Abstract: The coordination environment of Ag⁺, i.e., not only the atom coordinated with the silver(I) ion, but also the structure around the silver(I) ion and the ease of ligand replacement, plays an important role in the antimicrobial activities of silver(I) complexes. Water-soluble neutral and anionic silver(I) complexes with histidine (*D*-1, *L*-1 and *L*-4) and water-insoluble ones (*D*-2, *L*-2 and *DL*-3) were prepared depending on the reaction conditions, including the reaction time and pH. They exhibited a wide spectrum of effective antimicrobial activities against both Gram-negative (*Escherichia coli* and *Pseudomonas aeruginosa*) and Gram-positive (*Bacillus subtilis* and *Staphylococcus aureus*) bacteria as well as yeasts (*Candida albicans* and *Saccharomyces cerevisiae*). Various structures of silver(I) complexes with basic amino acids suggest that histidine as well as arginine and lysine residues can uptake silver(I) ion in peptides and proteins and transfer metal ions outside the cell depending on local proton concentrations in the cell.

Keywords: Silver(I) complexes, basic amino acid, histidine, antimicrobial activity, EXAFS, ESI-MS

序論

金属イオンは生体内で様々な重要な役割を果たしているとともに、医薬品やMRI造影剤などの病態診断として重要な無機化合物や金属錯体も数多く存在する^{1,2)}。

生理活性を示す無機化合物として、無機系抗菌剤の一群がある。やけど、褥瘡、皮膚潰瘍の外用感染治療薬として、銀化合物を含む塗り薬がある（スルフジアジン銀 (I) (silver sulfadiazine) (Fig. 1))。

無機系抗菌剤の一般的な特徴として、広範な抗菌スペクトルを示すこと、古くから用いられているため安全性が高いとされていること、有機抗菌剤より熱に安定であることが挙げられる。

無機抗菌性化合物の応用分野は、水処理、家庭用

品への抗菌性付加、繊維製品の抗菌、防臭加工、生活資材、機械・器具、土建・塗料と広い。無機抗菌性化合物は、1) 光触媒機能を持つ酸化チタン及び2) ケイ酸塩、リン酸塩に銀、銅、亜鉛イオンを担持させたものに大別されている³⁾。

我々は、これまで無機系抗菌剤の中で、広い抗菌

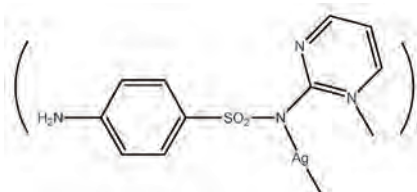


Fig. 1. Silver sulfadiazine.

スペクトルを持つ銀(I)錯体に着目してきた。銀(I)イオンは膜結合型酵素のチオール基と銀(I)イオンが結合し、それらの酵素に影響すると言われているが、詳細は明らかになっていない⁴⁾。銀(I)イオンに有機化合物が配位した銀(I)錯体の抗菌作用については、さらに不明である。そこで、高純度の新規銀(I)錯体を合成し、分子構造決定後、実用的に抗菌作用が望まれているバクテリア (*E. coli*, *B. subtilis*, *S. aureus*, *P. aeruginosa*)、酵母 (*C. albicans*, *S. cerevisiae*)、カビ (*A. brasiliensis (niger)*, *P. citrinum*) を選んで、それらの抗菌活性評価を最小発育阻止濃度 (Minimum inhibitory concentration, MIC $\mu\text{g/mL}$) により行ってきた。供与原子 (O, N, P, S) ごとに銀(I)錯体を分類し、配位子の交換しやすさと抗菌活性の相関を調べてきたところ、配位子交換性が高い Ag-N, Ag-O 結合性の銀(I)錯体が、Ag-S, Ag-P 結合性銀(I)錯体よりも抗菌スペクトルが広く、優れた抗菌活性を示す⁵⁾。

以上から、タンパク質を構成する α アミノ酸を配位子とする銀(I)錯体は関心が持たれるが、これまで光に不安定な銀(I)錯体が多く、単離が難しいとされてきた。原料の銀塩として酸化銀を用いることにより、いくつかのホモレプティックな中性の銀(I)アミノ酸錯体 (∞ $\{[\text{Ag}(\text{DL-Hasp})]_2\} \cdot 1.5\text{H}_2\text{O}$ アスパラギン酸 (H_2asp)、 ∞ $\{[\text{Ag}(\text{L-asn})]\}$ アスパラギン (Hasn) を単離し、報告してきた^{5), 6)}。S 原子を含まない中性、酸性のアミノ酸銀(I)錯体は、 α 炭素のアミノ基、カルボキシル基と、酸性官能基の供与原子が銀(I)イオンに配位する。銀(I)イオンに配位するのは窒素原子と酸素原子であるが、配位様式は4種類ある。i) 2つの Ag...Ag を2つの COO^- が架橋する様式、ii) Ag に2つの供与原子が O-Ag-O、N-Ag-N で連結する直線2配位と、iii) Ag に2つの供与原子が O-Ag-N で連結する直線2配位、iv) 窒素原子のみで連結する直線2配位である (Fig. 2)。

α アミノ酸の中で、側鎖、置換基 R が、イミダズリルメチル基、3-グアニジノプロピル基、4-アミノブチル基を持つヒスチジン、アルギニン、リシンは、塩基性アミノ酸に分類される。塩基性アミノ酸を配位子とした銀(I)錯体は、pH により塩基性官能基がアニオン、中性、カチオンすべての状態をとることが可能であることから、中性、酸性のアミノ酸配位子からなる銀(I)錯体より多様な結合様式を持つ銀(I)錯体が形成されることが予想される。今回はそのような配位子としてヒスチジン (Fig. 3)⁷⁾ に着目し、条件により多様なヒスチジン銀(I)錯体が形成されることを明らかにし、抗菌活性試験結果とともに報告する。また関連のあるアルギニン銀(I)錯体について

も分子構造、抗菌活性について触れる。

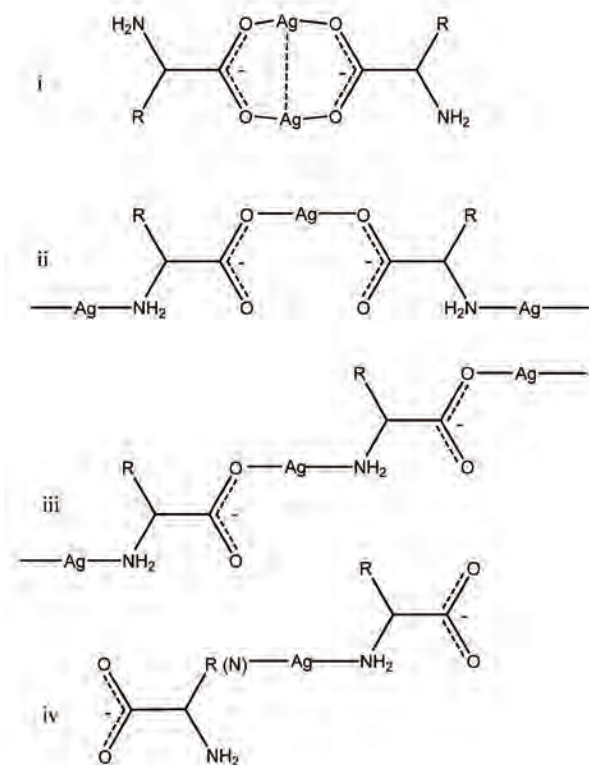


Fig. 2. Classification of silver (I) complexes with amino acid ligands with N and O donor atoms and without an S atom.

材料と方法

材料

Ag_2O 、 AgNO_3 、ヒスチジン (H_2his)、アルギニン (Harg)、リシン (Hlys)、 EtOH 、 D_2O は市販品をそのまま用いた。

水溶性 *D*-または *L*-ヒスチジン銀(I)錯体 ∞ $\{[\text{Ag}(\text{D-His}) \cdot 0.2\text{EtOH}]_2\}$ (*D*-1)、 ∞ $\{[\text{Ag}(\text{L-His}) \cdot 0.2\text{EtOH}]_2\}$ (*L*-1)、水に不溶性 *D*-または *L*-ヒスチジン銀(I)錯体 ∞ $\{[\text{Ag}(\text{D-His})]\}$ (*D*-2)、 ∞ $\{[\text{Ag}(\text{L-His})]\}$ (*L*-2)、水に不溶性 *DL*-ヒスチジン銀(I)錯体 ∞ $\{[\text{Ag}_2(\text{D-His})]\}$ (*DL*-3)、粘性の ∞ $\{[\text{Na}[\text{Ag}_3(\text{L-His})_2]]\}$ (*L*-4) はスキーム (Fig. 4) に従って合成した。

アルギニン銀(I)錯体は硝酸銀とアルギニンを水中

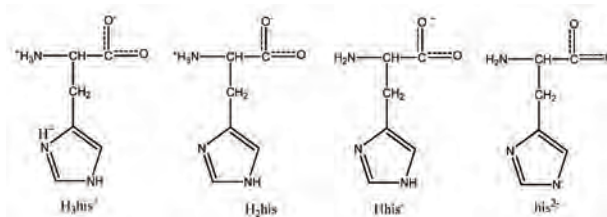


Fig. 3. Various structures of histidine (H_2his).

で1:1のモル比で反応させpHを調整後、有機溶媒に沈殿させて得た。

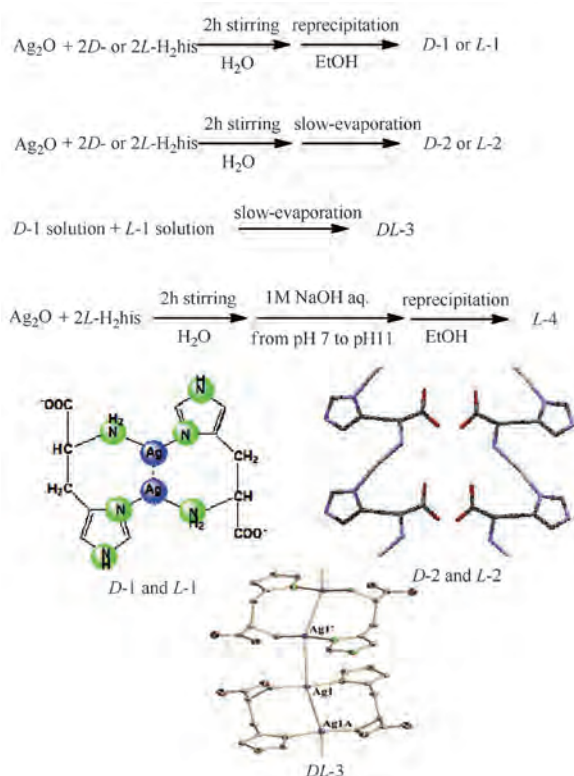


Fig. 4. Synthetic diagram of silver(I) complexes with histidine ligand.

測定方法

CHN 元素分析は Perkin-Elmer PE2400series II CHNS/O を用いた。熱分析データ (TG/DTA) は Rigaku Thermo Plus 2 TG 8120 を使用し、30 °C から 500 °C まで 1 分間に 4 °C 温度上昇させながら測定した。赤外吸収スペクトルは日本分光 FT-IR 4100 で測定した。¹H, ¹³C NMR スペクトルは日本電子 ECP300 または ECP500NMR 装置で DSS を内部標準として測定した。単結晶 X 線構造解析は Bruker SMART APEX CCD または Rigaku Saturn CCD 回折計と解析ソフトウェア SHELX-TL または Yadokari-XG2009 を使用した。ESI-MS および ESI-MS スペクトルは日本電子 JMS-T100LC で測定した。粘度計は東機産業の TVC-5 粘度計を用いた。XANES と EXAFS 測定は東レリサーチセンターに依頼した。

バクテリア (グラム陰性菌の大腸菌 (*E. coli*), 緑膿菌 (*P. aeruginosa*)) グラム陽性菌の枯草菌 (*B. subtilis*), 黄色ブドウ球菌 (*S. aureus*) の 4 種類)、酵母 (*C. albicans*, *S. cerevisiae* の 2 種類)、カビ (*A. brasiliensis*, *P. citrinum* の 2 種類) に対する最少発育阻止濃度 (MIC, μg/mL または mmol/L) 測定は秦

野食品安全センターに依頼した⁸⁾。

結果

中性のヒスチジン銀 (I) 錯体 L-1, D-1, D-2, L-2, DL-3

中性のヒスチジン銀 (I) 錯体は、いずれもイミダゾール環とアミノ基の窒素原子が銀イオンに配位した type IV の配位様式をとっていた。副生成物は水以外なく、粉体では銀 (I) 錯体はほぼ定量的に得られる。結晶化しても 50% ほどの収率で単結晶が生成した。D-1 と L-1 を混合すると DL-3 が生成したことから、水溶液中で Ag-N 結合は交換可能であることが示された⁹⁾。

アニオン性のヒスチジン銀 (I) 錯体 L-4

L-1 の水溶液は pH が 7 (中性付近) であるが、1M NaOH 水溶液を加え、アルカリ性になると粘性がでてきた。エタノールに再沈殿するとナトリウムを含む吸湿性の粉体が得られた。粉末 X 線回折装置ではシグナルが現れなかったことから、アモルファスな物質であり、元素分析、ESI-MS (Fig. 5) の結果から $\text{Na}^+ : \text{Ag}^+ : \text{his}^{2-} = 1 : 3 : 2$ の組成であることが示された。他のアルカリ金属塩 (Li, K, Cs 塩) の調製も行ったが、ナトリウム塩の純度が一番高かったので、ナトリウム塩のキャラクタリゼーションを行った¹⁰⁾。

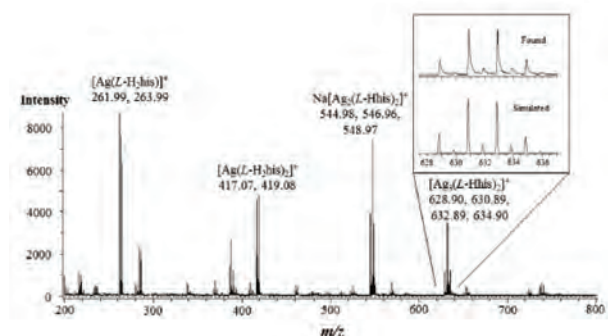


Fig. 5. Positive-ion ESI-MS of an aqueous solution of L-4.¹⁰⁾

討論

アニオン性のヒスチジン銀 (I) 錯体 L-4 の構造

元素分析や MS より銀 (I) の 3 核錯体であること、また XRD の結果から L-4 はアモルファスであることがわかった。構造に関する情報は NMR と EXAFS, EXAFS (Fig. 6) から得た。それらの結果からアニオン性ヒスチジン銀 (I) 錯体は、Ag-Ag 結合を含むポリマーであることが示唆された。配位供与原子はヒスチジンの窒素原子と水分子の酸素原子が考えられ、溶液の濃度、アルカリ金属イオンの濃度により Fig.

7のいずれか、または2つの構造が混在していると推定される。

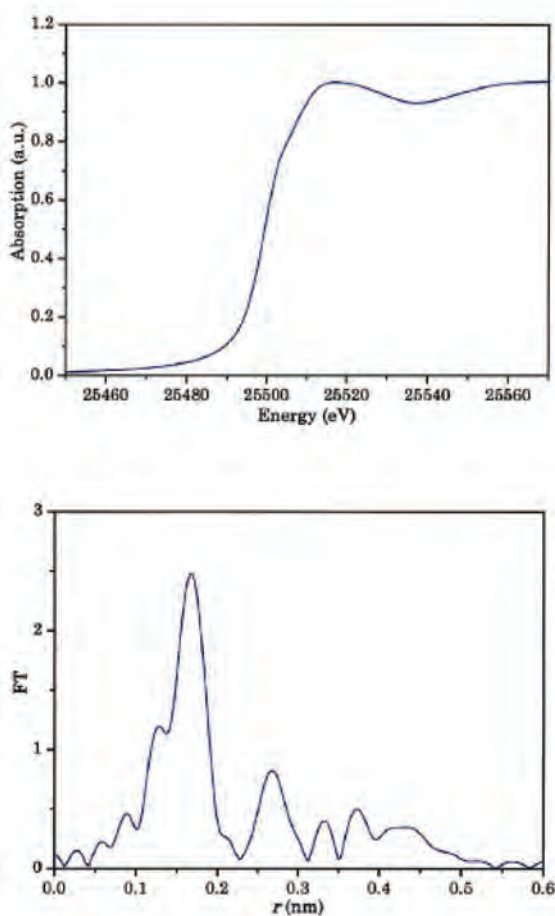


Fig. 6. The Ag K-edge X-ray absorption spectrum (above) and radial distribution function (below) of L-4.¹⁰

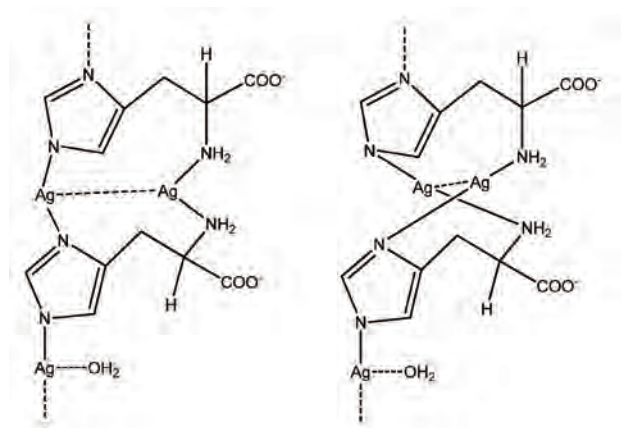


Fig. 7. Plausible structures of L-4.

長らく銀イオンに耐性を持つ細菌は知られていなかったが、最近銀イオンに耐性を持つ細菌が報告された。その耐性メカニズムの一つに、SilEの(a periplasmic silver-binding protein)が挙げられており、そのモデル化合物としてFrommらは

2種類のカチオン性ヒスチジン銀(I)錯体を報告している (Fig. 8)。彼らはSilE中のヒスチジン残基が銀(I)イオンなどの重金属イオンに中性条件で配位し、細胞中の局所pH環境の変化によりそれらのイオン放出に参与している可能性を示した (Fig. 9)¹¹。

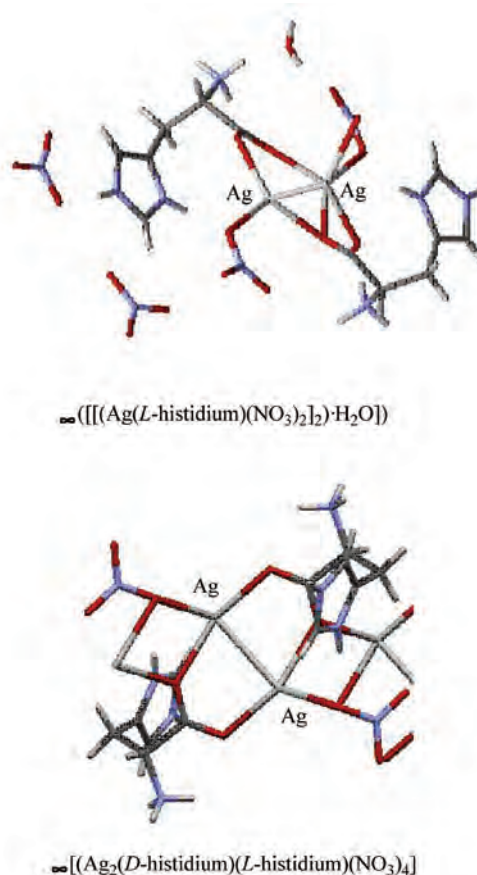


Fig. 8. Two cationic silver(I) complexes with histidine ligands¹¹.

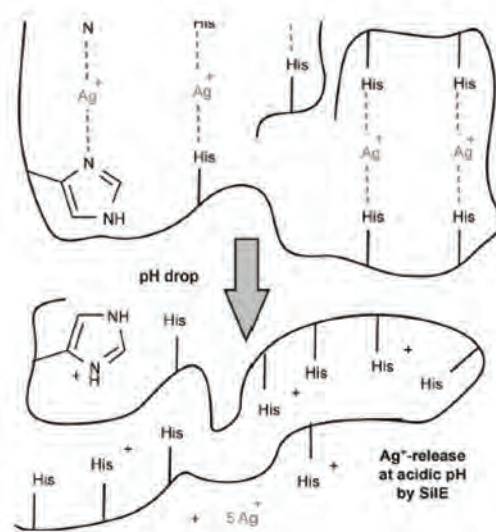


Fig. 9. Proposed mode of action of SilE by Fromm *et al.*¹¹

L-4を得た我々は、中性条件下に加えて、アニオン性条件下でも銀(I)イオンがペプチド、タンパク質のヒスチジン残基に取り込まれることを示した。塩基性アミノ酸であるアルギニンやリシンについても硝酸銀と反応させると、反応時のpHに依存して中性、カチオン性の銀(I)錯体を得られることもわかった。アルギニン銀(I)錯体の例をFig. 10に示す¹²⁾。耐性たんぱく質中で、ヒスチジン以外にアルギニン残基やリシン残基、またはそれらの組み合わせが金属イオン輸送等に関与している可能性がある。

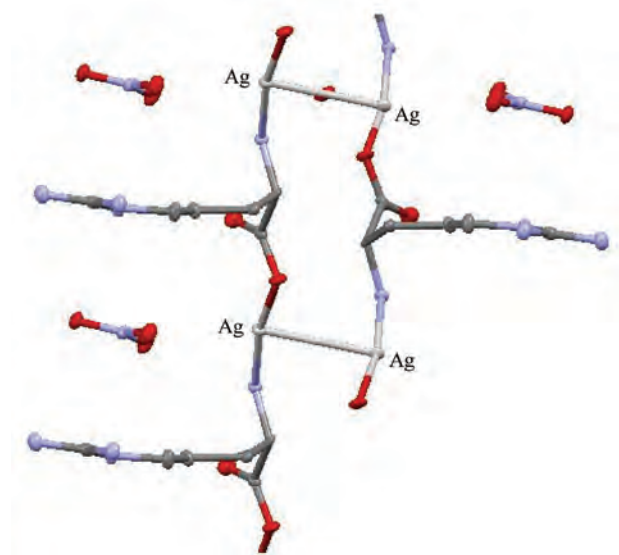


Fig. 10. Crystal structure of $\infty \{[Ag(L-Harg)](NO_3)_2 \cdot H_2O\} \cdot 12H_2O$.

ヒスチジン銀(I)錯体の抗菌活性

グラム陽性菌の枯草菌 (*B. subtilis*)、黄色ブドウ球菌 (*S. aureus*)、グラム陰性菌の大腸菌 (*E. coli*)、緑膿菌 (*P. aeruginosa*)、酵母 (*C. albicans*, *S. cerevisiae*)、カビ (*A. brasiliensis*, *P. citrinum*) に対する、各ヒスチジン銀(I)錯体の抗菌活性をMICにより評価した。結果をTable 1に示す。ヒスチジン、L-1, L-4は水溶液を菌液に加え、水に不溶のL-2, DL-3は懸濁液を菌液に加えて、最小発育阻止濃度を決めた。

Ag-N及びAg-O結合性銀(I)錯体としていずれも広いスペクトルの抗菌活性が見られた。水溶性銀(I)錯体L-1, L-4、不溶性のL-2, DL-3ともにグラム陽性、陰性菌、さらに酵母、カビに抗菌作用を示すことがわかる。水溶性の錯体はバクテリアに対する抗菌活性が不溶性の銀(I)錯体より強めであった。アルギニン銀(I)、リシン銀(I)錯体にもバクテリアに対する抗菌活性があった。チオール残基は銀イオンとの結合が強く放出が難しい。しかし塩基性アミノ酸ではAg-N結合が配位子交換やプロトンネーション可能であるため、輸送蛋白中に含まれる残基として適していると考えられる。

以上、ヒスチジンに加えアルギニン、リシンといった塩基性アミノ酸およびそれらの残基が銀(I)イオン耐性タンパク質に関与する可能性を示した。

Table 1. Antimicrobial activities of silver complexes with histidine ligand and related complexes evaluated by minimum inhibitory concentration (MIC; $\mu\text{g mL}^{-1}$)

| | L-H ₂ his ⁸ | L-1 ⁸ | L-2 ⁸ | DL-3 ⁹ | L-4 ⁹ | $\infty \{[Ag(L-Harg)](NO_3)_2 \cdot H_2O\} \cdot 12H_2O$ ¹² | $\infty \{[Ag(L-Hlys)](NO_3)_2\}$ |
|---|-----------------------------------|------------------|------------------|-------------------|------------------|---|-----------------------------------|
| <i>Escherichia coli</i> | >1000 | 15.7 | 125 | 125 | 31.3 | 125 | 15.7 |
| <i>Bacillus subtilis</i> | >1000 | 62.5 | 250 | 125 | 31.3 | 125 | 15.7 |
| <i>Staphylococcus aureus</i> | >1000 | 62.5 | 250 | 31.3 | 62.5 | 125 | 31.3 |
| <i>Pseudomonas aeruginosa</i> | >1000 | 15.7 | 250 | 125 | 15.7 | 62.5 | 7.9 |
| <i>Candida albicans</i> | >1000 | 15.7 | 125 | 125 | 500 | >1000 | 7.9 |
| <i>Saccharomyces cerevisiae</i> | >1000 | 15.7 | 125 | 31.3 | 62.5 | 125 | 15.7 |
| <i>Aspergillus brasiliensis (niger)</i> | >1000 | 125 | 250 | 250 | 250 | >1000 | 125 |
| <i>Penicillium citrinum</i> | >1000 | 500 | 250 | 1000 | 1000 | >1000 | >1000 |

謝辞

この研究は神奈川県総合化学研究所共同研究助成「塩基性アミノ酸（アルギニン、リシン）を配位子とするポリマー性銀(I)錯体の合成、構造解析及び抗菌活性」(RIIS201403)の援助を受けて行いました。ここに謝意を表します。

文献

- 1) Mjos KD and Orvig C (2014) Metallo drugs in medicinal inorganic chemistry *Chem. Rev.* **114**: 4540-4563.
- 2) 梶本哲也 (2008) クスリの化学 (31). *化学と教育* **56**: 518-519.
- 3) 特許庁 (2001) 抗菌性化合物とその応用.
- 4) Yamanaka M, Matsui N, Hara K and Kudo J (2006) Ag⁺ イオンによる抗菌防臭コート技術. *シャープ技報* **94**: 30-34.
- 5) Nomiya K, Kasuga NC and Takayama A (2014) Synthesis, structure and antimicrobial activities of polymeric and nonpolymeric silver and other metal complexes. In: *Polymeric Materials with Antimicrobial Activity From Synthesis to Applications*. Muñoz-Bonilla A, Cerrada M and Fernández-García M, eds., RSC, Cambridge, UK. pp. 156-207.
- 6) Nomiya K and Yokoyama H (2002) Synthesis, crystal structures and antimicrobial activities of polymeric silver(I) complexes with three aminoacids *J. Chem. Soc. Dalton Trans.* **2002**: 2483-2490.
- 7) Li S and Hong M (2011) Protonation, tautomerization, and rotameric structure of histidine: A comprehensive study of magic-angle-spinning solid-state NMR. *J. Am. Chem. Soc.* **133**: 1534-1544.
- 8) Nomiya K, Takahashi S, Noguchi R, Nemoto S, Takayama T and Oda M (2000) Synthesis and characterization of water-soluble silver(I) complexes with *L*-histidine (H₂his) and (*S*)-(-)-2-pyrrolidone-5-carboxylic acid (H₂pyrrld) showing a wide spectrum of effective antibacterial and antifungal activities. Crystal structures of chiral helical polymers [Ag(His)]_n and {(Ag(Hpyrrld))₂}_n in the solid state. *Inorg. Chem.* **39**: 3301-3311.
- 9) Kasuga NC, Takagi Y, Tsuruta S, Kuwana W, Yoshikawa R and Nomiya K (2011) Synthesis, structure and antimicrobial activities of meso silver(I) histidine [Ag₂(*D*-his)(*L*-his)]_n (H₂his=histidine) showing different self-assembly from those of chiral silver(I) histidines. *Inorg. Chem. Acta* **368**: 44-48.
- 10) Takayama A, Takagi Y, Yanagita K, Inoue C, Yoshikawa R, Kasuga NC and Nomiya K (2014) Synthesis, characterization and antimicrobial activities of sodium salt of *L*-histidinatoargentate(I) derived from the pH 11 solution. *Polyhedron* **80**:151-156.
- 11) Mirolo L, Schmidt T, Eckhardt S, Meuwly M and Fromm KM (2013) pH-Dependent coordination of AgI ions by histidine: Experiment, theory and a model for SilE. *Chem. Eur. J.* **19**: 1754-1761.
- 12) Takayama A, Yoshikawa R, Iyoku S, Kasuga CN and Nomiya K (2013) Synthesis, structure and antimicrobial activity of *L*-argininesilver(1⁺) nitrate. *Polyhedron* **52**: 844-847.